

S.R.-22 Smart Pavement: Response Characteristics of a Jointed Plain Concrete Pavement to Applied and Environmental Loads

Phase II Final Report



Prepared by:

Jennifer K. McCracken
Rania E. Asbahan
Julie M. Vandenbossche

University of Pittsburgh
Department of Civil and Environmental Engineering
Pittsburgh, Pennsylvania 15261

Prepared for:

Pennsylvania Department of Transportation,
Federal Highway Administration

February 2008

1. Report No. FHWA-PA-2008-007-22021-2B-013	2. Government Accession No.	3. Recipient's Catalog No.	
4. Title and Subtitle S.R.-22 Smart Pavement: Response Characteristics of a Jointed Plain Concrete Pavement to Applied and Environmental Loads – Phase II Final Report		5. Report Date February 2008	
		6. Performing Organization Code	
7. Author(s) J.K. McCracken, R.E. Asbahan and J. M. Vandenbossche		8. Performing Organization Report No.	
9. Performing Organization Name and Address University of Pittsburgh 3700 Ohara St. Pittsburgh, PA 15261		10. Work Unit No. (TRAIS)	
		11. Contract or Grant No.	
12. Sponsoring Agency Name and Address		13. Type of Report and Period Covered Phase II Final Report	
		14. Sponsoring Agency Code	
15. Supplementary Notes			
16. Abstract <p>The primary objective of this study is to develop tools used in the design and construction of more cost-effective concrete pavements. One of the project goals is to establish the inputs suitable for the Pennsylvania Department of Transportation to use in the new Guide for the Design of New and Rehabilitated Pavement Structures (MEPDG) (ver. 1.0) by establishing the following for the site conditions on SR 22 in Murrysville, Pennsylvania: concrete material properties; strength correlations; gradients that develop throughout the pavement structure; construction and seasonal curling and warping and pavement response under environmental and applied loads. A summary of the MEPDG inputs as well as the sensitivity of the performance prediction of the Smart Pavement to inputs defined using different hierarchical levels was provided. The measured temperature and moisture conditions throughout the pavement structure were compared to those predicted by the Enhanced Integrated Climatic Model, which is embedded in the MEPDG.</p> <p>The change in the shape of the slab as a result of seasonal gradients and was defined based on the static strain and pressure gage data and slab profile measurements. Dynamic strain data were collected in conjunction with known truck loads and axle configurations and falling weight deflectometer testing. While the sensor data was collected continuously every 15 minutes since the time of construction, field data measurements were made seasonally for the first three years after paving. Finally, a finite element model was developed and validated using strain measurements from the dynamic strain testing. Findings have been provided based on the first three years of measurements. A subsequent report will be published under Contract 510601/WO-003 that will discuss the stress generated by these applied loads. The stress determined using the validated finite element model will then be used to evaluate the performance prediction of the MEPDG based on the accumulated damage produced by the calculated stress.</p>			
17. Key Words Concrete, instrumentation, gradients, JPCP, curl, warp, applied loads		18. Distribution Statement	
19. Security Classif. (of this report) Unclassified	20. Security Classif. (of this page) Unclassified	21. No. of Pages 359	22. Price

ACKNOWLEDGEMENTS

The success of a project of this magnitude is not possible without the assistance and expertise of many individuals. First, the authors gratefully acknowledge the financial and technical support provided by the Pennsylvania Department of Transportation (PennDOT) and the Federal Highway Administration (FHWA).

The time and effort in assisting with the coordination of this research effort by Mr. Gary Barber of the PennDOT District 12 is also greatly appreciated. Mr. Barber's assistance was immeasurable and it was a great pleasure to work with him. The authors would also like to thank Mr. Patrick Richter of District 12 and Ms. Michelle Tarquino of Central Office for their assistance. The assistance of Mr. Vince Blair and Mr. Gary Mendola of Westmorland County Maintenance and the PennDOT Weigh Team out of District 12 with the field data collection was also very much appreciated. The field data collection effort takes a significant amount of coordination and resources. Their time and effort is greatly appreciated. The authors would also like to extend their gratitude to Mr. Michael Long, Mr. Rodney Urban, Mr. Calvin Heinel and Mr. Kirit Pandya of the PennDOT Central Office for providing falling weight deflectometer testing of the Smart Pavement each season for the last several years.

Finally, the authors would like to thank the many graduate and undergraduate students at the University of Pittsburgh who assisted with this research effort. The authors would also like to extend their sincere gratitude to Mr. Michael Dufalla (formerly of the PennDOT District 12) who provided vision that was critical in the development of the research objectives and persistence that was essential in turning this research idea into a funded project. Lastly, the authors would like to extend a sincere appreciation of gratitude to Mr. Joeseeph Szczur of the District 12 PennDOT Office for his continued support throughout this effort.

DISCLAIMER

The contents of the report reflect the views of the author who is responsible for the facts and accuracy of the data presented herein. The contents do not necessarily reflect the views or policies of the Pennsylvania Department of Transportation. This report does not constitute a standard, specification, or regulations.

TABLE OF CONTENTS

	<i>Page Number</i>
<i>List of Appendices</i>	<i>viii</i>
<i>List of Figures</i>	<i>ix</i>
<i>List of Tables</i>	<i>xlvi</i>
CHAPTER 1: INTRODUCTION.....	1
1.1.0 Primary Goals of the Smart Pavement Project.....	1
1.1.1 Goals Completed in Phase I	1
1.1.2 Goals Completed in Phase II	1
1.2.0. Project Location and Site Description.....	2
1.3.0. Layout of Test Sections	3
1.4.0. Pavement Design.....	6
1.5.0. Structure of the Report	7
CHAPTER 2: TEMPERATURE AND MOISTURE DATA ANALYSIS.....	9
2.1.0. Introduction.....	9
2.2.0. Ambient Climatic Conditions	9
2.3.0. Measured Temperature Conditions in the Pavement Structure.....	15
2.3.1. Temperature Instrumentation	15
2.3.2. Temperature Measurements within the Concrete Slabs	17
2.3.3. Temperature Measurements within the Underlying Layers.....	28
2.3.4. Summary	30
2.4.0. Measured Moisture Conditions in the Pavement Structure	30
2.4.1. Moisture Instrumentation.....	31
2.4.2. Moisture Measurements within the Concrete Slabs.....	34
2.4.3. Moisture Measurements within the Granular Layers.....	47
2.4.4. Summary	51
2.5.0. Conclusions	52

CHAPTER 3: DEFINING THE BUILT-IN CONSTRUCTION GRADIENT.....	53
3.1.0 Introduction.....	53
3.2.0 Early-Age Concrete Temperature and Moisture Conditions	55
3.3.0 Instrumentation of Static Sensors	60
3.4.0 Early-Age Strains within the JPCP Slab	61
3.4.1 Static Strain Gages	62
3.4.2 Restrained Slabs.....	63
3.4.3 Unrestrained Slabs.....	70
3.4.4 Comparison between Restrained and Unrestrained Slabs	77
3.4.5 Built-in Temperature Gradient based on Concrete Strain Measurements	78
3.5.0 Early-Age Pressure along the Slab/Base Interface	80
3.5.1 Static Pressure Cells.....	81
3.5.2 Restrained Slabs.....	83
3.5.3 Unrestrained Slabs.....	85
3.5.4 Built-in Temperature Gradient Based on Pressure Measurements	87
3.6.0 Built-in Construction Gradient	88
3.6.1 Set Time and Corresponding Built-in Temperature Gradient...	88
3.6.2 Built-in Moisture Gradient	90
3.7.0 Summary and Conclusions.....	90
 CHAPTER 4: INPUTS OF THE MECHANISTIC-EMPIRICAL DESIGN GUIDE	 92
4.1.0 Introduction.....	92
4.2.0 General Information and Pavement Design Inputs	93
4.3.0 Traffic Inputs	94
4.3.1 Traffic Volume Inputs	95
4.3.2 Traffic Volume Adjustment Factor Inputs.....	96
4.3.3 Axle Load Distribution Factor Inputs.....	99
4.3.4 General Traffic Inputs.....	101

4.4.0	<i>Environmental Inputs</i>	103
4.4.1	<i>Weather-Related Inputs</i>	104
4.4.2	<i>Ground Water Related Inputs</i>	105
4.4.2.1	<i>Groundwater Table Depth</i>	105
4.4.3	<i>Drainage and Surface Property Inputs</i>	105
4.4.3.1	<i>Surface Shortwave Absorptivity</i>	105
4.4.3.2	<i>Infiltration</i>	106
4.4.3.3	<i>Drainage Path Length</i>	106
4.4.4	<i>Pavement Structure Material Inputs</i>	106
4.4.4.1	<i>Asphalt Material Properties</i>	107
4.4.4.2	<i>Concrete Material Properties</i>	107
4.4.4.3	<i>Compacted Unbound Material Inputs</i>	108
4.5.0	<i>PCC Material Property Inputs</i>	110
4.5.1	<i>PCC Mix Component Inputs</i>	111
4.5.2	<i>PCC Modulus of Elasticity</i>	111
4.5.3	<i>Poisson's ratio of PCC Materials</i>	115
4.5.4	<i>PCC Flexural Strength</i>	115
4.5.5	<i>Unit Weight of PCC Materials</i>	118
4.5.6	<i>PCC Coefficient of Thermal Expansion</i>	118
4.5.7	<i>PCC Shrinkage</i>	120
4.5.7.1	<i>Time to develop 50 Percent of Ultimate Shrinkage</i>	122
4.5.7.2	<i>Anticipated Amount of Reversible Shrinkage</i>	123
4.6.0	<i>ATPB Material Property Inputs</i>	123
4.6.1	<i>General Asphalt Inputs</i>	123
4.6.2	<i>Asphalt Mix and Binder Inputs</i>	124
4.7.0	<i>Unbound Granular Materials and Subgrade Material Property Inputs</i>	125
4.8.0	<i>Predicted Temperature and Moisture Conditions in the Pavement Structure</i>	128
4.8.1	<i>Overview of the EICM</i>	128
4.8.2	<i>Climatic Databases</i>	130

4.8.3	<i>Temperature Predictions within the Concrete Slab.....</i>	135
4.8.4	<i>Temperature Predictions within the Underlying Layers</i>	145
4.8.5	<i>Moisture Predictions within the Granular Layers.....</i>	153
4.9.0	<i>Effect of the Hierarchical Levels on Pavement Performance.....</i>	157
4.9.1	<i>Performance of the Pavement with Restrained Slabs.....</i>	157
4.9.2	<i>Performance of the Pavement with Unrestrained Slabs.....</i>	160
4.9.3	<i>Effect of the Design Parameter Hierarchical Level on Performance.....</i>	163
4.9.3.1	<i>Effect of the Hierarchical Traffic Inputs on Performance Prediction.....</i>	163
4.9.3.2	<i>Effect of the Different Sources of Climatic Data on Performance Prediction.....</i>	164
4.9.3.3	<i>Effect of Hierarchical Level for Defining PCC Strength on Performance Prediction.....</i>	166
4.9.3.4	<i>Effect of Hierarchical Level for Defining PCC Coefficient of Thermal Expansion on Performance Prediction.....</i>	168
4.9.3.5	<i>Effect of Hierarchical Level for Defining Subgrade Resilient Modulus on Performance Prediction.....</i>	170
4.10.0	<i>Comparison between the Design Thickness of the Smart Pavement Based on the 1993 AASHTO Design Guide and the MEPDG.....</i>	171
4.11.0	<i>Conclusions</i>	172
 CHAPTER 5: PAVEMENT RESPONSE TO ENVIRONMENTAL LOADING ...		
5.1.0.	<i>Introduction</i>	175
5.2.0.	<i>Instrumentation of Static Sensors.....</i>	175
5.3.0.	<i>Static Strain Measurements</i>	176
5.3.1.	<i>Background</i>	176
5.3.2.	<i>Seasonal Static Strain Measurements</i>	177
5.3.3.	<i>Effect of the Slab Restraining Conditions</i>	184
5.3.4.	<i>Slab curvature</i>	190

5.3.5. Summary	192
5.4.0. Static Pressure Measurements	193
5.4.1. Seasonal Variations in Temperature and Pressure.....	194
5.4.2. Effect of Freezing of the Base Layer on Pressure.....	198
5.4.3. Effect of Temperature Gradients on Pressure.....	200
5.4.4. Summary	205
5.5.0. Concrete Surface Profile Measurements.....	205
5.5.1. Temperature and Moisture Conditions during Seasonal Dipstick Testing	208
5.5.2. Surface Profile Measurements for Restrained and Unrestrained Slabs	216
5.5.3. Slab Curvature	222
5.5.4. Corner Displacements.....	226
5.5.5. Summary.....	230
5.6.0. Effect of Moisture on Concrete Drying Shrinkage	231
5.6.1. Restrained Slabs.....	231
5.6.2. Unrestrained Slabs.....	235
5.6.3. Comparison between Restrained and Unrestrained Slabs.....	238
5.6.4. Summary.....	239
5.7.0. Conclusions.....	240
 CHAPTER 6: PAVEMENT RESPONSE TO APPLIED LOADS	 242
6.1.0 Introduction	242
6.2.0 Dynamic Sensor Locations.....	242
6.3.0 Falling Weight Deflectometer Testing.....	245
6.4.0 Concrete Temperature and Moisture Distributions during FWD Testing.....	247
6.4.1 Concrete Temperature Distributions	247
6.4.2 Concrete Moisture Distributions	256
6.5.0 Joint Performance	259
6.5.1 Effect of Temperature Gradients on Load Transfer Efficiency	262

6.5.2	<i>Relationship between Strain and Load Transfer Efficiency</i>	266
6.6.0	<i>Void Detection.....</i>	271
6.7.0	<i>Support Conditions</i>	278
6.8.0	<i>Deflections at Each Location</i>	283
6.9.0	<i>Truck Load Testing</i>	287
6.10.0	<i>Concrete Temperature and Moisture Distributions During Truck Testing.....</i>	290
6.10.1	<i>Concrete Temperature Distribution.....</i>	290
6.10.2	<i>Concrete Moisture Distribution.....</i>	306
6.11.0	<i>Comparison of Strains Measured at Different Locations within the Slab.....</i>	308
6.11.1	<i>Strain in the Restrained Slabs.....</i>	308
6.11.2	<i>Strain in the Unrestrained Slabs.....</i>	311
6.12.0	<i>Effect of Axle Configuration on Measured Strain.....</i>	313
6.13.0	<i>Effect of Axle Load Magnitude on Measured Strain.....</i>	318
6.14.0	<i>Dynamic Strains Measured at the Top and Bottom of the Slab</i>	320
6.14.1	<i>Strain at the Top and Bottom of the Restrained Slabs.....</i>	320
6.14.2	<i>Strain at the Top and Bottom of the Unrestrained Slabs.....</i>	322
6.15.0	<i>Effect of Slab Temperature and Gradients of Dynamic Strain</i>	323
6.16.0	<i>Conclusions.....</i>	327

CHAPTER 7: DEVELOPMENT AND VALIDATION OF FINITE ELEMENT

MODELS	329
7.1.0. Introduction.....	329
7.2.0. Model Inputs.....	329
7.2.1. <i>Mesh-Slab Model Inputs.....</i>	330
7.2.2. <i>Inputs for Modeling Slab Joints</i>	333
7.2.3. <i>Modeling the Loads Applied to the Pavement Structure.....</i>	334
7.3.0. Finite Element Model Validation	336
7.3.1. <i>Validation Using Group 1 Sensors (Adjacent to the Transverse Joint).....</i>	337

7.3.1.1. Validation of the Restrained Slabs Using Group 1 Sensors	337
7.3.1.2. Validation of the Unrestrained Slabs Using Group 1 Sensors	339
7.3.2. Validation Using Group 2 Sensors (Along the Lane/Shoulder Joint).....	341
7.3.2.1. Validation of the Restrained Slabs Using Group 2 Sensors	342
7.3.2.2. Validation of the Unrestrained Slabs Using Group 2 Sensors	344
7.3.3. Validation Using Group 3 Sensors (Midpanel).....	346
7.3.3.1. Validation of the Restrained Slabs Using Group 3 Sensors	346
7.3.3.2. Validation of the Unrestrained Slabs Using Group 3 Sensors	348
7.4.0. Conclusions.....	351
CHAPTER 8: SUMMARY OF FINDINGS	352
References	356

Appendices

<i>Appendix</i>	<i>Page Number</i>
<i>Appendix A: Temperature and Moisture Measurements</i>	<i>A-1</i>
<i>Appendix B: Early Age Vibrating Wire Gage Measurements</i>	<i>B-1</i>
<i>Appendix C: Design Inputs for the MEPDG.....</i>	<i>C-1</i>
<i>Appendix D: Vibrating Wire Gage Measurements</i>	<i>D-1</i>
<i>Appendix E: Surface Profile Measurements</i>	<i>E-1</i>
<i>Appendix F: Slab Curvature</i>	<i>F-1</i>
<i>Appendix G: Pavement Response to Applied Loads</i>	<i>G-1</i>

Figures

Figure Title	Page Number
Figure 1.1. Layout of the Smart Pavement section [1, 2].....	5
Figure 1.2. Design thicknesses of the pavement layers [1, 2].	6
Figure 2.1. Monthly maximum and minimum ambient temperature conditions over three years after construction of the pavement.	10
Figure 2.2. Monthly maximum and minimum ambient relative humidity the first three years after construction.....	11
Figure 2.3. Monthly maximum, minimum and average ambient wind speed over three years after construction of the pavement.	11
Figure 2.4. Monthly rainfall over the first three years after construction.	12
Figure 2.5. Frequency of occurrence of rain events and the monthly average precipitation per event between August 2004 and October 2007.	13
Figure 2.6. Location of temperature sensors in Cell 4.	15
Figure 2.7. Depth of thermocouple sensors.....	16
Figure 2.8. Weighted average temperature at slab midpanel during the three years following construction of the pavement.....	18
Figure 2.9. Monthly maximum and minimum ambient temperature and weighted average slab temperature.....	19
Figure 2.10. Midpanel concrete temperature for a one-week period representing the summer of 2004.	22
Figure 2.11. Midpanel concrete temperature for a one-week period representing the fall of 2004.	23
Figure 2.12. Midpanel concrete temperature for a one-week period representing the winter of 2005.....	23
Figure 2.13. Midpanel concrete temperature for a one-week period representing the spring of 2005.....	24
Figure 2.14. Edge concrete temperatures for a one-week period representing the summer 2004 season.....	25
Figure 2.15. Midpanel equivalent linear temperature gradients for one-week periods representing the summer.	26
Figure 2.16. Midpanel equivalent linear temperature gradients for one-week periods representing the fall.....	26
Figure 2.17. Midpanel equivalent linear temperature gradients for one-week periods representing the winter.....	27
Figure 2.18. Midpanel equivalent linear temperature gradients for one-week periods representing the spring.....	27
Figure 2.19. Asphalt temperatures at mid-depth variations with time.....	29
Figure 2.20. Variation of temperature within the 2A-subbase and subgrade layers. ...	30
Figure 2.21. Location of concrete moisture sensors in the restrained slabs (Cell 4)....	31
Figure 2.22. Depths of concrete moisture sensors in the restrained slabs (Cell 4).	31
Figure 2.23. Location of moisture sensors within the granular layers in Cell 4.....	32
Figure 2.24. Depths of moisture sensors within the granular layers in Cell 4.....	33

Figure 2.25. Concrete relative humidity at midpanel during the three years after construction of the pavement.....	35
Figure 2.26. Concrete relative humidity at slab edge during the three years after construction of the pavement.....	35
Figure 2.27. Monthly maximum and minimum concrete relative humidity at midpanel and slab edge in comparison to ambient relative humidity.....	36
Figure 2.28. Monthly maximum and minimum concrete relative humidity at midpanel and slab edge in comparison to monthly precipitation.	37
Figure 2.29. Monthly maximum and minimum concrete relative humidity at midpanel and slab edge in comparison to frequency of occurrence of daily rain events.	38
Figure 2.30. Midpanel concrete relative humidity for a ten-day period representing the summer 2004 season.....	39
Figure 2.31. Edge concrete relative humidity for a ten-day period representing the summer 2004 season.....	39
Figure 2.32. Midpanel concrete relative humidity for a ten-day period representing the fall 2004 season.	40
Figure 2.33. Edge concrete relative humidity for a ten-day period representing the fall 2004 season.	41
Figure 2.34. Midpanel concrete relative humidity for a ten-day period representing the winter 2005 season.	42
Figure 2.35. Edge concrete relative humidity for a ten -day period representing the winter 2005 season.	42
Figure 2.36. Midpanel concrete relative humidity for a ten -day period representing the spring 2005 season.	43
Figure 2.37. Edge concrete relative humidity for a ten -day period representing the spring 2005 season.	44
Figure 2.38. Midpanel concrete relative humidity for a ten-day period representing the summer 2005 season.....	45
Figure 2.39. Edge concrete relative humidity for a ten-day period representing the summer 2005 season.....	45
Figure 2.40. Seasonal average midpanel concrete relative humidity.	46
Figure 2.41. Seasonal average edge concrete relative humidity.....	47
Figure 2.42. Volumetric water content measured by midpanel sensor TD05 in the 2A-subbase at a depth of 19 inches.	48
Figure 2.43. Bulk soil conductivity recorded by midpanel sensor TD05 in the 2A-subbase at a depth of 19 inches.	49
Figure 2.44. Average monthly VWC measurements based on midpanel sensors TD05 to TD08.....	51
Figure 3.1. Early-age variation of temperatures in the concrete midpanel of the restrained slab.	55
Figure 3.2. Early-age variation in temperature gradients in the concrete slab.....	56
Figure 3.3. Early-age variation of concrete moisture in the restrained slab.	57
Figure 3.4. Location of static strain gages and static pressure cells in Cells 3 and 4.	61
Figure 3.5. Depth of static strain gages and static pressure cells in Cells 3 and 4.	61

Figure 3.6. Early-age variation in the total strain with temperature, in the longitudinal direction, for the top sensor located at midpanel of restrained Slab B.....	63
Figure 3.7. Early-age variation in the total strain with temperature, in the longitudinal direction, for the bottom sensor located at midpanel of restrained Slab B.....	64
Figure 3.8. Set times in the restrained slabs.....	66
Figure 3.9. Variation in average concrete set time with depth, for restrained slabs. ...	67
Figure 3.10. Average maturity at time of set for restrained slabs.....	69
Figure 3.11. Maturity at time of set with respect to sensor depth for restrained slabs.	69
Figure 3.12. Effect of restraining conditions on maturity at set time for restrained slabs.....	70
Figure 3.13. Early-age variation in the total strain with temperature, in the longitudinal direction, for the top sensor located at midpanel of unrestrained Slab B.....	71
Figure 3.14. Early-age variation in the total strain with temperature, in the longitudinal direction, for the bottom sensor located at midpanel of unrestrained Slab B.	72
Figure 3.15. Set times in the unrestrained slabs.....	72
Figure 3.16. Variation in average concrete set time with depth, for unrestrained slabs.	74
Figure 3.17. Average maturity at time of set for unrestrained slabs.....	76
Figure 3.18. Maturity at time of set with respect to sensor depth for unrestrained slabs.....	76
Figure 3.19. Effect of restraining conditions on maturity at set time for unrestrained slabs.....	77
Figure 3.20. Maturity at time of set with respect to depth for restrained and unrestrained slabs.	77
Figure 3.21. Effect of restraining conditions on maturity at set time for restrained and unrestrained slabs.	78
Figure 3.22. Range of temperature profiles at the time of set for the restrained and unrestrained slabs based on VW data.	79
Figure 3.23. Gradients at set time in restrained and unrestrained slabs.....	80
Figure 3.24. Early-age variation in pressure with time for the restrained slabs.	82
Figure 3.25. Early-age variation in pressure with time for the unrestrained slabs.	83
Figure 3.26. Early-age variation in pressure with changes in the temperature gradient for the corner of restrained Slab A.....	84
Figure 3.27. Early-age variation in pressure with changes in the temperature gradient for the midpanel of restrained Slab A.....	84
Figure 3.28. Early-age variation in pressure with changes in the temperature gradient for the midpanel of restrained Slab B.....	85
Figure 3.29. Early-age variation in pressure with changes in the temperature gradient for the corner of restrained Slab B.....	85
Figure 3.30. Early-age variation in pressure with changes in the temperature gradient for the corner of unrestrained Slab A.....	86
Figure 3.31. Early-age variation in pressure with changes in the temperature gradient for the midpanel of unrestrained Slab A.....	87

Figure 3.32. Early-age variation in pressure with changes in the temperature gradient for the midpanel of unrestrained Slab B.....	87
Figure 3.33. Temperature profiles at the time of set of the restrained and unrestrained slabs based on pressure measurements.....	88
Figure 4.1. PCC modulus of elasticity.....	112
Figure 4.2. PCC compressive strength.....	114
Figure 4.3. PCC modulus of rupture.....	117
Figure 4.4. PCC drying shrinkage during the first year after paving.....	121
Figure 4.5. Locations of the weather stations with respect to the site [22]	130
Figure 4.6. Measured hourly air temperatures for the different weather stations.....	132
Figure 4.7. Average measured hourly rainfall for the different weather stations.....	132
Figure 4.8 Maximum measured hourly rainfall for the different weather stations	133
Figure 4.9. Average measured hourly wind speed for the different weather stations.....	133
Figure 4.10. Maximum measured hourly wind speed for the different weather stations.....	134
Figure 4.11. Summary of average measured hourly percent sunshine for the different weather stations	135
Figure 4.12. Average measured hourly ambient relative humidity for the different weather stations.....	135
Figure 4.13. Predicted and measured monthly weighted average temperature.....	136
Figure 4.14. Predicted and measured seasonal weighted average temperature.....	137
Figure 4.15. Predicted versus measured weighted average temperature (Pittsburgh station).....	139
Figure 4.16. Residual versus measured weighted average temperature (Pittsburgh station).	140
Figure 4.17. Seasonal maximum positive equivalent linear temperature gradient based on the predicted and measured temperature.	141
Figure 4.18. Seasonal maximum negative equivalent linear temperature gradient based on the temperature predicted at 1-hour intervals and the temperature measured at 15-minute intervals.	141
Figure 4.19. Seasonal average equivalent linear temperature gradient based on the temperature predicted at 1-hour intervals and the temperature measured at 15-minute intervals.	142
Figure 4.20. Weighted average temperature based on predicted and measured temperatures over a three-year period.	143
Figure 4.21. Equivalent linear temperature gradient based on predicted and measured temperatures over a three-year period.	144
Figure 4.22. Average predicted and measured concrete temperature profiles during the summer.....	144
Figure 4.23. Average predicted and measured concrete temperature profiles during the fall.	145
Figure 4.24. Average predicted and measured concrete temperature profiles during the winter.....	145
Figure 4.25. Average predicted and measured concrete temperature profiles during the spring.....	146

Figure 4.26. Average seasonal predicted and measured temperatures at mid-depth of the ATPB.	147
Figure 4.27. Average seasonal predicted and measured temperatures at mid-depth of the subbase.	148
Figure 4.28. Average seasonal predicted fill temperatures (6-12 inches) and measured temperatures (6-24 inches) in the fill layer.	159
Figure 4.29. Average seasonal predicted and measured subgrade temperatures (0-24 inches).	150
Figure 4.30. Average seasonal temperature profiles within the underlying layers during the summer.	151
Figure 4.31. Average seasonal temperature profiles within the underlying layers during the fall.	151
Figure 4.32. Average seasonal temperature profiles within the underlying layers during the winter.	152
Figure 4.33. Average seasonal temperature profiles within the underlying layers during the spring.	153
Figure 4.34. Predicted volumetric water content within the granular layers based on climatic data from the Pittsburgh station.	154
Figure 4.35. Predicted VWC within the subbase.	155
Figure 4.36. Predicted and measured VWC within the subbase (Pittsburgh station).	156
Figure 4.37. Predicted and measured VWC within the fill (Pittsburgh station).	156
Figure 4.38. Predicted and measured VWC within the subgrade (Pittsburgh station).	157
Figure 4.39. Predicted faulting for the restrained slabs.	158
Figure 4.40. Predicted percent cracking in the restrained slabs.	159
Figure 4.41. IRI predicted for the pavement with restrained slabs.	159
Figure 4.42. Predicted percent cracking in the unrestrained slabs.	160
Figure 4.43. Predicted faulting for the unrestrained slabs.	161
Figure 4.44. Predicted IRI for the pavement with unrestrained slabs.	162
Figure 4.45. Percent cracking in the restrained slabs for Level 2 and Level 3 traffic inputs.	163
Figure 4.46. Predicted faulting in the unrestrained slabs for Level 2 and Level 3 traffic inputs.	164
Figure 4.47. Percent cracking in the restrained slabs for different sources of climatic data.	165
Figure 4.48. Faulting in the unrestrained slabs for different sources of climatic data.	166
Figure 4.49. Percent cracking in the restrained slabs for PCC strength defined using Level 1, 2 and 3 inputs.	167
Figure 4.50. Faulting in the unrestrained slabs for PCC strength defined using Level 1, 2 and 3 inputs.	167
Figure 4.51. Percent cracking in the restrained slabs for the PCC coefficient of thermal expansion defined using Level 1, 2 and 3 inputs.	169
Figure 4.52. Faulting in the unrestrained slabs for the PCC coefficient of thermal expansion defined using Level 1, 2 and 3 inputs.	169
Figure 4.53. Percent cracking in the restrained slabs for the subgrade resilient modulus defined using Level 1, 2 and 3 inputs.	170

<i>Figure 4.2. Predicted faulting in the unrestrained slabs for the subgrade resilient modulus defined using Level 1, 2 and 3 inputs.....</i>	<i>171</i>
<i>Figure 5.1. Strain in the longitudinal direction at midpanel at the top of the restrained slabs.....</i>	<i>178</i>
<i>Figure 5.2. Strain in the longitudinal direction at midpanel at the top of the unrestrained slabs.</i>	<i>179</i>
<i>Figure 5.3. Seasonal contributions of the various components to the development of total strain in the longitudinal direction at midpanel at the top of the restrained and unrestrained slabs.</i>	<i>180</i>
<i>Figure 5.4. Variation in strain with temperature, in the longitudinal direction at midpanel for top of restrained slabs.....</i>	<i>182</i>
<i>Figure 5.5. Variation in strain with temperature, in the longitudinal direction at midpanel for top of unrestrained slabs.....</i>	<i>182</i>
<i>Figure 5.6. Variation in strain with temperature, in the transverse direction along the transverse joints for top of unrestrained slabs.</i>	<i>184</i>
<i>Figure 5.7. Total strain at the top and bottom of the restrained and unrestrained slabs at midpanel in the longitudinal direction.</i>	<i>185</i>
<i>Figure 5.8. Temperature-induced strain at the top and bottom of the restrained and unrestrained slabs at midpanel in the longitudinal direction.</i>	<i>186</i>
<i>Figure 5.9. Strain due to moisture and other factors at the top and bottom of the restrained and unrestrained slabs at midpanel in the longitudinal direction.</i>	<i>187</i>
<i>Figure 5.10. Total strain at the top of the restrained and unrestrained slabs along the transverse joint in the transverse direction.</i>	<i>188</i>
<i>Figure 5.11. Total strain at the top of the restrained and unrestrained slabs along the centerline longitudinal joint in the longitudinal direction.</i>	<i>189</i>
<i>Figure 5.12. Total strain along the centerline longitudinal joints (longitudinal direction) and the transverse joints (transverse direction) at the top of the unrestrained slabs.....</i>	<i>190</i>
<i>Figure 5.13. Average curvature for the restrained slabs, based on the corner strain in the diagonal direction along the shoulder.....</i>	<i>191</i>
<i>Figure 5.14. Average curvature for the unrestrained slabs, based on the corner strain in the diagonal direction along the shoulder.</i>	<i>191</i>
<i>Figure 5.15. Variation in average curvature with equivalent linear temperature gradient for the restrained and unrestrained slabs (April 2006).</i>	<i>192</i>
<i>Figure 5.16. Temperatures recorded by pressure cell gauges throughout the first three years after construction.</i>	<i>194</i>
<i>Figure 5.17. Pressure measured at the edge at the slab-base interface for the restrained and unrestrained slabs (gages SP01).</i>	<i>196</i>
<i>Figure 5.18. Pressure measured at midslab at the slab-base interface for the restrained and unrestrained slabs (gages SP02).</i>	<i>196</i>
<i>Figure 5.19. Pressure measured at midslab at the slab-base interface for the restrained and unrestrained slabs (gages SP03).</i>	<i>197</i>
<i>Figure 5.20. Pressure measured at the edge at the slab-base interface for the restrained slab (gage SP04).....</i>	<i>197</i>

Figure 5.21. Pressure recorded at the slab edge for the unrestrained and restrained slabs during the freezing period of January 20 to February 6, 2005.....	198
Figure 5.22. Pressure recorded at midslab for the unrestrained and restrained slabs during the freezing period of January 20 to February 6, 2005.....	199
Figure 5.23. Pressure recorded at the slab edge for the unrestrained and restrained slabs during the freezing period of January 29 to February 19, 2007.....	200
Figure 5.24. Variation in pressure with equivalent linear gradient for the edge sensor SP01 of unrestrained Slab A, during the spring for the first three years after construction.	201
Figure 5.25. Variation in pressure with equivalent linear gradient for the midpanel sensor SP03 of unrestrained Slab B, during the spring for the first three years after construction.....	201
Figure 5.26. Variation in pressure with equivalent linear gradient for the midpanel sensor SP03 of restrained Slab B, during the spring for the first three years after construction.....	202
Figure 5.27. Variation in pressure with equivalent linear gradient for the edge sensor SP04 of restrained Slab B, during the spring for the first three years after construction.	202
Figure 5.28. Average pressure for each range of equivalent linear gradients for the unrestrained slabs (Cell 3).	203
Figure 5.29. Average pressure for each range of equivalent linear gradient for the sensors in the restrained slabs (Cell 4).	204
Figure 5.30. Surface profile measurements using the dipstick.....	206
Figure 5.31. Surface profile measurement paths along the concrete slabs [1].....	206
Figure 5.32. Midpanel weighted average concrete temperatures during dipstick testing.	209
Figure 5.33. Midpanel equivalent linear temperature gradients during dipstick testing.	210
Figure 5.34. Moisture content of the concrete at midslab during dipstick testing.	211
Figure 5.35. Moisture content of the concrete at the edge of the slab during dipstick testing.	211
Figure 5.36. Temperature difference equivalent to moisture warping during profile test dates.....	215
Figure 5.37. Measured and assumed slab moisture profiles during profile test dates for the third year after construction.	216
Figure 5.38. Restrained Slab C diagonal surface profiles for the winter of 2007.	217
Figure 5.39. Restrained Slab C diagonal surface profiles for the spring of 2007.	218
Figure 5.40. Restrained Slab C diagonal surface profiles for the summer of 2007....	218
Figure 5.41. Restrained Slab C diagonal surface profiles for the fall of 2007.	219
Figure 5.42. Unrestrained Slab A diagonal surface profiles for the winter of 2007...	220
Figure 5.43. Unrestrained Slab A diagonal surface profiles for the spring of 2007...	220
Figure 5.44. Unrestrained Slab A diagonal surface profiles for the summer of 2007.	221
Figure 5.45. Unrestrained Slab A diagonal surface profiles for the fall of 2007.....	221
Figure 5.46. Curvature versus equivalent linear gradient for the diagonal profile of restrained Slab C.	223

Figure 5.47. Curvature versus equivalent linear gradient for the diagonal profile of unrestrained Slab A.	224
Figure 5.48. Curvature versus equivalent linear gradient for the diagonal profiles of restrained and unrestrained slabs.	225
Figure 5.49. Plan showing the start point of the surface profiles in all directions [2].	226
Figure 5.50. Corner displacement versus equivalent linear gradient for the diagonal profiles of restrained Slab C.	228
Figure 5.51. Corner displacement versus equivalent linear gradient for the diagonal profiles of unrestrained Slab A.	229
Figure 5.52. Curvature estimated using surface profiles and vibrating wire gages for restrained Slab A during the winter of 2007.	232
Figure 5.53. Curvature estimated using surface profiles and vibrating wire gages for restrained Slab A during the spring of 2007.	232
Figure 5.54. Curvature estimated using surface profiles and vibrating wire gages for restrained Slab A during the summer of 2007.	233
Figure 5.55. Curvature estimated using surface profiles and vibrating wire gages for restrained Slab A during the fall of 2007.	233
Figure 5.56. Difference in slab curvature for the restrained slabs in the diagonal direction.	235
Figure 5.57. Curvature estimated using surface profiles and vibrating wire gages for unrestrained Slab A during the summer of 2007.	237
Figure 5.58. Curvature estimated using surface profiles and vibrating wire gages for unrestrained Slab A during the fall of 2007.	237
Figure 5.59. Difference in slab curvatures for the unrestrained slabs in the diagonal direction.	238
Figure 5.60. Comparison between the difference in corner curvatures for the restrained and unrestrained slabs in the diagonal direction.	239
Figure 6.1. Sensor layout for Cell 1 and Cell 2.	243
Figure 6.2. Typical dimensions of dynamic strain gages, and dynamic pressure cells.	244
Figure 6.3. Falling weight deflectometer used on S.R. 22.	245
Figure 6.4. FWD test locations.	246
Figure 6.5. Midpanel temperature conditions during FWD testing performed in the fall of 2004.	249
Figure 6.6. Midpanel temperature conditions during FWD testing performed in the fall of 2006.	249
Figure 6.7. Midpanel temperature conditions during FWD testing performed in the fall of 2007.	250
Figure 6.8. Midpanel temperature conditions during FWD testing performed in the winter of 2005.	251
Figure 6.9. Midpanel temperature conditions during FWD testing performed in the winter of 2006.	251
Figure 6.10. Midpanel temperature conditions during FWD testing performed in the winter of 2007.	252

<i>Figure 6.11. Midpanel temperature conditions during FWD testing performed in the spring of 2005.....</i>	<i>253</i>
<i>Figure 6.12. Midpanel temperature conditions during FWD testing performed in the spring of 2006.....</i>	<i>253</i>
<i>Figure 6.13. Midpanel temperature conditions during FWD testing performed in the spring of 2007.....</i>	<i>254</i>
<i>Figure 6.14. Midpanel temperature conditions during FWD testing performed in the summer of 2005.</i>	<i>255</i>
<i>Figure 6.15. Midpanel temperature conditions during FWD testing performed in the summer of 2006.</i>	<i>255</i>
<i>Figure 6.16. Midpanel temperature conditions during FWD testing performed in the summer of 2007.</i>	<i>256</i>
<i>Figure 6.17. Midpanel moisture distribution throughout the PCC slab during FWD testing.</i>	<i>257</i>
<i>Figure 6.18. Edge moisture distribution throughout the PCC slab during FWD testing.</i>	<i>257</i>
<i>Figure 6.19. Load transfer efficiencies measured for each cell.</i>	<i>260</i>
<i>Figure 6.20. Relationship between load transfer efficiency and equivalent linear temperature gradient of the unrestrained Cell 3.....</i>	<i>263</i>
<i>Figure 6.21. Relationship between load transfer efficiency and age of the pavement for the unrestrained Cell 3.</i>	<i>264</i>
<i>Figure 6.22. Relationship between load transfer efficiency and equivalent linear temperature gradient of the unrestrained Cell 2.....</i>	<i>265</i>
<i>Figure 6.23. Relationship between load transfer efficiency and equivalent linear temperature gradient of the restrained Cell 1.....</i>	<i>266</i>
<i>Figure 6.24. Relationship between load transfer efficiency and strain measured in the wheelpath on the bottom of the restrained slabs.</i>	<i>267</i>
<i>Figure 6.25. Relationship between load transfer efficiency and strain measured in the wheelpath 1 in from the surface of the restrained slabs.....</i>	<i>267</i>
<i>Figure 6.26. Relationship between load transfer efficiency and strain measured in the corner on the bottom of the restrained slabs.</i>	<i>268</i>
<i>Figure 6.27. Relationship between load transfer efficiency and strain measured in the corner 1 in from the surface of the restrained slabs.</i>	<i>268</i>
<i>Figure 6.28. Relationship between load transfer efficiency and strain measured in the wheelpath on the bottom of the unrestrained slabs.</i>	<i>270</i>
<i>Figure 6.29. Relationship between load transfer efficiency and strain measured in the wheelpath 1 in from the surface of the unrestrained slabs.....</i>	<i>270</i>
<i>Figure 6.30. Relationship between load transfer efficiency and strain measured in the corner on the bottom of the unrestrained slabs.....</i>	<i>271</i>
<i>Figure 6.31. Relationship between load transfer efficiency and strain measured in the corner 1 in from the surface of the unrestrained slabs.</i>	<i>271</i>
<i>Figure 6.32. Estimating the presence of a void using FWD data.....</i>	<i>272</i>
<i>Figure 6.33. Void parameters calculated along the Smart Pavement for each cell. ...</i>	<i>273</i>
<i>Figure 6.34. Relationship between the Void parameter and the equivalent linear temperature gradient present for unrestrained Slab A in Cell 2.....</i>	<i>275</i>

Figure 6.35. Relationship between the Void parameter and the equivalent linear temperature gradient present for unrestrained Slab B in Cell 3.....	276
Figure 6.36. Relationship between the Void parameter and the equivalent linear temperature gradient for restrained Slab B in Cell 1.....	277
Figure 6.37. The calculated k-value across the Smart Pavement.....	278
Figure 6.38. Average annual seasonal support conditions across the Smart Pavement.	279
Figure 6.39. The cumulative monthly precipitation measured since construction of the Smart Pavement.....	280
Figure 6.40. Comparison of the support conditions beneath the slab and the average temperature of the asphalt treated permeable base throughout testing.....	281
Figure 6.41. Comparison of the support conditions beneath the slab and the equivalent linear temperature gradient of the slab during testing for unrestrained Slab A in Cell 3.	282
Figure 6.42. Comparison of the support conditions beneath the slab and the equivalent linear temperature gradient of the slab during testing for restrained Slab A in Cell 1.	283
Figure 6.43. Deflections measured in the corner of each slab.....	284
Figure 6.44. Deflections measured along the lane/shoulder joint.....	285
Figure 6.45. Deflections measured at midpanel.....	286
Figure 6.46. Deflections measured in the wheelpath, adjacent to the transverse joint.	287
Figure 6.47. Axle configurations for truck testing.....	289
Figure 6.48. Verification of axle loads.....	290
Figure 6.49. Midpanel temperature conditions during Class 10 truck testing performed in the fall of 2004.....	292
Figure 6.50. Midpanel temperature conditions during Class 6 and 7 truck testing performed in the fall of 2004.....	293
Figure 6.51. Midpanel temperature conditions during Class 10 truck testing performed in the fall of 2005.....	293
Figure 6.52. Midpanel temperature conditions during Class 6 truck testing performed in the fall of 2005.....	294
Figure 6.53. Midpanel temperature conditions during Class 10 truck testing performed in the fall of 2006.....	294
Figure 6.54. Midpanel temperature conditions during Class 6 and 7 truck testing performed in the fall of 2006.....	295
Figure 6.55. Midpanel temperature conditions during Class 6, 7, and 10 truck testing performed in the fall of 2007.....	295
Figure 6.56. Midpanel temperature conditions during Class 10 truck testing performed in the winter of 2005.....	296
Figure 6.57. Midpanel temperature conditions during Class 6 and 7 truck testing performed in the winter of 2005.....	297
Figure 6.58. Midpanel temperature conditions during Class 10 truck testing performed in the winter of 2006.....	297
Figure 6.59. Midpanel temperature conditions during Class 6 and 7 truck testing performed in the winter of 2006.....	298

Figure 6.60. Midpanel temperature conditions during Class 10 truck testing performed in the winter of 2007.....	298
Figure 6.61. Midpanel temperature conditions during Class 6 and 7 truck testing performed in the winter of 2007.	299
Figure 6.62. Midpanel temperature conditions during Class 10 truck testing performed in the spring of 2005.....	300
Figure 6.63. Midpanel temperature conditions during Class 6 and 7 truck testing performed in the spring of 2005.	300
Figure 6.64. Midpanel temperature conditions during Class 10 truck testing performed in the spring of 2006.....	301
Figure 6.65. Midpanel temperature conditions during Class 6 and 7 truck testing performed in the spring of 2006.	301
Figure 6.66. Midpanel temperature conditions during Class 10 truck testing performed in the spring of 2007.....	302
Figure 6.67. Midpanel temperature conditions during Class 6 and 7 truck testing performed in the spring of 2007.	302
Figure 6.68. Midpanel temperature conditions during Class 10 truck testing performed in the summer of 2005.	303
Figure 6.69. Midpanel temperature conditions during Class 6 and 7 truck testing performed in the summer of 2005.....	304
Figure 6.70. Midpanel temperature conditions during Class 10 truck testing performed in the summer of 2006.	304
Figure 6.71. Midpanel temperature conditions during Class 6 and 7 truck testing performed in the summer of 2006.....	305
Figure 6.72. Midpanel temperature conditions during Class 6, 7, and 10 truck testing performed in the summer of 2007.....	305
Figure 6.73. Midpanel moisture distribution throughout the PCC slab during truck testing.	306
Figure 6.74. Edge moisture distribution throughout the PCC slab during Class 10 truck testing.	307
Figure 6.75. Average strains measured at various locations at the top of the restrained slabs during the first three years after construction.	309
Figure 6.76. Average strains measured at various locations at the bottom of the restrained slabs during the first three years after construction.	310
Figure 6.77. Average strains measured at various locations at the bottom of the unrestrained slabs during the first three years after construction.	313
Figure 6.78. Average normalized strains measured along the edge of the restrained and unrestrained slabs for the Class 6 truck with 25,000 lb axle loads.	314
Figure 6.79. Average normalized strains measured along the edge of the restrained and unrestrained slabs for the Class 7 truck with 25,000 lb axle loads.	315
Figure 6.80. Average normalized strains measured along the edge of the restrained and unrestrained slabs for the Class 10 truck with 25,000 lb axle loads.	316
Figure 6.81. Average normalized strains measured along the edge of the restrained and unrestrained slabs for the tandem axle of the Class 6 and 10 trucks.....	317
Figure 6.82. Average normalized strains measured along the edge of the restrained and unrestrained slabs for the tridem axle of the Class 7 and 10 trucks.	317

Figure 6.83. Strains measured along the edge for the critical axle of the Class 6 truck for various load levels.	318
Figure 6.84. Strains measured along the edge for the critical axle of the Class 7 truck for various load levels.	319
Figure 6.85. Strains measured along the edge in the unrestrained slabs for the critical axle of the Class 10 truck for various load levels.	319
Figure 6.86. Strains measured along the edge of the slabs for the critical axle of all the truck classes and load levels.	320
Figure 6.87. Strain measured at the top and bottom of the slab along the edge of the cell.	321
Figure 6.88. Strain measured at the top and bottom of the slab along the edge of the unrestrained cell.	323
Figure 6.89. Relationship between strains measured in the wheelpath at the top of the restrained slabs and slab temperature.	324
Figure 6.90. Relationship between strains measured in the corner at the top of the restrained slabs and slab temperature.	324
Figure 6.91. Relationship between strains measured in the wheelpath at the bottom of the unrestrained slabs and slab temperature.	325
Figure 6.92. Relationship between strains measured in the wheelpath at the top of the restrained slabs and the temperature gradient in the slab.	326
Figure 6.93. Relationship between strains measured in the wheelpath at the top of the unrestrained slabs and the temperature gradient in the slab.	327
Figure 7.1. Axle configuration and tire spacing of the Class 6 truck.	335
Figure 7.2. Axle configuration and tire spacing of the Class 7 truck.	335
Figure 7.3. Axle configuration and tire spacing of the Class 10 truck.	335
Figure 7.4. Dynamic strain sensor layout.	336
Figure 7.5. Validation results for the sensors located adjacent to the transverse joint in the restrained slabs for the Class 6 truck.	338
Figure 7.6. Validation results for the sensors located adjacent to the transverse joint in the restrained slabs for the Class 7 truck.	339
Figure 7.7. Validation results for the sensors located adjacent to the transverse joint in the restrained slabs for the Class 10 truck.	339
Figure 7.8. Validation results for the sensors located adjacent to the transverse joint in the unrestrained slabs for the Class 6 truck.	340
Figure 7.9. Validation results for the sensors located adjacent to the transverse joint in the unrestrained slabs for the Class 7 truck.	341
Figure 7.10. Validation results for the sensors located adjacent to the transverse joint in the unrestrained slabs for the Class 10 truck.	341
Figure 7.11. Validation results for the sensors located adjacent to lane/shoulder joint in the restrained slabs for the Class 6 truck.	343
Figure 7.12. Validation results for the sensors located adjacent to lane/shoulder joint in the restrained slabs for the Class 7 truck.	343
Figure 7.13. Validation results for the sensors located adjacent to lane/shoulder joint in the restrained slabs for the Class 10 truck.	344

Figure 7.14. Validation results for the sensors located adjacent to lane/shoulder joint in the unrestrained slabs for the Class 6 truck.	345
Figure 7.15. Validation results for the sensors located adjacent to lane/shoulder joint in the unrestrained slabs for the Class 7 truck.	345
Figure 7.16. Validation results for the sensors located adjacent to lane/shoulder joint in the unrestrained slabs for the Class 10 truck.	346
Figure 7.17. Validation results for the sensors at midpanel in the restrained slabs for the Class 6 truck.	347
Figure 7.18. Validation results for the sensors at midpanel in the restrained slabs for the Class 7 truck.	348
Figure 7.19. Validation results for the sensors at midpanel in the restrained slabs for the Class 10 truck.	348
Figure 7.20. Validation results for the sensors at midpanel in the unrestrained slabs for the Class 6 truck.	349
Figure 7.21. Validation results for the sensors at midpanel in the unrestrained slabs for the Class 7 truck.	350
Figure 7.22. Validation results for the sensors at midpanel in the unrestrained slabs for the Class 10 truck.	350
Figure A.1. Midpanel concrete temperature for a 1-week period representing the summer 2004 season.....	A-2
Figure A.2. Midpanel concrete temperature for a 1-week period representing the fall 2004 season.	A-2
Figure A.3. Midpanel concrete temperature for a 1-week period representing the winter 2005 season.	A-3
Figure A.4. Midpanel concrete temperature for a 1-week period representing the spring 2005 season.	A-3
Figure A.5. Midpanel concrete temperature for a 1-week period representing the summer 2005 season.....	A-4
Figure A.6. Midpanel concrete temperature for a 1-week period representing the fall 2005 season.	A-4
Figure A.7. Midpanel concrete temperature for a 1-week period representing the winter 2006 season.	A-5
Figure A.8. Midpanel concrete temperature for a 1-week period representing the spring 2006 season.	A-5
Figure A.9. Midpanel concrete temperature for a 1-week period representing the summer 2006 season.....	A-6
Figure A.10. Midpanel concrete temperature for a 1-week period representing the fall 2006 season.	A-6
Figure A.11. Midpanel concrete temperature for a 1-week period representing the winter 2007 season.	A-7
Figure A.12. Midpanel concrete temperature for a 1-week period representing the spring 2007 season.	A-7
Figure A.13. Midpanel concrete temperature for a 1-week period representing the summer 2007 season.....	A-8

Figure A.14. Midpanel concrete temperature for a 1-week period representing the fall 2007 season.	A-8
Figure A.15. Edge concrete temperature for a 1-week period representing the summer 2004 season.	A-9
Figure A.16. Edge concrete temperature for a 1-week period representing the fall 2004 season.	A-9
Figure A.17. Edge concrete temperature for a 1-week period representing the winter 2005 season.	A-10
Figure A.18. Edge concrete temperature for a 1-week period representing the spring 2005 season.	A-10
Figure A.19. Edge concrete temperature for a 1-week period representing the summer 2005 season.	A-11
Figure A.20. Edge concrete temperature for a 1-week period representing the fall 2005 season.	A-11
Figure A.21. Edge concrete temperature for a 1-week period representing the winter 2006 season.	A-12
Figure A.22. Edge concrete temperature for a 1-week period representing the spring 2006 season.	A-12
Figure A.23. Edge concrete temperature for a 1-week period representing the summer 2006 season.	A-13
Figure A.24. Edge concrete temperature for a 1-week period representing the fall 2006 season.	A-13
Figure A.25. Edge concrete temperature for a 1-week period representing the winter 2007 season.	A-14
Figure A.26. Edge concrete temperature for a 1-week period representing the spring 2007 season.	A-14
Figure A.27. Edge concrete temperature for a 1-week period representing the summer 2007 season.	A-15
Figure A.28. Edge concrete temperature for a 1-week period representing the fall 2007 season.	A-15
Figure A.29. Midpanel concrete moisture content for a 10-day period representing the fall 2005 season.	A-16
Figure A.30. Midpanel concrete moisture content for a 10-day period representing the winter 2006 season.	A-16
Figure A.31. Midpanel concrete moisture content for a 10-day period representing the spring 2006 season.	A-17
Figure A.32. Midpanel concrete moisture content for a 10-day period representing the summer 2006 season.	A-17
Figure A.33. Midpanel concrete moisture content for a 10-day period representing the fall 2006 season.	A-18
Figure A.34. Midpanel concrete moisture content for a 10-day period representing the winter 2007 season.	A-18
Figure A.35. Midpanel concrete moisture content for a 10-day period representing the spring 2007 season.	A-19
Figure A.36. Midpanel concrete moisture content for a 10-day period representing the summer 2007 season.	A-19

<i>Figure A.37. Midpanel concrete moisture content for a 10-day period representing the fall 2007 season.</i>	<i>A-20</i>
<i>Figure A.38. Edge concrete moisture content for a 10-day period representing the fall 2005 season.</i>	<i>A-20</i>
<i>Figure A.39. Edge concrete moisture content for a 10-day period representing the winter 2006 season.</i>	<i>A-21</i>
<i>Figure A.40. Edge concrete moisture content for a 10-day period representing the spring 2006 season.</i>	<i>A-21</i>
<i>Figure A.41. Edge concrete moisture content for a 10-day period representing the summer 2006 season.</i>	<i>A-22</i>
<i>Figure A.42. Edge concrete moisture content for a 10-day period representing the fall 2006 season.</i>	<i>A-22</i>
<i>Figure A.43. Edge concrete moisture content for a 10-day period representing the winter 2007 season.</i>	<i>A-23</i>
<i>Figure A.44. Edge concrete moisture content for a 10-day period representing the spring 2007 season.</i>	<i>A-23</i>
<i>Figure A.45. Edge concrete moisture content for a 10-day period representing the summer 2007 season.</i>	<i>A-24</i>
<i>Figure A.46. Volumetric water content measured by midpanel sensor TD06 in the fill material at a depth of 22 inches.</i>	<i>A-24</i>
<i>Figure A.47. Volumetric water content measured by midpanel sensor TD07 in the fill material at a depth of 36 inches.</i>	<i>A-25</i>
<i>Figure A.48. Volumetric water content measured by midpanel sensor TD08 in the subgrade at a depth of 48 inches.</i>	<i>A-25</i>
<i>Figure B.1. Variation of strain with temperature, in the longitudinal direction, for the top sensor located at the corner along the centerline joint in restrained Slab A.</i>	<i>B-2</i>
<i>Figure B.2. Variation of strain with temperature, in the longitudinal direction, for the middepth sensor located at the corner along the centerline joint in restrained Slab A.</i>	<i>B-2</i>
<i>Figure B.3. Variation of strain with temperature, in the longitudinal direction, for the bottom sensor located at the corner along the centerline joint in restrained Slab A.</i>	<i>B-3</i>
<i>Figure B.4. Variation of strain with temperature, in the diagonal direction, for the top sensor located at the corner along the centerline joint in restrained Slab A.</i>	<i>B-3</i>
<i>Figure B.5. Variation of strain with temperature, in the diagonal direction, for the bottom sensor located at the corner along the centerline joint in restrained Slab A.</i>	<i>B-4</i>
<i>Figure B.6. Variation of strain with temperature, in the transverse direction, for the top sensor located at the corner along the centerline joint in restrained Slab A.</i>	<i>B-4</i>
<i>Figure B.7. Variation of strain with temperature, in the transverse direction, for the middepth sensor located at the corner along the centerline joint in restrained Slab A.</i>	<i>B-5</i>

Figure B.8. Variation of strain with temperature, in the transverse direction, for the bottom sensor located at the corner along the centerline joint in restrained Slab A.	B-5
Figure B.9. Variation of strain with temperature, in the longitudinal direction, for the top sensor located along the centerline joint in restrained Slab A.	B-6
Figure B.10. Variation of strain with temperature, in the longitudinal direction, for the bottom sensor located along the centerline joint in restrained Slab A.	B-6
Figure B.11. Variation of strain with temperature, in the longitudinal direction, for the top sensor located at midpanel in restrained Slab A.	B-7
Figure B.12. Variation of strain with temperature, in the longitudinal direction, for the bottom sensor located at midpanel in restrained Slab A.	B-7
Figure B.13. Variation of strain with temperature, in the longitudinal direction, for the top sensor located along the lane/shoulder joint in restrained Slab A.	B-8
Figure B.14. Variation of strain with temperature, in the longitudinal direction, for the bottom sensor located along the lane/shoulder joint in restrained Slab A.	B-8
Figure B.15. Variation of strain with temperature, in the transverse direction, for the top sensor located along the transverse joint in restrained Slab A.	B-9
Figure B.16. Variation of strain with temperature, in the transverse direction, for the bottom sensor located along the transverse joint in restrained Slab A.	B-9
Figure B.17. Variation of strain with temperature, in the longitudinal direction, for the top sensor located at the corner along the lane/shoulder joint in restrained Slab A.	B-10
Figure B.18. Variation of strain with temperature, in the longitudinal direction, for the middepth sensor located at the corner along the lane/shoulder joint in restrained Slab A.	B-10
Figure B.19. Variation of strain with temperature, in the longitudinal direction, for the bottom sensor located at the corner along the lane/shoulder joint in restrained Slab A.	B-11
Figure B.20. Variation of strain with temperature, in the diagonal direction, for the top sensor located at the corner along the lane/shoulder joint in restrained Slab A.	B-11
Figure B.21. Variation of strain with temperature, in the diagonal direction, for the bottom sensor located at the corner along the lane/shoulder joint in restrained Slab A.	B-12
Figure B.22. Variation of strain with temperature, in the transverse direction, for the top sensor located at the corner along the lane/shoulder joint in restrained Slab A.	B-12
Figure B.23. Variation of strain with temperature, in the transverse direction, for the middepth sensor located at the corner along the lane/shoulder joint in restrained Slab A.	B-13
Figure B.24. Variation of strain with temperature, in the transverse direction, for the bottom sensor located at the corner along the lane/shoulder joint in restrained Slab A.	B-13
Figure B.25. Variation of strain with temperature, in the longitudinal direction, for the top sensor located at the corner along the centerline joint in restrained Slab B.	B-14

Figure B.26. Variation of strain with temperature, in the longitudinal direction, for the middepth sensor located at the corner along the centerline joint in restrained Slab B.	B-14
Figure B.27. Variation of strain with temperature, in the diagonal direction, for the top sensor located at the corner along the centerline joint in restrained Slab B.	B-15
Figure B.28. Variation of strain with temperature, in the diagonal direction, for the middepth sensor located at the corner along the centerline joint in restrained Slab B.	B-15
Figure B.29. Variation of strain with temperature, in the diagonal direction, for the bottom sensor located at the corner along the centerline joint in restrained Slab B.	B-16
Figure B.30. Variation of strain with temperature, in the transverse direction, for the top sensor located at the corner along the centerline joint in restrained Slab B.	B-16
Figure B.31. Variation of strain with temperature, in the transverse direction, for the middepth sensor located at the corner along the centerline joint in restrained Slab B.	B-17
Figure B.32. Variation of strain with temperature, in the transverse direction, for the bottom sensor located at the corner along the centerline joint in restrained Slab B.	B-17
Figure B.33. Variation of strain with temperature, in the longitudinal direction, for the top sensor located along the centerline joint in restrained Slab B.	B-18
Figure B.34. Variation of strain with temperature, in the longitudinal direction, for the bottom sensor located along the centerline joint in restrained Slab B.	B-18
Figure B.35. Variation of strain with temperature, in the longitudinal direction, for the top sensor located at midpanel in restrained Slab B.	B-19
Figure B.36. Variation of strain with temperature, in the longitudinal direction, for the bottom sensor located at midpanel in restrained Slab B.	B-19
Figure B.37. Variation of strain with temperature, in the longitudinal direction, for the top sensor located along the lane/shoulder joint in restrained Slab B.	B-20
Figure B.38. Variation of strain with temperature, in the longitudinal direction, for the bottom sensor located along the lane/shoulder joint in restrained Slab B. ..	B-20
Figure B.39. Variation of strain with temperature, in the transverse direction, for the top sensor located along the transverse joint in restrained Slab B.	B-21
Figure B.40. Variation of strain with temperature, in the transverse direction, for the bottom sensor located along the transverse joint in restrained Slab B.	B-21
Figure B.41. Variation of strain with temperature, in the longitudinal direction, for the top sensor located at the corner along the lane/shoulder joint in restrained Slab B.	B-22
Figure B.42. Variation of strain with temperature, in the longitudinal direction, for the middepth sensor located at the corner along the lane/shoulder joint in restrained Slab B.	B-22
Figure B.43. Variation of strain with temperature, in the longitudinal direction, for the bottom sensor located at the corner along the lane/shoulder joint in restrained Slab B.	B-23

Figure B.44. Variation of strain with temperature, in the diagonal direction, for the top sensor located at the corner along the lane/shoulder joint in restrained Slab B.	B-23
Figure B.45. Variation of strain with temperature, in the diagonal direction, for the middepth sensor located at the corner along the lane/shoulder joint in restrained Slab B.	B-24
Figure B.46. Variation of strain with temperature, in the diagonal direction, for the bottom sensor located at the corner along the lane/shoulder joint in restrained Slab B.	B-24
Figure B.47. Variation of strain with temperature, in the transverse direction, for the top sensor located at the corner along the lane/shoulder joint in restrained Slab B.	B-25
Figure B.48. Variation of strain with temperature, in the transverse direction, for the middepth sensor located at the corner along the lane/shoulder joint in restrained Slab B.	B-25
Figure B.49. Variation of strain with temperature, in the transverse direction, for the bottom sensor located at the corner along the lane/shoulder joint in restrained Slab B.	B-26
Figure B.50. Variation of strain with temperature, in the longitudinal direction, for the top sensor located at the corner along the centerline joint in restrained Slab C.	B-26
Figure B.51. Variation of strain with temperature, in the diagonal direction, for the top sensor located at the corner along the centerline joint in restrained Slab C.	B-27
Figure B.52. Variation of strain with temperature, in the diagonal direction, for the middepth sensor located at the corner along the centerline joint in restrained Slab C.	B-27
Figure B.53. Variation of strain with temperature, in the diagonal direction, for the bottom sensor located at the corner along the centerline joint in restrained Slab C.	B-28
Figure B.54. Variation of strain with temperature, in the transverse direction, for the top sensor located at the corner along the centerline joint in restrained Slab C.	B-28
Figure B.55. Variation of strain with temperature, in the transverse direction, for the middepth sensor located at the corner along the centerline joint in restrained Slab C.	B-29
Figure B.56. Variation of strain with temperature, in the transverse direction, for the bottom sensor located at the corner along the centerline joint in restrained Slab C.	B-29
Figure B.57. Variation of strain with temperature, in the longitudinal direction, for the top sensor located along the centerline joint in restrained Slab C.	B-30
Figure B.58. Variation of strain with temperature, in the longitudinal direction, for the bottom sensor located along the centerline joint in restrained Slab C.	B-30
Figure B.59. Variation of strain with temperature, in the longitudinal direction, for the top sensor located at midpanel in restrained Slab C.	B-31

Figure B.60. Variation of strain with temperature, in the longitudinal direction, for the bottom sensor located at midpanel in restrained Slab C.	B-31
Figure B.61. Variation of strain with temperature, in the longitudinal direction, for the top sensor located along the lane/shoulder joint in restrained Slab C.	B-32
Figure B.62. Variation of strain with temperature, in the longitudinal direction, for the bottom sensor located along the lane/shoulder joint in restrained Slab C. ..	B-32
Figure B.63. Variation of strain with temperature, in the transverse direction, for the top sensor located along the transverse joint in restrained Slab C.	B-33
Figure B.64. Variation of strain with temperature, in the transverse direction, for the bottom sensor located along the transverse joint in restrained Slab C.	B-33
Figure B.65. Variation of strain with temperature, in the longitudinal direction, for the top sensor located at the corner along the lane/shoulder joint in restrained Slab C.	B-34
Figure B.66. Variation of strain with temperature, in the longitudinal direction, for the middepth sensor located at the corner along the lane/shoulder joint in restrained Slab C.	B-34
Figure B.67. Variation of strain with temperature, in the longitudinal direction, for the bottom sensor located at the corner along the lane/shoulder joint in restrained Slab C.	B-35
Figure B.68. Variation of strain with temperature, in the diagonal direction, for the top sensor located at the corner along the lane/shoulder joint in restrained Slab C.	B-35
Figure B.69. Variation of strain with temperature, in the diagonal direction, for the middepth sensor located at the corner along the lane/shoulder joint in restrained Slab C.	B-36
Figure B.70. Variation of strain with temperature, in the diagonal direction, for the bottom sensor located at the corner along the lane/shoulder joint in restrained Slab C.	B-36
Figure B.71. Variation of strain with temperature, in the transverse direction, for the top sensor located at the corner along the lane/shoulder joint in restrained Slab C.	B-37
Figure B.72. Variation of strain with temperature, in the transverse direction, for the middepth sensor located at the corner along the lane/shoulder joint in restrained Slab C.	B-37
Figure B.73. Variation of strain with temperature, in the transverse direction, for the bottom sensor located at the corner along the lane/shoulder joint in restrained Slab C.	B-38
Figure B.74. Variation of strain with temperature, in the longitudinal direction, for the top sensor located at the corner along the centerline joint in unrestrained Slab A.	B-38
Figure B.75. Variation of strain with temperature, in the longitudinal direction, for the middepth sensor located at the corner along the centerline joint in unrestrained Slab A.	B-39
Figure B.76. Variation of strain with temperature, in the longitudinal direction, for the bottom sensor located at the corner along the centerline joint in unrestrained Slab A.	B-39

Figure B.77. Variation of strain with temperature, in the diagonal direction, for the top sensor located at the corner along the centerline joint in unrestrained Slab A.	B-40
Figure B.78. Variation of strain with temperature, in the diagonal direction, for the middepth sensor located at the corner along the centerline joint in unrestrained Slab A.	B-40
Figure B.79. Variation of strain with temperature, in the diagonal direction, for the bottom sensor located at the corner along the centerline joint in unrestrained Slab A.	B-41
Figure B.80. Variation of strain with temperature, in the transverse direction, for the top sensor located at the corner along the centerline joint in unrestrained Slab A.	B-41
Figure B.81. Variation of strain with temperature, in the transverse direction, for the bottom sensor located at the corner along the centerline joint in unrestrained Slab A.	B-42
Figure B.82. Variation of strain with temperature, in the longitudinal direction, for the top sensor located along the centerline joint in unrestrained Slab A.	B-42
Figure B.83. Variation of strain with temperature, in the longitudinal direction, for the bottom sensor located along the centerline joint in unrestrained Slab A.	B-43
Figure B.84. Variation of strain with temperature, in the longitudinal direction, for the top sensor located at midpanel in unrestrained Slab A.	B-43
Figure B.85. Variation of strain with temperature, in the longitudinal direction, for the bottom sensor located at midpanel in unrestrained Slab A.	B-44
Figure B.86. Variation of strain with temperature, in the longitudinal direction, for the top sensor located along the lane/shoulder joint in unrestrained Slab A.	B-44
Figure B.87. Variation of strain with temperature, in the longitudinal direction, for the bottom sensor located along the lane/shoulder joint in unrestrained Slab A.	B-45
Figure B.88. Variation of strain with temperature, in the transverse direction, for the top sensor located along the transverse joint in unrestrained Slab A.	B-45
Figure B.89. Variation of strain with temperature, in the transverse direction, for the bottom sensor located along the transverse joint in unrestrained Slab A.	B-46
Figure B.90. Variation of strain with temperature, in the longitudinal direction, for the top sensor located at the corner along the lane/shoulder joint in unrestrained Slab A.	B-46
Figure B.91. Variation of strain with temperature, in the longitudinal direction, for the middepth sensor located at the corner along the lane/shoulder joint in unrestrained Slab A.	B-47
Figure B.92. Variation of strain with temperature, in the longitudinal direction, for the bottom sensor located at the corner along the lane/shoulder joint in unrestrained Slab A.	B-47
Figure B.93. Variation of strain with temperature, in the diagonal direction, for the top sensor located at the corner along the lane/shoulder joint in unrestrained Slab A.	B-48

Figure B.94. Variation of strain with temperature, in the diagonal direction, for the bottom sensor located at the corner along the lane/shoulder joint in unrestrained Slab A.	B-48
Figure B.95. Variation of strain with temperature, in the transverse direction, for the top sensor located at the corner along the lane/shoulder joint in unrestrained Slab A.	B-49
Figure B.96. Variation of strain with temperature, in the transverse direction, for the middepth sensor located at the corner along the lane/shoulder joint in unrestrained Slab A.	B-49
Figure B.97. Variation of strain with temperature, in the transverse direction, for the bottom sensor located at the corner along the lane/shoulder joint in unrestrained Slab A.	B-50
Figure B.98. Variation of strain with temperature, in the longitudinal direction, for the top sensor located at the corner along the centerline joint in unrestrained Slab B.	B-50
Figure B.99. Variation of strain with temperature, in the longitudinal direction, for the middepth sensor located at the corner along the centerline joint in unrestrained Slab B.	B-51
Figure B.100. Variation of strain with temperature, in the diagonal direction, for the top sensor located at the corner along the centerline joint in unrestrained Slab B.	B-51
Figure B.101. Variation of strain with temperature, in the diagonal direction, for the middepth sensor located at the corner along the centerline joint in unrestrained Slab B.	B-52
Figure B.102. Variation of strain with temperature, in the diagonal direction, for the bottom sensor located at the corner along the centerline joint in unrestrained Slab B.	B-52
Figure B.103. Variation of strain with temperature, in the transverse direction, for the top sensor located at the corner along the centerline joint in unrestrained Slab B.	B-53
Figure B.104. Variation of strain with temperature, in the transverse direction, for the middepth sensor located at the corner along the centerline joint in unrestrained Slab B.	B-53
Figure B.105. Variation of strain with temperature, in the transverse direction, for the bottom sensor located at the corner along the centerline joint in unrestrained Slab B.	B-54
Figure B.106. Variation of strain with temperature, in the longitudinal direction, for the top sensor located along the centerline joint in unrestrained Slab B.	B-54
Figure B.107. Variation of strain with temperature, in the longitudinal direction, for the bottom sensor located along the centerline joint in unrestrained Slab B.	B-55
Figure B.108. Variation of strain with temperature, in the longitudinal direction, for the top sensor located at midpanel in unrestrained Slab B.	B-55
Figure B.109. Variation of strain with temperature, in the longitudinal direction, for the bottom sensor located at midpanel in unrestrained Slab B.	B-56
Figure B.110. Variation of strain with temperature, in the longitudinal direction, for the top sensor located along the lane/shoulder joint in unrestrained Slab B.	B-56

Figure B.111. Variation of strain with temperature, in the longitudinal direction, for the bottom sensor located along the lane/shoulder joint in unrestrained Slab B.	B-57
Figure B.112. Variation of strain with temperature, in the transverse direction, for the top sensor located along the transverse joint in unrestrained Slab B.	B-57
Figure B.113. Variation of strain with temperature, in the transverse direction, for the bottom sensor located along the transverse joint in unrestrained Slab B.	B-58
Figure B.114. Variation of strain with temperature, in the longitudinal direction, for the top sensor located at the corner along the lane/shoulder joint in unrestrained Slab B.	B-58
Figure B.115. Variation of strain with temperature, in the longitudinal direction, for the middepth sensor located at the corner along the lane/shoulder joint in unrestrained Slab B.	B-59
Figure B.116. Variation of strain with temperature, in the longitudinal direction, for the bottom sensor located at the corner along the lane/shoulder joint in unrestrained Slab B.	B-59
Figure B.117. Variation of strain with temperature, in the diagonal direction, for the top sensor located at the corner along the lane/shoulder joint in unrestrained Slab B.	B-60
Figure B.118. Variation of strain with temperature, in the diagonal direction, for the middepth sensor located at the corner along the lane/shoulder joint in unrestrained Slab B.	B-60
Figure B.119. Variation of strain with temperature, in the diagonal direction, for the bottom sensor located at the corner along the lane/shoulder joint in unrestrained Slab B.	B-61
Figure B.120. Variation of strain with temperature, in the transverse direction, for the top sensor located at the corner along the lane/shoulder joint in unrestrained Slab B.	B-61
Figure B.121. Variation of strain with temperature, in the transverse direction, for the middepth sensor located at the corner along the lane/shoulder joint in unrestrained Slab B.	B-62
Figure B.122. Variation of strain with temperature, in the transverse direction, for the bottom sensor located at the corner along the lane/shoulder joint in unrestrained Slab B.	B-62
Figure B.123. Variation of strain with temperature, in the longitudinal direction, for the top sensor located at the corner along the centerline joint in unrestrained Slab C.	B-63
Figure B.124. Variation of strain with temperature, in the longitudinal direction, for the middepth sensor located at the corner along the centerline joint in unrestrained Slab C.	B-63
Figure B.125. Variation of strain with temperature, in the longitudinal direction, for the bottom sensor located at the corner along the centerline joint in unrestrained Slab C.	B-64
Figure B.126. Variation of strain with temperature, in the diagonal direction, for the top sensor located at the corner along the centerline joint in unrestrained Slab C.	B-64

Figure B.127. Variation of strain with temperature, in the diagonal direction, for the middepth sensor located at the corner along the centerline joint in unrestrained Slab C.	B-65
Figure B.128. Variation of strain with temperature, in the diagonal direction, for the bottom sensor located at the corner along the centerline joint in unrestrained Slab C.	B-65
Figure B.129. Variation of strain with temperature, in the transverse direction, for the top sensor located at the corner along the centerline joint in unrestrained Slab C.	B-66
Figure B.130. Variation of strain with temperature, in the transverse direction, for the bottom sensor located at the corner along the centerline joint in unrestrained Slab C.	B-66
Figure B.131. Variation of strain with temperature, in the longitudinal direction, for the top sensor located along the centerline joint in unrestrained Slab C.	B-67
Figure B.132. Variation of strain with temperature, in the longitudinal direction, for the bottom sensor located along the centerline joint in unrestrained Slab C.	B-67
Figure B.133. Variation of strain with temperature, in the longitudinal direction, for the top sensor located at midpanel in unrestrained Slab C.	B-68
Figure B.134. Variation of strain with temperature, in the longitudinal direction, for the bottom sensor located at midpanel in unrestrained Slab C.	B-68
Figure B.135. Variation of strain with temperature, in the longitudinal direction, for the top sensor located along the lane/shoulder joint in unrestrained Slab C.	B-69
Figure B.136. Variation of strain with temperature, in the transverse direction, for the top sensor located along the transverse joint in unrestrained Slab C.	B-69
Figure B.137. Variation of strain with temperature, in the transverse direction, for the bottom sensor located along the transverse joint in unrestrained Slab C. ...	B-70
Figure B.138. Variation of strain with temperature, in the longitudinal direction, for the top sensor located at the corner along the lane/shoulder joint in unrestrained Slab C.	B-70
Figure B.139. Variation of strain with temperature, in the longitudinal direction, for the middepth sensor located at the corner along the lane/shoulder joint in unrestrained Slab C.	B-71
Figure B.140. Variation of strain with temperature, in the longitudinal direction, for the bottom sensor located at the corner along the lane/shoulder joint in unrestrained Slab C.	B-71
Figure B.141. Variation of strain with temperature, in the diagonal direction, for the top sensor located at the corner along the lane/shoulder joint in unrestrained Slab C.	B-72
Figure B.142. Variation of strain with temperature, in the diagonal direction, for the middepth sensor located at the corner along the lane/shoulder joint in unrestrained Slab C.	B-72
Figure B.143. Variation of strain with temperature, in the diagonal direction, for the bottom sensor located at the corner along the lane/shoulder joint in unrestrained Slab C.	B-73

Figure B.144. Variation of strain with temperature, in the transverse direction, for the top sensor located at the corner along the lane/shoulder joint in unrestrained Slab C.	B-73
Figure B.145. Variation of strain with temperature, in the transverse direction, for the middepth sensor located at the corner along the lane/shoulder joint in unrestrained Slab C.	B-74
Figure B.146. Variation of strain with temperature, in the transverse direction, for the bottom sensor located at the corner along the lane/shoulder joint in unrestrained Slab C.	B-74
Figure D.1. Strains in the longitudinal direction at midpanel at the top of the restrained slabs.	D-2
Figure D.2. Strains in the longitudinal direction at midpanel at the bottom of the restrained slab.	D-2
Figure D.3. Strains in the longitudinal direction along the lane/shoulder joint at the top of the restrained slabs.	D-3
Figure D.4. Strains in the longitudinal direction along the lane/shoulder joint at the bottom of the restrained slabs.	D-3
Figure D.5. Strains in the longitudinal direction along the centerline joint at the top of the restrained slabs.	D-4
Figure D.6. Strains in the longitudinal direction along the centerline joint at the bottom of the restrained slabs.	D-4
Figure D.7. Strains in the transverse direction along the transverse joint at the top of the restrained slabs.	D-5
Figure D.8. Strains in the transverse direction along the transverse joint at the bottom of the restrained slabs.	D-5
Figure D.9. Strains in the longitudinal direction at the corner along the centerline joint at the top of the restrained slabs.	D-6
Figure D.10. Strains in the longitudinal direction at the corner along the centerline joint at the middepth of the restrained slabs.	D-6
Figure D.11. Strains in the longitudinal direction at the corner along the centerline joint at the bottom of the restrained slabs.	D-7
Figure D.12. Strains in the diagonal direction at the corner along the centerline joint at the top of the restrained slabs.	D-7
Figure D.13. Strains in the diagonal direction at the corner along the centerline joint at the middepth of the restrained slabs.	D-8
Figure D.14. Strains in the diagonal direction at the corner along the centerline joint at the bottom of the restrained slabs.	D-8
Figure D.15. Strains in the transverse direction at the corner along the centerline joint at the top of the restrained slabs.	D-9
Figure D.16. Strains in the transverse direction at the corner along the centerline joint at the middepth of the restrained slabs.	D-9
Figure D.17. Strains in the transverse direction at the corner along the centerline joint at the bottom of the restrained slabs.	D-10
Figure D.18. Strains in the longitudinal direction at the corner along the lane/shoulder joint at the top of the restrained slabs.	D-10

Figure D.19. Strains in the longitudinal direction at the corner along the lane/shoulder joint at the middepth of the restrained slabs.	D-11
Figure D.20. Strains in the longitudinal direction at the corner along the lane/shoulder joint at the bottom of the restrained slabs.	D-11
Figure D.21. Strains in the diagonal direction at the corner along the lane/shoulder joint at the top of the restrained slabs.	D-12
Figure D.22. Strains in the diagonal direction at the corner along the lane/shoulder joint at the middepth of the restrained slabs.	D-12
Figure D.23. Strains in the diagonal direction at the corner along the lane/shoulder joint at the bottom of the restrained slabs.	D-13
Figure D.24. Strains in the transverse direction at the corner along the lane/shoulder joint at the top of the restrained slabs.	D-13
Figure D.25. Strains in the transverse direction at the corner along the lane/shoulder joint at the middepth of the restrained slabs.	D-14
Figure D.26. Strains in the transverse direction at the corner along the lane/shoulder joint at the bottom of the restrained slabs.	D-14
Figure D.27. Strains in the longitudinal direction at midpanel at the top of the unrestrained slabs.	D-15
Figure D.28. Strains in the longitudinal direction at midpanel at the bottom of the unrestrained slabs.	D-15
Figure D.29. Strains in the longitudinal direction along the lane/shoulder joint at the top of the unrestrained slabs.	D-16
Figure D.30. Strains in the longitudinal direction along the lane/shoulder joint at the bottom of the unrestrained slabs.	D-16
Figure D.31. Strains in the longitudinal direction along the centerline joint at the top of the unrestrained slabs.	D-17
Figure D.32. Strains in the longitudinal direction along the centerline joint at the bottom of the unrestrained slabs.	D-17
Figure D.33. Strains in the transverse direction along the transverse joint at the top of the unrestrained slabs.	D-18
Figure D.34. Strains in the transverse direction along the transverse joint at the bottom of the unrestrained slabs.	D-18
Figure D.35. Strains in the longitudinal direction at the corner along the centerline joint at the top of the unrestrained slabs.	D-19
Figure D.36. Strains in the longitudinal direction at the corner along the centerline joint at the middepth of the unrestrained slabs.	D-19
Figure D.37. Strains in the longitudinal direction at the corner along the centerline joint at the bottom of the unrestrained slabs.	D-20
Figure D.38. Strains in the diagonal direction at the corner along the centerline joint at the top of the unrestrained slabs.	D-20
Figure D.39. Strains in the diagonal direction at the corner along the centerline joint at the middepth of the unrestrained slabs.	D-21
Figure D.40. Strains in the diagonal direction at the corner along the centerline joint at the bottom of the unrestrained slabs.	D-21
Figure D.41. Strains in the transverse direction at the corner along the centerline joint at the top of the unrestrained slabs.	D-22

Figure D.42. Strains in the transverse direction at the corner along the centerline joint at the middepth of the unrestrained slabs.....	D-22
Figure D.43. Strains in the transverse direction at the corner along the centerline joint at the bottom of the unrestrained slabs.	D-23
Figure D.44. Strains in the longitudinal direction at the corner along the lane/shoulder joint at the top of the unrestrained slabs.	D-23
Figure D.45. Strains in the longitudinal direction at the corner along the lane/shoulder joint at the middepth of the unrestrained slabs.	D-24
Figure D.46. Strains in the longitudinal direction at the corner along the lane/shoulder joint at the bottom of the unrestrained slabs.....	D-24
Figure D.47. Strains in the diagonal direction at the corner along the lane/shoulder joint at the top of the unrestrained slabs.	D-25
Figure D.48. Strains in the diagonal direction at the corner along the lane/shoulder joint at the middepth of the unrestrained slabs.	D-25
Figure D.49. Strains in the diagonal direction at the corner along the lane/shoulder joint at the bottom of the unrestrained slabs.	D-26
Figure D.50. Strains in the transverse direction at the corner along the lane/shoulder joint at the top of the unrestrained slabs.	D-26
Figure D.51. Strains in the transverse direction at the corner along the lane/shoulder joint at the middepth of the unrestrained slabs.	D-27
Figure D.52. Strains in the transverse direction at the corner along the lane/shoulder joint at the bottom of the unrestrained slabs.	D-27

Figure E.1. Restrained Slab A diagonal surface profiles for the winter of 2006.	E-2
Figure E.2. Restrained Slab B diagonal surface profiles for the winter of 2006.	E-2
Figure E.3. Restrained Slab C diagonal surface profiles for the winter of 2006.	E-3
Figure E.4. Restrained Slab A diagonal surface profiles for the spring of 2006.	E-3
Figure E.5. Restrained Slab B diagonal surface profiles for the spring of 2006.	E-4
Figure E.6. Restrained Slab C diagonal surface profiles for the spring of 2006.	E-4
Figure E.7. Restrained Slab A diagonal surface profiles for the summer of 2006.....	E-5
Figure E.8. Restrained Slab B diagonal surface profiles for the summer of 2006.....	E-5
Figure E.9. Restrained Slab C diagonal surface profiles for the summer of 2006.....	E-6
Figure E.10. Restrained Slab A diagonal surface profiles for the winter of 2007.	E-6
Figure E.11. Restrained Slab B diagonal surface profiles for the winter of 2007.	E-7
Figure E.12. Restrained Slab C diagonal surface profiles for the winter of 2007.	E-7
Figure E.13. Restrained Slab A diagonal surface profiles for the spring of 2007.	E-8
Figure E.14. Restrained Slab B diagonal surface profiles for the spring of 2007.	E-8
Figure E.15. Restrained Slab C diagonal surface profiles for the spring of 2007.	E-9
Figure E.16. Restrained Slab A diagonal surface profiles for the summer of 2007....	E-9
Figure E.17. Restrained Slab B diagonal surface profiles for the summer of 2007..	E-10
Figure E.18. Restrained Slab C diagonal surface profiles for the summer of 2007..	E-10
Figure E.19. Restrained Slab A diagonal surface profiles for the fall of 2007.	E-11
Figure E.20. Restrained Slab B diagonal surface profiles for the fall of 2007.	E-11
Figure E.21. Restrained Slab C diagonal surface profiles for the fall of 2007.	E-12
Figure E.22. Unrestrained Slab A diagonal surface profiles for the winter of 2006.	E-12

<i>Figure E.23. Unrestrained Slab B diagonal surface profiles for the winter of 2006.</i>	E-13
<i>Figure E.24. Unrestrained Slab C diagonal surface profiles for the winter of 2006.</i>	E-13
<i>Figure E.25. Unrestrained Slab A diagonal surface profiles for the spring of 2006.</i>	E-14
<i>Figure E.26. Unrestrained Slab B diagonal surface profiles for the spring of 2006.</i>	E-14
<i>Figure E.27. Unrestrained Slab C diagonal surface profiles for the spring of 2006.</i>	E-15
<i>Figure E.28. Unrestrained Slab A diagonal surface profiles for the summer of 2006.</i>	E-15
<i>Figure E.29. Unrestrained Slab B diagonal surface profiles for the summer of 2006.</i>	E-16
<i>Figure E.30. Unrestrained Slab C diagonal surface profiles for the summer of 2006.</i>	E-16
<i>Figure E.31. Unrestrained Slab A diagonal surface profiles for the winter of 2007.</i>	E-17
<i>Figure E.32. Unrestrained Slab B diagonal surface profiles for the winter of 2007.</i>	E-17
<i>Figure E.33. Unrestrained Slab C diagonal surface profiles for the winter of 2007.</i>	E-18
<i>Figure E.34. Unrestrained Slab A diagonal surface profiles for the spring of 2007.</i>	E-18
<i>Figure E.35. Unrestrained Slab B diagonal surface profiles for the spring of 2007.</i>	E-19
<i>Figure E.36. Unrestrained Slab C diagonal surface profiles for the spring of 2007.</i>	E-19
<i>Figure E.37. Unrestrained Slab A diagonal surface profiles for the summer of 2007.</i>	E-20
<i>Figure E.38. Unrestrained Slab B diagonal surface profiles for the summer of 2007.</i>	E-20
<i>Figure E.39. Unrestrained Slab C diagonal surface profiles for the summer of 2007.</i>	E-21
<i>Figure E.40. Unrestrained Slab A diagonal surface profiles for the fall of 2007.</i>	E-21
<i>Figure E.41. Unrestrained Slab B diagonal surface profiles for the fall of 2007.</i>	E-22
<i>Figure E.42. Unrestrained Slab C diagonal surface profiles for the fall of 2007.</i>	E-22
<i>Figure E.43. Restrained Slab A Line A transverse surface profiles for the winter of 2006.</i>	E-23
<i>Figure E.44. Restrained Slab B Line A transverse surface profiles for the winter of 2006.</i>	E-23
<i>Figure E.45. Restrained Slab B Line B transverse surface profiles for the winter of 2006.</i>	E-24
<i>Figure E.46. Restrained Slab C Line B transverse surface profiles for the winter of 2006.</i>	E-24

Figure E.47. Restrained Slab A Line A transverse surface profiles for the spring of 2006.	E-25
Figure E.48. Restrained Slab B Line A transverse surface profiles for the spring of 2006.	E-25
Figure E.49. Restrained Slab B Line B transverse surface profiles for the spring of 2006.	E-26
Figure E.50. Restrained Slab C Line B transverse surface profiles for the spring of 2006.	E-26
Figure E.51. Restrained Slab A Line A transverse surface profiles for the summer of 2006.	E-27
Figure E.52. Restrained Slab B Line A transverse surface profiles for the summer of 2006.	E-27
Figure E.53. Restrained Slab B Line B transverse surface profiles for the summer of 2006.	E-28
Figure E.54. Restrained Slab C Line B transverse surface profiles for the summer of 2006.	E-28
Figure E.55. Restrained Slab A Line A transverse surface profiles for the winter of 2007.	E-29
Figure E.56. Restrained Slab B Line A transverse surface profiles for the winter of 2007.	E-29
Figure E.57. Restrained Slab B Line B transverse surface profiles for the winter of 2007.	E-30
Figure E.58. Restrained Slab C Line B transverse surface profiles for the winter of 2007.	E-30
Figure E.59. Restrained Slab A Line A transverse surface profiles for the spring of 2007.	E-31
Figure E.60. Restrained Slab B Line A transverse surface profiles for the spring of 2007.	E-31
Figure E.61. Restrained Slab B Line B transverse surface profiles for the spring of 2007.	E-32
Figure E.62. Restrained Slab C Line B transverse surface profiles for the spring of 2007.	E-32
Figure E.63. Restrained Slab A Line A transverse surface profiles for the summer of 2007.	E-33
Figure E.64. Restrained Slab B Line A transverse surface profiles for the summer of 2007.	E-33
Figure E.65. Restrained Slab B Line B transverse surface profiles for the summer of 2007.	E-34
Figure E.66. Restrained Slab C Line B transverse surface profiles for the summer of 2007.	E-34
Figure E.67. Restrained Slab A Line A transverse surface profiles for the fall of 2007.	E-35
Figure E.68. Restrained Slab B Line A transverse surface profiles for the fall of 2007.	E-35
Figure E.69. Restrained Slab B Line B transverse surface profiles for the fall of 2007.	E-36

Figure E.70. Restrained Slab C Line B transverse surface profiles for the fall of 2007.	E-36
Figure E.71. Unrestrained Slab A Line A transverse surface profiles for the winter of 2006.	E-37
Figure E.72. Unrestrained Slab B Line A transverse surface profiles for the winter of 2006.	E-37
Figure E.73. Unrestrained Slab B Line B transverse surface profiles for the winter of 2006.	E-38
Figure E.74. Unrestrained Slab C Line B transverse surface profiles for the winter of 2006.	E-38
Figure E.75. Unrestrained Slab A Line A transverse surface profiles for the spring of 2006.	E-39
Figure E.76. Unrestrained Slab B Line A transverse surface profiles for the spring of 2006.	E-39
Figure E.77. Unrestrained Slab B Line B transverse surface profiles for the spring of 2006.	E-40
Figure E.78. Unrestrained Slab C Line B transverse surface profiles for the spring of 2006.	E-40
Figure E.79. Unrestrained Slab A Line A transverse surface profiles for the summer of 2006.	E-41
Figure E.80. Unrestrained Slab B Line A transverse surface profiles for the summer of 2006.	E-41
Figure E.81. Unrestrained Slab B Line B transverse surface profiles for the summer of 2006.	E-42
Figure E.82. Unrestrained Slab C Line B transverse surface profiles for the summer of 2006.	E-42
Figure E.83. Unrestrained Slab A Line A transverse surface profiles for the winter of 2007.	E-43
Figure E.84. Unrestrained Slab B Line A transverse surface profiles for the winter of 2007.	E-43
Figure E.85. Unrestrained Slab B Line B transverse surface profiles for the winter of 2007.	E-44
Figure E.86. Unrestrained Slab C Line B transverse surface profiles for the winter of 2007.	E-44
Figure E.87. Unrestrained Slab A Line A transverse surface profiles for the spring of 2007.	E-45
Figure E.88. Unrestrained Slab B Line A transverse surface profiles for the spring of 2007.	E-45
Figure E.89. Unrestrained Slab B Line B transverse surface profiles for the spring of 2007.	E-46
Figure E.90. Unrestrained Slab C Line B transverse surface profiles for the spring of 2007.	E-46
Figure E.91. Unrestrained Slab A Line A transverse surface profiles for the summer of 2007.	E-47
Figure E.92. Unrestrained Slab B Line A transverse surface profiles for the summer of 2007.	E-47

Figure E.93. Unrestrained Slab B Line B transverse surface profiles for the summer of 2007.	E-48
Figure E.94. Unrestrained Slab C Line B transverse surface profiles for the summer of 2007.	E-48
Figure E.95. Unrestrained Slab A Line A transverse surface profiles for the fall of 2007.	E-49
Figure E.96. Unrestrained Slab B Line A transverse surface profiles for the fall of 2007.	E-49
Figure E.97. Unrestrained Slab B Line B transverse surface profiles for the fall of 2007.	E-50
Figure E.98. Unrestrained Slab C Line B transverse surface profiles for the fall of 2007.	E-50
Figure E.99. Restrained Slab A longitudinal surface profiles for the winter of 2006.	E-51
Figure E.100. Restrained Slab B longitudinal surface profiles for the winter of 2006.	E-51
Figure E.101. Restrained Slab C longitudinal surface profiles for the winter of 2006.	E-52
Figure E.102. Restrained Slab A longitudinal surface profiles for the spring of 2006.	E-52
Figure E.103. Restrained Slab B longitudinal surface profiles for the spring of 2006.	E-53
Figure E.104. Restrained Slab C longitudinal surface profiles for the spring of 2006.	E-53
Figure E.105. Restrained Slab A longitudinal surface profiles for the summer of 2006.	E-54
Figure E.106. Restrained Slab B longitudinal surface profiles for the summer of 2006.	E-54
Figure E.107. Restrained Slab C longitudinal surface profiles for the summer of 2006.	E-55
Figure E.108. Restrained Slab A longitudinal surface profiles for the winter of 2007.	E-55
Figure E.109. Restrained Slab B longitudinal surface profiles for the winter of 2007.	E-56
Figure E.110. Restrained Slab C longitudinal surface profiles for the winter of 2007.	E-56
Figure E.111. Restrained Slab A longitudinal surface profiles for the spring of 2007.	E-57
Figure E.112. Restrained Slab B longitudinal surface profiles for the spring of 2007.	E-57
Figure E.113. Restrained Slab C longitudinal surface profiles for the spring of 2007.	E-58
Figure E.114. Restrained Slab A longitudinal surface profiles for the summer of 2007. ..	E-58
Figure E.115. Restrained Slab B longitudinal surface profiles for the summer of 2007.	E-59

<i>Figure E.116. Restrained Slab C longitudinal surface profiles for the summer of 2007.</i>	E-59
<i>Figure E.117. Restrained Slab A longitudinal surface profiles for the fall of 2007...</i>	E-60
<i>Figure E.118. Restrained Slab B longitudinal surface profiles for the fall of 2007...</i>	E-60
<i>Figure E.119. Restrained Slab C longitudinal surface profiles for the fall of 2007...</i>	E-61
<i>Figure E.120. Unrestrained Slab A longitudinal surface profiles for the winter of 2006.</i>	E-61
<i>Figure E.121. Unrestrained Slab B longitudinal surface profiles for the winter of 2006.</i>	E-62
<i>Figure E.122. Unrestrained Slab C longitudinal surface profiles for the winter of 2006.</i>	E-62
<i>Figure E.123. Unrestrained Slab A longitudinal surface profiles for the spring of 2006.</i>	E-63
<i>Figure E.124. Unrestrained Slab B longitudinal surface profiles for the spring of 2006.</i>	E-63
<i>Figure E.125. Unrestrained Slab C longitudinal surface profiles for the spring of 2006.</i>	E-64
<i>Figure E.126. Unrestrained Slab A longitudinal surface profiles for the summer of 2006.</i>	E-64
<i>Figure E.127. Unrestrained Slab B longitudinal surface profiles for the summer of 2006.</i>	E-65
<i>Figure E.128. Unrestrained Slab C longitudinal surface profiles for the summer of 2006.</i>	E-65
<i>Figure E.129. Unrestrained Slab A longitudinal surface profiles for the winter of 2007.</i>	E-66
<i>Figure E.130. Unrestrained Slab B longitudinal surface profiles for the winter of 2007.</i>	E-66
<i>Figure E.131. Unrestrained Slab C longitudinal surface profiles for the winter of 2007.</i>	E-67
<i>Figure E.132. Unrestrained Slab A longitudinal surface profiles for the spring of 2007.</i>	E-67
<i>Figure E.133. Unrestrained Slab B longitudinal surface profiles for the spring of 2007.</i>	E-68
<i>Figure E.134. Unrestrained Slab C longitudinal surface profiles for the spring of 2007.</i>	E-68
<i>Figure E.135. Unrestrained Slab A longitudinal surface profiles for the summer of 2007.</i>	E-69
<i>Figure E.136. Unrestrained Slab B longitudinal surface profiles for the summer of 2007.</i>	E-69
<i>Figure E.137. Unrestrained Slab C longitudinal surface profiles for the summer of 2007.</i>	E-70
<i>Figure E.138. Unrestrained Slab A longitudinal surface profiles for the fall of 2007.</i>	E-70
<i>Figure E.139. Unrestrained Slab B longitudinal surface profiles for the fall of 2007.</i>	E-71

Figure E.140. Unrestrained Slab C longitudinal surface profiles for the fall of 2007.	E-71
--	------

Figure F.1. Curvature estimated from surface profiles and vibrating wire gages for restrained Slab A during the winter of 2006.	F-2
Figure F.2. Curvature estimated from surface profiles and vibrating wire gages for restrained Slab B during the winter of 2006.	F-2
Figure F.3. Curvature estimated from surface profiles and vibrating wire gages for restrained Slab C during the winter of 2006.	F-3
Figure F.4. Curvature estimated from surface profiles and vibrating wire gages for restrained Slab A during the spring of 2006.	F-3
Figure F.5. Curvature estimated from surface profiles and vibrating wire gages for restrained Slab B during the spring of 2006.	F-4
Figure F.6. Curvature estimated from surface profiles and vibrating wire gages for restrained Slab C during the spring of 2006.	F-4
Figure F.7. Curvature estimated from surface profiles and vibrating wire gages for restrained Slab A during the summer of 2006.	F-5
Figure F.8. Curvature estimated from surface profiles and vibrating wire gages for restrained Slab B during the summer of 2006.	F-5
Figure F.9. Curvature estimated from surface profiles and vibrating wire gages for restrained Slab C during the summer of 2006.	F-6
Figure F.10. Curvature estimated from surface profiles and vibrating wire gages for restrained Slab A during the winter of 2007.	F-6
Figure F.11. Curvature estimated from surface profiles and vibrating wire gages for restrained Slab B during the winter of 2007.	F-7
Figure F.12. Curvature estimated from surface profiles and vibrating wire gages for restrained Slab C during the winter of 2007.	F-7
Figure F.13. Curvature estimated from surface profiles and vibrating wire gages for restrained Slab A during the spring of 2007.	F-8
Figure F.14. Curvature estimated from surface profiles and vibrating wire gages for restrained Slab B during the spring of 2007.	F-8
Figure F.15. Curvature estimated from surface profiles and vibrating wire gages for restrained Slab C during the spring of 2007.	F-9
Figure F.16. Curvature estimated from surface profiles and vibrating wire gages for restrained Slab A during the summer of 2007.	F-9
Figure F.17. Curvature estimated from surface profiles and vibrating wire gages for restrained Slab B during the summer of 2007.	F-10
Figure F.18. Curvature estimated from surface profiles and vibrating wire gages for restrained Slab C during the summer of 2007.	F-10
Figure F.19. Curvature estimated from surface profiles and vibrating wire gages for restrained Slab A during the fall of 2007.	F-11
Figure F.20. Curvature estimated from surface profiles and vibrating wire gages for restrained Slab B during the fall of 2007.	F-11
Figure F.21. Curvature estimated from surface profiles and vibrating wire gages for restrained Slab C during the fall of 2007.	F-12

Figure F.22. Curvature estimated from surface profiles and vibrating wire gages for unrestrained Slab A during the winter of 2006.	F-12
Figure F.23. Curvature estimated from surface profiles and vibrating wire gages for unrestrained Slab B during the winter of 2006.	F-13
Figure F.24. Curvature estimated from surface profiles and vibrating wire gages for unrestrained Slab C during the winter of 2006 (VW Data is not available). ..	F-13
Figure F.25. Curvature estimated from surface profiles and vibrating wire gages for unrestrained Slab A during the spring of 2006.	F-14
Figure F.26. Curvature estimated from surface profiles and vibrating wire gages for unrestrained Slab B during the spring of 2006.	F-14
Figure F.27. Curvature estimated from surface profiles and vibrating wire gages for unrestrained Slab C during the spring of 2006 (VW Data is not available). ..	F-15
Figure F.28. Curvature estimated from surface profiles and vibrating wire gages for unrestrained Slab A during the summer of 2006.	F-15
Figure F.29. Curvature estimated from surface profiles and vibrating wire gages for unrestrained Slab B during the summer of 2006.	F-16
Figure F.30. Curvature estimated from surface profiles and vibrating wire gages for unrestrained Slab C during the summer of 2006 (VW Data is not available).	F-16
Figure F.31. Curvature estimated from surface profiles and vibrating wire gages for unrestrained Slab A during the winter of 2007.	F-17
Figure F.32. Curvature estimated from surface profiles and vibrating wire gages for unrestrained Slab B during the winter of 2007.	F-17
Figure F.33. Curvature estimated from surface profiles and vibrating wire gages for unrestrained Slab C during the winter of 2007(VW Data is not available). ..	F-18
Figure F.34. Curvature estimated from surface profiles and vibrating wire gages for unrestrained Slab A during the spring of 2007.	F-18
Figure F.35. Curvature estimated from surface profiles and vibrating wire gages for unrestrained Slab B during the spring of 2007.	F-19
Figure F.36. Curvature estimated from surface profiles and vibrating wire gages for unrestrained Slab C during the spring of 2007(VW Data is not available).. ..	F-19
Figure F.37. Curvature estimated from surface profiles and vibrating wire gages for unrestrained Slab A during the summer of 2007.	F-20
Figure F.38. Curvature estimated from surface profiles and vibrating wire gages for unrestrained Slab B during the summer of 2007.	F-20
Figure F.39. Curvature estimated from surface profiles and vibrating wire gages for unrestrained Slab C during the summer of 2007(VW Data is not available).. ..	F-21
Figure F.40. Curvature estimated from surface profiles and vibrating wire gages for unrestrained Slab A during the fall of 2007.	F-21
Figure F.41. Curvature estimated from surface profiles and vibrating wire gages for unrestrained Slab B during the fall of 2007.	F-22
Figure F.42. Curvature estimated from surface profiles and vibrating wire gages for unrestrained Slab C during the fall of 2007(VW Data is not available).	F-22

Figure G.1. Relationship between load transfer efficiency and age of the pavement for the unrestrained Cell 2	G-2
Figure G.2. Relationship between load transfer efficiency and age of the pavement for the unrestrained Cell 2.	G-2
Figure G.3. Relationship between load transfer efficiency and age of the pavement for the unrestrained Cell 2.	G-3
Figure G.4. Relationship between load transfer efficiency and age of the pavement for the unrestrained Cell 3.	G-3
Figure G.5. Relationship between load transfer efficiency and age of the pavement for the unrestrained Cell 3.	G-4
Figure G.6. Relationship between load transfer efficiency and equivalent linear temperature gradient for the unrestrained Cell 2.	G-4
Figure G.7. Relationship between load transfer efficiency and equivalent linear temperature gradient for the unrestrained Cell 2.	G-5
Figure G.8. Relationship between load transfer efficiency and equivalent linear temperature gradient for the unrestrained Cell 3.	G-5
Figure G.9. Relationship between load transfer efficiency and equivalent linear temperature gradient for the unrestrained Cell 3.	G-6
Figure G.10. Relationship between load transfer efficiency and equivalent linear temperature gradient for the unrestrained Cell 3.	G-6
Figure G.11. Relationship between load transfer efficiency and equivalent linear temperature gradient for the restrained Cell 1.	G-7
Figure G.12. Relationship between load transfer efficiency and equivalent linear temperature gradient for the restrained Cell 1.	G-7
Figure G.13. Relationship between load transfer efficiency and equivalent linear temperature gradient for the restrained Cell 1	G-8
Figure G.14. Relationship between load transfer efficiency and equivalent linear temperature gradient for the restrained Cell 4.	G-8
Figure G.15. Relationship between load transfer efficiency and equivalent linear temperature gradient for the restrained Cell 4.	G-9
Figure G.16. Relationship between load transfer efficiency and equivalent linear temperature gradient for the restrained Cell 4.	G-9
Figure G.17. Relationship between load transfer efficiency and equivalent linear temperature gradient for the restrained Cell 4.	G-10
Figure G.18. Relationship between the Void parameter and the equivalent linear temperature gradient present during testing for the restrained Slab A in Cell 1.....	G-10
Figure G.19. Relationship between the Void parameter and the equivalent linear temperature gradient present during testing for unrestrained Slab B in Cell 2.....	G-11
Figure G.20. Relationship between the Void parameter and the equivalent linear temperature gradient present during testing for the unrestrained Slab A in Cell 3.	G-11
Figure G.21. Relationship between the Void parameter and the equivalent linear temperature gradient present during testing for the unrestrained Slab B in Cell 3.....	G-12

Figure G.22. Relationship between the Void parameter and the equivalent linear temperature gradient present during testing for unrestrained Slab C in Cell 3.....	G-12
Figure G.23. Relationship between the Void parameter and the equivalent linear temperature gradient present during testing for the restrained Slab A in Cell 4.....	G-13
Figure G.24. Relationship between the Void parameter and the equivalent linear temperature gradient present during testing for the restrained Slab B in Cell 4.....	G-13
Figure G.25. Relationship between the Void parameter and the equivalent linear temperature gradient present during testing for the restrained Slab C in Cell 4.....	G-14
Figure G.1. Comparison of the support conditions beneath the slab and the equivalent linear temperature gradient of the slab during testing for restrained Slab B in Cell 1.	G-14
Figure G.2. Comparison of the support conditions beneath the slab and the equivalent linear temperature gradient of the slab during testing for unrestrained Slab B in Cell 2.	G-15
Figure G.3. Comparison of the support conditions beneath the slab and the equivalent linear temperature gradient of the slab during testing for unrestrained Slab A in Cell 3.	G-15
Figure G.4. Comparison of the support conditions beneath the slab and the equivalent linear temperature gradient of the slab during testing for unrestrained Slab B in Cell 3.	G-16
Figure G.5. Comparison of the support conditions beneath the slab and the equivalent linear temperature gradient of the slab during testing for unrestrained Slab C in Cell 3.	G-16
Figure G.6. Comparison of the support conditions beneath the slab and the equivalent linear temperature gradient of the slab during testing for restrained Slab A in Cell 4.	G-17
Figure G.7. Comparison of the support conditions beneath the slab and the equivalent linear temperature gradient of the slab during testing for restrained Slab B in Cell 4.	G-17
Figure G.8. Comparison of the support conditions beneath the slab and the equivalent linear temperature gradient of the slab during testing for restrained Slab C in Cell 4.	G-18
Figure G.9. Comparison of the support conditions beneath the slab and the equivalent linear temperature gradient of the slab during testing for restrained Slab D in Cell 4.	G-18
Figure G.10. Comparison of the support conditions beneath the slab and the equivalent linear temperature gradient of the slab during testing for restrained Slab E in Cell 4.	G-19
Figure G.11. Relationship between strain measured in the wheelpath at the bottom of the restrained slabs and slab temperature.	G-19
Figure G.12. Relationship between strain measured in the wheelpath at the top of the unrestrained slabs and slab temperature	G-20

<i>Figure G.13. Relationship between strain measured in the corner at the bottom of the restrained slabs and slab temperature.</i>	<i>G-20</i>
<i>Figure G.14. Relationship between strain measured in the corner at the top of the unrestrained slabs and slab temperature.</i>	<i>G-21</i>
<i>Figure G.15. Relationship between strain measured in the corner at the bottom of the unrestrained slabs and slab temperature.</i>	<i>G-21</i>
<i>Figure G.16. Relationship between strain measured in the wheelpath at the bottom of the restrained slabs and the temperature gradient in the slab.</i>	<i>G-22</i>
<i>Figure G.17. Relationship between strain measured in the wheelpath at the bottom of the unrestrained slabs and the temperature gradient in the slab.</i>	<i>G-22</i>
<i>Figure G.18. Relationship between strain measured in the corner at the top of the restrained slabs and the temperature gradient in the slab.</i>	<i>G-23</i>
<i>Figure G.19. Relationship between strain measured in the corner at the bottom of the restrained slabs and the temperature gradient in the slab.</i>	<i>G-23</i>
<i>Figure G.20. Relationship between strain measured in the corner at the top of the unrestrained slabs and the temperature gradient in the slab.</i>	<i>G-24</i>
<i>Figure G.21. Relationship between strain measured in the corner at the bottom of the unrestrained slabs and the temperature gradient in the slab.</i>	<i>G-24</i>

Tables

Table	Page Number
<i>Table 1.1. Summary of sensors installed in the Smart Pavement Project [1, 2].</i>	<i>4</i>
<i>Table 2.1. Summary of frequency of occurrence of daily rain events.</i>	<i>14</i>
<i>Table 2.2. Monthly maximum positive and negative temperature differences across the concrete slab.</i>	<i>20</i>
<i>Table 2.3. Monthly maximum positive and negative equivalent linear temperature gradients.</i>	<i>21</i>
<i>Table 3.1. Concrete material parameters needed for the estimation of an equivalent temperature gradient for a moisture gradient.</i>	<i>59</i>
<i>Table 3.2. Concrete set time based on early-age vibrating wire data for restrained slabs.</i>	<i>66</i>
<i>Table 3.3. Concrete maturity corresponding to the estimated set times for restrained slabs.</i>	<i>68</i>
<i>Table 3.4. Concrete set time based on early-age vibrating wire data for unrestrained slabs.</i>	<i>73</i>
<i>Table 3.5. Concrete maturity corresponding to the estimated set times for unrestrained slabs.</i>	<i>75</i>
<i>Table 3.6. Time of set, built-in temperature gradients and weighted average temperatures based on the two methods.</i>	<i>89</i>
<i>Table 4.1. General inputs for the Smart pavement.</i>	<i>94</i>
<i>Table 4.2. Pavement structure inputs for the Smart pavement.</i>	<i>94</i>
<i>Table 4.3. MEPDG traffic volume inputs for the Smart Pavement.</i>	<i>96</i>
<i>Table 4.4. Monthly traffic adjustment factors for SR 22.</i>	<i>97</i>
<i>Table 4.5. Vehicle class distribution for SR 22.</i>	<i>97</i>
<i>Table 4.6. Hourly traffic distribution factors for SR 22.</i>	<i>99</i>
<i>Table 4.7. Single axle load distribution default values for each vehicle class (ARA 2004).</i>	<i>100</i>
<i>Table 4.8. Tandem axle load distribution default values for each vehicle class (ARA 2004).</i>	<i>101</i>
<i>Table 4.9. Average number of axles per truck class for SR 22.</i>	<i>102</i>
<i>Table 4.10. Axle configurations for SR 22.</i>	<i>103</i>
<i>Table 4.11. Truck wheelbases for traffic on SR 22.</i>	<i>103</i>
<i>Table 4.12. Inputs needed for characterizing drainage.</i>	<i>106</i>
<i>Table 4.13. Level 3 mass-volume inputs for the compacted unbound layers of the Smart Pavement.</i>	<i>109</i>
<i>Table 4.14. Level 1 mass-volume inputs for the compacted unbound layers of the Smart Pavement.</i>	<i>109</i>
<i>Table 4.15. Additional inputs for the compacted unbound layers of the Smart pavement.</i>	<i>110</i>

Table 4.16. Mixture properties for the Smart Pavement.	111
Table 4.17. PCC modulus of elasticity values determined through laboratory testing.	112
Table 4.18. PCC modulus of elasticity values required for Level 1.	113
Table 4.19. Results of compressive strength testing performed at the University of Pittsburgh.	113
Table 4.20. PCC compressive strength values required for Level 2.	114
Table 4.21. PCC modulus of elasticity values for Level 3.	115
Table 4.22. Poisson's ratios for the Smart Pavement.	115
Table 4.23. Moduli of rupture for the Smart Pavement.	116
Table 4.24. Moduli of rupture values required for Level 1.	117
Table 4.25. Unit weight at the three hierarchical levels.	118
Table 4.26. Mixture design for the PCC used to pave SR22.	119
Table 4.27. Thermal coefficient of expansion at the three hierarchical levels.	120
Table 4.28. Ultimate shrinkage at the three hierarchical levels.	122
Table 4.29. Time to develop 50 percent of ultimate shrinkage at all three hierarchical levels.	123
Table 4.30. General asphalt inputs for SR 22.	124
Table 4.31. Asphalt mix characteristics for the SR 22 ATPB.	125
Table 4.32. Resilient moduli of the unbound granular layers and subgrade for SR 22.	126
Table 4.33. Resilient moduli of the unbound granular layers and subgrade for the three hierarchical levels.	127
Table 4.34. Weather stations used in the analysis.	131
Table 4.35. Seasonal ranges of concrete weighted average temperatures.	138
Table 4.36. Statistical analysis of predicted and measured concrete weighted average temperature.	139
Table 4.37. Summary statistics for comparing predicted with measured equivalent linear temperature gradient.	142
Table 4.38. Required thickness for SR 22 based on the AASHTO and MEPDG design methods.	172
Table 5.1. Temperatures at transverse joints lock-up for the restrained and unrestrained slabs.	183
Table 5.2. Surface profile measurements test dates representing each season.	207
Table 5.3. Seasonal slab temperatures and equivalent linear gradients during profile testing.	209
Table 5.4. Temperature difference equivalent to moisture warping during profile test dates.	214
Table 5.5. Ranges of displacement at the corner for different equivalent linear temperature gradients based on unrestrained and restrained Slabs A, B and C.	230
Table 6.1. Seasonal temperature variation during FWD testing.	248
Table 6.2. Seasonal equivalent linear temperature gradients present during FWD testing.	274
Table 6.3. Axle loads for truck testing.	289

<i>Table 6.4. Temperature variation during truck testing.....</i>	<i>291</i>
<i>Table 6.5. Variation in the depth of the dynamic sensors of the restrained cell.</i>	<i>310</i>
<i>Table 6.6. Variation in the depth of the dynamic sensors in the unrestrained cell. ...</i>	<i>312</i>
<i>Table 7.1. Number of elements used for generating the finite element models.</i>	<i>330</i>
<i>Table 7.2. PCC model inputs for each slab type based on measured values.</i>	<i>331</i>
<i>Table 7.3. ATPB model inputs based on measured values.</i>	<i>331</i>
<i>Table 7.4. Average seasonal elastic moduli of the ATPB for the restrained and unrestrained slabs.</i>	<i>332</i>
<i>Table 7.5. Average seasonal backcalculated static k-values for the restrained and unrestrained slabs.</i>	<i>332</i>
<i>Table 7.6. The measured load transfer efficiency along the transverse joint of the restrained and unrestrained slabs.</i>	<i>333</i>
<i>Table 7.7. The measured load transfer efficiency along the longitudinal joint used to model the unrestrained slabs.</i>	<i>334</i>
<i>Table C.1. Traffic volume adjustment factors for Level 1 & 2 analysis.</i>	<i>C-2</i>
<i>Table C.2. Hourly truck traffic distribution for Level 1 & 2 analysis.</i>	<i>C-2</i>
<i>Table C.3. Vehicle class distribution for Level 1 & 2 analysis.</i>	<i>C-2</i>
<i>Table C.4. Traffic growth factors for Level 1 & 2 analysis.</i>	<i>C-3</i>
<i>Table C.5. General traffic inputs for Level 1 & 2 analysis.</i>	<i>C-3</i>
<i>Table C.6. Traffic volume adjustment factors for Level 3 analysis.</i>	<i>C-4</i>
<i>Table C.7. Hourly truck traffic distribution for Level 3 analysis.</i>	<i>C-4</i>
<i>Table C.8. Vehicle class distribution for Level 3 analysis.</i>	<i>C-4</i>
<i>Table C.9. Traffic growth factors for Level 3 analysis.</i>	<i>C-5</i>
<i>Table C.10. General traffic inputs for Level 3 analysis.</i>	<i>C-5</i>
<i>Table C.11. PCC general, thermal, and mix properties for Level 1 analysis.</i>	<i>C-6</i>
<i>Table C.12. PCC strength characterization for Level 1 analysis.</i>	<i>C-6</i>
<i>Table C.13. PCC general, thermal, and mix properties for Level 2 analysis.</i>	<i>C-6</i>
<i>Table C.14. PCC strength characterization for Level 2 analysis.</i>	<i>C-7</i>
<i>Table C.15. PCC general, thermal, and mix properties for Level 3 analysis.</i>	<i>C-7</i>
<i>Table C.16. PCC strength characterization for Level 3 analysis.</i>	<i>C-7</i>
<i>Table C.17. Asphalt treated permeable base properties for all hierarchical levels... </i>	<i>C-8</i>
<i>Table C.18. Subbase characterization for Level 1 analysis.....</i>	<i>C-9</i>
<i>Table C.19. Subbase characterization for Level 2 analysis.....</i>	<i>C-10</i>
<i>Table C.20. Subbase characterization for Level 3 analysis.....</i>	<i>C-11</i>
<i>Table C.21. Characterization of the fill material for Level 1 analysis.....</i>	<i>C-12</i>
<i>Table C.22. Characterization of the fill material for Level 2 analysis.....</i>	<i>C-13</i>
<i>Table C.23. Characterization of the fill material for Level 3 analysis.....</i>	<i>C-14</i>
<i>Table C.24. Subgrade characterization for Level 1 analysis.....</i>	<i>C-15</i>
<i>Table C.25. Subgrade characterization for Level 2 analysis.....</i>	<i>C-16</i>
<i>Table C.26. Subgrade characterization for Level 3 analysis.....</i>	<i>C-17</i>

CHAPTER 1: INTRODUCTION

1.1.0 Primary Goals of the Smart Pavement Project

The Smart Pavement research initiative is a joint effort among the Pennsylvania Department of Transportation (PennDOT), the Federal Highway Administration (FHWA), Mascaro Construction and the University of Pittsburgh. One of the primary objectives of the Smart Pavement study is to evaluate the ability of High Performance Paving (HIPERPAV) software to predict strength gain and early-age stress development. The second objective is to establish inputs for a pavement constructed in Pennsylvania to use in the Mechanistic-Empirical Pavement Design Guide (MEPDG). Version 1.0 of the MEDPG was used throughout this study. The approach taken to accomplish these objectives is to construct an instrumented pavement section, perform an extensive laboratory study to characterize the materials properties of the paving concrete and finally perform seasonal load testing and surface profile measurements on the instrumented pavement. The final portion

1.1.1 Goals Completed Under Phase I

The project consists of two phases. Phase I involved the instrumentation of a pavement section, evaluation of the early-age (first 28 days) concrete material properties, evaluation of HIPERPAV and analysis of the early-age (first 28 days) pavement response characteristics. A summary of these findings can be found in the Phase I report submitted in October 2005 [1].

1.1.2 Goals Completed Under Phase II

Phase II began with performing the one-year material property testing of the concrete on cores extracted from the test section. Seasonal load testing and profile measurements were also made for a three-year period so that the slab response to vehicle and environmental loads could be characterized. Finally, the data collected throughout the study was used to evaluate the use of the MEPDG for designing a pavement in Pennsylvania. A Phase II Interim Report was published in November 2006 summarizing the results from the load testing and surface profile measurements for the first year after the pavement was constructed as well as the one-year material properties of the concrete [2].

The focus of this report is on the data collected over the three-year period following construction. Throughout this time approximately 25 million readings have been taken from the static sensors alone. Surface profile measurements, truck load testing and FWD testing were performed twelve separate times throughout this three-year period. This data has been used to

1. characterize the design inputs needed for MEPDG based on a typical PennDOT design and compare the thickness determined using the MEPDG to that obtained using the current PennDOT design philosophy prescribed in Publication 242 Pavement Policy Manual (2003 Edition).
2. characterize seasonal temperature and moisture conditions in the pavement structure
3. describing seasonal trends in the response of the slab to environmental and applied loads for different restraint conditions
4. use finite element models calibrated using field data to estimate the stress in the slab

A brief section is first provided that describes the project location, site description pavement cross-section and pavement design details. A general overview of the location of the dynamic, environmental and static sensors embedded in the pavement is also included. For the sake of brevity, just a brief description of the test section is provided below. A more detailed description can be found in the Phase I Report [1].

1.2.0 Project Location and Site Description

The site location for the instrumented test sections was selected based on a number of criteria including construction schedule, roadway grade, subgrade support characteristics, and traffic patterns. After careful consideration, a section of highway along construction Section B01 of U.S. Route 22 was chosen. Section B01 is a 3.4 mile stretch of highway running from stations 513+45.144 to 0+08.573 in Allegheny County and from stations 0+08.573 to 166+99.475 in Westmoreland County. It is one of 10 designated construction sections (B01 through B10) that are part of PennDOT's Renew 22 reconstruction project that runs primarily through Westmoreland County between the Allegheny and Indiana County lines.

The Smart Pavement research section is located in the westbound truck lane between Tarr Hollow Road and School Road. The Smart Pavement test section consists of fourteen portland cement concrete (PCC) slabs running between stations 94+82 and 96+92. The test section is located in front of a shopping plaza (Franklin Plaza) on the westbound side of the highway and a manufacturing facility (Cleaveland Brothers Machinery Company) on the eastbound side.

1.3.0 Layout of the Test Sections

The layout of the test sections is provided in Figure 1.1. Nearly 400 sensors were installed at various depths throughout pavement structure. The sensors were installed in groups of slabs (panels) referred to as “cells”. There are a total of four cells consisting of three panels each. The cells are labeled 1 through 4, with numbers increasing in the westward direction. Cells 1 and 2 are used for measuring seasonal dynamic strains and Cells 3 and 4 are instrumented to measure both static strain and temperature and moistures conditions in the slabs. The sensors in Cells 1 and 2 are of the same type, quantity, depth, and location. The same is true for Cells 3 and 4 with the exception that Cell 4 also contains environmental monitoring sensors.

While the sensor arrangements in these two sets of cells are repetitive, there is one key variable that sets them apart. Cells 2 and 3 are unrestrained by dowel and tie bars while Cells 1 and 4 contain dowels and tie bars. One of the key research objectives is to investigate the effects of the restraint condition induced by the dowel and tie bars on pavement response. Non-instrumented transition panels act to isolate the two unrestrained cells (Cells 2 and 3) from the restrained cells (Cells 1 and 4). Of the 14 panels that comprise the instrumentation section, twelve were instrumented with the remaining two acting as transition panels between the restrained and unrestrained sections.

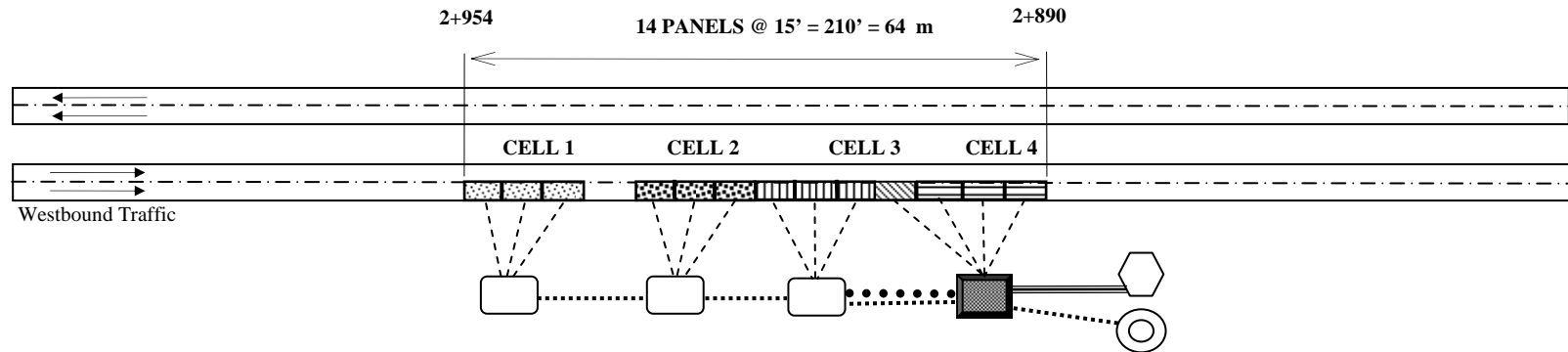
The sensors were installed in each of the 4 cells and wired to a set of datalogging equipment specific to that cell. A total of over three miles of wire was used to connect all the sensors into the dataloggers. The dataloggers for each cell are housed within cabinets that were constructed directly adjacent to the instrumented panels and approximately twelve feet away from the edge of the curb. Electricity is provided for each of these cabinets and phone service is provided for the enclosures for Cells 3 and 4. A schematic of the general sensor

layout, enclosure arrangement, and wiring is provided in figure 1.3. A summary of the sensors, including quantity and location appears in Table 1.1.

Table 1.1. Summary of sensors installed in the Smart Pavement Project [1, 2].

Sensor Type	Sensor Name	Qty.	Measurement	Cell
Environmental	Thermocouple	60	Temperature	4
Environmental	Moisture Sensor	24	Relative Humidity	4
Environmental	Time Domain Reflectometer	16	Moisture Content	4
Static Load	Vibrating Wire Strain Gage	156	Static Strain	3, 4
Static Load	Static Pressure Cell	8	Static Pressure	3, 4
Dynamic Load	Dynamic Strain Gage	112	Dynamic Strain	1, 2
Dynamic Load	Dynamic Pressure Cell	8	Dynamic Pressure	1, 2

S.R. - 22 SMART PAVEMENT PROJECT LAYOUT



LEGEND

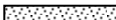

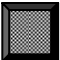










<div>Slabs with Dynamic Strain Sensors</div> <div><div> Cell 1: 3 Restrained Slabs</div><div> Cell 2: 3 Unrestrained Slabs</div></div>	<div> Datalogger Enclosure with Remote Communications System</div> <div> Datalogger Enclosure without Remote Communications System</div> <div> Power Supply</div> <div> Phone Supply</div>	<div> Power Cable</div> <div> Phone Cable</div> <div> Sensor Lead Wires</div> <div> Coaxial/Fiber Optic Cable</div>
<div>Slabs with Static Strain and Environmental Sensors</div> <div><div> Cell 3: 3 Unrestrained Slabs</div><div> Cell 4: 1 Intermediate Slab</div><div> Cell 4: 3 Restrained Slabs</div></div>		

Figure 1.1. Layout of the Smart Pavement section [1, 2].

1.4.0 Pavement Design

The newly constructed roadway is a four-lane urban major arterial divided by a concrete median. At the time of design in June 2002, the two-way average daily traffic (ADT) was 26,950 vehicles with 5 percent being truck traffic. The projected ADT at the end of the design life in 2022 is 36,780 vehicles. The design hourly volume in June 2002 was 3,678 vehicles with a directional split of 60 percent in the predominate direction of travel. The posted speed limit is 35 miles per hour, with several traffic signals and business entrances occurring along the roadway.

The new pavement structure is a jointed plain concrete pavement (JPCP) with 15-ft transverse joints and 12-ft wide lanes. This section of roadway is crowned with a 2.0 percent transverse slope. The longitudinal slope along the research section is approximately 2.4 percent. The concrete medians vary in width from 14.4 ft to 2.0 ft with concrete mountable curbs. The Smart Pavement section contains 2.6-ft wide concrete curb-and-gutter shoulders at an 8 percent transverse slope.

A description of the layers and layer thicknesses of the pavement structure are provided in Figure 1.2. Originally, the pavement was to be constructed directly on the subgrade but the poor soil conditions required the removal of a portion of the subgrade material and backfilling using a gap-graded soil and aggregate mixture.

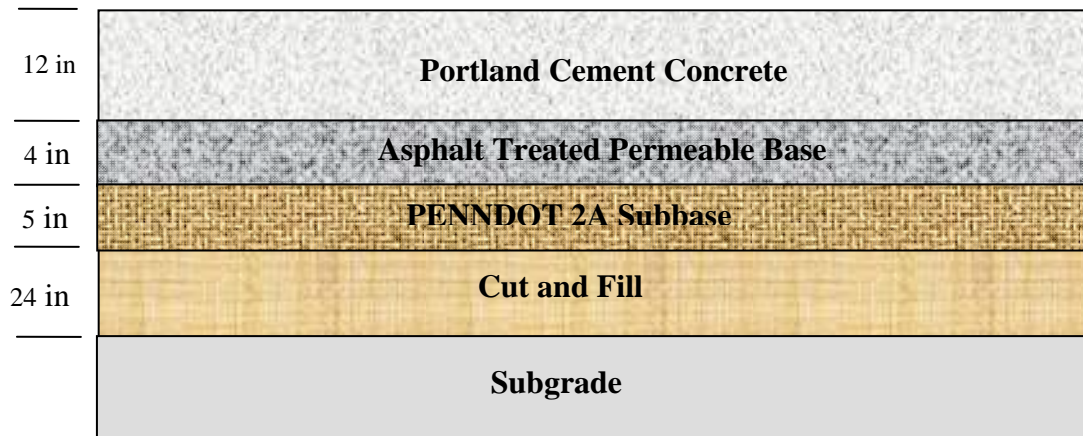


Figure 1.2. Design thicknesses of the pavement layers [1, 2].

For the restrained slabs in Cells 1 and 4, No. 5 epoxy-coated tie bars were placed every 2.5 ft along both the lane/shoulder and centerline joints and 1.5-in epoxy-coated dowel bars were spaced every 12 ft along the transverse joints.

Six-in corrugated, polyvinyl chloride (PVC), longitudinal edge drains are present beneath the curb at a depth of approximately 8 in below the bottom of the subgrade. The longitudinal drainage trenches are lined with a geotextile and filled with a American Association of State Highway and Transportation Officials (AASHTO) No. 57 coarse aggregate. The drainage inlets are spaced at approximately 260 ft.

1.5.0 Structure of the Report

This report is a compilation and analysis of the results of the data collected from the Smart Pavement for the first three years after construction. It is subdivided into eight chapters covering the following topics.

Chapter 2 involves the analysis of data collected from temperature and moisture sensors. This chapter presents the variations in ambient climatic conditions and the resulting affect it has on the temperature and moisture conditions throughout the pavement system throughout the first three years after construction.

Chapter 3 details the process established for determining the built-in construction gradient of the restrained and unrestrained slabs of the Smart Pavement. The built-in temperature gradient greatly affects pavement performance and is an input in the new Mechanistic-Empirical Design Guide (MEPDG). This chapter details the methodology adopted to determine the built-in construction gradient and presents and compares two approaches for determining the concrete set time used to establish the built-in construction gradient. The first approach uses early-age data collected from strain gages embedded in the concrete slabs and the second approach uses early-age data from static pressure cells embedded along the interface between the concrete slabs and the base layer.

Chapter 4 presents the characterization of the MEPDG design inputs for the restrained and unrestrained slabs of the Smart Pavement. This includes determination of the inputs at the three hierarchical levels defined in the new MEPDG. This chapter also presents a summary of the predicted pavement faulting, cracking and IRI of each

hierarchical level. A sensitivity analysis of the hierarchical level of individual design inputs is also investigated.

Chapter 5 presents an analysis of the response of the slabs to environmental loads during the first three years after paving. This chapter includes analysis of data collected from the static strain sensors and static pressure cells, in addition to an analysis of seasonal surface profile measurements. The analysis of the data collected by the strain gages includes seasonal variation of strains within the slabs and the effects of different environmental factors on strain measurements. The analysis of the data collected by the pressure cells includes the seasonal variations and the effects of several factors on the measurements. In addition, surface profile measurements were made shortly after paving and during each season throughout the three years after construction to capture the change in the shape of the slab under various temperature and moisture gradients. The static strain and pressure data and the surface profile measurements were used to analyze the seasonal effects on curling and warping of the pavement.

Chapter 6 presents the results of the load testing performed with the falling weight deflectometer (FWD) and trucks with known axle weights and configurations throughout the first three years after pavement construction. This chapter presents the characterization of seasonal and long-term trends in the response of the pavement to applied loads.

Chapter 7 presents the development and calibration of a finite element model for predicting stress in the Smart Pavement. The results of the seasonal FWD testing are used to define the model inputs. The finite element model is validated using strain measurements recorded during the truck load testing.

A summary of the findings presented throughout this report are provided in Chapter 8 along with some recommendations on future work needed. A subsequent report will be published under Contract 510601/WO-003 that will discuss the stress generated by these applied loads. The stress determined using the validated finite element models will then be used to evaluate the performance prediction of the MEPDG based on the accumulated damage produced by the calculated stress.

CHAPTER 2: TEMPERATURE AND MOISTURE DATA ANALYSIS

2.1.0. Introduction

Daily and seasonal variations in temperature and moisture conditions cause the development of temperature and moisture gradients in the concrete slab. These gradients cause slab curling and warping in which upward and downward curvature depends on whether the gradients are negative or positive. However, concrete slabs are not fully free to move and therefore, restraint in slab movement caused by thermal or moisture changes contributes to the development of stresses in concrete pavements. As a result, temperature and moisture gradients affect the long-term performance of concrete pavements.

This chapter discusses the daily and seasonal variations in the environmental conditions affecting the performance of the concrete pavement during the first three years after construction of the pavement. This chapter is subdivided into four major sections. The first section presents the variations in ambient climatic conditions. The second and third sections characterize the variations in the temperature and moisture conditions within the pavement. The last section summarizes the results of the work carried out in this chapter.

2.2.0. Ambient Climatic Conditions

The ambient climatic conditions influence the temperature and moisture conditions inside the pavement system. Daily and seasonal variations in the ambient temperature and moisture cause daily and seasonal variations inside the concrete slabs and throughout the underlying layers. Additionally, ambient climatic conditions are a major component of the environmental inputs in the EICM of the MEPDG. These variables constitute the main input to the EICM and characterization of the ambient climatic conditions will be used to develop the EICM inputs for a Level 1 characterization. In this section, the variations in the ambient climatic conditions during the first three years after construction of the pavement are presented. The climatic conditions presented include ambient temperatures, relative humidity and wind speed collected from the onsite weather station, and precipitation recorded by the Allegheny County Airport weather station.

The onsite weather station monitors ambient temperature, relative humidity, and wind speed at 15-minute intervals. The monthly maximum and minimum ambient temperature are presented in Figure 2.1. The temperature reached a peak high value of 99°F in August 2005

and a peak low of -9°F in January 2005. The difference between the monthly maximum and minimum temperature is lowest for the summer season and highest for the winter season.

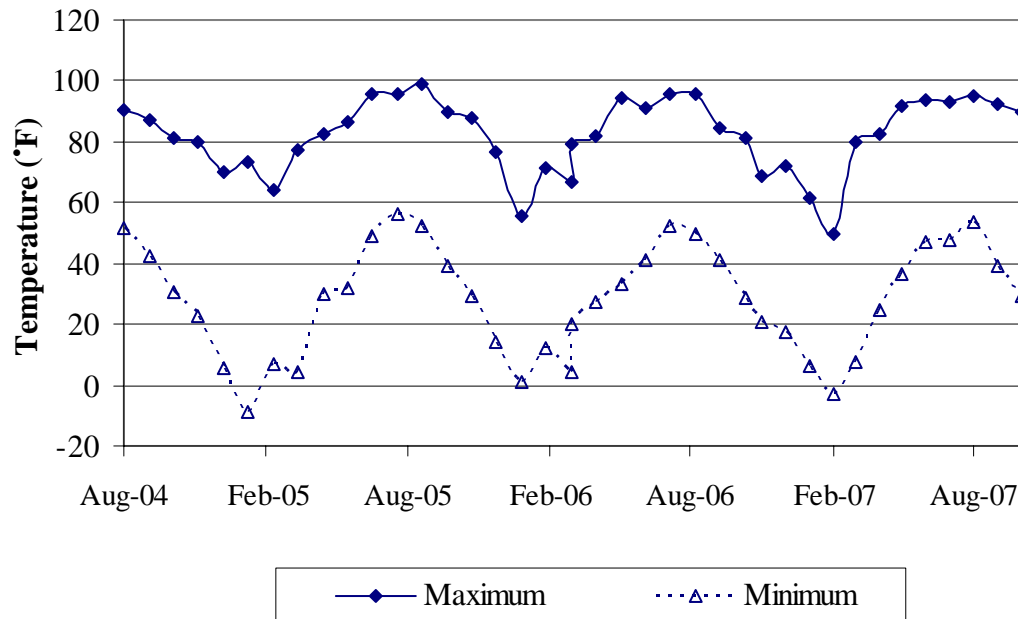


Figure 2.1. Monthly maximum and minimum ambient temperature conditions over three years after construction of the pavement.

The monthly maximum and minimum relative humidity is presented in Figure 2.2. The maximum monthly relative humidity does not vary seasonally and is at 95 to 100 percent during the first three years after construction of the pavement since it rains quite frequently in this area. The minimum monthly ambient relative humidity varies between 9 and 34 percent, with the lowest levels recorded during the spring and the highest levels during the summer.

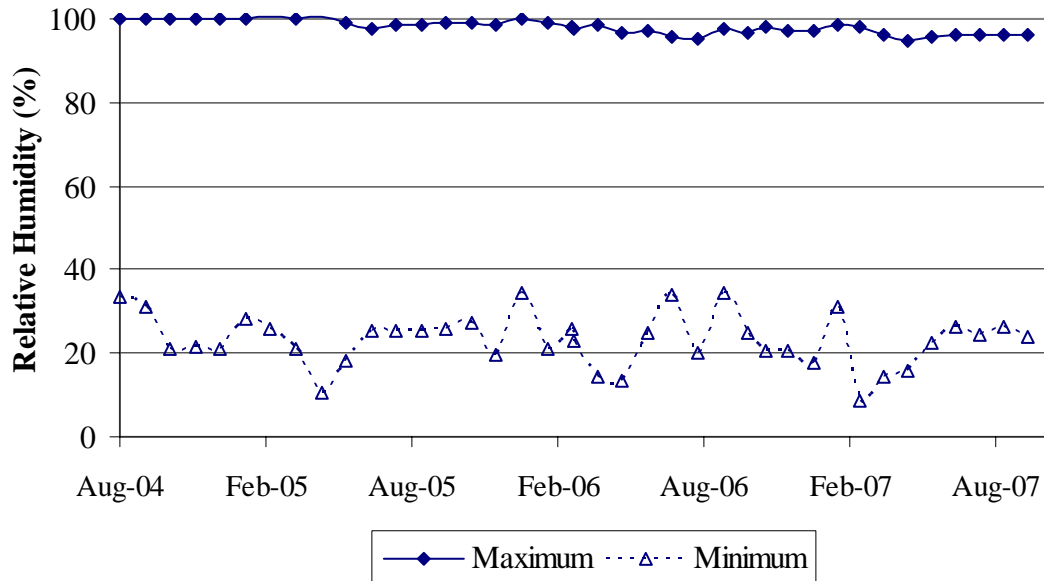


Figure 2.2. Monthly maximum and minimum ambient relative humidity the first three years after construction.

The monthly maximum, minimum and average wind speed is presented in Figure 2.3. The monthly maximum wind speed fluctuates between 12 and 27 mph, with the highest values recorded during the winter and the lowest values during the summer. The monthly average wind speeds ranged between 1 and 4 mph, with an average of 3 mph.

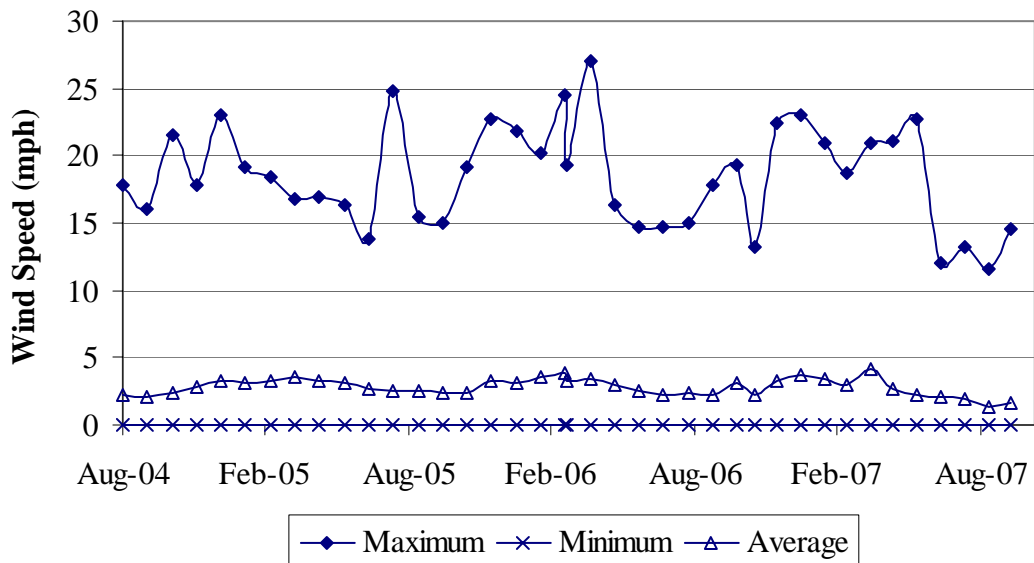


Figure 2.3. Monthly maximum, minimum and average ambient wind speed over three years after construction of the pavement.

The onsite weather station does not provide precipitation readings therefore, daily and hourly precipitation recorded by the weather station located at the Allegheny County Airport was used to represent field conditions. The precipitation data is obtained from the website maintained by the National Oceanic & Atmospheric Administration Satellite and Information Service and the National Climatic Data Center. Figure 2.4 shows the monthly precipitation recorded during the first three years after construction of the pavement. The largest monthly precipitation was recorded during the month of September 2004. This extremely high level of precipitation is the result of the storms generated by hurricane Ivan.

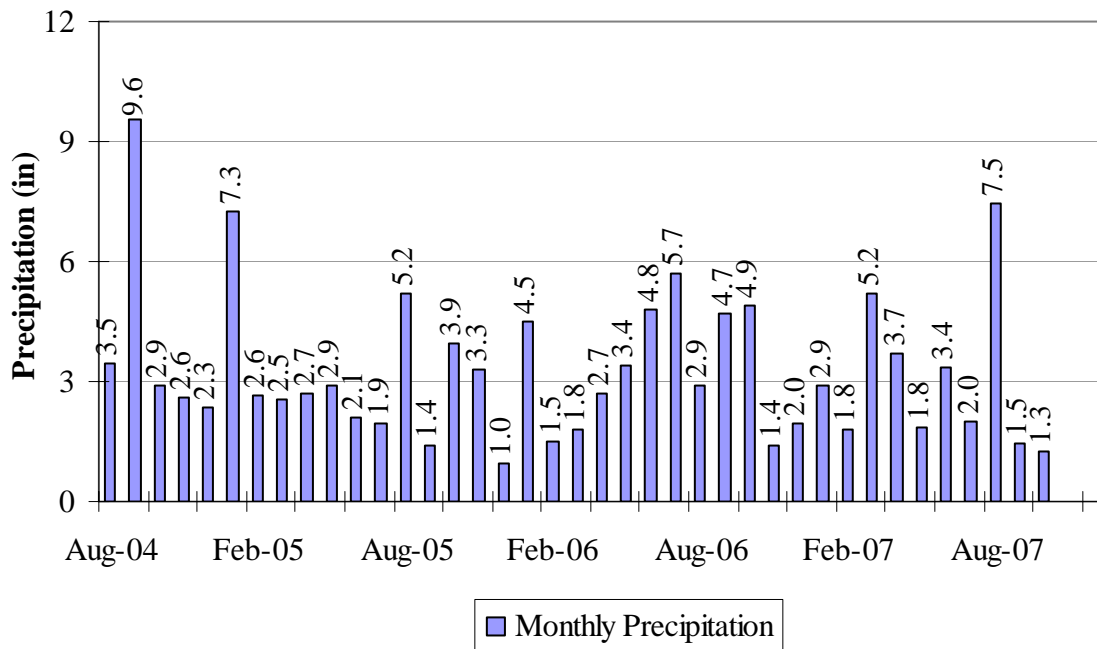


Figure 2.4. Monthly rainfall over the first three years after construction.

The frequency of occurrence, duration and intensity of the rain events also plays a role in the moisture content at the surface of the slab. The frequency of occurrence of rain events is presented in Table 2.1 and Figure 2.5 for the three-year period following construction of the pavement. The frequency of occurrence of each rain event fluctuates between 6 and 20 rain events per month. The largest number of rain events was recorded during the spring of 2005 and the lowest during the summer of 2007. The average monthly precipitation per event varies between 0.1 and 0.9 in.

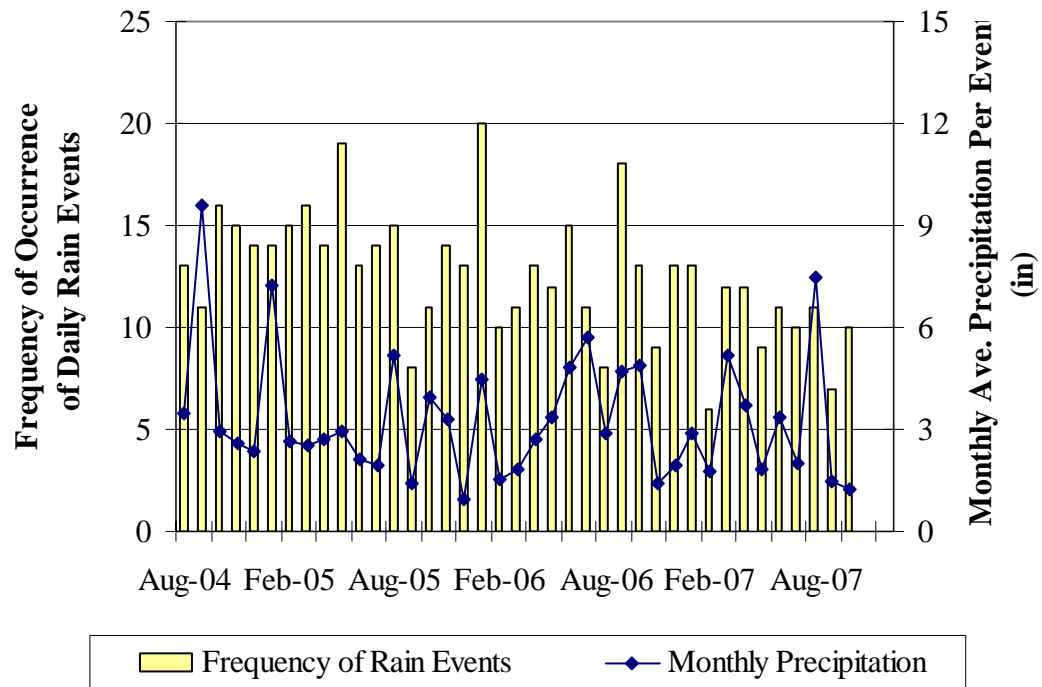


Figure 2.5. Frequency of occurrence of rain events and the monthly average precipitation per event between August 2004 and October 2007.

Table 2.1. Summary of frequency of occurrence of daily rain events.

Season	Month	Frequency of occurrence of daily rain events	Seasonal Totals
Summer 04	Aug-04	13	24
	Sep-04	11	
Fall 04	Oct-04	16	45
	Nov-04	15	
	Dec-04	14	
Winter 05	Jan-05	14	45
	Feb-05	15	
	Mar-05	16	
Spring 05	Apr-05	14	46
	May-05	19	
	Jun-05	13	
Summer 05	Jul-05	14	37
	Aug-05	15	
	Sep-05	8	
Fall 05	Oct-05	11	38
	Nov-05	14	
	Dec-05	13	
Winter 06	Jan-06	20	41
	Feb-06	10	
	Mar-06	11	
Spring 06	Apr-06	13	40
	May-06	12	
	Jun-06	15	
Summer 06	Jul-06	11	37
	Aug-06	8	
	Sep-06	18	
Fall 06	Oct-06	13	35
	Nov-06	9	
	Dec-06	13	
Winter 07	Jan-07	13	31
	Feb-07	6	
	Mar-07	12	
Spring 07	April-07	12	32
	May-07	9	
	Jun-07	11	
Summer 07	July-07	10	28
	Aug-07	11	
	Sep-07	7	
Fall 07	Oct-07	10	N/A

2.3.0. Measured Temperature Conditions in the Pavement Structure

In the previous section, seasonal variations in the ambient climatic conditions were presented. The influence of ambient conditions on pavement temperature is examined in this section.

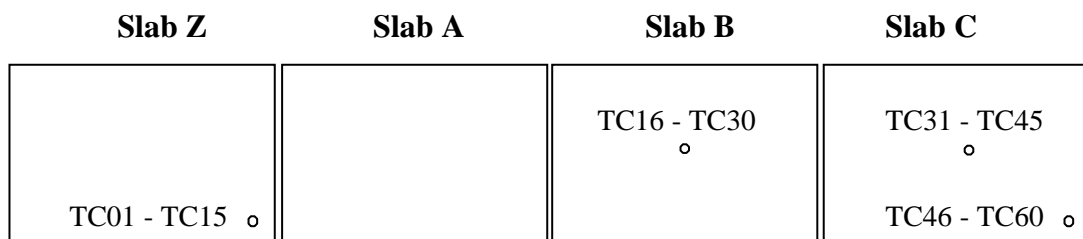
A brief summary of the instrumentation providing temperature measurements in the field is presented, followed by an analysis of the temperature measurements in the concrete slabs and underlying layers during the first three years after construction of the pavement.

2.3.1. Temperature Instrumentation

Type T thermocouples were installed to monitor the temperature throughout the pavement structure. A total of 60 thermocouples were installed at four locations in Cell 4, as follows:

- in the corners of Slabs Z and C, and
- at midpanel of Slabs B and C.

Locations of the thermocouples are shown in Figure 2.6. At each location, fifteen sensors were placed; seven in the Portland cement concrete slab, two in the asphalt treated permeable base, two in the 2A-subbase, three in the fill material and one in the subgrade. The approximate depths at which they were placed are provided in Figure 2.7. The thermocouples have been operational and recording temperature data along the various depths of the pavement layers since construction.



CELL 4

○ Thermocouples (TC)

Figure 2.6. Location of temperature sensors in Cell 4.

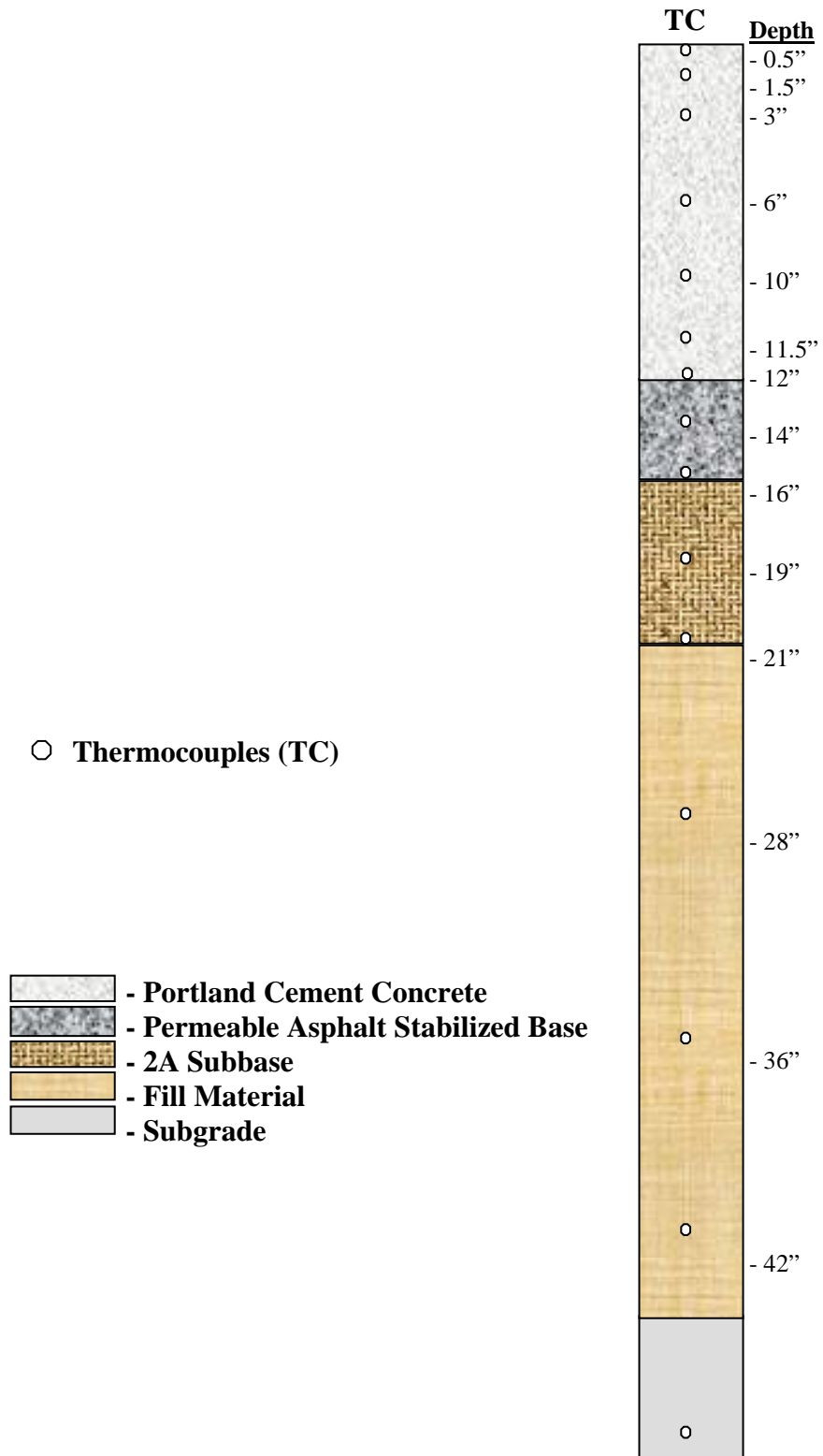


Figure 2.7. Depth of thermocouple sensors.

The original construction report took on the task of validating the measurements made by the four thermocouple trees. It was found that the temperature measurements recorded by the thermocouple trees placed at similar locations were similar [1]. As a result, the midpanel tree of Slab B and the corner tree of Slab Z will be used in this section to represent the temperature conditions at midpanel and the corner of the slab.

2.3.2. Temperature Measurements within the Concrete Slab

The effect of seasonal and daily environmental conditions on temperature measurements within the concrete is examined in this section. The average slab temperature will affect the stress state in the slab as a function of the set temperature. It will also dictate the restraint provided at the undoweled joints since the average slab temperature will influence the crack width at the joint.

The weighted average temperature of the concrete slab follows the same seasonal trend as the ambient temperature, as shown in Figure 2.8. This figure presents the weighted average temperature based on the thermocouple data collected at midpanel during the first three years after construction of the pavement. The lowest weighted average temperature reached 13°F and was recorded in February 2007 and the highest weighted average temperature reached 99°F and was recorded in August 2006. The temperatures recorded by the thermocouples located at the slab edge showed the same weighted average temperatures and similar seasonal trends.

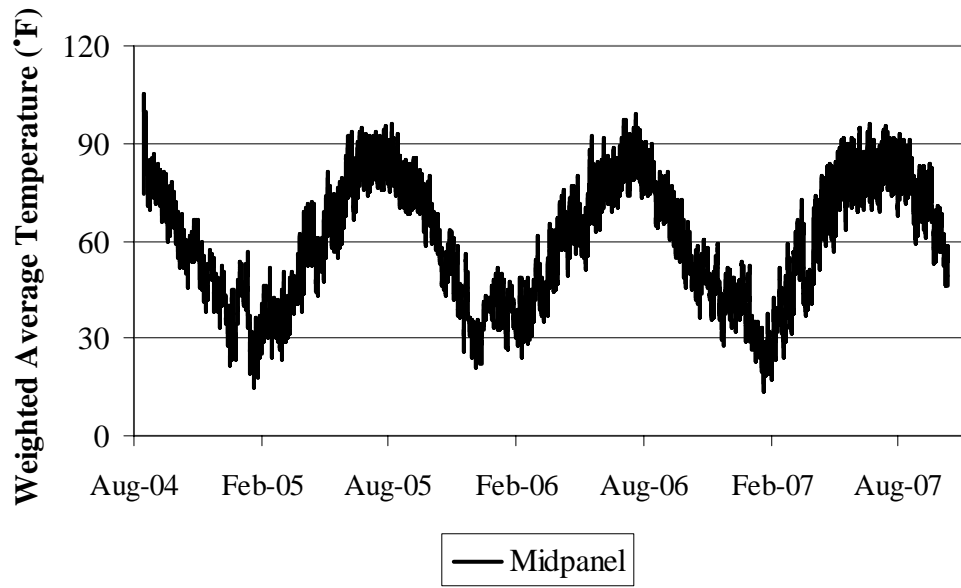


Figure 2.8. Weighted average temperature at slab midpanel during the three years following construction of the pavement.

During the first three years after construction of the pavement, the minimum weighted average temperature at midpanel varied between 15°F and 74°F and the maximum weighted average temperatures varied between 44°F and 104°F, confirming that the concrete slab experiences large fluctuations in temperature throughout the year. The maximum and minimum monthly ambient and concrete temperatures are both plotted in Figure 2.9.

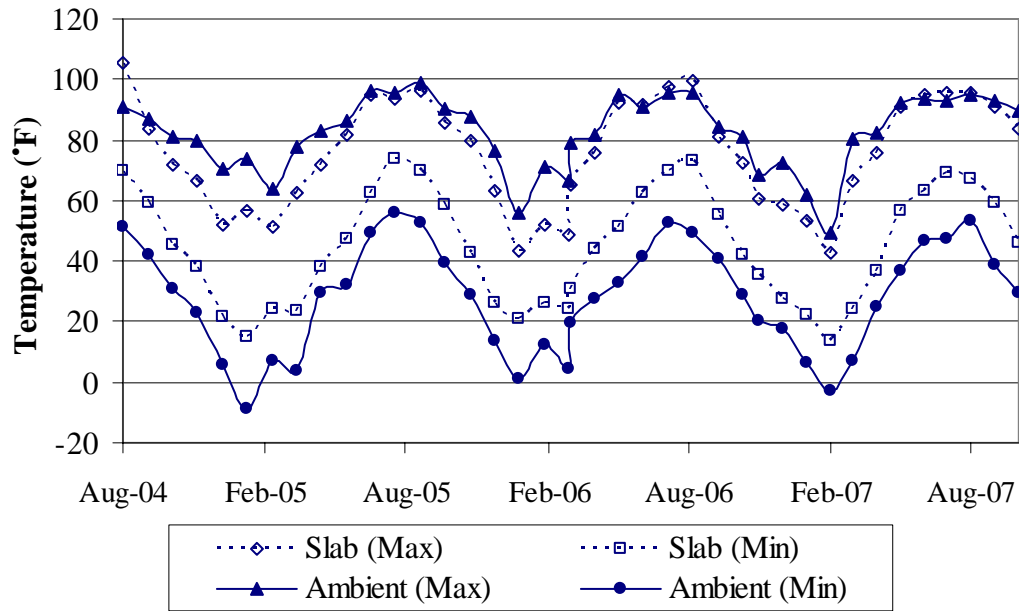


Figure 2.9. Monthly maximum and minimum ambient temperature and weighted average slab temperature.

Table 2.2 presents the monthly maximum and minimum temperature differences between the top and bottom of the slab, based on the temperatures measured during the first three years after construction of the pavement. It is important to characterize the temperature difference that develops throughout the life of the slab so the magnitude of curling in the slab can be characterized. Positive differences indicate that the top of the slab is at a higher temperature than the bottom of the slab. Temperature differences range between -16°F and 28°F during the summer, -17°F and 21°F during the fall, -17°F and 28°F during the winter and -18°F and 32°F during the spring. The monthly maximum negative temperature difference does not exhibit a large amount of variation during the different seasons and the value ranges between -12°F and -18°F throughout the three years. On the other hand, the monthly maximum positive temperature difference is highest during the spring and lowest during the fall, and the values range between 14°F and 32°F throughout the three-year period.

Table 2.2. Monthly maximum positive and negative temperature differences across the concrete slab.

Season	Month	Maximum Temperature Difference (°F) ²		Month	Maximum Temperature Difference (°F) ²	
		Positive	Negative		Positive	Negative
Summer				Jul-06	28	-14
	Aug-04 ¹	18	-16	Aug-06	26	-16
	Sep-04	20	-14	Sep-06	23	-12
Fall	Oct-04	19	-14	Oct-06	21	-16
	Nov-04	16	-14	Nov-06	18	-14
	Dec-04	15	-17	Dec-06	17	-14
Winter	Jan-05	15	-17	Jan-07	15	-15
	Feb-05	22	-14	Feb-07	19	-16
	Mar-05	27	-15	Mar-07	27	-14
Spring	Apr-05	31	-15	Apr-07	32	-18
	May-05	30	-13	May-07	31	-17
	Jun-05	31	-13	Jun-07	31	-14
Summer	Jul-05	26	-12	Jul-07	28	-16
	Aug-05	26	-14	Aug-07	27	-15
	Sep-05	23	-16	Sep-07	24	-16
Fall	Oct-05	21	-14	Oct-07	23	-15
	Nov-05	19	-15	---	---	---
	Dec-05	14	-14	---	---	---
Winter	Jan-06	19	-13	---	---	---
	Feb-06	22	-16	---	---	---
	Mar-06	28	-13	---	---	---
Spring	Apr-06	27	-14	---	---	---
	May-06	32	-16	---	---	---
	Jun-06	29	-15	---	---	---

¹ Temperature difference = $T_{\text{top of slab}} - T_{\text{bottom of slab}}$.

² Temperature difference = $T_{\text{top of slab}} - T_{\text{bottom of slab}}$.

The temperature distribution across the slab depth can also be characterized as a temperature gradient. The temperature distribution is typically nonlinear so it is useful to characterize this nonlinear distribution using an equivalent linear gradient. This method, developed by Janssen and Snyder (2000), accounts for nonlinear temperature gradients in concrete slabs, by estimating the moment about the bottom of the slab. The temperature moment can be converted into an equivalent linear gradient by determining the linear gradient that produces the same magnitude of temperature moment as the measured surface profile [3]. A positive gradient refers to when the top of the slab is warmer than the bottom, and likewise, a negative temperature gradient occurs when the top of the slab is cooler than

the bottom of the slab. Table 2.3 summarizes the monthly maximum positive and negative equivalent linear temperature gradients within the slab during the first three years after construction, based on the midpanel temperatures.

The equivalent linear temperature gradient varies between -1.41°F/in and 2.51°F/in throughout the three years. Based on the summary provided in Table 2.3, the largest gradients occur during the spring and the gradients that develop during the fall are relatively small.

Table 2.3. Monthly maximum positive and negative equivalent linear temperature gradients.

Season	Month	Max. Equivalent Linear Temp. Gradient ($^{\circ}\text{F/in}$)		Month	Max. Equivalent Linear Temp. Gradient ($^{\circ}\text{F/in}$)	
		Positive	Negative		Positive	Negative
Summer		---	---	Jul-06	2.16	-1.08
	Aug-04 ¹	1.40	-1.28	Aug-06	1.98	-1.25
	Sep-04	1.59	-1.08	Sep-06	1.78	-0.97
Fall	Oct-04	1.48	-1.14	Oct-06	1.63	-1.25
	Nov-04	1.29	-1.06	Nov-06	1.35	-1.11
	Dec-04	1.19	-1.35	Dec-06	1.29	-1.14
Winter	Jan-05	1.13	-1.39	Jan-07	1.12	-1.21
	Feb-05	1.74	-1.09	Feb-07	1.48	-1.31
	Mar-05	2.13	-1.16	Mar-07	2.12	-1.14
Spring	Apr-05	2.42	-1.15	Apr-07	2.51	-1.41
	May-05	2.33	-1.00	May-07	2.37	-1.37
	Jun-05	2.35	-0.99	Jun-07	2.40	-1.14
Summer	Jul-05	2.02	-0.97	Jul-07	2.16	-1.27
	Aug-05	1.99	-1.12	Aug-07	2.10	-1.18
	Sep-05	1.78	-1.28	Sep-07	1.87	-1.26
Fall	Oct-05	1.62	-1.08	Oct-07	1.79	-1.19
	Nov-05	1.45	-1.21	---	----	---
	Dec-05	1.06	-1.15	---	----	---
Winter	Jan-06	1.47	-1.04	---	----	---
	Feb-06	1.67	-1.29	---	----	---
	Mar-06	2.22	-1.07	---	----	---
Spring	Apr-06	2.11	-1.15	---	----	---
	May-06	2.47	-1.23	---	----	---
	Jun-06	2.23	-1.17	---	----	---

¹ The test section was constructed on August 16, 2004.

Daily fluctuations in the concrete temperature are examined herein. During the first three years after construction, the pavement structure is subjected to four climatic cycles.

The temperatures recorded by the sensors along the various depths of the slab are compared to the ambient temperatures for a one-week period representing each season. Figure 2.10 to Figure 2.13 present the daily temperature fluctuations at midpanel for one-week periods representing the different seasons along with the ambient temperatures during the same time periods. The figures show the climatic cycles during the first year after construction of the pavement. The remaining figures showing the climatic cycles during the second and third year after construction of the pavement are included in appendix A.

The ambient and concrete temperatures are similar during the spring and fall but the temperature fluctuations are a lot larger in the spring and therefore larger temperature gradients develop. The range of temperatures recorded during the spring and summer seasons is the highest compared to the remaining seasons. The lowest concrete temperatures are always higher than the lowest ambient temperatures; however, the concrete reaches temperatures that are higher than the highest ambient temperatures, during most of the seasons due to solar radiation.

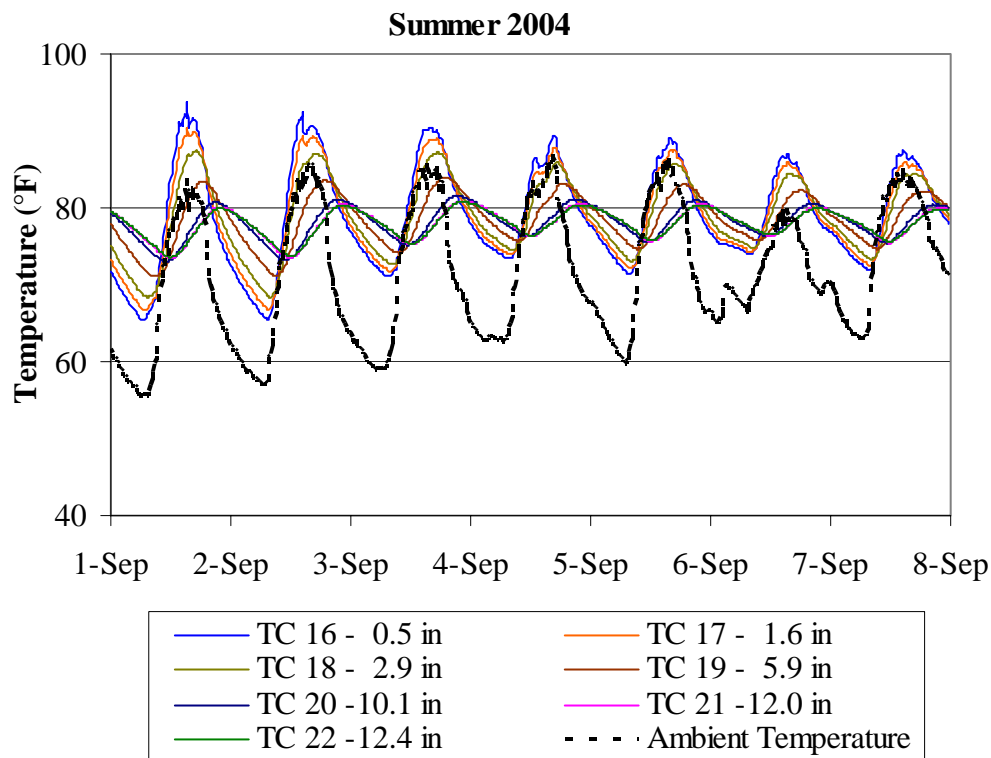


Figure 2.10. Midpanel concrete temperature for a one-week period representing the summer of 2004.

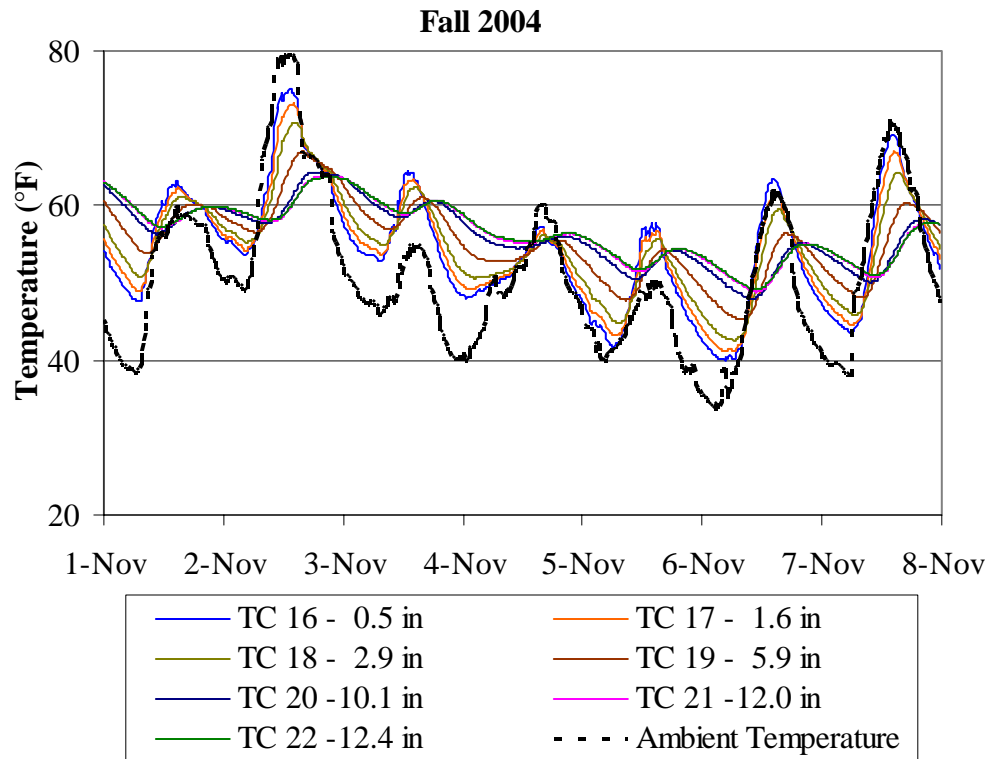


Figure 2.11. Midpanel concrete temperature for a one-week period representing the fall of 2004.

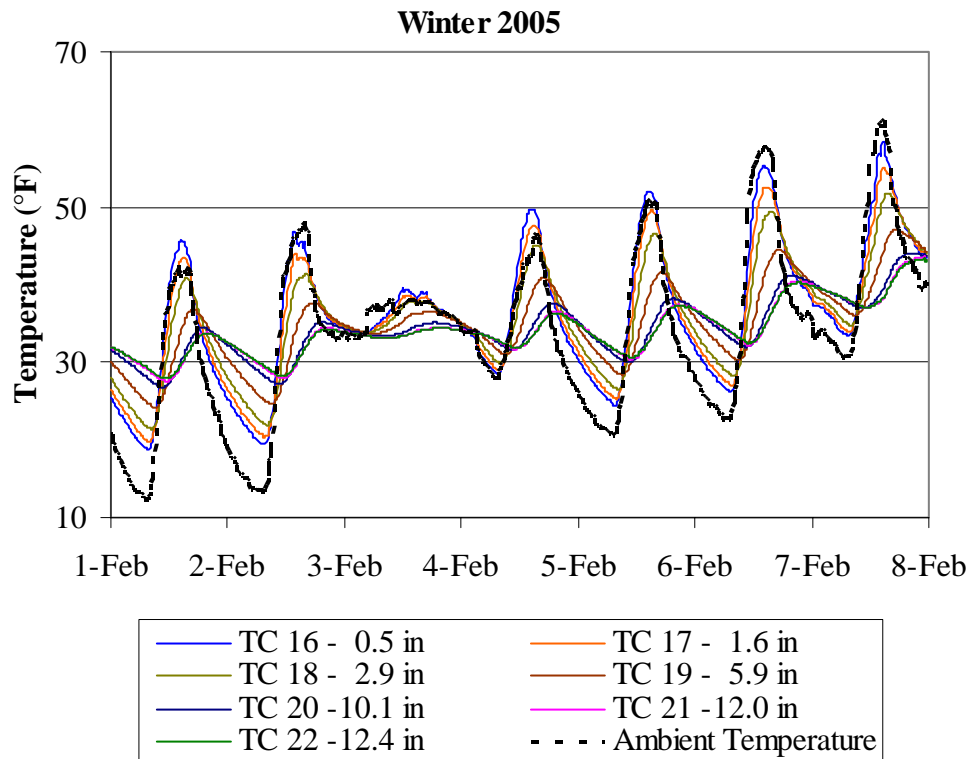


Figure 2.12. Midpanel concrete temperature for a one-week period representing the winter of 2005.

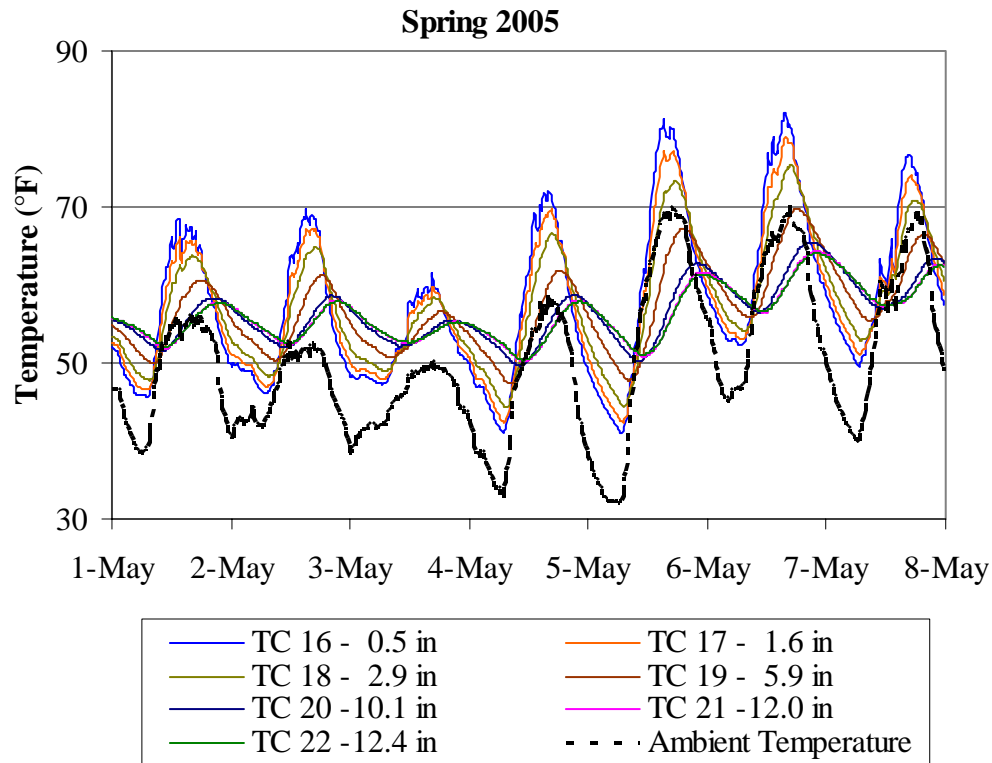


Figure 2.13. Midpanel concrete temperature for a one-week period representing the spring of 2005.

The temperatures recorded by the thermocouples located along the slab edge are also compared to the ambient temperatures. Figure 2.14 shows the daily temperature fluctuations at the slab edge for a one-week period representing the summer of 2004. The figures showing the climatic cycles during the first three years after construction of the pavement are presented in appendix A. The edge temperature follows the same daily trends as the midpanel temperature. Irrespective of the season, the midpanel exhibits a wider range of temperatures than the slab edge. It has been shown in a previous study that the midpanel temperatures are a better predictor of pavement response since it is more representative of the temperature profile in the majority of the mass of concrete [17].

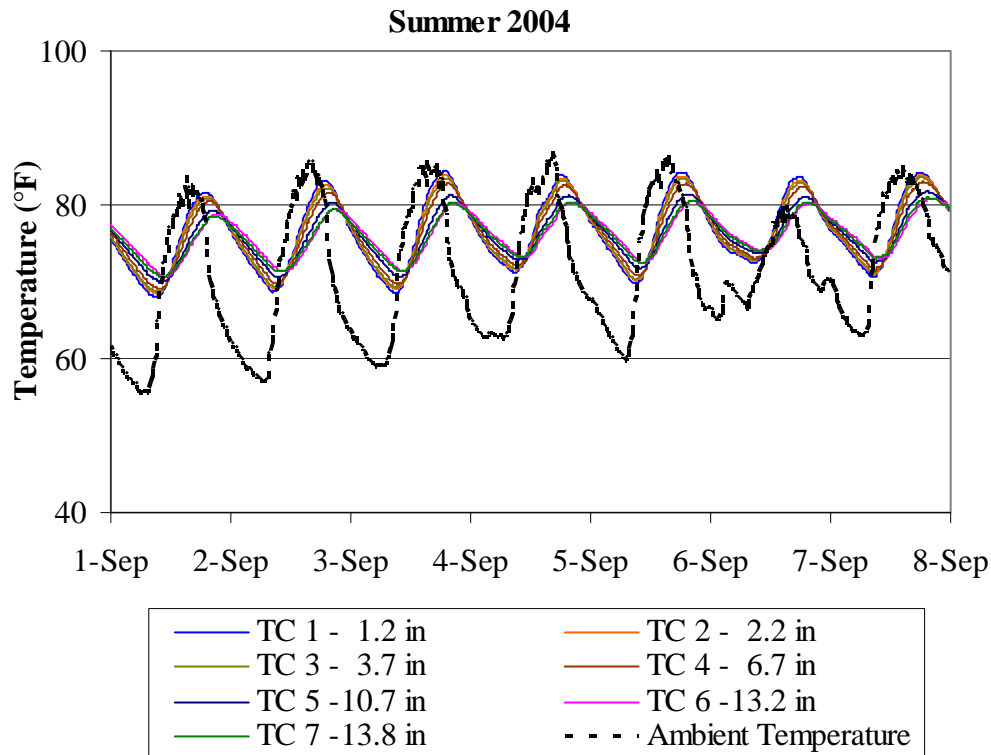


Figure 2.14. Edge concrete temperatures for a one-week period representing the summer 2004 season.

The equivalent linear temperature gradients are presented in Figure 2.15 through Figure 2.18 for the different climatic seasons. The figures confirm the previous statements that the range of temperature gradients is largest during the spring and summer, and smallest during the winter. The figures also show that the time of the day when no gradient is present changes depending on the ambient conditions. In addition, the duration of time when the concrete slab is subjected to positive temperature gradients is different depending on the climatic conditions. Positive gradients are present for a duration of approximately twelve hours per day during the summer and spring (noon to midnight), a duration of approximately nine hours per day during the fall (10:00 AM to 7:00 PM), and a duration of approximately six hours per day during the winter (noon to 6:00 PM).

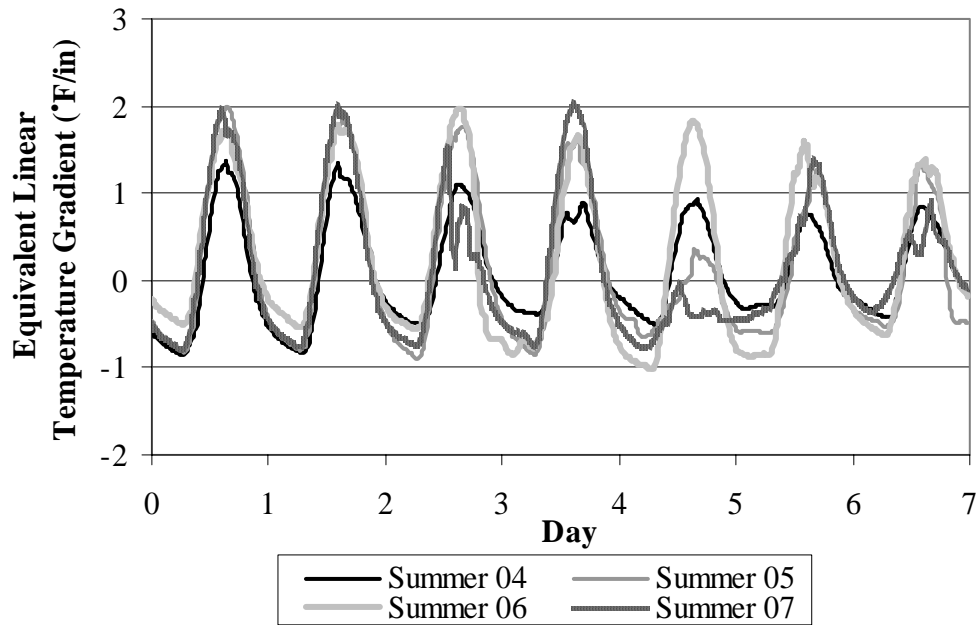


Figure 2.15. Midpanel equivalent linear temperature gradients for one-week periods representing the summer.

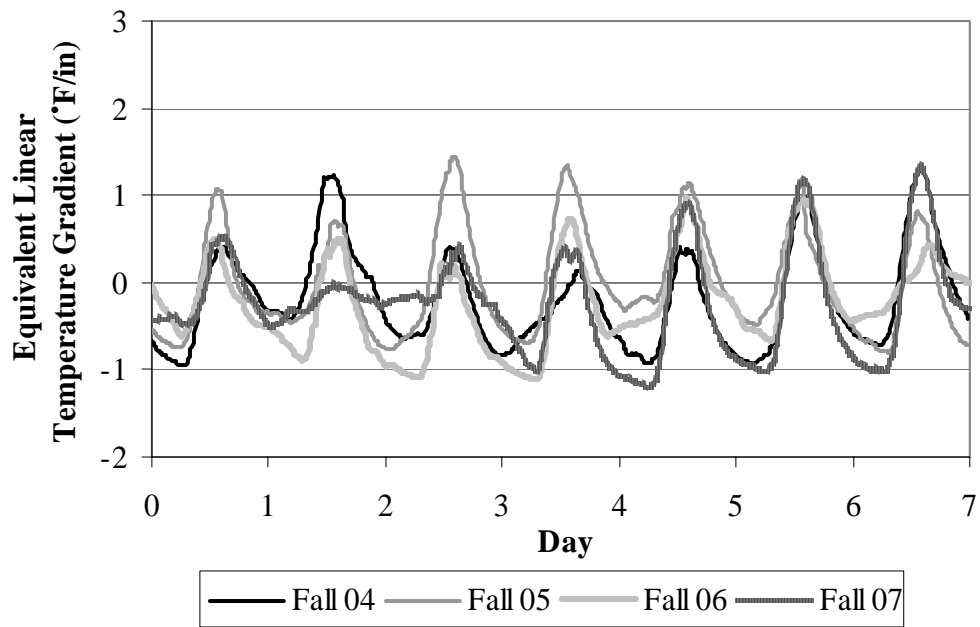


Figure 2.16. Midpanel equivalent linear temperature gradients for one-week periods representing the fall.

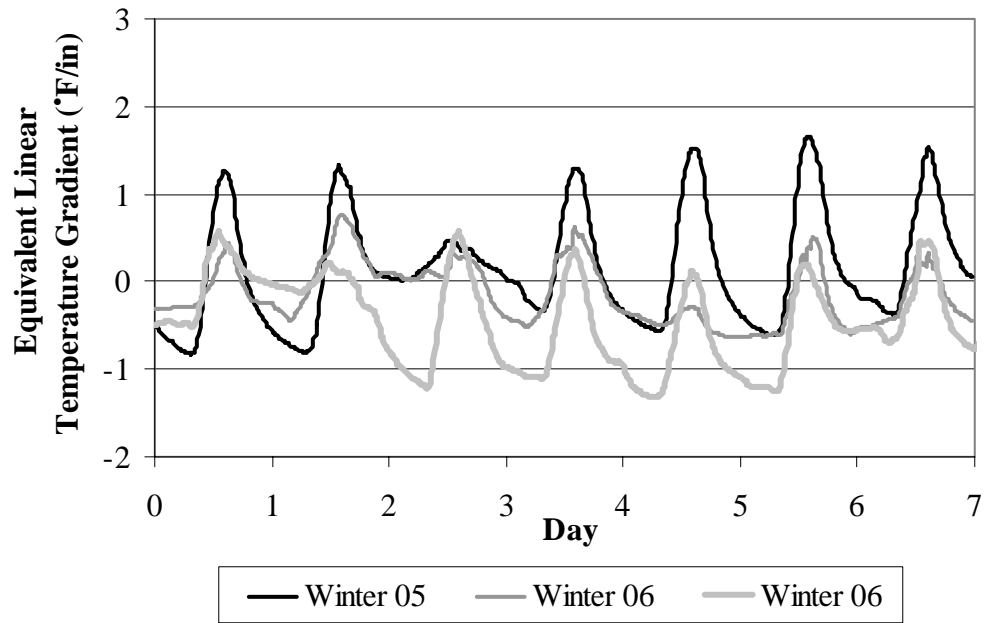


Figure 2.17. Midpanel equivalent linear temperature gradients for one-week periods representing the winter.

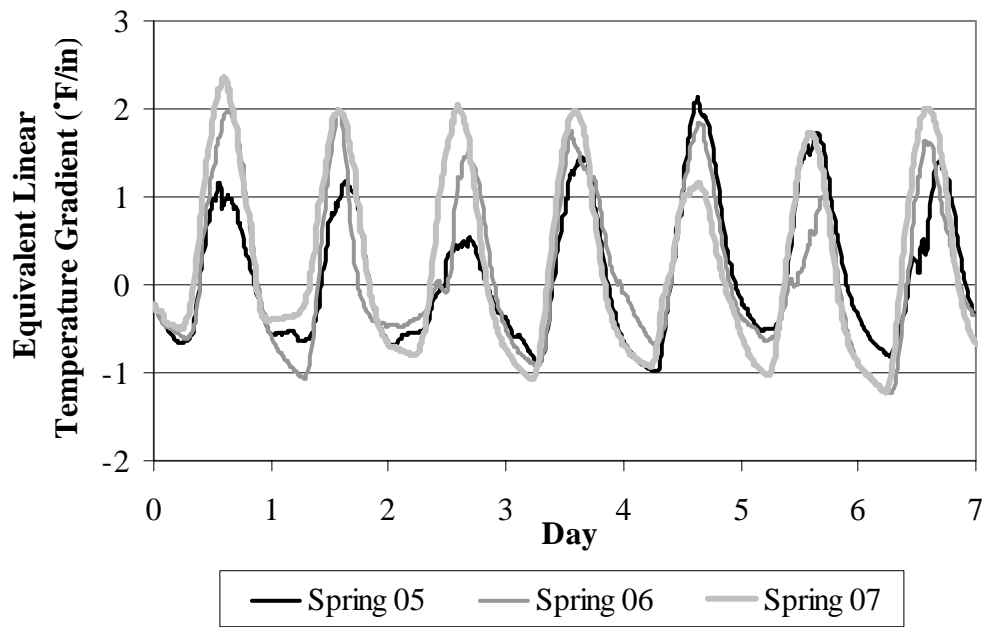


Figure 2.18. Midpanel equivalent linear temperature gradients for one-week periods representing the spring.

2.3.3. Temperature Measurements within the Underlying Layers

This section presents the temperature measurements within the underlying layers throughout the first three years after construction. Determination of temperature in the underlying layers is necessary to characterize the temperature variations in the overall pavement structure and provides insight into the stiffness and support of the underlying layers. As previously discussed, the Smart Pavement consists of concrete placed on an asphalt treated permeable base (ATPB) layer, which is placed on a granular layer. The variation in temperatures in the ATPB layer is discussed first.

The stiffness of the underlying layers is highly influenced by the stiffness of the ATPB and the stiffness of the ATPB is largely a function of the temperature of the ATPB throughout the year. Figure 2.19 shows the variation in the temperature in the ATPB during the first three years after construction of the pavement. The mid-depth temperature of the ATPB follows the same trend as the ambient climatic temperatures (reference 2.2.0). The ATPB temperature ranged between 29°F and 92°F with an average of 41°F during the winter, 52°F during the fall, 63°F during the spring and 78°F during the summer.

The coldest temperatures were recorded during the periods of December 16 to 29, 2004, January 25 to February 6, 2005, December 14 to 22, 2005, and January 29 to February 20, 2007. During these periods, the thermocouples embedded in the ATPB recorded temperatures at or below the freezing temperature (32°F). This indicates that during these periods, the ATPB was frozen down to a depth of fourteen in below the pavement surface.

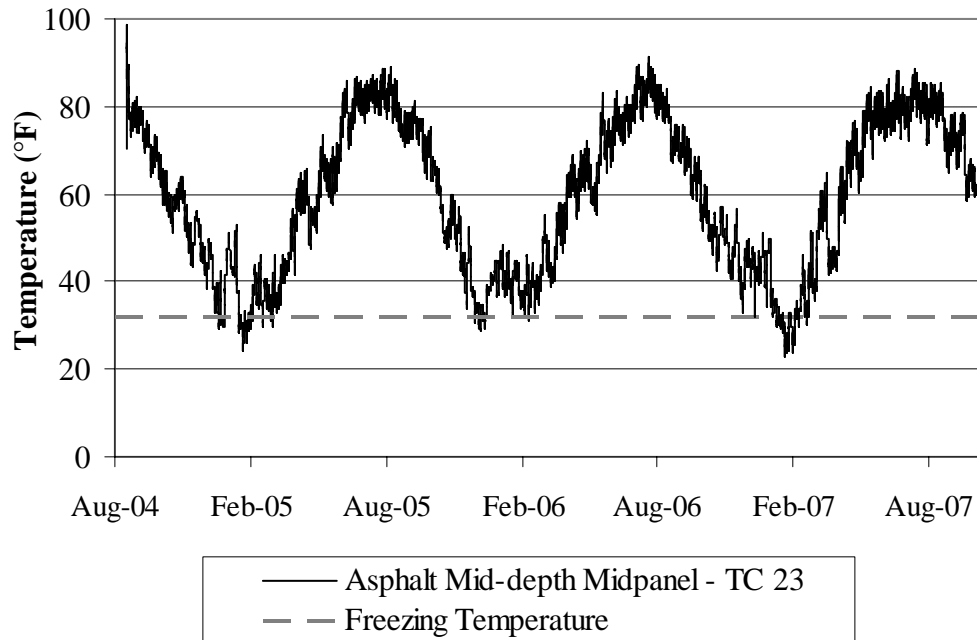


Figure 2.19. Asphalt temperatures at mid-depth variations with time.

The temperature variations in the underlying layers during the first three years after construction are presented in Figure 2.20. The coldest temperature was recorded during the periods of January 25 to February 6, 2005 and January 29 to February 20, 2007. During these periods, the thermocouples within the 2A-subbase recorded temperatures at or close to freezing, implying that the pavement structure was frozen to a depth of 21 in. Therefore, the frost depth for this pavement structure in the winter can be estimated to be 21 in or 1.75 feet.

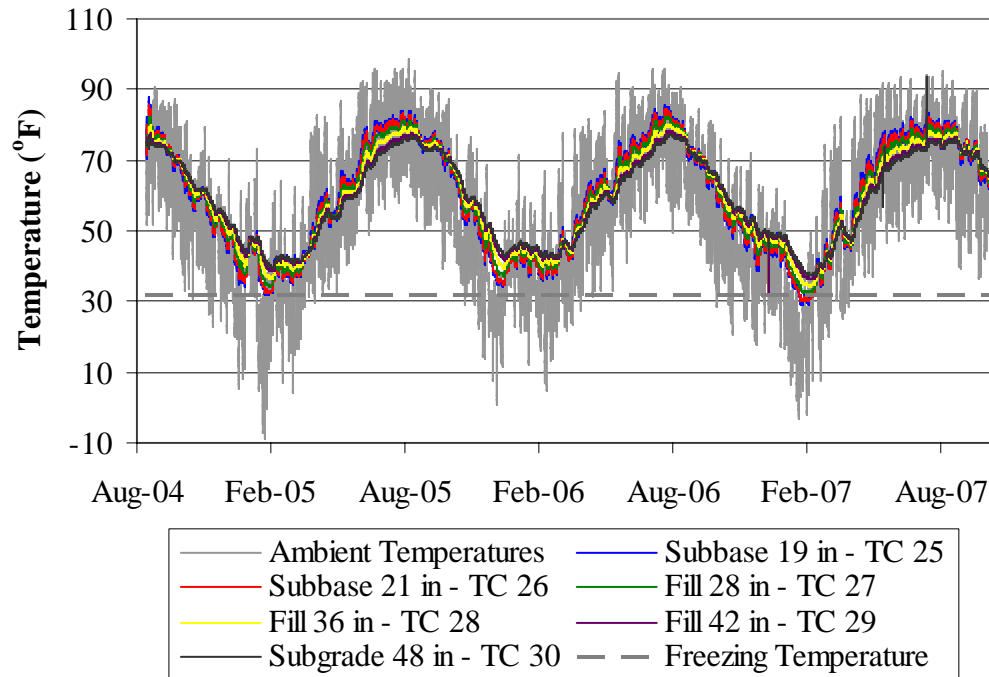


Figure 2.20. Variation in temperature within the 2A-subbase and subgrade layers.

2.3.4. Summary

The weighted average temperature within the pavement structure indicated that the pavement experiences large fluctuations in temperature throughout the year. Both seasonal and daily climatic cycles affect the pavement temperature. Irrespective of the season, the slab is subjected to alternating cycles of negative and positive temperature gradients on a daily basis. The equivalent linear temperature gradients varied between $-1.41^{\circ}\text{F}/\text{in}$ and $2.51^{\circ}\text{F}/\text{in}$ throughout the three years after construction. In addition, the midpanel exhibited more variation in temperature than the slab edge.

The pavement structure is subjected to four different climatic cycles representing the four seasons of the year. Throughout the year, the weighted average concrete temperature follows the same trend as the ambient temperature; however, the ambient temperature experiences a wider range of values than the concrete temperature.

2.4.0. Measured Moisture Conditions in the Pavement Structure

As previously discussed, moisture in the pavement structure is another major factor that is known to affect pavement performance. This section presents the variation in

moisture content within the concrete slab and underlying layers during the first three years after construction. A brief summary of the instrumentation providing moisture measurements in the field is presented first, followed by an analysis of the moisture measurements in the concrete slab and underlying layers during the first three years after construction of the pavement.

2.4.1. Moisture Instrumentation

The Sensirion SHT75 relative humidity and temperature sensors were installed at various depths in the PCC layer to capture the variation of moisture within the slab. They were installed at four locations at the restrained slab corners and midslabs. A total of 24 moisture sensors were installed at four locations as shown in Figure 2.21 and Figure 2.22.

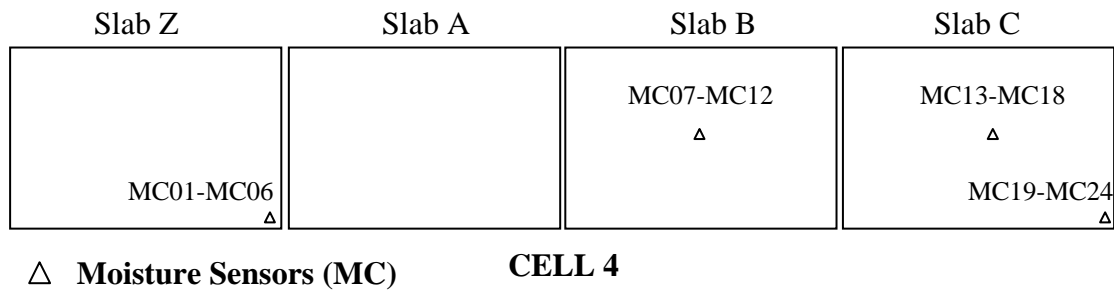


Figure 2.21. Location of concrete moisture sensors in the restrained slabs (Cell 4).

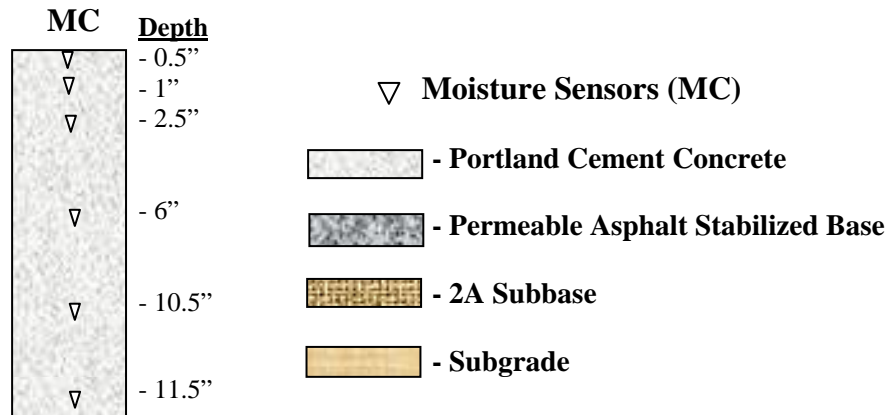
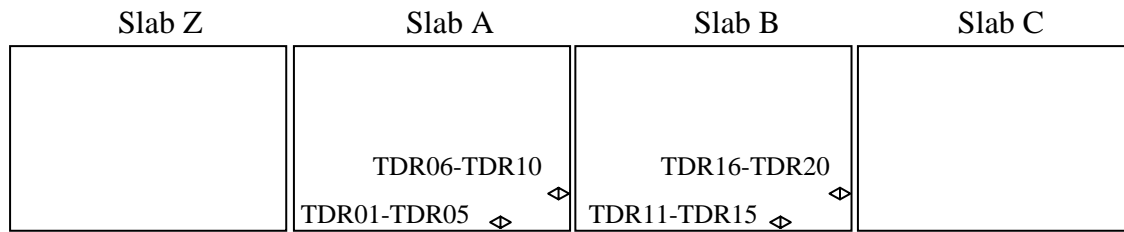


Figure 2.22. Depths of concrete moisture sensors in the restrained slabs (Cell 4).

A TDR system from Campbell Scientific was used to log moisture content and frost depth data within the subgrade and subbase. The sixteen CS605L wave guide probes were placed at various depths in the wheelpath and along the longitudinal slab edge of the restrained slabs, as shown in Figure 2.23 and Figure 2.24.



CELL 4

◊ Time Domain Reflectometry

Figure 2.23. Location of moisture sensors within the granular layers in Cell 4.

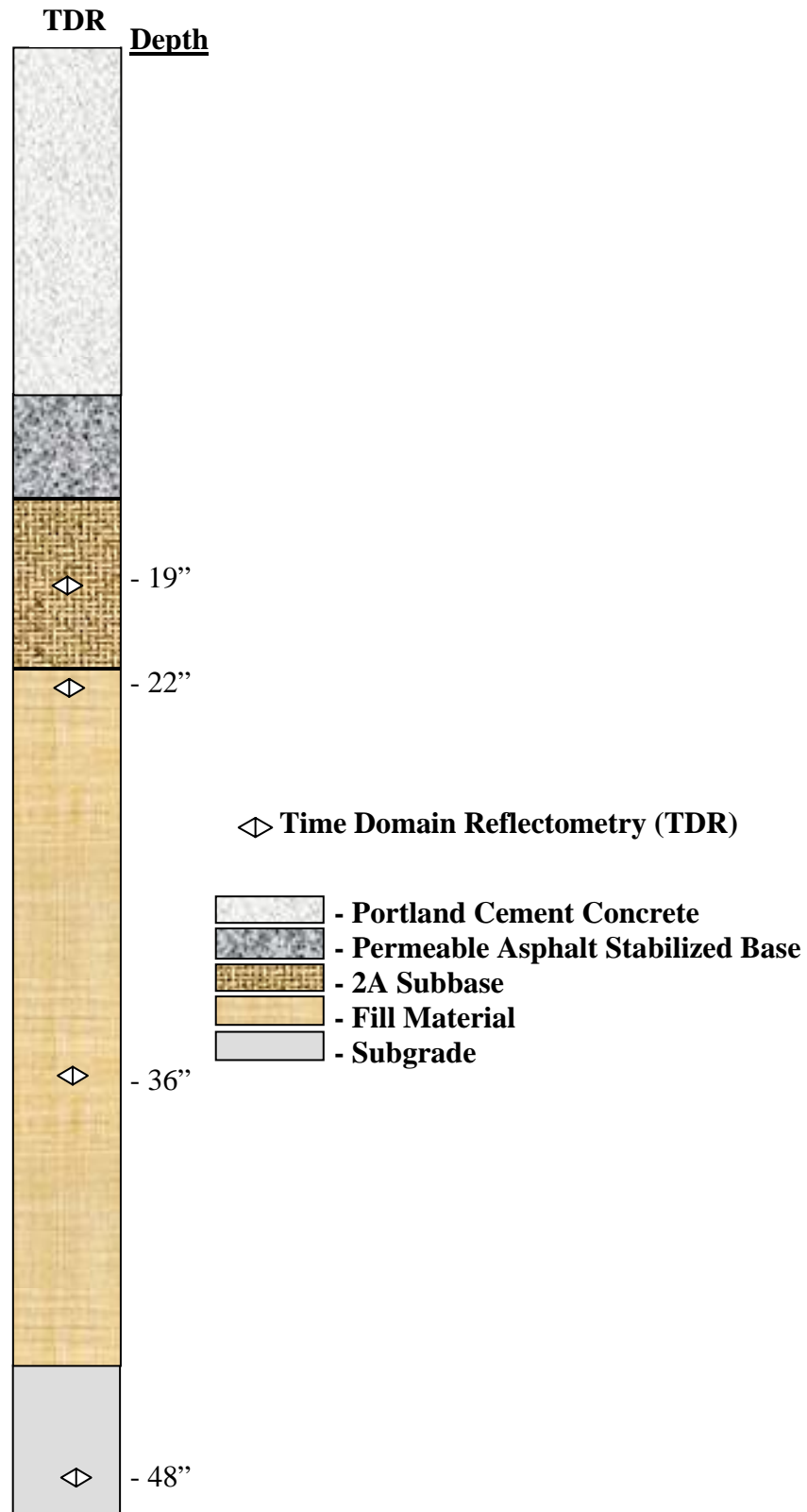


Figure 2.24. Depths of moisture sensors within the granular layers in Cell 4.

2.4.2. Moisture Measurements within the Concrete Slabs

The variation of moisture content within the concrete follows seasonal trends, as shown in Figure 2.25 and Figure 2.26. These figures present the concrete moisture content based on data collected from the slab midpanel and edge during the first three years after construction of the pavement. The figures show that there are some gaps in the collected data, which are due to communication problems with the data acquisition system.

At both locations, moisture content increases with increasing slab depth. Additionally, moisture content follows the same seasonal trends irrespective of the location of the sensor within the concrete slab. At midpanel and the slab edge, the moisture content of the concrete stabilized three to four weeks after construction and remained relatively constant throughout the remainder of the fall season. The moisture content stabilized to average values of 80 percent in the top two in, 95 percent at mid-depth and 100 percent in the bottom half of the slab. The moisture content reached a minimum during the winter, and increased there after reaching a maximum during the spring. The moisture content followed the same seasonal trends for the first three years after construction; however, moisture content during the second year was lower than the first year, and moisture content during the third year was lower than the second year. This indicates that the moisture content is decreasing with time.

At midpanel, only two sensors were operational during the three year period. At a depth of 0.7-in, moisture content varied between 73 and 81 percent during the first year, 57 and 66 percent during the second year, and 54 and 63 percent during the third year. At a depth of 1.0-in, moisture content varied between 87 and 93 percent during the first year, 62 and 74 percent during the second year, and 60 and 68 percent the third year.

As Figure 2.26 shows, moisture content at the slab edge is larger than midpanel. At this location, four sensors were operational; however two of the sensors at the bottom of the slab recorded relative humidities higher than 100 percent a majority of the time. This may be due to condensation along the sensor tips. Throughout the three year analysis period, the moisture content varied between 71 and 86 percent at a depth of 1.6-in, between 75 and 100 at 6.6-in and below 10.5 in the concrete slab remained saturated.

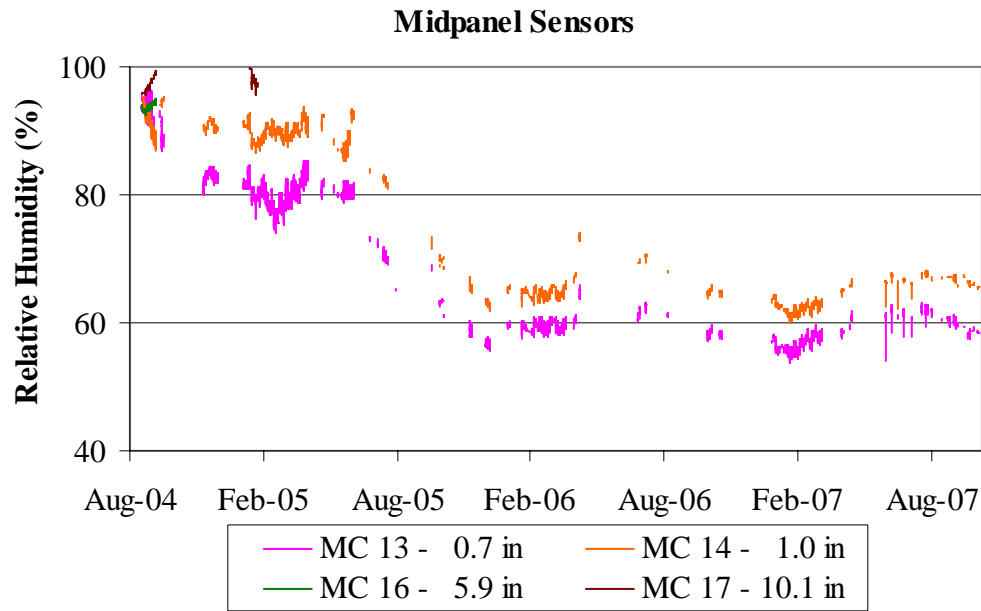


Figure 2.25. Concrete relative humidity at midpanel during the first three years after construction of the pavement.

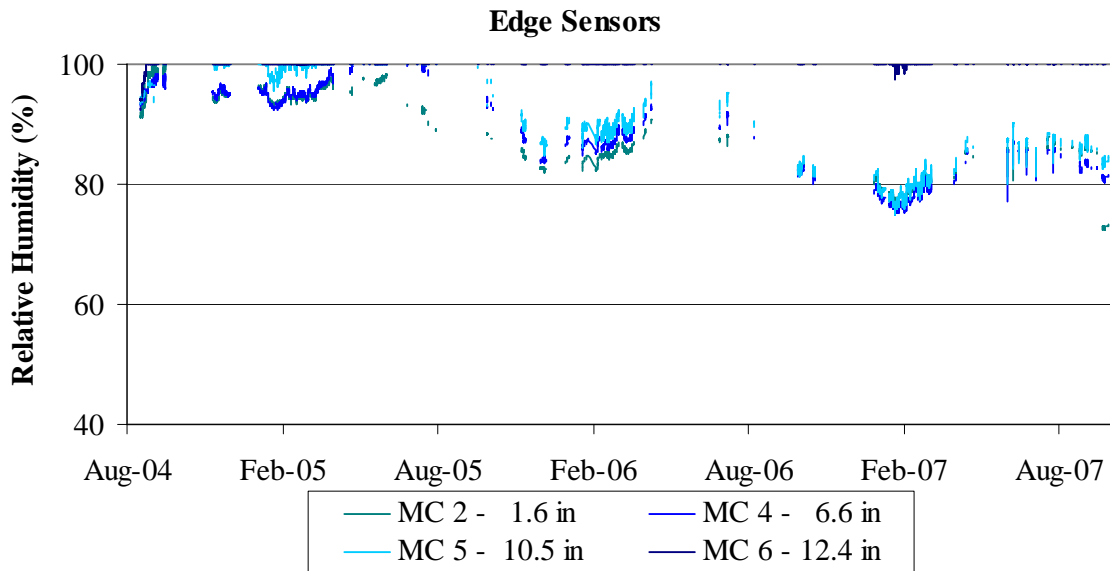


Figure 2.26. Concrete relative humidity at slab edge during the first three years after construction of the pavement.

The ambient climatic factors studied include variations in ambient relative humidity and the frequency of occurrence of precipitation events. In this analysis, the moisture content

measured within the top two in of the slabs was considered, since moisture content at deeper portions of the slabs was not affected by changes in ambient climatic conditions.

During the first three years after construction, the ambient relative humidity ranged between 20 and 100 percent with an average range of 60 to 80 percent. The minimum and maximum concrete moisture content was compared to the ambient relative humidity and is presented in Figure 2.27. As would be expected, the concrete moisture content in the top two in of the slab is not significantly affected by variations in the ambient relative humidity.

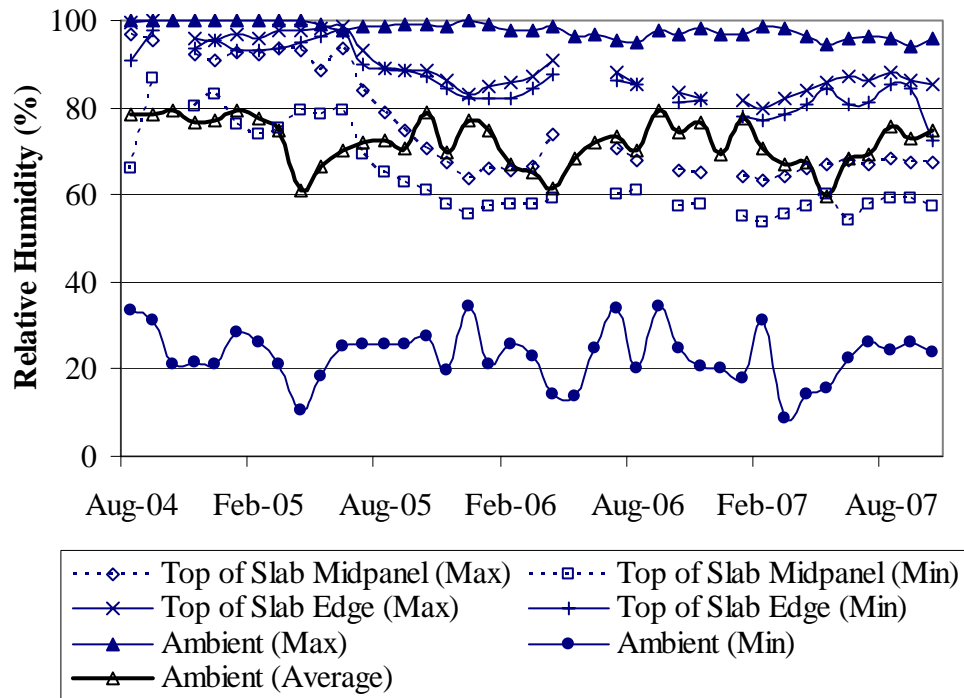


Figure 2.27. Monthly maximum and minimum concrete relative humidity at midpanel and slab edge in comparison to ambient relative humidity.

During the first three years after pavement construction, the seasonal average rainfall precipitation varied between 2.7 and 4.4 in per month. The highest precipitation was recorded during the summer and the lowest during the fall. The frequency of occurrence of the rain events does not vary much throughout the three years. During the summer, a monthly average of twelve daily rain events was recorded, compared to a monthly average of thirteen daily rain events during the remaining seasons. The minimum and maximum concrete moisture content was compared to monthly precipitation and the frequency of

occurrence of daily rain events and is presented in Figure 2.28 and Figure 2.29. These graphs show the moisture content in the upper portion of the slab increases during the spring and summer season. The graphs do not show a clear relationship between monthly precipitation or frequency of rain events and the moisture content in the upper portion of the slab.

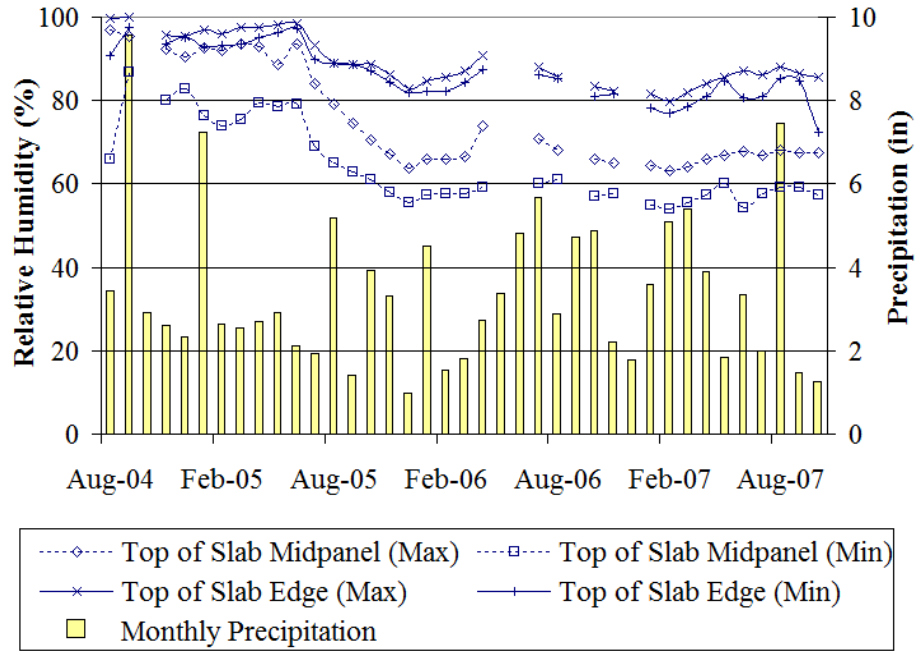


Figure 2.28. Monthly maximum and minimum concrete relative humidity at midpanel and slab edge in comparison to monthly precipitation.

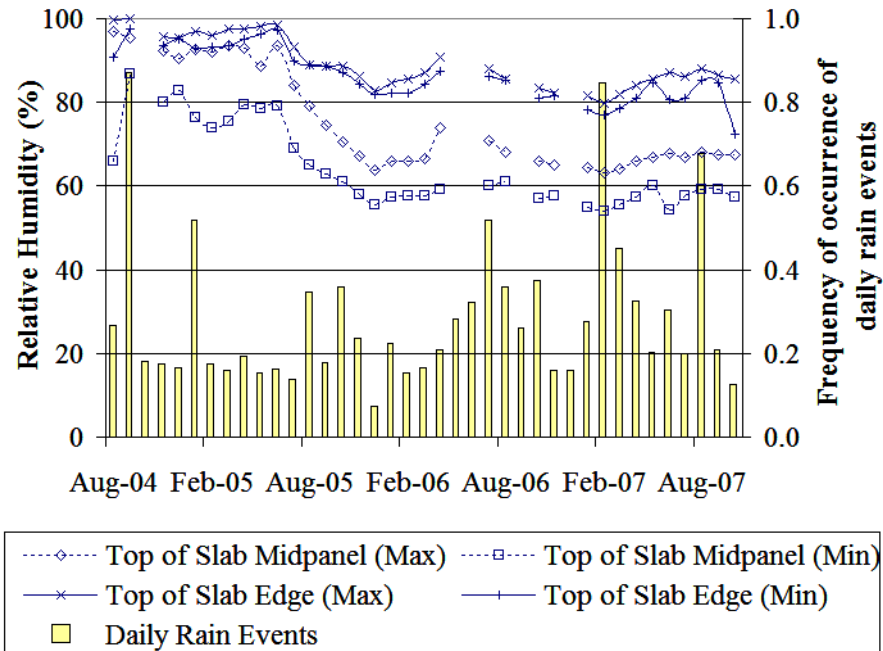


Figure 2.29. Monthly maximum and minimum concrete relative humidity at midpanel and slab edge in comparison to frequency of occurrence of daily rain events.

According to the previous analyses, moisture content in the top two in of the concrete slab varies seasonally. However, a comparison between concrete moisture content and the ambient climatic conditions showed no correlation. Therefore, seasonal variations in concrete moisture content will be investigated to explore a possible correlation between the concrete moisture content and climatic conditions. Since the effect of rainfall on concrete moisture is not instantaneous, an analysis was performed while considering a time period of ten days. A full set of figures showing the concrete moisture content during 10-day periods representing seasonal variations for the first three years after construction are included in appendix A.

Figure 2.30 and Figure 2.31 show the daily moisture content at midpanel and slab edge for a 10-day period representing the summer of 2004, shortly after construction. The vertical dashed lines in the figures represent points in time when rain events exceeding 0.1 in occurred. At both locations, the moisture content is relatively constant, with slight variations in the top portion of the slab. In the top portion of the slab, the moisture content varied between 90 and 95 percent at midpanel and between 85 and 90 percent at the slab edge.

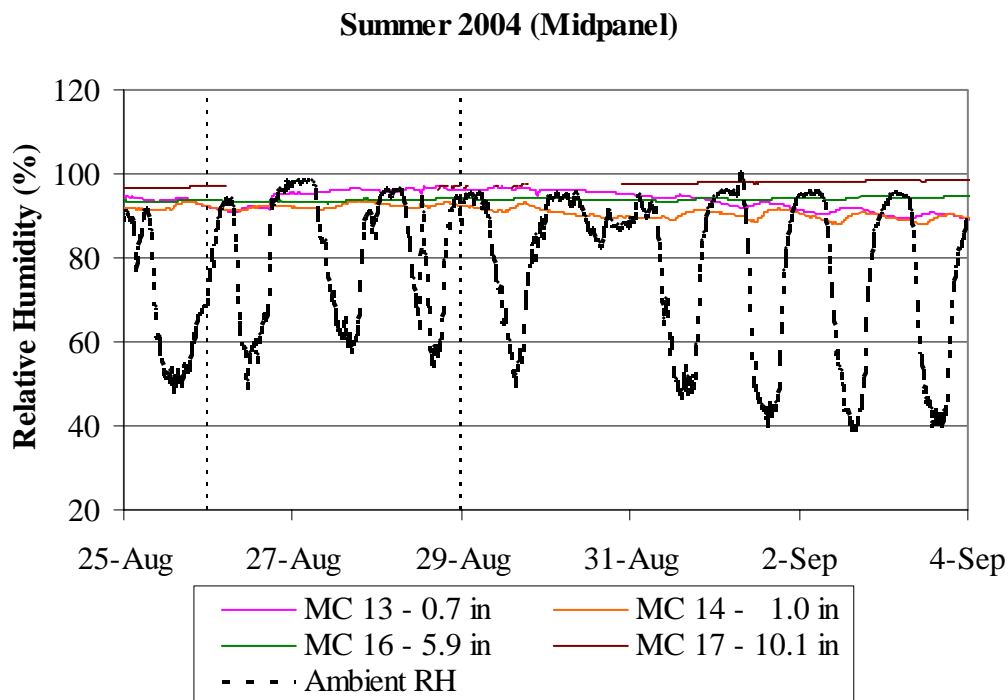


Figure 2.30. Midpanel concrete relative humidity for a ten-day period representing the summer 2004 season.

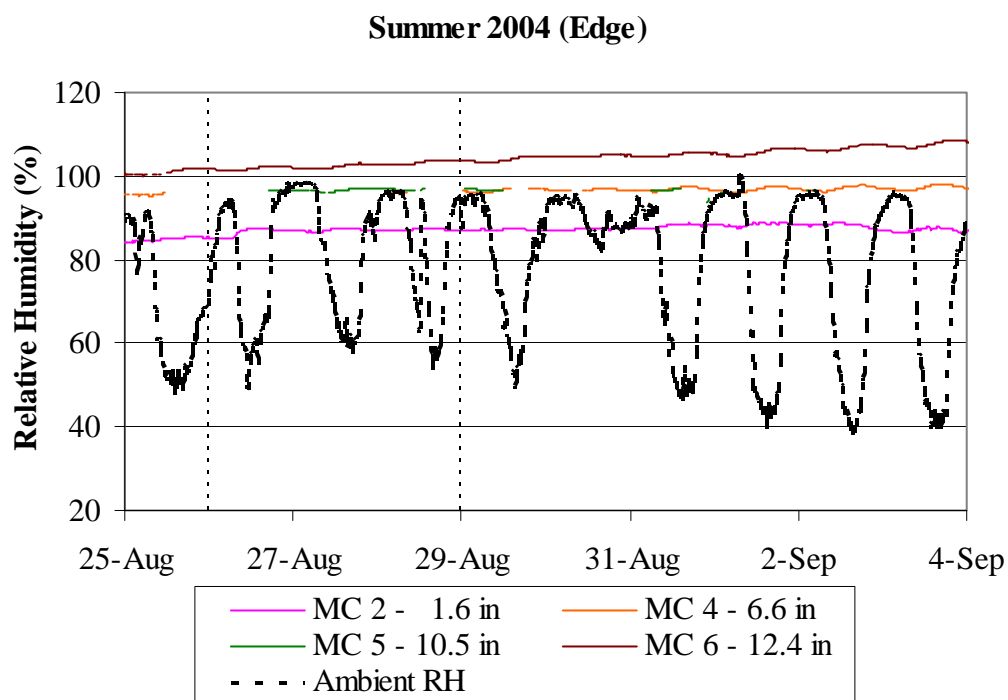


Figure 2.31. Edge concrete relative humidity for a ten-day period representing the summer 2004 season.

Figure 2.32 and Figure 2.33 present the daily relative humidity at midpanel and slab edge for a 10-day period representing the fall of 2004 just a couple of months after construction. The midpanel sensors show variations between 80 and 92 percent, which is a relatively large difference considering that the difference in depth between the two sensors is only 0.3 in. There is no indication of malfunction or erroneous readings on either of the two sensors, and therefore, both will be used as representative of the moisture at midpanel. These readings further confirm that moisture content can vary significantly in the top two in of the slab. At the slab edge, moisture content is approximately 82 percent at the top of slab, 95 percent at mid-depth, and it is saturated at the bottom.

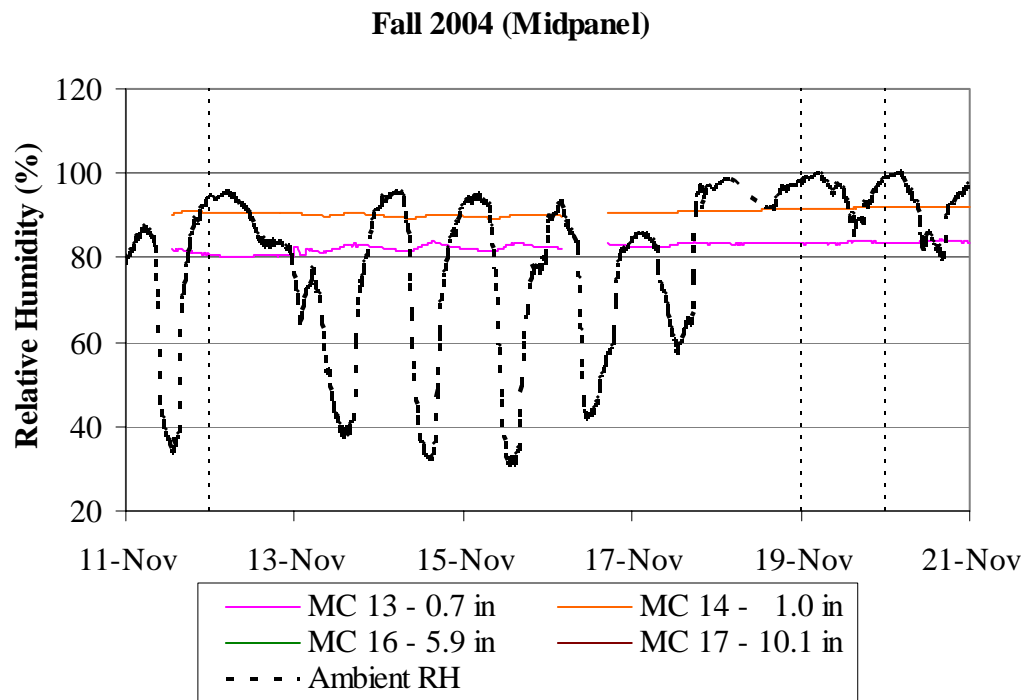


Figure 2.32. Midpanel concrete relative humidity for a ten-day period representing the fall 2004 season.

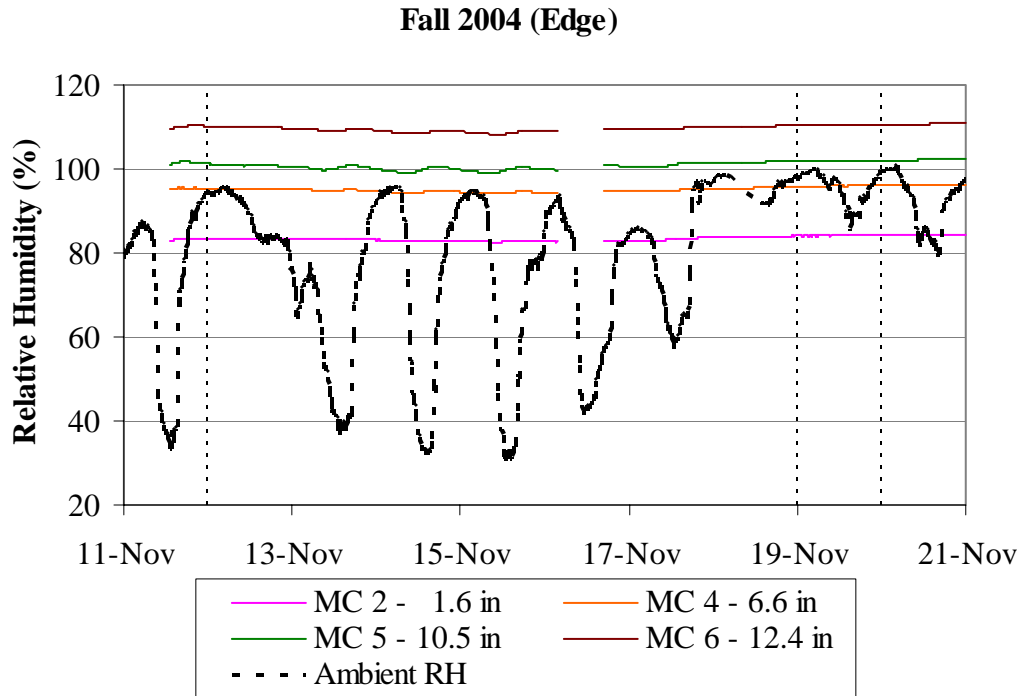


Figure 2.33. Edge concrete relative humidity for a ten-day period representing the fall 2004 season.

Figure 2.34 and Figure 2.35 present the daily relative humidity at midpanel and slab edge for a 10-day period representing the winter of 2005. Similarly to the data collected in the previous fall season, only two top sensors were operational at midpanel. These sensors measured variations between 78 and 92 percent, which is a relatively large difference across a concrete depth of 0.3 in. At the slab edge, moisture content is approximately 83 percent at the top of slab, 95 percent at mid-depth, and it is saturated at the bottom. As Figure 2.35 shows, the moisture concrete in the slab increases slightly after precipitation events with the increase being more pronounced at the top of the slab and not substantially affected at mid-depth.

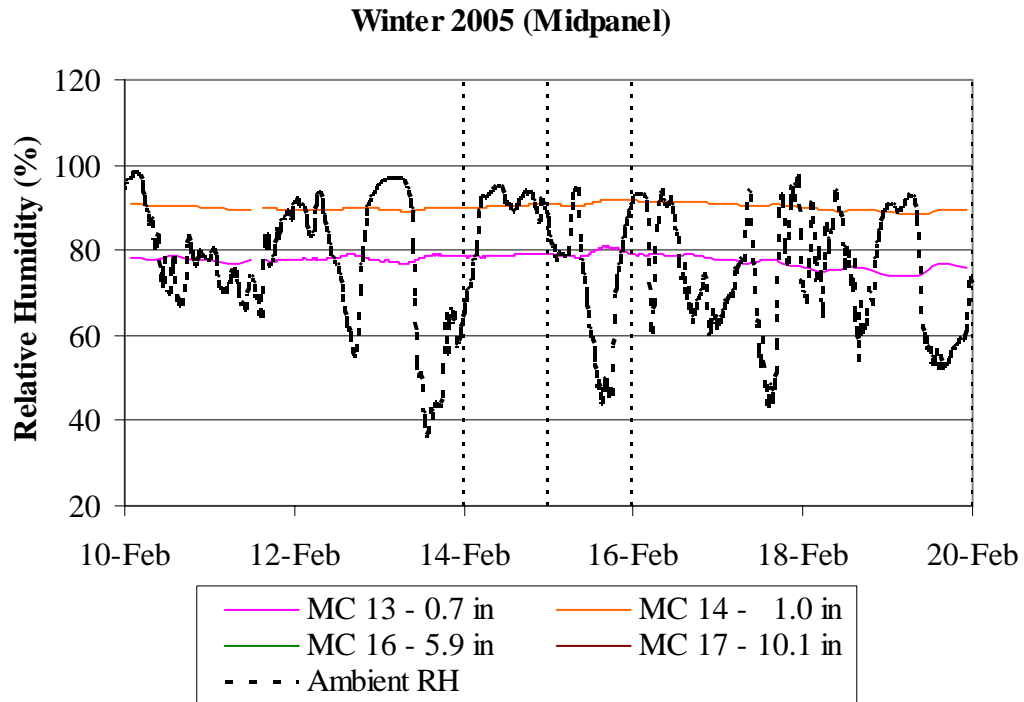


Figure 2.34. Midpanel concrete relative humidity for a ten-day period representing the winter 2005 season.

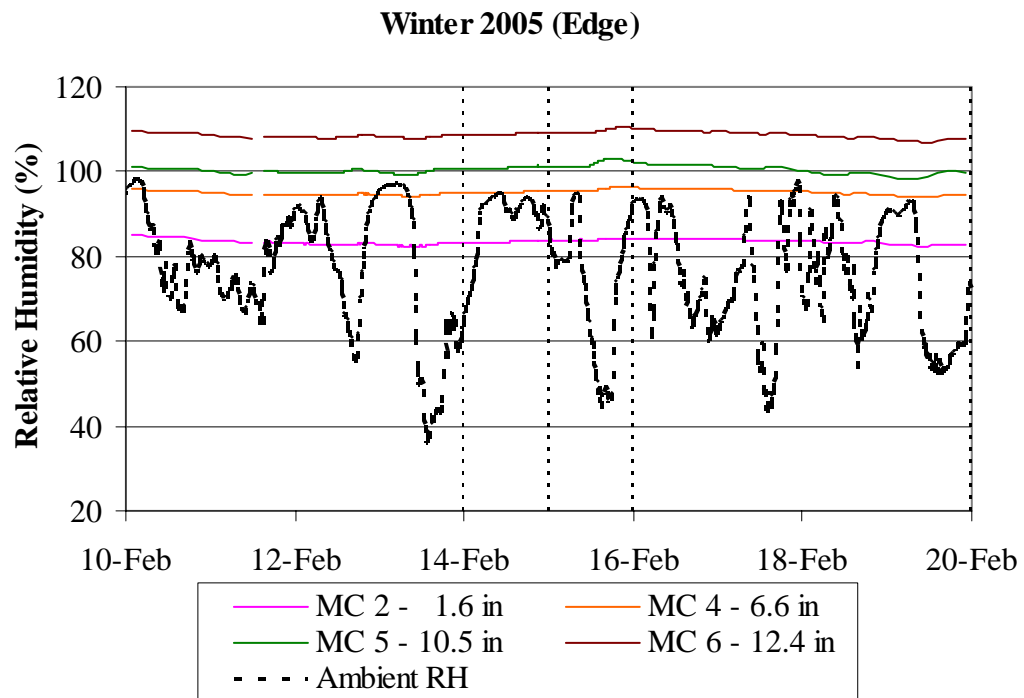


Figure 2.35. Edge concrete relative humidity for a ten-day period representing the winter 2005 season.

Figure 2.36 and Figure 2.37 show the daily relative humidity at midpanel and slab edge for a 10-day period representing the spring of 2005. The observed trends are similar to the previous seasons. The moisture content at midpanel varied between 81 and 92 percent. At the slab edge, the relative humidity at the top of slab is 83 percent, at mid-depth, it is 97 percent, and the bottom of the slab is saturated.

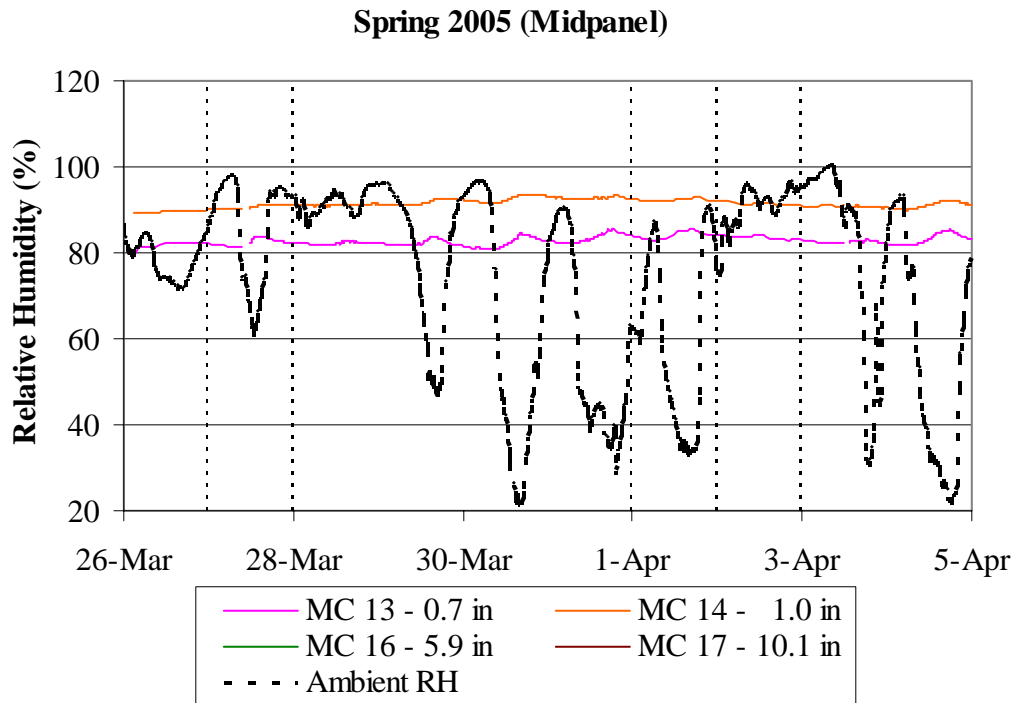


Figure 2.36. Midpanel concrete relative humidity for a ten -day period representing the spring 2005 season.

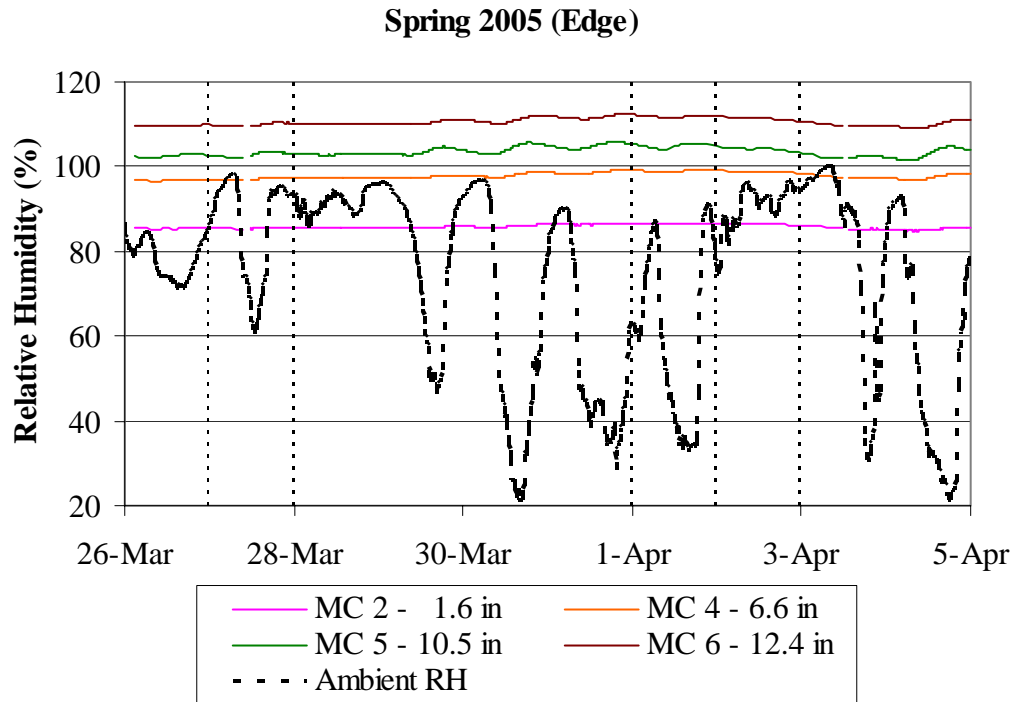


Figure 2.37. Edge concrete relative humidity for a ten -day period representing the spring 2005 season.

Figure 2.38 and Figure 2.39 present the daily moisture content at midpanel and the slab edge for a 10-day period representing the summer of 2005. The observed trends are similar to those experienced in the previous three seasons. At midpanel, the top two sensors varied between 70 and 82 percent but the average relative humidity has dropped substantially. At the slab edge, moisture content is approximately 80 percent at the top of slab, and is saturated at mid-depth and bottom portion of the slab.

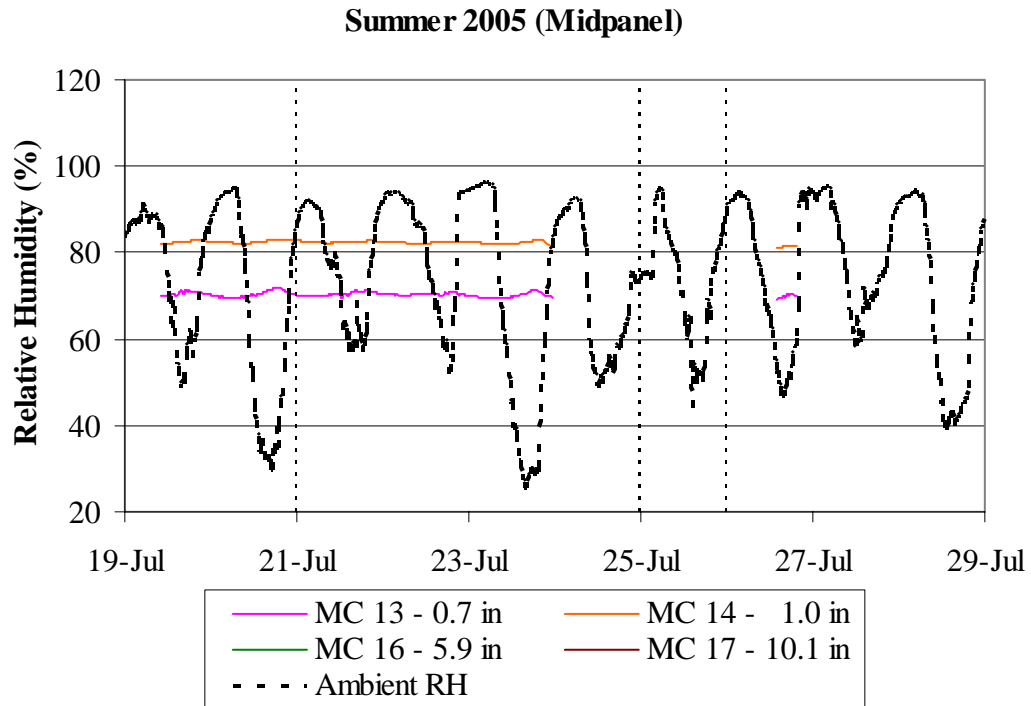


Figure 2.38. Midpanel concrete relative humidity for a ten-day period representing the summer 2005 season.

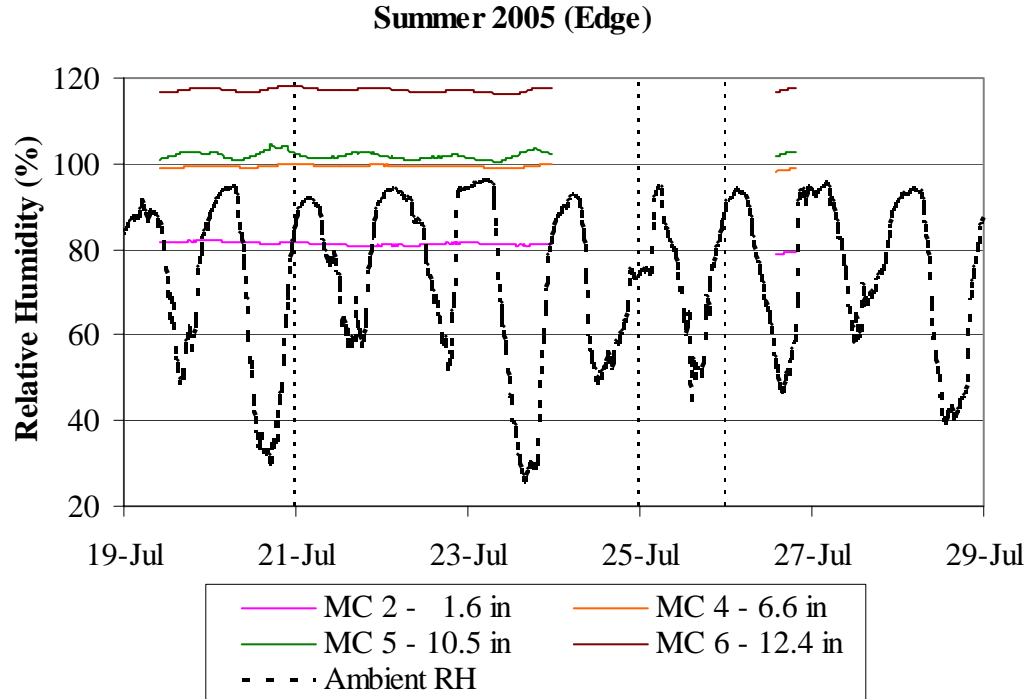


Figure 2.39. Edge concrete relative humidity for a ten-day period representing the summer 2005 season.

The trends observed for the second and third year after paving are similar to those observed for the first year. Figures showing the daily moisture content at midpanel and slab edge for ten-day periods representing the remaining seasons are included in appendix A.

The average concrete relative humidity was calculated for every climatic season during the three years following the construction of the pavement. The averages of the data recorded by the midpanel and edge sensors are presented Figure 2.40 and Figure 2.41. The figures show that the concrete moisture content increases with increasing slab depth. The moisture content is higher along the edge of the slab than at midpanel, which is justified by the proximity to the joints. The moisture content recorded during the second and third years after construction are lower than those recorded during the first. This is observed at both midpanel and the slab edge. At the bottom of the slab, the concrete moisture is at 100 percent or larger throughout the three years and is not affected by variations in seasonal climatic conditions. There is a clear seasonal trend in the upper portion of the slab with the relative humidity increasing during the spring and summer and decreasing during the fall and winter. This occurs at midpanel and the edge.

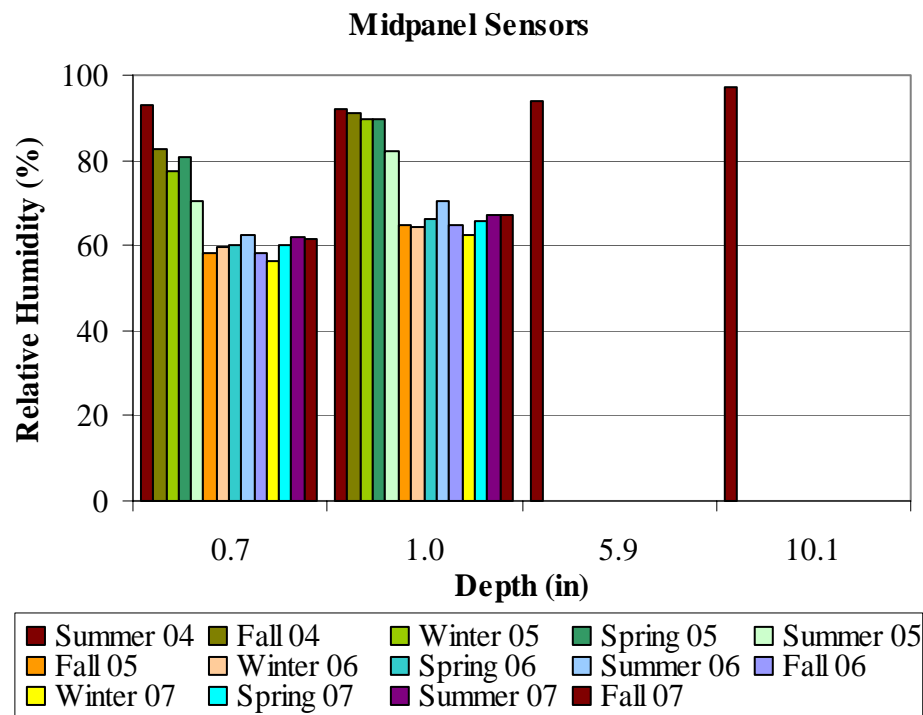


Figure 2.40. Seasonal average midpanel concrete relative humidity.

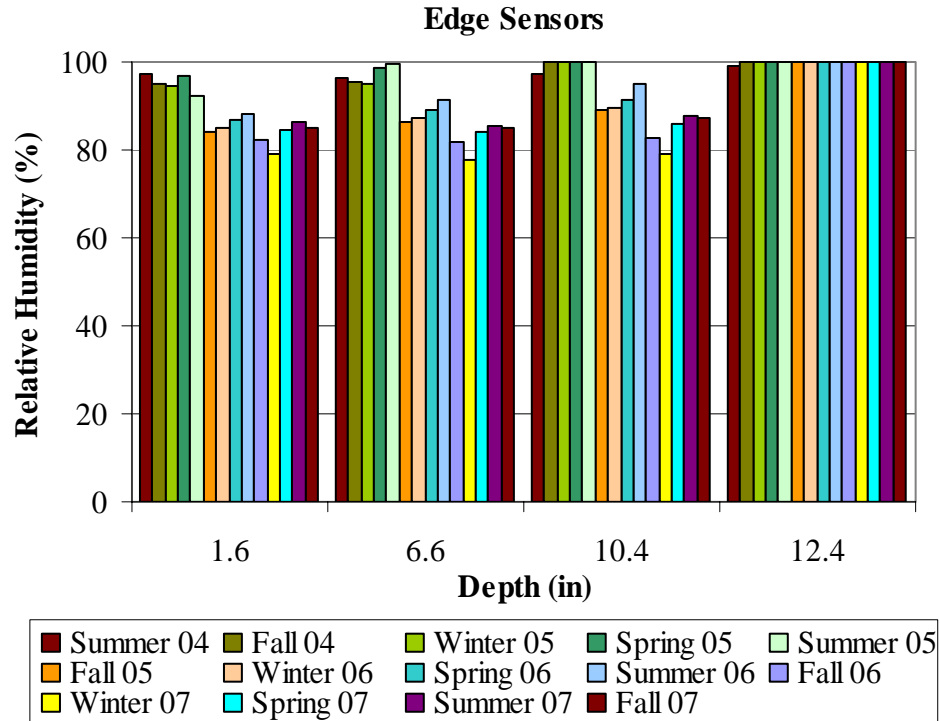


Figure 2.41. Seasonal average edge concrete relative humidity.

2.4.3. Moisture Measurements within the Granular Layers

TDR probes were installed in the subbase and subgrade layers to monitor the moisture levels within the granular layers. In addition to estimating the moisture content in the soil, the TDR system can be used to detect the frost depth within the pavement structure. This is based on the fact that, as temperatures decrease and the water within the soil particles freezes, the soil particles become insulated from each other causing a rapid decrease in the electrical conductivity (EC).

The variation in volumetric water content (VWC) with time during the first three years after paving is presented in Figure 2.42 for TD05, located in the subbase layer at midpanel. The VWC is a unitless quantity varying between 0 and 1, indicating moisture levels varying between 0 and 100 percent. This figure is presented after a considerable effort to show only valid data points and eliminate the large amount of noise recorded by the sensors. The figure shows that the VWC measurements and the noise level fluctuate during the three year period. The measurements recorded by the other sensors show similar patterns in the variation in moisture content and variation in noise during the three year period and can be found in appendix A. However, the data collected by TD01 to TD04 located at the

slab edge do not exhibit any distinguishable patterns in moisture variation and contain a large amount of noise throughout the three year period.

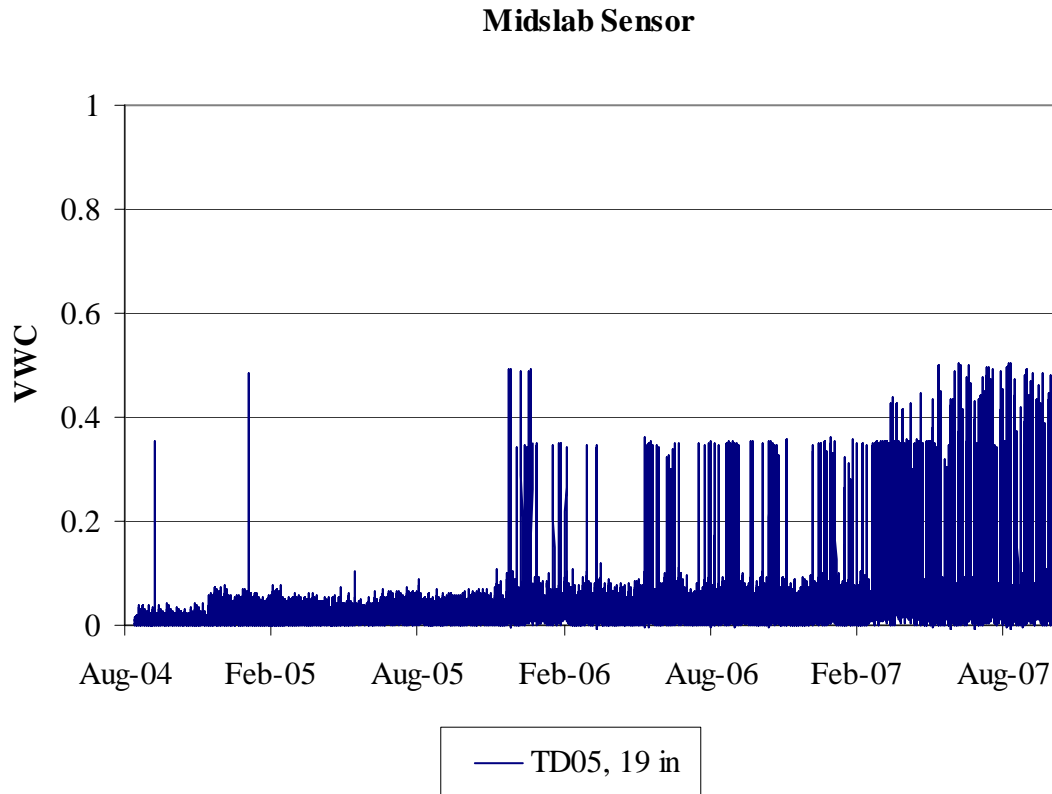


Figure 2.42. Volumetric water content measured by midpanel sensor TD05 in the 2A-subbase at a depth of 19 in.

In an attempt to identify whether the VWC data collected by the sensors is valid and contains a large amount of noise or whether it is simply invalid and needs to be disregarded, variations in the electrical conductivity made by the same sensors was examined. The variation in bulk soil EC with time during the first three years after paving is presented in Figure 2.43 for TD05, located in the subbase layer at midpanel. The figure shows that the EC varies seasonally, decreasing during the fall to reach the lowest values in the winter, then increasing during the spring to reach the highest values in the summer. The figure also shows that the increase in EC during the spring takes place along a step-wise pattern.

The seasonal variations in EC are attributed to variations in the ambient climatic conditions. During the winter, the temperature of the concrete pavement and underlying

layers are at or below the freezing point. The lowest temperatures were observed between mid-January and mid-February 2005. During this period, Figure 2.43 shows a relatively rapid decrease in EC, which would be typical for a frozen soil condition. Starting in mid-February 2005, temperatures in the underlying layers started rising, causing thawing of the water present in these layers. This increase in water content causes an increase in bulk electrical conductivity of the soil and accounts for the high EC values shown in the figure.

In addition, EC fluctuates daily, and the range of these daily fluctuations increases significantly during the spring and summer seasons. The daily fluctuations recorded for the second year after paving are larger than those recorded for the first year during all the seasons. The manufacturer of the TDR probes, Campbell Scientific, Inc., was contacted for technical support regarding the wide bands in the EC measurements and the undistinguishable trends in the VWC measurements. Campbell Scientific's support team concluded that the probes installed in this project are not appropriate in soils where conductivity is higher than 0.14 Siemens/m. According to the collected data, the soil conductivities reach levels higher than 0.14 Siemens/m during the spring and summer. This accounts for the wide bands in EC measurements and the high noise levels in the VWC measurements. These soil conductivity levels were not anticipated at the time of selection and installation of the TDR probes.

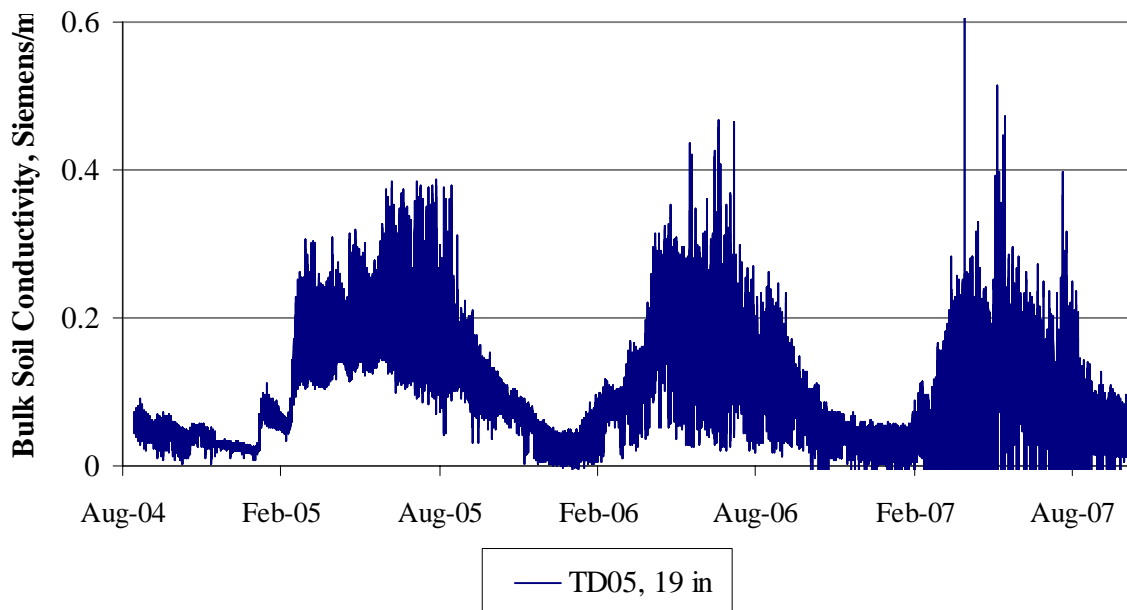


Figure 2.43. Bulk soil conductivity recorded by midpanel sensor TD05 in the 2A-subbase at a depth of 19 in.

The electrical conductivity at different depths in the pavement structure were compared to each other. The trends in variations of EC with time were the same as those observed for TD05. In addition, the conductivity of the different materials were of the same values and differences could not be detected. As a result, the EC data could not be used to estimate the conductivity of the different materials of the pavement structure. Moreover, the rapid decrease in EC recorded between mid-January and mid-February 2005 was also recorded by the sensors located at the different locations and depths. This makes it difficult to use the EC graphs to determine the exact frost depth or to confirm the frost depth of 21 in previously determined based on the thermocouple data in section 2.3.3.

Based on the EC measurements, it can be concluded that the TDR sensors are operational but the moisture measurements are influenced by the large amount of noise entering the system. The presence of noise may be due to the presence of some external magnetic and/or electric source near the site causing interference with the TDR system. An electric power regulator is present on site and is located approximately 120 feet away from the datalogger recording the TDR data. It is not clear whether this power source is influencing the TDR readings.

Since the TDR probes are operational and collecting valid trends of variation of EC data, another look at the VWC measurements was taken in an attempt to make observations regarding the seasonal fluctuation of moisture content in the granular layers. The VWC data collected by the midpanel sensors TD05 to TD08 was analyzed. The VWC measurements indicate that the data with the least noise is the data that was recorded between March and October of 2005. This was unexpected since the EC data indicated the highest level of noise during that period. The average VWC measurements during this period are summarized in Figure 2.44. According to the figure, the volumetric moisture content decreases during the spring and increases during the summer. The increase during the summer is due to larger precipitation levels recorded during that period. In addition, the volumetric moisture content in the subbase, fill and subgrade material are within 10 percent of each other. This is not considered a significant difference because the average moisture content varies between 1.8 and 2.4 percent and the maximum moisture content varies between 5 and 10 percent in the granular layers.

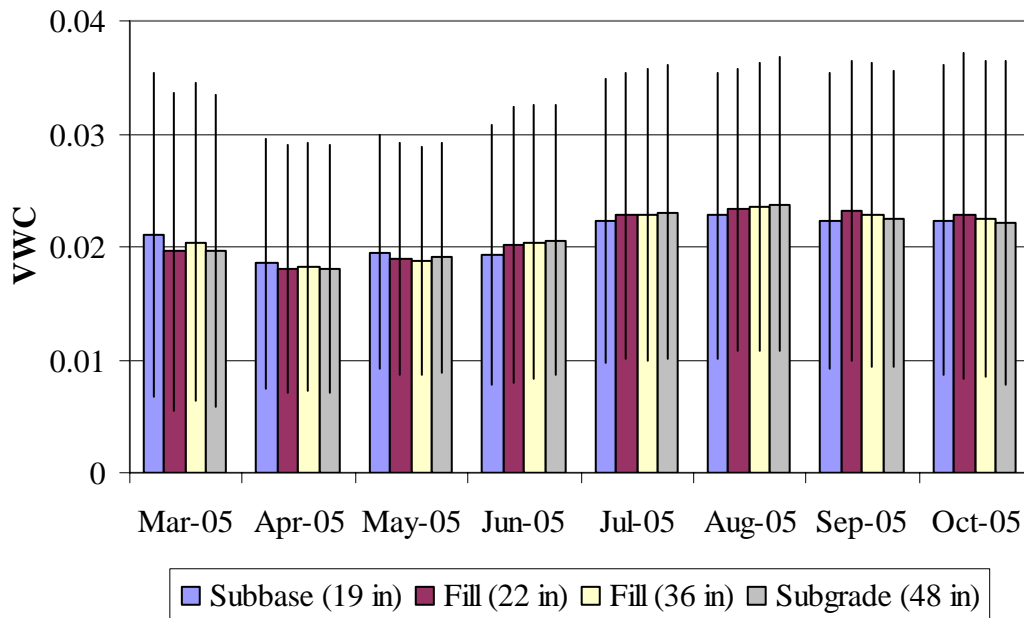


Figure 2.44. Average monthly VWC measurements based on midpanel sensors TD05 to TD08.

The volumetric moisture content of the granular layers corresponding to full saturation can be estimated using available literature based on the material properties. The volumetric moisture content corresponding to 100 percent saturation are 27 percent for the subbase, 28 percent for the fill, and 19 percent for the subgrade. During the three year period, the volumetric moisture content measured by the TDRs varied between 5 and 90 percent for the different layers. Assuming that the TDRs are collecting valid data, this analysis indicates that all the granular layers are in wet to saturated conditions during most of the three-year period. However, according to Figure 2.44, the granular layers are below saturation between March and October of 2005.

2.4.4. Summary

The concrete moisture content shows the same seasonal trends irrespective of the location of the sensor within the concrete slab. The concrete moisture content reaches minimum values during the winter, after which moisture content increases and reaches a maximum during the spring and summer. The seasonal trends are similar for all three years after construction. However, the relative humidity in the slab during the second and third

year are lower than those measured during the first year. The relative humidity is also higher at the edge than midpanel.

At midpanel, the concrete relative humidity in the top two in of the slab varies between 73 and 93 percent during the first year, between 57 and 74 percent during the second year and between 54 and 67 during the third year. At mid-depth, the relative humidity varies between 93 and 100 percent during the first year, between 80 and 94 percent during the second year and between 75 and 85 percent during the third year and the slab remains saturated at the bottom.

An analysis of the moisture content of the granular layers determined that the TDR probes installed in the underlying layers do not provide consistent readings and do not allow for a proper analysis of moisture content. However, based on the available data, it can be concluded that the granular layers are in a wet to saturated condition during most of the three year period.

2.5.0. Conclusions

The temperature and moisture data collected showed the pavement structure is subjected to four climatic cycles representing the seasons of the year. The temperature and moisture profile as well as the average slab temperature and relative humidity vary constantly throughout the year. The moisture content also varies from year to year as the average relative humidity in the slab continues to decline. The effects of the temperature and moisture conditions on the slab response will be evaluated in subsequent chapters.

CHAPTER 3: DEFINING THE BUILT-IN CONSTRUCTION GRADIENT

3.1.0. Introduction

The climatic conditions at the time the concrete sets influences the response of the slab at later ages. The temperature and moisture conditions inside the concrete at the time of set result in the development of a built-in construction gradient in the slab. A built-in construction gradient is defined as the gradient due to temperature and moisture that is present in the slab when it sets [4; 5; 6]. The magnitude of the built-in construction gradient influences slab curling and warping and thus affects the development of stress and strain within the concrete at later ages.

If the concrete sets when the top of the slab is exposed to higher temperatures than the bottom of the slab, the built-in gradient is positive, and if the top of the slab is exposed to lower temperatures, the built-in gradient is negative. The larger the difference between the top and bottom of the slab, the larger the gradient. At the time the concrete sets, the slab remains flat since the concrete is still in its plastic state and has not yet developed sufficient stiffness [4]. This implies that, at any point in time, when the gradient in the slab is of the same magnitude as that corresponding to the built-in construction gradient, the slab is flat with zero stress. When the slab is in a zero gradient condition, it curls instead of remaining flat. The curling is upward if the built-in gradient is positive and downward if it is negative [7].

To determine the magnitude of the built-in construction gradient, it is necessary to define the time of set of the concrete. The time of set of concrete represents the time when the concrete reaches a solid state, and when the development of stresses and strains within the concrete is initiated [8]. Researchers have been using a wide variety of methods to estimate the built-in construction gradient. Most of these methods are based on analyzing surface movements of the slab with respect to changes in temperature gradients along the slab depth. These analyses usually involve the use of prediction models to estimate slab curvatures for different temperature gradients and the selection of the gradient that results in the least error between predicted and measured curvatures. The built-in construction gradient estimated by these different methods was found to cover a wide range of values and vary with several factors including type of base, type of curing, concrete mixture design and material properties and climatic conditions at the time of construction [9; 10; 11; 12]. However, a standard methodology to accurately determine the built-in construction gradient of concrete pavements is not available.

The built-in construction gradient has proven to be an important factor in estimating stresses in concrete pavements, especially when adopting the new mechanistic-empirical pavement design approach [13; 4; 10]. Since the new design approach takes into account the effects of climatic conditions on the performance of the pavement, selecting a non-representative construction gradient value in the MEPDG could result in under-designed or over-designed pavement structures. The first objective of this research is to establish a methodology for determining the built-in construction gradient of a jointed plain concrete pavement and evaluate its effect on the performance of the concrete pavement. This chapter details the methodology adopted to determine the built-in construction gradient in the slabs as accurately as possible. The analysis involves studying the early-age behavior of two types of slabs: restrained slabs and unrestrained slabs. For this purpose, two approaches for determining the concrete set time are followed and compared.

The first approach involves analyzing data collected from strain gages embedded at different locations and depths in the concrete slabs. The strain data is analyzed for the first 42 hours after placement to identify the time when the concrete starts experiencing strain corresponding to changes in temperature. The second approach involves analyzing data collected from static pressure cells embedded at different locations along the interface between the concrete slabs and the base layer. The pressure cell data is analyzed for the first 42 hours after placement to identify the time when the base layer starts experiencing uniform changes in pressure along with changes in temperature gradients within the slab. The results of these two methods are analyzed and compared to determine the time of set. Once the set time is determined, data from the thermocouples embedded in the concrete slabs are used to estimate the corresponding built-in construction gradient.

The first section of this chapter presents the temperature and moisture conditions in the slab during the first 24 hours after placement of the concrete. The corresponding range of values of the temperature and moisture gradients contributing to the built-in construction gradient is also presented. The second section presents the number, locations and depths of the static strain and pressure sensors in the slabs. The third section describes the set times and corresponding built-in construction gradients determined based on the early-age vibrating wire data in the restrained and unrestrained slabs. Next, the set time and built-in construction gradient determined based on the early-age pressure cell data in the restrained and unrestrained slabs are discussed. After that, a

comparison between the set times and built-in construction gradients determined based on the two methods is presented. Finally, the last section summarizes the results and conclusions made regarding the determination of the built-in construction gradient for the jointed plain concrete slabs.

3.2.0. Early-Age Concrete Temperature and Moisture Conditions

The built-in construction gradient is a function of the temperature and moisture conditions at the time of set. Before quantifying this parameter, the variations in the temperature and moisture conditions in the slab during the first 24 hours are examined and presented in this section, along with the corresponding temperature and moisture gradients.

The variation of temperature within the concrete slab was monitored using thermocouples embedded at seven different depths throughout the 12.5-in concrete slab. The slab temperature measured in the field during the first 24 hours after paving is shown in Figure 3.1 based on the thermocouples located at midpanel of restrained Slab B. The concrete temperature increases from 70°F to 110°F during the first 12 hours, after which it decreases. The increase in temperature is due to the hydration of the cement and the increase in the ambient temperature. The decrease in temperature is caused by the decrease in ambient temperature during the evening and nighttime hours.

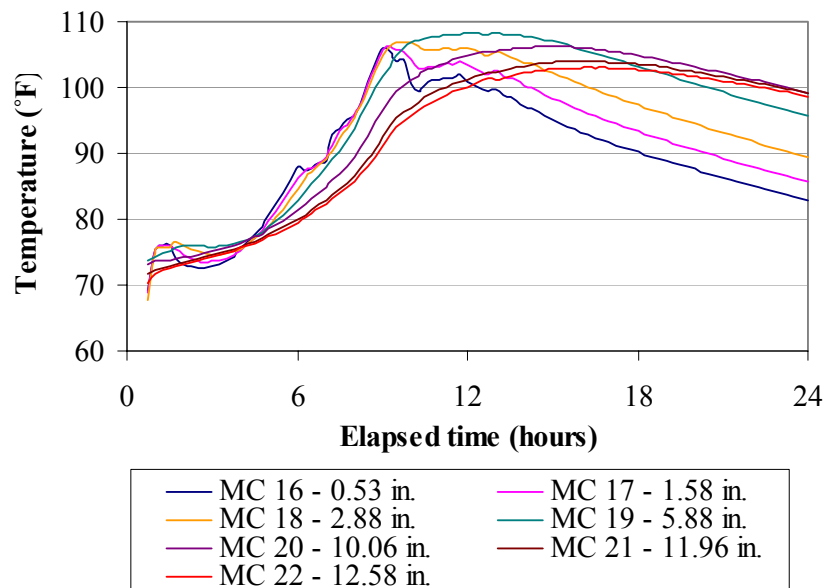


Figure 3.1. Early-age variation of temperatures in the concrete midpanel of the restrained slab.

To account for nonlinear temperature gradients in slab, Janssen and Snyder (2000) presented a method for estimating the moment produced by a nonlinear temperature profile about the bottom of the slab. This was previously presented in Chapter 2. The equivalent linear temperature gradient can be estimated based on the variation in the temperatures along the slab depth. The variation in the equivalent linear temperature gradient during the first 24 hours after paving is presented in Figure 3.2. The figure shows that the equivalent linear temperature gradient fluctuates between 0 and 1.1°F/in during the first 12 hours and then decreases to -1.25°F/in during the subsequent 12 hours. This is equivalent to a temperature difference of -15.7°F to +13.8°F between the top and bottom of the 12.5-in slab. Negative temperature difference indicates upward slab curvatures and a positive difference indicates downward slab curvatures when moisture gradients are not present. The range of temperature differences indicate that an appropriate selection of the built-in temperature gradient is necessary to differentiate between situations when the slab is curved upwards and downwards when exposed to different ambient temperature conditions.

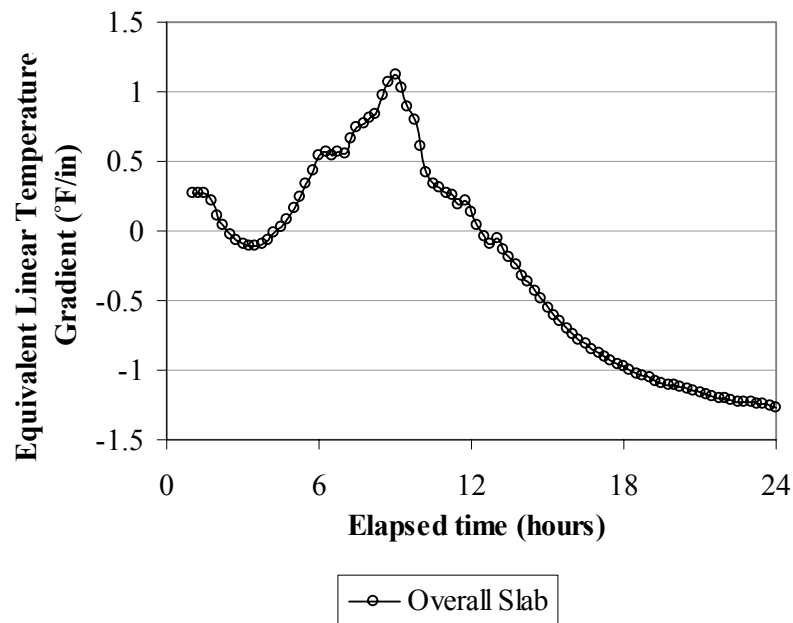


Figure 3.2. Early-age variation in temperature gradients in the concrete slab.

The built-in construction gradient represents the temperature and moisture conditions at the time the concrete sets. The variation in the temperature gradient during

the first 24 hours after paving was presented earlier in this section. Next, a discussion is provided on the magnitude of the moisture gradient during the early-age of the slab.

The moisture in the slab was monitored using relative humidity sensors embedded at four different depths throughout the 12.5-in slab. Unfortunately, moisture data during the first 24 hours after paving is not available. As previously presented and discussed in Chapter 2, moisture in the concrete slabs does not vary significantly on a daily basis [14]. As a result, the concrete moisture levels during the first 24 hours after paving are expected to be similar to those measured during the second day after paving. The concrete moisture levels measured during the second day after paving are available and are presented in Figure 3.3, based on relative humidity sensors located at midpanel of the restrained slabs. The concrete moisture levels vary between 94 and 96 percent along the slab depth. This indicates that the change in relative humidity is relatively small throughout the depth of the slab. Based on this, it is expected that the built-in gradient due to moisture will not be significant.

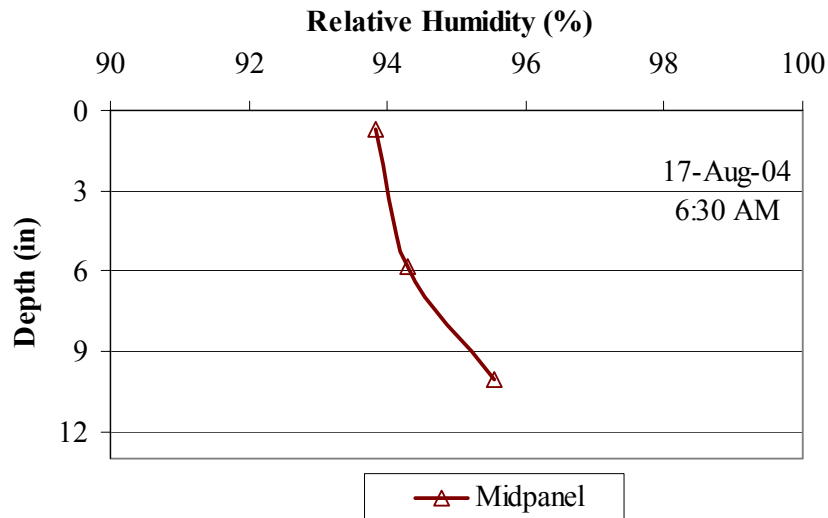


Figure 3.3. Early-age variation of concrete moisture in the restrained slab.

In the new design guide, the moisture gradient through the slab is represented by an equivalent temperature difference along the slab depth. However, since the new design procedure incorporates the impact of climate and aging on material properties throughout the entire design life, moisture warping needs to be adjusted monthly based on atmospheric relative humidity. The effects of monthly variation in moisture warping are expressed in terms of equivalent temperature difference and are added to the equivalent

linear temperature difference during stress calculations [15]. Equation 3-1 presents the equivalent temperature difference representing deviations in moisture warping from the annual average adjusted based on the ambient relative humidity.

$$ETG_{Shi} = \frac{3(\phi \cdot \epsilon_{su})(S_{hi} - S_{h\text{ave}})h_s \left(\frac{h}{2} - \frac{h_s}{3} \right)}{\alpha h^2 \cdot 100} \quad (\text{Equation 3-1})$$

Where: ETG_{Shi} = Temperature difference equivalent of the deviation of moisture warping in month i from the annual average, °F

ϕ = Reversible shrinkage factor, fraction of total shrinkage. A value of 0.5 is recommended for use unless more accurate information is available

ϵ_{su} = Ultimate shrinkage based on PCC mix properties, $\times 10^6$

S_{hi} = Relative humidity factor for month i:

$$\begin{aligned} S_{hi} &= 1.1 RH_a && \text{for } RH_a < 30 \% \\ S_{hi} &= 1.4 - 0.01 RH_a && \text{for } 30 \% < RH_a < 80 \% \\ S_{hi} &= 3.0 - 0.03 RH_a && \text{for } RH_a \geq 80 \% \end{aligned}$$

RH_a = Ambient average relative humidity, percent

$S_{h\text{ave}}$ = Annual average relative humidity factor. Annual average of S_{hi}

h_s = Depth of shrinkage zone, typically 2 in

h = PCC slab thickness, in

α = PCC coefficient of thermal expansion, /°F

The above equation is based on the ultimate shrinkage of the concrete, which requires time to fully develop. To estimate the temperature difference equivalent of the deviation of moisture warping at any time from placement, equation 3-2 was developed and is presented in the new design guide [15].

$$ETG_{Sht} = \left(\frac{Age}{n + Age} \right) ETG_{Shi} \quad (\text{Equation 3-2})$$

Where: ETG_{Sht} = ETG_{Shi} at any time t days from PCC placement, °F

Age = PCC age, days since placement

n = time to develop 50% of ultimate shrinkage strain, days

Based on the above, the moisture gradient can be converted into an equivalent linear temperature gradient. This procedure calculates the equivalent temperature difference representing slab warping due to moisture, based on relative changes in

monthly ambient relative humidity with respect to the annual average ambient relative humidity. The use of this equation requires several parameters characterizing the concrete material properties along with parameters characterizing the effects of the ambient relative humidity conditions on the concrete. The concrete material parameters were determined by laboratory testing and are presented in detail in the construction report [1] and the one-year report [2]. The relevant concrete material properties needed to estimate the equivalent temperature gradient are listed in Table 3.1.

Table 3.1. Concrete material parameters needed for the estimation of an equivalent temperature gradient for a moisture gradient.

Concrete Parameter	Value
Surface shrinkage, ϵ_s	945 $\mu\epsilon$
PCC slab thickness, h	12.5 in
Depth of the shrinkage zone, t	2 in
PCC coefficient of thermal expansion, α	$5.5 \times 10^{-6} / ^\circ\text{F}$
Reversible shrinkage factor, ϕ	0.5 (assumed)

At early age, equation 3-1 is not representative of the temperature difference due to concrete moisture. As a result, the equation will be used along with the ambient relative humidity corresponding to the worst-case scenario during the first year after paving. It was shown in chapter 2 that, during the first year after construction, the concrete relative humidity varies between 73 and 93 percent in the top 2 in of the slab, varies between 93 and 100 percent at mid-depth, and the slab remains saturated at the bottom. The month during which the concrete relative humidity is lowest in the top 2 in of the slab is expected to result in the largest moisture gradient across the slab depth. Based on section 2.4.2, the lowest concrete relative humidity during the first year after paving is measured during the month of February 2008. During that month, the average ambient relative humidity was 78 percent, and the yearly average during the first year after construction was 74 percent, based on the relative humidity data collected from the onsite weather station. From this, the relative humidity factors can be calculated as:

$$S_{hi} = 1.4 - 0.01 RH_a = 1.4 - 0.01 (78) = 0.62 \text{ for February 2005, and}$$

$$S_{have} = 1.4 - 0.01 RH_a = 1.4 - 0.01 (74) = 0.66 \text{ for the first year after paving.}$$

Using equation 3-1, the material properties provided in Table 3.1 and the relative humidity factors determined in this paragraph, the temperature difference across the slab

depth equivalent to the deviation of moisture during the week of construction is calculated as:

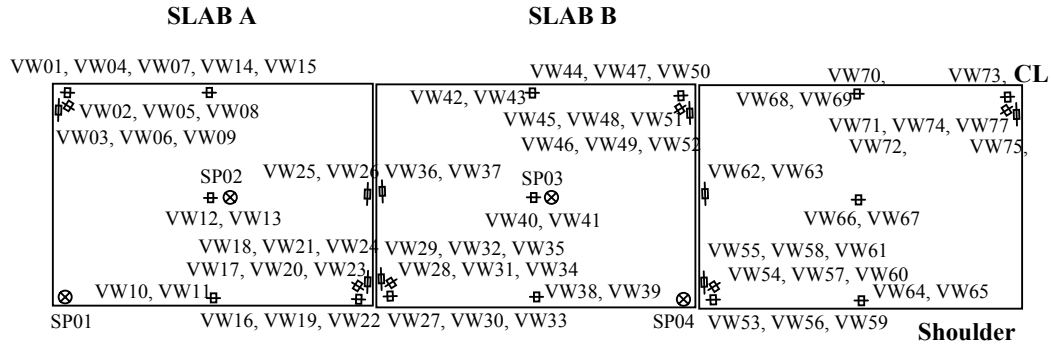
$$\begin{aligned}
 ETG_{shi} &= \frac{3(\phi \cdot \varepsilon_{su})(S_{hi} - S_{h\ ave})h_s\left(\frac{h}{2} - \frac{h_s}{3}\right)}{\alpha h^2 \cdot 100} \\
 &= \frac{3(0.5)(945 \times 10^{-6})(0.62 - 0.66)(2)\left(12.5/2 - 2/3\right)}{5.5 \times 10^{-6}(12)^2(100)} = -0.008^\circ F
 \end{aligned}$$

Comparing the contributions of the temperature and moisture to the built-in construction gradient, the effect of temperature is much more significant than the effect of moisture. The temperature gradient during the first 24 hours after paving varies between -1.25°F/in and 1.1°F/in and the corresponding range of temperature difference across the slab depth is -15.7°F to +13.8°F. While the temperature difference equivalent for the moisture gradient is estimated to be -0.008°F. It can be concluded that moisture effects contribute to less than 1 percent of the overall built-in gradient. As a result, neglecting the effect of moisture when estimating the built-in construction gradient in the slab is expected to result in minimal errors. Therefore, the built-in construction gradient will be estimated solely based on the temperature conditions in the slab.

3.3.0. Instrumentation of Static Sensors

Vibrating wire (VW) strain gages were installed at various depths in the PCC layer at four critical slab locations: the corners, midpanels and along the transverse and longitudinal edges. A total of 156 VW strain gages were installed at 60 locations in the unrestrained and restrained slabs, as shown in Figure 3.4. Three VW gages were placed at each corner location, and two were placed at each edge and midpanel location. Strain readings are automatically taken at 15-minute intervals. Depths at which the gages were placed are provided in Figure 3.5.

Pressure induced by the PCC slabs on the base layer is measured using Geokon 4800 Earth Pressure Cells. These cells, also referred to as static pressure cells, are positioned at the ATPB/PCC interface at locations of critical static stresses: at both midpanel and at the corners. Pressure values at these locations would indicate the magnitude of the pressure being exerted on the base layers by the PCC due to curling and warping. A total of 8 pressure cells were installed at the slab corners and at midslab in the unrestrained and restrained slabs, as shown in Figure 3.4. The depth at which the pressure cells were placed is provided in Figure 3.5.



- ⊞ Static Strain Gages (VW)
 ⊗ Static Pressure Cell (SP)

Figure 3.4. Location of static strain gages and static pressure cells in Cells 3 and 4.

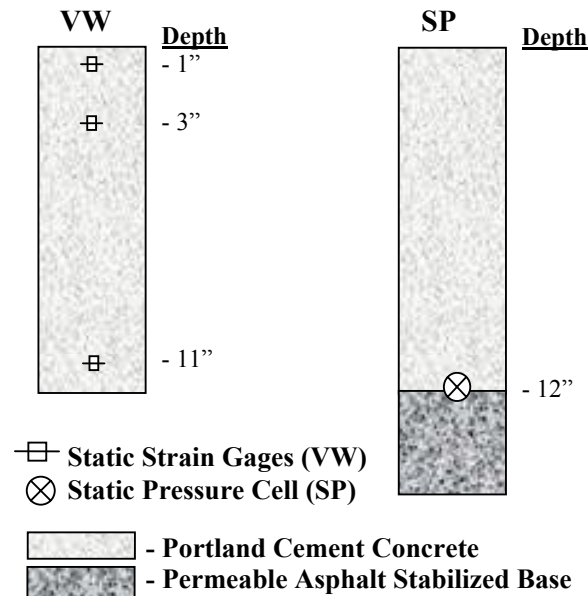


Figure 3.5. Depth of static strain gages and static pressure cells in Cells 3 and 4.

3.4.0. Early-Age Strains within the JPCP Slab

As previously mentioned, the time of final set defines the point at which concrete starts gaining strength, which also marks the transition between the plastic and solid states of the concrete. Before the concrete sets, it is in a plastic state and can experience large changes in temperatures with little to no change in strain. At the time of set, the concrete experiences movements that accompany changes in temperature. At that point, strain measurements can be recorded. Stress is generated in the slab when the movement of the concrete is restrained by tie bars, friction along the slab/base interface, dowel bars, or any other restraining factor that might be present.

Data was collected from the vibrating wire gages embedded in the concrete slab at different locations and depths. The variation in measured strain with respect to temperature changes during the first 42 hours after placement is used to identify the concrete set time. The time of final set is selected as that corresponding to the time when expansion/contraction is measured with changes in temperature. The analysis of the early-age variations in strain with respect to temperature included all the vibrating wire sensors of the restrained and unrestrained slabs. The general trends observed are presented in this section, along with some of the figures that were used. The remaining figures showing the early age data from all the sensors of the restrained and unrestrained slabs are included in appendix B. As a result of the analysis of the early age variations in strain measurements, the time of set is established. Finally, the built-in temperature gradient corresponding to the time of set is estimated. A general overview of the static strain gage used is presented first.

3.4.1. Static Strain Gages

The raw strain reading represents the slab deformation due to the effects of temperature changes, moisture changes, shrinkage and creep. The strain readings are also affected by factors that restrain the movement of the slabs. As a result, the strain measurements based on the sensors embedded in the restrained and unrestrained slabs are expected to be different.

The raw strain readings are first corrected for the effect of temperature on the steel wire in the gages and then converted into total strain, which reflects the total deformations measured in the slab [1]. The corrections are accounted for by using equation 3-3 to calculate the total strain experienced by the concrete. In this chapter, the strain measurements are zeroed based on the time the concrete was placed and will be used to determine the time of set of the concrete.

$$\varepsilon_{total} = (R_1 - R_0)B + (T_1 - T_0)\alpha_s \quad \text{(Equation 3-3)}$$

where: ε_{total} = Total strain in the concrete

R_0 = Raw strain at time 0 (initial concrete set)

R_1 = Raw strain at time 1

T_0 = Temperature at time 0 (initial concrete set)

T_1 = Temperature at time 1

α_s = Thermal coefficient of expansion of steel in strain gage = $6.78 \mu\epsilon/^\circ\text{F}$

B = Batch calibration factor (provided by the manufacturer)

3.4.2. Restrained Slabs

The variation in the measured strain with respect to temperature changes during the first 42 hours after placement is used to identify the concrete set time. The time of final set is selected as that corresponding to the time when expansion/contraction is measured with changes in temperature. The early-age variation in the total strain for the midpanel sensors oriented in the longitudinal direction and located at the top and bottom of the restrained Slab B are illustrated in Figure 3.6 and Figure 3.7. Based on these figures, the set times were found to correspond to 2:46 PM for the top of the slab and 4:01 PM for the bottom of the slab. These times are then zeroed to the time when concrete mixing was initiated, which is assumed to be 45 minutes prior to concrete placement, as will be explained in the next paragraph. According to the thermistor readings, the concrete was placed at 6:31 AM at the midpanel of restrained Slab B. Accordingly, the concrete set times for the midpanel of restrained Slab B are found to correspond to elapsed time of 8.25 hours (top of slab) and 9.5 hours (bottom of slab) after mixing.

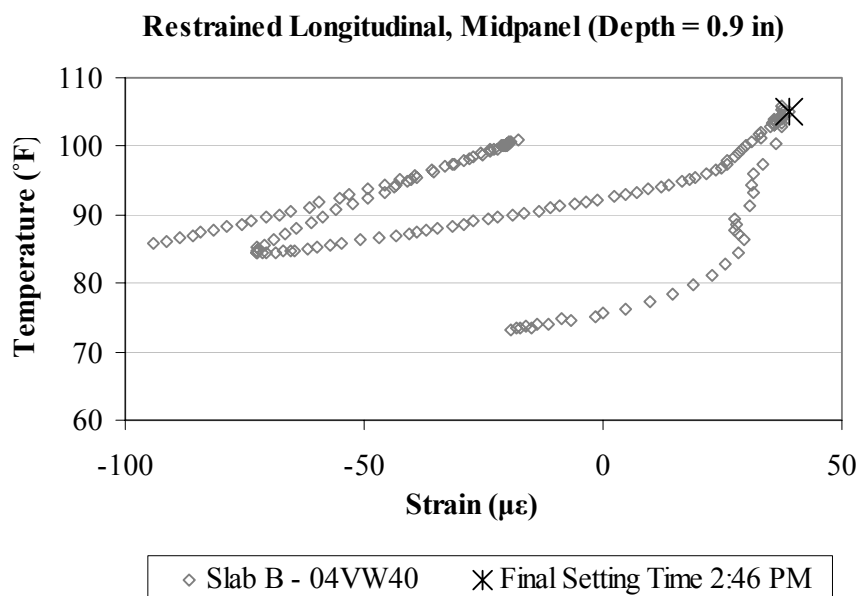


Figure 3.6. Early-age variation in the total strain with temperature, in the longitudinal direction, for the top sensor located at midpanel of restrained Slab B.

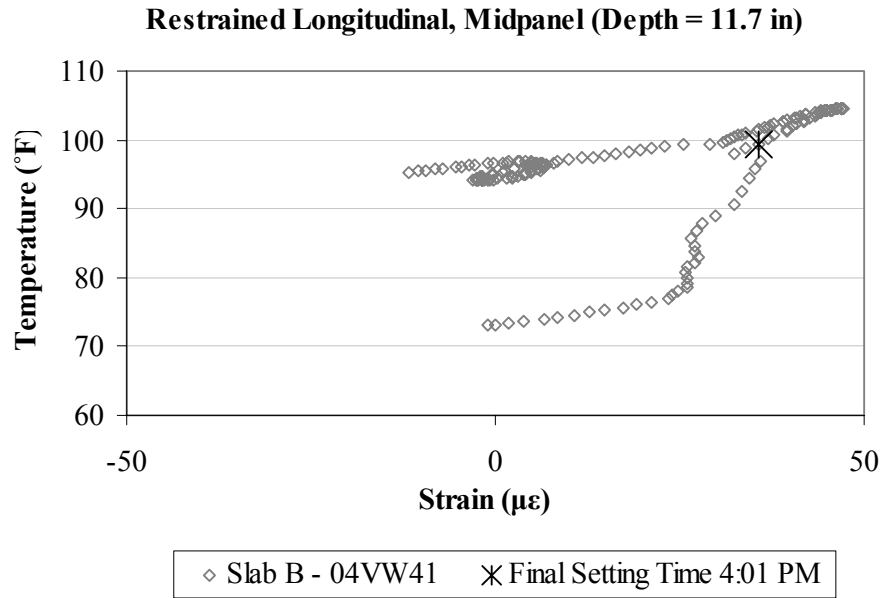


Figure 3.7. Early-age variation in the total strain with temperature, in the longitudinal direction, for the bottom sensor located at midpanel of restrained Slab B.

The concrete was mixed at a portable plant located approximately five miles east of the project site in Export, Pennsylvania and was delivered to the site via front-discharge trucks. The time from when the water hits the cement in the batching process to the time the concrete truck pulls away to head to the job site, including the time for mixing and loading the truck, was estimated at eight minutes. The travel time needed to reach the job site was estimated at twelve minutes. Once on the site, the time for testing of the concrete was estimated at fifteen minutes. And, the time to place the concrete on the grade was estimated at ten minutes. In total, an additional 45 minutes are accounted for between the time water hits the cement and the time the thermocouples begin recording temperatures.

A similar procedure was followed to determine the concrete set times for every sensor at every depth and location within restrained Slabs A, B and C. The figures illustrating the early-age variation in total strain with temperature are included in appendix B. Based on the early-age variation in the strain data, the set times are presented in Table 3.2 and Figure 3.8 for the restrained slabs.

The results indicate that the average concrete set time varies between 9 and 12.25 hours after mixing, with an overall average of 10.62 hours. At each location, the set times estimated based on the sensors located at the top, middepth and bottom of the slab are similar. The largest difference between top and bottom of the slab was recorded at the

midpanel of restrained Slab B and amounts to 1.25 hours. To further illustrate this point, the average set times at the top, middepth and bottom of the slab were calculated based on the data collected from the sensors in all the slabs, and are compared to each other in Figure 3.9. The figure shows that the set times at the top, middle and bottom portions of the slabs are within 4 percent of each other. Moreover, the concrete set times estimated at the different locations within the slabs are within 18 percent of each other and do not show any specific pattern of variation. This implies that the slab restraining conditions do not significantly affect the concrete set time. This is expected since the set time describes a concrete material property, irrespective of the slab restraining conditions. However, the slab restraining conditions are expected to affect the built-in stress within the slab.

Table 3.2. Concrete set time based on early-age vibrating wire data for restrained slabs.

Location	Direction ¹	Depth	Concrete Set Time ^{2,3} (hours)			
			Slab A	Slab B	Slab C	Average
Corner; Centerline	L	Top	10.5	10.75	11.25	10.83
		Middepth	10.5	10.75	--	10.63
		Bottom	10.5	--	--	10.50
	D	Top	10.75	10.5	10.75	10.67
		Middepth	--	10.5	11	10.75
		Bottom	10.75	10.5	12	11.08
	T	Top	10.25	9.75	10.75	10.25
		Middepth	10.5	9.75	10.75	10.33
		Bottom	11.25	10.25	11	10.83
Edge; Centerline	L	Top	10.5	9.75	10.75	10.33
		Bottom	10.5	10.25	10.75	10.50
Midpanel	L	Top	10.75	9	11.5	10.42
		Bottom	10.75	10.25	11.5	10.83
Edge; Lane/Shoulder	L	Top	10.5	9.5	9.75	9.92
		Bottom	11	10	9.75	10.25
Transverse Joint	T	Top	11.25	11.25	11.25	11.25
		Bottom	11.25	11.75	12.25	11.75
Corner; Lane/Shoulder	L	Top	10.25	10.5	11.5	10.75
		Middepth	9.75	10.5	10.25	10.17
		Bottom	11	11	11	11.00
	D	Top	10.25	10.75	9.5	10.17
		Middepth	--	10.75	9.75	10.25
		Bottom	10.75	10.75	9.75	10.42
	T	Top	10.5	10.25	10.75	10.50
		Middepth	10.5	10.25	10.75	10.50
		Bottom	11.75	10.5	11.25	11.17

¹ L: Longitudinal direction; D: Diagonal direction; T: Transverse direction

² Set time is zeroed to the concrete mixing time (45 minutes prior to placement)

³ Dashed lines indicate that VW data is not available or cannot be interpreted

Restrained Slabs											
Slab A				Slab B				Slab C			
10.5 ± 0.25 (T)	10.5 (T)			9.75 (T)	10.33 ± 0.52 (T)			10.75 (T)	10.92 ± 0.29 (T)		
10.5 ± 0.0 (M)	10.5 (B)			10.25 (B)	10.33 ± 0.52 (M)			10.75 (B)	10.88 ± 0.18 (M)		
10.83 ± 0.38 (B)					10.38 ± 0.18 (B)				11.5 ± 0.71 (B)		
	10.75 (T)	11.25 (T)		11.25 (T)	9 (T)			11.25 (T)	11.5 (T)		
	10.75 (B)	11.25 (B)		11.75 (B)	10.25 (B)			12.25 (B)	11.5 (B)		
		10.33 ± 0.16 (T)		10.5 ± 0.25 (T)				10.58 ± 1.01 (T)			
	10.5 (T)	10.13 ± 0.53 (M)		10.5 ± 0.25 (M)	9.5 (T)			10.25 ± 0.5 (M)	9.75 (T)		
	11 (B)	11.17 ± 0.52 (B)		10.75 ± 0.25 (B)	10 (B)			10.67 ± 0.8 (B)	9.75 (B)		

T: Top of slab;

M: Middepth;

B: Bottom of slab

Figure 3.8. Set times in the restrained slabs.

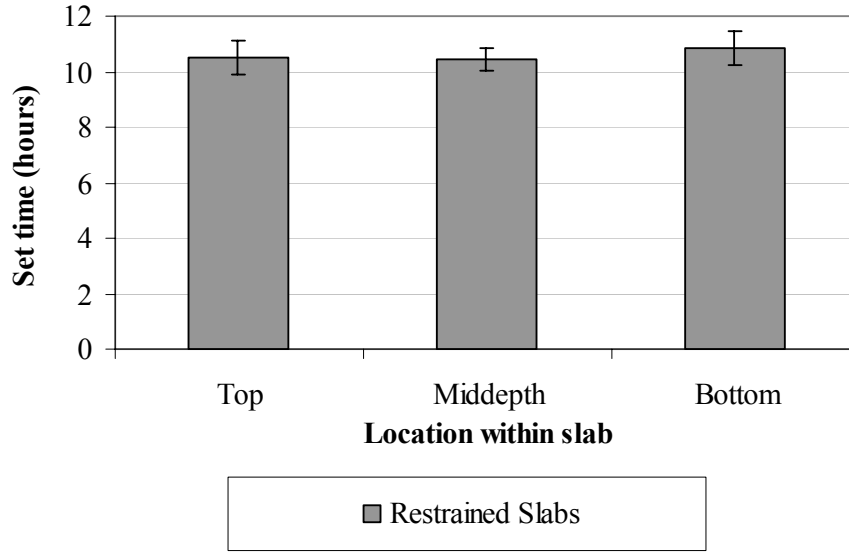


Figure 3.9. Variation in average concrete set time with depth, for restrained slabs.

Since the strength, and therefore stiffness, of the concrete is a function of maturity, the stiffness of the concrete at different locations in the slab can be assessed by using the maturity concept. Additional stiffness needed by the concrete to overcome the restraint can be quantified by evaluating the difference in the concrete maturity at the time of set. For this purpose, the maturity of the concrete at different locations and depths were estimated for the time of set at each location. The maturity concept assumes that the strength of a particular concrete mixture is a function of the maturity of that concrete, regardless of the time-temperature combinations leading to that maturity. Since concrete strength is a function of time and temperature, different combinations of time and temperature can be used to determine the maturity of the concrete. Concrete maturity represents the area under the temperature versus time graph, with reference to a datum temperature, and can be estimated by using the Nurse-Saul expression provided in equation 3-4 [16].

$$\text{Maturity Function} = M(t) = \sum (T_a - T_0) \Delta t \quad (\text{Equation 3-4})$$

Where: $M(t)$ = Temperature-time factor at age t (degree-hours)

Δt = Time interval

T_a = Average concrete temperature during the time interval Δt

T_0 = Datum temperature below which there is no strength gain, assumed to be equal to 14°F.

The temperatures recorded by the vibrating wire gages were used in calculating the maturity. The maturity corresponding to the time of set of each gage is presented in Table 3.3 and illustrated in Figure 3.10. The maturity at the time of set indicates that the maturity at the top, middle and bottom portions of the slab are similar (within 20 percent of each other). This confirms the previous observation that the concrete sets uniformly within the slab, irrespective of the slab restraining conditions.

Table 3.3. Concrete maturity corresponding to the estimated set times for restrained slabs.

Location	Direction ¹	Depth	Maturity at Concrete Set (°F-hour)			
			Slab A	Slab B	Slab C	Average
Corner; Centerline	L	Top	754	794	844	797
		Middepth	761	795	--	778
		Bottom	725	--	--	725
	D	Top	788	774	800	787
		Middepth	--	775	808	792
		Bottom	757	738	860	785
	T	Top	752	706	795	751
		Middepth	767	707	791	755
		Bottom	804	721	778	768
Edge; Centerline	L	Top	736	671	746	718
		Bottom	705	682	717	701
Midpanel	L	Top	780	641	886	769
		Bottom	739	718	837	764
Edge; Lane/Shoulder	L	Top	736	663	666	689
		Bottom	756	679	669	701
Transverse Joint	T	Top	830	823	817	823
		Bottom	793	832	864	830
Corner; Lane/Shoulder	L	Top	732	761	841	778
		Middepth	687	764	739	730
		Bottom	779	772	766	772
	D	Top	729	786	671	729
		Middepth	--	784	690	737
		Bottom	732	741	662	712
	T	Top	756	742	781	760
		Middepth	747	742	776	755
		Bottom	816	728	777	774

¹ L: Longitudinal direction; D: Diagonal direction; T: Transverse direction

The variation in the concrete maturity at the time of set along the slab depth is further examined in Figure 3.11. The figure presents the maturity versus a normalized depth parameter. The normalized depth parameter is calculated by dividing the depth of the sensor by the slab thickness at the location of the sensor. This parameter is introduced

to take into account the variability of the slab thickness during construction and provides a non-dimensional value that can be used to compare maturity for sensors located at varying depths with respect to the slab thickness. The figure confirms that, at the time of set, the maturity is not affected by the depth within the slab.

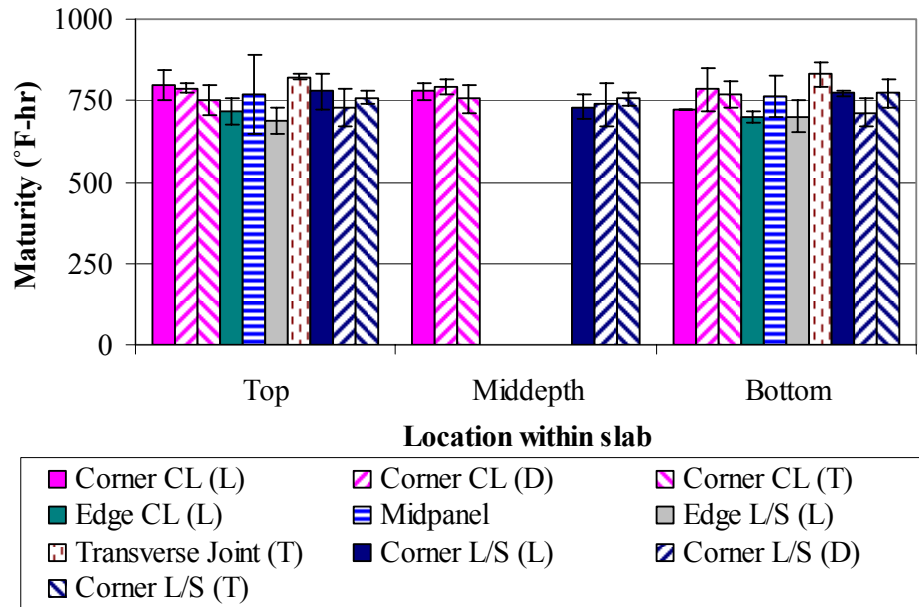


Figure 3.10. Average maturity at time of set for restrained slabs.

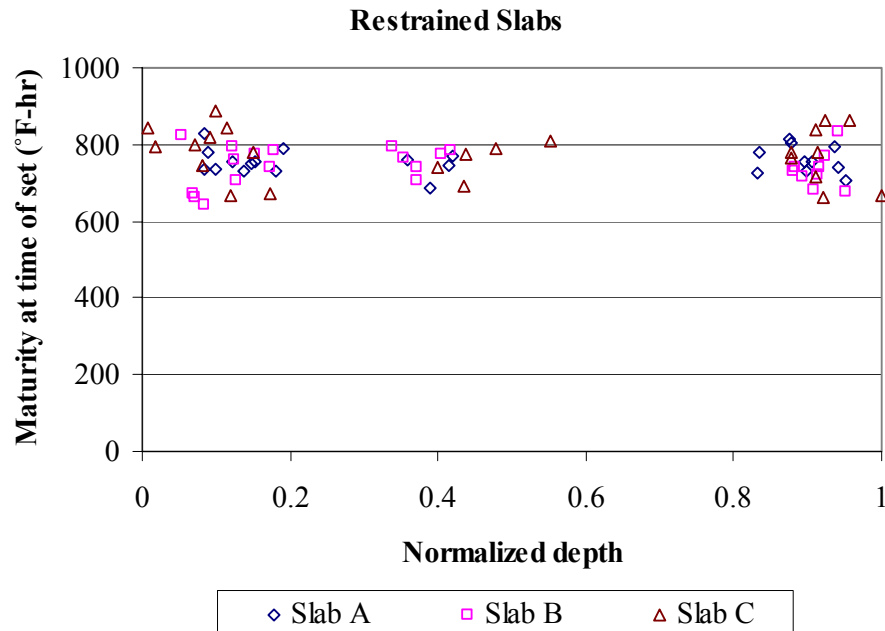


Figure 3.11. Maturity at time of set with respect to sensor depth for restrained slabs.

Moreover, Figure 3.12 presents the maturity at the time of set depending on the type of restraint affecting the movements recorded by the sensors. The investigated restraints are: presence of the tie bars, presence of dowel bars, presence of an adjacent slab, and friction along the slab/base interface. The figure is based on data from the corner sensors at the centerline joint and the lane/shoulder joint. According to the figure, the maturity at the time of set established using the VW gages is not affected by the slab restraining conditions.

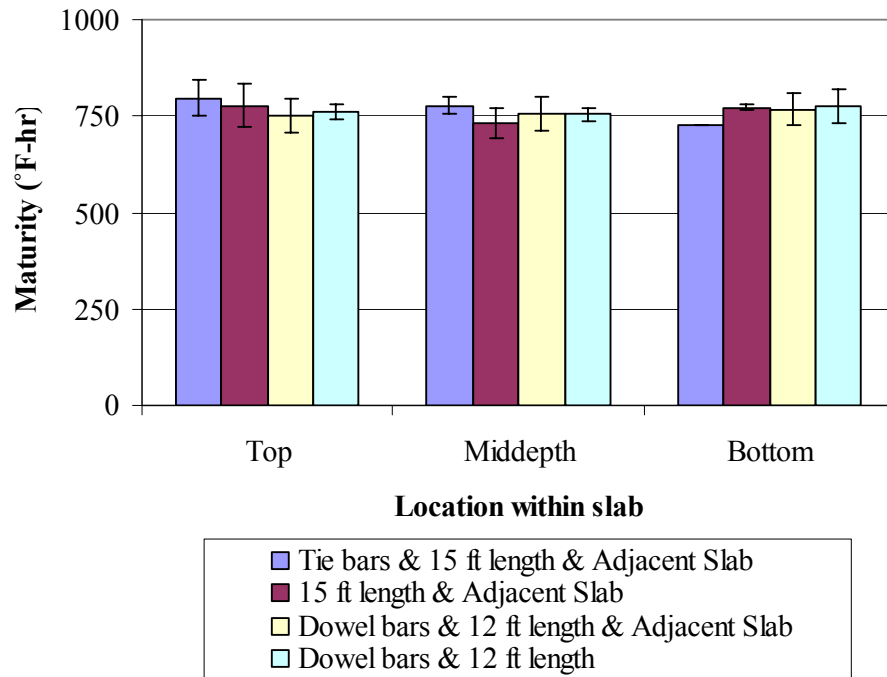


Figure 3.12. Effect of restraining conditions on maturity at set time for restrained slabs.

3.4.3. Unrestrained Slabs

Similarly to what was carried out for the restrained slabs, the variation in the measured strain with respect to temperature changes during the first 42 hours after placement are used to identify the concrete set time for the unrestrained slabs. The time of final set of the concrete is selected as that corresponding to the time when expansion/contraction is measured with changes in temperature. The early-age variation in the total strain for the midpanel sensors oriented in the longitudinal direction and located at the top and bottom of the unrestrained Slab B are illustrated in Figure 3.13 and Figure 3.14. Based on these figures, the set times were found to correspond to 5:15 PM for the top of the slab and 4:30 PM for the bottom of the slab. These times are then zeroed

to the time when concrete mixing was initiated, which is assumed to be 45 minutes prior to concrete placement, as previously explained. According to the thermistor readings, the concrete was placed at 7:00 AM at the midpanel of unrestrained Slab B. Accordingly, the concrete set time for the midpanel of unrestrained Slab B is found to correspond to elapsed time of 10.25 hours (top of slab) and 9.5 hours (bottom of slab) after mixing.

A similar procedure was followed to determine the concrete set time for every sensor at every depth and location within unrestrained Slabs A, B and C. The figures illustrating the early age variations of total strains with temperature are included in appendix B. The set times established based on the early-age variation in the strain data, are presented in Table 3.4 and Figure 3.15 for the unrestrained slabs.

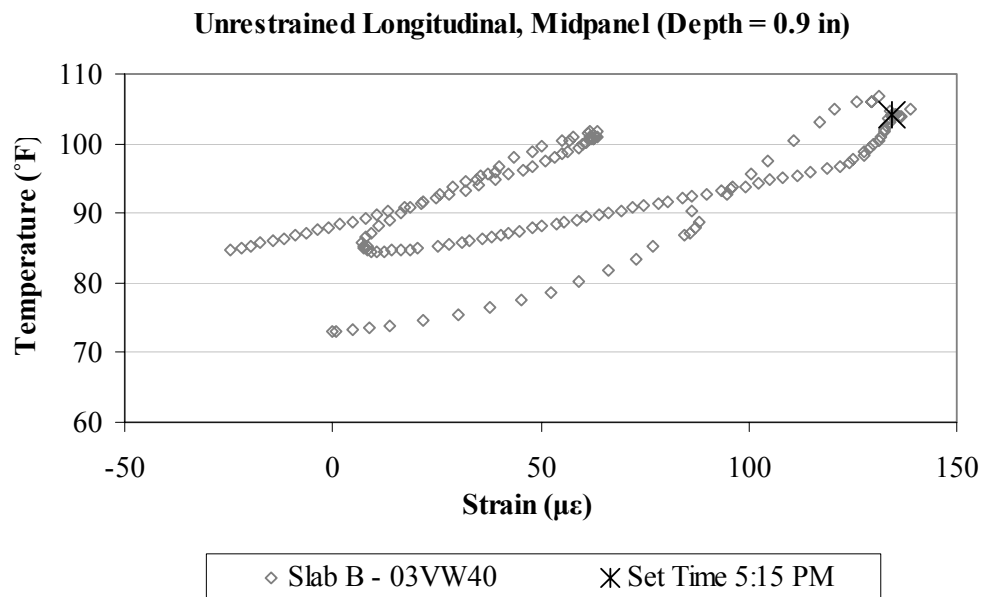


Figure 3.13. Early-age variation in the total strain with temperature, in the longitudinal direction, for the top sensor located at midpanel of unrestrained Slab B.

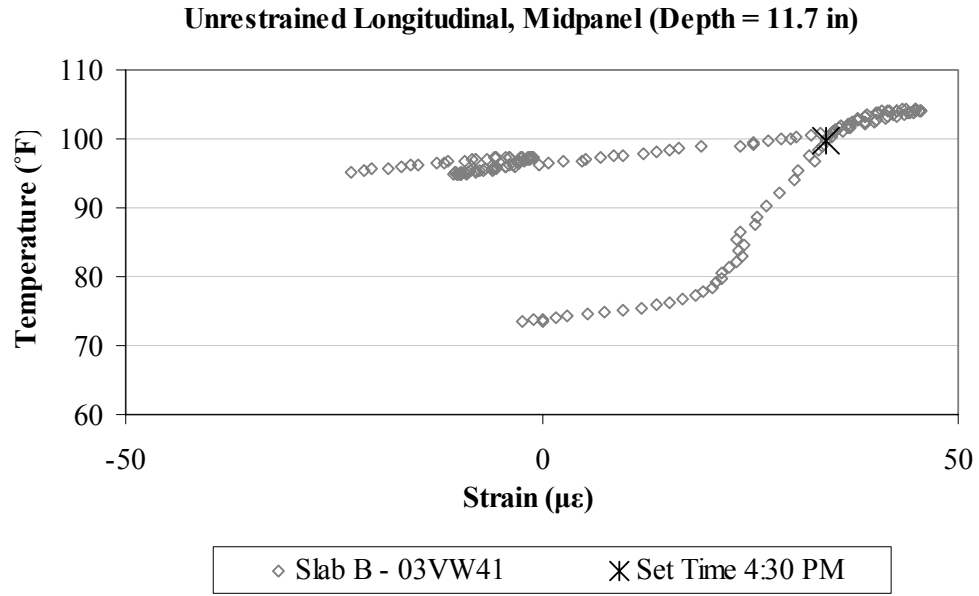


Figure 3.14. Early-age variation in the total strain with temperature, in the longitudinal direction, for the bottom sensor located at midpanel of unrestrained Slab B.

Unrestrained Slabs											
Slab A				Slab B				Slab C			
9.92 ± 0.14 (T)	10 (T)			10 (T)	9.92 ± 0.14 (T)			10.5 (T)	10.83 ± 0.29 (T)		
10.13 ± 0.18 (M)	10 (B)			10.25 (B)	10.17 ± 0.14 (M)			9.75 (B)	10.63 ± 0.18 (M)		
10.67 ± 0.76 (B)					10.63 ± 0.18 (B)				11.25 ± 0.90 (B)		
	10 (T)	9.75 (T)		10 (T)	11 (T)			10.75 (T)	10.5 (T)		
	10.75 (B)	10.75 (B)		11.5 (B)	10.25 (B)			10.75 (B)	11.75 (B)		
		9.83 ± 0.29 (T)		9.50 ± 0.0 (T)				9.58 ± 0.14 (T)			
	10 (T)	10.13 ± 0.18 (M)		10.0 ± 0.43 (M)	11.75 (T)			9.58 ± 0.52 (M)	10.5 (T)		
	9.5 (B)	10.67 ± 0.76 (B)		10.42 ± 0.14 (B)	12 (B)			10.17 ± 0.14 (B)	N/A (B)		

T: Top of slab; M: Middepth; B: Bottom of slab

Figure 3.15. Set times in the unrestrained slabs.

Table 3.4. Concrete set time based on early-age vibrating wire data for unrestrained slabs.

Location	Direction ¹	Depth	Concrete Set Time ^{2,3} (hours)			
			Slab A	Slab B	Slab C	Average
Corner; Centerline	L	Top	10	10	10.5	10.17
		Middepth	10.25	10	10.5	10.25
		Bottom	11.5	--	10.5	11.00
	D	Top	9.75	9.75	11	10.17
		Middepth	10	10.25	10.75	10.33
		Bottom	10.5	10.75	11	10.75
	T	Top	10	10	11	10.33
		Middepth	--	10.25	--	10.25
		Bottom	10	10.5	12.25	10.92
Edge; Centerline	L	Top	10	10	10.5	10.17
		Bottom	10	10.25	9.75	10.00
Midpanel	L	Top	10	11	10.5	10.50
		Bottom	10.75	10.25	11.75	10.92
Edge; Lane/Shoulder	L	Top	10	11.75	10.5	10.75
		Bottom	9.5	12	--	10.75
Transverse Joint	T	Top	9.75	10	10.75	10.17
		Bottom	10.75	11.5	10.75	11.00
Corner; Lane/Shoulder	L	Top	9.5	9.5	9.75	9.58
		Middepth	10.25	9.5	9	9.58
		Bottom	10.5	10.5	10.25	10.42
	D	Top	10	9.5	9.5	9.67
		Middepth	--	10.25	9.75	10.00
		Bottom	10	10.25	10	10.08
	T	Top	10	9.5	9.5	9.67
		Middepth	10	10.25	10	10.08
		Bottom	11.5	10.5	10.25	10.75

¹ L: Longitudinal direction; D: Diagonal direction; T: Transverse direction

² Set time is zeroed to the concrete mixing time (45 minutes prior to placement)

³ Dashed lines indicate that VW data is not available or cannot be interpreted

The results indicate that the average concrete set time varies between 9.5 and 12 hours after mixing, with an overall average of 10 hours. At each location, the set times estimated based on the sensors located at the top, middepth and bottom of the slab are similar. The largest difference between top and bottom of the slab was recorded at the midpanel of unrestrained Slab C and amounts to 1.25 hours. To further illustrate this point, the average set times at the top, middepth and bottom of the slab were calculated based on the data collected from the sensors in all the slabs, and are compared to each other in Figure 3.16. The figure shows that the set times of the top, middle and bottom

portions of the slabs are within 6 percent of each other. Moreover, the concrete set times estimated at the different locations within the slab are within 26 percent from each other and do not show any specific pattern of variation. This implies that the slab restraining conditions do not significantly affect the concrete set time. Similarly to what was observed for the restrained slabs, this was also expected since the set time describes a concrete material property, irrespective of the slab restraining conditions.

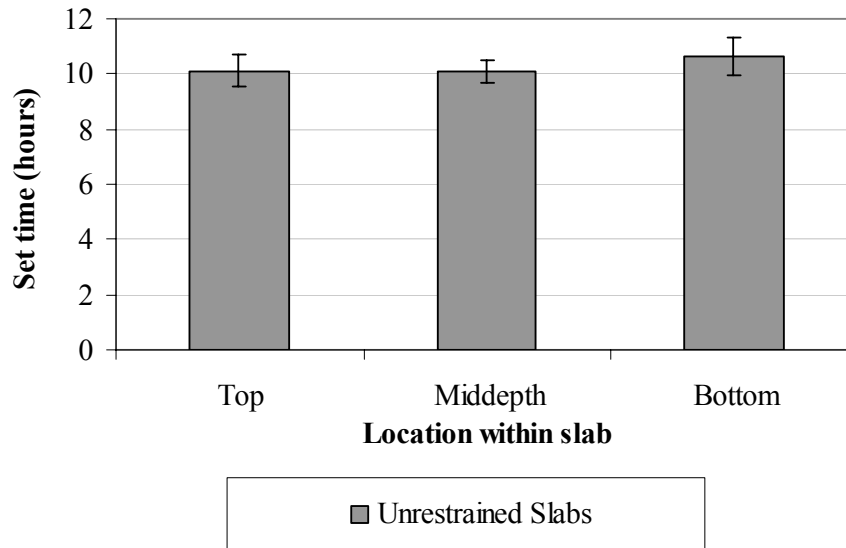


Figure 3.16. Variation in average concrete set time with depth, for unrestrained slabs.

Similarly to the analysis carried out for the restrained slabs, the maturity of the concrete at different locations and depths were estimated for the time of set at each location. The procedure described in the previous section was adopted and the temperatures recorded by the vibrating wire gages were used in calculating the maturity. The maturity corresponding to the time of set of each gage is presented in Table 3.5 and illustrated in Figure 3.17. The maturity at the time of set indicates that the maturity at the top, middle and bottom portions of the slab are not significantly different, within 19 percent of each other. This confirms the previous observation that the concrete uniformly sets within the same time period, irrespective of the slab restraining conditions.

Table 3.5. Concrete maturity corresponding to the estimated set times for unrestrained slabs.

Location	Direction ¹	Depth	Maturity at Concrete Set (°F-hour)			
			Slab A	Slab B	Slab C	Average
Corner; Centerline	L	Top	745	720	786	750
		Middepth	764	717	789	757
		Bottom	837	--	753	795
	D	Top	722	623	834	726
		Middepth	743	667	811	740
		Bottom	749	682	800	744
	T	Top	748	720	835	768
		Middepth	--	738	--	738
		Bottom	709	732	912	784
Edge; Centerline	L	Top	--	715	746	731
		Bottom	670	694	657	674
Midpanel	L	Top	746	832	782	787
		Bottom	779	724	861	788
Edge; Lane/Shoulder	L	Top	718	841	714	757
		Bottom	654	854	--	754
Transverse Joint	T	Top	736	754	801	764
		Bottom	777	887	747	804
Corner; Lane/Shoulder	L	Top	687	687	712	695
		Middepth	750	692	639	694
		Bottom	745	756	713	738
	D	Top	732	617	689	679
		Middepth	--	685	708	697
		Bottom	692	650	699	680
	T	Top	736	691	690	706
		Middepth	729	760	728	739
		Bottom	816	745	716	759

¹ L: Longitudinal direction; D: Diagonal direction; T: Transverse direction

The variation of the concrete maturity at the time of set along the slab depth is examined in Figure 3.18. The figure presents the maturity at the time of set versus the normalized depth. As previously explained in section 3.4.2, the normalized depth parameter is calculated by dividing the depth of the sensor by the slab thickness at the location of the sensor. The figure confirms that, at the time of set, the maturity is not affected by the depth within the slab.

Moreover, Figure 3.19 presents the maturity at the time of set depending on the type of restraint affecting the movements recorded by the sensors. The investigated restraints are: presence of an adjacent slab, and friction along the slab/base interface. The figure is based on data from the corner sensors at the centerline joint and the

lane/shoulder joint. According to the figure, the maturity at set time is not affected by the slab restraining conditions.

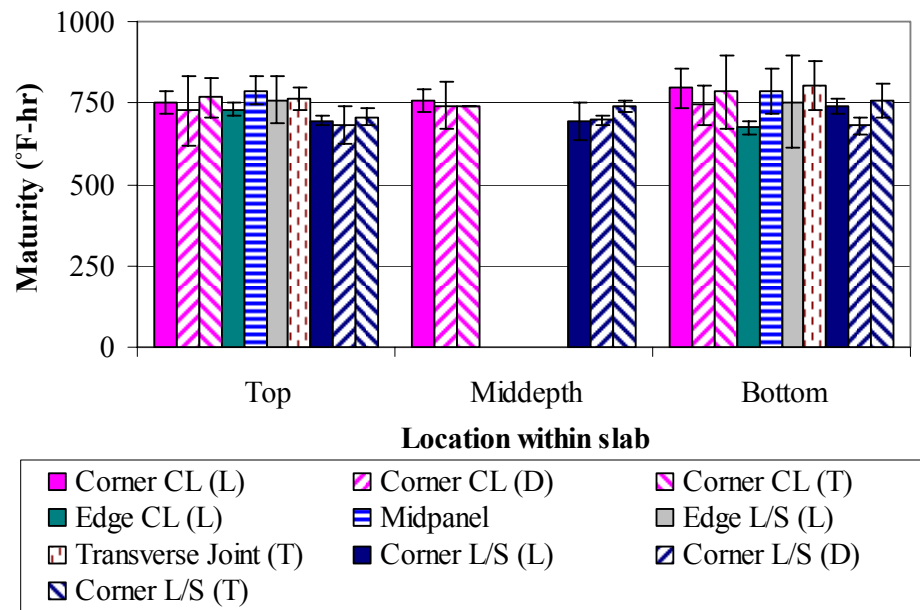


Figure 3.17. Average maturity at time of set for unrestrained slabs.

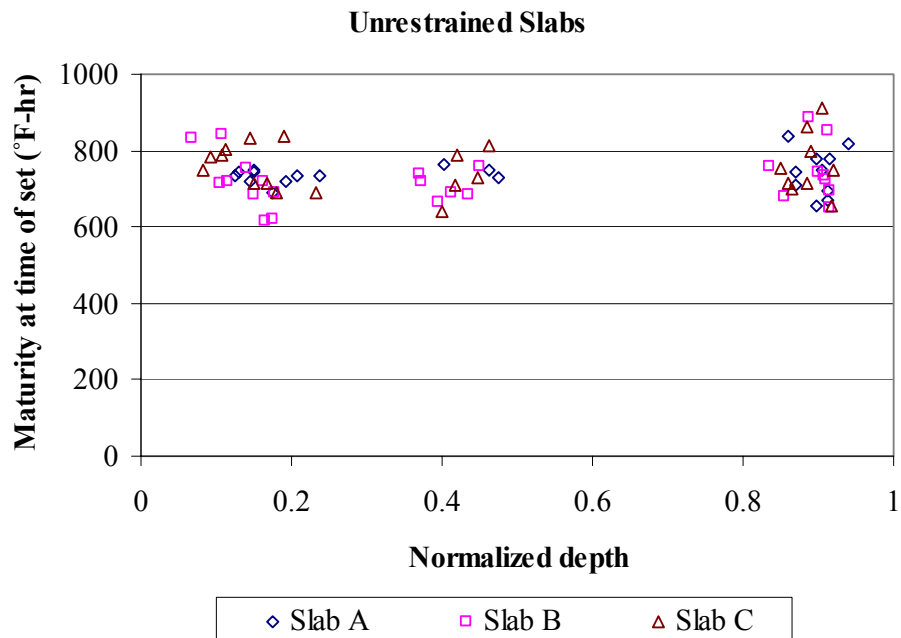


Figure 3.18. Maturity at time of set with respect to sensor depth for unrestrained slabs.

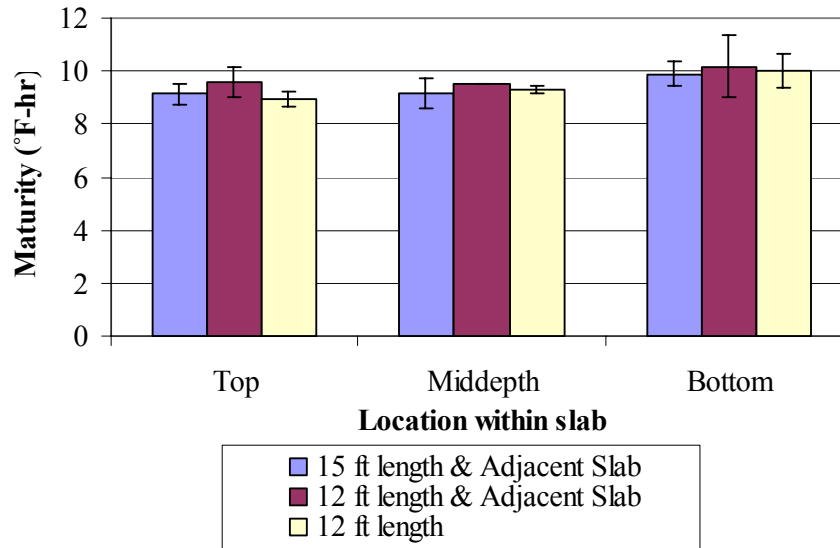


Figure 3.19. Effect of restraining conditions on maturity at set time for unrestrained slabs.

3.4.4. Comparison between Restrained and Unrestrained Slabs

The concrete set time is similar for both restrained and unrestrained slabs, irrespective of the sensor location within the slab and the slab restraining conditions. Figure 3.20 presents the variation of the concrete maturity at the time of set with the normalized slab depths for both types of slabs. The figure confirms the previous statements that the concrete set time is similar across the slab depth. The figure also shows that the maturity at set time is not affected by the slab restraining conditions.

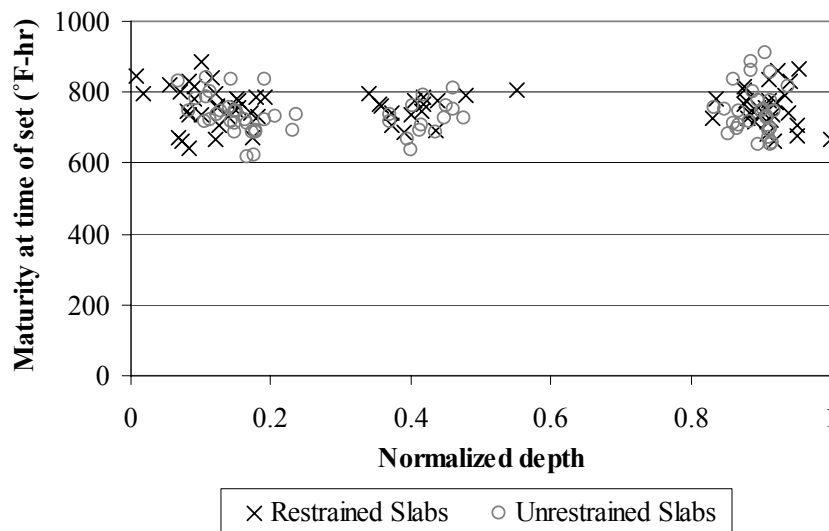


Figure 3.20. Maturity at time of set with respect to depth for restrained and unrestrained slabs.

Moreover, Figure 3.21 compares the maturity at the time of set depending on the type of restraint affecting the movements recorded by the sensors in the restrained and unrestrained slabs. The figure is based on data from the corner sensors at the centerline joint and the lane/shoulder joint. The figure confirms the previous observations that the slab restraining conditions do not affect the set time of the concrete. The maturity values are within 16 percent of each other.

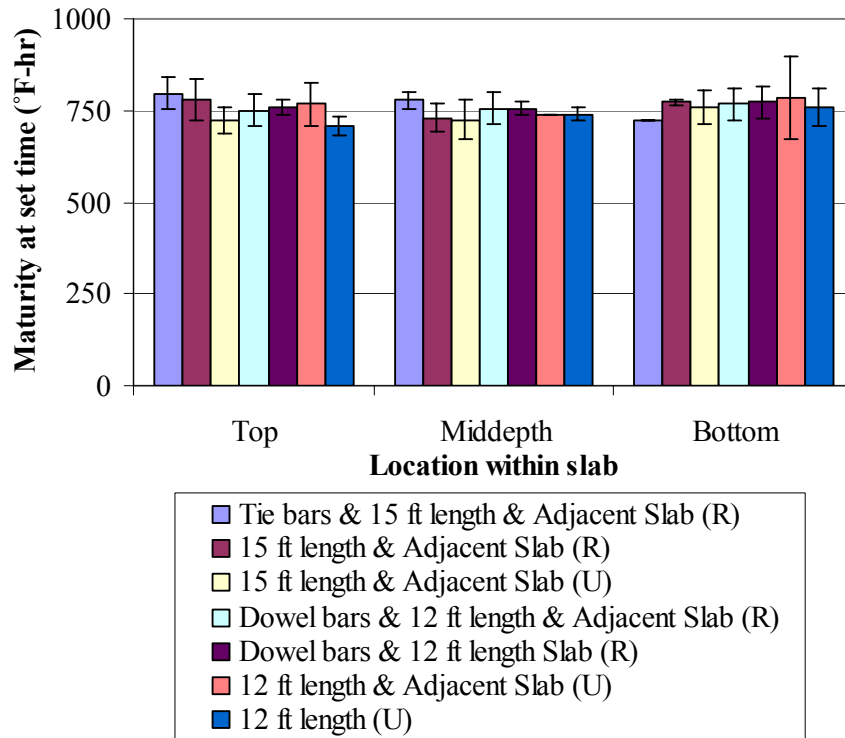


Figure 3.21. Effect of restraining conditions on maturity at set time for restrained and unrestrained slabs.

3.4.5. Built-in Temperature Gradient based on Concrete Strain Measurements

As determined in sections 3.4.2 and 3.4.3, the final set time of the restrained slabs takes place between 2:46 PM and 6:01 PM on the day of construction, and the final set time of the unrestrained slabs takes place between 3:15 PM and 6:15 PM on the day of construction. During these time periods, the concrete temperature conditions and the corresponding equivalent linear temperature gradients vary significantly, as presented in section 3.2.0. The temperature profiles corresponding to the upper and lower limits of the time ranges are presented in Figure 3.22. The corresponding equivalent linear temperature gradients are presented in Figure 3.23 for the restrained and unrestrained

slabs. The temperature gradients vary between 1.12 and 0.05°F/in for the case of the restrained slabs, and between 0.90 and 0.14°F/in for the case of the unrestrained slabs. This constitutes a relatively large range of temperature gradients.

Previous research studying the behavior of JPCP slabs in response to temperature and moisture changes has shown that the response of the slab is controlled by the temperature and moisture conditions at midpanels, and not at the edges [17]. As a result, the temperature conditions at midpanel will be considered in establishing the built-in construction gradient. Moreover, relaxation of the concrete at the slab surface might affect the time of set. Therefore, it would be logical to use the data based on the sensors located at the bottom portion of the slab. In this case, the midpanel gradients (sensors at bottom of slab) vary between 0.19 and 0.42°F/in for the restrained slabs, with an average of 0.31°F/in. For the unrestrained slabs, the midpanel gradients (sensors at bottom of slab) vary between 0.21 and 0.42°F/in for the restrained slabs, with an average of 0.31°F/in. As a result, the built-in temperature gradient is established as 0.31°F/in, for both restrained and unrestrained slabs. This built-in gradient is equivalent to a 3.9°F temperature difference across the slab depth.

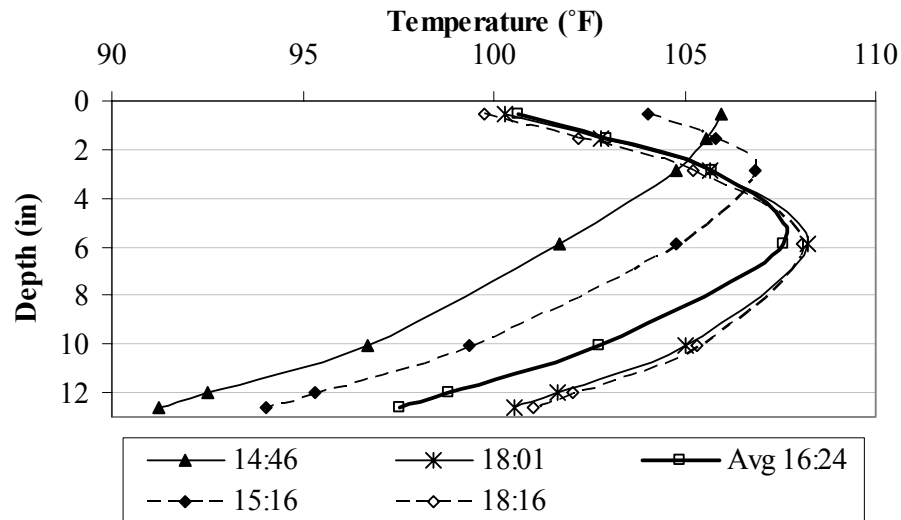


Figure 3.22. Range of temperature profiles at the time of set for the restrained and unrestrained slabs based on VW data.

Restrained Slabs					
Slab A		Slab B		Slab C	
0.36 ± 0.06 (T)	0.34 (T)	0.80 (T)	0.48 ± 0.27 (T)	0.31 (T)	0.29 ± 0.03 (T)
0.34 ± 0.0 (M)	0.34 (B)	0.42 (B)	0.48 ± 0.27 (M)	0.31 (B)	0.29 ± 0.03 (M)
0.30 ± 0.04 (B)			0.38 ± 0.05 (B)		0.20 ± 0.10 (B)
	0.31 (T)	0.26 (T)	0.26 (T)	1.12 (T)	0.26 (T)
	0.31 (B)	0.26 (B)	0.21 (B)	0.42 (B)	0.05 (B)
		0.39 ± 0.04 (T)	0.36 ± 0.06 (T)		0.47 ± 0.38 (T)
	0.34 (T)	0.57 ± 0.32 (M)	0.36 ± 0.06 (M)	0.90 (T)	0.51 ± 0.26 (M)
	0.27 (B)	0.26 ± 0.05 (B)	0.31 ± 0.04 (B)	0.60 (B)	0.44 ± 0.31 (B)
T: Top of slab;		M: Middepth;		B: Bottom of slab	

Unrestrained Slabs					
Slab A		Slab B		Slab C	
0.67 ± 0.11 (T)	0.60 (T)	0.60 (T)	0.67 ± 0.11 (T)	0.34 (T)	0.29 ± 0.04 (T)
0.51 ± 0.13 (M)	0.60 (B)	0.42 (B)	0.48 ± 0.11 (M)	0.80 (B)	0.33 ± 0.02 (M)
0.38 ± 0.21 (B)			0.33 ± 0.02 (B)		0.22 ± 0.15 (B)
	0.60 (T)	0.80 (T)	0.60 (T)	0.27 (T)	0.31 (T)
	0.31 (B)	0.31 (B)	0.19 (B)	0.42 (B)	0.31 (B)
		0.70 ± 0.17 (T)	0.90 ± 0.0 (T)		0.86 ± 0.06 (T)
	0.60 (T)	0.51 ± 0.13 (M)	0.58 ± 0.28 (M)	0.21 (T)	0.84 ± 0.26 (M)
	0.90 (B)	0.38 ± 0.21 (B)	0.37 ± 0.04 (B)	0.14 (B)	0.48 ± 0.11 (B)
T: Top of slab;		M: Middepth;		B: Bottom of slab	

Figure 3.23. Gradients at set time in restrained and unrestrained slabs.

3.5.0. Early-Age Pressure along the Slab/Base Interface

Static pressure cells were placed at the interface between the JPCP slabs and the asphalt treated permeable base layer. The pressure cells were placed at the midpanel and corner locations in two restrained and two unrestrained slabs. Pressure values at these locations would indicate the change in pressure exerted on the base layers by the concrete due to curling and warping. Positive gradients cause pressures at the slab edges to be larger than those at midpanel due to the downward curvature of the slab. Similarly, the upward curvature produced by negative gradients produces higher pressures at the midpanel compared to those at slab edges.

Once the concrete slabs set, the pressure exerted by the slabs on the base is expected to vary along uniform rates. At the slab corners, the pressure is expected to increase with increasing concrete temperature gradients and at midpanels, the pressure is expected to decrease with increasing concrete temperature gradients. Before the concrete sets, the pressure exerted on the base layer is not expected to vary along a uniform rate. Data was collected from the static pressure cells and the variation in the measured pressure with respect to changes in the concrete temperature gradients during the first 42 hours after placement is used to identify the slab set time. The time of final set of the slabs is selected as that corresponding to the time when uniform changes in pressure are measured with changes in temperature gradients.

The analysis of the early-age variations in pressure with respect to temperature gradients included all the pressure cells of the restrained and unrestrained slabs. The general trends observed are presented in sections 3.5.2 and 3.5.3. As a result of the analysis of the early-age variation in pressure measurements, the time of set of the slabs is determined. Finally, the built-in temperature gradients corresponding to the time of set are estimated in section 3.5.4. A general overview of the static pressure cells is presented first.

3.5.1. Static Pressure Cells

The static earth pressure cells consist of two stainless steel plates welded together around their periphery and separated by a narrow gap filled with hydraulic fluid. External pressures cause the two plates to come closer together thus exerting an equal pressure on the internal fluid. The fluid filled cavity is connected to a vibrating wire transducer that converts the fluid pressure into an electric signal transmitted to the datalogger. Temperature changes cause the internal fluid to expand at a different rate than the surrounding material. The pressure measurements need to be corrected for the effects of temperature on the vibrating wire transducers. The pressure cells are equipped with a thermistor to monitor temperature changes [18]. The pressure readings are automatically corrected for the effect of temperature on the vibrating wires in the pressure cells. This is done internally by the datalogger based on equation 3-5, provided by the manufacturer. The calibration factor and the thermal factor are provided by the manufacturer for every pressure cell.

$$P_{corrected} = (R_0 - R_1)C + (T_1 - T_0)K \quad \text{(Equation 3-5)}$$

where: $P_{corrected}$ = Thermally corrected pressure

R_0 = Initial reading

R_1 = Current reading

C = Calibration factor (provided by the manufacturer)

T_1 = Current temperature

T_0 = Initial temperature

K = Thermal factor (provided by the manufacturer)

The pressure measurements are zeroed based on the pressure recorded prior to loading of the cells (or placement of the concrete). The variation in the pressure

measurements during the first 48 hours after placement of the concrete is presented in Figure 3.24 for the restrained slabs and Figure 3.25 for the unrestrained slabs. Both figures show that during the first couple of hours, the pressure increases with increasing time at all locations. This reflects the time needed by the pressure cell to adjust to the weight of the concrete that had just been placed. After approximately 10 hours, the pressures along the corners decrease while those at midpanel increase. The concrete temperatures and resulting gradients affect the recorded pressure. When subjected to positive temperature gradients, the slab curls downward, resulting in a decrease in pressure at midpanel and increase in pressure at the slab edge. The situation is reversed when the temperature gradients are negative. Approximately ten hours after construction, the temperature variations are uniform along the slab depth and the gradients approach zero values and keep decreasing. The negative gradients cause the slabs to curl upwards; this accounts for the decrease in pressure at the slab edge and the increase in pressures at midpanel.

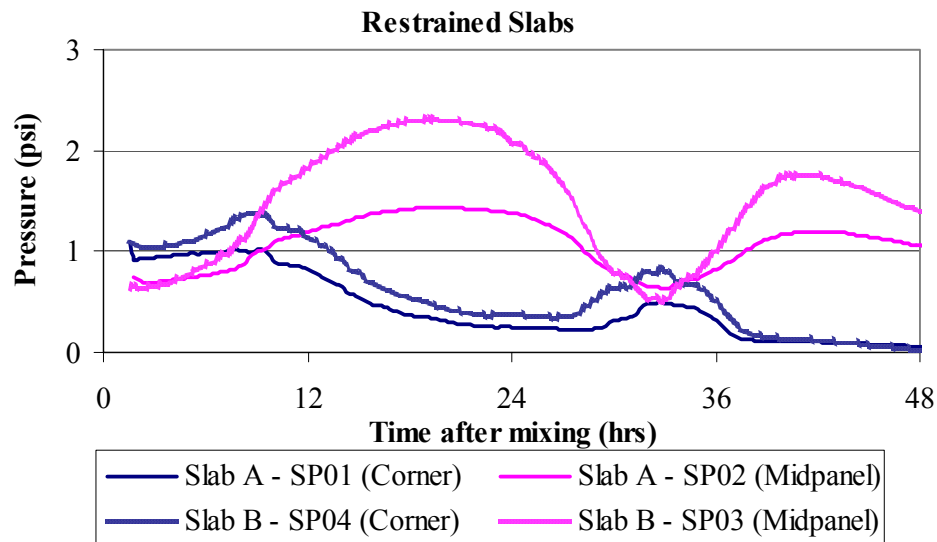


Figure 3.24. Early-age variation in pressure with time for the restrained slabs.

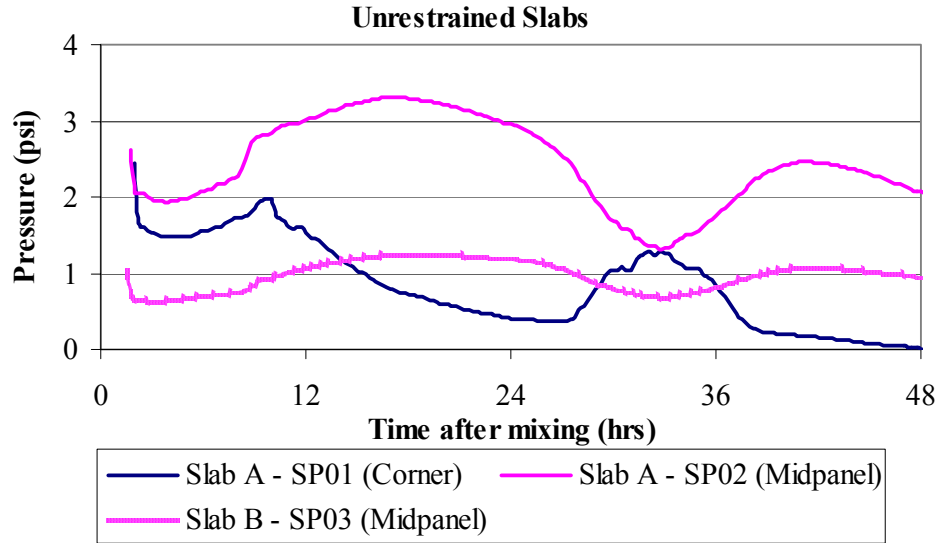


Figure 3.25. Early-age variation in pressure with time for the unrestrained slabs.

3.5.2. Restrained Slabs

Having established that the pressure at the slab/base interface is affected by temperature variations, the pressure readings at early ages can be used to estimate the time of set of the overall slab. It has already been mentioned that the concrete sets as it approaches a certain level of maturity. It has also been mentioned that the concrete maturity is a function of temperature and time. As a result, by comparing the pressure measurements to the temperature gradients inside the slab, the time of set at the slab/base interface can be determined. As the concrete temperature increases due to hydration, and as long as the concrete is still in its plastic state, pressure measurements do not vary uniformly with temperature. As the concrete sets, the pressure measurements become a function of the temperature gradient in the concrete. The point in time when pressure measurements are uniform with changes in temperature gradients is considered as representative of the slab set time at the corresponding locations.

The variation in pressure measurements with temperature gradients is plotted for the four pressure cells in the restrained Slab A and Slab B, and are presented in Figure 3.26 to Figure 3.29. According to the figures, the time of set for the restrained slabs takes place between 3:46 PM and 4:01 PM. These times are zeroed to the time when concrete mixing was initiated, which was assumed to be 45 minutes prior to concrete placement. Concrete placement was initiated at 6:46 AM for restrained Slab A, and at 6:31 AM for

restrained Slab B. This indicates that the restrained slabs set after an elapsed time of 9.25 hours after placement of the concrete, or 10 hours after mixing of the concrete.

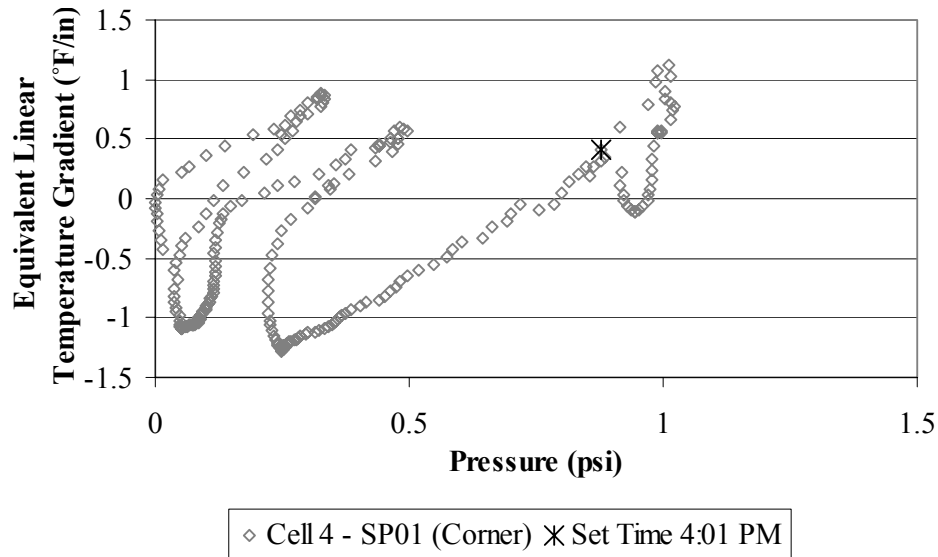


Figure 3.26. Early-age variation in pressure with changes in the temperature gradient for the corner of restrained Slab A.

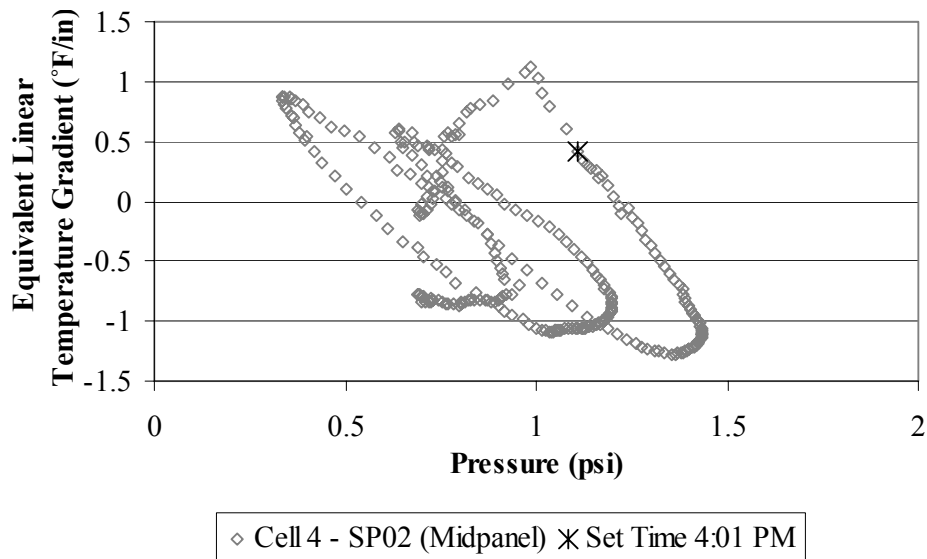


Figure 3.27. Early-age variation in pressure with changes in the temperature gradient for the midpanel of restrained Slab A.

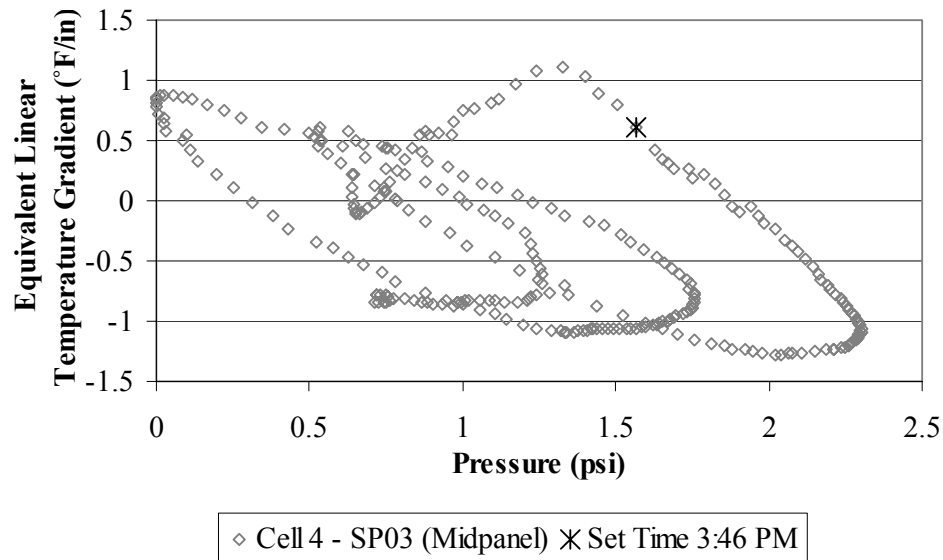


Figure 3.28. Early-age variation in pressure with changes in the temperature gradient for the midpanel of restrained Slab B.

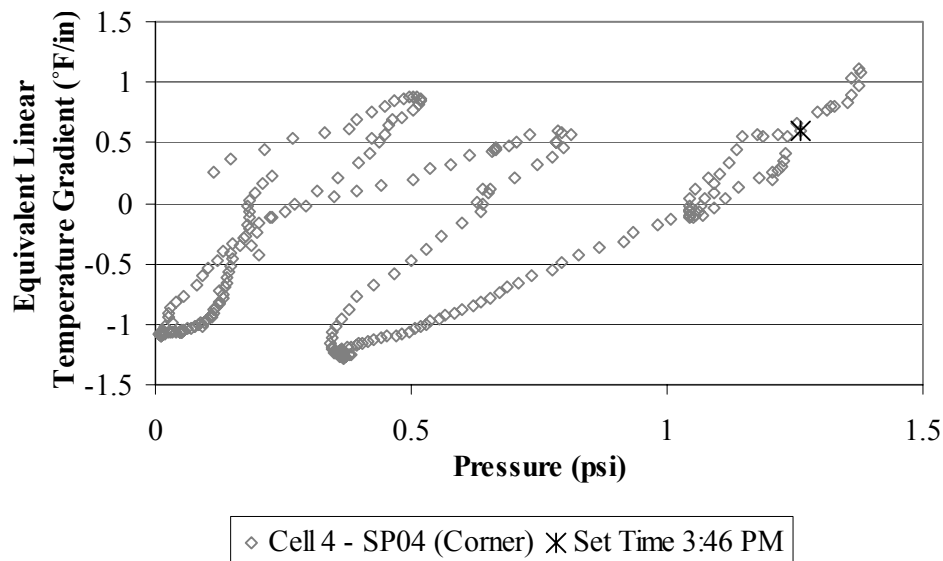


Figure 3.29. Early-age variation in pressure with changes in the temperature gradient for the corner of restrained Slab B.

3.5.3. Unrestrained Slabs

Similarly to the procedure carried out for the restrained slabs, the early-age variation in the pressure measurements in the unrestrained slabs is also examined. Unfortunately, the pressure cell located at the corner of Slab B has not been recording valid data since construction. The variations in pressure measurements with temperature gradients are plotted for the three remaining pressure cells in the unrestrained Slab A and

Slab B, and are presented in Figure 3.30 to Figure 3.32. According to the figures, the time of set of the unrestrained slabs takes place at 4:00 PM. The set time is zeroed to the time when concrete mixing was initiated, which is estimated to be 45 minutes prior to concrete placement, as previously explained. Concrete placement was initiated at 7:00 AM for unrestrained Slabs A and B. This indicates that the unrestrained slabs set after an elapsed time of 9 hours after placement of the concrete or 9.75 hours after mixing of the concrete.

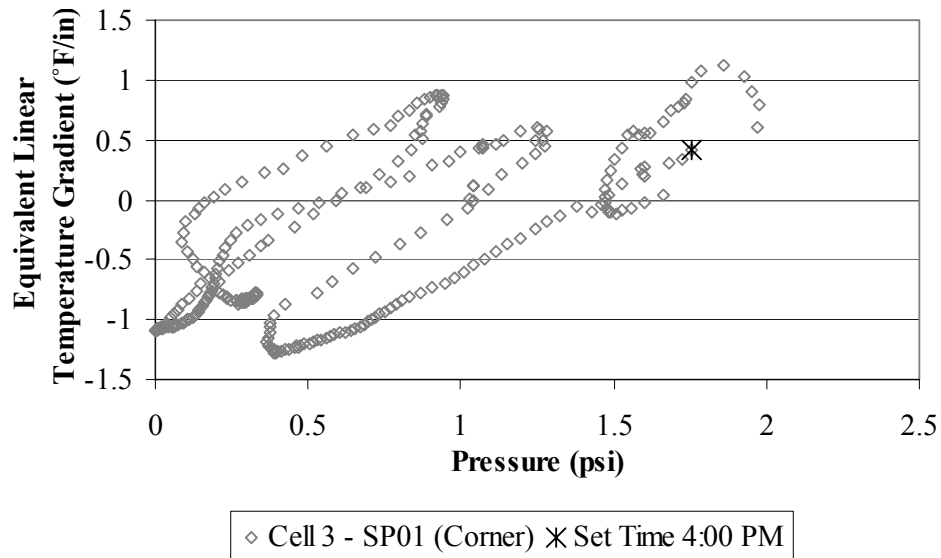


Figure 3.30. Early-age variation in pressure with changes in the temperature gradient for the corner of unrestrained Slab A.

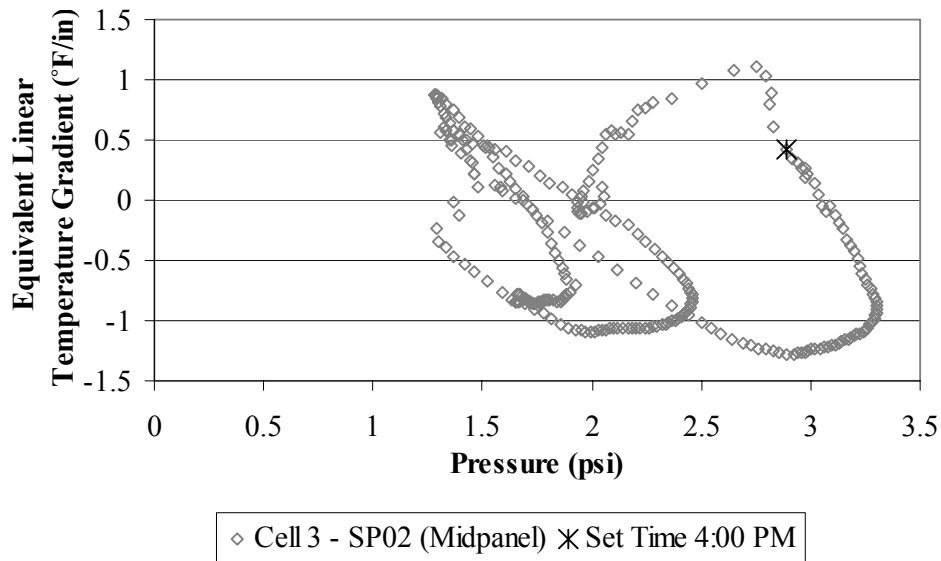


Figure 3.31. Early-age variation in pressure with changes in the temperature gradient for the midpanel of unrestrained Slab A.

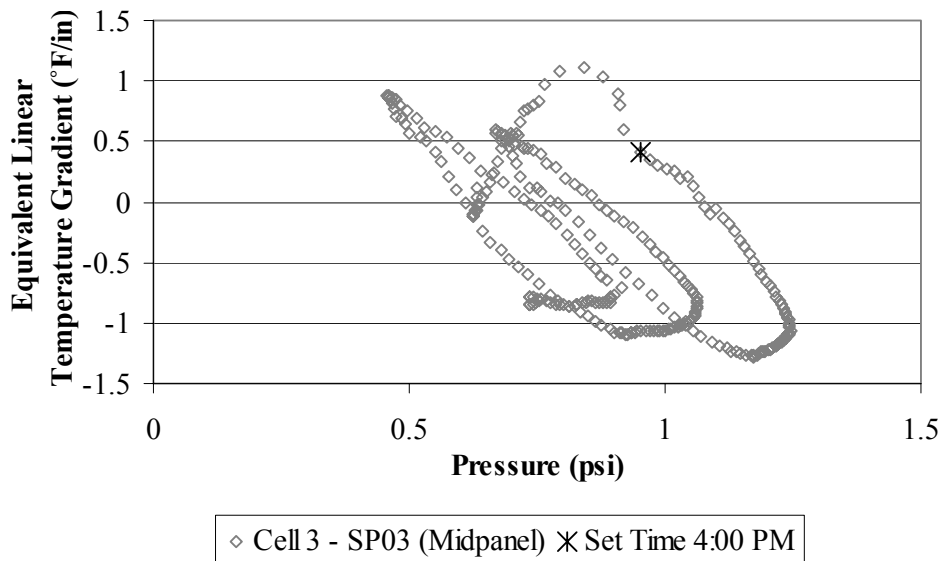


Figure 3.32. Early-age variation in pressure with changes in the temperature gradient for the midpanel of unrestrained Slab B.

3.5.4. Built-in Temperature Gradient Based on Pressure Measurements

The final set time of the restrained slabs takes place between 3:46 PM and 4:01 PM, and the final set time of the unrestrained slabs takes place at approximately 4:00 PM. The temperature profiles do not vary much during this time period, as shown in Figure 3.33. The corresponding equivalent linear temperature gradients vary between 0.60 and 0.42°F/in. The difference in gradients during these times is not significant, and it can be

concluded that the built-in temperature gradient based on the pressure cell data is, on average, $0.51^{\circ}\text{F}/\text{in}$ for the restrained slabs and $0.42^{\circ}\text{F}/\text{in}$ for the unrestrained slabs. These gradients are equivalent to a 6.4°F temperature difference across the restrained slab depth and 5.3°F temperature difference across the unrestrained slab depth.

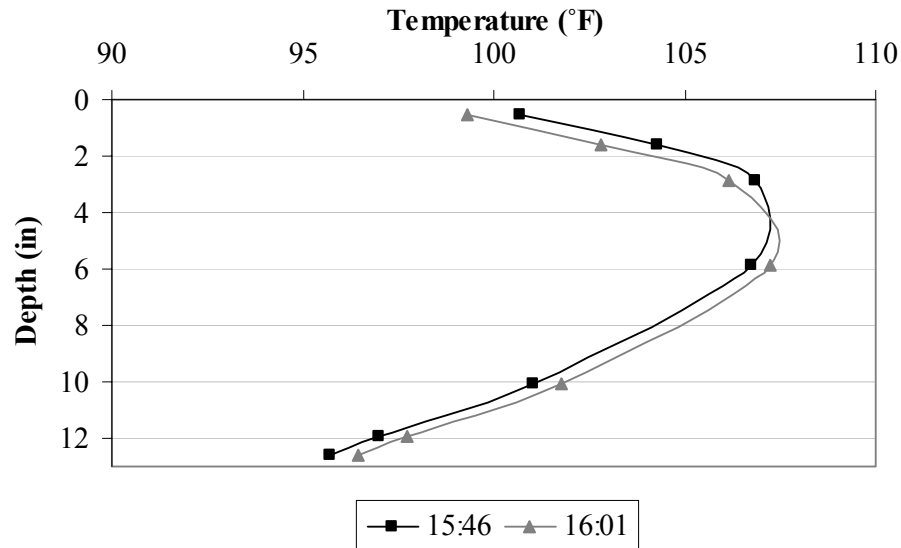


Figure 3.33. Temperature profiles at the time of set of the restrained and unrestrained slabs based on pressure measurements.

3.6.0. Built-in Construction Gradient

Static strain and pressure data were analyzed during the first 42 hours after construction of the pavement to estimate the set time and the corresponding built-in temperature gradient in the restrained and unrestrained slabs. The results of the two methods are compared and summarized in this section, and the appropriate built-in construction gradient in the JPCP slabs is established.

3.6.1. Set Time and Corresponding Built-in Temperature Gradient

The set time, built-in temperature gradient, and weighted average slab temperature based on the vibrating wire data and the pressure measurements are summarized in Table 3.6. The set times determined based on the static strain data are longer than those determined based on the static pressure data. The time of set based on the static pressure data takes place approximately 0.83 to 1.17 hours (50 to 90 minutes) after that determined based on the static strain data. The corresponding weighted average slab temperature based on both methods is similar, as is the equivalent linear temperature gradient.

Table 3.6. Time of set, built-in temperature gradients and weighted average temperatures based on the two methods.

Method	Time of set (hours)¹	Weighted Average Temperature (°F)²	Equivalent Linear Temperature Gradient (°F/in)²	Type of Slab³
Static Strain Measurements	10.83	104.3	0.31	R
	10.92	104.4	0.31	UR
Static Pressure Measurements	10.0	103.6	0.51	R
	9.75	103.6	0.42	UR

¹ After mixing of the concrete

² Based on thermocouples located at slab midpanel

³ R: Restrained; UR: Unrestrained

There are several advantages and disadvantages associated with the procedures followed for the determination of the set times based on the two methods. The differences are discussed in this section for the purpose of establishing the most suitable method for selecting the time of set and the corresponding built-in temperature gradient for the restrained and unrestrained slabs.

When carrying out the analysis of the early-age variations in strain measurements, the following disadvantage is noted. The strain gages may have been slightly displaced or shifted during placement of the concrete. This might cause the sensors to measure strains that are occurring in locations or directions that are different than what was analyzed in section 3.4.0. However, since the results were similar for the restrained and unrestrained slabs, at different locations and depths within the slabs, this implies that any displacement of the sensors during construction is not significant enough to affect the results. On the other hand, the main advantage of this method is that the determination of the set time based on the variation in strain with temperature graphs reflects the time when the concrete starts experiencing movement. Even though this may not reflect the exact time when the concrete sets, the temperature gradient that is present in the slabs at the time when concrete starts experiencing movement is defined as the built-in temperature gradient [15]. This method eliminates the need for going through a determination of the time of set using an analysis of the slab surface movements and the use of prediction models to correlate back to the time when movement starts taking place.

When carrying out the analysis of the early-age variations in pressure measurements, the following disadvantages are noted. First, the graphs showing the variations in pressure along the slab/base interface with temperature gradients all showed a slight increase in pressure during the first couple of hours. There is not an explanation

for this increase in pressure. After this point, the relationship between pressure and the measured temperature gradient follows the anticipated trends (increased pressure at midpanel and decreased pressure at slab corners with negative temperature gradients in the slabs, and vice versa).

Based on the above, it can be concluded that the time when concrete starts experiencing movement, as determined based on the static strain sensors, is the most appropriate time to use in determining the built-in temperature gradient in the slabs. Accordingly, the corresponding built-in temperature gradient is found to be $0.31^{\circ}\text{F}/\text{in}$ for the restrained and unrestrained slabs. Although, the difference between the two methods is not substantially different.

3.6.2. Built-in Moisture Gradient

As previously mentioned in section 3.2.0, the contribution of the moisture component to the built-in construction gradient consists of an equivalent temperature difference of -0.008°F across the slab thickness. Since the effect of moisture is insignificant compared to that of temperature, it will not be included in the determination of the overall built-in construction gradient.

3.7.0. Summary and Conclusions

In this chapter, two methods were followed to estimate the time of set and the corresponding built-in construction gradient in the concrete slabs. The first method consisted of analyzing the strain measurements in the concrete slabs, and the second method consisted of analyzing the pressure measurements exerted by the slabs on the underlying base layer.

A comparison between the results of the two methods and an analysis of the advantages and disadvantages associated with each method revealed that the time when concrete starts experiencing movement, as determined based on the static strain sensors, is the most appropriate time to use in determining the built-in temperature gradient in the slabs. Accordingly, the corresponding built-in temperature gradient is found to be $0.31^{\circ}\text{F}/\text{in}$ for the restrained and unrestrained slabs. Moreover, the contribution of the moisture component to the built-in construction gradient consists of an equivalent temperature difference of -0.008°F across the slab thickness. Since the effect of moisture is insignificant compared to that of temperature, it is not included in the determination of the overall built-in construction gradient. In conclusion, the restrained and unrestrained

slabs set with a built-in construction gradient of $0.31^{\circ}\text{F}/\text{in}$, and a weighted average slab temperature of 104.3°F .

CHAPTER 4: INPUTS OF THE MECHANISTIC-EMPERICAL DESIGN GUIDE

4.1.0. Introduction

This chapter presents the characterization of the design inputs for the MEPDG. The main objective of this chapter is to provide guidance in the determination of traffic, environmental and material inputs for the design of JPCP, based on the knowledge gained from the Smart Pavement.

The Mechanistic-Empirical Design Guide considers three hierarchical input levels depending on the amount of information available to the designer and criticality of the project. This hierarchical approach is utilized for the all of the inputs discussed in this chapter (traffic, material and environmental). Therefore, classification of these input levels is useful to the comprehension of the various inputs. There are three levels of input which are provided herein:

- Level 1: Level 1 inputs provide the highest level of accuracy and would typically be used when designing pavements that have a high volume of traffic, such as interstates. Level 1 inputs are directly measured through laboratory or field testing; therefore they require the most resources, both time and monetary, to define.
- Level 2: Level 2 inputs provide an intermediate level of accuracy and would typically be used when resources are unavailable for direct measurement. Level 2 inputs can be estimated through correlations of available data, selected by the user from an agency database, or can be derived from limited testing.
- Level 3: Level 3 inputs provide the user with the lowest level of accuracy and can be used for the design of low volume roads where early failure has a minimum consequence. Level 3 inputs are typical values chosen from available sources and experience.

This chapter will begin with defining the appropriate inputs within each of the following categories:

MEPDG Inputs

1. General design information
2. Structural design
3. Traffic
4. Environmental

Each of these inputs will be defined for the Smart Pavement in the order in which they were listed above. The material inputs for the MEPDG will be provided; this includes the determination of the mechanical (e.g. strength parameters) and thermal properties for the PCC, ATPB, and unbound layers.

Following this, the pavement structure will be modeled using the Enhanced Integrated Climatic Model (EICM) to estimate temperature and moisture conditions in the pavement structure. The EICM, which is embedded in the new MEPDG, models the effects of ambient conditions on the pavement material properties and on infiltration through the pavement structure. Climatic data from the onsite weather station and from other weather stations close to the site will be used as inputs. The predicted conditions will then be compared to those measured in the field to validate the EICM predictions.

Upon determination of all the design inputs at the three hierarchical levels, an analysis of their effect on performance will be investigated for both the restrained and unrestrained slabs. This will include a summary of the predicted pavement faulting, cracking and IRI for each hierarchical level. Following this, the effect of the three input levels on individual design parameters will be investigated. This chapter will conclude with a summary of the findings.

4.2.0. General Information and Pavement Design Inputs

The characterization of the general design inputs define the analysis period and type of design. These inputs also include characterization of the pavement construction and the month the section was opened to traffic. The general information for the Smart Pavement is found in Table 4.1.

Table 4.1. General inputs for the Smart Pavement.

Design life	20 years
Construction month	August-04
Traffic opening month	September-04
Type of Design	JPCP

The structural design inputs for SR 22 are provided in Table 4.2. As stated in the previous chapters, the Smart Pavement consists of the following layers: a 12-in PCC slab, a 4-in asphalt treated permeable base, a 5-in PennDOT 2A subbase and 24 in of fill. Table 4.2 shows inputs for undoweled and doweled pavement structures because both pavement types exist in the Smart Pavement. An analysis of the performance of doweled versus undoweled pavements will be evaluated.

Table 4.2. Structure inputs for the Smart Pavement.

Permanent curl/warp unrestrained	- 4 °F
Permanent curl/warp restrained	- 4 °F
Joint spacing	15 feet
Sealant type	Liquid
Dowel diameter	1.5 in
Dowel spacing	12 in
Edge support	Tied PCC shoulder
Long-term LTE shoulder	40%
Base type	Asphalt treated
Erodibility index	very erosion resistant (2)
PCC-base interface	full friction contact
Loss of full friction	229 months

4.3.0. Traffic Inputs

Characterization of traffic data is one of the fundamental data elements required for the structural design and analysis of pavements. Traffic data is required for estimating loads applied to the pavement and frequency of the applied loads throughout the design life. There are several inputs required for characterization of traffic in the new MEPDG. These include:

- Base year truck traffic volume (ADTT)
- Vehicle operational speed
- Truck-traffic directional and lane distributions
- Vehicle class distributions
- Monthly adjustment factors
- Hourly adjustment factors
- Axle load distribution factors
- Axle and wheel base configurations
- Tire characteristics and inflation pressure
- Truck lateral distribution factor
- Truck growth rates

The following provides an analysis of the characterization of the traffic design inputs for the Smart Pavement.

The hierarchical input of traffic data in the MEPDG can be classified as Levels 1 through 3. At input Level 1, a good knowledge of past and future traffic characteristics should be known. This can be found from site specific WIM, AVC, or traffic counts. Level 2 inputs are used when a modest knowledge of traffic is known by using regional WIM, AVC, or traffic counts. Level 3 accounts for a poor knowledge of traffic where national averages determined from various LTPP sites that are incorporated in the MEPDG may be used.

The characterization of the traffic data for SR 22 will be from a combination of all three hierarchical input levels. Originally, a WIM device installed within the project limits was to be used to characterize all traffic data for the Smart Pavement. Unfortunately, a modem was never installed with the system and data has never been collected. Therefore, the University of Pittsburgh research team used traffic counts provided by PennDOT and data collected by a traffic sensor located approximately 2.8 miles from the project site to characterize the MEPDG inputs for traffic on SR 22.

4.3.1. Traffic Volume Inputs

Traffic volume inputs provide characterization of traffic during the base year (first year roadway is opened to traffic). These inputs include classification of the following

parameters:

- Two-way annual average daily truck traffic (AADTT)
- Number of lanes in the design direction
- Percent trucks in design direction
- Percent trucks in the design lane
- Vehicle operational speed

These inputs have been established for the Smart Pavement and are provided in Table 4.3. SR 22 is a four-lane urban major arterial divided by a concrete median. At the time of construction in August 2004, the one-way average daily traffic (ADT) volume was 14,196 vehicles with 6 percent being truck traffic. Typically, for a four lane divided roadway the lane distribution is 90 percent [19]. The posted speed limit is 35 miles per hour, with several traffic signals and business entrances occurring along the roadway.

Table 4.3. MEPDG traffic volume inputs for the Smart Pavement.

Input Parameter	Value for SR 22
One-way average annual daily truck traffic (AADTT)	852
Number of lanes in the design direction	2
Percent trucks in design direction	100
Percent trucks in design lane	90
Vehicle operational speed (MPH)	35

4.3.2. Traffic Volume Adjustment Factor Inputs

Classification of the traffic volume adjustment factors provides the following inputs for the MEPDG:

- Monthly adjustment factors
- Vehicle class distribution factors
- Hourly truck distribution factors
- Traffic growth factors

These inputs used for the Smart Pavement and are provided below.

The monthly adjustment factor represents the proportion of annual truck traffic for a given truck class that occurs in a specific month. This parameter was determined by dividing the monthly truck traffic by the yearly truck traffic and multiplying by 12. This

parameter is sensitive for pavement design because variations in the amount of traffic per month affect stress development. Therefore, if reliable information is not available then an even distribution should be used. Table 4.4 provides the monthly adjustment factors for the Smart Pavement. These monthly adjustment factors should be used for all vehicle classifications.

Table 4.4. Monthly traffic adjustment factors for SR 22.

Month	Adjustment Factor
January	0.80
February	0.80
March	1.02
April	1.06
May	1.07
June	1.09
July	1.06
August	1.05
September	0.96
October	1.02
November	1.03
December	1.05

The vehicle class distribution was determined from vehicle counts provided by PennDOT. The input provides the vehicle class (using FHWA classifications) distribution for each truck class (Classes 4 through 13) within the base year. Table 4.5 provides the vehicle class distribution for SR 22.

Table 4.5. Vehicle class distribution for SR 22.

FHWA Truck Classification	Distribution for SR 22 (%)
Class 4	2
Class 5	39
Class 6	3
Class 7	1

Class 8	7
Class 9	48
Class 10	0
Class 11	0
Class 12	0
Class 13	0

The hourly distribution factors represent the percentage of the AADTT within each hour of the day. This parameter is especially important for JPCP because larger volumes of traffic during periods of large positive or negative gradients can greatly affect stress development in the pavement. The hourly distribution factors for SR 22 are provided in Table 4.6. These hourly adjustment factors should be used for all vehicle classifications. The hourly adjustment factors were based on the hourly traffic volumes for a section of SR 22 located approximately 2.8 miles from the project site.

Accurately estimating the traffic growth for a roadway has a substantial impact on the ability to predict pavement performance. Traffic can be characterized within the design guide as having no growth, linear growth or compound growth. The design of SR 22 was completed in 2002 and at this time the average two-way daily traffic was 26,950 vehicles. At the time of design, it was projected that average daily traffic would be 36,780 vehicles at the end of the 20-year design life. Therefore, the rate can be computed using a linear growth model. The growth rate for SR 22 is 1.8 percent.

Table 4.6. Hourly traffic distribution factors for SR 22.

Hour	Distribution for SR 22
MIDNIGHT	0.7
1:00 AM	0.4
2:00 AM	0.4
2:00 AM	0.5
4:00 AM	1.1
5:00 AM	4.1
6:00 AM	7.3
7:00 AM	7.9
8:00 AM	6.9
9:00 AM	6.0
10:00 AM	5.8
11:00 AM	5.8
NOON	5.6
1:00 PM	5.5
2:00 PM	5.5
3:00 PM	5.6
4:00 PM	5.6
5:00 PM	6.2
6:00 PM	5.4
7:00 PM	4.2
8:00 PM	3.4
9:00 PM	3.0
10:00 PM	1.9
11:00 PM	1.3

4.3.3. Axle Load Distribution Factor Inputs

The axle load distribution factors simply represent the percentage of the total number of applications of each axle type for each load interval. The axle types include single, tandem, tridem, and quad axles. The load levels range from 3,000 to 14,000 lbs for single axles, 6,000 to 80,000 lbs for tandem axles, and 12,000 to 102,000 lbs for tridem and quad

axles. This data can only be determined from WIM data provided from project specific or regional devices. If this data is not available, as is the case for the Smart Pavement, the MEPDG provides default values at input Level 3 that were determined from data provided from LTPP sites across the country. Table 4.7 and Table 4.8 provide these values for the single and tandem axle classifications, the tridem and quad axle load distributions can be found in the MEPDG literature.

Table 4.7. Single axle load distribution default values for each vehicle class [15].

Mean Axle Load, lbs.	Vehicle/Truck Class									
	4	5	6	7	8	9	10	11	12	13
3000	1.80	10.03	2.47	2.14	11.62	1.74	3.64	3.55	6.68	8.88
4000	0.96	13.19	1.78	0.55	5.36	1.37	1.24	2.91	2.29	2.67
5000	2.91	16.40	3.45	2.42	7.82	2.84	2.36	5.19	4.87	3.81
6000	3.99	10.69	3.95	2.70	6.98	3.53	3.38	5.27	5.86	5.23
7000	6.80	9.21	6.70	3.21	7.98	4.93	5.18	6.32	5.97	6.03
8000	11.45	8.26	8.44	5.81	9.69	8.43	8.34	6.97	8.85	8.10
9000	11.28	7.11	11.93	5.26	9.98	13.66	13.84	8.07	9.57	8.35
10000	11.04	5.84	13.55	7.38	8.49	17.66	17.33	9.70	9.95	10.69
11000	9.86	4.53	12.12	6.85	6.46	16.69	16.19	8.54	8.59	10.69
12000	8.53	3.46	9.47	7.41	5.18	11.63	10.30	7.28	7.09	11.11
13000	7.32	2.56	6.81	8.99	4.00	6.09	6.52	7.16	5.86	7.34
14000	5.55	1.92	5.05	8.15	3.38	3.52	3.94	5.65	6.58	3.78
15000	4.23	1.54	2.74	7.77	2.73	1.91	2.33	4.77	4.55	3.10
16000	3.11	1.19	2.66	6.84	2.19	1.55	1.57	4.35	3.63	2.58
17000	2.54	0.90	1.92	5.67	1.83	1.10	1.07	3.56	2.56	1.52
18000	1.98	0.68	1.43	4.63	1.53	0.88	0.71	3.02	2.00	1.32
19000	1.53	0.52	1.07	3.50	1.16	0.73	0.53	2.06	1.54	1.00
20000	1.19	0.40	0.82	2.64	0.97	0.53	0.32	1.63	0.98	0.83
21000	1.16	0.31	0.64	1.90	0.61	0.38	0.29	1.27	0.71	0.64
22000	0.66	0.31	0.49	1.31	0.55	0.25	0.19	0.76	0.51	0.38
23000	0.56	0.18	0.38	0.97	0.36	0.17	0.15	0.59	0.29	0.52
24000	0.37	0.14	0.26	0.67	0.26	0.13	0.17	0.41	0.27	0.22
25000	0.31	0.15	0.24	0.43	0.19	0.08	0.09	0.25	0.19	0.13
26000	0.18	0.12	0.13	1.18	0.16	0.06	0.05	0.14	0.15	0.26
27000	0.18	0.08	0.13	0.26	0.11	0.04	0.03	0.21	0.12	0.28
28000	0.14	0.05	0.08	0.17	0.08	0.03	0.02	0.07	0.08	0.12
29000	0.08	0.05	0.08	0.17	0.05	0.02	0.03	0.09	0.09	0.13
30000	0.05	0.02	0.05	0.08	0.04	0.01	0.02	0.06	0.02	0.05
31000	0.04	0.02	0.03	0.72	0.04	0.01	0.03	0.03	0.03	0.05
32000	0.04	0.02	0.03	0.06	0.12	0.01	0.01	0.04	0.01	0.08
33000	0.04	0.02	0.03	0.03	0.01	0.01	0.02	0.01	0.01	0.06
34000	0.03	0.02	0.02	0.03	0.02	0.01	0.01	0.01	0.01	0.02
35000	0.02	0.02	0.01	0.02	0.02	0.00	0.01	0.01	0.01	0.01
36000	0.02	0.02	0.01	0.02	0.01	0.01	0.01	0.01	0.01	0.01
37000	0.01	0.01	0.01	0.01	0.01	0.00	0.01	0.00	0.01	0.01
38000	0.01	0.01	0.01	0.01	0.00	0.00	0.01	0.02	0.01	0.01
39000	0.01	0.00	0.01	0.01	0.01	0.00	0.01	0.01	0.00	0.01
40000	0.01	0.00	0.01	0.01	0.00	0.00	0.04	0.02	0.00	0.00
41000	0.00	0.00	0.00	0.00	0.00	0.00	0.00	0.00	0.00	0.00

Table 4.8. Tandem axle load distribution default values for each vehicle class [15].

Mean Axle Load, lbs.	Vehicle/Truck Class									
	4	5	6	7	8	9	10	11	12	13
6000	5.88	7.06	5.28	13.74	18.95	2.78	2.45	7.93	5.23	6.41
8000	1.44	35.42	8.42	6.71	8.05	3.92	2.19	3.15	1.75	3.85
10000	1.94	13.23	10.81	6.49	11.15	6.51	3.65	5.21	3.35	5.58
12000	2.73	6.32	8.99	3.46	11.92	7.61	5.40	8.24	5.89	5.66
14000	3.63	4.33	7.71	7.06	10.51	7.74	6.90	8.88	8.72	5.73
16000	4.96	5.09	7.50	4.83	8.25	7.00	7.51	8.45	8.37	5.53
18000	7.95	5.05	6.76	4.97	6.77	5.82	6.99	7.08	9.76	4.90
20000	11.58	4.39	6.06	4.58	5.32	5.59	6.61	5.49	10.85	4.54
22000	14.20	2.31	5.71	4.26	4.13	5.16	6.26	5.14	10.78	6.45
24000	13.14	2.28	5.17	3.85	3.12	5.05	5.95	5.99	7.24	4.77
26000	10.75	1.53	4.52	3.44	2.34	5.28	6.16	5.73	6.14	4.34
28000	7.47	1.96	3.96	6.06	1.82	5.53	6.54	4.37	4.93	5.63
30000	5.08	1.89	3.21	3.68	1.58	6.13	6.24	6.57	3.93	7.24
32000	3.12	2.19	3.91	2.98	1.20	6.34	5.92	4.61	3.09	4.69
34000	1.87	1.74	2.12	2.89	1.05	5.67	4.99	4.48	2.74	4.51
36000	1.30	1.78	1.74	2.54	0.94	4.46	3.63	2.91	1.73	3.93
38000	0.76	1.67	1.44	2.66	0.56	3.16	2.79	1.83	1.32	4.20
40000	0.53	0.38	1.26	2.50	0.64	2.13	2.24	1.12	1.07	3.22
42000	0.52	0.36	1.01	1.57	0.28	1.41	1.69	0.84	0.58	2.28
44000	0.30	0.19	0.83	1.53	0.28	0.91	1.26	0.68	0.51	1.77
46000	0.21	0.13	0.71	2.13	0.41	0.59	1.54	0.32	0.43	1.23
48000	0.18	0.13	0.63	1.89	0.20	0.39	0.73	0.21	0.22	0.85
50000	0.11	0.14	0.49	1.17	0.14	0.26	0.57	0.21	0.22	0.64
52000	0.06	0.20	0.39	1.07	0.11	0.17	0.40	0.07	0.23	0.39
54000	0.04	0.06	0.32	0.87	0.06	0.11	0.38	0.13	0.20	0.60
56000	0.08	0.06	0.26	0.81	0.05	0.08	0.25	0.15	0.12	0.26
58000	0.01	0.02	0.19	0.47	0.03	0.05	0.16	0.09	0.07	0.18
60000	0.02	0.02	0.17	0.49	0.02	0.03	0.15	0.03	0.19	0.08
62000	0.10	0.01	0.13	0.38	0.06	0.02	0.09	0.06	0.09	0.14
64000	0.01	0.01	0.08	0.24	0.02	0.02	0.08	0.01	0.04	0.07
66000	0.02	0.01	0.06	0.15	0.02	0.02	0.06	0.01	0.02	0.08
68000	0.01	0.00	0.07	0.16	0.00	0.02	0.05	0.01	0.04	0.03
70000	0.01	0.02	0.04	0.06	0.00	0.01	0.11	0.00	0.12	0.01
72000	0.00	0.01	0.04	0.13	0.00	0.01	0.04	0.00	0.01	0.04
74000	0.00	0.00	0.02	0.06	0.00	0.01	0.01	0.00	0.01	0.02
76000	0.00	0.00	0.01	0.06	0.00	0.00	0.01	0.00	0.01	0.04
78000	0.00	0.00	0.00	0.02	0.00	0.00	0.01	0.00	0.01	0.02
80000	0.00	0.00	0.00	0.02	0.00	0.00	0.00	0.00	0.00	0.08
82000	0.00	0.00	0.00	0.00	0.00	0.00	0.00	0.00	0.00	0.00

4.3.4. General Traffic Inputs

The general traffic inputs primarily provide information necessary for calculating pavement response. These inputs define axle load configuration and provide loading details such as: traffic wander, design lane width, and mean wheel location. Unfortunately, since this data was not available, Level 3 analysis of these parameters is necessary. Level 3 general traffic inputs are default values provided by the MEPDG, these values were determined from a national database of traffic information. The parameters that define the

general traffic inputs include:

- Mean wheel location
- Traffic wander standard deviation
- Design lane width
- Number of axle types per truck class
- Axle configuration
- Wheelbase

The mean wheel location is simply the distance from the outer edge of the wheel to the pavement marking. To determine this parameter at input Level 1, direct measurements at the site need to be made. The national average of mean wheel location, which is the SR 22 input, is 18 in. The traffic wander standard deviation is used to determine the number of axle load applications over a point for predicting stresses and performance. This value was determined for SR 22 from the national average, which is 10 in. The design lane width for SR 22 is 12 feet. The number of axles for each truck class (FHWA Classes 4-13) was determined from the LTPP database. The suggested values provided by the MEPDG as default values are shown in Table 4.9 and will be used for classification of SR 22 traffic.

Table 4.9. Average number of axles per truck class for SR 22.

Truck Classification	Number of Single Axles per Truck	Number of Tandem Axles per Truck	Number of Tridem Axles per Truck
4	1.62	0.39	0.00
5	2.00	0.00	0.00
6	1.02	0.99	0.00
7	1.00	0.26	0.83
8	2.38	0.67	0.00
9	1.13	1.93	0.00
10	1.19	1.09	0.89
11	4.29	0.26	0.06
12	3.52	1.14	0.06
13	2.15	2.13	0.35

Classification of the axle configuration inputs includes the determination of several parameters. These parameters include: the average axle width, dual tire spacing, axle spacing,

and average tire pressure. These values can be obtained directly from a manufacturer's database or measured directly in the field. If this information is unavailable to the designer, as is the case for SR 22, then typical values are provided as defaults in the MEPDG. The default values assumed for SR 22 are provided in Table 4.10.

Table 4.10. Axle configurations for SR 22.

Input parameter	Value for SR 22
Average axle width (ft)	8.5
Dual tire spacing (in)	12.0
Tire pressure (psi)	120.0
Axle spacing - tandem (in)	51.6
Axle spacing - tridem (in)	49.2
Axle spacing - quad (in)	49.2

The final input needed for classification of design traffic is the vehicle wheelbase information that is needed for computing pavement response. These values can be obtained directly from a manufacturer's database or measured directly in the field. If this information is unavailable, then national averages determined from LTPP projects are used as default values in the MEPDG. These default values used for SR 22 are provided in Table 4.11.

Table 4.11. Truck wheelbases for traffic on SR 22.

	Short	Medium	Long
Average Axle Spacing (ft)	12	15	16
Percent of truck	33	33	34

4.4.0. Environmental Inputs

Characterization of environmental factors is a very important component of the MEPDG. The environmental factors significantly affect performance of JPCP. Factors such as precipitation, temperature, and moisture determine the shape and critical stresses of a concrete slab, which effects performance. As previously mentioned, in the MEPDG, the environmental analysis is performed by the EICM. The EICM of the MEPDG simulates changes in the pavement and subgrade materials that are caused by seasonal changes in

environmental conditions. A more detailed overview of the EICM is presented in section 4.8.1

This section provides the determination of the environmental inputs of the MEPDG. It will begin a brief description of the weather-related inputs obtained by weather station records. Following this, the characterization of environmental inputs can be separated into three additional categories: ground water related inputs, drainage and surface property inputs, and pavement structure and material inputs.

4.4.1. Weather-Related Inputs

Weather-related variables are a major component of the environmental inputs. These variables constitute the main input to the EICM and can be determined for any weather station across the USA. Currently, the MEPDG has information from over 800 weather stations, making it possible to have very reliable weather data for virtually any geographic point. This information is provided by a database of weather data populated by the National Climatic Data Center. The designing engineer is able to define which weather station, or combination of weather stations, best represents the weather conditions that act on the pavement being analyzed. Additionally, the engineer has the ability to create a weather station from site-specific weather data. Therefore, the user has three options:

- *Choose one specific weather station.* This option lets the user choose the closest weather station to the design site, or the one that best represents actual conditions.
- *Input latitude, longitude and elevation of the site.* When this option is chosen, the MEPDG software returns six weather stations that are closest to the construction site. The designer then has the opportunity to choose any combination among these six, according to judgement of distances and directions.
- *Import a previously generated climatic data file.* This option gives the user the ability to import site-specific climatic data.

The input variables supplied by the selected weather station(s) include:

- Hourly air temperature
- Hourly precipitation

- Hourly wind speed
- Hourly percentage sunshine
- Hourly relative humidity

4.4.2. Ground Water Related Inputs

Ground water related inputs are the second classification of environmental inputs. It is important to recognize that ground water related inputs play a significant role in the overall accuracy of the foundation/pavement moisture contents and therefore, should be determined as accurately as possible.

4.4.2.1. Groundwater Table Depth

The depth of the groundwater table is to be a best estimate of the average annual depth or seasonal average depth of the water table. Only Level 1 and 3 input levels exist for this input. Level 1 is determined using borings and Level 3, is estimated based on annual or seasonal averages. If Level 1 data is not available, then county soil reports may be used.

The depth to the water table for the Smart Pavement was identified from the results of soil borings pulled near the test section. According to the boring log, the water table for the test section at stations 95+145 and 97+11 is 9 ft below the surface of the soil.

4.4.3. Drainage and Surface Property Inputs

Drainage and surface property inputs are the third classification of environmental inputs. These inputs classify the infiltration of water into the pavement, the drainage of the pavement, and the ability of the pavement to absorb solar energy.

4.4.3.1. Surface Shortwave Absorptivity

The surface shortwave absorptivity is a measure of the amount of solar energy that is absorbed by the pavement structure. At Level 1, this parameter is to be estimated through laboratory testing. Unfortunately, this parameter was not estimated for the SR 22 mix because there is no current AASHTO certified standard for estimating shortwave absorptivity. The surface shortwave absorptivity can not be determined at input Level 2 therefore, Level 3 typical values were used. The shortwave absorptivity of the surface of the Smart Pavement was defined as 0.85.

4.4.3.2. Infiltration

The MEPDG uses three classifications for infiltration, based on the type of shoulder present and if edge drains exist. This input also considers whether the design is for new, rehabilitated or reconstructed pavements. The three classifications are:

- Minor: Tied or sealed concrete shoulders, widened PCC lanes, or full width HMA paving
- Moderate: All other shoulder types, PCC restoration, and HMA overlays
- Extreme: Typically not used for new or reconstructed pavement design

According to the following classification, the Smart Pavement infiltration input is minor since it has tied curb and gutter.

4.4.3.3. Drainage Path Length

The drainage path length is the resultant of the cross and longitudinal slope lengths of the pavement and is measured from the highest point on the cross section to the point where a drain is located. This parameter is used in the EICM model of infiltration and drainage to compute the time required to drain an unbound layer or a subgrade from an initial wet condition. The following inputs are needed for determination of the drainage path length in the DRIP (Drainage Requirements in Pavements) program: the pavement cross and longitudinal slopes, lane width, edge drain trench width, and the cross-section geometry. Table 4.12 shown below, displays these inputs for the Smart Pavement.

Table 4.12. Inputs needed for characterizing drainage.

SR 22 cross slope	2.0 %
SR 22 longitudinal slope	2.4 %
SR 22 lane width	12 feet
SR 22 edge drain trench width	6 in
SR 22 cross-section geometry	Crowned

4.4.4. Pavement Structure Material Inputs

Material inputs characterizing the pavement structure are the fourth classification of environmental inputs. These inputs characterize material properties of the asphalt and concrete that control heat flow through the pavement system. These inputs will affect

changes in temperature and moisture conditions throughout the pavement.

4.4.4.1. Asphalt Material Properties

The asphalt material properties affected by environmental action on the pavement are thermal conductivity and heat capacity. The following material property magnitudes can only be set on a Level 3 basis, since Level 1 requires laboratory testing and this testing was not part of the scope of this research effort.

The thermal conductivity may be measured using ASTM E1952, but if this is not available then typical values or agency data can be used. Level 2 input is not applicable for the thermal conductivity. Typical values for asphalt concrete range from 0.44 to 0.81 Btu/(ft)(hr)(°F). The average of the high and the low (0.62 Btu/(ft)(hr)(°F)) was selected.

Just as for thermal conductivity, heat capacity determination is considered in the MEPDG under only Level 1 or Level 3. On a Level 1 basis, it is recommended that the heat capacity of asphalt concrete be found through direct testing (ASTM D2766). When direct measurement is not feasible, then agency data or typical values should be used. Typical values for asphalt concrete range from 0.22 to 0.40 Btu/(lb)(°F). The average value of this range will be used (0.31 Btu/(lb)(°F)).

4.4.4.2. Concrete Material Properties

Similar to the asphalt materials, thermal conductivity and heat capacity must also be estimated for PCC materials in the MEPDG. These inputs allow the EICM to estimate temperature and moisture distributions in the pavement structure.

The thermal conductivity of concrete materials can only be estimated from Level 1 or 3 data in the MEPDG. Level 1 data would be obtained by measuring the thermal conductivity in accordance with ASTM E 1952. This parameter was not measured so it must be estimated using Level 3. Typical values for thermal conductivity range from 1.0 to 1.5 Btu/(ft)(hr)(°F). An average value of 1.25 Btu/(ft)(hr)(°F) was determined representative for the Smart Pavement.

In conjunction with thermal conductivity, heat capacity is a thermal property that controls the ability of a material to transfer heat. The heat capacity reflects the actual amount of heat energy necessary to change the temperature of a unit mass by one degree.

At input Level 1, heat capacity can be estimated in accordance with ASTM D 2766. This testing was not carried out at the University of Pittsburgh and therefore the heat capacity

for the Smart Pavement was determined using Level 3 data. Typically, heat capacity of PCC materials varies between 0.2 and 0.28 $Btu/(ft)(^{\circ}F)$. Again, the average value (0.24 $Btu/(ft)(^{\circ}F)$) was used.

4.4.4.3. Compacted Unbound Material Inputs

This subsection presents the determination of the mass-volume parameters that ultimately define the resilient modulus of the unbound sub-layers with respect to changes in moisture and temperature conditions throughout the life of the pavement. There are three basic inputs that need to be defined by the user. The three basic input variables are the maximum dry density ($\gamma_{d\ max}$), specific gravity (G_s) and the optimum gravimetric water content (w_{opt}). Upon determination of these parameters, the EICM internally computes all other mass-volume parameters.

All three inputs can only be determined through direct measurement (Level 1) in accordance with standard test procedures or correlated from other available information about the unbound material (Level 2). The first input, oven-dried specific gravity, can be directly measured based on AASHTO T100. If a specific gravity-test is not preformed, it can be determined from the percent material passing the 200 sieve and the plasticity index for unbound materials.

The optimum gravimetric water content and maximum dry density can be directly measured using AASTHO T180 for the base layer and AASTHO T99 for other unbound layers. If this test is not performed, these inputs can be correlated using the percent of material passing the 200 sieve (P_{200}), the plasticity index (PI), and the particle size passed by 60 percent of the material (D_{60}). These inputs were determined, using Level 3 inputs for the various compacted unbound layers (subgrade, fill, and subbase) of the Smart Pavement. These inputs are provided in Table 4.13. The Level 1 compacted unbound material inputs were calculated using the MEPDG literature and are provided in Table 4.14. The subgrade on SR 22 is an A-6 AASHTO soil classification, which is a fair to poor subgrade. In order to comply with PennDOT specifications, two feet of this material was removed and replaced with a more suitable gap graded fill material. The fill contains a significant amount of rock, with some stones having a diameter as large as 22 in. The fill is classified as an A-1 material due to its small amount of fines. The subbase consists of PennDOT 2-A subbase material. This subbase is classified as an A-2 soil.

Table 4.13. Level 3 mass-volume inputs for the compacted unbound layers of the Smart Pavement.

Layer	P₂₀₀	D₆₀ (in)	PI
Subbase	5%	0.462	10
Fill	8%	1.063	6
Subgrade	77%	0.0006	11

Table 4.14. Level 1 mass-volume inputs for the compacted unbound layers of the Smart Pavement.

Layer	G_s	γ_{d max} (lb/ft³)	w_{opt}
Subbase	2.68	121.6	11.8
Fill	2.69	121.0	12.2
Subgrade	2.73	110.7	17.2

Additional inputs are required for the environmental classification of the compacted unbound layers. These inputs include the saturated hydraulic conductivity (k_{sat}), the dry thermal conductivity (K), and the dry heat capacity (Q).

The saturated hydraulic conductivity is needed to determine the transient moisture profiles in the compacted unbound layers and also helps in computing their drainage characteristics. This parameter can be measured using input Levels 1 and 2 only. Level 1 is a direct measurement using AASHTO T215. This test was not performed for the unbound materials so it will be defined using Level 2 information, which estimates this parameter using the P₂₀₀, D₆₀, and the PI.

The dry thermal conductivity (K) can be determined using input Levels 1 and 3. For Level 1 this parameter is directly measured using ASTM E1952. This parameter was not measured for the Smart Pavement and therefore is determined for each unbound material based on the AASTHO classification. The dry heat capacity (Q) can also only be determined using input Levels 1 and 3. The dry heat capacity is determined from ASTM 2766 for Level 1 input. If Level 1 data is not available, like for the Smart Pavement, then a typical value or an agency determined value is used. Table 4.15 displays the saturated hydraulic conductivity, dry thermal conductivity, and dry heat capacity values for the compacted unbound materials

of the Smart Pavement.

Table 4.15. Additional inputs for the compacted unbound layers of the Smart Pavement.

Layer	k_{sat} (ft/hr)	K (BTU/(ft)(hr)(°F))	Q (BTU/(lb)(°F))
Subbase	0.60	0.20	0.18
Fill	2.97	0.30	0.18
Subgrade	5.68×10^{-6}	0.18	0.18

4.5.0. PCC Material Property Inputs

PCC properties are among the most important input variables in the design of JPCP within the MEPDG. Material inputs play a significant role in the performance of slabs in response to environmental and applied loads and are very important inputs for the distress prediction models of the MEPDG. PCC properties can be classified under three major conceptual groups:

- Strength/mechanical behaviour related: Modulus of elasticity, Poisson's ratio, modulus of rupture, indirect tensile strength, compressive strength, PCC unit weight and coefficient of thermal expansion.
- Shrinkage related: Ultimate shrinkage, reversible shrinkage, time to reach 50% ultimate shrinkage.
- Thermal behaviour related: Thermal conductivity, specific heat and surface short wave absorptivity.

Most of the input variables within the first group vary with PCC age in the short and long term. Due to the incremental nature of the distress prediction models used in the MEPDG, a time dependent variation of these properties is considered throughout the design life.

The following provides an analysis of the PCC material property inputs included in the MEPDG. Each section will begin with a brief description of that specific property, followed by an analysis of each property at all three input levels.

4.5.1. PCC Mix Component Inputs

The MEPDG requires the following PCC mix-related inputs for modeling material behavior:

- Cement type
- Cement content
- Water/cement ratio
- Aggregate type
- PCC zero-stress temperature

These inputs were determined for the SR 22 concrete and are provided in Table 4.16.

Table 4.16. Mixture properties for the Smart Pavement.

Cement type	Type I
Cementitious material content	588 lb/yd ³
Water/cement ratio	0.44
Aggregate type	Limestone
PCC-zero stress temperature	104 °F

4.5.2. PCC Modulus of Elasticity

The PCC modulus of elasticity, E_c , is a very important property in the analysis of pavement response in the MEPDG. The modulus of elasticity greatly effects deflections and stresses throughout the pavement structure. Therefore, proper determination of this parameter is essential. The modulus of elasticity may be determined at all three hierarchical levels and is provided for the Smart Pavement herein.

The modulus of elasticity must be determined directly by laboratory testing at input Level 1; characterization of the modulus of elasticity is obtained from ASTM C469. For Level 1 characterization, the modulus of elasticity is needed at several ages (7, 14, 28, and 90 days). Upon determination of these values, an estimate of the 20-year to 28-day elastic modulus ratio must be defined. The MEPDG then develops a modulus gain curve using the test data and long-term modulus ratio to predict the modulus of elasticity at any point over the design life of the pavement.

Testing performed at the testing University of Pittsburgh was based on ASTM C469 and is summarized in Table 4.17. The MEPDG recommends a maximum value of 1.2 for the

20-year to 28-day E_c ratio unless more accurate information is available.

Table 4.17. PCC modulus of elasticity values determined through laboratory testing.

Age (days)	Cylinders (psi)	Cores (psi)
1	3.0×10^6	--
3	3.0×10^6	--
7	3.1×10^6	--
28	3.7×10^6	4.6×10^6
365	5.1×10^6	5.0×10^6

The MEPDG PCC strength characterization is based on the modulus of elasticity for days 7, 14, 28 and 90. However, testing performed at the University of Pittsburgh was performed at 1, 3, 7, 28, and 365 days. One approach to estimate the values at the required ages (7, 14, 28, and 90 days) is to use a logarithmic regression that includes the available data. However, when using this approach at least two of the required values are needed. Figure 4.1 provides the analysis of the regression performed to determine the modulus of elasticity at 14 and 90 days and Table 4.18 shows the modulus of elasticity values required for Level 1 input.

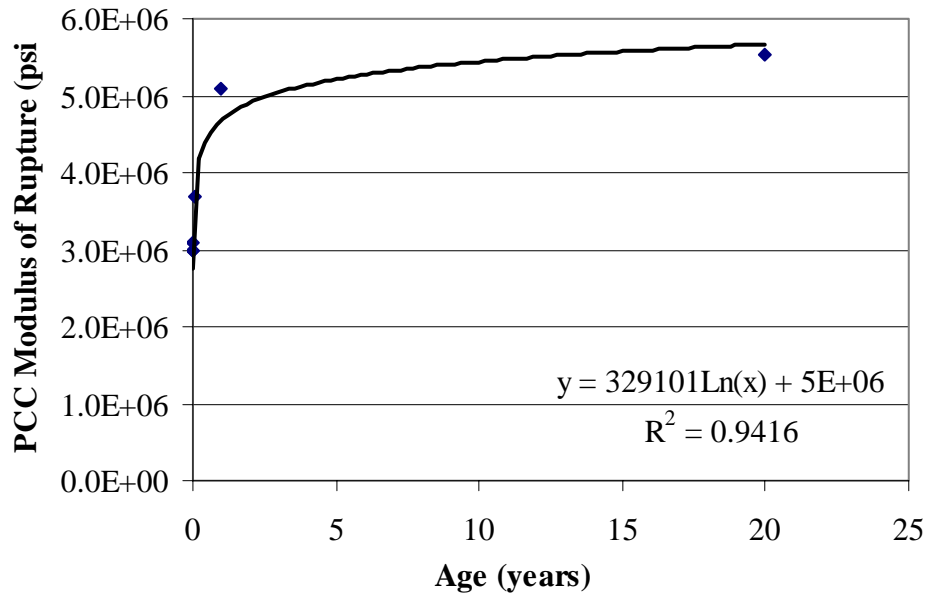


Figure 4.1. PCC modulus of elasticity.

Table 4.18. PCC modulus of elasticity values required for Level 1.

Age (days)	Modulus of Elasticity (psi)
7	3.1×10^6
14	3.3×10^6
28	3.7×10^6
90	4.69×10^6

At Level 2, the modulus of elasticity is estimated through a correlation with the compressive strength of the concrete. Therefore, compressive strength testing must be determined at 7-, 14-, 28-, and 90-days from direct measurement through AASHTO T22 test procedures. Additionally, the 20-year to 28-day compressive strength ratio must also be determined. A maximum value of 1.35 for the 20-year to 28-day compressive strength is recommended. A value of 1.20 is suggested in regions where low relative humidity is experienced; however, if historical agency data is available to determine this relationship, it should be used to find this correlation. Testing was performed at the University of Pittsburgh to determine the compressive strength of the Smart Pavement and is shown in Table 4.19.

Table 4.19. Results of compressive strength testing performed at the University of Pittsburgh.

Age (days)	Compressive Strength (psi)
1	2,141
3	3,580
7	4,443
28	5,868
365	7,196

Given that data ages available are 1-, 3-, 7-, 28-, and 365-days a logarithmic regression was used to find the required values of compressive strength. Figure 4.2 shows the logarithmic regression and

Table 4.20 contains the compressive strength values needed for Level 2 characterization in the MEPDG.

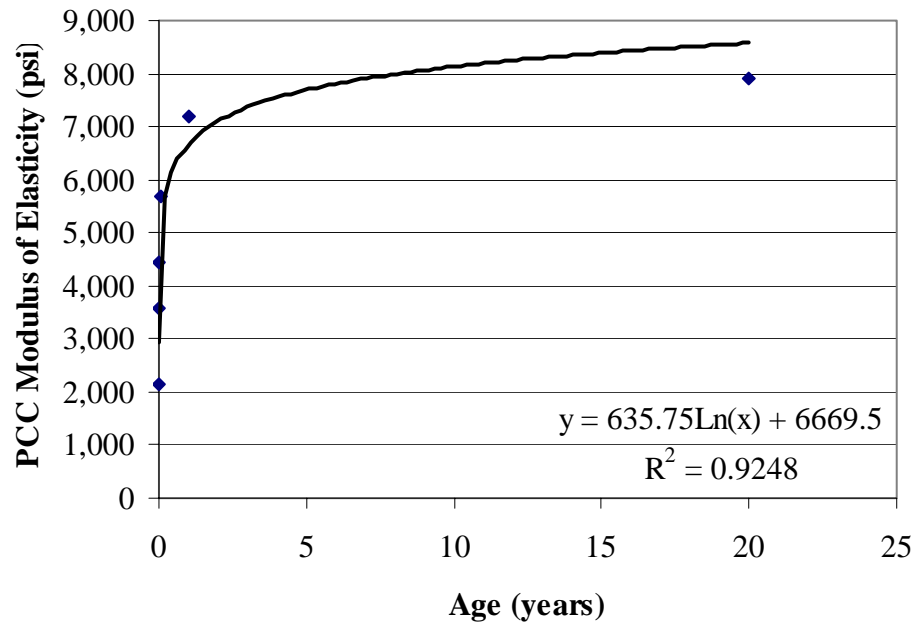


Figure 4.2. PCC compressive strength.

Table 4.20. PCC compressive strength values required for Level 2.

Age (days)	Compressive Strength (psi)
7	4,443
14	4,597
28	5,690
90	5,780

At Level 3, the modulus of elasticity is determined indirectly from 28-day estimates of flexural or compressive strength. Additionally, the 28-day modulus of elasticity may also be input at this level. The flexural strength of the concrete is estimated from laboratory testing using AASTHO T97 or from historical data. Likewise, the compressive strength and modulus of elasticity can also be directly measured utilizing AASTHO T22 and ASTM C469, respectively or historical agency data may be used. These inputs were determined through direct measurement for the concrete used on SR 22 and can be found in Table 4.21.

Table 4.21. PCC modulus of elasticity values for Level 3.

28-day Elastic Modulus (psi)	3,700,000
28-day Compressive Strength (psi)	5,868
28 day Flexural Strength (psi)	1,106

4.5.3. Poisson's ratio of PCC Materials

Poisson's ratio is a mechanical property that relates transverse and longitudinal strain of a homogenous and isotropic material when stress is applied. Although, this property does not have a significant influence on pavement mechanical response, it is considered within the MEPDG.

Poisson's ratio can be estimated using either Level 1 or 3. Level 2 is not applicable for this parameter because correlations do not exist between Poisson's ratio and other PCC material characteristics. Level 1 requires determination of Poisson's ratio in conjunction with elastic modulus testing following ASTM C469 test procedures. This testing was performed for the Smart Pavement and is shown in Table 4.22. According to the data, a value of 0.17 is most representative of the SR 22 concrete.

Table 4.22. Poisson's ratios for the Smart Pavement.

Age (days)	Cylinders	Cores
1	0.27	--
3	0.17	--
7	0.21	--
28	0.18	0.17
365	0.16	0.18

At Level 3, typical values of Poisson's ratio should be used. Typical values for normal concrete range between 0.11 and 0.21 and a value between 0.15 and 0.18 is typically assumed for PCC design.

4.5.4. PCC Flexural Strength

The flexural strength (modulus of rupture) of concrete is the most important strength parameter in JPCP. The flexural strength of concrete is simply the maximum tensile stress at

the bottom of a simply supported beam at rupture. This flexural strength has a significant effect on the cracking potential of PCC slabs; therefore, care must be taken when characterizing this parameter for rigid pavements. Flexural strength can be determined at all three hierarchical levels and is provided for the Smart Pavement herein.

At Level 1, the flexural strength of concrete (MR) should be measured directly utilizing AASTO T97 test procedures. The flexural strength should be determined at 7-, 14-, 28-, and 90-days. In addition, an estimate of the 20-year to 28-day flexural strength must be determined. A maximum value of 1.20 is recommended for this parameter. Testing was performed at the University of Pittsburgh to determine the modulus of rupture of the SR 22 mix in accordance to AASTHO T97 and is provided in Table 4.23.

Table 4.23. Moduli of Rupture for the Smart Pavement.

Age (days)	Average Flexural Strength (psi)
1	521
3	844
7	878
28	1106
365	1043

According to the testing performed at the University of Pittsburgh, the flexural strength at 28 days was larger than 365 days. A possible explanation for this was reported previously [1] and has to do with the fact that large coarse aggregate was found at the failure plane (greater than 2.5 in), influencing the strength of the beams. Given that the required input values are restrained to 7, 14, 28, and 90 days a logarithmic regression was performed to determine the 14 and 90 day modulus of rupture values and is shown in Figure 4.3. Table 4.24 contains the values needed for Level 1 in the MEPDG.

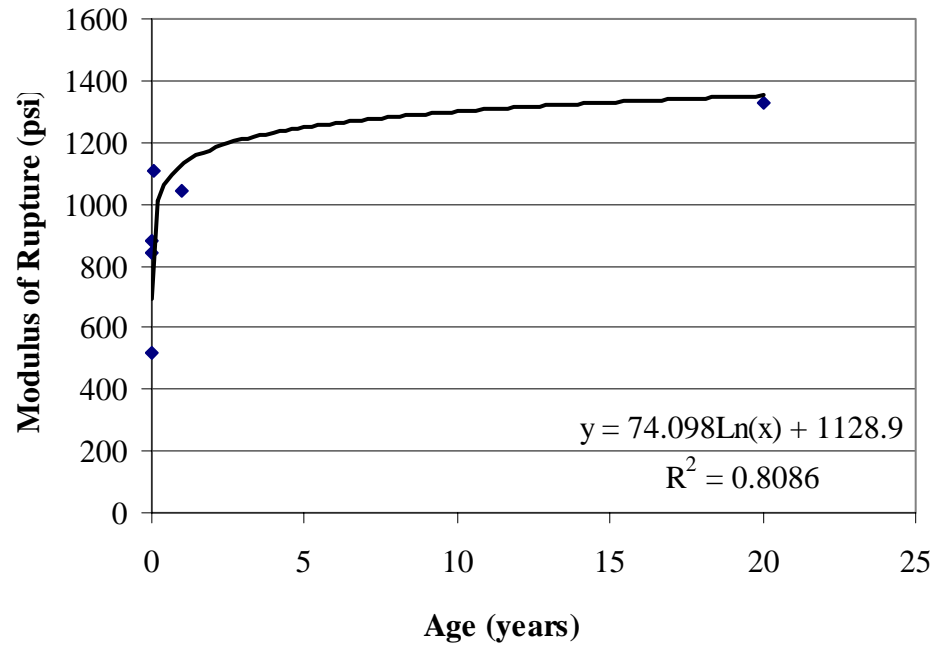


Figure 4.3. PCC modulus of rupture.

Table 4.24. Moduli of rupture values required for Level 1.

Age (days)	Modulus of Rupture (psi)
7	878
14	888
28	939
90	1025

Level 2 characterization requires direct determination of the compressive strength of the concrete at 7, 14, 28, and 90 days and is to follow AASHTO T22 test procedures. In addition the 20-year to 28-day compressive strength ratio must be determined. This was previously reported in the analysis of the modulus of elasticity for SR 22 and inputs can be found in Table 4.11.

The MEPDG accepts either values of 28-day compressive strength or modulus of rupture at Level 3. These values were previously reported and can be found in Table 4.21.

4.5.5. Unit Weight of PCC Materials

The unit weight of concrete is an important parameter in the MEPDG. Unit weight, which is affected by the quantity of the aggregate, air content, water content and density, affects critical stresses in the slab. Therefore, proper characterization of this parameter is helpful when determining the performance of a PCC pavement to transverse cracking. The unit weight of concrete can be determined at inputs Levels 1 and 3 in the MEPDG.

At Level 1, the unit weight of concrete should be measured directly using proper test procedures (AASHTO T121). The average measured unit weight of the PCC on SR 22 was characterized, in accordance to AASHTO T121, and found to be 144 lb/ft^3 . At input Level 3, the unit weight should be selected from historical agency data or typical values. Typical values of concrete range between 140 and 160 lb/ft^3 , with 150 lb/ft^3 being the most common unit weight of concrete. A summary of the hierarchical unit weight of the concrete inputs is provided in Table 4.25.

Table 4.25. Unit weight at the three hierarchical levels.

	Level 1	Level 2	Level 3
Unit Weight (lb/ft ³)	143.4	-	150

4.5.6. PCC Coefficient of Thermal Expansion

The PCC coefficient of thermal expansion (CTE) is an important thermal property of concrete, primarily controlled by the type of coarse aggregate used in the mix. This property is defined as the change in unit length per degree of temperature change. The coefficient of thermal expansion greatly affects the magnitude of curling stresses in PCC pavements and is a major component of joint design. The CTE can be determined at all three hierarchical levels.

At Level 1, CTE is characterized through the AASHTO TP 60 test procedures. This test was performed by the University of Pittsburgh team for several specimens and the average coefficient of thermal expansion was found to be $5.9 \times 10^{-6} / ^\circ\text{F}$.

At input Level 2, CTE can be estimated with the following expression:

$$\alpha_{PCC} = \alpha_{AGG} V_{AGG} + \alpha_{PASTE} V_{PASTE} \quad (\text{Equation 4-1})$$

where,

α_{AGG} = coefficient of thermal expansion of aggregate

V_{AGG} = volumetric proportion of the aggregate in the PCC mix

α_{PASTE} = coefficient of thermal expansion of cement mix

V_{PASTE} = volumetric proportion of the paste in the PCC mix

Table 4.26 contains the proportions of the mix design used on SR 22. The MEPDG literature provides typical values of CTE for various aggregates, which can be used to determine the coefficient of thermal expansion of the concrete if direct measurement is unavailable.

According to Table 4.26, the total proportional volume of aggregates is 0.70. Thus, the proportional volume of the paste is 0.30. The CTE of the limestone aggregate is $2.8 \times 10^{-6}/^{\circ}\text{F}$ and was determined from an average of typical values. The sand has a CTE of $6.3 \times 10^{-6}/^{\circ}\text{F}$. For the paste, the MEPDG literature suggests a range between $10 \times 10^{-6}/^{\circ}\text{F}$ and $11 \times 10^{-6}/^{\circ}\text{F}$ corresponding to a water-to-cement ratio of 0.4 to 0.6. A value of $10.5 \times 10^{-6}/^{\circ}\text{F}$ was used for the paste. Using these inputs and equation 4-1, the PCC CTE was estimated for the SR 22 mix. Based on Level 2, the PCC coefficient of thermal expansion for SR 22 is $7.14 \times 10^{-6}/^{\circ}\text{F}$.

Table 4.26. Mixture design for the PCC used to pave SR 22.

Material	Specific Gravity	Absorption	Batch Weight (lb/yd³)	Proportional Volume of Components (yd³/yd³)
Type I Cement (St. Lawrence)	3.15	n/a	382	-
Ground Granulated Blast Furnace Slag (Holcim)	2.89	n/a	206	0.04
Fine Aggregate (Hanson, PennDOT Spec. Type A)	2.61	1.15%	1248	0.28
Coarse Aggregate (Hanson, AASHTO No. 57)	2.68	0.50%	1881	0.42
Air Entrainment – Catexol 360 (Axim)	n/a	n/a	5.7 oz	-
Water Reducer – Catexol 100N (Axim)	-	n/a	17 oz	-
Water Content (City Water)	1	n/a	286	-

At input Level 3, CTE should be estimated from historical averages or typical values. The MEPDG suggests a typical value of $5.4 \times 10^{-6}/^{\circ}\text{F}$ based on the average of LTPP sites in which limestone was the source of aggregate used in the mix. However, it is highly recommended that historical agency data of typical ranges for various aggregate and cement types be used due to the importance of this parameter in determining distress. A summary of the CTE of the concrete at the three hierarchical input levels is provided in Table 4.27.

Table 4.27. Thermal coefficient of expansion at the three hierarchical levels.

	Level 1	Level 2	Level 3
Thermal coefficient of expansion ($/^{\circ}\text{F}$)	5.9×10^{-6}	7.14×10^{-6}	5.4×10^{-6}

4.5.7. PCC Shrinkage

The drying shrinkage of concrete is a long term process that influences strains in the material. Drying shrinkage can increase crack susceptibility and joint opening, which affects the performance of JPCP pavements. The MEPDG has several inputs that characterize drying shrinkage these include: ultimate shrinkage strain, time required to develop 50 percent of the ultimate shrinkage strain, and anticipated amount of reversible shrinkage. The following sections determine these inputs at the various hierarchical levels.

Determination of the ultimate shrinkage of concrete should be established through laboratory testing. However, there is no practical method since it takes several years to determine the ultimate shrinkage strain of concrete. The MEPDG recommends the use of the AASHTO T160 protocol to measure short-term shrinkage. The determination of this value is helpful when confirming results of Level 2 and 3 analyses.

The team at the University of Pittsburgh used ASTM C157.99 during a one year analysis to establish the drying shrinkage of the concrete used on SR 22. The results of this testing are shown in Figure 4.4. It can be seen that the ultimate shrinkage appears to be stabilizing at 945 microstrain.

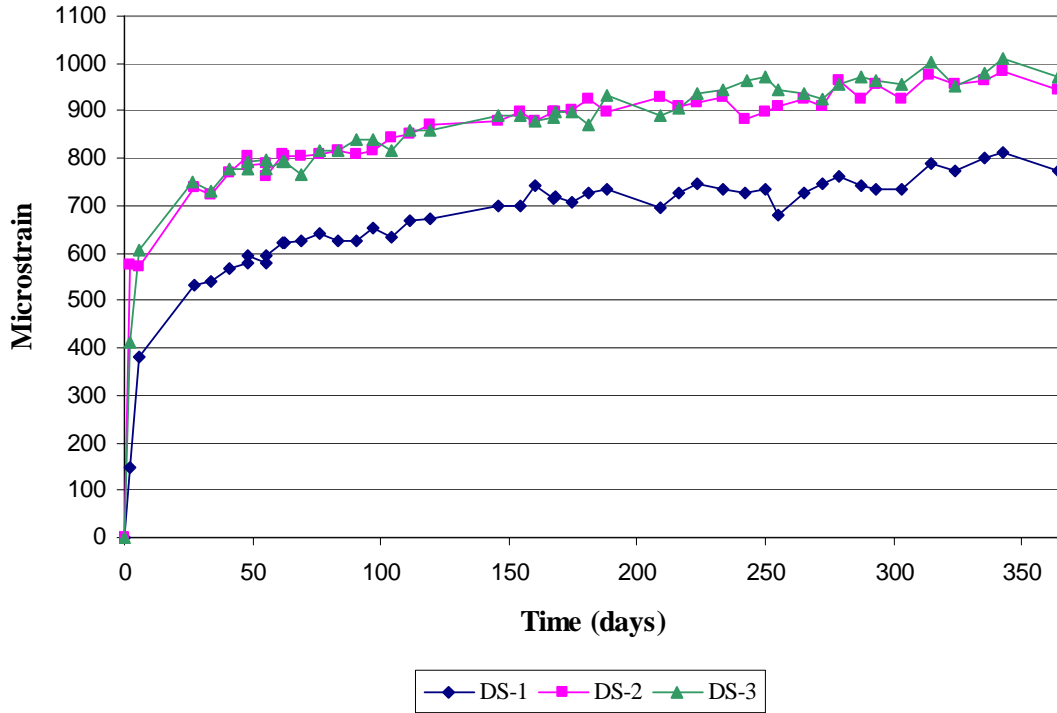


Figure 4.4. PCC drying shrinkage during the first year after paving.

At input Level 2, ultimate shrinkage can be estimated using the following correlation:

$$\varepsilon_{su} = C_1 \cdot C_2 \cdot [26w^{2.1}(f'_c)^{-0.28} + 270] \quad (\text{Equation 4-2})$$

where:

ε_{su} = Ultimate shrinkage strain ($\times 10^{-6}$)

C_1 = Cement type factor

1.0 for type I cement

0.85 for type II cement

1.1 for type III cement

C_2 = Type of curing factor

0.75 if steam cured

1.0 if cured in water or 100% relative humidity

1.2 if sealed during curing (curing compound)

w = Water content of the mix under consideration, lb/ft^3

f'_c = 28-day PCC compressive strength, psi

The following factors and materials properties are available for the Smart Pavement PCC mix:

$$C_1 = 1.0 \text{ for type I cement}$$

$$C_2 = 1.2 \text{ for curing compound}$$

$$w = 10.6 \text{ lb/ft}^3$$

$$f'_c = 5996 \text{ psi}$$

$$\epsilon_{su} = (1.0)(1.2) \left[26(10.6)^{2.1} (5996)^{-0.28} + 270 \right] (10^{-6})$$

$$\epsilon_{su} = 713 \times 10^{-6}$$

Therefore, an ultimate shrinkage of 713 microstrain can be used as the Level 2 input for the Smart Pavement. For Level 3, equation 4-2 can be utilized. This procedure differs from Level 2, in that typical agency values of w (10.2 lb/ft³) and f'_c (4544 psi) should be used. Table 4.28 provides the ultimate shrinkage of the concrete at the three hierarchical levels.

Table 4.28. Ultimate shrinkage at the three hierarchical levels.

	Level 1	Level 2	Level 3
Ultimate Shrinkage, microstrain	945	713	711

4.5.7.1. Time to develop 50 Percent of Ultimate Shrinkage

The MEPDG recommends a value of 35 days at all input levels unless more reliable information is available. Referring to the measured data, see Figure 4.4, by setting the 50 percent ultimate shrinkage value at half of the estimated ultimate shrinkage $\epsilon_{50\%} = 472.5 \times 10^{-6}$; the following interpolated number of days were estimated for each of the beams tested:

DS-1: 18.7 days

DS-2: 1.6 days

DS-3: 3.3 days

If an average of these three values is used, then a value of 8 days is needed for the SR 22 concrete to reach 50 percent of its ultimate shrinkage. Table 4.29 provides the time to develop 50 percent of the ultimate shrinkage at the three hierarchical levels.

Table 4.29. Time to develop 50 percent of ultimate shrinkage at all three hierarchical levels.

	Level 1	Level 2	Level 3
Time to Develop 50% Ultimate Shrinkage	8 days	35 days	35 days

4.5.7.2. Anticipated Amount of Reversible Shrinkage

At all input levels, the MEPDG suggests a value of 50 percent unless more reliable information is available. This value was not determined through testing performed at the University of Pittsburgh and a value of 50 percent is assumed for the Smart Pavement.

4.6.0. ATPB Material Property Inputs

An asphalt treated permeable base was utilized for the Smart Pavement. Therefore, determination of the MEPDG input parameters for this material follow characterization for an asphalt material. The characterization of asphalt materials in the MEPDG can be separated into three classifications:

- General asphalt inputs
- Asphalt mix inputs
- Asphalt binder inputs

The following provides the characterization of the MEPDG inputs for the ATPB of the Smart Pavement. Although asphalt materials can be characterized at all three hierarchical input levels, it will only be classified according to input Level 3 for the Smart Pavement. The MEPDG has been in development for several years and when SR 22 was constructed the determination of the specifications to define the binder and mix of asphalt materials was not complete. Therefore, testing in accordance to the specifications established today was not completed and the ATPB of SR 22 can only be determined through Level 3 analysis.

4.6.1. General Asphalt Inputs

The general asphalt inputs of the MEPDG are the same at all three hierarchical levels. These inputs are needed for prediction of thermal cracking in the HMA layer. The following parameters are needed for general characterization of the asphalt material:

- Reference temperature

- Effective binder content
- Percent of air voids
- Total unit weight of asphalt
- Thermal conductivity and heat capacity
- Poisson's ratio

The preceding parameters were determined for the ATPB on SR 22, according to proper standards and specifications, and are provided in Table 4.30. The reference temperature, or temperature at the time of set, was determined from thermocouples embedded in the ATPB. The thermal conductivity and heat capacity were determined by taking the average of the range of typical values for asphalt concrete. Typically the thermal conductivity of asphalt concrete ranges between 0.44 and 0.81 Btu/(ft)(hr)(°F), and heat capacity varies between 0.22 and 0.44 Btu/(lb)(°F).

Table 4.30. General asphalt inputs for SR 22.

Input parameter	Value for SR 22
Reference temperature (°F)	68
Effective binder content (%)	2.5
Air voids (%)	8.5
Total unit weight (lb/ft ³)	148
Poisson's ratio	0.35
Thermal Conductivity (Btu/(ft)(hr)(°F))	0.62
Heat Capacity (Btu/(lb)(°F))	0.31

4.6.2. Asphalt Mix and Binder Inputs

The MEPDG uses asphalt mix and binder inputs to develop a master curve that relates the dynamic modulus of the asphalt to various temperatures. The dynamic modulus is the primary stiffness property of interest for asphalt materials. This parameter is a function of many parameters including: age, binder stiffness, aggregate gradation, binder content, air voids, and rate of loading. Therefore, if direct measurement of the dynamic modulus (Level 1 input) is not available proper characterization of the binder stiffness and aggregate gradation is necessary to determine the stiffness of the base throughout the design life.

At input Level 3, the asphalt is characterized through sieve analysis. The required

inputs include the cumulative percent of material retained on the 3/4 in, 3/8 in, and #4 sieves and the percent passing the #200 sieve. These inputs were determined for the ATPB on SR 22 and are shown in Table 4.31.

Table 4.31. Asphalt mix characteristics for the SR 22 ATPB.

Input Parameter	Value
Cumulative % Retained 3/4" sieve	28
Cumulative % Retained 3/8" sieve	67.5
Cumulative % Retained #4 sieve	84
% Passing #200 sieve	3

Level 3 characterization of the asphalt binder involves classification of the type of binder utilized in construction. Asphalt binders can be classified by three different grading systems, the Superpave binder grading, conventional viscosity grading, and the conventional penetration grade. The ATPB on SR 22 is a PG64-22 classified by the Superpave grading system. This is the only needed input for classification of the binder at input Level 3.

4.7.0. Unbound Granular Materials and Subgrade Material Property Inputs

The material inputs required for characterization of unbound granular materials and the subgrade of a pavement structure can be classified as follows:

- Pavement response model material inputs
- EICM material inputs
- Other material inputs

The pavement response material inputs include determination of the resilient modulus and Poisson's ratio of the various materials. These inputs are used to characterize the behaviour of the material when subjected to stresses. The material properties associated with the EICM include grain size distribution, the Atterberg limits, specific gravity, and hydraulic conductivity. These parameters are used to predict temperature and moisture conditions throughout the pavement system and were previously discussed, reference section 4.3.4.3. The final classification of unbound material properties are those required for the design solution, such as the coefficient of lateral pressure. The pavement response and other material inputs will be identified for the subbase and subgrade of the Smart Pavement herein.

The resilient modulus is a very important in the characterization of unbound granular materials. This parameter has a significant effect on the computed pavement responses and the dynamic modulus of subgrade reaction computed by the MEPDG. The resilient modulus can be determined at all input Levels 2 and 3. At Level 2, the resilient modulus can be estimated from cyclic triaxial tests in accordance to AASTO T307 or NCHRP 1-28A. The resilient modulus can also be estimated at input Level 2 through correlation with other material properties such as CBR. At Level 3, typical values or historical agency data should be utilized to characterize the resilient modulus of unbound granular materials.

The MEPDG considers the estimation of resilient modulus through backcalculation based on non-destructive deflection testing only in the cases of rehabilitation or reconstruction. However, this was the procedure followed by the University of Pittsburgh team for the Smart Pavement. The 5 in of 2A-subbase and the 24 in of backfill material that make up the subbase of the Smart Pavement have similar stiffness properties based on their soil classifications. Therefore, they are treated as a single layer. Deflection data from the FWD testing performed on the ATPB prior to the construction of the PCC slabs was used to backcalculate the resilient modulus of the subbase and subgrade material, using linear elastic layered analysis. The resilient moduli MEPDG inputs of the unbound layers and subgrade are provided in Table 4.32.

Table 4.32. Resilient moduli of the unbound granular layers and subgrade for SR 22.

Layer	Modulus of Resilience (psi)
2A subbase and backfill	19,500
Subgrade	4,500

The user of the guide faces two alternatives in regard to the input of the resilient modulus for various environmental (monthly) conditions:

1. Input the representative value of resilient modulus (discussed above) and let the EICM adjust the values for different seasonal variations
2. Input a value of resilient modulus for each month

It is recommended that the user chose to allow the EICM to adjust the modulus seasonally unless the resilient modulus has been determined seasonally through testing or backcalculation. Table 4.33 provides the resilient modulus inputs of the unbound granular

layers for the three hierarchical levels, the typical values provided for the Level 3 analysis were provided from LTPP historical data.

Table 4.33. Resilient moduli of the unbound granular layers and subgrade for the three hierarchical levels.

Resilient Modulus, psi	Level 1	Level 2	Level 3
2A subbase (A-2)	-	19,500	16,000
Backfill (A-1)	-	19,500	18,000
Subgrade (A-6)	-	4,500	14,000

Poisson's ratio must also be determined for each of the unbound granular layers of the pavement structure. This property is rarely measured because its influence on the mechanical response is minor. The MEPDG does allow it to be characterized at all three hierarchical levels. At Level 1, Poisson's ratio may be determined from cyclic triaxial tests on prepared samples using data obtained from resilient modulus testing. Although, there are models and correlations available to estimate Poisson's ratio, the MEPDG does not recommend using them. Instead, correlations and models based on local experience are suggested for input Level 2. At Level 3, the MEPDG suggests the use of typical values or historical agency data. The Poisson's ratio of the subbase and fill material on SR 22 was estimated from the classification of the soil to be 0.4. The subgrade material also has a Poisson's ratio of 0.4. These values will be used at all three hierarchical levels.

The coefficient of lateral pressure is used to express the ratio of the lateral earth pressure to the vertical earth pressure. Typically for unbound granular and subgrade materials, the coefficient of lateral pressure ranges between 0.4 and 0.6. Additionally, the coefficient of lateral pressure can be estimated through the following models:

$$k_0 = \frac{\mu}{1 - \mu} \quad (\text{Equation 4-3})$$

Where:

k_0 = Coefficient of lateral pressure

μ = Poisson's ratio

$$k_0 = 1 - \sin \phi \quad \text{(Equation 4-4)}$$

Where:

k_0 = Coefficient of lateral pressure

ϕ = Angle of effective internal friction

The coefficient of lateral pressure was characterized through correlation for the subbase, fill and subgrade material on SR 22 and was found to be 0.5 for all materials; this value will be used at all hierarchical levels.

4.8.0. Predicted Temperature and Moisture Conditions in the Pavement Structure

Models have been developed by researchers to estimate variations in temperature and moisture conditions in the pavement structure based on changes in ambient climatic conditions. The most recent modeling tool incorporating the effects of ambient conditions on the pavement material properties and on the infiltration through the pavement structure has been embedded in the new MEPDG and is referred to as the EICM [15].

The seasonal variations in ambient climatic conditions and the accompanying temperature and moisture measurements in the pavement structure were presented in Chapter 2. In this section, the pavement structure will be modeled using the EICM to estimate the temperature and moisture conditions in the pavement structure. Climatic data from the onsite weather station and from other weather stations close to the site will be used as inputs. The predicted conditions will then be compared to those measured in the field to validate the EICM predictions. First, a general overview of the EICM is presented. This is followed by a brief summary of the data collected by the climatic weather stations close to the site. Finally, the predicted temperature and moisture conditions inside the pavement structure are compared to those measured in the field.

4.8.1. Overview of the EICM

As previously discussed, the new MEPDG uses the EICM as a climatic modeling tool to account for changes in temperature and moisture conditions inside the pavement structure. The EICM simulates changes in the moisture, temperature and material properties of the pavement and subgrade materials as the ambient climatic conditions fluctuate over the design life of the pavement. The EICM is a combination of three separate models that evaluate the

effects of heat and moisture flow in a one-dimensional direction through the pavement structure [15]. The three models composing the EICM are:

- The Climatic-Materials-Structural Model developed at the University of Illinois [19].
- The CRREL Frost Heave and Thaw Settlement Model developed at the United States Army Cold Regions Research and Engineering Laboratory [20].
- The Infiltration and Drainage Model developed at Texas A&M University [21].

The EICM predicts temperature, resilient modulus adjustment factors, pore water pressure, water content, frost and thaw depth, frost heave, and drainage throughout the entire pavement structure. The results obtained from the EICM analysis include the following:

- a set of adjustment factors for unbound material layers that account for the effects of environmental parameters and conditions such as moisture content changes, freezing, thawing, and recovery from thawing,
- in-situ temperatures at the midpoints of each bound layer,
- temperature profiles within the asphalt and concrete layers (at eleven evenly spaced points through the thickness of the concrete) for every hour, and
- average monthly moisture contents for each layer in the pavement structure.

The output from the EICM is used by the structural response models and performance prediction models of the MEPDG to evaluate the performance of the trial design pavement over the design life. When the MEPDG uses the damage accumulation model, the design analysis period is divided into monthly time increments to analyze the proposed pavement structure. Each month is then subdivided into 2-hour periods to establish the temperature profiles in the slab. For each time increment, the equivalent linear temperature difference through the concrete slab is accounted for in increments of 2°F for both positive (daytime) and negative (nighttime) top-to-bottom temperature differences. In addition, all other factors that affect pavement response and damage are held constant within each time increment; they include: concrete strength and modulus, base modulus, subgrade modulus and joint load transfer across transverse and longitudinal joints. For each time increment, critical stresses, strains and deflections are determined along with damage accumulated during that time increment.

The fatigue damage due to the combined effect of environmental and traffic loads is

accumulated according to Miner's damage hypothesis by summing the damage over the entire design period. When the estimated value of accumulated damage is small, the pavement structure is not expected to have physical distresses. When the accumulated damage is large, physical distresses can be expected.

4.8.2. Climatic Databases

The effect of the climatic data on the predictions made by the EICM will be evaluated using climatic data from different weather stations. Data collected from the onsite weather station will be used as an input in the EICM to predict the temperature and moisture conditions in the pavement structure. In addition, the climatic data collected from the two weather stations closest to the site will be used as the climatic inputs and the predicted conditions will be compared to those measured. In total, three runs of the EICM using different climatic data will be analyzed. The locations of the selected weather stations are presented in Figure 4.5 and listed in Table 4.34. The table also includes the proximity of the weather stations to the site and the number of available data for each station.

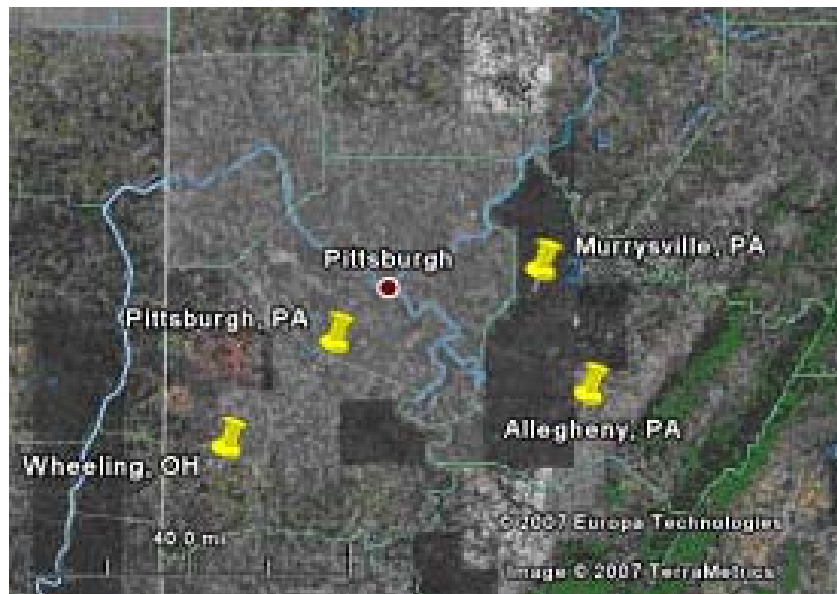


Figure 4.5. Locations of the weather stations with respect to the site [22].

Table 4.34. Weather stations used in the analysis.

	Latitude (degrees)	Longitude (degrees)	Elevation (ft)	Distance from site (miles)	Available data (months)
Murrysville (onsite)	40.43 N	79.66 W	935	--	38
Pittsburgh International Airport	40.30 N	80.14 W	1175	19.3	116
Allegheny County Airport	40.21 N	79.55 W	1281	25.7	85

A comparison of the climatic data collected by the different weather stations is presented in this section. The air temperature, rainfall, wind speed, sunshine and relative humidity are compared. The climatic data available from the onsite weather station covers a period of 38 months from September 1, 2004 to October 31, 2007, and the data available from the remaining weather stations covers a period of 7.1 to 9.7 years, as indicated in Table 4.34

A summary of the measured hourly air temperature is presented in Figure 4.6. The boxes in the figure represent the range of temperature extending between the average and plus and minus one standard deviation. The lines extending from the boxes represent the overall range of temperature extending between the minimum and maximum values. With the exception of the onsite weather station, referred to as the Murrysville station, the air temperature is in the range 0°F to 95°F and the averages are both 33°F. For the onsite weather station, the air temperature covers a slightly wider range (between -9°F and 98°F) and the average air temperature is 54°F, which is 62 percent higher than the temperature measured at the other stations. The higher average air temperature and the larger standard deviation of the Murrysville data is due to the small amount of available data from that station.

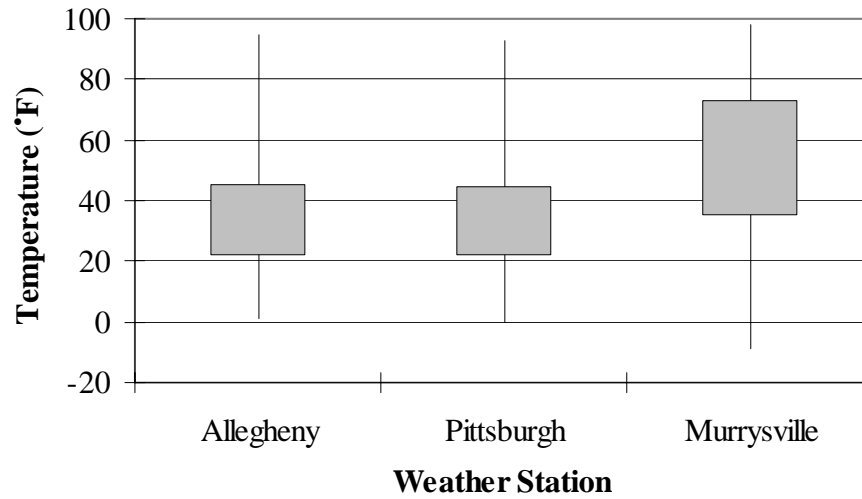
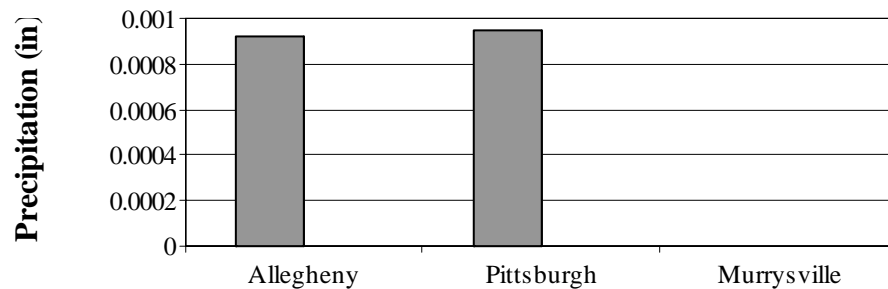


Figure 4.6. Measured hourly air temperatures for the different weather stations.

A summary of the measured rainfall is presented in Figure 4.7 and Figure 4.8. The Allegheny and Pittsburgh stations recorded a similar average rainfall; with the average varying between 0.00092 and 0.00094 in, with a standard deviation of 0.034 and 0.036 in. The maximum hourly rainfall reached 6 in for the Allegheny and Pittsburgh stations. Precipitation data is not collected by the onsite weather station.



Average	0.00092	0.00094	Data is not
Standard deviation	0.034	0.036	available

Figure 4.7. Average measured hourly rainfall for the different weather stations.

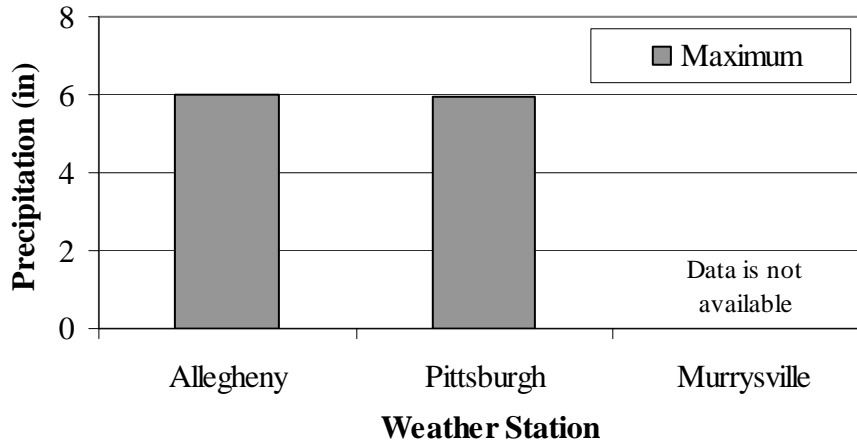


Figure 4.8 Maximum measured hourly rainfall for the different weather stations.

A summary of the average and maximum measured wind speed is presented in Figure 4.9 and Figure 4.10. The minimum measured wind speed was equal to zero for all stations. The average hourly wind speed recorded by all the weather stations varied between 1.2 and 1.3 mph, with the exception of the onsite station which recorded an average hourly wind speed of 2.8 mph. This indicates that the wind speed at the site is more than two times higher than those recorded at the other stations. The maximum wind speed is largest for the Pittsburgh station at 33 mph and lowest for the onsite station at 22.3 mph.

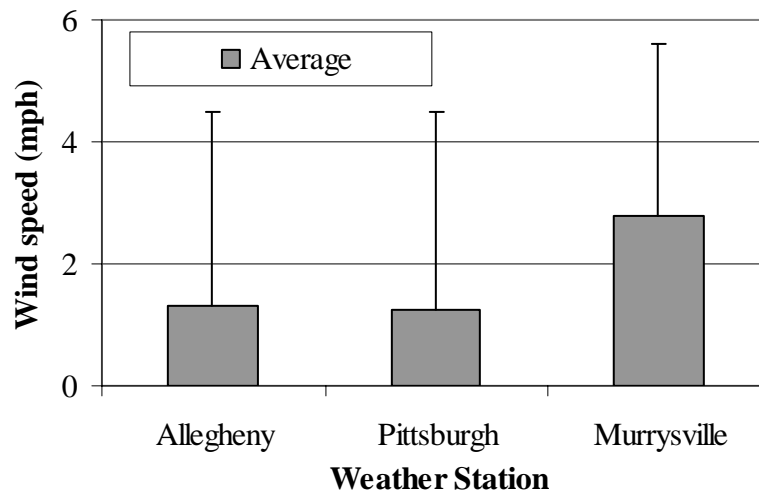


Figure 4.9. Average measured hourly wind speed for the different weather stations.

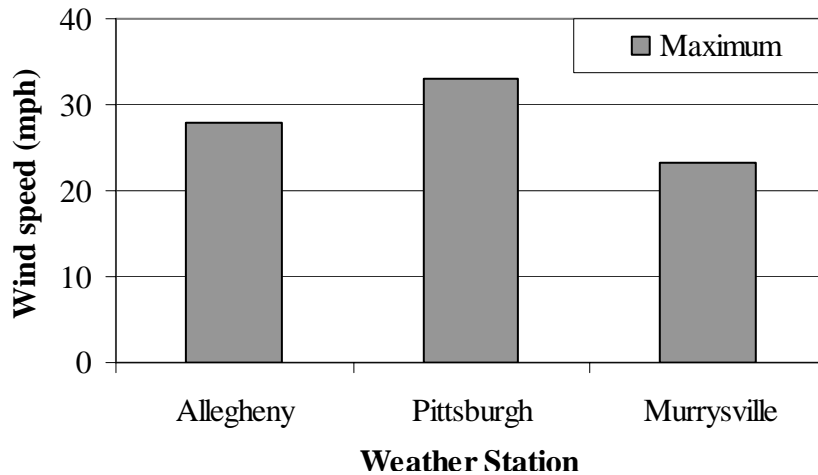


Figure 4.10. Maximum measured hourly wind speed for the different weather stations.

A summary of the average measured hourly percent sunshine is presented in Figure 4.11. The average percent sunshine varies between 6.1 percent for the Pittsburgh station and 10.2 percent for the Allegheny station. Sunshine data is not collected by the onsite weather station.

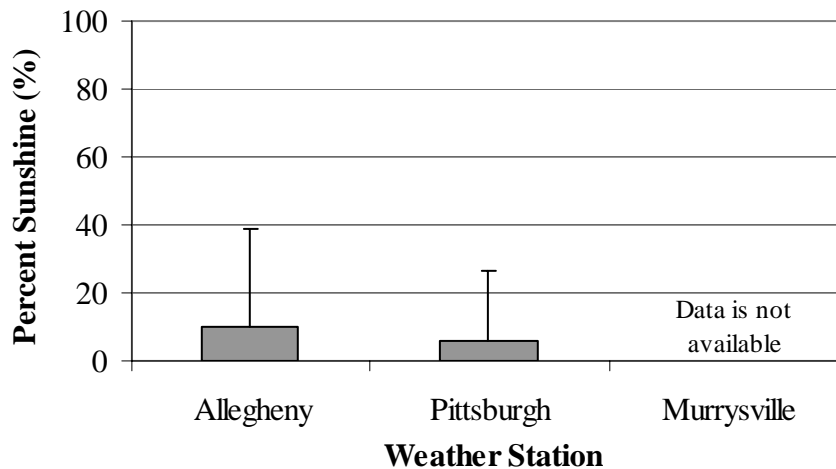


Figure 4.11. Summary of average measured hourly percent sunshine for the different weather stations.

A summary of the measured hourly ambient relative humidity is presented in Figure 4.12. The minimum ambient relative humidity varies between 62 and 63 percent for all the stations, except the onsite station where the minimum relative humidity is 9 percent. The average relative humidity is 94 percent for the Allegheny and Pittsburgh stations, compared

to an average of 72 percent measured by the onsite weather station.

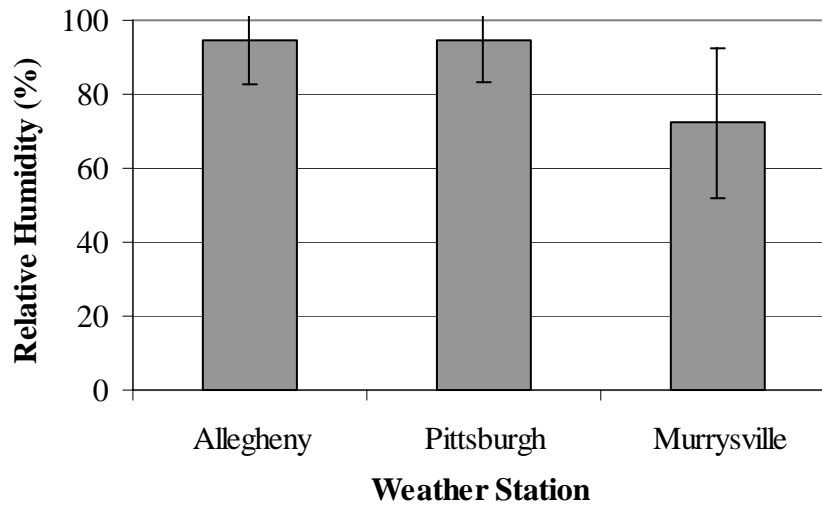


Figure 4.12. Average measured hourly ambient relative humidity for the different weather stations.

Since the onsite weather station does not include data for the percent sunshine or precipitation, and since the data collected by the two closest weather stations (Pittsburgh and Allegheny) are similar, the percent sunshine and precipitation data from the Pittsburgh station was used as representative of the conditions at the site and was appended to the remaining data collected onsite.

4.8.3. Temperature Predictions within the Concrete Slabs

The EICM was used to predict the temperature conditions within the concrete at eleven evenly spaced locations within the slab, by using the weather data from the climatic stations presented in the previous section. In this section, the predicted concrete temperatures during the first three years after construction of the pavement are presented and compared to those measured.

The monthly averages of the predicted and measured concrete weighted average temperature during the first three years after construction are compared in Figure 4.13. The predicted and measured temperatures follow the same seasonal trends. The temperatures predicted by the different weather stations are close to each other and close to those measured.

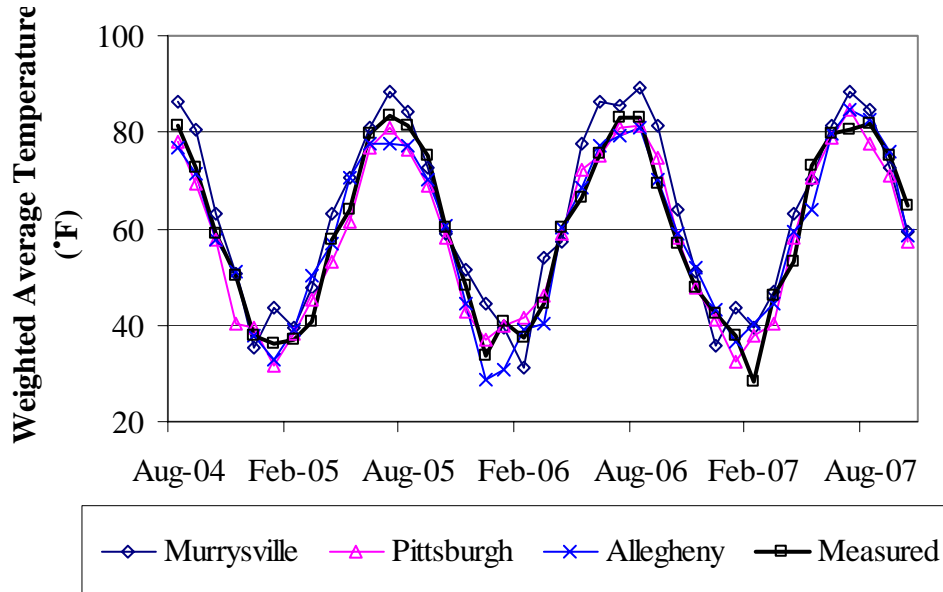


Figure 4.13. Predicted and measured monthly weighted average temperature.

The seasonal variation in the predicted temperature is presented in Figure 4.14. The figure presents the seasonal average and standard deviation of the weighted average temperature. The predicted temperature using the Murrysville (onsite) weather station is the highest compared to those predicted using the remaining weather stations. This is due to the fact that the ambient temperature measured by the onsite station is higher than that measured by the remaining stations. The average ambient temperature over the three-year period was found to be 54°F. This is 62 percent higher than the average ambient temperature, which was 33°F, measured at the other stations, as previously presented in section 4.8.2.

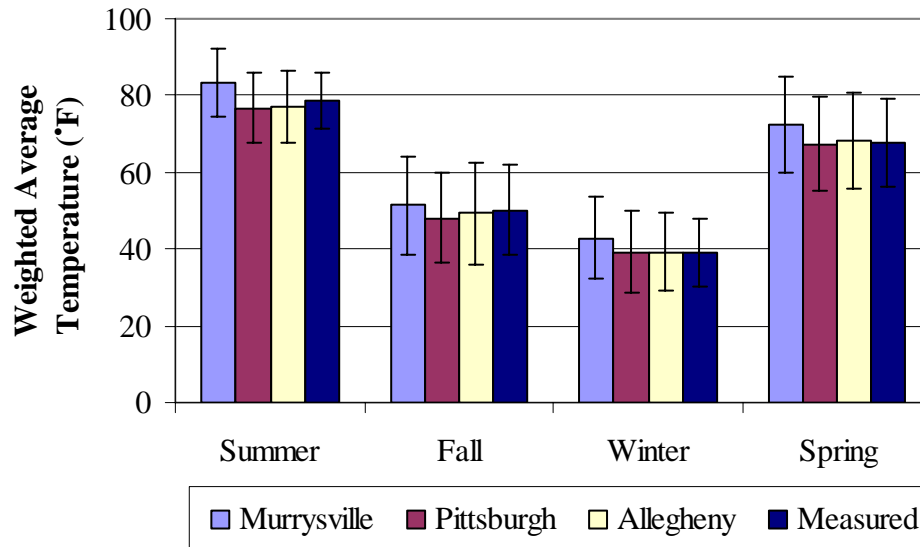


Figure 4.14. Predicted and measured seasonal weighted average temperature.

The average of all predicted weighted average temperatures within each season for each weather station is compared to the average of all measured weighted average temperatures are presented in Table 4.35. The average temperature predicted based on the Pittsburgh and Allegheny stations is within 10 percent of the measured weighted average temperature.

Table 4.35. Seasonal ranges of concrete weighted average temperatures.

	Weighted Average Temperatures (°F)	
	Predicted	Measured
Summer	79	79
Fall	50	50
Winter	40	39
Spring	69	68

The accuracy of the climatic model in predicting the weighted average concrete temperature is evaluated using statistical analysis. First, the predicted temperature is plotted versus the measured temperature, as shown in Figure 4.15. This figure shows the data predicted based on data from the Pittsburgh weather station. The correlation coefficient (R^2) between predicted and measured for the Pittsburgh station was equal to 0.88, indicating that the climatic model explains 88 percent of the total variability in temperature predictions for the 18,526 data points. This same procedure was carried out for the data predicted based on the Allegheny and Murrysville climatic databases. A summary of the correlation coefficients determined for each prediction case is presented in Table 4.36. The correlation coefficient varies between 88 and 94 percent, indicating that the climatic model is accurately predicting concrete temperatures. Moreover, the standard error of the estimate varies between 5.1 and 6.5 percent, indicating reasonable levels of error. The standard error of the estimate is also included in Table 4.36. The highest correlation coefficient was that corresponding to the Murrysville (onsite) weather station and it was accompanied with the lowest standard error. This indicates that the slab temperature predicted using the climatic data from the three climatic databases is accurately predicting the slab temperature.

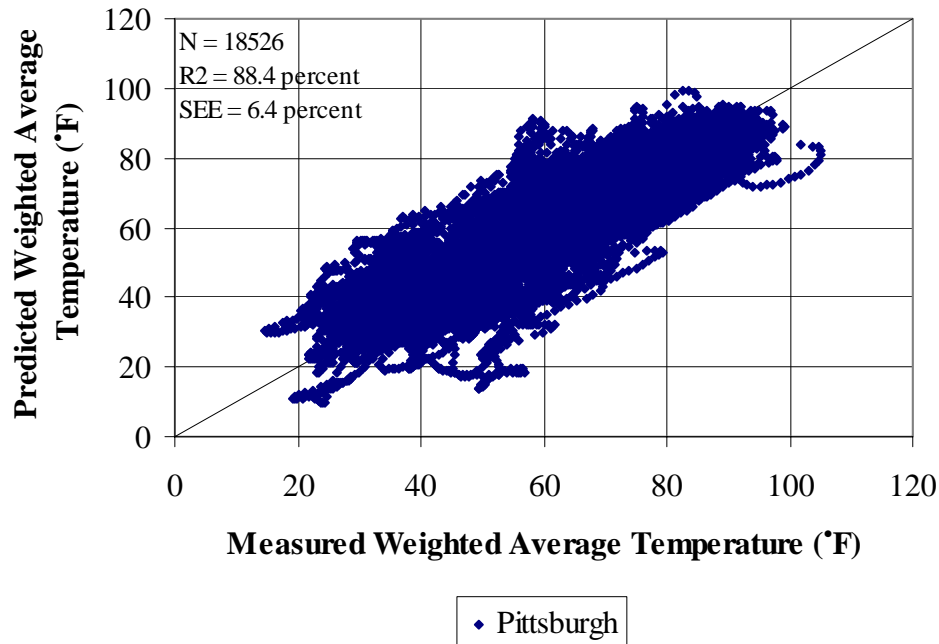


Figure 4.15. Predicted versus measured weighted average temperature (Pittsburgh station).

Table 4.36. Statistical analysis of predicted and measured concrete weighted average temperature.

Weather Station	R ² (%)	Standard error of the estimate	N
Murrysville	94	0.05126	18,526
Pittsburgh	88	0.06447	18,526
Allegheny	89	0.06451	18,526

In addition, the scatter around the one-to-one line in Figure 4.15 is an indication of the residual error involved in the temperature prediction. If there are more data points above or below this line, this might indicate a bias in the prediction. The residuals representing the difference between the predicted and measured weighted average temperature were plotted against the measured temperature, and are presented in Figure 4.16, which corresponds to the predictions based on the Pittsburgh station. The figure shows a horizontal band with no abnormalities or trends, implying that the data used in the analysis is independent. This was also carried out for the data predicted by the three climatic data files and the results were similar.

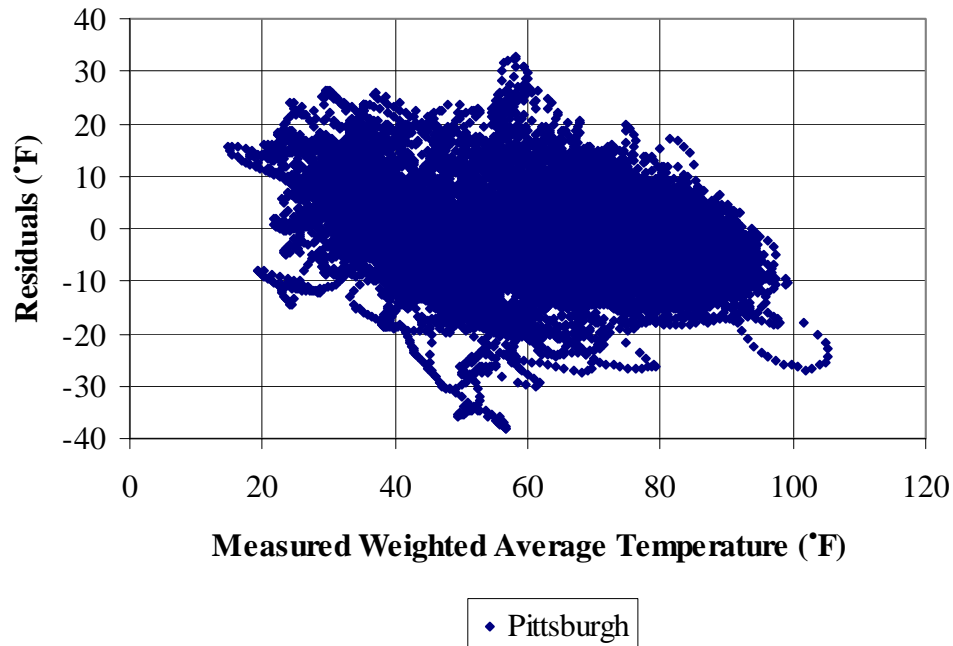


Figure 4.16. Residual versus measured weighted average temperature (Pittsburgh station).

Having established that the predicted weighted average concrete temperature is similar to that measured, another aspect of the predicted temperature also needs to be examined. The temperature predicted along the slab depth influences the temperature gradients within the slab. Therefore, the equivalent linear temperature gradient based on the predicted temperature is compared to those based on the measured temperature.

The seasonal variation in the equivalent linear temperature gradient calculated using the predicted and measured temperatures is presented in Figure 4.17 to Figure 4.19. The figures show the maximum positive, negative and average equivalent linear temperature gradient. According to Figure 4.17, the maximum positive gradient based on the predicted temperature is higher than that based on the measured temperature for all seasons, with the exception of the predicted temperature determined using the onsite weather station for the spring season. This indicates that the predicted temperature tends to over-estimate the maximum positive temperature gradient in the slab for the conditions considered. Similarly, the predicted temperature over-estimates the maximum negative temperature gradient in the slab, as shown in Figure 4.18. The over-estimation of the predicted maximum positive and negative gradient could result in over-estimation of the damage caused by these gradients. As a result, the predicted performance of the pavement would be underestimated when

compared to the actual performance.

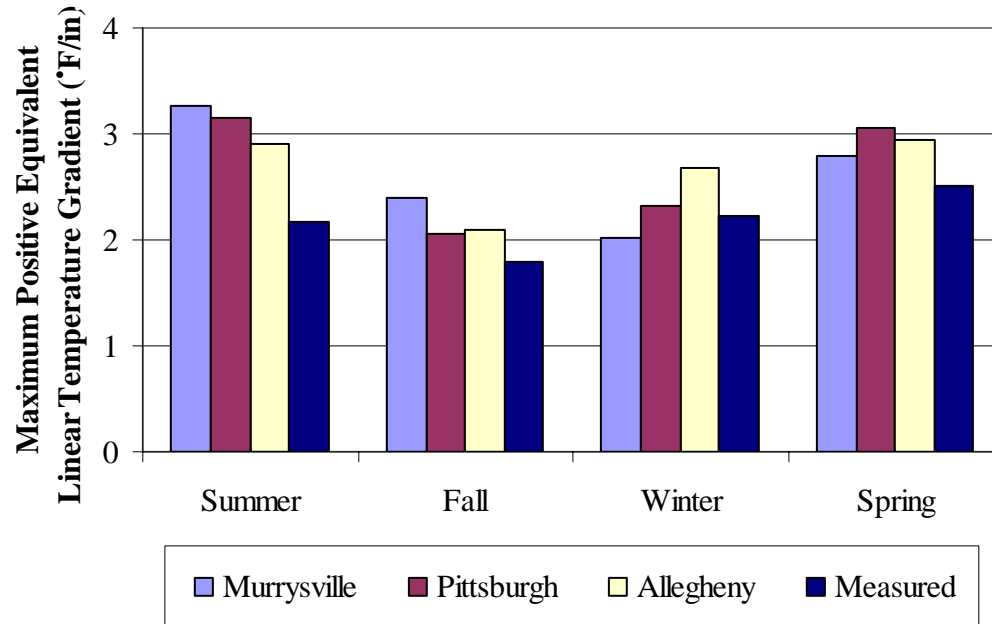


Figure 4.17. Seasonal maximum positive equivalent linear temperature gradient based on the predicted and measured temperature.

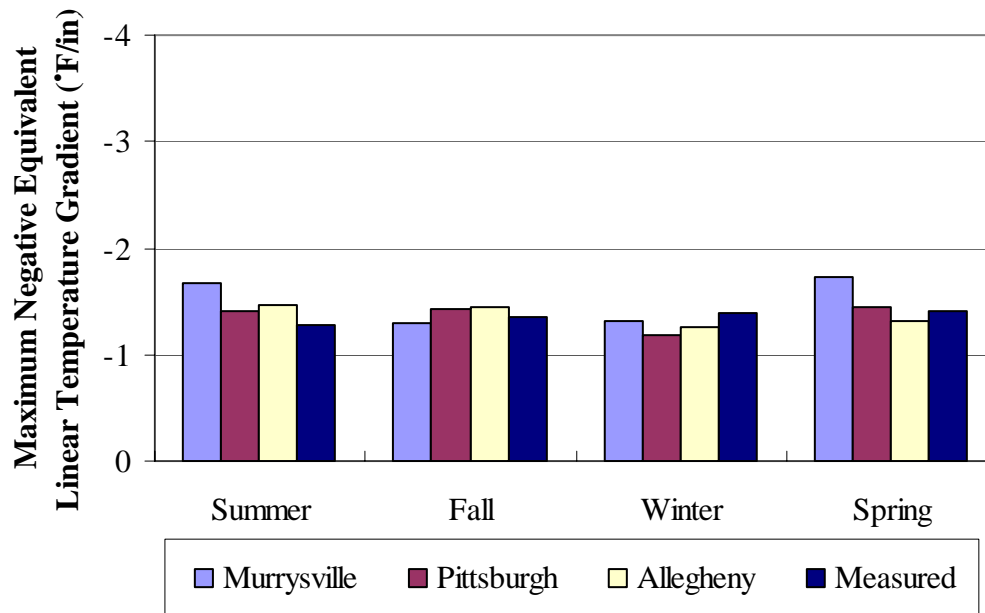


Figure 4.18. Seasonal maximum negative equivalent linear temperature gradient based on the temperature predicted at 1-hour intervals and the temperature measured at 15-minute intervals.

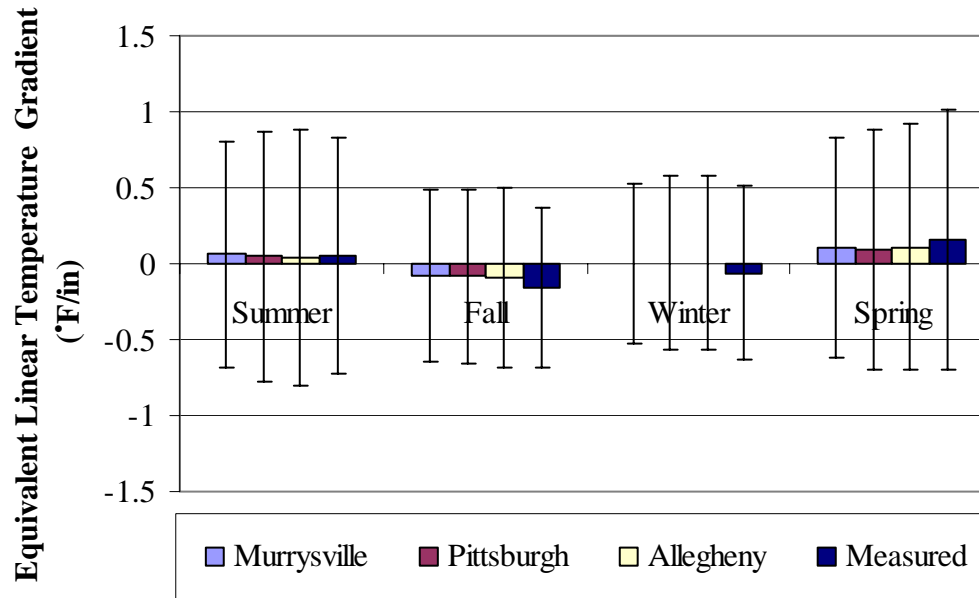


Figure 4.19. Seasonal average equivalent linear temperature gradient based on the temperature predicted at 1-hour intervals and the temperature measured at 15-minute intervals.

Similar to the statistical analysis carried out for the weighted average temperature, the accuracy of the climatic model in estimating the equivalent linear temperature gradient is was also evaluated. The correlation coefficient and the standard error of the estimate between the gradient based on the predicted and measured temperature is presented in Table 4.37. The correlation coefficient varies between 58 and 66 percent, indicating that the climatic model is not as accurate in predicting the temperature gradient. The standard error of the predicted gradient is 0.5 percent, which indicates that the level of error in the prediction model is reasonable. Similar to the observation made regarding the weighted average temperature, the prediction made based on the Murrysville station resulted in the highest correlation coefficient and lowest standard error.

Table 4.37. Summary statistics for comparing predicted with measured equivalent linear temperature gradient.

Weather Station	R ² (%)	Standard error of the estimate	N
Murrysville	66	0.00454	18,526

Pittsburgh	58	0.00518	18,526
Allegheny	61	0.00514	18,526

In summary, the weighted average temperature and the equivalent linear temperature gradient over the three-year period are compared in Figure 4.20 and Figure 4.21. In these figures, the box represents the range of values between the average plus and minus one standard deviation. The lines extending from the box represents the overall range of values showing the minimum and maximum value. The weighted average temperature predicted by the different weather stations are similar to each other and to those measured. The equivalent linear gradient based on the predicted and measured temperatures are also similar.

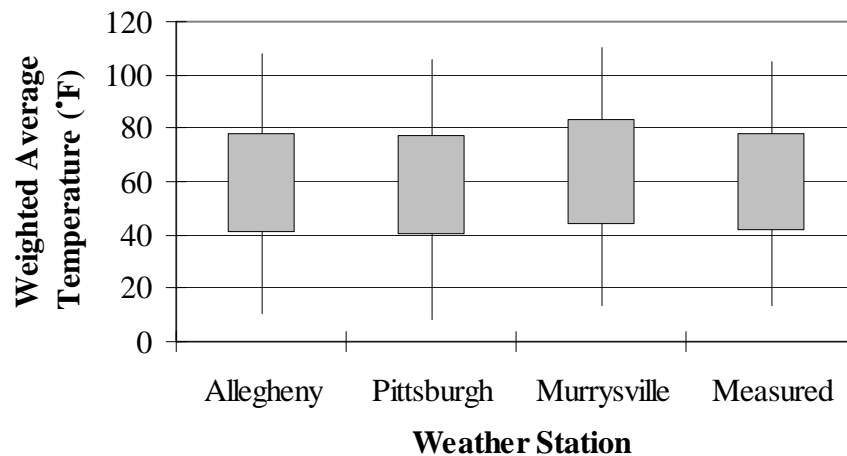


Figure 4.20. Weighted average temperature based on predicted and measured temperatures over a three-year period.

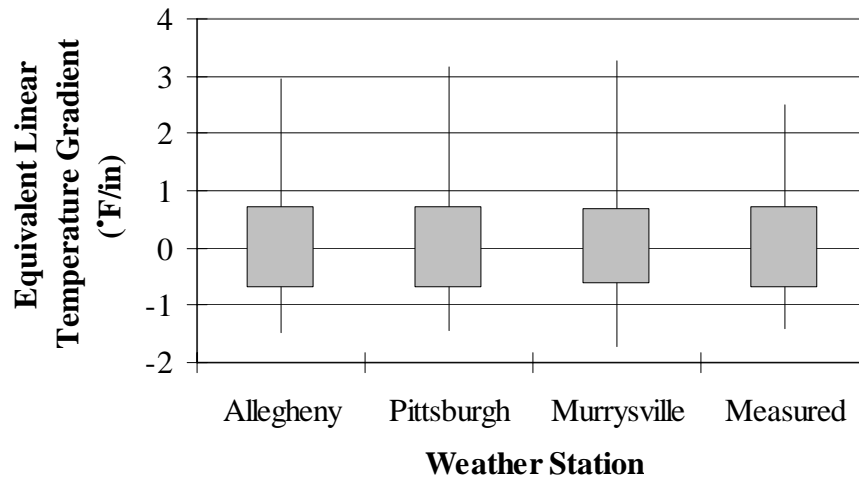


Figure 4.21. Equivalent linear temperature gradient based on predicted and measured temperatures over a three-year period.

The predicted and measured seasonal variation in temperature along the depth of the concrete slab was calculated for the four climatic seasons based on the data collected during the first three years after construction. The average temperature profile for the summer season is presented in Figure 4.22. Unexpectedly, the average temperature predicted based on the climatic data from the onsite weather station is substantially larger than the measured values. The predicted temperatures based on the climatic data from the two remaining weather stations are close to each other and lower than the measured temperatures. The gradients for the temperature profiles in Figure 4.22 vary between 0.04 and 0.06°F/in.

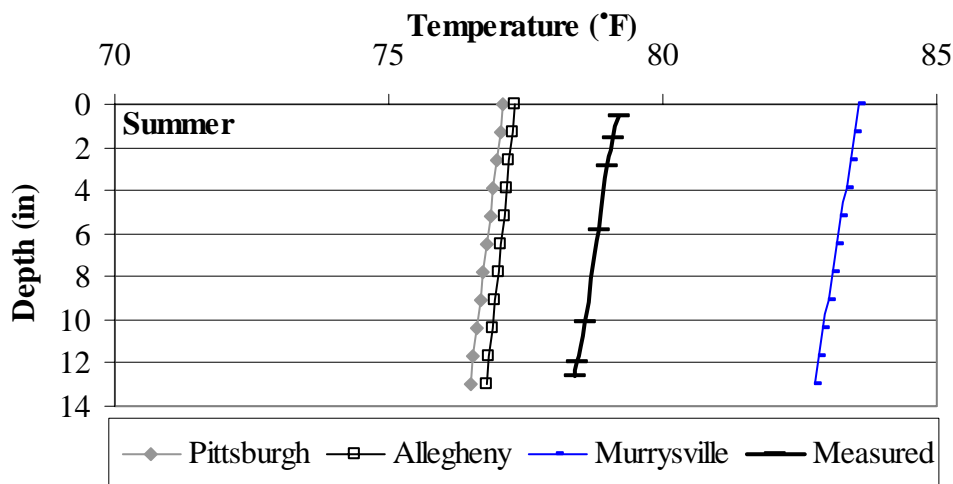


Figure 4.22. Average predicted and measured concrete temperature profiles during the summer.

The average temperature profiles for the fall are presented in Figure 4.23. All of the predicted temperatures were within a couple degrees of the measured temperatures. The gradients for the temperature profiles in Figure 4.23 vary between -0.08 and $-0.16^{\circ}\text{F/in.}$

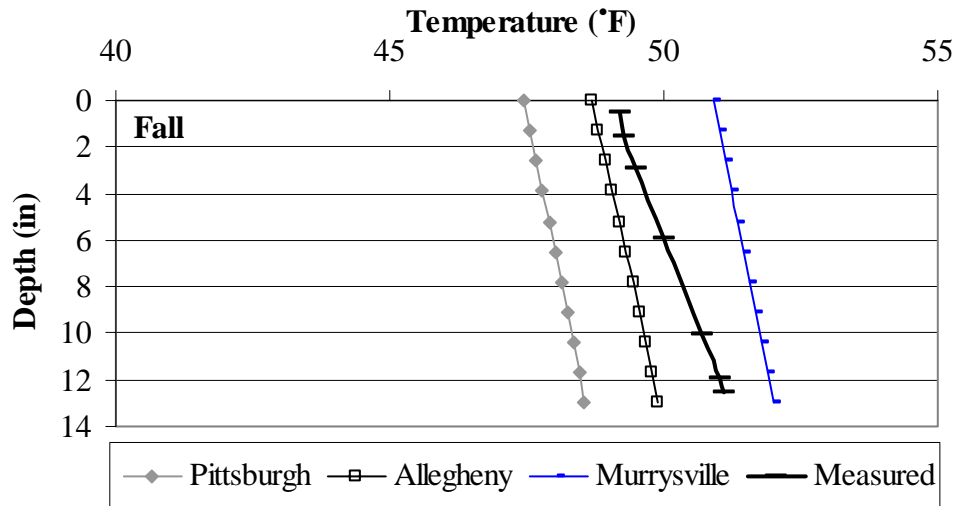


Figure 4.23. Average predicted and measured concrete temperature profiles during the fall.

The average temperature profiles for the winter are presented in Figure 4.24. Most of the predicted temperatures are within a few degrees of the measured temperatures. A significant gradient is not present in any of the profiles.

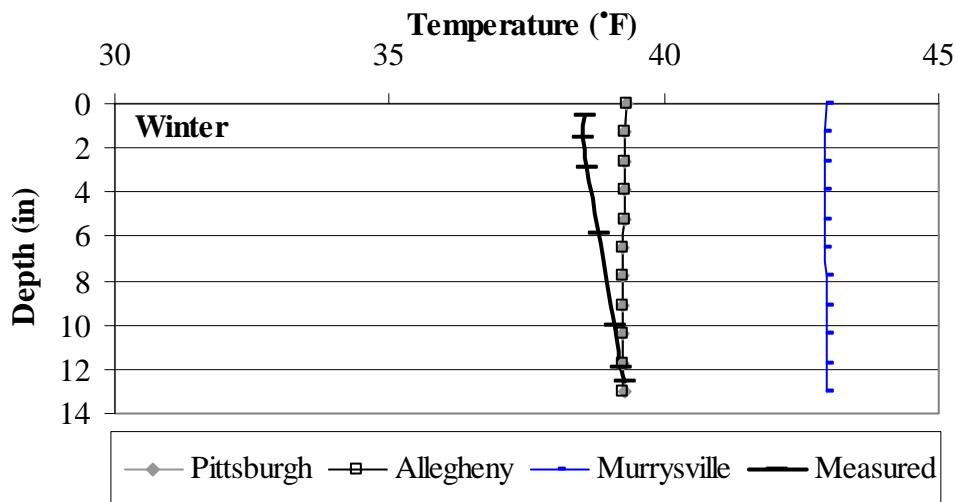


Figure 4.24. Average predicted and measured concrete temperature profiles during the winter.

The average temperature profiles for the spring are presented in Figure 4.25. All predicted temperatures are within a couple of degrees of the measured temperatures. The temperature gradients for the predicted temperature profiles vary between 0.09 and 0.11°F/in. The gradient for the measured temperature profile is 0.16°F/in, which is very close to the predicted values.

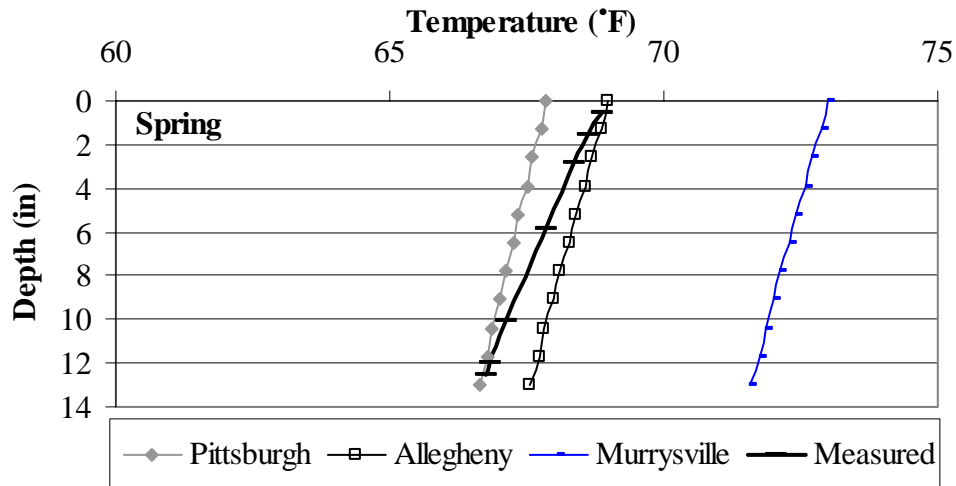


Figure 4.25. Average predicted and measured concrete temperature profiles during the spring.

In general, the temperature generated using climatic data from weather stations close to the site (within 30 miles) predicted the average temperatures within a couple of degrees. The predicted average gradients were also very close to the measured average gradient. It is surprising that the average temperature profiles predicted using the onsite weather station are so different from the measured values. The reason for this is not clear.

4.8.4. Temperature Predictions within the Underlying Layers

In addition to predicting temperatures in the concrete slab, the EICM also predicts temperatures within the stabilized and granular layers. In relatively thick layers, the layer is subdivided into thinner layers and the temperature is predicted at mid-depth of the layer. In thin layers, the temperature is simply predicted at mid-depth. The 24-in fill layer was automatically subdivided into four equal layers 6-in thick, and the top 24 in of the subgrade layer is treated as a separate layer. In this section, the predicted temperature in the granular

layers during the first three years after construction of the pavement are presented and compared to those measured.

Starting with the 4-in ATPB layer, the temperature was predicted at mid-depth of the layer. The thermocouples measuring temperature in this layer are located at approximate depths of 14 and 16 in from the top of the pavement, which correspond to the middepth of the ATPB and the bottom of the ATPB. The predicted and measured average seasonal temperature is presented in Figure 4.26. The average temperature predicted based on the climatic data from the Murrys ville (onsite) station is the highest. Overall, the predicted temperature is similar to the measured temperature.

Moving to the 5-in thick subbase layer, the temperature was also predicted at mid-depth of the layer. The thermocouples measuring temperature in this layer were located at approximate depths of 19 and 21 in from the top of the pavement, which correspond to depths of 2 in (middepth of the subbase) and 4 in (bottom of the subbase) from the top of the subbase layer. The predicted and measured average seasonal temperature is presented in Figure 4.27. The average temperature predicted based on the climatic data from the Murrys ville (onsite) station is the highest. Overall, the predicted temperature is similar to the measured.

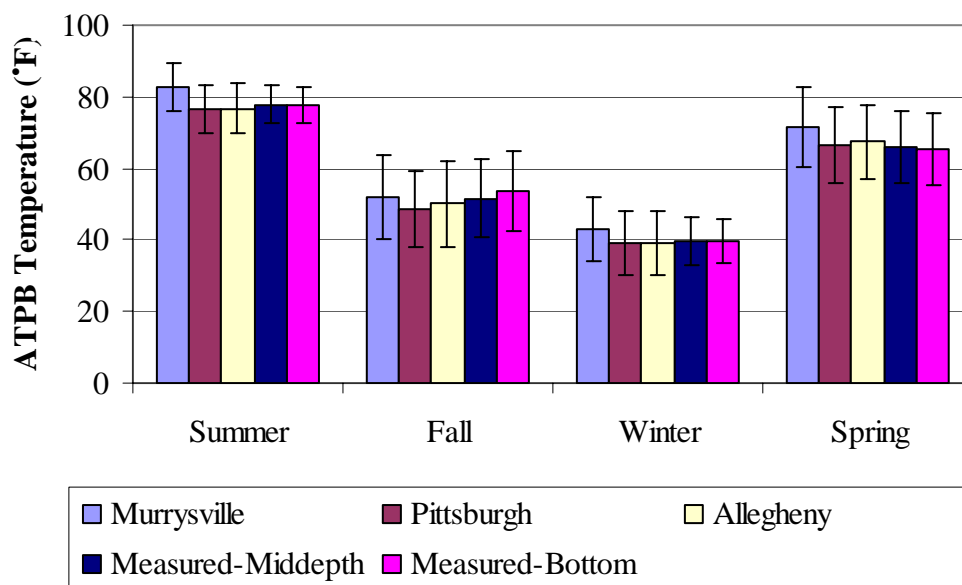


Figure 4.26. Average seasonal predicted and measured temperatures at mid-depth of the ATPB.

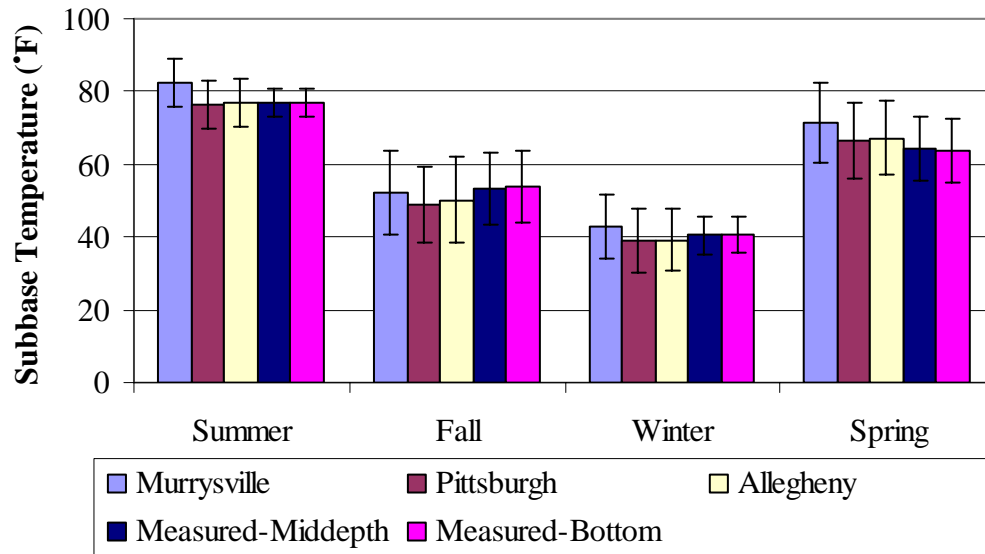


Figure 4.27. Average seasonal predicted and measured temperatures at mid-depth of the subbase.

Going deeper into the pavement structure, the fill layer was automatically subdivided into four sublayers, 6 in thick. The temperature was predicted at mid-depth of each sublayer. The thermocouples measuring temperature in this layer were located at approximate depths of 28, 36 and 42 in from the top of the pavement, which correspond to depths of 6, 14 and 20 in from the top of the fill layer, or 0 in from the top of the second sublayer, 2 in from the top of the third sublayer and 2 in from the top of the fourth sublayer. The seasonal trends of the predicted temperatures were similar in the four sublayers. To minimize repetition, only the predicted average seasonal temperature for the second sublayer is presented in Figure 4.28, along with the measured average temperature for the second, third and fourth sublayers. The average temperature predicted based on the climatic data from the Murrysville (onsite) station is the highest. Overall, the predicted temperature is similar to the measured.

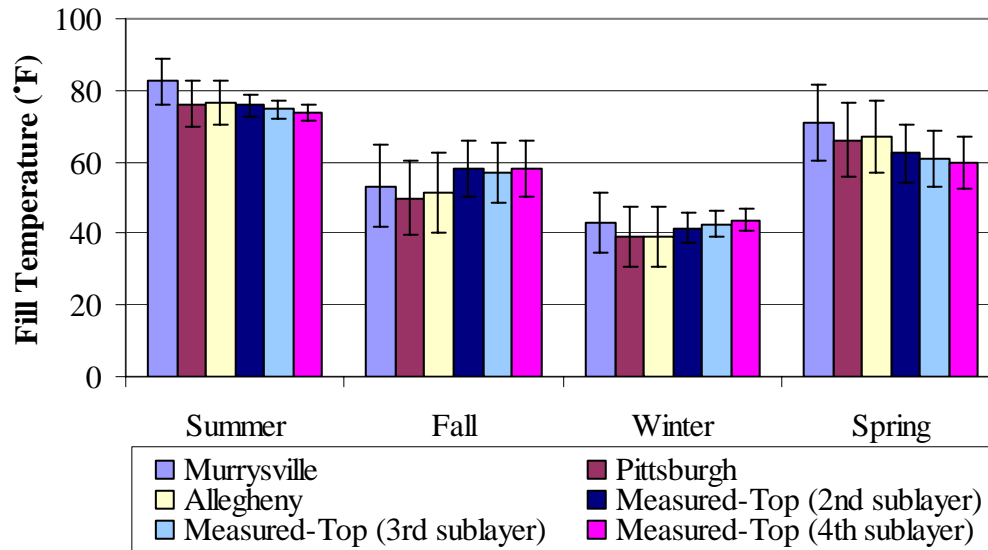


Figure 4.28. Average seasonal predicted temperatures (6-12 in) and measured temperatures (6-24 in) in the fill layer.

The subgrade layer was automatically subdivided into two sublayers. The first sublayer is 24 in and the second consists of the remaining of the modeled thickness. The temperature was predicted at mid-depth of each sublayer. The thermocouples measuring temperature in this layer were located at an approximate depth of 48 in from the top of the pavement, which corresponds to a depth of 2 in from the top of the subgrade layer. The seasonal trends of the predicted temperature are similar in the two sublayers. To minimize repetition, only the predicted and measured average seasonal temperature for the first sublayer is presented in Figure 4.29. The average temperature predicted based on the climatic data from the Murrysville (onsite) station is the highest. Overall, the predicted temperature is similar to the measured.

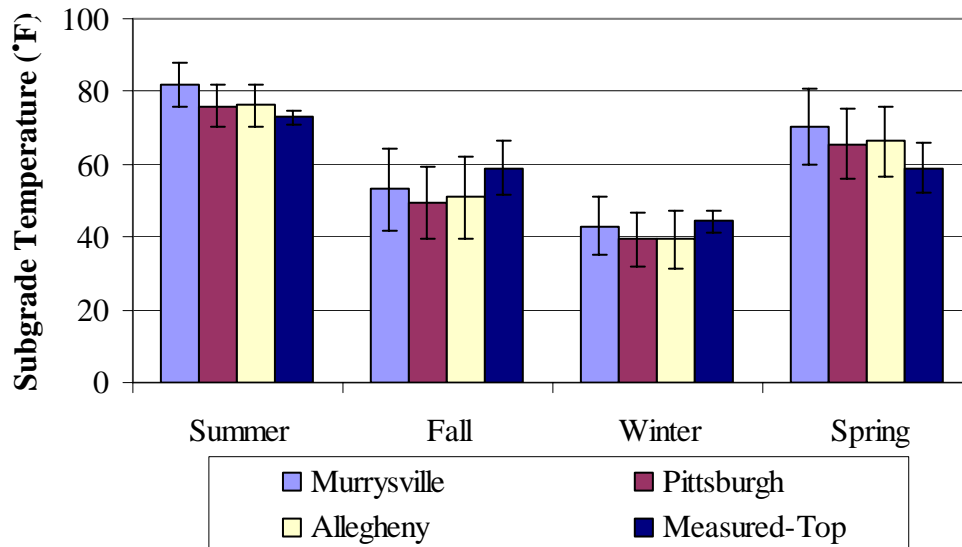


Figure 4.29. Average seasonal predicted and measured subgrade temperatures (0-24 in).

The predicted and measured seasonal variation in temperature along the depth of the layers underlying the concrete slab was calculated for the four climatic seasons based on the data for the three years. The average profiles for the summer season are presented in Figure 4.30. Based on the figure, the predicted temperature profiles are different from the measured profile. The average temperature predicted based on the climatic data from the onsite weather station shows the most significant difference from the measured temperature. The predicted temperature based on the Allegheny and Pittsburgh climatic data files are close to each other.

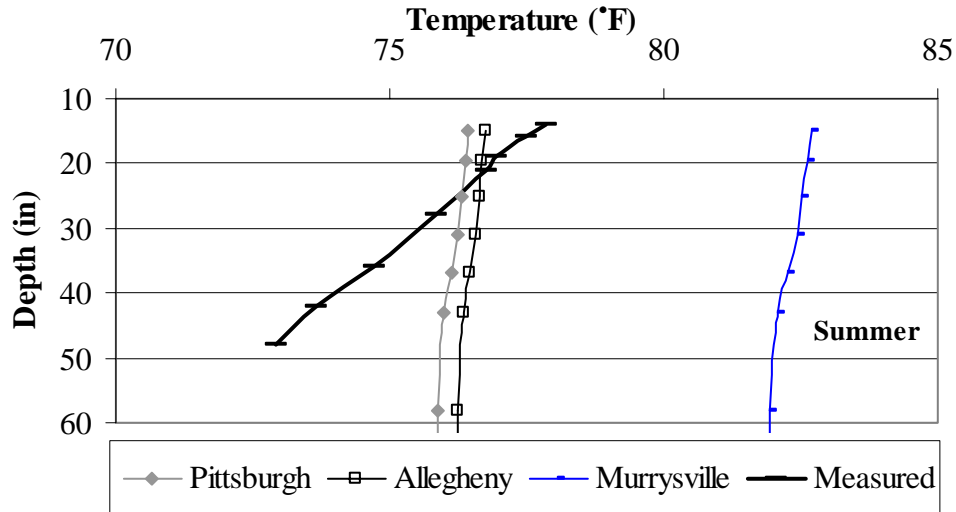


Figure 4.30. Average seasonal temperature profiles within the underlying layers during the summer.

The average profiles for the fall season are presented in Figure 4.31. Based on the figure, the predicted temperature profiles are different from the measured profile. The predicted temperature profiles are similar to the measured values in the upper portion of the pavement structure during the fall but are substantially different in the lower layers. This might be attributed to the fact that the material properties of the layers were estimated primarily based on estimations using the particle distribution and plasticity characteristics.

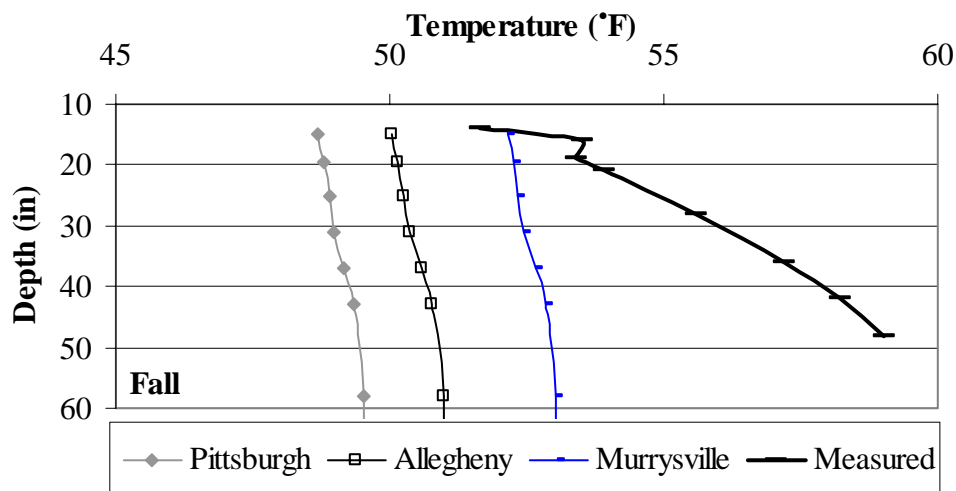


Figure 4.31. Average seasonal temperature profiles within the underlying layers during the fall.

The average profiles for the winter season are presented in Figure 4.32. The predicted temperature profiles are similar to the measured temperature. As with the fall season, the predicted temperature in the lower portion of the structure tends to underestimate the measured temperature during the winter.

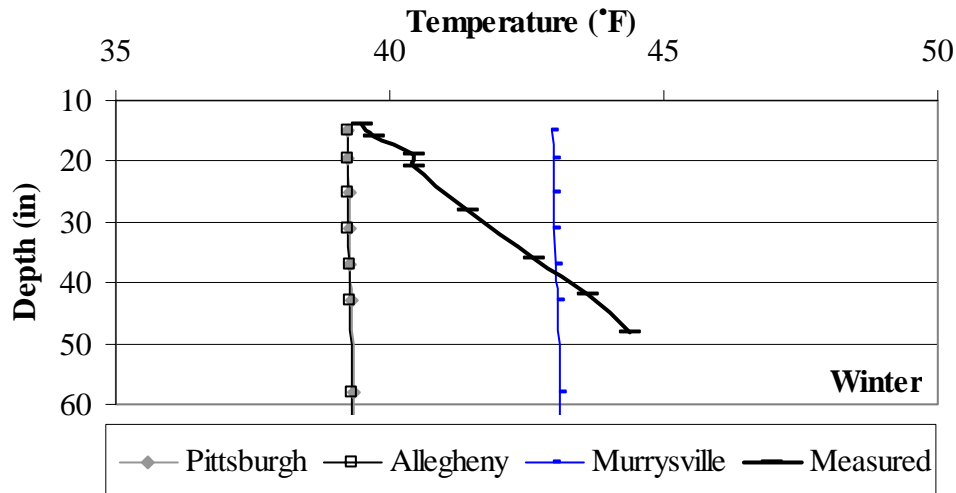


Figure 4.32. Average seasonal temperature profiles within the underlying layers during the winter.

The average profiles for the spring season are presented in Figure 4.33. Unlike during the winter and fall seasons, the predicted temperature tends to overestimate the measured temperature by about 10°F during the spring. The onsite weather station drastically overestimates the measured temperature.

In summary, it can be concluded that the temperature predicted in the underlying layers is not representative of the measured conditions. The largest influence in the temperature of the underlying layers on the pavement response is when the granular layers are frozen. Fortunately, the frost depth is shallow and the lower layers do not freeze and therefore errors in the temperature are not very influential. It has been shown that the weather stations within a distance of 50 miles from the test section predicted temperature well. In a subsequent section, the effect of these differences in temperature on pavement performance will be evaluated to confirm the theory that these differences in temperature predictions are not significant on pavement design for SR-22. These errors between predicted and measured temperatures might have an impact on pavement designs for different locations when the temperatures are closer to freezing.

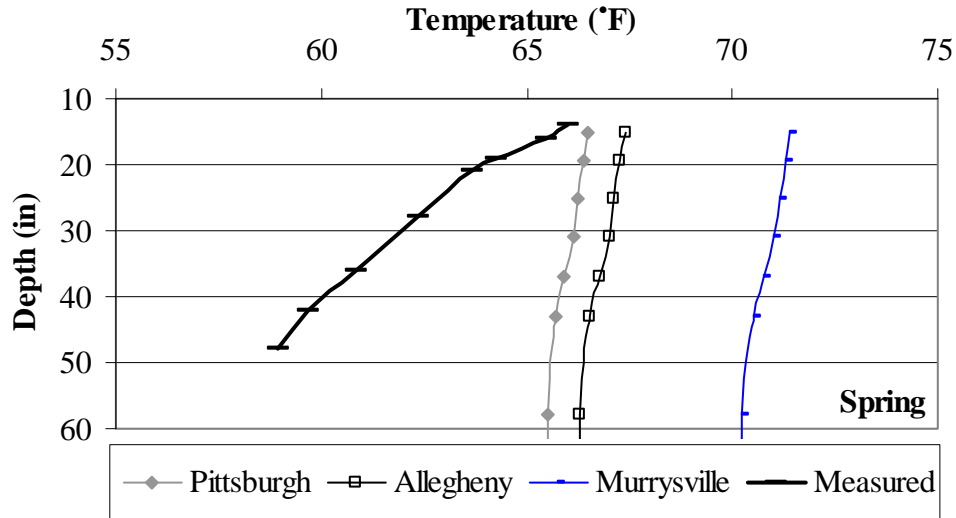


Figure 4.33. Average seasonal temperature profiles within the underlying layers during the spring.

4.8.5. Moisture Predictions within the Granular Layers

In addition to predicting temperature, the EICM also predicts the moisture content within the granular layers; it does not predict moisture content in the concrete or in stabilized layers. This is because the change in moisture content for the bound layer will not impact the stiffness of that layer. Similarly to the temperature predictions in granular layers, thick layers are subdivided into thinner sublayers and the moisture contents are predicted at mid-depth of the layer. In thin layers, the moisture content is simply predicted at mid-depth. The 24-in fill layer was automatically subdivided into four 6-in layers. The top 24 in of the subgrade layer was treated as a separate layer. In this section, the predicted moisture content in the granular layers during the first three years after construction of the pavement are presented and compared to measured moisture content.

The volumetric water content predicted based on the climatic data from the Pittsburgh weather station is presented in Figure 4.34 for the first three years after construction of the pavement. The moisture content did not vary much throughout the three-year period but clearly indicates a sharp decrease during the first and second winter season. This decrease in VWC is attributed to the freezing of the underlying layers during that period. The VWC increases with depth. During the three-year period, the subbase has a moisture content of 10 percent, the fill has a moisture content of 15 to 18 percent, and the subgrade has a moisture content of 34 to 35 percent. The same trends were obtained based on the climatic data from

the remaining weather stations, with the exception of the predictions based on the onsite station. The predicted moisture content based on the onsite weather station showed slightly lower moisture contents in all the layers during the three-year period. According to the material characteristics, the volumetric moisture content corresponding to 100 percent saturation are equal to 27 percent for the subbase, 28 percent for the fill, and 19 percent for the subgrade. Based on the predicted moisture levels, the subgrade layer is fully saturated during the three-year period, irrespective of the climatic season.

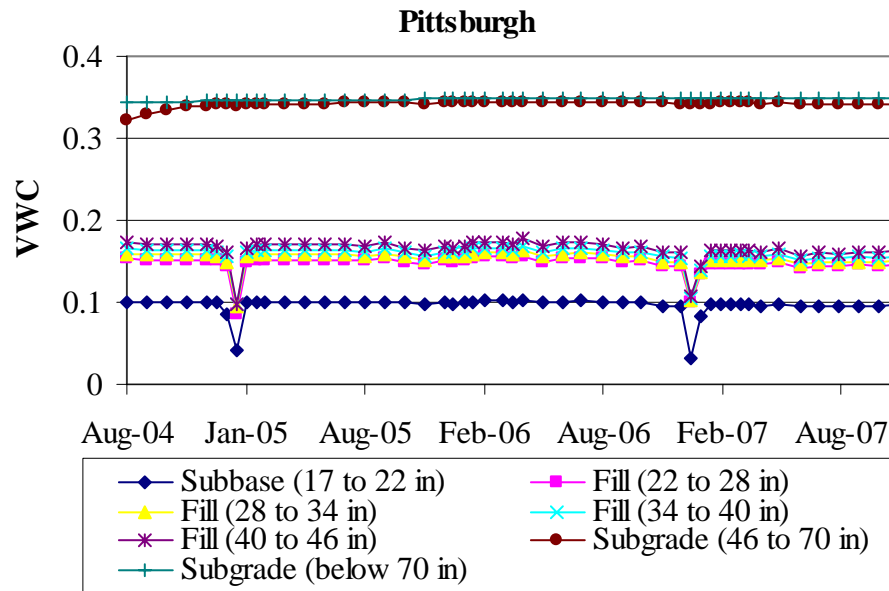


Figure 4.34. Predicted volumetric water content within the granular layers based on climatic data from the Pittsburgh station.

The predicted moisture content based on the climatic data from the different weather stations are compared to each other for the case of the subbase layer, and are presented in Figure 4.35. Data from the onsite weather station shows the lowest moisture content predicted. This is consistent in all the layers. This difference is not significant.

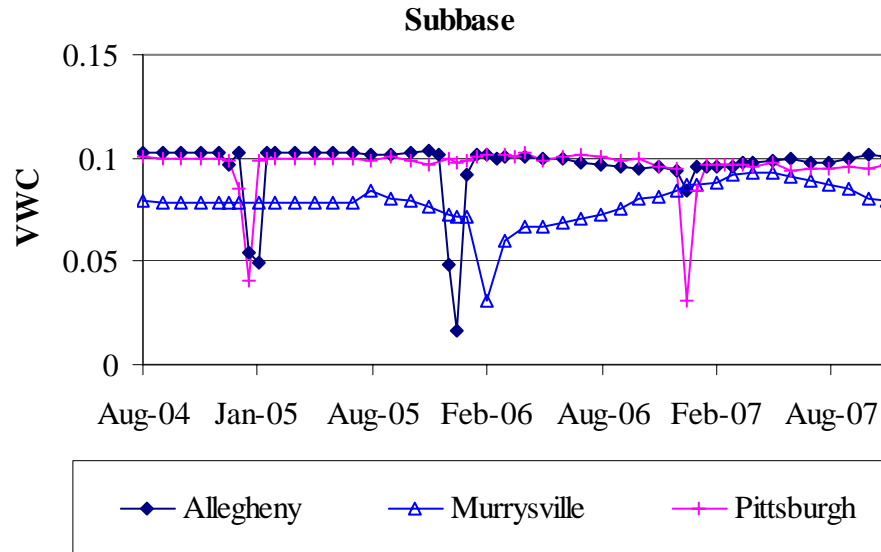


Figure 4.35. Predicted VWC within the subbase.

The predicted volumetric moisture content is compared to that measured by the Time Domain Reflectometers (TDR) at midpanel. The comparison is presented in Figure 4.36 for the subbase layer. The predicted moisture content is based on the climatic data from the Pittsburgh weather station. The predicted and measured VWC in the fill and subgrade layers are compared in Figure 4.37 and Figure 4.38 based on the same climatic data. The figures show that the predictions overestimate the moisture content, and that they are closest for the subbase layer. However, as discussed in section 2.4.3 of Chapter 2, most of the TDR graphs do not show any patterns, which made interpretation of the data difficult. This makes it difficult to interpret the predicted data and evaluate whether the predictions are close to those measured or not.

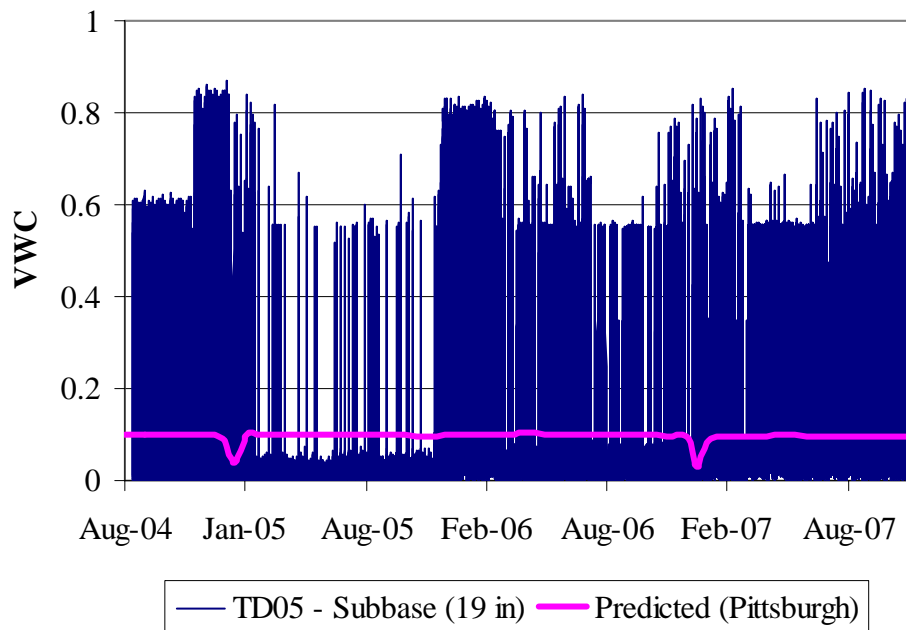


Figure 4.36. Predicted and measured VWC within the subbase (Pittsburgh station).

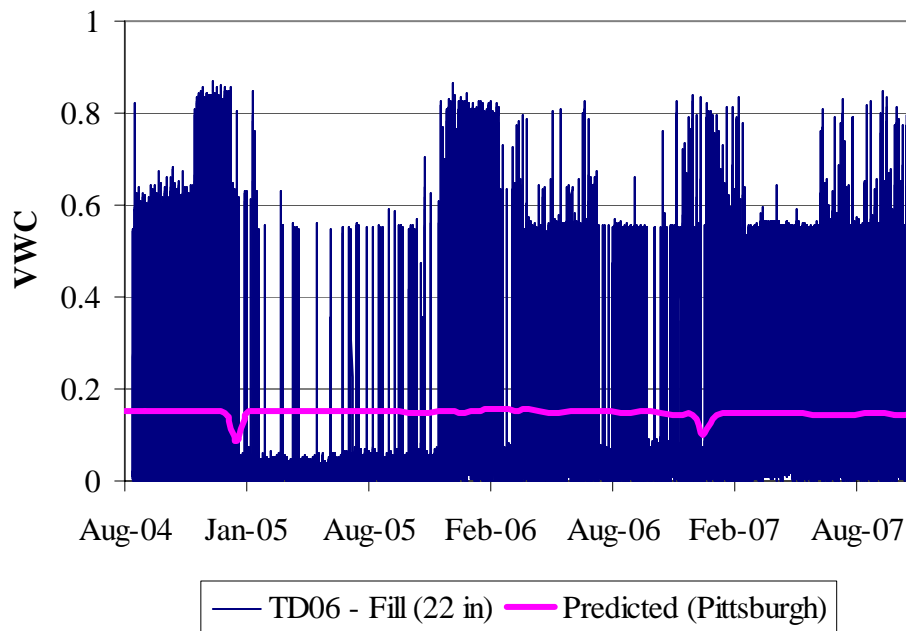


Figure 4.37. Predicted and measured VWC within the fill (Pittsburgh station).

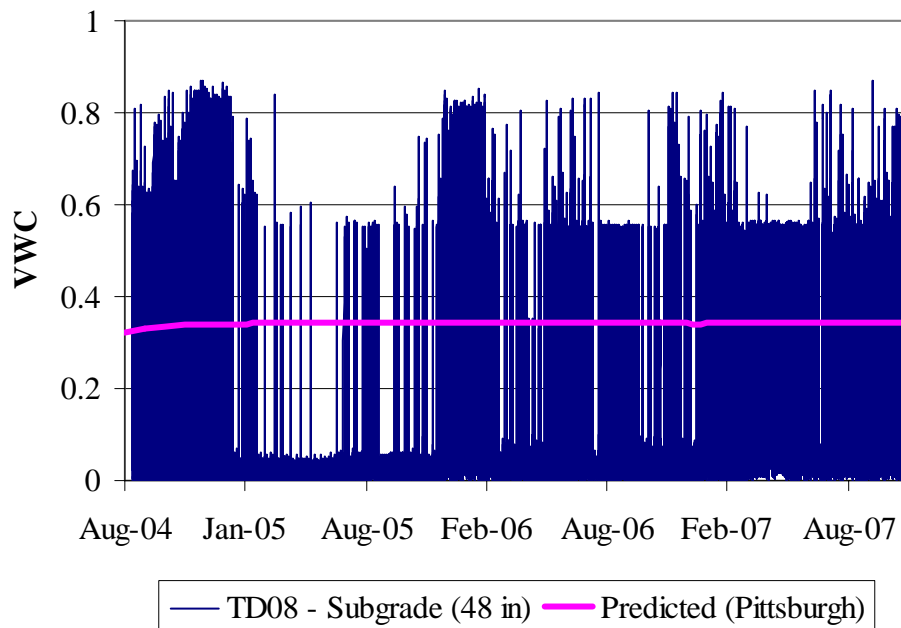


Figure 4.38. Predicted and measured VWC within the subgrade (Pittsburgh station).

4.9.0. Effect of Hierarchical Levels on Pavement Performance Prediction

This section evaluates the difference in the prediction of the performance of the Smart Pavement at the three hierarchical input levels. This includes the results of slab faulting, cracking, and IRI of the roadway throughout the 20-year design period. Appendix C presents the summary of the design inputs for the restrained and unrestrained slabs of the Smart Pavement at the three hierarchical levels. After the effect of the hierarchical levels for the selected variables has been quantified, a comparison is made between the Smart Pavement thickness design based on the 1993 AASHTO Guide and the MEPDG.

4.9.1. Performance of the Pavement with Restrained Slabs

This section presents the results of the predicted performance of the restrained slabs throughout the 20-year design life for three different designs. The first design used Level 1 inputs, the second used Level 2 inputs and the third used Level 3 inputs. A design thickness of 7 in was determined for the restrained slabs using the MEPDG and Level 1 inputs. Therefore, this analysis was performed using a design thickness of 7 in. All results represent a level of reliability of 50 percent (solid lines) and 95 percent (dashed lines).

As Figure 4.39 shows, there is little variation in the amount of pavement faulting

between the three hierarchical levels. This is largely due to the fact that the primary mode of failure for the restrained slabs is cracking. The 1.5-in dowel bars for the restrained slabs provide good load transfer and therefore limit the amount of faulting at all three hierarchical levels.

Figure 4.40 presents variations in the slab cracking throughout the design life for inputs determined using the three different hierarchical levels. As the figure shows, the predicted performance of the pavement with restrained slabs is acceptable throughout the design life, at all three levels. At the end of the 20-year design life, 4 percent cracking was predicted when designing the pavement using Level 1 or Level 2 inputs and 0.1 percent cracking was predicted when using Level 3 input. All three designs were based on a 50 percent reliability. For this case, using different levels inputs did not significantly affect the design.

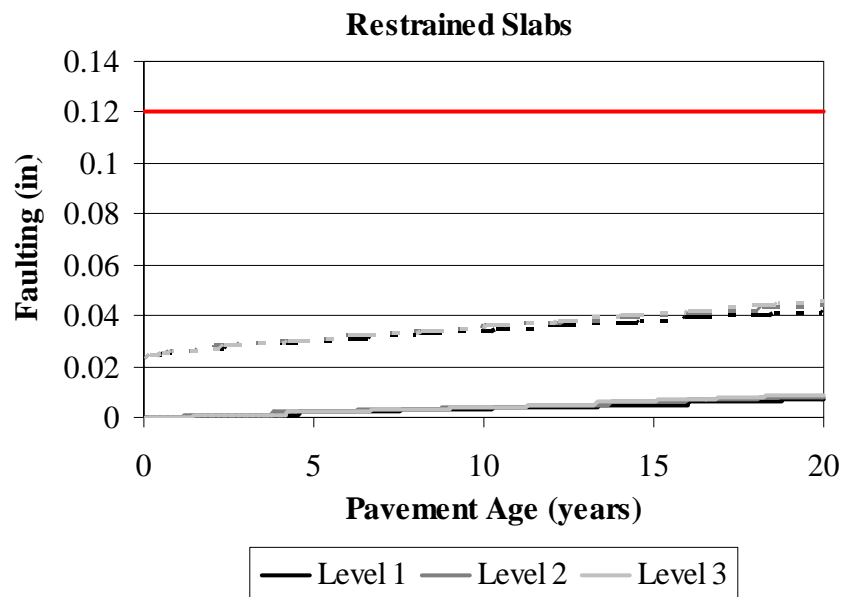


Figure 4.39. Predicted faulting for the restrained slabs.



Figure 4.40. Predicted percent cracking in the restrained slabs.

Figure 4.41 presents the variation in the international roughness index (IRI) of the pavement surface throughout the design life for the three hierarchical levels. At the end of the 20-year design life, an IRI of 86 in/mile was predicted when designing the pavement using Level 1 inputs, 82 in/mile for Level 2 inputs, and 74 in/mile for Level 3 inputs. There is not a substantial difference between the predicted IRI using the three different levels of inputs.

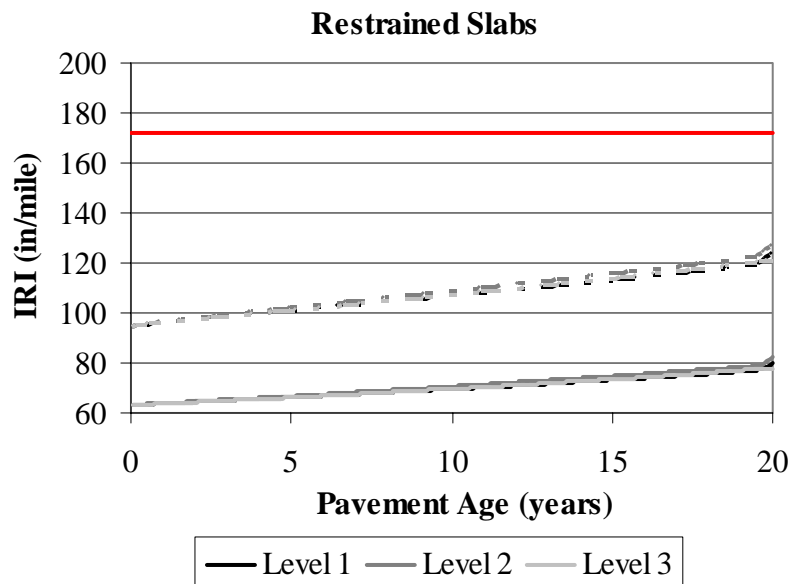


Figure 4.41. IRI predicted for the pavement with restrained slabs.

4.9.2. Performance of the Pavement with Unrestrained Slabs

This section presents the results of the predicted performance of the unrestrained slabs throughout the 20-year design life for three different designs. As in the previous analysis, the first design used Level 1 inputs, the second used Level 2 inputs and the third used Level 3 inputs. A design thickness of 13 in was determined for the restrained slabs using the MEPDG and Level 1 inputs. Therefore, this analysis was performed using a design thickness of 13 in instead of 7 in. The predicted performance of the pavement represents a level of reliability of 50 percent (solid lines) and 95 percent (dashed lines) in each graph.

As Figure 4.42 shows, there is no variation in the amount of pavement cracking predicted for the three runs made using each different hierarchical level inputs since the primary mode of failure for the unrestrained slabs is faulting. The thickness of the slab had to be increased substantially to limit the amount of faulting to an acceptable level since this is only an indirect means of limiting the faulting.



Figure 4.42. Predicted percent cracking in the unrestrained slabs.

Figure 4.43 presents the variation in the amount of faulting between the three designs using the three different hierarchical levels to define the inputs. At the end of the 20-year design life, the design using Level 1 inputs predicted 0.06 in of faulting. For the design based on Level 2 and 3 inputs, 0.06 in and 0.07 in of faulting, respectively, was predicted. The analysis was performed based on a 50 percent level of reliability. A significant difference was not found between the predicted faulting regardless of level of the inputs used. At 95 percent reliability the design thickness would need to be increased by 0.5 in to limit the faulting to below 0.12 in for the length of the 20-year design period. As shown in Figure 4.44, the IRI will also exceed the threshold value of if Level 3 inputs are used and the reliability of the design is 95 percent.

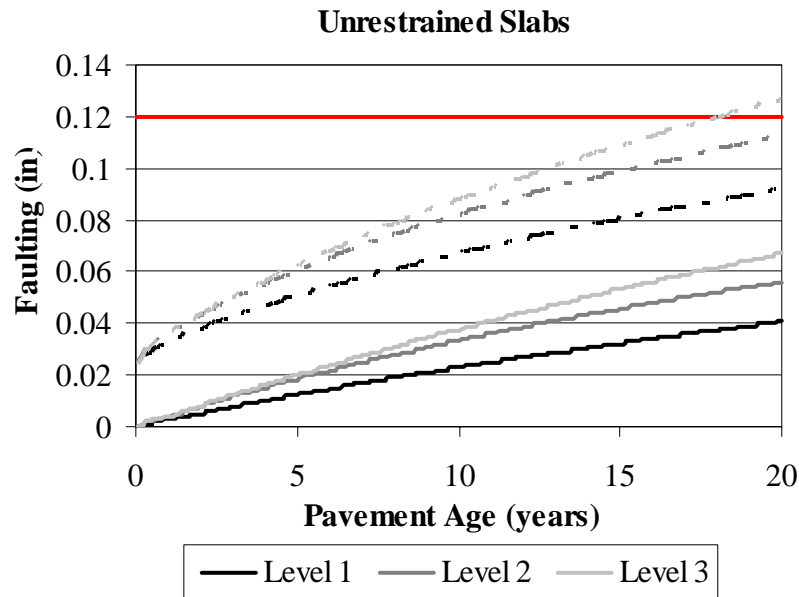


Figure 4.43. Predicted faulting for the unrestrained slabs.

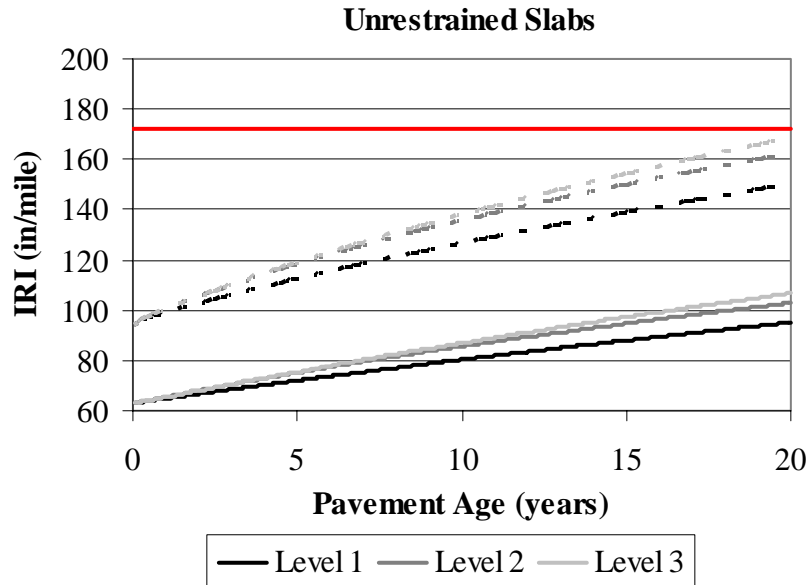


Figure 4.44. Predicted IRI for the pavement with unrestrained slabs.

4.9.3. Effect of Hierarchical Level for Defining all Design Inputs on Performance Prediction

The following sub-sections present the performance of the pavements for the restrained and unrestrained slabs on SR 22 as the hierarchical level of selected individual design parameters are varied. All parameters will be evaluated at a reliability of 50 percent and 95 percent. The following parameters will be investigated due to their significance in predicting pavement damage through the faulting and cracking models of the MEPDG:

- Traffic (Level 2 and 3)
- Climate (varying weather stations)
- PCC Strength (Level 1, 2, and 3)
- PCC Coefficient of Thermal Expansion (Level 1, 2, and 3)
- Subgrade Resilient Modulus (Level 2 and 3)

In each analysis, each individual design parameter is varied between the hierarchical Levels (1, 2, and 3). All other inputs are defined using the lowest level of hierarchical data available. The performance of the pavement section with the doweled slabs will be evaluated based the percent slabs cracked, while the performance of the section with undoweled slabs will be based on the faulting since these are the primary modes of failure for each pavement section.

4.9.3.1. Effect of Hierarchical Level for Defining Traffic Inputs on Performance Prediction

The effect of the traffic inputs hierarchical level on pavement performance was evaluated using the Level 2 and 3 data available for SR 22. Level 1 characterization was not performed because site specific WIM data was not available. Therefore, in both analyses (Level 2 and 3) national averages of axle load distributions were used. In the Level 2 analysis, the monthly adjustment factors, vehicle class distribution, and hourly distribution were determined for SR 22. For the Level 3 analysis, national averages of these parameters, determined from various LTPP sites, were used.

Figure 4.45 presents the predicted slab cracking of the restrained slabs throughout the 20-year design life at 50 and 95 percent reliability. There is a significant difference between the predicted cracking when traffic is predicted using Levels 2 inputs compared to Level 3 inputs. The analysis with Level 2 inputs predicted approximately 4 percent of the slabs would crack, while analysis with the Level 3 inputs predicted approximately 12 percent at a reliability of 50 percent. Therefore, the analysis with Level 3 inputs predicted three times more damage than when Level 2 inputs were used. The design thickness obtained based on using Level 3 traffic data would be 0.5 in thicker based a 95 percent level of reliability.



Figure 4.45. Percent cracking in the restrained slabs for Level 2 and Level 3 traffic inputs.

Figure 4.46 presents the variation in the predicted faulting for the pavement with unrestrained slabs when the traffic inputs are defined using Levels 2 and Level 3 inputs. At the end of the 20-year design life, 0.04 in of faulting was predicted when Level 2 inputs were used and 0.07 in with Level 3 inputs at a level of reliability of 50 percent. At 95 percent reliability, the faulting exceeds the threshold value of 0.12 in after 17 years when Level 3 data is used. The design thickness using Level 3 traffic data would be 0.5 in thicker.

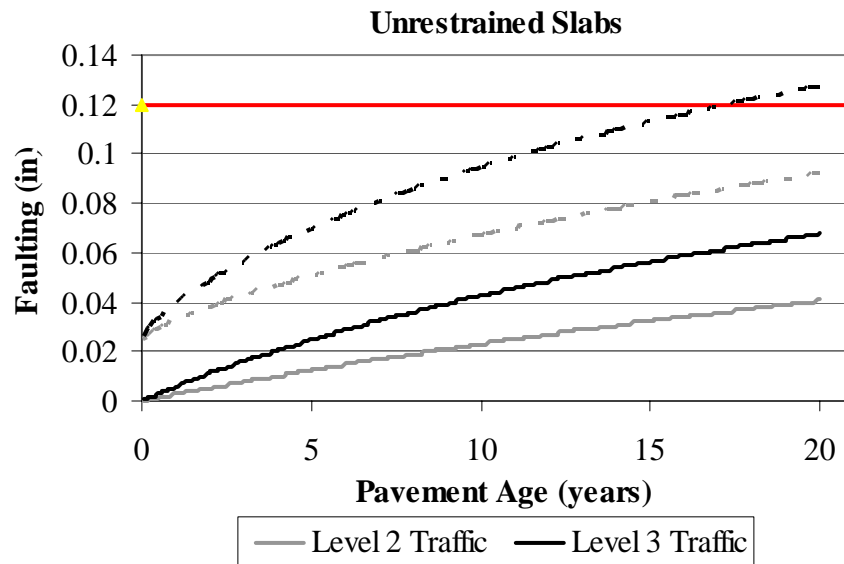


Figure 4.46. Predicted faulting in the unrestrained slabs for Level 2 and Level 3 traffic inputs.

4.9.3.2. Effect of Different Sources of Climatic Data on Performance Prediction

The effect of the climatic data on the predicted performance will be evaluated using climatic data from different weather stations. The performance of the pavement when the climatic data was collected from the onsite weather station was compared to climatic data collected by the two closest weather stations to the site, the Pittsburgh International Airport and the Allegheny Airport, as discussed in section 4.8.0.

Figure 4.47 presents the predicted slab cracking of the restrained slabs throughout the 20-year design life at 50 percent reliability. There is a significant difference between the predicted cracking although the proximity of the three weather stations is within a 30 mile radius. The onsite weather station and Allegheny County Airport weather station predicted 4

percent of the slabs would crack while the Pittsburgh International Airport weather station predicted 1 percent at 50 percent reliability. The onsite (Murrysville) and Allegheny County Airport weather stations predicted approximately six times more damage than the Pittsburgh weather station. These two weather stations have substantially less data than the Pittsburgh weather station, which is most likely contributing to the difference between the predicted performances. Even though there was a difference in the predicted performance, this difference was not sufficiently significant to affect the overall design thickness.

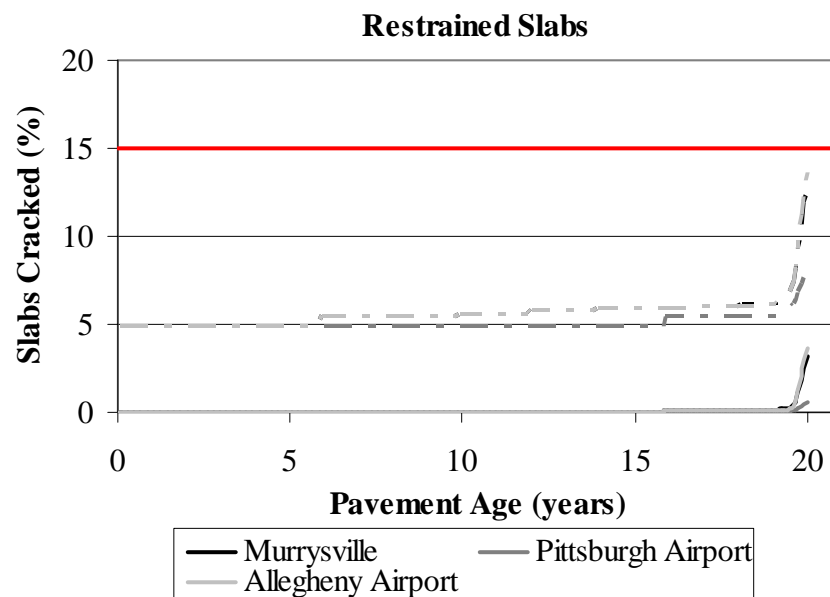


Figure 4.47. Percent cracking in the restrained slabs for different sources of climatic data.

Figure 4.48 shows a similar trend in the unrestrained slabs of the Smart Pavement, with faulting varying approximately 17 percent between the three weather stations within a 30 mile radius. The onsite (Murrysville) weather station is predicting the lowest amount of faulting and the Pittsburgh and Allegheny weather stations show more faulting. The use of the different climatic sources did not affect the designed thickness for either the unrestrained or restrained slabs. This was not the case when earlier versions of the MEPDG were used and the climatic database was limited. In earlier versions of the MEPDG, the use of these different weather stations did have an effect on the design thickness.

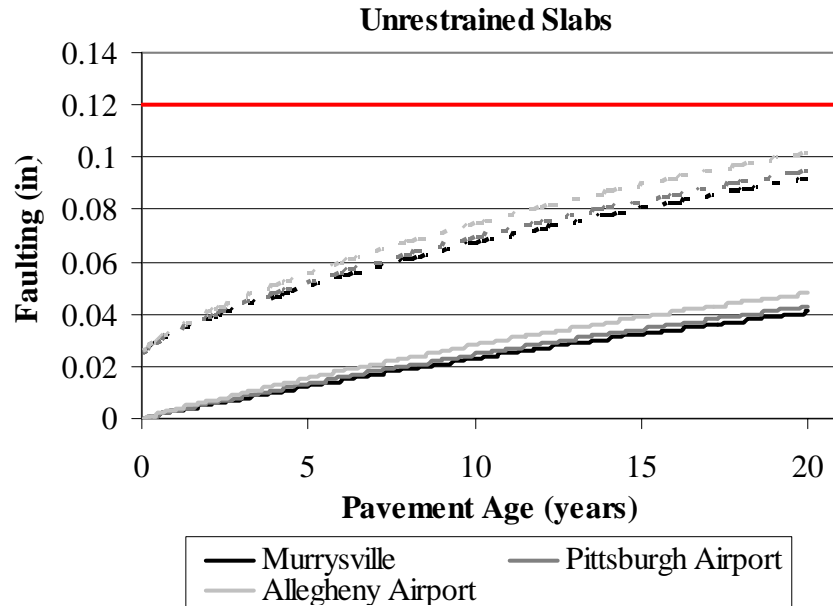


Figure 4.48. Faulting in the unrestrained slabs for different sources of climatic data.

4.9.3.3. Effect of Hierarchical Level for Defining PCC Strength on Performance Prediction

The effect of the hierarchical level used to define the PCC strength on pavement performance is now investigated. Figure 4.49, shown below, presents the predicted slab cracking for the restrained slabs throughout the 20-year design life at a 50 and 95 percent level of reliability. At 50 percent reliability, the use of Level 1 and 2 inputs produced 3 percent cracking and 1 percent cracking was predicted when Level 3 inputs were used. As Figure 4.50 demonstrates, the predicted faulting of the undoweled slabs increased as the hierarchical level of inputs used decreased. The use of different levels of input for the PCC strength did not affect the design thickness for the restrained or unrestrained slabs.

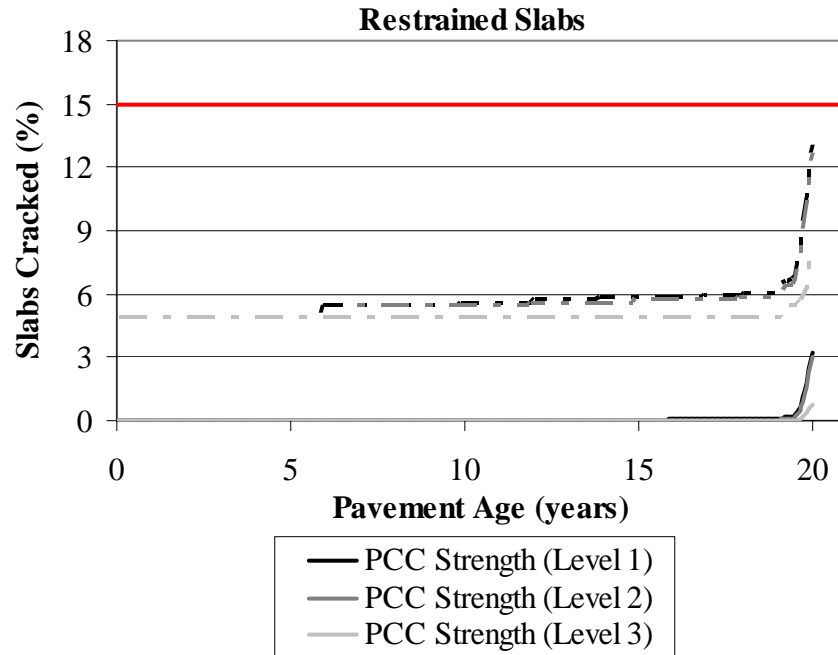


Figure 4.49. Percent cracking in the restrained slabs for PCC strength defined using Level 1, 2 and 3 inputs.

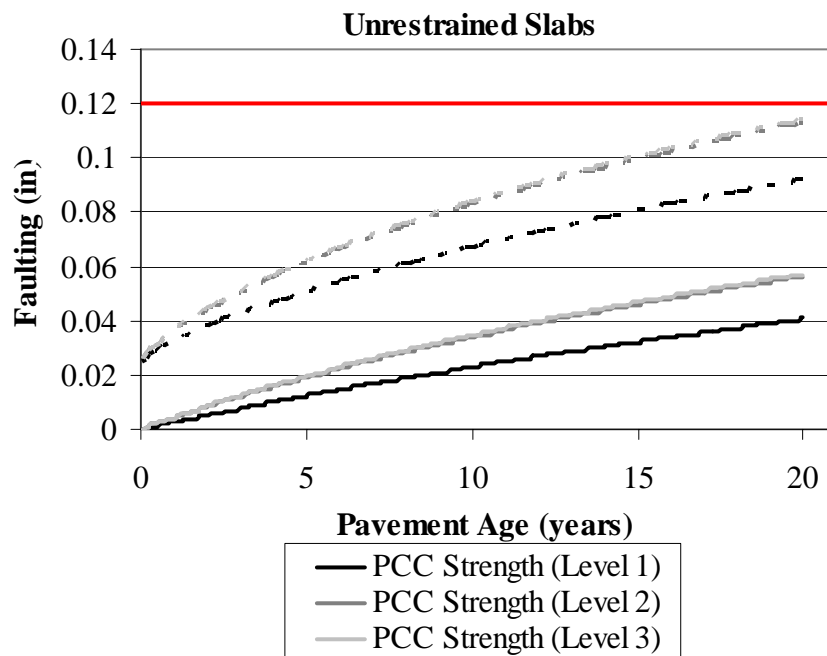


Figure 4.50. Faulting in the unrestrained slabs for PCC strength defined using Level 1, 2 and 3 inputs.

4.9.3.4. Effect of Hierarchical Level for Defining PCC Coefficient of Thermal Expansion on Performance Prediction

Figure 4.51 and Figure 4.52 present the predicted performance of the restrained and unrestrained slabs as the hierarchical level of the inputs used in defining the PCC coefficient of thermal expansion (CTE) is varied. At a reliability of 50 percent, the predicted percent cracking for the doweled slab varies considerably as the hierarchical level is changed. The Level 1 analysis predicted that 4 percent of the slabs would crack, while the Level 2 and Level 3 analyses predicted 16 percent and 2 percent, respectively. The Level 2 input predicted more distress because the value, which was estimated using the coefficient of thermal expansion of the paste and aggregate and their volumes in the concrete mixture, was much larger than the other two values at $7.1 \times 10^{-6}/^{\circ}\text{F}$. The design thickness achieved using a Level 2 data to define the CTE would have to be increased by 0.5 in to produce an acceptable level of performance throughout the design life. The Level 3 input resulted in less distress because the typical value used in the analysis was less than the actual measured value.

The predicted faulting for the unrestrained slabs also varied significantly as the hierarchical level of the data used to define the CTE varied. The Level 2 analysis, which had the largest CTE, predicted the most faulting and only meets the design criteria for 13 years at a reliability of 95 percent. The design thickness would need to be increased by 2 in if a Level 2 input was used.

The results of this analysis stress the importance of obtaining an accurate value for the PCC CTE when designing a concrete pavement. The CTE has a wide range of possible values for some aggregates. Historically this parameter has not been well documented by agencies for concrete paving mixtures.

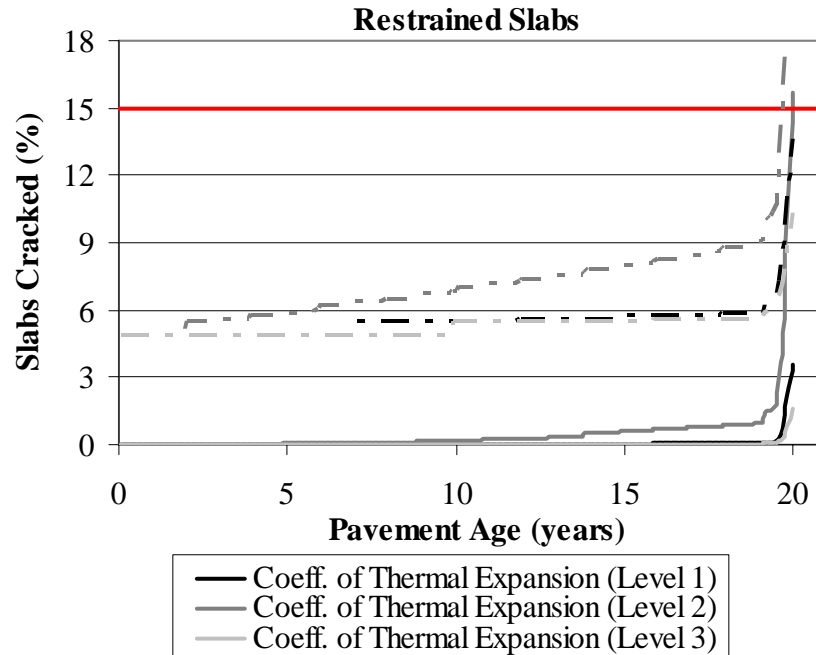


Figure 4.51. Percent cracking in the restrained slabs for the PCC coefficient of thermal expansion defined using Level 1, 2 and 3 inputs.

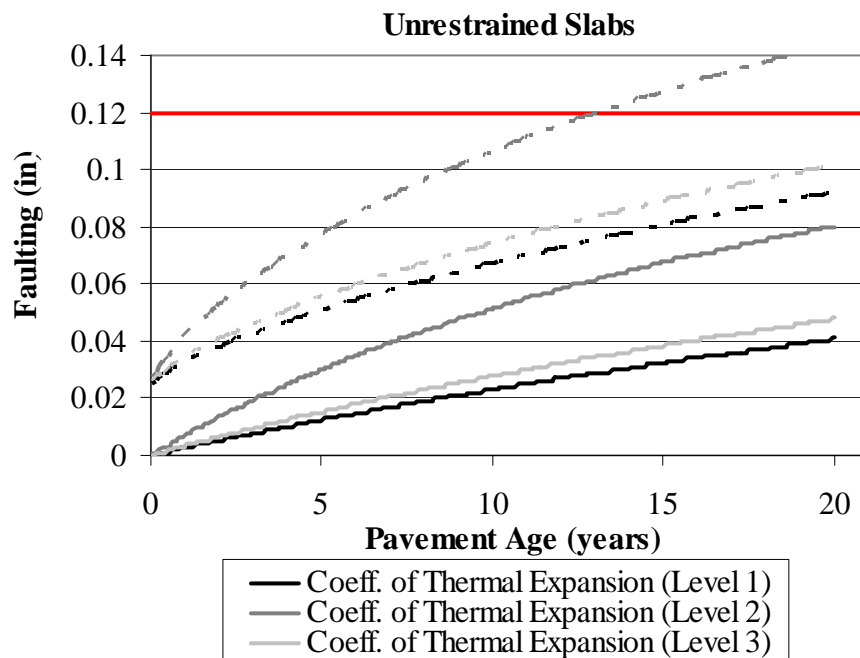


Figure 4.52. Faulting in the unrestrained slabs for the PCC coefficient of thermal expansion defined using Level 1, 2 and 3 inputs.

4.9.3.5. Effect of Hierarchical Level for Defining Subgrade Resilient Modulus on Performance Prediction

Figure 4.53 and Figure 4.54 present the predicted performance of the restrained and unrestrained slabs as the hierarchical level of inputs for defining subgrade resilient modulus is varied. The Level 2 analysis represents a resilient modulus of 4500 psi. The Level 3 input results in a resilient modulus of 14,000 psi, which is the MEPDG recommended value determined from the LTPP data. Although the resilient modulus value changed drastically between the hierarchical inputs levels, the predicted performance did not. At 50 percent reliability, the Level 2 analysis predicted that 3 percent of the slabs would crack while the Level 3 analyses predicted 4 percent. This trend was also experienced in the predicted faulting for the unrestrained slabs, as shown in Figure 4.54. This difference in predicted cracking and faulting can be considered negligible therefore; the hierarchical level of the subgrade resilient modulus does not significantly affect performance for the pavement conditions considered.

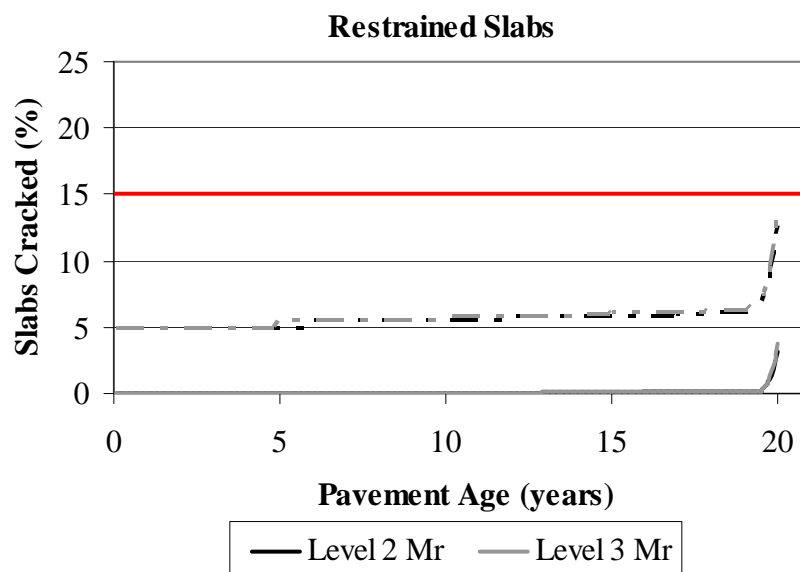


Figure 4.53. Percent cracking in the restrained slabs for the subgrade resilient modulus defined using Level 1, 2 and 3 inputs.

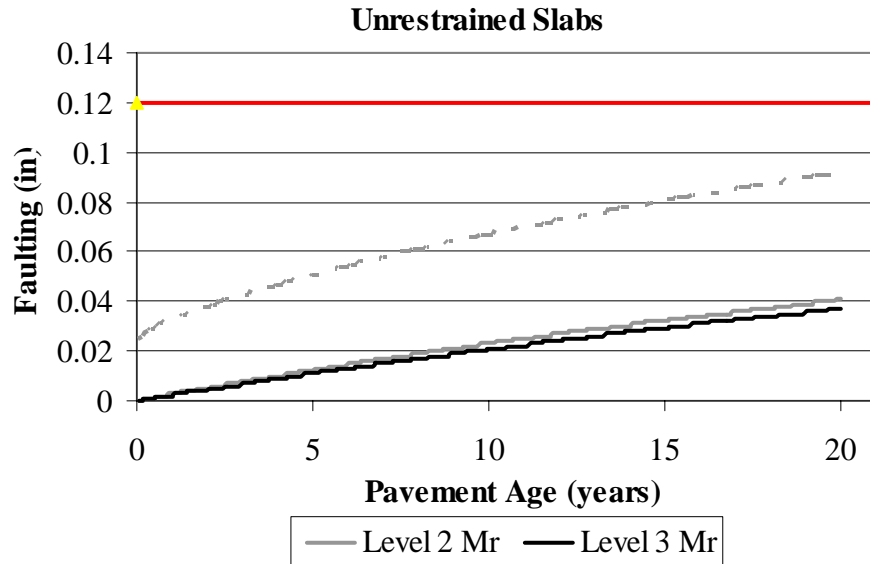


Figure 4.54. Predicted faulting in the unrestrained slabs for the subgrade resilient modulus defined using Level 1, 2 and 3 inputs.

4.10.0. Comparison between the Design Thickness of the Smart Pavement Based on the 1993 AASHTO Design Guide and the MEPDG

A comparison was also made between the thickness design of the Smart Pavement based on the MEPDG and the 1993 AASHTO Design Guide. The design thicknesses for the doweled and undoweled slabs were determined using the MEPDG, along with Level 1 inputs, and the 1993 AASHTO Design Guide. As Table 4.38 shows, the pavement thickness determined using the 1993 Guide and standard PennDOT inputs, as defined in *Pub. 242 Pavement Policy Manual*, [20] was 12 in for both the restrained and unrestrained slabs. A design thickness of 13 in was determined for the unrestrained slabs and 7 in for the restrained slabs using the MEPDG. Based on the MEPDG, the service life of the 12-in restrained slabs is 45 years and 17 years for the 12-in unrestrained slabs at a 95 percent level of reliability. Therefore, designing this pavement section with restrained slabs using the AASHTO 1993 Guide would produce a slab 5 in thicker than if the MEPDG was used. The unrestrained slab would be 1 in thinner.

Table 4.38. Required thickness for SR 22 based on the AASHTO and MEPDG design methods.

	Thickness Required for a 20-yr Design Life (in)	
	MEPDG	AASHTO 93
Unrestrained Slabs	13	12
Restrained Slabs	7	12

4.11.0. Conclusions

In conclusion, the new MEPDG provides a versatile and state-of-the-art tool for the design of pavement structures using mechanistic-empirical principles. The MEPDG represents a major change in the way pavement design is performed. The designer must first consider site conditions and construction conditions in proposing a trial design for a new pavement. This includes the evaluation of a more detailed analysis of traffic and characterization of pavement materials. Additionally, the new Enhanced Integrated Climatic Model (EICM), a powerful climatic modeling tool, is used to model temperature and moisture within each pavement layer and the subgrade. The design is then evaluated for adequacy through prediction of key distresses and smoothness. The designer has the ability and flexibility to consider different design features and materials in order to optimize the design and insure that specific distresses will not develop.

The temperature and moisture conditions inside the pavement structure were predicted based on ambient climatic data from the onsite weather station and two of the closest stations to the site. The temperature predications in the concrete slabs showed that the predicted temperature is close to the measured. The correlation coefficients between the predicted and measured weighted average temperature of the concrete was higher than 86 percent, indicating excellent correlation between both variables. The correlation coefficients between the predicted and measured concrete equivalent linear temperature gradients were higher than 58 percent, indicating an acceptable level of correlation between both variables. Moreover, the predicted temperature overestimates the maximum positive and negative gradients, implying that the use of these over-predicted gradients would result in conservative predictions in the performance of the pavement. In addition, the average seasonal temperature gradient in the concrete based on the predicted temperature was similar to those based on measured temperatures.

The temperature and moisture conditions inside the pavement structure were predicted based on ambient climatic data from the onsite weather station and two of the closest stations to the site using the EICM of the MEPDG. The temperature predictions in the concrete slab showed that the predicted temperature is close to the measured. However, the predicted temperature overestimates the maximum positive and negative gradients, implying that the use of these over-predicted gradients would result in conservative predictions in the performance of the pavement. In addition, the average seasonal temperature gradient in the concrete based on the predicted temperature was similar to those based on measured temperature. An analysis of predicted versus measured temperature showed that the temperature predictions in the asphalt and granular layers do not provide a good estimate of the measured conditions.

The moisture predictions in the granular layers showed that the predicted moisture content does not vary much throughout the seasons. A comparison between the predicted and measured moisture content could not be properly carried out since the measured moisture content could not be interpreted.

The results of the analysis of the hierarchical levels showed that the restrained slab would have the same design thickness regardless of the level of inputs used. The thickness of the unrestrained slab would have to be a half in thicker if Level 3 data was used when compared to Level 1 or 2 data.

The results of the analyses of the hierarchical level of individual design inputs used on SR 22 provided insight into the sensitivity of traffic, climate, PCC strength, PCC CTE, and subgrade resilient modulus on predicting pavement performance. The use of Level 3 data for characterizing traffic would result in a slab 0.5 in thicker than Level 2 data for both the restrained and unrestrained slabs. The use of Level 2 data for the PCC CTE would result in a slab design thickness that is 2 in thicker than the design thickness determined using Level 1 or Level 3 data for the unrestrained slabs. Both Level 2 and Level 3 inputs would require an increase in slab thickness compared to a design thickness established using Level 1 inputs for the restrained slabs. Varying the input levels used in defining the PCC strength did not impact the design thickness nor did the use of different climatic weather stations. This study shows that the use of different hierarchical levels for the critical inputs can have an effect on the design thickness. The input level producing the least conservative design also varies.

Based on the results from the MEPDG, the restrained slabs on SR 22 will provide an acceptable level of service for 45 years and the unrestrained slabs for 17 years. A comparison of the thickness designs from the MEPDG and AASTHO 1993 Guide showed the restrained slabs to be over-designed by 5 in and the undoweled slabs to be under-designed by 1 in.

CHAPTER 5: PAVEMENT RESPONSE TO ENVIRONMENTAL LOADING

5.1.0. Introduction

A primary objective of this research is to examine the pavement response to environmental loading, characterized by seasonal variations in temperature and moisture throughout the slab depth. The pavement response is presented in terms of seasonal variations in the concrete strain and slab surface profiles during the first three years after construction.

Static strain and pressure gages were installed for measuring the response of the slab to environmental loads. They have been operational and recording data along the various depths of the concrete since construction. This section presents an analysis of the results obtained from the static sensors for the first three years after construction between August 16, 2004 and October 31, 2007. In addition, seasonal surface profile measurements were made to capture the change in the shape of the slab under various temperature and moisture gradients. These results are also presented in this section.

A brief summary of the instrumentation providing strain and pressure measurements in the field is presented first. Then, the seasonal variations in static strain and pressure measurements during the first three years after construction of the pavement are analyzed. Finally, a summary of the findings of this section is included.

5.2.0. Instrumentation of Static Sensors

As previously mentioned in section 3.3.1, a total of 156 VW strain gages were installed at 60 locations in the unrestrained and restrained slabs. VW gages were placed at three different depths within the slab for each corner location, and two different depths at each edge and midpanel location. Strain readings are automatically taken at 15-minute intervals [1].

Similarly, as discussed in section 3.4.1, static pressure cells were placed at the interface between the JPCP slabs and the asphalt treated permeable base layer at the midpanel and corner locations in two restrained and two unrestrained slabs. A total of eight static pressure cells were installed at eight locations at the interface between the slab and the base layer. Pressure readings are also automatically recorded at 15-minute intervals [1].

More details regarding the exact locations and depths of the VW gages and static pressure cells can be found in the Phase I Final Report [1].

5.3.0. Static Strain Measurements

This section examines the effects of seasonal variation in temperature and moisture on strain measurements. In addition, the effects of the different slab restraining conditions on slab movements are also analyzed. The factors considered include depth of gage within the slab and the presence of dowel bars or tie bars along the joints. A brief background on the strain measurements is presented first, followed by an analysis of the seasonal strain measurements.

5.3.1. Background

The raw strain readings represent the slab deformations due to the effects of concrete temperature and moisture changes and concrete creep. The raw readings also include the effects of temperature on the steel wire inside the gage. The raw strain readings are first corrected for the effect of temperature on the steel wire in the gage and then converted into total strain readings, which reflect the total deformations measured in the slabs. The corrections are accounted for by using equation 3-3 to calculate the total strain experienced by the concrete. The strain measurements are zeroed based on the time the concrete set. The set times corresponding to each sensor were presented in chapter 3.

The total strain calculated using the previous equation is then separated into strain due to temperature effects and strain due to other remaining factors including moisture, creep, and slab restraining conditions. Strain due to uniform temperature change is estimated using equation 5-1 and those due to other components are estimated by subtracting the thermal strains from the total strains, as shown in equation 5-2. Equation 5-1 does not represent the strain that the slab experiences due to the total effect of temperature, since it does not take into account the strain induced by temperature gradients. Moreover, the equation does not represent an actual measured thermal strain and assumes that the coefficient of expansion of the concrete is the same as that of the slab, without taking into account the effect of the restraints.

$$\varepsilon_{thermal} = (T_1 - T_0)\alpha_c \quad \text{(Equation 5-1)}$$

$$\varepsilon_{other} = \varepsilon_{total} - \varepsilon_{thermal} \quad (\text{Equation 5-2})$$

where: $\varepsilon_{thermal}$ = Thermal strain in the concrete

ε_{other} = Strain in the concrete due to all factors that are not temperature related

α_c = Thermal coefficient of expansion of the concrete = $5.67 \mu\text{E}/^\circ\text{F}$

Moreover, as the slab is subjected to different moisture and temperature conditions, slab deformations vary throughout the depth of the concrete. Based on the difference between the strains measured at the top and bottom of the slabs at the corner locations, the curvature of the slab can be calculated by using equation 5-3. The slab curvatures are presented in section 5.3.4.

$$\rho = -\frac{\varepsilon_t - \varepsilon_b}{D(1 + \varepsilon_t)} \quad (\text{Equation 5-3})$$

where: ρ = Slab curvature (positive values indicate upward curvature), in units of 1/ft

ε_t = Measured strain at the slab top at the time of interest

ε_b = Measured strain at the bottom of the slab at the time of interest

D = Distance between the sensors at the top and bottom of the slab where strain measurements are taken, ft.

5.3.2. Seasonal Static Strain Measurements

This section investigates the effects of environmental factors on strain development at different locations and depths within the slab. The environmental factors include variations in seasonal temperature and moisture conditions, freezing of the underlying layers and joint locking.

Figure 5.1 and Figure 5.2 provide a comparison between the total strain, the temperature-induced strain, and the strain due to moisture, creep and other factors. The strain presented in these two figures is measured in the longitudinal direction, at the top of the restrained and unrestrained midpanels. The strain is negative throughout the first three years after construction, for both the restrained and unrestrained slabs, indicating that the slabs are in a state of contraction. The variation in strain follows seasonal trends. The total and the temperature-induced strain increases in magnitude until reaching a maximum in the winter, after which strain decreases throughout the spring, and reaches a minimum value in

the summer. Decreasing temperature causes the concrete to contract and increasing temperature causes the concrete to expand. Therefore, it is expected that the lower temperatures observed during the winter season would cause the largest amount of contraction in the slab, while the smallest contraction is observed in the summer. This is observed in both the restrained and unrestrained slabs.

In addition, the strain due to moisture and other factors does not vary much throughout the different seasons, while the temperature-induced strain exhibits a larger amount of fluctuation. This is due to the fact that the temperature conditions inside the concrete fluctuate greatly during the different climatic seasons, as previously discussed in chapter 2, while the concrete moisture conditions do not vary substantially throughout the year.

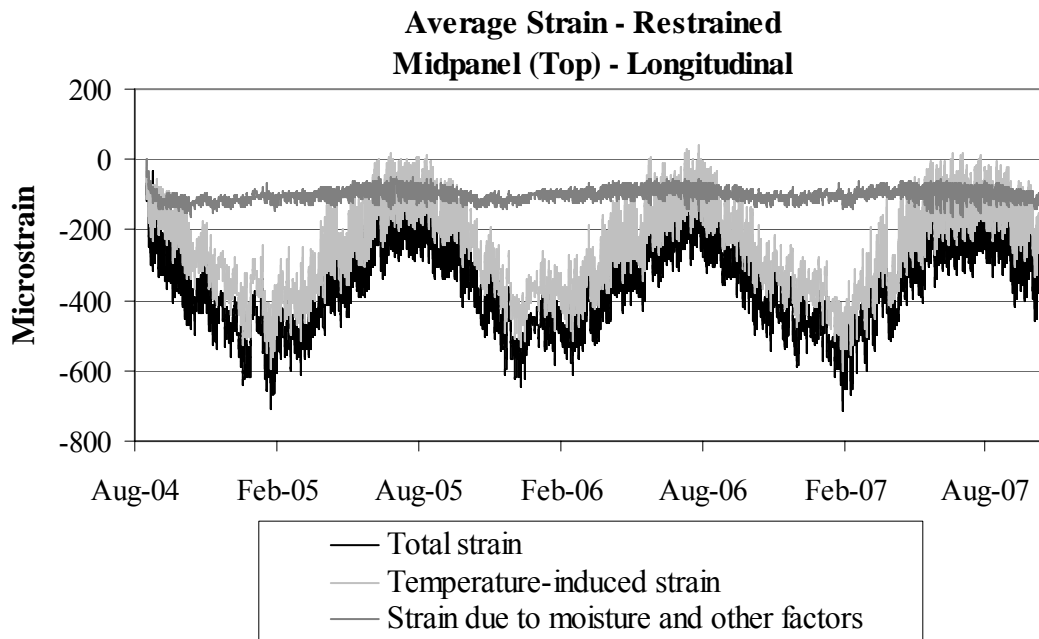


Figure 5.1. Strain in the longitudinal direction at midpanel at the top of the restrained slabs.

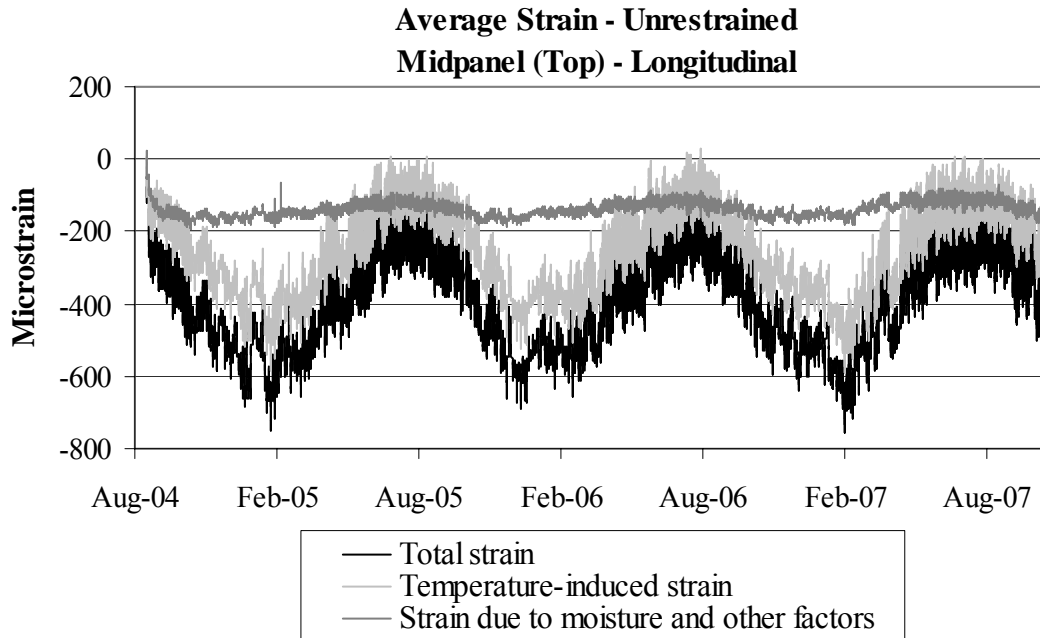


Figure 5.2. Strain in the longitudinal direction at midpanel at the top of the unrestrained slabs.

The seasonal contribution of both components to the total strain was compared to each other and is presented in Figure 5.3, for strains in the longitudinal direction, at the top of the restrained and unrestrained midpanels. For the restrained slabs, the temperature-induced strain varies between -144 microstrain during the summer and -481 microstrain during the winter. The smaller strain during the summer is expected, since during the summer, the higher temperatures contribute to an expansion of the slab, which is exhibited by a decrease in the contraction of the slab. The contribution of the temperature-induced strain is lowest during the summer, constituting 61 percent of the total strain, and highest during the winter, constituting 79 percent of the total strain. The strain due to moisture and other factors varies between -88 microstrain during the spring and -112 microstrain during the fall, on average. The smaller strain during the spring is expected, since during the spring, the higher amount of precipitation causes the slab to expand (as discussed in chapter 2), which is exhibited by a decrease in the slab contraction. The contribution of the moisture-induced strain is lowest during the winter, constituting 21 percent of the total strain, and highest during the summer, constituting 39 percent of the total strain. The magnitude of the temperature-induced strain is much higher than the magnitude of the strain due to other factors (including moisture). As a

result, variations in the temperature conditions are the dominant factor contributing to the development of total strain in the concrete slab.

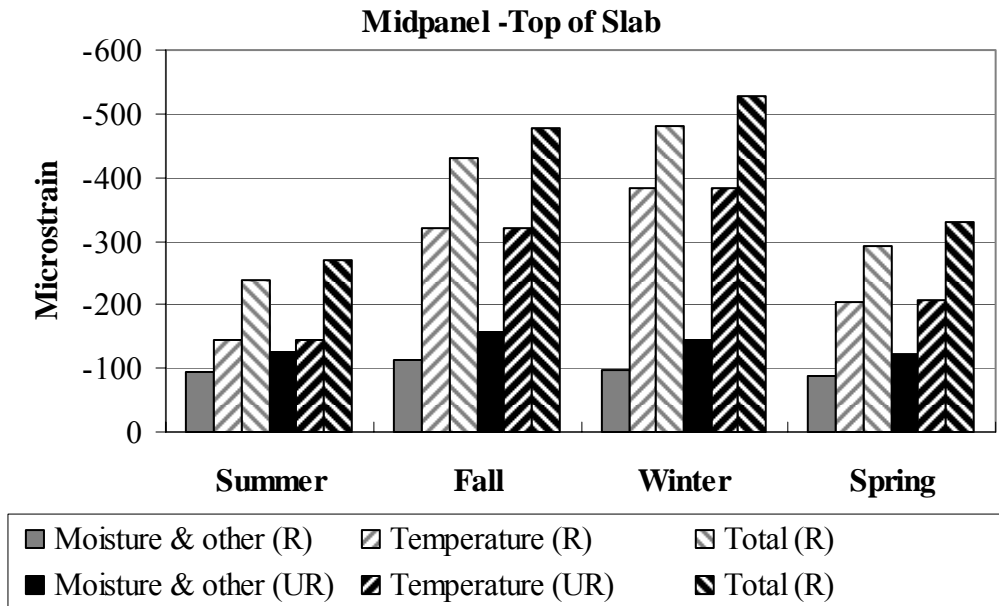


Figure 5.3. Seasonal contributions of the various components to the development of total strain in the longitudinal direction at midpanel at the top of the restrained and unrestrained slabs.

Similarly, the same trends are observed for the strain at midpanel of the unrestrained slab. The temperature-induced strain varies between -145 microstrain during the summer and -382 microstrain during the winter, indicating that the higher temperatures during the summer contribute to expansion of the slab. The contribution of the temperature-induced strain is lowest during the summer, constituting 53 percent of the total strain, and highest during the winter, constituting 73 percent of the total strain. The strain due to moisture and other factors varies between -122 microstrain during the spring and -156 microstrain during the fall, indicating that the higher amount of precipitation during the spring contributes to the expansion of the slab. The contribution of the moisture-induced strain is lowest during the winter, constituting 27 percent of the total strain, and highest during the summer, constituting 46 percent of the total strain. These seasonal changes in the relative humidity in the slab were discussed in chapter 2. The variation in temperature conditions is the dominant factor in contributing to the development of total strain in the slab. However, for the case of the restrained slab, the magnitude of the strain due to moisture and other factors is 28 percent

smaller than that for the unrestrained slabs, indicating that the slab restraints cause a 28 percent decrease in strain.

Similar trends regarding the seasonal contribution of temperature, moisture and other factors to total concrete strain were also observed based on strain measured at different locations and depths within the restrained and unrestrained slabs. A full set of figures showing the variation in strains with time during the three-year period after construction of the pavement is included in appendix D.

The influence of temperature variations in the underlying layers is examined in this paragraph. For example, subjecting the asphalt treated base layer to very low temperatures causes an increase in the stiffness of the ATPB. This implies that the bond between the slab and the base is stronger and poses an additional restraint on the structure. In such a case, the strain in the concrete is expected to be smaller as a result of this increased restraint.

According to the temperature measurements presented in chapter 2, the coldest temperatures were recorded during the periods between January 25 to February 6, 2005 and January 29 to February 20, 2007. During these periods, the thermocouples within the 2A subbase recorded temperatures at or close to the freezing temperature, implying that the resilient modulus of the ATPB layer was higher than usual. During these periods, the total strain and the temperature-induced strain decrease in magnitude, as shown in Figure 5.1 and Figure 5.2. This confirms that the stronger base layer poses an additional restraint on the concrete slab and causes a decrease in strain.

For the top of the slab, the average total strain during the frozen period is -445 microstrain for the restrained slabs and -484 microstrain for the unrestrained slabs. These are 7 and 8 percent smaller than the average for the winter season. The average temperature-induced strain is -348 microstrain for the restrained slabs and -439 microstrain for the unrestrained slabs, which are 9 and 11 percent smaller than the average for the winter season. The average strain due to moisture and other factors is -98 microstrain for the restrained slabs and -145 microstrain for the unrestrained slabs, which are similar to the average for the winter season. The strain at the bottom of the slab also decreases by the same percentages with respect to the average strain measured during the winter season.

As temperatures increase and the concrete expands, the width of the joint decreases to accommodate the increase in length of the slabs. The joint width will continue to decrease

with increasing temperature until the joint locks-up. Strain measurements are used to determine the temperatures at which the joints will lock. The variation in average total strain with respect to temperature change is plotted for the midpanel sensors measuring concrete movement in the longitudinal direction at the top of the restrained and unrestrained slabs. The strain versus temperature variations is presented in Figure 5.4 and Figure 5.5. At the top of the unrestrained and restrained slabs, temperatures range between 0°F and 111°F, and the transverse joints lock-up starting at a temperature of 96°F.

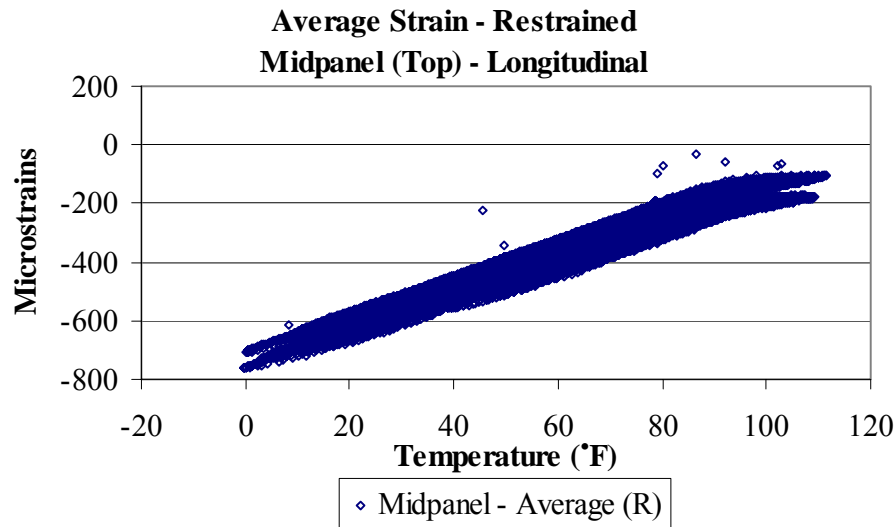


Figure 5.4. Variation in strain with temperature, in the longitudinal direction at midpanel for top of restrained slabs.

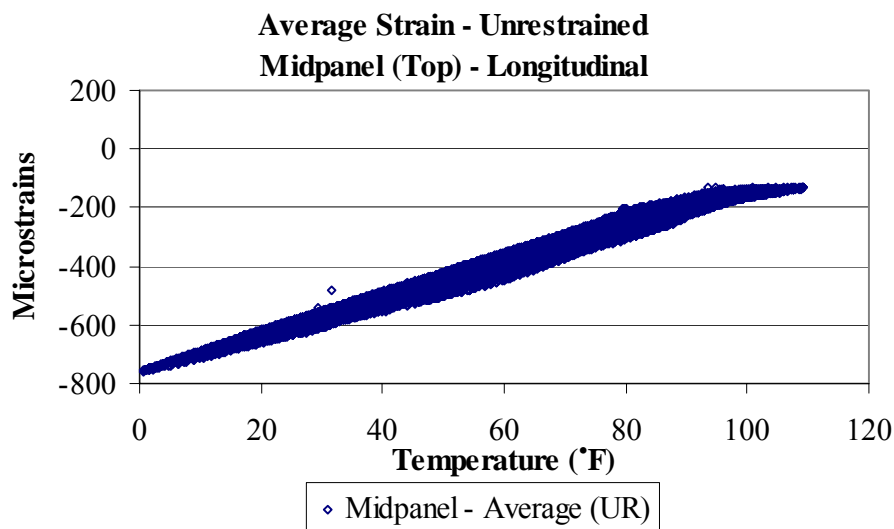


Figure 5.5. Variation in strain with temperature, in the longitudinal direction at midpanel for top of unrestrained slabs.

During seasons when temperatures are high, strains increase until the joints lock-up. During seasons when temperatures are low, strains are not large enough to cause lock-up of the joints. The seasonal range of concrete temperatures recorded by the static strain gages is presented in Table 5.1 for both the restrained and unrestrained slabs. The table summarizes data collected from the sensors measuring strains in the longitudinal direction at the top at the midpanel locations. It indicates that lock-up of the transverse joint does not occur during the fall and winter, but takes place during the spring and summer seasons. The minimum strain recorded by the midpanel sensors at the time the transverse joints were locked reach -105 microstrain for the restrained slabs and -130 microstrain for the unrestrained slabs. At lock-up, the magnitudes of the strain in the unrestrained slabs is 24 percent larger than for the restrained slabs. This confirms that the restraining conditions of the slab cause a decrease in the total allowable joint opening in the slab, when compared to similar slabs with no restraint.

Table 5.1. Temperatures at transverse joint lock-up for the restrained and unrestrained slabs.

	Range of Temperatures (°F)		Temperature at joint lock-up (°F)
	Restrained slabs	Unrestrained slabs	
Summer	50 - 111	51 - 109	96
Fall	11 - 89	12 - 87	--
Winter	0 - 77	0 - 75	--
Spring	31 - 108	32 - 106	96

The variation in total strain with temperature was also plotted for strain measured in the transverse direction to determine whether the longitudinal joints also lock-up at high temperatures. Figure 5.6 presents the variation in average total strain with respect to temperature changes for the sensors measuring movement in the transverse direction along the transverse joints at the top of the unrestrained slabs. The figure shows that expansion in the transverse direction is not restricted to a maximum limit, even though concrete temperatures recorded by the sensors exceed the 96°F limit at which transverse joints lock-up. This indicates that the presence of the curb and gutter does not restrain the slab sufficiently to prevent expansion of the slab in the transverse direction. This was observed in

all strains measured in the transverse direction by sensors located at the transverse joints of the unrestrained and restrained slabs.

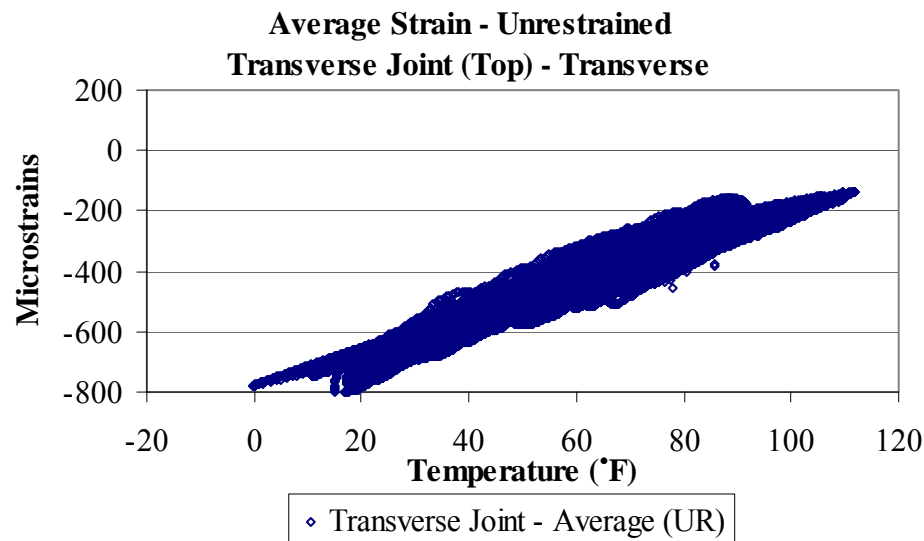


Figure 5.6. Variation in strain with temperature, in the transverse direction along the transverse joints for top of unrestrained slabs.

5.3.3. Effect of the Slab Restraining Conditions

In this section, the effects of the different slab restraining conditions on the development of strain in the slab are examined. The investigated factors include depth within the slab, presence of dowel bars or tie bars, and slab length in the direction of movement.

The boundary conditions at the top and bottom of the slab are different. The bottom of the slab is fully bonded to the asphalt treated permeable base (See Phase I Report. [1]), while the slab surface is free from restraint. The total strain measured at the midpanel locations at the top and bottom portions of the restrained and unrestrained slabs are compared to each other in Figure 5.7. The total strain measured at the bottom portion of the restrained slabs is 11 percent lower than that at the top portion of the slabs, and the total strain at the top of the unrestrained slabs is 22 percent lower than that at the top portion of the slabs. Since the sensors are equidistant from the surface and the base layer, the comparison between the strain measured at the top and bottom of the slab gives an indication of the effect of the base restraint on the strain measurements.

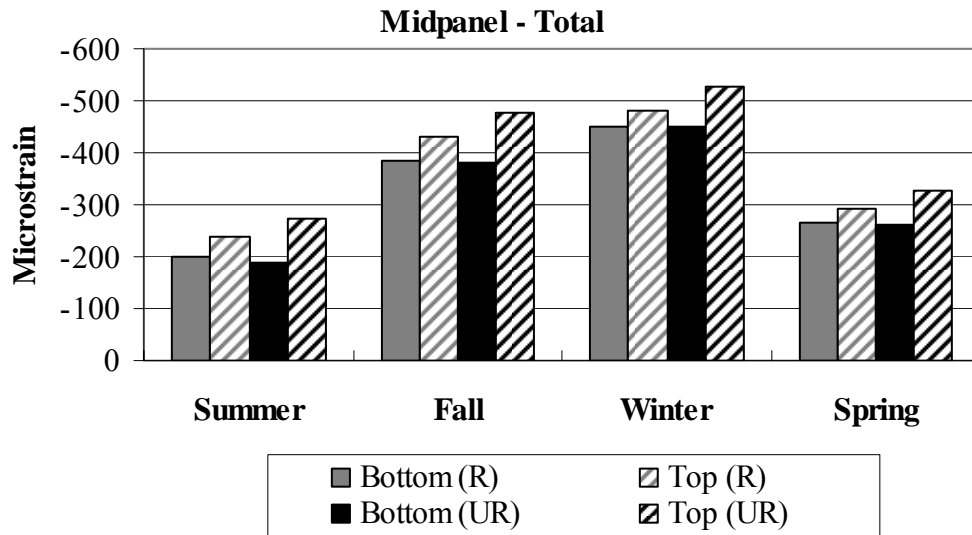


Figure 5.7. Total strain at the top and bottom of the restrained and unrestrained slabs at midpanel in the longitudinal direction.

The total strain can be separated into that due to temperature effects and that due to other remaining factors including moisture, creep and slab restraining conditions. As stated in section 5.3.3, the thermal strain is that due to uniform temperature changes across the slab depth, and does not take into account the daily changes in temperature gradients. As a result, it is expected that the temperature-induced strain presented does not vary depending on the sensor location within the slab depth. This is shown in Figure 5.8, which presents a comparison between the temperature-induced strain measured in the longitudinal direction at midpanel. Based on this figure, the temperature-induced strain measured at the bottom portion of the restrained slabs is 8 percent lower than that at the top portion of the slabs. The temperature-induced strain at the top of the unrestrained slabs is 10 percent lower than that at the top portion of the slabs. This difference in temperature-induced strain does not account for the 11 and 22 percent differences in total strain between the top and bottom portions of the slab. Therefore, a comparison between the midpanel strain due to the remaining factors, which include moisture and restraining conditions, is also plotted and presented in Figure 5.9. Based on this figure, the strain due to the remaining factors is 20 percent lower at the bottom of the restrained slabs, and 43 percent lower at the bottom of the unrestrained slabs, when compared to the strain at the top portions of the slabs.

Similarly, a comparison between the strain measured at the top and bottom portions of the slabs was carried out for the sensors located at all locations within the restrained and unrestrained slabs. The comparison showed that the temperature-induced strain at the bottom of the slabs is 2 to 12 percent lower than the strain measured at the top for the restrained slabs, and 3 to 23 percent for the unrestrained slabs. On the other hand, at the bottom portions of the slabs, the strain due to the remaining factors is significantly smaller in magnitude than that at the top of the slabs. These strains at the bottom of the slabs are 13 to 75 percent smaller than those measured at the top of the restrained slabs, and 25 to 72 percent smaller than those measured at the top of the unrestrained slabs.

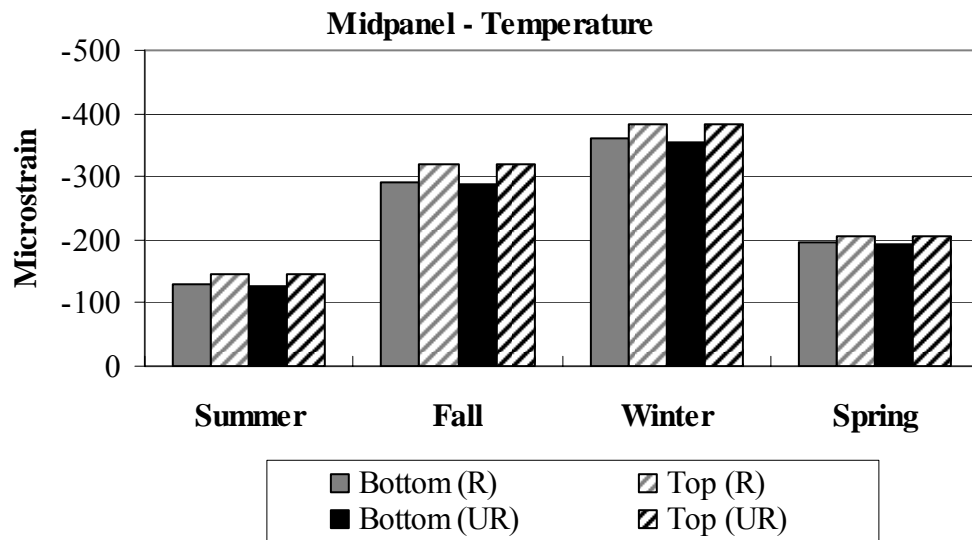


Figure 5.8. Temperature-induced strain at the top and bottom of the restrained and unrestrained slabs at midpanel in the longitudinal direction.

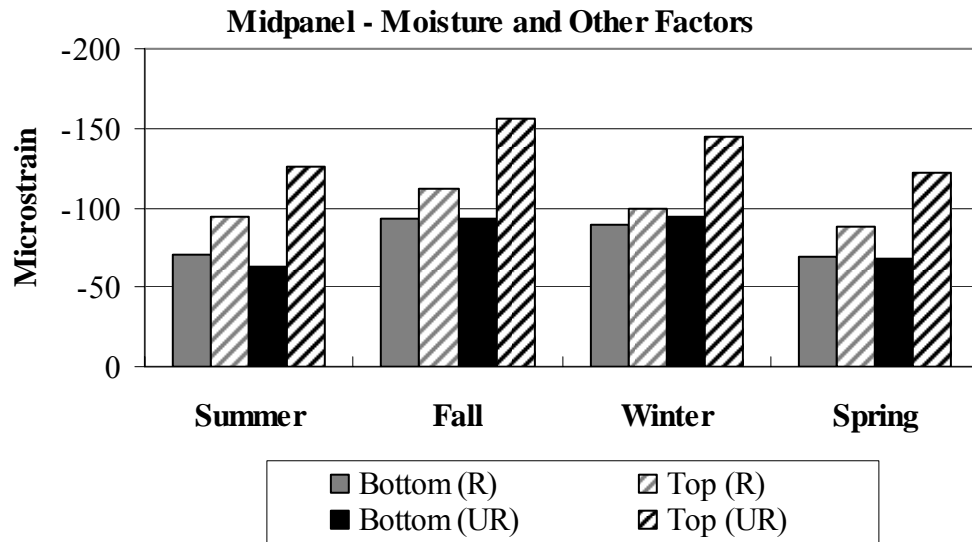


Figure 5.9. Strain due to moisture and other factors at the top and bottom of the restrained and unrestrained slabs at midpanel in the longitudinal direction.

Another factor restraining slab movement is the presence of dowel bars along the transverse joints. As previously mentioned, dowel bars were placed along the transverse joints for the purpose of minimizing joint faulting. Dowels restrict the slab from free contraction, reduce slab deflections along the transverse joint and affect the curling-induced stresses, especially in the regions surrounding the dowels [25; 26; 27]. Dowels also restrict the slab curvature causing a redistribution of stresses in the slabs [28; 17]. In this section, the effect of the presence of dowel bars along the transverse joints on the development of strain in the concrete is examined. For this purpose, strain data collected from the restrained and unrestrained slabs is compared to each other.

Figure 5.10 presents a comparison between the total strain measured in the transverse direction along the transverse joints of the restrained and unrestrained slabs. At the top of the slab, the total strain measured in the unrestrained slabs is 21 percent higher than that in the restrained slabs. At the bottom of the slab, the measured strains are similar and within 2 percent of each other. Separating the total strain into the different components, it was found that the temperature-induced strain is not affected by the presence of dowel bars. However, the strain due to the restraining conditions showed a 39 percent increase in measured strain in the absence of dowel bars, compared to the case when dowel bars are present.

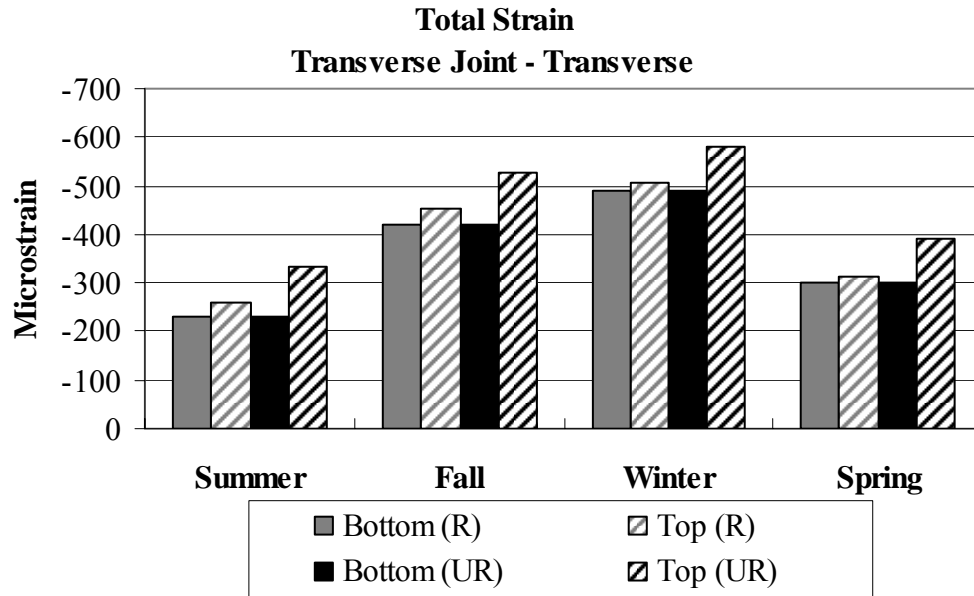


Figure 5.10. Total strain at the top of the restrained and unrestrained slabs along the transverse joint in the transverse direction.

Tie bars were placed along the longitudinal joints to keep the joints tight and prevent the infiltration of water into the pavement structure. Keeping the joint tight allows the load to be transferred from one slab to the other through aggregate interlock [25]. In this section, the effect of the presence of tie bars along the longitudinal joints on the development of strain in the concrete is examined. For this purpose, strain data collected from the restrained and unrestrained slabs will be compared to each other.

Figure 5.11 presents a comparison between the total strain measured in the longitudinal direction along the centerline longitudinal joints of the restrained and unrestrained slabs. At the top and bottom portions of the slabs, the total strain measured in the restrained and unrestrained slabs are similar and within 8 percent of each other. Separating the total strain into the different components, it was found that the temperature-induced strain and the strain due to the remaining factors are also not affected by the presence of tie bars along the joints.

Similarly, a comparison between the strains measured in the longitudinal direction at the restrained and unrestrained slab corners along the centerline joint was also carried out. The total strain is similar and within 13 percent of each other, also indicating that the tie bars

do not affect the development of strain in the slabs. The same observations were made for the sensors located at the top, middepth and bottom of the slabs.

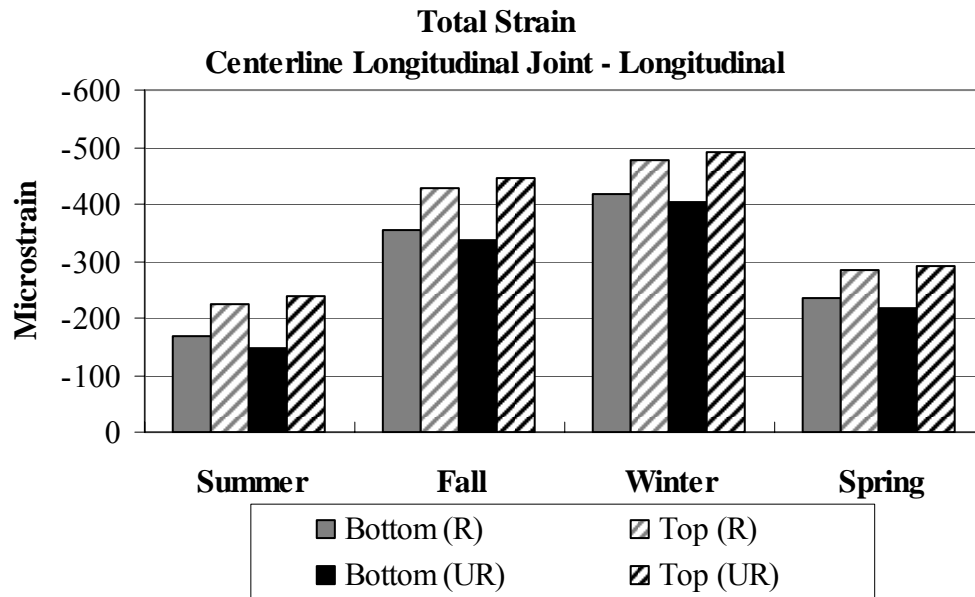


Figure 5.11. Total strain at the top of the restrained and unrestrained slabs along the centerline longitudinal joint in the longitudinal direction.

The effect of the slab length and type of adjacent boundary conditions on the development of strain in the concrete is examined herein. In the transverse direction, the slab is approximately 12 ft wide and is restrained by the curb and gutter on one side and by the eastbound lane on the other side. In the longitudinal direction, the slab is approximately 15 ft long and is restrained by the adjacent slabs on both sides, with dowels in the case of the restrained slabs. Strain data collected from the sensors located along the longitudinal joint and measuring strain in the longitudinal direction is compared to data collected from sensors located along the transverse joint and measuring strain in the transverse direction of the unrestrained slabs.

Figure 5.12 presents a comparison between the total strain measured in the longitudinal and transverse directions along the longitudinal and transverse joints of the unrestrained slabs. At the top portion of the slab, the total strain measured in the transverse direction is 6 to 21 percent larger than that measured in the longitudinal direction. At the bottom portion of the slab, the difference is 7 to 9 percent. This indicates that when the slab

length is longer and is restrained by adjacent slabs, the restraint is increased and the measured strain is smaller.

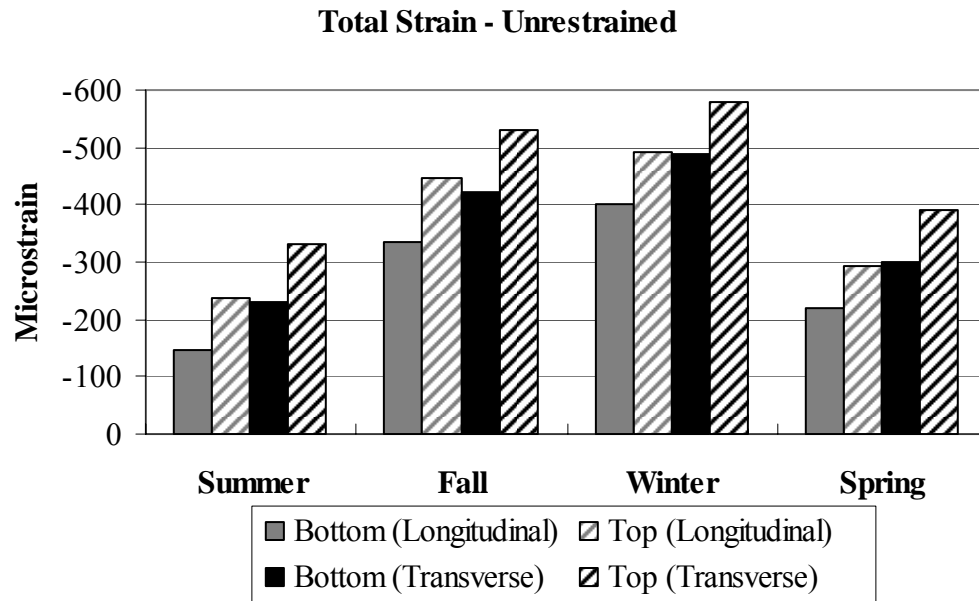


Figure 5.12. Total strain along the centerline longitudinal joints (longitudinal direction) and the transverse joints (transverse direction) at the top of the unrestrained slabs.

In summary, it was found that the bond provided at the slab/base interface reduces the slab surface strain by 11 to 22 percent, the presence of dowel bars reduces the strain by 21 percent, and the longer slab length with adjacent slabs reduces the strain by 6 to 21 percent. On the other hand, it was found that the presence of tie bars does not affect the strain at the slab surface.

5.3.4. Slab curvature

Equation 5-3 was used to calculate the curvature based on the strain measured by the static strain sensors located at the top and bottom of the slab corners, in a rosette configuration. Figure 5.14 and Figure 5.13 show the average curvature based on the strain measured in the diagonal direction for the restrained and unrestrained slabs during the first three years after construction. The curvatures from both figures exhibit the same trends, with a relatively small range of curvatures during the winter and a larger range of curvatures during the summer seasons. This is expected since the slabs are subjected to small temperature gradients during the winter season, which causes the slabs to undergo small

amounts of curvatures. The slabs are subjected to larger temperature gradients during the summer seasons, thus causing the slabs to undergo larger amounts of curvatures.

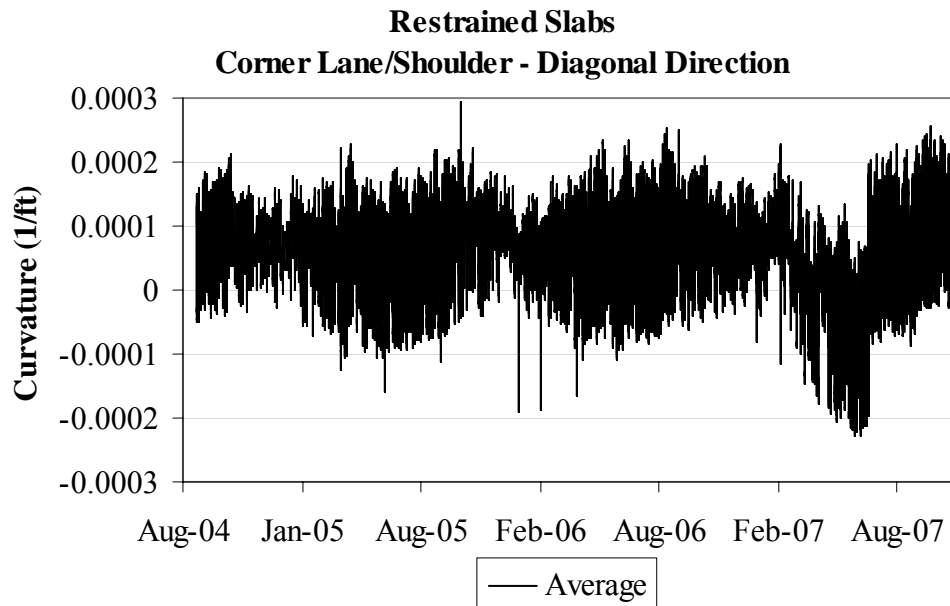


Figure 5.13. Average curvature for the restrained slabs, based on the corner strain in the diagonal direction along the shoulder.

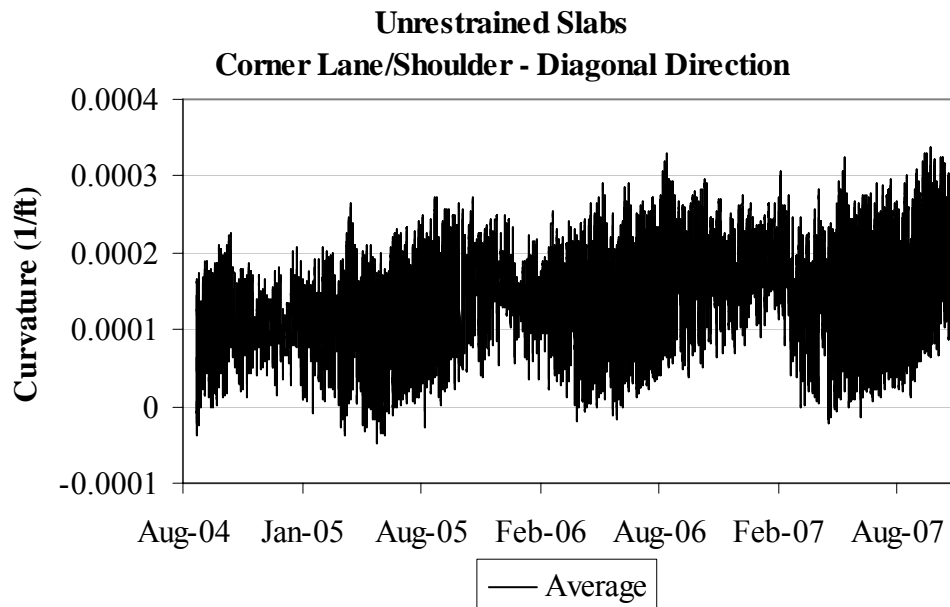


Figure 5.14. Average curvature for the unrestrained slabs, based on the corner strain in the diagonal direction along the shoulder.

The curvature for the restrained slab is 20 to 50 percent lower compared to the unrestrained slab, as shown in Figure 5.15. This was also expected, since the restraint provided by the dowel bars and tie bars along the joints causes the restrained slabs to undergo a smaller amount of curvature than the unrestrained slabs. Similar trends were observed for the curvature estimated from strain in the longitudinal and transverse directions. Moreover, at the same location, the curvature estimated based on strain in the three different directions was similar.

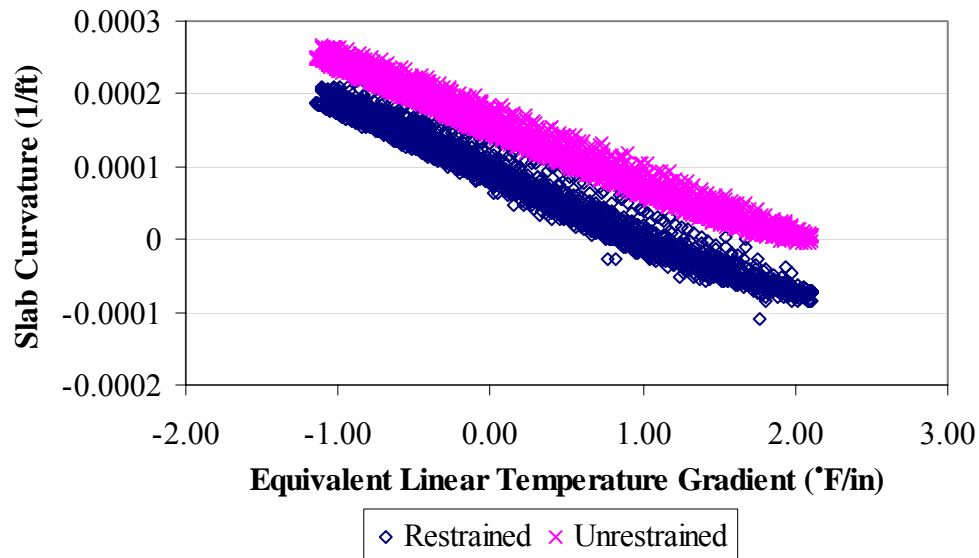


Figure 5.15. Variation in average curvature with equivalent linear temperature gradient for the restrained and unrestrained slabs (April 2006).

The slab curvature calculated in this section will be compared to those calculated based on the surface profile testing and the difference between them will be used to estimate the effect of moisture on the drying shrinkage of the concrete. This will be presented in section 5.6.0.

5.3.5. Summary

An analysis of the static strain measurements has lead to a better understanding of the change in shape of the slab both diurnally and seasonally. A summary of these findings is provided below.

The strain is negative throughout the first three years after construction indicating that the slabs are in a state of contraction. The variation in strain follows seasonal trends. The

low temperature observed during the winter season causes the slab to contract and thereby results in the lowest strain measurements. While, the higher temperature observed during the summer causes the least amount of contraction in the slabs and therefore the strain measurements are largest. This was observed in both the restrained and unrestrained slabs.

Moisture and creep induced strains do not fluctuate much throughout the different seasons, while the temperature induced strains exhibit a larger amount of fluctuation. This is due to the fact that the moisture and creep conditions do not vary much throughout the year when compared to the temperature conditions, which are continuously changing. This is supported by the temperature and moistures measurements in the slab discussed in chapter 2. During the fall and summer, temperature has the greatest effect on strain; while during the winter and spring, moisture and creep induced strains are larger than temperature induced strains. This is also observed in both the restrained and unrestrained slabs.

The joint width continues to decrease with increasing temperature until the joints lock-up. Lock-up of the transverse joint occurs at temperatures higher than 96°F. On the other hand, the curb and gutter do not provide enough restraint to cause lock-up of the longitudinal joint.

Strain data from the restrained and unrestrained slabs was compared to investigate the different restraint conditions. It was found that the bond at the slab/base interface, the presence of dowel bars and the slab length all provide comparable restraint in the slab. On the other hand, it was found that the presence of tie bars does not provide sufficient restraint to affect the strain in the slab.

The curvatures estimated from strains in the longitudinal, diagonal and transverse directions show that curvatures for the restrained slab are 20 to 50 percent lower when compared to those of the unrestrained slab. The dowel and tie bars restrict upward and downward movement at the outer portion of the slab, and cause the majority of the curvature to develop in the central portion of the slab.

5.4.0. Static Pressure Measurements

Pressure cells are used to look at the changes in pressure applied by the slab onto the base. In this section, an analysis of data collected from the static pressure cells will be discussed. This analysis will investigate the seasonal variation in pressure measurements and

the effects of changes in temperature gradients within the slab on pressure measurements along the interface between the concrete and underlying base.

5.4.1. Seasonal Variations in Temperature and Pressure

The temperatures measured by the pressure cells are similar for all the sensors. The measured temperature at the slab base interface varied between 20°F and 91°F, as shown in Figure 5.16, found below.

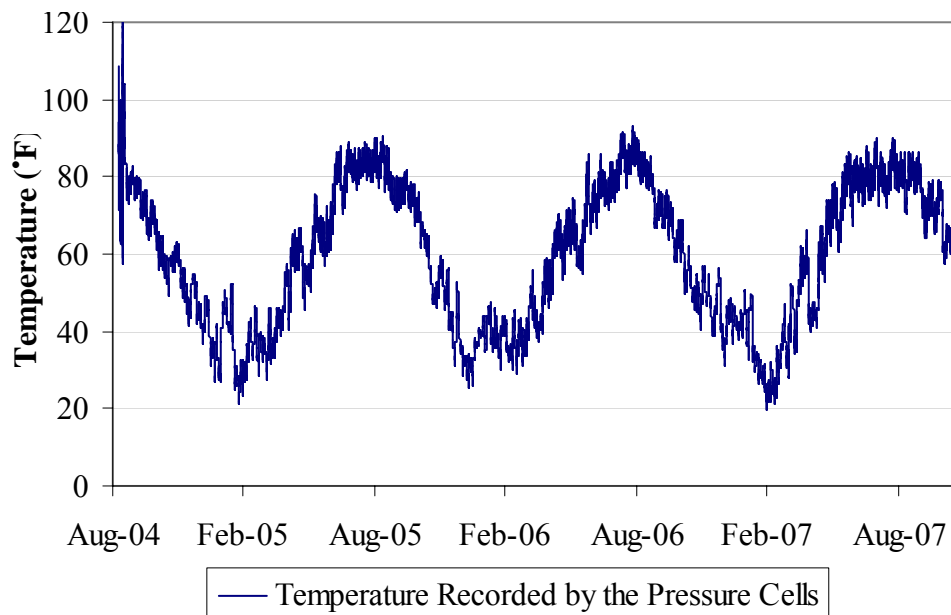


Figure 5.16. Temperatures recorded by pressure cell gauges throughout the first three years after construction.

The measured pressure for the unrestrained and restrained slabs is shown in Figure 5.17 through Figure 5.20. Unfortunately, the edge sensor SP04 of unrestrained Slab B was not recording valid data since construction and therefore, no data is available for analysis. The pressures varied between 8 and 30 psi for both types of slabs, except for a localized increase in pressure observed in the pressure cells located at the corners of restrained Slabs A and B (SP01 and SP04) during the first two weeks of February 2005 and February 2007. These periods correspond to the coldest recorded temperatures within the concrete and underlying layers. During these periods, the ATPB temperature was at or below the freezing point, and the stiffness of the overall pavement structure is significantly increased. As a result, when the slab is subjected to temperature gradients and is attempting to curl, it is

resisted by the base layer. This indicates that the pressure along the slab/base interface is also increased. The strains recorded by the static strain sensors show a decrease in strain measurements during these periods, confirming that the stronger base layer poses an additional restraint on the concrete slab. The effect of freezing of the base layers is discussed in more detail in section 5.4.2.

There are several observable trends in the pressure data. First, the restrained slabs produce larger pressures than the unrestrained slabs in the edge sensors. For the midslab sensors, the opposite is true and the unrestrained slabs exhibits larger pressure than the restrained slabs. There are several factors present that produce these differences in the restrained and unrestrained slabs at various locations. The construction gradient present in the slab was estimated to be $0.31^{\circ}\text{F}/\text{in}$, as previously described in chapter 3, due to the moisture and temperature conditions at the time the concrete set. This positive construction gradient produces a constant upward curvature in the slab, which reduces the pressure applied by the slab to the base along the edges and increases the pressure applied at midslab. In the restrained slabs, this curvature is limited by the restraint produced by the dowel and tie bars. The presence of the restraint at the edges reduces the slab movement at that location, resulting in a redistribution of the load and causing the point in the slab that is furthest away from the restraints, in this case midpanel, to undergo a larger amount of movement. The graphs also show that the edge pressures fluctuate more in the unrestrained slab while the midslab pressures fluctuate more in the restrained slab.

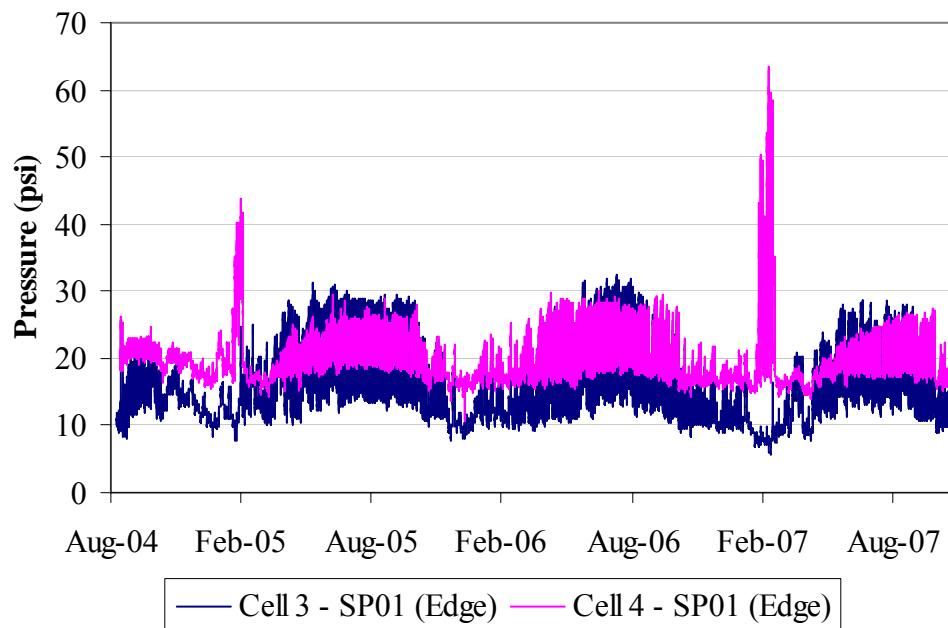


Figure 5.17. Pressure measured at the edge at the slab-base interface for the restrained and unrestrained slabs (gages SP01).

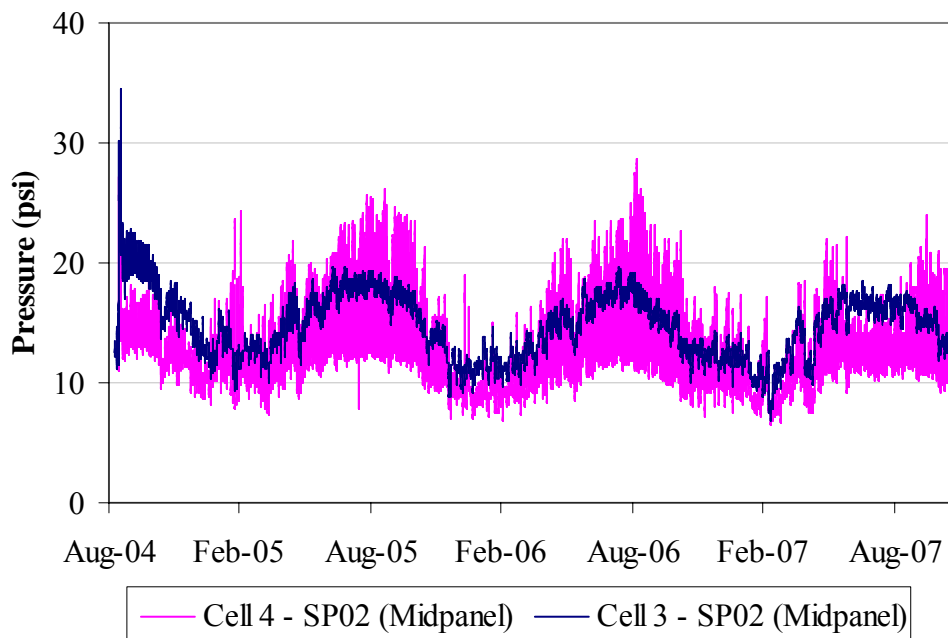


Figure 5.18. Pressure measured at midslab at the slab-base interface for the restrained and unrestrained slabs (gages SP02).

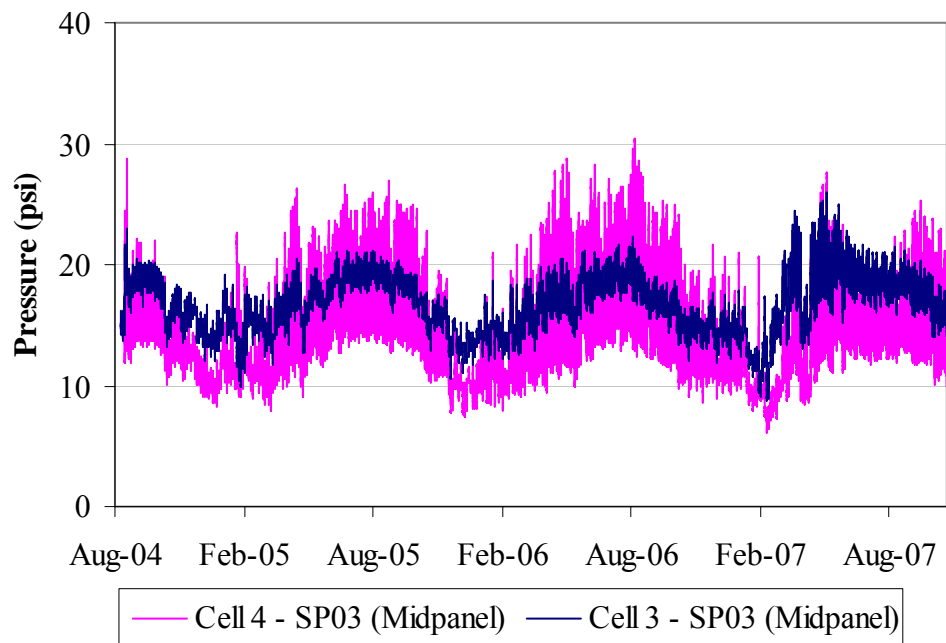


Figure 5.19. Pressure measured at midslab at the slab-base interface for the restrained and unrestrained slabs (gages SP03).

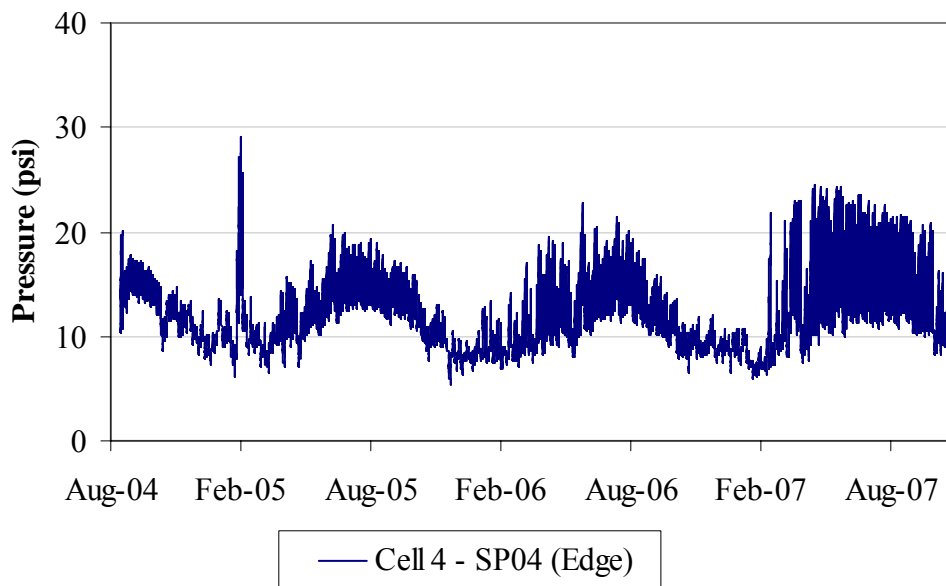


Figure 5.20. Pressure measured at the edge at the slab-base interface for the restrained slab (gage SP04).

Moreover, the figures also indicate that the pressure variation for the unrestrained slabs exhibit a larger amount of fluctuation, compared to the restrained slabs. This indicates

that, for the same temperature gradients, the unrestrained slabs are allowed to curl more than the restrained slabs.

5.4.2. Effect of Freezing of the Base Layer on Pressure

It was previously determined that the pavement structure was frozen down to a depth of 21 in during the period of January 20 to February 6, 2005 and January 29 to February 20, 2007. Freezing of the base layer results in an increase in the resilient modulus of the ATPB layer. As moisture and temperature gradients develop in the slab, the underlying layers have a higher resistance to loads, and therefore, larger pressures are exerted on the base layer. Figure 5.21 and Figure 5.22 show that the pressure increased during the 2005 freezing period, at slab edge and midpanel. The pressure recorded during the freezing period reached values twice as large as those recorded during other days. This holds true for the pressure gages at the unrestrained and restrained slab edges, and at the restrained midslab locations. The unrestrained slabs show an increase in pressure at midslab but to a much lesser extent than that observed for the restrained slabs.

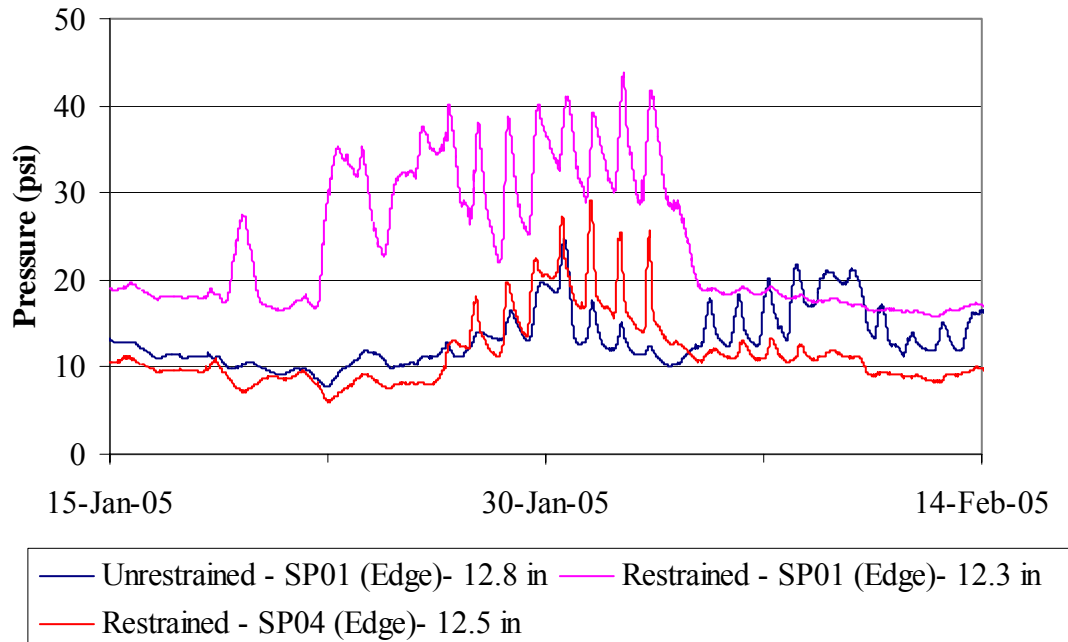


Figure 5.21. Pressure recorded at the slab edge for the unrestrained and restrained slabs during the freezing period of January 20 to February 6, 2005.

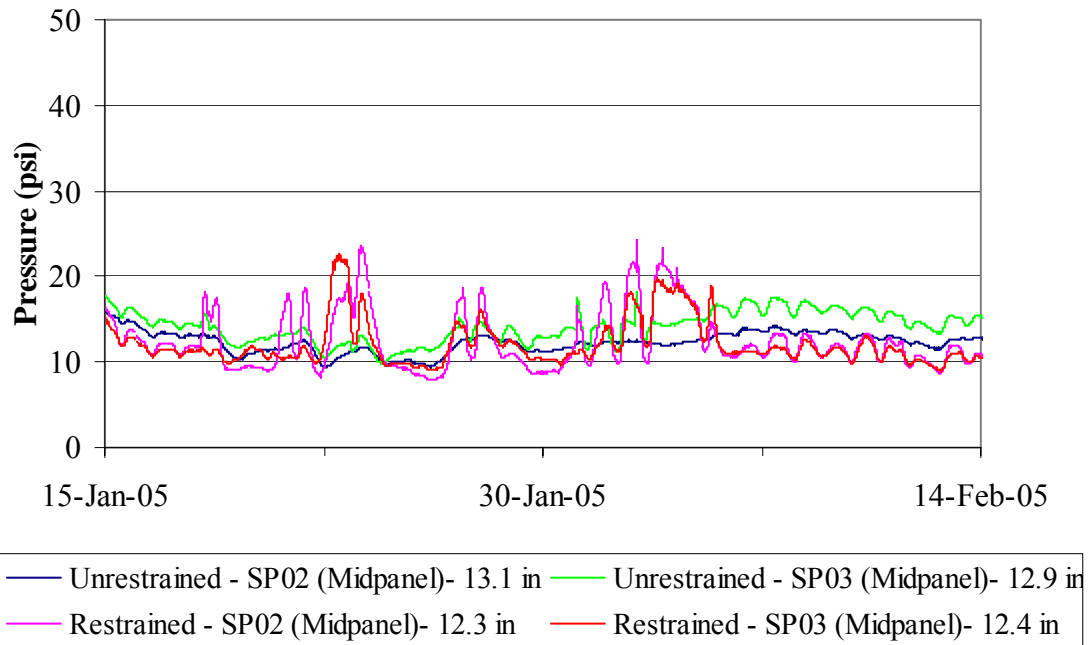


Figure 5.22. Pressure recorded at midslab for the unrestrained and restrained slabs during the freezing period of January 20 to February 6, 2005.

A similar trend of increased pressure during freezing was experienced during the 2007 freezing period and can be seen in Figure 5.23. The pressure recorded by the edge sensor (SP01) of the unrestrained Slab A increased by four times during the freezing period due to the increase in support under the slab. This magnitude of increase was not observed at any of the other locations. It appears that the validity of the readings for this sensor might be in question when temperatures are extremely low. The low temperatures recorded during the 2007 freezing period are the lowest throughout the three years after construction.

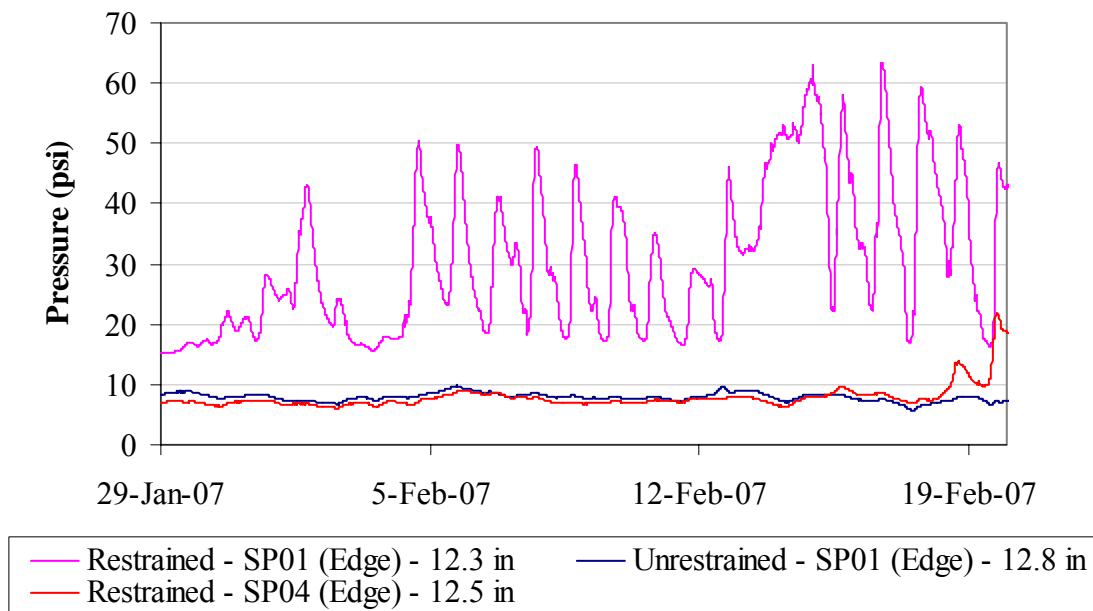


Figure 5.23. Pressure recorded at the slab edge for the unrestrained and restrained slabs during the freezing period of January 29 to February 19, 2007.

5.4.3. Effect of Temperature Gradients on Pressure

The effect of temperature gradients in the slab has been extensively studied in order to characterize the response of the pavement. Gradients that develop daily in the pavement affect slab curvature, which in turn affects the slab pressure at the edge and midpanel. Positive gradients, which cause the slab to curl downward, increase pressure at the slab edge and decrease it at midpanel. Similarly, the upward curvature produced by negative gradients produces higher pressures at midpanel compared to those at the slab edge. Figure 5.24 through Figure 5.27 show the variation in pressure with changes in equivalent linear gradient in the slab for the spring season of the first three years after construction. The figures show that at the edge, the pressure is increasing with increasing equivalent linear gradient for both the restrained and unrestrained slabs. It is also observed that as the equivalent linear gradient decreases, pressure at midpanel increases.

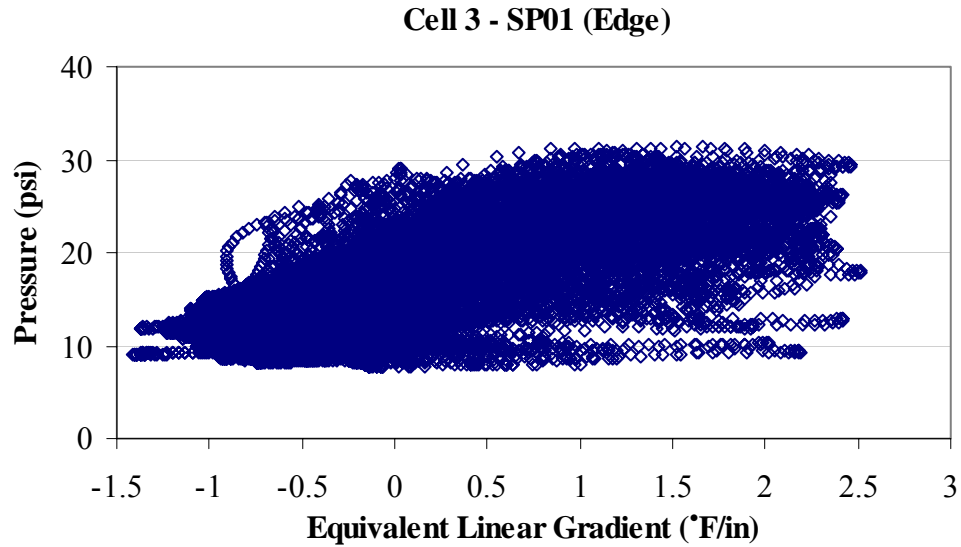


Figure 5.24. Variation in pressure with equivalent linear gradient for the edge sensor SP01 of unrestrained Slab A, during the spring for the first three years after construction.

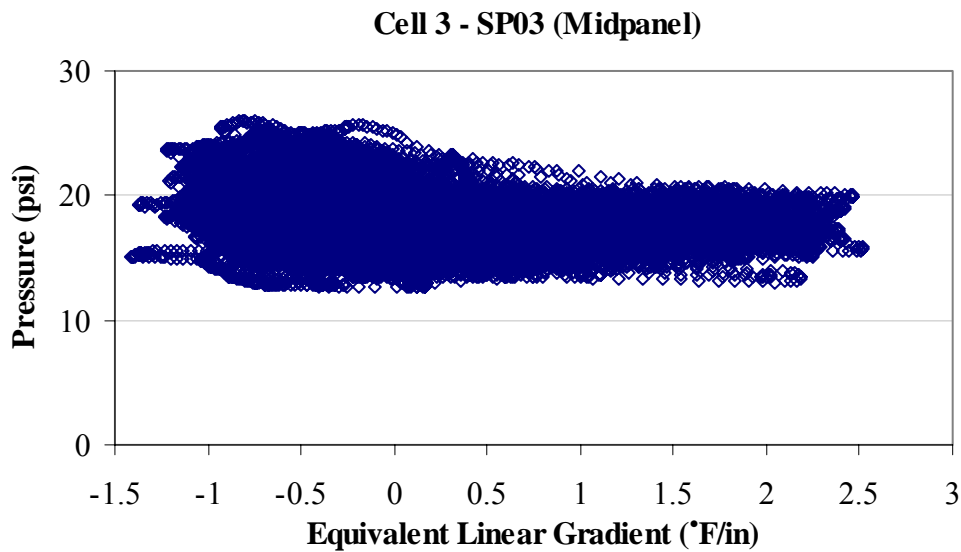


Figure 5.25. Variation in pressure with equivalent linear gradient for the midpanel sensor SP03 of unrestrained Slab B, during the spring for the first three years after construction.

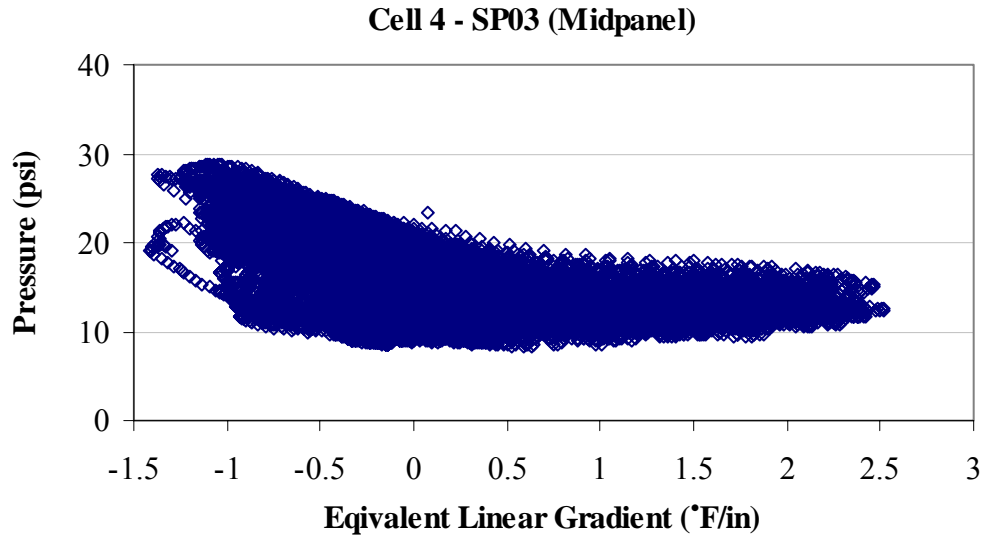


Figure 5.26. Variation in pressure with equivalent linear gradient for the midpanel sensor SP03 of restrained Slab B, during the spring for the first three years after construction.

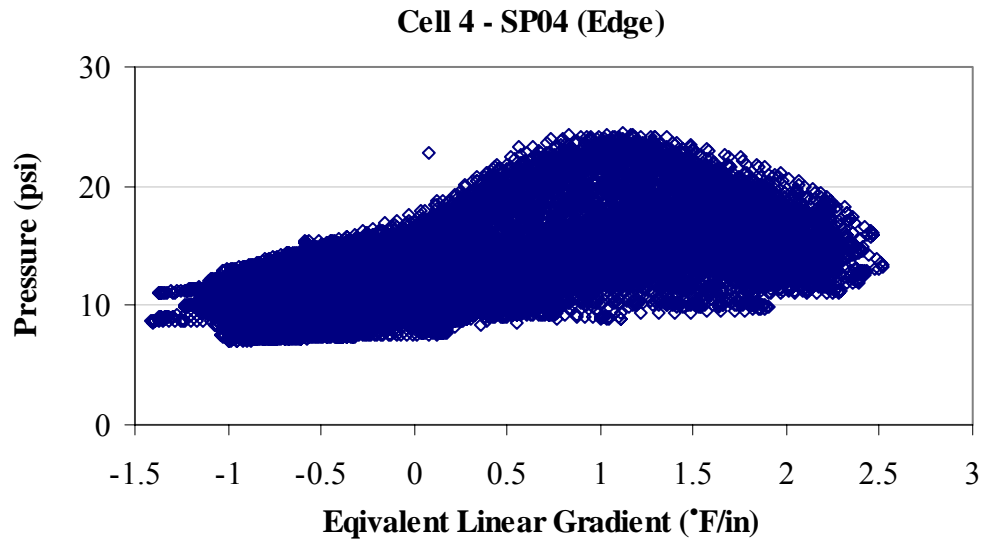


Figure 5.27. Variation in pressure with equivalent linear gradient for the edge sensor SP04 of restrained Slab B, during the spring for the first three years after construction.

Figure 5.28 and Figure 5.29, shown below, display the statistical average of the pressure for each 0.5°F/in change in the equivalent linear temperature gradient since construction of the pavement for restrained and unrestrained slabs. As previously stated, there is a trend of increased pressure at the slab edge with increasing positive gradients, and

increased pressure at midpanel when negative gradients increase. At the edge of the unrestrained slabs, pressure increased 36 percent when the gradient changed from the range of -1.5 to -1.0°F/in to between 0 to 0.5°F/in and increased an additional 22 percent when gradients increased to a range of 1.5 to 2.0°F/in. Similar results were also exhibited in the restrained slabs, as shown in Figure 5.29. Pressure increased approximately 15 percent when the gradient increased from the range of 0 to 0.5°F/in to the range of 1.5 to 2.0°F/in. At the midpanel of the unrestrained slabs, pressure increased approximately 7 percent when negative gradients increased from the range of 0 and 0.5°F/in to the range of -1.5 and -1.0°F/in. At the midpanel location, pressure remained relatively constant between a zero gradient and a large positive gradient with an average of approximately 16 psi.

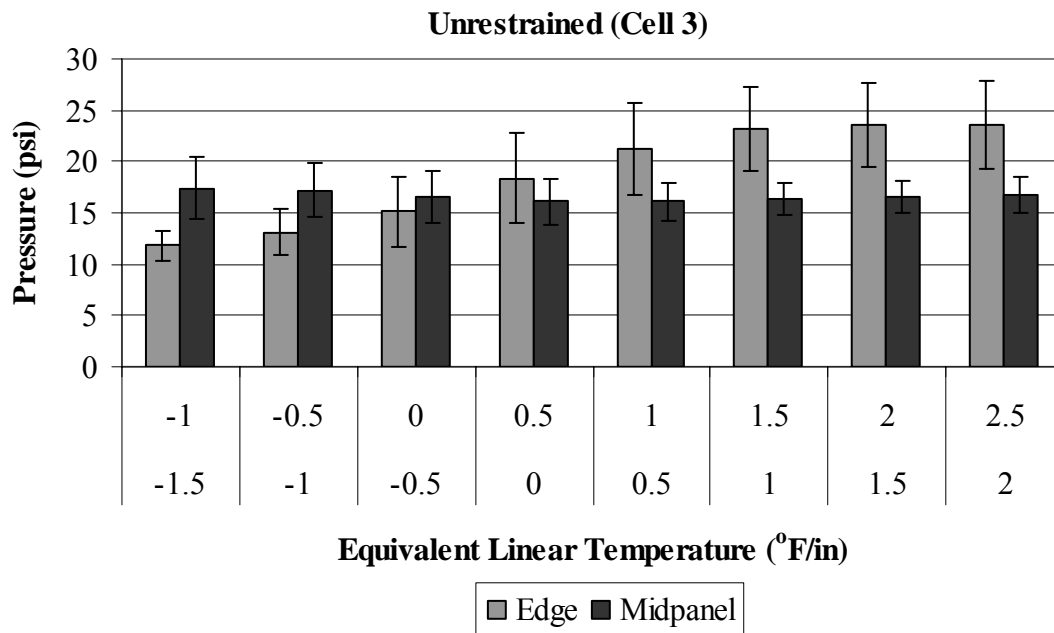


Figure 5.28. Average pressure for each range of equivalent linear gradients for the unrestrained slabs (Cell 3).

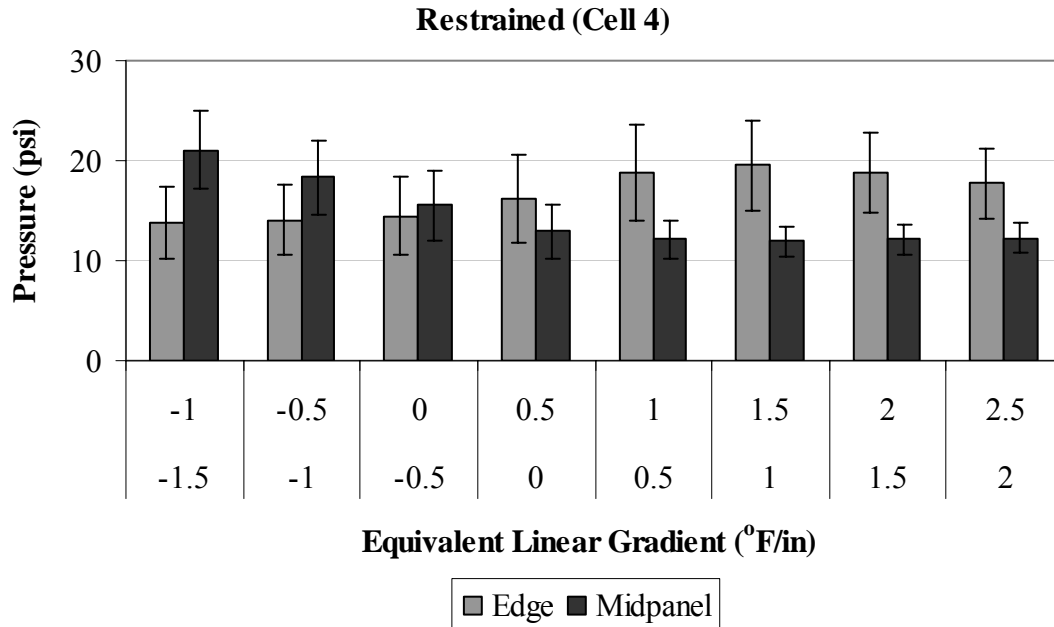


Figure 5.29. Average pressure for each range of equivalent linear gradient for the sensors in the restrained slabs (Cell 4).

The figures also show that when the temperature gradient is less than 0.31°F/in , the pressure at midpanel is larger than at the slab edge. The opposite is true when the gradient is greater than 0.31°F/in . When negative gradients are between the range of -1.5 and -1.0°F/in , pressure at the midpanel of the slab is approximately 32 percent greater at the edge in the unrestrained slabs, and 34 percent larger in the restrained. Similarly, when positive gradients range between 1.5 and 2.0°F/in , pressure at the slab edge is approximately 42 percent larger than at midpanel for the restrained slabs and 55 percent greater in the unrestrained slab. An analysis of the statistical average of the restrained and unrestrained slabs for various gradients showed several trends. For periods when large negative gradients (-1.5 to -1.0°F/in) are present, pressure at both slab edge and midpanel is 15 percent larger in the restrained slabs compared to the unrestrained slabs. This increase in pressure is caused by the restraint provided by the dowel and tie bars. The opposite is true when large positive gradients are present. When the gradient in the slab varies between 2 and 2.5°F/in , the pressure at the unrestrained slab edge is approximately 33 percent larger than the pressure at the restrained slab edge, and the pressure at the unrestrained midpanel is 37 percent larger. In the presence of large negative gradients, the slabs curl downward and the pressure is

increased at midpanel, and decreased at the slab edge. In the case when large positive gradients are present, the opposite is true.

5.4.4. Summary

An analysis of the static pressure measurements along the interface between the concrete and underlying base layer has lead to a better understanding of the change in shape of the slab both diurnally and seasonally. A summary of these findings is provided below.

The variation of pressure on top of the base increases with increasing equivalent linear gradient at the edge. At midpanel, pressure is decreasing with increasing equivalent linear gradient. The pressure appears to stabilize as the magnitude of the gradients increase in both the positive and negative direction. This indicates that gradients larger than this cause a larger degree of curvature but the contact area between the slab and base remains constant. Pressure on top of the base also increases when the base freezes. Freezing of the base layers results in an increase in the resilient modulus of the ATPB layer. As moisture and temperature gradients develop in the slab, the underlying layers have a higher resistance to load, and therefore, larger pressures are exerted on the base layers.

5.5.0. Concrete Surface Profile Measurements

In this section, the curling and warping of the slab due to seasonal temperature and moisture conditions are discussed. For this, seasonal surface profile measurements were made to capture changes in the shape of the slab under various temperature and moisture gradients.

Surface profile measurements were made using a Dipstick, manufactured by Face Construction Technologies, Inc. [30]. The dipstick, shown in Figure 5.30, is a highly sensitive device that measures the relative difference in elevation between successive points along the slab surface. Surface profile measurements were made on the restrained and unrestrained slabs in the longitudinal, diagonal, and transverse directions, as shown in Figure 5.31. The dipstick runs were initiated from the top of invar rods located near the transverse joints along the shoulder. The invar rods are used as benchmarks for all slab profile measurements to allow all relative elevations measured with the dipstick to be turned into actual elevations [1].



Figure 5.30. Surface profile measurements using the dipstick.

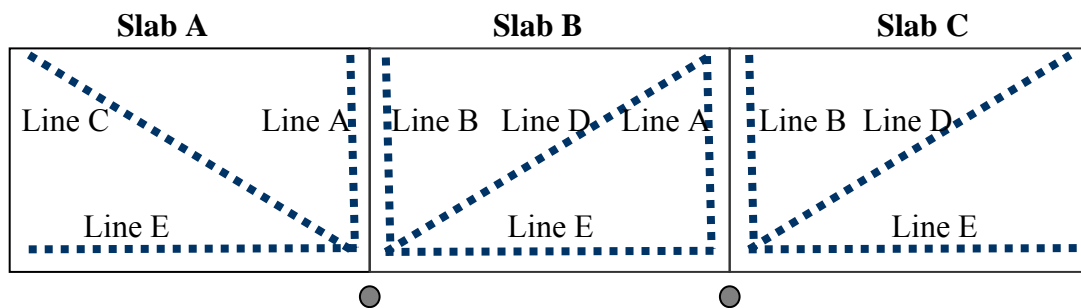


Figure 5.31. Surface profile measurement paths along the concrete slabs [1].

The data collected from the dipstick was first corrected for the slope of the slab in the transverse, longitudinal and diagonal directions. This section of the roadway has, on average, a 2 percent transverse slope and a 2.4 percent longitudinal slope. As a result, the slopes of the slabs affect the surface profiles being measured. Each measured profile consisted of walking the dipstick back and forth along the lines drawn on the slab, starting and ending with on top of the invar rod. The difference between the data measured in both directions was calculated for every point along the line, and the average of the differences was considered to be the bias of the operator. Then, the readings were corrected for the bias and the average between the readings taken in the approach direction and those taken in the

leave direction is used to calculate the slope of the profile. Finally, the average profile data was corrected for the calculated slope of the profile. This procedure helps ensure that surface irregularities are removed from the profiles.

The next and final step in the data manipulation process is to make sure that the measured profile is zeroed to the same slab profile. This was carried out by subtracting out the profile present at a temperature gradient corresponding to the built-in gradient, for every profile and every seasonal outing. As previously mentioned in chapter 3, the restrained and unrestrained slabs set with a built-in construction gradient of 0.31°F/in. This implies that the slabs will be curved upward whenever the gradient is less than 0.31°F/in.

During the 3-year period after construction of the pavement, surface profile measurements were carried out seasonally, four times a year. The seasonal data collection includes continuously walking the Dipstick across the paths shown in Figure 5.31 for a one-day period extending between midnight and 6:00 P.M. The dates of the data collection outings representing each season are provided in Table 5.2. Surface profile measurements were taken for a 1-week period shortly after paving. Unfortunately, dipstick testing was not carried out for the fall 2005 and fall 2006 seasons.

Table 5.2. Surface profile measurement test dates representing each season.

Season	Test Date
Summer 2004	August 16 to 19 and August 22, 2004
Fall 2004	November 16, 2004
Winter 2005	March 3, 2005
Spring 2005	April 6, 2005
Summer 2005	September 22, 2005
Fall 2005	---
Winter 2006	February 1, 2006
Spring 2006	April 18, 2006
Summer 2006	July 20, 2006
Fall 2006	---
Winter 2007	February 28, 2007
Spring 2007	May 3, 2007
Summer 2007	August 15, 2007
Fall 2007	October 31, 2007

The slab temperature and moisture conditions during the Dipstick test dates are presented first followed by the results of the seasonal surface profile measurements. In addition, the curvatures of the slabs were estimated based on the surface profiles and the

corresponding corner displacements were calculated, as presented in sections 5.5.3 and 5.5.4. Finally, a summary of the findings of this section is presented.

5.5.1. Temperature and Moisture Conditions during Seasonal Dipstick Testing

Dipstick testing was performed under different temperature and moisture conditions representing the different seasons. The concrete temperature is characterized in terms of the weighted average temperature and the equivalent linear temperature gradient, while the concrete moisture content is characterized in terms of the relative humidity profile and the corresponding equivalent temperature differences across the slab. The variation in the measured temperature and relative humidity in the slab over the three-year period were presented in chapter 2. The concrete temperature and moisture conditions during the Dipstick test dates are presented in this section.

The temperature of the slab during Dipstick testing is summarized in Table 5.3. Since each test date represents a season, the table lists the weighted average temperature and the equivalent linear gradient by season. The average slab temperature ranged between 31°F (winter 2005) and 90°F (summer 2006). The daily variation in the concrete weighted average temperature during the Dipstick test dates is presented in Figure 5.32.

During the Dipstick test dates, the equivalent linear temperature gradient covered positive and negative values. The widest range of values throughout the day during testing was recorded in the spring season, followed by the summer season, as discussed in chapter 2. The narrowest range of values throughout the day during testing was recorded in the winter season. The largest positive gradient during testing was 2.42°F/in and occurred in the spring 2005. The largest negative gradient was -1.01°F/in and it occurred in the fall 2007 test date. The daily variation in the concrete equivalent linear temperature gradient during testing is presented in Figure 5.33.

Table 5.3. Seasonal slab temperatures and equivalent linear gradients during profile testing.

Season	Weighted Average Slab Temperature (°F)			Equivalent Linear Temperature Gradient (°F/in)		
	Maximum	Minimum	Average	Maximum	Minimum	Average
Summer 04	81	71	75	0.98	-0.97	-0.16
Fall 04	49	42	45	0.72	-0.60	-0.06
Winter 05	36	27	31	0.92	-0.85	-0.25
Spring 05	69	52	60	2.42	-0.51	0.65
Summer 05	82	68	75	1.67	-0.88	0.08
Fall 05	--	--	--	--	--	--
Winter 06	42	39	40	0.44	-0.32	-0.12
Spring 06	74	57	65	2.11	-0.94	0.31
Summer 06	97	83	90	1.85	-0.73	0.29
Fall 06	--	--	--	--	--	--
Winter 07	43	35	39	1.14	-0.11	0.24
Spring 07	80	64	72	2.04	-0.79	0.28
Summer 07	86	74	80	1.65	-0.87	0.02
Fall 07	59	46	53	1.32	-1.01	-0.12

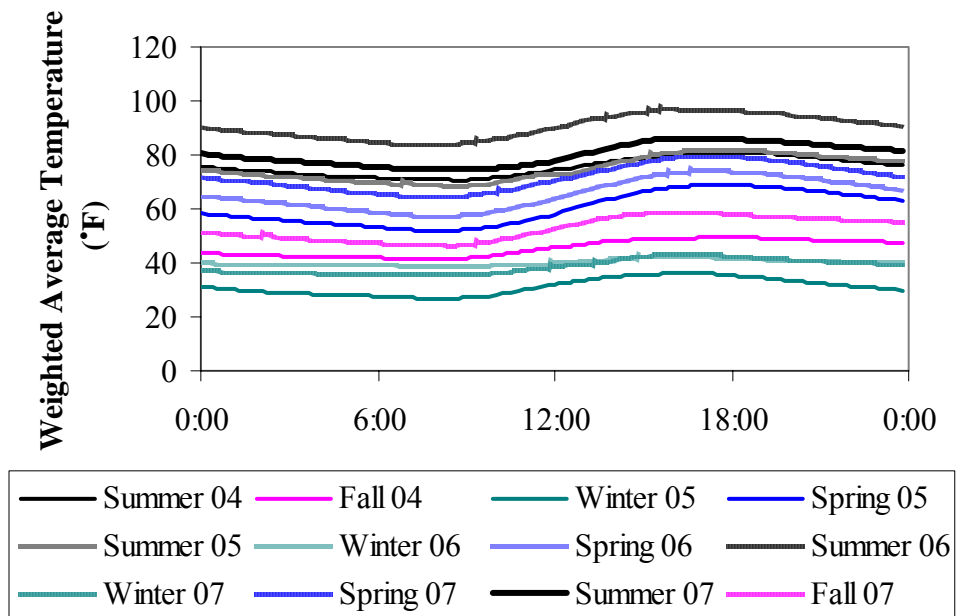


Figure 5.32. Midpanel weighted average concrete temperatures during dipstick testing.

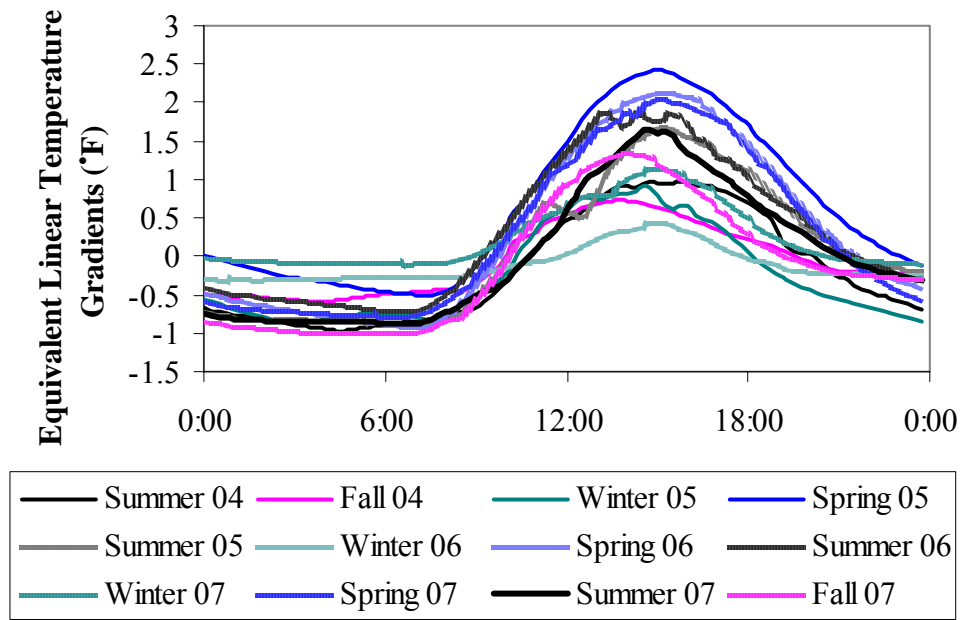


Figure 5.33. Midpanel equivalent linear temperature gradients during dipstick testing.

The concrete moisture content during the Dipstick testing is presented in Figure 5.34 and Figure 5.35. These figures were generated based on the moisture sensors located at midpanel and along the slab edge. The figures show the average concrete relative humidity for each season. As previously stated in chapter 2, the concrete relative humidity is highest during the first year after paving and decreases with time. The moisture is highest during the spring of 2005 and lowest during the winter and fall of 2007.

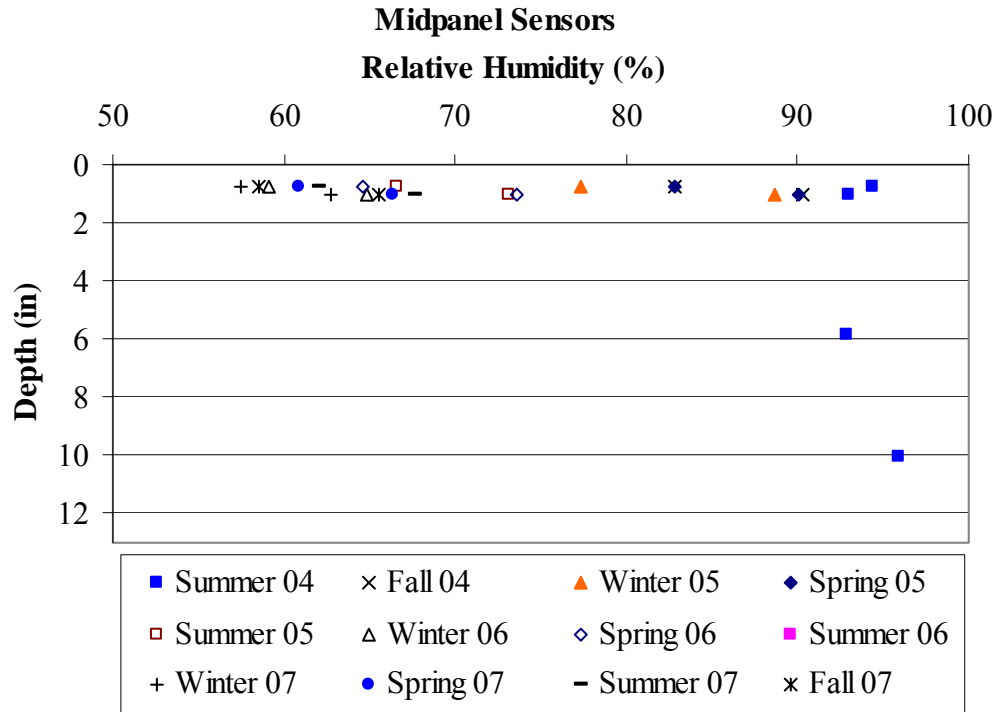


Figure 5.34. Moisture content of the concrete at midslab during dipstick testing.

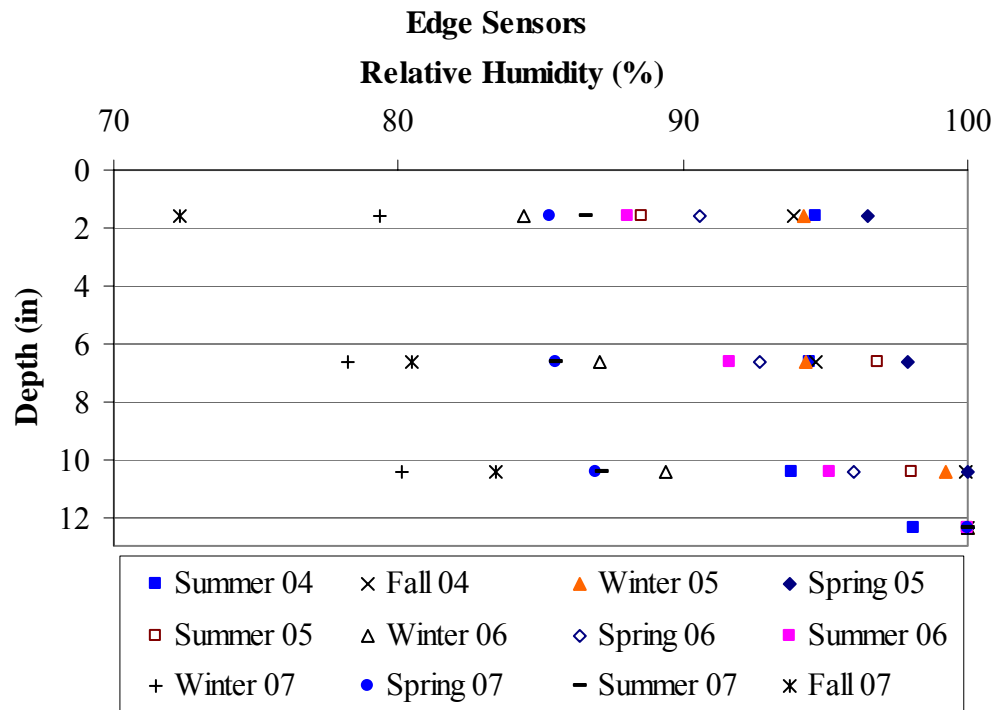


Figure 5.35. Moisture content of the concrete at the edge of the slab during dipstick testing.

The new design guide represents the moisture gradient through the slab by an equivalent temperature difference along the slab depth. However, since the new design procedure incorporates the impact of climate and aging on material properties throughout the entire design life, moisture warping needs to be adjusted monthly based on atmospheric relative humidity. The effects of monthly variation in moisture warping are expressed in terms of equivalent temperature difference and are added to the equivalent linear temperature difference during stress calculations [15]. This was previously presented in equation 3-1, which presents the equivalent temperature difference representing deviations in moisture warping from the annual average adjusted based on atmospheric relative humidity. This equation represents the warping due to a negative moisture gradient, i.e., a positive temperature difference indicates a negative gradient and an upward curvature while a negative temperature difference indicates a positive gradient and a downward curvature.

The relative humidity factors corresponding to the moisture conditions encountered during the test dates were calculated based on the ambient relative humidity, RH_a , and are listed in

Table 5.4. The ambient relative humidity listed in the table is that corresponding to the monthly averages. Also, the moisture gradient is converted into an equivalent linear temperature gradient and the corresponding temperature difference across the top 2 in of the slab, ETG_{Shi} , is calculated. The calculated temperature differences are also presented in the same table. The equivalent temperature gradient representing the combined effect of the moisture gradient in upper two in and the drying shrinkage that has occurred over time is represented by ETG_{Sht} . The temperature difference equivalent to moisture warping during the profile test dates are also illustrated in Figure 5.36.

Moisture warping is calculated based on the assumption that concrete moisture varies in the top 2 in of the slab, depending on the ambient relative humidity, and the concrete moisture in the deeper portion of the slab remains constant at a saturation level of 85 percent or higher [15]. This was verified by the concrete moisture measurements during the three years after construction, which were presented in section 2.4.2. Since the bottom portion of the slab has a higher moisture than the top portion, the moisture gradient is expected to be negative throughout the year resulting in an upward slab curvature due to warping. However, the calculations presented in the previous paragraph and in

Table 5.4 and Figure 5.36 indicate that the equivalent temperature difference fluctuates between positive and negative values throughout the three-year period. This is misleading and is explained by the method of calculation of the equivalent temperature difference, which estimates the temperature difference in the top 2 in of the slab with respect to the annual average ambient relative humidity, while maintaining an 85 percent saturation level in the deeper portion of the slab [15].

Based on

Table 5.4 and Figure 5.36, the equivalent temperature difference starts out with small negative values of -0.001°F to -0.003°F shortly after construction and during the first couple of months after paving. The ambient relative humidity during these months varies between 75 and 78 percent, which is close to the average annual relative humidity during the first year after construction (74 percent). As a result, slab movement due to the moisture gradient is minimal during this time period. During the spring of 2005, the ambient relative humidity significantly decreases to 61 percent, and is accompanied by an increase in the temperature difference due to slab warping of 0.022°F , which represents a more negative gradient. During the second and third year after paving, the annual average relative humidity is 71 percent. During the months when the ambient relative humidity is lower than 71 percent, an equivalent positive temperature difference is calculated and during the months when the ambient relative humidity is higher than 71 percent, an equivalent negative temperature difference is calculated.

Table 5.4. Temperature difference equivalent to moisture warping during profile test dates.

Season	Test Date	$RH_a^{(1)}$ (%)	$S_{hi}^{(2)}$	$S_{h,ave}^{(3)}$	$ETG_{Shi}^{(4,6)}$ (°F)	Age (days)	$ETG_{Sht}^{(5,6)}$ (°F)
Summer 04	22-Aug-04	78	0.616	0.658	-0.009	6	-0.001
Fall 04	11-Nov-04	76	0.636	0.658	-0.004	87	-0.003
Winter 05	3-Mar-05	75	0.652	0.658	-0.001	199	-0.001
Spring 05	6-Apr-05	61	0.789	0.658	0.025	233	0.022
Summer 05	22-Sep-05	71	0.694	0.686	0.002	402	0.001
Fall 05	--	--	--	--	0.000	--	
Winter 06	1-Feb-06	67	0.731	0.686	0.009	534	0.008
Spring 06	18-Apr-06	61	0.787	0.686	0.019	610	0.018
Summer 06	20-Jul-06	74	0.664	0.686	-0.004	703	-0.004
Fall 06	--	--	--	--		--	
Winter 07	28-Feb-07	71	0.693	0.689	0.001	926	0.001
Spring 07	3-May-07	60	0.805	0.689	0.022	990	0.021
Summer 07	15-Aug-07	76	0.641	0.689	-0.009	1094	-0.009
Fall 07	31-Oct-07	75	0.650	0.689	-0.007	1171	-0.007

Notes: (1) RH_a = Ambient Relative Humidity

(2) $S_{hi} = 1.4 - 0.01 RH_a$ for $30\% < RH_a < 80\%$

(3) $S_{h,ave}$ = Annual average of S_{hi}

(4) ETG_{Shi} = Temperature difference equivalent of the deviation of moisture warping in month i from the annual average

(5) $ETG_{Sht} = ETG_{Shi}$ at any time t days from PCC placement

(6) Negative values indicate downward curvature and positive values indicate upward curvature

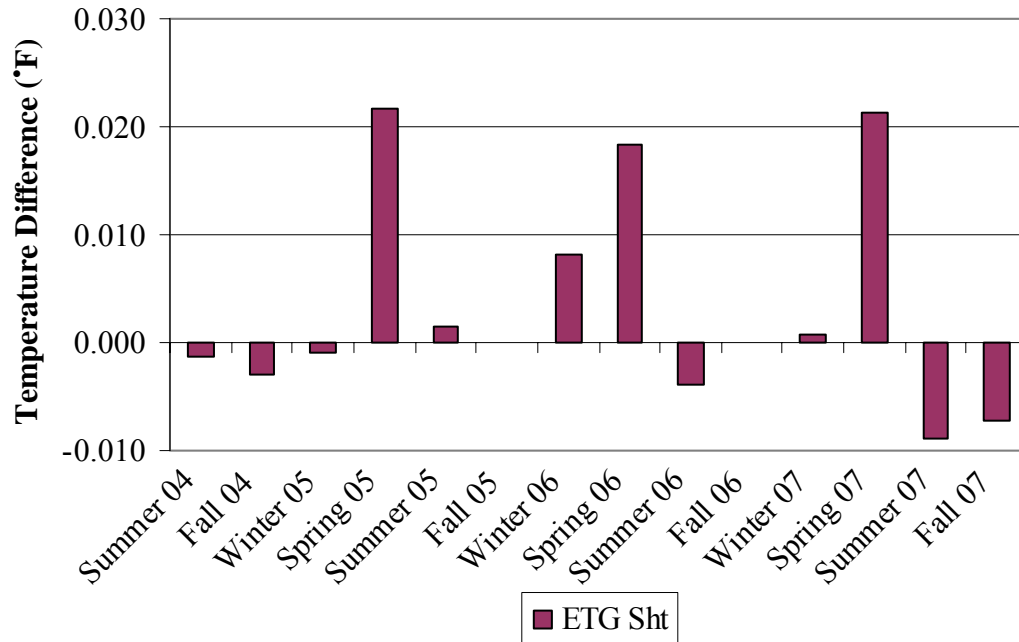


Figure 5.36. Temperature difference equivalent to moisture warping during profile test dates.

Figure 5.37 presents a comparison between the measured and assumed slab moisture profiles during the Dipstick test dates for the third year after paving. The assumed profiles are based on the criteria followed in the MEPDG: in the lower portion of the slab, moisture is at 85 percent, and in the top 2 in of the slab, moisture varies between 85 percent and the ambient relative humidity. Noting that the annual average ambient relative humidity for the third year after construction was 71 percent, the moisture gradient is more negative during the spring and winter and less negative during the fall and summer. According to the figure, the assumed moisture profile overestimates the moisture in the top 2 in of the slab and slightly underestimates the moisture in the lower portion of the slab.

It was shown in section 2.4.2 that the moisture content in the upper portion of the slab increases during the spring and summer season, when the precipitation levels are higher than in the remaining seasons. The highest precipitation was recorded during the summer and the lowest during the fall. This suggests that estimating the moisture gradient in the top 2 in of the concrete slab based solely on the ambient relative humidity may not be fully representative of the actual moisture gradient present in the slab. A more suitable method of estimating the concrete moisture gradient might be to account for the effect of precipitation events on the concrete as well as the ambient relative humidity.

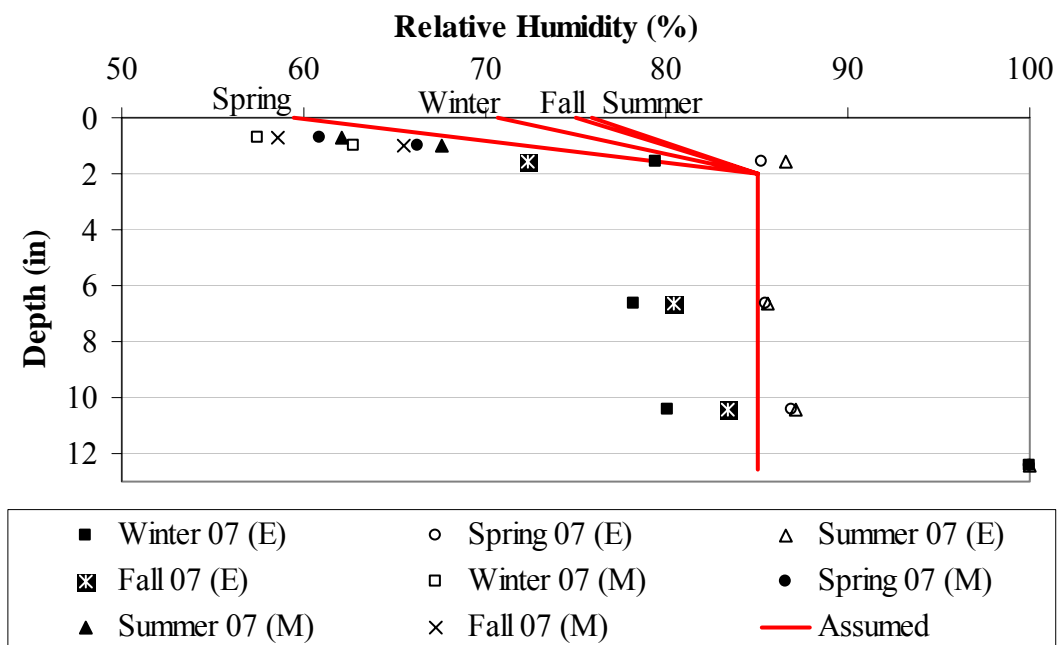


Figure 5.37. Measured and assumed slab moisture profiles during profile test dates for the third year after construction.

5.5.2. Surface Profile Measurements for Restrained and Unrestrained Slabs

The Dipstick was able to provide a dynamic representation of the surface profile of the slab as daily temperature gradients caused it to curl. When plotting the surface profiles, surface irregularities were removed from the profiles by subtracting out the profile present at about 0.31°F/in (corresponding to the construction gradient), as explained earlier in this section.

Seasonal profiles were measured in the longitudinal, transverse and diagonal directions of the restrained and unrestrained Slabs A, B and C. A complete set of the profile measurements carried out during the first year after paving are available in the one-year report [2]. A complete set of all profile measurements for the restrained and unrestrained slabs in the diagonal, longitudinal and transverse directions for the second and third year after construction (seven data collection outings) is provided in appendix E; only some of the figures are presented in this section. The profile measurements made in August 2004 immediately following paving were provided in the Phase I Report [1] and will not be included in this report. The general seasonal trends observed for the slab surface profiles are presented in this section, for the restrained and unrestrained slabs.

Profiles measured for restrained Slab C in the diagonal direction during four of the test dates representing each of the winter, spring, summer and fall seasons are shown in Figure 5.38 to Figure 5.41. The figures indicate that the restrained slab is subjected to positive and negative curvatures during each test date. During the early morning hours, when the temperature gradient is negative, the slabs tend to curl upward, and during the afternoon hours, when the temperature gradient is positive, the slabs tend to curl downward. During the fall and winter, in the case of positive curvature, the maximum range of slab displacement at midpanel is 0.02 in, while during the summer and spring, the range of slab displacement at midpanel reaches 0.04 in. This is expected since the slabs are subjected to a wider range of temperature gradients during the summer and spring, compared to the fall and winter seasons. In addition, the displacement at the slab edge varies within 0.02 in, during the summer and spring seasons, and is much less than that during the fall and winter. To verify this statement, the curvature of the slab and the corresponding corner displacements will be calculated based on the measured profiles, and will be presented in sections 5.5.3 and 5.5.4. Similar trends were observed for the longitudinal and transverse profiles of restrained Slab C and the diagonal, longitudinal and transverse profiles of restrained slabs A and B.

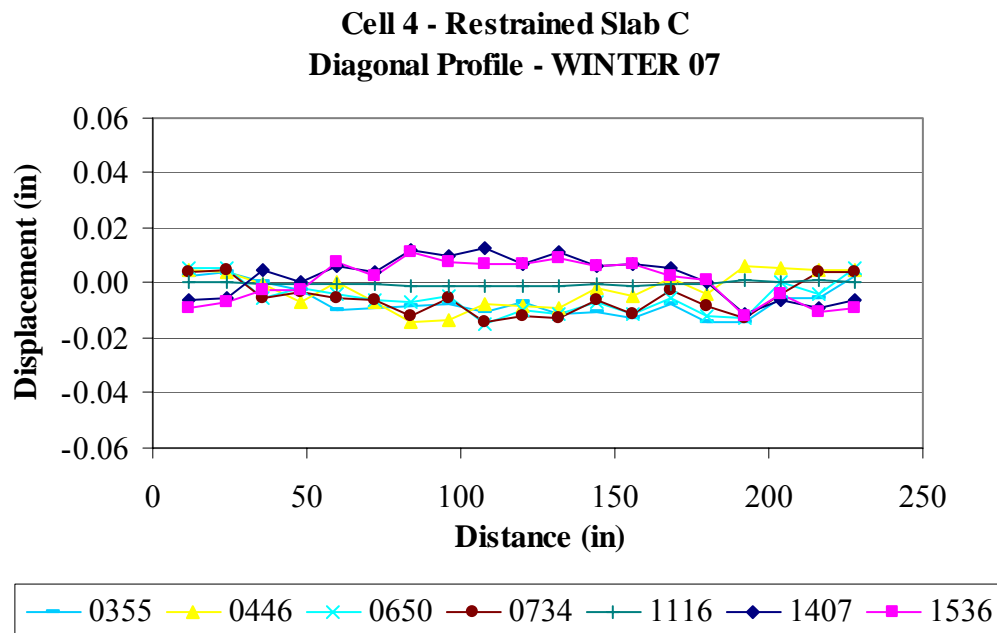


Figure 5.38. Restrained Slab C diagonal surface profiles for the winter of 2007.

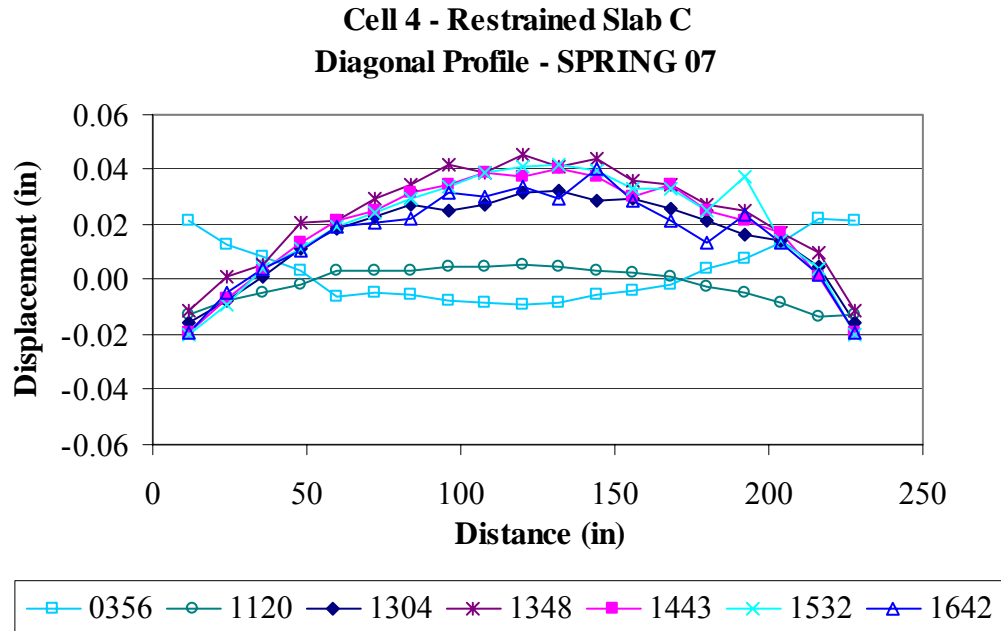


Figure 5.39. Restrained Slab C diagonal surface profiles for the spring of 2007.

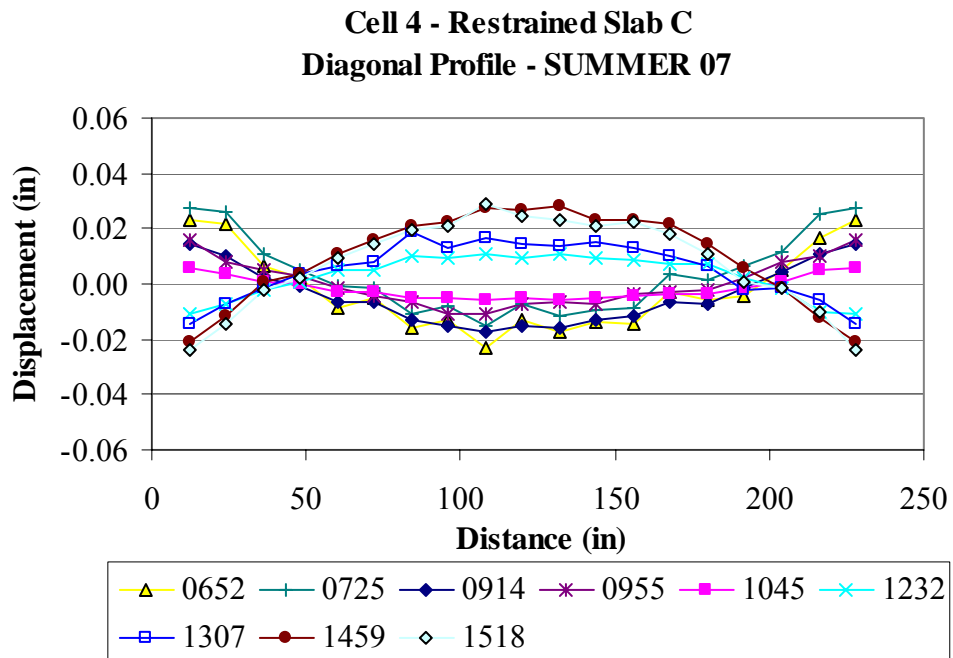


Figure 5.40. Restrained Slab C diagonal surface profiles for the summer of 2007.

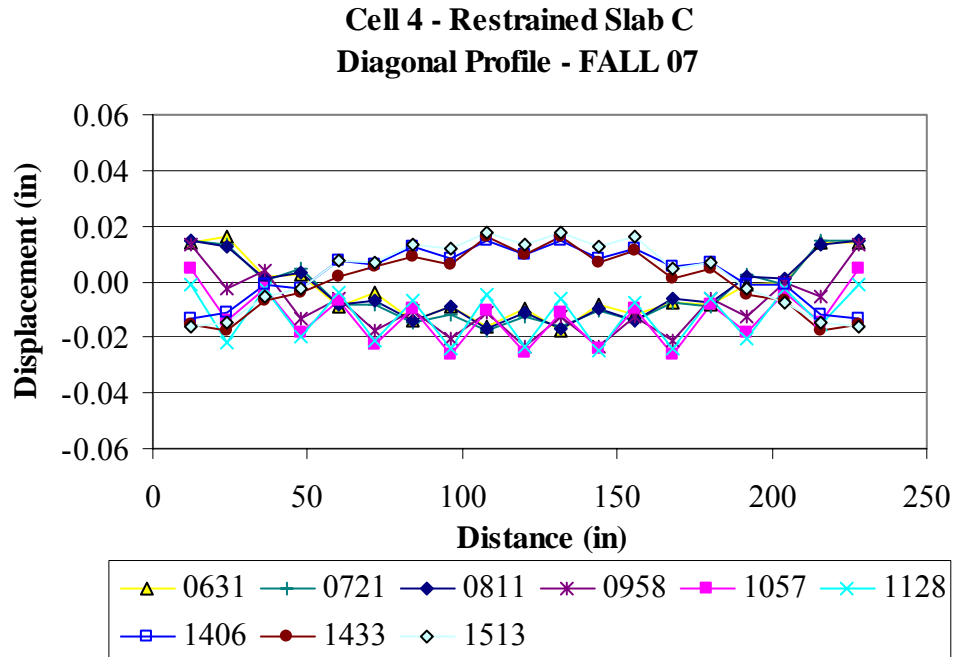


Figure 5.41. Restrained Slab C diagonal surface profiles for the fall of 2007.

As for the surface profiles of the unrestrained slabs, profiles measured for unrestrained Slab A in the diagonal direction during the four test dates representing the winter, spring, summer and fall seasons are shown in Figure 5.42 to Figure 5.45. The figures indicate that the unrestrained slab is also subjected to positive and negative curvatures during each test date. During the early morning hours, when the temperature gradient is negative, the slabs tend to curve upwards, and during the afternoon hours, when the temperature gradient is positive, the slabs tend to curve downwards. The maximum slab displacement at midpanel varies within 0.02 in during the winter and fall, and varies within 0.04 in during the spring and summer. This is similar to what was observed for the case of the restrained slabs. The larger curvature (both negative and positive) is expected during the summer and spring due to the wider range of temperature gradients experienced during these two seasons. In addition, the displacement at the unrestrained slab edge varies within 0.03 in, during the summer and spring seasons, and is much less than that during the fall and winter. To verify this statement, the curvature of the slabs and the corresponding corner displacements will be calculated and compared to the temperature gradients in the slabs at the time of the profile measurements. This will be presented in sections 5.5.3 and 5.5.4. Similar trends were

observed for the longitudinal and transverse profiles of unrestrained Slab A and the diagonal, longitudinal and transverse profiles of unrestrained Slabs B and C.

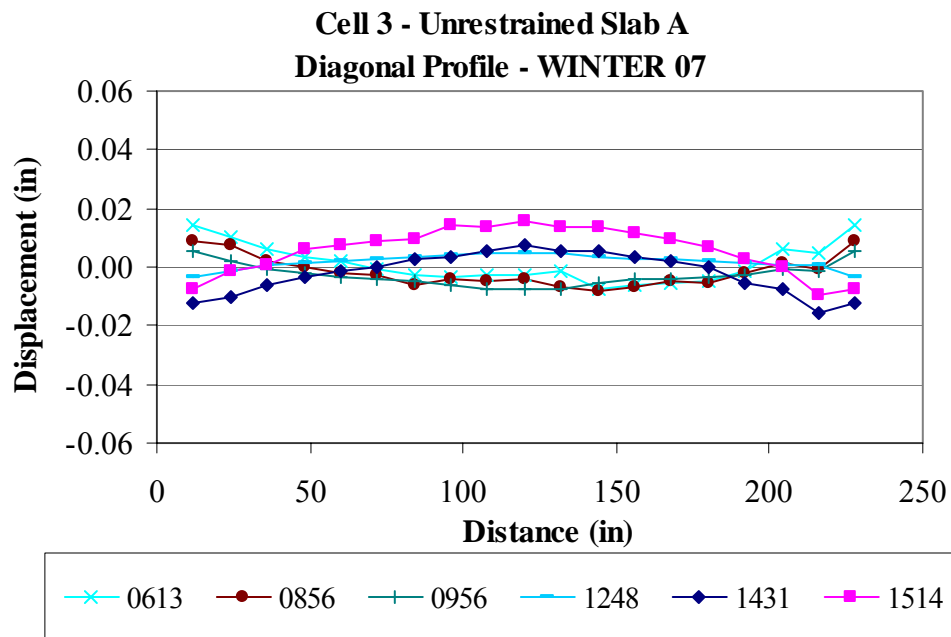


Figure 5.42. Unrestrained Slab A diagonal surface profiles for the winter of 2007.

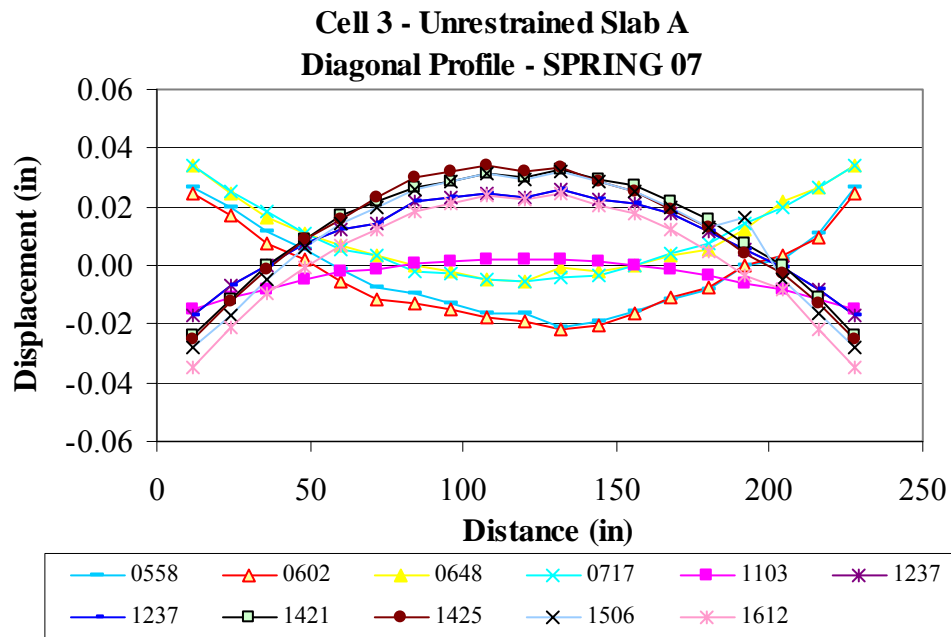


Figure 5.43. Unrestrained Slab A diagonal surface profiles for the spring of 2007.

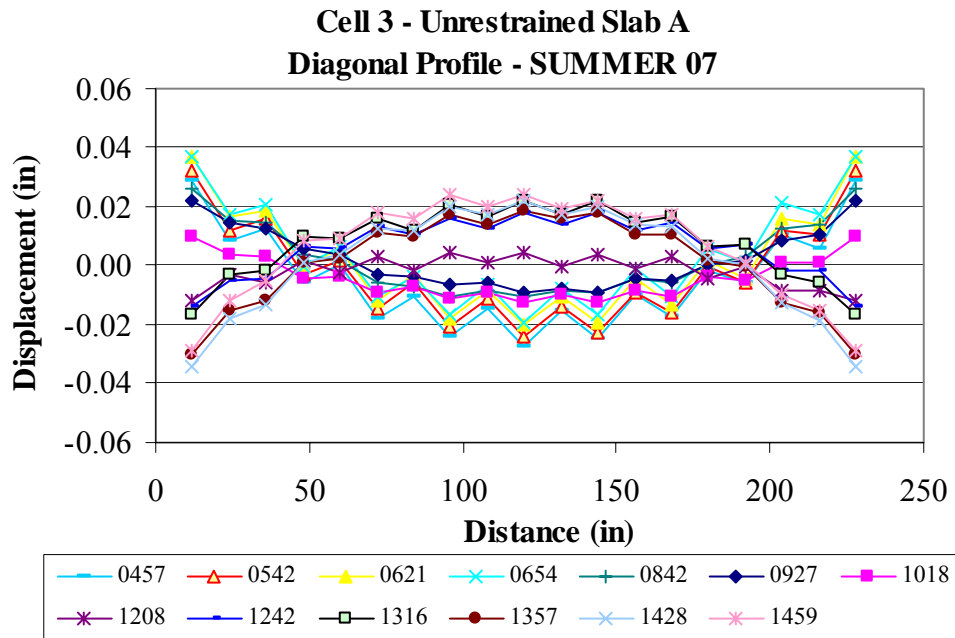


Figure 5.44. Unrestrained Slab A diagonal surface profiles for the summer of 2007.

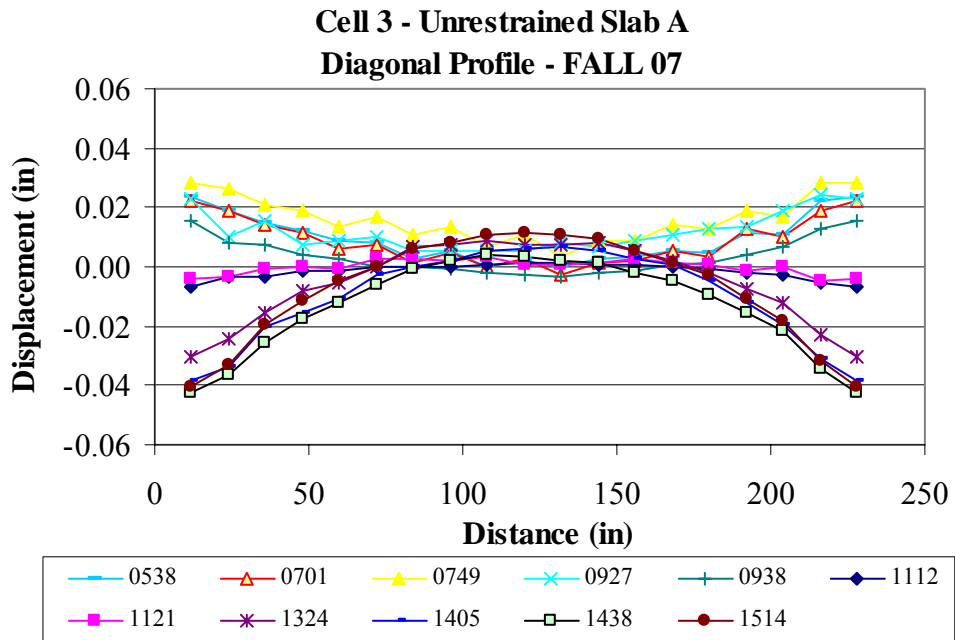


Figure 5.45. Unrestrained Slab A diagonal surface profiles for the fall of 2007.

Based on the surface profiles provided in this section and in appendix E, the unrestrained slabs exhibit larger movements at the edge and the restrained slabs exhibit larger movements at midpanel. The restraint provided by the dowels at the transverse joint reduces

the displacement at the edge of the slab from ± 0.03 in to ± 0.02 in. Due to this restraint imposed on the restrained slab edges, the stresses increase at the edge. The redistribution of stresses within the slab causes a reduction in the stress at midpanel, which in turn allows the midpanel to deflect more than the edge [1]. This behavior was observed for the profiles measured in all slabs and in each of the three directions.

5.5.3. Slab Curvature

In this section, slab curvature is estimated based on the measured surface profile and a relationship between slab curvature and temperature gradient is developed. The slab curvature was calculated by fitting a second order polynomial to the measured profiles. By combining the profile data with the equivalent linear temperature gradient derived from the midpanel thermocouples, the relationship between slab curvature and equivalent linear temperature gradient was defined. Plots of curvature versus equivalent linear temperature gradient for the diagonal, longitudinal and transverse profiles of both unrestrained and restrained slabs were generated and included with the Phase II Interim Report, for data collected during the first year after paving [2]. Surface profile data collected during the first three years after construction was used to generate the plots presented in Figure 5.46 and Figure 5.47, which are based on the diagonal profiles of restrained Slab C and unrestrained Slab A. Similarly to the plots presented in the Phase II Interim Report, only the curvatures calculated for the profiles measured after the joints cracked were used to generate the plots for the August 2004 test period.

A linear relationship between slab curvature and equivalent linear temperature gradient can be distinguished. The slope of the line indicates the rate of change in curvature with changes in equivalent linear gradient. As the temperature gradient in the slab increases, the curvature of the slab decreases; negative curvatures indicate downward slab curvature and positive curvatures indicate upward curvature. In general, the graphs are consistent in showing that the slopes of the lines are relatively close to each other throughout the seasons. An exception is the slope estimated for the September 2005 (Summer 2005) and February 2007 (Winter 2007) test periods, which are somewhat steeper than for the remaining seasons.

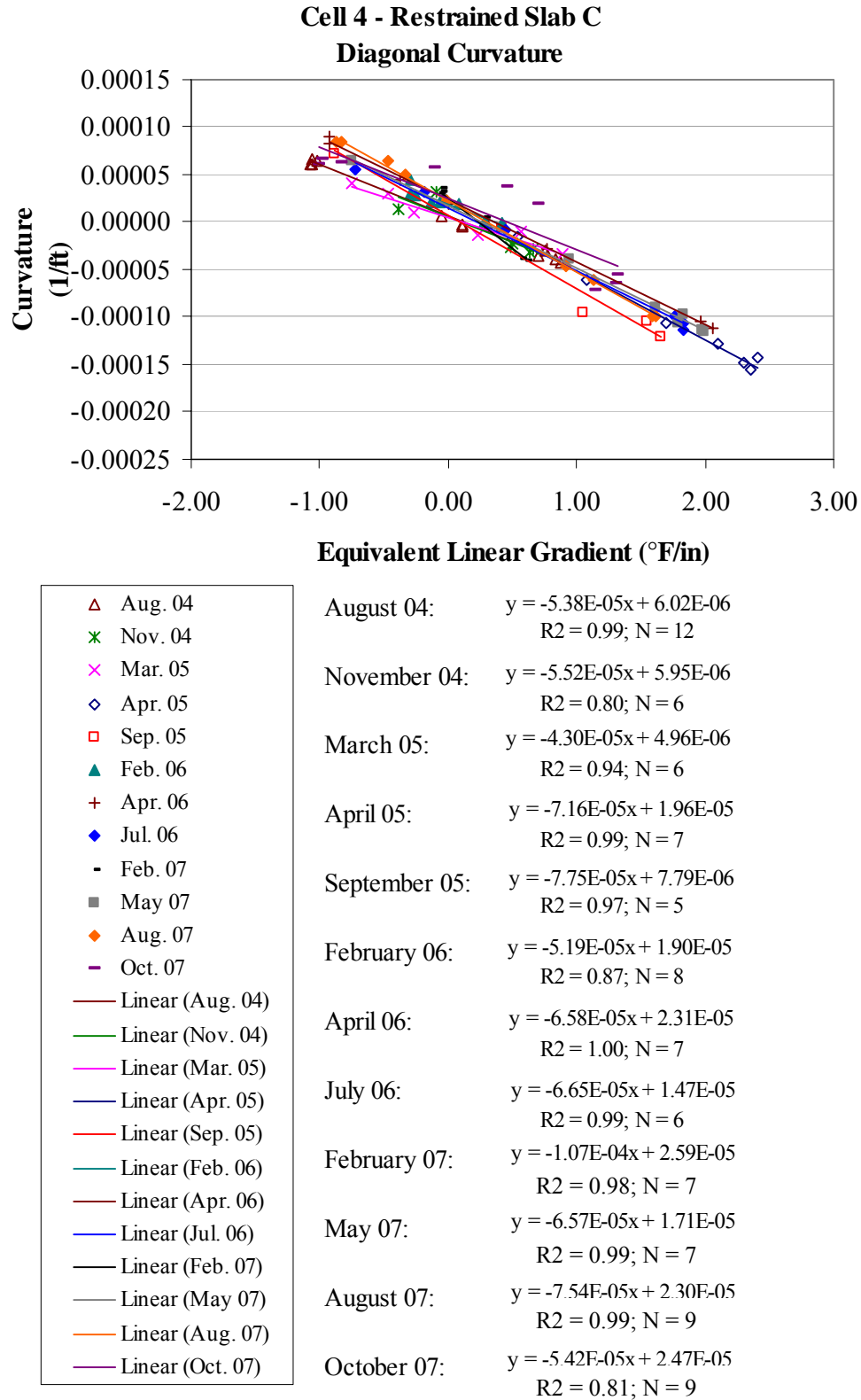
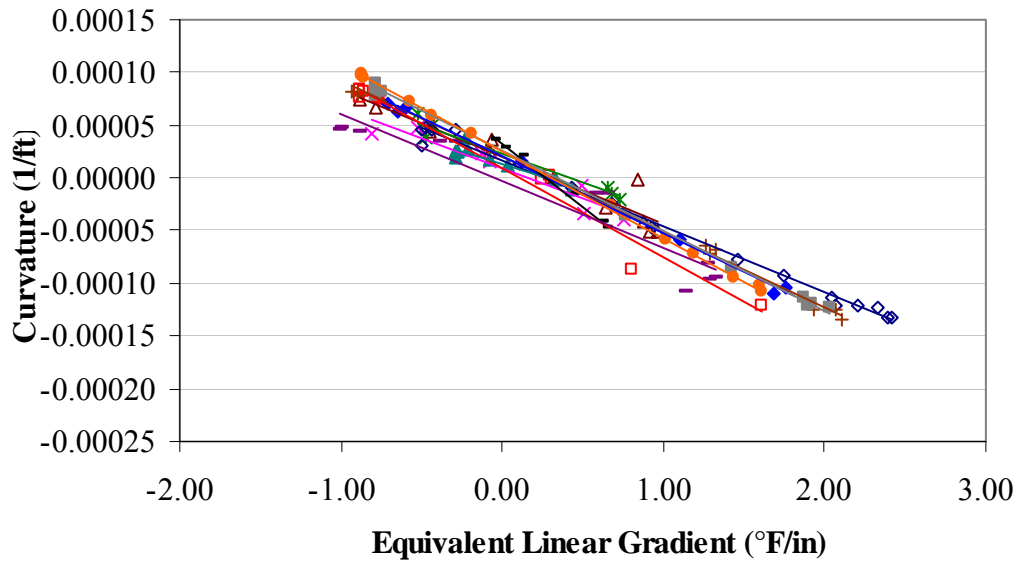


Figure 5.46. Curvature versus equivalent linear gradient for the diagonal profile of restrained Slab C.

Cell 3 - Unrestrained Slab A
Diagonal Curvature



△ Aug. 04	August 04:	$y = -6.35E-05x + 1.97E-05$ $R^2 = 0.93$; $N = 11$
✱ Nov. 04	November 04:	$y = -5.50E-05x + 2.30E-05$ $R^2 = 0.96$; $N = 6$
✕ Mar. 05	March 05:	$y = -5.70E-05x + 8.90E-06$ $R^2 = 0.91$; $N = 7$
◇ Apr. 05	April 05:	$y = -6.23E-05x + 1.58E-05$ $R^2 = 0.99$; $N = 17$
□ Sep. 05	September 05:	$y = -8.44E-05x + 9.51E-06$ $R^2 = 0.97$; $N = 10$
▲ Feb. 06	February 06:	$y = -4.88E-05x + 1.33E-05$ $R^2 = 0.83$; $N = 10$
+ Apr. 06	April 06:	$y = -7.12E-05x + 2.00E-05$ $R^2 = 0.89$; $N = 11$
◆ Jul. 06	July 06:	$y = -7.31E-05x + 1.99E-05$ $R^2 = 1.00$; $N = 9$
- Feb. 07	February 07:	$y = -1.20E-04x + 3.20E-05$ $R^2 = 1.00$; $N = 6$
■ May. 07	May 07:	$y = -7.55E-05x + 2.54E-05$ $R^2 = 1.00$; $N = 10$
● Aug. 07	August 07:	$y = -8.21E-05x + 2.57E-05$ $R^2 = 1.00$; $N = 13$
- Oct. 07	October 07:	$y = -6.32E-05x - 3.29E-06$ $R^2 = 0.91$; $N = 11$
— Linear (Aug. 04)		
— Linear (Nov. 04)		
— Linear (Mar. 05)		
— Linear (Apr. 05)		
— Linear (Sep. 05)		
— Linear (Feb. 06)		
— Linear (Apr. 06)		
— Linear (Jul. 06)		
— Linear (Feb. 07)		
— Linear (May. 07)		
— Linear (Aug. 07)		
— Linear (Oct. 07)		

Figure 5.47. Curvature versus equivalent linear gradient for the diagonal profile of unrestrained Slab A.

The slopes for the restrained slabs are slightly smaller than those for the unrestrained. On average, the rate of variation in curvature with changes in the gradient is 8 percent less for the restrained slabs for curvature along the diagonal, 10 percent less for curvature along the transverse joint and 7 percent less for curvature along the longitudinal joint. A comparison between the variation in the curvature with changes in equivalent linear temperature gradient of the restrained and unrestrained slabs is presented in Figure 5.48 based on the diagonal profiles.

When subjected to similar temperature gradients, the restraint provided by the dowel bars along the transverse joint prevents the slab from attaining the magnitude of curvature measured for the unrestrained slabs. This is observed in the 10 percent difference in the slope in the curvature along the transverse joints.

Moreover, the restrained slabs are tied to the curb and gutter on one side and to the adjacent inside lane on the other side, while no tie bars are provided for the unrestrained slabs. Based on this, the curvatures estimated for the restrained slabs are expected to be smaller than those of the unrestrained, which was observed in the 7 percent difference in the slopes of the curvatures along the longitudinal lane/shoulder joints.

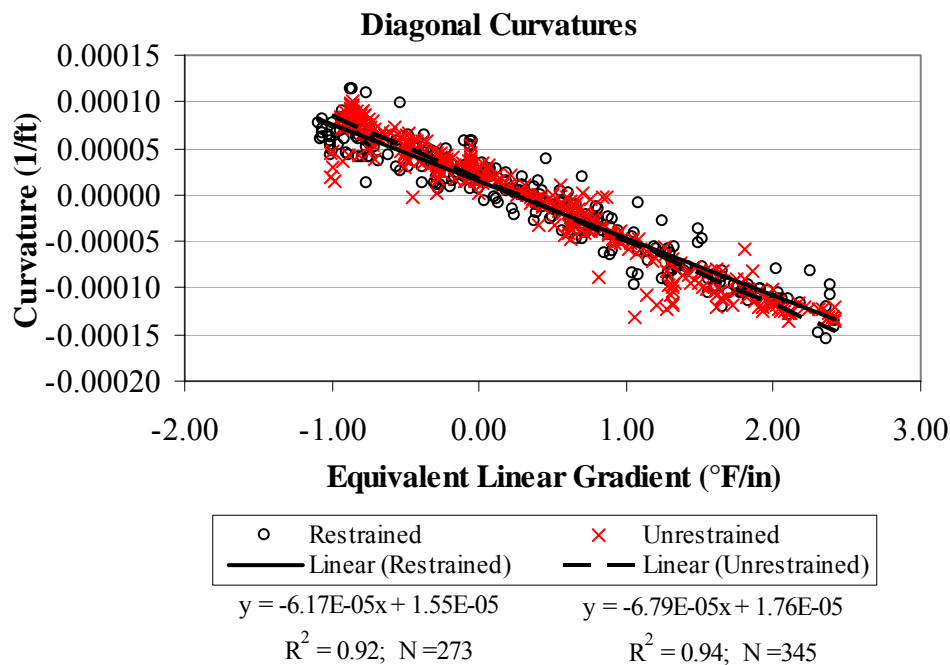


Figure 5.48. Curvature versus equivalent linear gradient for the diagonal profiles of restrained and unrestrained slabs.

5.5.4. Corner Displacements

In this section, the corner displacement is calculated based on the slab curvature and a relationship between corner displacement and equivalent linear temperature gradient is presented.

The profile measurement starts from the top of the invar rod. The subsequent Dipstick reading is taken on the curb and gutter and the third reading is taken at a marked point on the slab located at a distance of four in away from each edge, as shown in Figure 5.49. Based on the estimated curvature, and knowing the exact point where the profile is initiated, the displacement of the slab corner can be calculated. The corner displacement is estimated for each profile by using the first surface profile measurement located on the slab and backcalculating the displacement at the corresponding distance away based on the profile curvature. The diagonal profiles are used to estimate the corner displacements, the transverse profiles are used to estimate the displacements 4 in away from the corner in the longitudinal direction. The longitudinal profiles are used to estimate the displacements 4 in away from the corner in the transverse direction [2].

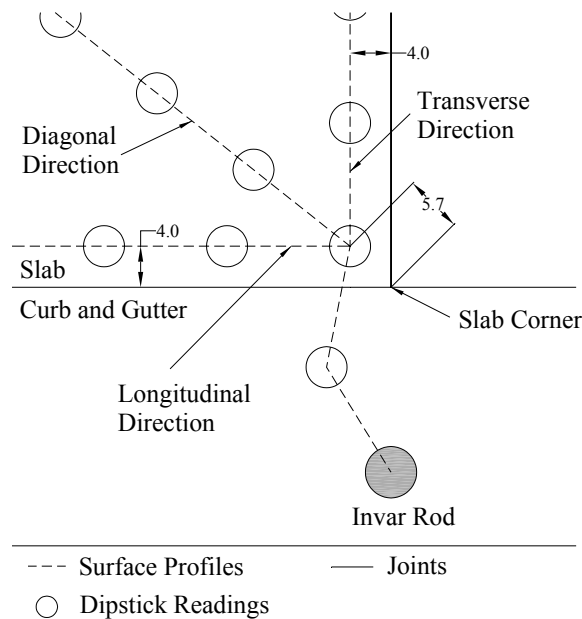


Figure 5.49. Plan showing the start point of the surface profiles in all directions [2].

Figure 5.50 and Figure 5.51 show the variation in the corner displacement estimated using the diagonal profiles for restrained Slab C and unrestrained Slab A with respect to the equivalent linear temperature gradient. The slope of the line indicates the rate of change in corner displacement with changes in equivalent linear gradient. The corner displacements decrease with increasing gradients. However, Figure 5.50 indicates that the rates of change for the November 2004 and March 2005 test dates are smaller than the rates for the other data collection outings. The range of equivalent linear gradients covered during both these test dates is the smallest compared to the other outings, as well. This indicates that there was not sufficient data to give an accurate depiction of the change in corner displacement that accompanies changes in temperature gradient. In addition, for the November 2004 testing, the coefficient of correlation is approximately 16 percent, which indicates that the relationship between the temperature gradient and the corner displacement is poor for that data set.

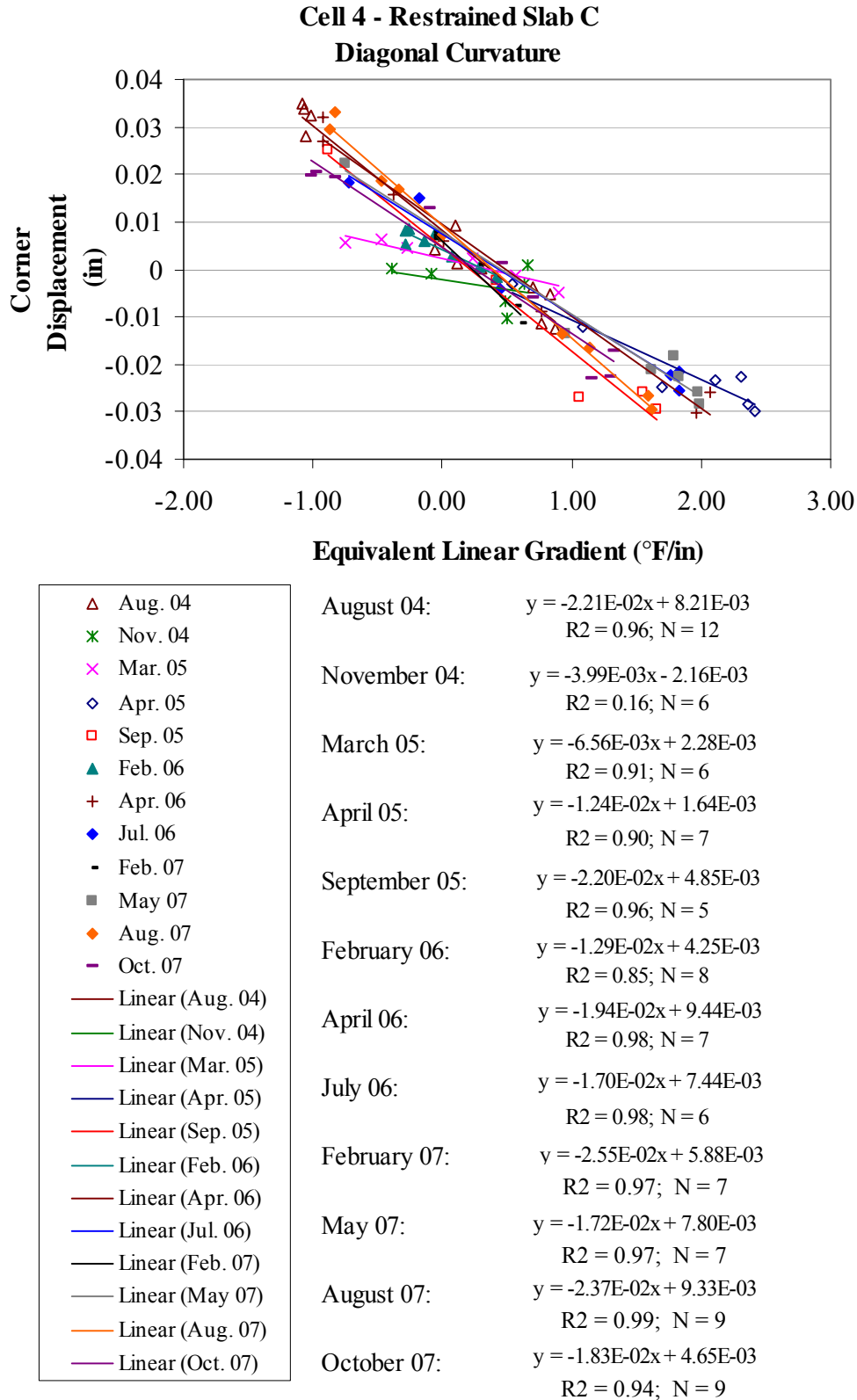


Figure 5.50. Corner displacement versus equivalent linear gradient for the diagonal profiles of restrained Slab C.

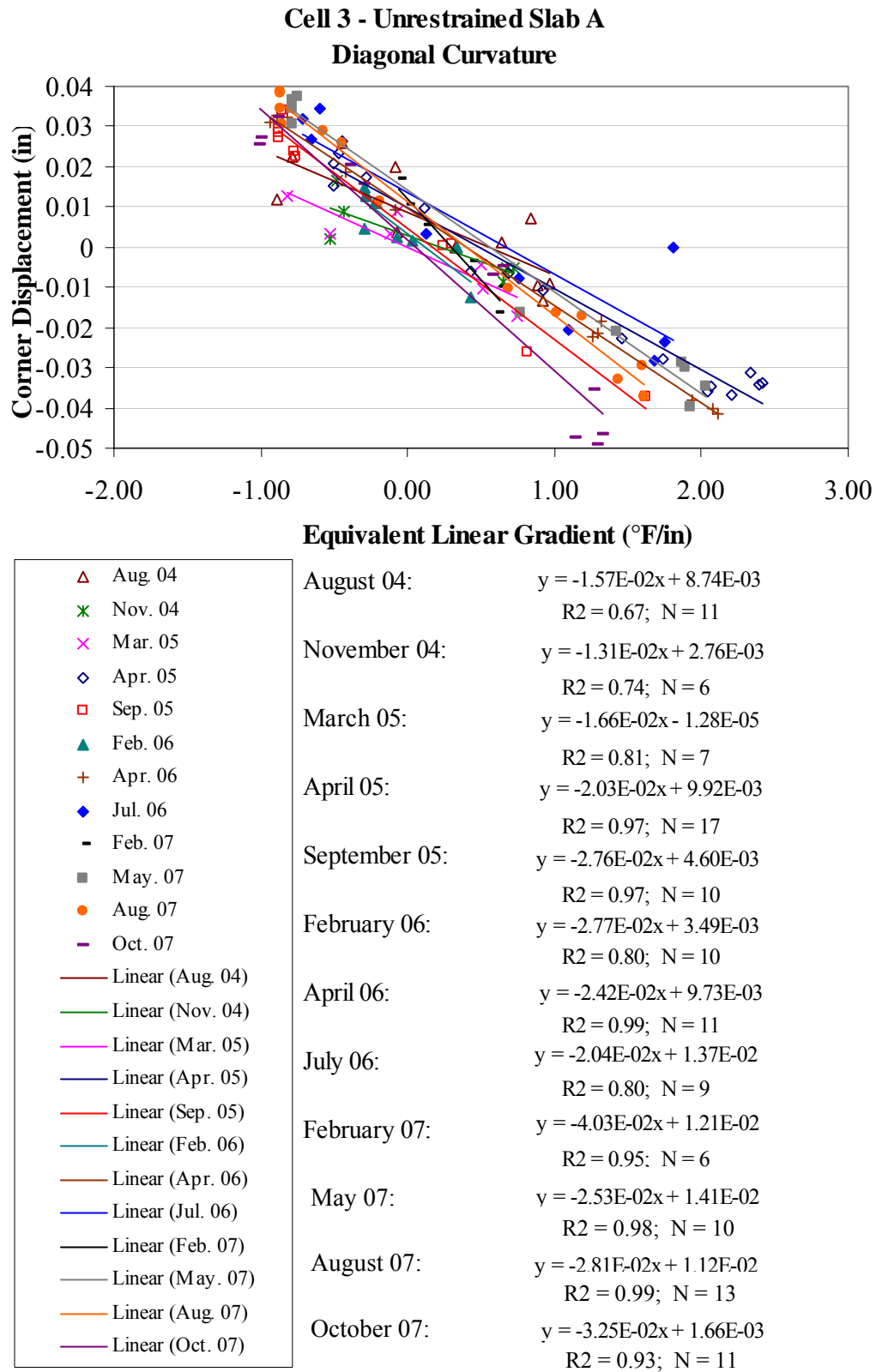


Figure 5.51. Corner displacement versus equivalent linear gradient for the diagonal profiles of unrestrained Slab A.

The corner deflections for the diagonal profiles of the unrestrained and restrained slabs are compared to each other for the same equivalent linear temperature gradients. The equivalent linear temperature gradient varied between -1.0°F/in to 2.5°F/in during the time periods when surface profile measurements were being taken. The range of corner displacements for the restrained and unrestrained slabs is provided in Table 5.5. This represents the range of corner deflections for all slabs (Slabs A, B and C). For the same gradient, the estimated corner displacements are similar for the restrained and unrestrained slabs. The maximum upward corner displacement is 40 mils for both the restrained and unrestrained slabs, and the maximum downward corner displacement is -35 mils for the restrained slabs and -50 mils for the unrestrained slabs. This indicates that the slabs encounter comparable maximum displacement, irrespective of the restraint provided by the dowel bars and tie bars along the transverse and longitudinal joints, respectively.

Table 5.5. Ranges of displacement at the corner for different equivalent linear temperature gradients based on unrestrained and restrained Slabs A, B and C.

Equivalent Linear Temperature Gradient, °F/in	Corner Deflections from Diagonal Profiles (Slabs A, B and C), mils					
	Restrained Slabs			Unrestrained Slabs		
-1.0	5	to	40	-10	to	40
0.0	-10	to	20	-20	to	20
0.31	-15	to	15	-15	to	15
1.0	-35	to	5	-30	to	-5
2.0	-35	to	-15	-50	to	-20

5.5.5. Summary

The unrestrained slabs exhibit larger movements at the sides and the restrained slabs exhibit larger movements at midslab. The restraint provided by the dowels along the transverse joint reduces the curvature at the end of the slab. Due to this restraint imposed on the restrained slab edge, the stress increase at the edge. This behavior was observed in the transverse, longitudinal and diagonal directions.

The seasonal profiles show positive curvature during the fall season and both positive and negative curvature during the remaining seasons. The slab deformation is relatively small during the winter season to the point where the slabs are almost flat. Large deformations occur during the spring and summer. The largest upward curvature was measured in the spring and the largest downward curvature in the fall and summer.

Slab curvatures decrease with increasing equivalent linear gradients at a constant rate irrespective of season of the year. This was confirmed by all data collected throughout one year, with some exceptions. The rate of the change in curvature with a change in gradient is lower for the restrained slabs than the unrestrained.

5.6.0. Effect of Moisture on Concrete Drying Shrinkage

In the previous sections 5.3.4 and 5.5.3, the slab curvature was estimated based on the strain measurements and based on the surface profile measurements. In this section, the slab curvature estimated from both types of data are compared to each other for the days when Dipstick testing was performed during the 3-year period after construction. The results are used in evaluating the effect of moisture on drying shrinkage for the restrained and unrestrained slabs.

5.6.1. Restrained Slabs

The slab curvature was estimated based on the strain measurements and the seasonal surface profiles. Figure 5.52 to Figure 5.55 compare the curvatures that were estimated based on the strain data and those based on the surface profile data for restrained Slab A, for the Dipstick test dates during the third year after paving. The curvatures provided in the figures are estimated based on strain data collected from sensors in the corner of the slab adjacent to the lane/shoulder joint and in the longitudinal, diagonal and transverse directions. The curvatures estimated using the dipstick data are based on surface profiles measured at the slab corner adjacent to the lane/shoulder joint in the same three directions. The figures show that the curvatures estimated from the surface profiles and the strain data follow similar daily trends, with the curvatures estimated based on the strain data smaller in value, in most cases.

Appendix F includes a full set of figures comparing curvatures estimated from the surface profiles to those from the strain gages, for restrained slabs A, B and C, for the second and third years after construction (seven dipstick outings). The figures showing data collected from the first two years after construction show that the curvature estimated using the surface profiles is shifted downward compared to the curvatures obtained from the strain gages. The measured curvature based on the surface profile measurements is smaller when compared to those estimated from the strain data; the positive curvatures are underestimated and the negative curvatures are overestimated. The figures showing data from the third year

after construction show similar trends, but in some cases, the curvatures calculated based on strain data is not consistent in the three directions (longitudinal, diagonal, and transverse). In such cases, the trends observed are similar to those observed during the previous years, with some exceptions.

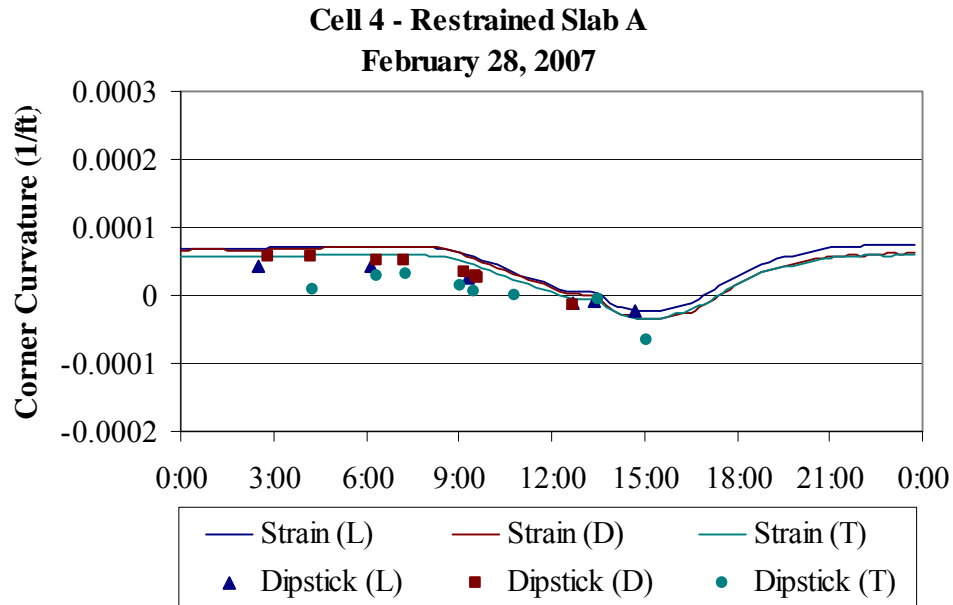


Figure 5.52. Curvature estimated using surface profiles and vibrating wire gages for restrained Slab A during the winter of 2007.

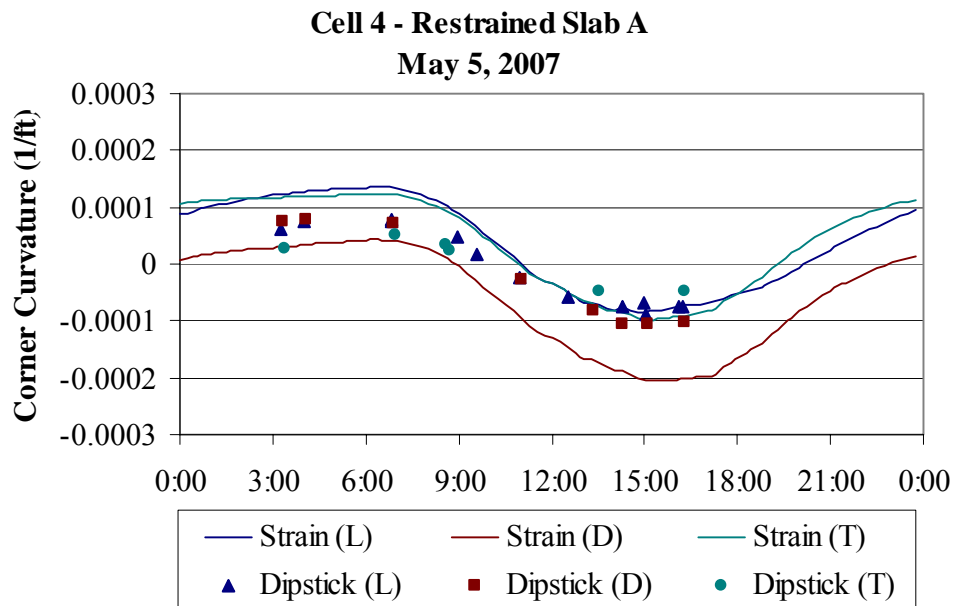


Figure 5.53. Curvature estimated using surface profiles and vibrating wire gages for restrained Slab A during the spring of 2007.

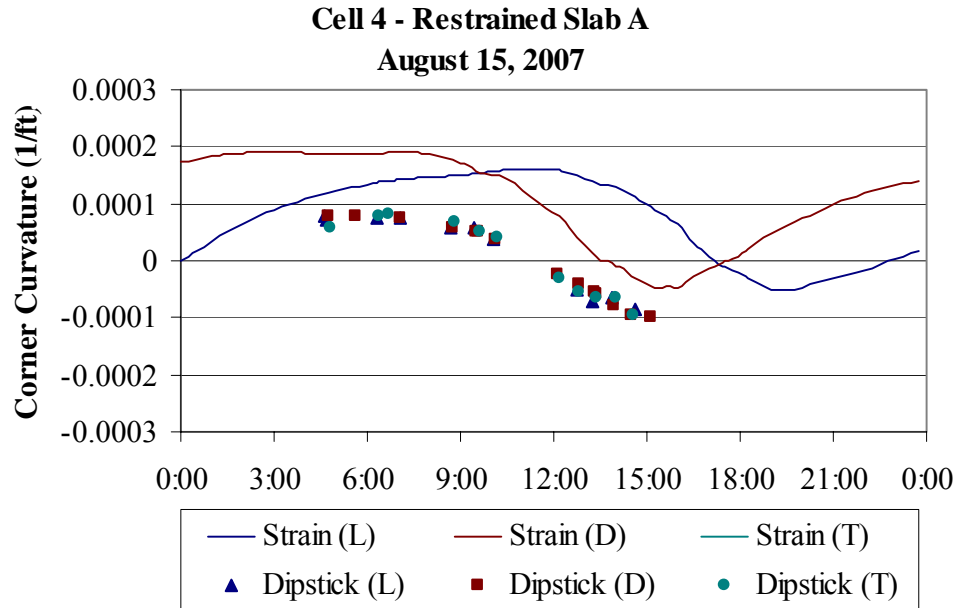


Figure 5.54. Curvature estimated using surface profiles and vibrating wire gages for restrained Slab A during the summer of 2007.

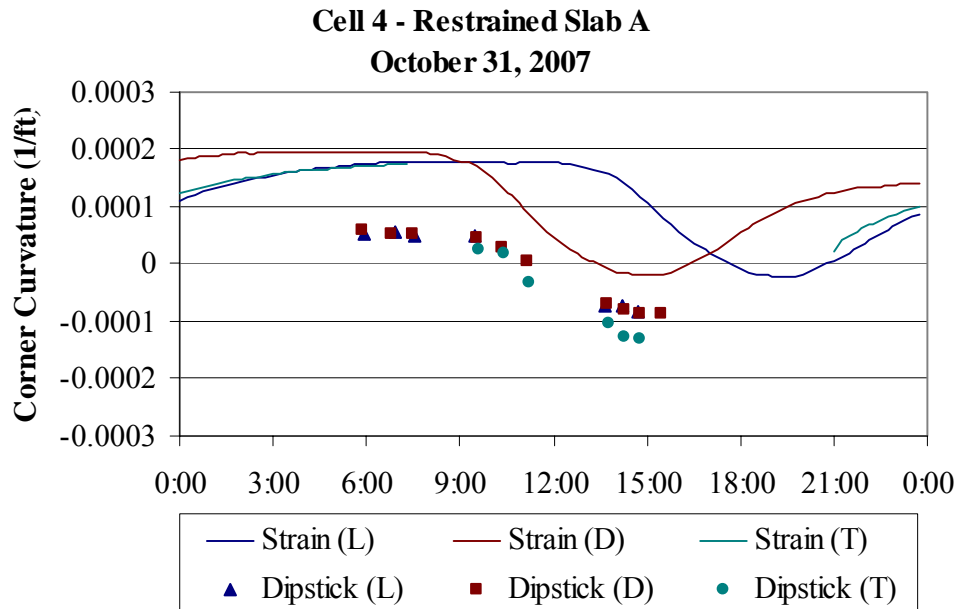


Figure 5.55. Curvature estimated using surface profiles and vibrating wire gages for restrained Slab A during the fall of 2007.

The curvature estimated using the two methods is different because of the different components that are accounted for when using each method. Slab curling and warping is due to several factors, including the following: daily and seasonal variations in temperature,

seasonal variations in moisture and the presence of a built-in construction gradient. The response of the slab to these different factors is highly affected by concrete material properties such as coefficient of thermal expansion, drying shrinkage, creep and elastic modulus. In addition, the response of the slab is also highly affected by factors that reduce the slab movement, which include: slab self-weight, friction at the slab/base interface and restraints along the transverse and longitudinal joints.

Estimating the slab curvature based on strain gage data takes into account the variations in temperature and moisture conditions, the built-in construction gradient, as well as factors affecting the slab movement such as concrete shrinkage and slab restraining conditions. However, the slab curvature estimated based on the surface profile measurements does not take into account all these factors. As previously mentioned in section 5.5.0, for each Dipstick test date, the surface profiles are zeroed to a profile representing the built-in construction gradient. This establishes that the slab is flat when the temperature gradient is equal to the built-in gradient.. This is not entirely true because it does not take into account the effect of moisture changes on concrete drying shrinkage over time.

The majority of the drying shrinkage that will occur throughout the life of the slab will occur within the first couple of years after casting. Upon rewetting, concrete expands to reverse a portion of the drying shrinkage but some of the shrinkage that occurs on first drying is irreversible. The main factors that affect the reversible portion of drying shrinkage are the seasonal climatic conditions [15]. As a result, the difference in slab curvature as estimated from the two methods can be attributed to the effects of drying shrinkage of concrete.

The difference between the curvatures estimated from the strain data and those estimated from the surface profile measurements were calculated for every profile measured during every outing. The differences for the restrained slabs are presented in Figure 5.56 for the 3-year period following construction. The figure shows that, with the exception of the spring 2007 data, the calculated differences are mostly positive indicating that the curvature based on the strain data are in general larger than the curvature based on the surface profile measurements. This implies that the surface profile measurements underestimate the slab curvature. The figure also shows that the difference in curvatures is not constant throughout the 3-year period, and a distinct trend of variation cannot be clearly detected. This implies that the drying shrinkage at the slab surface is increasing with time. As previously shown in

chapter 2 and section 5.5.1, the concrete moisture is decreasing over the three-year period. After construction, moisture was at 80 percent in the top two in, 95 percent at mid-depth and 100 percent in the bottom half of the slab, and after three years, the moisture was 60 to 65 percent in the top portion of the slab and 81 percent in the bottom portion of the slab. Similar trends were observed for the curvatures of the restrained slabs in the longitudinal and transverse directions.

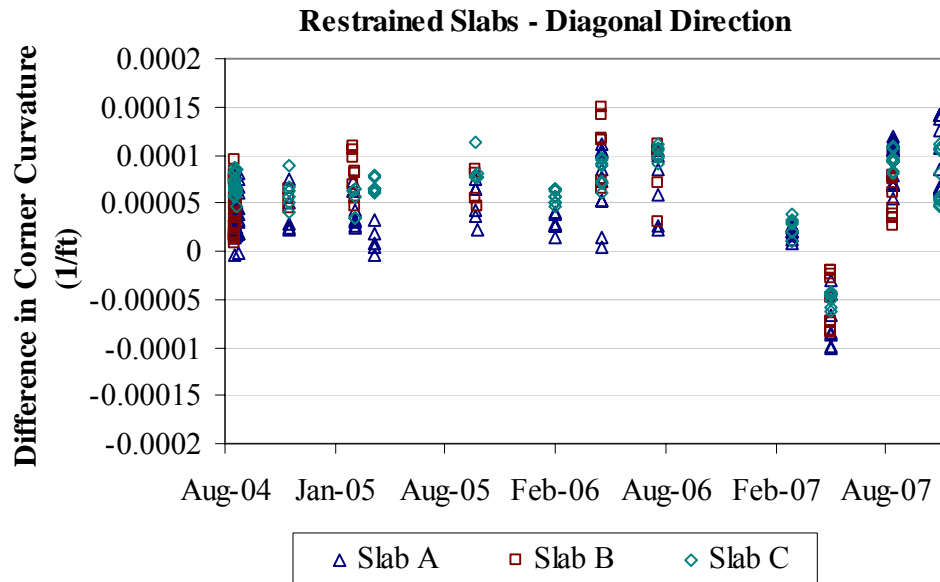


Figure 5.56. Difference in slab curvature for the restrained slabs in the diagonal direction.

Moreover, the differences indicate a scatter in the data for every test day. This is most likely due to differences in the restraining conditions along the slabs. For example, it is highly possible that the dowel bars or tie bars get slightly shifted from their original position during construction, indicating that the same exact restraining conditions are not replicated for the three slabs. Also, the joint cracking pattern will potentially have an effect on the crack widths at the transverse joints. Joints that cracked first were wider than the joints that cracked later.

5.6.2. Unrestrained Slabs

Similar to the procedure followed for the restrained slabs, the curvature estimated based on the strain data and the surface profile data for unrestrained Slab A is presented in Figure 5.57 and Figure 5.58. This data is for the summer and fall 2007 data collection outings. The curvatures provided in the figures are estimated based on strain data collected

from sensors in the corner of the slab adjacent to the lane/shoulder joint and in the longitudinal, diagonal and transverse directions. The curvature estimated based on the Dipstick data is based on the surface profiles measured at the slab corner adjacent to the lane/shoulder joint in the same three directions. The same trends that were observed for the restrained slabs are also observed for the unrestrained slabs. The curvature estimated based on the strain data is greater than that for the surface profiles. As expected, the curvatures show a decrease during the early hours of the day and an increase during the early hours of the night. This is consistent with the peak positive curvature (upward), which occurs in the early morning hours, and the peak negative curvature (downward), which occurs in the late afternoon/early evening.

Appendix F also includes a full set of figures comparing curvature estimated using the surface profiles to those using the strain gages, for unrestrained slabs A, B and C, for the second and third years after construction (seven data collection outings). The observed trends are similar to those for the restrained slabs. All the figures showing data collected from the first two years after construction show that the curvature estimated from the surface profiles is shifted downward compared to the curvatures obtained from the strain gages. While, the figures showing data from the third year after construction show similar trends, with some exceptions. Based on the discussion presented previously, the difference in slab curvature estimated from the two methods can be attributed to the effects of moisture on the drying shrinkage of concrete.

The difference between the curvature estimated from the strain data and that estimated from the surface profile measurements were calculated for every profile measured during every seasonal outing. The differences for the unrestrained slabs are presented in Figure 5.59 for the three-year period following construction. With the exception for the differences calculated for the summer 2004 season, the figure shows that the calculated differences are positive indicating that the curvature based on the strain data is larger than the curvature based on the surface profile measurements. This implies that the surface profile measurements underestimate the slab curvature. The figure also shows that the difference in curvature increases throughout the three-year period. The trends are similar to those of the restrained slabs. Similar trends were observed for the curvatures of the unrestrained slabs in the longitudinal and transverse directions.

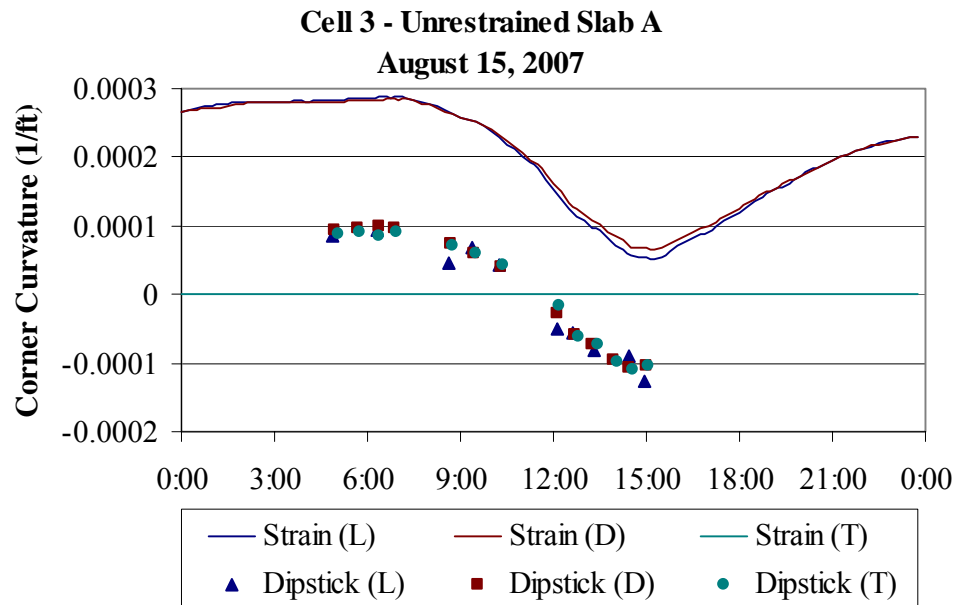


Figure 5.57. Curvature estimated using surface profiles and vibrating wire gages for unrestrained Slab A during the summer of 2007.

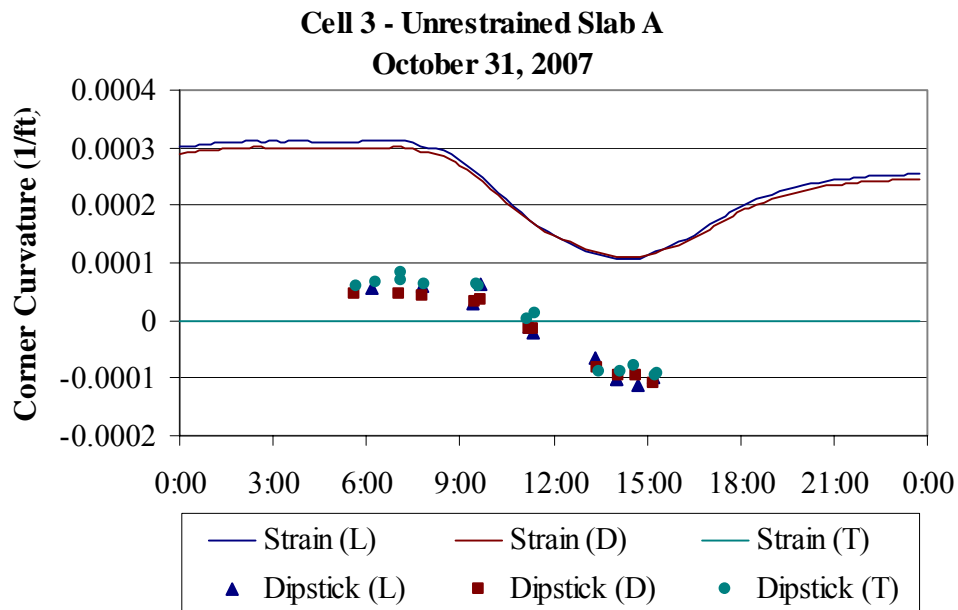


Figure 5.58. Curvature estimated using surface profiles and vibrating wire gages for unrestrained Slab A during the fall of 2007.

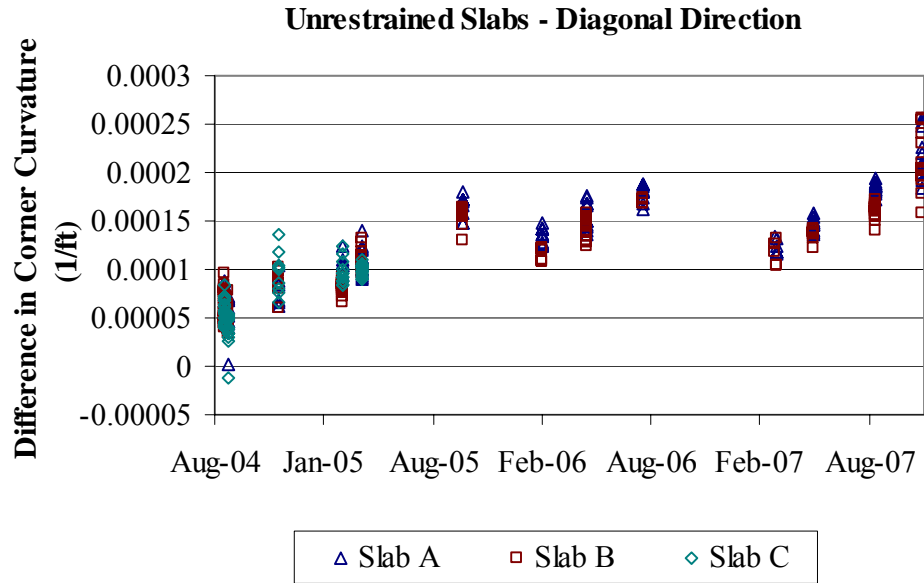


Figure 5.59. Difference in slab curvatures for the unrestrained slabs in the diagonal direction.

In addition, Figure 5.59 does not show a wide range of scatter in the differences calculated for every test day for the unrestrained slabs, when compared to Figure 5.56 showing the same data for the restrained slabs. This indicates that the unrestrained slabs exhibit a more repeatable pattern of behavior. Part of this might be attributed to the fact that the measured curvatures are higher for the unrestrained slab.

5.6.3. Comparison between Restrained and Unrestrained Slabs

The differences in corner curvatures are compared for both cases of restrained and unrestrained slabs, as presented in Figure 5.60. The differences are smaller for the restrained slabs, confirming the previous findings that the presence of the restraint at the edge is counteracting the curvature produced by the moisture gradient. In addition, the rate of increase in the differences over time for the unrestrained slabs is on average five times larger than that of the restrained slabs. This also indicates that the restraint provided by the dowel bars along the joint is significantly affecting the slab curvature.

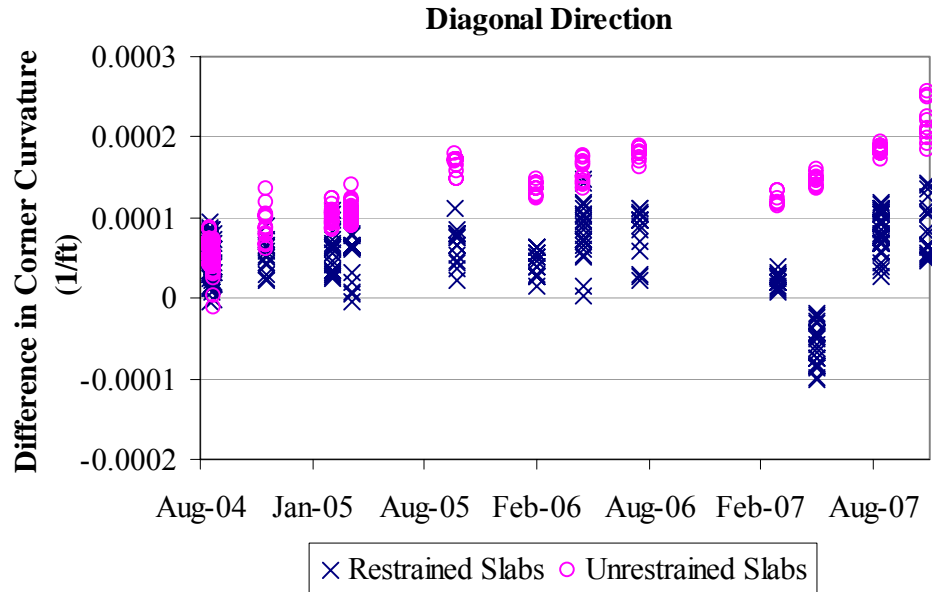


Figure 5.60. Comparison between the difference in corner curvatures for the restrained and unrestrained slabs in the diagonal direction.

5.6.4. Summary

The slab curvature was estimated based on the strain measurements and the seasonal surface profiles. The curvatures estimated based on both sets of data were compared for the Dipstick test dates during the first three years after paving. It was found that the curvatures estimated from the surface profiles and the strain data follow the same daily trends, with curvature estimated using the surface profiles shifted downward compared to the curvature obtained from the strain gages. This difference can be attributed to the effects of moisture on the drying shrinkage of concrete.

The difference between the curvatures estimated from the strain data and those estimated from the surface profile measurements were compared for every profile measured during every seasonal outing. The calculated differences are mostly positive indicating that the surface profile measurements underestimate the slab curvatures. In addition, the difference in curvature is increasing throughout the three-year period, implying that the drying shrinkage at the slab surface is increasing with time.

5.7.0. Conclusions

An analysis of the static strain and pressure sensors showed that the slabs undergo daily and seasonal changes in shape due to environmental loading (changes in temperature and moisture). Surface profile measurements were performed seasonally and confirmed the results of the static data analysis. A summary of these findings is provided below.

The total strain is negative throughout the first three years after construction indicating that the restrained and unrestrained slabs are in a state of contraction. Moisture and creep induced strain does not fluctuate much throughout the different seasons, while the temperature induced strain exhibits a larger amount of fluctuation. This is due to the fact that the moisture and creep conditions do not vary much throughout the year when compared to the temperature conditions, which are continuously changing. During the fall and summer, temperature has the greatest effect on strain; while during the winter and spring, moisture and creep induced strain is larger than temperature induced strain.

Strain data from the restrained and unrestrained slabs was compared to investigate the different restraint conditions. It was found that the bond provided at the slab/base interface reduces the slab surface strain by 11 to 22 percent, the presence of dowel bars reduces the strain by 21 percent, and the longer slab length with adjacent slabs reduce the strain by 6 to 21 percent. However, it was found that the presence of tie bars does not affect the strain at the slab surface. The dowel and tie bars restrict upward and downward movement at the outer portion of the slab, and cause the majority of the curvature to develop in the central portion of the slab. This results in smaller slab curvature for the restrained slab. Surface profile measurements confirmed the findings based on the static strain measurements. The unrestrained slabs exhibit larger movements at the sides and the restrained slabs exhibit larger movements at midslab. Due to the restraint provided by the dowels at the transverse joint, the curvature is reduced at the end of the slab and the stress at the edge is increased.

The slab curvatures determined based on the strain measurements were compared to those obtained based on the seasonal surface profiles, for the Dipstick test dates during the first three years after paving. It was found that the curvature estimated using the surface profiles and the strain data follow the same daily trends, with curvature estimated using the surface profiles shifted downward compared to the curvatures obtained from the strain gages. This difference can be attributed to the effects of moisture on the drying shrinkage of

concrete. The difference between the curvatures estimated using both methods showed that the calculated differences are mostly positive indicating that the surface profile measurements underestimate the slab curvature. In addition, the difference in curvature is increasing throughout the three-year period, implying that the drying shrinkage at the slab surface is increasing with time.

An analysis of the static pressure cells showed that the pressure on top of the base increases with increasing equivalent linear gradient at the edge and decreases with increasing equivalent linear gradient at midpanel. Pressure on top of the base also increases when the base freezes. Freezing of the base layers results in an increase in the modulus of subgrade reaction of the layers under the PCC slab. As moisture and temperature gradients develop in the slab, the underlying layers have a higher resistance to loads, and therefore, larger pressures are exerted on the base layers.

CHAPTER 6: PAVEMENT RESPONSE TO APPLIED LOADS

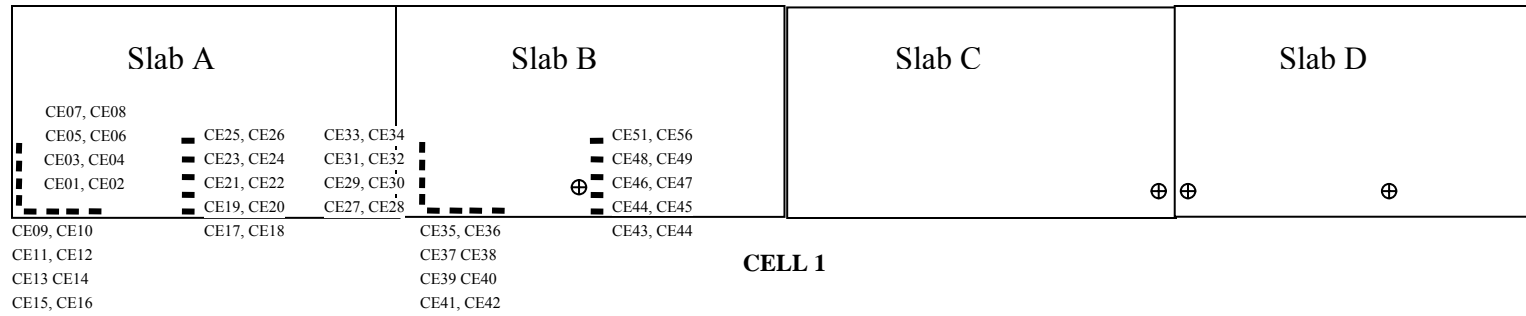
6.1.0. Introduction

Static strain and deflection measurements were used to define the pavement response to applied loads. Load testing with both the FWD and trucks with known axle weights and configurations was performed four times a year so seasonal and long-term effects could be characterized. A summary of the testing results for the first three years after construction is provided below following a brief description of the type and location of the dynamic sensors installed in the restrained (Cell 1) and unrestrained (Cell 2) test sections.

6.2.0. Dynamic Sensor Locations

Figure 6.1 outlines the locations of the dynamic strain gages and dynamic pressure cells located in Cells 1 and 2. Longitudinally oriented gages are located in the wheelpath at the center of the slab and in the slab corner along the edge. The transversely oriented dynamic strain gages measure strains in the wheelpath near the transverse joints. As shown in Figure 6.1 the sensor layout for the unrestrained cell (Cell 2) is almost identical to that of the restrained cell (Cell 1). Figure 6.2 shows the typical dimensions of the sensor layout. The top sensor is half an inch below the surface of the slab and the bottom sensor is located 11.5 in below the slab surface.

Instrumented Restrained Panels (Dowel and Tie Bars)



Instrumented Unrestrained Panels (No Dowel and Tie Bars)

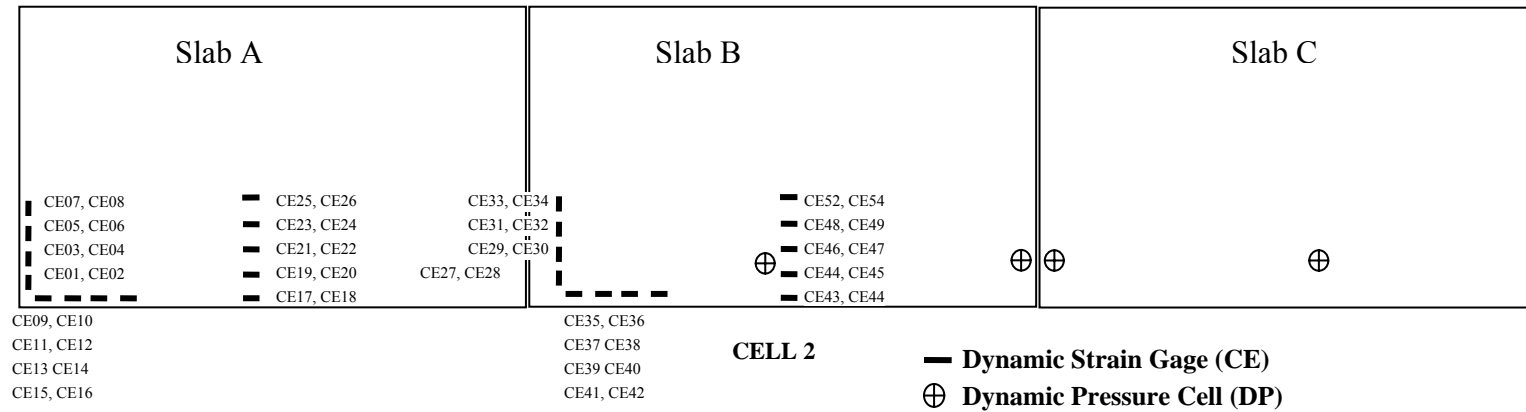


Figure 6.1. Sensor layout for Cell 1 and Cell 2.

Representative Dimensions – Cells 1 and 2

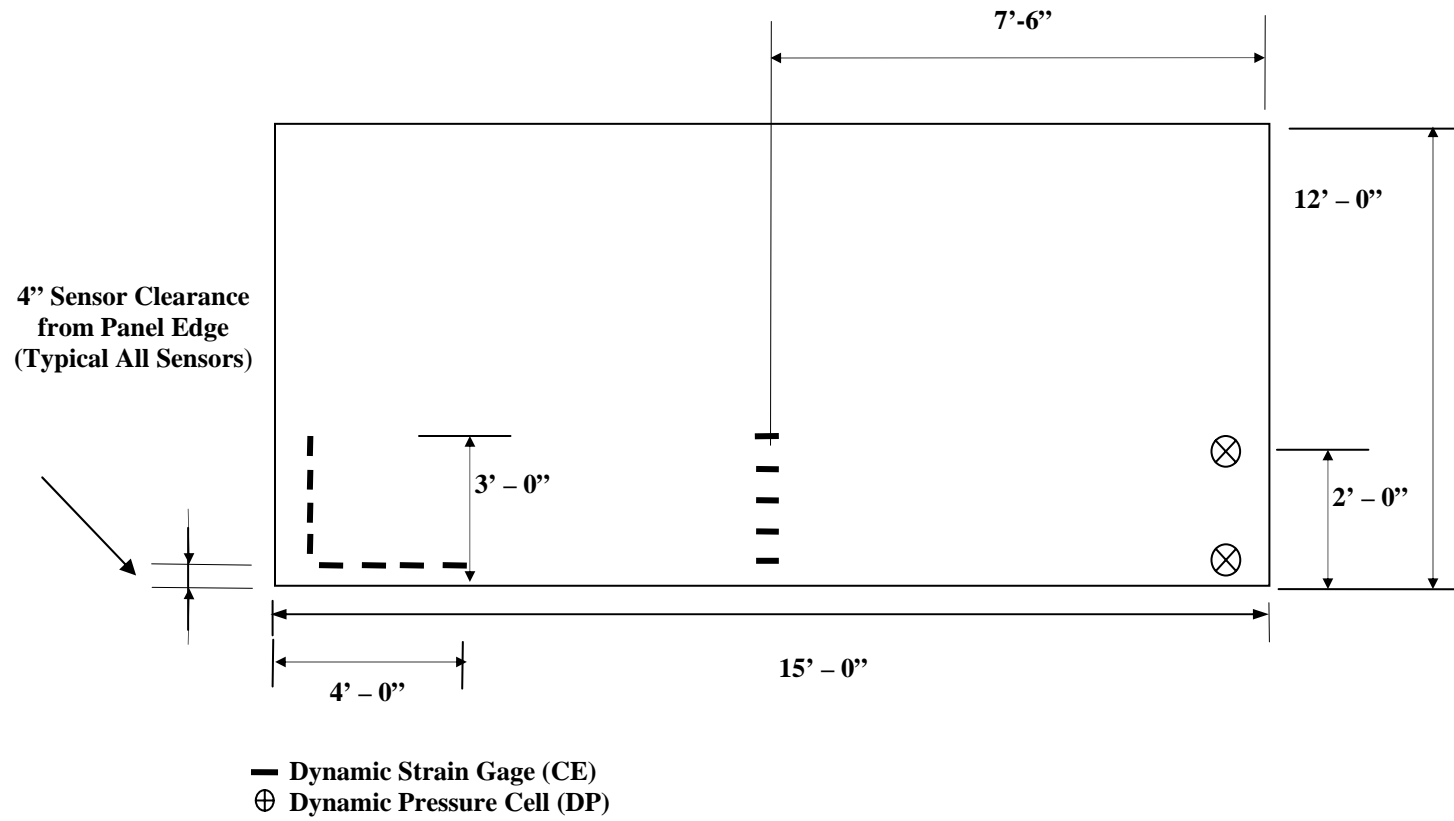


Figure 6.2. Typical dimensions of dynamic strain gages, and dynamic pressure cells.

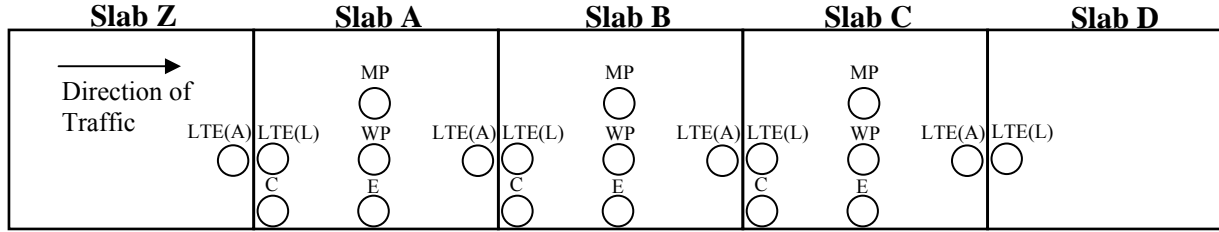
6.3.0. Falling Weight Deflectometer Testing

PennDOT provided a KUAB FWD and operator who performed all FWD testing. The device used is shown in Figure 6.3. The FWD is used to apply a dynamic impulse load to the pavement surface and the resulting deflections are recorded at various distances away from the applied load. These FWD drops were performed at various locations on the pavement, such as the corner, midpanel, and edge. The FWD test locations are provided in Figure 6.4. Each test consisted of three drops, one at each of 9,000, 12,000, and 16,000 lbs load levels.

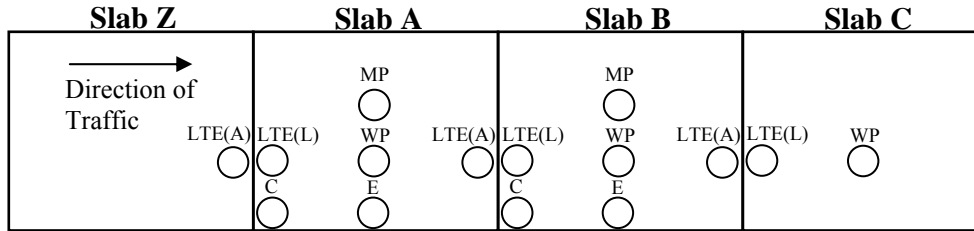


Figure 6.3. Falling weight deflectometer used on S.R. 22.

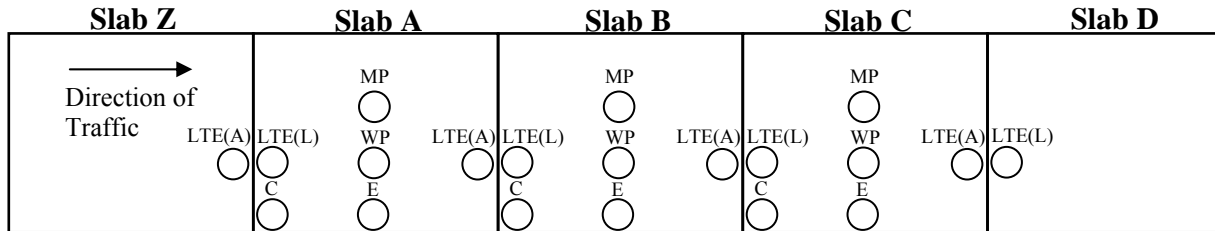
The FWD data was used to evaluate joint performance, the support conditions under the corner of the slab, deflection basins at known locations, and to backcalculate layer moduli. Strain data was also collected in conjunction with the FWD testing. FWD testing was performed each season for a total of three years after paving. Winter testing was performed in March of 2005 and February of 2006 and 2007, spring testing was performed in April of 2005, 2006, and 2007 and summer testing took place in October of 2005, July of 2006 and August of 2007. In October 2005, the temperatures were unseasonably warm and the conditions were considered more representative of typical summer conditions than typical fall conditions, therefore testing during this time was considered summer testing. Although this test outing is representative of summer conditions, the amount of daylight and the angle of the sun are not typical of summer conditions. Fall testing was performed in October of 2004, November of 2006 and October of 2007.



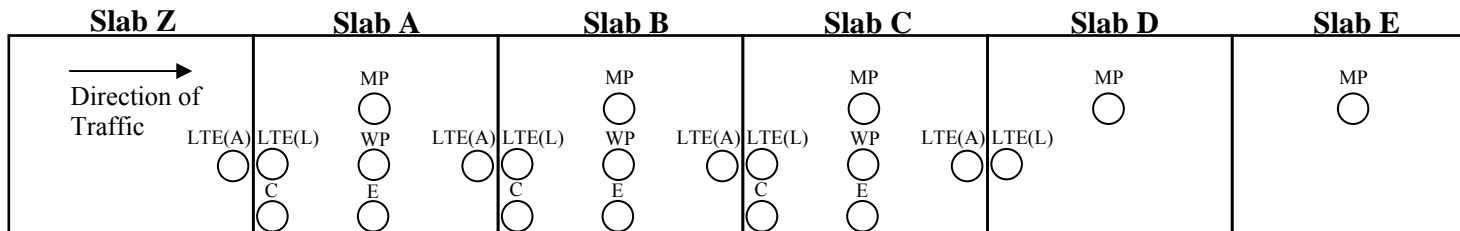
CELL 1



CELL 2



CELL 3



CELL 4

Note: Panels are in the outside lane or truck lane

LEGEND:

MP – Midpanel
 LTE(A) – Load Transfer Efficiency (Approach)
 LTE(L) – Load Transfer Efficiency (Leave)
 WP – Wheelpath
 C – Corner
 E - Edge

Figure 6.4. FWD test locations.

6.4.0. Concrete Temperature and Moisture Distributions during FWD Testing

The characterization of the temperature and moisture distributions throughout the PCC slab during FWD testing is critical in analyzing pavement response. The weighted average temperature, equivalent linear temperature gradient, and temperature of the ATPB affect the shape and critical stress and deflection locations in the slab. Therefore, characterization of joint performance, support conditions under the corner of the slab, deflection basins at known locations, and to backcalculate layer moduli can not be performed without defining the climatic conditions during testing.

A variation in moisture throughout the depth of the slab also affects the shape (See chapter 2) of the slab and therefore the location of the critical stress and peak deflections. Therefore, characterization of this difference in moisture content throughout the depth of the slab is also beneficial in the analysis of the pavement to FWD loadings.

6.4.1. Concrete Temperature Distribution

Table 6.1, shown below, provides the variation of the weighted average temperature in the slab at midpanel during FWD testing. The largest variation in temperature was experienced during the spring of 2006 and 2007 with a range of 16 °F. The smallest variation in temperature was experienced during the first three test outings in the fall of 2004, and winter and spring of 2005. All results are typical of seasonal temperature variation.

Table 6.1. Seasonal temperature variation during FWD testing.

Season	Testing Time	Weighted Average Temperature, °F		
		Maximum	Minimum	Average
Fall 2004	9:45 am - 12:30 pm	58	53	55
Winter 2005	8:00 am - 11:45 am	34	29	31
Spring 2005	7:30 am - 10:30 am	55	52	53
Summer 2005	12:30 pm - 3:15 pm	77	72	75
Winter 2006	12:30 pm - 4:00 pm	45	39	42
Spring 2006	8:30 am - 1:00 pm	75	59	65
Summer 2006	10:00 am - 2:00 pm	96	83	89
Fall 2006	11:00 am - 2:00 pm	52	43	47
Winter 2007	11:00 am - 2:00 pm	37	28	32
Spring 2007	11:00 am - 2:00 pm	75	59	66
Summer 2007	11:30 am - 2:00 pm	84	73	78
Fall 2007	10:30 am - 2:00 pm	58	46	53

Figure 6.5 through Figure 6.16 show the variation in weighted average temperature and equivalent linear temperature gradient of the slab, and the mid-depth temperature of the ATPB during testing periods. Summary statistics of all test seasons are discussed below. Each season for all three years was combined to determine the overall range and average values of each factor.

During the fall testing periods the weighted average temperature in the PCC slab ranged between 43 and 58 °F with an average of 52 °F. The equivalent linear temperature gradient of the PCC slab varied between -0.86 and 1.17 °F/in during fall testing, with an average of 0.31 °F/in. The temperature at middepth of the ATPB ranged between 46 and 58 °F with an average of 52 °F. See Figure 6.5 through Figure 6.7. As shown in the proceeding figures, the weighted average temperature of the concrete varied minimally during the three test outings. The fall testing encountered the least variation in weighted average temperature with an average range of 15 °F.

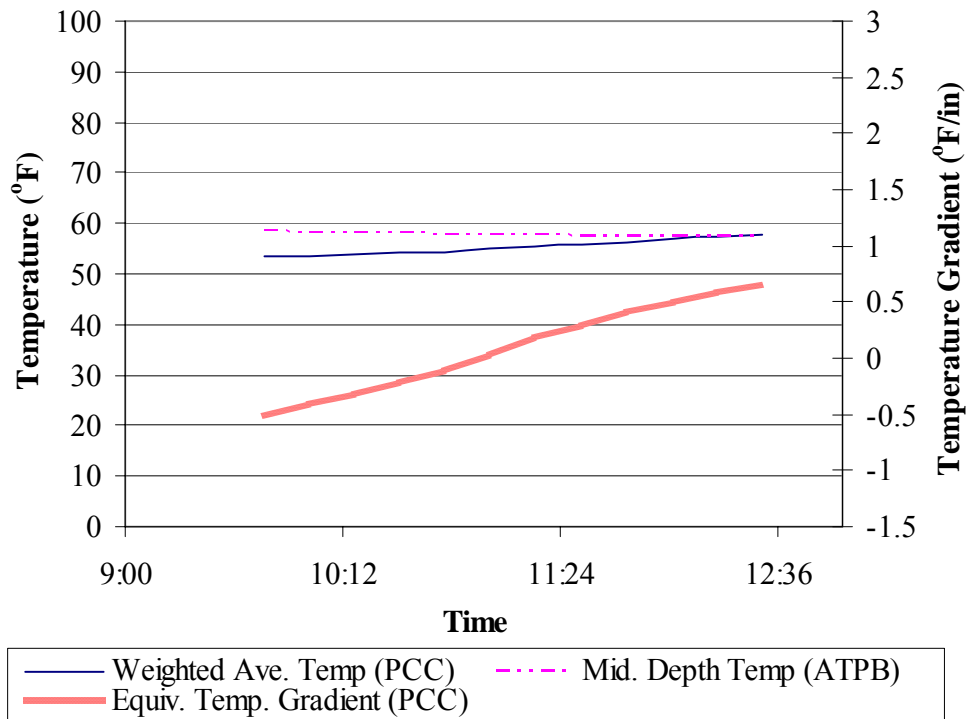


Figure 6.5. Midpanel temperature conditions during FWD testing performed in the fall of 2004.

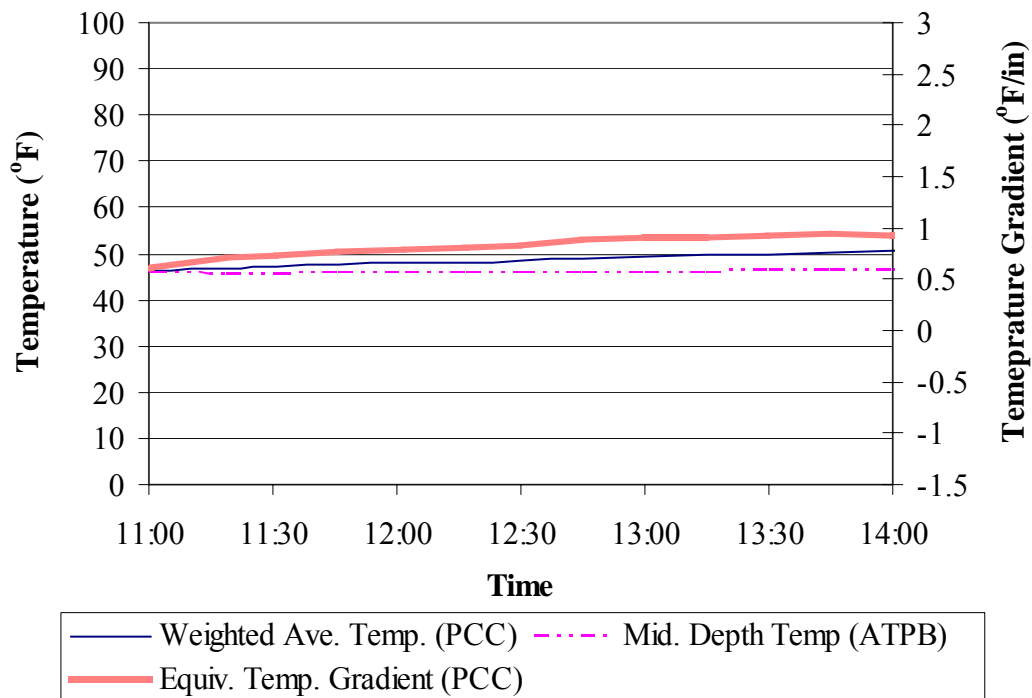


Figure 6.6. Midpanel temperature conditions during FWD testing performed in the fall of 2006.

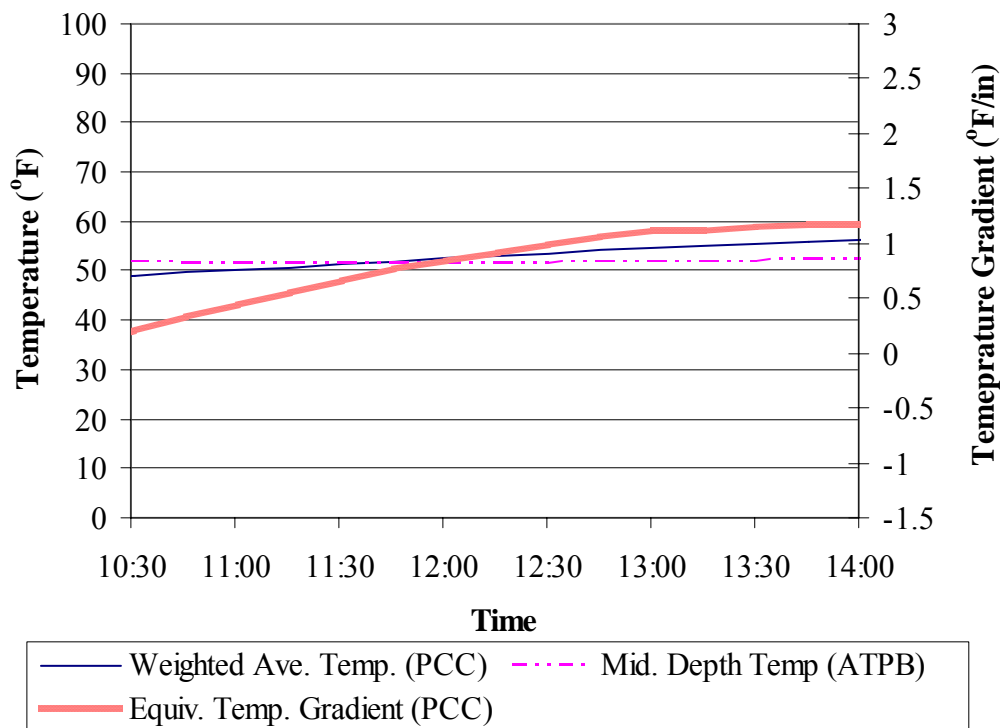


Figure 6.7. Midpanel temperature conditions during FWD testing performed in the fall of 2007.

Figure 6.8 through Figure 6.10 present the temperature of the concrete and ATPB and gradient of the slab during winter testing. The weighted average temperature for the winter testing periods ranged between 28 and 45 °F with an average of 35 °F. The equivalent linear temperature gradient varied between -0.61 and 1.34 °F/in with an average of 0.30 °F/in. The mid-depth temperature of the ATPB, measured during the FWD winter periods, fluctuated between 29 and 41 °F with an average of 35 °F. Additionally, the smallest variations in temperature gradients were experienced during winter testing, with an average range of 1.95 °F/in.

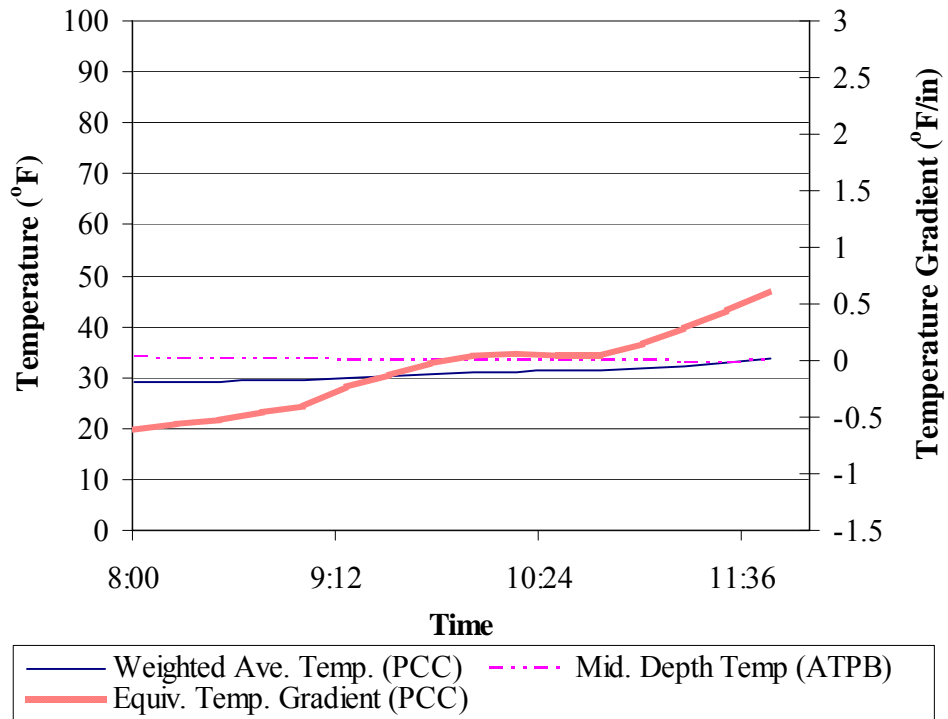


Figure 6.8. Midpanel temperature conditions during FWD testing performed in the winter of 2005.

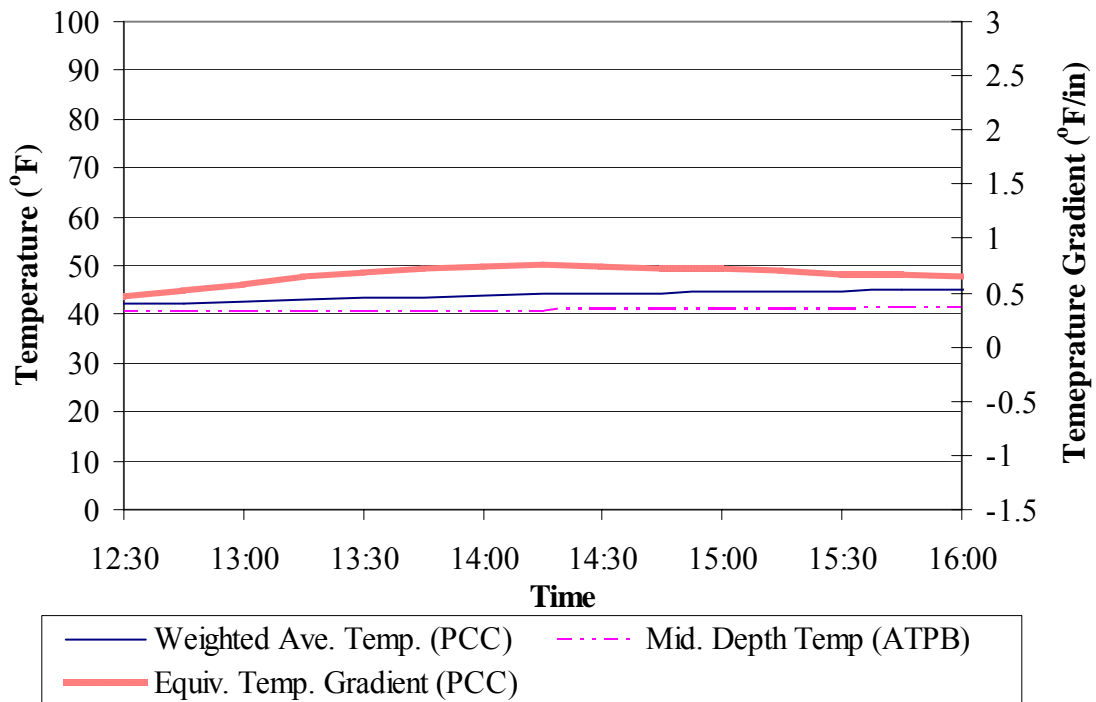


Figure 6.9. Midpanel temperature conditions during FWD testing performed in the winter of 2006.

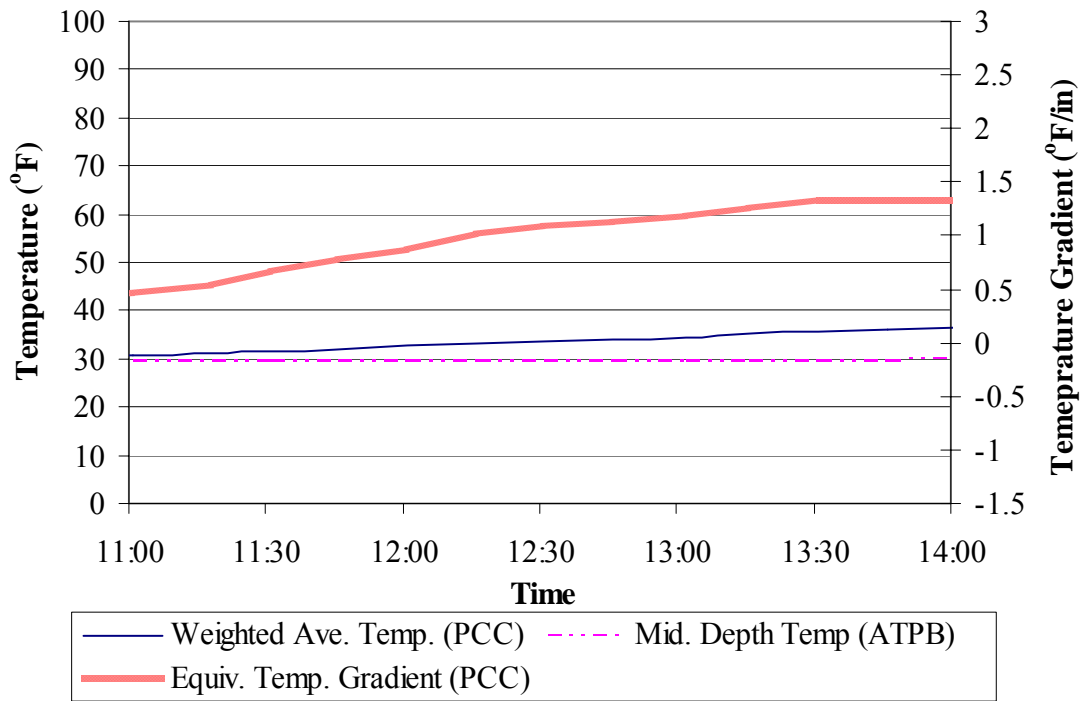


Figure 6.10. Midpanel temperature conditions during FWD testing performed in the winter of 2007.

During the spring test periods, the weighted average temperature in the PCC slab ranged between 52 and 75 °F with an average of 61 °F. The equivalent linear temperature gradient of the PCC slab varied between -0.85 and 2.28 °F/in during spring testing, with an average of 0.71 °F/in. The temperature at middepth of the ATPB ranged between 53 and 64 °F with an average of 58 °F. As shown in Figure 6.11 through Figure 6.13, the equivalent linear temperature gradient of the concrete varied significantly during spring testing. The largest average variation in temperature gradients was experienced with an average range of 3.14 °F/in. Although the temperature of the concrete varied significantly, throughout the depth of the slab during the spring, the ATPB remained relatively constant and showed the lowest variation with an average range of 11°F.

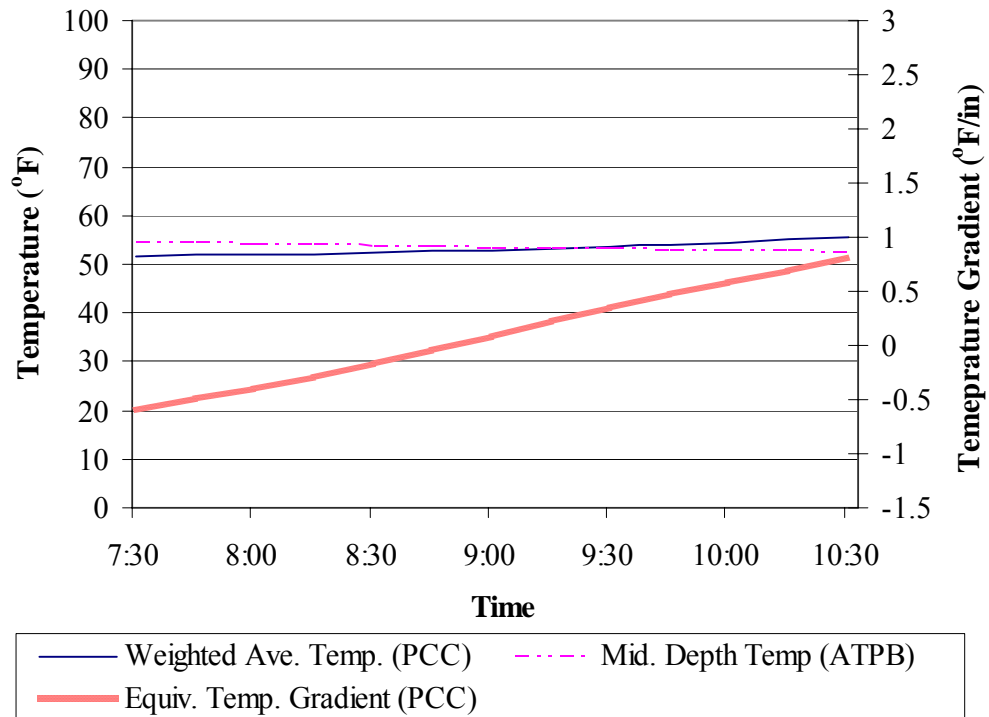


Figure 6.11. Midpanel temperature conditions during FWD testing performed in the spring of 2005.

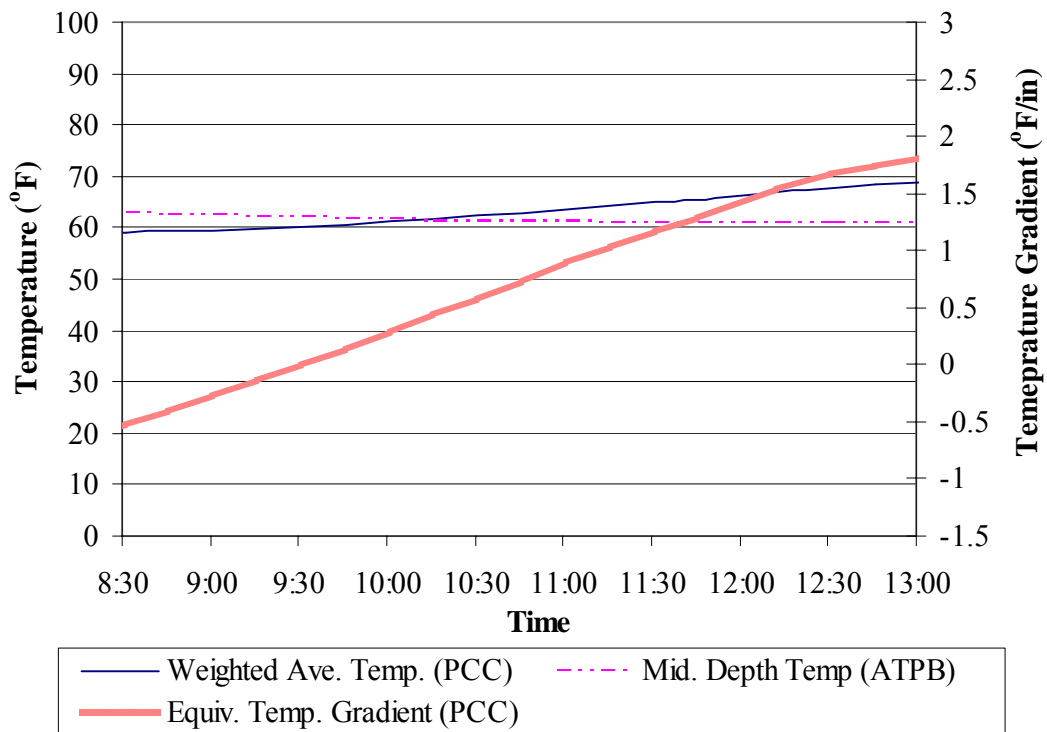


Figure 6.12. Midpanel temperature conditions during FWD testing performed in the spring of 2006.

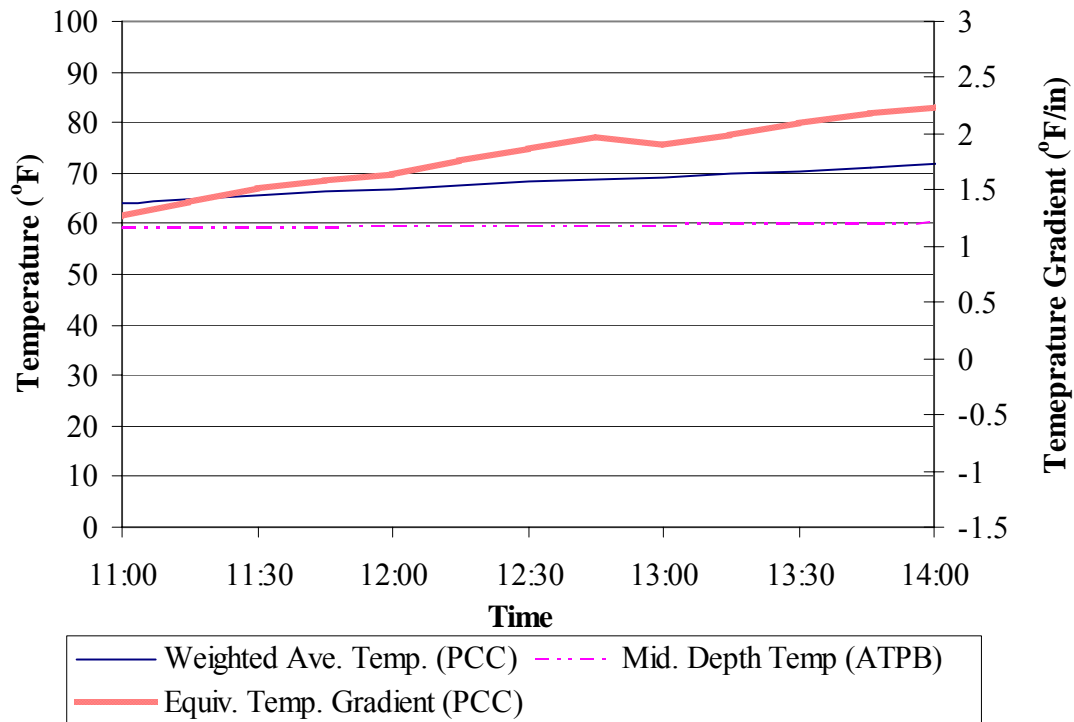


Figure 6.13. Midpanel temperature conditions during FWD testing performed in the spring of 2007.

The weighted average temperature for the summer testing periods ranged between 72 and 96 °F with an average of 80 °F. The equivalent linear temperature gradient varied between -0.73 and 2.07 °F/in with an average of 1.03 °F/in. The mid-depth temperature of the ATPB, measured during the FWD summer periods, fluctuated between 69 and 86 °F with an average of 76 °F. As shown in Figure 6.14 through Figure 6.16, the weighted average temperature of the concrete varied considerably during summer testing. The largest average variation in weighted average temperature of the concrete was experienced with an average range of 24 °F. Additionally, the ATPB also experienced the largest variation during summer testing with an average range of 18°F.

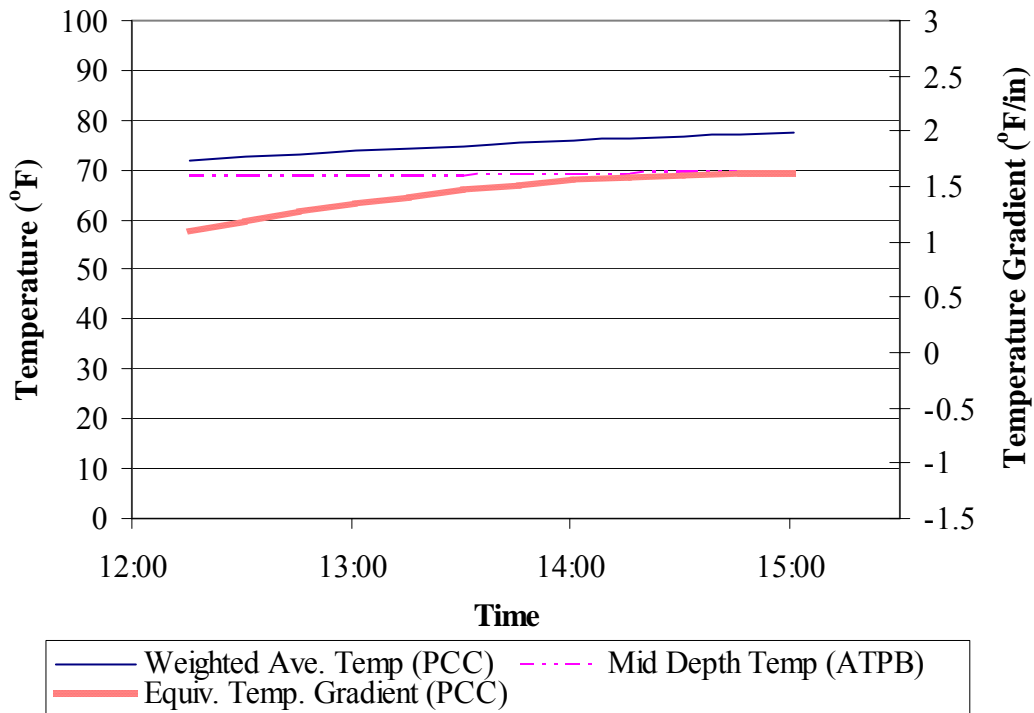


Figure 6.14. Midpanel temperature conditions during FWD testing performed in the summer of 2005.

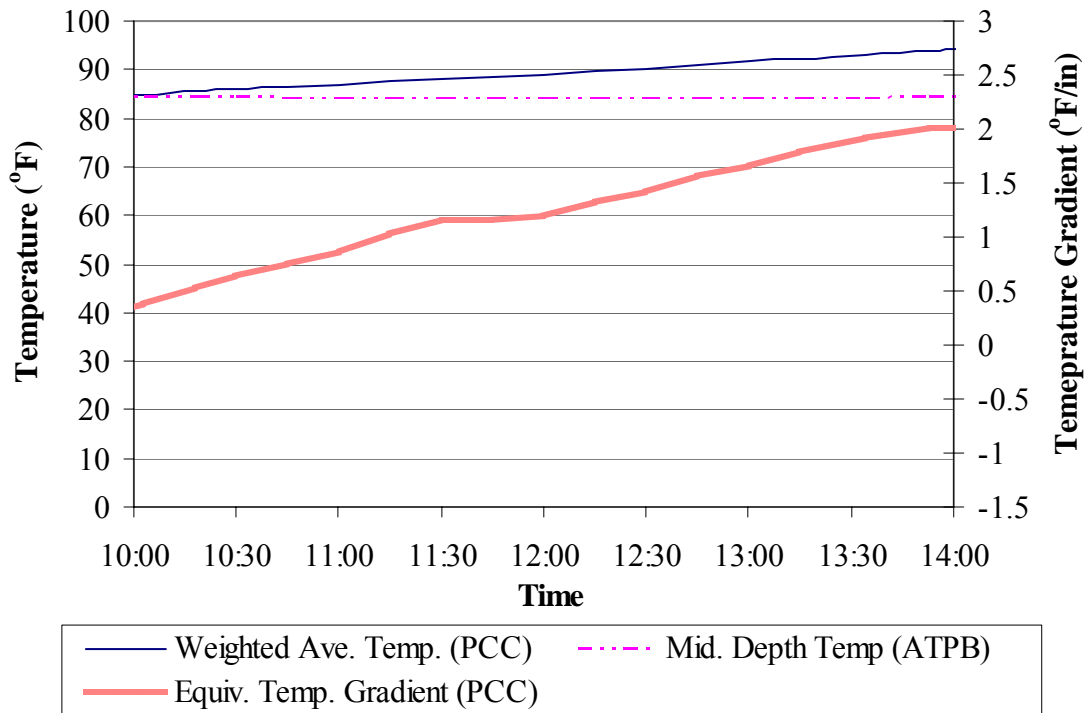


Figure 6.15. Midpanel temperature conditions during FWD testing performed in the summer of 2006.

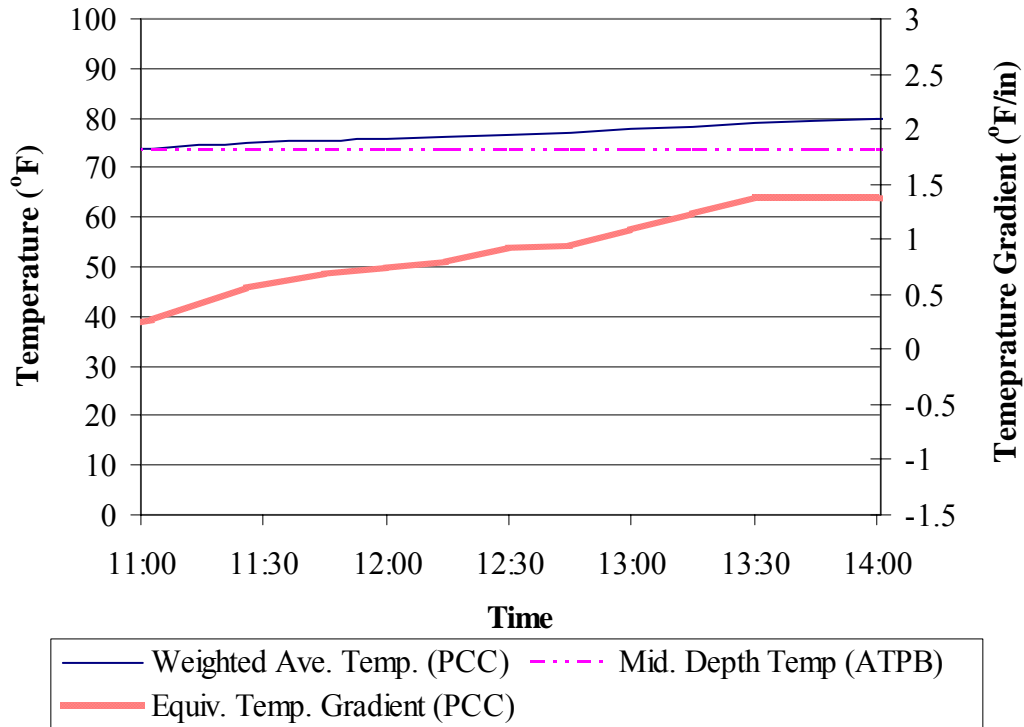


Figure 6.16. Midpanel temperature conditions during FWD testing performed in the summer of 2007.

6.4.2. Concrete Moisture Distribution

Figure 6.17 and Figure 6.18, shown below, present the variation in relative humidity throughout the PCC slab at the midpanel and edge during FWD testing. As previously discussed, the two factors affecting the response of the slab to an applied load are the change in moisture content throughout the depth of the slab (slab shape) and the change in the average relative humidity across the slab profile (crack width).

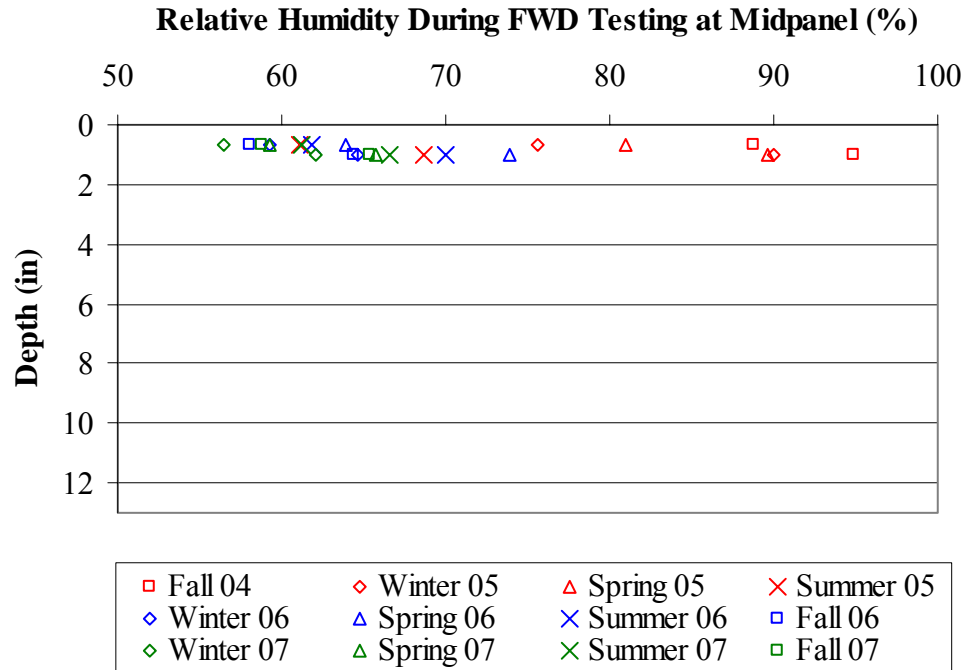


Figure 6.17. Midpanel moisture distribution throughout the PCC slab during FWD testing.

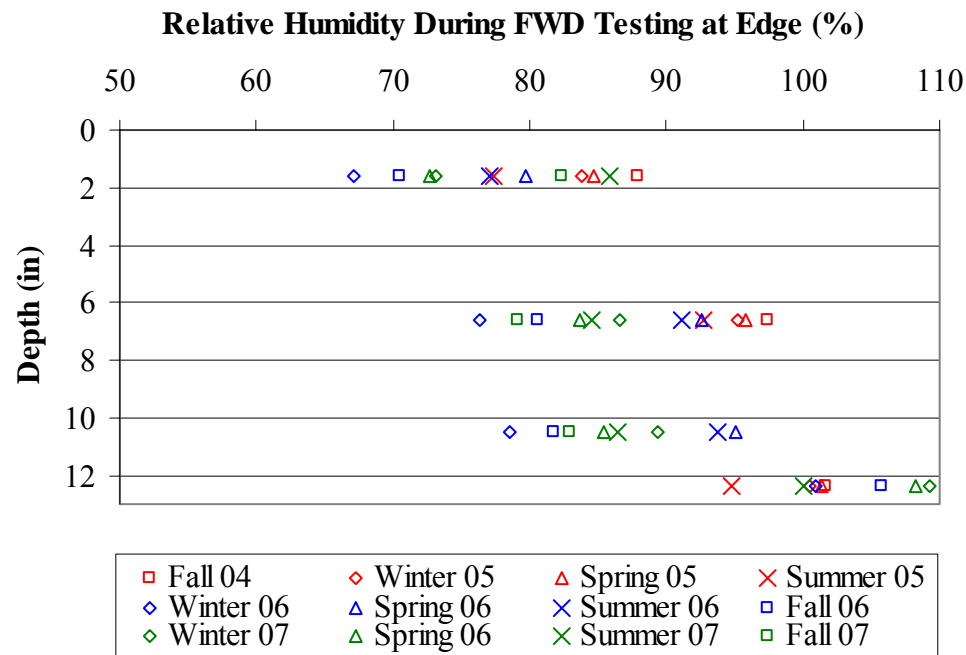


Figure 6.18. Edge moisture distribution throughout the PCC slab during FWD testing.

First the uniform change in the moisture throughout the depth of the slab will be discussed since it will affect the width of the crack at the joint. The uniform moisture content throughout the depth of the slab has continually declined since the construction of the pavement. Starting out at 100 percent relative humidity immediately after construction the relative humidity throughout the slab dropped to approximately 95 percent the first year after construction, 93 percent the second year and 83 percent the third year. The crack width at the joint will continue to increase with time until the relative humidity within the slab stabilizes.

Next, the change in moisture content throughout the depth of the slab will be discussed. The relative humidity near the slab surface fluctuates more over time compared to other depths within the slab since it is exposed to the ambient climatic conditions. The lowest measured relative humidity, within these 2 in, was found during the winter with an average of 75 percent. The largest was measured during the summer and fall with an average of 80 percent. The spring relative humidity was between the winter and summer and had an average of 79 percent. Beyond the top two inches, the relative humidity was found to be approximately 76 percent and above during all test periods. At mid-depth of the slab, the relative humidity varied between 80 and 100 percent and the bottom of the slab remained saturated. Although moisture levels above 100 percent were measured, this unrealistic and most likely indicates condensation on the sensor. The largest change in relative humidity throughout the depth of the slab was experienced during the winter of 2007 with a difference of 32 percent between the top and bottom of the slab. The smallest variation in relative humidity was experienced during the first test outing in the fall of 2004, with a 12 percent difference. The largest variation in relative humidity throughout the depth of the slab was found during the winter with an average difference of 25 percent. The fall and spring seasons had the smallest variation in relative humidity with an average of 21 percent. The summer relative humidity fell between these two values with an average difference in relative humidity of 23 percent.

6.5.0. Joint Performance

Joint performance was evaluated by calculating the load transfer efficiency in the wheelpath using the equation provided below.

$$LTE = \frac{\delta_{ul}}{\delta_l} \times 100\% \quad (\text{Equation 6-1})$$

LTE = Load transfer efficiency, percent

δ_{ul} = Deflection measured on the unloaded side of the joint

δ_l = Deflection measured on the loaded side of the joint

Figure 6.19 shows the load transfer efficiencies and the stations at which they were measured throughout the first three years after paving.

At higher slab temperatures, the concrete expands and the joints lock-up. This allows the aggregate interlock provided by the surface texture at the crack face to engage to better facilitate transferring loads from one side of the joint to the other. Likewise, when the slab temperatures are low and the slab contracts, the joints open and aggregate interlock will not effectively transfer load from one side of the joint to the other. Therefore, determination of temperature at the time of testing is imperative for the analysis of load transfer efficiency. The range of slab temperatures present during testing are summarized in Table 6.1. Figure 6.5 through Figure 6.16 presents the weighted average slab temperature, the temperature in the middle of the ATPB and the temperature gradients that were present throughout each test period.

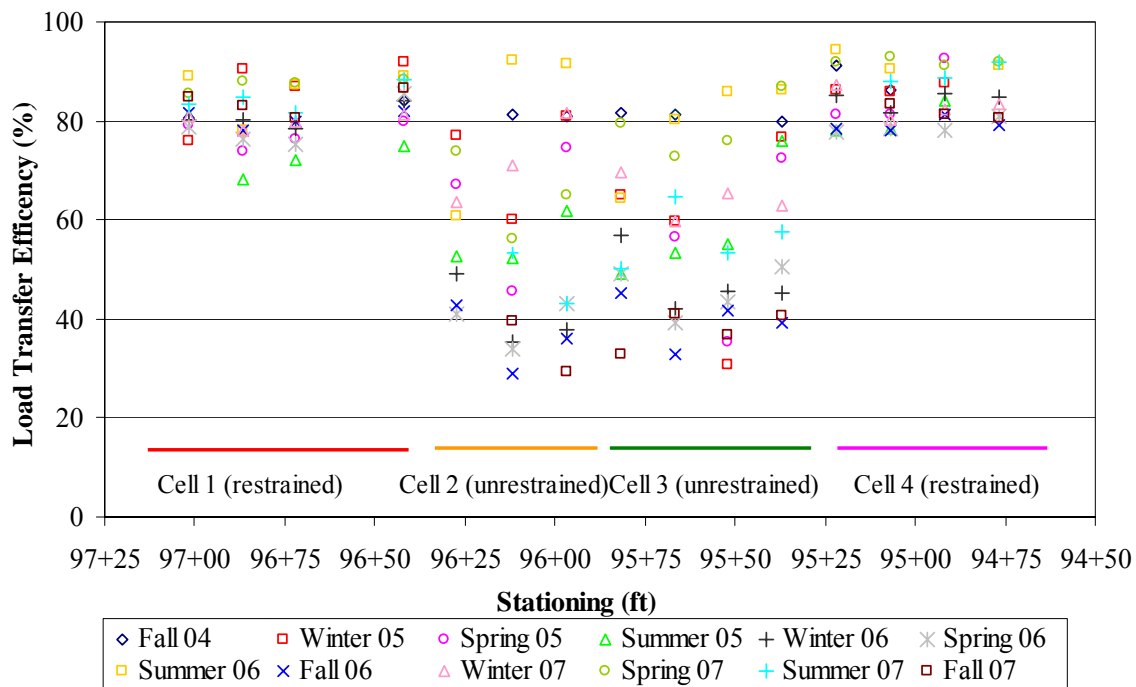


Figure 6.19. Load transfer efficiencies measured for each cell.

The initial load transfer efficiencies were measured on October 11, 2004, between 9:45 AM and 12:30 PM just shortly after the section was constructed. The load transfer efficiencies ranged between 80 and 95 percent for both the doweled and undoweled joints. The final load transfer efficiency was measured on October 30, 2007, between 10:30 am and 2:00 pm. The load transfer at this time ranged between 29 and 87 percent for both joint types. Therefore, in the three years since project construction the load transfer efficiency has decreased approximately 30 percent. This indicates significantly decreased performance in the joints of the Smart Pavement during the three years period.

During the first year, the fall testing produced the highest load transfer efficiency for both the doweled and undoweled joints. This was expected since this was the first test period after construction. The lowest values were measured during the summer for both joint types. This was unexpected; typically LTE is highest in the summer due to small joint openings from increased temperatures. All of the undoweled joints and six of the seven doweled joints tested fell below 80 percent in the first year. This was anticipated for the undoweled joints but the load transfer efficiencies for the doweled

joints should be higher this short of a time after construction. The load transfer efficiencies ranged between 68 and 92 percent throughout the first year for the doweled joints and between 38 and 89 percent for the undoweled joints.

The load transfer efficiencies ranged between 75 and 94 percent for the doweled joints and between 28 and 92 percent for the undoweled joints throughout the second year of testing. The load transfer efficiencies measured for the doweled joints during the spring were the lowest with an average of 80 percent and the highest were measured during the summer with an average of 87 percent. This is only an 8 percent difference which indicates an insignificant difference between the seasonal averages. The undoweled joints had the lowest load transfer efficiencies during the fall and the highest during the summer.

The undoweled joints, which rely on aggregate interlock to provide load transfer, experienced joint openings of approximately 0.046 in during fall testing. Typically, load transfer efficiency decreases significantly once joint openings exceed 0.03 in, therefore the increased joint openings during fall testing attributes to the lower measured load transfer efficiencies.

At the end of the second year all of the undoweled joints fell below 70 percent, with five of the seven falling below 40 percent load transfer efficiency during some data collection periods. This is significant because the Federal Highway Administration (FHWA) suggests restoring joints that have less than 70 percent load transfer to prevent further damage to the pavement [32]. This emphasizes the need for load transfer devices for long-term performance. Figure 6.19 indicates that some of the joints would exhibit an acceptable level of load transfer efficiency if the perfect conditions were present, such as, high pavement temperatures, small crack width, and good support conditions. As previously discussed, when slab temperatures are high the joints lock-up and load transfer efficiency increases. As previously discussed in section 5.3.2, the undoweled joints start locking up at 96 °F. During one FWD test outing, slab temperatures were high enough for the joints to lock-up, however, for the majority of test outings slab temperatures were much lower than 96 °F with an average slab temperature during FWD testing of 57 °F. Therefore, it can be concluded that undoweled pavements in a climate similar to that found in Pennsylvania will have low load transfer capabilities for a large portion of each

day and for several months in the year. This is regardless of the aggregate interlock surface texture available at the slab face for load transfer. The reason some of the slabs were undoweled in this pavement is so the effects of restraint conditions could be characterized in this study

The load transfer efficiencies measured during the third year ranged between 78 and 93 percent for the doweled joints and between 29 and 87 for the undoweled joints. The load transfer efficiencies measured during the fall for the doweled and undoweled joints was the lowest and was highest during the spring. These results are not typical of the Pennsylvania region. During the spring and fall seasons, increased moisture levels cause loss of support in the supporting layers of the pavement structure. The spring testing was performed on April 30, 2007. Typically the period of increased moisture and decreased support occurs at the beginning of the spring season when the pavement structure thaws. This period would have occurred prior to the end of April and the increased support conditions could be contributing to the increased load transfer experienced during the spring 2007 testing, along with the higher pavement temperatures.

As previously mentioned, the FHWA suggests restoring joints that have less than 70 percent load transfer efficiency. The majority (larger than 50 percent) of the undoweled joints experienced LTEs below 70 percent in three of the four test outings in 2007. During the spring testing only two of the seven joints fell below 70 percent. During the fall, which was the final test period, four of seven undoweled joints fell below 40 percent load transfer with some joints experiencing approximately 20 percent load transfer. The results of the analysis of load transfer during the third year further validates the statement that undoweled joints in climates like Pennsylvania will experience low load transfer the majority of the year.

6.5.1. Effect of Temperature Gradients on Load Transfer Efficiency

The calculated load transfer efficiency was plotted against equivalent linear temperature gradient for both doweled and undoweled joints to see if any trends existed. Figure 6.20 shows this relationship for one of the slabs of the unrestrained cell. The weighted average temperature of the slab at the time of testing is provided next to each data point.

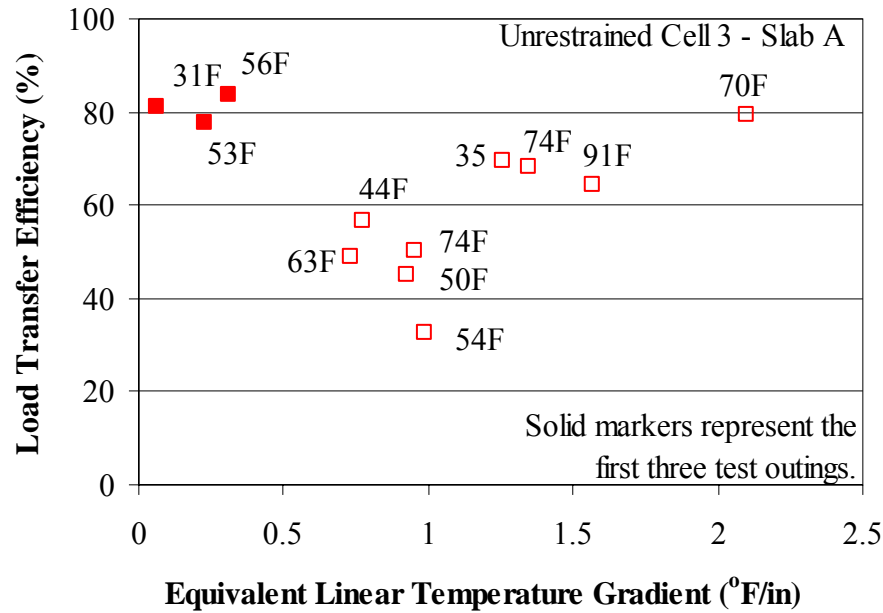


Figure 6.20. Relationship between load transfer efficiency and equivalent linear temperature gradient of the unrestrained Cell 3.

The load transfer measured for the unrestrained slabs is very dependent on the temperature gradient present at the time of testing. Load transfer efficiency increases as the gradient increases (downward slab curvature) and decreases when negative gradients (upward slab curvature) are present.

Positive gradients develop in the afternoon when the temperature of the slab is higher. These higher temperatures tend to increase the load transfer efficiency because the cracks at the joints close as the slab expands. However, Figure 6.20 shows that when testing is performed on a slab at times when the average temperature of the slab is the same but the gradients are different, then the load transfer efficiency will be different. For example, in Figure 6.20 two separate tests were performed when the average slab temperature ranged between 70°F and 74°F yet the load transfer efficiency for these tests ranged between 68 and 80 percent. The largest positive gradient corresponds with the largest load transfer efficiency and the largest negative gradient corresponds with the lowest load transfer efficiency.

The relationship between LTE versus gradient was not observed in the first three points in Figure 6.20. These first three points (shown by solid squares) were measured during the first three FWD testing periods; therefore time could be a factor. An analysis

of the load transfer efficiency and age of the pavement was carried out to determine if age was the contributing factor. The first three testing periods, performed within the first 10 months after construction, experienced only a 6 percent variation in load transfer efficiency. The joint exhibited high load transfer efficiency during the first winter and spring even though the pavement temperatures were lower.

The transverse joints cracked the first night after paving. Repeated loading was required to “break” the slab loose. As Figure 6.21 indicates, the slab did not “break” into more discrete, finite segments until after the first spring testing. This trend was observed in all of the unrestrained slabs but varied in the amount of time it took for the slabs to break loose. This most likely can be attributed to the large difference in initial crack widths observed the first 24 hours after paving. The comparisons of load transfer efficiency to pavement age for all the unrestrained slabs can be found in appendix G.

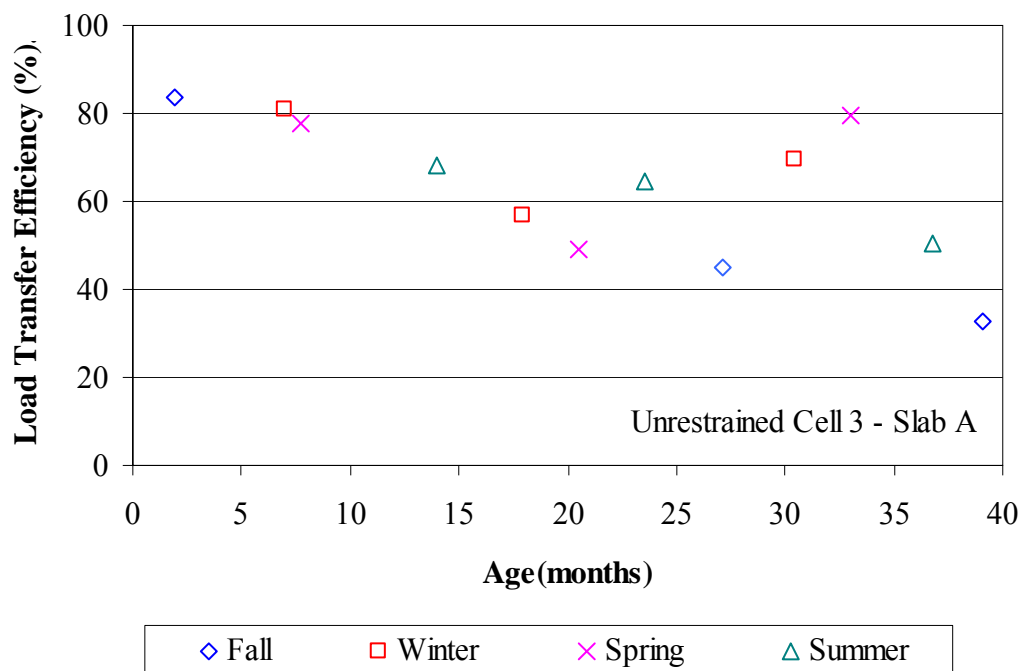


Figure 6.21. Relationship between load transfer efficiency and age of the pavement for the unrestrained Cell 3.

It was observed in Figure 6.22, that when the average slab temperature is 62°F, with a small positive gradient present, the load transfer efficiency is lower by approximately 45 percent compared to when the slab temperature is 69°F and a large

positive gradient is present. Load transfer efficiency was reduced by an average of 38 percent for all of the unrestrained cells when the gradient changed from 0.5 °F/in to 2.0 °F/in at similar temperatures.

The trend of increased load transfer with increasing positive temperature gradient was seen for all of the slabs in both of the unrestrained cells. Graphs of all of the slabs can be found in appendix G. This trend, of increasing load transfer with increasing positive gradients, was also experienced in a study performed at the Mn/ROAD test facility. Vandenbossche determined that load transfer efficiencies, measured for undoweled slabs, were greatly influenced by the presence of a gradient [33].

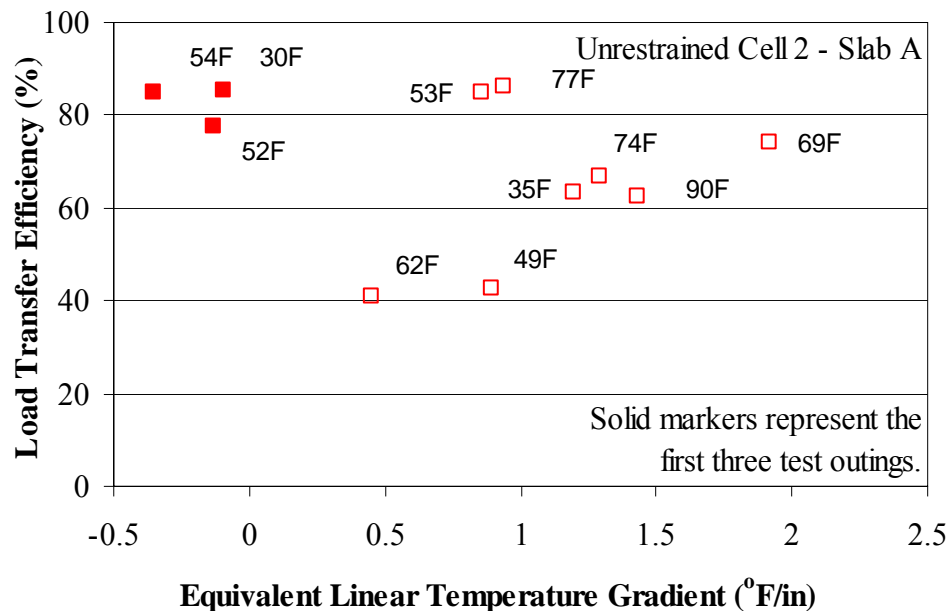


Figure 6.22. Relationship between load transfer efficiency and equivalent linear temperature gradient of the unrestrained Cell 2.

The load transfer measured for the doweled slabs was found to not be affected by temperature gradients or slab temperature, as shown in Figure 6.23. The load transfer efficiency varies between 69 and 91 percent, a 22 percent difference, while the range of gradients was large at 2.5 °F/in. This variation of 22 percent occurred over a temperature range of 61 °F. This trend, which was found in all of restrained slabs, can be seen in the figures of appendix G. This trend was also experienced in the Mn/ROAD study performed by Vandenbossche, in which doweled slabs were found to not be

affected by slab temperature or temperature gradients [33]. Additionally, in 2003 Khazonovich and Gotif found that LTE was affected by temperature differences and the resulting joint movement and slab curling in both unrestrained and restrained slabs. This supports the findings of this study and a previous study by Vandenbossche study for the restrained slabs but not the unrestrained slabs which were not affected by slab shape [34].

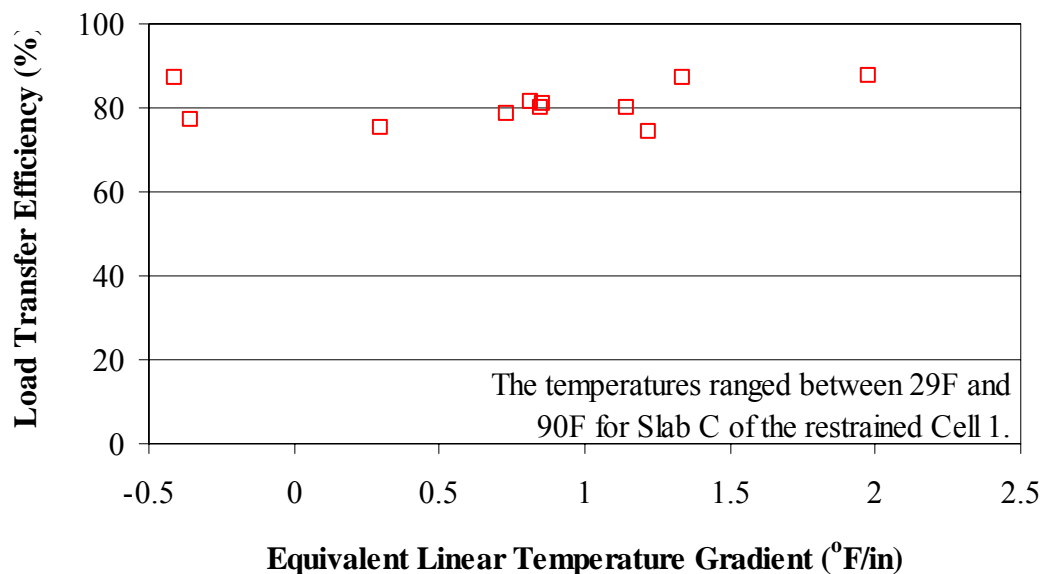


Figure 6.23. Relationship between load transfer efficiency and equivalent linear temperature gradient of the restrained Cell 1.

6.5.2. Relationship between Strain and Load Transfer Efficiency

Dynamic strain gages installed in both restrained and unrestrained slabs (Cells 1 and 2, respectively) were used to measure strains in conjunction with the FWD testing. As previously discussed, FWD testing was performed seasonally (winter, spring, summer, and fall) throughout the first three years following construction. Figure 6.24 through Figure 6.27 show the relationship between load transfer efficiency and measured strain at the top and bottom for the restrained slabs. Negative values indicate a compressive strain and positive values indicate tensile strains. These strains were linearly normalized to a 9,000 lb load. Each data point is defined in the legend according to the slab for which the data point was measured (Slab A or B). Although data was collected seasonally over the three years, excessive electronic noise and erroneous

measurements during field testing prohibited the use of some data collected and therefore, each graph does not have the same number of data points.

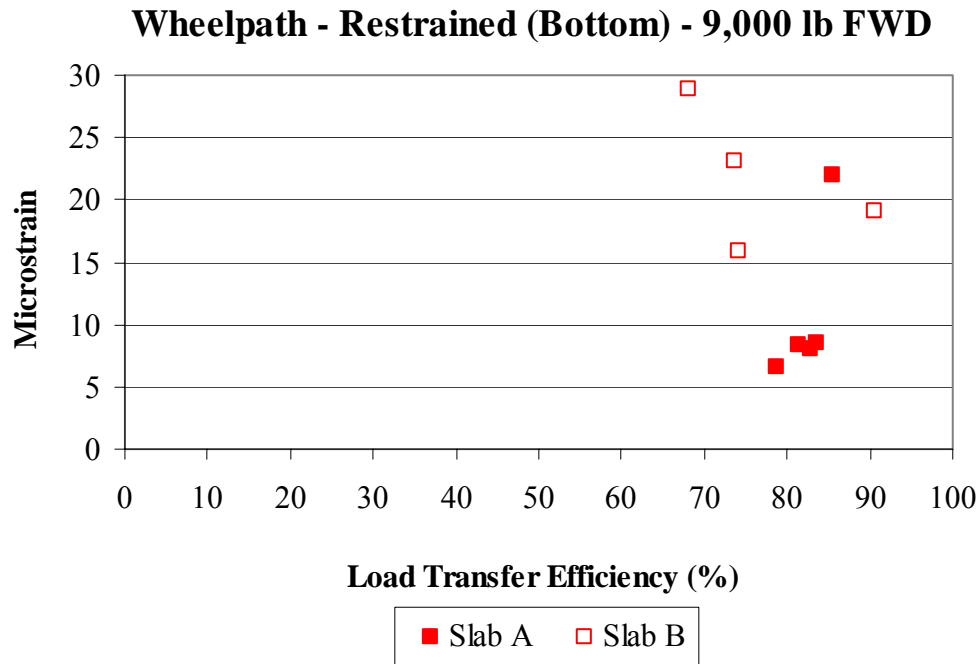


Figure 6.24. Relationship between load transfer efficiency and strain measured in the wheelpath on the bottom of the restrained slabs.

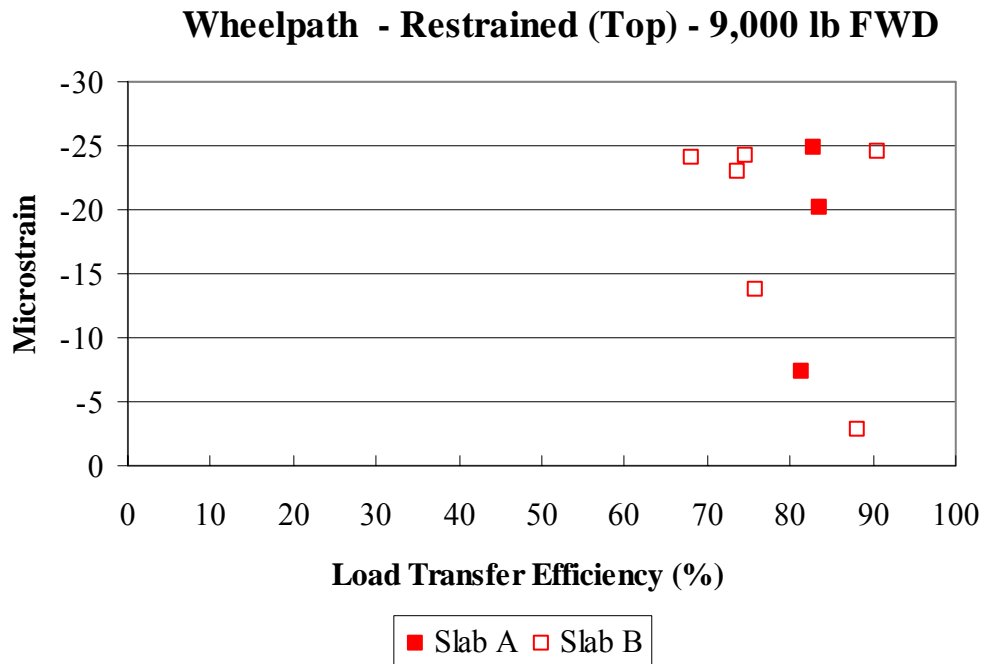


Figure 6.25. Relationship between load transfer efficiency and strain measured in the wheelpath 1 in from the surface of the restrained slabs.

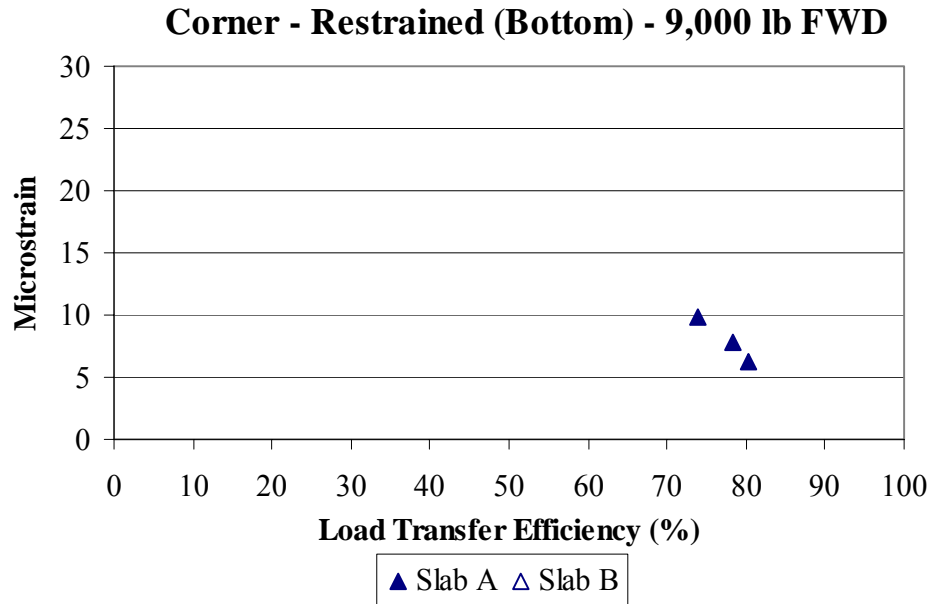


Figure 6.26. Relationship between load transfer efficiency and strain measured in the corner on the bottom of the restrained slabs.

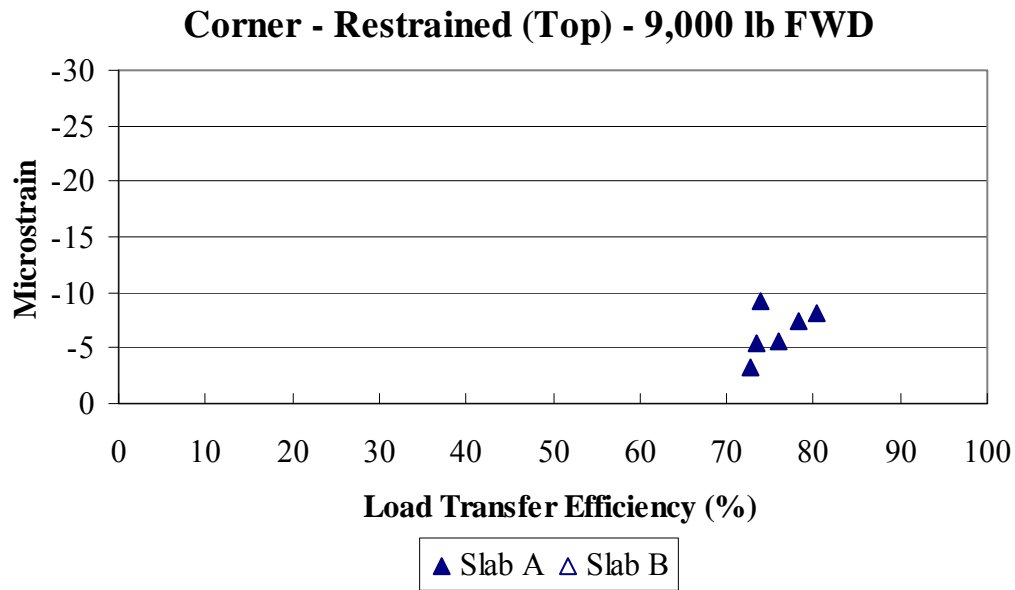


Figure 6.27. Relationship between load transfer efficiency and strain measured in the corner 1 in from the surface of the restrained slabs.

Figure 6.24 through Figure 6.27 show that strain measured along the transverse joint of the restrained slabs has no correlation to load transfer efficiency. It would be

anticipated that the strains would increase with decreasing load transfer efficiency since the loaded slab is forced to carry a larger portion of the load.

Along the transverse joint, the strain varies between 7 and 21 microstrain at the bottom of Slab A and between 6 and 29 at the bottom of Slab B. Although the strain varies drastically, there is minor variation in the load transfer efficiency with a 7 percent change in Slab A and a 22 percent variation in Slab B. Although a distinguishable relationship between LTE and strain was not experienced, there is a trend of larger variation in strain when a larger variation in load transfer efficiency is experienced. There is also less variation in the measured strains at the corner of the slab when compared to those measured in the wheelpath. This is due to the larger displacements experienced at the corner of the slabs due to temperature and moisture variation.

The relationship between microstrain and load transfer efficiency is shown in Figure 6.28 through Figure 6.31 for the unrestrained slabs. A similar trend is found for the unrestrained slabs since load transfer efficiency does not affect the magnitude of the measured strain in the restrained slabs either.

Strains measured along the transverse joint of the unrestrained slab, vary between 2 and 28 microstrain at the bottom of Slab A and between 6 and 19 in Slab B. There is a drastic variation in the measured strain and because the joints are undoweled, load transfer efficiency also varies significantly. The LTE varied approximately 44 percent in Slab A and 62 percent in Slab B. Therefore, variation in LTE was less in Slab A than Slab B. This is most likely related to the fact that the magnitude of load transfer efficiency was less for Slab B compared to Slab A. This is similar to the variation in strain observed for the restrained slabs, which varied more when there were large fluctuations in load transfer efficiency. The unrestrained slabs also exhibited a similar trend to the restrained slabs when comparing the magnitude of the strains measured in the wheelpath and corner locations. Strains measured in the corner are again less than strains measured in the wheelpath.

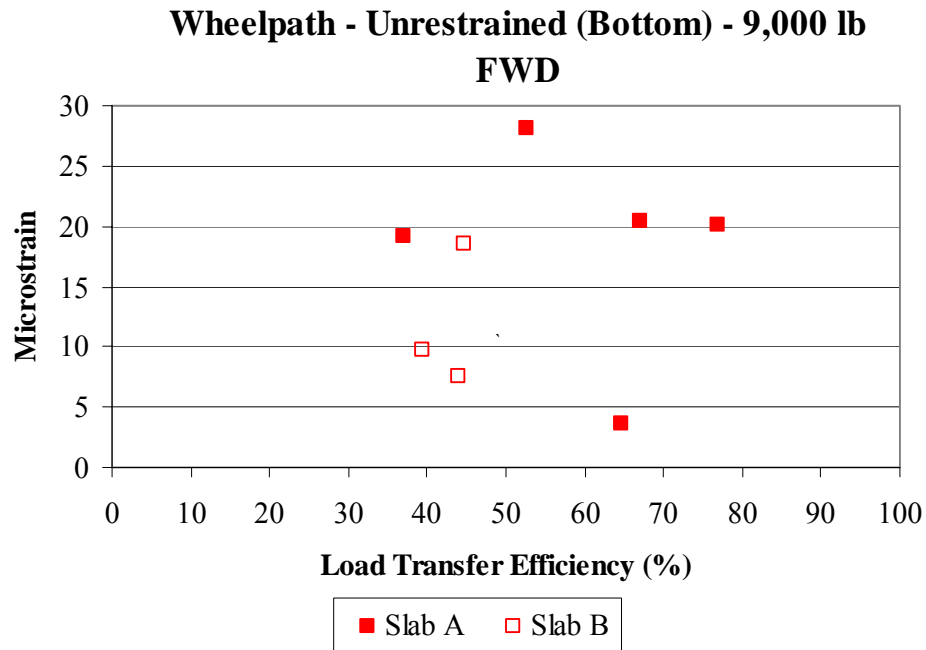


Figure 6.28. Relationship between load transfer efficiency and strain measured in the wheelpath on the bottom of the unrestrained slabs.

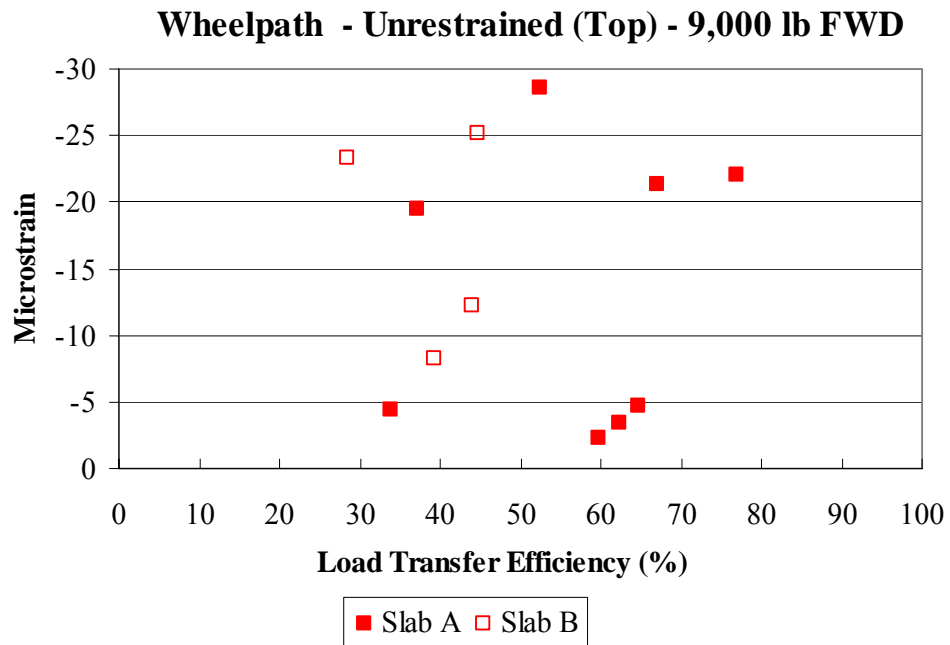


Figure 6.29. Relationship between load transfer efficiency and strain measured in the wheelpath 1 in from the surface of the unrestrained slabs.

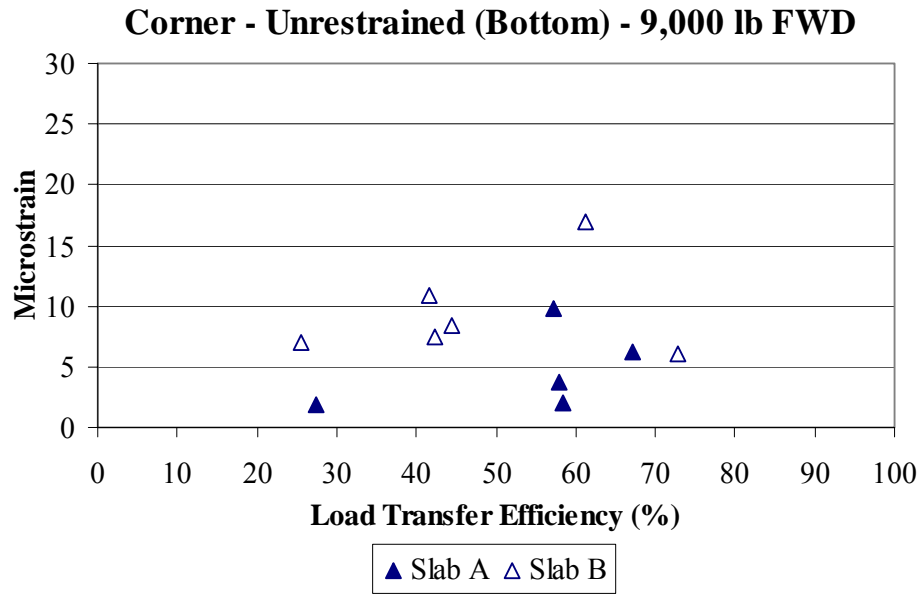


Figure 6.30. Relationship between load transfer efficiency and strain measured in the corner on the bottom of the unrestrained slabs.

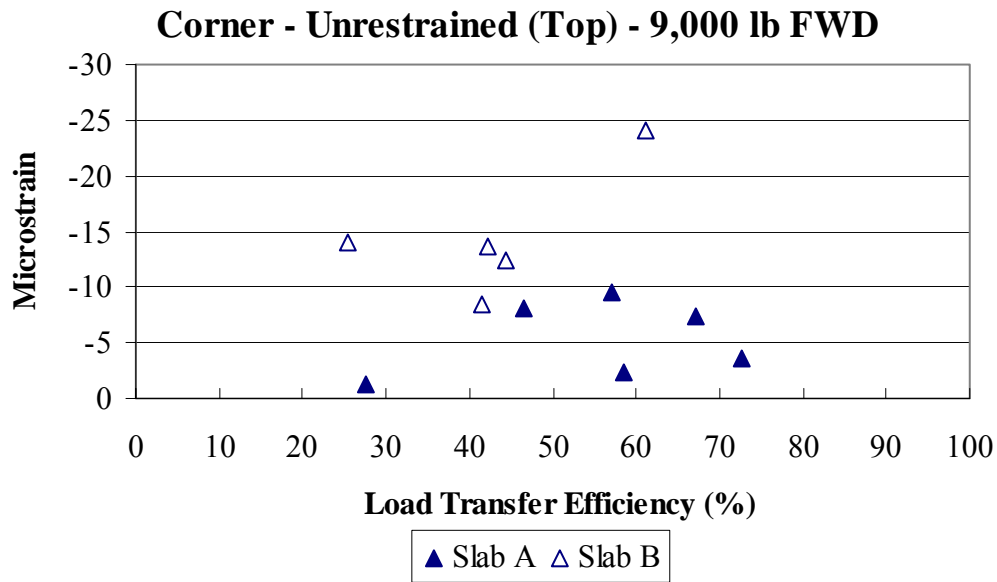


Figure 6.31. Relationship between load transfer efficiency and strain measured in the corner 1 in from the surface of the unrestrained slabs.

6.6.0. Void Detection

FWD testing conducted at the slab corners is used to evaluate the potential for voids beneath the slab. The deflections measured directly under the applied load were

plotted against load for the corner test locations. A linear regression was used to fit a line to these data points. The Void parameter is defined by the x-intercept. The Void parameter concept, which was developed by Darter and Crovetti (1985), is illustrated in Figure 6.32. A fully supported condition will have a Void parameter of less than 2 mils. An x-intercept greater than 2 mils indicates the presence of a void. The magnitude of the Void parameter also provides an indication of the void size, with the void size increasing with an increase in the magnitude of the Void parameter [35].

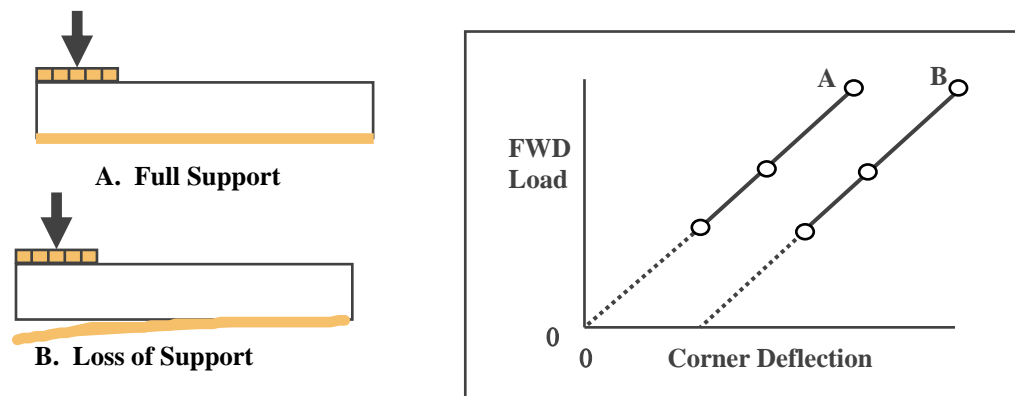


Figure 6.32. Estimating the presence of a void using FWD data.

Figure 6.33 presents the calculated Void parameters along the Smart Pavement. All Void parameters are less than 2 mils except at one joint for an unrestrained slab in Cell 2, indicating the presence of only one void at this location. This would be anticipated since the pavement is constructed on a stabilized base. There is no distinguishable difference between the Void parameters calculated in the restrained and unrestrained slabs. However, there is seasonal variability between the Void parameters. This can be attributed to curling/warping of the slab, which influences the support at the corner. Upward curvature (due to a negative gradient) can produce a false positive while downward curvature (due to a positive gradient) can produce a false negative.

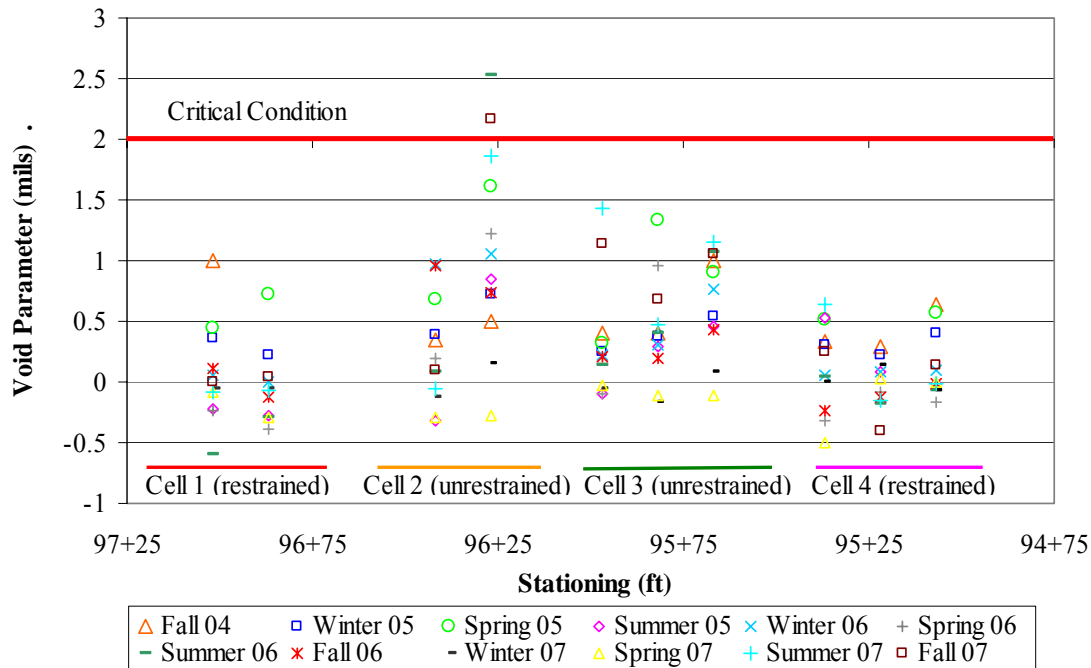


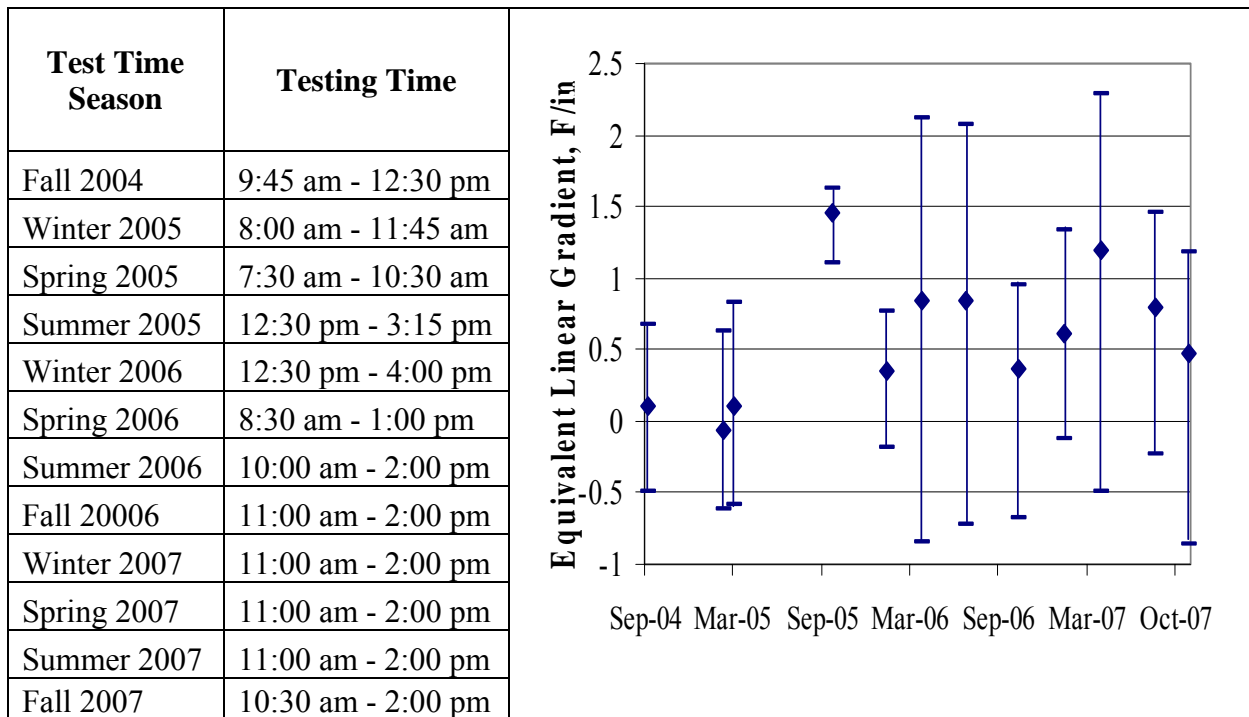
Figure 6.33. Void parameters calculated along the Smart Pavement for each cell.

Seasonally, the spring testing produced the largest variation in Void parameters and the winter testing produced the smallest variation in Void parameters for the restrained and unrestrained cells. This can be attributed to the variation in equivalent linear temperature gradients during testing. Table 6.2 shows the maximum, minimum, and average equivalent linear temperature gradients during FWD testing and Figures 6.5 through 6.16 shows this variation separately for each test outing. The spring testing varied on average 2.38 °F/in compared to the winter testing, which varied approximately 1.22 °F/in.

Warping of the slab, caused by moisture variations throughout the slab, also affects the Void parameters. Figure 6.17 and Figure 6.18, found in section 6.4.2, show the moisture distributions throughout the slab at the midpanel and edge during FWD testing. The edge location is of interest when analyzing the affect of moisture on the corner of the slab. The largest average variation in moisture occurred during winter testing with an average difference in relative humidity of 25 percent from the top of the slab to the bottom. The smallest variation in relative humidity occurred during spring testing with an average difference of 21 percent. Although moisture varied significantly

throughout winter testing, the Void parameters did not. The void parameters measured during the winter had the smallest variation due to the smaller variation in temperature gradients. Therefore, temperature has a larger affect on the Void parameter then moisture. This supports the findings in chapter 3, that temperature distributions have a larger contribution to changes in slab shape then moisture distributions.

Table 6.2. Seasonal equivalent linear temperature gradients present during FWD testing.



Comparing temperature gradients present at the time the data was collected with the calculated Void parameter in Figure 6.34 through Figure 6.36, a good correlation is found between the magnitude of the Void parameter and the size of the gradient. Large positive gradients produce negative Void parameters (indicating that a void is not present) while large negative gradients produce large positive Void parameters (indicating increased support conditions). This shows the effect of gradients on void detection.

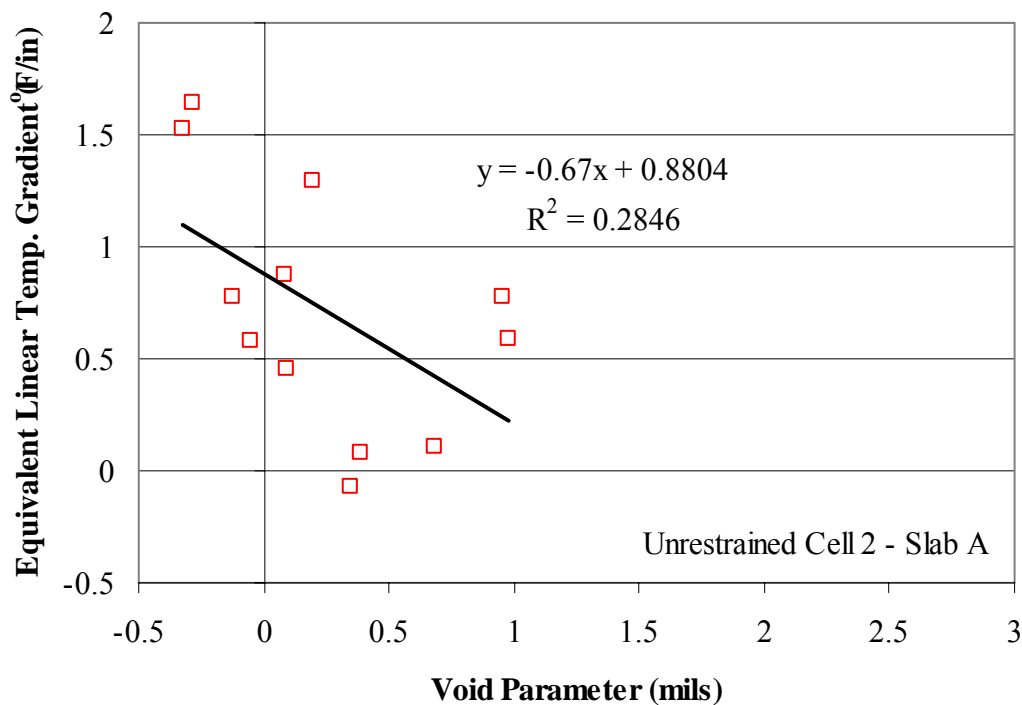


Figure 6.34. Relationship between the Void parameter and the equivalent linear temperature gradient present for unrestrained Slab A in Cell 2.

A linear regression was performed to determine if the y-intercept of the relationship between the equivalent linear temperature gradient and Void parameter is near the set gradient of the slab. The set gradient of both the restrained and unrestrained slabs was determined to be 0.31 °F/in. As Figure 6.34 shows, there is little correlation between the equivalent linear temperature gradient and Void parameter for the unrestrained slab and the y-intercept of 0.88 °F/in is larger than the set gradient. The unrestrained slabs show less correlation and subsequently a higher set gradient because the majority of the time the slab does not experience full support. Figure 6.35 shows the relationship between the equivalent linear temperature gradient and the Void parameter for unrestrained Slab B. A number is placed next to each data marker indicating the data collection periods that data point represents. For example, the first data collection period immediately following construction is represented by 1. This graph indicates factors other than the gradient present at the time of testing and the age of the pavement most likely have a greater impact on the estimated Void parameter. Of course, the age of the

pavement might be a more significant factor if the pavement was more than three years old.

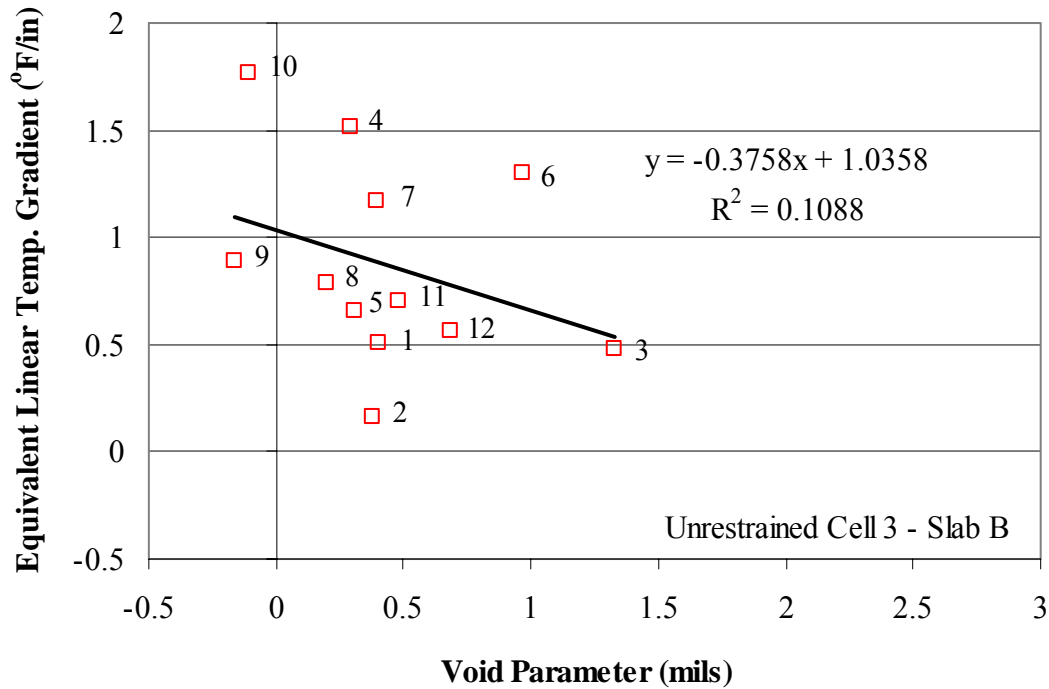


Figure 6.35. Relationship between the Void parameter and the equivalent linear temperature gradient present for unrestrained Slab B in Cell 3.

The Void calculated for the restrained slabs was dependent on the temperature gradient present at the time of testing for all cells as shown in Figure 6.36. The change in the estimated void size with changes in temperature gradient was substantially smaller for the restrained slabs when compared to the unrestrained slabs. This is due to the restraint provided by the dowel and tie-bars in the restrained slabs. A large positive temperature gradient of 1.5 °F/in produced an average Void parameter of -0.18 for the unrestrained slabs, but was only -0.11 for the restrained slabs. The restrained slabs exhibited a 37 percent reduction in Void parameter for the same temperature gradient, indicating the effectiveness of the dowel bars in limiting slab deformation do to temperature and moisture gradients. This observation indicated that restrained slabs have less potential for temperature gradients to significantly affect support conditions. Graphs similar to Figure 6.35 and Figure 6.36 have been developed for each cell in both the unrestrained

and restrained cells to confirm the relationship between Void parameter and temperature gradient. Graphs of this type for all of the slabs of both the restrained and unrestrained cells can be found in appendix G.

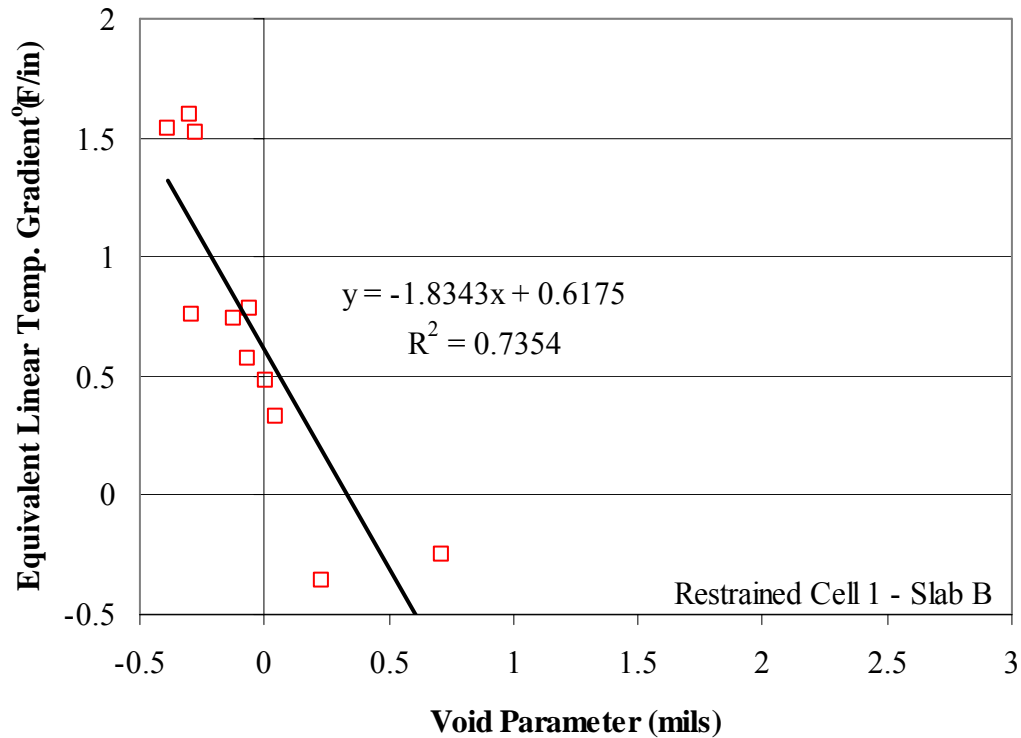


Figure 6.36. Relationship between the Void parameter and the equivalent linear temperature gradient for restrained Slab B in Cell 1.

A linear regression was performed to determine if the y-intercept of the restrained slabs was near the set gradient. As previously mentioned, the set gradient for all the restrained slabs is 0.31 °F/in. Figure 6.36 shows a better correlation between the temperature gradient and Void parameter in the restrained slabs. This is because the majority of the time full support or near full support is experienced in the restrained slabs (indicating no voids are present). Additionally, the regression provided a closer estimate of the set gradient with an intercept of approximately 0.62 °F/in.

6.7.0. Support Conditions

The k-value representing the composite stiffness of all layers beneath the slab was backcalculated seasonally for the first three years after construction. This value is backcalculated using the AREA method presented by Hall and et. al. using deflections collected at midpanel [36]. As Figure 6.37 shows, there is considerable variation in the magnitude of the k-values measured throughout the Smart Pavement section. All backcalculated k-values represent dynamic k-values. The restrained Cell 1 had the highest measured k-values throughout the three years of testing, indicating a stiffer support condition in this area. Cell 1 was approximately 21 percent larger than the restrained Cell 4, 31 percent larger than the unrestrained Cell 2 and 29 percent larger than Cell 3. This is a fairly high level of variability but still within an acceptable range. The unrestrained cells had lower k-values (average k-value 304 pci) than both of the restrained cells (average k-value 388 pci) and also showed less variation. The average deviation for the unrestrained cells was 62 pci, while the restrained cells had an average standard deviation of 79 pci.

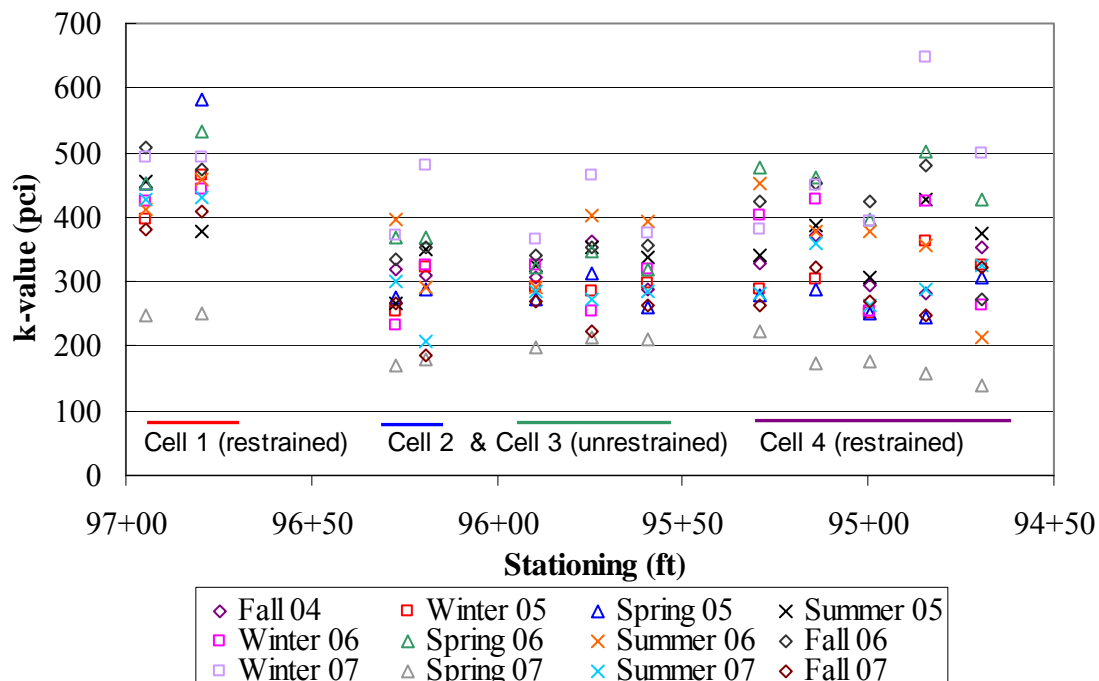


Figure 6.37. The calculated k-value across the Smart Pavement.

Figure 6.38 shows that support conditions beneath the slab do vary seasonally throughout the year. Typically, in climates like Pennsylvania, the highest k-value is found during the winter months due to the frozen subgrade. The spring and fall tend to show lower k-values due to the increase in moisture in the lower layers of the pavement structure. However, these typical support conditions were not experienced during the first and second years of testing. During the first year after construction, from the fall of 2004 to the summer of 2005, the k-value was relatively constant at approximately 320 pci. In the summer of 2005, the k-value indicated stiffer support conditions in summer than spring. There are several reasons for the unusually low winter k-value. Due to scheduling difficulties the winter FWD testing was not performed until March 10, 2005, which was less than a month before the spring testing performed on April 1, 2005. Throughout this time period there was also an increase in rainfall. Due to the significant rainfall the moisture content throughout the pavement increases, thus decreasing support beneath the slab. Even though a stabilized base is present, the stiffness of subbase and fill materials used are highly dependent on the moisture content.

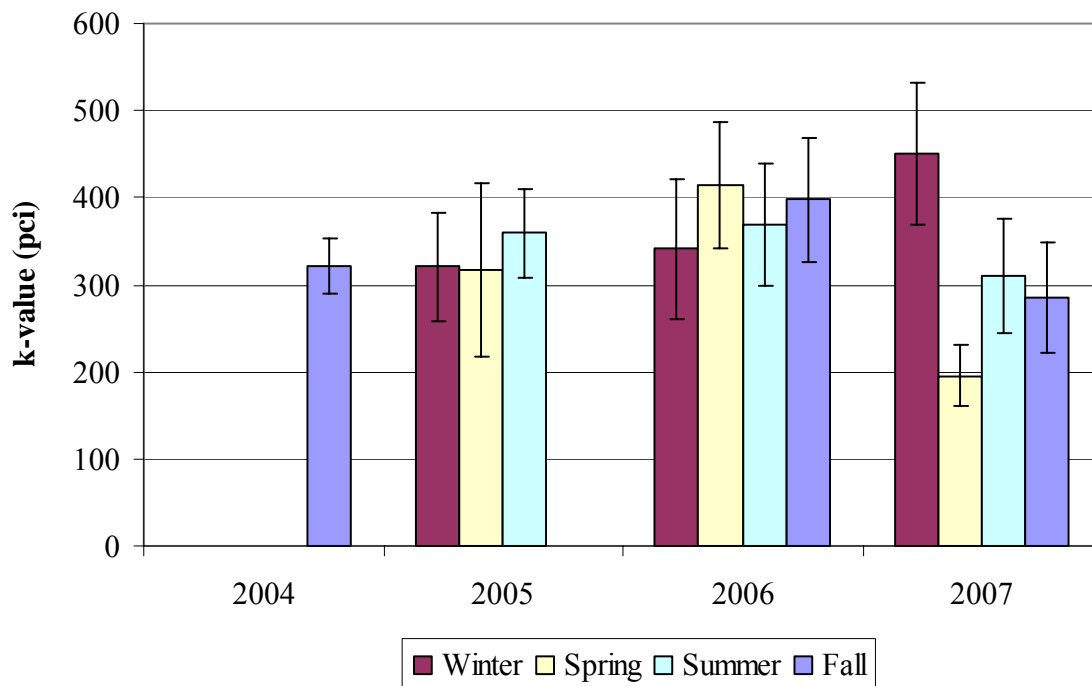


Figure 6.38. Average annual seasonal support conditions across the Smart Pavement.

Throughout the second year of testing (2006), measured k-values also did not behave typical to Pennsylvania climate and there was not a substantial difference between the k-values backcalculated. The spring had the highest measured k-value and in the winter the lowest k-value was observed. Although this may seem unusual, there are several reasons why the calculated k-value was low in the winter. The winter testing was conducted on February 2. During testing, the temperature of all the underlying layers varied between 40 and 46 degrees Fahrenheit. This signifies that the supporting layers were not frozen when winter testing was conducted. Also, the thawing that had recently taken place increased the moisture in the underlying layers, which decreased support beneath the slab. It can be concluded that the winter testing actually had conditions typical of early spring which decreased the support of the underlying layers. The spring testing, which was conducted April 19, had a higher average k-value than that of the summer measured three months later on July 19. As Figure 6.39 shows, the cumulative precipitation for April was approximately 3 in but in July this was doubled with 6 in of rainfall. Therefore, increased moisture levels caused lower measured k-values during the summer.

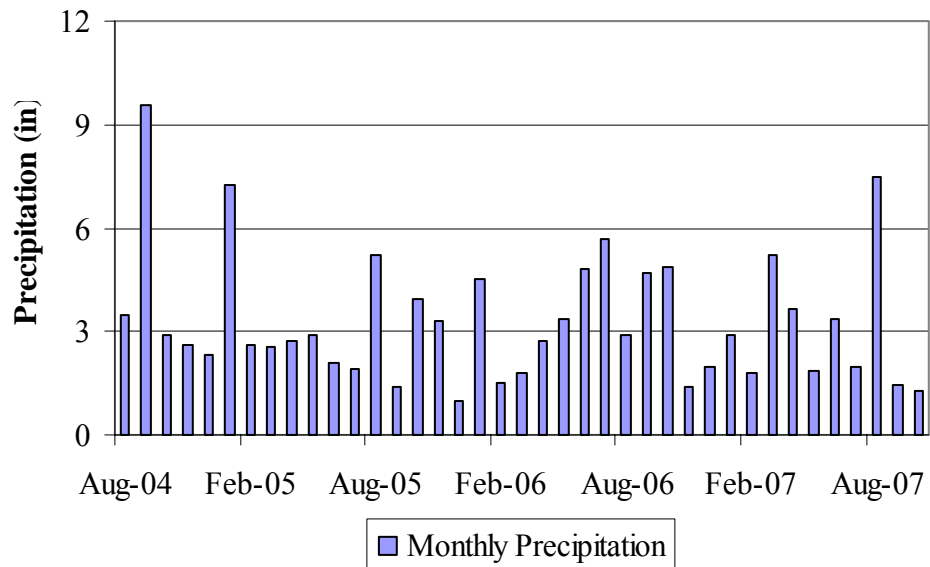


Figure 6.39. The cumulative monthly precipitation measured since construction of the Smart Pavement.

The k-values measured throughout year three (2007) show results typical of that anticipated for Pennsylvania climate. The winter had the highest average k-value of 451 pci and the spring had the lowest with an average of 195 pci. The summer season experienced the normal condition for the year with an average k-value of 310 pci and the k-value measured in the fall was approximately 285 pci.

As previously observed, seasonal trends are exhibited in the measured k-values. Also, it has been observed that temperature and moisture conditions of the supporting layers affect the backcalculated k-value. Therefore, a comparison was performed to investigate the average measured k-value and average mid-depth temperature of the ATPB during testing. As Figure 6.40 shows, there is no distinguishable trend between the measured k-value and the mid-depth temperature of the ATPB. The k-value varies substantially between the various slabs of the restrained and the unrestrained slabs during individual test outings even though the temperature of the base does not.

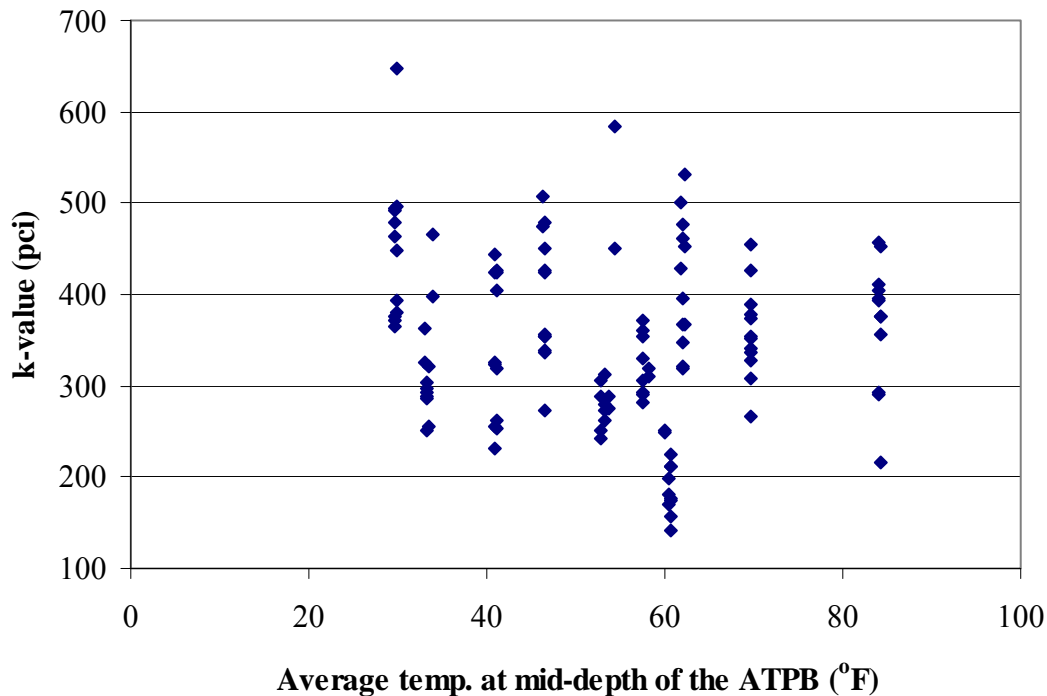


Figure 6.40. Comparison of the support conditions beneath the slab and the average temperature of the asphalt treated permeable base throughout testing.

A final analysis was performed to determine if any correlation existed between the measured k-value and equivalent linear temperature gradient of the slab during testing. As Figure 6.41 and Figure 6.42 show, there is no distinguishable trend between the measured k-value and the slab gradient in both the restrained and unrestrained slabs. The gradient varies considerably while the support conditions do not. A previous study by Khazanovich et al. determined that time of day of FWD testing can significantly affect the backcalculated k-value; this effect is most likely due to the slab gradient present during testing [37]. However, as Figure 6.41 shows, this trend was not experienced in the slabs of the Smart Pavement. The three squares represent backcalculated values from summer testing. The k-value varied between 412 and 455 pci as the gradient varied between 1.5 and 2.0 °F/in. FWD testing at the Smart Pavement was primarily conducted in the afternoons and typically the gradient did not vary significantly. Therefore, no trend was found between the backcalculated k-value and the slab gradient. Graphs similar to Figure 6.41 and Figure 6.42 have been developed for each slab in both the unrestrained and restrained cells to confirm that no relationship exists between the backcalculated k-value and gradient and can be found in appendix G.

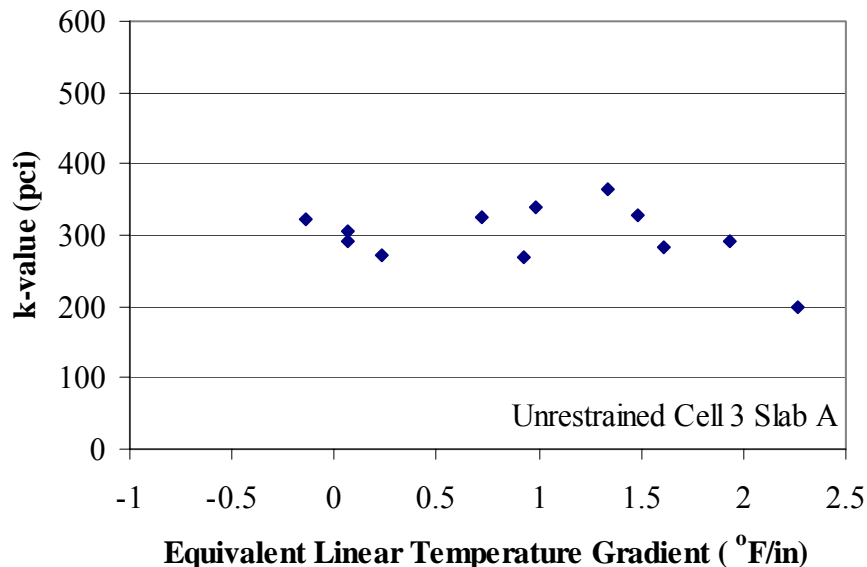


Figure 6.41. Comparison of the support conditions beneath the slab and the equivalent linear temperature gradient of the slab during testing for unrestrained Slab A in Cell 3.

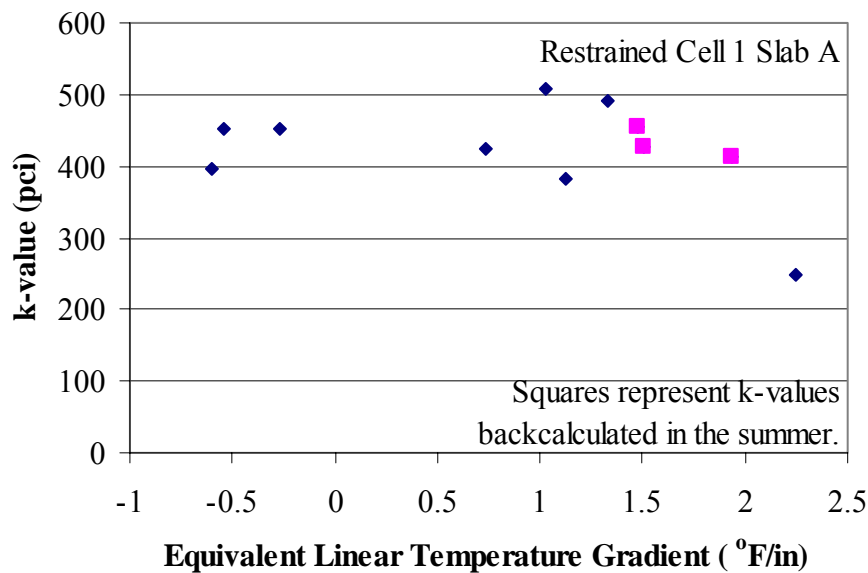


Figure 6.42. Comparison of the support conditions beneath the slab and the equivalent linear temperature gradient of the slab during testing for restrained Slab A in Cell 1.

6.8.0. Deflections at Each Location

Analyzing deflection data at various locations within the slab can be very useful in determining the performance of a pavement. Differential deflections along the transverse joint in the wheelpath are used in estimating joint performance and normalized deflections along at the corner of the slab can be used in predicting possible voids along a project. Additionally, deflections measured at any location within the slab can be used to access project variability.

Figure 6.43 through Figure 6.46 present the deflections measured at each test location throughout the three years of testing. Each deflection is normalized to a 9,000 lb load. Generally, as shown in the preceding figures, the unrestrained slabs exhibit larger deflections and more variation. This can be attributed not only to the unrestrained joints, but also to the weaker support layers in those locations.

The largest average deflections measured in both the restrained and unrestrained slabs were at the corner. Deflections at the corner of the unrestrained slabs were 2.5 times larger those measured at midpanel, 86 percent larger than those measured along the lane/shoulder joint, and 34 percent larger than the wheelpath, adjacent to the transverse joint. The deflections measured at the corner for the restrained slabs were 71 percent

larger those measured at midpanel, 38 percent larger than those measured along the lane/shoulder joint, and 22 percent larger than the wheelpath, adjacent to the transverse joint. The corner location also showed the most variation for the unrestrained slabs with an average standard deviation of 0.97 mils. The midpanel of the restrained slabs had the largest variation with an average standard deviation of 0.29 mils.

The corner and wheelpath along the transverse joint had the largest measured deflections and variation due to its proximity to the joint. Temperature gradients greatly affect the deflections measured at these locations. Large positive gradients decrease deflection while large negative gradients increase deflections. The performance of the joint also affects deflections at these locations. The unrestrained slabs are affected by joint opening, temperature of the PCC slab, and temperature gradients present during testing. For example deflections measured at the corner and wheelpath of the slab are decreased when temperature is high, joint opening is small, and temperature gradients are negative.

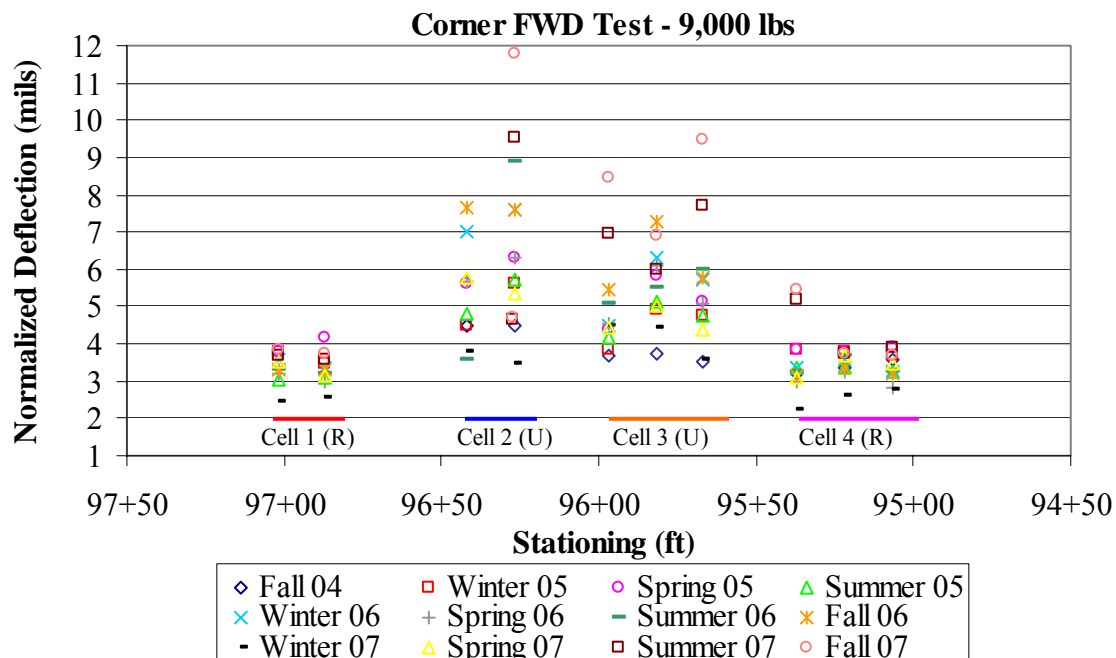


Figure 6.43. Deflections measured in the corner of each slab.

At the corner location, see Figure 6.43, the unrestrained slabs exhibit a 65 percent increase in deflection compared to the restrained slabs when averaged seasonally over the life of the pavement. This variation between the restrained and unrestrained slabs was greatest during summer testing and was lowest during spring. The summer testing was always completed during the afternoon when large positive gradients were present, this increases the deflections measured at the corner of the unrestrained slabs. The restrained slabs, due to the presence of dowel and tie bars, are unable to deform to the same magnitude as the unrestrained slabs therefore, reducing the deflections measured in the corner. The deviation in the deflections measured in the unrestrained slabs at the corner was also greater than that of the restrained. The average deviation in the unrestrained slabs was 0.97 mils while the restrained was only 0.26 mils. The largest average deflections, measured at the corner location, were in the fall for both the restrained and unrestrained slabs.

As previously discussed, deflections measured at the corner can be used in predicting possible voids beneath the slab. In section 6.6.0 the variable corner deflection analysis was used in predicting voids beneath the slab and it was determined that there was one possible void at station 96+25. Figure 6.43 also shows large deflections at this station which further suggests that a void may be present.

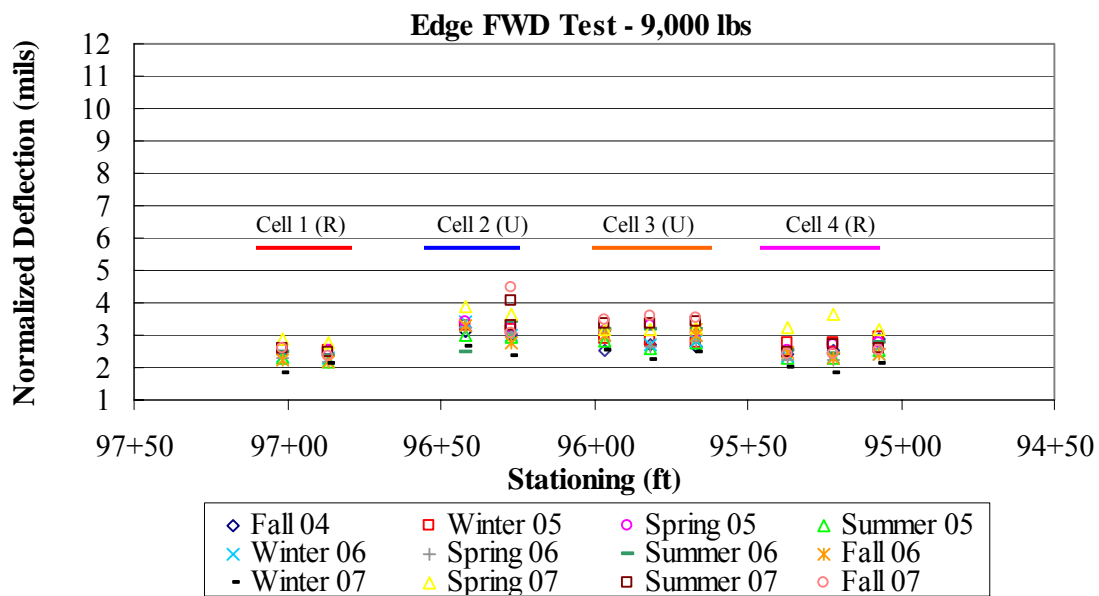


Figure 6.44. Deflections measured along the lane/shoulder joint.

Figure 6.44, shown above, displays the normalized deflections measured along the lane/shoulder joint for both restrained and unrestrained slabs. The total average deflection, along the lane/shoulder joint, for the unrestrained slab was 3 mils while the restrained slabs had an average of 2.5 mils. There is not a significant difference between these two averages indicating that increased support provided by the tied curb and gutter is not substantial. The deviation of the deflections measured in the unrestrained slabs was also greater with a standard deviation of 0.23 mils. The standard deviation of the restrained was 0.16 mils. The largest average deflections were measured during the spring testing for both restrained and unrestrained slabs. This can be attributed to the weakened support conditions of the underlying layers.

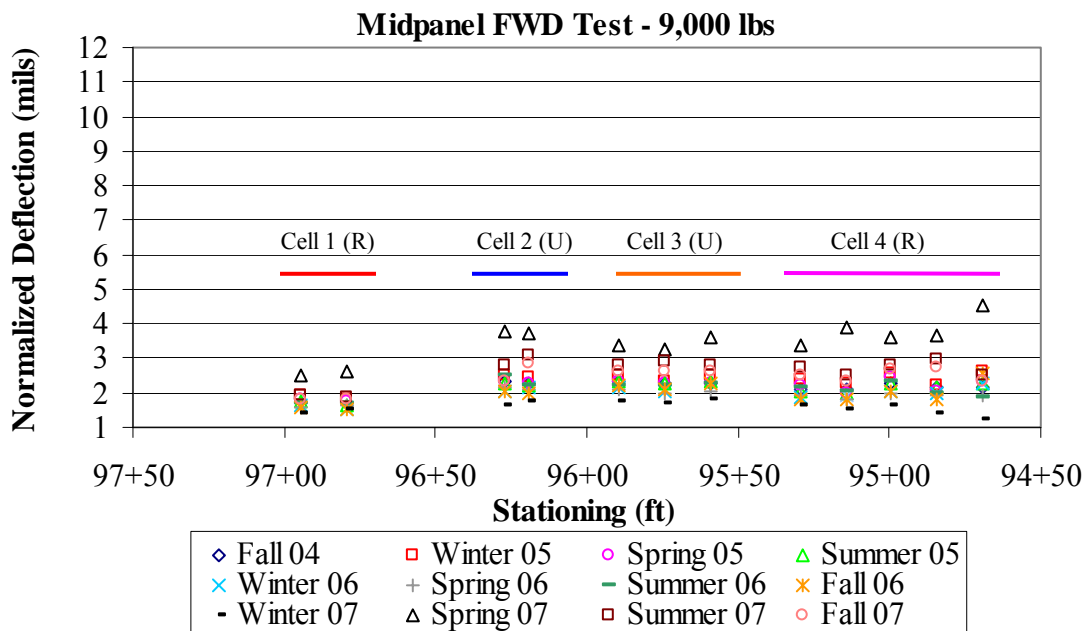


Figure 6.45. Deflections measured at midpanel.

At the midpanel location, see Figure 6.45, the unrestrained slabs exhibit 13 percent higher deflections than the restrained slabs when averaged seasonally over the life of the pavement. This variation was greatest during summer testing and was lowest during the spring. Due to the large positive gradients present during summer testing, support is lost between the slab and base layer, thus increasing the deflections at midpanel. The largest average deflections, measured at midpanel, were in the summer

for the unrestrained slabs and in the fall for the restrained slabs. This is most likely caused by the higher positive gradients experienced during the summer.

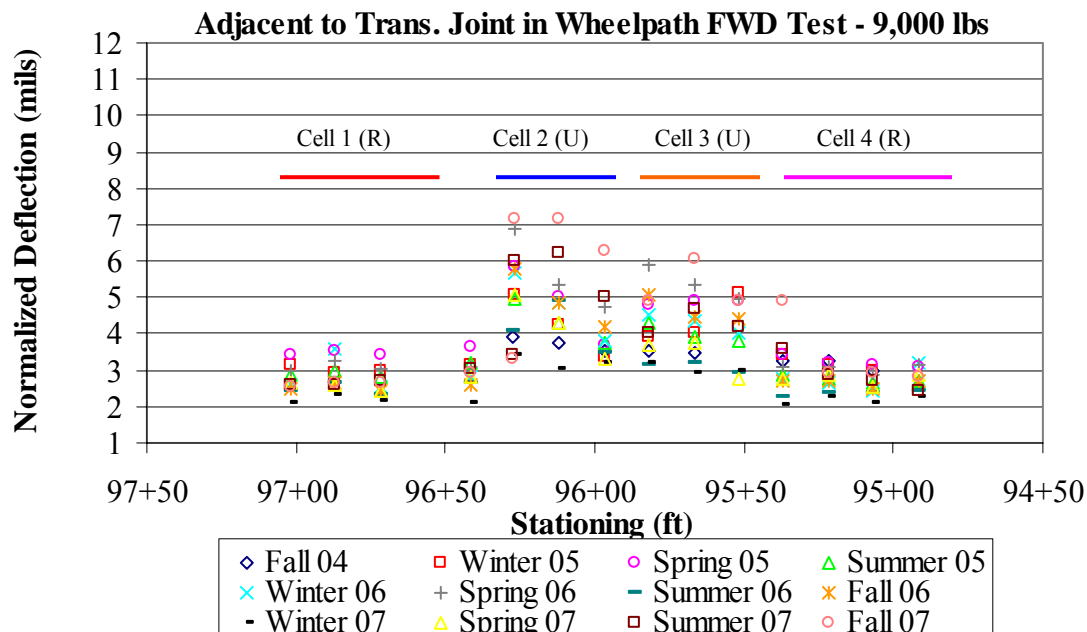


Figure 6.46. Deflections measured in the wheelpath, adjacent to the transverse joint.

Figure 6.46, shown above, displays the normalized deflections measured in the wheelpath, adjacent to the transverse joint, for both restrained and unrestrained slabs. The total average deflection, along for the unrestrained slabs was 4.2 mils while the restrained slabs had an average of 2.8 mils. At the wheelpath, the unrestrained slabs exhibited 51 percent higher deflections than the restrained slabs. The deviation of the deflections measured in the unrestrained slabs was also greater with a standard deviation of 0.65 mils. The standard deviation of the restrained was 0.29 mils. The largest average deflections were measured during the spring testing for both restrained and unrestrained slabs and the smallest were measured during the winter.

6.9.0. Truck Load Testing

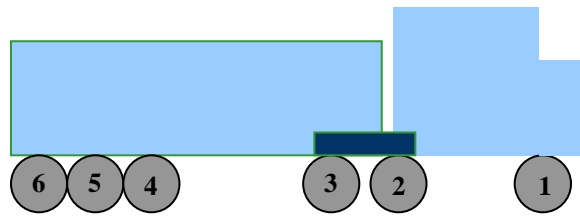
Seasonal truck load testing is conducted over the dynamic strain gages installed in Cells 1 and 2. Three different axle configurations were used, as shown in Figure 6.47. The three trucks consisted of the following:

1. 6-axle semi (FHWA Class 10);
2. 4-axle dump truck with a triple axle in the rear (FHWA Class 7) and
3. 3-axle dump truck with a tandem axle in the rear (FHWA Class 6).

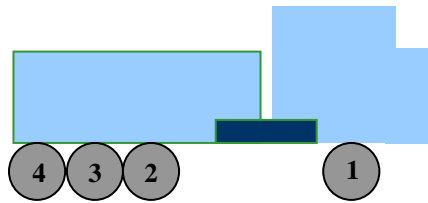
Each truck was loaded with three different loads representing an average, high and overload condition. The axle loads used for each axle configuration is shown in Table 6.3.

For each axle and load configuration, the truck made two passes over the test section. One pass was with the outside wheels passing along the lane/shoulder edge. The other pass was in the wheelpath, approximately two feet from the lane/shoulder. Each truck pass was completed at creep speed.

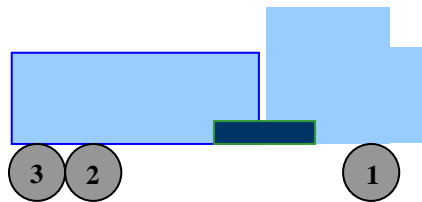
To ensure that the axles are loaded to the appropriate weights prior to each run, a weigh team was provided by PennDOT to weigh each axle, as shown in Figure 6.48. The load of the truck was adjusted until the desired axle loads were achieved. As the truck passed over each test cell, measurements were recorded from the dynamic strain and pressure gages.



**6- Axle Semi
FHWA Class 10**



**4- Axle Dump Truck
FHWA Class 7**



**3- Axle Dump Truck
FHWA Class 6**

Figure 6.47. Axle configurations for truck testing.

Table 6.3. Axle loads for truck testing.

	Weight on Axle (lbs)					
	1	2	3	4	5	6
Class 10	Standard	12,000	12,000	12,000	12,000	12,000
	Standard	18,000	18,000	18,000	18,000	18,000
	Standard	25,000	25,000	25,000	25,000	25,000
Class 7	Standard	15,000	15,000	15,000		
	Standard	20,000	20,000	20,000		
	Standard	25,000	25,000	25,000		
Class 6	Standard	15,000	15,000			
	Standard	20,000	20,000			
	Standard	25,000	25,000			



Figure 6.48. Verification of axle loads.

6.10.0. Concrete Temperature and Moisture Distributions During Truck Testing

The characterization of the temperature and moisture distributions throughout the PCC slab during truck testing is critical in analyzing pavement response. The weighted average temperature and equivalent linear temperature gradient significantly affect the shape and critical stress locations in the slab. The moisture content throughout the slab also will affect the shape and critical stress locations in the slab. Therefore, determination of these factors helps in the characterization of strain.

6.10.1. Concrete Temperature Distribution

Table 6.4, shown below, presents the variation of the weighted average temperature of the slabs at midpanel during truck testing. The largest variation in temperature during truck testing was experienced during the summer of 2005, spring of 2006, and summer of 2007 with a range of 9°F. The smallest variation in temperature was experienced during the winter of 2006 when the weighted average temperature did not fluctuate during testing.

Table 6.4. Temperature variation during truck testing.

Test Time Season	Truck Type	Testing Time	Ave. Weighted Ave. Temp, °F	Min. Weighted Ave. Temp, °F	Max. Weighted Ave. Temp, °F
Fall 2004	Class 10	11:00 am - 2:30 pm	72	69	75
Fall 2004	Class 6 & 7	9:00 am - 2:30 pm	55	52	58
Winter 2005	Class 10	9:00 am - 4:00 pm	40	38	42
Winter 2005	Class 6 & 7	8:30 am - 1:30 pm	38	37	40
Spring 2005	Class 6 & 7	3:00 pm - 5:30 pm	62	62	62
Spring 2005	Class 10	2:15 pm - 5:15 pm	69	67	70
Summer 2005	Class 10	11:15 am - 4:00 pm	74	69	79
Summer 2005	Class 6 & 7	9:30 am - 4:00 pm	67	64	69
Fall 2005	Class 10	8:45 am - 11:45 am	45	42	46
Fall 2005	Class 6	11:30 am - 4:00 pm	43	42	46
Winter 2006	Class 6 & 7	9:00 am - 3:00 pm	44	40	46
Winter 2006	Class 10	9:00 am - 3:00 pm	42	42	42
Spring 2006	Class 10	12:30 pm - 5:00 pm	60	55	64
Spring 2006	Class 6 & 7	8:45 am - 12:00 pm	53	50	57
Summer 2006	Class 10	11:00 am - 1:00 pm	81	78	83
Summer 2006	Class 6 & 7	8:45 am - 11:30 pm	79	77	81
Fall 2006	Class 10	8:30 am - 10:45 am	52	51	53
Fall 2006	Class 6 & 7	8:45 am - 11:30 am	53	52	54
Winter 2007	Class 6 & 7	10:00 am - 2:30 pm	30	27	32
Winter 2007	Class 10	10:00 am - 1:45 pm	18	15	21
Spring 2007	Class 6 & 7	8:45 am - 12:45 pm	50	47	53
Spring 2007	Class 10	8:45 am - 12:00 pm	70	67	72
Summer 2007	ALL	9:00 am - 2:30 pm	80	76	85
Fall 2007	ALL	8:45 am - 1:30 pm	65	63	67

Figure 6.49 through Figure 6.72 show the variation in weighted average temperature, equivalent linear temperature gradient of the slab, and middepth temperature of the asphalt treated permeable base (ATPB) during testing periods. Summary statistics of all test seasons are discussed below. Each season for all three years was combined to determine the overall range and average values of each variable.

During the fall testing the weighted average temperature in the PCC slab ranged between 42 and 75 °F with an average of 55 °F. The equivalent linear temperature gradient of the PCC slab varied between -0.46 and 1.36 °F/in during fall testing, with an average of 0.36 °F/in. The middepth temperature of the ATPB varied between 49 and 69 °F with an average of 57 °F. As shown in the proceeding figures, the weighted average temperature of the concrete varied minimally during the three test periods. The fall testing encountered the least variation in weighted average temperature with an average range of less than 1 °F.

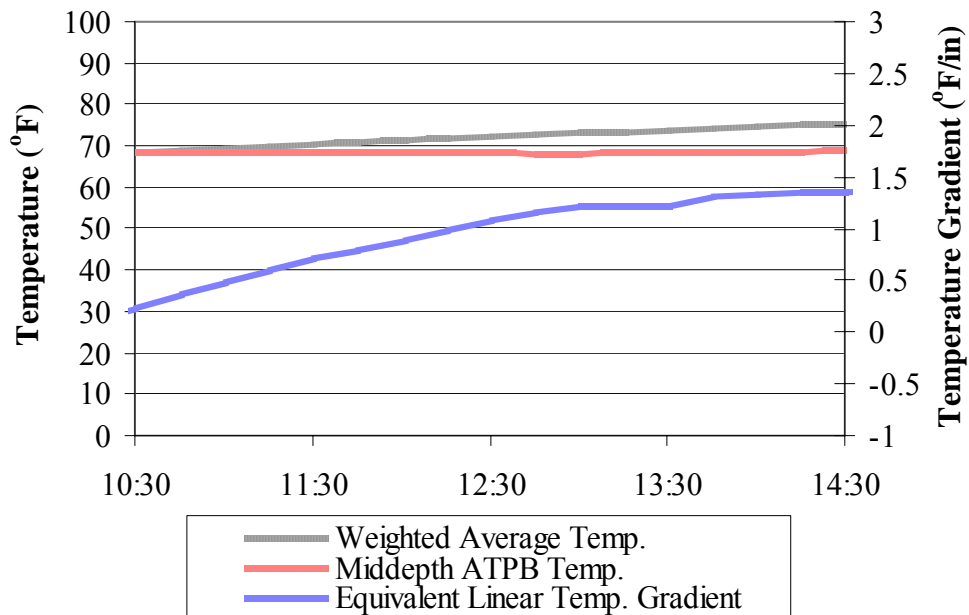


Figure 6.49. Midpanel temperature conditions during Class 10 truck testing performed in the fall of 2004.

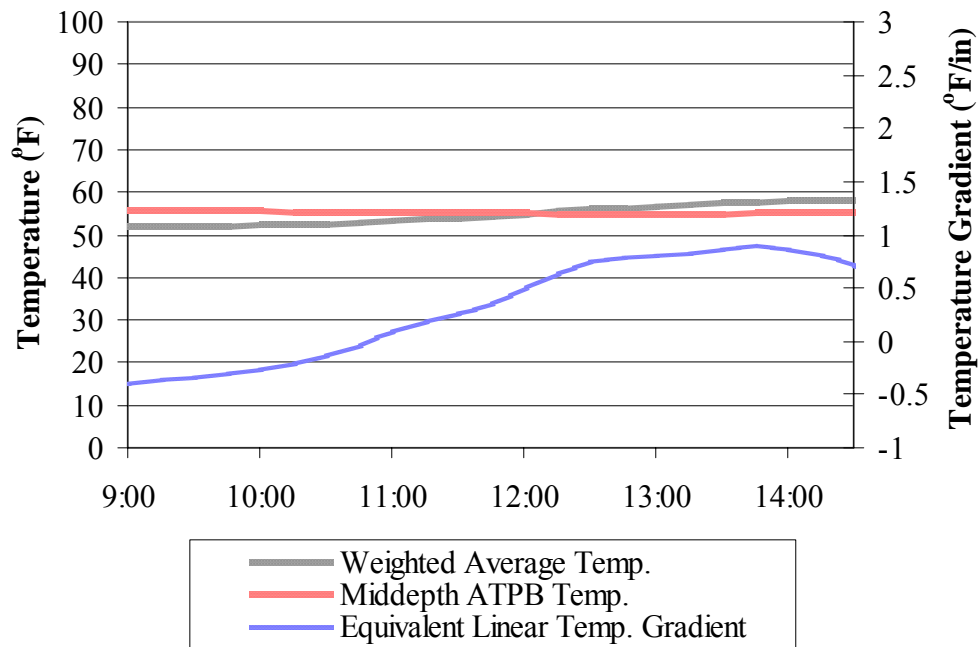


Figure 6.50. Midpanel temperature conditions during Class 6 and 7 truck testing performed in the fall of 2004.

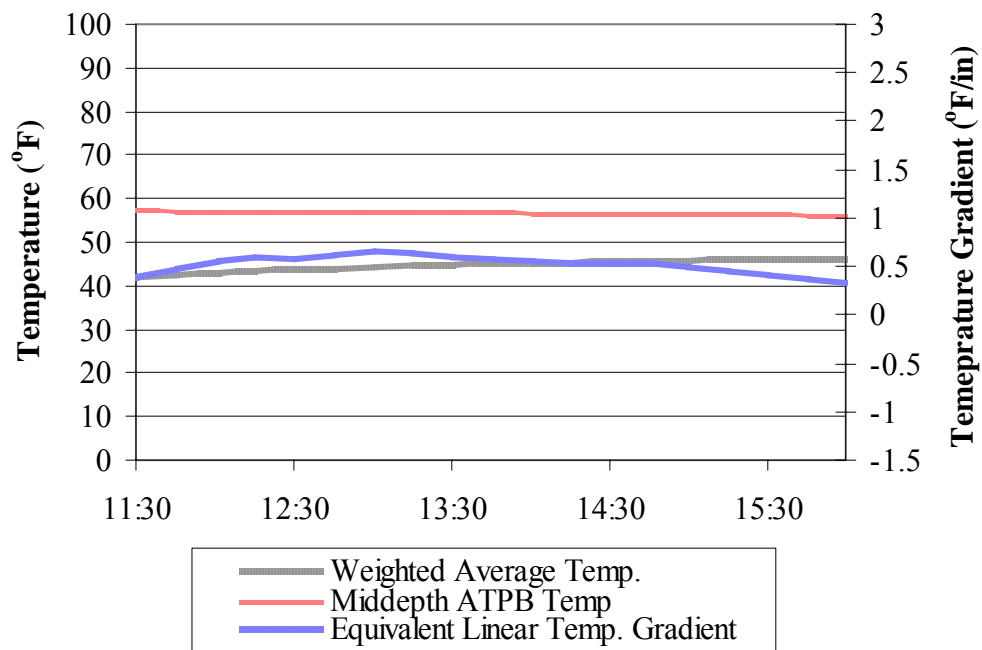


Figure 6.51. Midpanel temperature conditions during Class 10 truck testing performed in the fall of 2005.

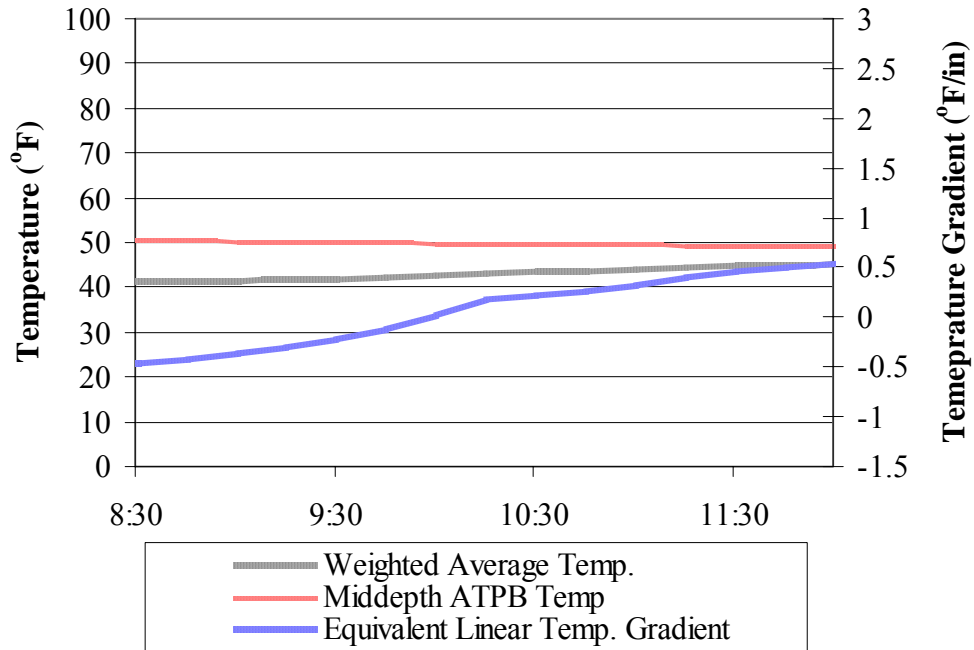


Figure 6.52. Midpanel temperature conditions during Class 6 truck testing performed in the fall of 2005.

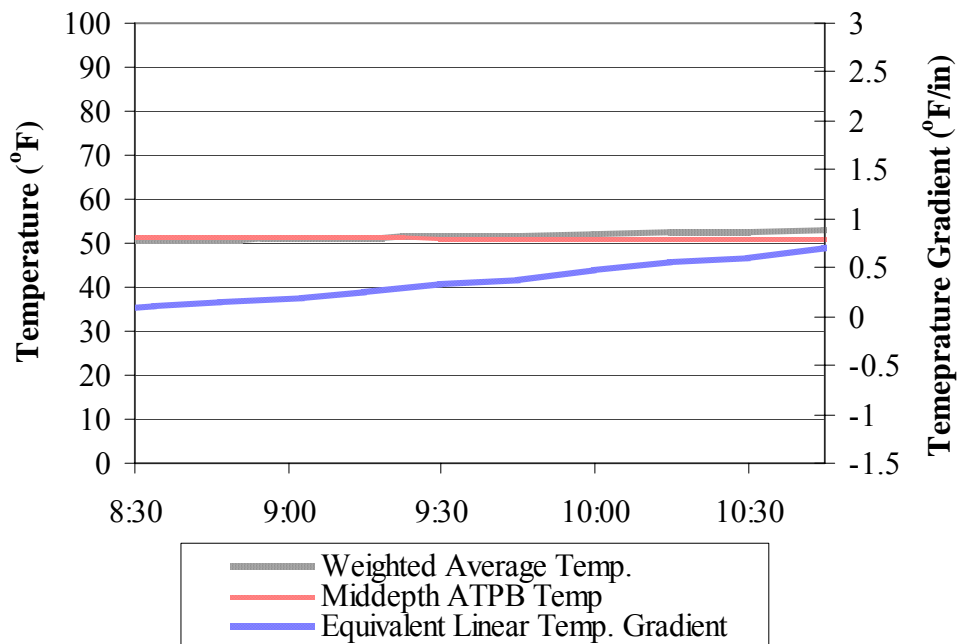


Figure 6.53. Midpanel temperature conditions during Class 10 truck testing performed in the fall of 2006.

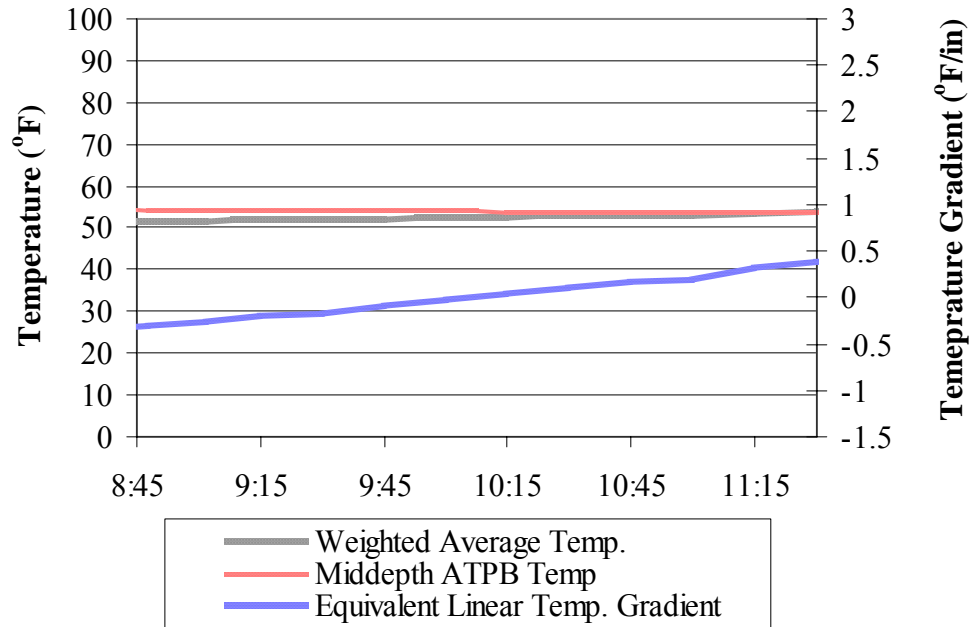


Figure 6.54. Midpanel temperature conditions during Class 6 and 7 truck testing performed in the fall of 2006.

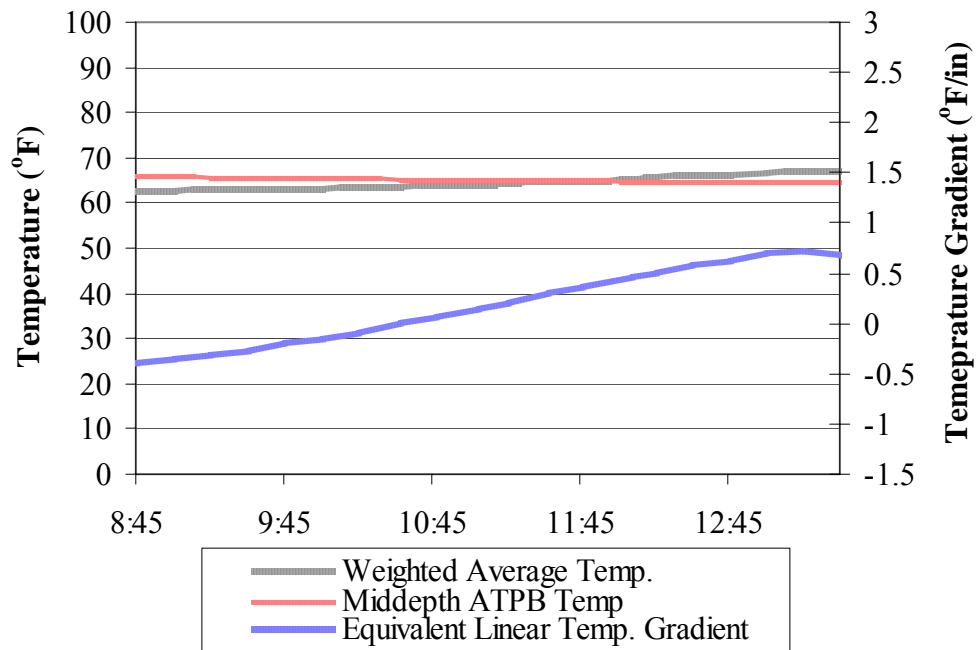


Figure 6.55. Midpanel temperature conditions during Class 6, 7, and 10 truck testing performed in the fall of 2007.

Figure 6.56 through Figure 6.61 present the temperature of the concrete and ATPB and gradient of the slab during winter testing. The weighted average temperature

for winter testing ranged between 15 and 46 °F with an average of 35 °F. The equivalent linear temperature gradient varied between -0.61 and 0.86 °F/in with an average of 0.18 °F/in. The middepth temperature of the ATPB, measured during the winter truck testing, fluctuated between 23 and 44 °F with an average of 36 °F. Additionally, the smallest variation in the temperature and gradient in the slab was experienced during winter testing with an average range of 4 °F and approximately 0.7 °F/in.

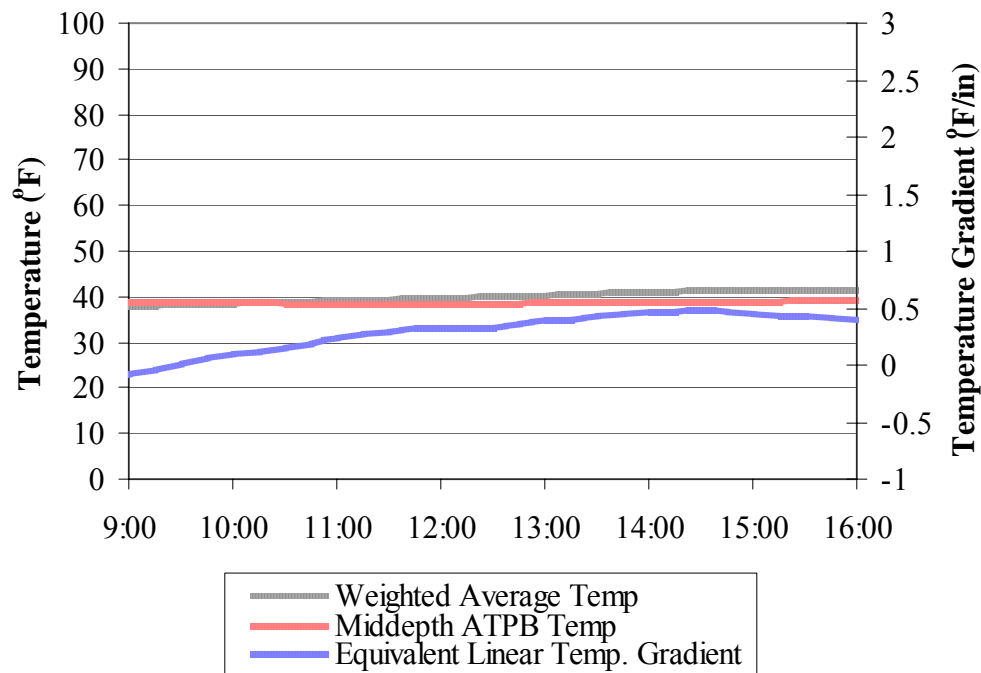


Figure 6.56. Midpanel temperature conditions during Class 10 truck testing performed in the winter of 2005.

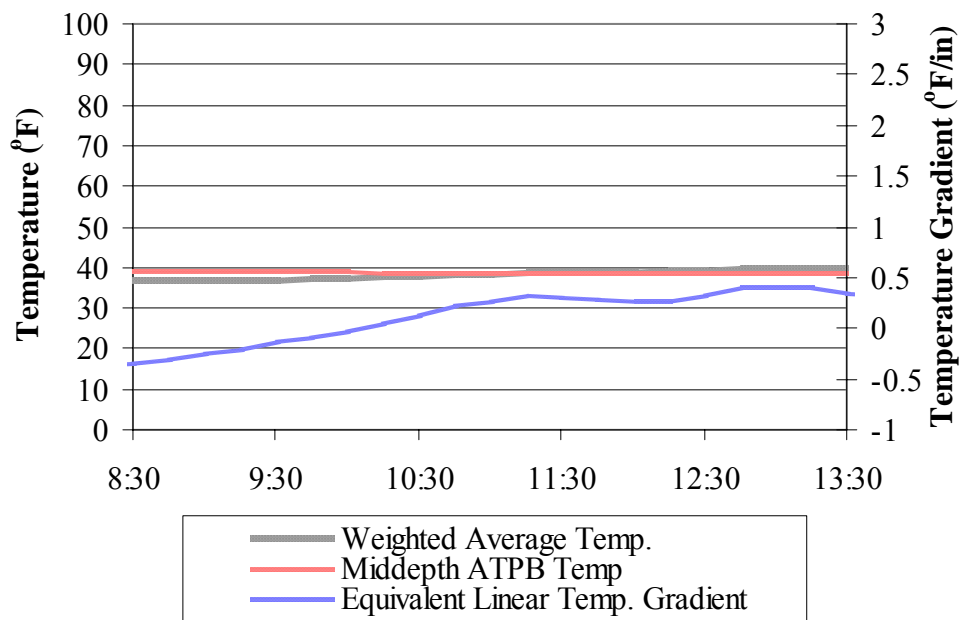


Figure 6.57. Midpanel temperature conditions during Class 6 and 7 truck testing performed in the winter of 2005.

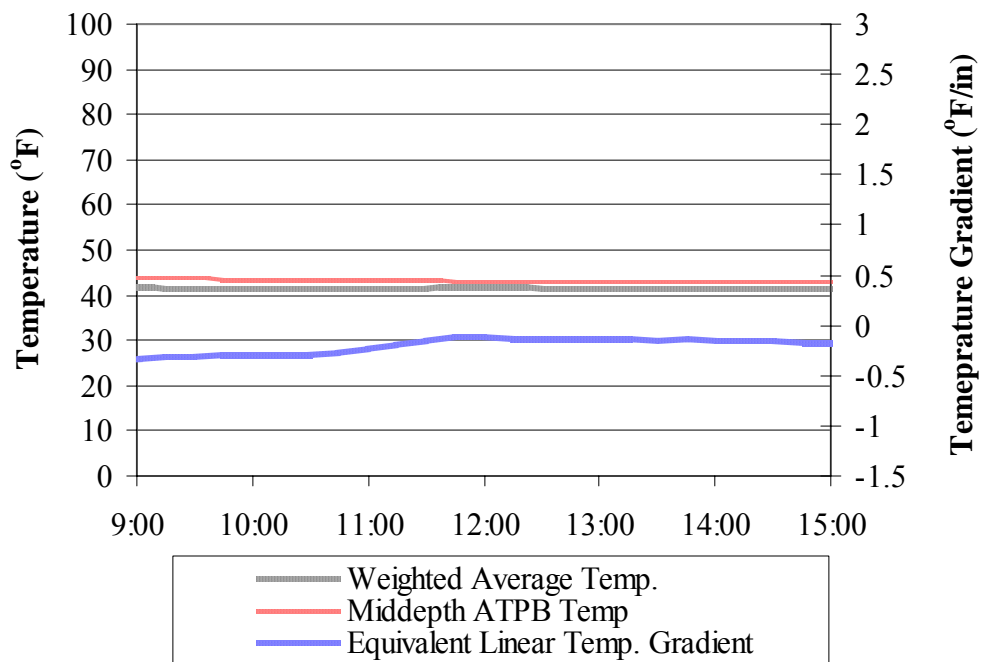


Figure 6.58. Midpanel temperature conditions during Class 10 truck testing performed in the winter of 2006.

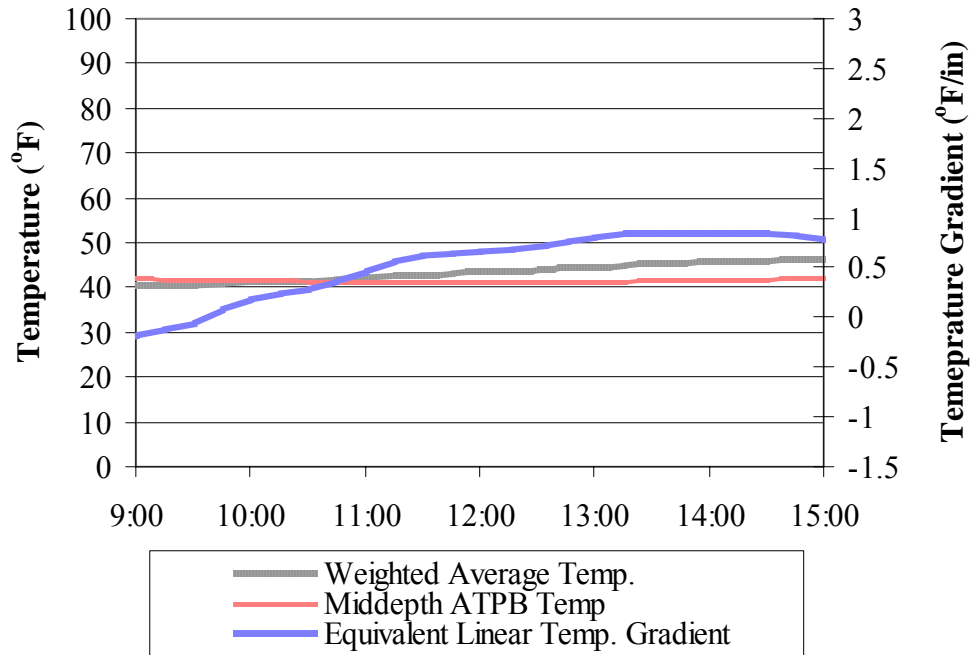


Figure 6.59. Midpanel temperature conditions during Class 6 and 7 truck testing performed in the winter of 2006.

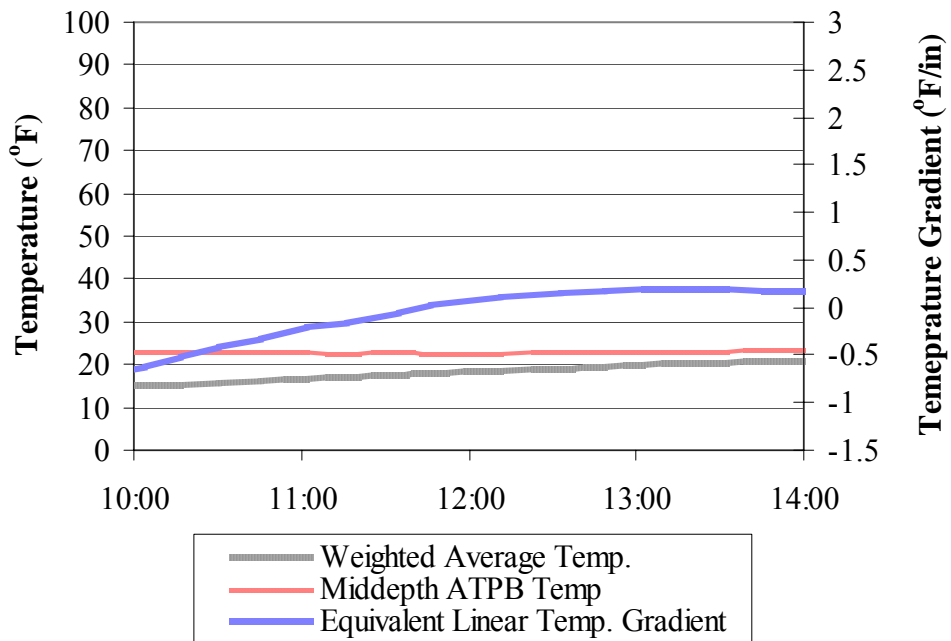


Figure 6.60. Midpanel temperature conditions during Class 10 truck testing performed in the winter of 2007.

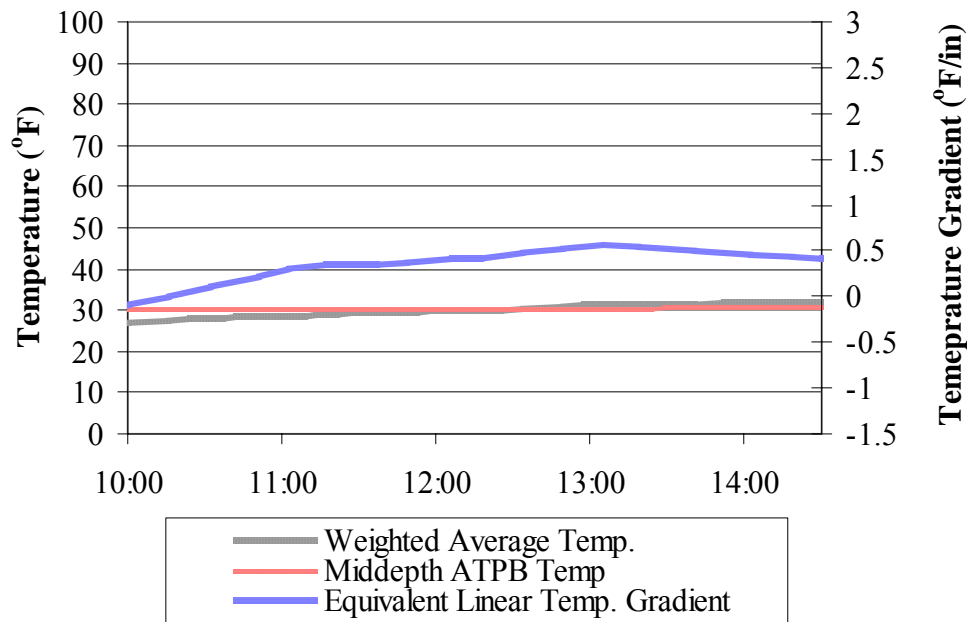


Figure 6.61. Midpanel temperature conditions during Class 6 and 7 truck testing performed in the winter of 2007.

During spring testing the weighted average temperature in the PCC slab ranged between 47 and 72 °F with an average of 61 °F. The equivalent linear temperature gradient of the PCC slab varied between -0.52 and 2.11 °F/in during spring testing, with an average of 1.06 °F/in. The temperature at middepth of the ATPB ranged between 46 and 67 °F with an average of 55 °F. As shown in Figure 6.62 through Figure 6.67, the equivalent linear temperature gradient of the concrete varied significantly during most of the spring test period. The average difference between the peak maximum and peak minimum equivalent linear gradient for all spring test periods is 0.9 °F/in. The temperature of the ATPB also remained relatively constant.

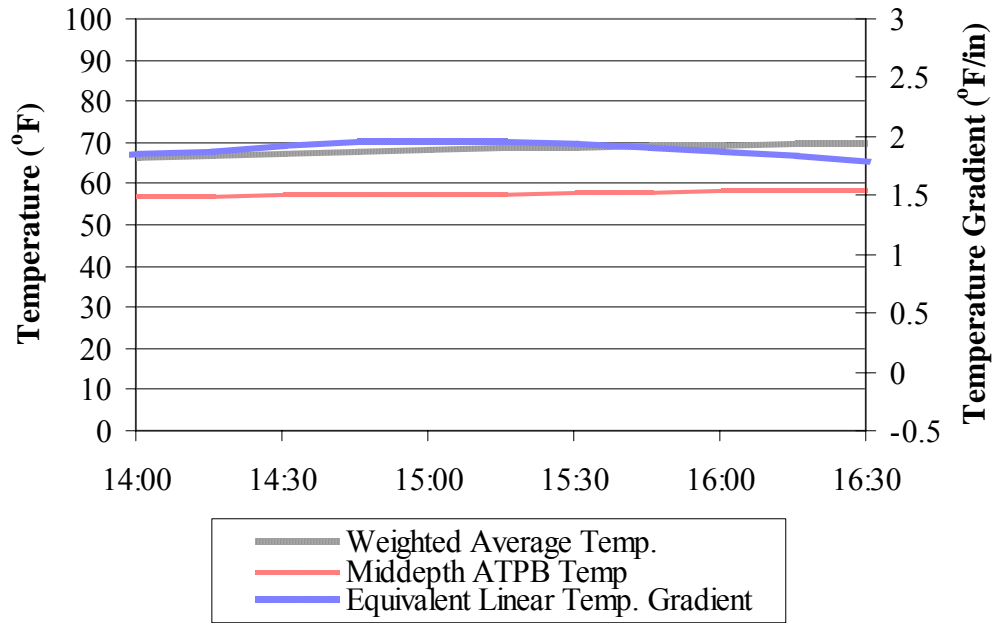


Figure 6.62. Midpanel temperature conditions during Class 10 truck testing performed in the spring of 2005.

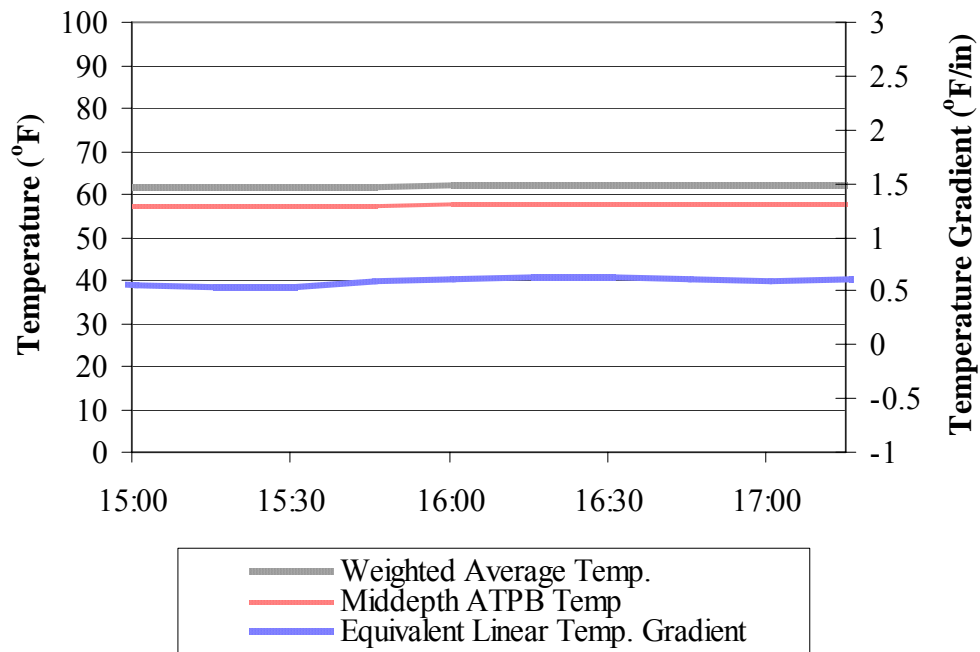


Figure 6.63. Midpanel temperature conditions during Class 6 and 7 truck testing performed in the spring of 2005.

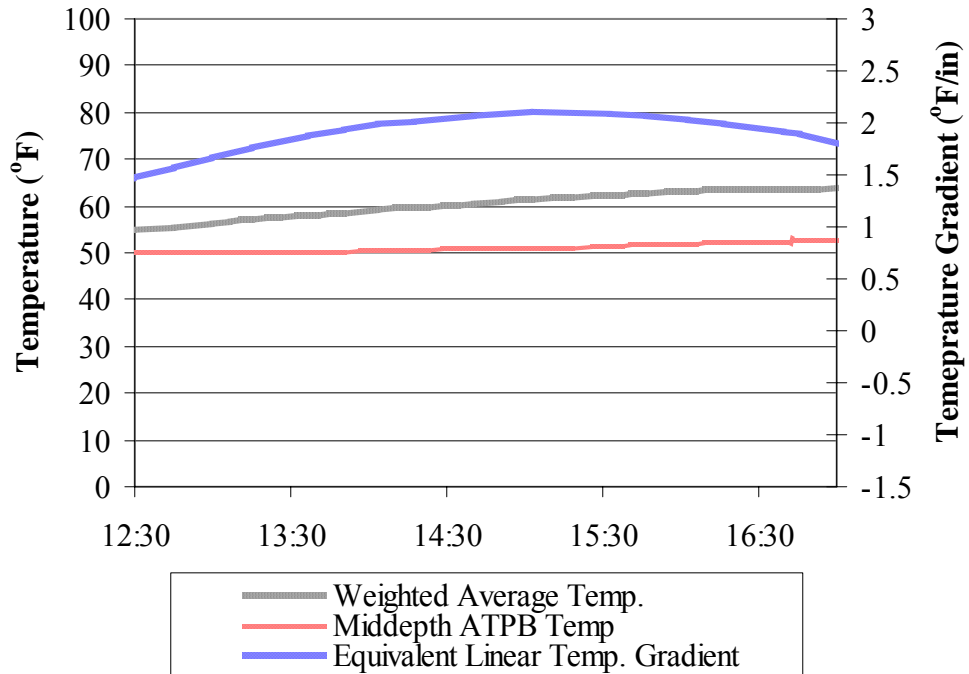


Figure 6.64. Midpanel temperature conditions during Class 10 truck testing performed in the spring of 2006.

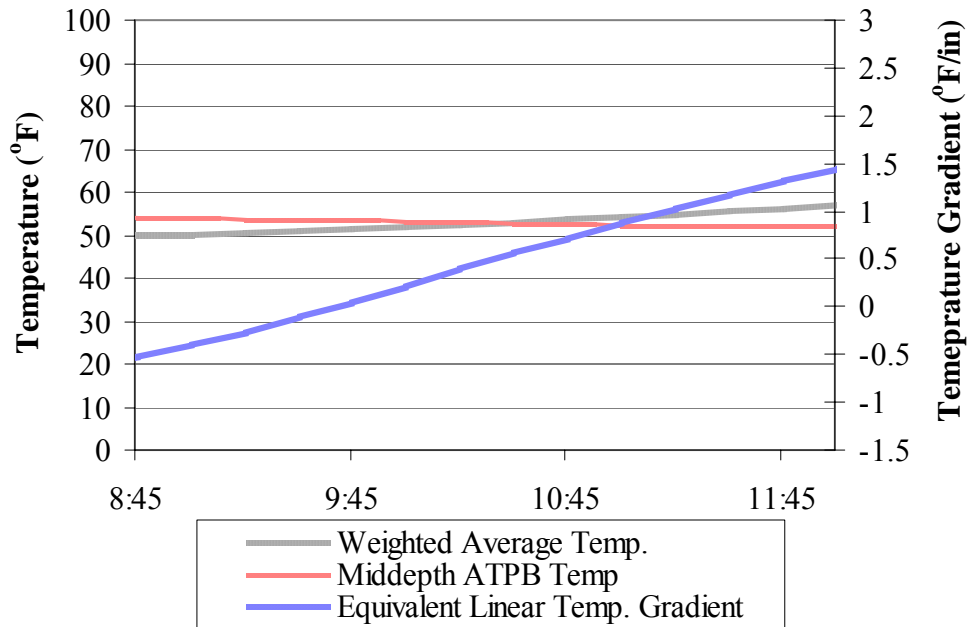


Figure 6.65. Midpanel temperature conditions during Class 6 and 7 truck testing performed in the spring of 2006.

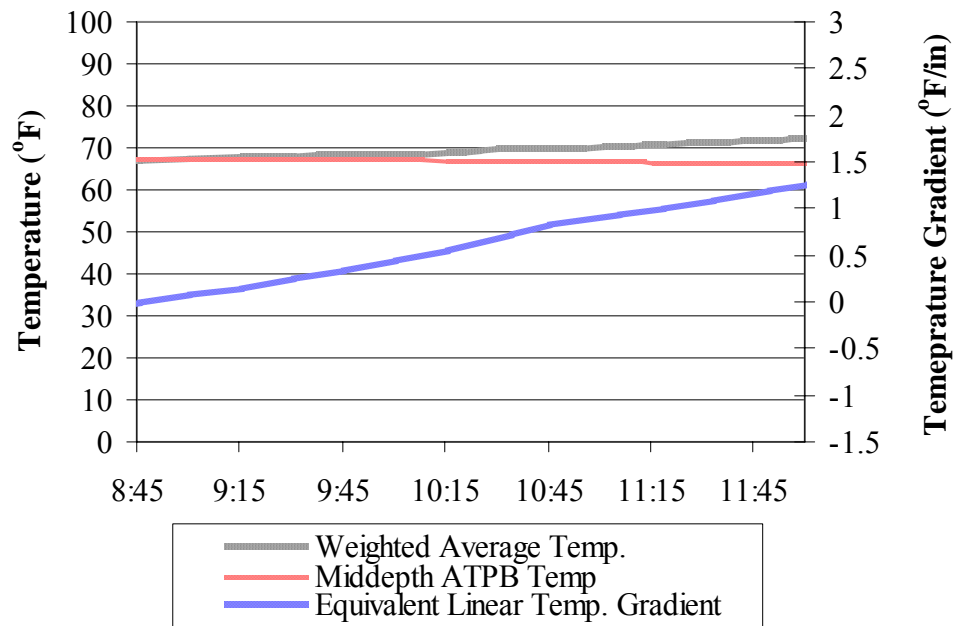


Figure 6.66. Midpanel temperature conditions during Class 10 truck testing performed in the spring of 2007.

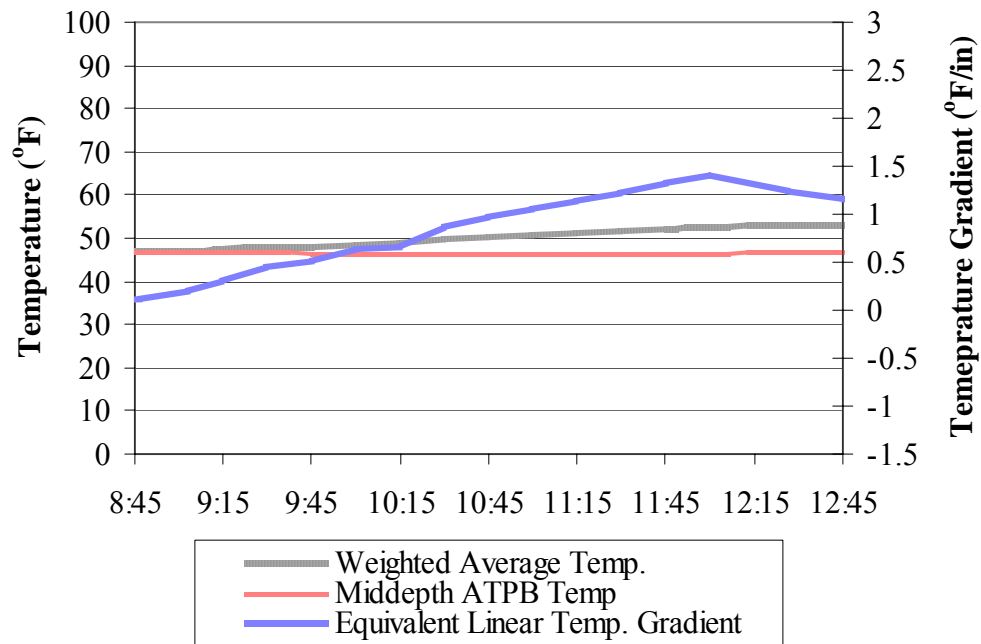


Figure 6.67. Midpanel temperature conditions during Class 6 and 7 truck testing performed in the spring of 2007.

The weighted average temperature for the summer test periods ranged between 64 and 85 °F with an average of 76 °F. The equivalent linear temperature gradient varied

between -0.62 and 1.67 °F/in with an average of 0.83 °F/in. The mid-depth temperature of the ATPB fluctuated between 65 and 81 °F with an average of 73 °F. As shown in Figure 6.68 through Figure 6.72, the weighted average temperature of the concrete varied considerably (approximately 7 °F on average) during summer testing. Both the average temperature and the temperature gradient in the slab experienced the largest fluctuation during summer. The average difference between the peak minimum and peak maximum temperature gradient for the summer test periods is 1.2°F/in.

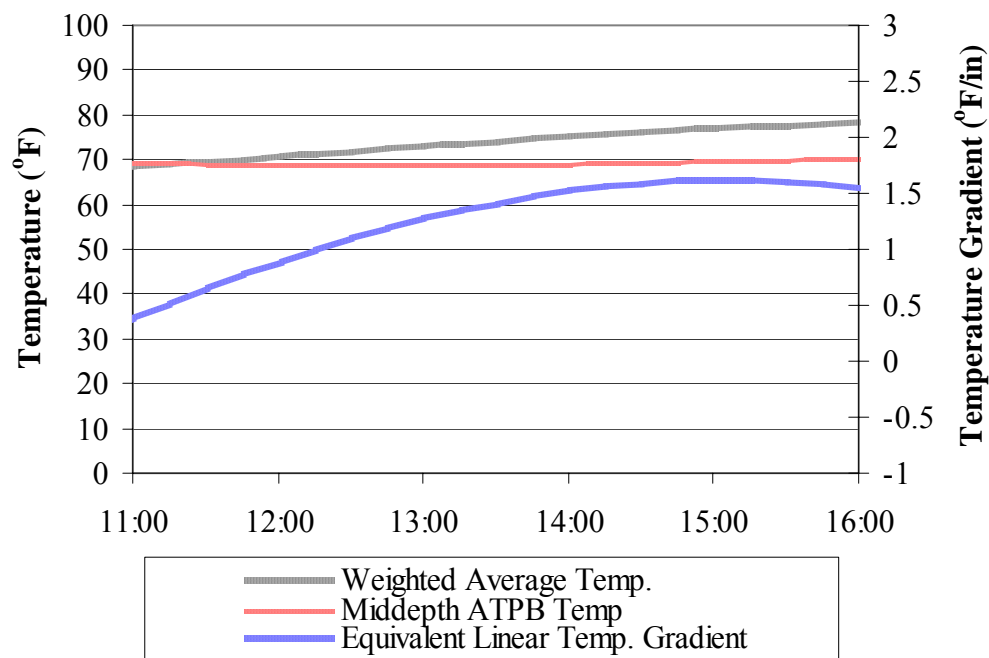


Figure 6.68. Midpanel temperature conditions during Class 10 truck testing performed in the summer of 2005.

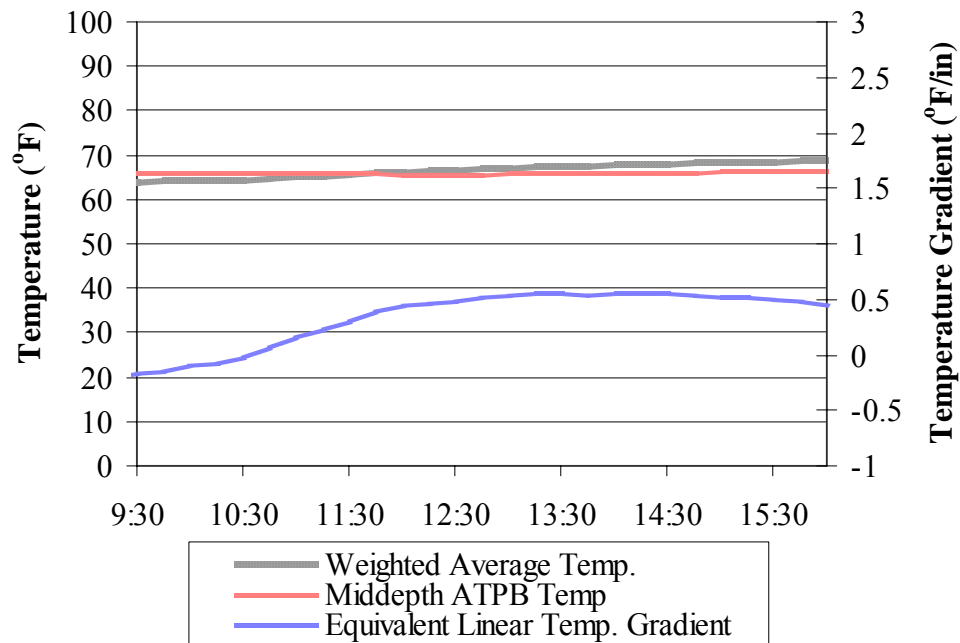


Figure 6.69. Midpanel temperature conditions during Class 6 and 7 truck testing performed in the summer of 2005.

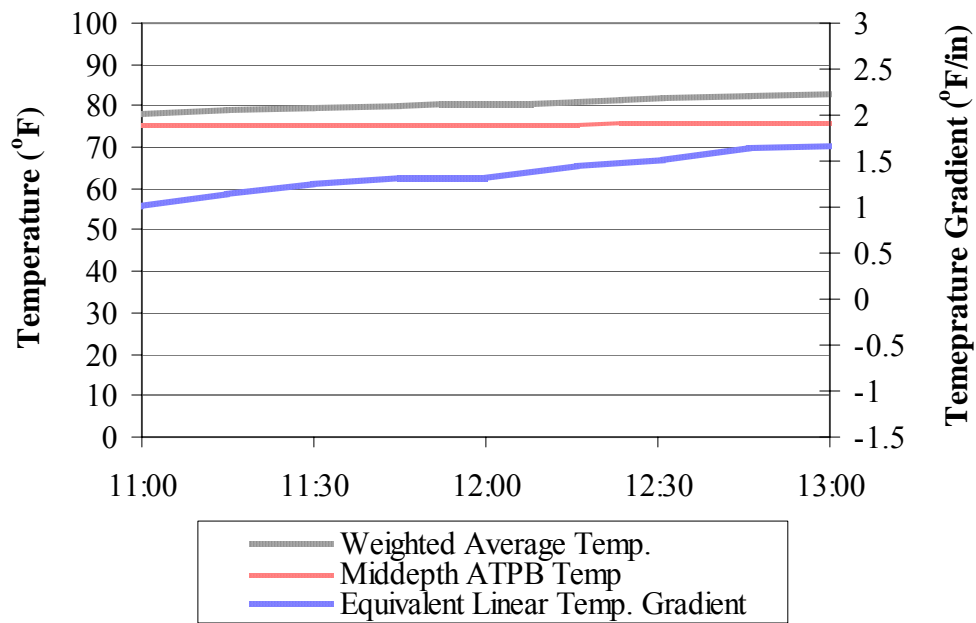


Figure 6.70. Midpanel temperature conditions during Class 10 truck testing performed in the summer of 2006.

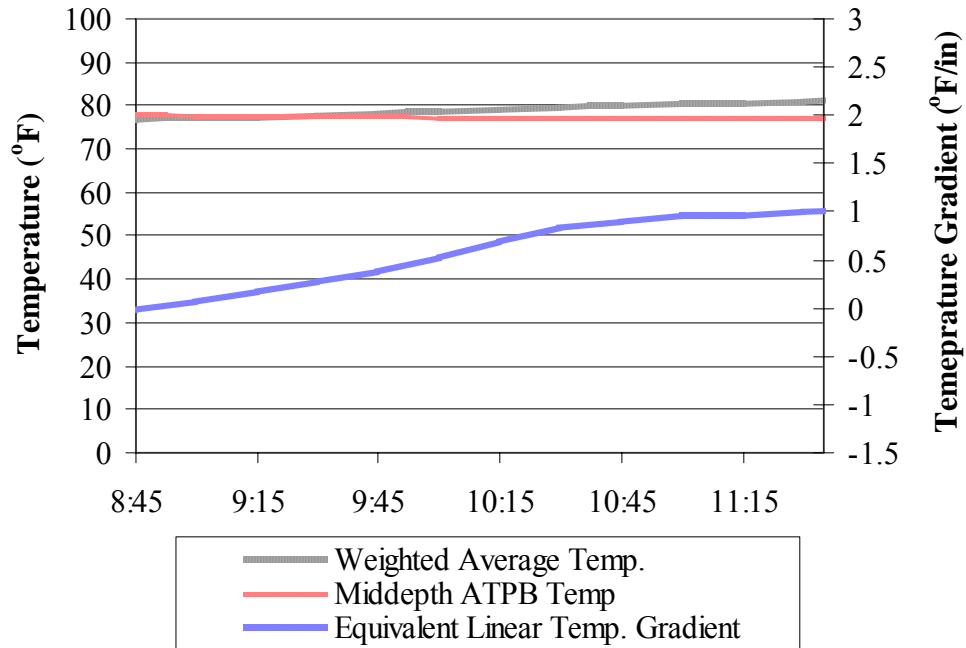


Figure 6.71. Midpanel temperature conditions during Class 6 and 7 truck testing performed in the summer of 2006.

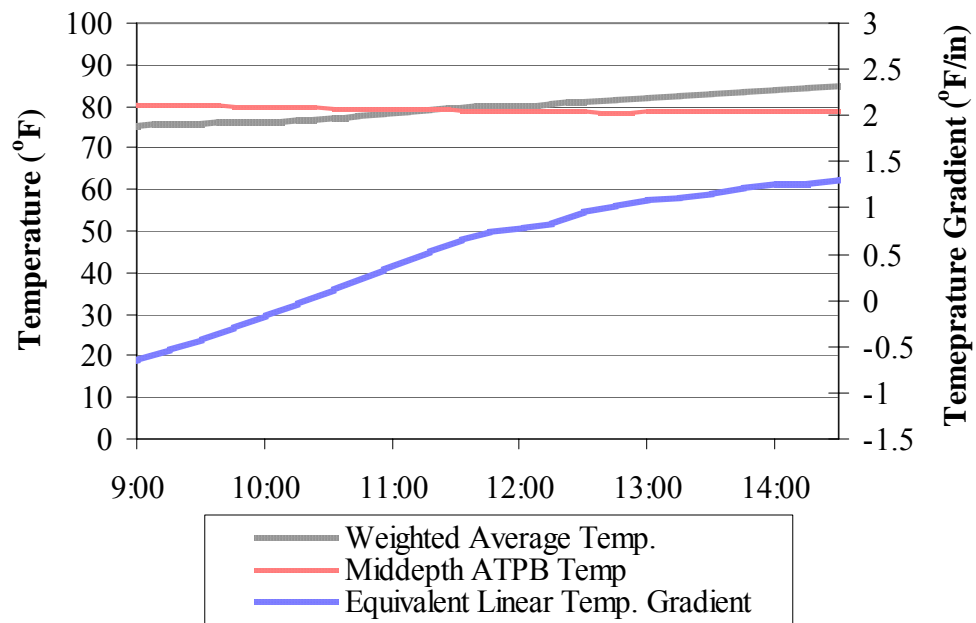


Figure 6.72. Midpanel temperature conditions during Class 6, 7, and 10 truck testing performed in the summer of 2007.

6.10.2. Concrete Moisture Distribution

Figure 6.73 and Figure 6.74, shown below, present the relative humidity throughout the PCC slab at the midpanel and edge during truck testing. The largest moisture gradient was observed during the winter of 2007 with a difference of 22 percent between the top and bottom of the slab. The moisture gradient was observed during the first test outing in the fall of 2004, with a 1 percent difference. Summary statistics for all test seasons are discussed below.

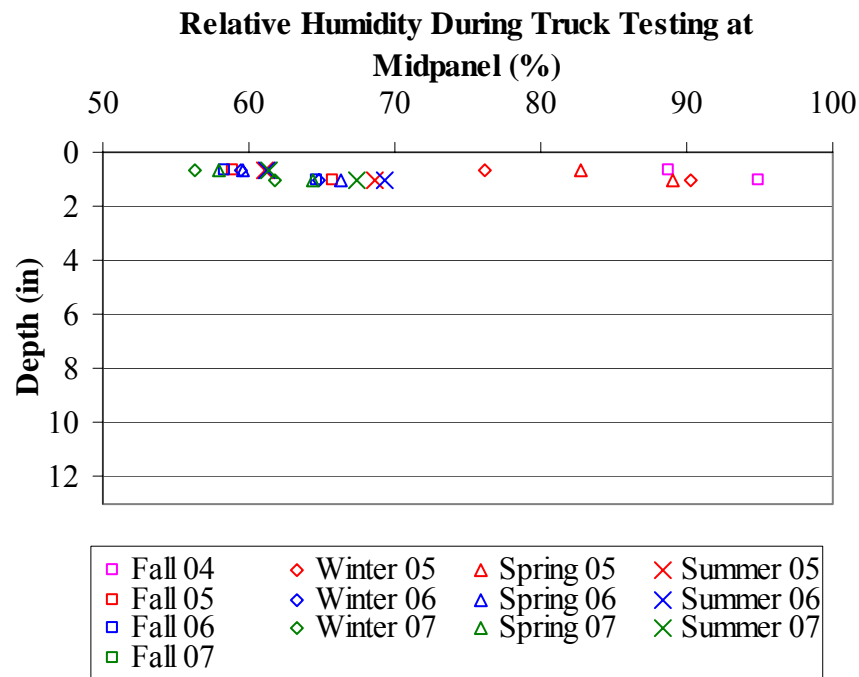


Figure 6.73. Midpanel moisture distribution throughout the PCC slab during truck testing.

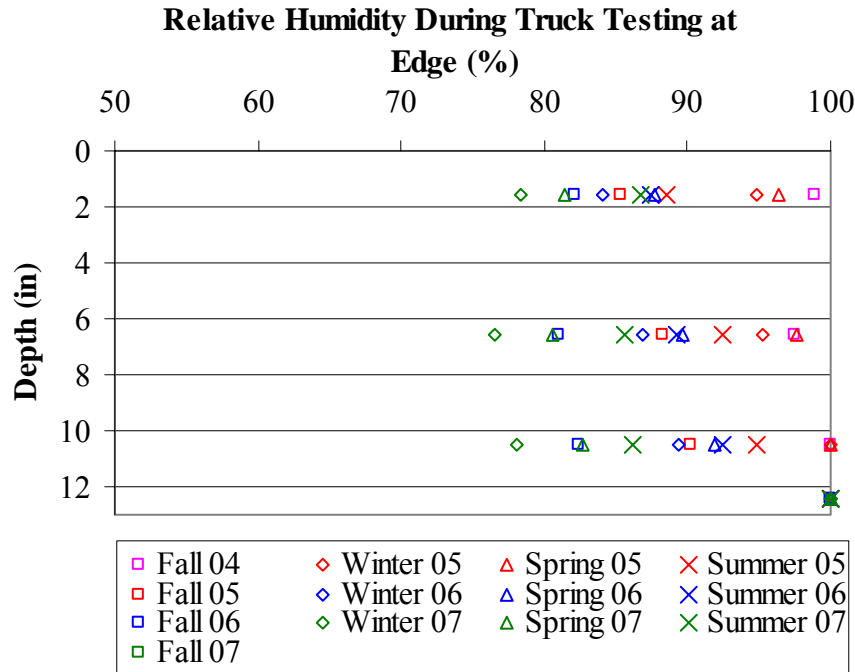


Figure 6.74. Edge moisture distribution throughout the PCC slab during truck testing.

First the uniform change in the moisture throughout the depth of the slab will be discussed because it affects the width of the crack at the joint. The uniform moisture content throughout the depth of the slab has continually declined since the construction of the pavement. Starting out at 100 percent relative humidity immediately after construction the relative humidity throughout the slab dropped to approximately 92 percent the first year after construction, 89 percent the second year and 81 percent the third year. The crack width at the joint will continue to increase with time until the relative humidity within the slab stabilizes.

Now, the change in moisture content throughout the depth of the slab will be discussed. The relative humidity near the slab surface fluctuates more over time compared to other depths within the slab since it is exposed to the ambient climatic conditions. The lowest measured relative humidity in the upper 2 in of the slab was found during the winter at 56 percent. The largest was measured during the summer with an average of 87 percent. The fall and spring relative humidity was between the winter and spring and typically ranged between of 81 and 88 percent. At mid-depth of the slab, the relative humidity varied between 78 and 100 percent and the bottom of the slab

remained saturated. The largest variation in relative humidity throughout the depth of the slab was found during the winter with an average difference of 14 percent. The spring had the smallest variation in relative humidity with an average of 11 percent. The summer and fall relative humidity fell between these two values with an average difference in relative humidity of 12 percent for both seasons.

6.11.0. Comparison of Strains Measured at Different Locations within the Slab

The first task was to compare strains measured at different locations within the slab. In this analysis, strains measured from the Class 10 truck for a 25,000 lb load level were used. Each strain measurement was normalized to help eliminate variations in strain due to variations between the target load level and the actual load applied for each of the test dates. Both the restrained (Cell 1) and unrestrained (Cell 2) test sections were analyzed. Strain measurements were measured seasonally throughout the first three years after construction and averaged to determine the strain at each location.

The strain locations evaluated were in the corner; in the wheelpath adjacent to the transverse joint; and at midpanel, adjacent to the lane/shoulder longitudinal joint. The sensors used for the corner location are CE01-02 and CE35-36, edge sensors are CE17-18 and CE43-44, and wheelpath sensors are CE05-06 and CE31-32. See Figure 6.1. The corner and edge strains represent the strains measured for the truck pass that traverses directly along the edge of the lane/shoulder joint. Strains measured in the wheelpath were generated when the truck ran along the wheelpath (approximately two feet from the edge of the pavement). These passes were used for the analysis because the truck travels directly over the corner and edge strain sensors when it is traveling along the edge of the lane/shoulder joint so maximum strains are being measured.

6.11.1. Strain in the Restrained Slabs

Figure 6.75 and Figure 6.76 display the variation in strain at different locations within the restrained slabs at the top and bottom of the slab. As Figure 6.75 shows, there is considerable variation in the strain measured in Slab A compared to that in Slab B at the top of the restrained cell. This variation in strain between the slabs can be attributed to variations in the depth of the top sensor from the top of the pavement. For example, the average strain measured at the wheelpath, adjacent to the transverse joint, is -14

microstrain in Slab A and -11 microstrain in Slab B while the sensor in Slab A is 1.28 in below the surface of the pavement and is 0.68 in for Slab B. However, strain in the corner varies approximately 1 microstrain between the two slabs, but the variation in sensor depth is significantly less with a difference of 0.08 in.

As Figure 6.76 shows, there is significantly less variation between strains measured in the two slabs at the bottom. This is because the bottom strain sensors were grouted directly to the top of the ATPB limiting the variation in the depth of the sensors between the two slabs. Therefore, strains measured at the bottom of the slab will be used to analyze strains at various locations within the slab.

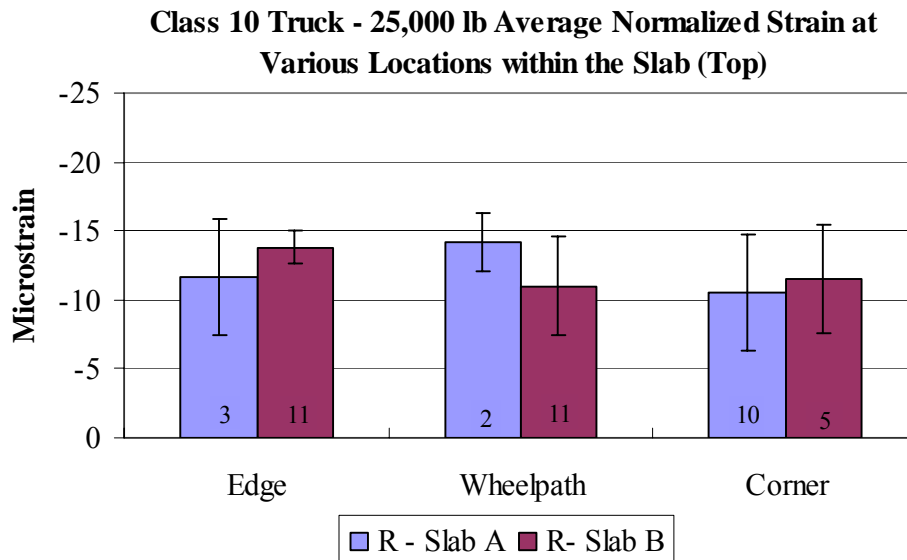


Figure 6.75. Average strains measured at various locations at the top of the restrained slabs during the first three years after construction.

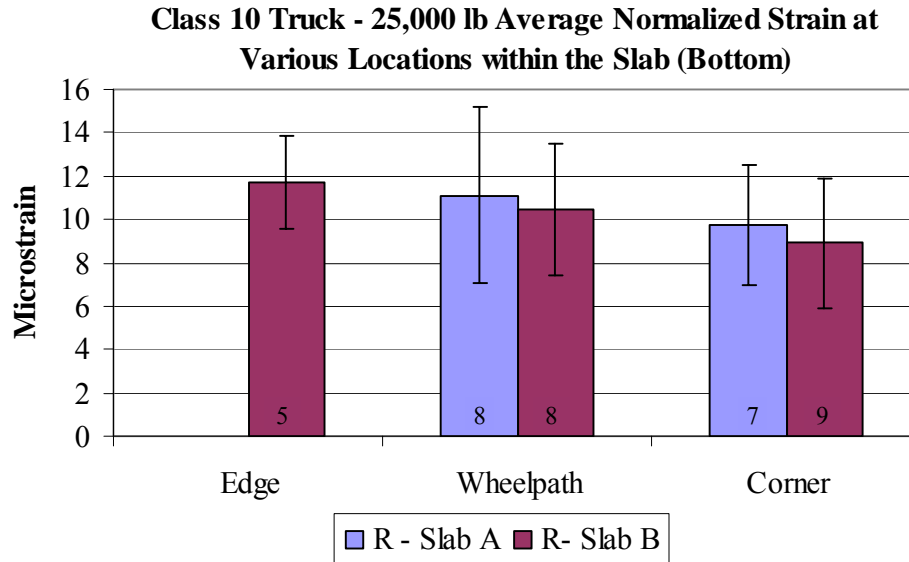


Figure 6.76. Average strains measured at various locations at the bottom of the restrained slabs during the first three years after construction.

Table 6.5. Variation in the depth of the dynamic sensors of the restrained cell.

Restrained Slabs (Cell 1)				
Sensor	Slab	Location	Depth of Sensor (in)	Slab Thickness(in)
CE01	A	Corner	0.86	14.26
CE02	A	Corner	13.99	
CE05	A	Wheelpath	1.28	14.68
CE06	A	Wheelpath	14.17	
CE17	A	Edge	0.88	14.65
CE18	A	Edge	14.37	
CE31	B	Wheelpath	0.68	14.41
CE32	B	Wheelpath	14.08	
CE35	B	Corner	0.94	14.53
CE36	B	Corner	14.12	
CE43	B	Edge	1.09	14.47
CE44	B	Edge	14.02	

The average strain at the edge for the restrained Slab B is 12 microstrain. In the corner and wheelpath locations the measured strain is 9 and 10 microstrain respectively. The average strain measured in the restrained slabs along the edge of the lane/shoulder

joints is approximately 12 percent larger than strain measured in the wheelpath along the transverse joints and 31 percent larger than strain measured in the corners. There are several possible reasons why the edge strains are larger in the restrained slabs. First, the edge location was measured at the midpanel of the slab and because of the restraint provided by the dowel and tie-bars and daily curling and warping of the slabs, stress/strain at this location is higher. Also, because of the proximity of the wheelpath and corner locations to the transverse joint and presence of a positive built-in temperature gradient strains in these locations are reduced due to increased support and restraint.

The standard deviation for the strains was large in areas that had the greatest variability in the edge support conditions. For example the corner gages, which had a standard deviation of 3 microstrain, are adjacent to two edges and the support provided by these edges varies seasonally as a function of the width of the transverse and longitudinal joints. The change in the transverse joint width also affects the edge support conditions for the strains measured adjacent to the transverse joint. The strains measured along the edge are affected by the width of the lane/shoulder joint. The width of the lane/shoulder joint varies less than the width of the transverse joint, which resulted in a higher standard deviation in the strains measured along the wheelpath adjacent to the transverse joint compared to that measured at midslab adjacent to the lane/shoulder joint. The strains measured in the wheelpath are also in close proximity to the lane/shoulder joint so the change in support conditions at the lane/shoulder joint also influences the strains measured in the wheelpath.

In an analysis of the response of a pavement to wheel loads Guo and Pecht determined that strains, measured in the slab interior, showed the least variability due to the distance from the joints [38]. Unfortunately, strain data in the interior of the slab is not available due to malfunctions with the strain gages. However, a similar trend is expected from the results of the variability in strain measured along the longitudinal and transverse joints of the slab.

6.11.2. Strain in the Unrestrained Slabs

Like the restrained slabs, the unrestrained slabs experienced considerable variation in the location of the top sensor beneath the slab (see Table 6.6). Therefore,

strains at the bottom of the slab were used to analyze the variation in strain at various locations within the slab.

Table 6.6. Variation in the depth of the dynamic sensors in the unrestrained cell.

Unrestrained Slabs (Cell 2)				
Sensor	Slab	Location	Depth of Sensor (in)	Slab Thickness(in)
CE01	A	Corner	1.06	11.76
CE02	A	Corner	11.43	
CE05	A	Wheelpath	0.87	11.93
CE06	A	Wheelpath	11.52	
CE17	A	Edge	0.80	11.69
CE18	A	Edge	11.25	
CE31	B	Wheelpath	1.17	12.14
CE32	B	Wheelpath	11.94	
CE35	B	Corner	1.37	12.14
CE36	B	Corner	11.49	
CE43	B	Edge	0.84	11.96
CE44	B	Edge	11.56	

As Figure 6.77 shows the unrestrained slabs also have the largest average strain at the edge location. The average strain measured at the edge location of Slab B is approximately 18 microstrain, in the corner and wheelpath locations the strain is 15 microstrain. The strain at the edge location is approximately 20 percent larger than strains in the corner and along the wheelpath.

Although strains observed in the corner location were the smallest, the deviation of these strains was the largest in the unrestrained slabs with an average of 4 standard deviations. This variation can be attributed to the affect changing support conditions and daily temperature and moisture fluctuations have on strains measured in the corner of the slab.

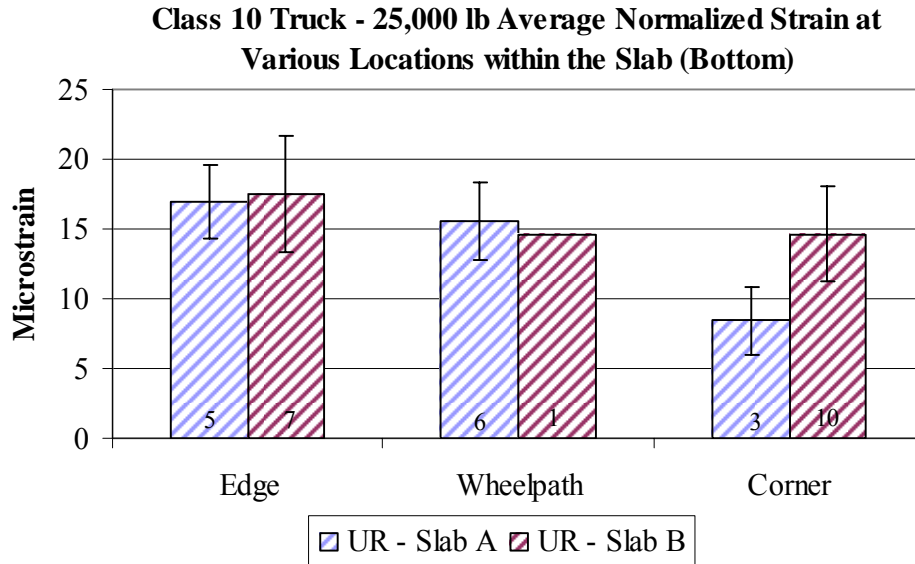


Figure 6.77. Average strains measured at various locations at the bottom of the unrestrained slabs during the first three years after construction.

6.12.0. Effect of Axle Configuration on Measured Strain

A closer examination of the strains measured at the edge location was performed to analyze the response of the pavement to various axle configurations. The average strain measured for the 25,000-lb load for each truck type (Class 6, 7, and 10) is reported in Figure 6.78 through Figure 6.80. All loads were normalized to a 25,000-lb load. Additionally, the first axle (standard axle) of each truck was not included in the analysis because the actual load applied was typically much less (approximately 10,000 lbs) than the target load. This load difference is too large for applying a linear interpolation between load and strain.

As Figure 6.78 shows, the critical axle for the Class 6 truck is axle three (second axle of the tandem) in both the restrained and unrestrained cells. The average strain for the third axle of the Class 6 truck was 11 microstrain for the restrained cell and 16 microstrain for the unrestrained cell. Strain measured for the third axle was approximately 15 percent larger than the second axle in the restrained slabs and 13 percent larger in the unrestrained when averaged over the three year period. The variation in the strain measured for each of the two axles of the tandem axle was 2 microstrain in the restrained slabs and 3 microstrain in the unrestrained slabs. It was

expected that strains in the unrestrained slabs would be larger and have more variation than the restrained slabs because they are free to move.

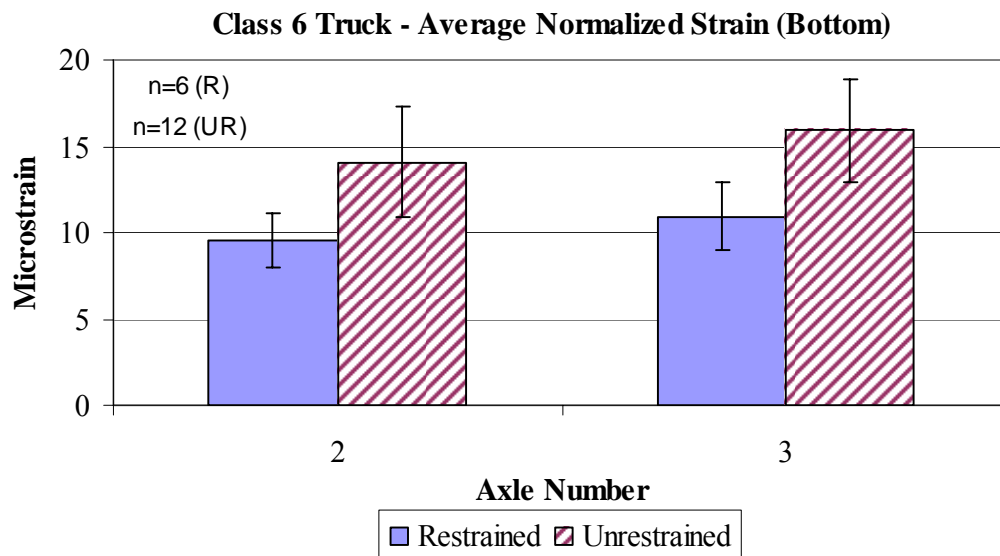


Figure 6.78. Average normalized strains measured along the edge of the restrained and unrestrained slabs for the Class 6 truck with 25,000 lb axle loads.

The fourth axle (third axle of tridem) was found to be the critical axle for the Class 7 truck, as shown in Figure 6.79. The average strain for the fourth axle of the Class 7 truck was 10 microstrain for the restrained cell and 16 microstrain for the unrestrained cell. In the unrestrained slabs, the fourth axle is 26 percent larger than the second and 14 percent larger than the third. The same trend was also found in the restrained slabs with the fourth axle having on average a 14 percent larger strain than the remaining axles. A similar trend to the Class 6 truck was experienced with strains in unrestrained slabs being larger and having more variation than the restrained slabs.

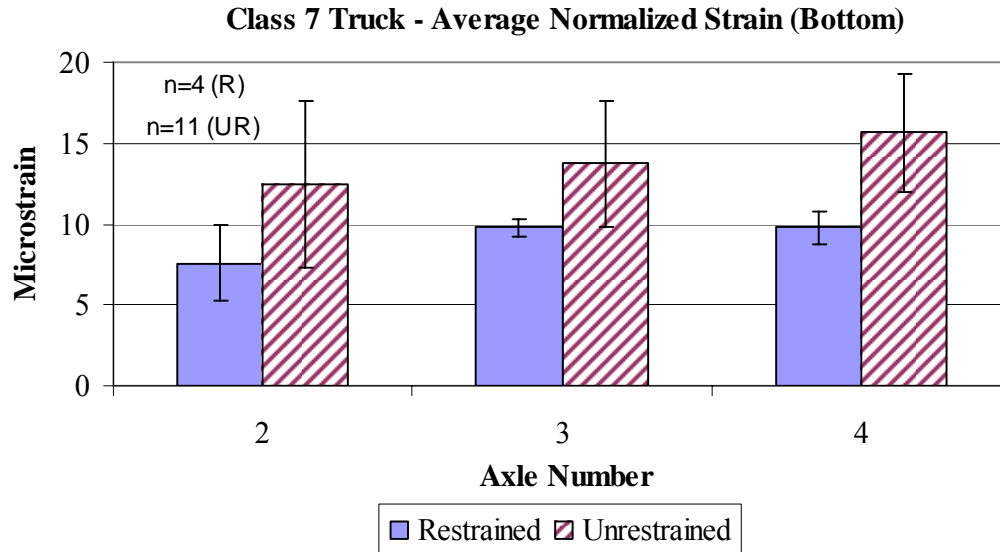


Figure 6.79. Average normalized strains measured along the edge of the restrained and unrestrained slabs for the Class 7 truck with 25,000 lb axle loads.

As Figure 6.80 shows, the third axle (second axle of tandem) exhibited the largest strain in the restrained and unrestrained slabs for the Class 10 truck. The average strain for the third axle of the Class 10 truck was 12 microstrain for the restrained cell and 18 microstrain for the unrestrained cell. In the restrained slabs, the third axle is approximately 34 percent larger than the second and 27 percent larger than the fourth, 7 percent larger than the fifth, and 22 percent than the sixth axle. The same trend was also found in the unrestrained slabs with the fourth axle having an average 18 percent larger strain than the remaining axles. Strains measured when the Class 10 truck traversed the edge of the slab were larger and had more variation in the unrestrained slabs, as would be expected.

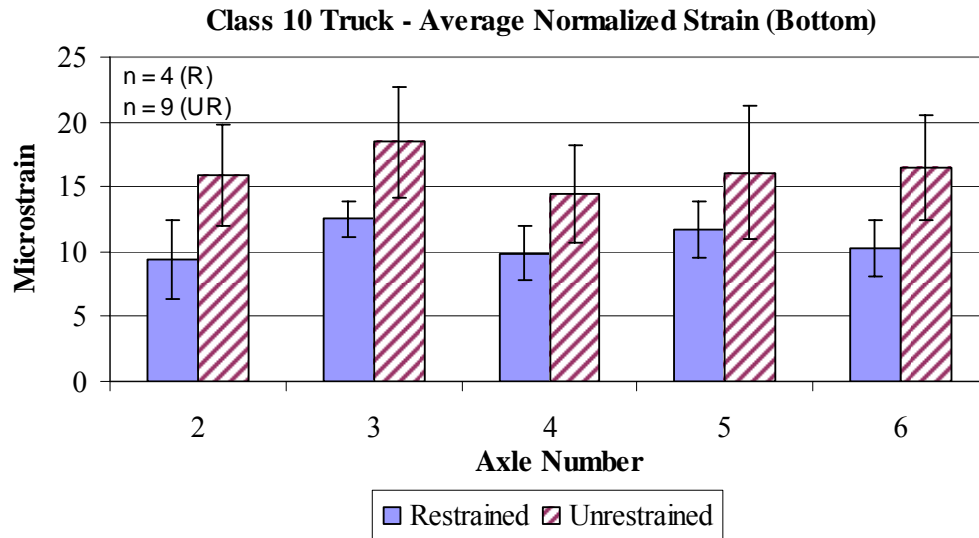


Figure 6.80. Average normalized strains measured along the edge of the restrained and unrestrained slabs for the Class 10 truck with 25,000 lb axle loads.

The Class 6 and Class 10 trucks both have a tandem axle, therefore an analysis was performed to investigate the measured strain for the tandem axle of the different truck classifications. As Figure 6.81 shows, the strain measured in the first axle for the tandem was approximately the same in the restrained slabs but in the unrestrained slabs the difference between the Class 6 and 10 trucks was approximately 1.6 microstrain. The larger difference in the unrestrained slabs may be attributed to wheel wander as the different trucks traversed the sensor or differences in the temperature and gradient present at the time of testing between the trucks. The affect of slab temperature and gradient affects the unrestrained slabs more because there is no restraint provided by dowel and tie-bars.

Strain measured for the second axle of the tandem was larger for the Class 10 truck in both the restrained and unrestrained slabs. The difference in axle spacing between the trucks contributes to the difference between strains measured in the Class 6 and 10 trucks. The Class 6 truck axle spacing is 54 in while the Class 10 truck spacing is less at 50 in. Therefore, strains measured by the Class 10 truck are larger in the second axle since a higher percentage of the load contributed by the adjacent axle is distributed to the location of the gage.

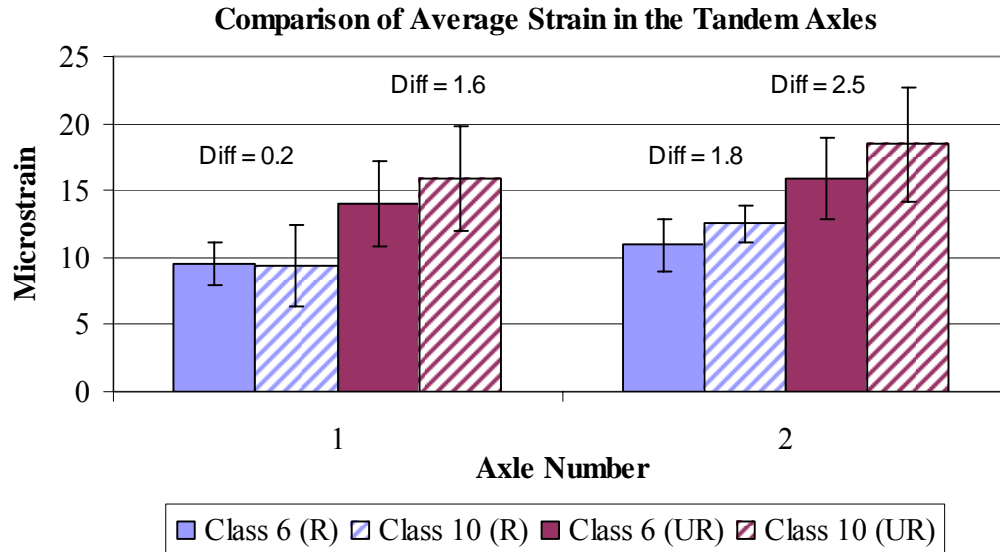


Figure 6.81. Average normalized strains measured along the edge of the restrained and unrestrained slabs for the tandem axle of the Class 6 and 10 trucks.

As Figure 6.82 displays, similar trends were experienced between the tridem axle of the Class 7 and 10 trucks. The unrestrained slabs experience a larger difference in measured strains between the different truck classifications. Additionally, differences between the measured strains of each axle can be attributed to differences in the spacing of the axles between the Class 7 and 10 trucks.

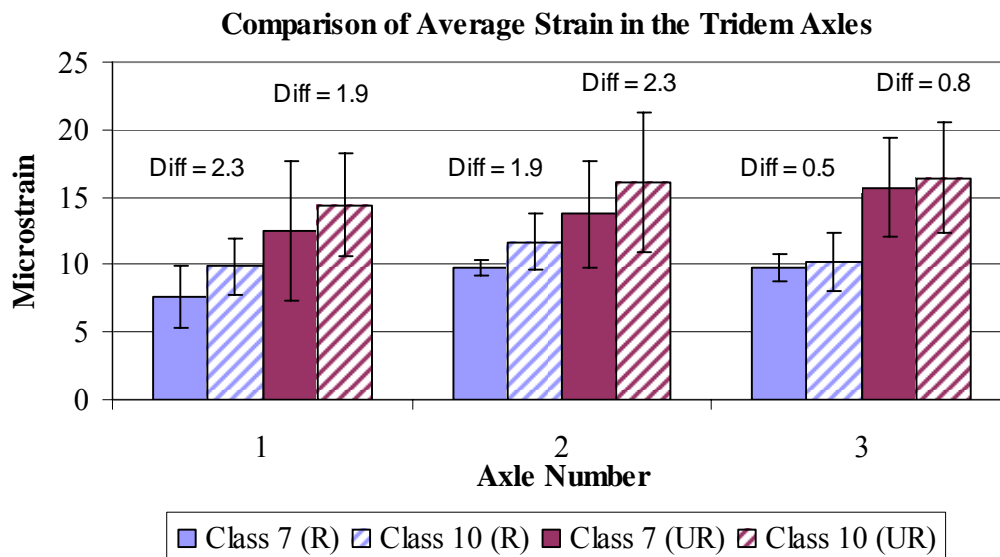


Figure 6.82. Average normalized strains measured along the edge of the restrained and unrestrained slabs for the tridem axle of the Class 7 and 10 trucks.

6.13.0. Effect of Axle Load Magnitude on Measured Strain

This section examines the effects of the magnitude of the load on the measured strains. Figure 6.83 through Figure 6.85 display the average strain normalized to the target load level for each truck class (Class 6, 7 and 10). The critical axle determined in the previous section (reference section 5.4) was used for each truck type.

As observed in Figure 6.83, there is a significant difference in strain generated at the three different load levels (15,000, 20,000 and 25,000 lb) for the Class 6 truck in both the restrained and unrestrained cells. The 15,000-lb load level generated an average strain of 7 microstrain; the 20,000-lb load produced an average of 9 microstrain and the 25,000-lb load measured 12 microstrain in the restrained cell. As expected, the unrestrained cell experiences higher strains at each load level. The 15,000 lb-load has an average strain of 10 microstrain, the 20,000-lb load has an average of 13 microstrain and average strain for the 25,000-lb load is 16 microstrain.

There is an average difference of 4 microstrain between the minimum and maximum load level and a 2.5 microstrain difference between the 20,000 and 25,000-lb load levels. The strain observed from the 25,000-lb load level is 64 percent greater than strain observed by the 15,000-lb load level and 23 percent greater than strain observed by the 20,000-lb load. Therefore, it can be concluded that strain induced by different loads increases with increasing load in a non-linear manner.

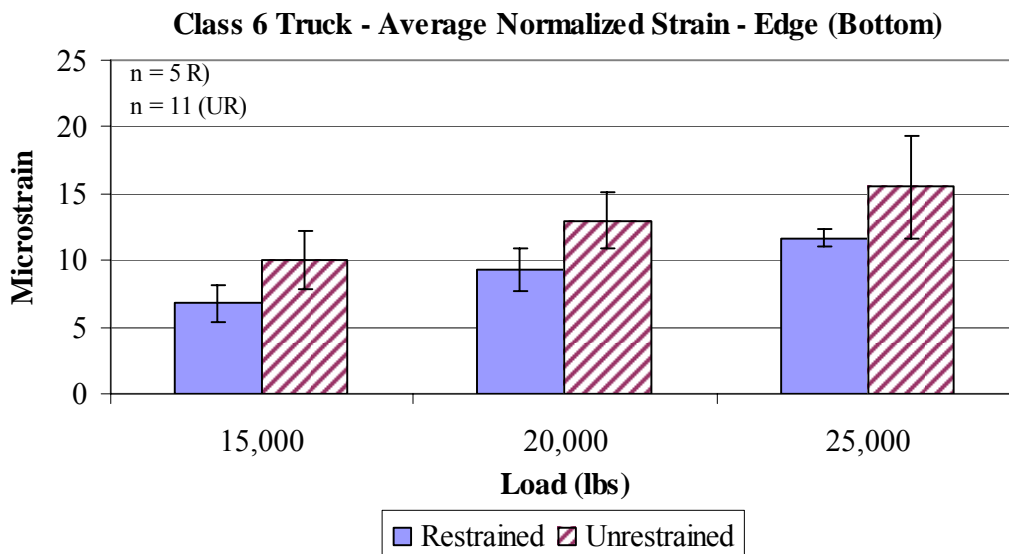


Figure 6.83. Strains measured along the edge for the critical axle of the Class 6 truck for various load levels.

Like the Class 6 truck, a similar trend of increasing strain with increasing load magnitude was observed in the Class 7 and 10 trucks (Figure 6.84 and Figure 6.85). As Figure 6.84 shows, the strain increases an average of 2 microstrain between the 15,000-lb and 20,000-lb load levels and increases 2.5 microstrain between the 20,000-lb and 25,000-lb load levels. The results are very similar in the Class 10 truck, but it appears as though the increase is larger, this is due to the larger load increase between the load levels.

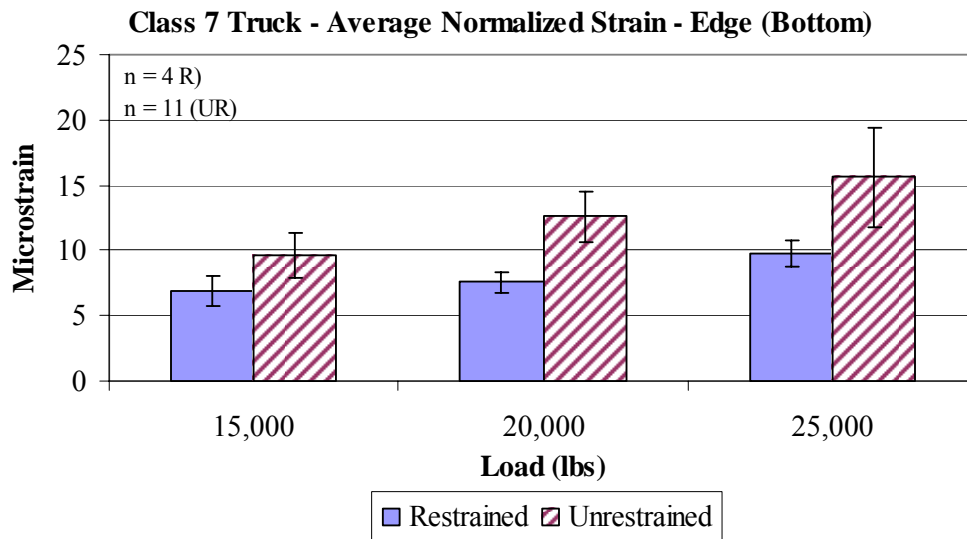


Figure 6.84. Strains measured along the edge for the critical axle of the Class 7 truck for various load levels.

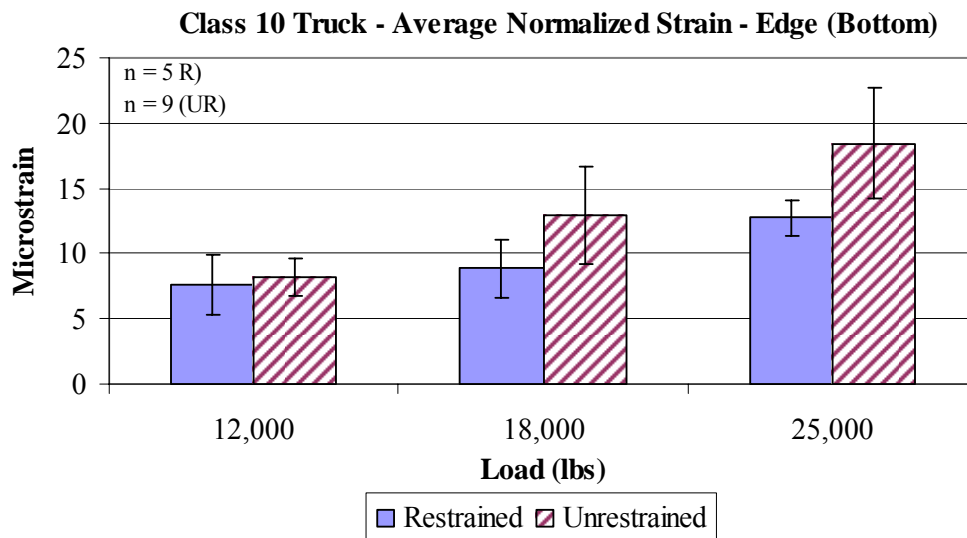


Figure 6.85. Strains measured along the edge in the unrestrained slabs for the critical axle of the Class 10 truck for various load levels.

A regression analysis was preformed to see if a correlation existed between load magnitude and measured strain. As Figure 6.86 shows, this relationship does exist in both the restrained and unrestrained cells. The restrained slab shows good correlation to an exponential fit with a coefficient of 0.72. The unrestrained slabs show a strong correlation with the power function with a correlation coefficient of 0.95.

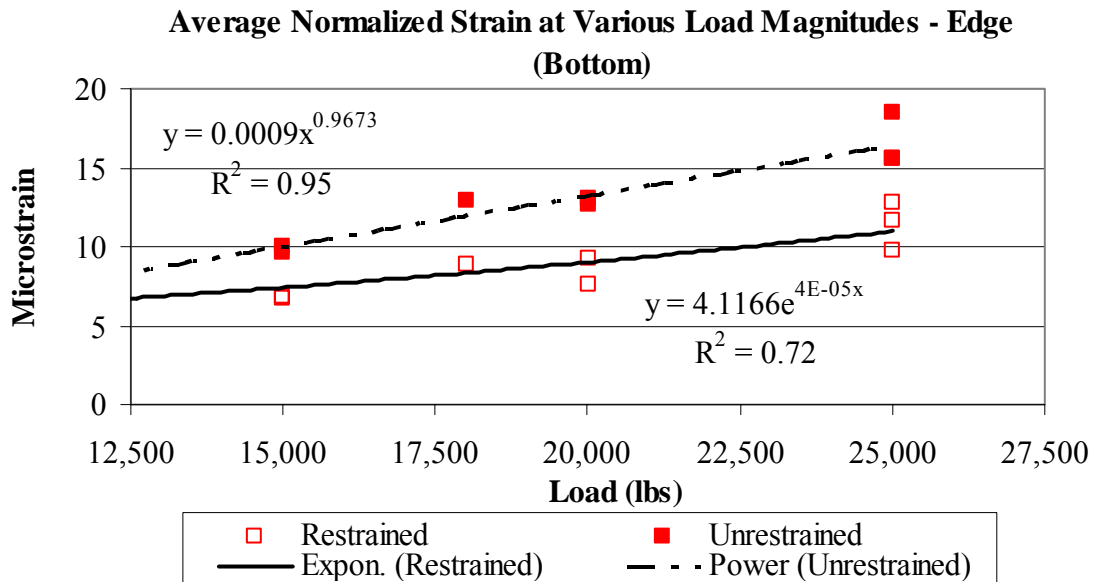


Figure 6.86. Strains measured along the edge of the slabs for the critical axle of all the truck classes and load levels.

6.14.0. Dynamic Strains Measured at the Top and Bottom of the Slab

A closer examination of the critical axle strains measured for each truck classification at the edge location was performed to compare strains measured at the top of the slab versus those measured at the bottom. The strains were normalized for a 25,000 lb load level. The strains were also extrapolated to the top of the slab using linear interpolation since the distance of the upper sensor to the slab surface was approximately 1 in. The survey data was used to define the exact distance of each sensor from the pavement surface. The following subsections provide the analysis for the restrained and unrestrained slabs respectively.

6.14.1. Strain at the Top and Bottom of the Restrained Slabs

Figure 6.87 displays the average strain at the top and bottom of the restrained slabs for the various truck classifications. There is a general trend of higher strains at the

surface of the slab compared to the bottom of the slab. An analysis of the average of all of the strains, measured at the top of the slab, for all three truck classifications shows that these strains are approximately 27 percent larger than those at the bottom of the slab. A paired t-test was performed to determine if the measured strain at the top is statistically different from strain at the bottom of the slab. It was determined with 95 percent confidence that strain at the top of the slab is indeed larger than the strain at the bottom of the slab. This difference, in the magnitude of the measured strains, indicates that the slab must be bonded to the asphalt treated permeable base.

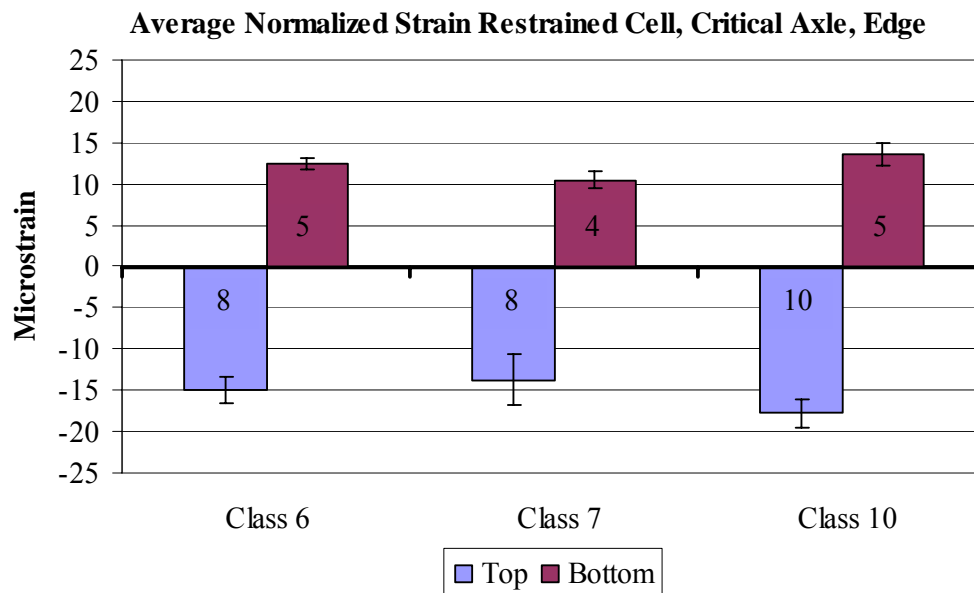


Figure 6.87. Strain measured at the top and bottom of the slab along the edge of the restrained cell.

As previously discussed, temperature gradients develop daily in the concrete slab. For example, during the evening when the temperature on top of the slab is colder than that at the bottom, the slab curves upward. Although the slab is deflecting upward, the base and slab remain in contact as long as the curvature does not exceed the precompression produced by the weight of the slab [25]. Therefore, the two layers act as one monolithic section and the neutral axis is shifted downward resulting in a higher strain/stress at the top of the slab will be higher than that at the bottom of the slab. This is beneficial to the service life of the slab since the tensile stresses at the bottom of the slab are reduced.

There is also a larger amount of variation among the extrapolated strains at the top of the slab compared to those measured at the bottom in the restrained slabs. An analysis of the variation, between the top and bottom strains, showed that strains at the top of the slab vary twice as much as those on the bottom. One explanation for this might be related to defining the exact position of the gage. The gages at the bottom of the slab were bonded to the surface of the base while the gages in the upper portion of the slab were hung from wooden dowel rods. The elevation and location of each gage was surveyed prior to the passing of the paver but the weight of the concrete head in front of the paver or errors in the survey could result in changes in the actual location of the sensor with respect to the surveyed location.

6.14.2. Strain at the Top and Bottom of the Unrestrained Slabs

As previously discussed, when the slab is bonded to the base, the two layers act as one monolithic section, the neutral axis is shifted downward and strain at the top of the slab will be higher than that at the bottom of the slab. However, when the slab is not bonded to the base, the strain at the top of the slab will be equal in magnitude and opposite in sign to the strain at the bottom of the slab. This trend is observed in the unrestrained slabs of Cell 2 and is shown in Figure 6.88.

Although Figure 6.88 shows that strain is larger at the bottom in the Class 6 and 7 trucks and at the top in the Class 10, significant variation was experienced between the measured strains. Therefore, a paired t-test was performed to determine if there is a statistical difference between strain at the top and bottom of the slab. It was determined with 95 percent confidence that there is no difference between strain measured at the top and bottom of the unrestrained slabs. Unlike the restrained slabs, the unrestrained slabs appear to be unbonded to the asphalt treated permeable base. This can contribute to the higher strains that were measured for the unrestrained slabs. The performance of a pavement as predicted by the MEPDG is significantly affected by the age at which friction (bond) between the slab and underlying layer is lost. Unfortunately, very limited information is available on the degradation of friction over time. These findings do shed some light on this phenomenon. It appears that the friction can degrade more readily for

an unrestrained slab when compared to a restrained slab as a result of the increased thermal- and moisture-related expansion and contraction of the slabs.

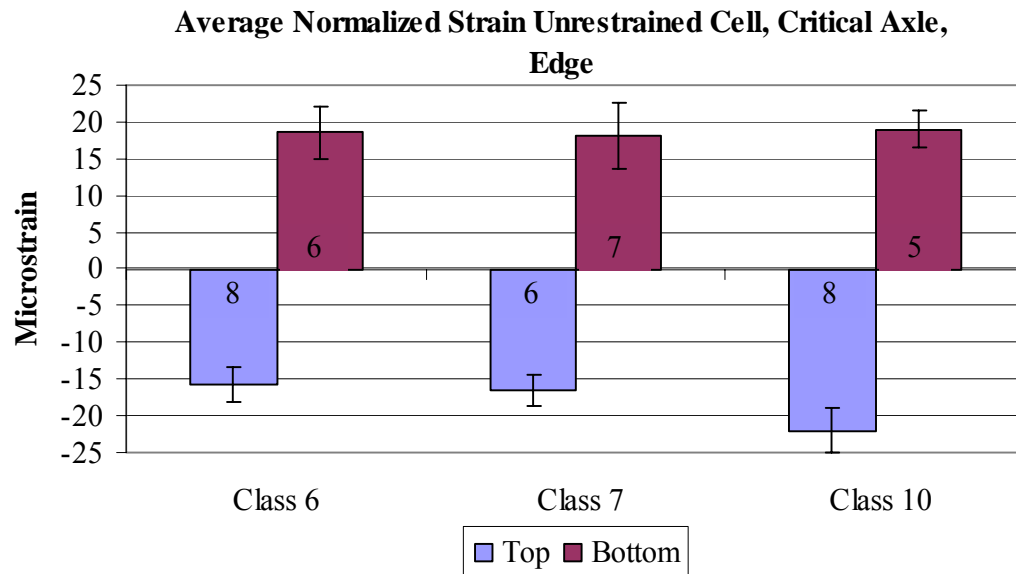


Figure 6.88. Strain measured at the top and bottom of the slab along the edge of the unrestrained cell.

6.15.0. Effect of Slab Temperature and Gradients of Dynamic Strain

The dynamic strain measurements collected in the corner and wheelpath during the first three years after construction were evaluated for both the restrained (Cell 1) and unrestrained (Cell 2) cells to characterize the effects of slab temperature and temperature gradients. These strains were plotted against the average slab temperature and equivalent linear gradient present at the time of testing to see if any correlation existed. The fourth axle for the Class 7 truck and the sixth axle for the Class 10 truck were evaluated at the 25,000-lb load level. Refer to Figure 6.89 through Figure 6.91.

The scatter in the data depicted in Figure 6.89 and Figure 6.90 indicates there is little to no relationship between the measured strain and change in temperature for either the corner or wheelpath locations for the restrained slabs. Figure 6.90 indicates that there is also not a relationship between the slab temperature and measured strain for the unrestrained slabs. Additional graphs supporting this conclusion can be found in appendix G.

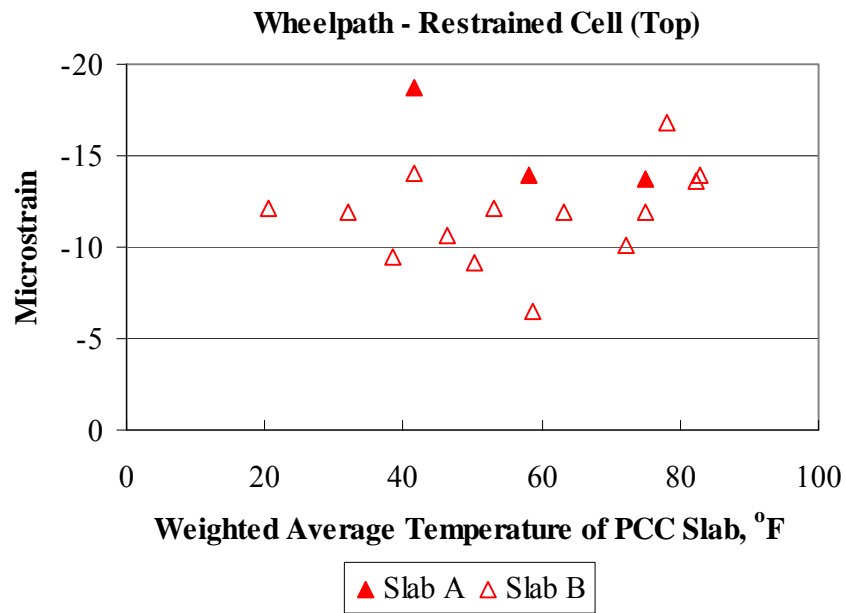


Figure 6.89. Relationship between strains measured in the wheelpath at the top of the restrained slabs and slab temperature.

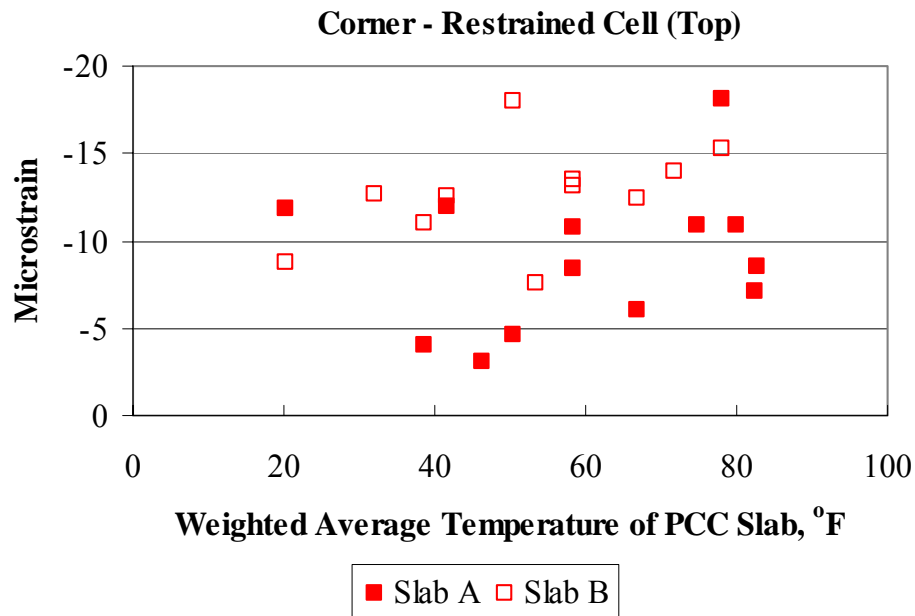


Figure 6.90. Relationship between strains measured in the corner at the top of the restrained slabs and slab temperature.

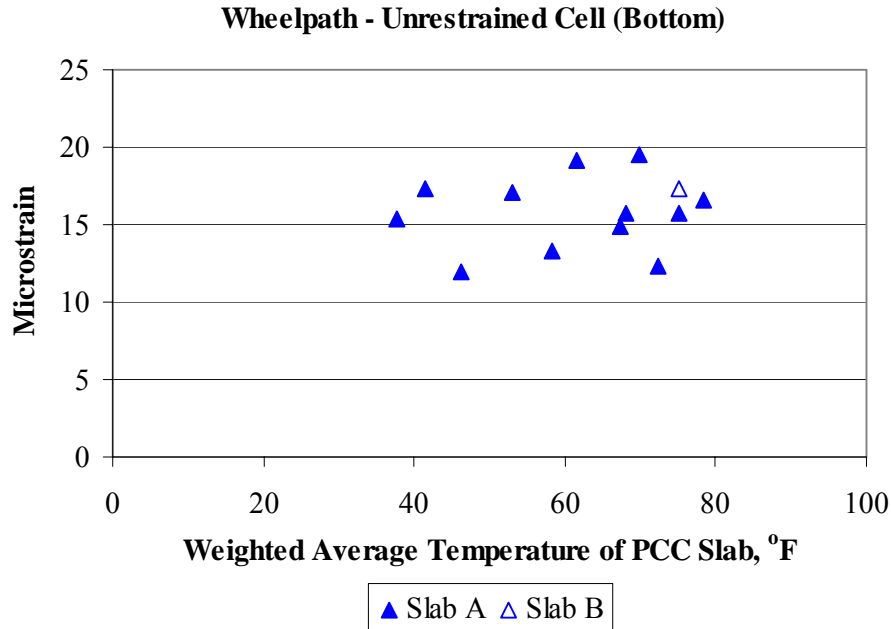


Figure 6.91. Relationship between strains measured in the wheelpath at the bottom of the unrestrained slabs and slab temperature.

The relationship between the strain measured in the wheelpath and the equivalent linear gradient present at the time of testing for both the restrained and unrestrained cells are provided in Figure 6.92 and Figure 6.93. These figures show that there is a trend of increased strain with increasing positive temperature gradients at the top of the slab in both the restrained and unrestrained slabs. As Figure 6.92 shows, when the gradient in Slab B was -0.15 °F/in the measured strain was -6 microstrain and when the gradient increased to 1.91 °F/in the strain increased to -14 microstrain. Similar results were experienced in the unrestrained Slab A (Figure 6.93), when the gradient was 0.05 °F/in strain was -5 microstrain, but when the gradient increased to 1.91 °F/in strain increased to -14 microstrain.

Other researchers have investigated the affect of the equivalent linear temperature gradient on dynamic strain with varying results. In 1998, Yu et al. determined that load induced strains are not significantly affected by temperature gradients, but a trend of increasing strain with increasing negative temperature gradients was experienced [10]. However, in 2002 Burnham showed that dynamic strain depends on slab shape and saw trends of increased strain with increasing positive temperature gradients [39]. The results

of this analysis support Burnham's finding that dynamic strain increases with increasing positive temperature gradients.

This trend of increasing strain with increasing positive temperature gradients was experienced in both the restrained and unrestrained slabs at both the top and bottom of the slab for both locations (corner and wheelpath). The figures of this relationship for the remaining locations can be found in appendix G.

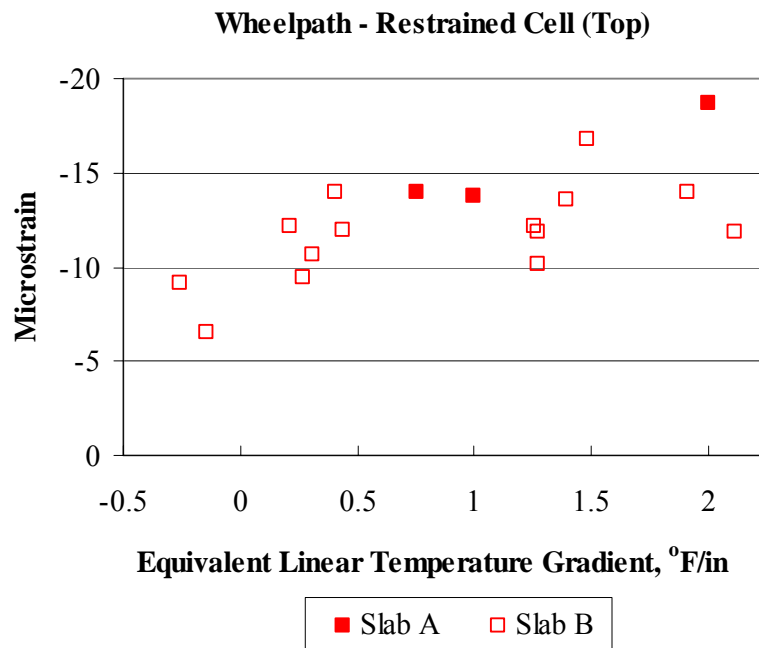


Figure 6.92. Relationship between strains measured in the wheelpath at the top of the restrained slabs and the temperature gradient in the slab.

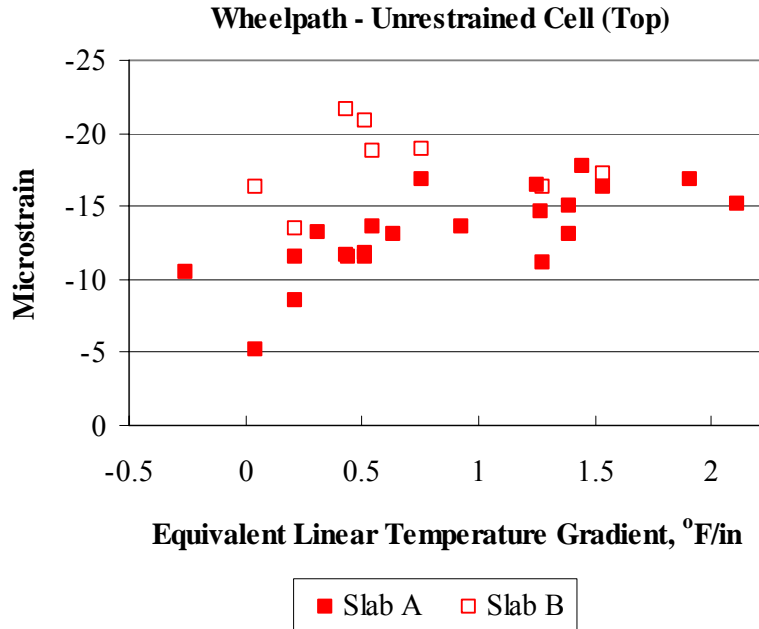


Figure 6.93. Relationship between strains measured in the wheelpath at the top of the unrestrained slabs and the temperature gradient in the slab.

6.16.0. Conclusions

This analysis had provided a better understanding of the response of a jointed plain concrete pavement to applied loads. The FWD and truck load testing provided valuable insight that will help in calibrating finite element models that will be used to characterize stress that develops in the pavement as a result of these applied loads.

Results from the FWD testing provided the following insight:

- Undoweled pavements in Pennsylvania will have low load transfer capabilities for a large portion of each day and for several months in the year even for a short 15-ft joint spacing.
- The load transfer measured for the unrestrained slabs is dependent on the temperature gradient present at the time of testing. The load transfer measured for the restrained slabs was found to not be affected by temperature gradients or slab temperature.
- Temperature gradients have a larger affect on measured deflections than moisture gradients.

- A good correlation was found between the magnitude of the Void parameter and the size of the gradient for both the restrained and unrestrained slabs.
- No correlation was found between the support conditions beneath the slab and the gradient of the slab during testing or the temperature of the ATPB.
- The unrestrained slabs exhibit larger deflections and more variation than the restrained slabs.

Seasonal truck load testing conducted over the dynamic strain gages installed in Cells 1 and 2 provided useful in determining the response of the pavement. Results from the trucking testing provided the following insight:

- The measured strains indicate the interface between the base and the slab is unbonded for the unrestrained slabs and bonded for the restrained slabs, indicating that the life of the bond might be a function of the restraint conditions.
- The average slab temperature did not affect the magnitude of the strain measured for either the restrained or unrestrained slabs.
- A relationship was found between the measured strain and the temperature gradient present in the slab at the time of testing for both the restrained and unrestrained slabs.

CHAPTER 7: DEVELOPMENT AND VALIDATION OF FINITE ELEMENT MODELS

7.1.0. Introduction

The performance of rigid pavements is predicted as a function of stress. Since it is not possible to measure stress directly, the measured strains are used in the development of finite element models that can be employed to determine the stress in the pavement. This chapter presents the development and validation of rigid pavement models for predicting stress. The results of the seasonal FWD data are used to define the model inputs including: elastic modulus, k-value, and load transfer efficiency. Upon determination of all inputs, the finite element program Illislab will be used to model the pavement structure. This program was chosen because it is frequently used in the pavement community, it is user-friendly and the modeling assumptions inherent to this program are representative of those used in the majority of the other finite element pavement analysis programs frequently used. The slab is modeled as a medium-thick plate and the pavement structure is modeled as an equivalent three-layer system. The Illislab model will be validated using strain measurements recorded during the dynamic testing of trucks with known axle weight and configurations.

7.2.0. Model Inputs

The development of a pavement model in finite element involves the determination of several inputs. These inputs can be grouped into three categories: mesh generation and material property inputs, joint inputs, and loading inputs. The mesh generation and material property inputs include: the determination of the optimal mesh fineness, the elastic modulus, Poisson's ratio, the unit weight of the concrete and ATPB, thickness of the slab and base, gradient at the time of loading, k-value and coefficient of thermal expansion. The joint stiffness was validated using the LTE's measured in the field. The third classification of model inputs are those related to the applied and temperature loads. The pertinent load information includes the type of vehicle loading (three axle truck, four axle trucks or six axle truck), axle spacing, axle configuration, tire

pressure, and contact area. The following sections provide the classification of the inputs for development of the finite element model of the Smart Pavement.

7.2.1. Mesh-Slab Model Inputs

The pavement was modeled as a six-slab system with three slabs in the longitudinal direction and two in the transverse direction. Each slab is 15 ft long and 12 ft wide. The number of elements used during the model validation was varied based on the location of the strain sensors in the slab. When predicting strain along the transverse joint, the sensors are spaced 10 in apart in the longitudinal direction and are located 6 in from the transverse joint. A mesh with 30 elements in the longitudinal direction and 72 in the transverse direction was used. All elements are the same size. Computational time for each model is minimal so it was not necessary to restrict the increased fineness in the mesh to the regions where sensors are located. Table 7.1 provides the slab meshing used for model validation of the three sensor groups (adjacent to transverse joint, adjacent to lane/shoulder joint and midpanel) of the Smart Pavement.

Table 7.1. Number of elements used for generating the finite element models.

Sensor Group	Elements in Transverse Direction	Elements in Longitudinal Direction
Adjacent to Transverse Joint	72	30
Adjacent to Shoulder Joint	36	60
Midpanel	72	30

The models consist of a concrete pavement and ATPB resting on a dense liquid foundation. The material properties for the concrete were measured for cores cast at the time of paving. The thickness of the pavement was determined using an average of the depths established based on the survey data for the restrained (Cell 1) and unrestrained (Cell 2) slabs. The concrete material inputs used in the models are provided in Table 7.2.

Table 7.2. PCC model inputs for each slab type based on measured values.

PCC Model Input	Restrained (Cell 1)	Unrestrained (Cell 2)
Thickness	14.5 in	12 in
Elastic Modulus (365-days)	5,050,000 psi	5,050,000 psi
Poisson's Ratio	0.17	0.17
Unit Weight	143 lbs/ft ³	143 lbs/ft ³
Coefficient of Thermal Expansion	5.90 $\mu\epsilon/^\circ\text{F}$	5.90 $\mu\epsilon/^\circ\text{F}$

The measured material properties for the ATPB were determined from laboratory testing following proper ASTM specifications. The material inputs for the ATPB are provided in Table 7.3.

Table 7.3. ATPB model inputs based on measured values.

ATPB Model Input	Cell 1 and 2
Thickness	4 inches
Elastic Modulus	(varies)
Poisson's Ratio	0.35
Coefficient of Thermal Expansion	1.10 $\mu\epsilon/^\circ\text{F}$
Unit Weight	148 lbs/ft ³
Interface with PCC layer	Bonded

As previously mentioned, the pavement was modeled as a three layer system with the slab and ATPB layers resting on a dense liquid foundation. The elastic modulus of the ATPB and modulus of subgrade reaction (k-value), representing the composite stiffness of all layers beneath the slab at the time the testing was performed, must be determined. FWD testing was performed during each season in conjunction with the truck testing so that an elastic modulus and k-value representative of the conditions during truck testing could be determined. A summary of these backcalculated values is provided in Chapter 6. The average seasonal elastic moduli for both the restrained and unrestrained cells are provided in Table 7.4 and the average seasonal k-values are provided in Table 7.5. The static k-value was taken as half of the dynamic k-value. Previous studies like the AASHO Road Test showed that reducing backcalculated

dynamic k-values by approximately two produced reasonable static k-values measured in the field [19].

Table 7.4. Average seasonal elastic moduli of the ATPB for the restrained and unrestrained slabs.

Year	Season	E _{ATPB} (ksi)		Standard Deviation	
		Cell 1	Cell 2	Cell 1	Cell 2
2004	Fall	327	360	72	7
2005	Winter	293	429	4	103
2005	Spring	198	390	19	11
2005	Summer	304	335	100	24
2006	Winter	325	578	43	268
2006	Spring	322	421	65	7
2006	Summer	329	403	15	166
2006	Fall	296	437	76	19
2007	Winter	396	639	5	277
2007	Spring	243	295	2	29
2007	Summer	245	317	24	11
2007	Fall	230	359	6	32

Table 7.5. Average seasonal backcalculated static k-values for the restrained and unrestrained slabs.

Year	Season	k-value (psi/in)		Standard Deviation	
		Cell 1	Cell 2	Cell 1	Cell 2
2004	Fall	163	157	38	7
2005	Winter	216	144	49	48
2005	Spring	259	141	94	8
2005	Summer	208	155	54	60
2006	Winter	217	139	14	65
2006	Spring	246	184	57	1
2006	Summer	217	172	32	73
2006	Fall	245	172	24	12
2007	Winter	246	213	1	77
2007	Spring	125	88	1	7
2007	Summer	214	127	4	65
2007	Fall	198	113	20	56

7.2.2. Inputs for Modeling Slab Joints

Insuring that the finite element model accurately represents the joint stiffness observed in the field is extremely important since the stiffness of the joint greatly affects stress development. The pavement consists of both restrained and unrestrained slabs. The restrained slabs contain No. 5 (5/8-in) epoxy-coated tie bars placed 2.5 ft apart along the lane/shoulder and centerline joints. The transverse joints have epoxy coated 1.5-in dowel bars spaced every 12 inches. Load transfer efficiency along the transverse joint was measured seasonally in the restrained and unrestrained slabs and will be used to specify the stiffness of these joints. The longitudinal LTE along the centerline joint will be estimated using a relationship between the geometry of the transverse and longitudinal joints for the unrestrained slabs. The LTE along the centerline joint for the restrained slab will be a function of the properties of the tie bars. As previously discussed in Chapter 6, the load transfer efficiency was determined for each of the joints during each season. Table 7.6 provides the LTE for the transverse joints of the restrained and unrestrained slabs and Table 7.7 provides the longitudinal LTE for the unrestrained slabs incorporated into the finite element models.

Table 7.6. The measured load transfer efficiency along the transverse joint of the restrained and unrestrained slabs.

Season	Restrained Cell		Unrestrained Cell	
	LTE (%)	St. Dev	LTE (%)	St. Dev
Fall 2004	88	1.8	87	1.2
Winter 2005	89	3.0	66	15.0
Spring 2005	83	4.0	60	15.5
Summer 2005	76	4.3	59	7.2
Fall 2005	-	-	-	-
Winter 2006	81	2.0	41	6.3
Spring 2006	80	3.8	39	4.6
Summer 2006	86	4.2	84	12.5
Fall 2006	81	2.3	37	5.6
Winter 2007	80	1.5	72	8.0
Spring 2007	87	2.5	67	4.9
Summer 2007	84	2.5	61	19.5
Fall 2007	84	3	51	30

Table 7.7. The load transfer efficiency along the longitudinal joint used to model the unrestrained slabs.

Season	Unrestrained
	LTE (%)
Fall 2004	100
Winter 2005	82
Spring 2005	74
Summer 2005	74
Fall 2005	-
Winter 2006	52
Spring 2006	49
Summer 2006	100
Fall 2006	46
Winter 2007	90
Spring 2007	84
Summer 2007	77
Fall 2007	64

7.2.3. Modeling the Loads Applied to the Pavement Structure

To properly model the loads applied to the Smart Pavement several parameters needed to be determined for the three trucks used for load testing. These parameters included: dimensions of the axle configuration, and tire spacing, and the tire size and pressure. The tire pressure for all truck types was determined from standard manufacturer's performance charts and a value of 100 psi was used. Figure 7.1 through Figure 7.3 provide the axle configuration, tire spacing, and tire size of the Class 6, 7, and 10 trucks used during truck testing on SR 22.

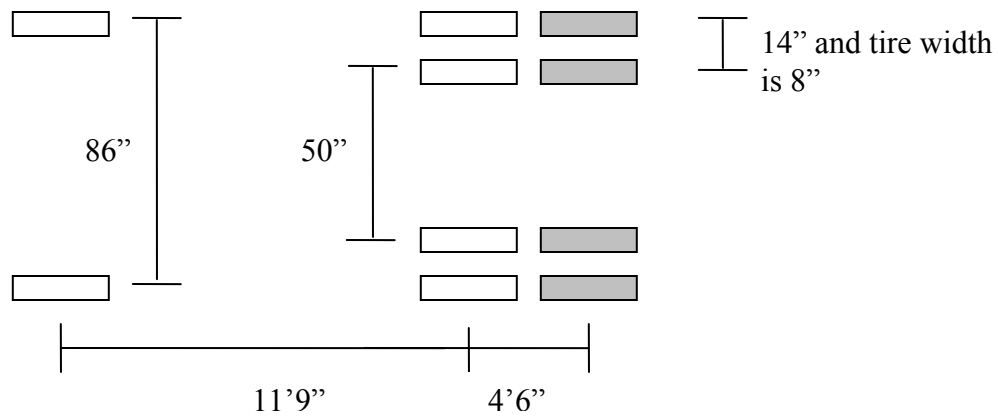


Figure 7.1. Axle configuration and tire spacing of the Class 6 truck.

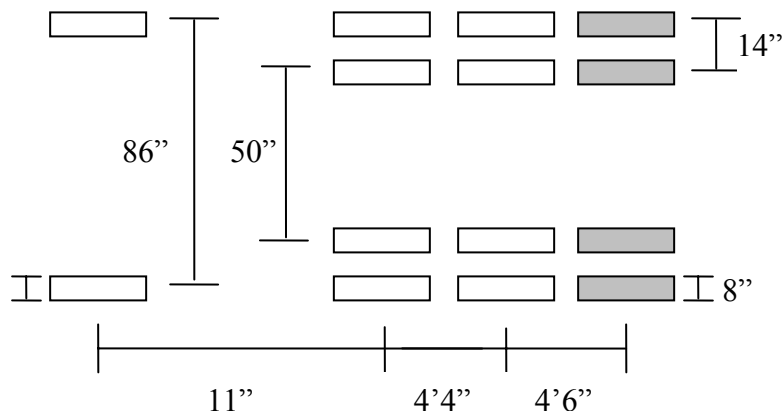


Figure 7.2. Axle configuration and tire spacing of the Class 7 truck.

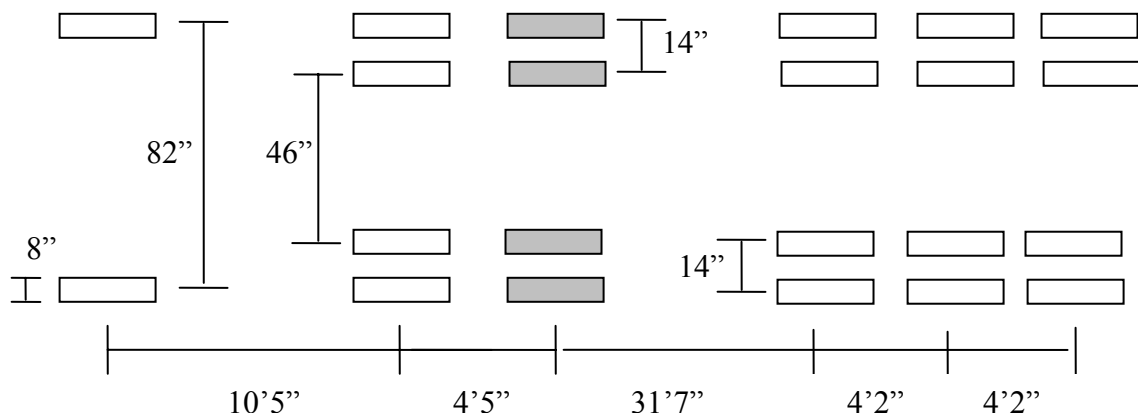


Figure 7.3. Axle configuration and tire spacing of the Class 10 truck.

7.3.0. Finite Element Model Validation

The following presents the results of the validation of the finite element models for the restrained and unrestrained slabs of the Smart Pavement. As previously discussed, the dynamic sensors of the Smart Pavement are arranged in three groups that correspond to different locations in the slab. As Figure 7.4 shows, the three sensor groups are located adjacent to the transverse joint (Group 1), along the edge/shoulder joint (Group 2), and at midpanel (Group 3). All three sensor groups for each of the three truck classes were used to validate the models. The gages used were restricted to the gages at the bottom of the slab since there was less variability compared to the top sensors, as previously discussed in Chapter 7.

The following subsections provide the results of the validation for the three sensors groups for each truck class (Class 6, 7, and 10). Strains measured from the critical axle identified in Chapter 6 for each truck type were used to validate the models. The critical axles for each truck type are highlighted in Figure 7.1 through Figure 7.3. Additionally, strains measured when the effective gradient in the slab was approximately zero were used for model validation. The strain gage measures changes in electrical resistance when an external force is applied to the concrete. This measure of resistance does not account for the additional expansion and contraction of the slab due to environmental changes, therefore the additional stress caused by the slab movement due to temperature differences between the top and bottom of the slab is not accounted for. The built-in gradient was established as $0.31\text{ }^{\circ}\text{F/in}$ so the strains measured when a gradient is $0.31\text{ }^{\circ}\text{F/in}$ is desired so that the slab is flat. This allows the models to be validated using loads that are applied on a flat slab so that strain that can not be accounted for in the strain gages is eliminated.

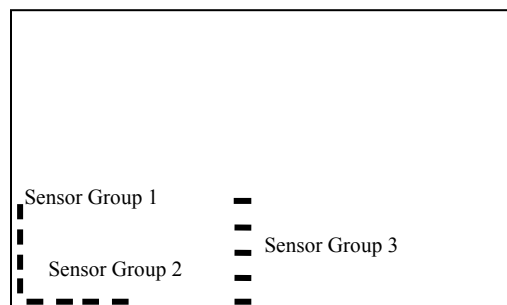


Figure 7.4. Dynamic strain sensor layout.

7.3.1. Validation Using Group 1 Sensors (Adjacent to the Transverse Joint)

The following presents the results of the validation of the Group 1 sensors located adjacent to the transverse joint in both the restrained and unrestrained slabs. This sensor group is located approximately 4 in from the transverse joint in the longitudinal direction. The four sensors are located at distances of 6, 16, 26, and 36 in from the lane/shoulder joint in the transverse direction. The gages measure strains in the wheelpath directly adjacent to the transverse joints. Only the strain measurements captured when the critical axle of each truck traversed the pavement in the wheelpath (approximately 24 inches from the lane/shoulder joint) were used. The following provides the validation results for the Class 6, 7, and 10 trucks for the Group 1 sensor in both the restrained and unrestrained slabs.

7.3.1.1. Validation of the Restrained Slabs Using the Group 1 Sensors

Figure 7.5 present the results of the measured and predicted Class 6 critical strain for the Group 1 sensors in the restrained slabs. Strains recorded in the summer of 2005 when the Class 6 truck traversed the slab in the wheelpath were used to investigate the correlation between predicted and measured strain since this is when the slab was close to flat. The truck was loaded with 15,000 lbs per axle and the gradient during testing was 0.16 °F/in. The values used to define the stiffness of the joints, the modulus of the ATPB, and the k-value were based on the average of the values determined using the FWD collected for the summer of 2005. As can be seen below, the predicted strain is following the same trend as the measured. Additionally, the predicted measurements are within 2 microstrain of the measured values.

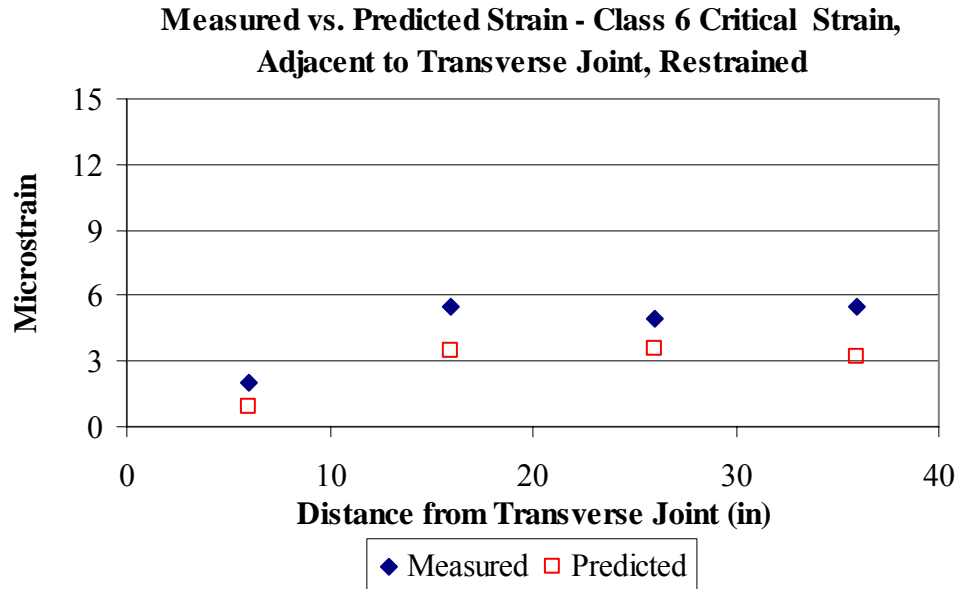


Figure 7.5. Validation results for the sensors located adjacent to the transverse joint in the restrained slabs for the Class 6 truck.

Figure 7.6 and Figure 7.7 present the measured and predicted strains along the transverse joint for the critical axle for the Class 7 and 10 trucks. Similar to the analysis for the Class 6 truck, the predicted strain along the transverse joint follows the same shape as the measured values and all strain measurements are within 2 microstrain indicating a good correlation between predicted and measured values. Although, the predicted and the measured strains do tend to diverge slightly when approaching the transverse joint, with the predicted strain underestimating the measured strain. The stiffness of the joint stiffness might be slightly higher in the model than that observed in the field.

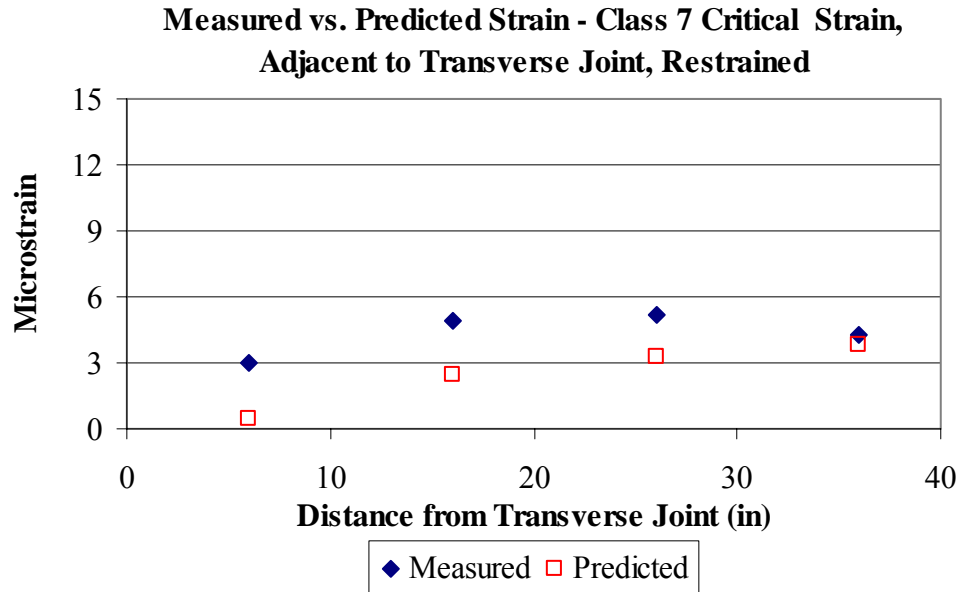


Figure 7.6. Validation results for the sensors located adjacent to the transverse joint in the restrained slabs for the Class 7 truck.

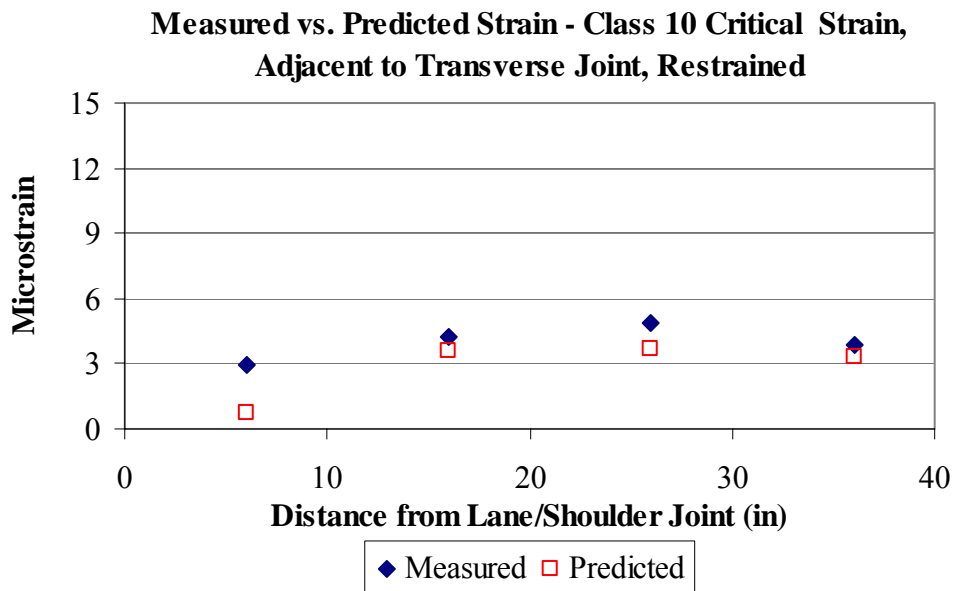


Figure 7.7. Validation results for the sensors located adjacent to the transverse joint in the restrained slabs for the Class 10 truck.

7.3.1.2. Validation of the Unrestrained Slabs Using the Group 1 Sensors

Figure 7.8 through Figure 7.10 present the results for the sensors adjacent to the transverse joint in the unrestrained slabs for the Class 6, 7, and 10 trucks with 18,000-lb axle loads. All of the predicted strain measurements are within two microstrain except

the strain predicted for the Class 6 truck at a distance of 26 in from the transverse joint. The predicted strain in this location was approximately 3 microstrain smaller than the measured value. This is an acceptable difference because the gradient of the slab during measurement was 0.18 °F/in, while the gradient present during the Class 7 and 10 trucks was closer to zero at 0.10 °F/in. The strain gages measure changes in electrical resistance when an external force is applied to the concrete. This measure of resistance does not account for the additional expansion and contraction of the slab due to environmental changes, therefore the additional stress caused by the slab movement due to temperature differences between the top and bottom of the slab is not accounted for. Therefore, a difference of 3 microstrain in this validation is acceptable.

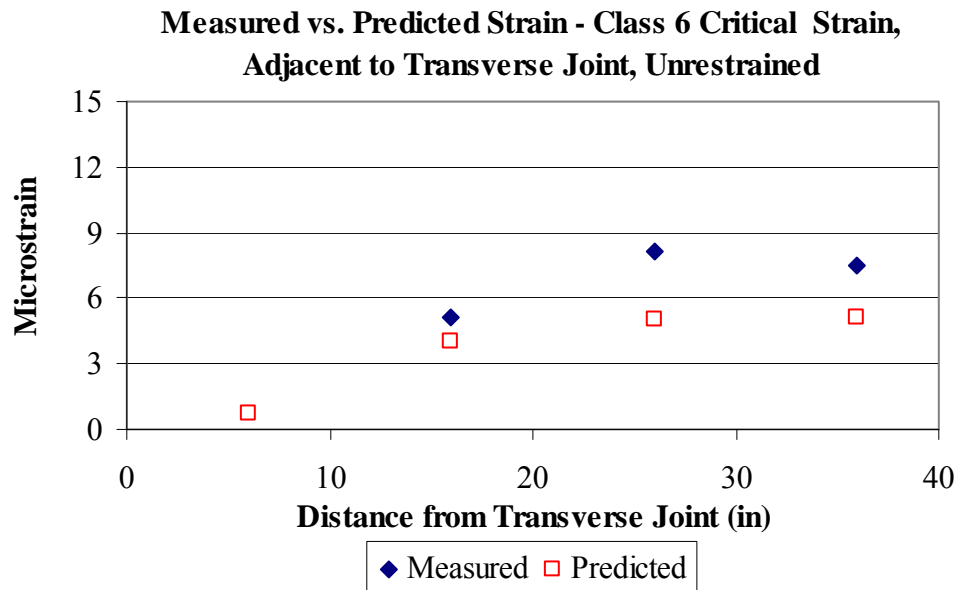


Figure 7.8. Validation results for the sensors located adjacent to the transverse joint in the unrestrained slabs for the Class 6 truck.

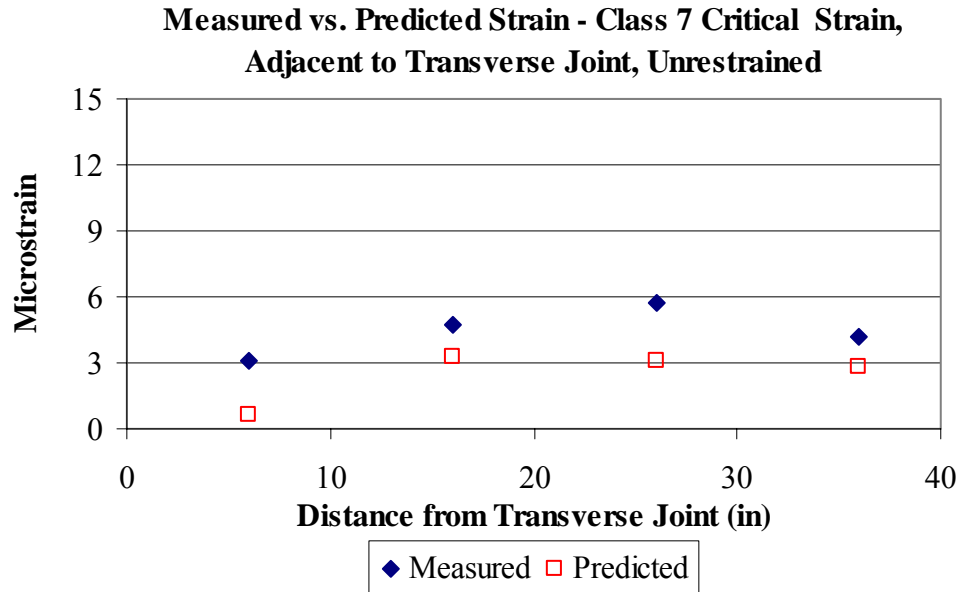


Figure 7.9. Validation results for the sensors located adjacent to the transverse joint in the unrestrained slabs for the Class 7 truck.

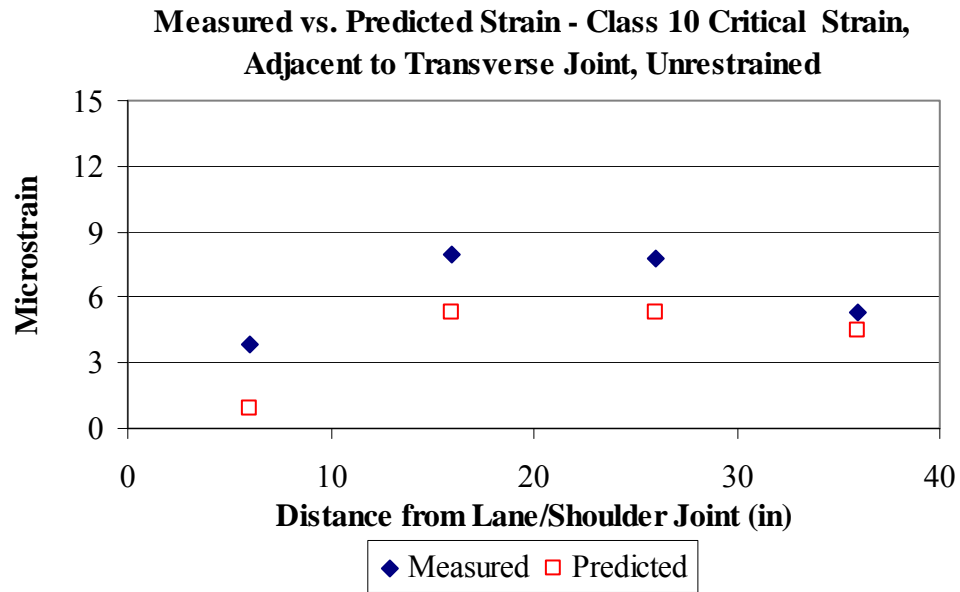


Figure 7.10. Validation results for the sensors located adjacent to the transverse joint in the unrestrained slabs for the Class 10 truck.

7.3.2. Validation Using Group 2 Sensors (Along the Lane/Shoulder Joint)

The following presents the results of the validation of the sensors in Group 2 located adjacent to the lane/shoulder joint in both the restrained and unrestrained slabs.

This sensor group is located approximately 4 in from the lane/shoulder joint in the transverse direction and the four sensors are located at distances of 20, 30, 39, and 49 in from the transverse joint in the longitudinal direction. These sensors are longitudinally oriented and measure strain in the longitudinal direction. Strain measurements captured when the critical axle of each truck traversed along the edge of the pavement were used in this analysis. The critical axle for each truck was placed directly on top of each sensor along the lane/shoulder joint. Strains measured for the load testing performed in the fall of 2004 were used for validation of the Class 7 and 10 trucks and strains measured in the winter of 2005 were used for the Class 6 truck. The gradient present at the time of testing was 0.17 °F/in for the Class 7 and 10 trucks and was -0.04 °F/in for the Class 6 truck.

7.3.2.1. Validation of the Restrained Slabs Using the Group 2 Sensors

Figure 7.11 through Figure 7.13 present the results from the analysis of measured versus predicted strain for the sensors located adjacent to the lane/shoulder joint in the restrained slabs. As can be seen below, the predicted strain is following the same trend as the measured. The predicted strain for the Class 6 and 10 trucks is within 1 microstrain of the measured values for all of the sensors along the lane/shoulder joint. The predicted strains for the Class 7 truck is within 2 microstrain of the measured values. This larger variation between predicted and measured values can be attributed to the larger temperature gradient (0.17 °F/in) during testing.

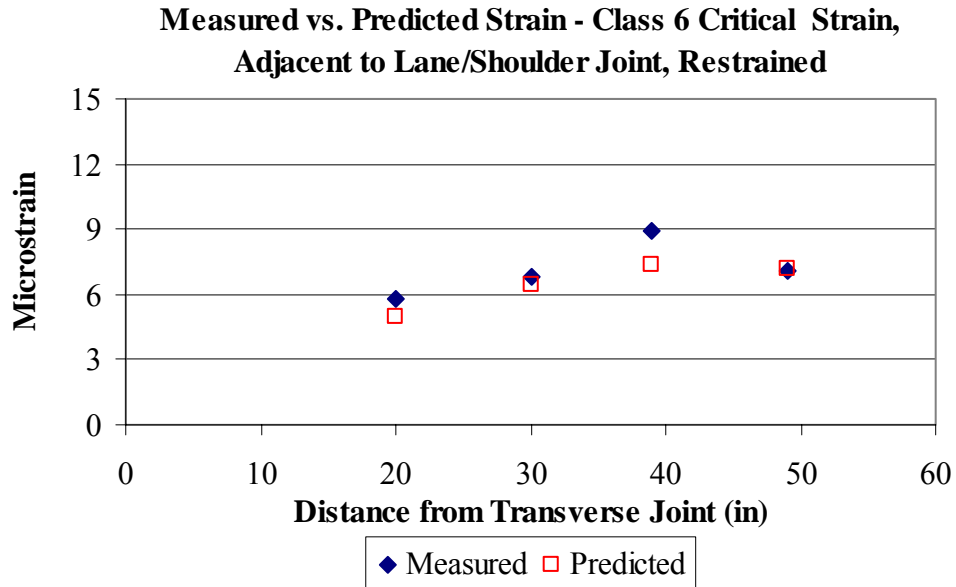


Figure 7.11. Validation results for the sensors located adjacent to lane/shoulder joint in the restrained slabs for the Class 6 truck.

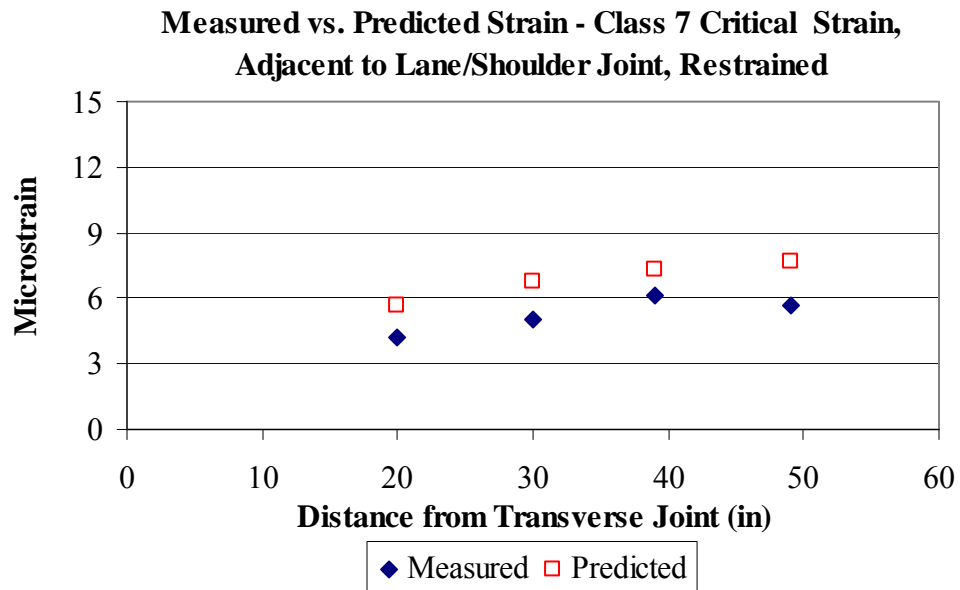


Figure 7.12. Validation results for the sensors located adjacent to lane/shoulder joint in the restrained slabs for the Class 7 truck.

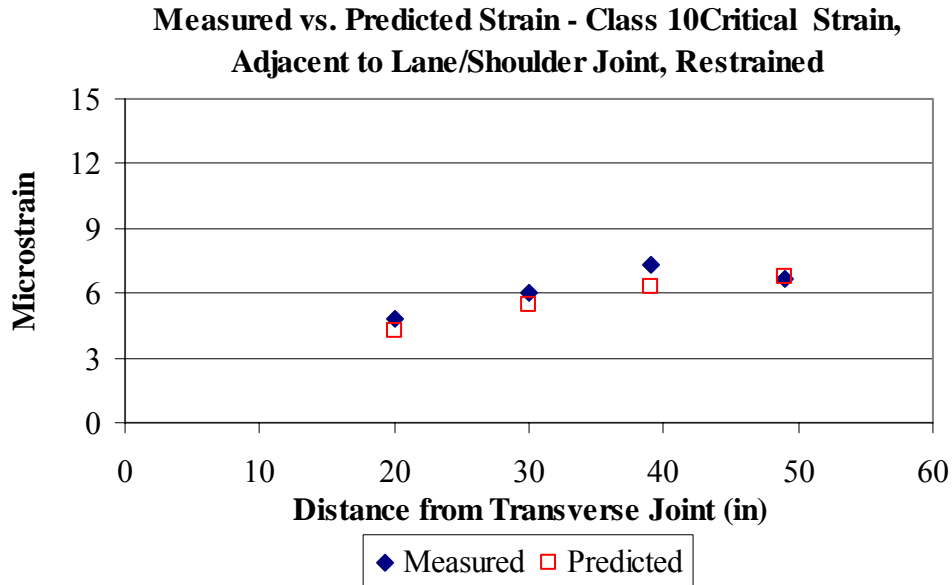


Figure 7.13. Validation results for the sensors located adjacent to lane/shoulder joint in the restrained slabs for the Class 10 truck.

7.3.2.2. Validation of the Unrestrained Slabs Using the Group 2 Sensors

Figure 7.14 through Figure 7.16 present the validation results of the sensors adjacent to the lane/shoulder joint in the unrestrained slabs for the Class 6, 7, and 10 critical strains. All of the predicted strain measurements are within two microstrain except the strain predicted for the Class 7 truck at a distance of 49 inches from the transverse joint. The predicted strain in this location was 3 microstrain larger than the measured value. As previously discussed, the dynamic strain gages can not account for stress/strain generated from slab restraint and movement. Therefore, this difference between predicted and measured strain is acceptable because the gradient of the slab during measurement was 0.17 °F/in.

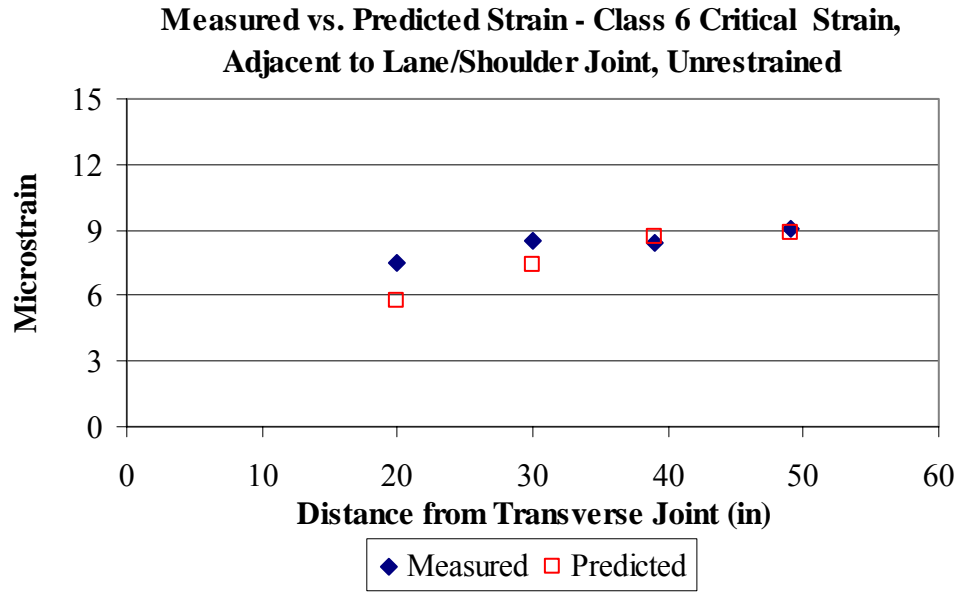


Figure 7.14. Validation results for the sensors located adjacent to lane/shoulder joint in the unrestrained slabs for the Class 6 truck.

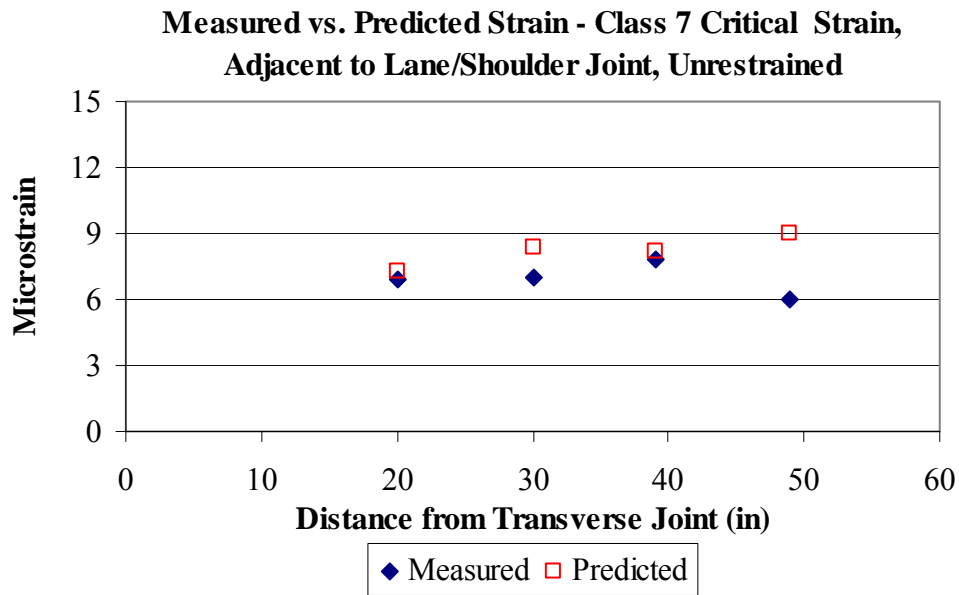


Figure 7.15. Validation results for the sensors located adjacent to lane/shoulder joint in the unrestrained slabs for the Class 7 truck.

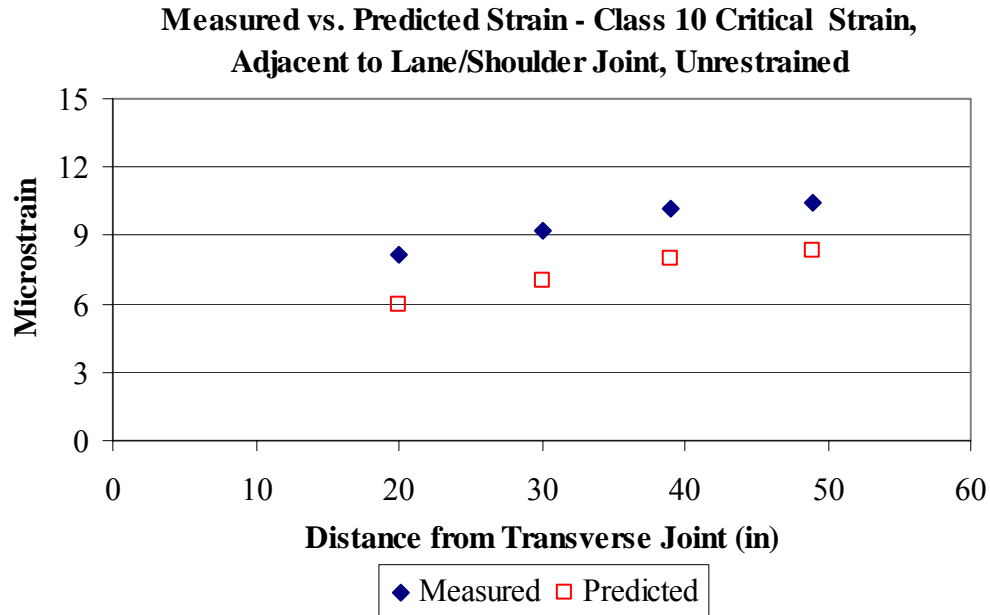


Figure 7.16. Validation results for the sensors located adjacent to lane/shoulder joint in the unrestrained slabs for the Class 10 truck.

7.3.3. Validation Using Group 3 Sensors (Midpanel)

The following presents the results of the validation of the model using sensor Group 3 located at midpanel in both the restrained and unrestrained slabs. This sensor group is located approximately 90 inches (midpanel) from the transverse joint in the longitudinal direction and the five sensors are located at distances of 10, 16, 22, 28, and 34 inches from the lane/shoulder joint in the transverse direction. These sensors measure strain in the longitudinal direction. The analysis used strain measurements captured when the critical axle of each truck traversed the pavement in the wheelpath (approximately 24 inches from the lane/shoulder joint). Strains measured during the winter of 2005 when the Class 7 and 10 trucks were loaded with 18,000 lbs per axle and strains measured during the summer of 2005 when the Class 6 truck was loaded with 15,000 lbs per axle were used to validate the model.

7.3.3.1. Validation of the Restrained Slabs Using the Group 3 Sensors

Figure 7.17 through Figure 7.19 present the results from the analysis of measured versus predicted strain for the Group 3 sensors in the restrained slabs. As can be seen below, the predicted strain is following the same trend as the measured. All of the

predicted strain measurements are within 2 microstrain of the measured values except the strain predicted for the Class 10 truck at a distance of 10 inches from the lane/shoulder joint. The predicted strain in this location was approximately 3 microstrain smaller than the measured value.

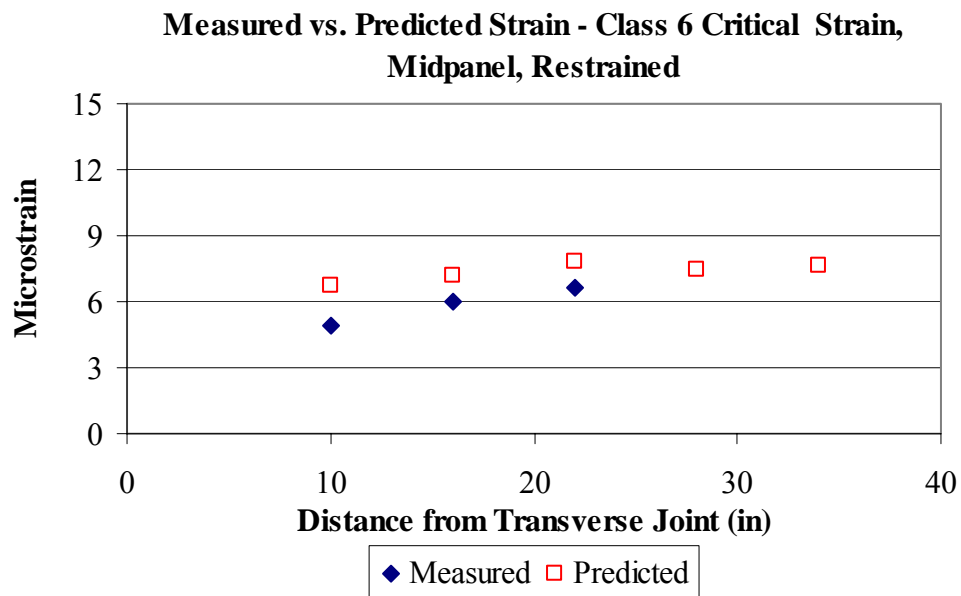


Figure 7.17. Validation results for the sensors at midpanel in the restrained slabs for the Class 6 truck.

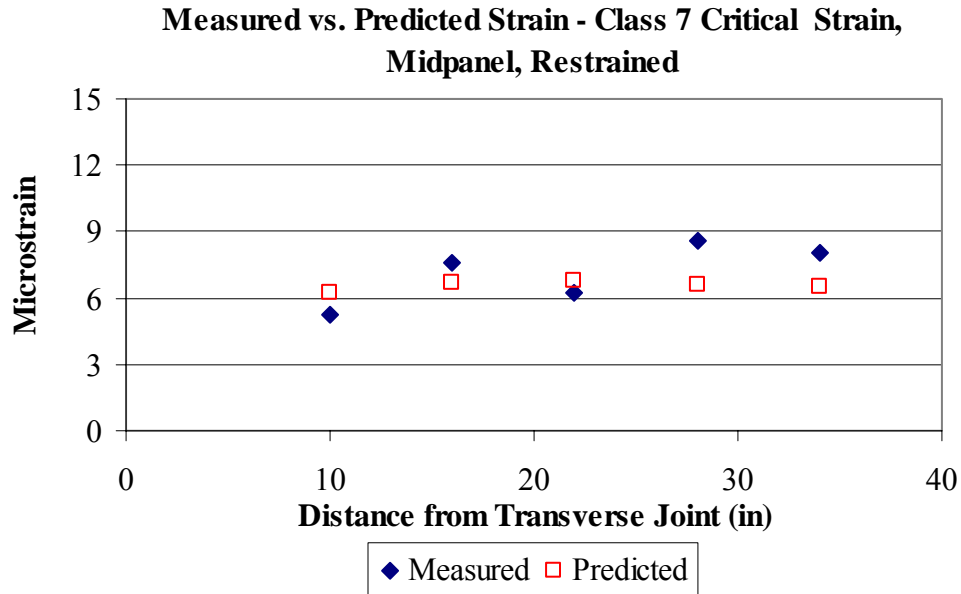


Figure 7.18. Validation results for the sensors at midpanel in the restrained slabs for the Class 7 truck.

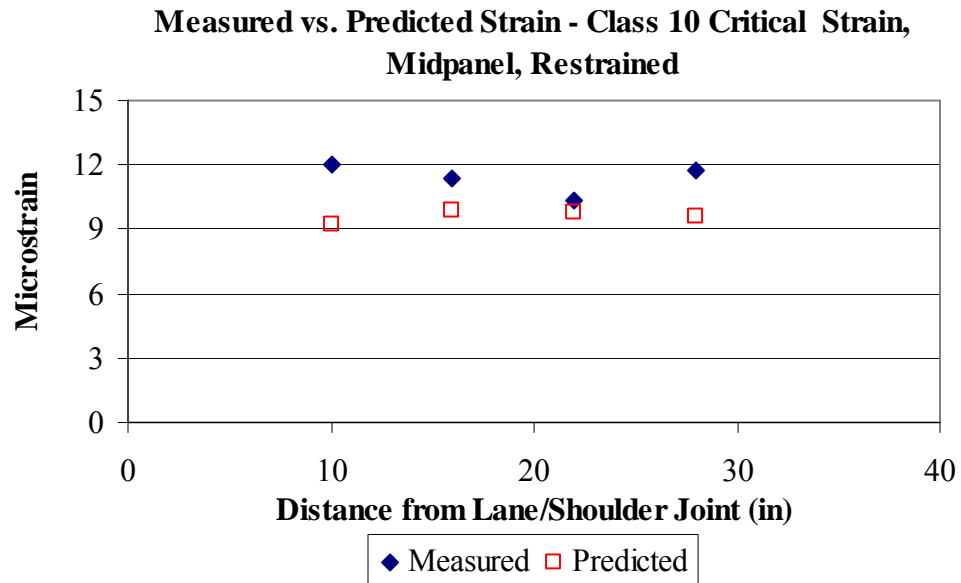


Figure 7.19. Validation results for the sensors at midpanel in the restrained slabs for the Class 10 truck.

7.3.3.2. Validation of the Unrestrained Slabs Using the Group 3 Sensors

Figure 7.20 through Figure 7.22 present the results for the sensors located at midpanel in the unrestrained slabs for the Class 6, 7, and 10 trucks. All of the predicted strain measurements are within 2 microstrain of the measured field values.

The finite element models generated using the inputs established with the FWD deflection data provide a relatively accurate estimate of the measured strain. The models were adjusted based on the inputs established for the season in which the truck load testing was performed. These seasonal inputs were established based on the FWD data representing that particular season. For all load cases considered, there was a good match between the measured and predicted strains for both the restrained and unrestrained slabs. Therefore, the strains measured in the field validated the finite element models and validation is not necessary. These models can now be used to predict stress in the slab for any combination of vehicle and environmental loads.

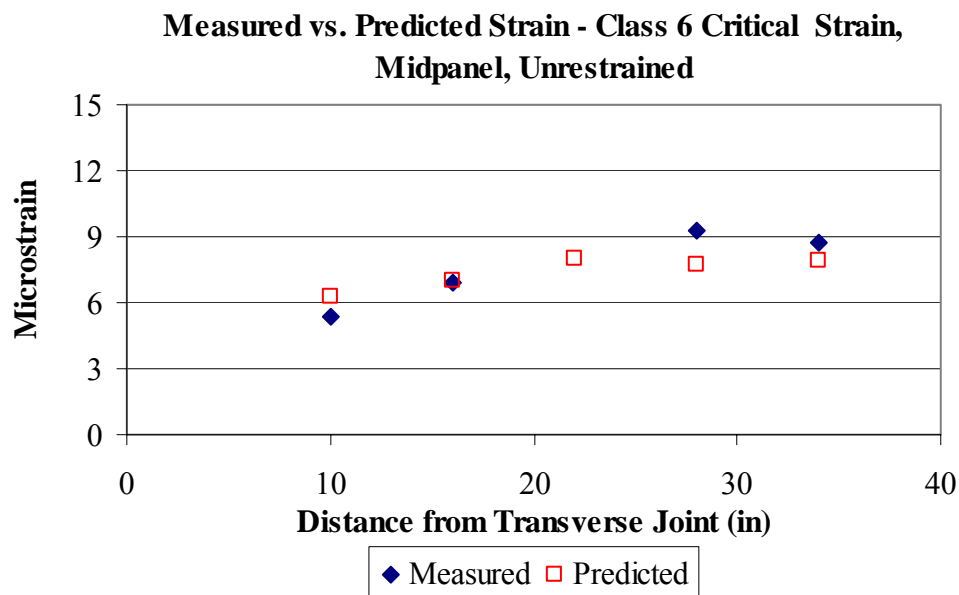


Figure 7.20. Validation results for the sensors at midpanel in the unrestrained slabs for the Class 6 truck.

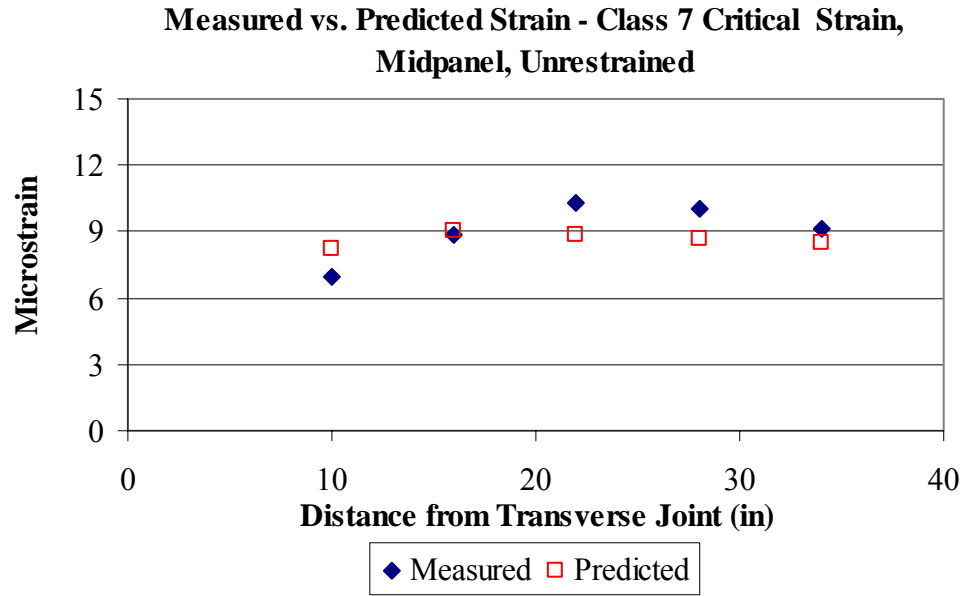


Figure 7.21. Validation results for the sensors at midpanel in the unrestrained slabs for the Class 7 truck.

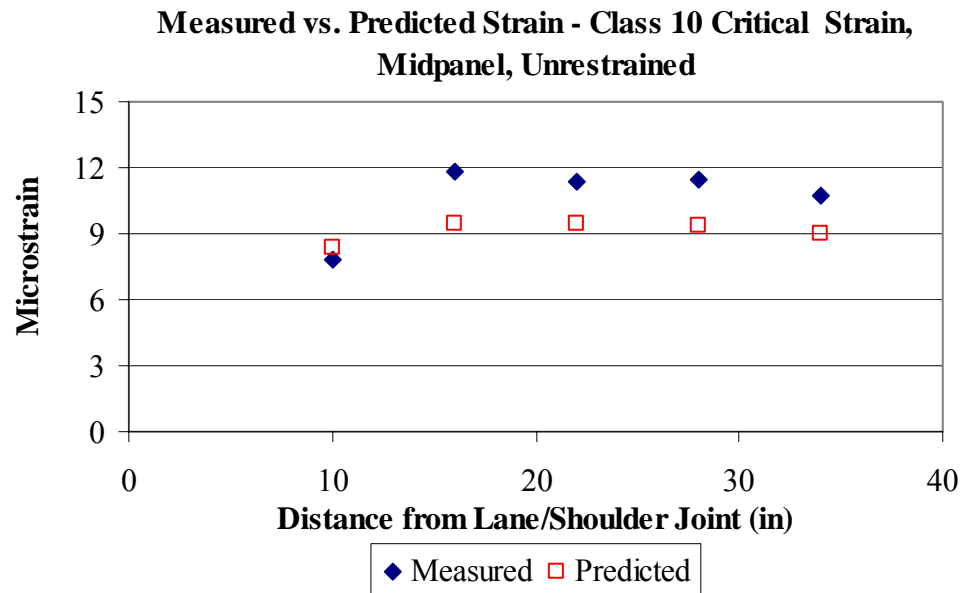


Figure 7.22. Validation results for the sensors at midpanel in the unrestrained slabs for the Class 10 truck.

7.4.0. Conclusions

The finite element models that were developed using inputs determined from FWD testing and proper test procedures and validated using field strain measurements was found to accurately predict strain in the pavement structure. These models can be used in future research to evaluate stress in the pavement for a wider range of temperature and moisture gradient, support conditions, and a wider range of vehicle loads and configurations. Additionally, the developed models should be used to evaluate the accuracy of the calculated stress and deflection in the MEPDG.

CHAPTER 8: SUMMARY OF FINDINGS

The major findings found for the Phase IIb portion of the study are summarized below. This chapter provides a quick reference of all primary findings. Additional details pertaining to each finding can be found in the body of the report. The findings are categorized by chapter for easy reference.

CHAPTER 2: TEMPERATURE AND MOISTURE DATA ANALYSIS

- The average moisture content in the slab has gradually decreased since construction. After three year since the time of construction, the average moisture content in the slab is still continuing to decline.

CHAPTER 3: DEFINING THE BUILT-IN CONSTRUCTION GRADIENT FOR A JOINTED PLAIN CONCRETE PAVEMENT

- Static strain sensors can be used in establishing the built-in temperature gradient in the slab. The time of set is 10.9 hours, and the corresponding built-in temperature gradient is $0.31^{\circ}\text{F}/\text{in}$ for the restrained and unrestrained slabs.
- The contribution of moisture to the built-in construction gradient consists of an equivalent temperature difference of -0.004°F . The effect of moisture is insignificant compared to that of temperature and is not included in the overall built-in construction gradient.
- The built-in construction gradient is $0.31^{\circ}\text{F}/\text{in}$ for the restrained and unrestrained slabs. This is equivalent to a temperature difference of 3.9°F throughout the slab depth. (*Input for the MEPDG*).

CHAPTER 4: INPUTS OF THE MECHANISTIC-EMPIRICAL DESIGN GUIDE

- The temperature and moisture conditions inside the pavement structure were predicted based on ambient climatic data from the onsite weather station and two of the closest stations to the site.
- The temperature predications in the concrete slabs showed that the predicted temperature using the EICM is close to the measured. However, the predicted temperature overestimates the maximum positive and negative gradients, implying that the use of these over-predicted gradients would result in conservative predictions in the performance of the pavement.

- An analysis of temperature predicted using the EICM and measured temperature showed that the temperature predictions in the asphalt and granular layers do not provide a good estimate of the measured conditions.
- The moisture predictions in the granular layers showed that the predicted moisture content does not vary much throughout the seasons. A comparison between the predicted and measured moisture content could not be properly carried out since the measured moisture content could not be interpreted.
- Based on the results from the MEPDG, the restrained slabs on SR 22 will provide an acceptable level of service for 45 years and the unrestrained slabs for 17 years.
- A comparison of the thickness designs from the MEPDG and AASTHO 1993 Guide showed the MEPDG provided a thickness design that was 5 in less for restrained slabs and 1 in thicker for the undoweled slabs compared to the AASHTO 1993 design thickness.
- The results of the analysis of the hierarchical levels showed that the restrained slab would have the same design thickness regardless of the level of inputs used. The thickness of the unrestrained slab would have to be a half inch thicker if Level 3 data was used when compared to Level 1 or 2 data.
- The use of Level 3 data for characterizing traffic would result in a slab 0.5-in thicker than Level 2 data for both the restrained and unrestrained slabs.
- The use of Level 2 data for the PCC CTE would result in a slab design thickness that is 2-in thicker than the design thickness determined using Level 1 or Level 3 data for the unrestrained slabs.
- Varying the input levels used in defining the PCC strength did not impact the design thickness nor did the use of different climatic weather stations.

CHAPTER 5: PAVEMENT RESPONSE TO ENVIRONMENTAL LOADING

- The total strain is negative throughout the first three years after construction indicating that the restrained and unrestrained slabs are in a state of contraction.
- The bond provided at the slab/base interface, the presence of dowel bars, and the longer slab length with adjacent slabs reduce the slab surface strain. This restricts upward and downward movement at the outer portion of the slab, and

causes the majority of the curvature to develop in the central portion of the slab.

- The unrestrained slabs exhibit larger deformations at the sides and the restrained slabs exhibit larger deformations at midslab.
- The presence of tie bars does not affect the strain at the slab surface.
- The surface profile measurements underestimate the slab curvature, compared to curvatures calculated based on the static strain gages. The difference in curvature between both methods is increasing throughout the three-year period, implying that the drying shrinkage at the slab surface is increasing with time.

CHAPTER 6: PAVEMENT RESPONSE TO APPLIED LOADS

- Undoweled pavements in Pennsylvania will have low load transfer capabilities for a large portion of each day and for several months in the year even for a short 15-ft joint spacing.
- The load transfer measured for the unrestrained slabs is dependent on the temperature gradient present at the time of testing. The load transfer measured for the restrained slabs was found to not be affected by temperature gradients or slab temperature.
- Temperature gradients have a larger affect on measured deflections than moisture gradients.
- A good correlation was found between the magnitude of the Void parameter and the size of the gradient for both the restrained and unrestrained slabs.
- The measured strains indicate the interface between the base and the slab is unbonded for the unrestrained slabs and bonded for the restrained slabs, indicating that the life of the bond might be a function of the restraint conditions.
- A relationship was found between the measured dynamic strain and the temperature gradient present in the slab at the time of testing for both the restrained and unrestrained slabs.

CHAPTER 7: DEVELOPMENT AND VALIDATION OF FINITE ELEMENT MODELS

- The finite element models that were developed based on inputs established using FWD and laboratory testing were validated using field strain measurements. The models were found to accurately predict the measured strain in the pavement.

The following recommendations were developed based on the findings from this study:

- The finite element models developed in this research should be used in future research to evaluate stress in the pavement for a wider range of temperature and moisture conditions, support conditions, and a wider range of vehicle loads and configurations.
- The finite element models developed in this research can be used to evaluate the accuracy of the calculated stress and deflection in the MEPDG.
- Further research is needed in determining the effect of the gradient in the slab and the slab temperature on backcalculated k-values, Void parameters, and load transfer efficiency. Establishing relationships between these parameters would provide the tools needed by practitioners for interpreting FWD data collected throughout the day. This would increase the hours available each day in which FWD testing could be performed.
- The collection of the moisture and static strain data should be continued for two to three additional years until the moisture content in the slab stabilizes.
- After the study is complete, dowels should be retrofit into the unrestrained slabs to increase the life of the pavement.

REFERENCES

1. Wells, S. A., B.M. Phillips, and J.M. Vandenbossche, (June 2005), "S.R.-22 Smart Pavement Phase I: Early-Age Material Properties and Pavement Response Characteristics for Jointed Plain Concrete Pavements; 28-Day Report Final Revision," *Submitted to the Pennsylvania Department of Transportation and the Federal Highway Administration*, University of Pittsburgh, Department of Civil and Environmental Engineering, Pittsburgh, Pennsylvania.
2. Asbahan, R., J. McCracken, and J.M. Vandenbossche, (November 2006), "S.R.-22 Smart Pavement Phase II: One-Year Material Properties and Pavement Response Characteristics for Jointed Plain Concrete Pavements," *Pennsylvania Department of Transportation and the Federal Highway Administration*, University of Pittsburgh, Department of Civil and Environmental Engineering, Pittsburgh, Pennsylvania.
3. Janssen, D. J. and M. B. Snyder, (June 2000), "Temperature-Moment Concept for Evaluating Pavement Temperature Data. Technical Note No. 19948," *Journal of Infrastructure Systems*, Vol. 6, No. 2, American Society of Civil Engineers. Reston, VA, pp. 81-83.
4. Wells, S.A., B.M. Phillips, and J.M. Vandenbossche, (2006), "Characterizing Strain Induced by Environmental Loads in Jointed Plain Concrete Pavements: Immediately after Paving and throughout First 10 Months," *Transportation Research Journal: Transportation Research Record 1947*: 36-48, National Research Council, Washington D.C.
5. Khazanovich, L. and T. Yu. "Modeling of Jointed Plain Concrete Pavement Fatigue Cracking in Pavespec 3.0," (2001), *Transportation Research Journal: Transportation Research Record 1778*: 33-42, National Research Council, Washington D.C.
6. Rao, S. and J.R. Roesler, (2005), "Characterizing Effective Built-In Curling from Concrete Pavement Field Measurements," *Journal of Transportation Engineering ASCE*, Vol. 131, No. 4, pp. 320–327.
7. Eisenmann, J. and G. Leykauf, (1990), "Simplified Calculation Method of Slab Curling Caused by Surface Shrinkage," *Proceedings, 2nd International Workshop on Theoretical Design of Concrete Pavements*: 185-197. Madrid, Spain.
8. Ruiz, J.M., P.J. Kim, A.K. Schindler, and R.O. Rasmussen, (2001), "Validation of HIPERPAV for Prediction of Early-age Jointed Concrete Pavement Behavior," *Transportation Research Journal: Transportation Research Record 1778*: 17–25, National Research Council, Washington, D.C.

9. Byrum, C.R., (2000), "Analysis of LTPP JCP Slab Curvatures Using High Speed Profiles," Paper Presented at the 79th Annual Meeting of Transportation Research Board, Washington, D.C.
10. Yu, H. T., L. Khazanovich, M.I. Darter, and A. Ardani, (1998), "Analysis of Concrete Pavement Responses to Temperature and Wheel Loads Measured from Instrumented Slabs," *Transportation Research Journal: Transportation Research Record* 1639, National Research Council, Washington, D.C.
11. Rao, C., E. Barenberg, M.B. Snyder, and S. Schmidt, (2001), "Effects of Temperature and Moisture on the Response of Jointed Concrete Pavements," Proceedings 7th International Conference on Concrete Pavements, Orlando, Florida, Sep. 9-13.
12. Beckemeyer, C. A., L. Khazanovich. and H.T. Yu, (2002), "Determining the Amount of Built-in Curling in JPCP: A Case Study of Pennsylvania I-80," Paper Presented at the 81st Annual Meeting of Transportation Research Board, Washington, D.C.
13. Hansen, W., Y. Wei., D.L. Smiley., Y. Peng. and E.A. Jensen, (2006), "Effects of Paving Conditions on Built-In Curling and Pavement Performance," *International Journal of Pavement Engineering*, Vol. 7, No. 4, pp. 291-296.
14. Asbahan, R. E., (2008), "Defining the Built-In Construction Gradient and Evaluating the Effects of Environmental Conditions on a Jointed Plain Concrete Pavement," Civil Engineering, Pittsburgh, University of Pittsburgh, Doctor of Philosophy Dissertation, Work-In-Progress.
15. ARA, Inc., ERES Consultants Division, (March 2004), "Guide for Mechanistic-Empirical Design of New and Rehabilitated Pavement Structures. Final Report," *National Cooperative Highway Research Program*, Transportation Research Board, National Research Council, Champaign, Illinois.
16. Mindness, S., J.F. Young. And D. Darwin, (2003), "Concrete." Pearson Education, Inc., New Jersey, USA.
17. Vandenbossche, J.M., (November 2003), "Interpreting Falling Weight Deflectometer Results for Curled and Warped Portland Cement Concrete Pavements," Civil Engineering, University of Minnesota, Doctor of Philosophy Dissertation.
18. GEOKON, (2006), "Earth Pressure Cells Technical Sheet Rev. E 09/06," Geokon Incorporated, NH, USA.
19. Dempsey, B. J., W. A. Herlach, and A. J. Patel, (1985), *The Climatic-Material-Structural Pavement Analysis Program*, FHWA/RD-84/115, Vol.3., Final Report, Federal Highway Administration, Washington D.C.

20. Guymon, G. L., R. L. Berg, and T. C. Johnson, (1986), *Mathematical Model of Frost Heave and Thaw Settlement in Pavement*, Report: U. S. Army Cold Region Research and Engineering Laboratory, Hanover, New Hampshire.
21. Lytton, R. L., D. E. Pufahl, C. H. Michalak, H. S. Liang, and B. J. Dempsey, (1990), *An Integrated Model of the Climatic Effects on Pavement*, Texas Transportation Institute, Texas A&M University, Report No. FHWA-RD-90-033, Federal Highway Administration, McLean, VA.
22. Explore, Search and Discover, 2007, Google, 13 March 2008, <<http://www.earth.google.com>>.
23. American Association of State Highway and Transportation Officials, (1993), "AASHTO Guide for Design of Pavement Structures," *AASHTO*, Washington, D.C.
24. Pennsylvania Department of Transportation, (2007), *Pavement Policy Manual Publication 242*, PennDOT, Harrisburg, PA.
25. William, G.W. and S.N. Shoukry, (2001), "3D Finite Element Analysis of Temperature Induced Stresses in Dowel Jointed Concrete Pavements," *International Journal of Geomechanics*, Vol. 1, No. 3, pp. 291–307.
26. Shoukry, S.N., G.W. William. And M. Riad, (2003), "Nonlinear Temperature Gradient Effects in Dowel Jointed Concrete Slabs," *International Journal of Pavement Engineering*, Vol. 4, No. 3, pp. 131-142.
27. Davids, G.W., (2000), "Effect of Dowel Looseness on Response of Jointed Concrete Pavements," *Journal of Transportation Engineering*, pp. 50-57.
28. Wells, S. A., (2005), "Early Age Response of Jointed Plain Concrete Pavements to Environmental Loads," Masters Thesis, University of Pittsburgh School of Engineering, Pittsburgh, PA.
29. Huang, Y. H., (2004), *Pavement Analysis and Design, Second Edition*, Pearson Prentice Hall, Upper Saddle River, NJ.
30. Face Construction Technologies, Inc., (2004), "Dipfloor 6.1. User's Guide," *Face Construction Technologies, Inc.*
31. Janssen, D., (1987), "Moisture in Portland Cement Concrete," *Transportation Research Journal: Transportation Research Record 1121*, National Research Council, Washington D.C.
32. Federal Highway Administration, (1997), "Concrete Pavement Rehabilitation Guide for Load Transfer Restoration," FHWA-SA-97103, Washington D.C.

33. Vandenbossche, J. M., (2007), "Effects of Slab Temperature Profiles on the Use of Falling Weight Deflectometer Data to Monitor Joint Performance and Detect Voids," *Transportation Research Journal: Transportation Research Record 2005*, National Research Council, Washington D.C.
34. Khazanovich, L. and A. Gotlif, (October 2003), "Evaluation of Joint and Crack Load Transfer Final Report," Technical Report FHWA-RD-02-088, Federal Highway Administration, McLean, VA.
35. Croveti, J.A. and M.I. Darter, (1985), "Void Detection for Jointed Concrete Pavements," *Transportation Research Journal: Transportation Research Record 1041*, National Research Council, Washington D.C.
36. Hall, K. T., M. I. Darter, T. E. Hoerner and L. Khazanovich, (1997), *LTPP Data Analysis-Phase I, Validation of Guidelines for k-Value Selection and Concrete Pavement Performance Prediction*, Technical Report FHWA-RD-96-198, Washington D.C.
37. Khazanovich, L. S.D. Tayabji, and M.I. Darter, (January 2001),"Backcalculation of Layer Parameters for LTPP Test Sections, Volume I: Slab on Elastic Solid and Slab on Dense-Liquid Foundation Analysis of Rigid Pavements," Technical Report FHWA-RD-00-086, Federal Highway Administration, McLean, VA.
38. Guo, E. and F. Pecht, (June 2006), "Critical Gear Configurations and Positions for Rigid Airport Pavements – Observations and Analysis," ASCE Geotechnical Special Publication No. 154. Pavement Mechanics and Performance, Proceedings of Sessions of Conference GeoShanghai, Shanghai, China.
39. Burnham, Tom, (2003), "Seasonal Load Response Behavior of a Thin Portland Cement Concrete Pavement," *Transportation Research Journal: Transportation Research Record 1819*, National Research Council, Washington D.C.

S.R.-22 Smart Pavement: Response Characteristics of a Jointed Plain Concrete Pavement to Applied and Environmental Loads

Phase II Final Report



APPENDIX

- A: Temperature and Moisture Measurements
- B: Early Age Vibrating Wire Gage Measurements
- C: Design Inputs for the MEPDG
- D: Vibrating Wire Gage Measurements
- E: Surface Profile Measurements
- F: Slab Curvature
- G: Pavement Response to Applied Loads

Prepared by:

Jennifer K. McCracken
Rania E. Asbahan
Julie M. Vandenbossche

University of Pittsburgh
Department of Civil and Environmental Engineering
Pittsburgh, Pennsylvania 15261

Prepared for:

Pennsylvania Department of Transportation,
Federal Highway Administration

February 2008

Appendix A: Temperature and Moisture Measurements

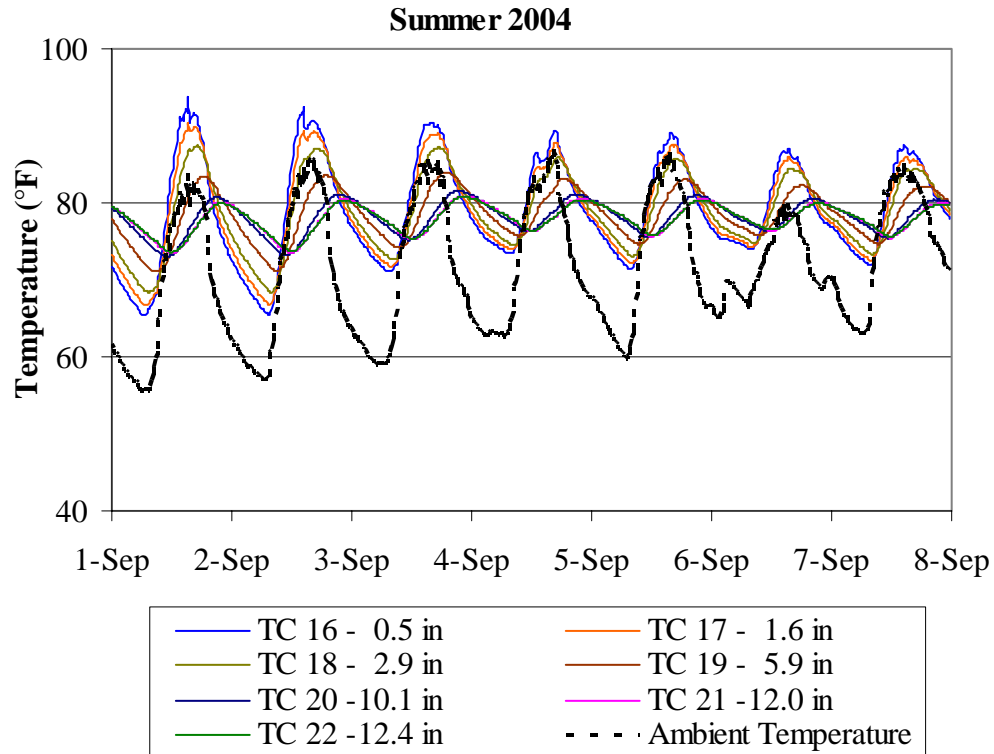


Figure A.1. Midpanel concrete temperature for a 1-week period representing the summer 2004 season.

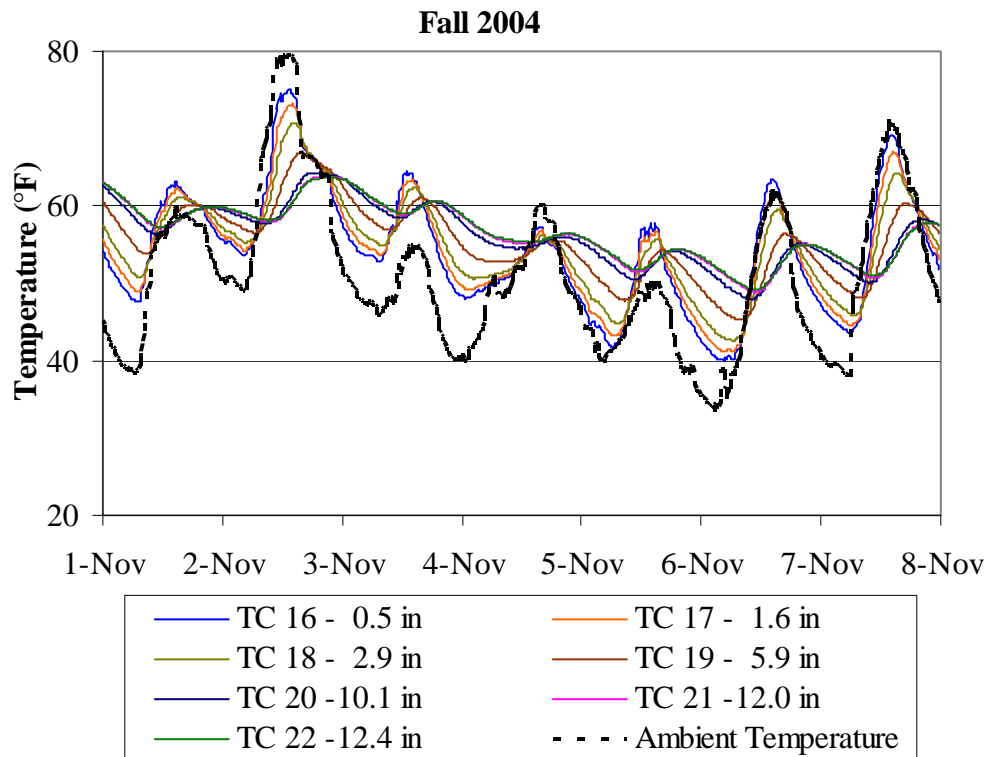


Figure A.2. Midpanel concrete temperature for a 1-week period representing the fall 2004 season.

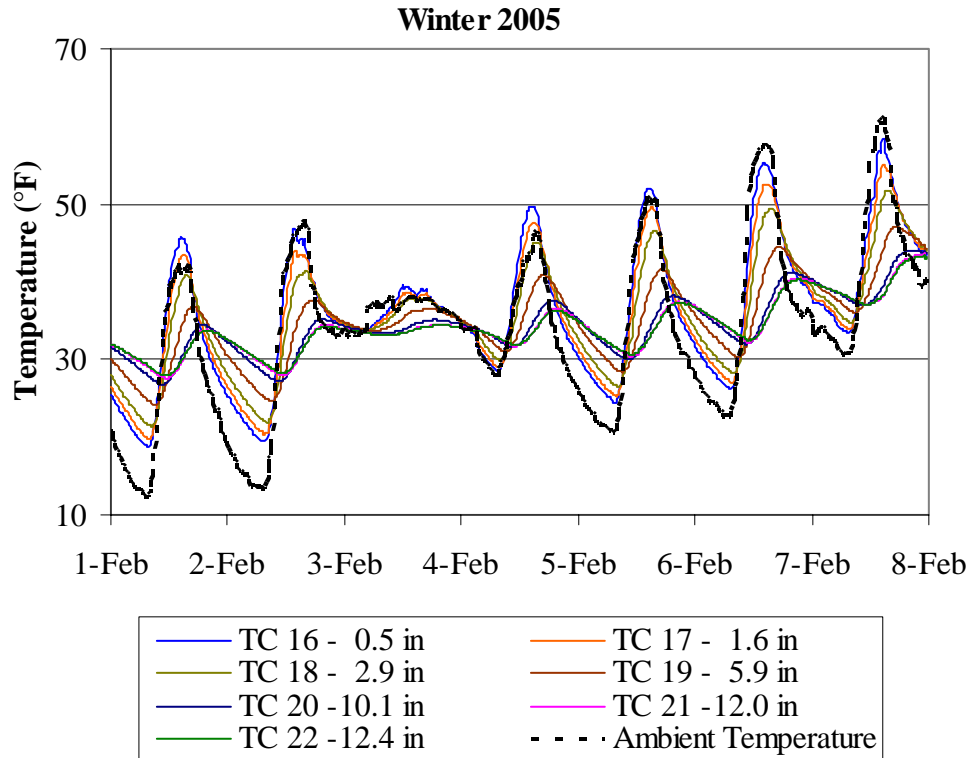


Figure A.3. Midpanel concrete temperature for a 1-week period representing the winter 2005 season.

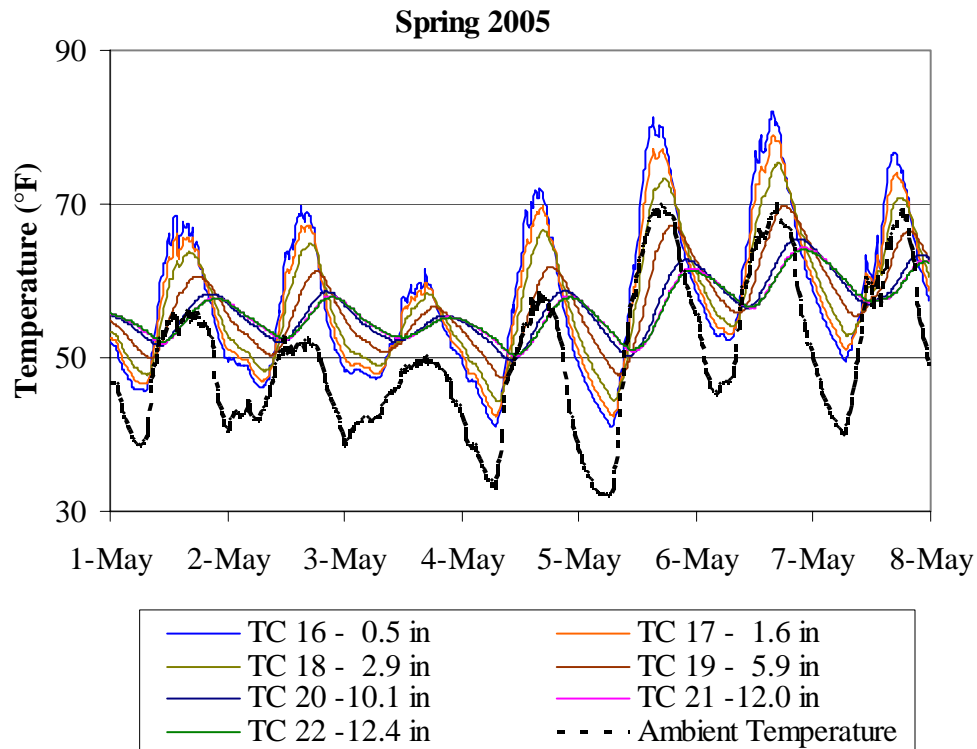


Figure A. 4. Midpanel concrete temperature for a 1-week period representing the spring 2005 season.

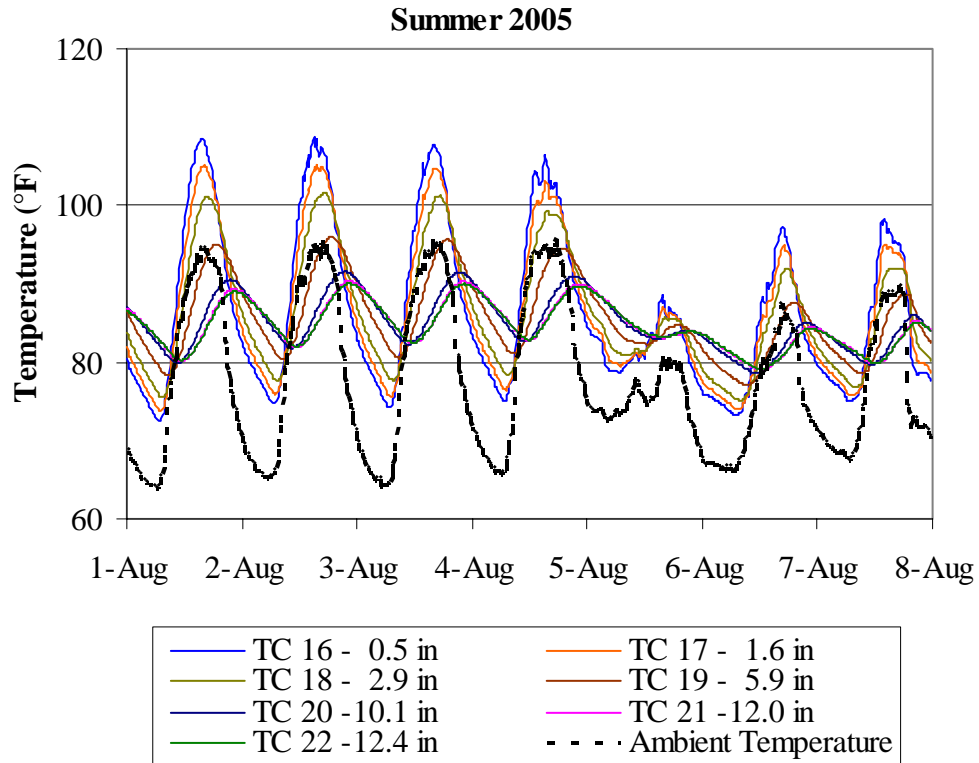


Figure A.5. Midpanel concrete temperature for a 1-week period representing the summer 2005 season.

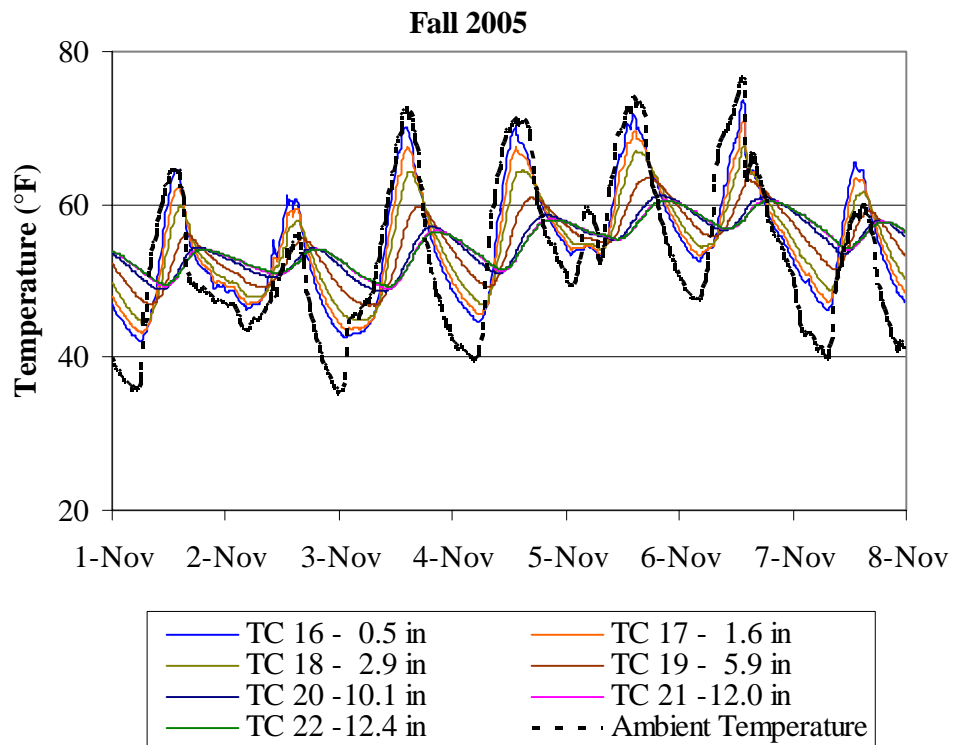


Figure A.6. Midpanel concrete temperature for a 1-week period representing the fall 2005 season.

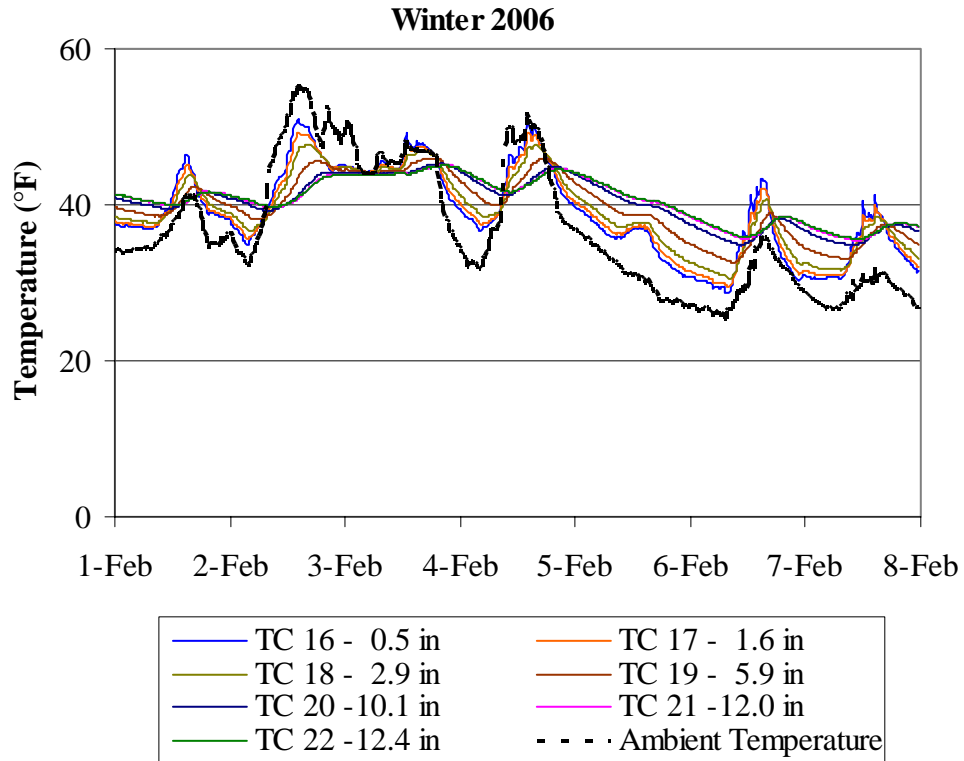


Figure A.7. Midpanel concrete temperature for a 1-week period representing the winter 2006 season.

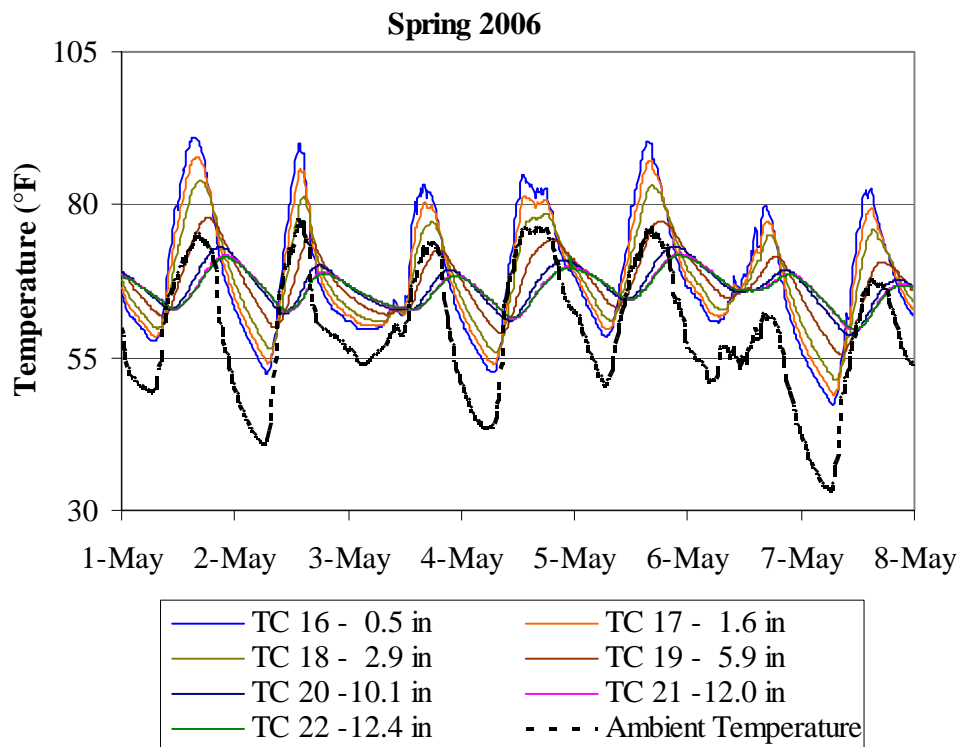


Figure A.8. Midpanel concrete temperature for a 1-week period representing the spring 2006 season.

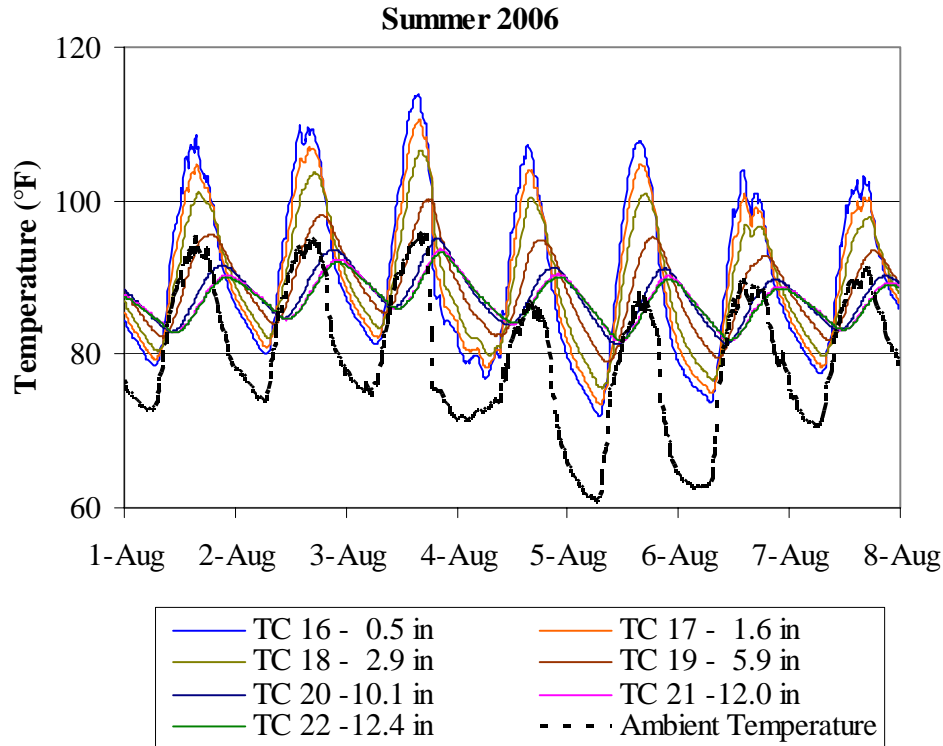


Figure A.9. Midpanel concrete temperature for a 1-week period representing the summer 2006 season.

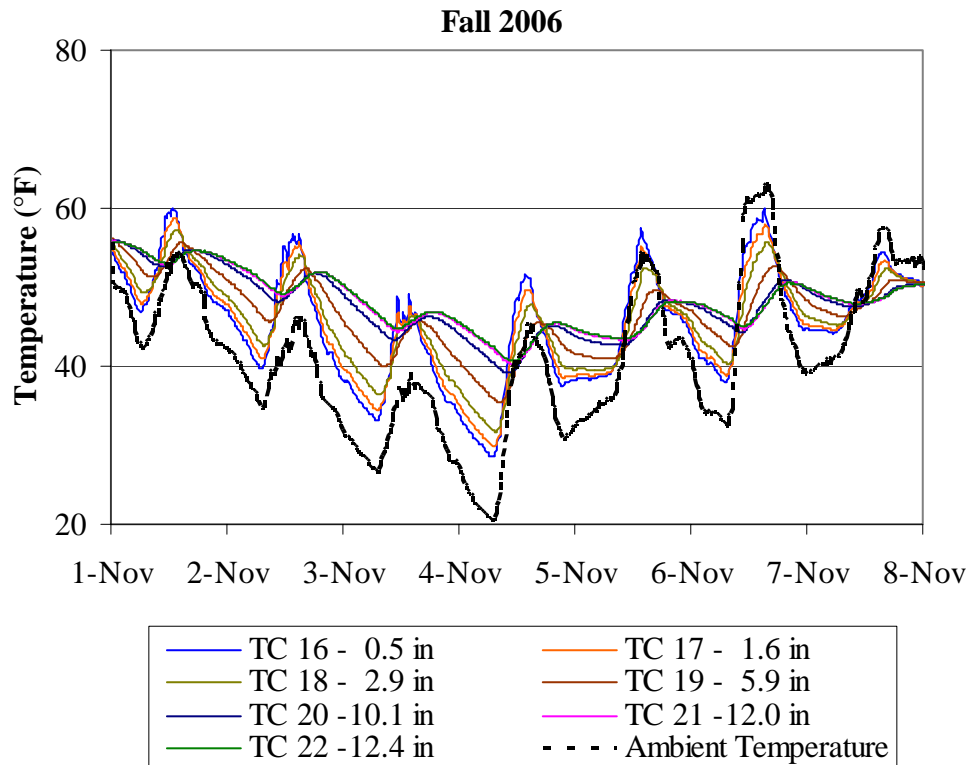


Figure A.10. Midpanel concrete temperature for a 1-week period representing the fall 2006 season.

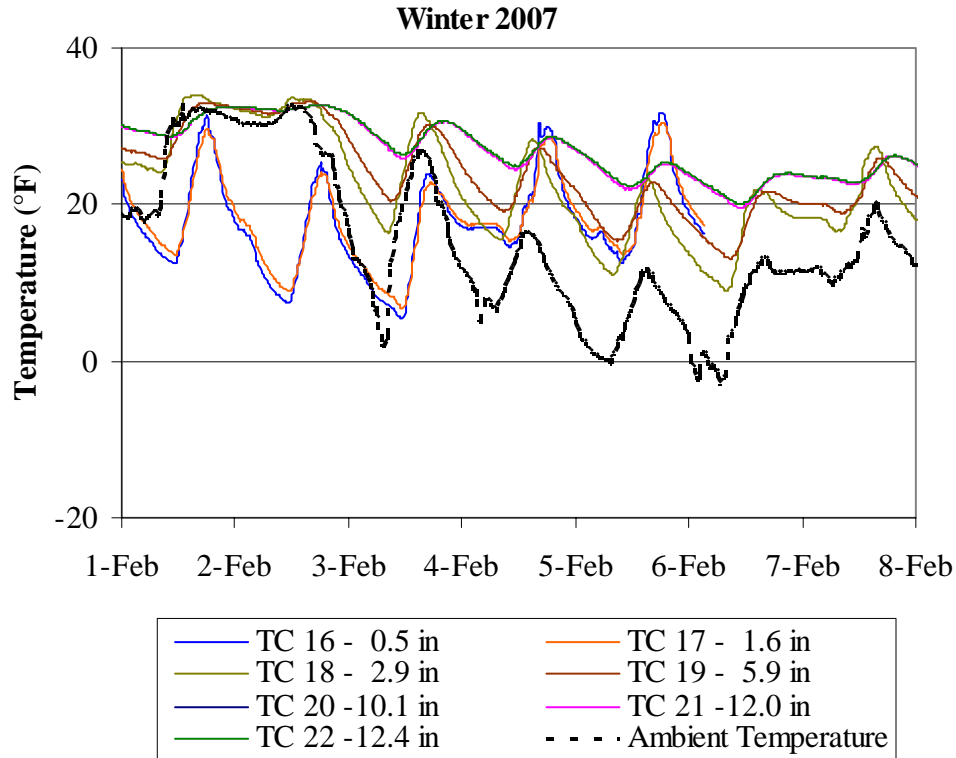


Figure A.11. Midpanel concrete temperature for a 1-week period representing the winter 2007 season.

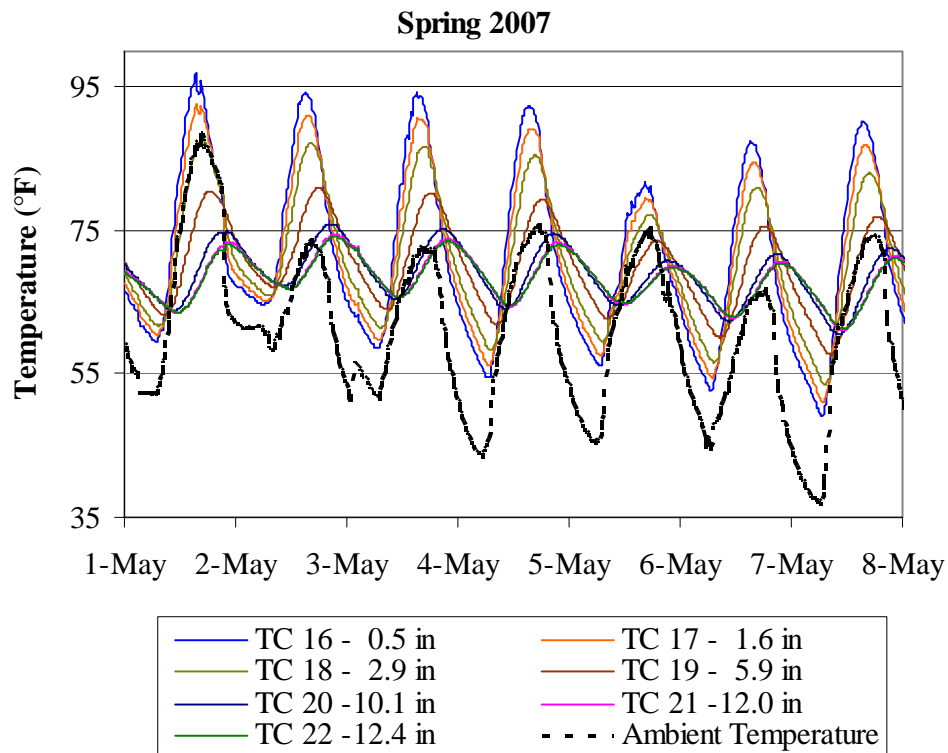


Figure A.12. Midpanel concrete temperature for a 1-week period representing the spring 2007 season.

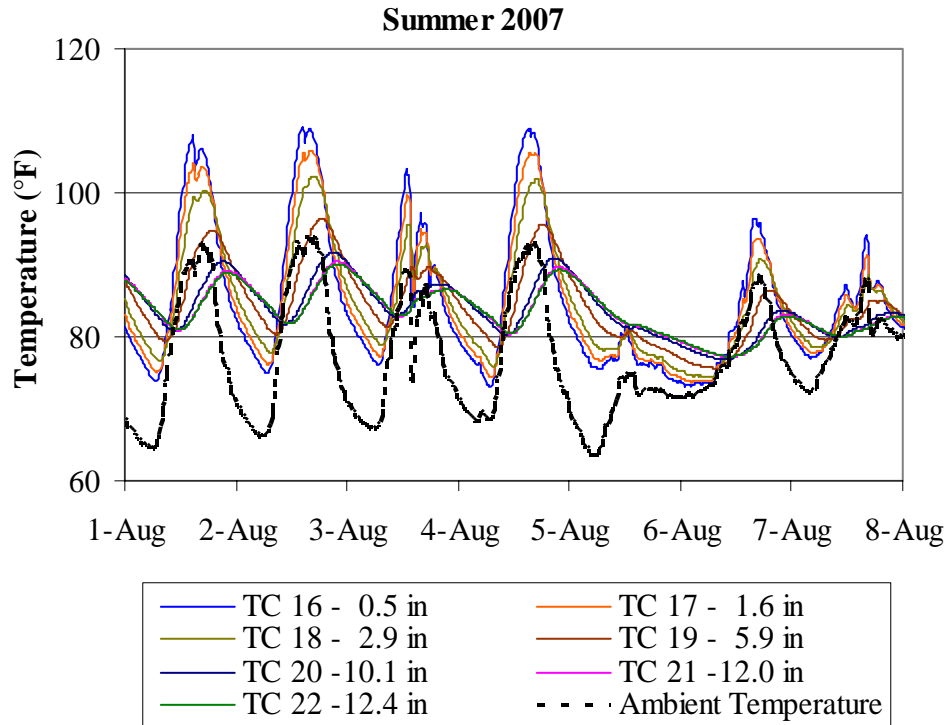


Figure A.13. Midpanel concrete temperature for a 1-week period representing the summer 2007 season.

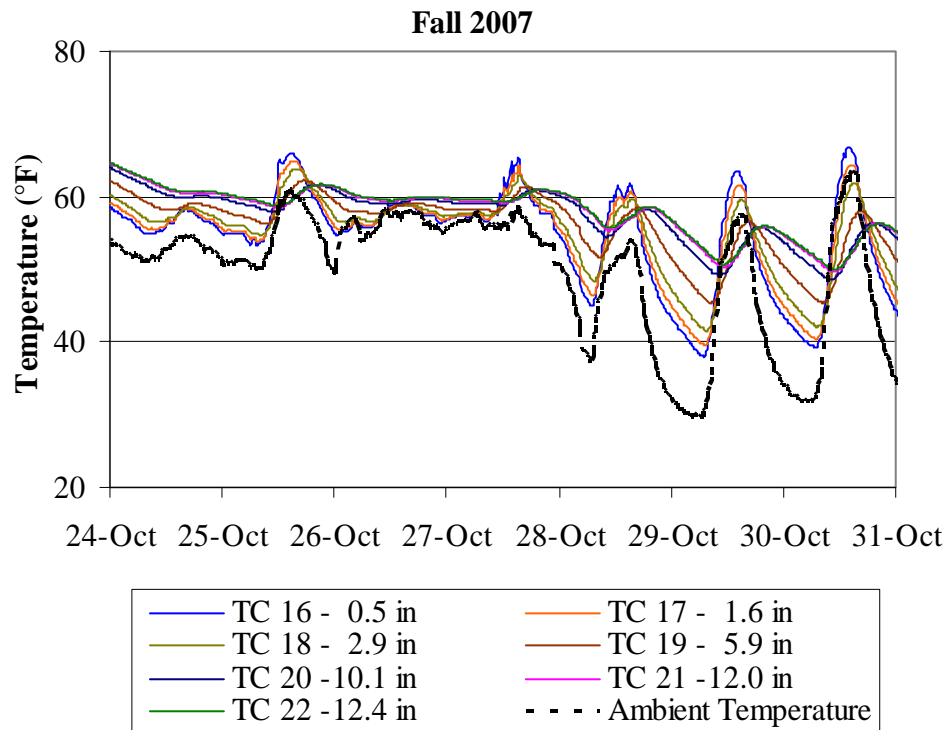


Figure A.14. Midpanel concrete temperature for a 1-week period representing the fall 2007 season.

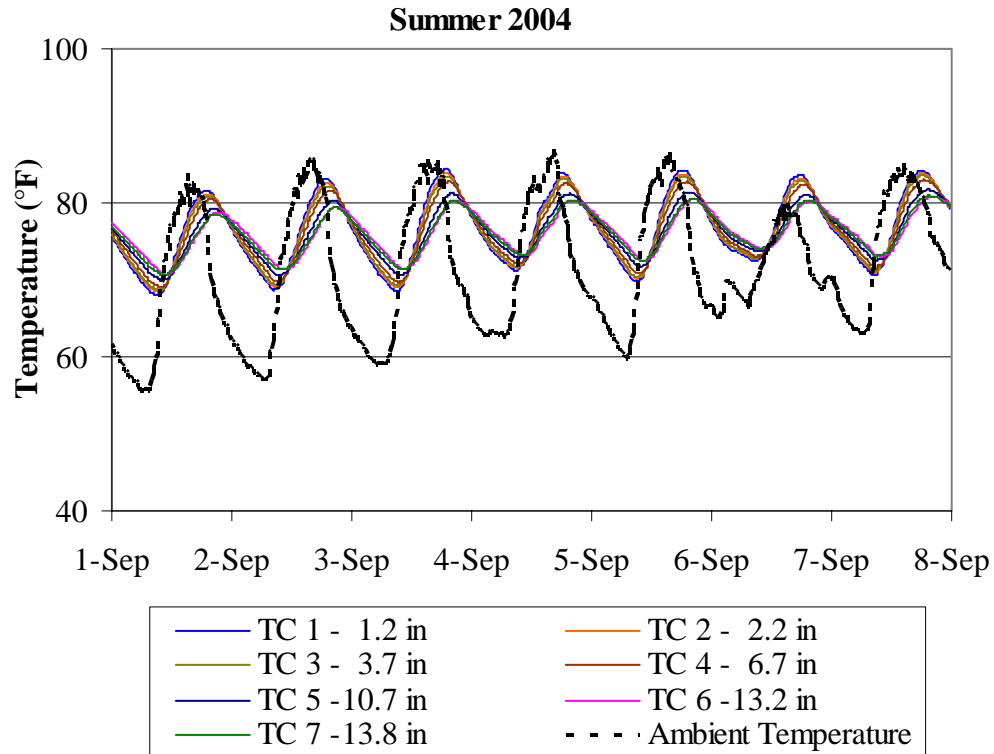


Figure A.15. Edge concrete temperature for a 1-week period representing the summer 2004 season.

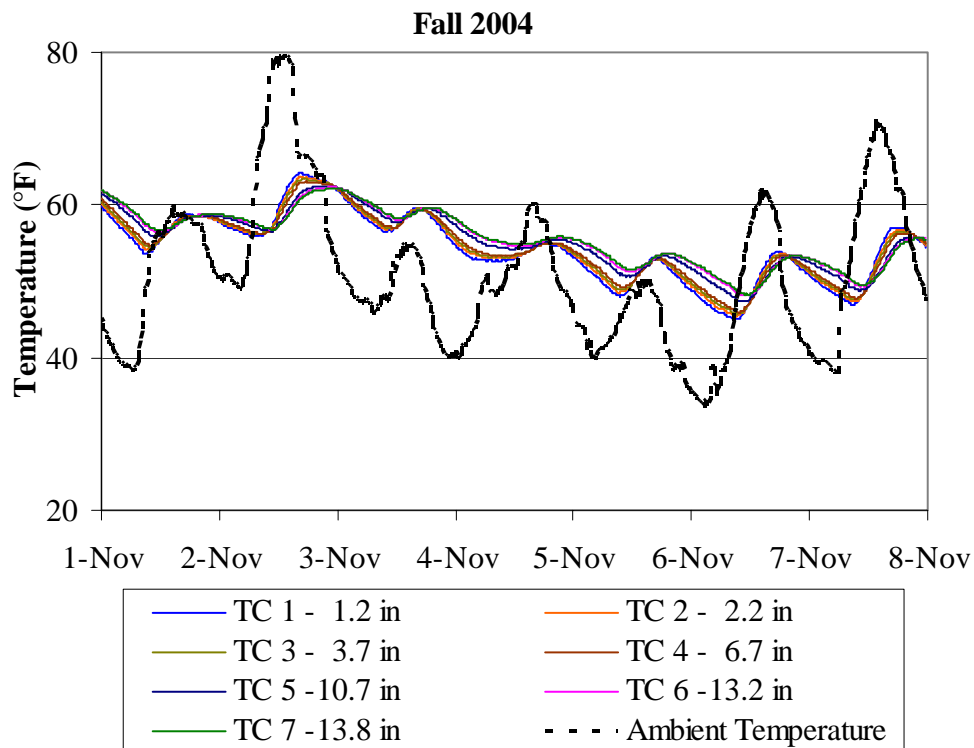


Figure A.16. Edge concrete temperature for a 1-week period representing the fall 2004 season.

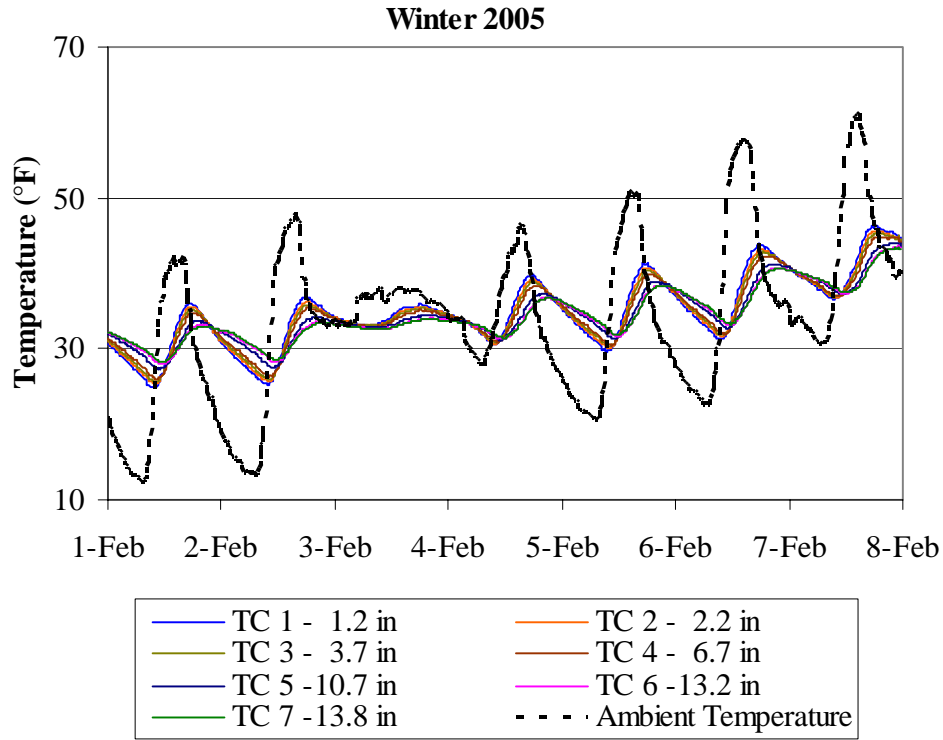


Figure A.17. Edge concrete temperature for a 1-week period representing the winter 2005 season.

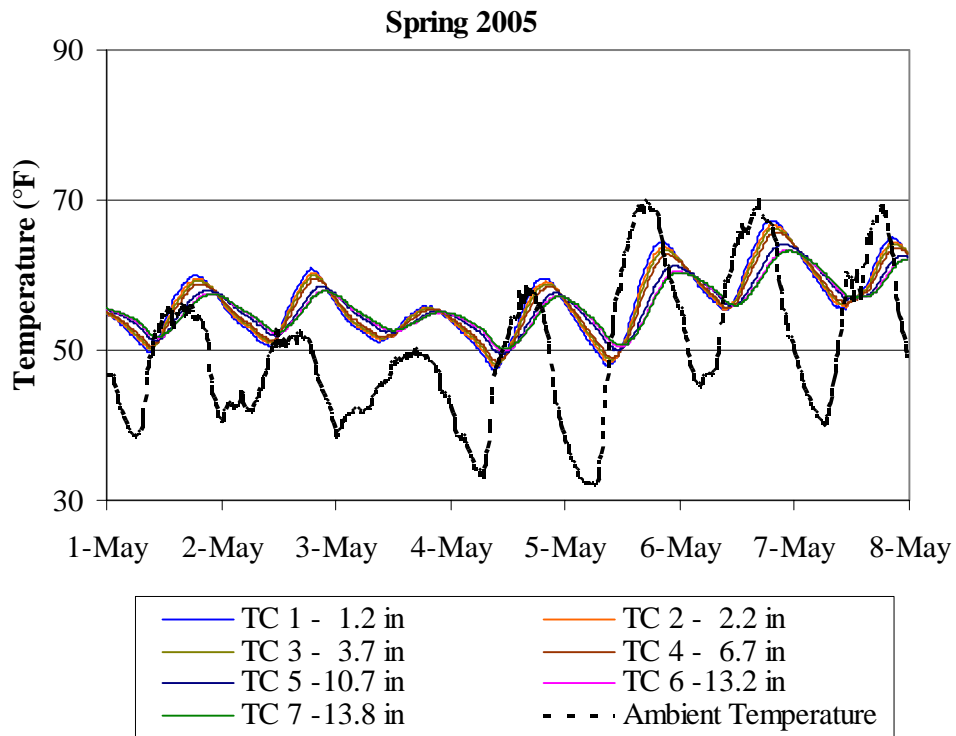


Figure A.18. Edge concrete temperature for a 1-week period representing the spring 2005 season.

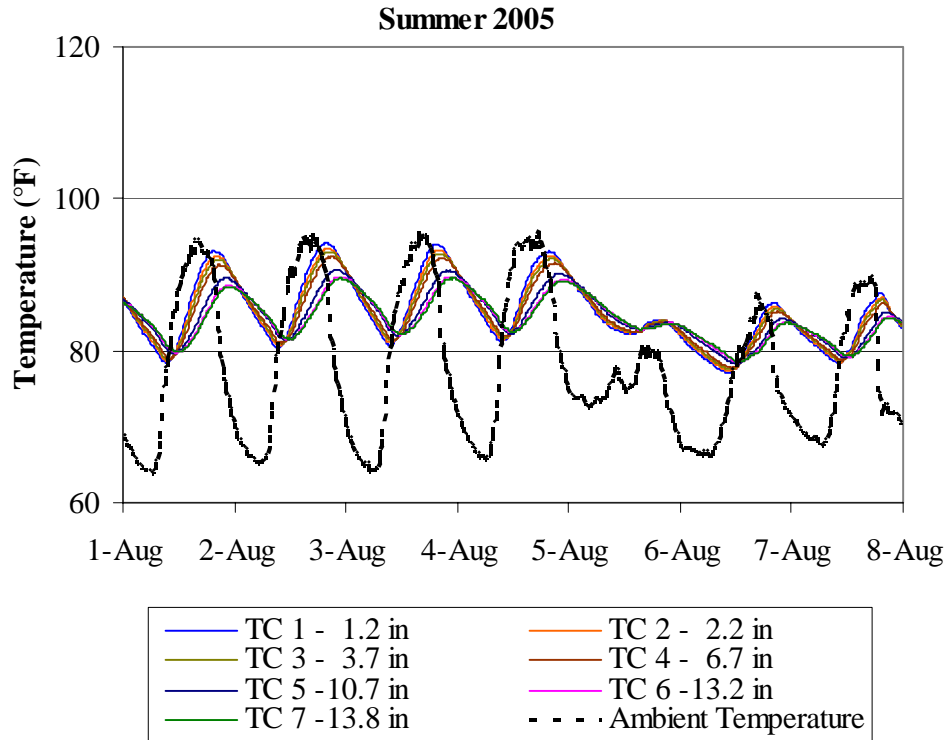


Figure A.19. Edge concrete temperature for a 1-week period representing the summer 2005 season.

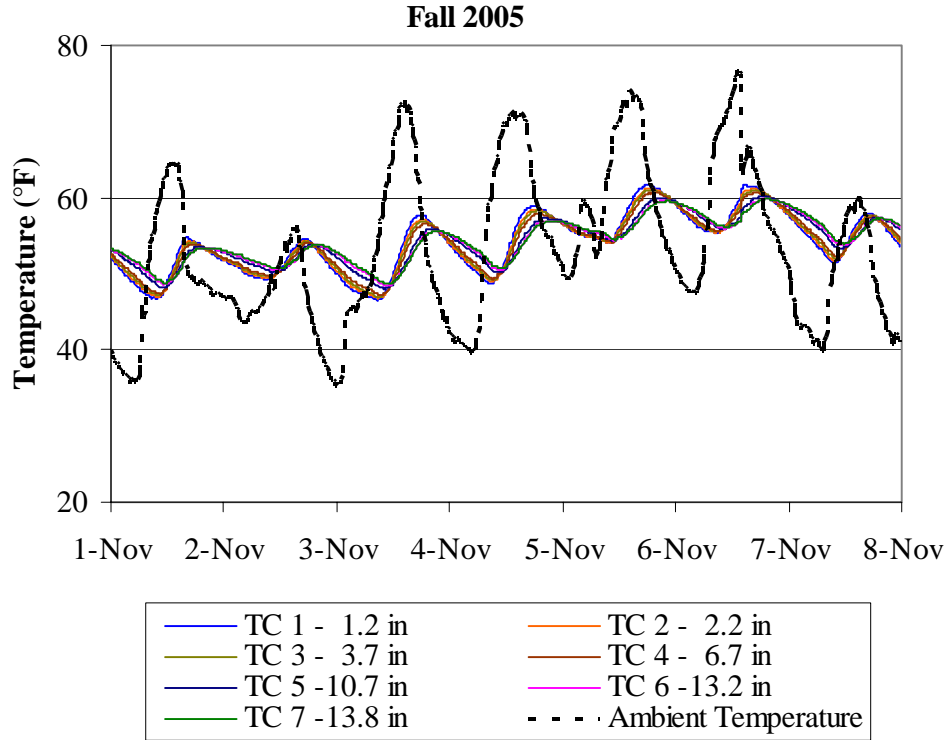


Figure A.20. Edge concrete temperature for a 1-week period representing the fall 2005 season.

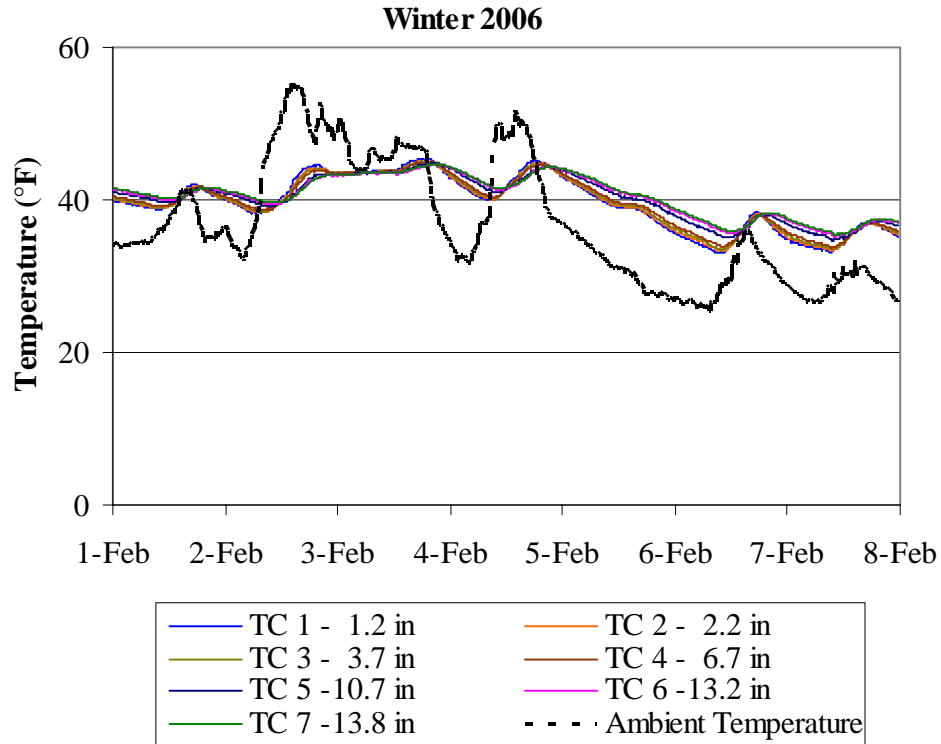


Figure A.21. Edge concrete temperature for a 1-week period representing the winter 2006 season.

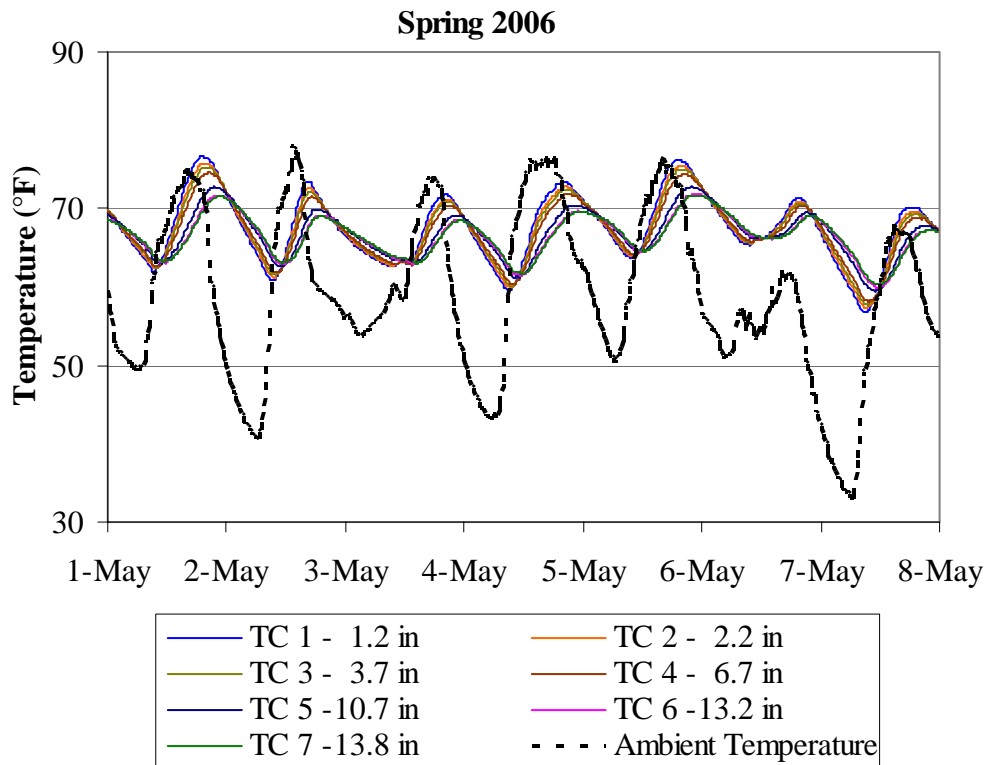


Figure A.22. Edge concrete temperature for a 1-week period representing the spring 2006 season.

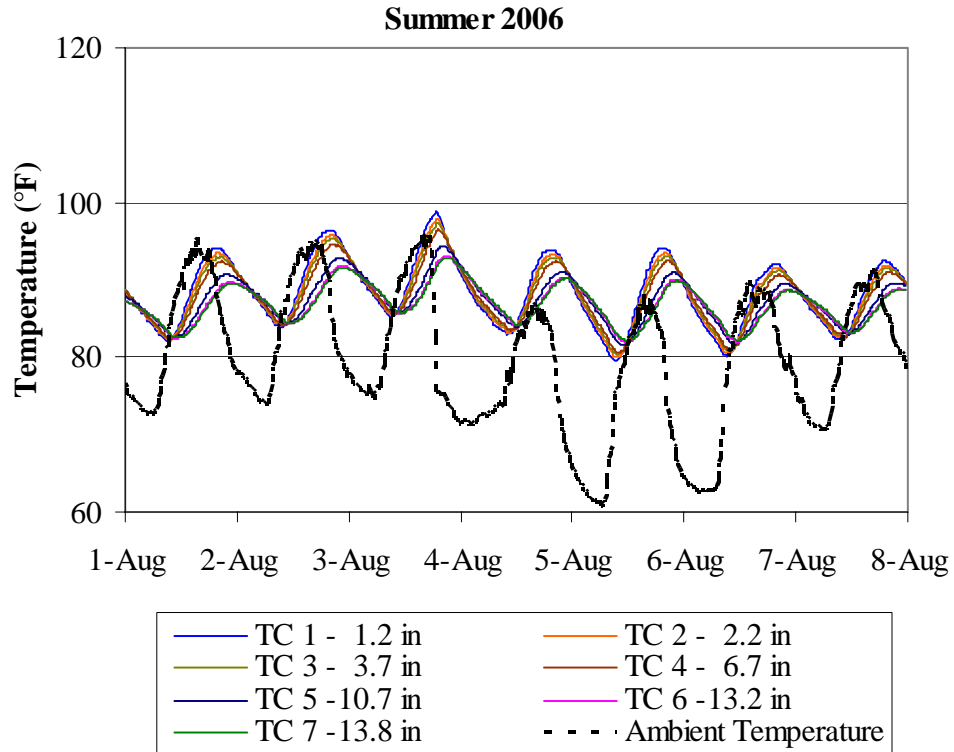


Figure A.23. Edge concrete temperature for a 1-week period representing the summer 2006 season.

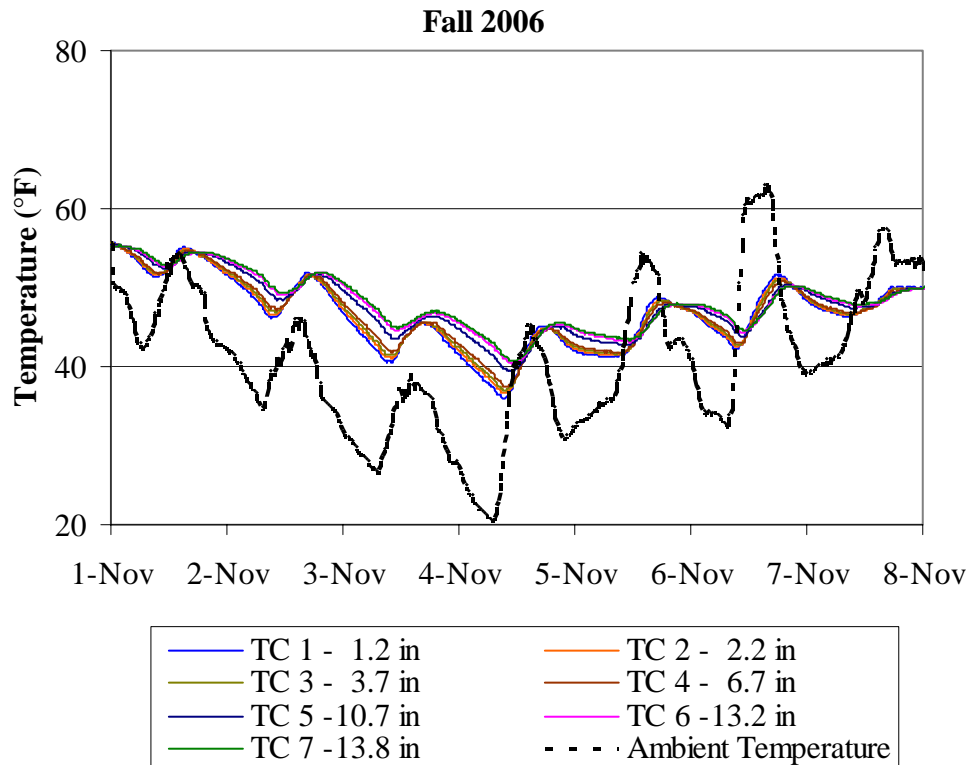


Figure A.24. Edge concrete temperature for a 1-week period representing the fall 2006 season.

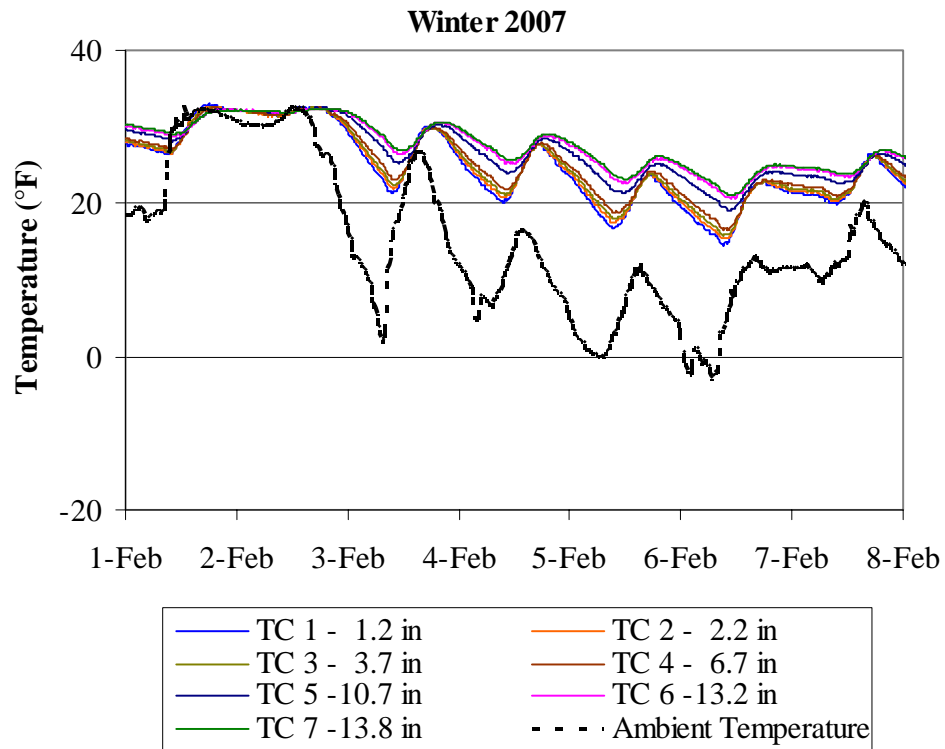


Figure A.25. Edge concrete temperature for a 1-week period representing the winter 2007 season.

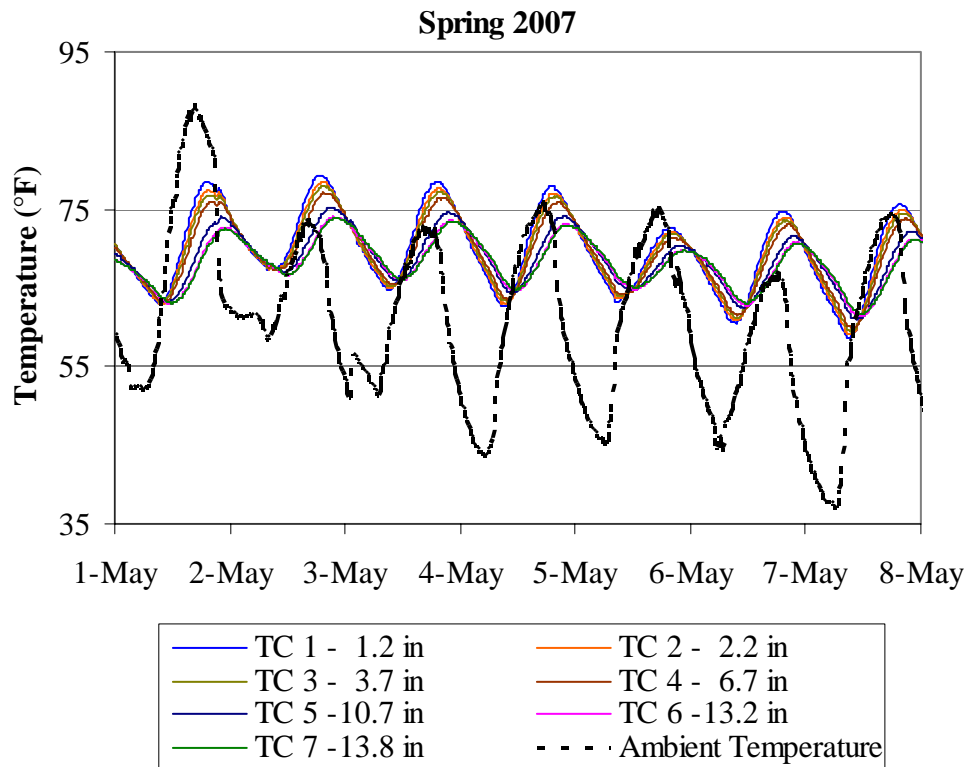


Figure A.26. Edge concrete temperature for a 1-week period representing the spring 2007 season.

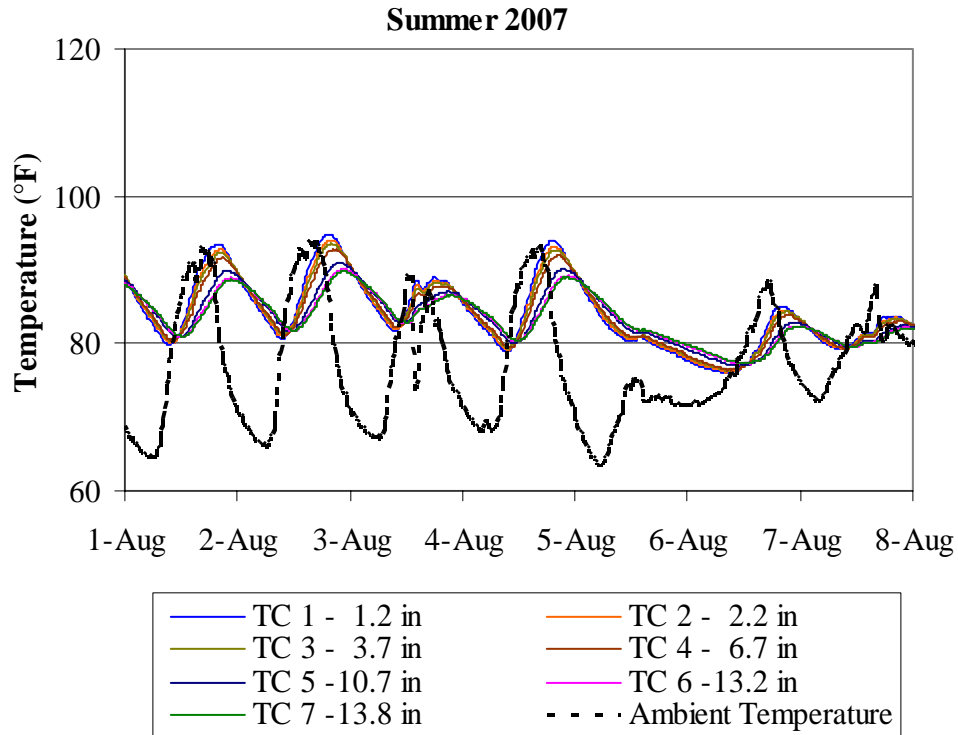


Figure A.27. Edge concrete temperature for a 1-week period representing the summer 2007 season.

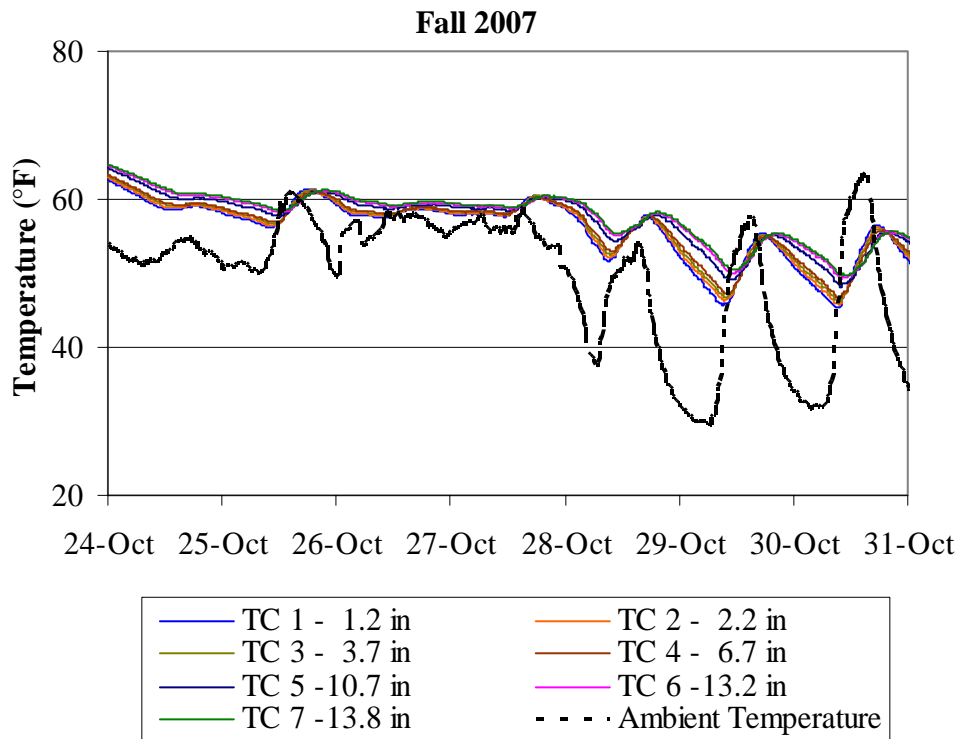


Figure A.28. Edge concrete temperature for a 1-week period representing the fall 2007 season.

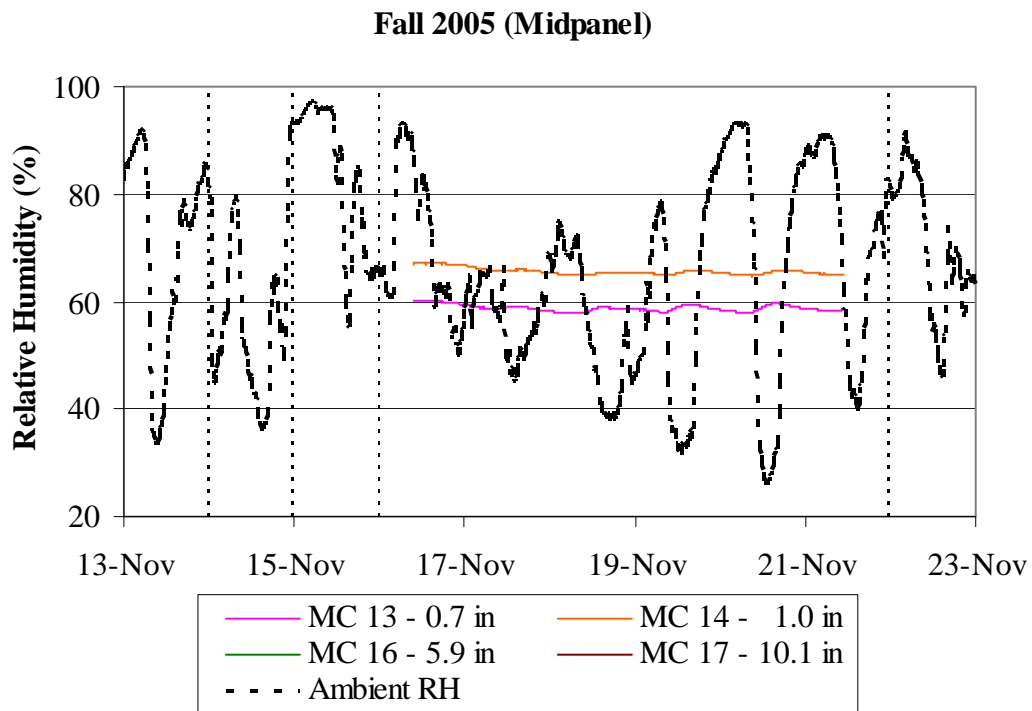


Figure A.29. Midpanel concrete moisture content for a 10-day period representing the fall 2005 season.

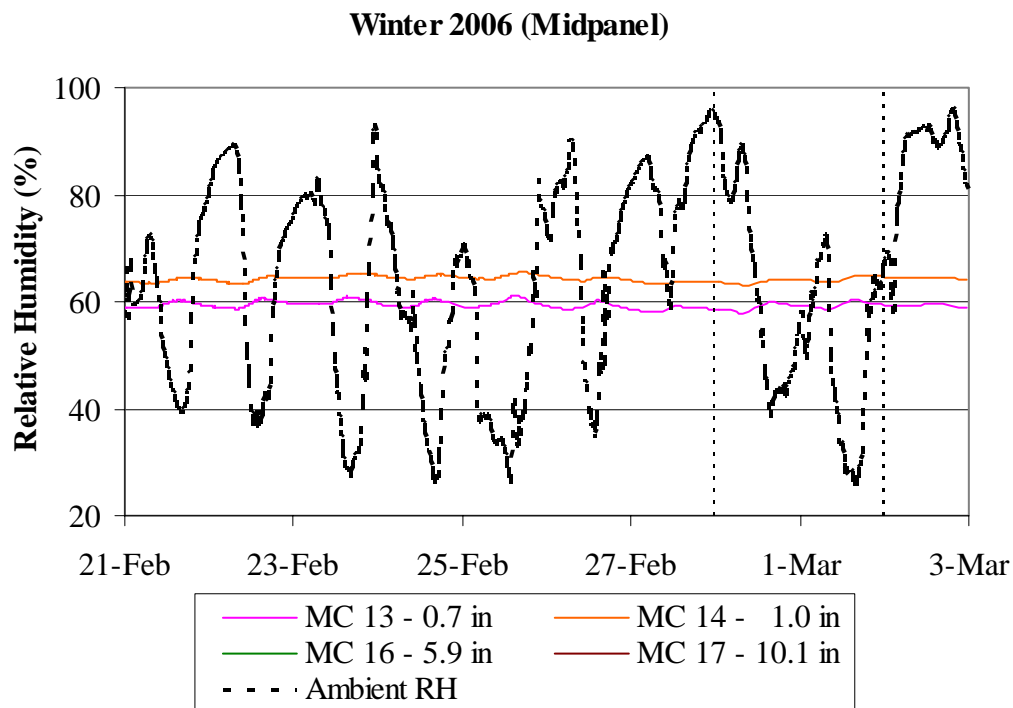


Figure A.30. Midpanel concrete moisture content for a 10-day period representing the winter 2006 season.

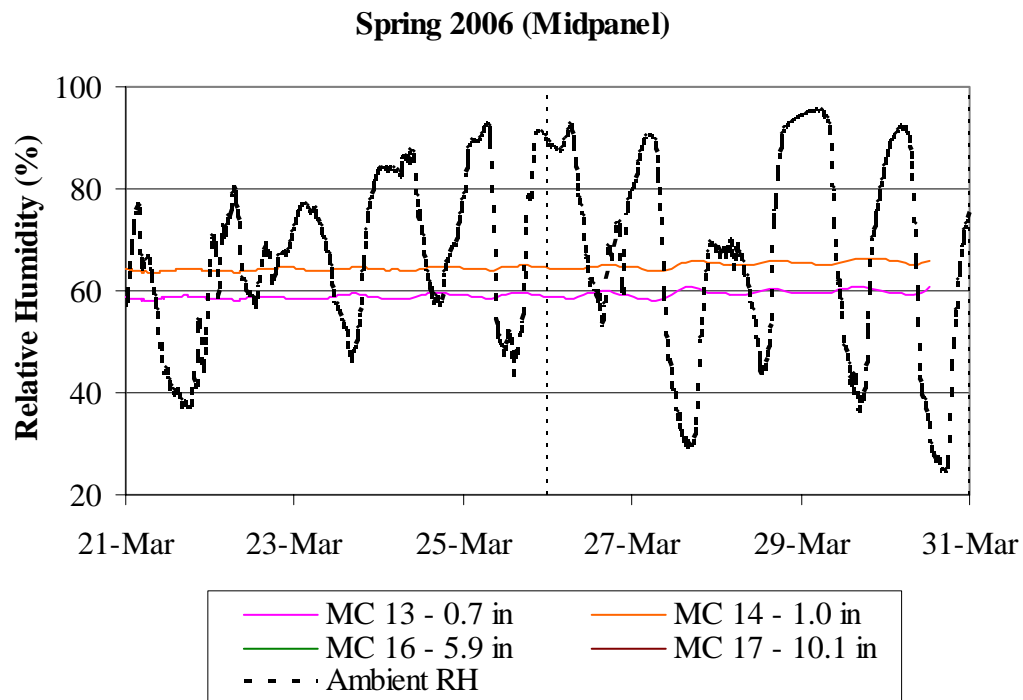


Figure A.31. Midpanel concrete moisture content for a 10-day period representing the spring 2006 season.

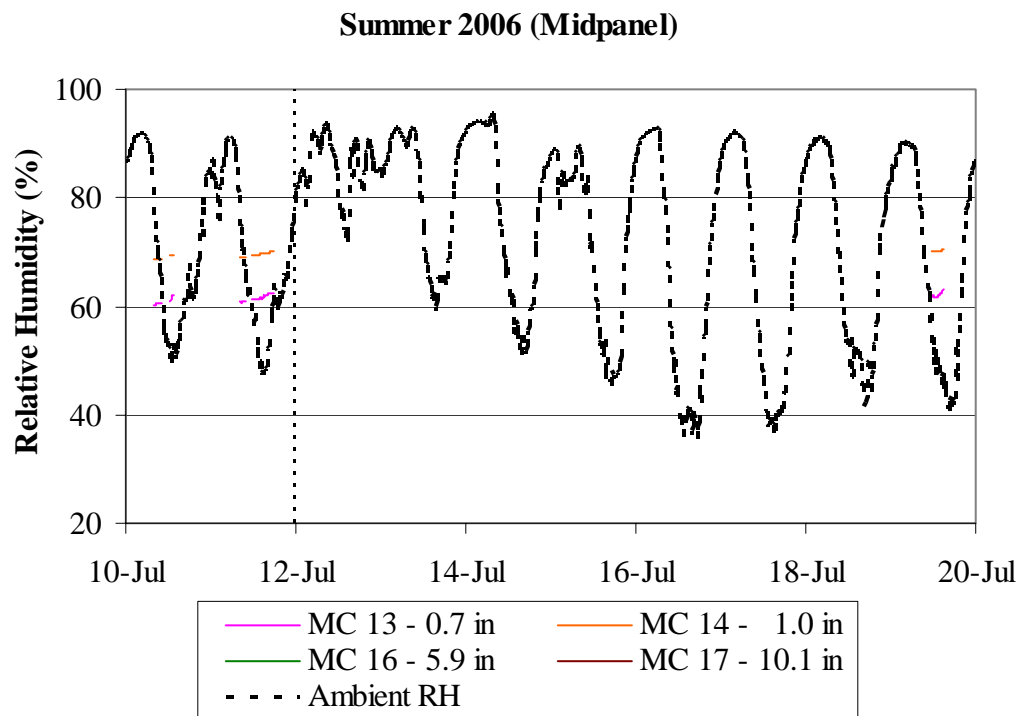


Figure A.32. Midpanel concrete moisture content for a 10-day period representing the summer 2006 season.

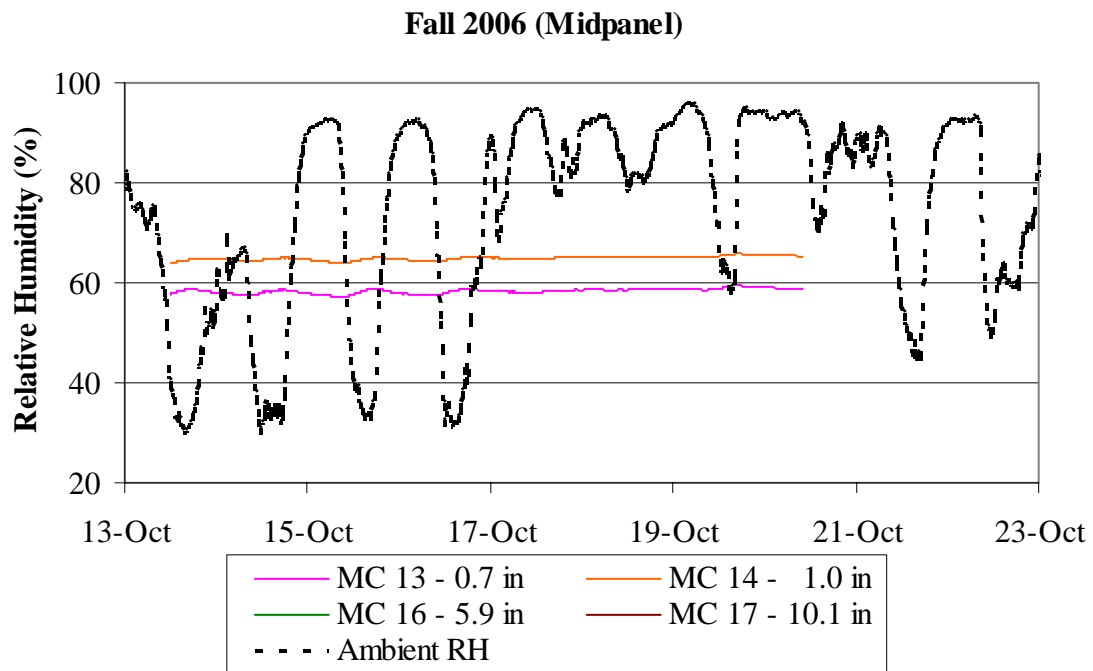


Figure A.33. Midpanel concrete moisture content for a 10-day period representing the fall 2006 season.

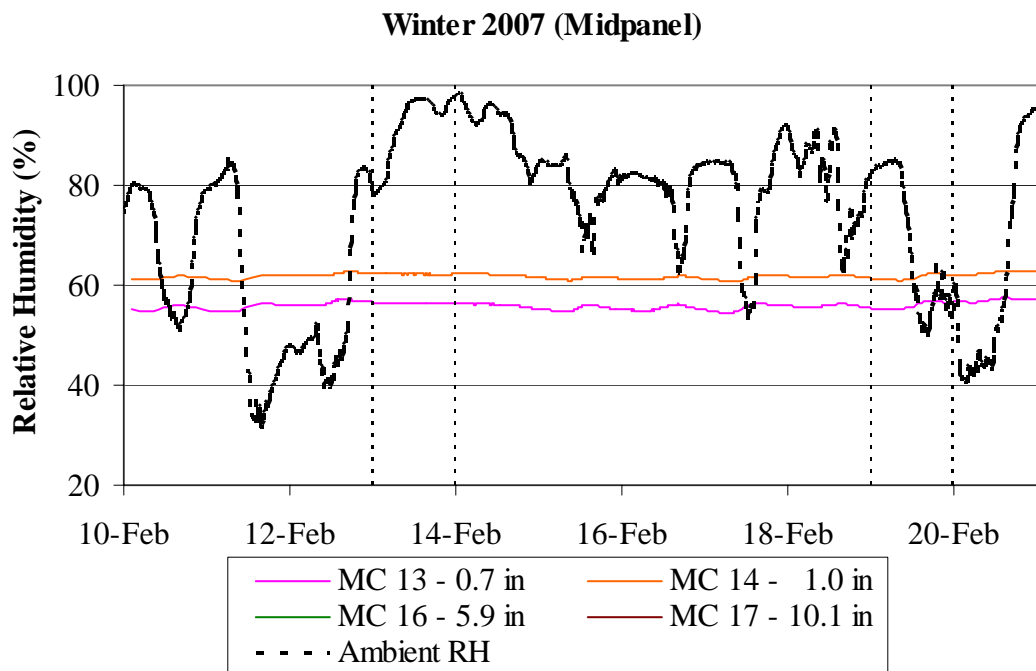


Figure A.34. Midpanel concrete moisture content for a 10-day period representing the winter 2007 season.

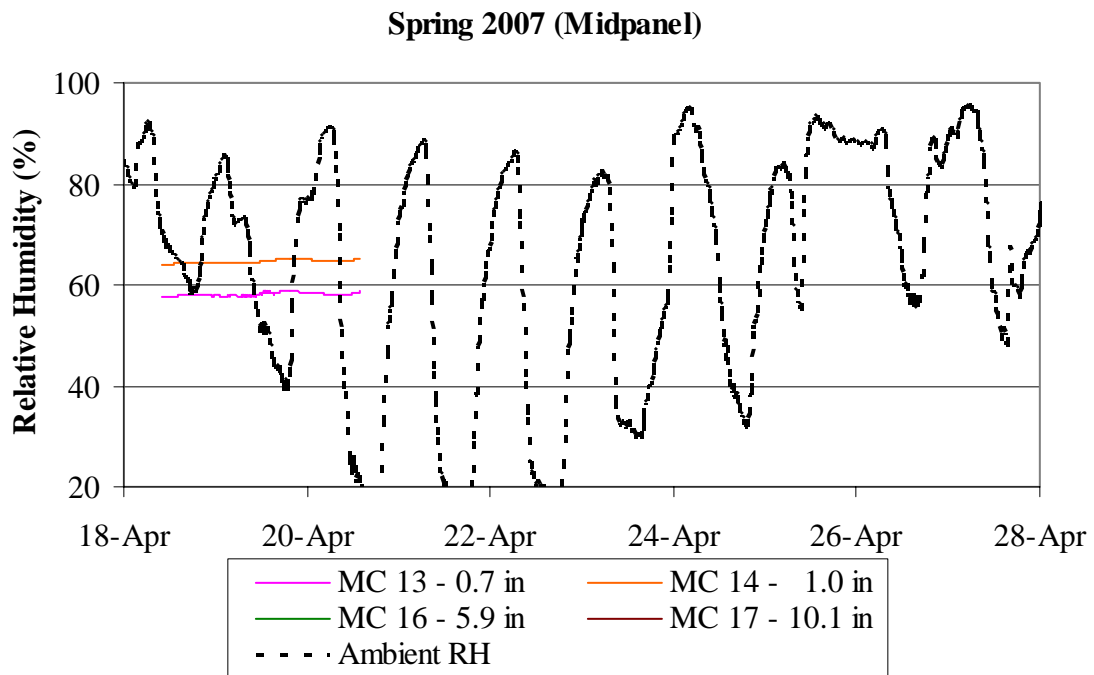


Figure A.35. Midpanel concrete moisture content for a 10-day period representing the spring 2007 season.

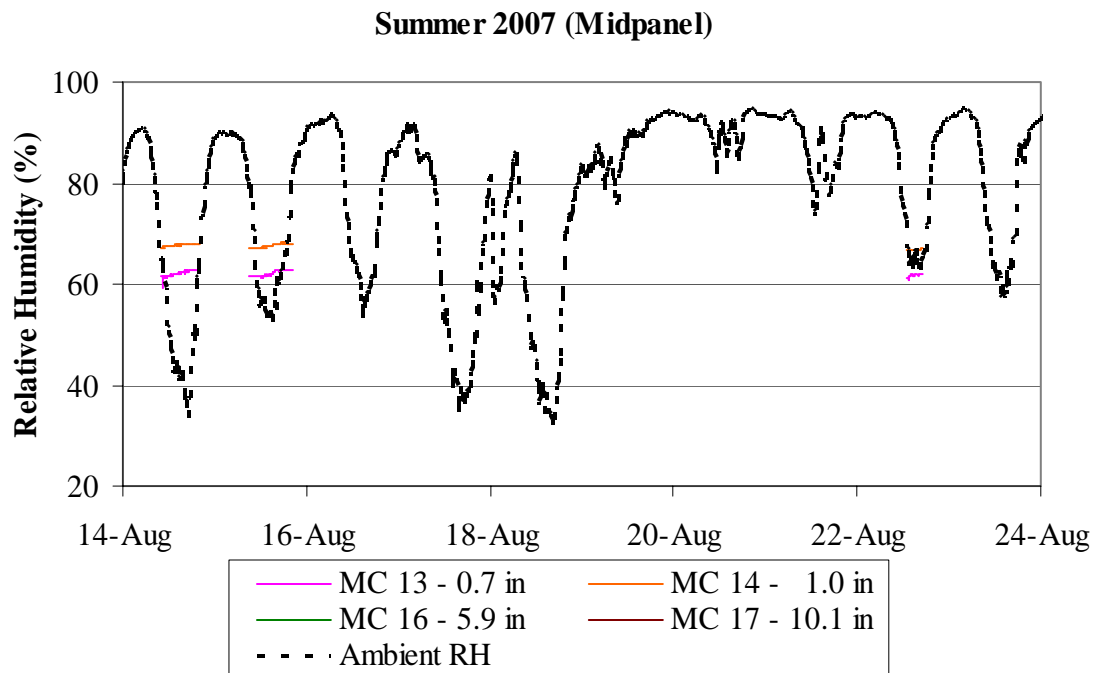


Figure A.36. Midpanel concrete moisture content for a 10-day period representing the summer 2007 season.

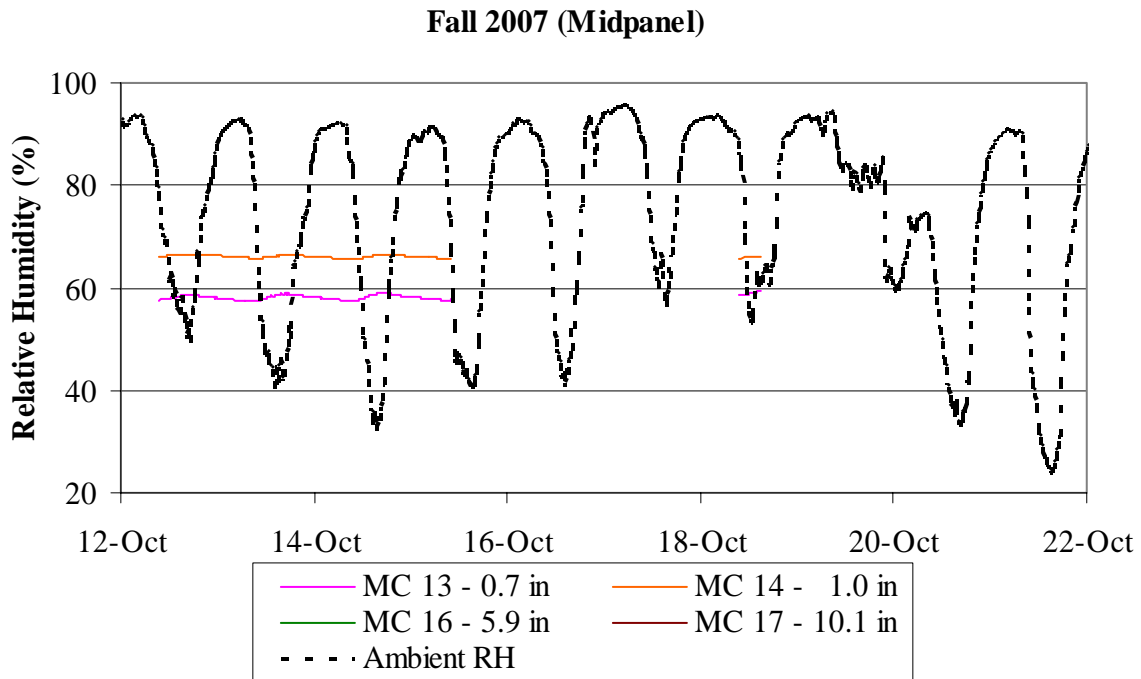


Figure A.37. Midpanel concrete moisture content for a 10-day period representing the fall 2007 season.

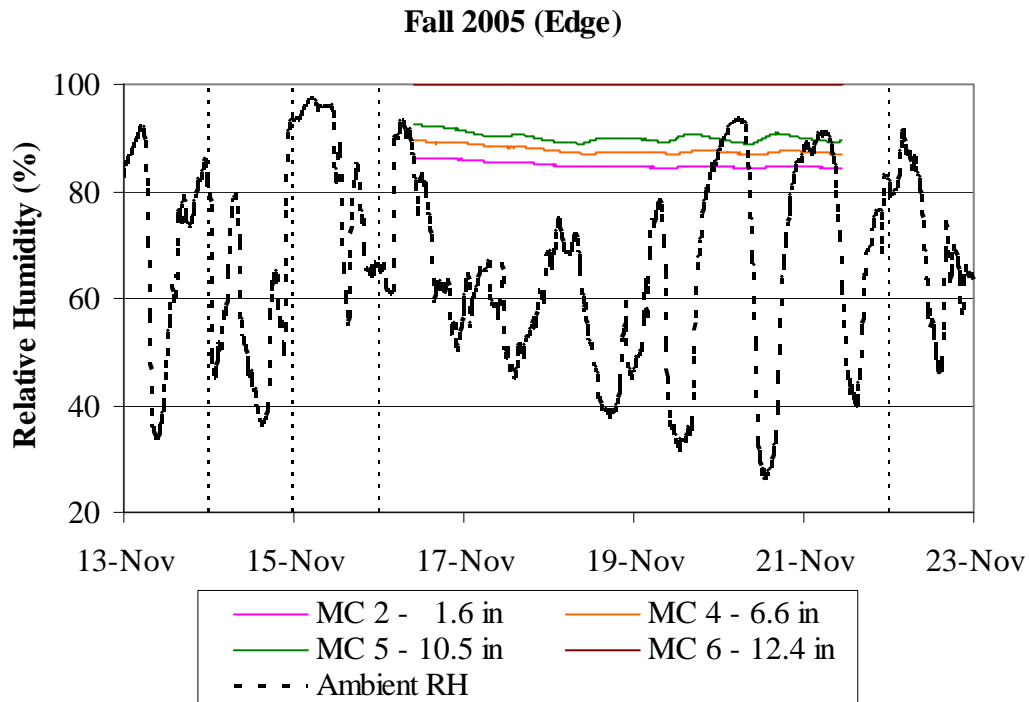


Figure A. 38. Edge concrete moisture content for a 10-day period representing the fall 2005 season.

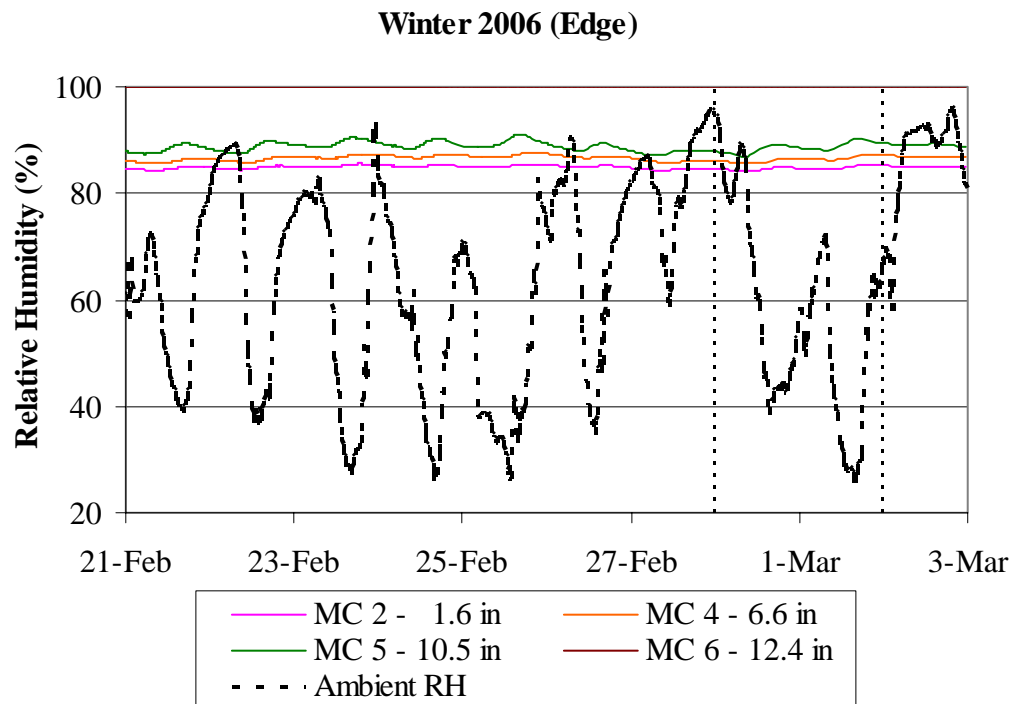


Figure A.39. Edge concrete moisture content for a 10-day period representing the winter 2006 season.

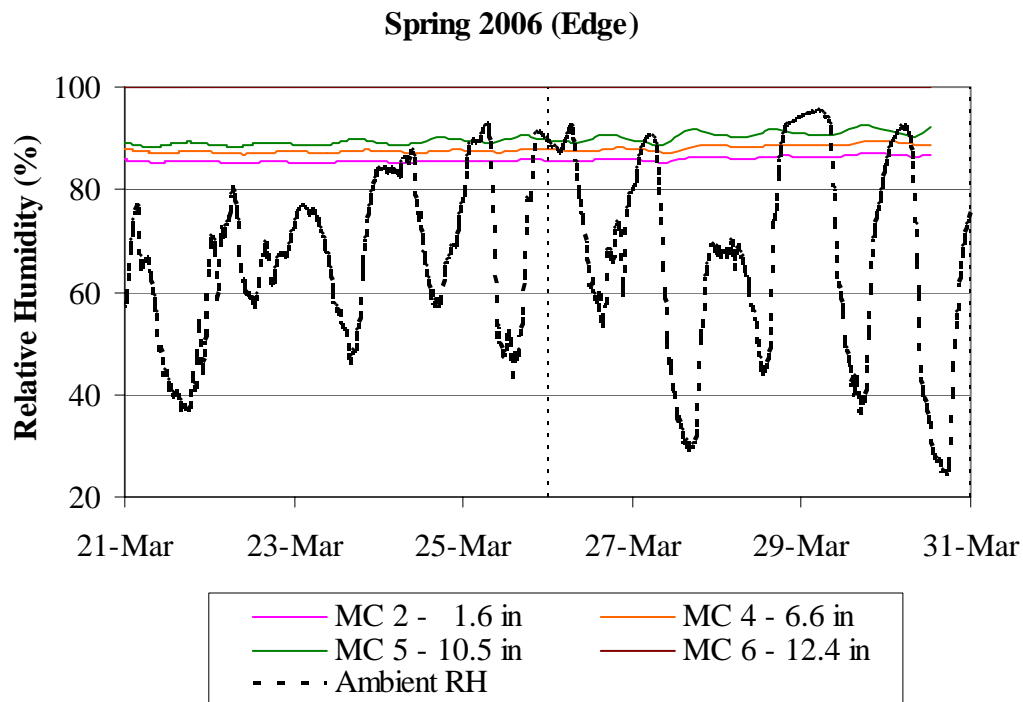


Figure A.40. Edge concrete moisture content for a 10-day period representing the spring 2006 season.

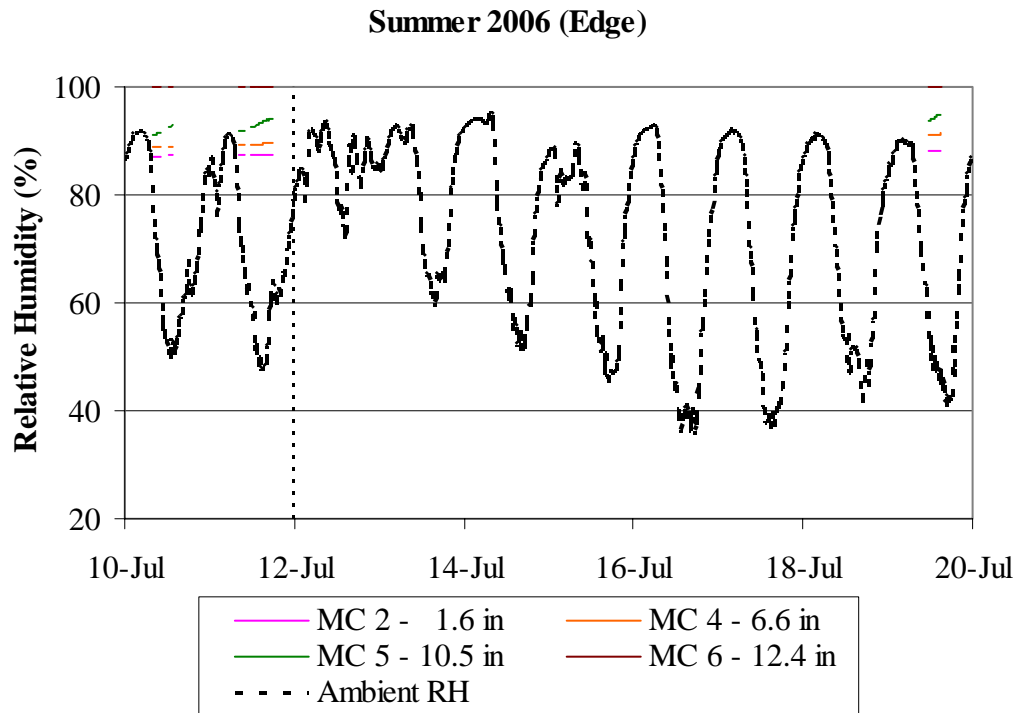


Figure A.41. Edge concrete moisture content for a 10-day period representing the summer 2006 season.

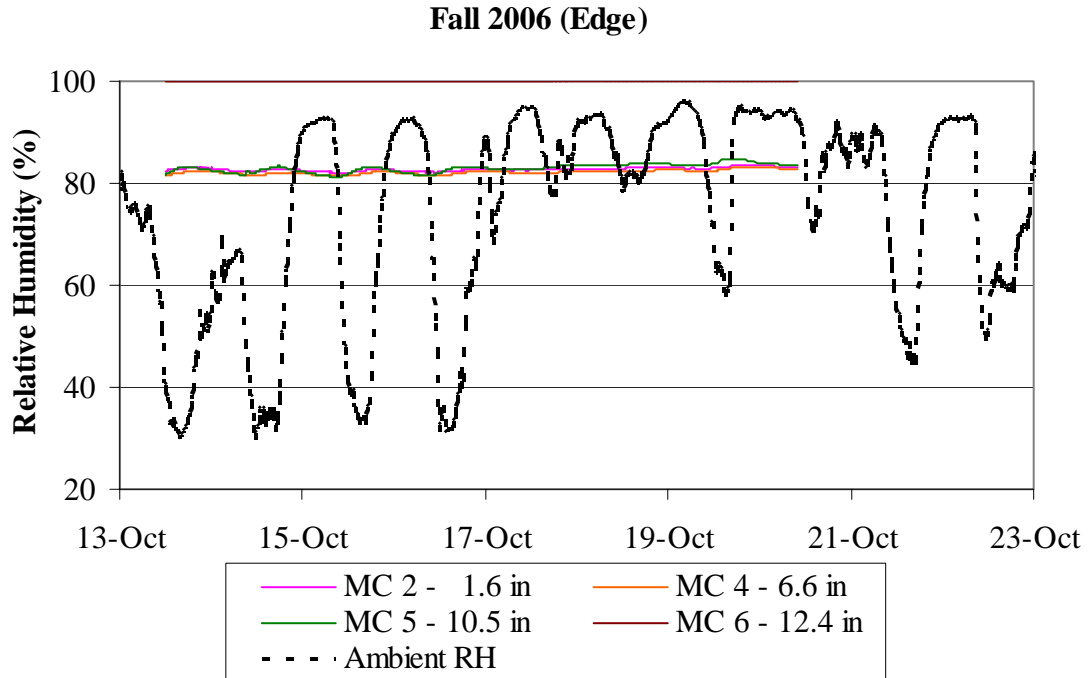


Figure A.42. Edge concrete moisture content for a 10-day period representing the fall 2006 season.

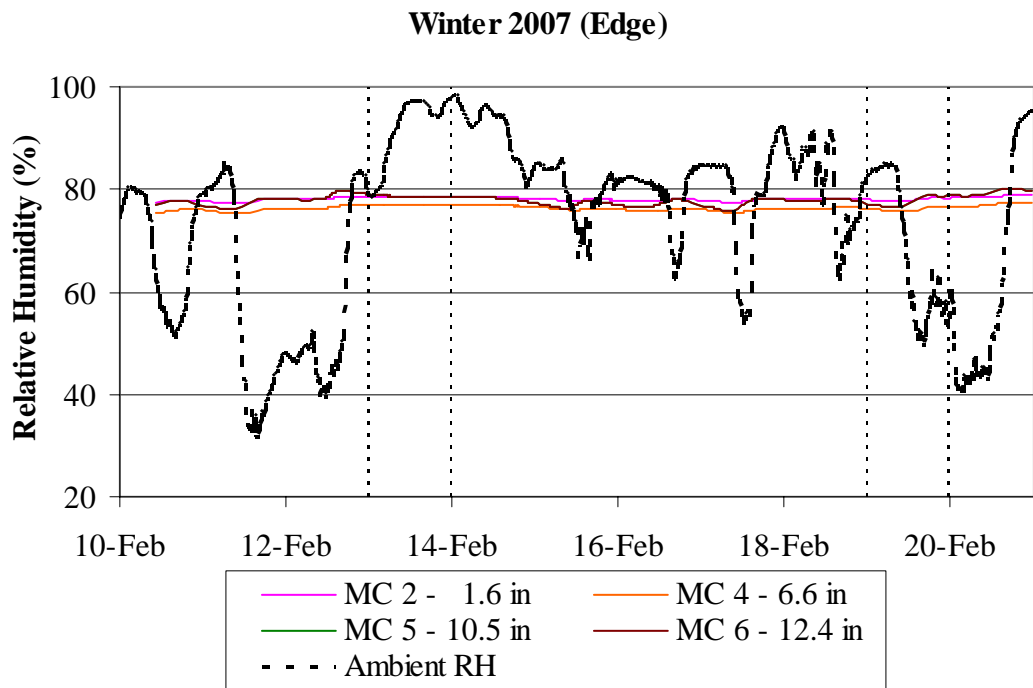


Figure A.43. Edge concrete moisture content for a 10-day period representing the winter 2007 season.

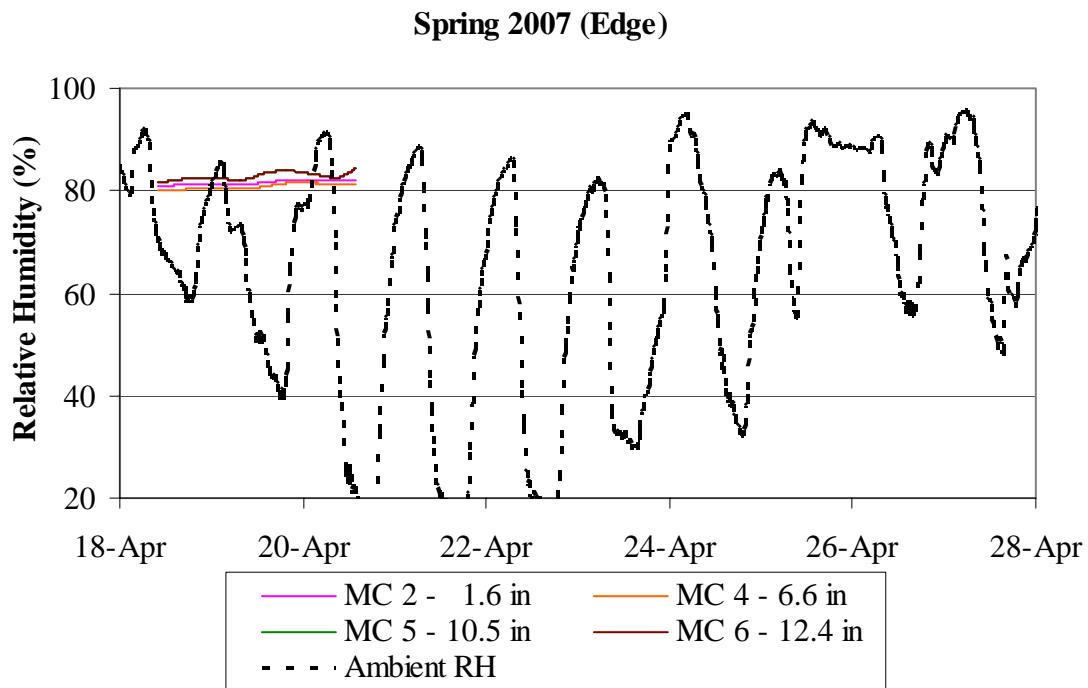


Figure A.44. Edge concrete moisture content for a 10-day period representing the spring 2007 season.

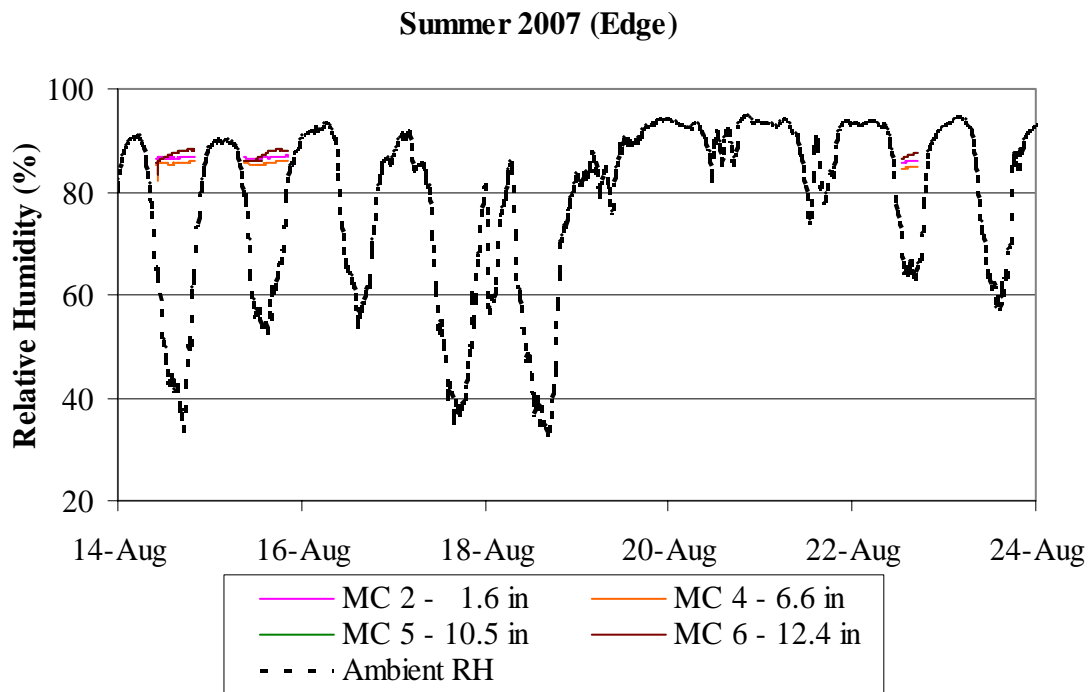


Figure A.45. Edge concrete moisture content for a 10-day period representing the summer 2007 season.

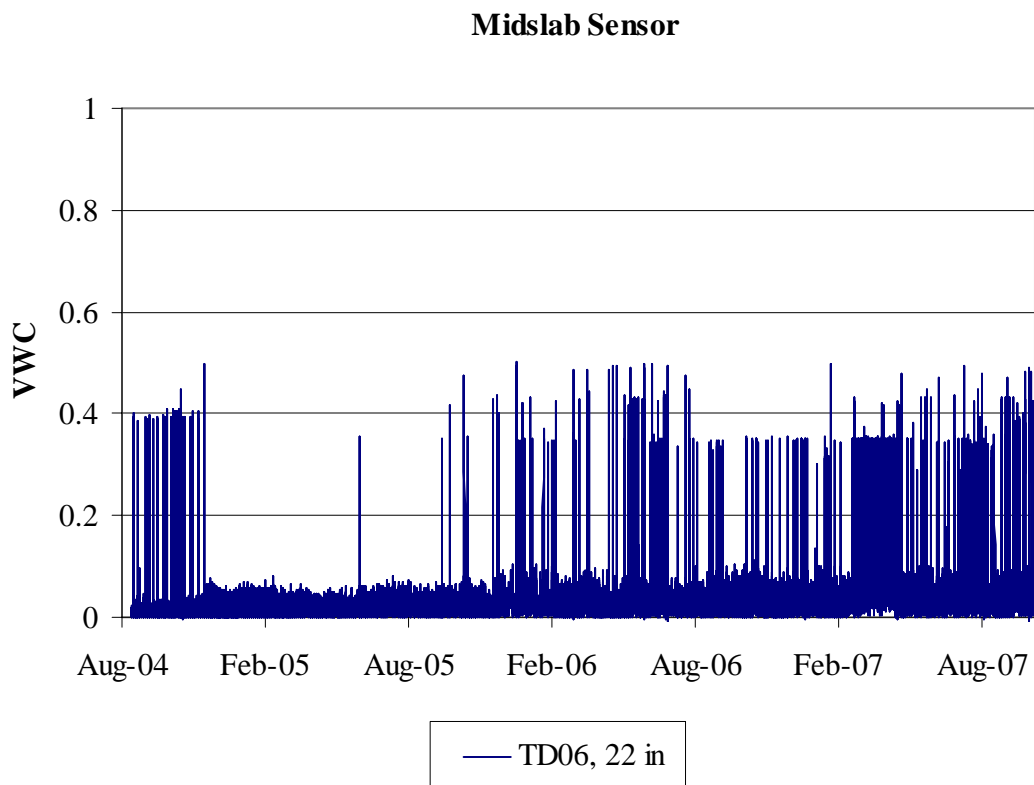


Figure A.46. Volumetric water content measured by midpanel sensor TD06 in the fill material at a depth of 22 inches.

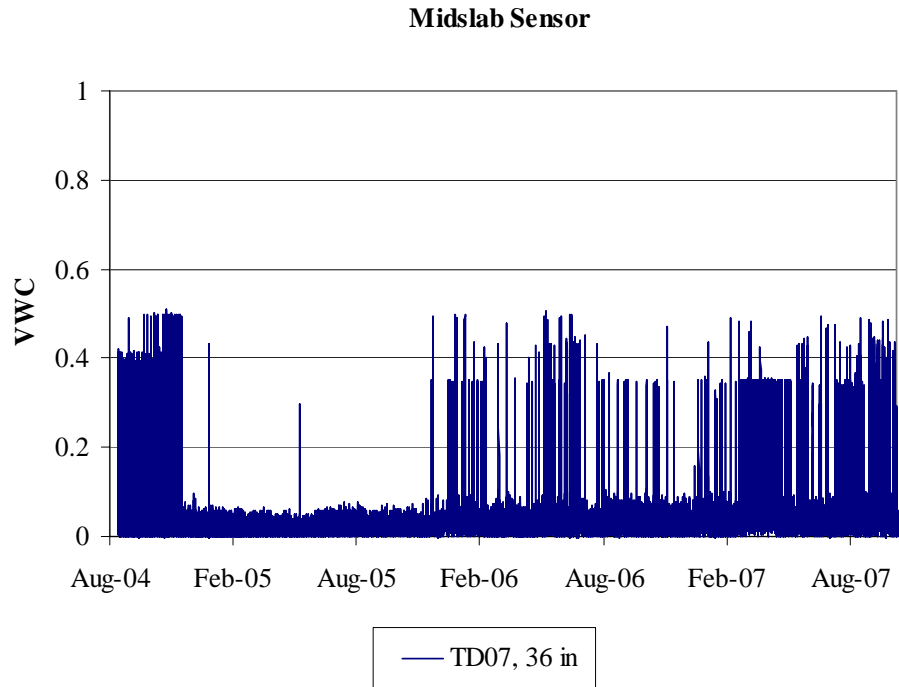


Figure A.47. Volumetric water content measured by midpanel sensor TD07 in the fill material at a depth of 36 inches.

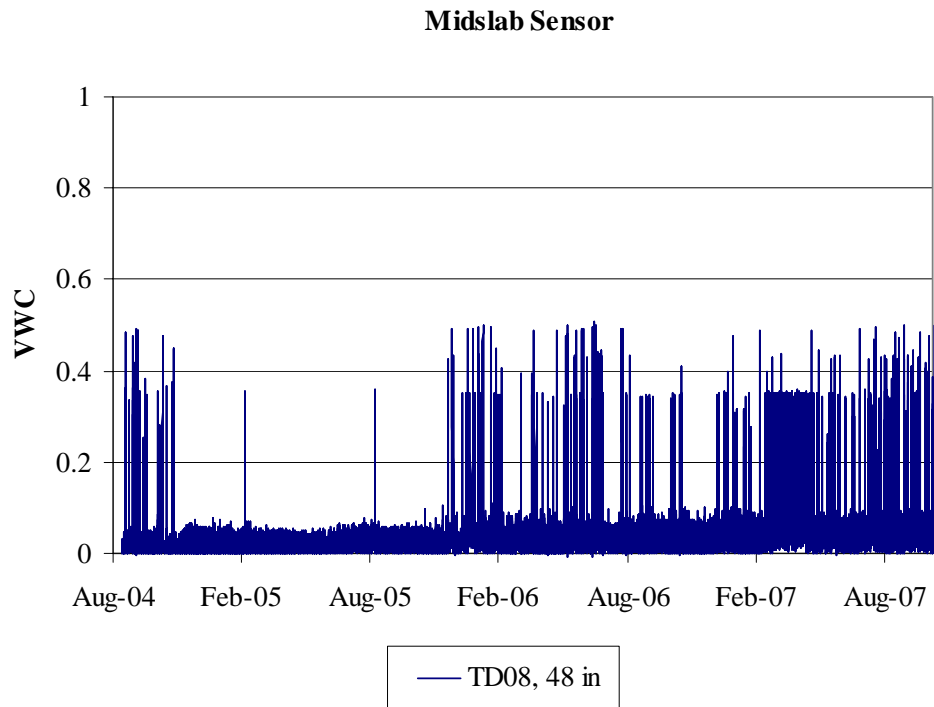


Figure A.48. Volumetric water content measured by midpanel sensor TD08 in the subgrade at a depth of 48 inches.

Appendix B: Early Age Vibrating Wire Gage Measurements

B.1 RESTRAINED SLAB A (CELL 4)

Restrained Longitudinal, Corner Centerline (Depth = 1.5 in)

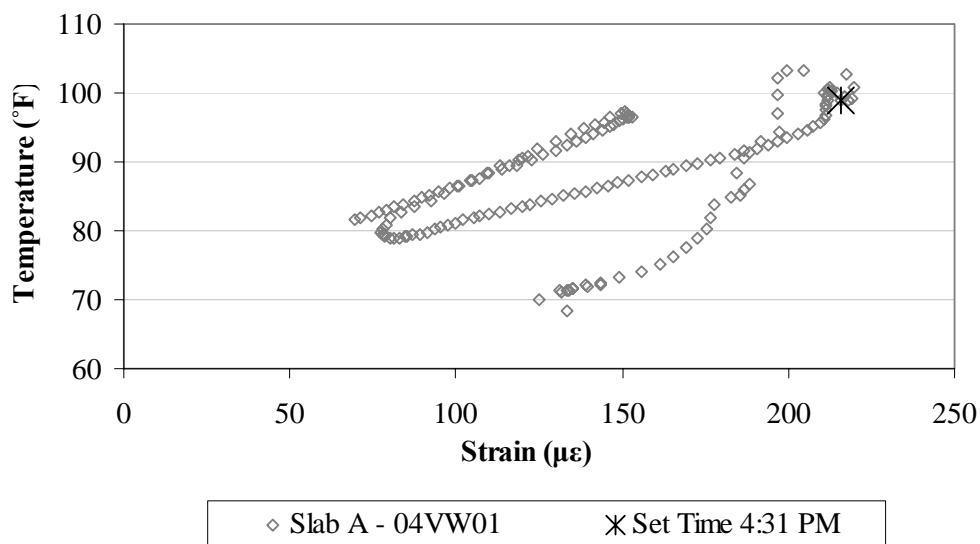


Figure B.1. Variation of strain with temperature, in the longitudinal direction, for the top sensor located at the corner along the centerline joint in restrained Slab A.

Restrained Longitudinal, Corner Centerline (Depth = 4.3 in)

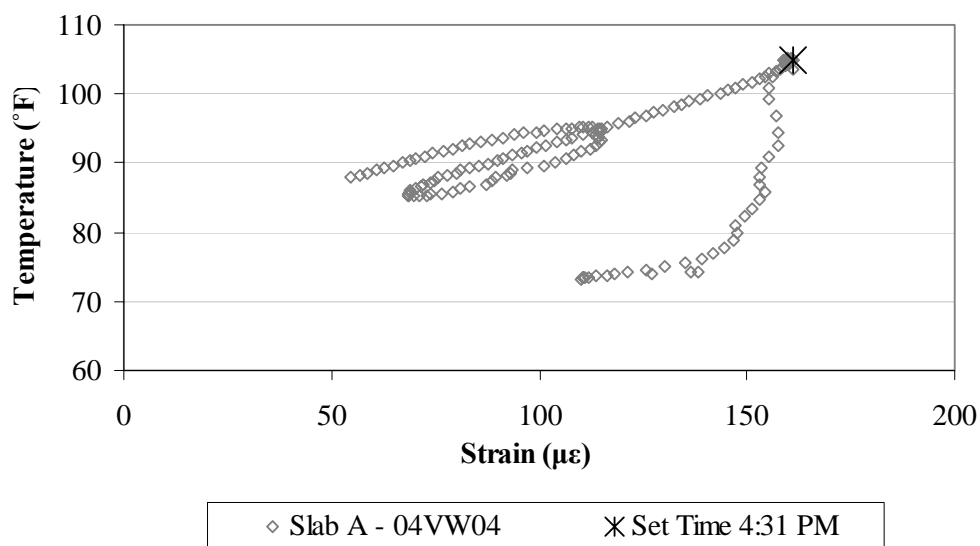


Figure B.2. Variation of strain with temperature, in the longitudinal direction, for the middepth sensor located at the corner along the centerline joint in restrained Slab A.

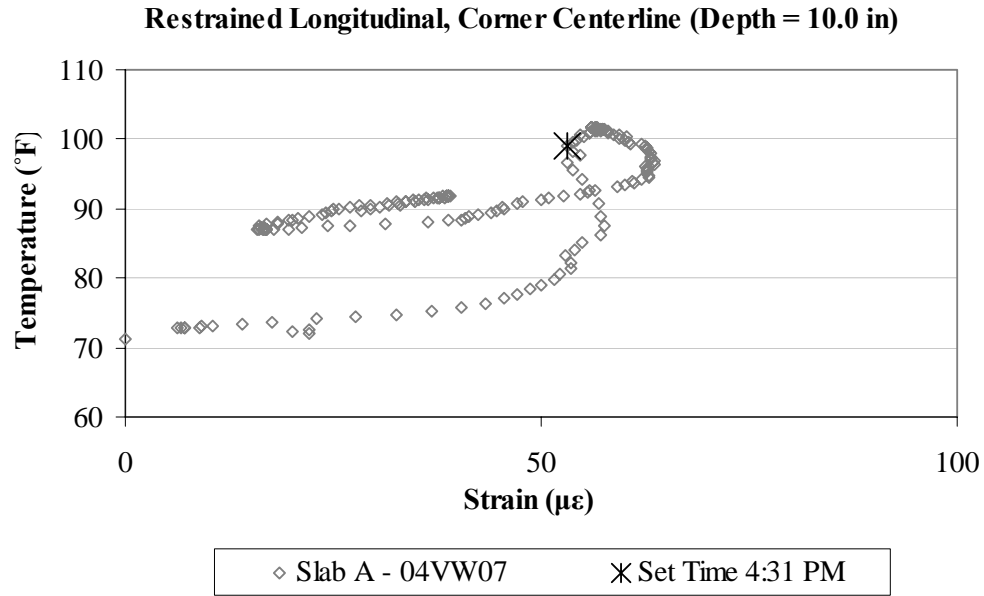


Figure B.3. Variation of strain with temperature, in the longitudinal direction, for the bottom sensor located at the corner along the centerline joint in restrained Slab A.

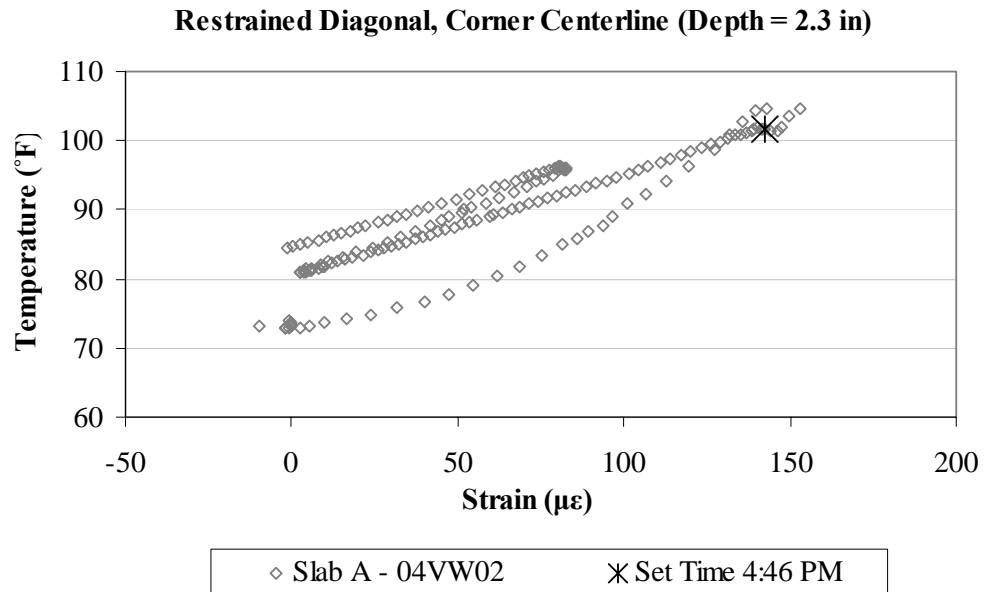


Figure B.4. Variation of strain with temperature, in the diagonal direction, for the top sensor located at the corner along the centerline joint in restrained Slab A.

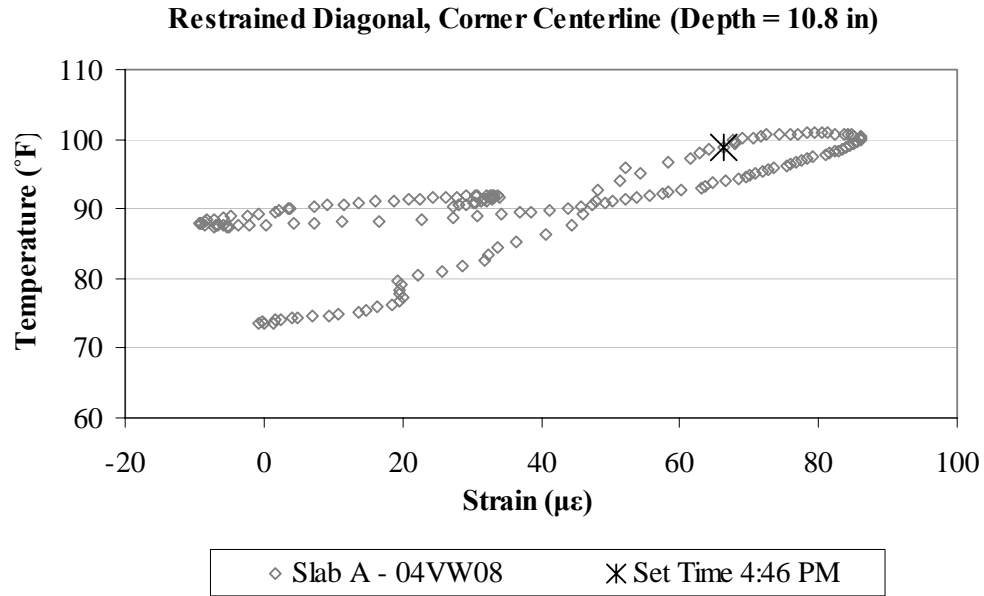


Figure B.5. Variation of strain with temperature, in the diagonal direction, for the bottom sensor located at the corner along the centerline joint in restrained Slab A.

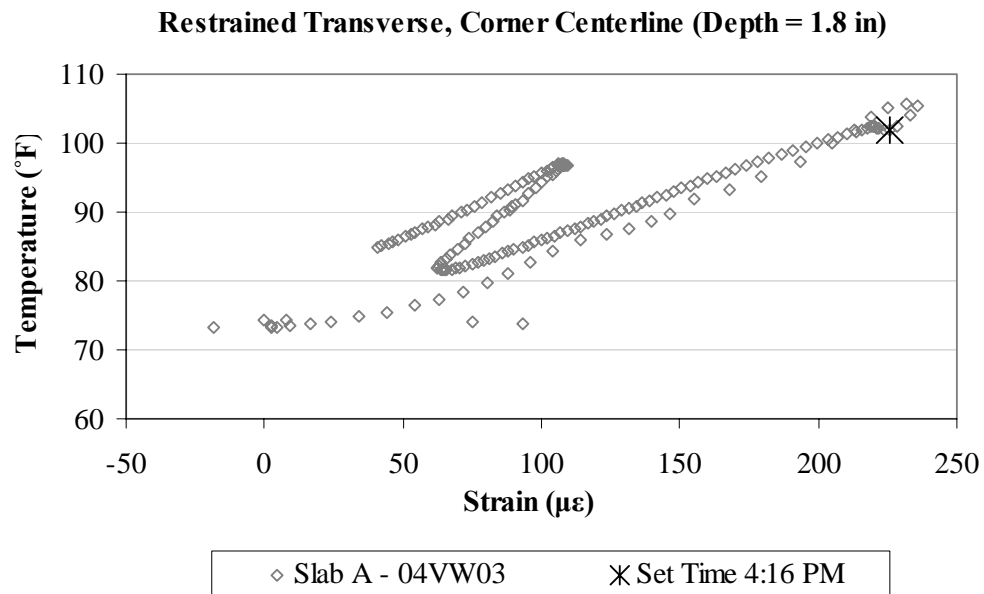


Figure B.6. Variation of strain with temperature, in the transverse direction, for the top sensor located at the corner along the centerline joint in restrained Slab A.

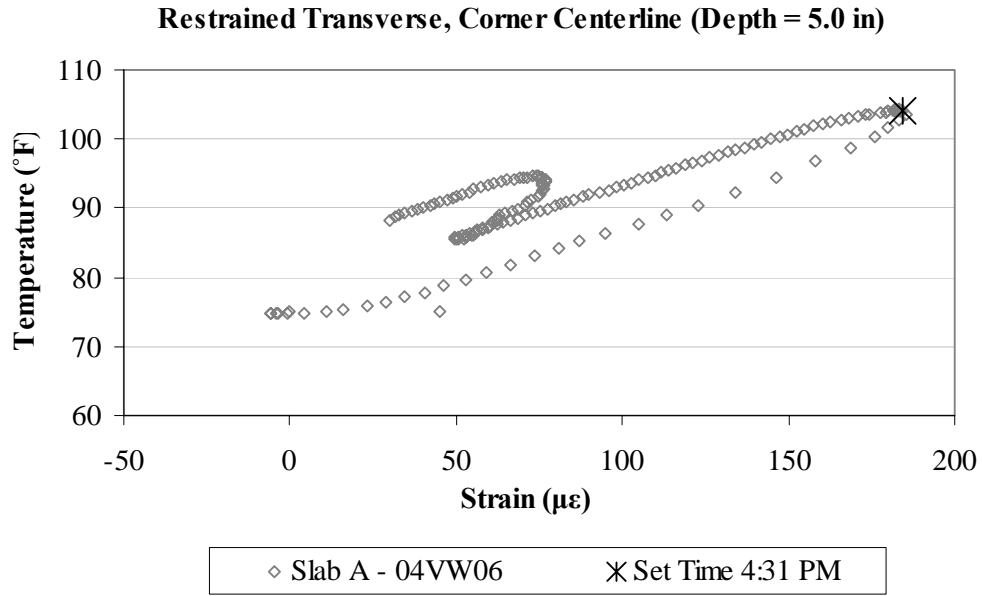


Figure B.7. Variation of strain with temperature, in the transverse direction, for the middepth sensor located at the corner along the centerline joint in restrained Slab A.

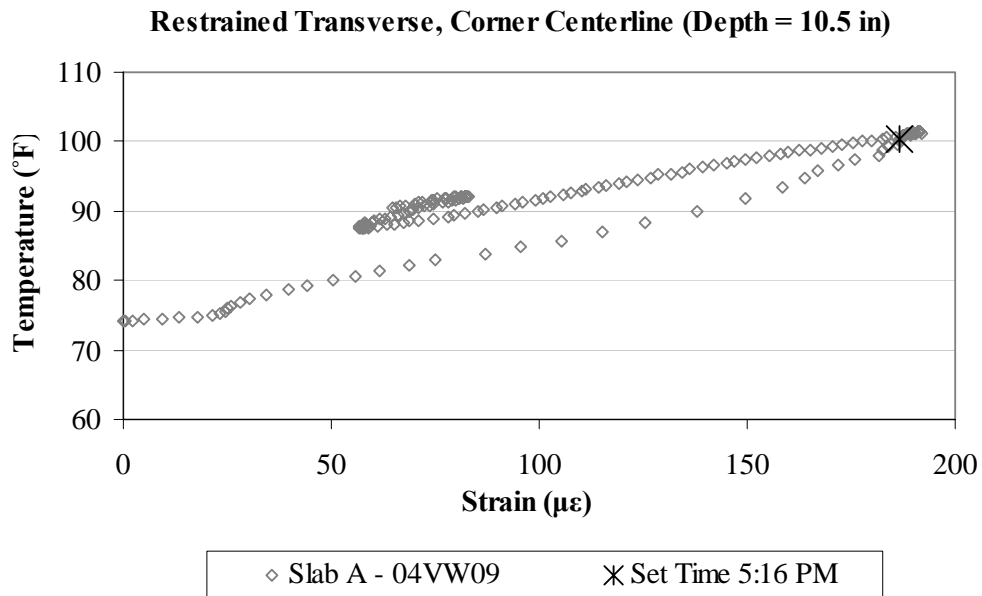


Figure B.8. Variation of strain with temperature, in the transverse direction, for the bottom sensor located at the corner along the centerline joint in restrained Slab A.

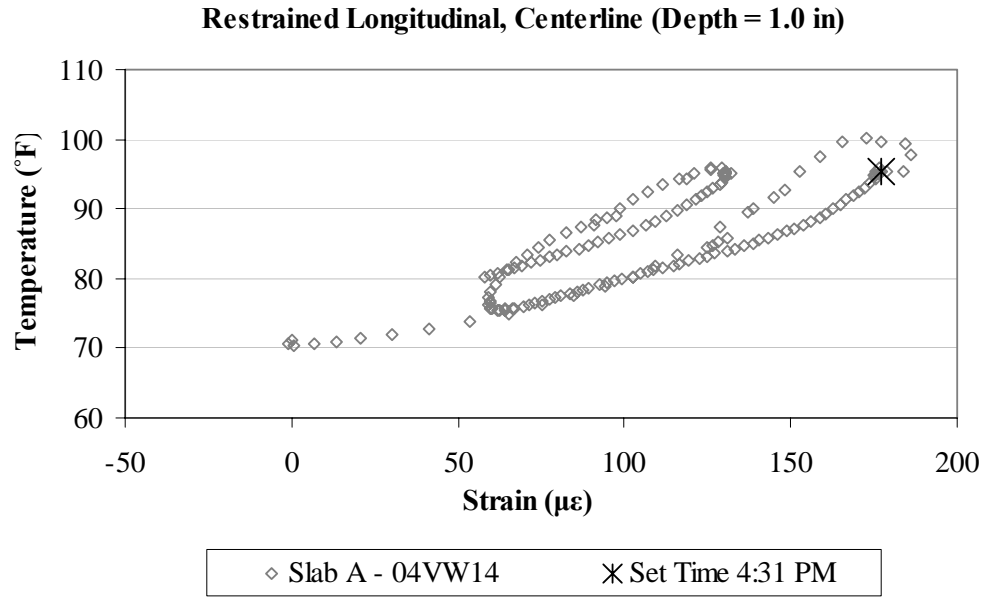


Figure B.9. Variation of strain with temperature, in the longitudinal direction, for the top sensor located along the centerline joint in restrained Slab A.

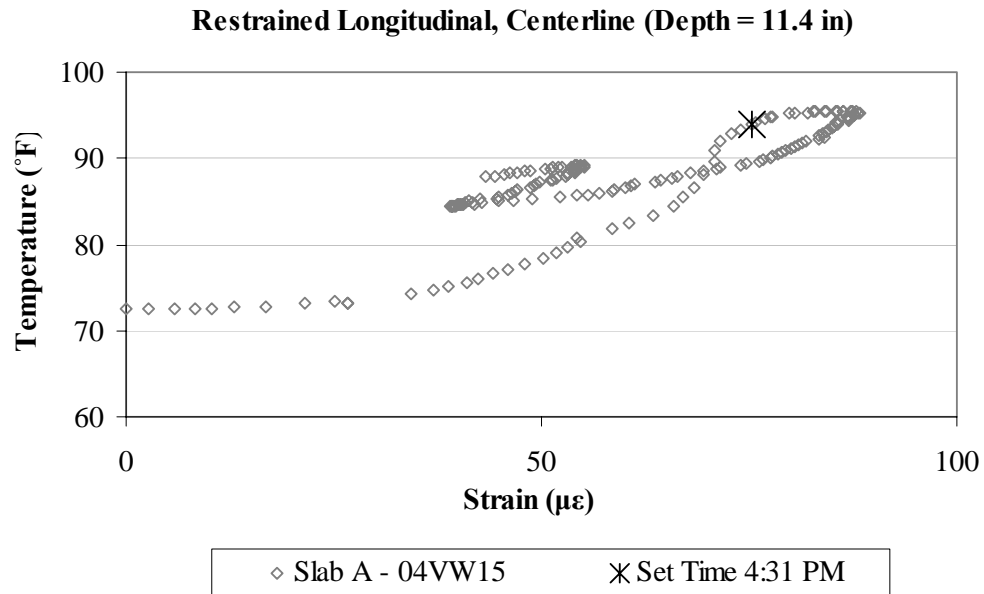


Figure B.10. Variation of strain with temperature, in the longitudinal direction, for the bottom sensor located along the centerline joint in restrained Slab A.

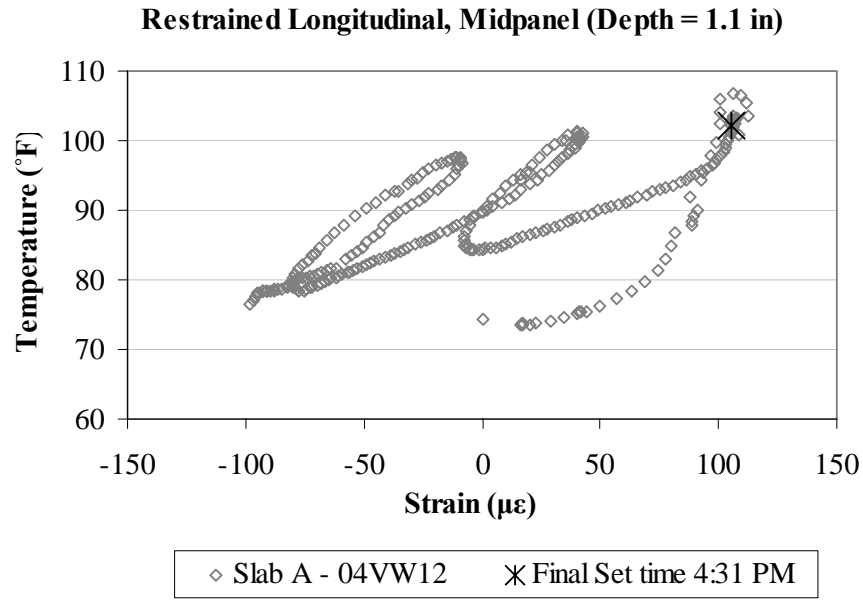


Figure B.11. Variation of strain with temperature, in the longitudinal direction, for the top sensor located at midpanel in restrained Slab A.

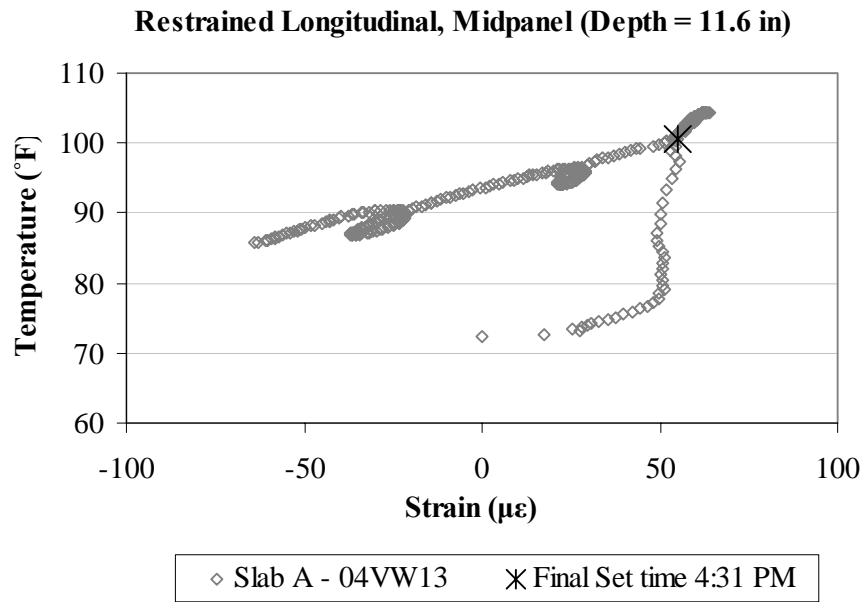


Figure B.12. Variation of strain with temperature, in the longitudinal direction, for the bottom sensor located at midpanel in restrained Slab A.

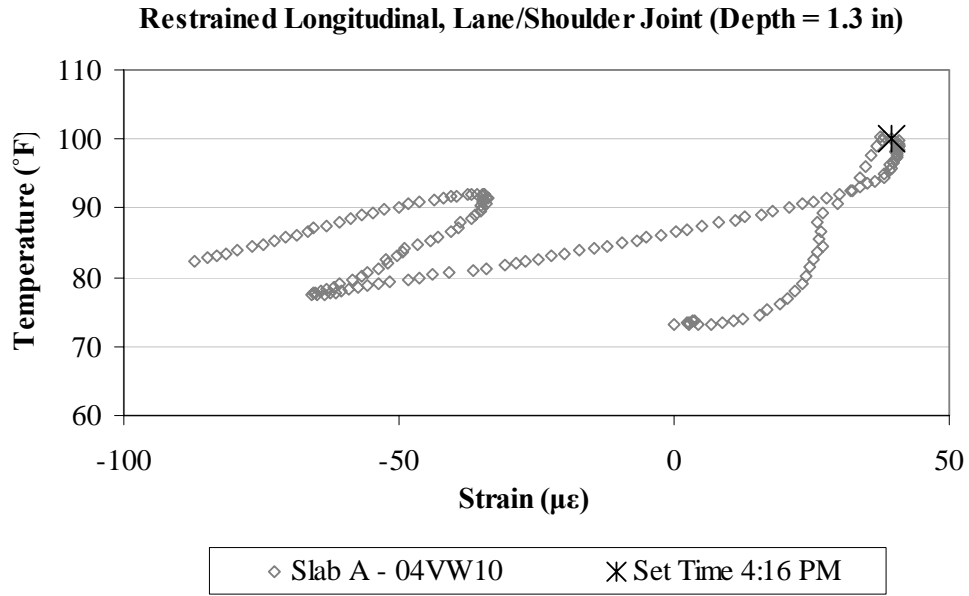


Figure B.13. Variation of strain with temperature, in the longitudinal direction, for the top sensor located along the lane/shoulder joint in restrained Slab A.

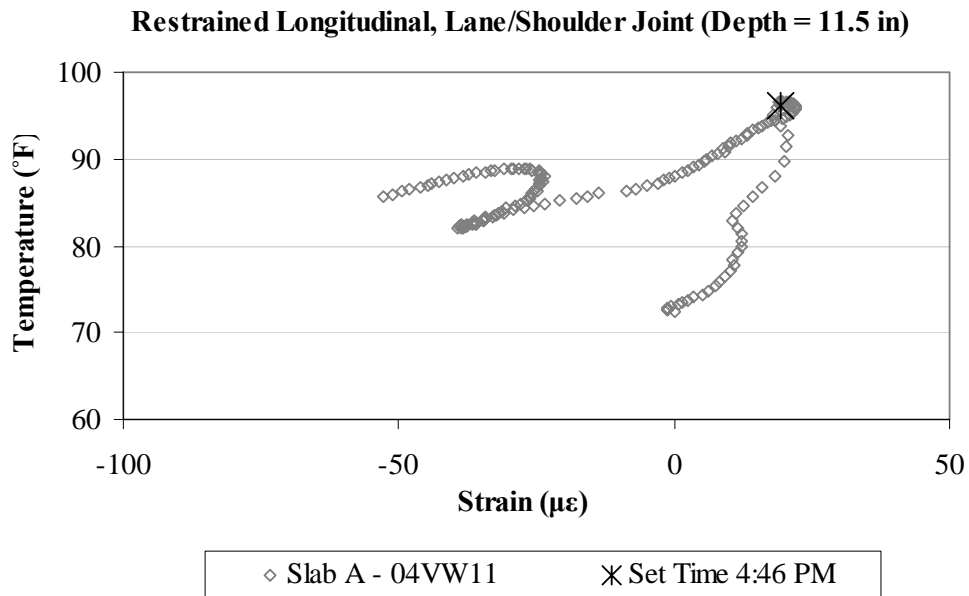


Figure B.14. Variation of strain with temperature, in the longitudinal direction, for the bottom sensor located along the lane/shoulder joint in restrained Slab A.

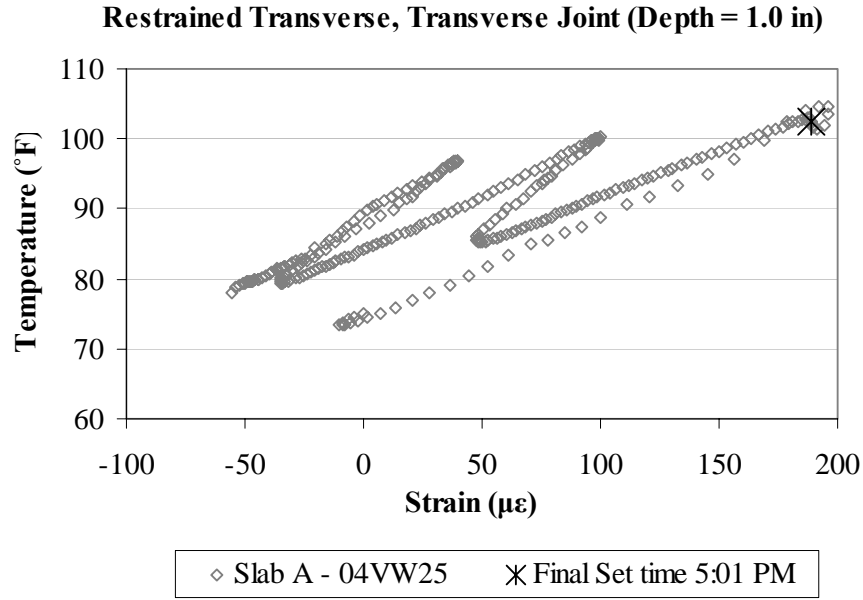


Figure B.15. Variation of strain with temperature, in the transverse direction, for the top sensor located along the transverse joint in restrained Slab A.

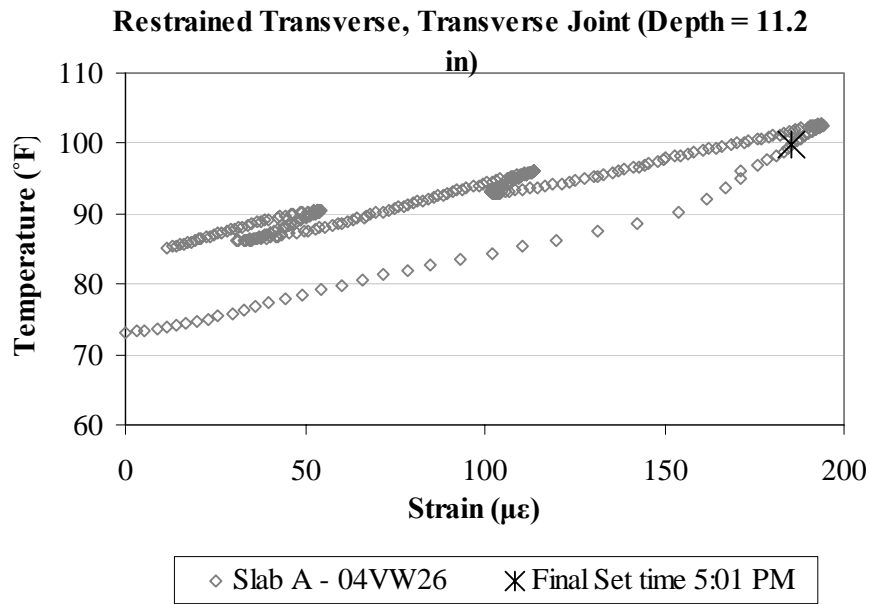


Figure B.16. Variation of strain with temperature, in the transverse direction, for the bottom sensor located along the transverse joint in restrained Slab A.

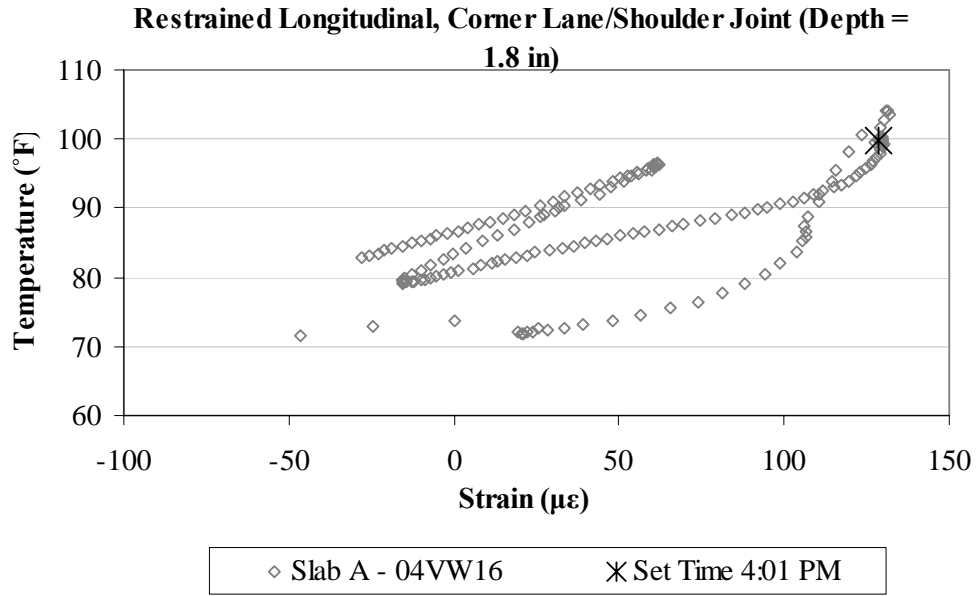


Figure B.17. Variation of strain with temperature, in the longitudinal direction, for the top sensor located at the corner along the lane/shoulder joint in restrained Slab A.

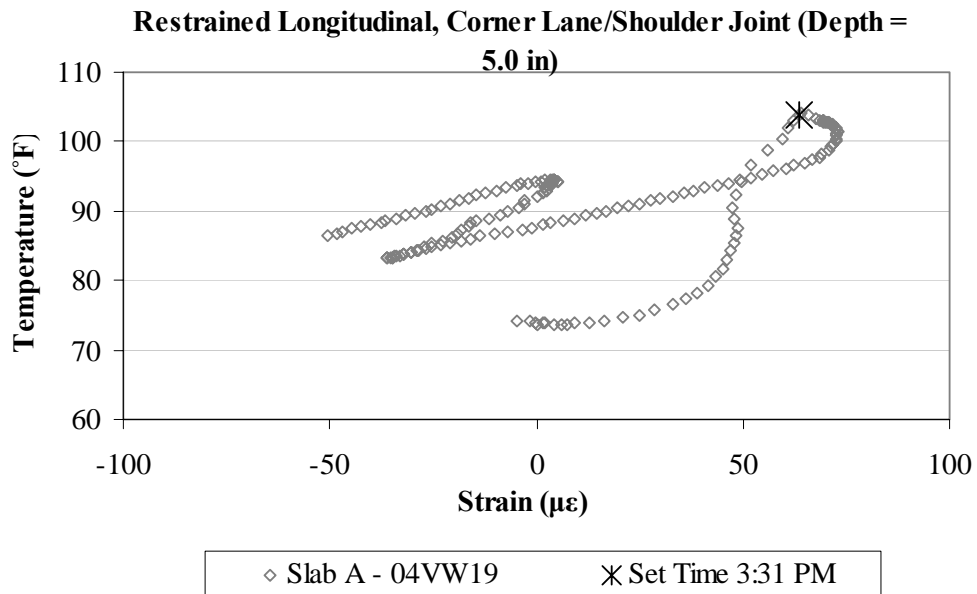


Figure B.18. Variation of strain with temperature, in the longitudinal direction, for the middepth sensor located at the corner along the lane/shoulder joint in restrained Slab A.

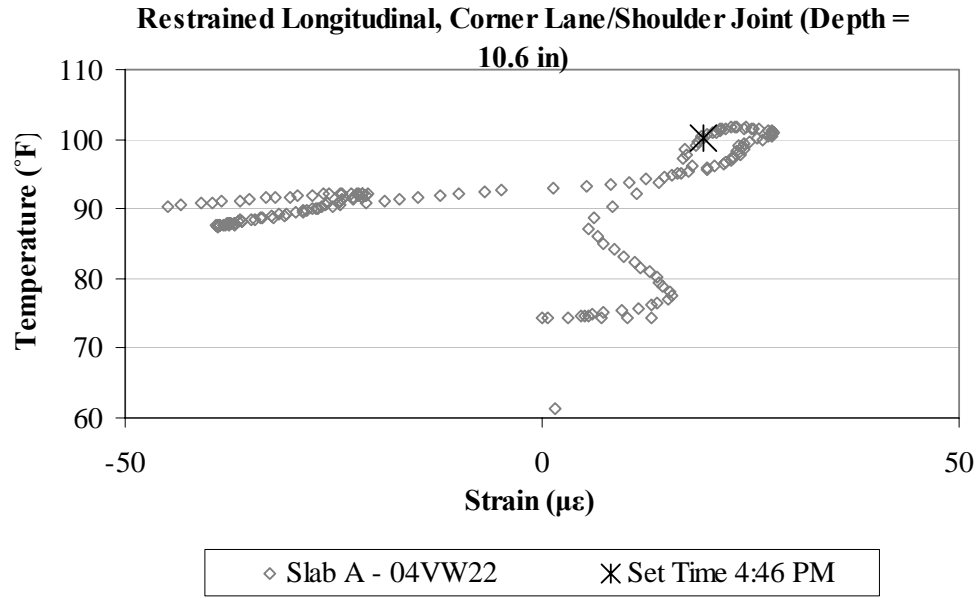


Figure B.19. Variation of strain with temperature, in the longitudinal direction, for the bottom sensor located at the corner along the lane/shoulder joint in restrained Slab A.

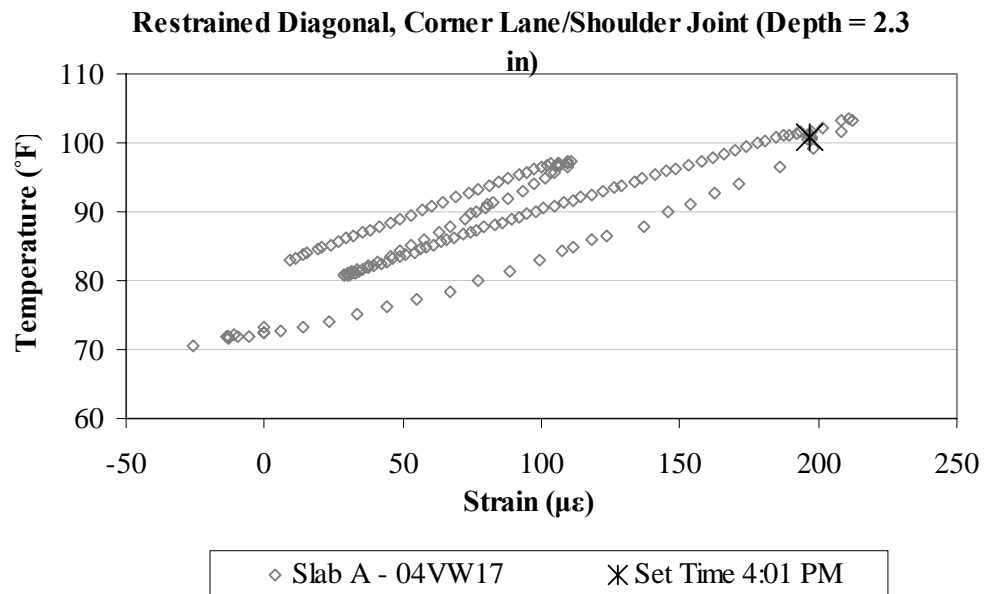


Figure B.20. Variation of strain with temperature, in the diagonal direction, for the top sensor located at the corner along the lane/shoulder joint in restrained Slab A.

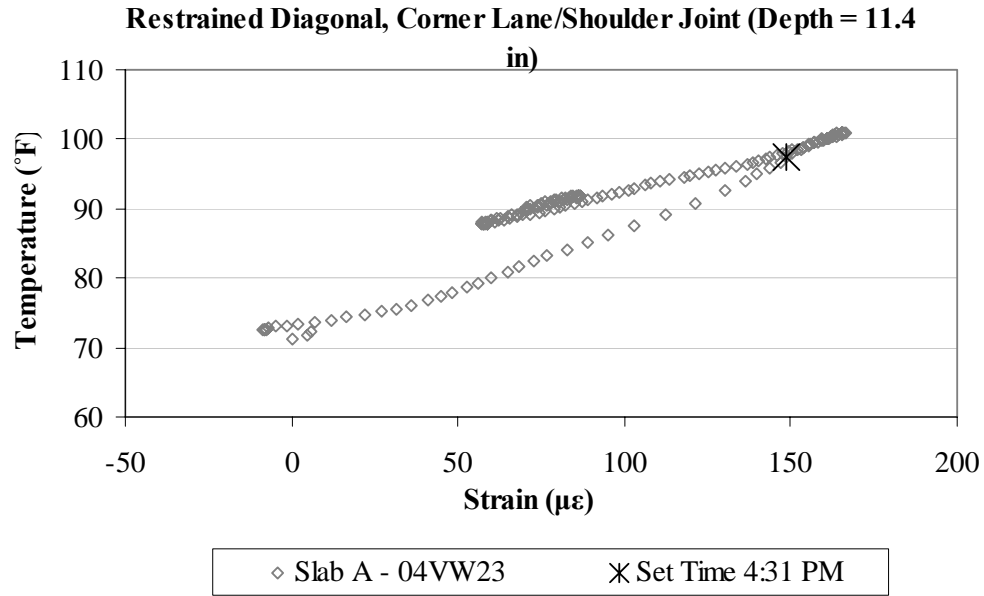


Figure B.21. Variation of strain with temperature, in the diagonal direction, for the bottom sensor located at the corner along the lane/shoulder joint in restrained Slab A.

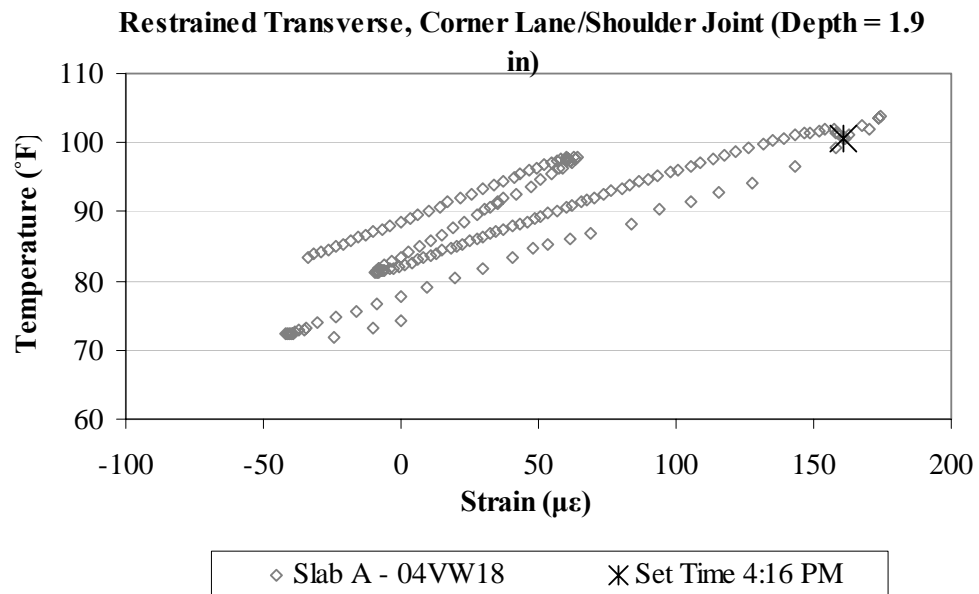


Figure B.22. Variation of strain with temperature, in the transverse direction, for the top sensor located at the corner along the lane/shoulder joint in restrained Slab A.

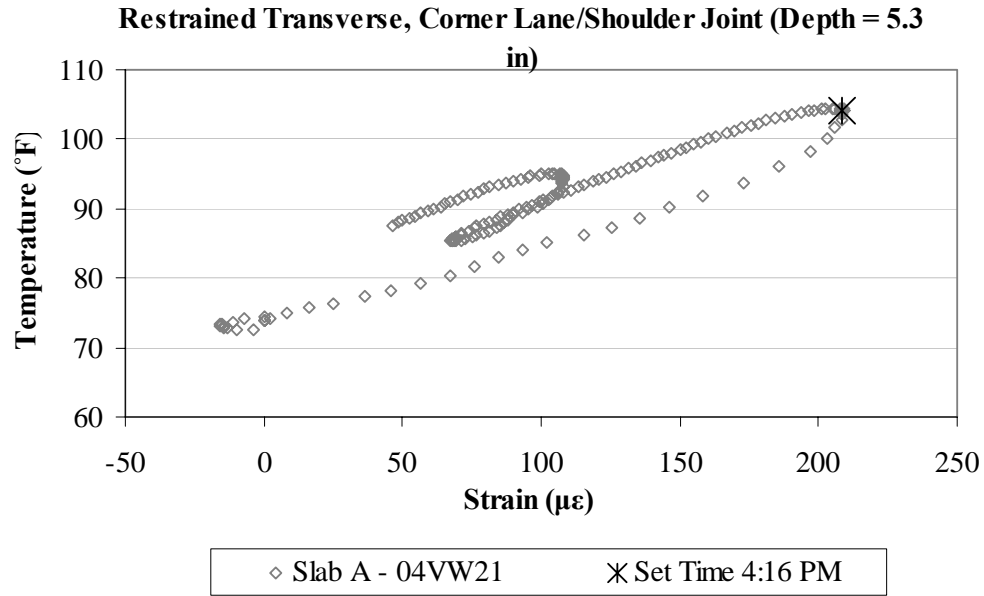


Figure B.23. Variation of strain with temperature, in the transverse direction, for the middepth sensor located at the corner along the lane/shoulder joint in restrained Slab A.

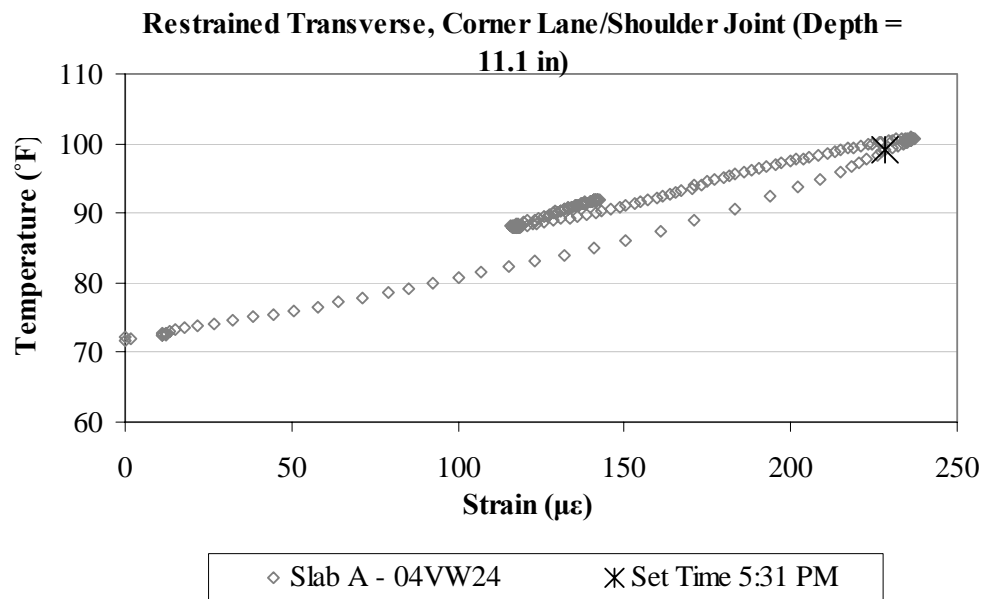


Figure B.24. Variation of strain with temperature, in the transverse direction, for the bottom sensor located at the corner along the lane/shoulder joint in restrained Slab A.

B.2 RESTRAINED SLAB B (CELL 4)

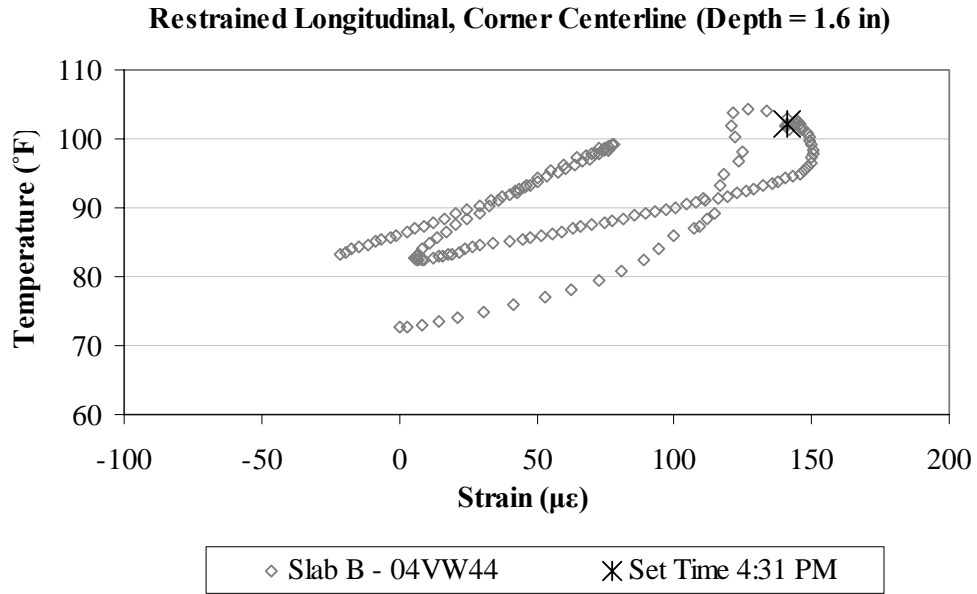


Figure B.25. Variation of strain with temperature, in the longitudinal direction, for the top sensor located at the corner along the centerline joint in restrained Slab B.

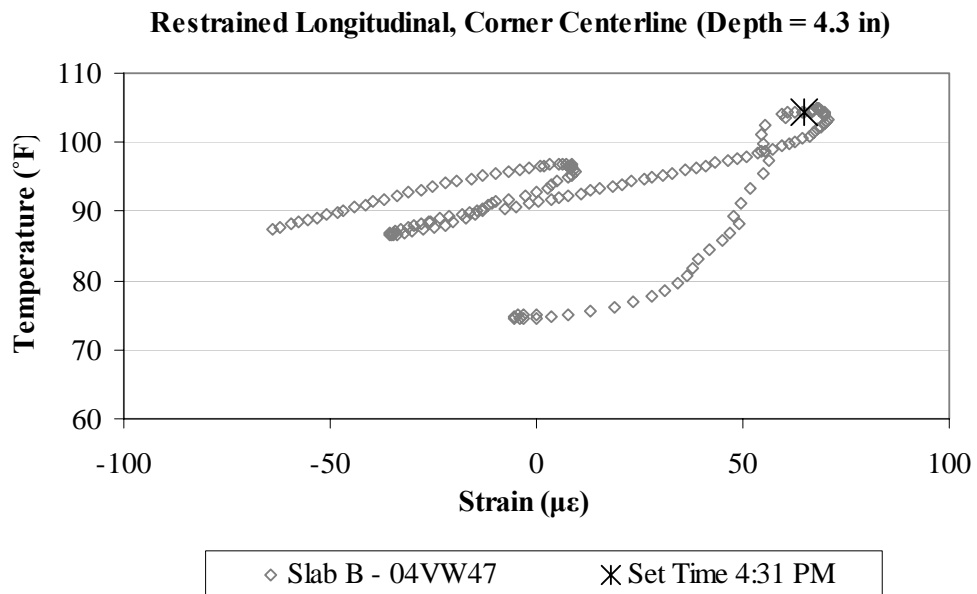


Figure B.26. Variation of strain with temperature, in the longitudinal direction, for the middepth sensor located at the corner along the centerline joint in restrained Slab B.

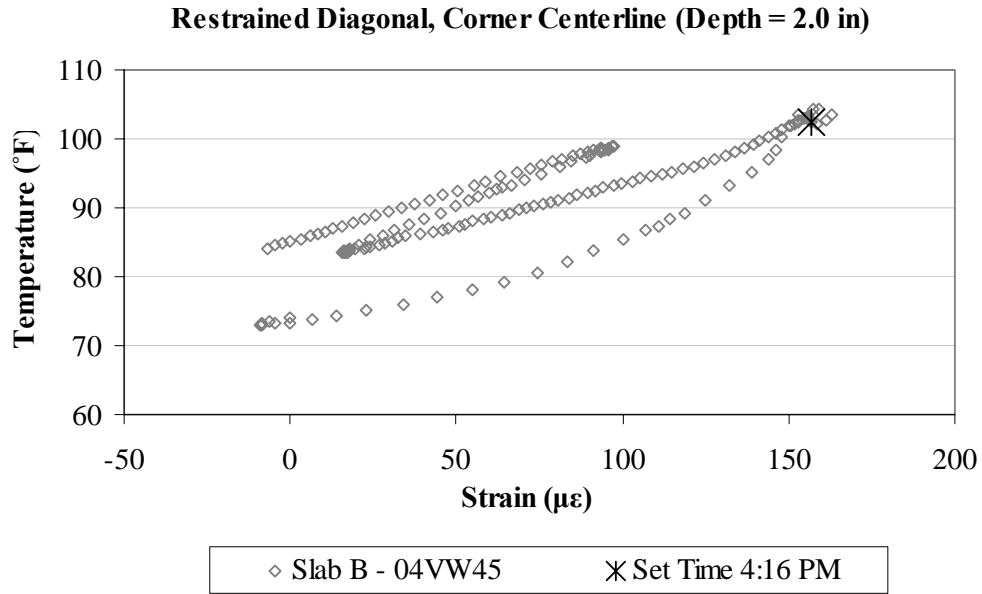


Figure B.27. Variation of strain with temperature, in the diagonal direction, for the top sensor located at the corner along the centerline joint in restrained Slab B.

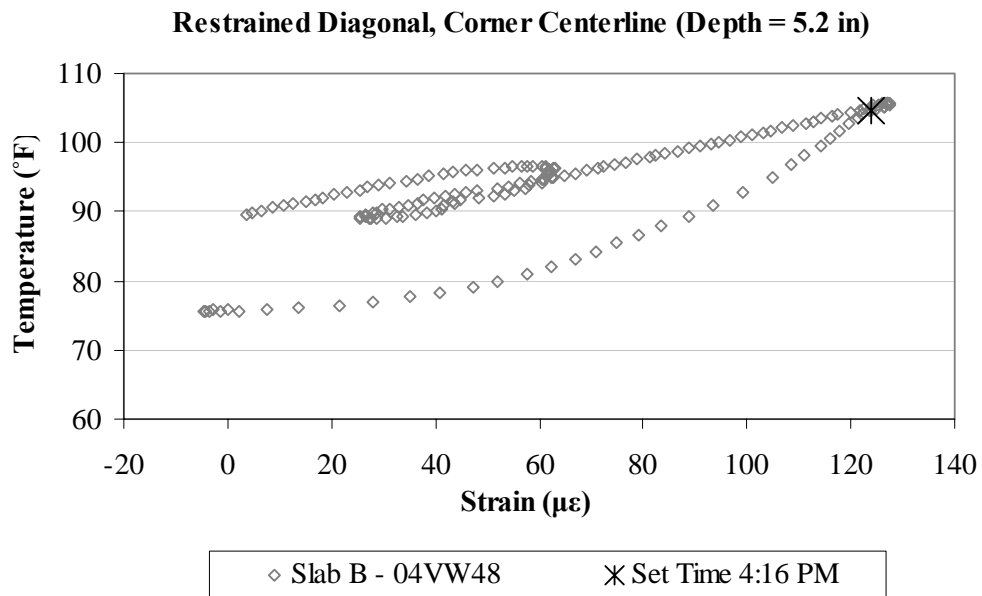


Figure B.28. Variation of strain with temperature, in the diagonal direction, for the middepth sensor located at the corner along the centerline joint in restrained Slab B.

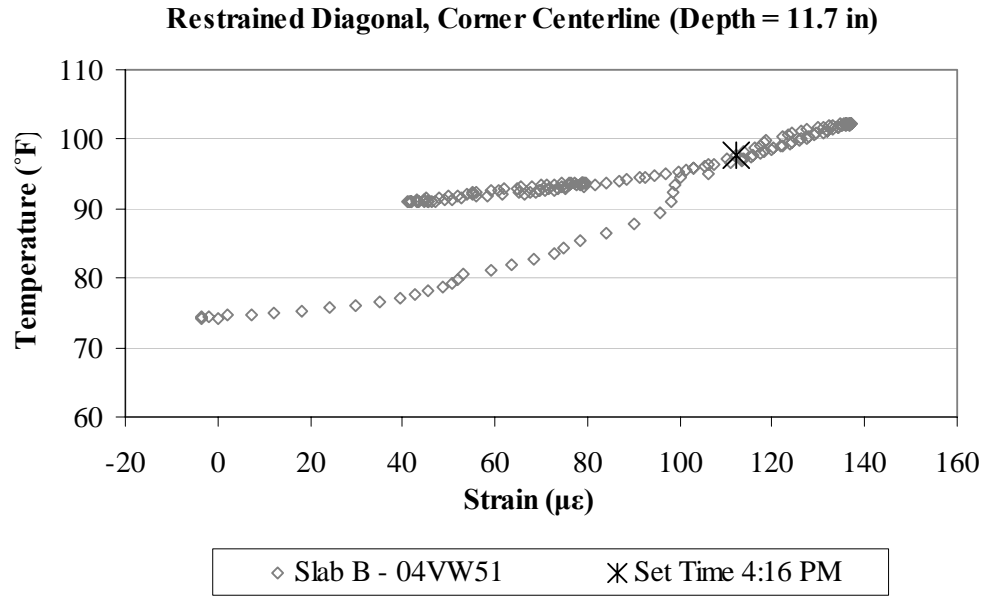


Figure B.29. Variation of strain with temperature, in the diagonal direction, for the bottom sensor located at the corner along the centerline joint in restrained Slab B.

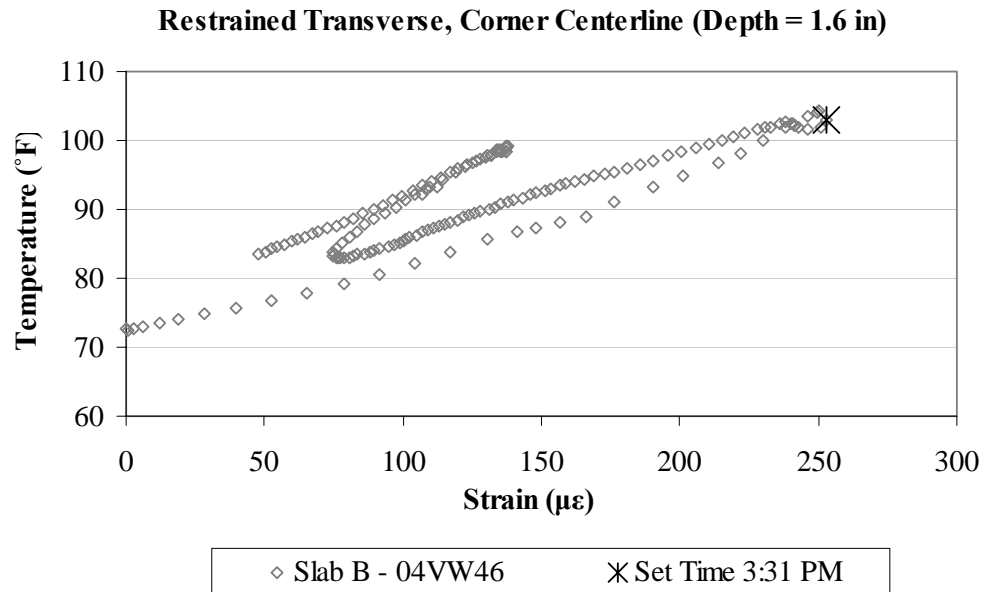


Figure B.30. Variation of strain with temperature, in the transverse direction, for the top sensor located at the corner along the centerline joint in restrained Slab B.

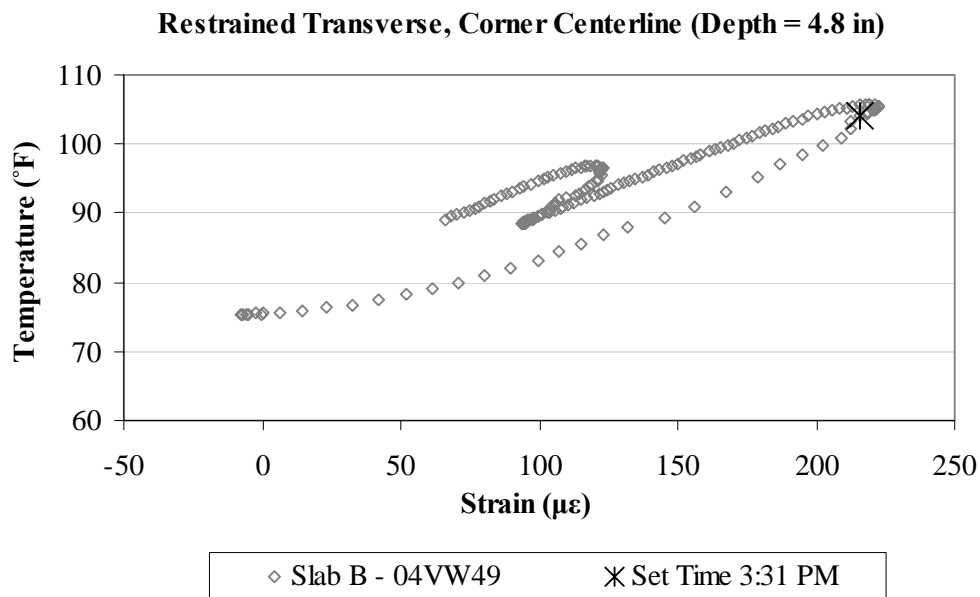


Figure B.31. Variation of strain with temperature, in the transverse direction, for the middepth sensor located at the corner along the centerline joint in restrained Slab B.

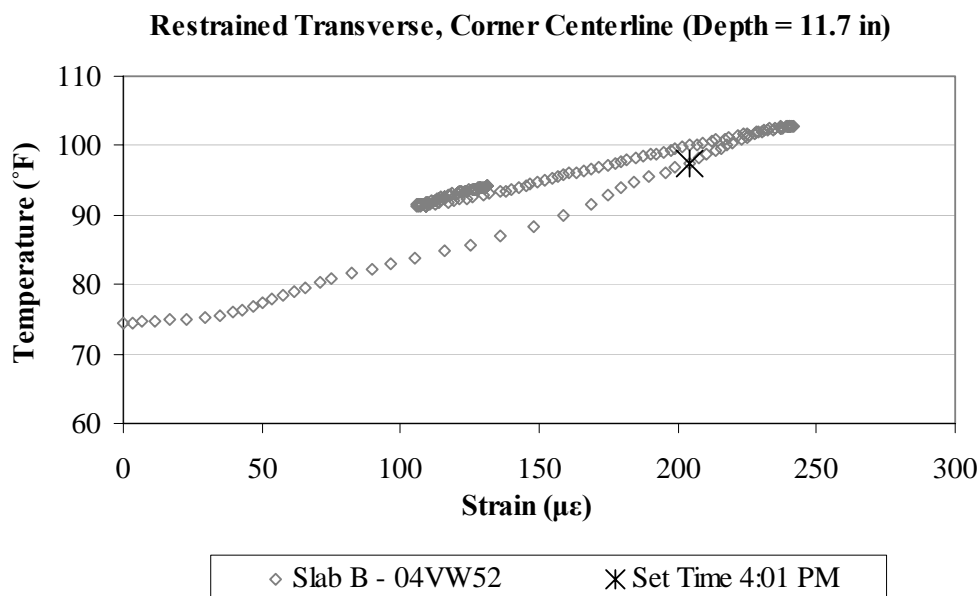


Figure B.32. Variation of strain with temperature, in the transverse direction, for the bottom sensor located at the corner along the centerline joint in restrained Slab B.

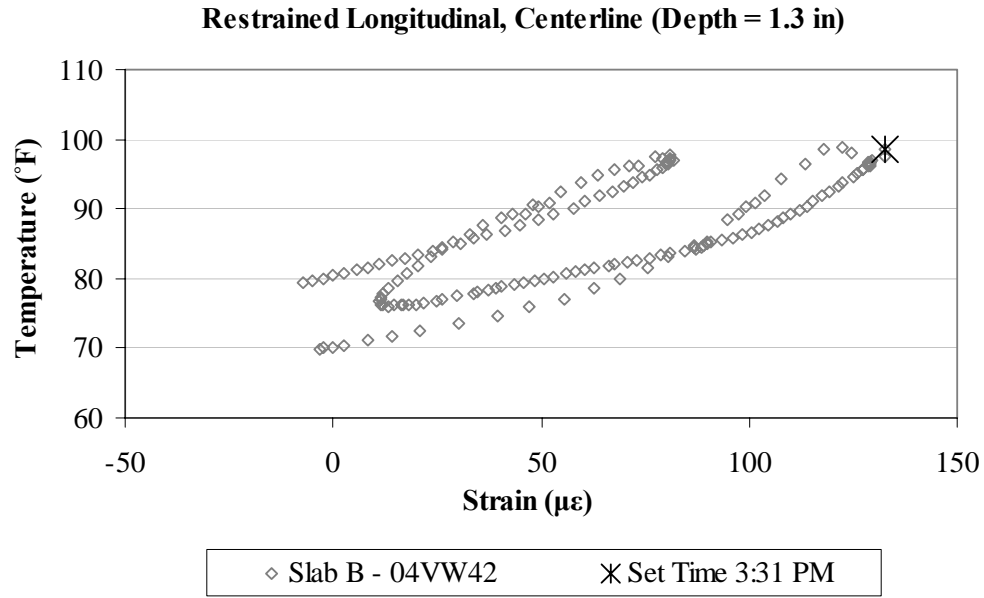


Figure B.33. Variation of strain with temperature, in the longitudinal direction, for the top sensor located along the centerline joint in restrained Slab B.

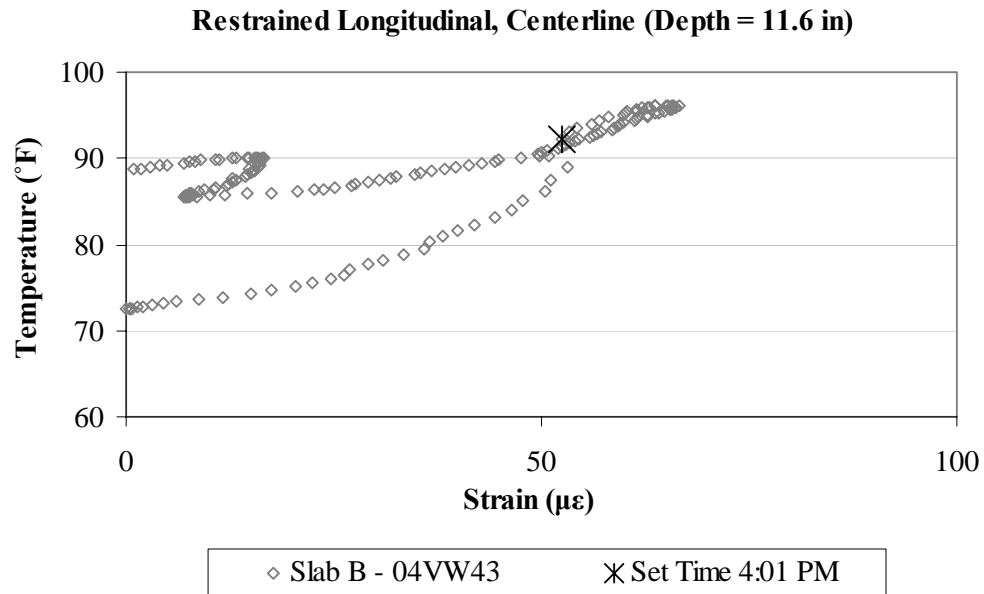


Figure B.34. Variation of strain with temperature, in the longitudinal direction, for the bottom sensor located along the centerline joint in restrained Slab B.

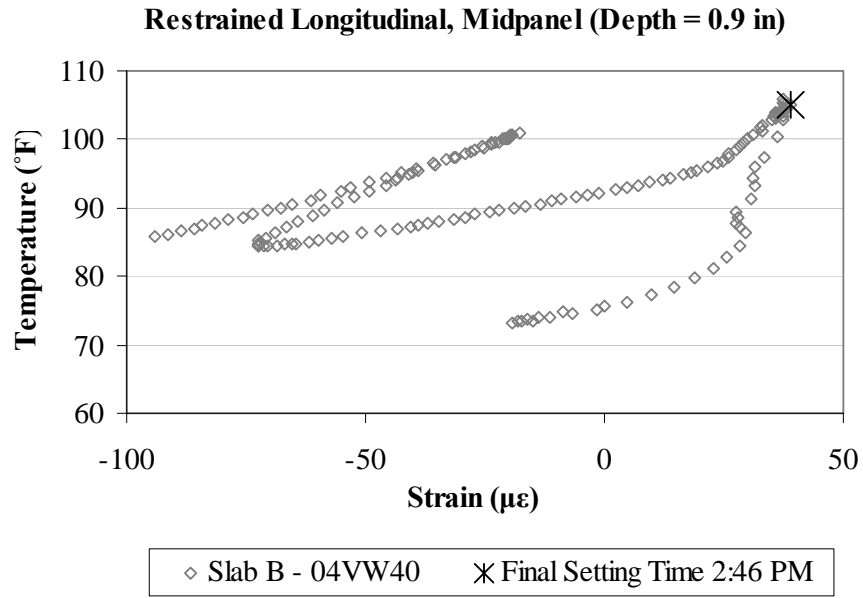


Figure B.35. Variation of strain with temperature, in the longitudinal direction, for the top sensor located at midpanel in restrained Slab B.

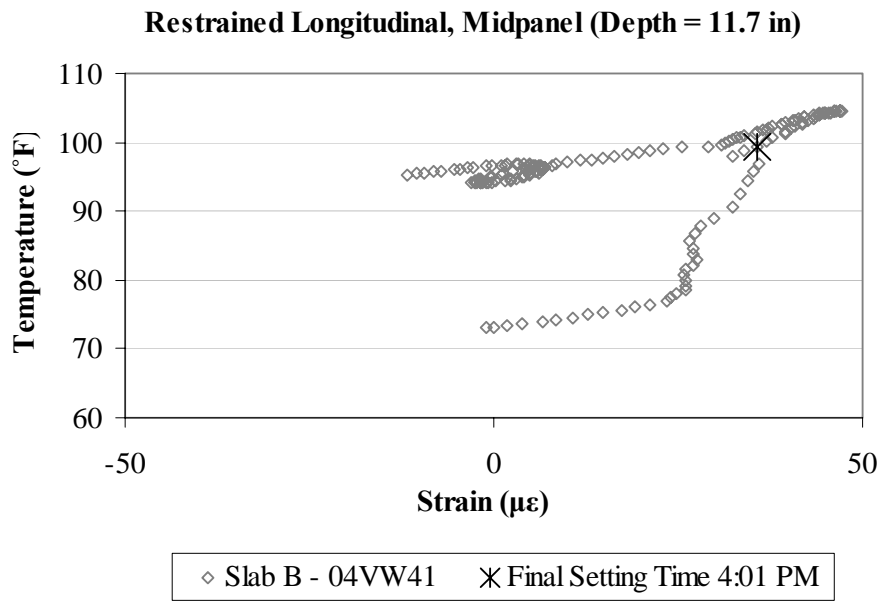


Figure B.36. Variation of strain with temperature, in the longitudinal direction, for the bottom sensor located at midpanel in restrained Slab B.

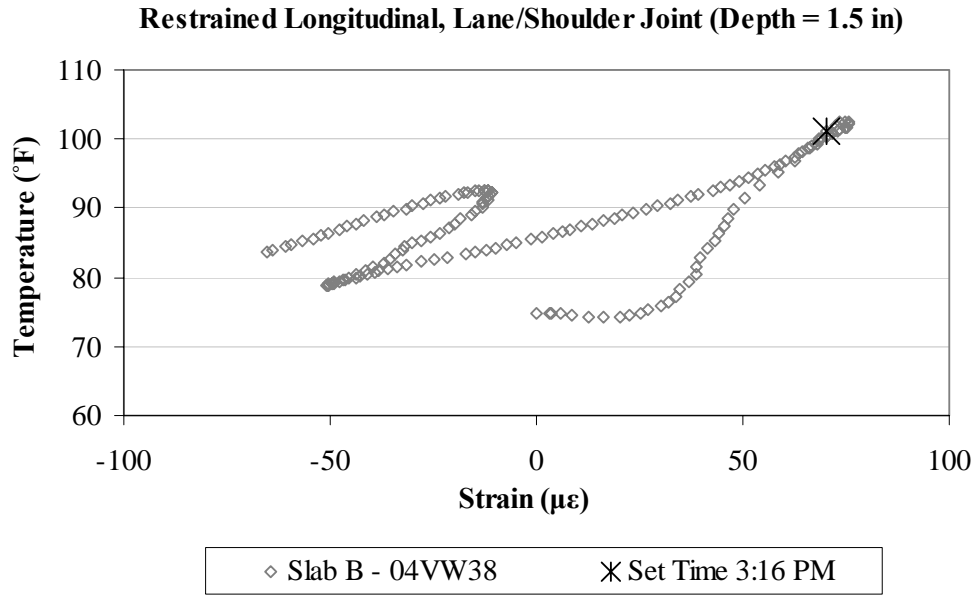


Figure B.37. Variation of strain with temperature, in the longitudinal direction, for the top sensor located along the lane/shoulder joint in restrained Slab B.

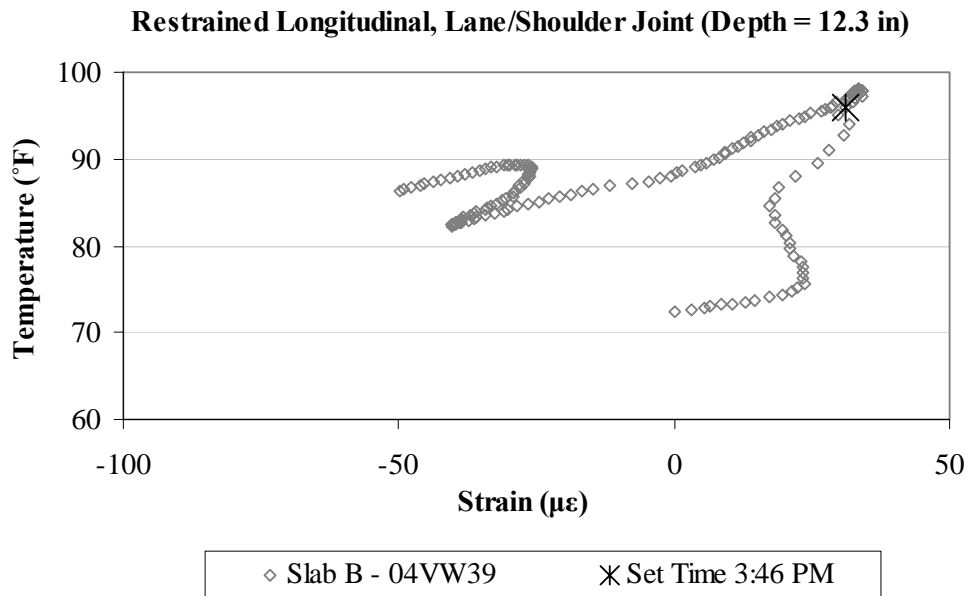


Figure B.38. Variation of strain with temperature, in the longitudinal direction, for the bottom sensor located along the lane/shoulder joint in restrained Slab B.

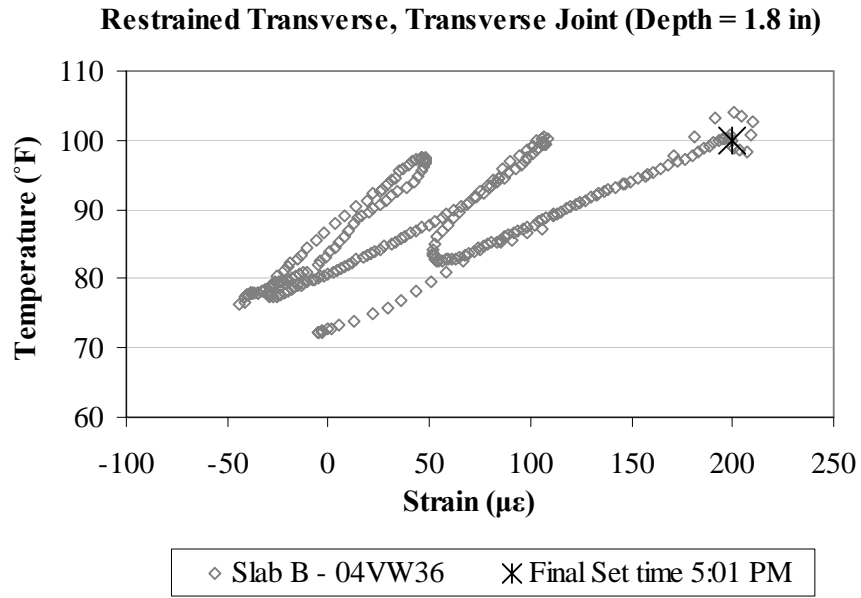


Figure B.39. Variation of strain with temperature, in the transverse direction, for the top sensor located along the transverse joint in restrained Slab B.

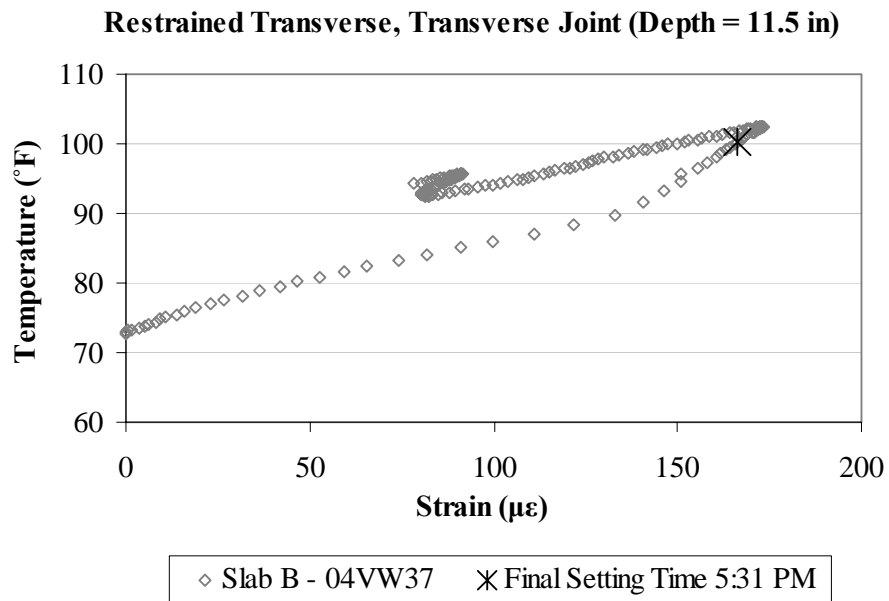


Figure B.40. Variation of strain with temperature, in the transverse direction, for the bottom sensor located along the transverse joint in restrained Slab B.

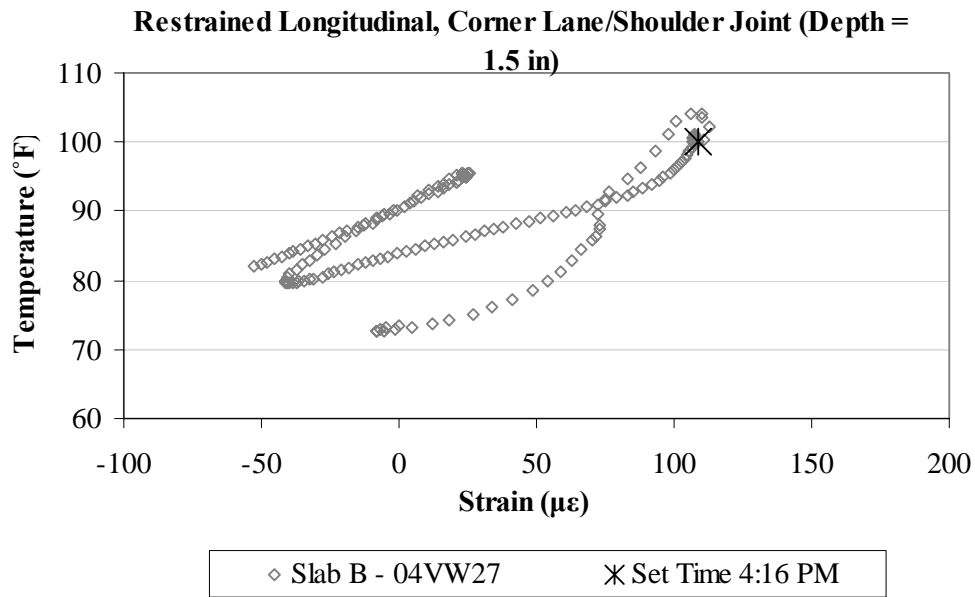


Figure B.41. Variation of strain with temperature, in the longitudinal direction, for the top sensor located at the corner along the lane/shoulder joint in restrained Slab B.

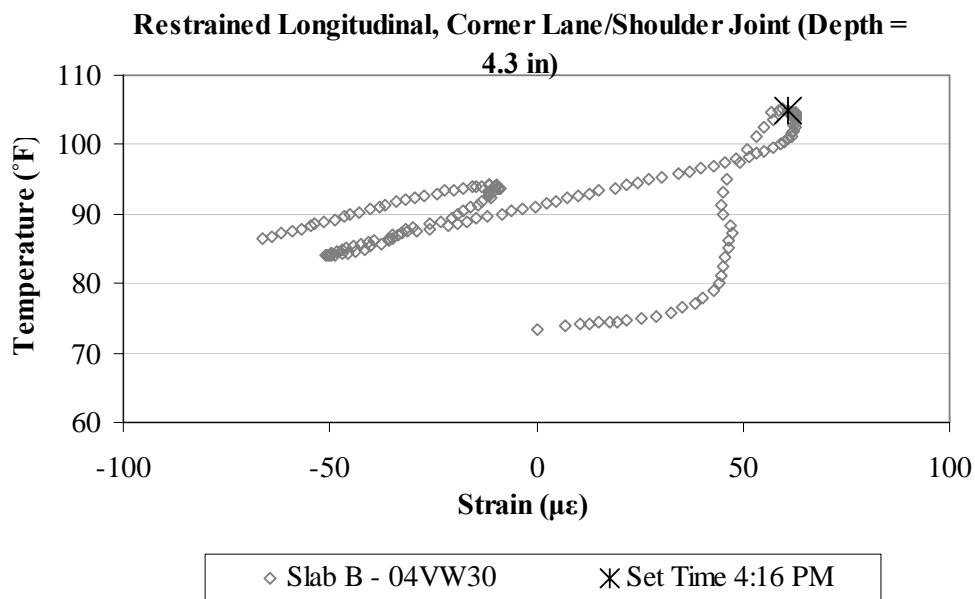


Figure B.42. Variation of strain with temperature, in the longitudinal direction, for the middepth sensor located at the corner along the lane/shoulder joint in restrained Slab B.

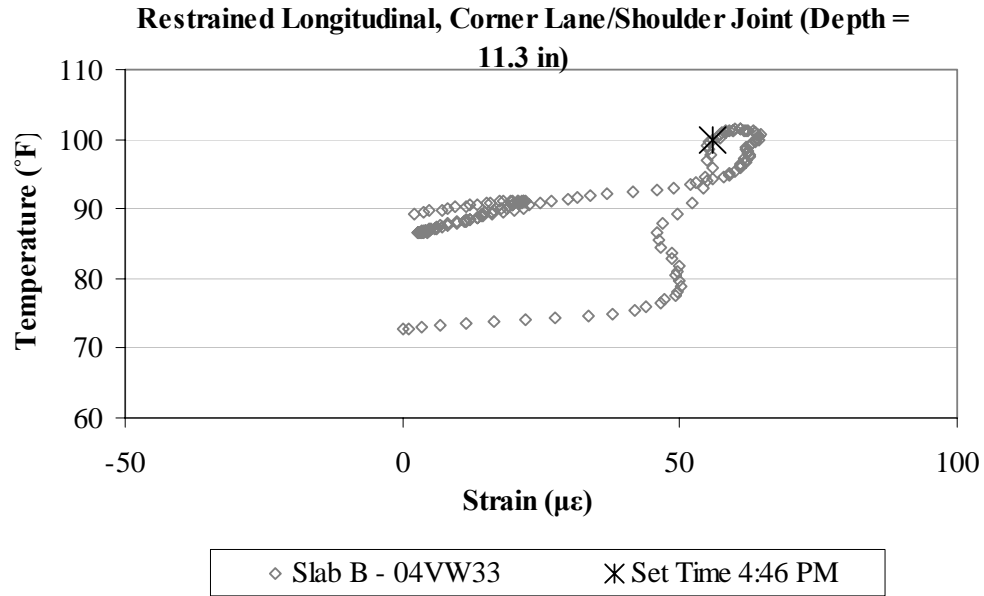


Figure B.43. Variation of strain with temperature, in the longitudinal direction, for the bottom sensor located at the corner along the lane/shoulder joint in restrained Slab B.

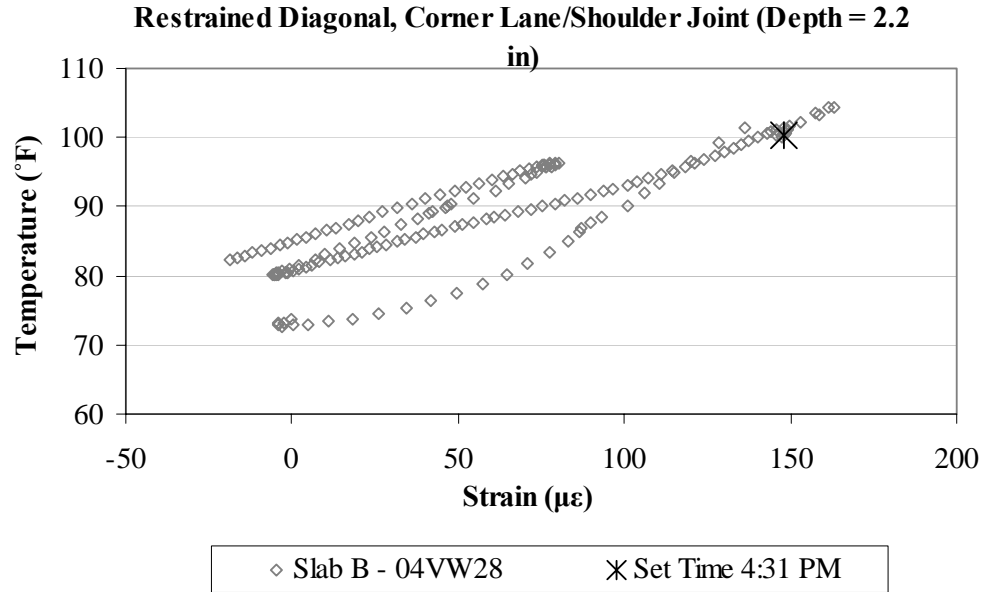


Figure B.44. Variation of strain with temperature, in the diagonal direction, for the top sensor located at the corner along the lane/shoulder joint in restrained Slab B.

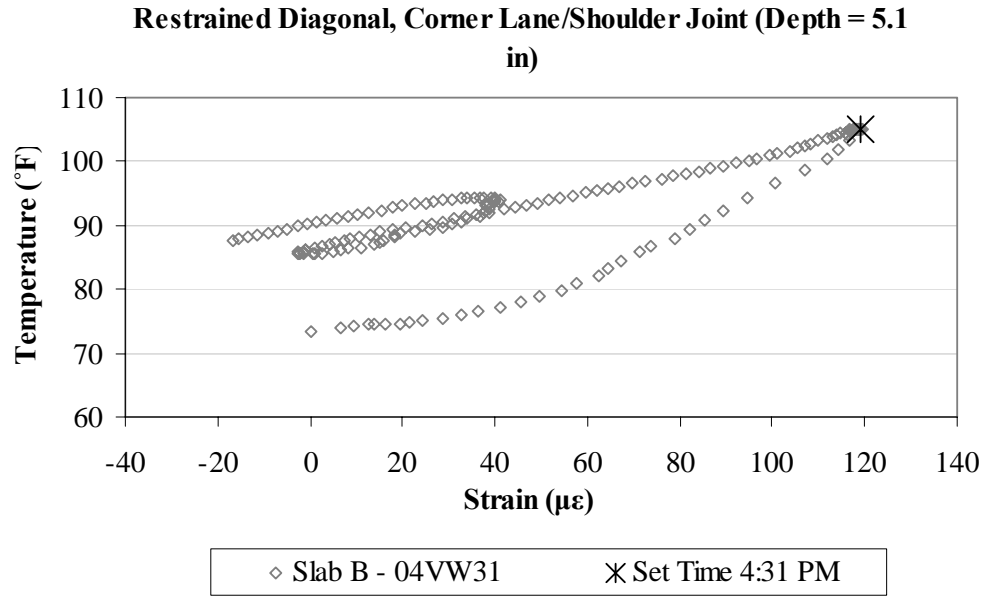


Figure B.45. Variation of strain with temperature, in the diagonal direction, for the middepth sensor located at the corner along the lane/shoulder joint in restrained Slab B.

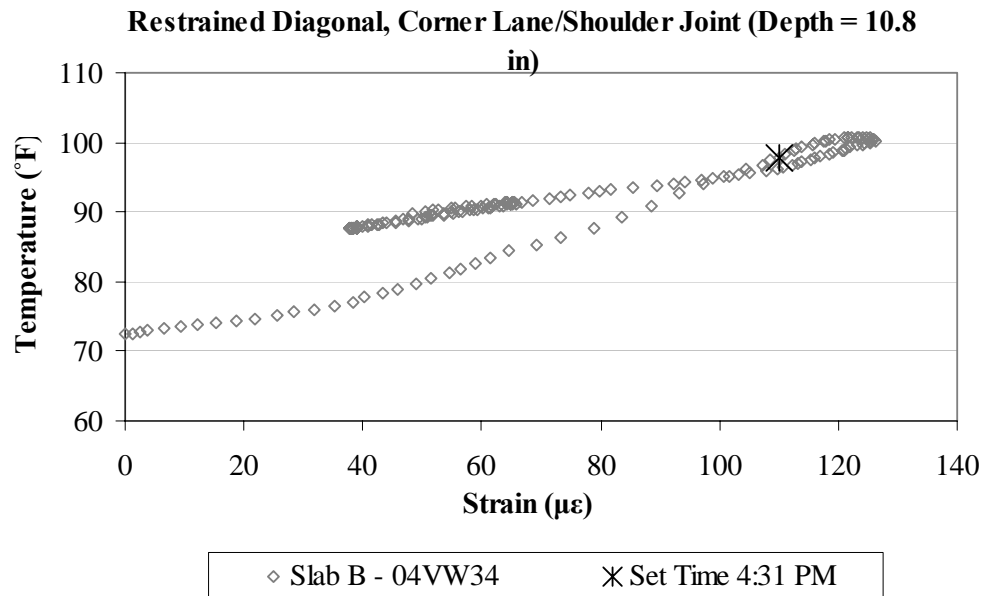


Figure B.46. Variation of strain with temperature, in the diagonal direction, for the bottom sensor located at the corner along the lane/shoulder joint in restrained Slab B.

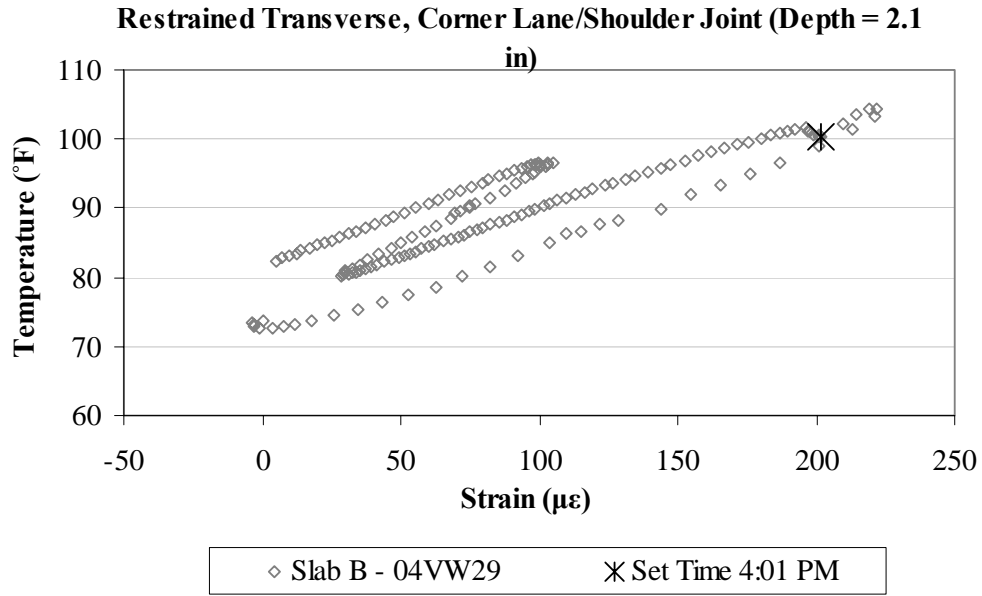


Figure B.47. Variation of strain with temperature, in the transverse direction, for the top sensor located at the corner along the lane/shoulder joint in restrained Slab B.

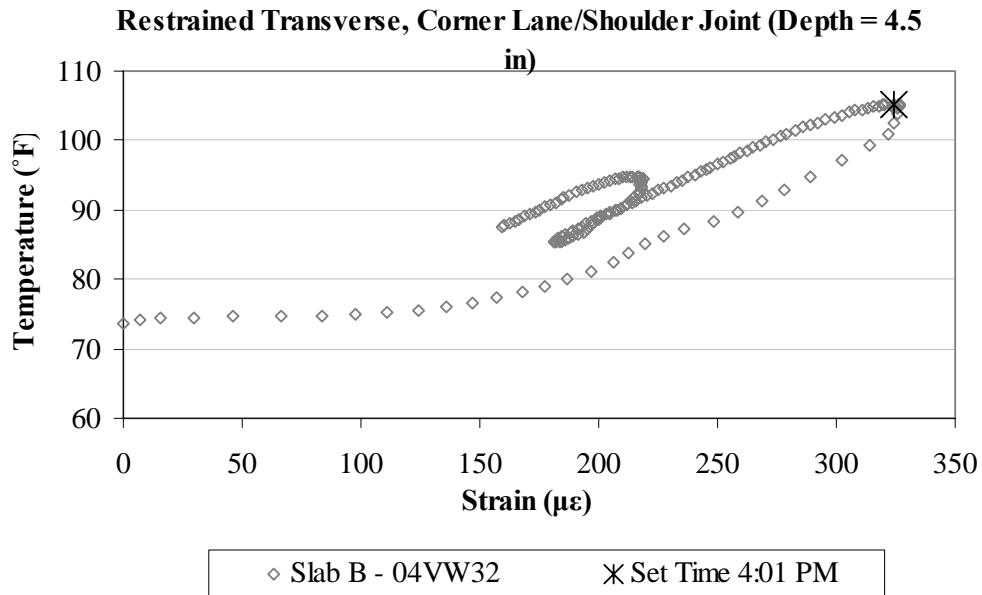


Figure B.48. Variation of strain with temperature, in the transverse direction, for the middepth sensor located at the corner along the lane/shoulder joint in restrained Slab B.

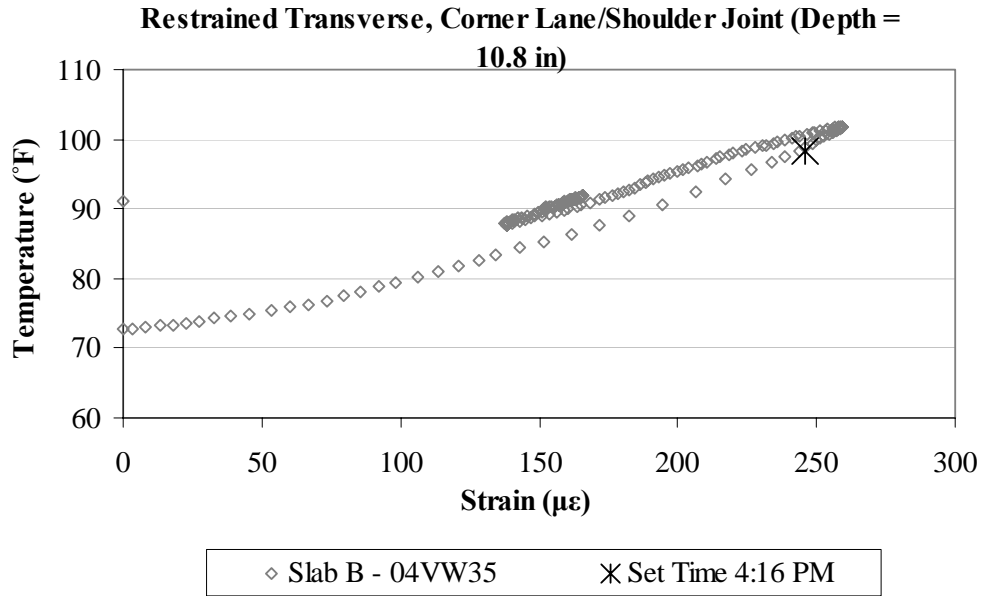


Figure B.49. Variation of strain with temperature, in the transverse direction, for the bottom sensor located at the corner along the lane/shoulder joint in restrained Slab B.

B.3 RESTRAINED SLAB C (CELL 4)

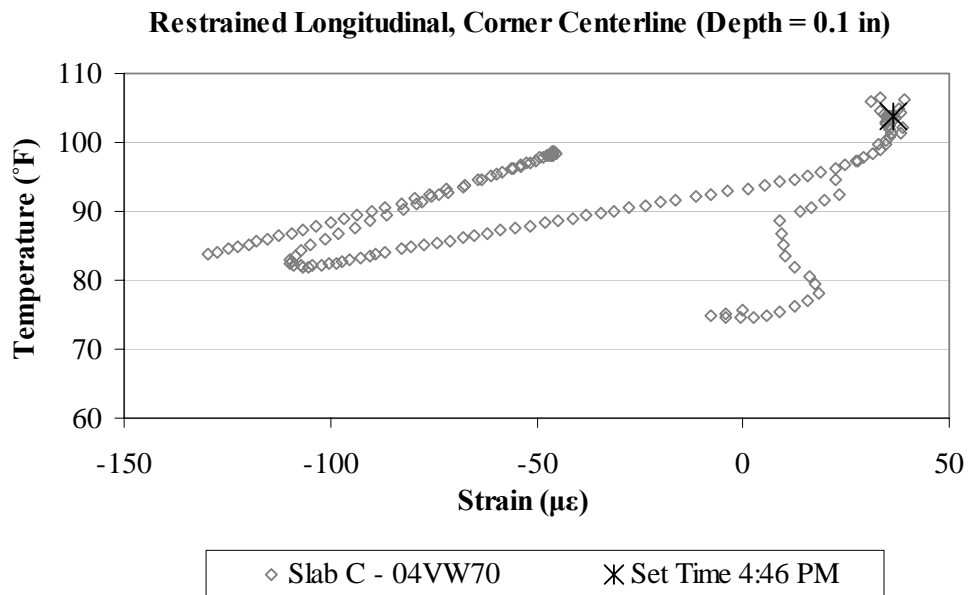


Figure B.50. Variation of strain with temperature, in the longitudinal direction, for the top sensor located at the corner along the centerline joint in restrained Slab C.

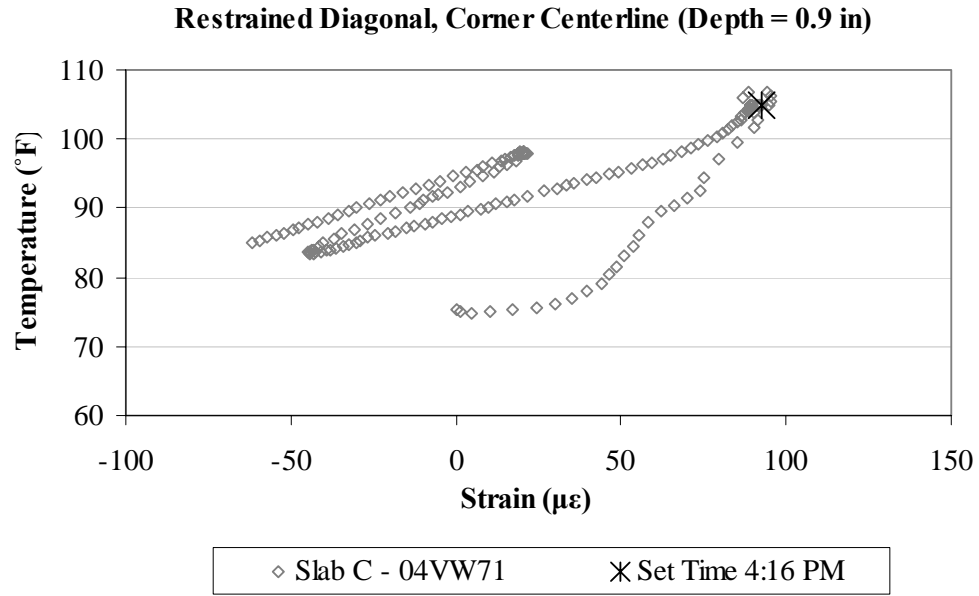


Figure B.51. Variation of strain with temperature, in the diagonal direction, for the top sensor located at the corner along the centerline joint in restrained Slab C.

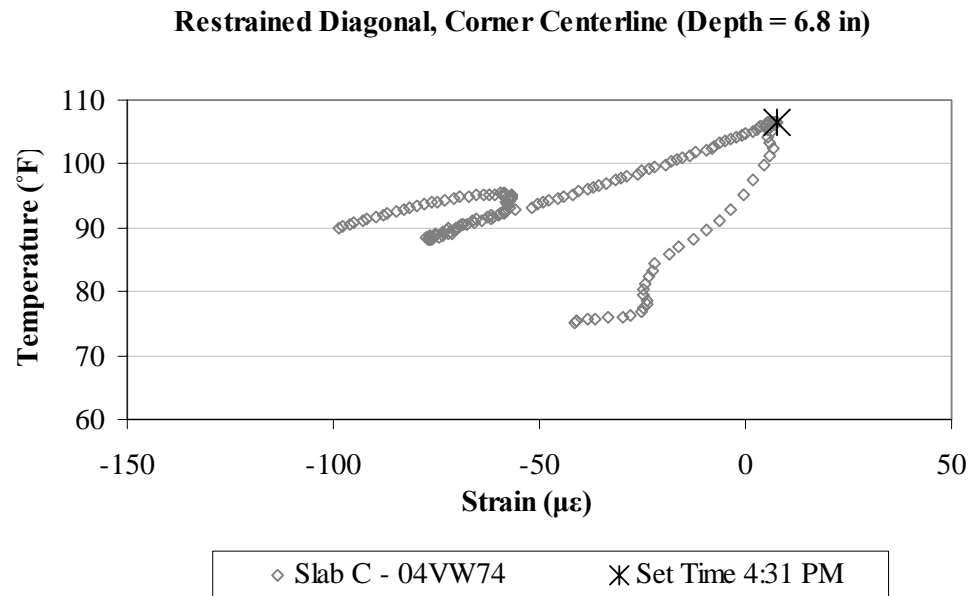


Figure B.52. Variation of strain with temperature, in the diagonal direction, for the middepth sensor located at the corner along the centerline joint in restrained Slab C.

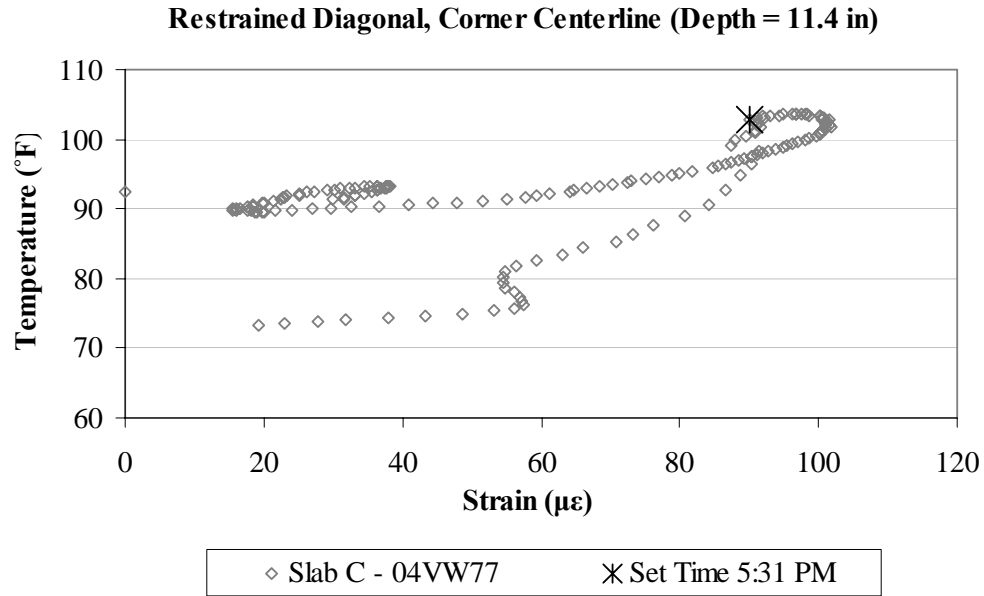


Figure B.53. Variation of strain with temperature, in the diagonal direction, for the bottom sensor located at the corner along the centerline joint in restrained Slab C.

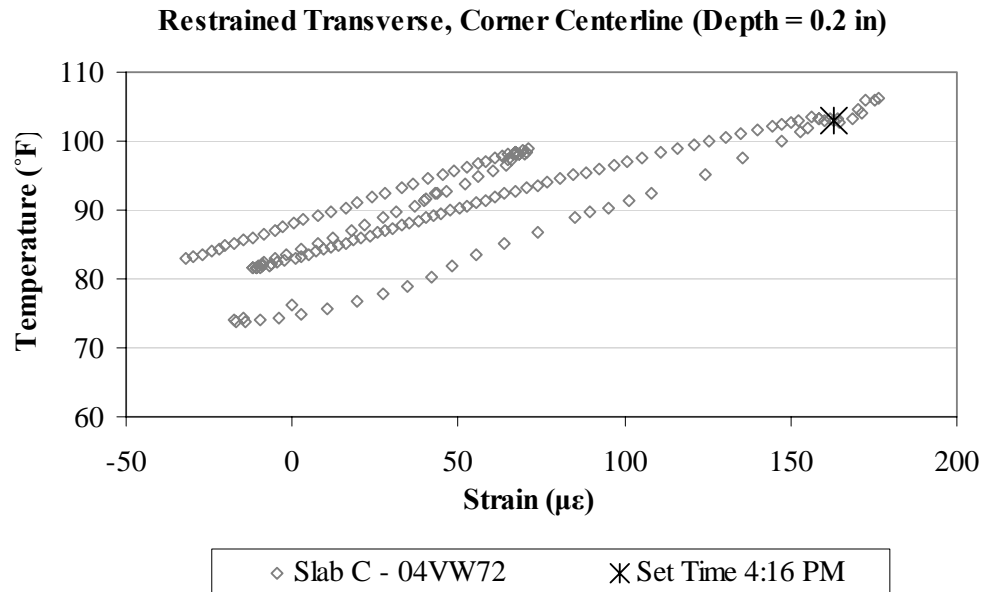


Figure B.54. Variation of strain with temperature, in the transverse direction, for the top sensor located at the corner along the centerline joint in restrained Slab C.

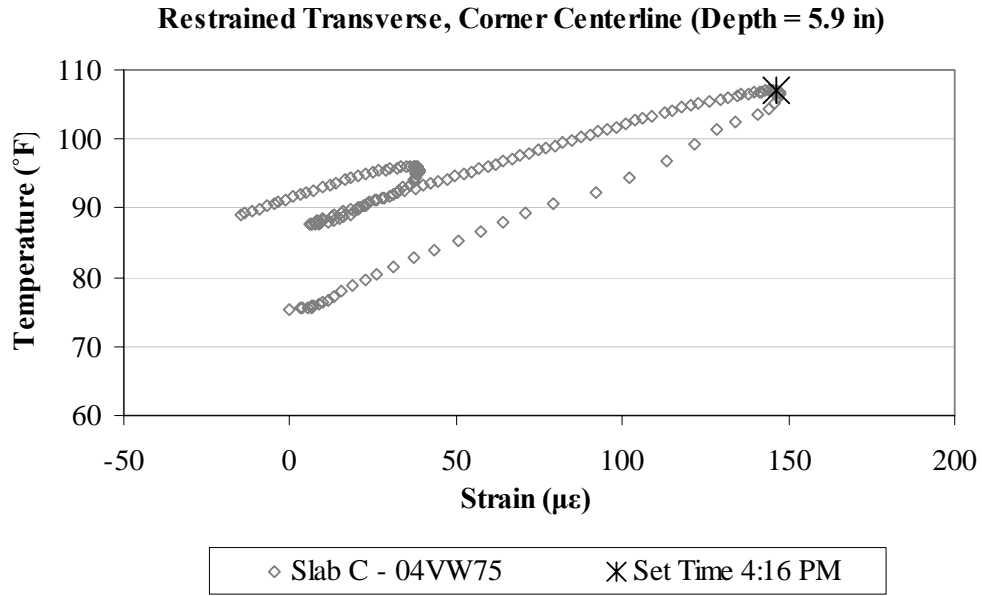


Figure B.55. Variation of strain with temperature, in the transverse direction, for the middepth sensor located at the corner along the centerline joint in restrained Slab C.

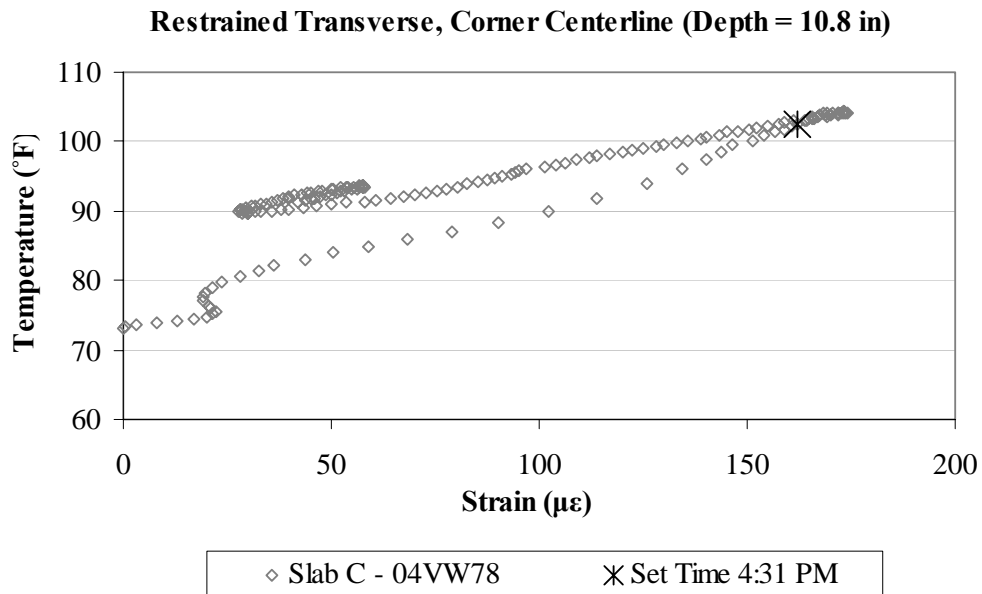


Figure B.56. Variation of strain with temperature, in the transverse direction, for the bottom sensor located at the corner along the centerline joint in restrained Slab C.

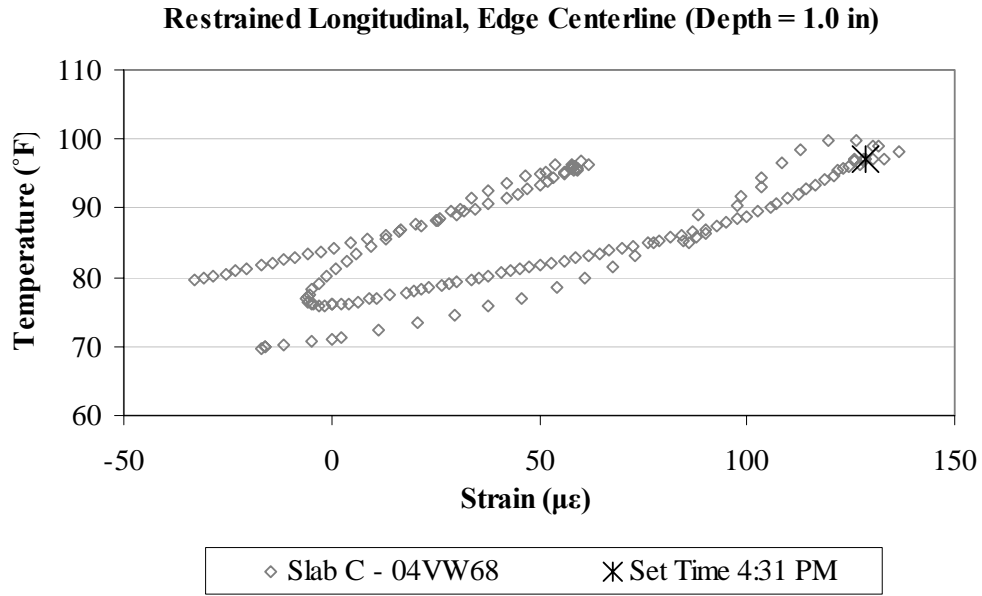


Figure B.57. Variation of strain with temperature, in the longitudinal direction, for the top sensor located along the centerline joint in restrained Slab C.

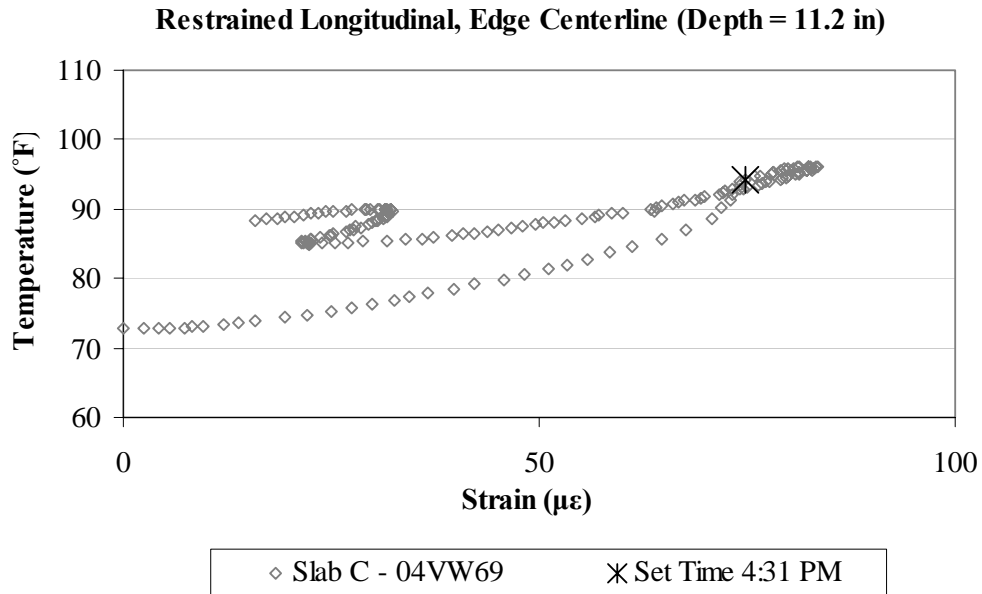


Figure B.58. Variation of strain with temperature, in the longitudinal direction, for the bottom sensor located along the centerline joint in restrained Slab C.

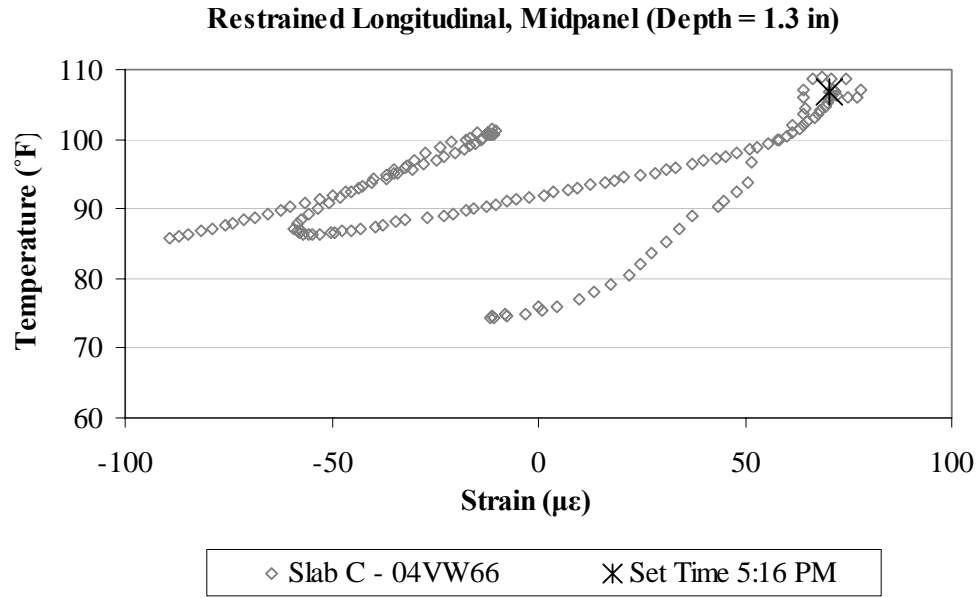


Figure B.59. Variation of strain with temperature, in the longitudinal direction, for the top sensor located at midpanel in restrained Slab C.

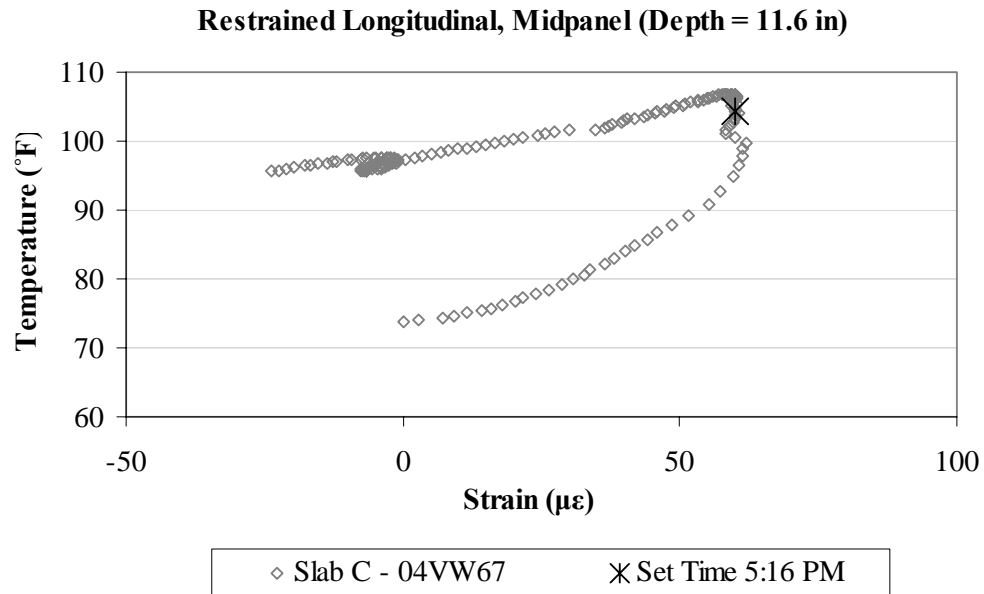


Figure B.60. Variation of strain with temperature, in the longitudinal direction, for the bottom sensor located at midpanel in restrained Slab C.

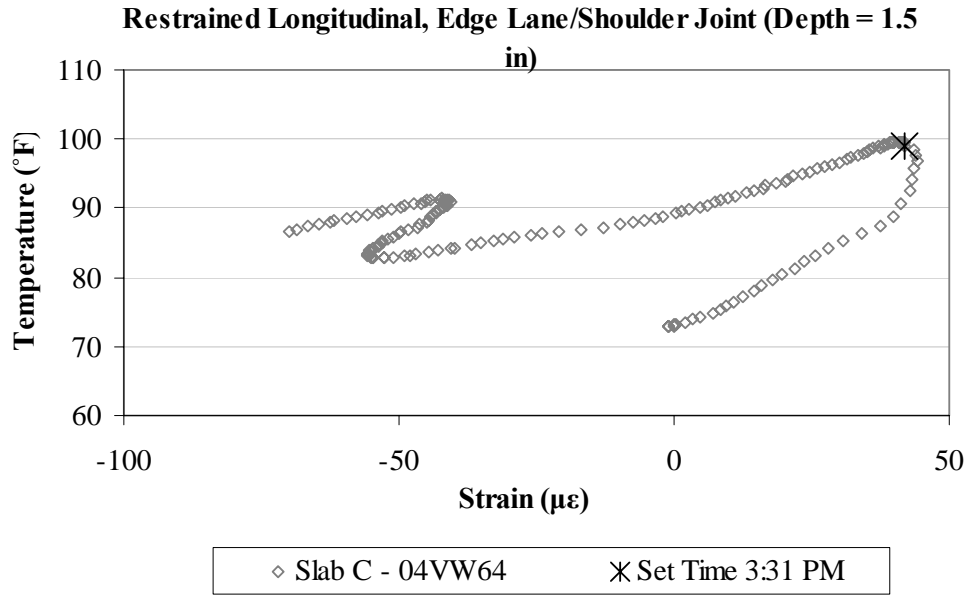


Figure B.61. Variation of strain with temperature, in the longitudinal direction, for the top sensor located along the lane/shoulder joint in restrained Slab C.

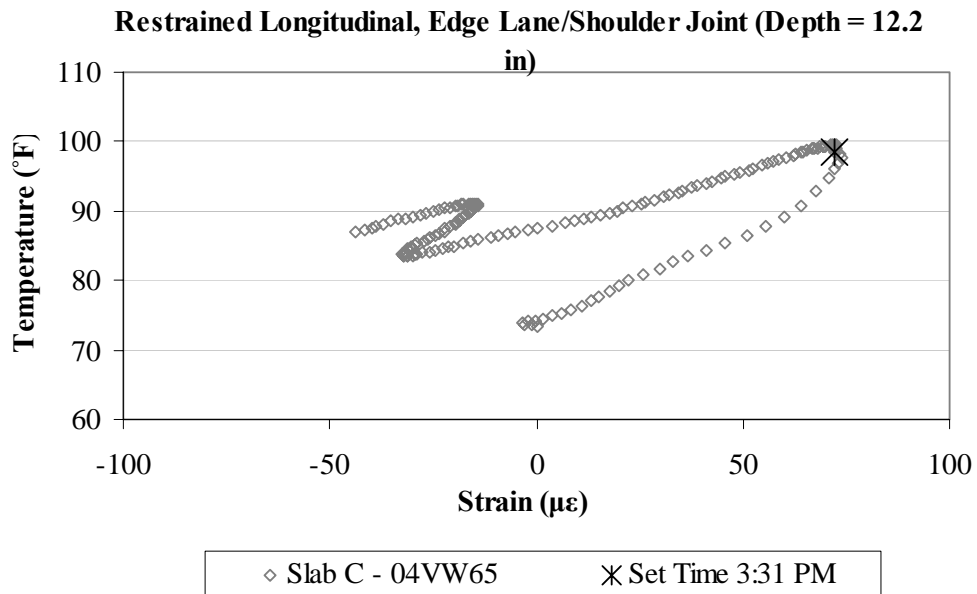


Figure B.62. Variation of strain with temperature, in the longitudinal direction, for the bottom sensor located along the lane/shoulder joint in restrained Slab C.

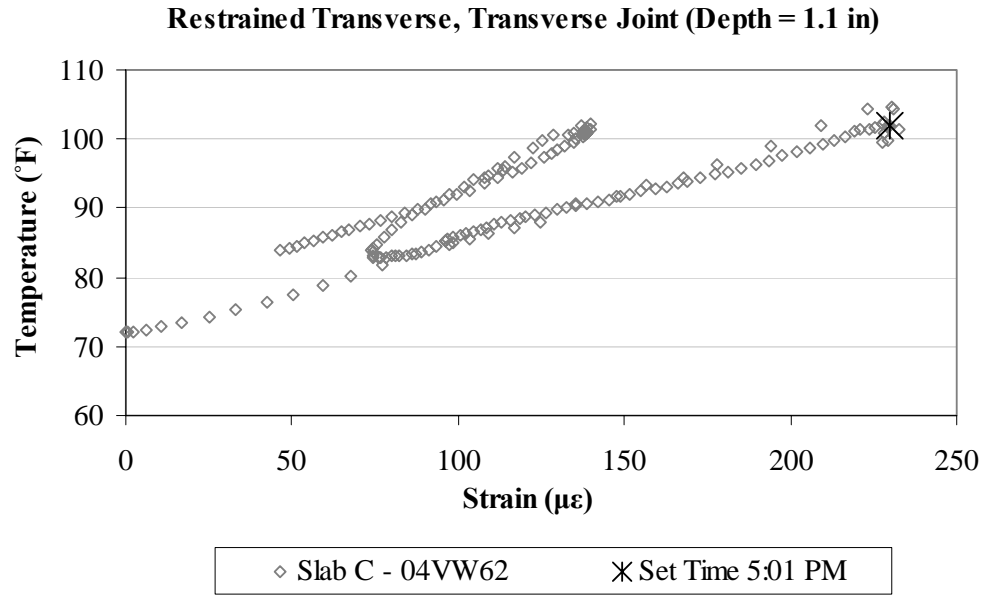


Figure B.63. Variation of strain with temperature, in the transverse direction, for the top sensor located along the transverse joint in restrained Slab C.

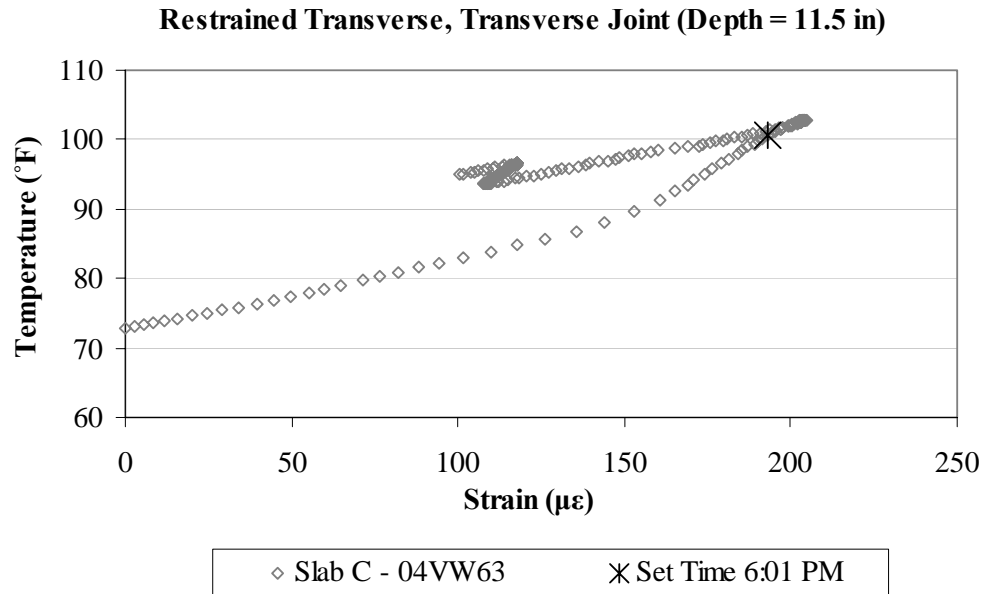


Figure B.64. Variation of strain with temperature, in the transverse direction, for the bottom sensor located along the transverse joint in restrained Slab C.

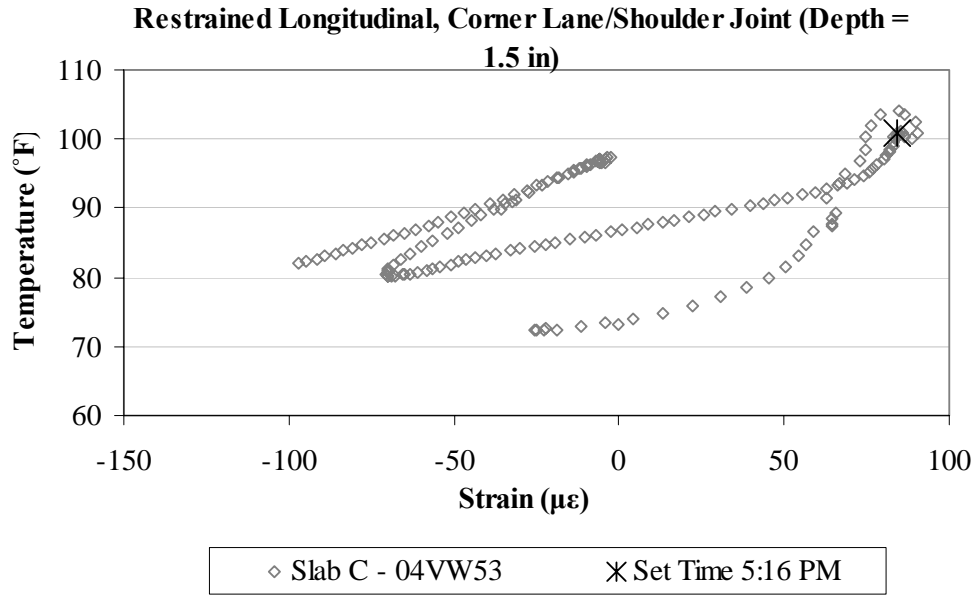


Figure B.65. Variation of strain with temperature, in the longitudinal direction, for the top sensor located at the corner along the lane/shoulder joint in restrained Slab C.

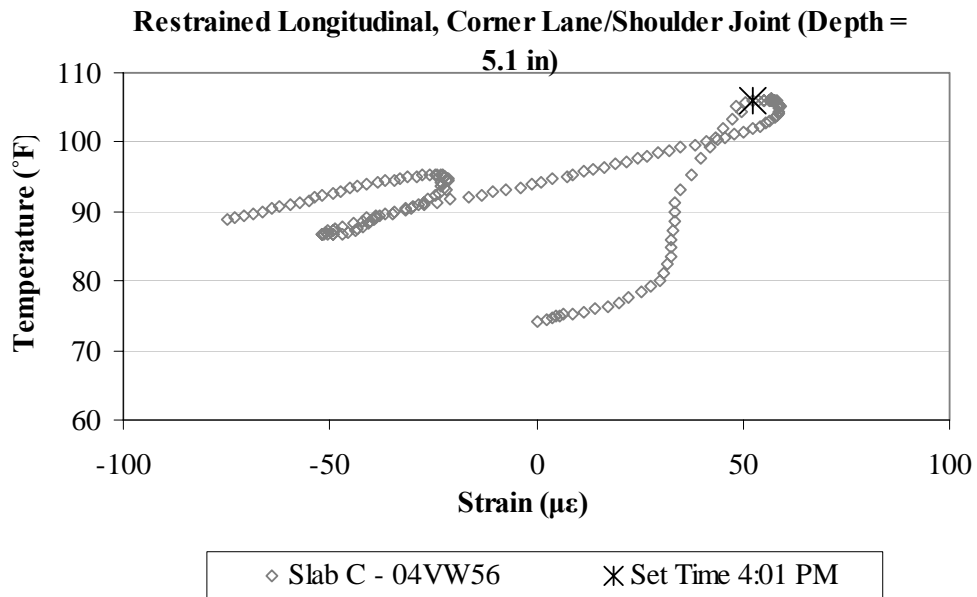


Figure B.66. Variation of strain with temperature, in the longitudinal direction, for the middepth sensor located at the corner along the lane/shoulder joint in restrained Slab C.

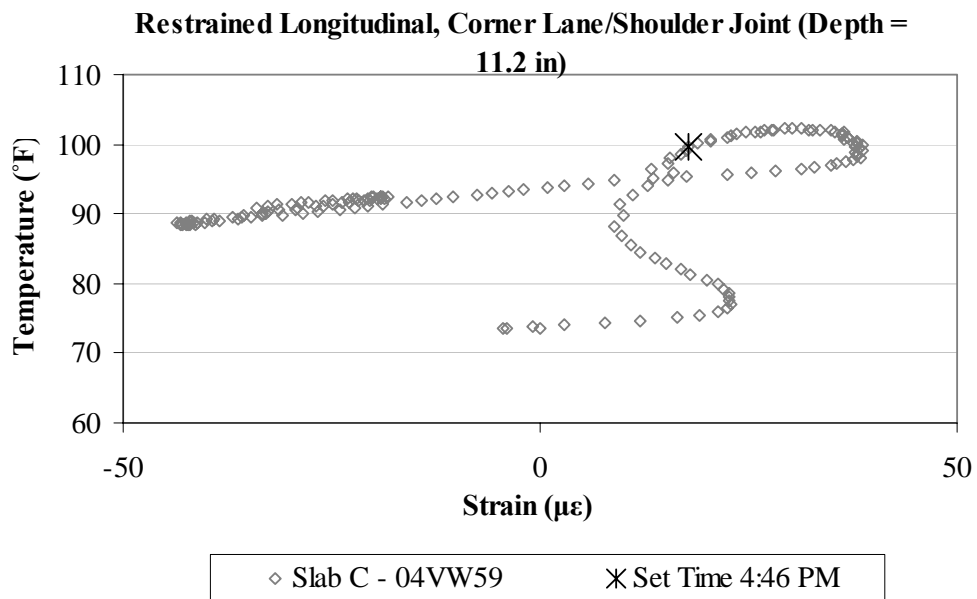


Figure B.67. Variation of strain with temperature, in the longitudinal direction, for the bottom sensor located at the corner along the lane/shoulder joint in restrained Slab C.

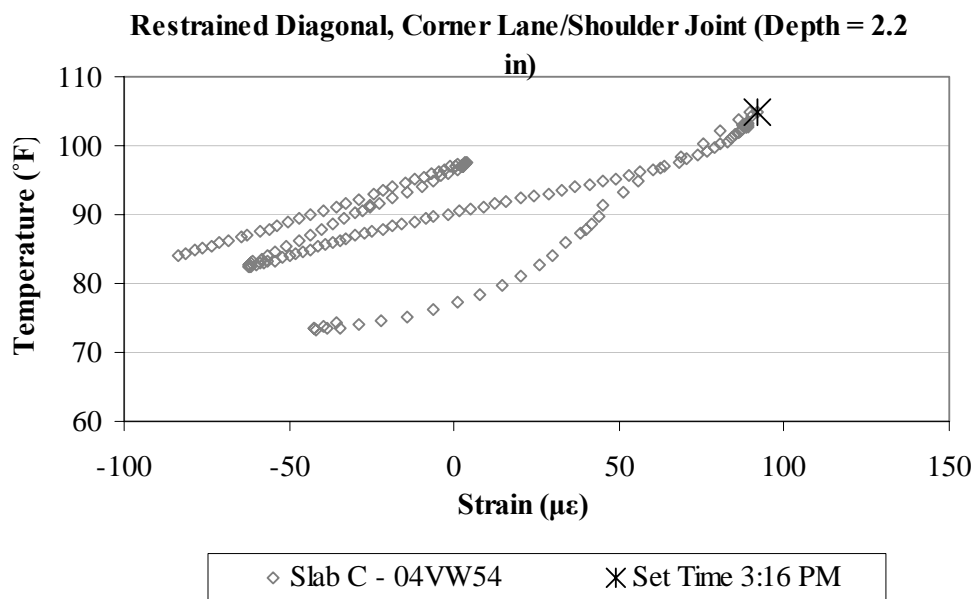


Figure B.68. Variation of strain with temperature, in the diagonal direction, for the top sensor located at the corner along the lane/shoulder joint in restrained Slab C.

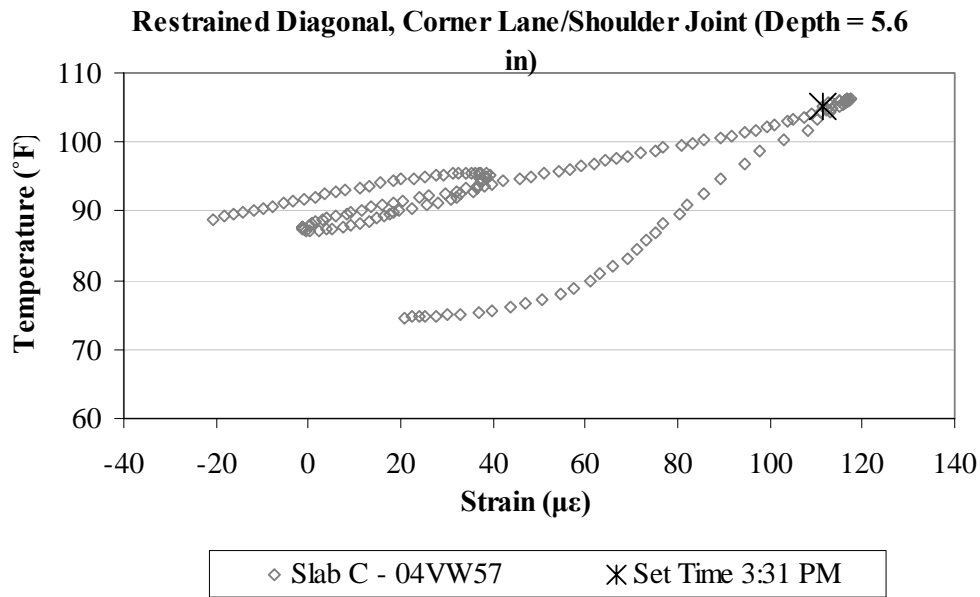


Figure B.69. Variation of strain with temperature, in the diagonal direction, for the middepth sensor located at the corner along the lane/shoulder joint in restrained Slab C.

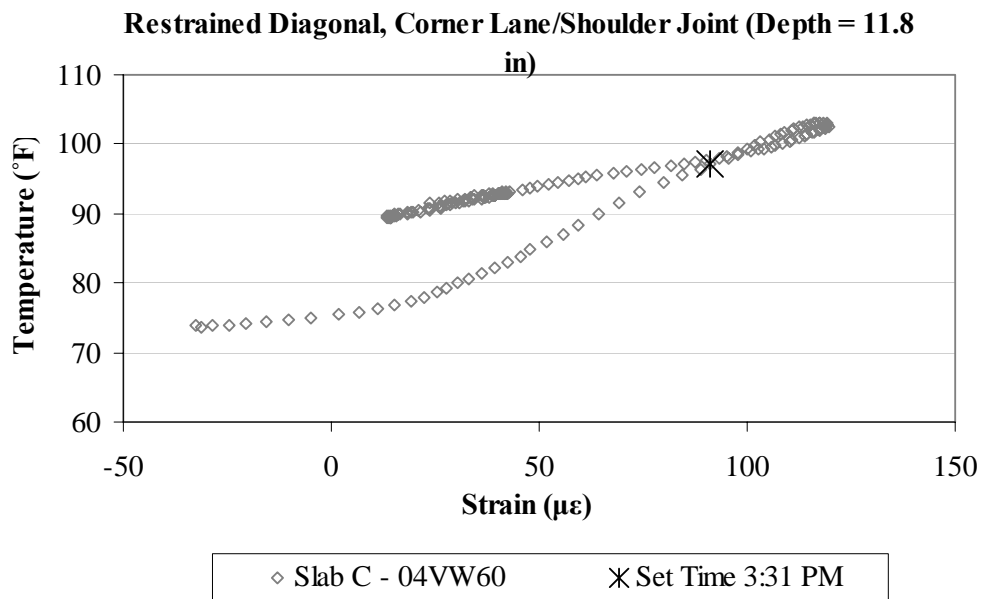


Figure B.70. Variation of strain with temperature, in the diagonal direction, for the bottom sensor located at the corner along the lane/shoulder joint in restrained Slab C.

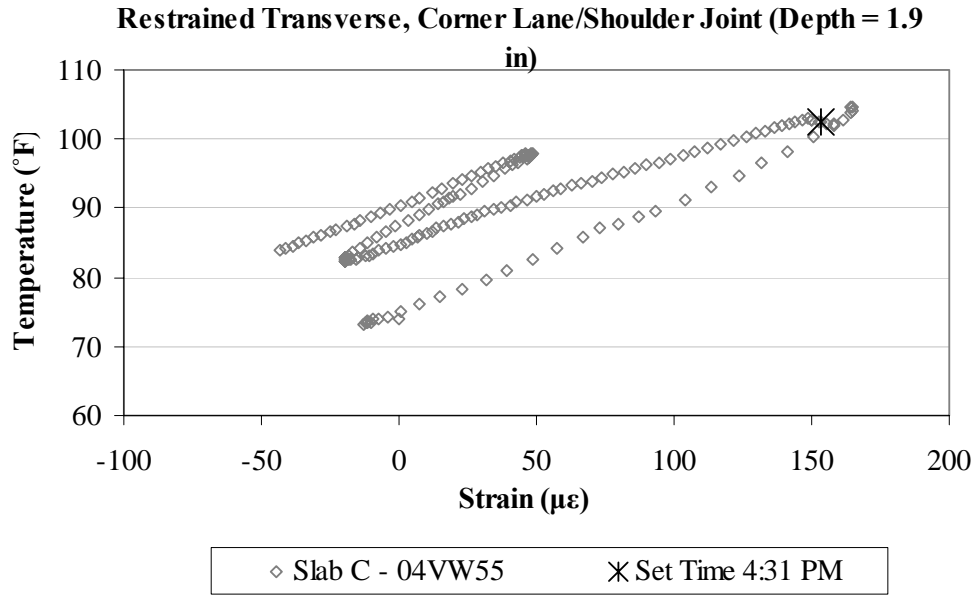


Figure B.71. Variation of strain with temperature, in the transverse direction, for the top sensor located at the corner along the lane/shoulder joint in restrained Slab C.

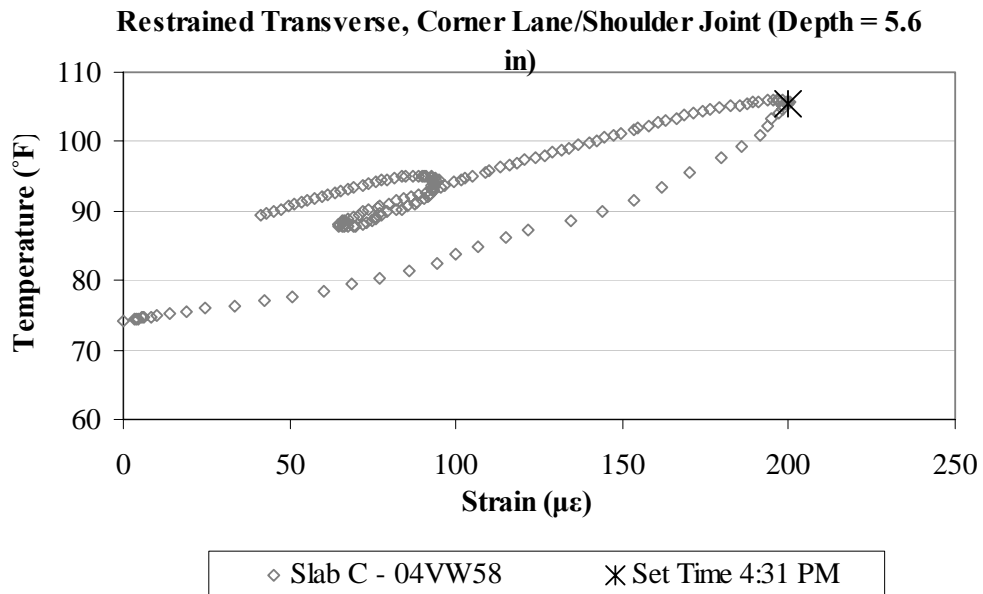


Figure B.72. Variation of strain with temperature, in the transverse direction, for the middepth sensor located at the corner along the lane/shoulder joint in restrained Slab C.

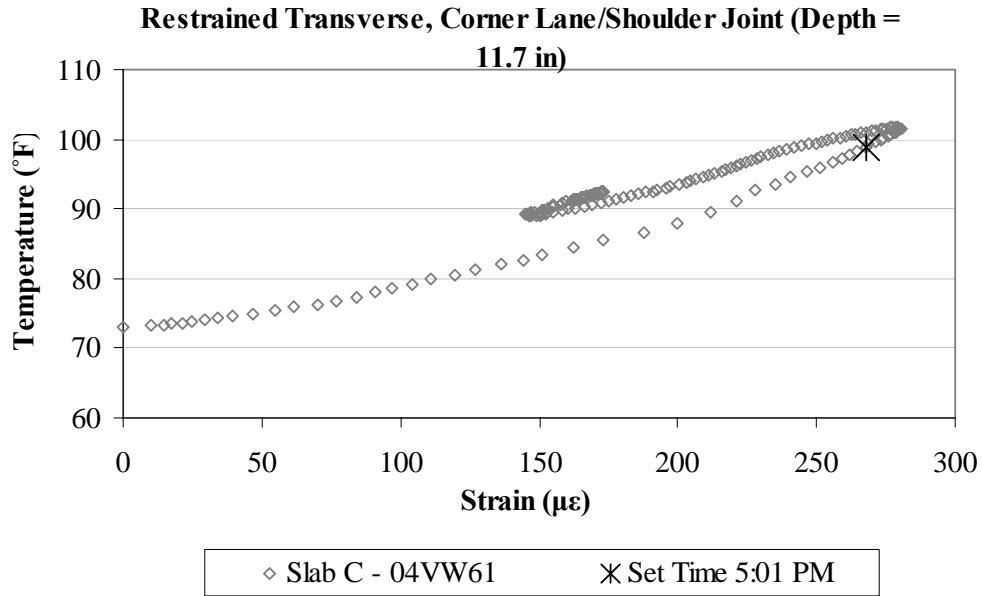


Figure B.73. Variation of strain with temperature, in the transverse direction, for the bottom sensor located at the corner along the lane/shoulder joint in restrained Slab C.

B.4 UNRESTRAINED SLAB A (CELL 3)

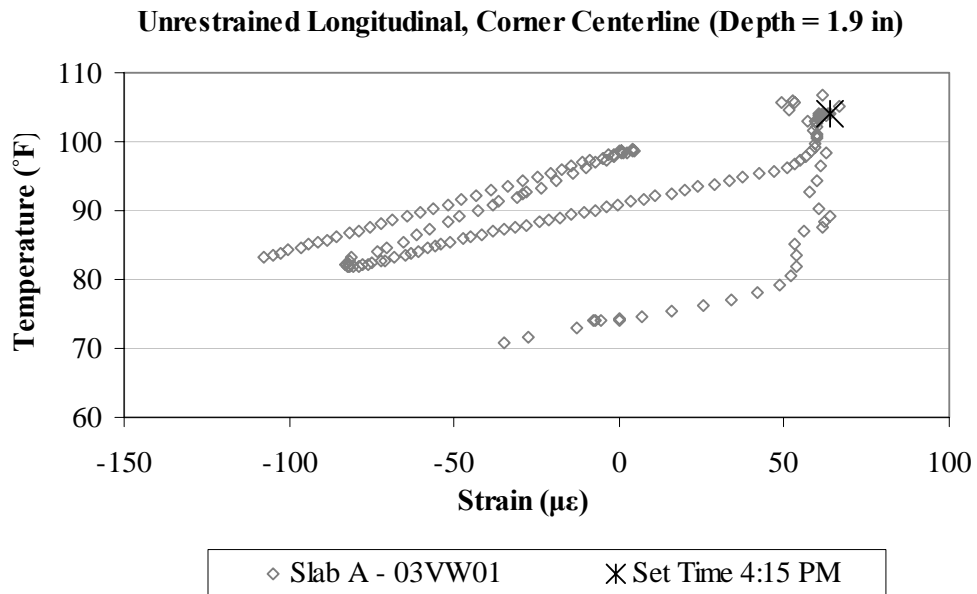


Figure B.74. Variation of strain with temperature, in the longitudinal direction, for the top sensor located at the corner along the centerline joint in unrestrained Slab A.

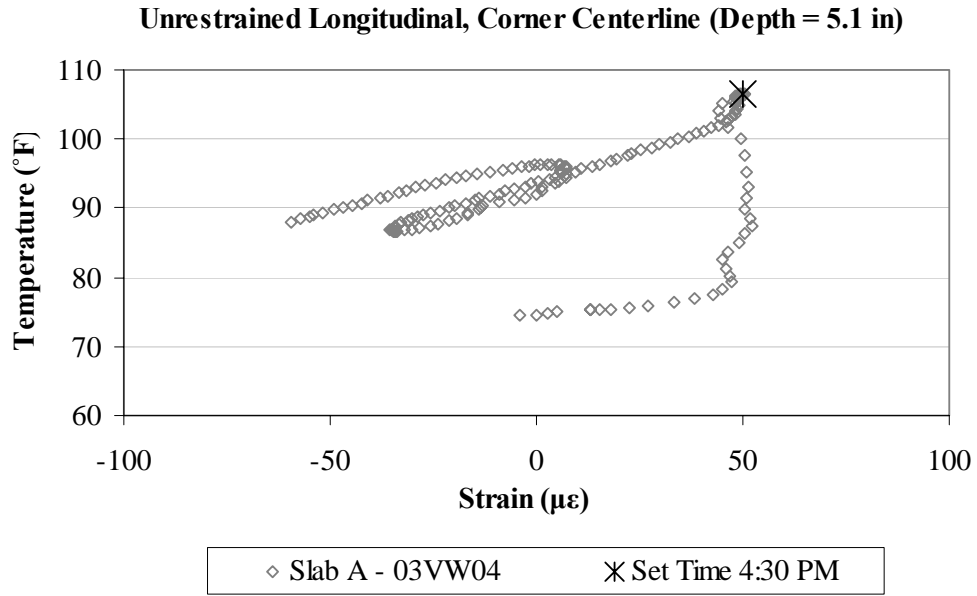


Figure B.75. Variation of strain with temperature, in the longitudinal direction, for the middepth sensor located at the corner along the centerline joint in unrestrained Slab A.

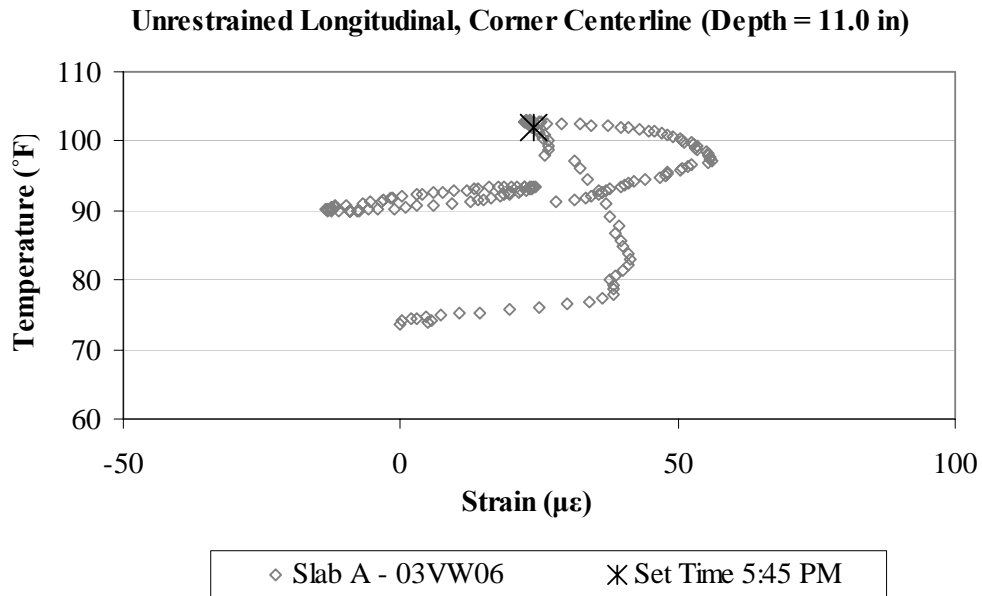


Figure B.76. Variation of strain with temperature, in the longitudinal direction, for the bottom sensor located at the corner along the centerline joint in unrestrained Slab A.

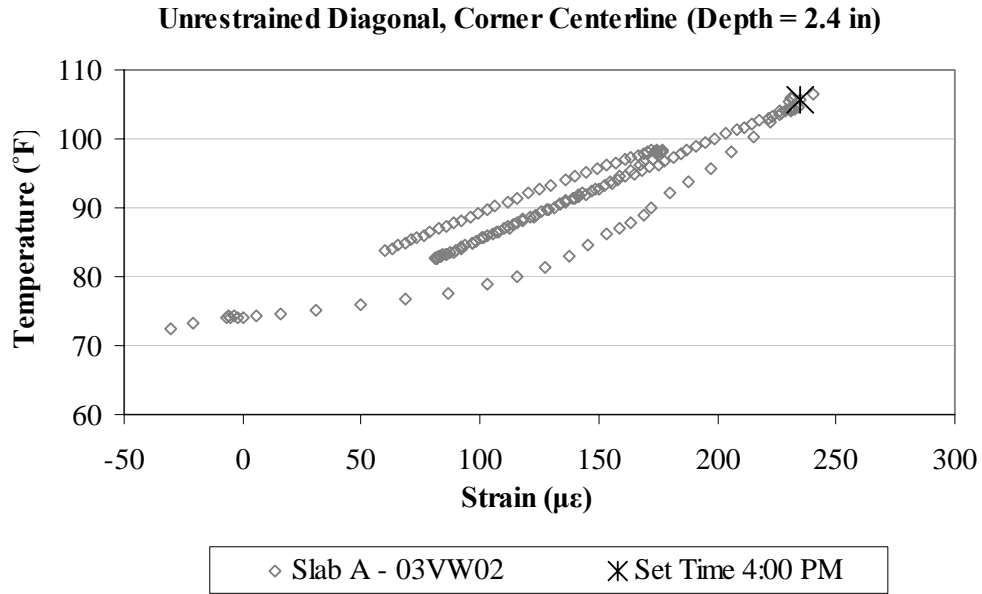


Figure B.77. Variation of strain with temperature, in the diagonal direction, for the top sensor located at the corner along the centerline joint in unrestrained Slab A.

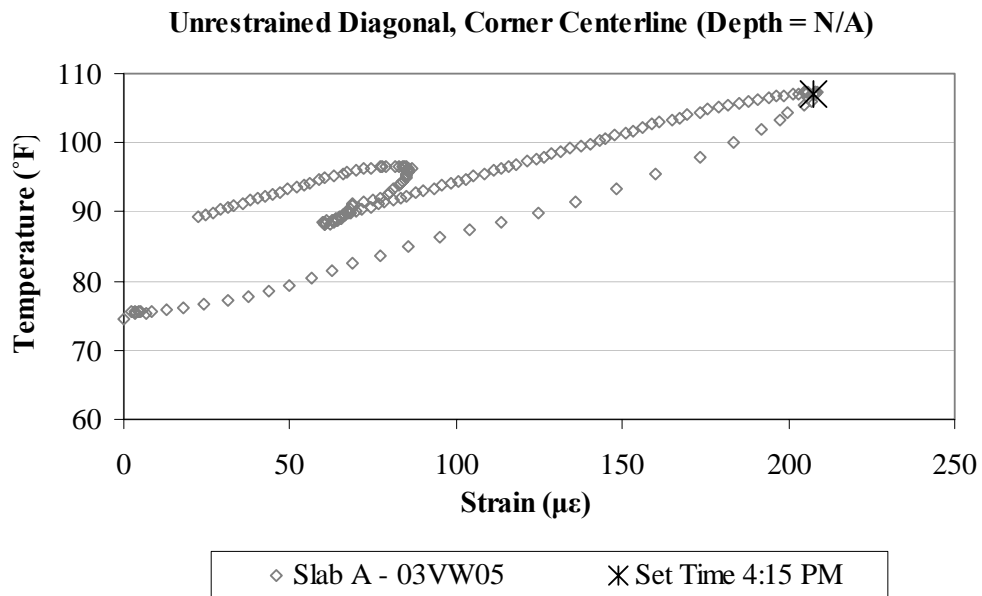


Figure B.78. Variation of strain with temperature, in the diagonal direction, for the middepth sensor located at the corner along the centerline joint in unrestrained Slab A.

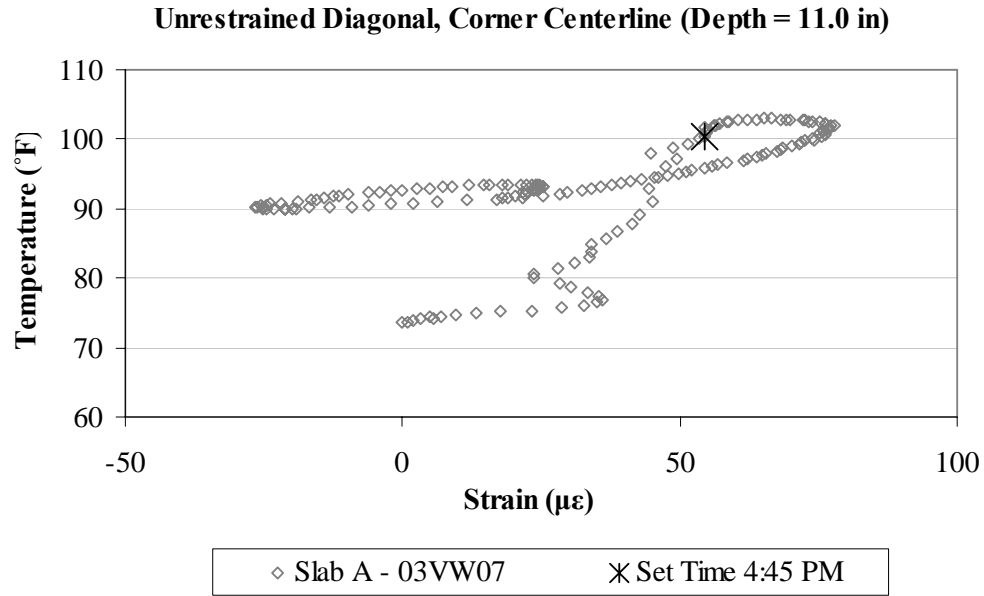


Figure B.79. Variation of strain with temperature, in the diagonal direction, for the bottom sensor located at the corner along the centerline joint in unrestrained Slab A.

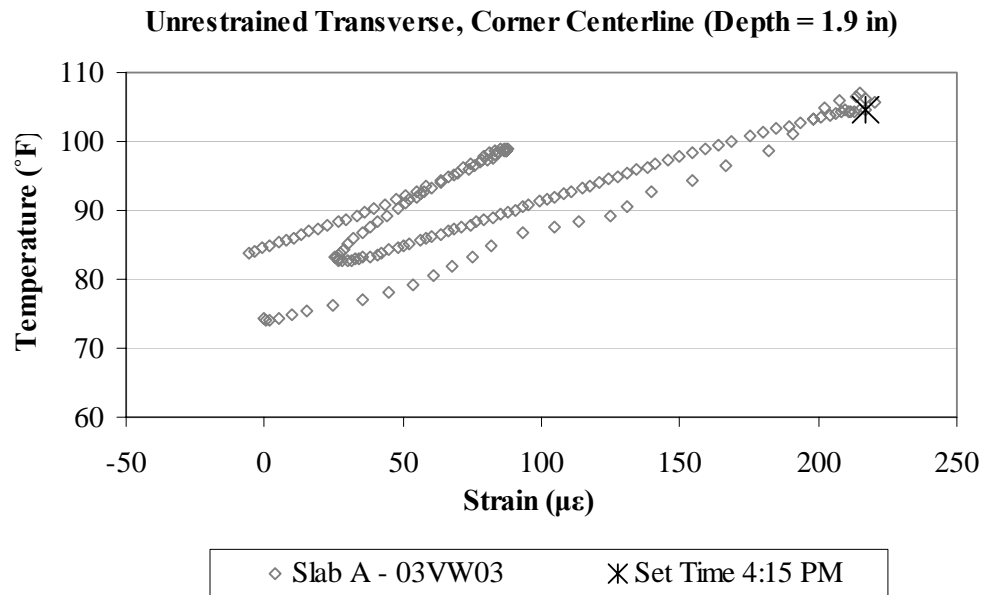


Figure B.80. Variation of strain with temperature, in the transverse direction, for the top sensor located at the corner along the centerline joint in unrestrained Slab A.

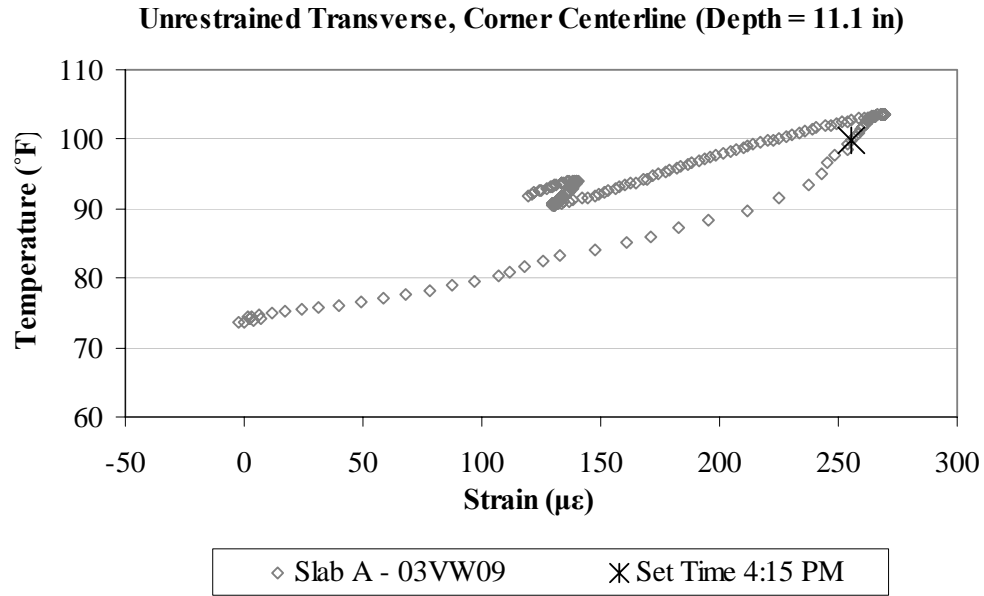


Figure B.81. Variation of strain with temperature, in the transverse direction, for the bottom sensor located at the corner along the centerline joint in unrestrained Slab A.

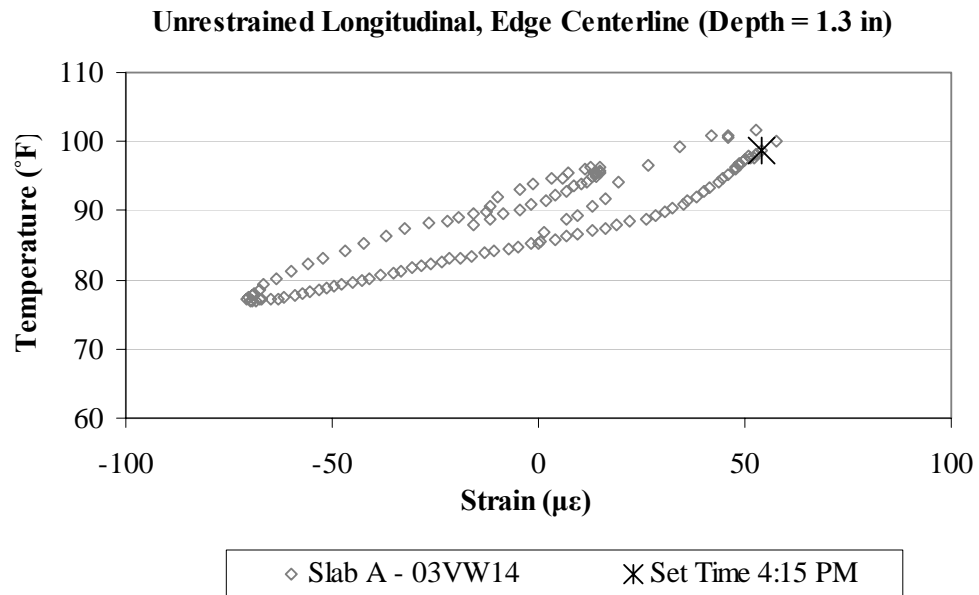


Figure B.82. Variation of strain with temperature, in the longitudinal direction, for the top sensor located along the centerline joint in unrestrained Slab A.

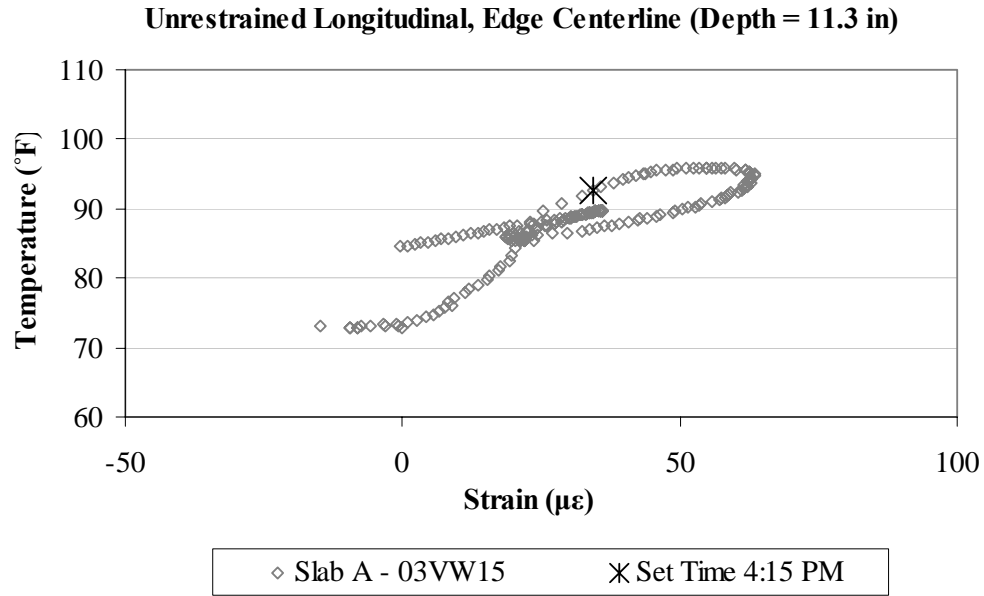


Figure B.83. Variation of strain with temperature, in the longitudinal direction, for the bottom sensor located along the centerline joint in unrestrained Slab A.

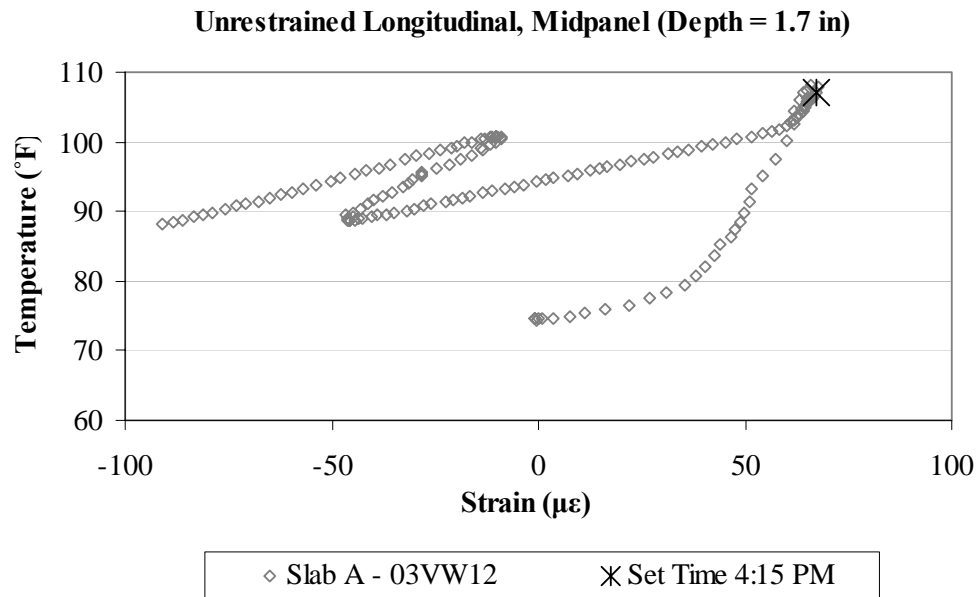


Figure B.84. Variation of strain with temperature, in the longitudinal direction, for the top sensor located at midpanel in unrestrained Slab A.

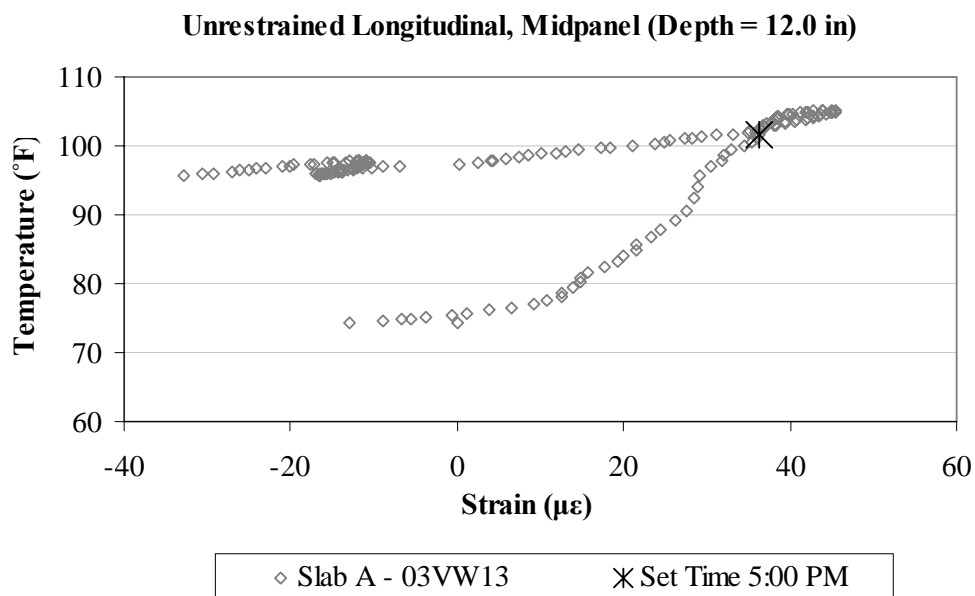


Figure B.85. Variation of strain with temperature, in the longitudinal direction, for the bottom sensor located at midpanel in unrestrained Slab A.

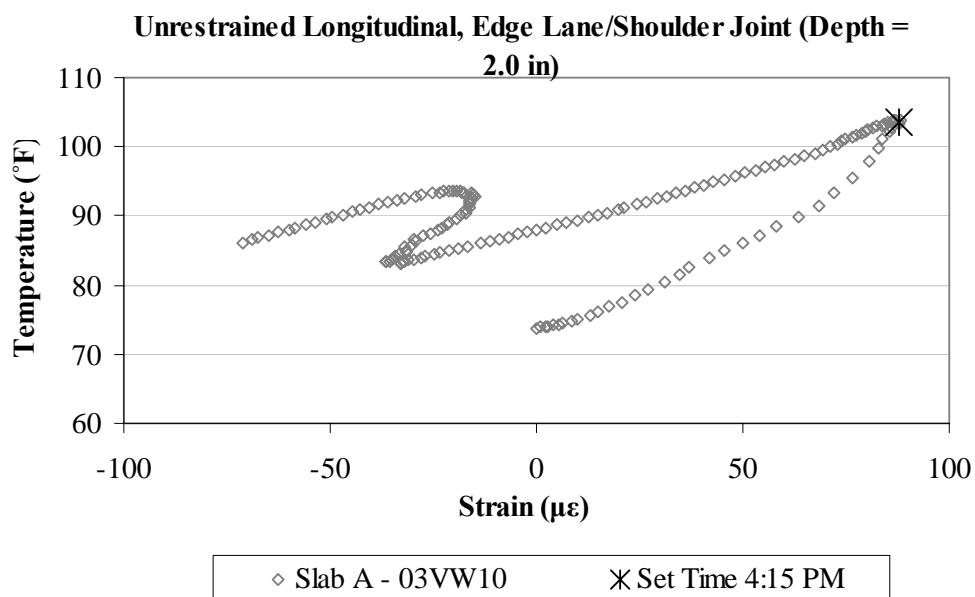


Figure B.86. Variation of strain with temperature, in the longitudinal direction, for the top sensor located along the lane/shoulder joint in unrestrained Slab A.

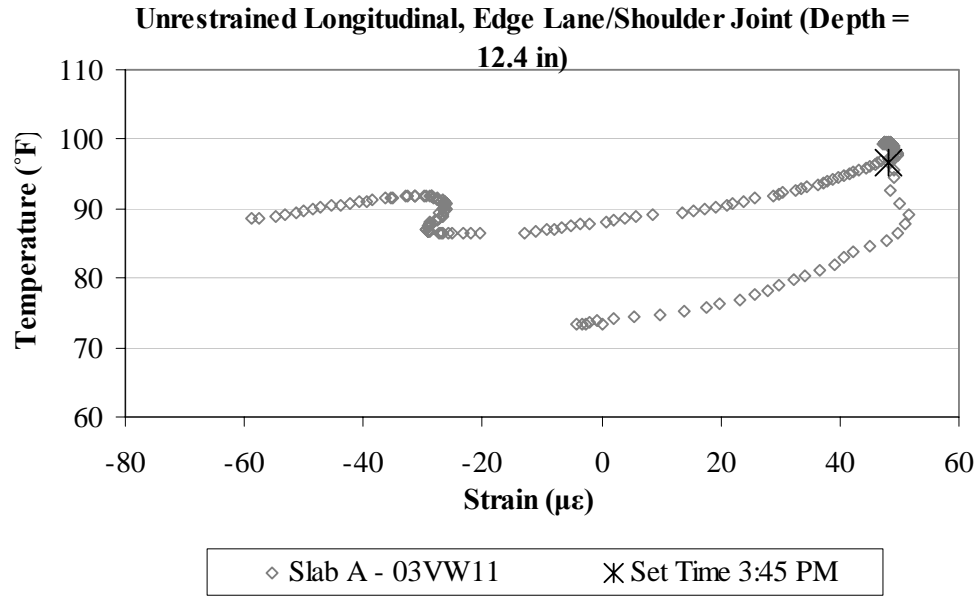


Figure B.87. Variation of strain with temperature, in the longitudinal direction, for the bottom sensor located along the lane/shoulder joint in unrestrained Slab A.

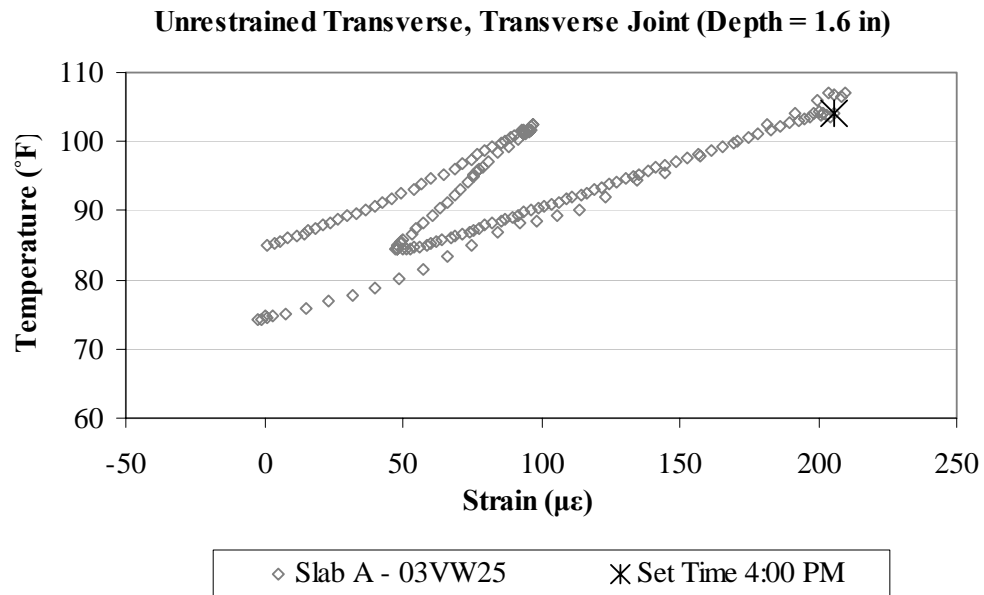


Figure B.88. Variation of strain with temperature, in the transverse direction, for the top sensor located along the transverse joint in unrestrained Slab A.

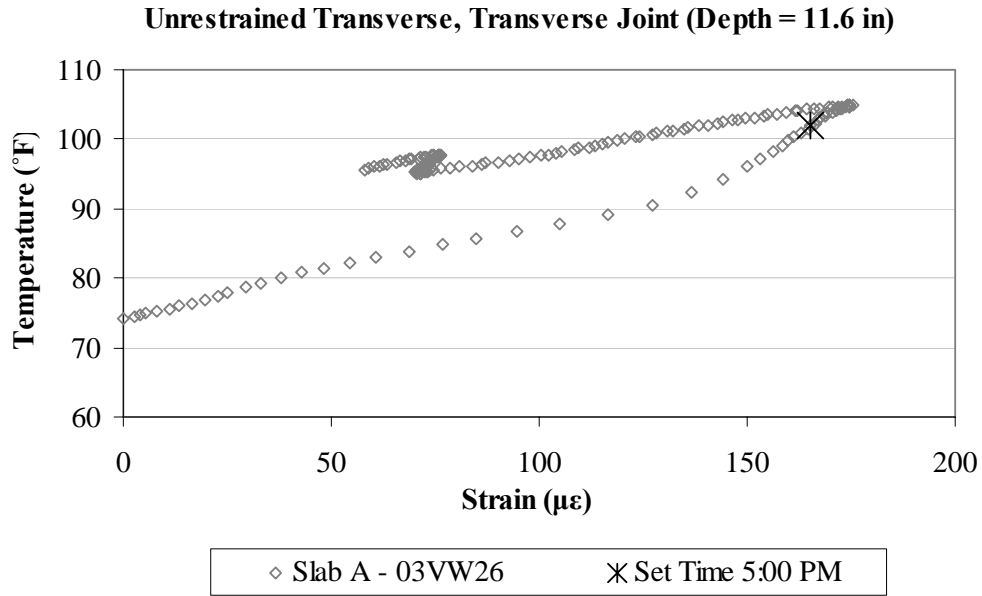


Figure B.89. Variation of strain with temperature, in the transverse direction, for the bottom sensor located along the transverse joint in unrestrained Slab A.

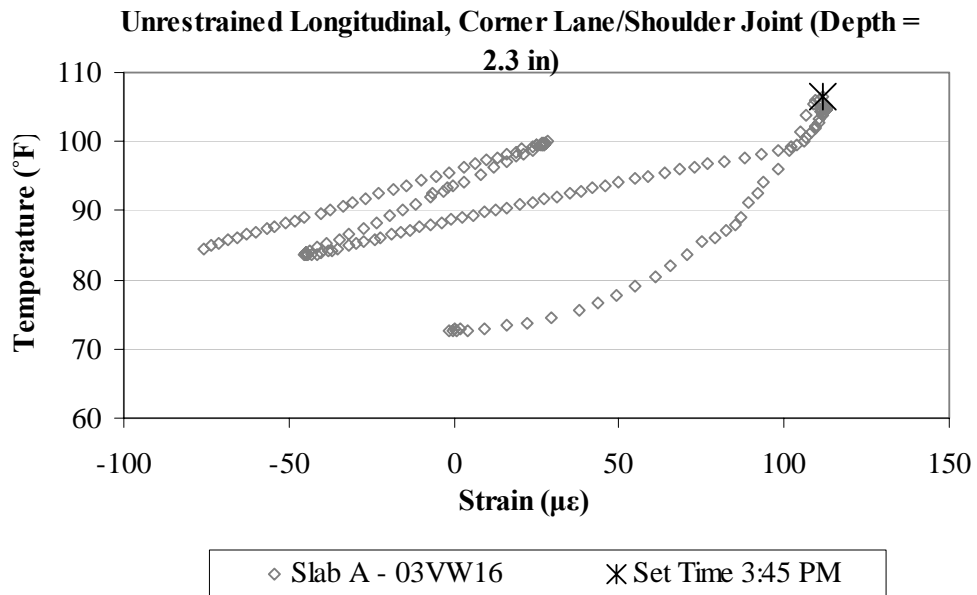


Figure B.90. Variation of strain with temperature, in the longitudinal direction, for the top sensor located at the corner along the lane/shoulder joint in unrestrained Slab A.

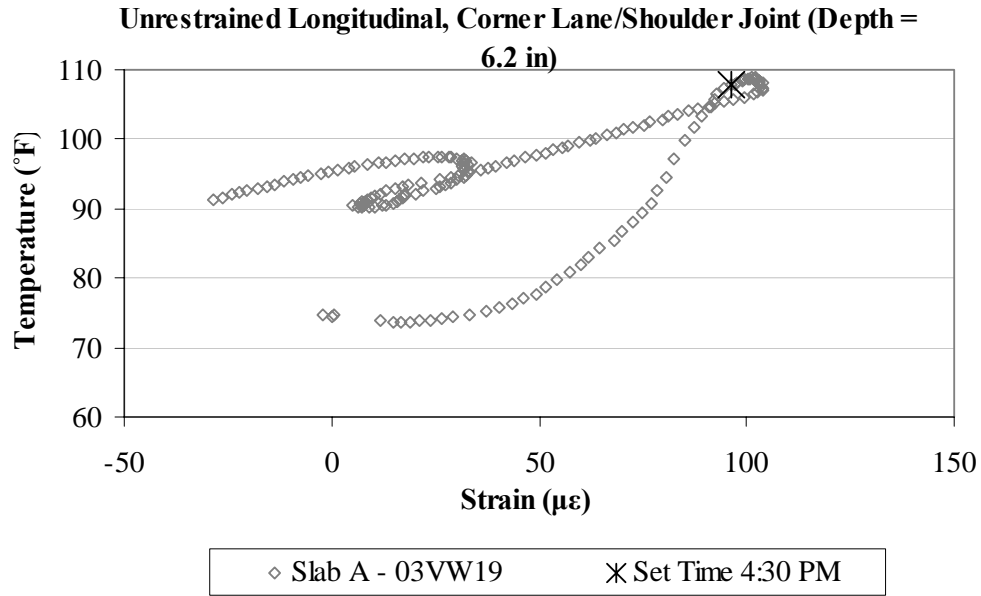


Figure B.91. Variation of strain with temperature, in the longitudinal direction, for the middepth sensor located at the corner along the lane/shoulder joint in unrestrained Slab A.

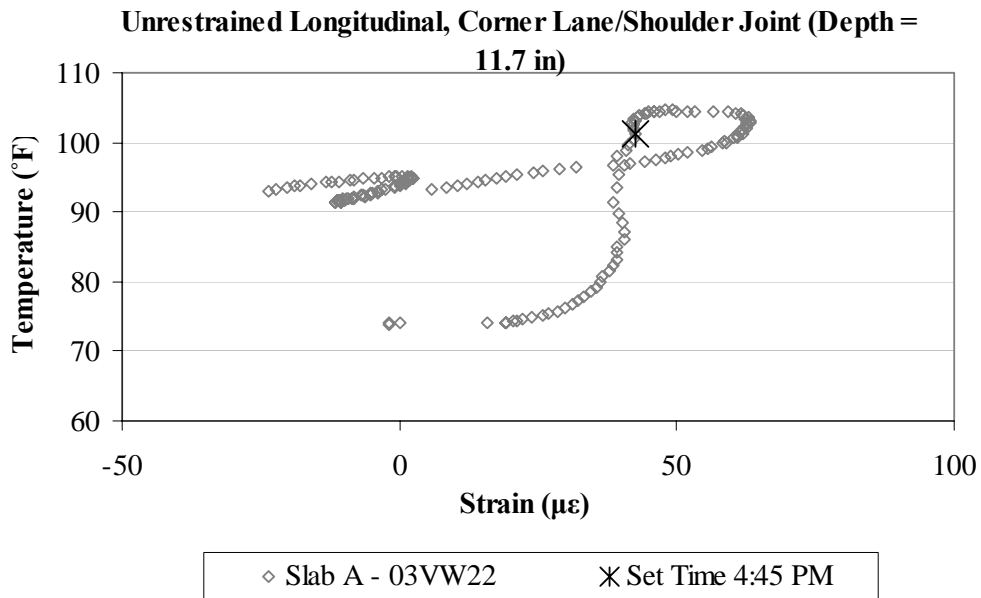


Figure B.92. Variation of strain with temperature, in the longitudinal direction, for the bottom sensor located at the corner along the lane/shoulder joint in unrestrained Slab A.

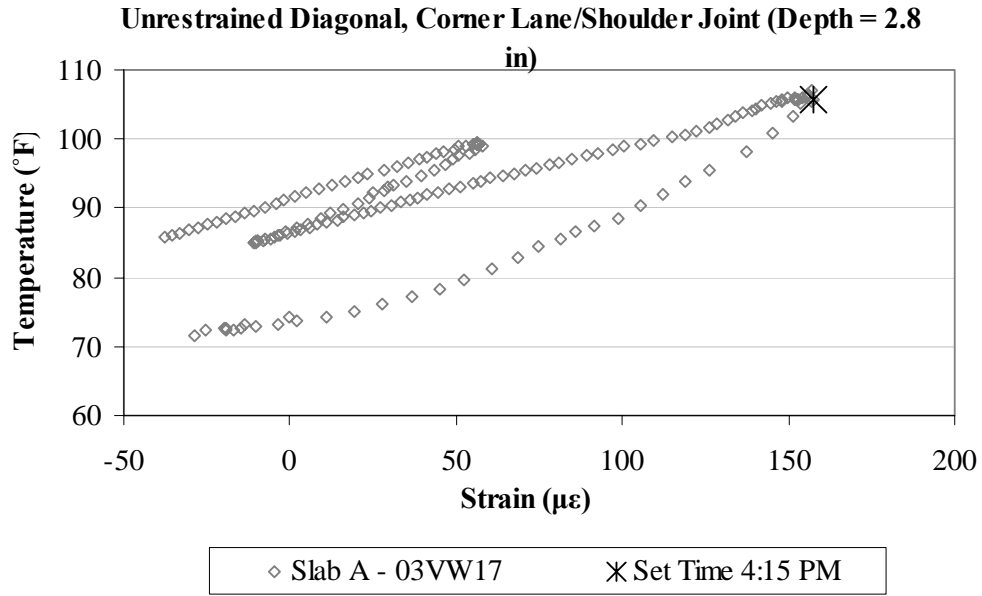


Figure B.93. Variation of strain with temperature, in the diagonal direction, for the top sensor located at the corner along the lane/shoulder joint in unrestrained Slab A.

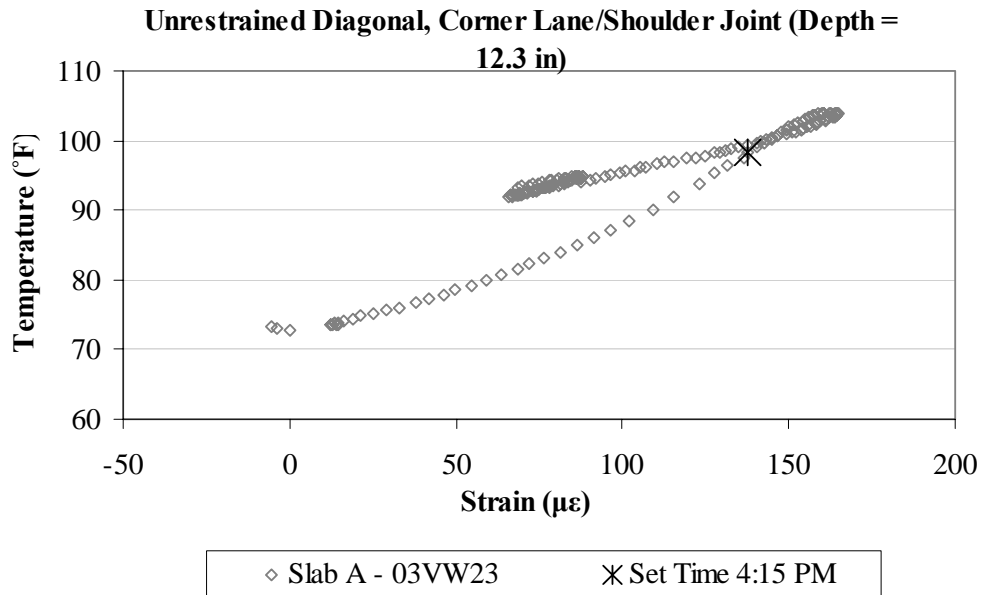


Figure B.94. Variation of strain with temperature, in the diagonal direction, for the bottom sensor located at the corner along the lane/shoulder joint in unrestrained Slab A.

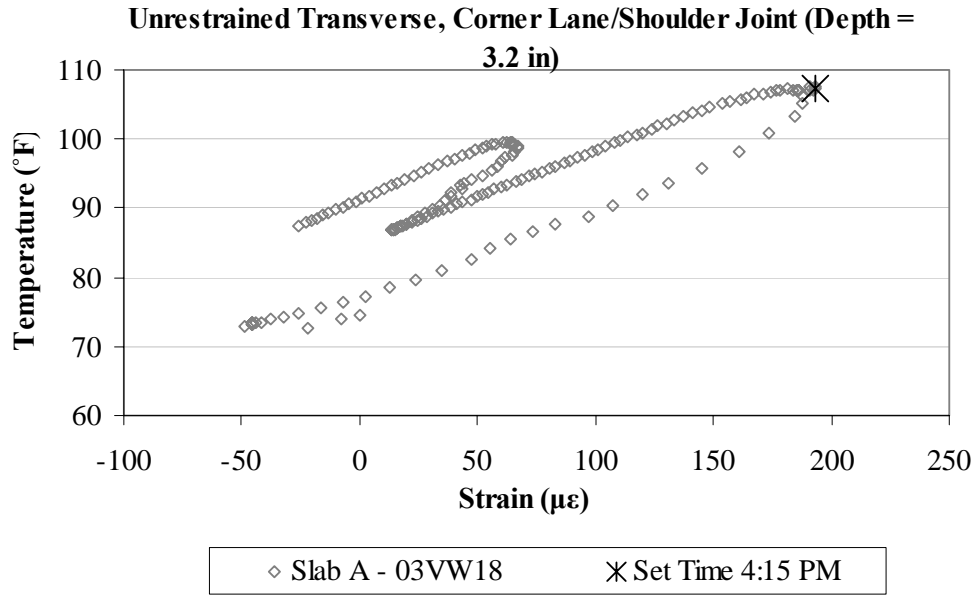


Figure B.95. Variation of strain with temperature, in the transverse direction, for the top sensor located at the corner along the lane/shoulder joint in unrestrained Slab A.

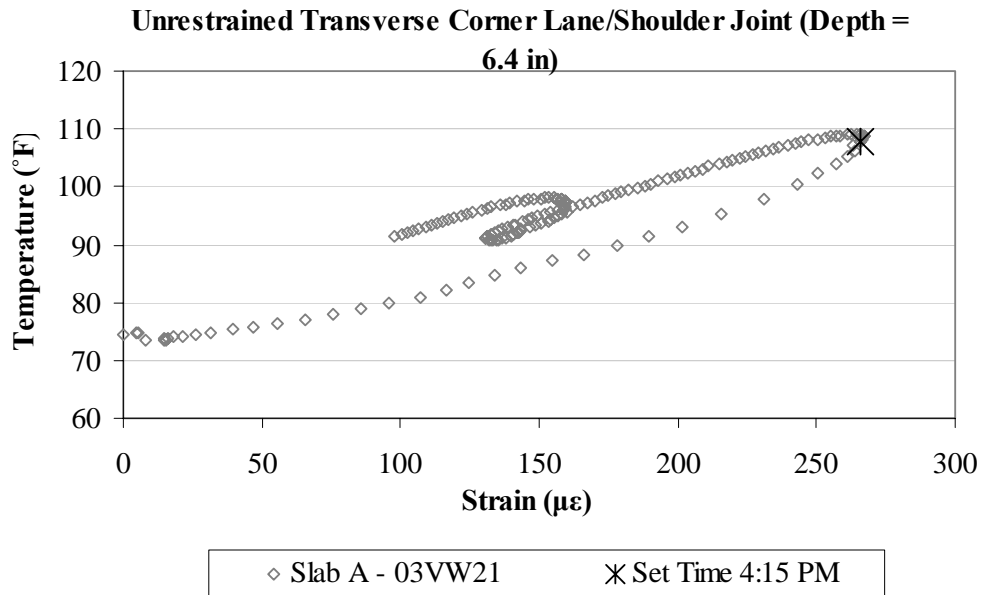


Figure B.96. Variation of strain with temperature, in the transverse direction, for the middepth sensor located at the corner along the lane/shoulder joint in unrestrained Slab A.

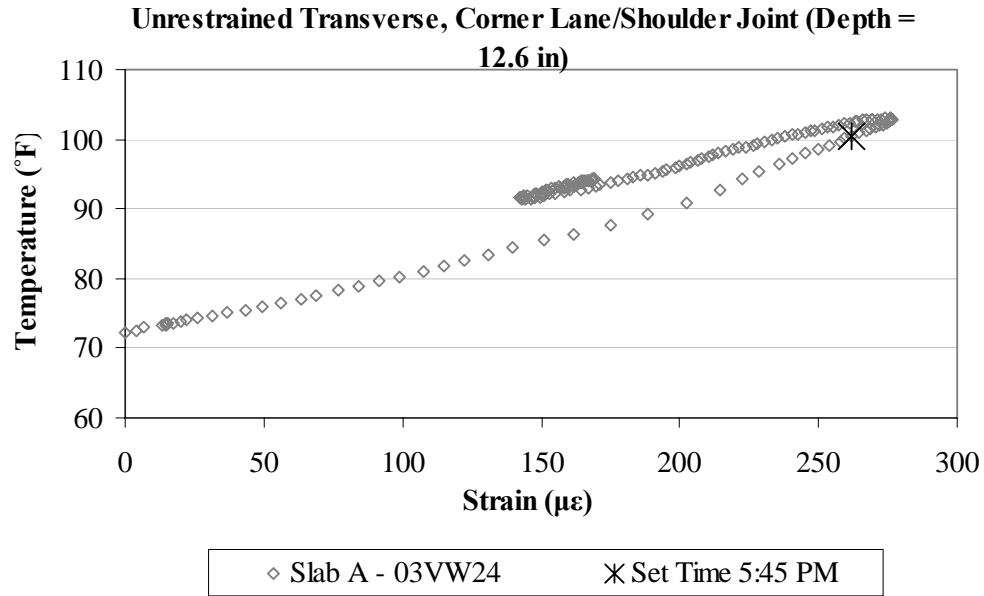


Figure B.97. Variation of strain with temperature, in the transverse direction, for the bottom sensor located at the corner along the lane/shoulder joint in unrestrained Slab A.

B.5 UNRESTRAINED SLAB B (CELL 3)

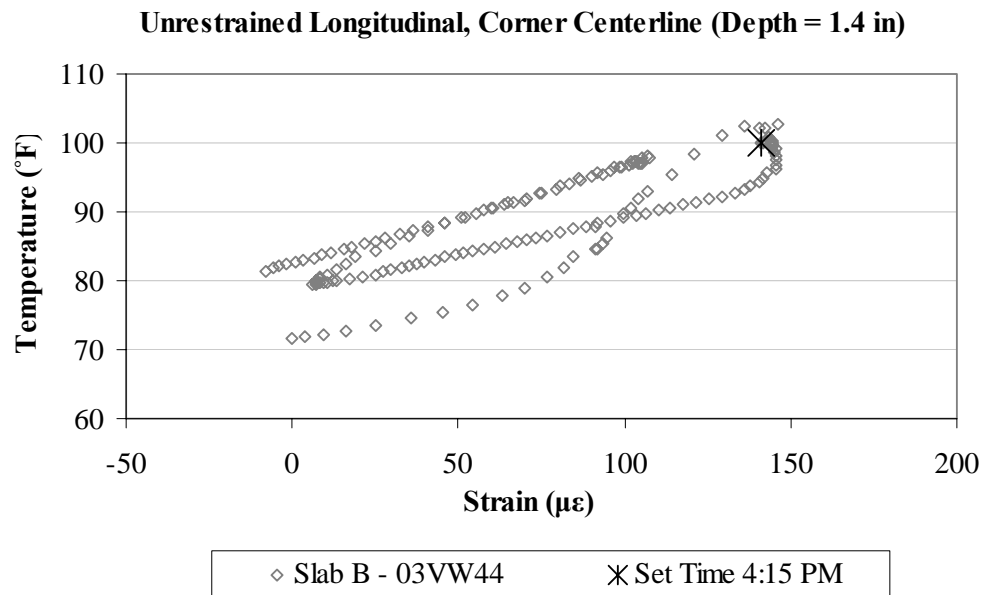


Figure B.98. Variation of strain with temperature, in the longitudinal direction, for the top sensor located at the corner along the centerline joint in unrestrained Slab B.

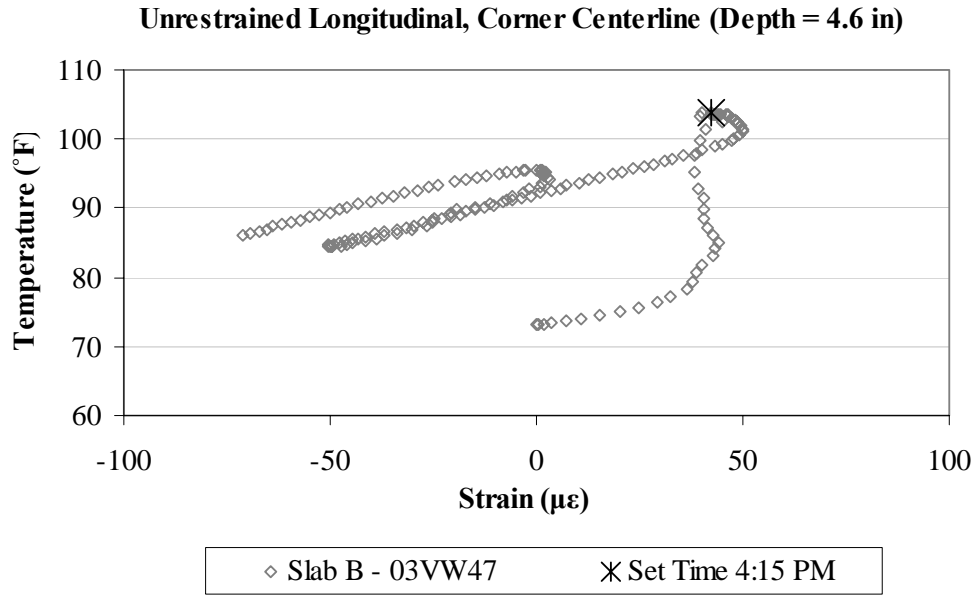


Figure B.99. Variation of strain with temperature, in the longitudinal direction, for the middepth sensor located at the corner along the centerline joint in unrestrained Slab B.

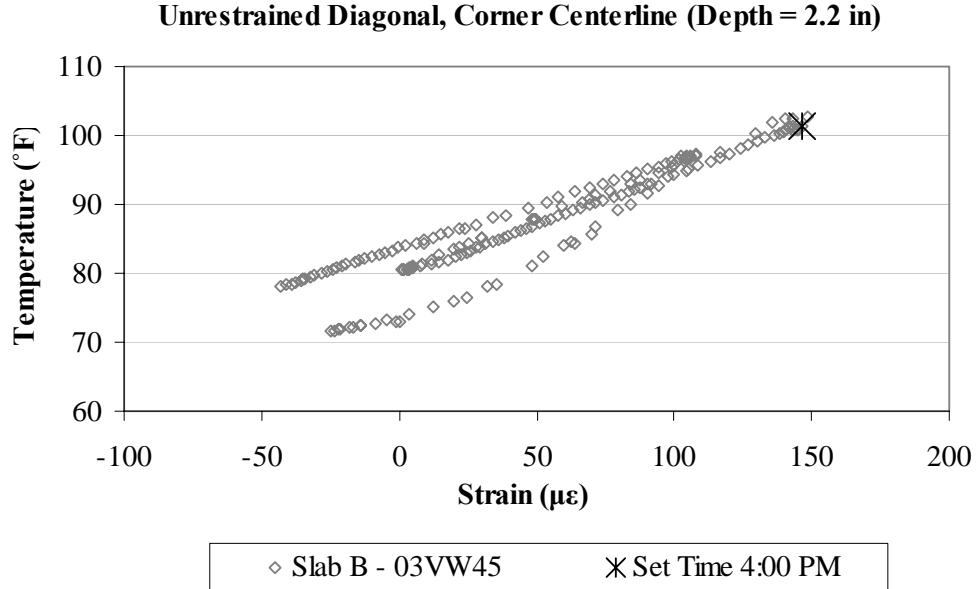


Figure B.100. Variation of strain with temperature, in the diagonal direction, for the top sensor located at the corner along the centerline joint in unrestrained Slab B.

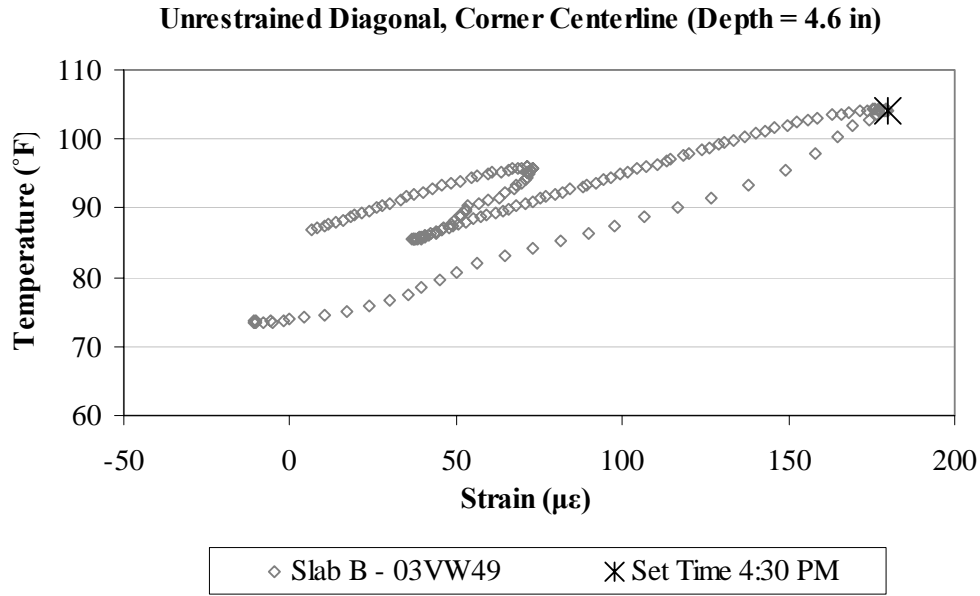


Figure B.101. Variation of strain with temperature, in the diagonal direction, for the middepth sensor located at the corner along the centerline joint in unrestrained Slab B.

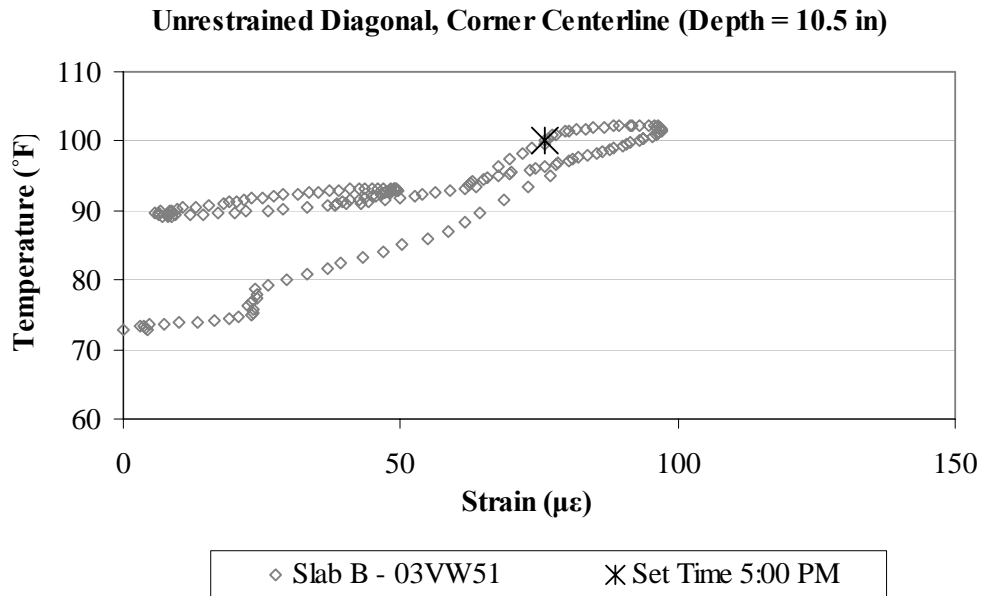


Figure B.102. Variation of strain with temperature, in the diagonal direction, for the bottom sensor located at the corner along the centerline joint in unrestrained Slab B.

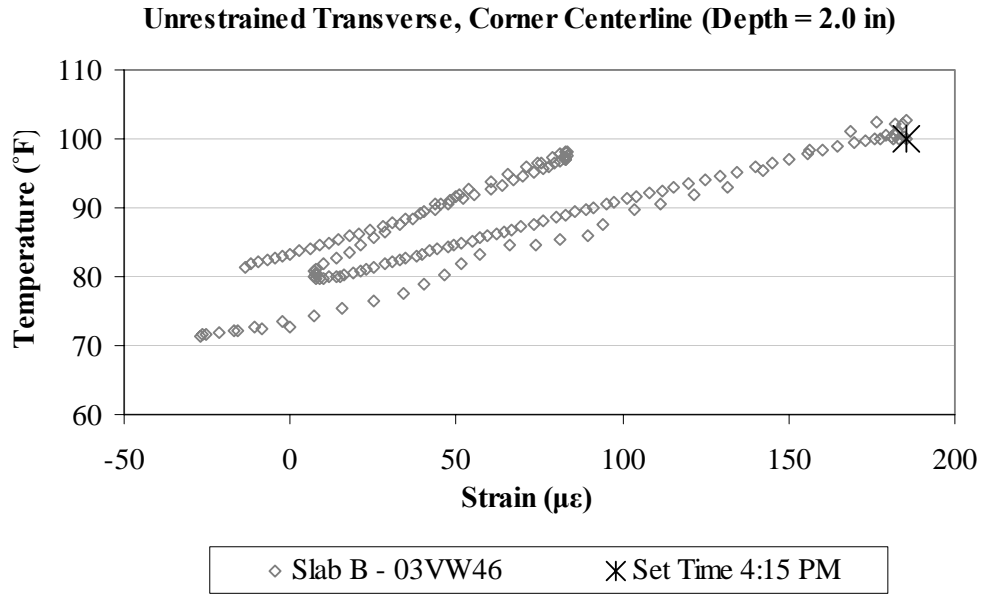


Figure B.103. Variation of strain with temperature, in the transverse direction, for the top sensor located at the corner along the centerline joint in unrestrained Slab B.

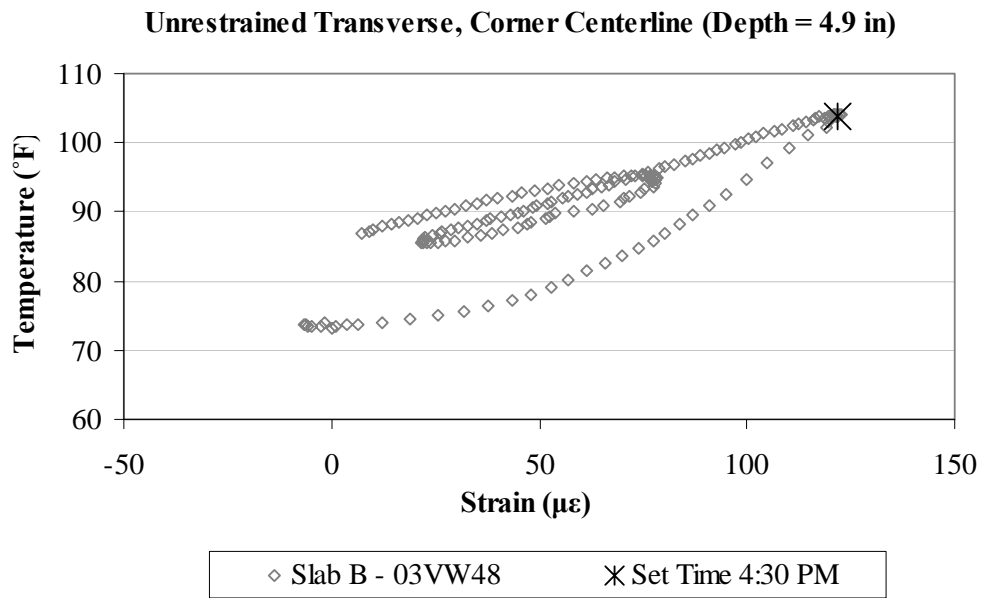


Figure B.104. Variation of strain with temperature, in the transverse direction, for the middepth sensor located at the corner along the centerline joint in unrestrained Slab B.

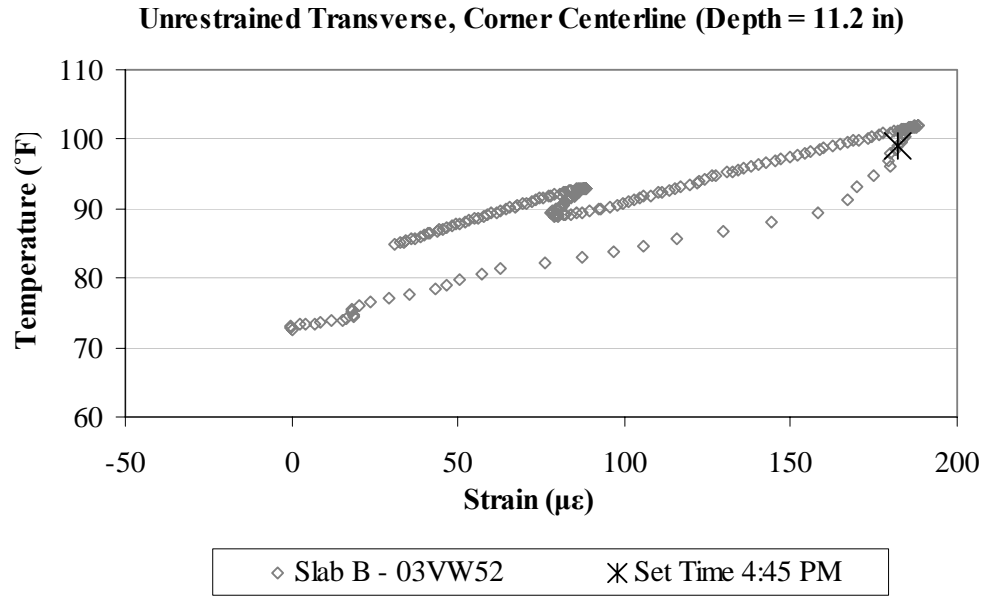


Figure B.105. Variation of strain with temperature, in the transverse direction, for the bottom sensor located at the corner along the centerline joint in unrestrained Slab B.

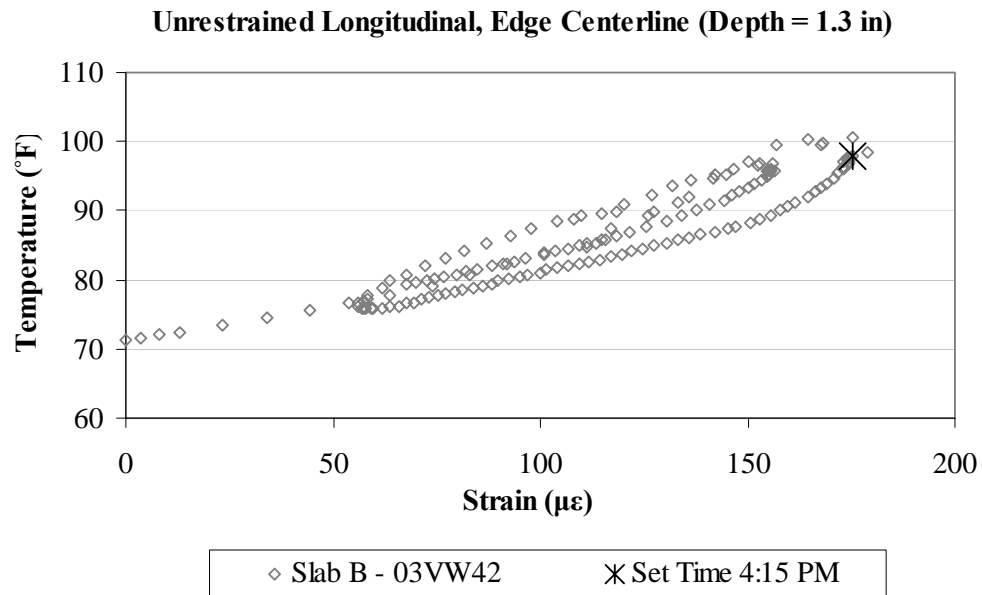


Figure B.106. Variation of strain with temperature, in the longitudinal direction, for the top sensor located along the centerline joint in unrestrained Slab B.

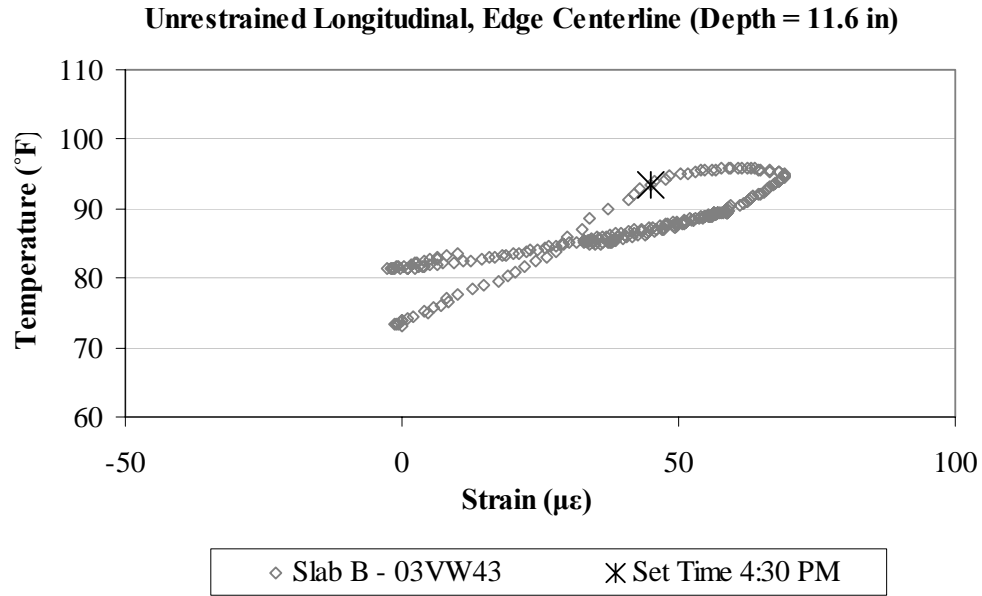


Figure B.107. Variation of strain with temperature, in the longitudinal direction, for the bottom sensor located along the centerline joint in unrestrained Slab B.

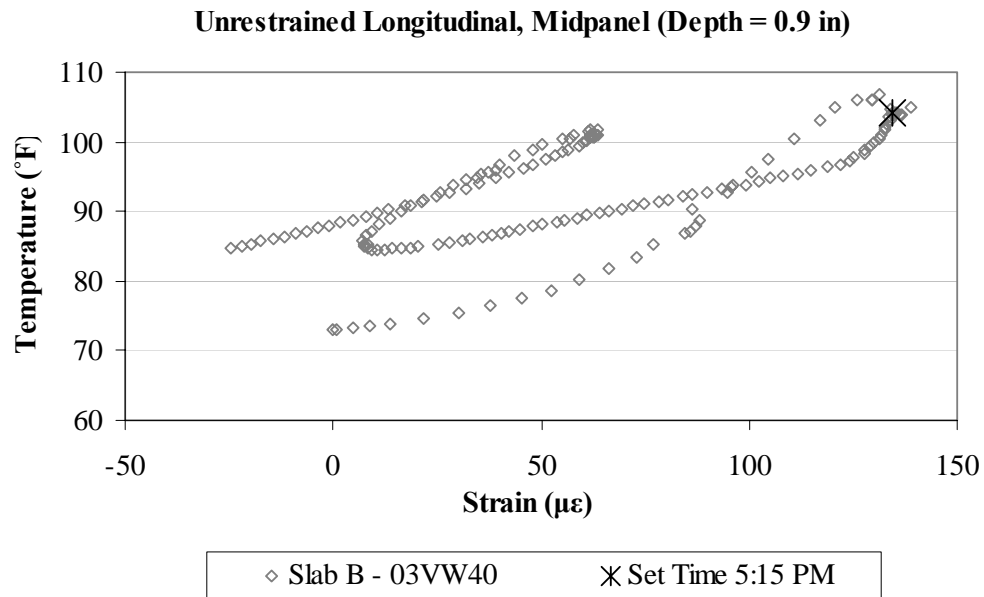


Figure B.108. Variation of strain with temperature, in the longitudinal direction, for the top sensor located at midpanel in unrestrained Slab B.

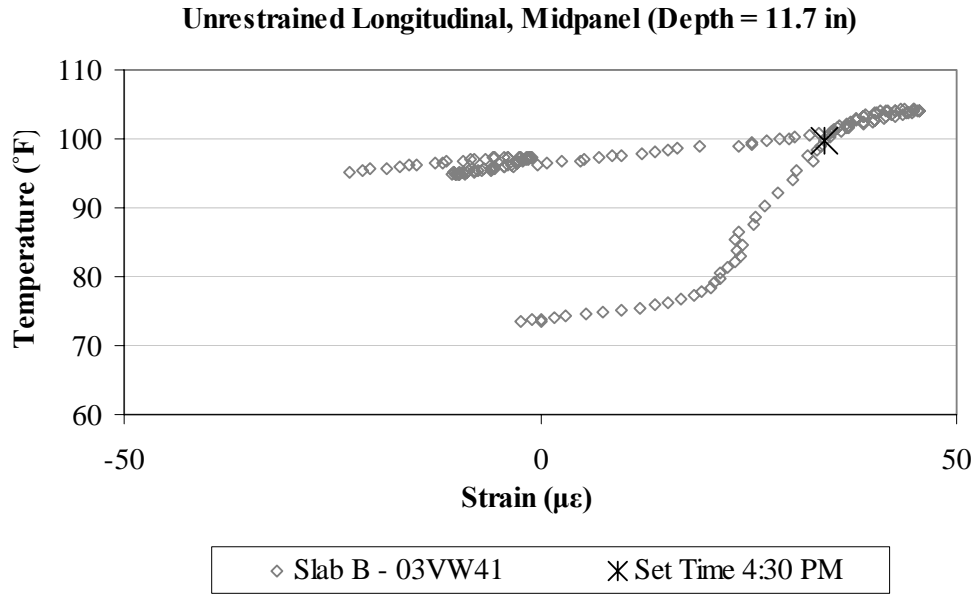


Figure B.109. Variation of strain with temperature, in the longitudinal direction, for the bottom sensor located at midpanel in unrestrained Slab B.

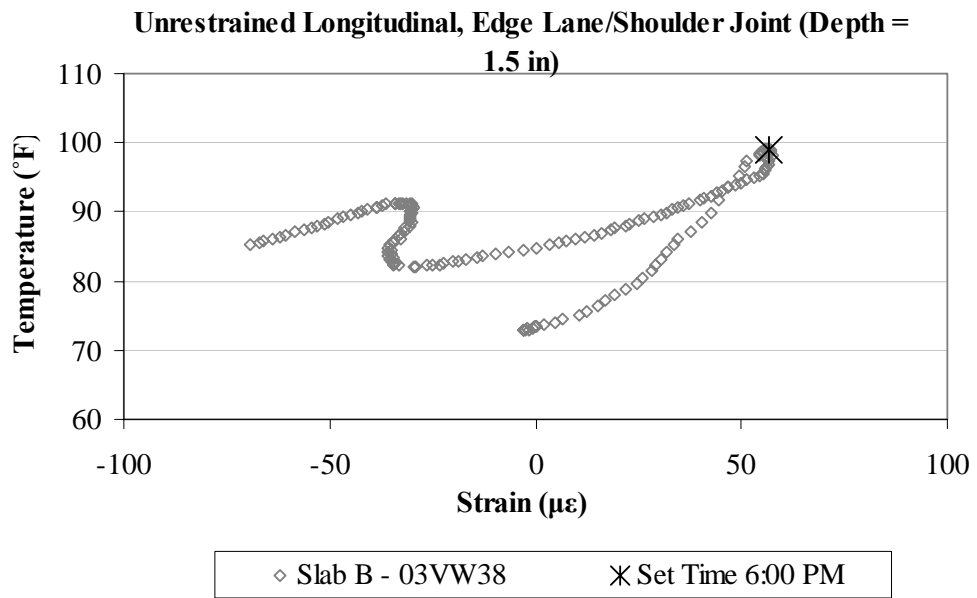


Figure B.110. Variation of strain with temperature, in the longitudinal direction, for the top sensor located along the lane/shoulder joint in unrestrained Slab B.

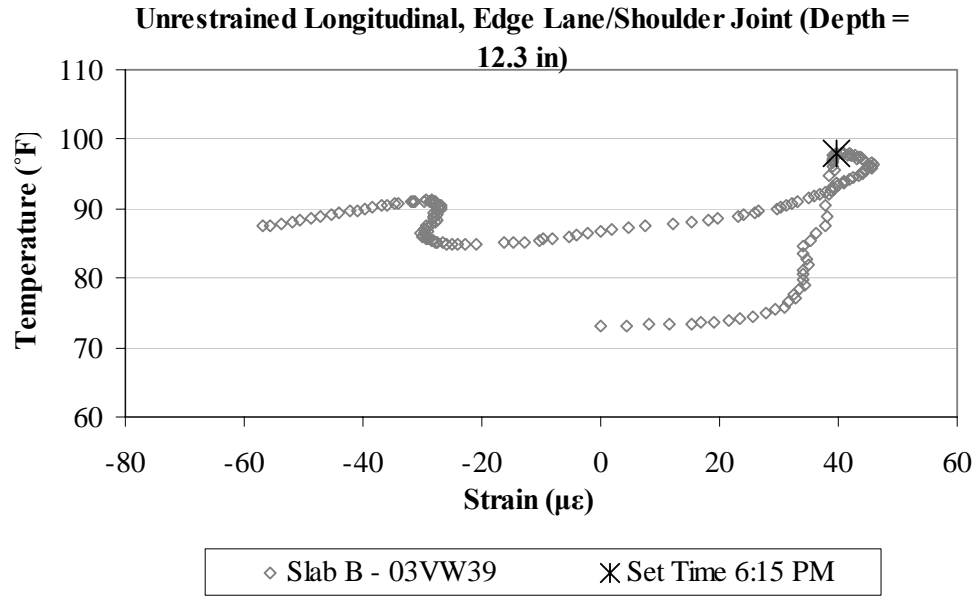


Figure B.111. Variation of strain with temperature, in the longitudinal direction, for the bottom sensor located along the lane/shoulder joint in unrestrained Slab B.

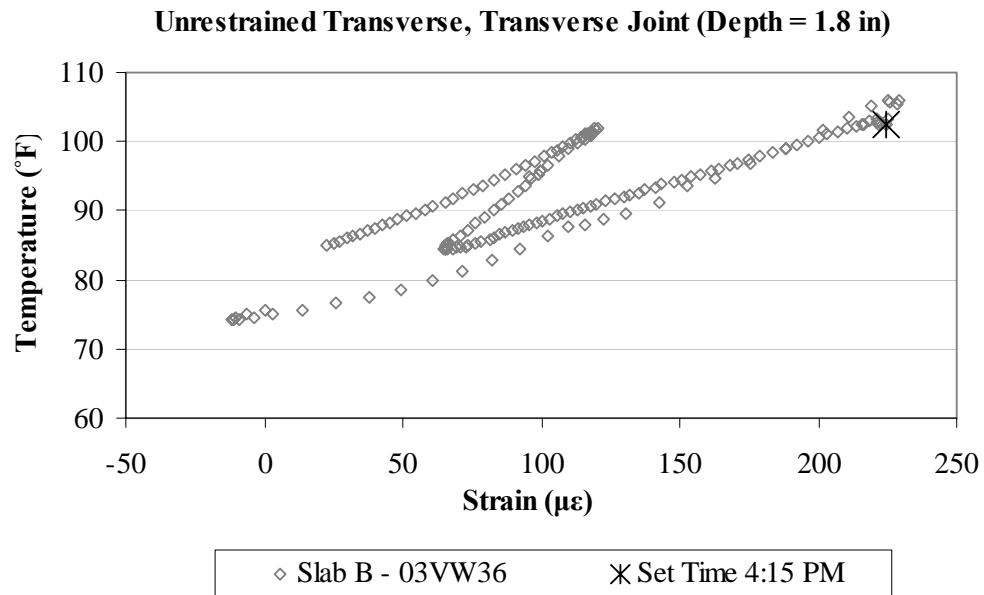


Figure B.112. Variation of strain with temperature, in the transverse direction, for the top sensor located along the transverse joint in unrestrained Slab B.

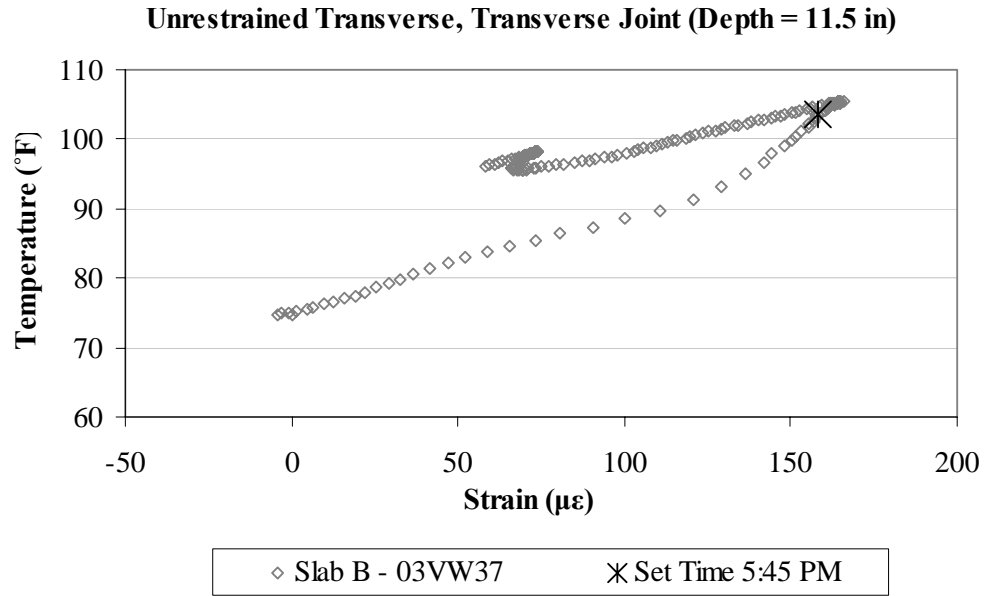


Figure B.113. Variation of strain with temperature, in the transverse direction, for the bottom sensor located along the transverse joint in unrestrained Slab B.

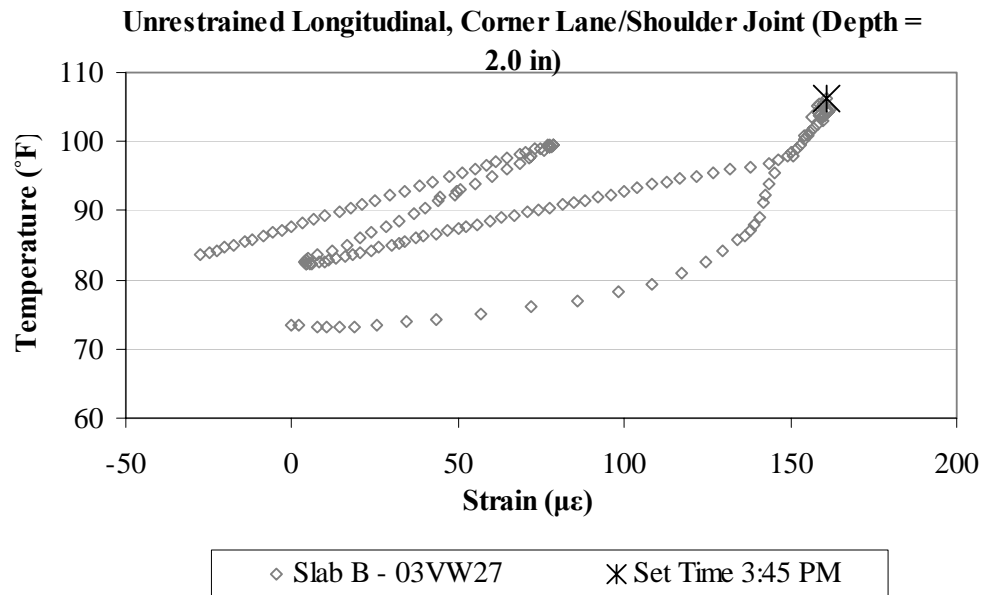


Figure B.114. Variation of strain with temperature, in the longitudinal direction, for the top sensor located at the corner along the lane/shoulder joint in unrestrained Slab B.

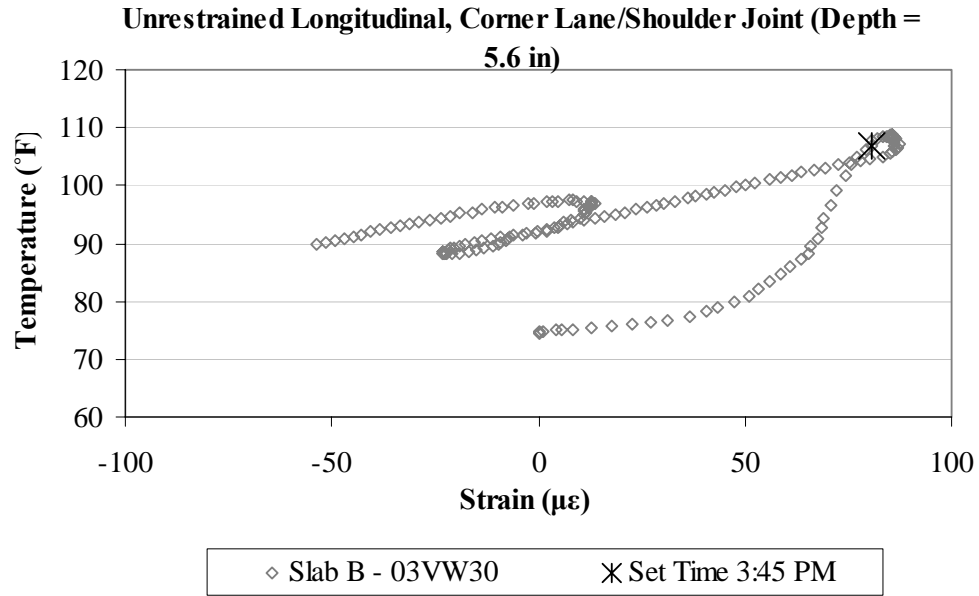


Figure B.115. Variation of strain with temperature, in the longitudinal direction, for the middepth sensor located at the corner along the lane/shoulder joint in unrestrained Slab B.

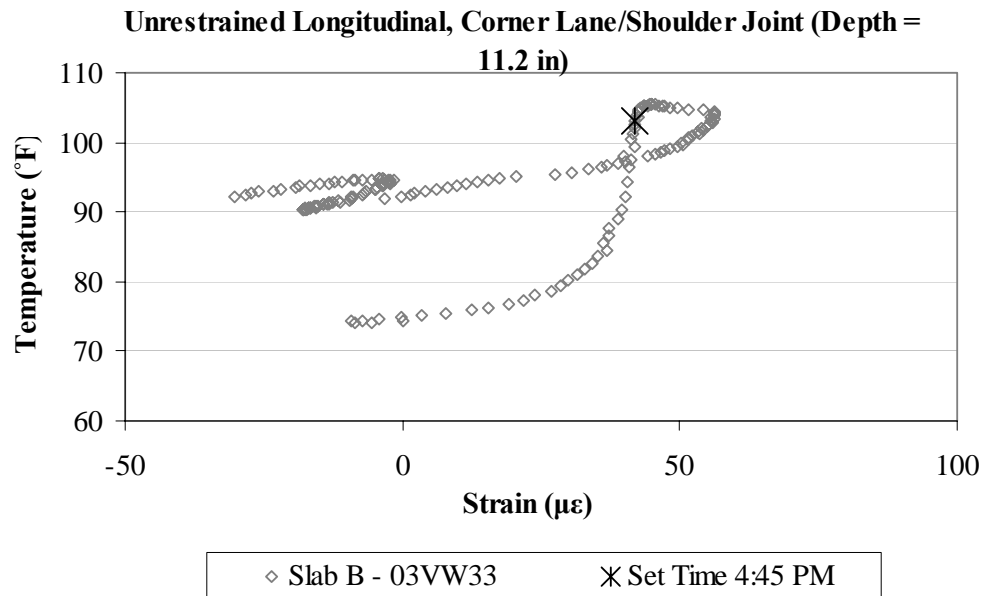


Figure B.116. Variation of strain with temperature, in the longitudinal direction, for the bottom sensor located at the corner along the lane/shoulder joint in unrestrained Slab B.

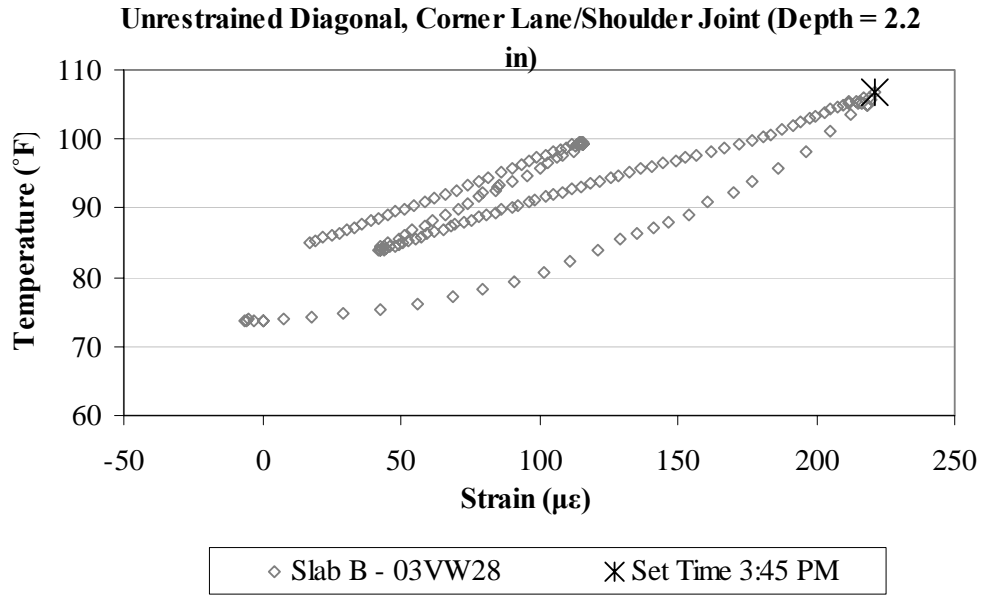


Figure B.117. Variation of strain with temperature, in the diagonal direction, for the top sensor located at the corner along the lane/shoulder joint in unrestrained Slab B.

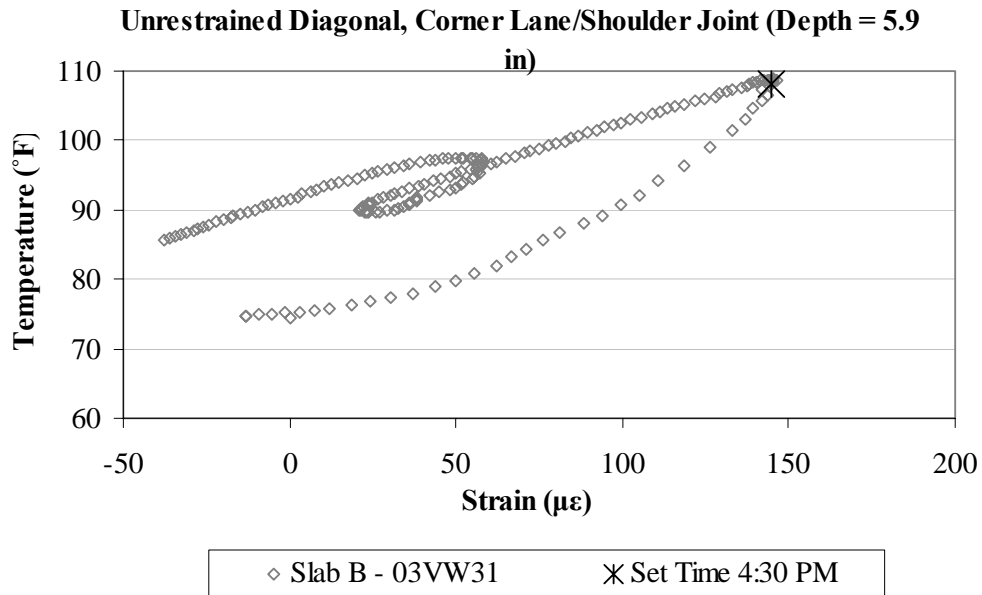


Figure B.118. Variation of strain with temperature, in the diagonal direction, for the middepth sensor located at the corner along the lane/shoulder joint in unrestrained Slab B.

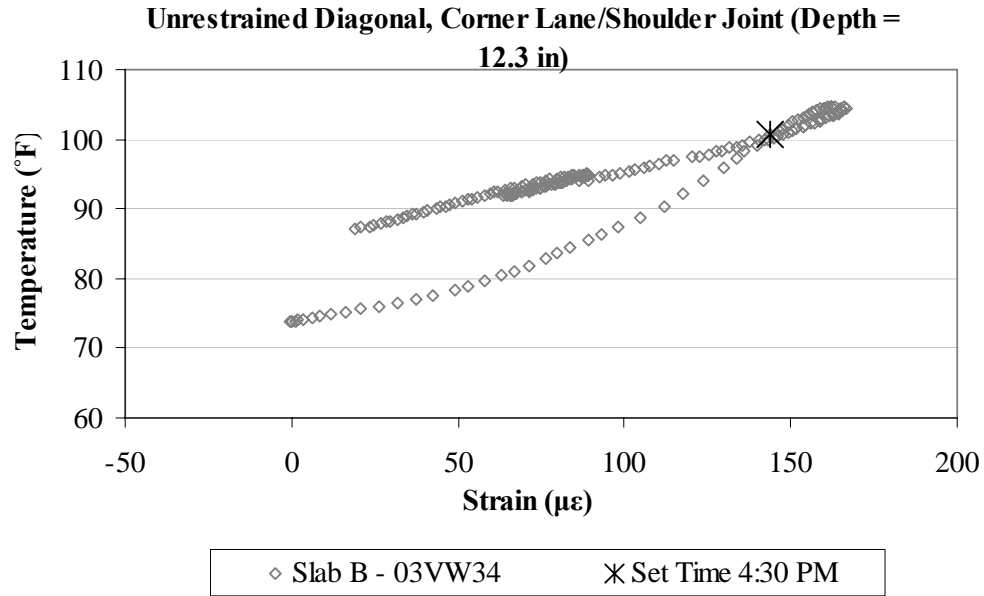


Figure B.119. Variation of strain with temperature, in the diagonal direction, for the bottom sensor located at the corner along the lane/shoulder joint in unrestrained Slab B.

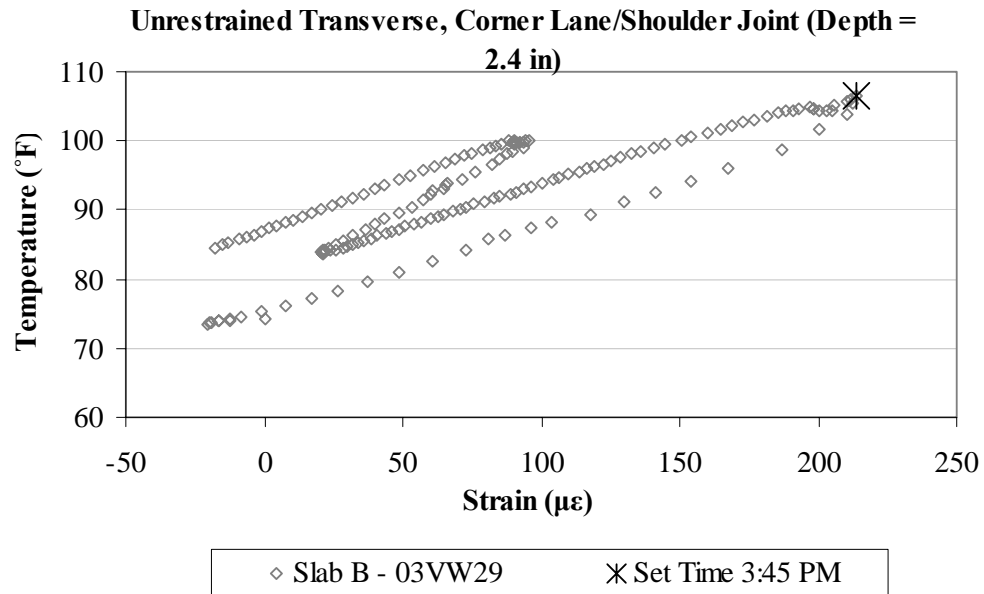


Figure B.120. Variation of strain with temperature, in the transverse direction, for the top sensor located at the corner along the lane/shoulder joint in unrestrained Slab B.

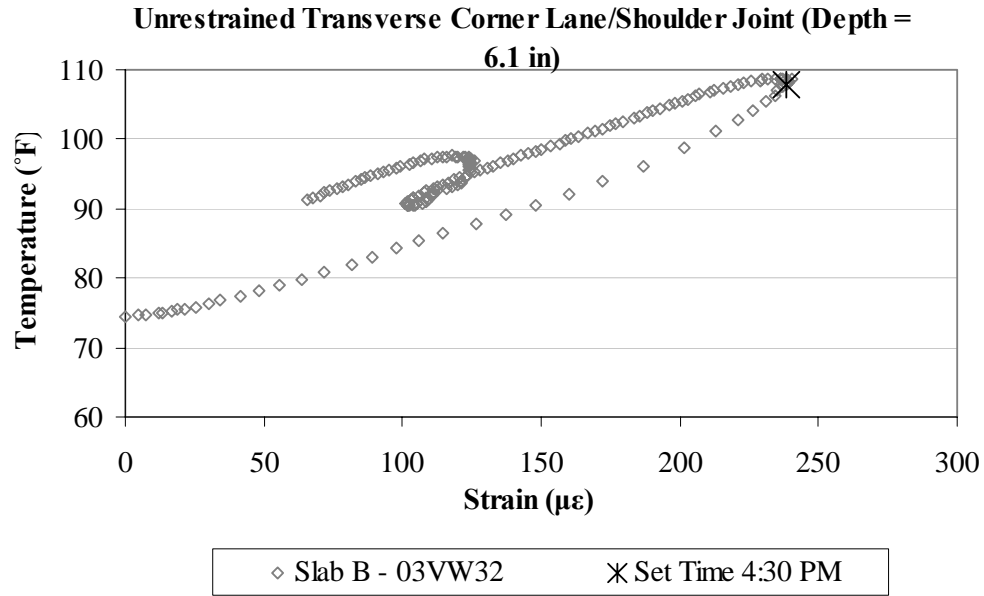


Figure B.121. Variation of strain with temperature, in the transverse direction, for the middepth sensor located at the corner along the lane/shoulder joint in unrestrained Slab B.

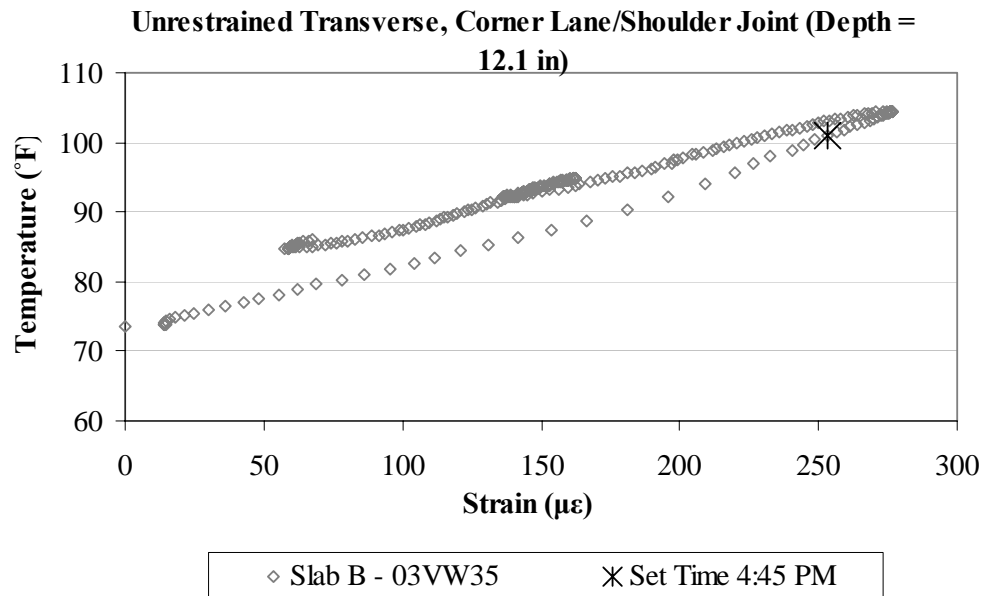


Figure B.122. Variation of strain with temperature, in the transverse direction, for the bottom sensor located at the corner along the lane/shoulder joint in unrestrained Slab B.

B.6 UNRESTRAINED SLAB C (CELL 3)

Unrestrained Longitudinal, Corner Centerline (Depth = 1.4 in)

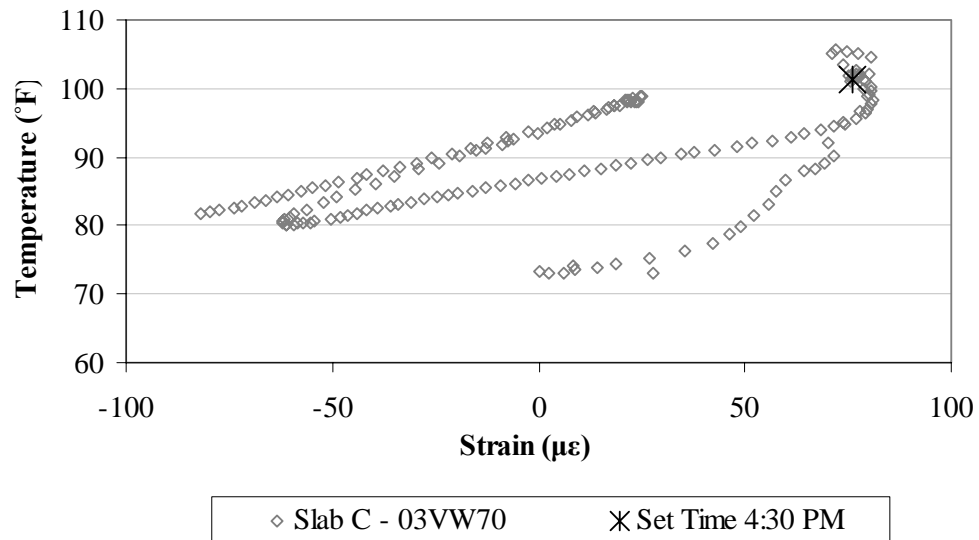


Figure B.123. Variation of strain with temperature, in the longitudinal direction, for the top sensor located at the corner along the centerline joint in unrestrained Slab C.

Unrestrained Longitudinal, Corner Centerline (Depth = 5.3 in)

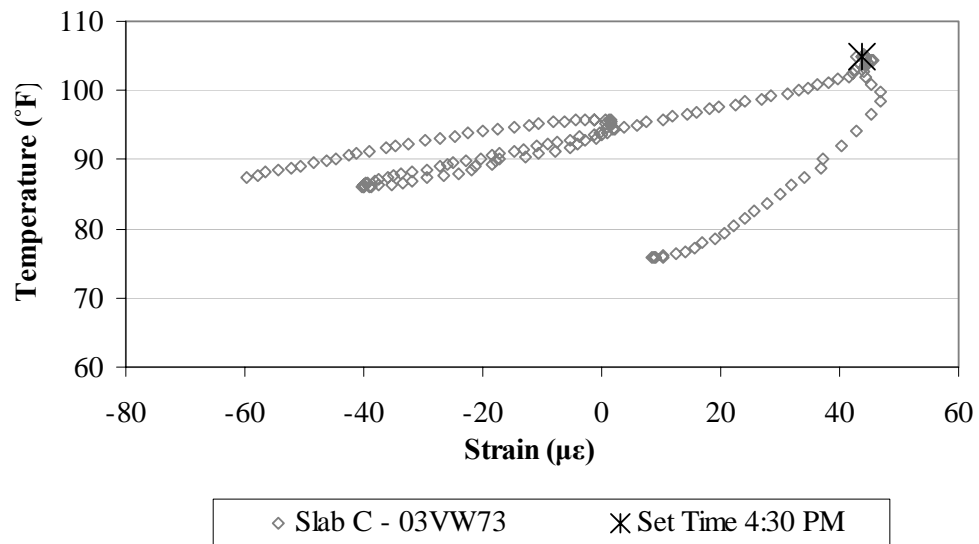


Figure B.124. Variation of strain with temperature, in the longitudinal direction, for the middepth sensor located at the corner along the centerline joint in unrestrained Slab C.

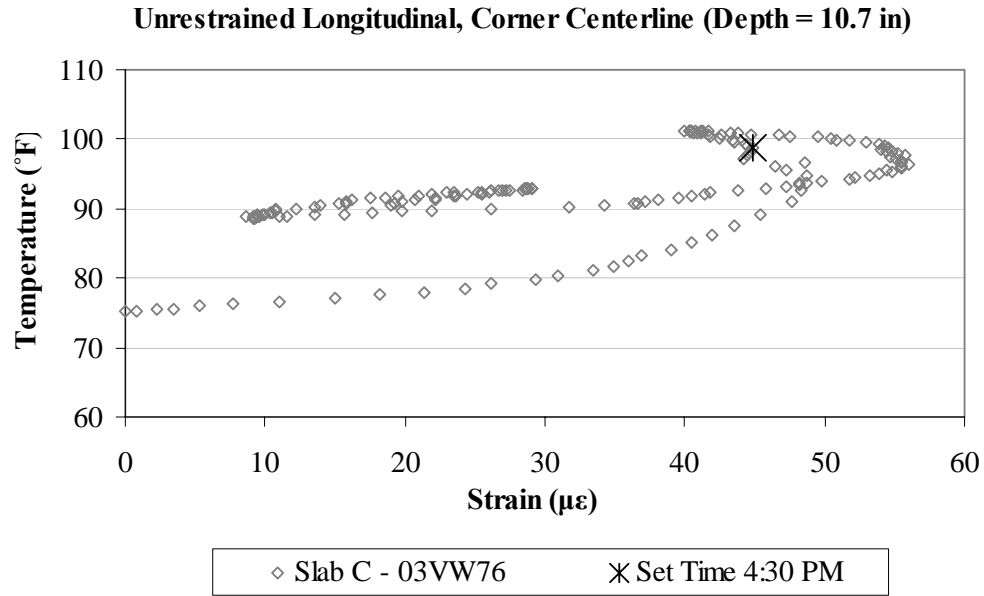


Figure B.125. Variation of strain with temperature, in the longitudinal direction, for the bottom sensor located at the corner along the centerline joint in unrestrained Slab C.

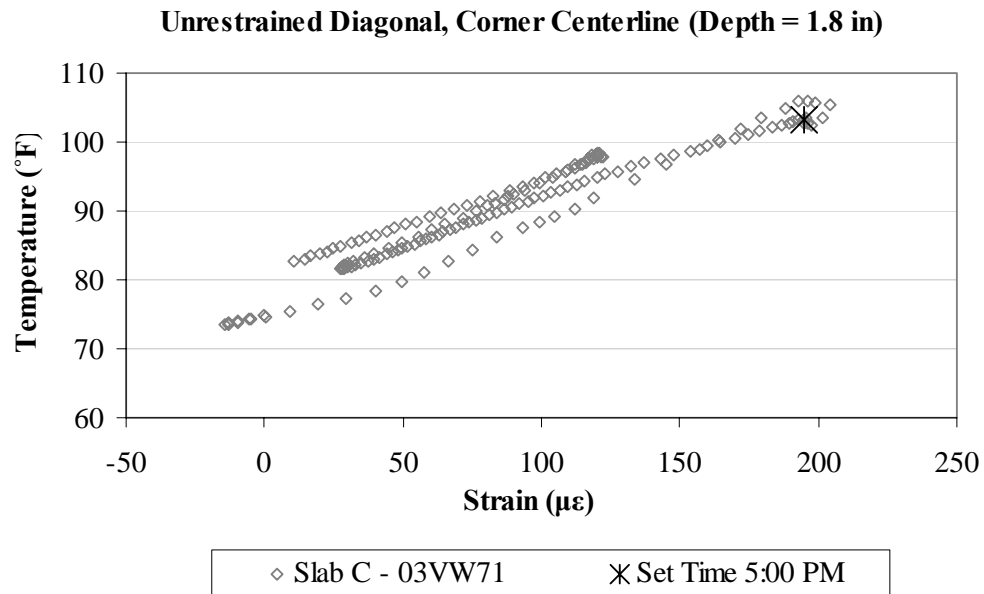


Figure B.126. Variation of strain with temperature, in the diagonal direction, for the top sensor located at the corner along the centerline joint in unrestrained Slab C.

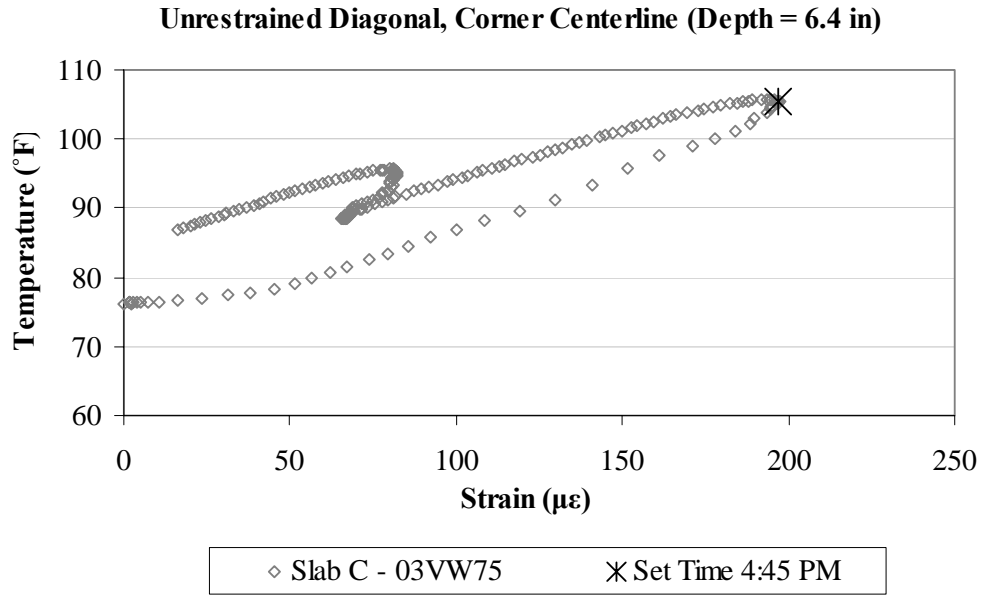


Figure B.127. Variation of strain with temperature, in the diagonal direction, for the middepth sensor located at the corner along the centerline joint in unrestrained Slab C.

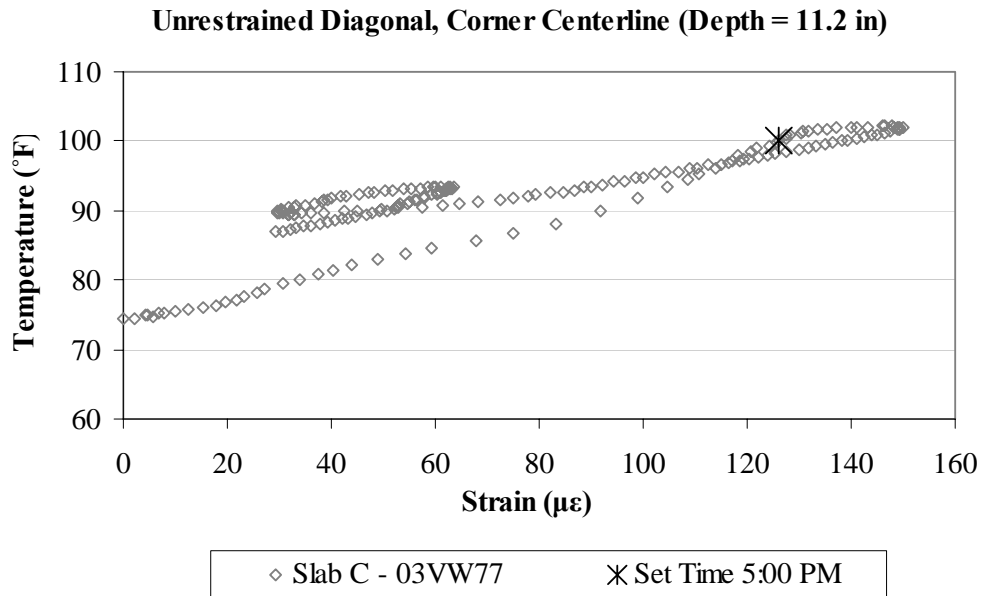


Figure B.128. Variation of strain with temperature, in the diagonal direction, for the bottom sensor located at the corner along the centerline joint in unrestrained Slab C.

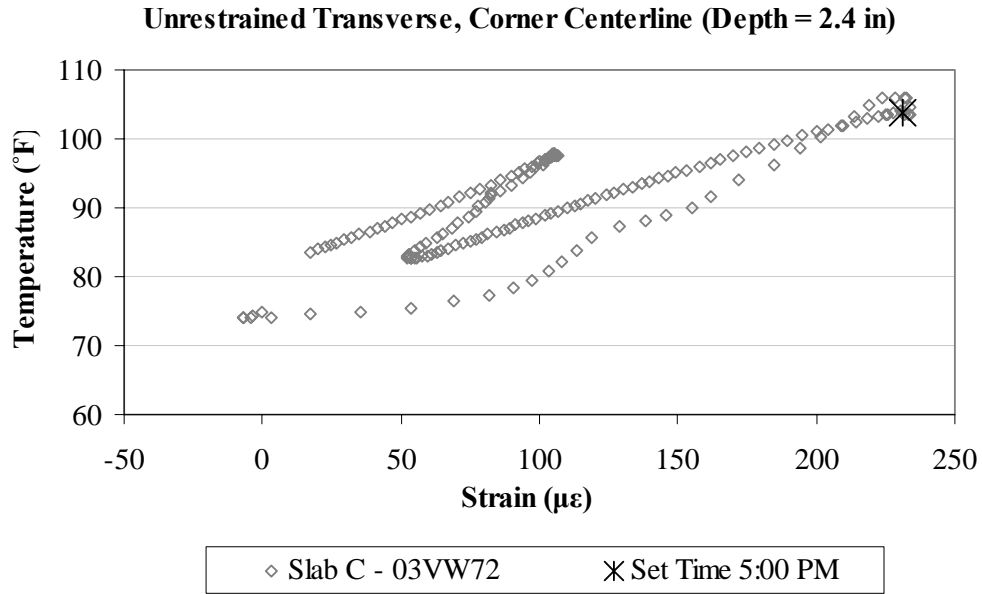


Figure B.129. Variation of strain with temperature, in the transverse direction, for the top sensor located at the corner along the centerline joint in unrestrained Slab C.

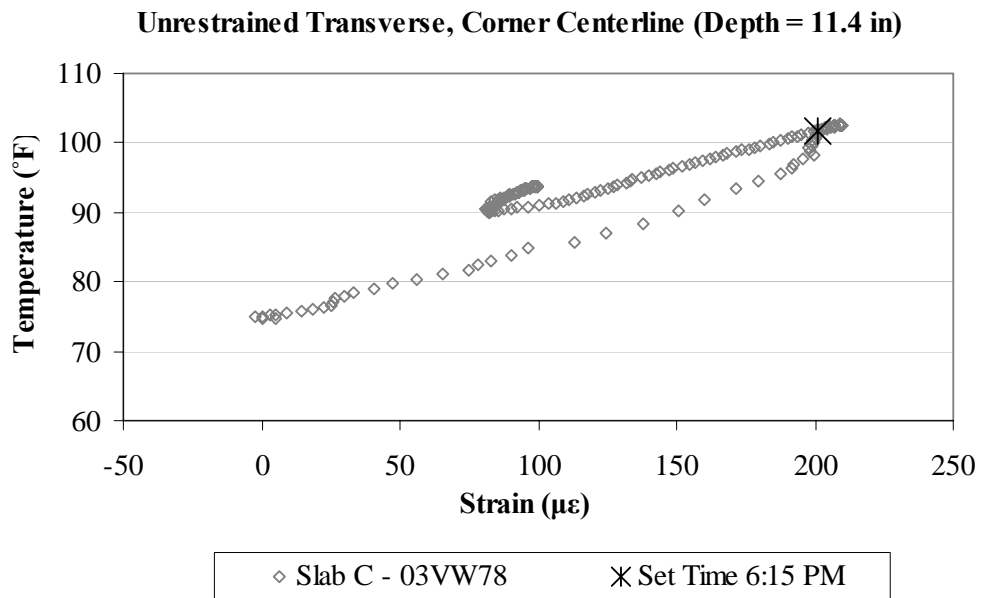


Figure B.130. Variation of strain with temperature, in the transverse direction, for the bottom sensor located at the corner along the centerline joint in unrestrained Slab C.

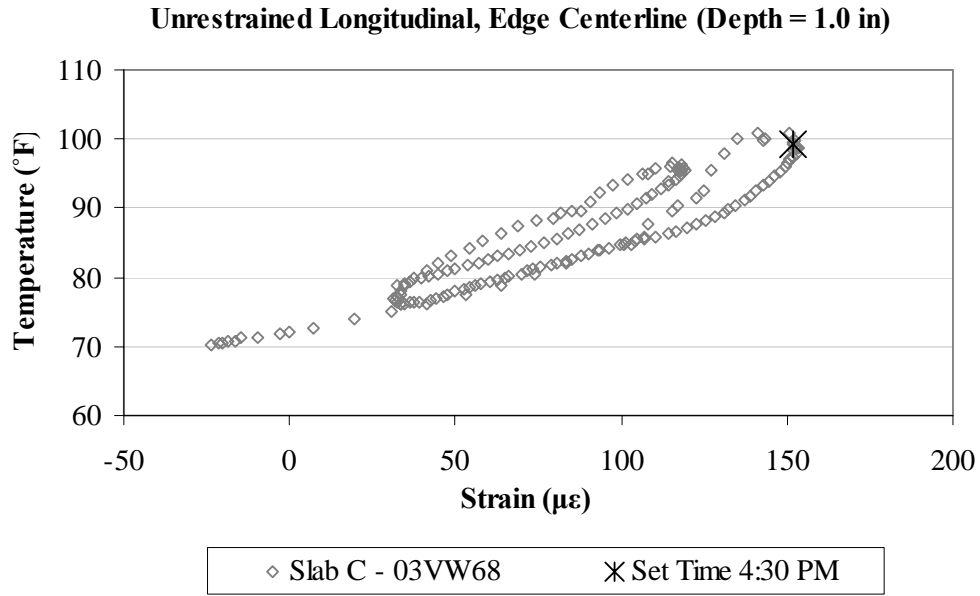


Figure B.131. Variation of strain with temperature, in the longitudinal direction, for the top sensor located along the centerline joint in unrestrained Slab C.

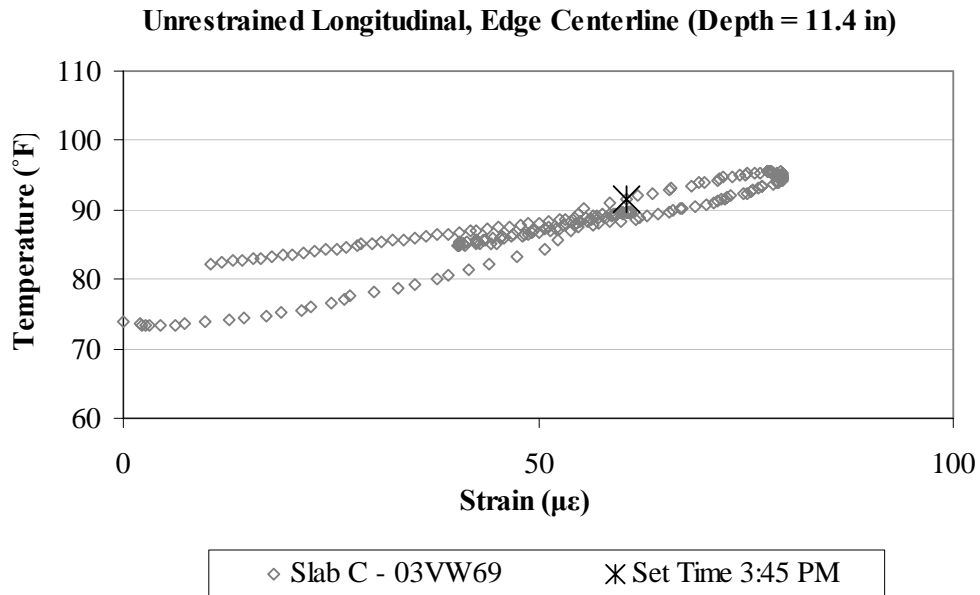


Figure B.132. Variation of strain with temperature, in the longitudinal direction, for the bottom sensor located along the centerline joint in unrestrained Slab C.

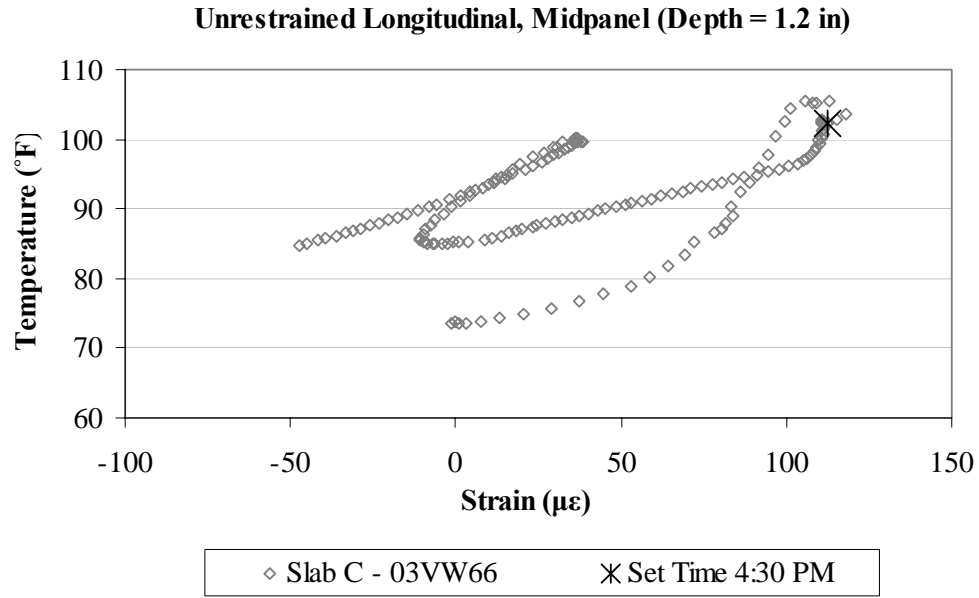


Figure B.133. Variation of strain with temperature, in the longitudinal direction, for the top sensor located at midpanel in unrestrained Slab C.

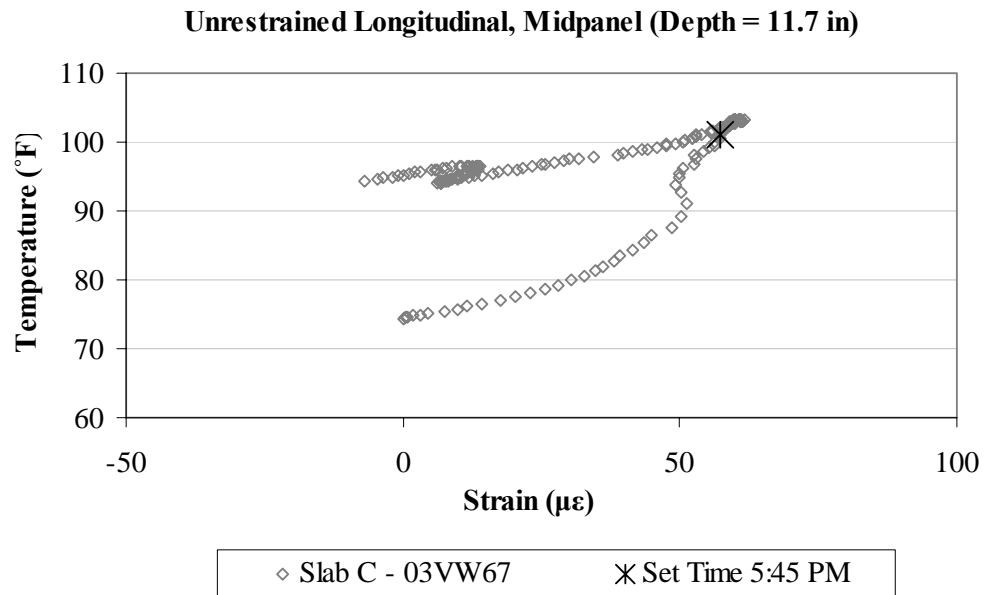


Figure B.134. Variation of strain with temperature, in the longitudinal direction, for the bottom sensor located at midpanel in unrestrained Slab C.

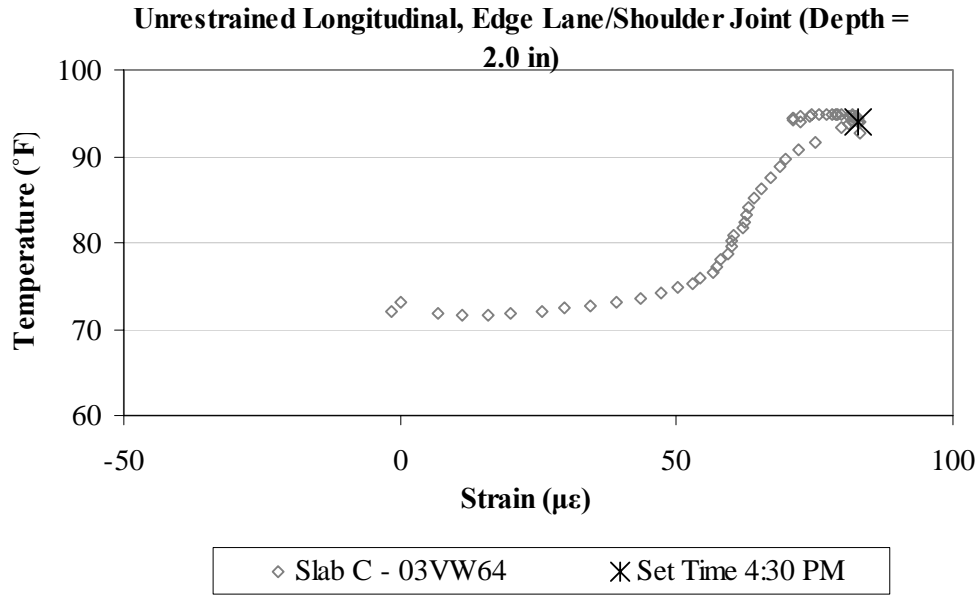


Figure B.135. Variation of strain with temperature, in the longitudinal direction, for the top sensor located along the lane/shoulder joint in unrestrained Slab C.

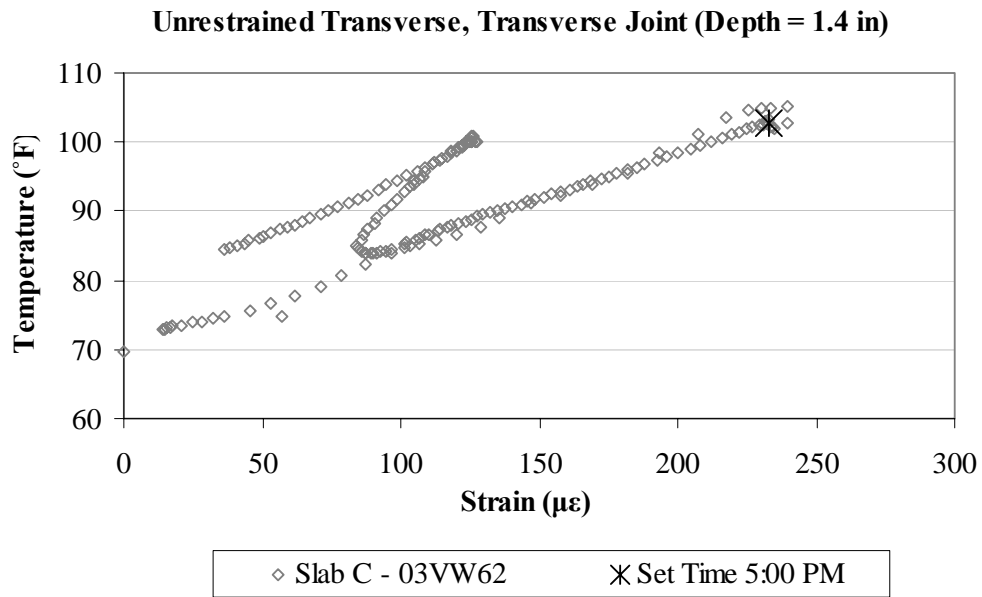


Figure B.136. Variation of strain with temperature, in the transverse direction, for the top sensor located along the transverse joint in unrestrained Slab C.

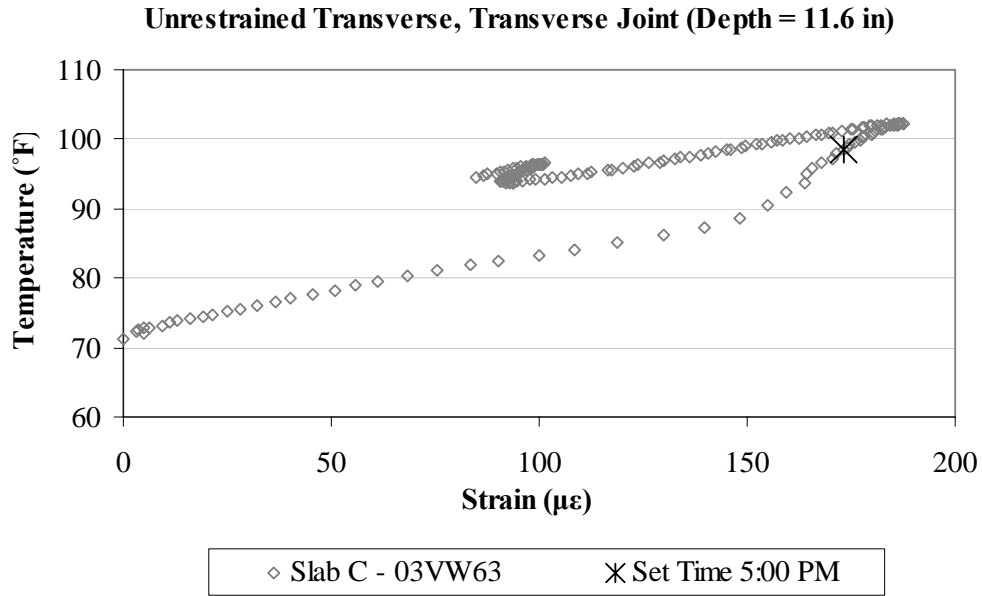


Figure B.137. Variation of strain with temperature, in the transverse direction, for the bottom sensor located along the transverse joint in unrestrained Slab C.

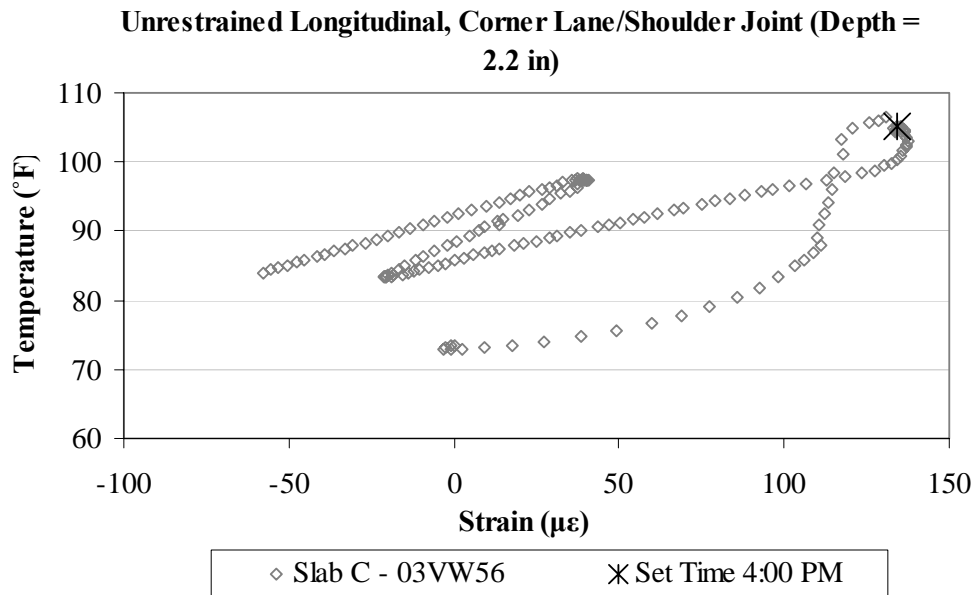


Figure B.138. Variation of strain with temperature, in the longitudinal direction, for the top sensor located at the corner along the lane/shoulder joint in unrestrained Slab C.

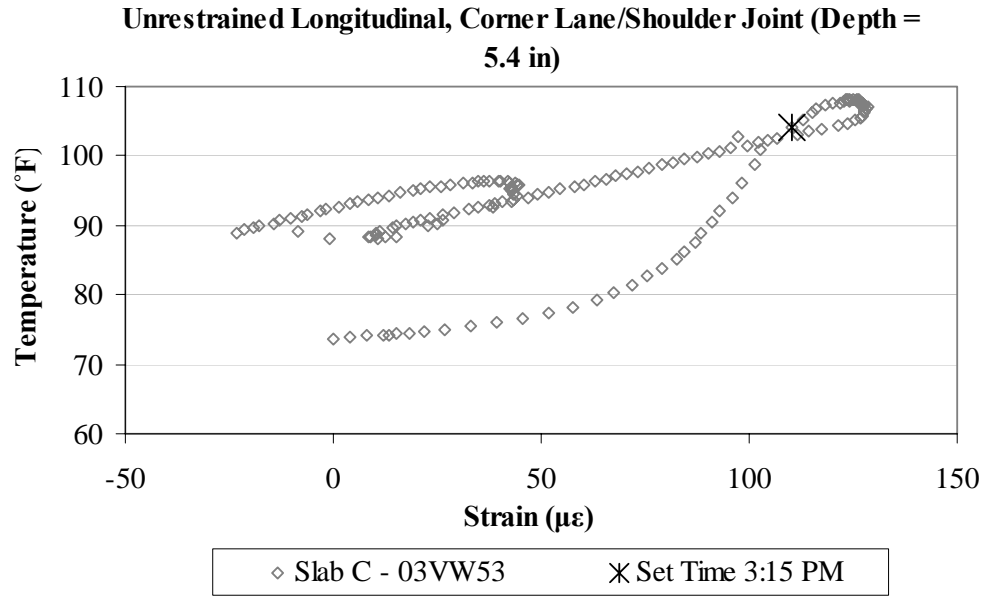


Figure B.139. Variation of strain with temperature, in the longitudinal direction, for the middepth sensor located at the corner along the lane/shoulder joint in unrestrained Slab C.

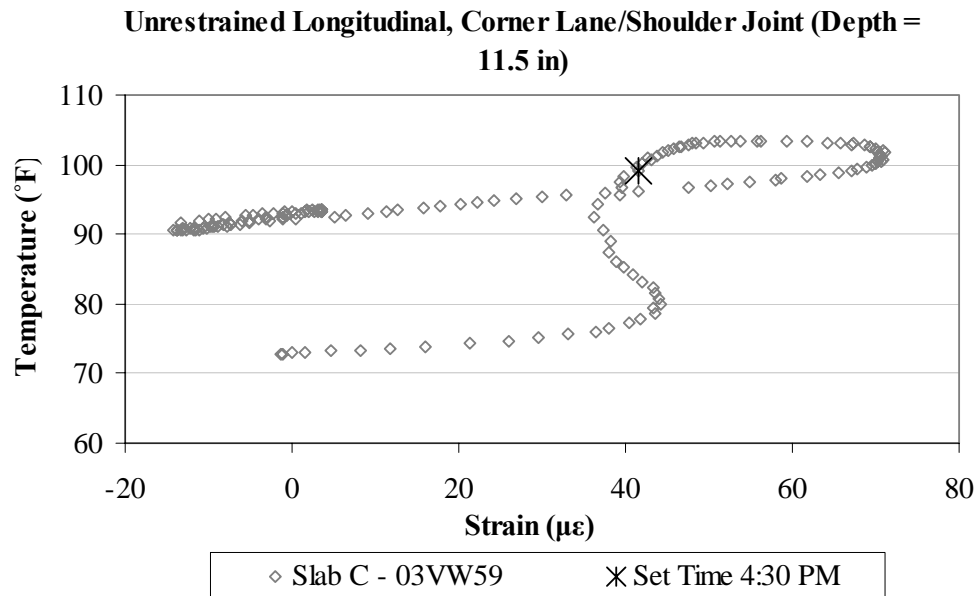


Figure B.140. Variation of strain with temperature, in the longitudinal direction, for the bottom sensor located at the corner along the lane/shoulder joint in unrestrained Slab C.

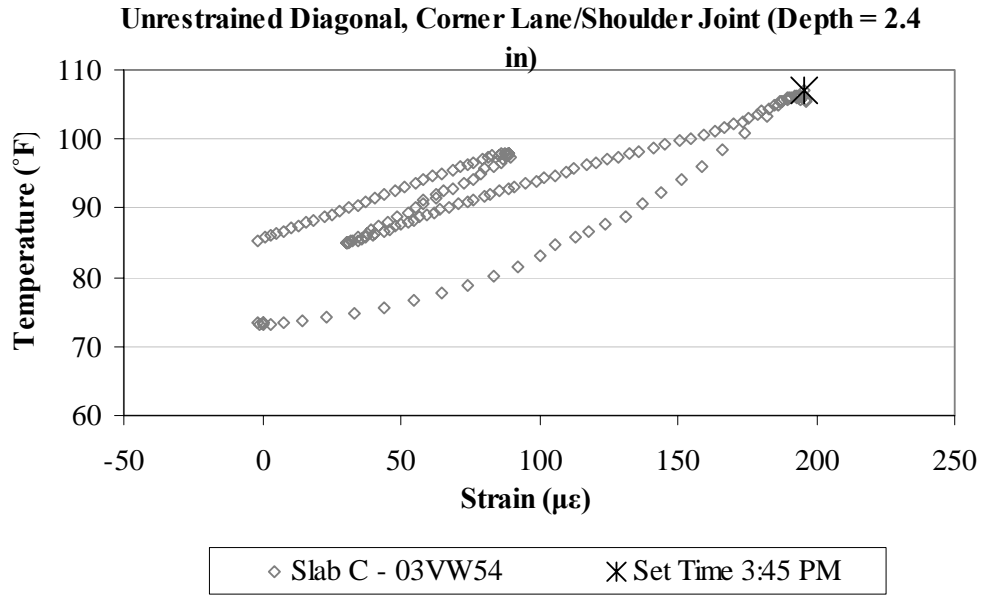


Figure B.141. Variation of strain with temperature, in the diagonal direction, for the top sensor located at the corner along the lane/shoulder joint in unrestrained Slab C.

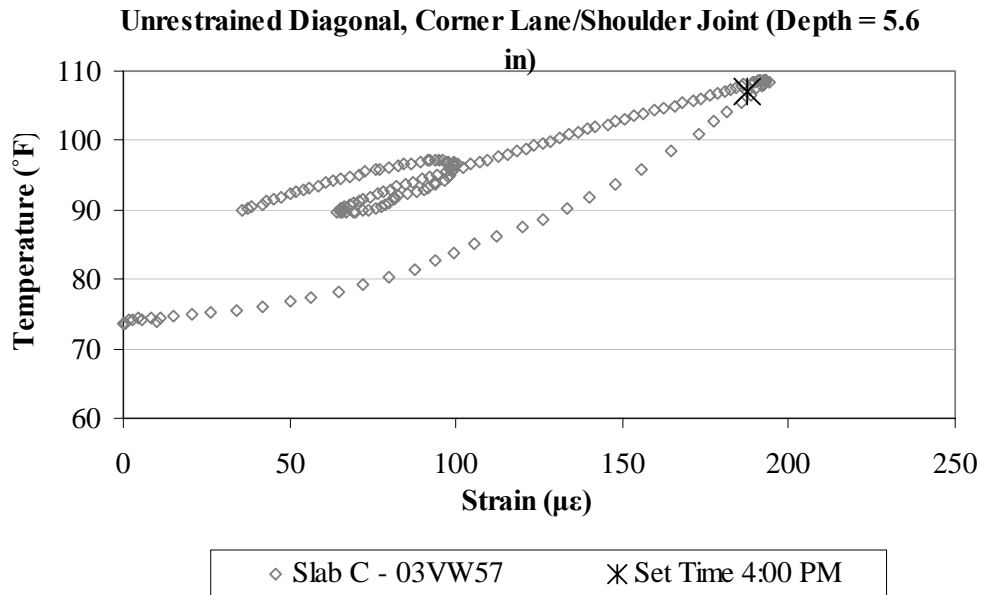


Figure B.142. Variation of strain with temperature, in the diagonal direction, for the middepth sensor located at the corner along the lane/shoulder joint in unrestrained Slab C.

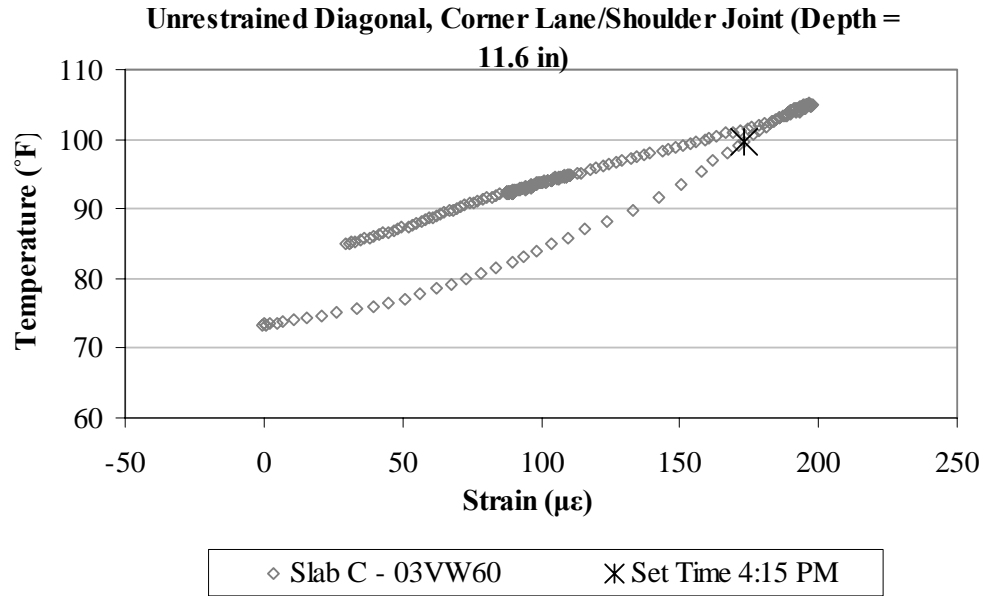


Figure B.143. Variation of strain with temperature, in the diagonal direction, for the bottom sensor located at the corner along the lane/shoulder joint in unrestrained Slab C.

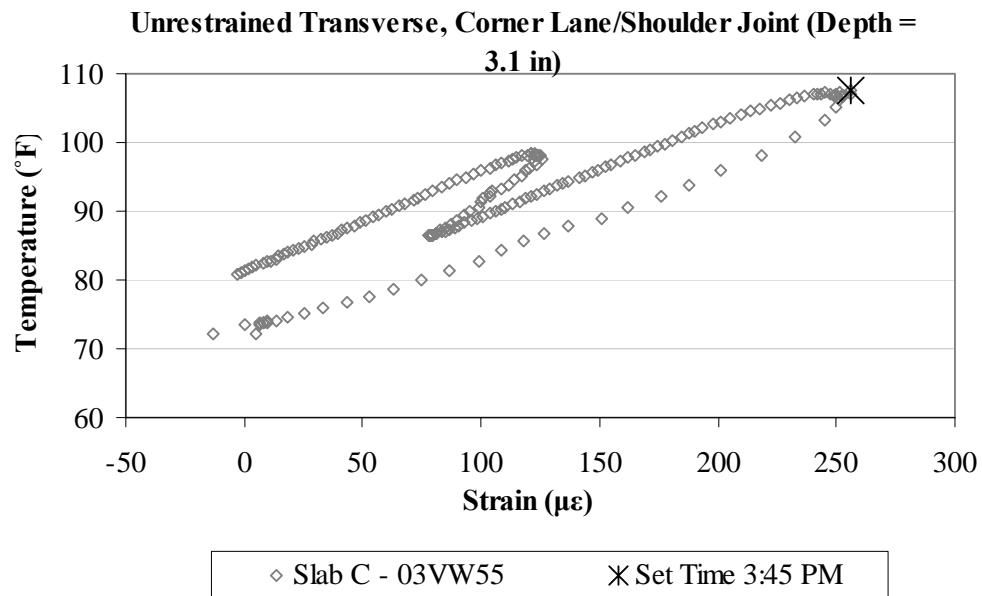


Figure B.144. Variation of strain with temperature, in the transverse direction, for the top sensor located at the corner along the lane/shoulder joint in unrestrained Slab C.

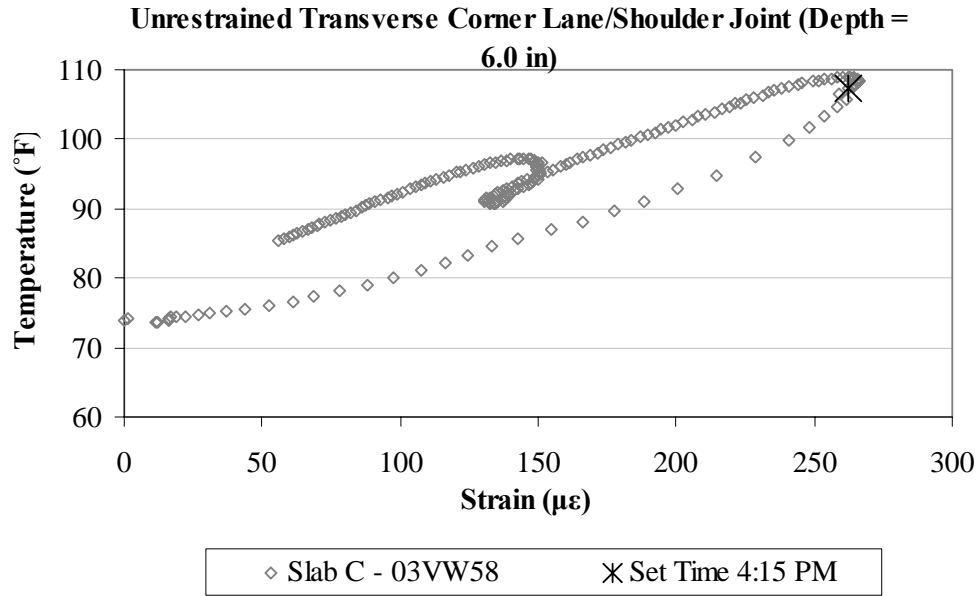


Figure B.145. Variation of strain with temperature, in the transverse direction, for the middepth sensor located at the corner along the lane/shoulder joint in unrestrained Slab C.

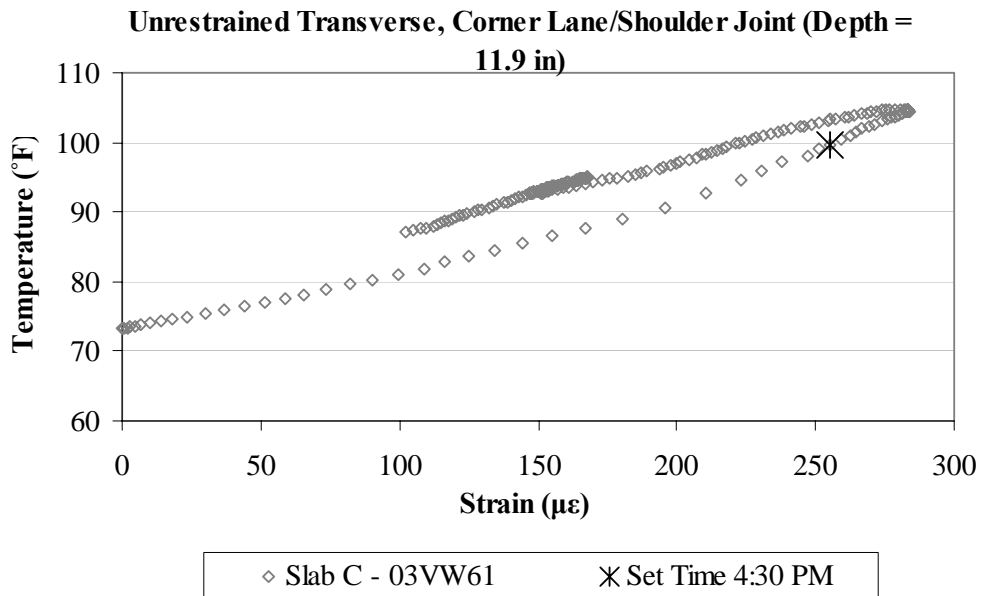


Figure B.146. Variation of strain with temperature, in the transverse direction, for the bottom sensor located at the corner along the lane/shoulder joint in unrestrained Slab C.

Appendix C: Design Inputs for the MEPDG

Table C.1. Traffic volume adjustment factors for Level 1 & 2 analysis.

Traffic -- Volume Adjustment Factors						
Monthly Adjustment Factors						
Month	Vehicle Class					
	Class 4	Class 5	Class 6	Class 7	Class 8	Class 9
January	0.80	0.80	0.80	0.80	0.80	0.80
February	0.80	0.80	0.80	0.80	0.80	0.80
March	1.02	1.02	1.02	1.02	1.02	1.02
April	1.06	1.06	1.06	1.06	1.06	1.06
May	1.07	1.07	1.07	1.07	1.07	1.07
June	1.09	1.09	1.09	1.09	1.09	1.09
July	1.06	1.06	1.06	1.06	1.06	1.06
August	1.05	1.05	1.05	1.05	1.05	1.05
September	0.96	0.96	0.96	0.96	0.96	0.96
October	1.02	1.02	1.02	1.02	1.02	1.02
November	1.03	1.03	1.03	1.03	1.03	1.03
December	1.05	1.05	1.05	1.05	1.05	1.05

Table C.2. Hourly truck traffic distribution for Level 1 & 2 analysis.

Hourly truck traffic distribution			
Midnight	0.7%	Noon	5.6%
1:00 am	0.4%	1:00 pm	5.5%
2:00 am	0.4%	2:00 pm	5.5%
3:00 am	0.5%	3:00 pm	5.6%
4:00 am	1.1%	4:00 pm	5.6%
5:00 am	4.1%	5:00 pm	6.2%
6:00 am	7.3%	6:00 pm	5.4%
7:00 am	7.9%	7:00 pm	4.2%
8:00 am	6.9%	8:00 pm	3.4%
9:00 am	6.0%	9:00 pm	3.0%
10:00 am	5.8%	10:00 pm	1.9%
11:00 am	5.8%	11:00 pm	1.2%

Table C.3. Vehicle class distribution for Level 1 & 2 analysis.

Vehicle Class Distribution	
AADTT distribution by vehicle class	
Class 4	2.0%
Class 5	39.0%
Class 6	3.0%
Class 7	1.0%
Class 8	7.0%
Class 9	48.0%
Class 10	0.0%
Class 11	0.0%
Class 12	0.0%
Class 13	0.0%

Table C.4. Traffic growth factors for Level 1 & 2 analysis.

Traffic Growth Factor		
Vehicle Class	Growth Rate	Growth Function
Class 4	1.6%	Linear
Class 5	1.6%	Linear
Class 6	1.6%	Linear
Class 7	1.6%	Linear
Class 8	1.6%	Linear
Class 9	1.6%	Linear
Class 10	1.6%	Linear
Class 11	1.6%	Linear
Class 12	1.6%	Linear
Class 13	1.6%	Linear

Table C.5. General traffic inputs for Level 1 & 2 analysis.

General Traffic Inputs				
Mean wheel location (inches from the lane marking):			18	
Traffic wander standard deviation (in):			10	
Design lane width (ft):			12	
Number of Axles per Truck				
Vehicle Class	Single Axle	Tandem Axle	Tridem Axle	Quad Axle
Class 4	1.62	0.39	0.00	0.00
Class 5	2.00	0.00	0.00	0.00
Class 6	1.02	0.99	0.00	0.00
Class 7	1.00	0.26	0.83	0.00
Class 8	2.38	0.67	0.00	0.00
Class 9	1.13	1.93	0.00	0.00
Class 10	1.19	1.09	0.89	0.00
Class 11	4.29	0.26	0.06	0.00
Class 12	3.52	1.14	0.06	0.00
Class 13	2.15	2.13	0.35	0.00
Axle Configuration				
Average axle width (edge-to-edge) outside dimensions,ft):			8.5	
Dual tire spacing (in):			12	
Tire Pressure (psi)			120	
Average Axle Spacing				
Tandem axle(psi):		51.6		
Tridem axle(psi):		49.2		
Quad axle(psi):		49.2		
Wheelbase Truck Tractor				
	Short	Medium	Long	
Average Axle Spacing (ft)	12	15	18	
Percent of trucks	33%	33%	34%	
Climate				
icm file:	C:\DG2002\Projects\onsite station Aug04 Oct07.icm			
Latitude (degrees.minutes)	40.43			
Longitude (degrees.minutes)	-79.66			
Elevation (ft)	935			
Depth of water table (ft)	9			

Table C.6. Traffic volume adjustment factors for Level 3 analysis.

Traffic -- Volume Adjustment Factors						
Monthly Adjustment Factors						
Month	Vehicle Class					
	Class 4	Class 5	Class 6	Class 7	Class 8	Class 9
January	1.00	1.00	1.00	1.00	1.00	1.00
February	1.00	1.00	1.00	1.00	1.00	1.00
March	1.00	1.00	1.00	1.00	1.00	1.00
April	1.00	1.00	1.00	1.00	1.00	1.00
May	1.00	1.00	1.00	1.00	1.00	1.00
June	1.00	1.00	1.00	1.00	1.00	1.00
July	1.00	1.00	1.00	1.00	1.00	1.00
August	1.00	1.00	1.00	1.00	1.00	1.00
September	1.00	1.00	1.00	1.00	1.00	1.00
October	1.00	1.00	1.00	1.00	1.00	1.00
November	1.00	1.00	1.00	1.00	1.00	1.00
December	1.00	1.00	1.00	1.00	1.00	1.00

Table C.7. Hourly truck traffic distribution for Level 3 analysis.

Hourly truck traffic distribution			
Midnight	2.3%	Noon	5.9%
1:00 am	2.3%	1:00 pm	5.9%
2:00 am	2.3%	2:00 pm	5.9%
3:00 am	2.3%	3:00 pm	5.9%
4:00 am	2.3%	4:00 pm	4.6%
5:00 am	2.3%	5:00 pm	4.6%
6:00 am	5.0%	6:00 pm	4.6%
7:00 am	5.0%	7:00 pm	4.6%
8:00 am	5.0%	8:00 pm	3.1%
9:00 am	5.0%	9:00 pm	3.1%
10:00 am	5.9%	10:00 pm	3.1%
11:00 am	5.9%	11:00 pm	3.1%

Table C.8. Vehicle class distribution for Level 3 analysis.

Vehicle Class Distribution	
AADTT distribution by vehicle class	
Class 4	1.3%
Class 5	8.5%
Class 6	2.8%
Class 7	0.2%
Class 8	7.6%
Class 9	74.0%
Class 10	1.2%
Class 11	3.4%
Class 12	0.6%
Class 13	0.3%

Table C.9. Traffic growth factors for Level 3 analysis.

Traffic Growth Factor		
Vehicle Class	Growth Rate	Growth Function
Class 4	4.0%	Compound
Class 5	4.0%	Compound
Class 6	4.0%	Compound
Class 7	4.0%	Compound
Class 8	4.0%	Compound
Class 9	4.0%	Compound
Class 10	4.0%	Compound
Class 11	4.0%	Compound
Class 12	4.0%	Compound
Class 13	4.0%	Compound

Table C.10. General traffic inputs for Level 3 analysis.

Traffic -- Axle Load Distribution Factors				
Level 3:		Default		
Traffic -- General Traffic Inputs				
Mean wheel location (inches from the lane marking):				18
Traffic wander standard deviation (in):				10
Design lane width (ft):				12
Number of Axles per Truck				
Vehicle Class	Single Axle	Tandem Axle	Tridem Axle	Quad Axle
Class 4	1.62	0.39	0.00	0.00
Class 5	2.00	0.00	0.00	0.00
Class 6	1.02	0.99	0.00	0.00
Class 7	1.00	0.26	0.83	0.00
Class 8	2.38	0.67	0.00	0.00
Class 9	1.13	1.93	0.00	0.00
Class 10	1.19	1.09	0.89	0.00
Class 11	4.29	0.26	0.06	0.00
Class 12	3.52	1.14	0.06	0.00
Class 13	2.15	2.13	0.35	0.00
Axle Configuration				
Average axle width (edge-to-edge) outside dimensions,ft):				8.5
Dual tire spacing (in):				12
Tire Pressure (psi)				120
Average Axle Spacing				
Tandem axle(psi):			51.6	
Tridem axle(psi):			49.2	
Quad axle(psi):			49.2	
Wheelbase Truck Tractor				
	Short	Medium	Long	
Average Axle Spacing (ft)	12	15	18	
Percent of trucks	33%	33%	34%	
Climate				
icm file:	C:\DG2002\Projects\Pittsburgh.icm			
Latitude (degrees.minutes)	40.43			
Longitude (degrees.minutes)	-79.66			
Elevation (ft)	935			
Depth of water table (ft)	9			

Table C.11. PCC general, thermal, and mix properties for Level 1 analysis.

JPCP	
General Properties	
PCC material	JPCP
Layer thickness (in):	7
Unit weight (pcf):	143.4
Poisson's ratio	0.17
Thermal Properties	
Coefficient of thermal expansion (per F° x 10- 6):	5.9
Thermal conductivity (BTU/hr-ft-F°) :	1.25
Heat capacity (BTU/lb-F°):	0.24
Mix Properties	
Cement type:	Type I
Cementitious material content (lb/yd^3):	588
Water/cement ratio:	0.44
Aggregate type:	Limestone
PCC zero-stress temperature (F°)	104
Ultimate shrinkage at 40% R.H (microstrain)	945
Reversible shrinkage (% of ultimate shrinkage):	50
Time to develop 50% of ultimate shrinkage (days):	10
Curing method:	Curing compound

Table C.12. PCC strength characterization for Level 1 analysis.

Strength Properties		
Time	Epcc (psi)	MR (psi)
7 Day	3100000	878
14 Day	3300000	888
28 Day	4274583	716.6
90 Day	4690000	950
20 Year/28 Day	1.2	1.2

Table C.13. PCC general, thermal, and mix properties for Level 2 analysis.

Layer 1 -- JPCP	
General Properties	
PCC material	JPCP
Layer thickness (in):	7
Unit weight (pcf):	143.4
Poisson's ratio	0.17
Thermal Properties	
Coefficient of thermal expansion (per F° x 10- 6):	7.14
Thermal conductivity (BTU/hr-ft-F°) :	1.25
Heat capacity (BTU/lb-F°):	0.24
Mix Properties	
Cement type:	Type I
Cementitious material content (lb/yd^3):	588
Water/cement ratio:	0.44
Aggregate type:	Limestone
PCC zero-stress temperature (F°)	104
Ultimate shrinkage at 40% R.H (microstrain)	713
Reversible shrinkage (% of ultimate shrinkage):	50
Time to develop 50% of ultimate shrinkage (days):	35
Curing method:	Curing compound

Table C.14. PCC strength characterization for Level 2 analysis.

Strength Properties	
Time	Compressive Strength
7 Day	4443 psi
14 Day	4597 psi
28 Day	5690 psi
90 Day	5780 psi
20 Year/28 Day	1.35

Table C.15. PCC general, thermal, and mix properties for Level 3 analysis.

Layer 1 -- JPCP	
General Properties	
PCC material	JPCP
Layer thickness (in):	7
Unit weight (pcf):	150
Poisson's ratio	0.18
Thermal Properties	
Coefficient of thermal expansion (per F° x 10 ⁻⁶):	5.4
Thermal conductivity (BTU/hr-ft-F°) :	1.25
Heat capacity (BTU/lb-F°):	0.24
Mix Properties	
Cement type:	Type I
Cementitious material content (lb/yd ³):	600
Water/cement ratio:	0.42
Aggregate type:	Limestone
PCC zero-stress temperature (F°)	Derived
Ultimate shrinkage at 40% R.H (microstrain)	713
Reversible shrinkage (% of ultimate shrinkage):	50
Time to develop 50% of ultimate shrinkage (days):	35
Curing method:	Curing compound

Table C.16. PCC strength characterization for Level 3 analysis.

Strength Properties	
28-day PCC compressive strength (psi)	5868

Table C.17. Asphalt treated permeable base properties for all hierarchical levels.

Layer 2 -- Asphalt treated permeable base	
Material type:	Asphalt permeable base
Layer thickness (in):	4
General Properties	
General Reference temperature (F°):	68
Volumetric Properties as Built	
Effective binder content (%):	2.5
Air voids (%):	8.5
Total unit weight (pcf):	148
Poisson's ratio:	0.35
Thermal Properties	
Thermal conductivity asphalt (BTU/hr-ft-F°):	0.62
Heat capacity asphalt (BTU/lb-F°):	0.31
Asphalt Mix	
Cumulative % Retained 3/4 inch sieve:	28
Cumulative % Retained 3/8 inch sieve:	67.5
Cumulative % Retained #4 sieve:	84
% Passing #200 sieve:	3
Asphalt Binder	
Option:	Superpave binder grading
A	10.9800 (correlated)
VTS:	-3.6800 (correlated)
Superpave Binder Grading	PG64-22

Table C.18. Subbase characterization for Level 1 analysis.

Layer 3 -- Crushed stone		
Unbound Material:		Crushed stone
Thickness(in):		5
Strength Properties		
Analysis Type:		ICM inputs (ICM Calculated Modulus)
Poisson's ratio:		0.4
Coefficient of lateral pressure,Ko:		0.5
Modulus (input) (psi):		19500
ICM Inputs		
Gradation and Plasticity Index		
Plasticity Index, PI:		10
Liquid Limit (LL)		10
Compacted Layer		Yes
Passing #200 sieve (%):		5
Passing #40		14.4
Passing #4 sieve (%):		37
D10(mm)		0.1879
D20(mm)		1.18
D30(mm)		2.911
D60(mm)		10.33
D90(mm)		28.06
Sieve	Minimum Percent Passing	Maximum Percent Passing
#200	0	10
#16	10	30
#8	16	38
#4	24	50
3/8"	36	70
1/2"	52	100
2"	100	100
Calculated/Derived Parameters		
Maximum dry unit weight (pcf):		121.6 (user input)
Specific gravity of solids, Gs:		2.68 (user input)
Saturated hydraulic conductivity (ft/hr):		0.6 (user input)
Optimum gravimetric water content (%):		11.8 (user input)
Calculated degree of saturation (%):		84.3 (calculated)
Soil water characteristic curve parameters:		Default values

Table C.19. Subbase characterization for Level 2 analysis.

Layer 3 -- Crushed stone		
Unbound Material:		Crushed stone
Thickness(in):		5
Strength Properties		
Analysis Type:		ICM inputs (ICM Calculated Modulus)
Poisson's ratio:		0.4
Coefficient of lateral pressure,Ko:		0.5
Modulus (input) (psi):		19500
ICM Inputs		
Gradation and Plasticity Index		
Plasticity Index, PI:		10
Liquid Limit (LL)		10
Compacted Layer		Yes
Passing #200 sieve (%):		5
Passing #40		14.4
Passing #4 sieve (%):		37
D10(mm)		0.1879
D20(mm)		1.18
D30(mm)		2.911
D60(mm)		10.33
D90(mm)		28.06
Sieve	Minimum Percent Passing	Maximum Percent Passing
#200	0	10
#16	10	30
#8	16	38
#4	24	50
3/8"	36	70
1/2"	52	100
2"	100	100
Calculated/Derived Parameters		
Maximum dry unit weight (pcf):		127.8 (derived)
Specific gravity of solids, Gs:		2.70 (derived)
Saturated hydraulic conductivity (ft/hr):		0.06011 (derived)
Optimum gravimetric water content (%):		7.3 (derived)
Calculated degree of saturation (%):		62.0 (calculated)
Soil water characteristic curve parameters:		Default values

Table C.20. Subbase characterization for Level 3 analysis.

Layer 3 -- A-2-5	
Unbound Material:	A-2-5
Thickness(in):	5
Strength Properties	
Analysis Type:	ICM inputs (ICM Calculated Modulus)
Poisson's ratio:	0.4
Coefficient of lateral pressure,Ko:	0.5
Modulus (input) (psi):	16000
ICM Inputs	
<u>Gradation and Plasticity Index</u>	
Plasticity Index, PI:	6
Liquid Limit (LL)	50
Compacted Layer	Yes
Passing #200 sieve (%):	30
Passing #40	61
Passing #4 sieve (%):	81
D10(mm)	0.0009086
D20(mm)	0.008255
D30(mm)	0.075
D60(mm)	0.4057
D90(mm)	12.5
Sieve	Percent Passing
#200	30
#80	46
#40	61
#10	75
#4	81
3/8"	88
1/2"	90
3/4"	94
1"	98
1 1/2"	100
2"	100
3 1/2"	100
4"	100
<u>Calculated/Derived Parameters</u>	
Maximum dry unit weight (pcf):	121.9 (derived)
Specific gravity of solids, Gs:	2.70 (derived)
Saturated hydraulic conductivity (ft/hr):	4.64e-007 (derived)
Optimum gravimetric water content (%):	10.1 (derived)
Calculated degree of saturation (%):	71.0 (calculated)
Soil water characteristic curve parameters:	Default values

Table C.21. Characterization of the fill material for Level 1 analysis.

FILL MATERIAL		
Unbound Material:		Crushed stone
Thickness(in):		24
Strength Properties		
Analysis Type:		ICM inputs (ICM Calculated Modulus)
Poisson's ratio:		0.4
Coefficient of lateral pressure,Ko:		0.5
Modulus (input) (psi):		19500
ICM Inputs		
Gradation and Plasticity Index		
Plasticity Index, PI:		6
Liquid Limit (LL)		6
Compacted Layer		Yes
Passing #200 sieve (%):		7.5
Passing #40		15
Passing #4 sieve (%):		36.6
D10(mm)		0.1337
D20(mm)		0.922
D30(mm)		2.906
D60(mm)		27.35
D90(mm)		64.78
Sieve	Minimum Percent Passing	Maximum Percent Passing
#200	0	15
#40	0	30
#10	0	50
3"	65	82
Calculated/Derived Parameters		
Maximum dry unit weight (pcf):		121.0 (user input)
Specific gravity of solids, Gs:		2.69 (user input)
Saturated hydraulic conductivity (ft/hr):		3 (user input)
Optimum gravimetric water content (%):		12.2 (user input)
Calculated degree of saturation (%):		84.7 (calculated)
Soil water characteristic curve parameters:		Default values

Table C.22. Characterization of the fill material for Level 2 analysis.

Layer 4 -- Crushed stone		
Unbound Material:		Crushed stone
Thickness(in):		24
Strength Properties		
Analysis Type:		ICM inputs (ICM Calculated Modulus)
Poisson's ratio:		0.4
Coefficient of lateral pressure,Ko:		0.5
Modulus (input) (psi):		19500
ICM Inputs		
Gradation and Plasticity Index		
Plasticity Index, PI:		6
Liquid Limit (LL)		6
Compacted Layer		Yes
Passing #200 sieve (%):		7.5
Passing #40		15
Passing #4 sieve (%):		36.6
D10(mm)		0.1337
D20(mm)		0.922
D30(mm)		2.906
D60(mm)		27.35
D90(mm)		64.78
Sieve	Minimum Percent Passing	Maximum Percent Passing
#200	0	15
#40	0	30
#10	0	50
3"	65	82
Calculated/Derived Parameters		
Maximum dry unit weight (pcf):		108.8 (derived)
Specific gravity of solids, Gs:		2.70 (derived)
Saturated hydraulic conductivity (ft/hr):		3.112 (derived)
Optimum gravimetric water content (%):		17.0 (derived)
Calculated degree of saturation (%):		83.7 (calculated)
Soil water characteristic curve parameters:		Default values

Table C.23. Characterization of the fill material for Level 3 analysis.

Layer 4 -- A-1-a	
Unbound Material:	A-1-a
Thickness(in):	24
Strength Properties	
Analysis Type:	ICM inputs (ICM Calculated Modulus)
Poisson's ratio:	0.4
Coefficient of lateral pressure,Ko:	0.5
Modulus (input) (psi):	18000
ICM Inputs	
Gradation and Plasticity Index	
Plasticity Index, PI:	1
Liquid Limit (LL)	6
Compacted Layer	Yes
Passing #200 sieve (%):	8.7
Passing #40	20
Passing #4 sieve (%):	44.7
D10(mm)	0.1035
D20(mm)	0.425
D30(mm)	1.306
D60(mm)	10.82
D90(mm)	46.19
Sieve	Percent Passing
#200	8.7
#80	12.9
#40	20
#10	33.8
#4	44.7
3/8"	57.2
1/2"	63.1
3/4"	72.7
1"	78.8
1 1/2"	85.8
2"	91.6
3 1/2"	97.6
4"	97.6
Calculated/Derived Parameters	
Maximum dry unit weight (pcf):	127.2 (derived)
Specific gravity of solids, Gs:	2.70 (derived)
Saturated hydraulic conductivity (ft/hr):	0.05054 (derived)
Optimum gravimetric water content (%):	7.4 (derived)
Calculated degree of saturation (%):	61.2 (calculated)
Soil water characteristic curve parameters:	Default values

Table C.24. Subgrade characterization for Level 1 analysis.

SUBGRADE	
Unbound Material:	A-6
Thickness(in):	Semi-infinite
Strength Properties	
Analysis Type:	ICM inputs (ICM Calculated Modulus)
Poisson's ratio:	0.4
Coefficient of lateral pressure,Ko:	0.5
Modulus (input) (psi):	4500
ICM Inputs	
Gradation and Plasticity Index	
Plasticity Index, PI:	11
Liquid Limit (LL)	11
Compacted Layer	Yes
Passing #200 sieve (%):	77
Passing #40	98
Passing #4 sieve (%):	100
D10(mm)	0.0002212
D20(mm)	0.0004894
D30(mm)	0.001189
D60(mm)	0.01849
D90(mm)	0.1789
Sieve	Percent Passing
0.001mm	29
0.002mm	33
#200	77
#60	95
#40	98
#20	99
#4	100
Calculated/Derived Parameters	
Maximum dry unit weight (pcf):	110.7 (user input)
Specific gravity of solids, Gs:	2.73 (user input)
Saturated hydraulic conductivity (ft/hr):	5.7e-006 (user input)
Optimum gravimetric water content (%):	17.2 (user input)
Calculated degree of saturation (%):	87.1 (calculated)
Soil water characteristic curve parameters:	Default values

Table C.25. Subgrade characterization for Level 2 analysis.

Layer 5 -- A-6	
Unbound Material:	A-6
Thickness(in):	Semi-infinite
Strength Properties	
Analysis Type:	ICM inputs (ICM Calculated Modulus)
Poisson's ratio:	0.4
Coefficient of lateral pressure,Ko:	0.5
Modulus (input) (psi):	4500
ICM Inputs	
Gradation and Plasticity Index	
Plasticity Index, PI:	11
Liquid Limit (LL)	11
Compacted Layer	Yes
Passing #200 sieve (%):	77
Passing #40	98
Passing #4 sieve (%):	100
D10(mm)	0.0002212
D20(mm)	0.0004894
D30(mm)	0.001189
D60(mm)	0.01849
D90(mm)	0.1789
Sieve	Percent Passing
0.001mm	29
0.002mm	33
#200	77
#60	95
#40	98
#20	99
#4	100
Calculated/Derived Parameters	
Maximum dry unit weight (pcf):	110.4 (derived)
Specific gravity of solids, Gs:	2.70 (derived)
Saturated hydraulic conductivity (ft/hr):	8.283e-005 (derived)
Optimum gravimetric water content (%):	16.2 (derived)
Calculated degree of saturation (%):	83.1 (calculated)
Soil water characteristic curve parameters:	Default values

Table C.26. Subgrade characterization for Level 3 analysis.

Layer 5 -- A-6	
Unbound Material:	A-6
Thickness(in):	Semi-infinite
Strength Properties	
Analysis Type:	ICM inputs (ICM Calculated Modulus)
Poisson's ratio:	0.4
Coefficient of lateral pressure,Ko:	0.5
Modulus (input) (psi):	14000
ICM Inputs	
Gradation and Plasticity Index	
Plasticity Index, PI:	16
Liquid Limit (LL)	33
Compacted Layer	Yes
Passing #200 sieve (%):	63.2
Passing #40	82.4
Passing #4 sieve (%):	93.5
D10(mm)	0.000285
D20(mm)	0.0008125
D30(mm)	0.002316
D60(mm)	0.05364
D90(mm)	1.922
Sieve	Percent Passing
#200	63.2
#80	73.5
#40	82.4
#10	90.2
#4	93.5
3/8"	96.4
1/2"	97.4
3/4"	98.4
1"	99
1 1/2"	99.5
2"	99.8
3 1/2"	100
4"	100
Calculated/Derived Parameters	
Maximum dry unit weight (pcf):	107.9 (derived)
Specific gravity of solids, Gs:	2.70 (derived)
Saturated hydraulic conductivity (ft/hr):	1.95e-005 (derived)
Optimum gravimetric water content (%):	17.1 (derived)
Calculated degree of saturation (%):	82.1 (calculated)
Soil water characteristic curve parameters:	Default values

APPENDIX D:
Vibrating Wire Strain Gage Measurements

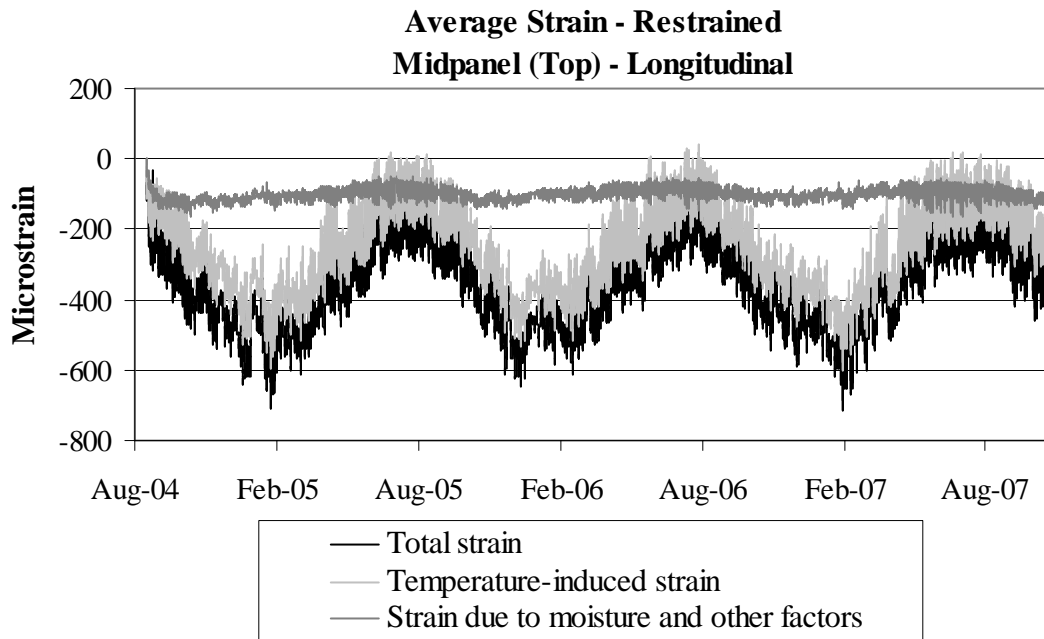


Figure D.1. Strains in the longitudinal direction at midpanel at the top of the restrained slabs.

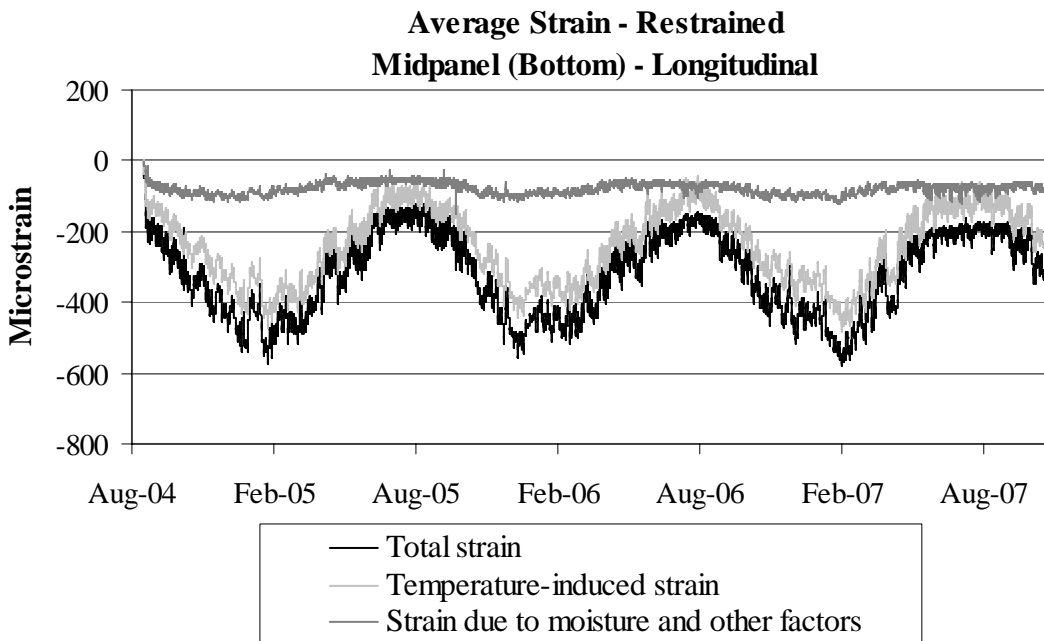


Figure D.2. Strains in the longitudinal direction at midpanel at the bottom of the restrained slabs.

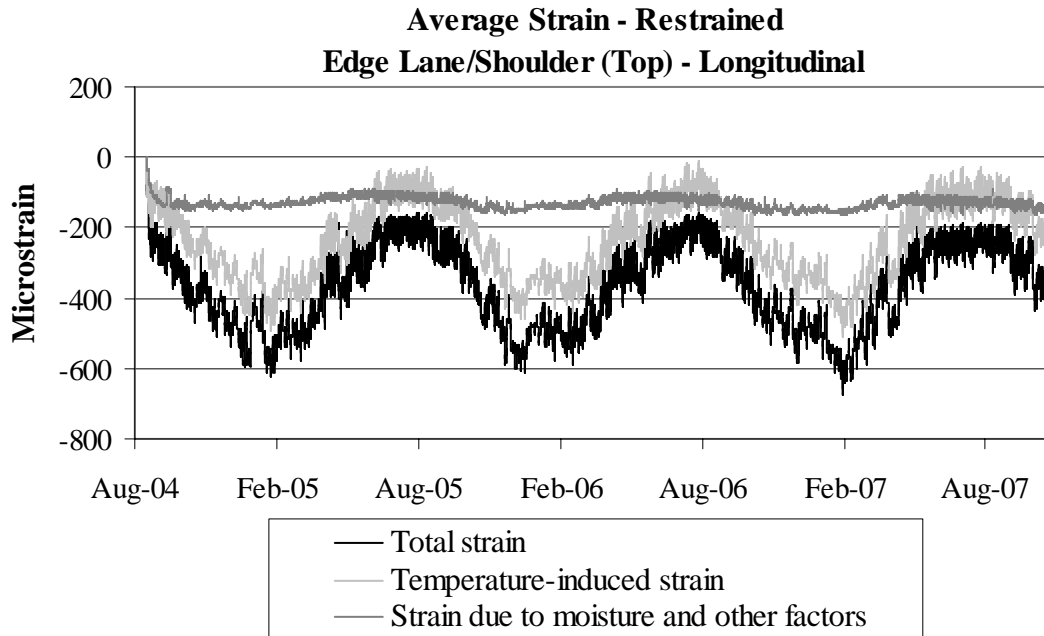


Figure D.3. Strains in the longitudinal direction along the lane/shoulder joint at the top of the restrained slabs.

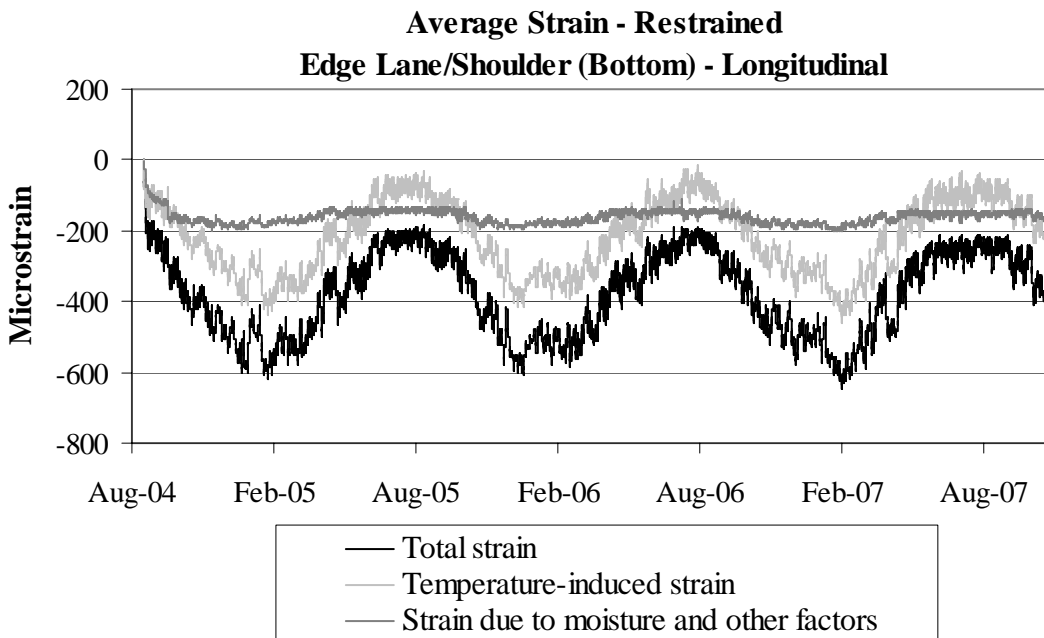


Figure D.4. Strains in the longitudinal direction along the lane/shoulder joint at the bottom of the restrained slabs.

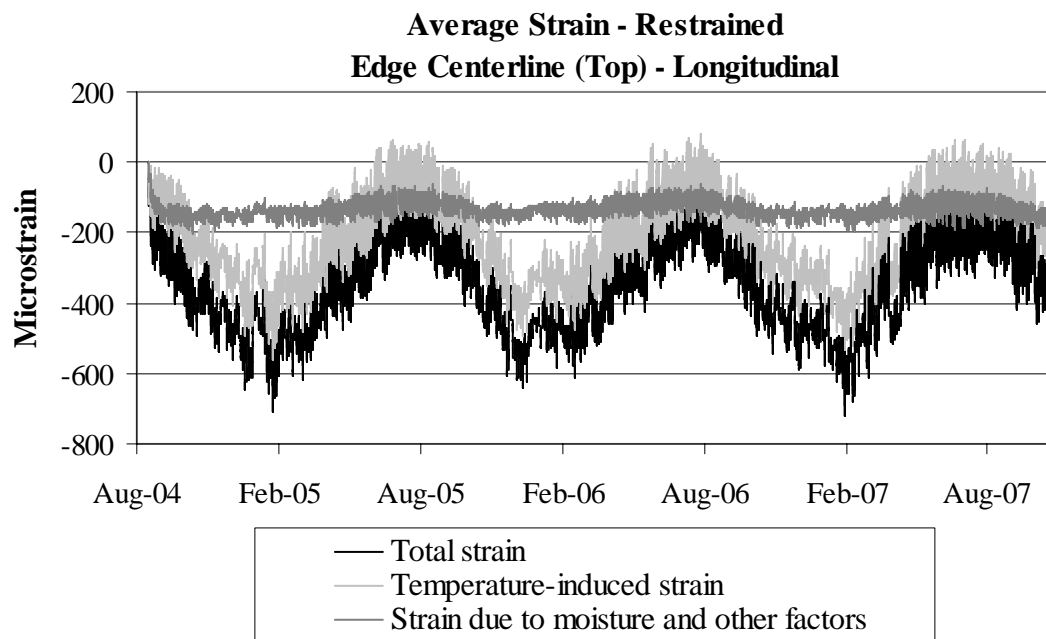


Figure D.5. Strains in the longitudinal direction along the centerline joint at the top of the restrained slabs.

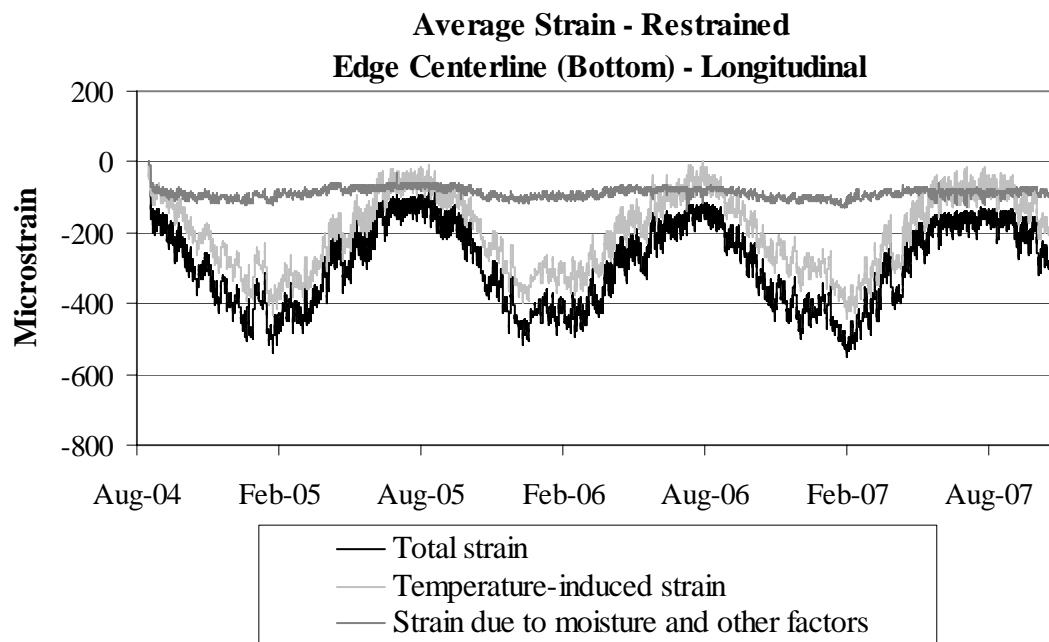


Figure D.6. Strains in the longitudinal direction along the centerline joint at the bottom of the restrained slabs.

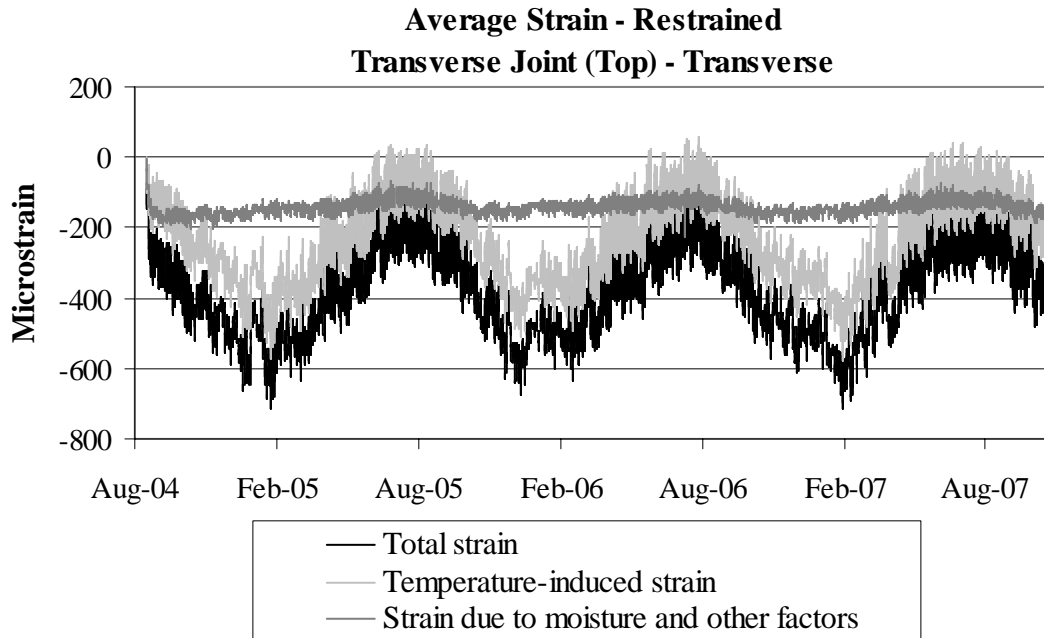


Figure D.7. Strains in the transverse direction along the transverse joint at the top of the restrained slabs.

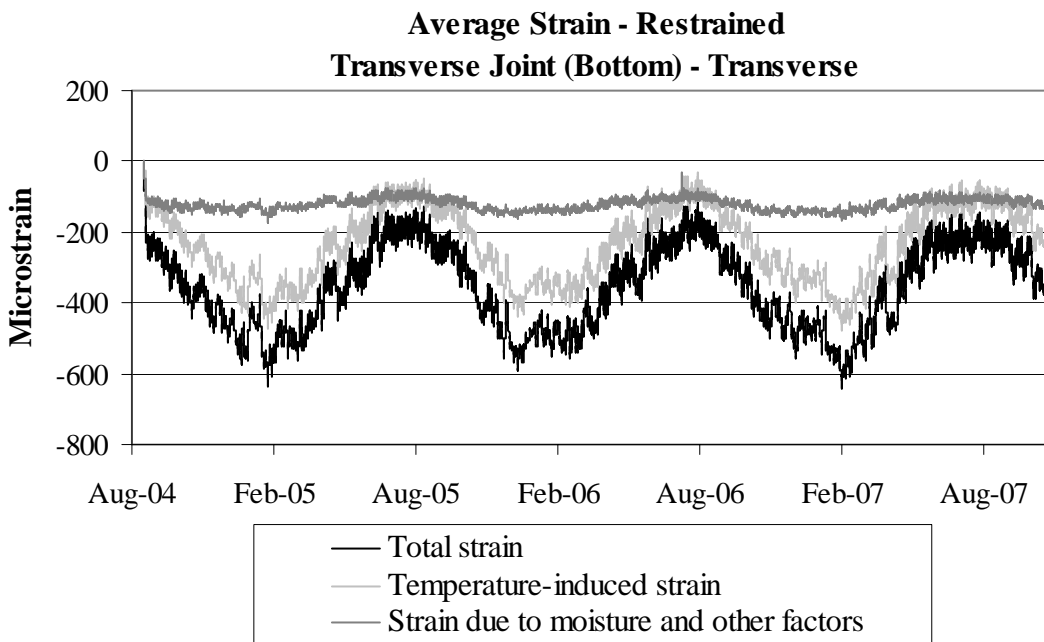


Figure D.8. Strains in the transverse direction along the transverse joint at the bottom of the restrained slabs.

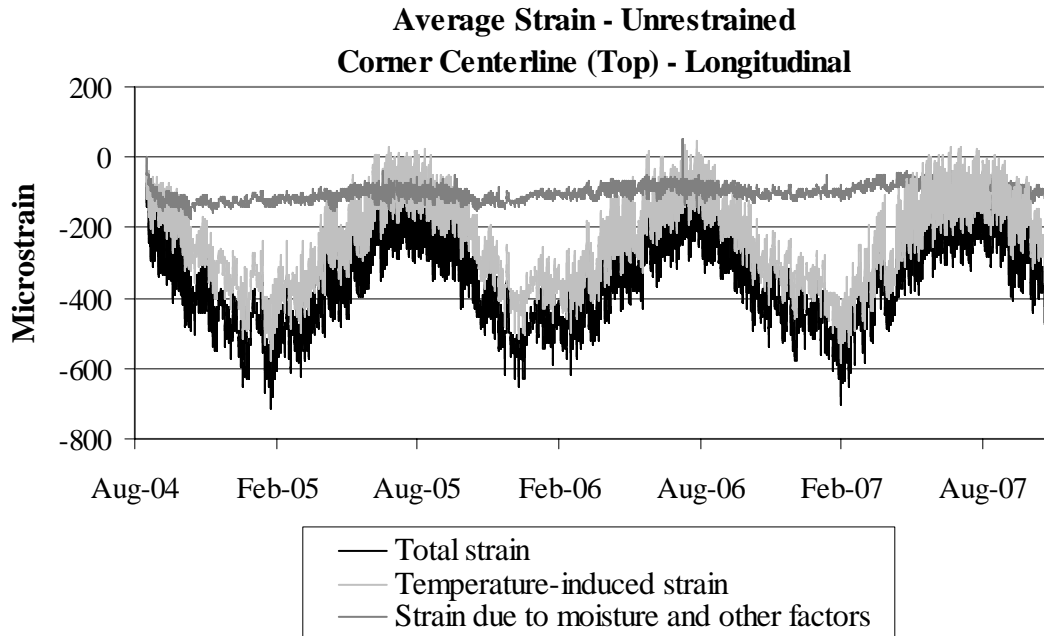


Figure D.9. Strains in the longitudinal direction at the corner along the centerline joint at the top of the restrained slabs.

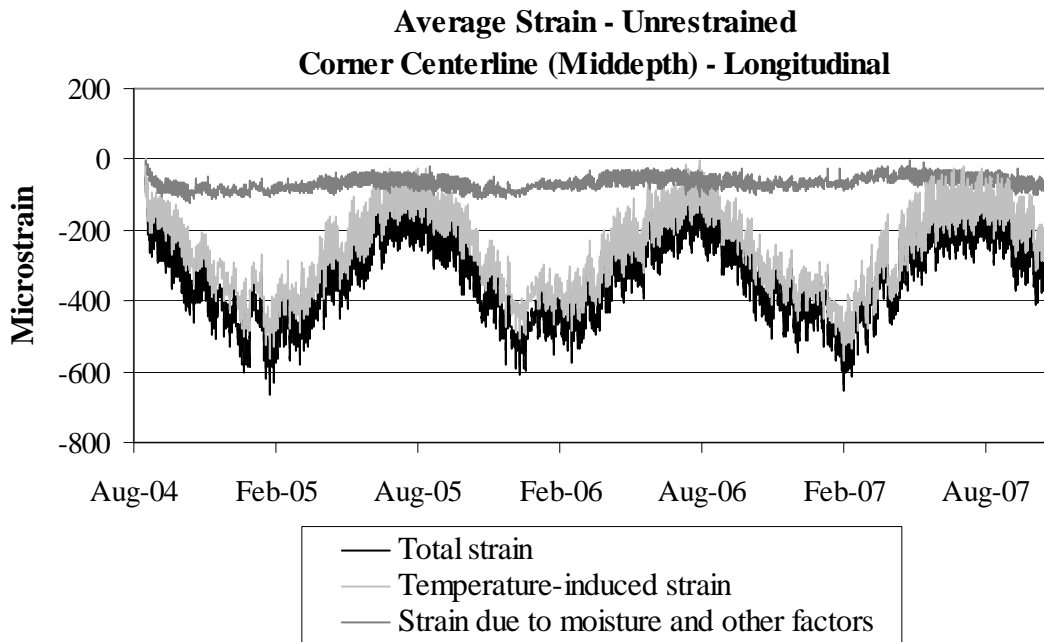


Figure D.10. Strains in the longitudinal direction at the corner along the centerline joint at the middepth of the restrained slabs.

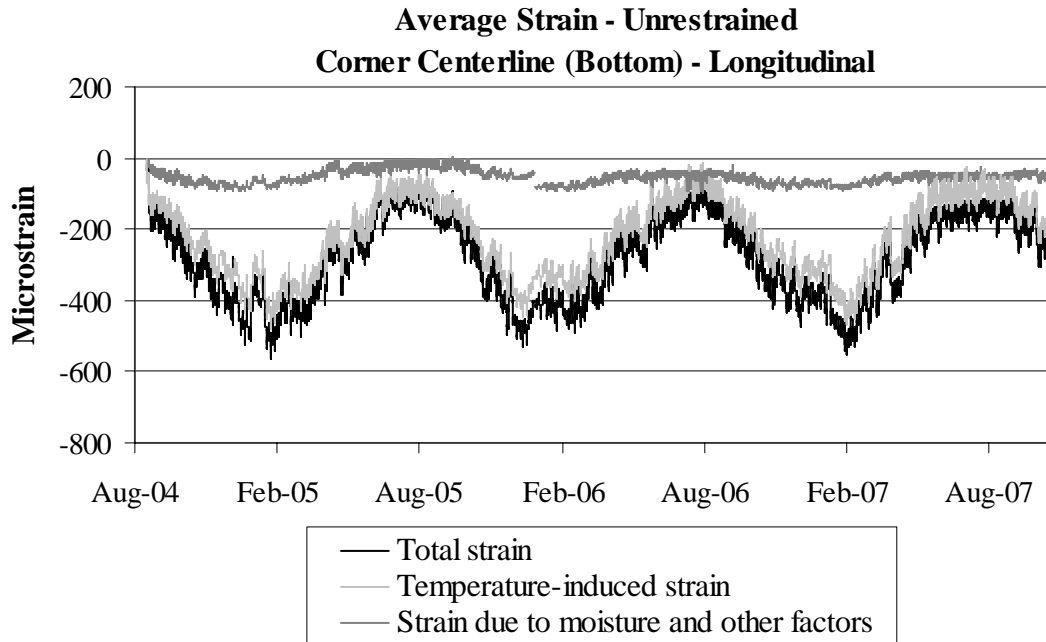


Figure D.11. Strains in the longitudinal direction at the corner along the centerline joint at the bottom of the restrained slabs.

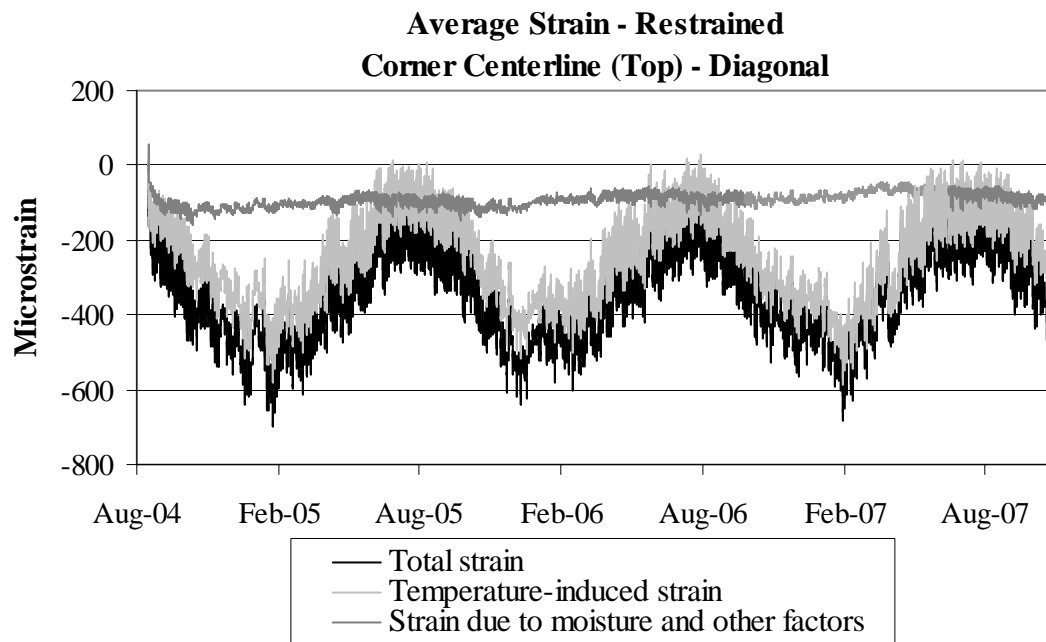


Figure D.12. Strains in the diagonal direction at the corner along the centerline joint at the top of the restrained slabs.

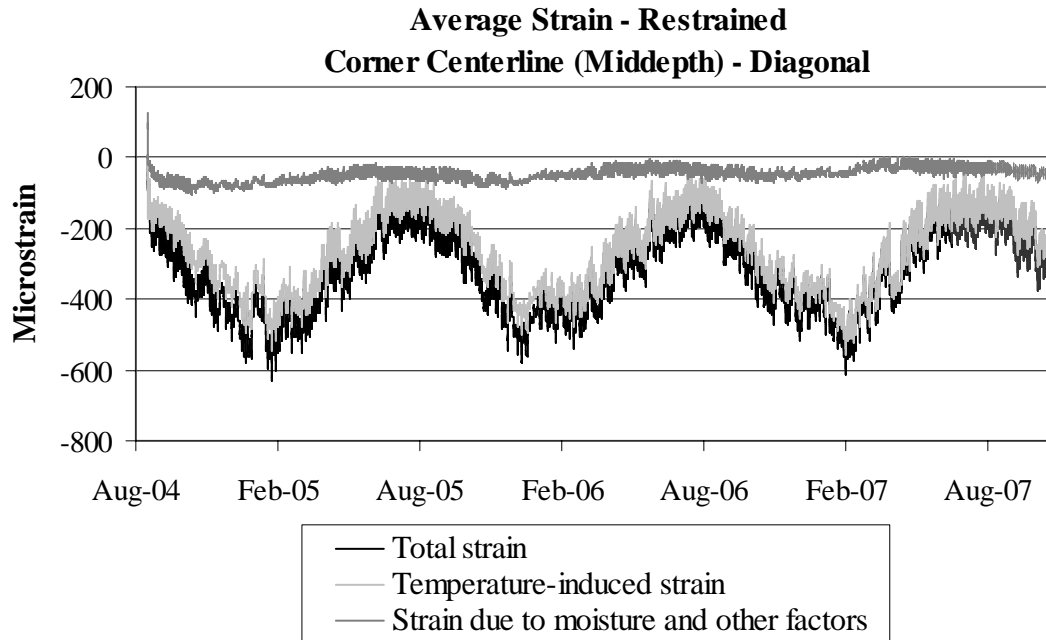


Figure D.13. Strains in the diagonal direction at the corner along the centerline joint at the middepth of the restrained slabs.

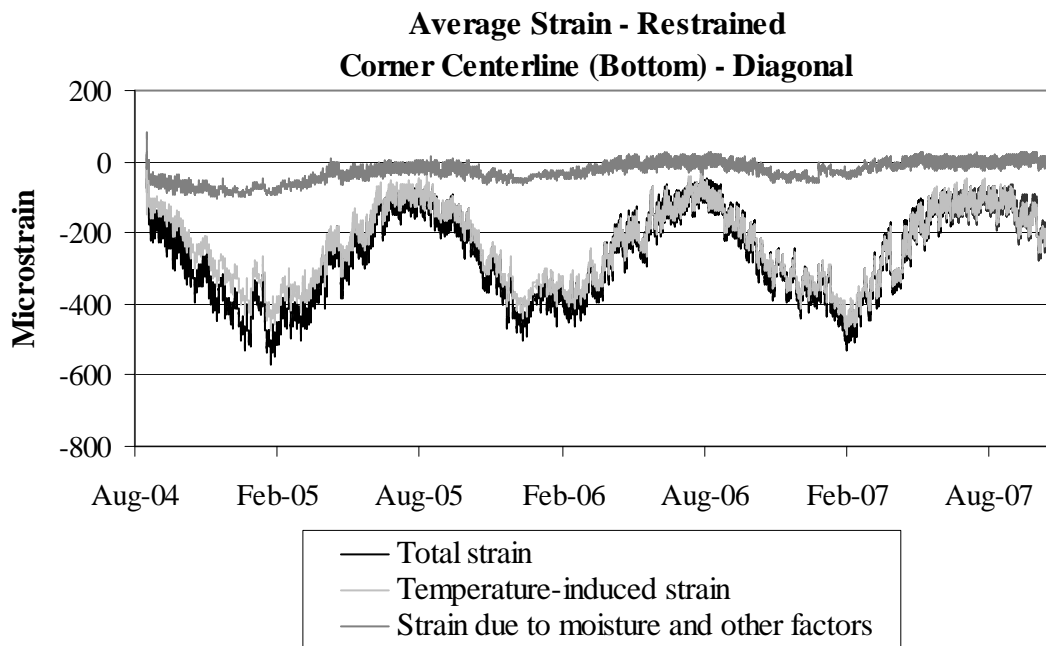


Figure D.14. Strains in the diagonal direction at the corner along the centerline joint at the bottom of the restrained slabs.

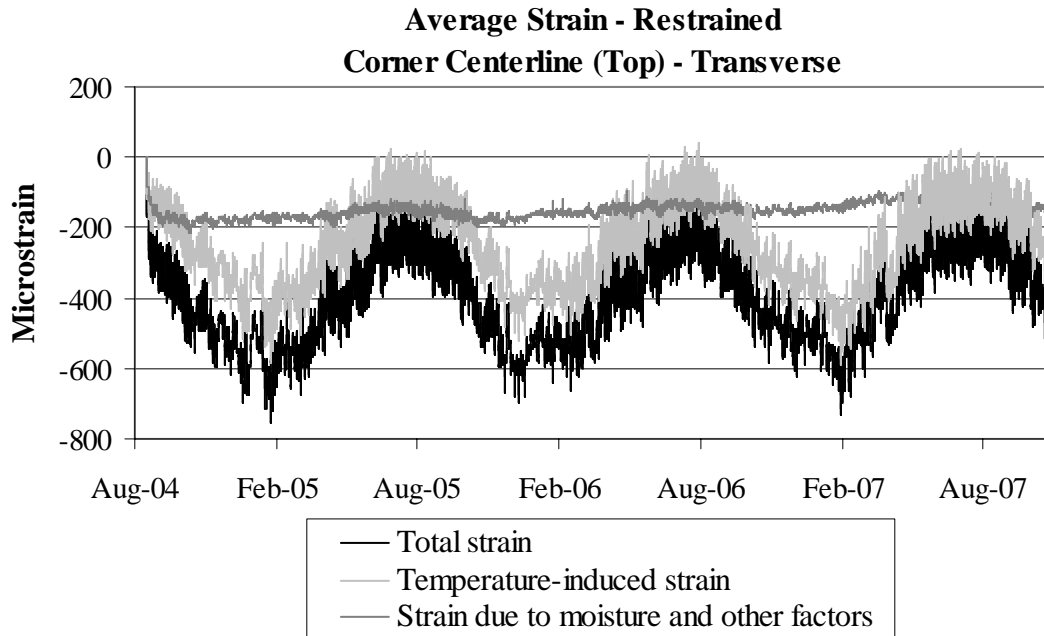


Figure D.15. Strains in the transverse direction at the corner along the centerline joint at the top of the restrained slabs.

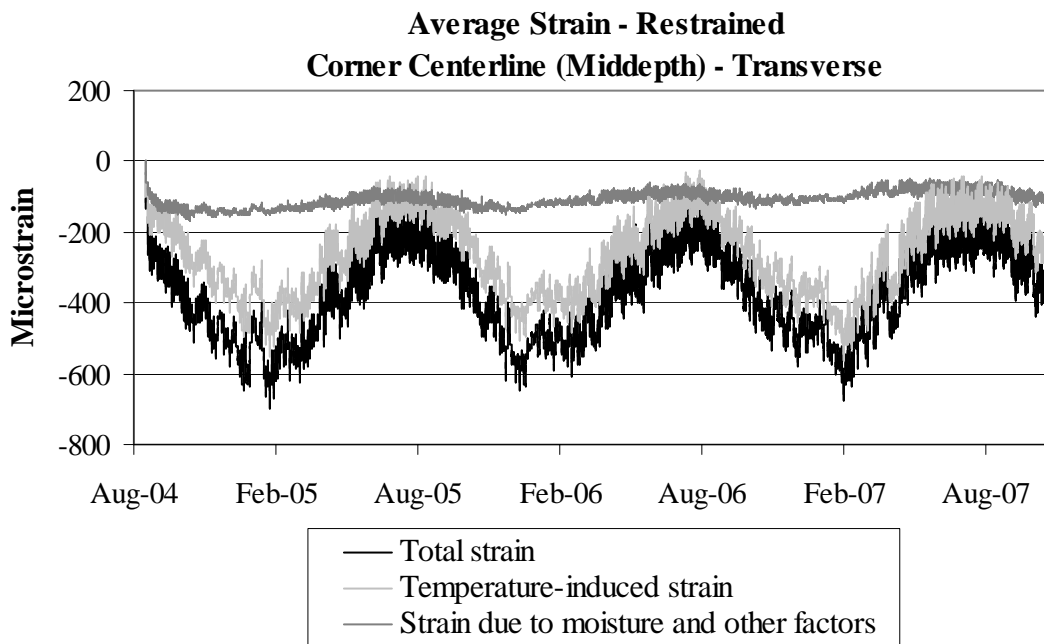


Figure D.16. Strains in the transverse direction at the corner along the centerline joint at the middepth of the restrained slabs.

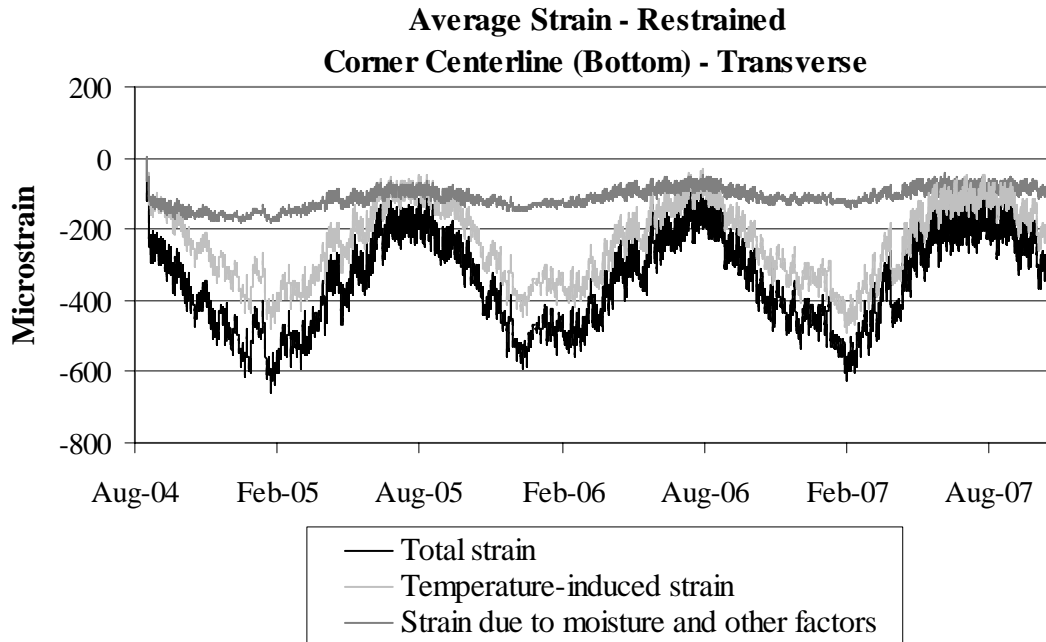


Figure D.17. Strains in the transverse direction at the corner along the centerline joint at the bottom of the restrained slabs.

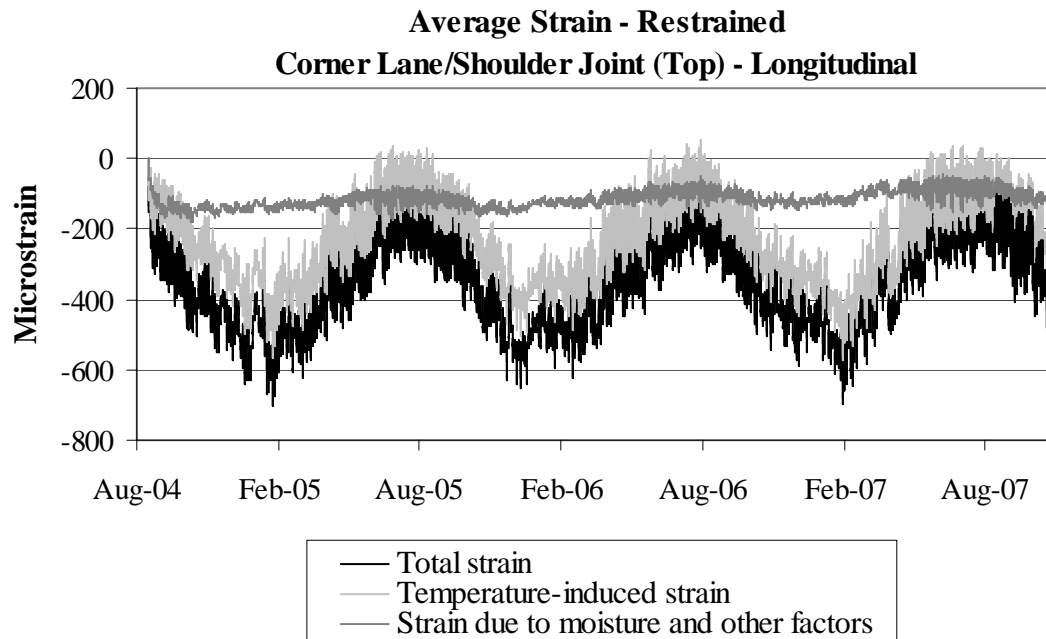


Figure D.18. Strains in the longitudinal direction at the corner along the lane/shoulder joint at the top of the restrained slabs.

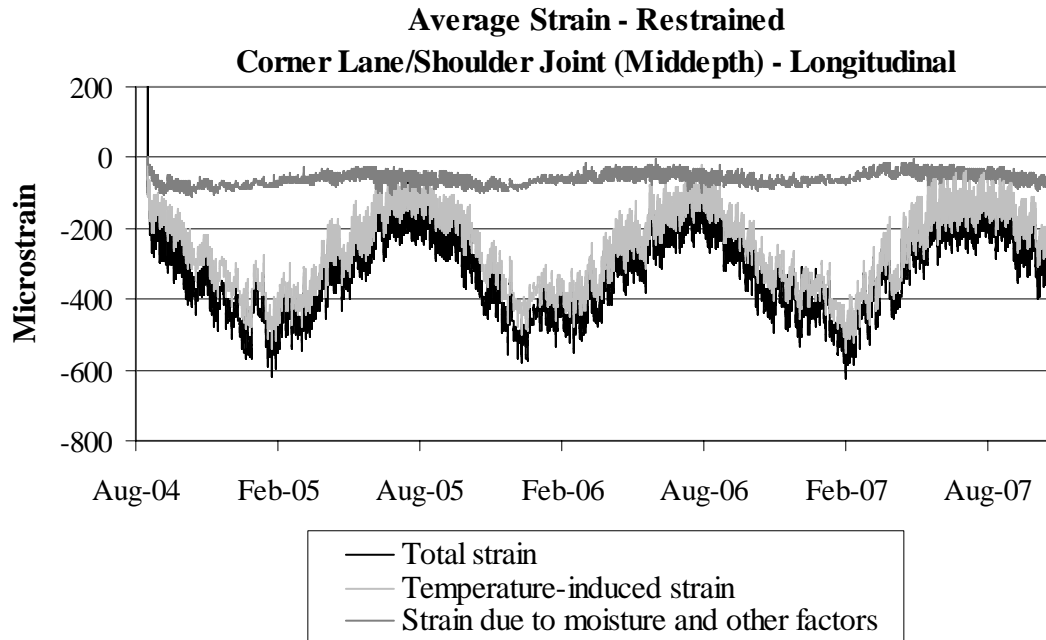


Figure D.19. Strains in the longitudinal direction at the corner along the lane/shoulder joint at the middepth of the restrained slabs.

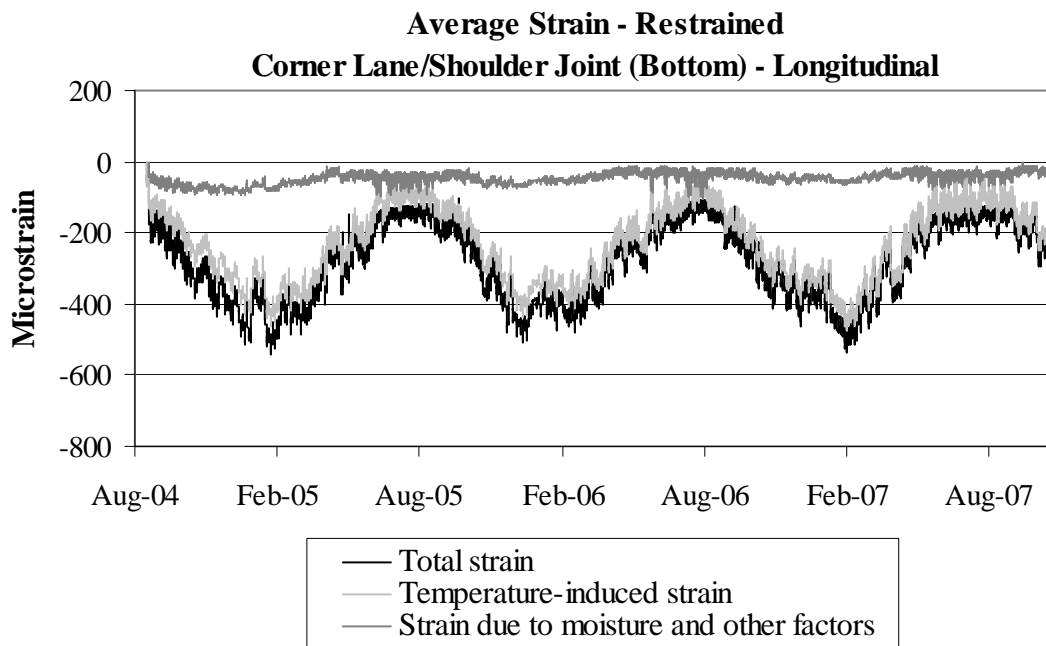


Figure D.20. Strains in the longitudinal direction at the corner along the lane/shoulder joint at the bottom of the restrained slabs.

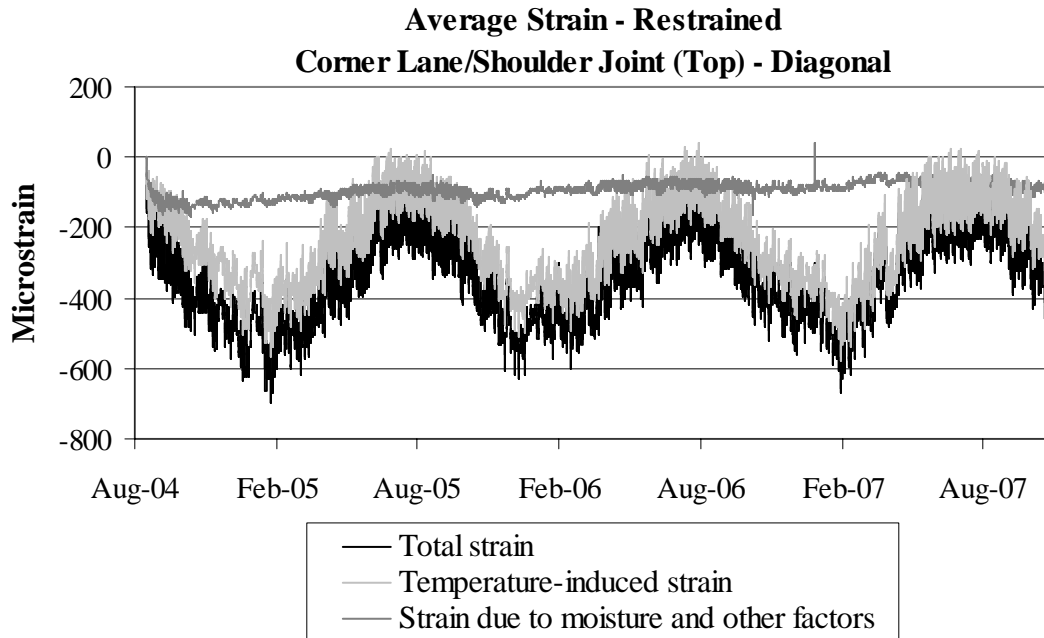


Figure D.21. Strains in the diagonal direction at the corner along the lane/shoulder joint at the top of the restrained slabs.

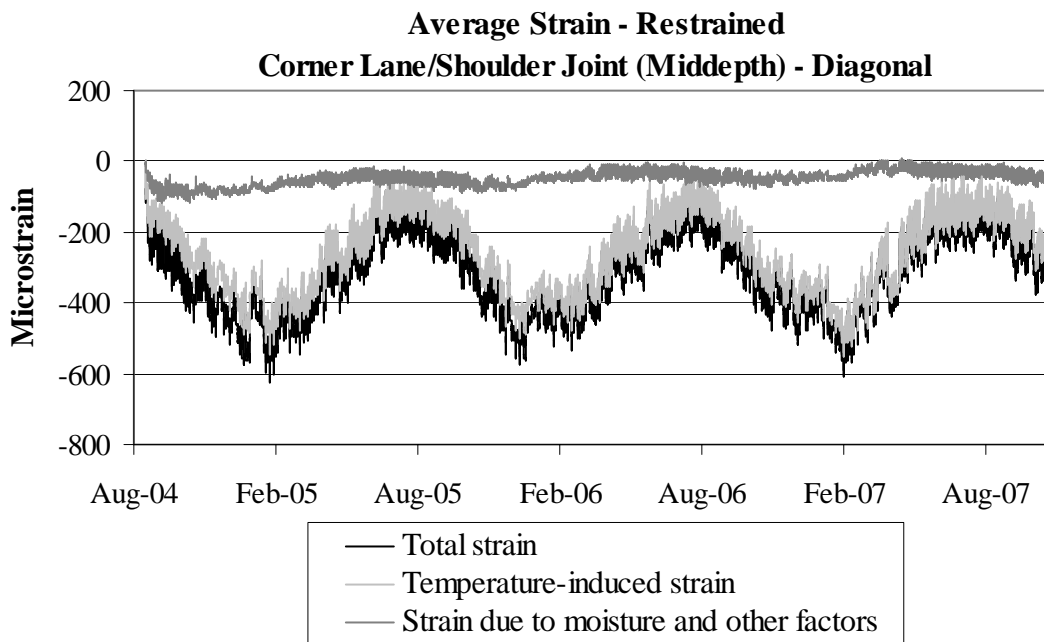


Figure D.22. Strains in the diagonal direction at the corner along the lane/shoulder joint at the middepth of the restrained slabs.

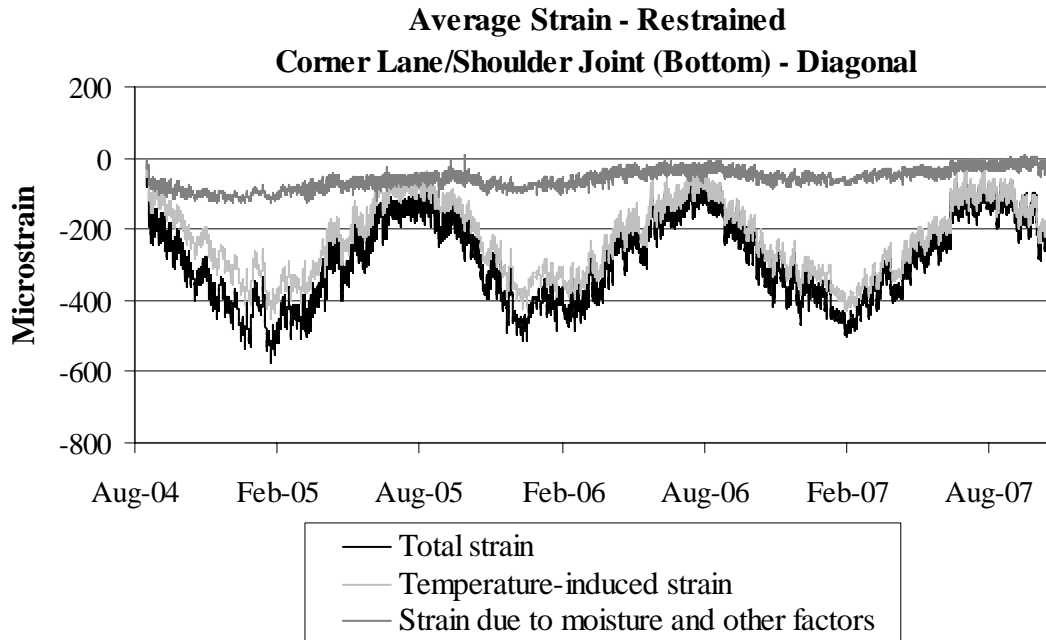


Figure D.23. Strains in the diagonal direction at the corner along the lane/shoulder joint at the bottom of the restrained slabs.

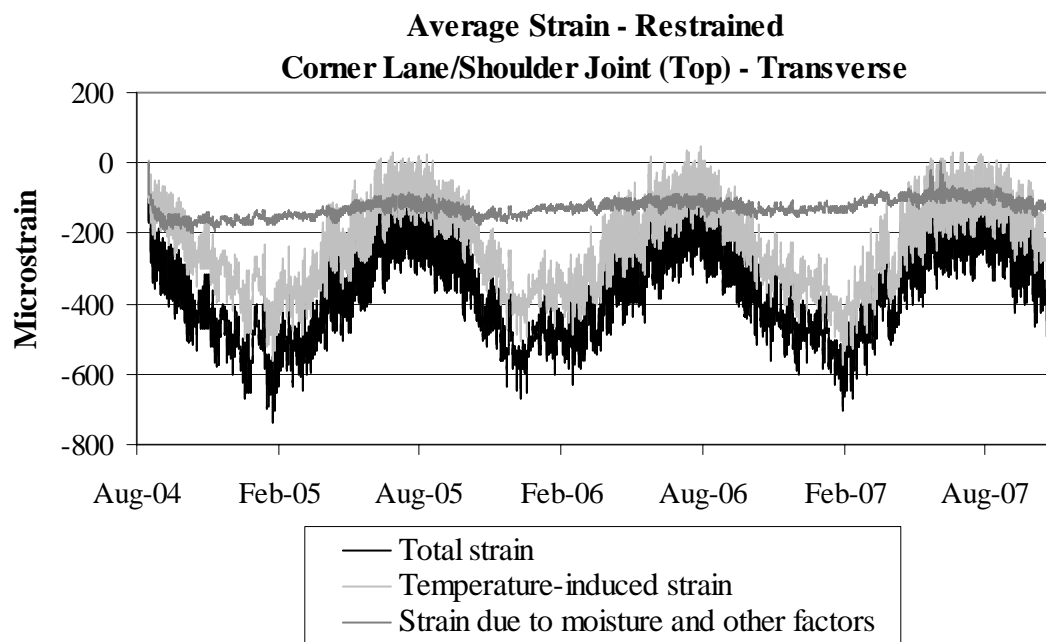


Figure D.24. Strains in the transverse direction at the corner along the lane/shoulder joint at the top of the restrained slabs.

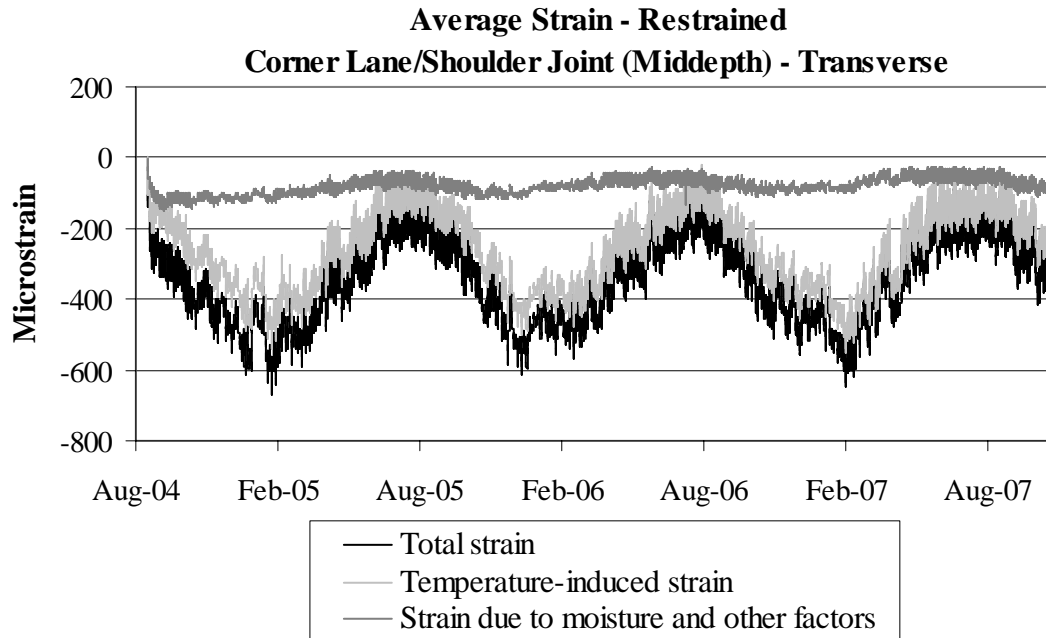


Figure D.25. Strains in the transverse direction at the corner along the lane/shoulder joint at the middepth of the restrained slabs.

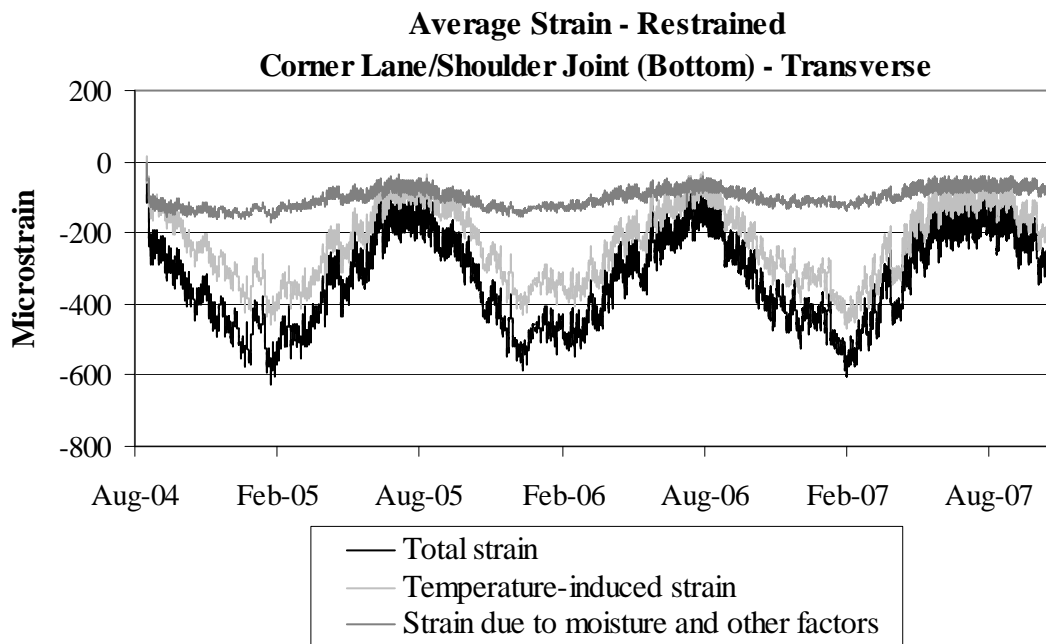


Figure D.26. Strains in the transverse direction at the corner along the lane/shoulder joint at the bottom of the restrained slabs.

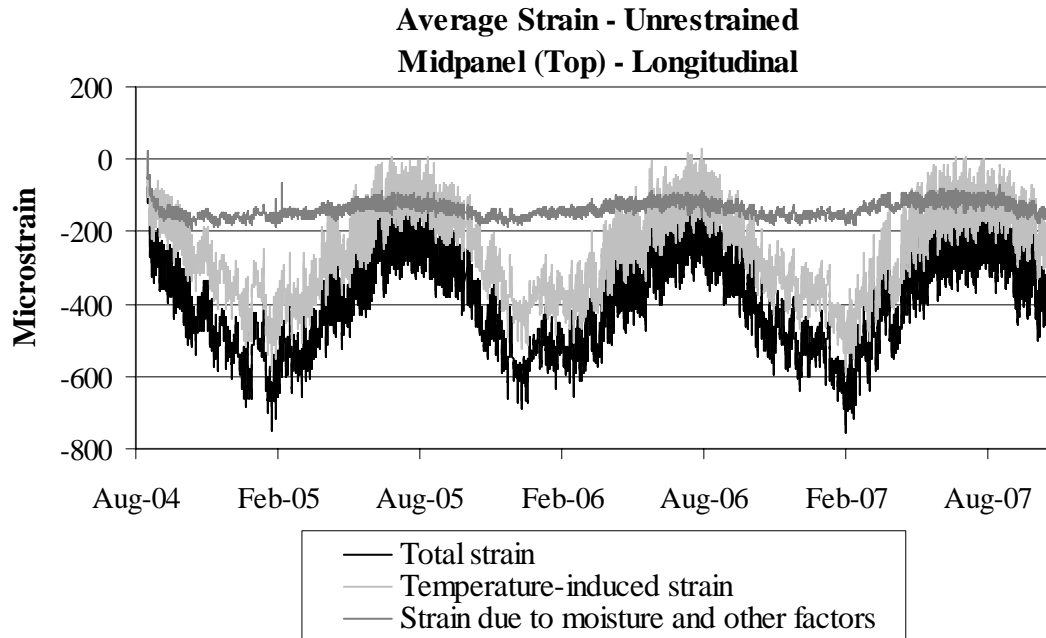


Figure D.27. Strains in the longitudinal direction at midpanel at the top of the unrestrained slabs.

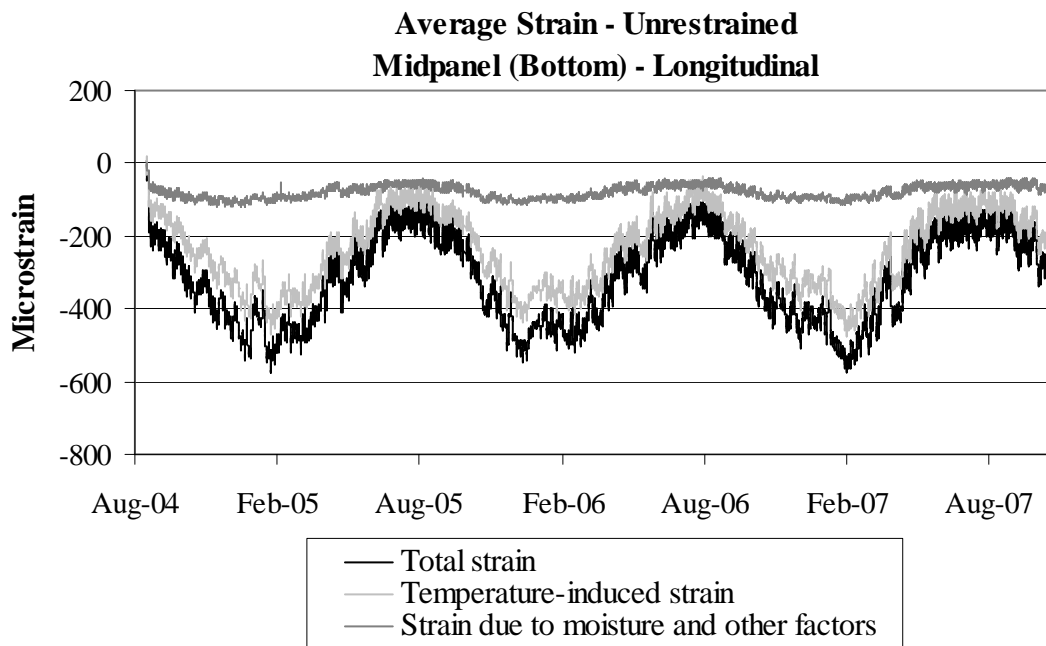


Figure D.28. Strains in the longitudinal direction at midpanel at the bottom of the unrestrained slabs.

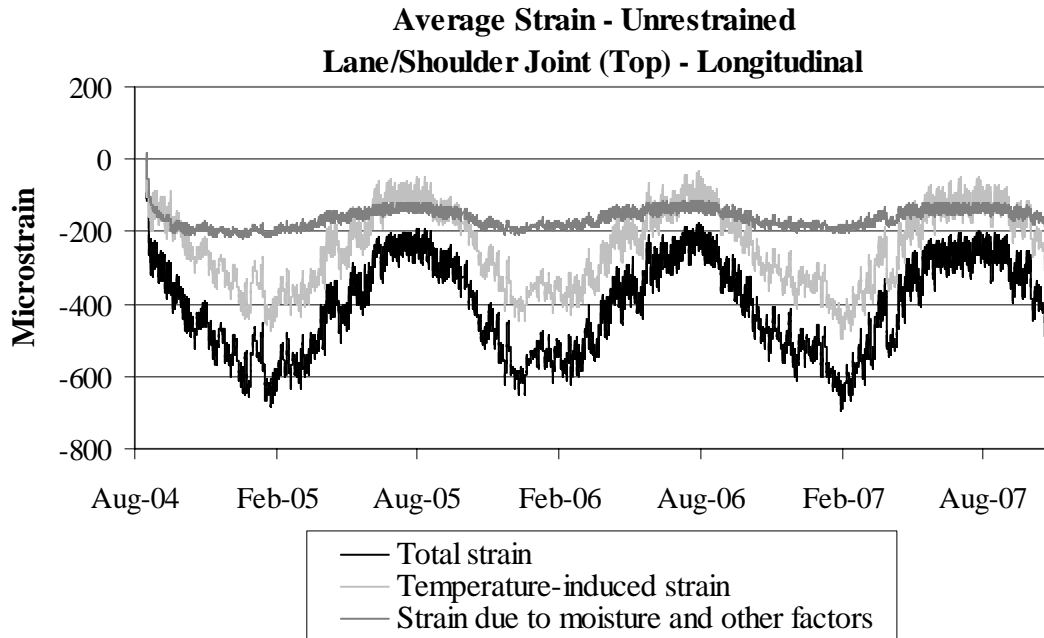


Figure D.29. Strains in the longitudinal direction along the lane/shoulder joint at the top of the unrestrained slabs.

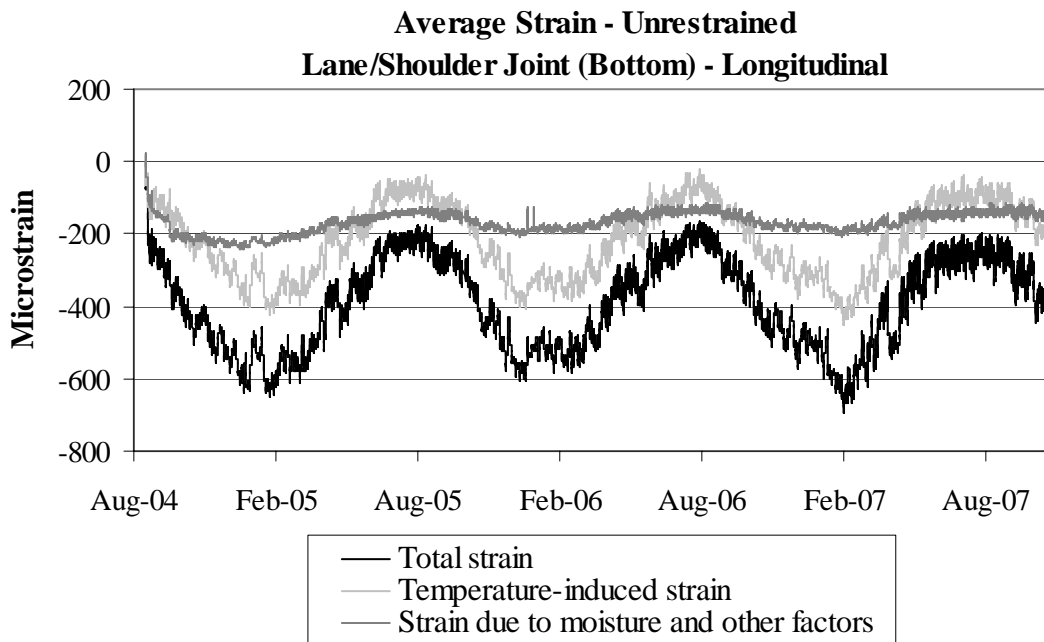


Figure D.30. Strains in the longitudinal direction along the lane/shoulder joint at the bottom of the unrestrained slabs.

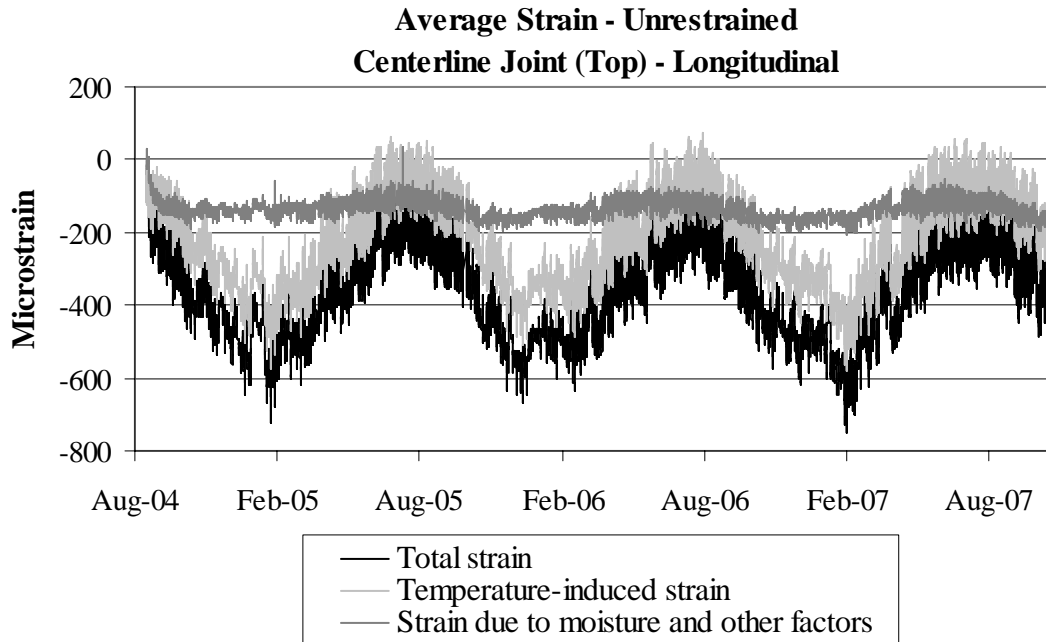


Figure D.31. Strains in the longitudinal direction along the centerline joint at the top of the unrestrained slabs.

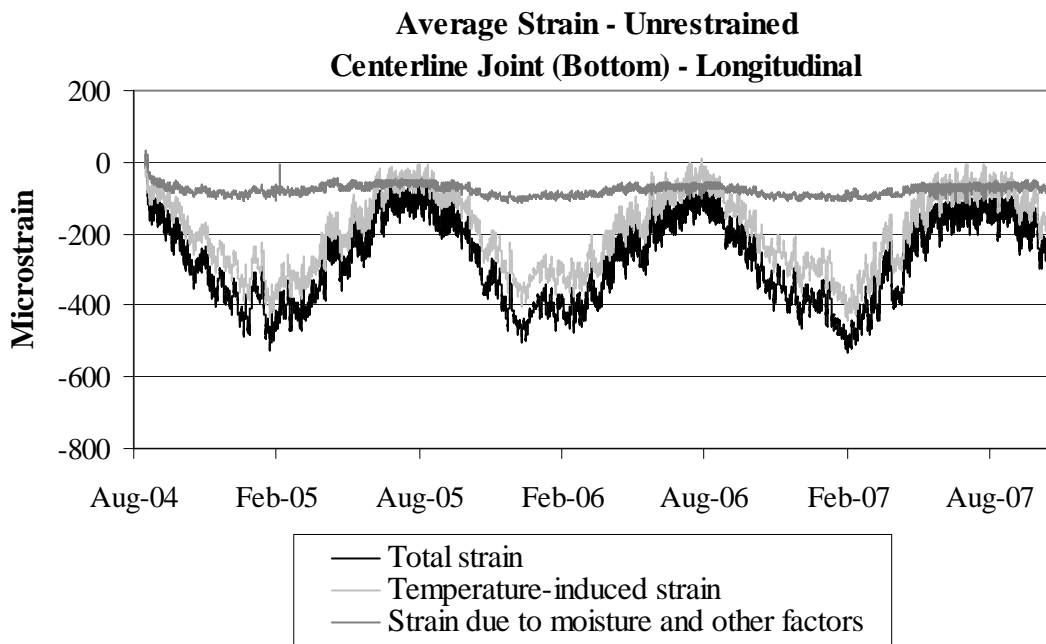


Figure D.32. Strains in the longitudinal direction along the centerline joint at the bottom of the unrestrained slabs.

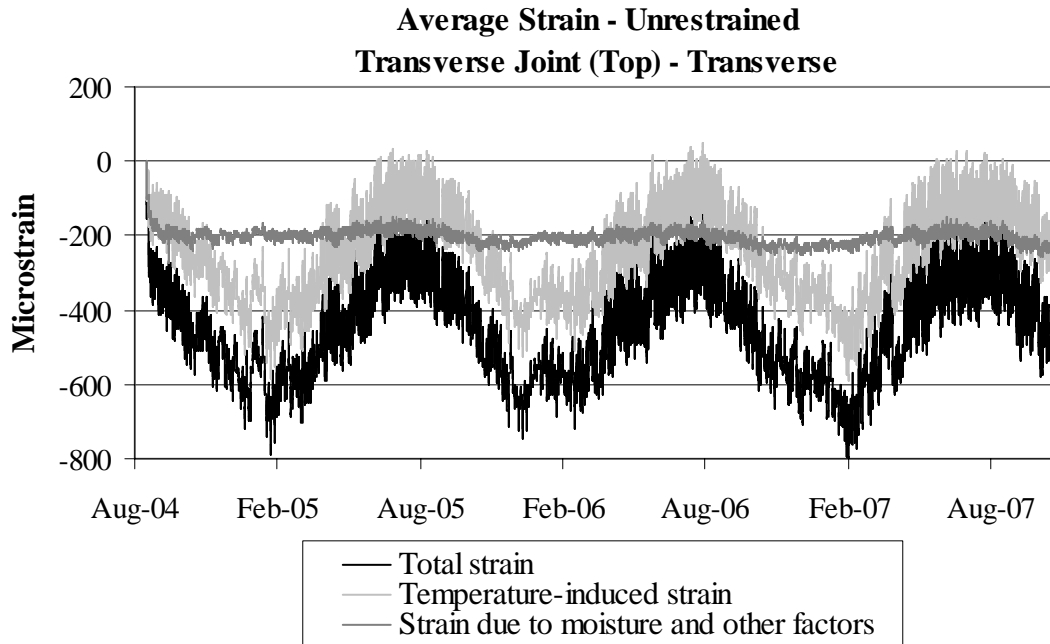


Figure D.33. Strains in the transverse direction along the transverse joint at the top of the unrestrained slabs.

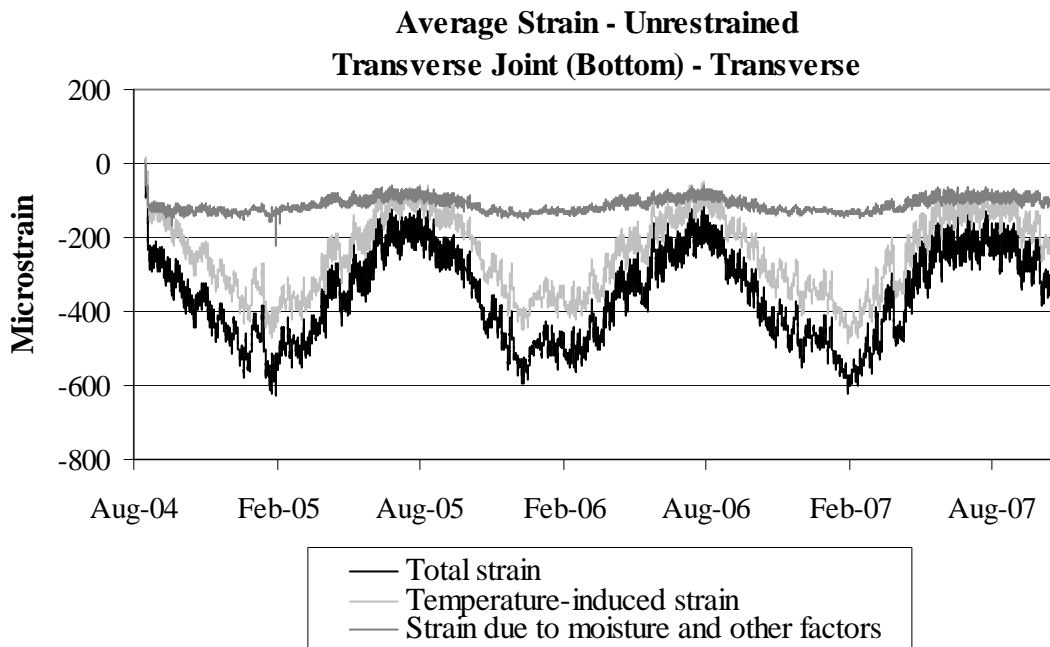


Figure D.34. Strains in the transverse direction along the transverse joint at the bottom of the unrestrained slabs.

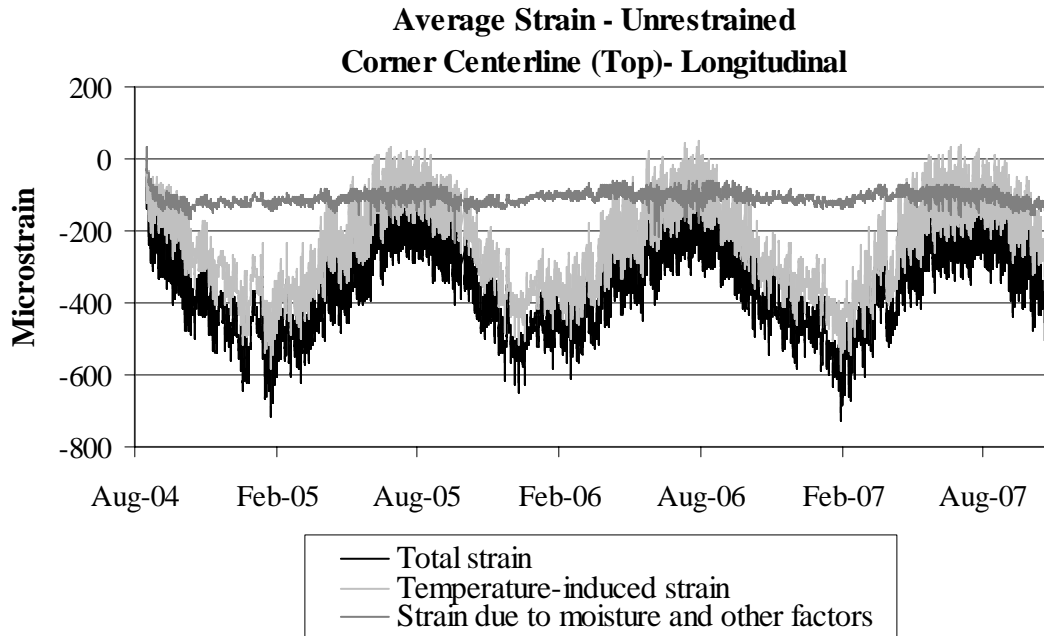


Figure D.35. Strains in the longitudinal direction at the corner along the centerline joint at the top of the unrestrained slabs.

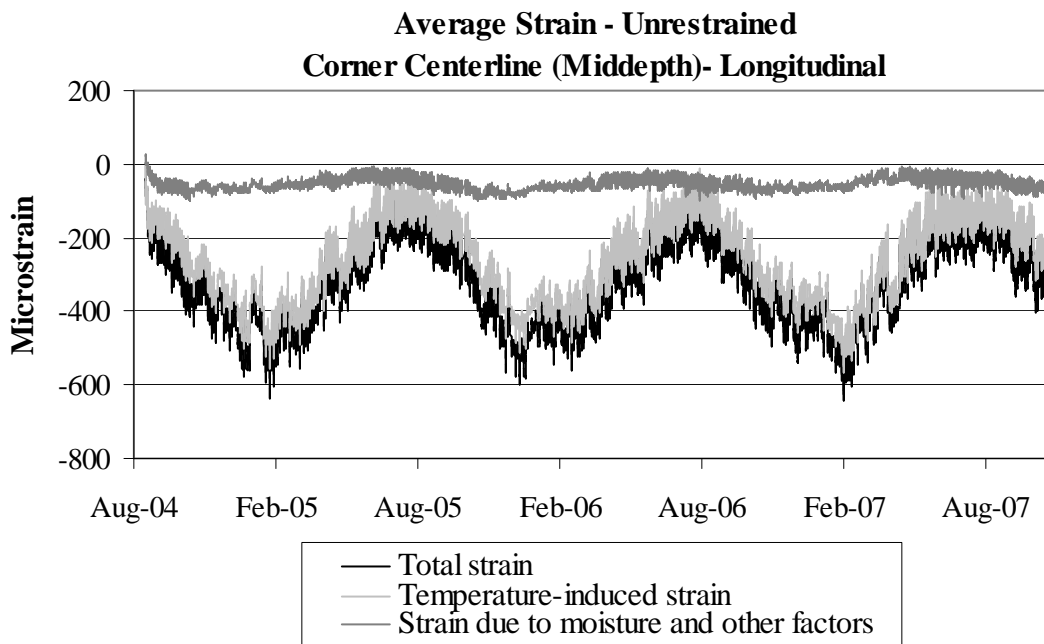


Figure D.36. Strains in the longitudinal direction at the corner along the centerline joint at the middepth of the unrestrained slabs.

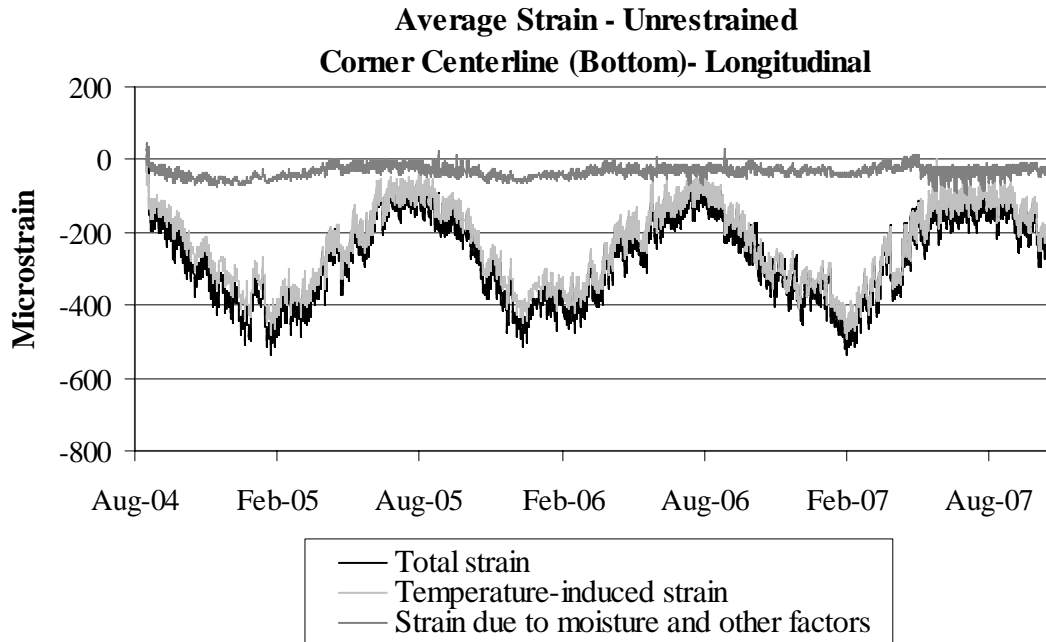


Figure D.37. Strains in the longitudinal direction at the corner along the centerline joint at the bottom of the unrestrained slabs.

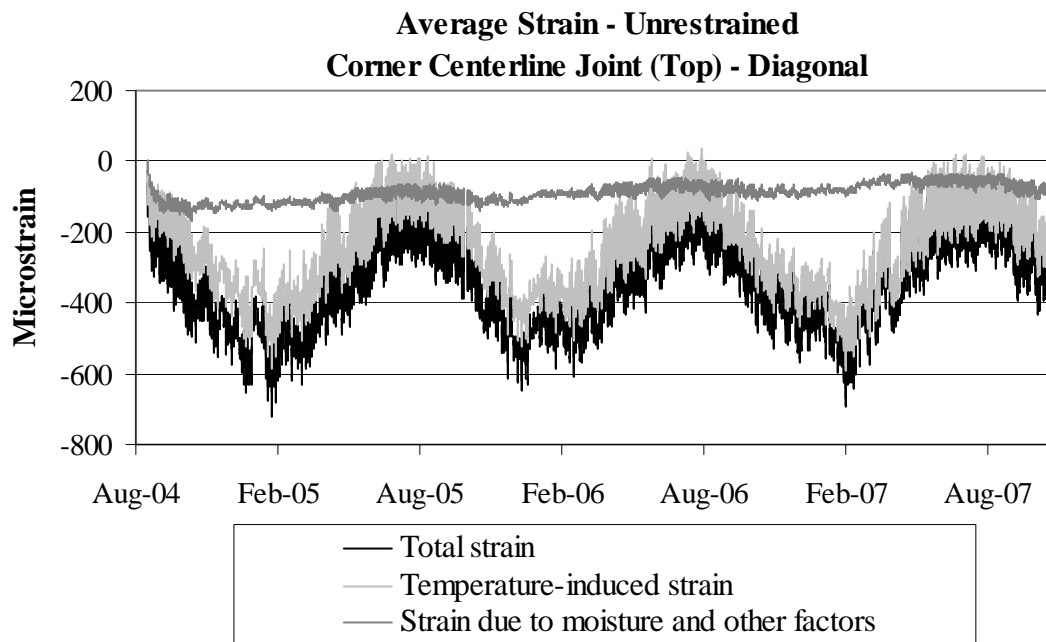


Figure D.38. Strains in the diagonal direction at the corner along the centerline joint at the top of the unrestrained slabs.

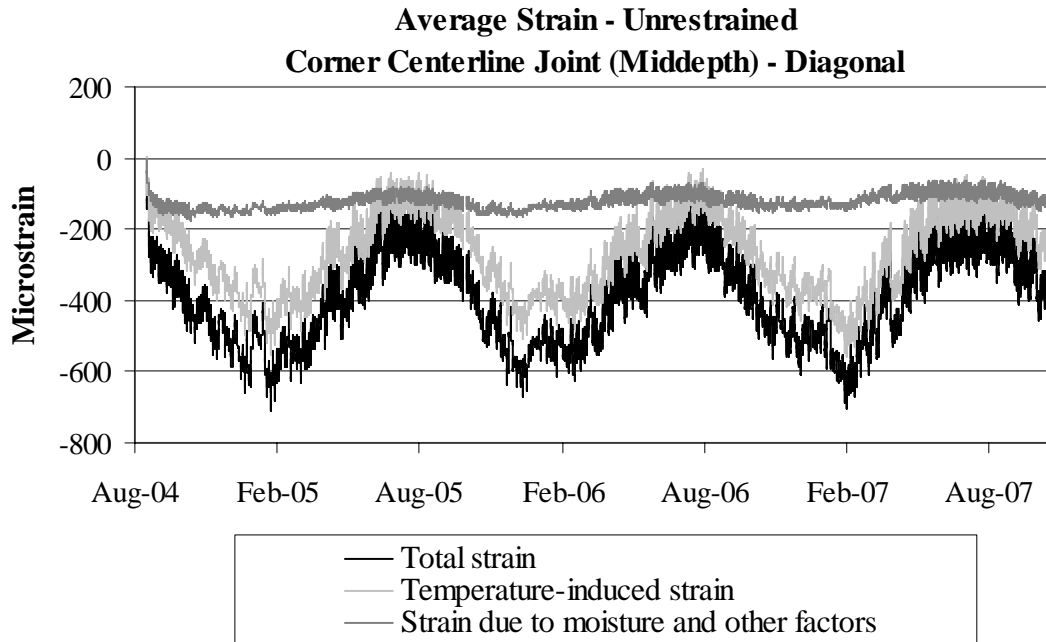


Figure D.39. Strains in the diagonal direction at the corner along the centerline joint at the middepth of the unrestrained slabs.

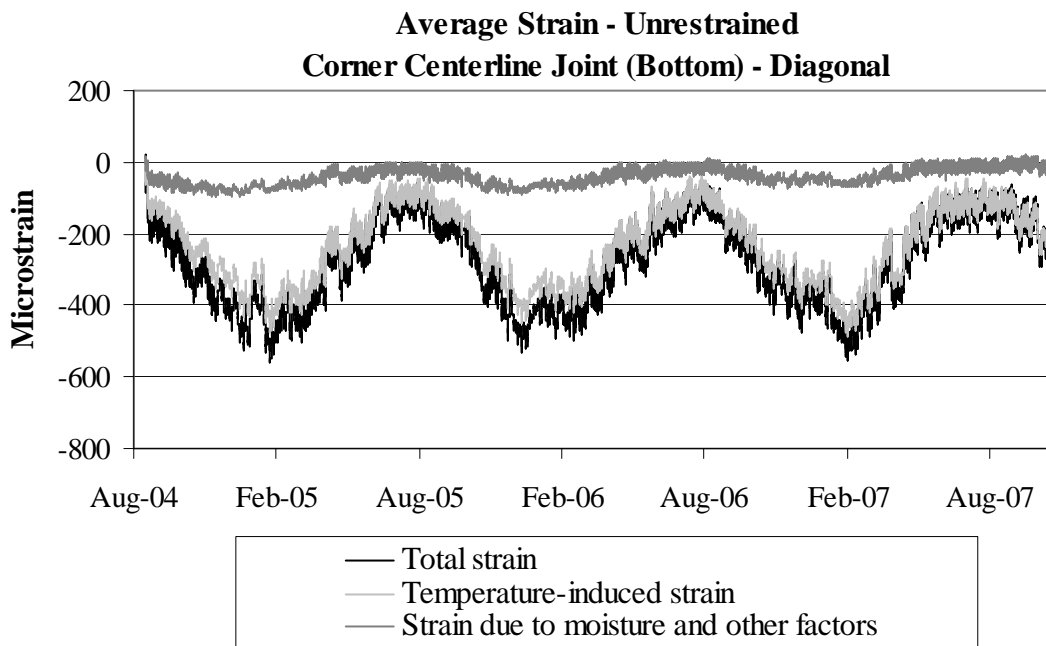


Figure D.40. Strains in the diagonal direction at the corner along the centerline joint at the bottom of the unrestrained slabs.

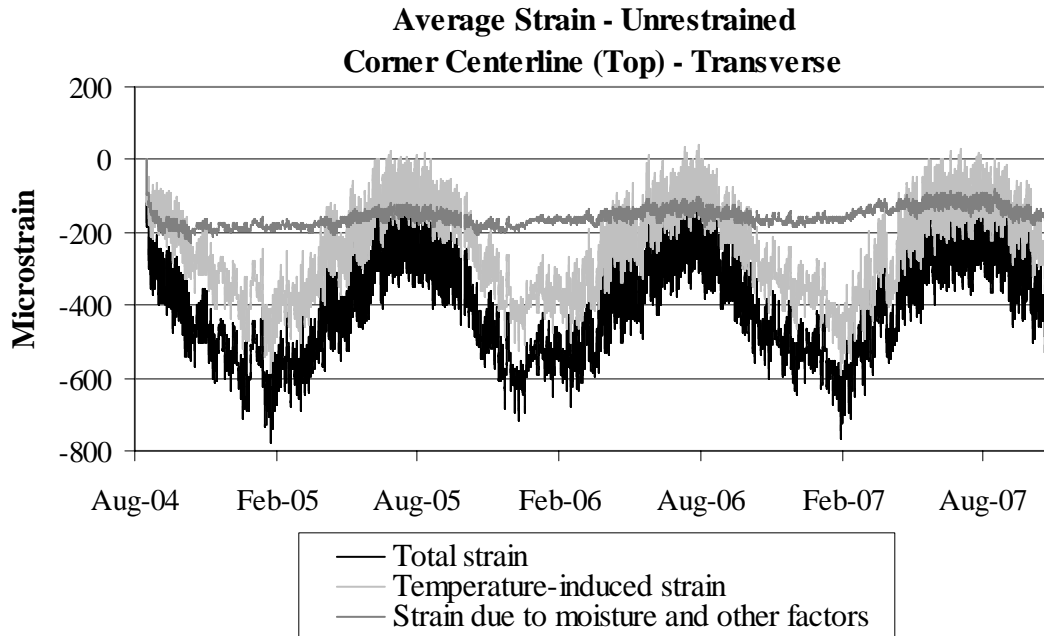


Figure D.41. Strains in the transverse direction at the corner along the centerline joint at the top of the unrestrained slabs.

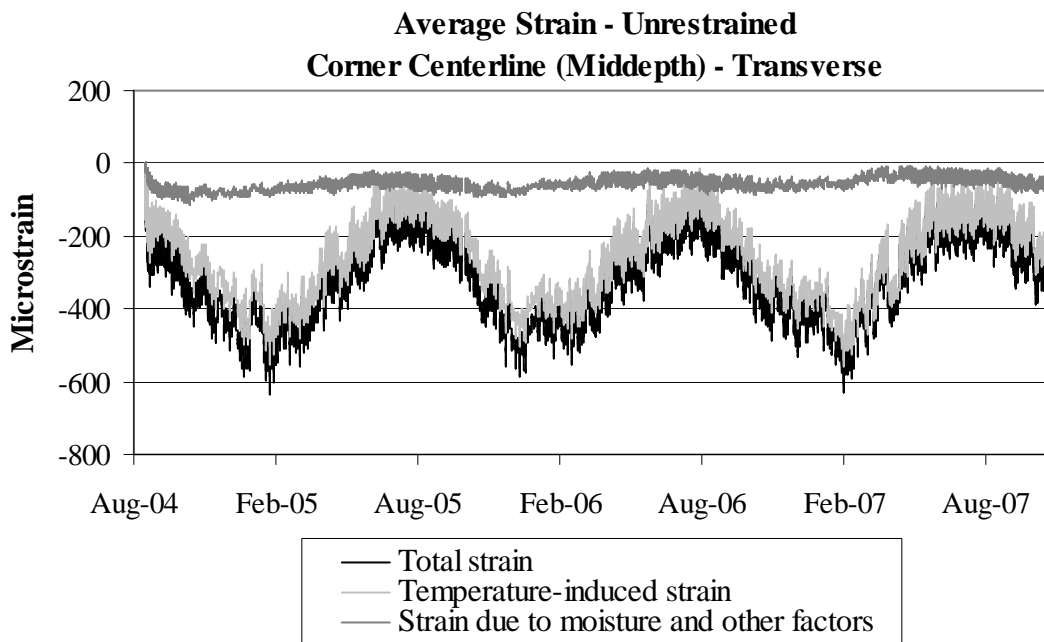


Figure D.42. Strains in the transverse direction at the corner along the centerline joint at the middepth of the unrestrained slabs.

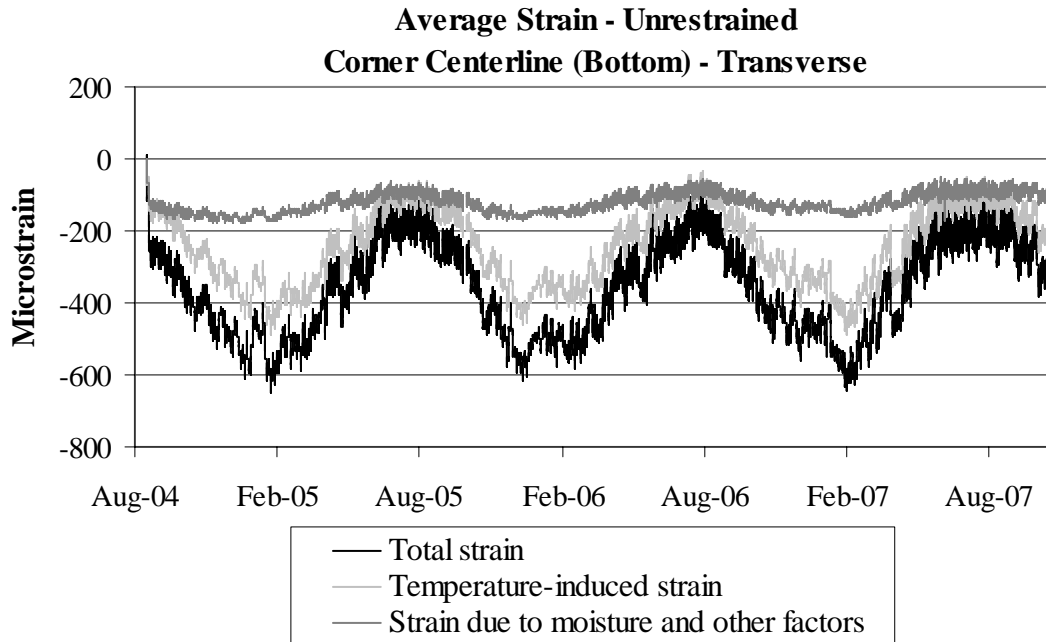


Figure D.43. Strains in the transverse direction at the corner along the centerline joint at the bottom of the unrestrained slabs.

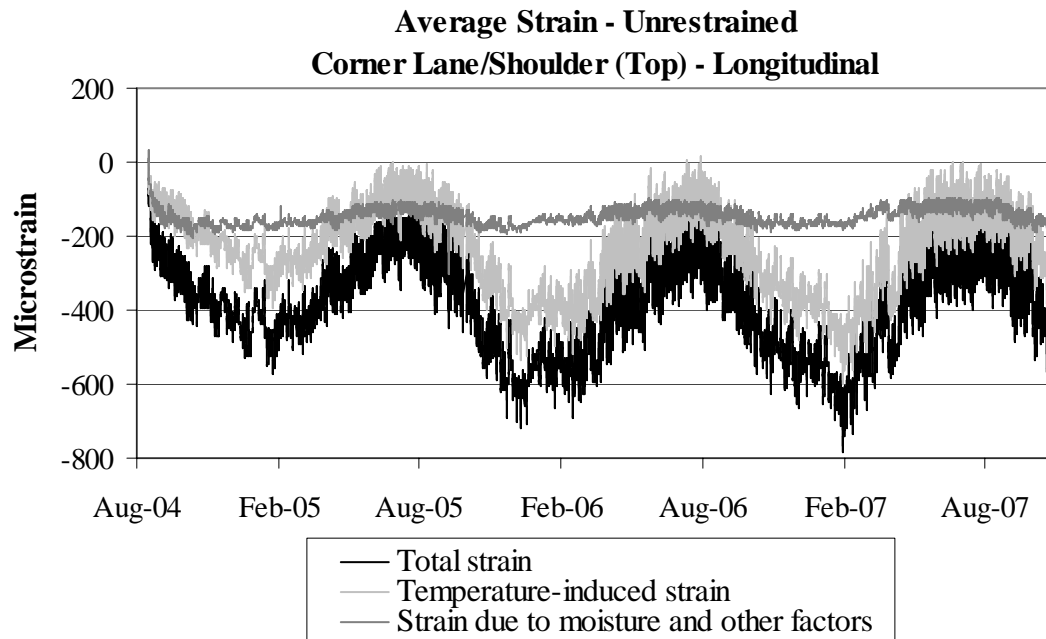


Figure D.44. Strains in the longitudinal direction at the corner along the lane/shoulder joint at the top of the unrestrained slabs.

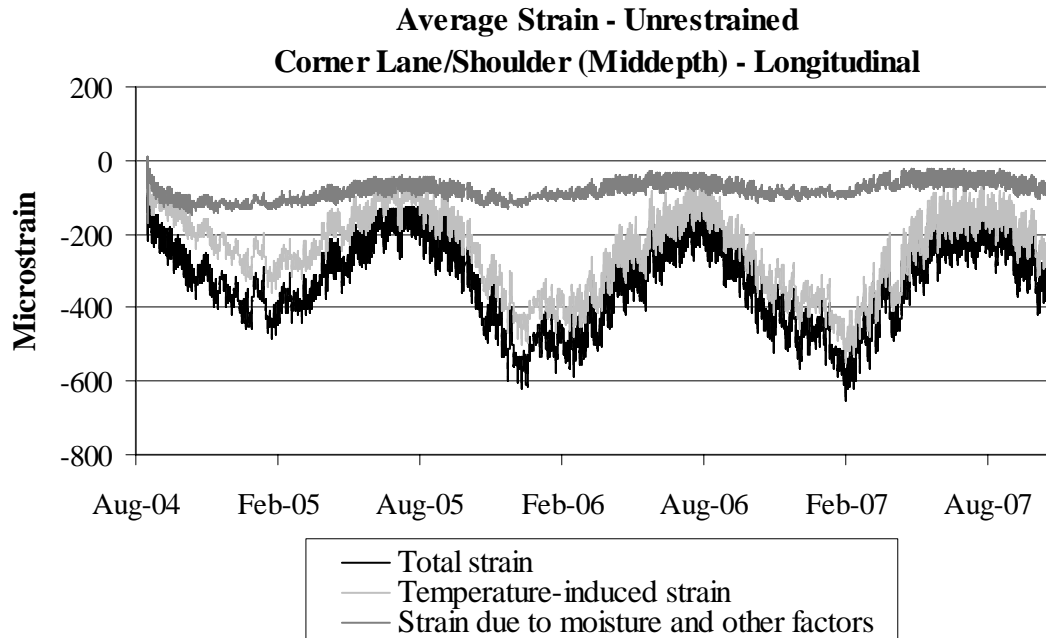


Figure D.45. Strains in the longitudinal direction at the corner along the lane/shoulder joint at the middepth of the unrestrained slabs.

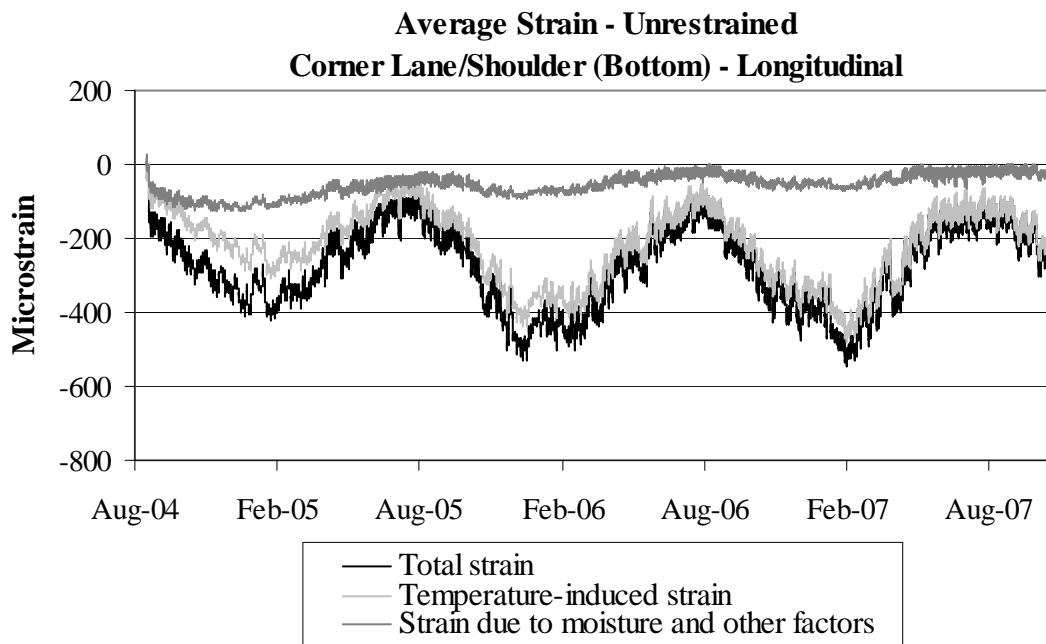


Figure D.46. Strains in the longitudinal direction at the corner along the lane/shoulder joint at the bottom of the unrestrained slabs.

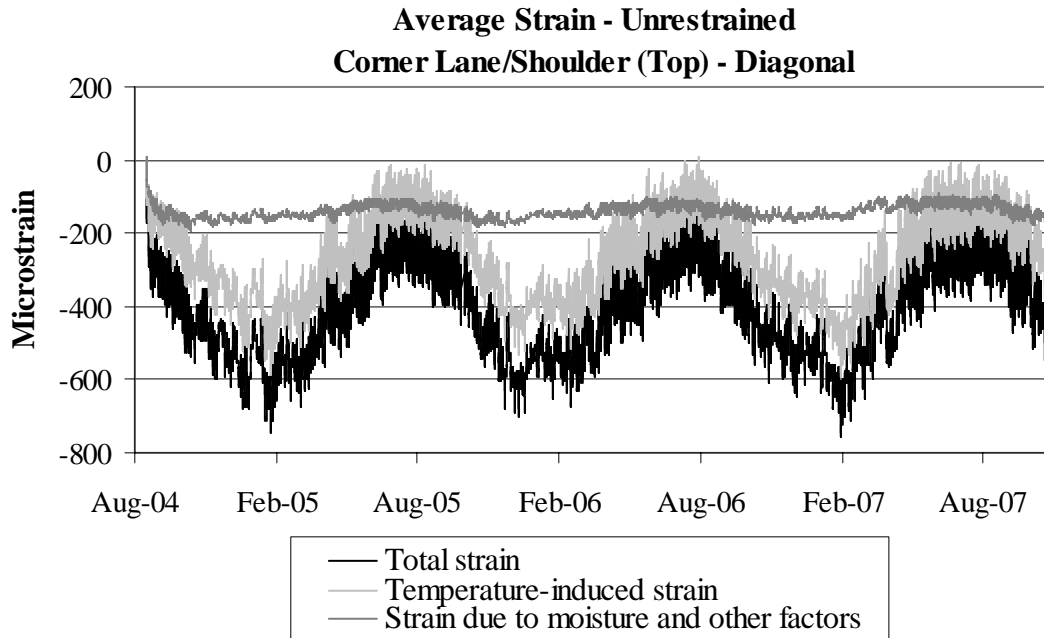


Figure D.47. Strains in the diagonal direction at the corner along the lane/shoulder joint at the top of the unrestrained slabs.

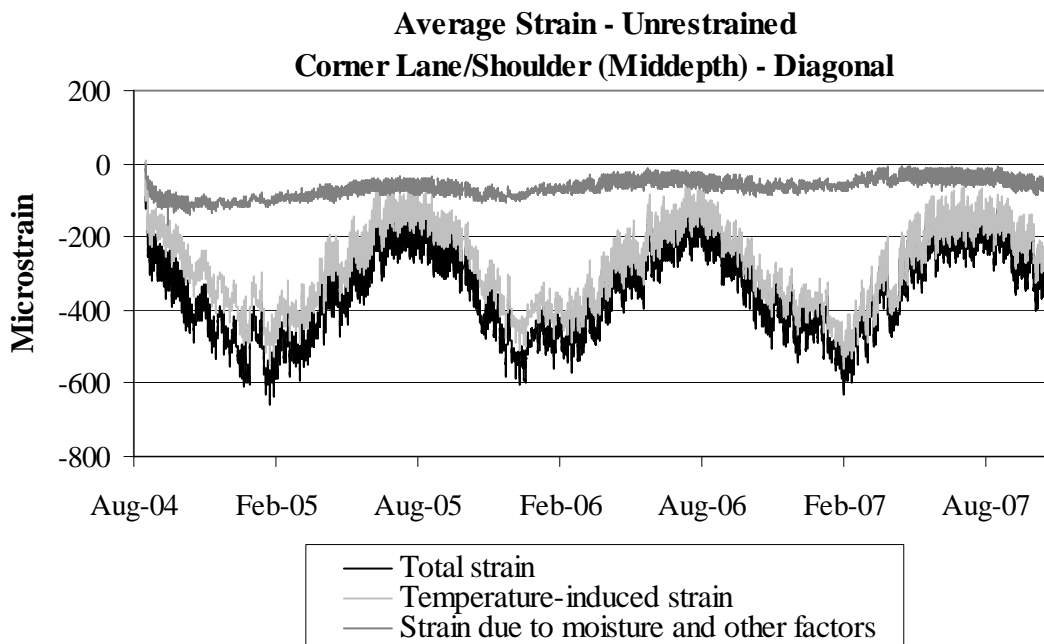


Figure D.48. Strains in the diagonal direction at the corner along the lane/shoulder joint at the middepth of the unrestrained slabs.

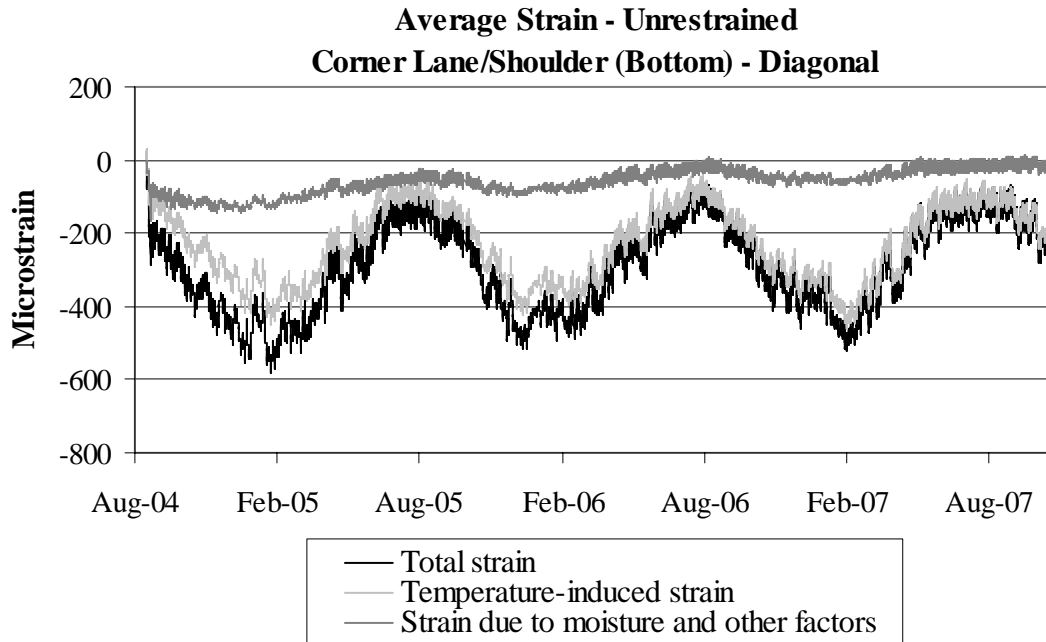


Figure D.49. Strains in the diagonal direction at the corner along the lane/shoulder joint at the bottom of the unrestrained slabs.

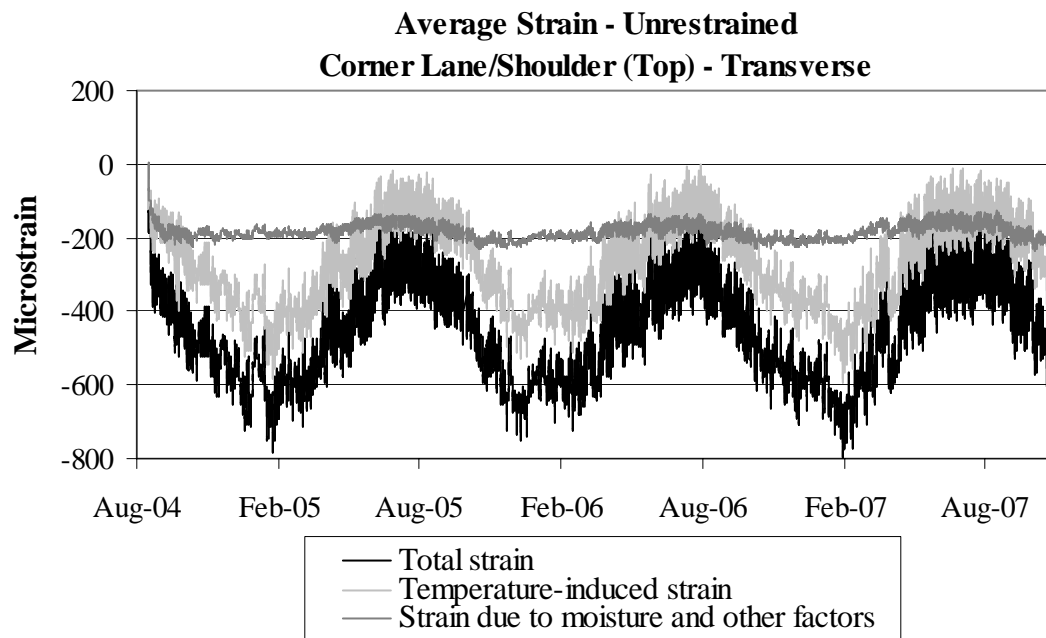


Figure D.50. Strains in the transverse direction at the corner along the lane/shoulder joint at the top of the unrestrained slabs.

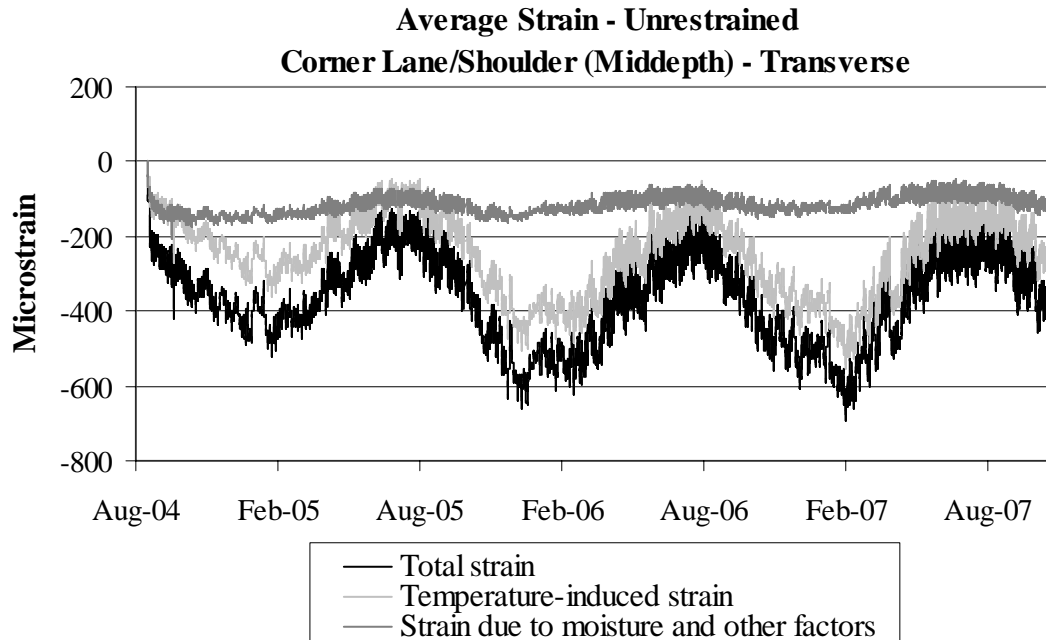


Figure D.51. Strains in the transverse direction at the corner along the lane/shoulder joint at the middepth of the unrestrained slabs.

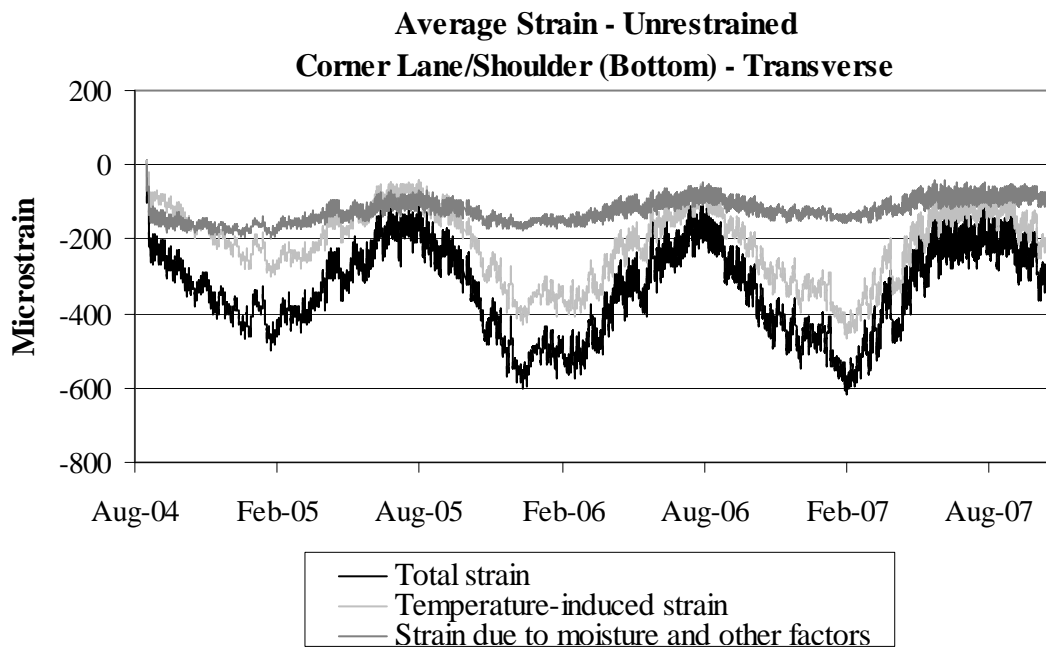


Figure D.52. Strains in the transverse direction at the corner along the lane/shoulder joint at the bottom of the unrestrained slabs.

Appendix E: Surface Profile Measurements

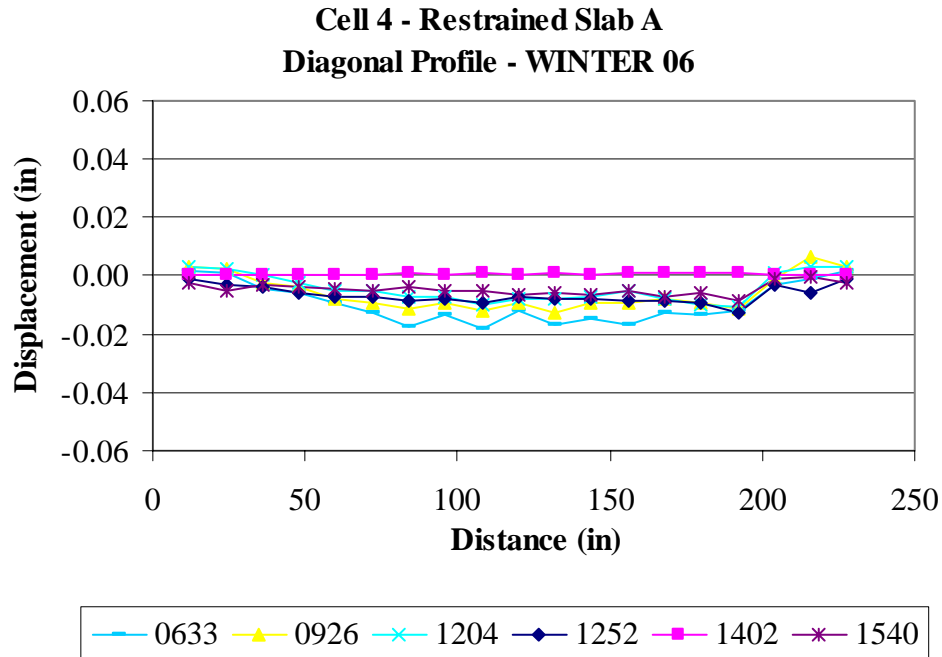


Figure E.1. Restrained Slab A diagonal surface profiles for the winter of 2006.

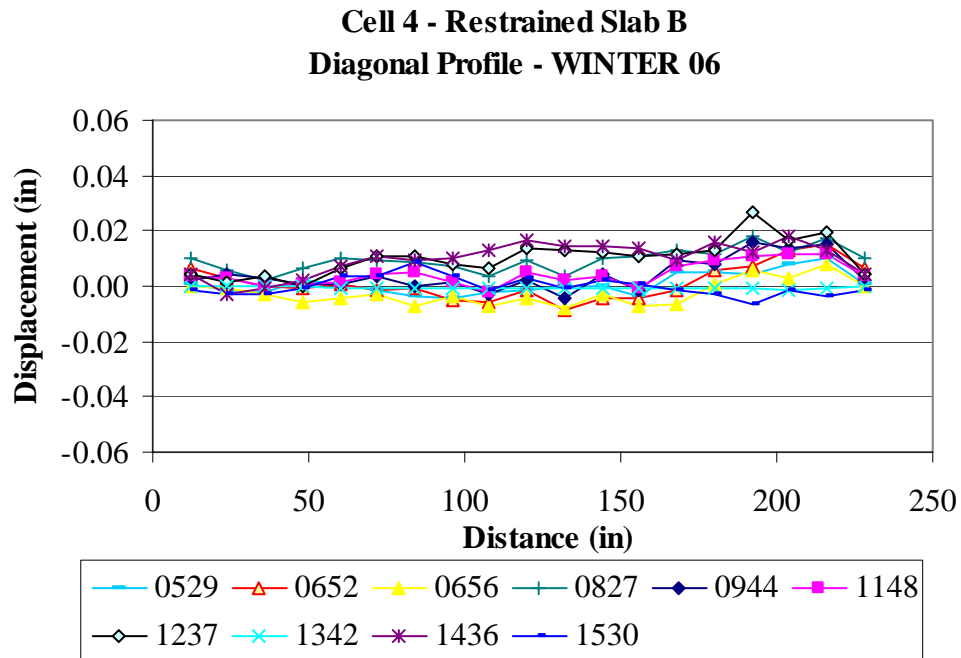


Figure E.2. Restrained Slab B diagonal surface profiles for the winter of 2006.

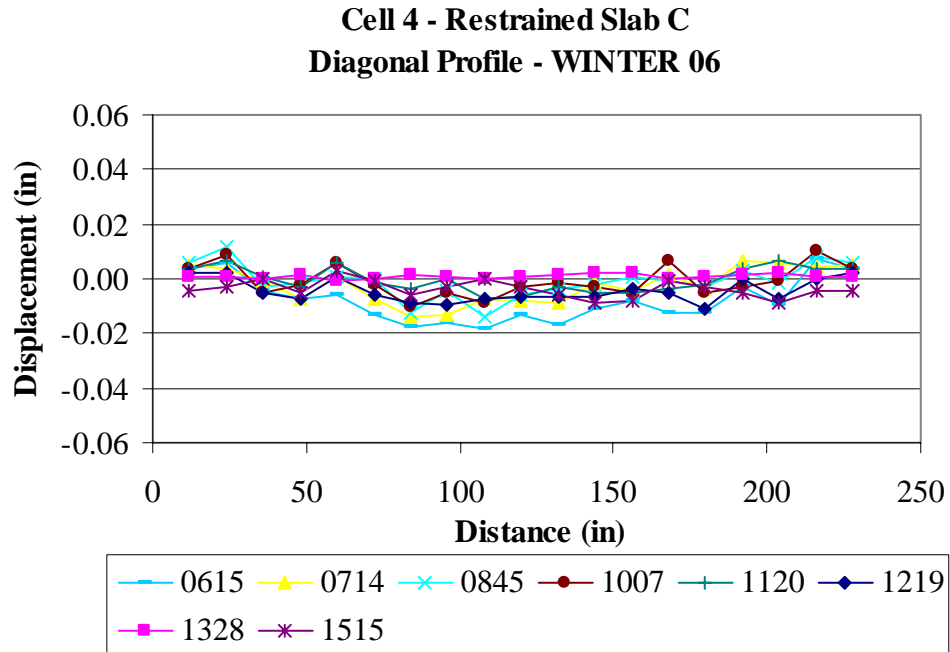


Figure E.3. Restrained Slab C diagonal surface profiles for the winter of 2006.

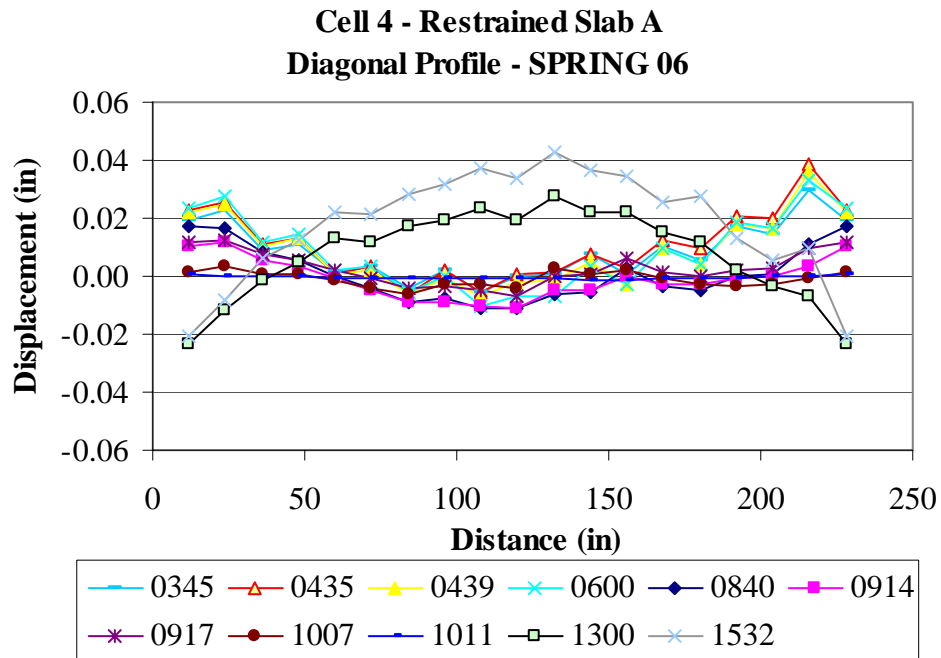


Figure E.4. Restrained Slab A diagonal surface profiles for the spring of 2006.

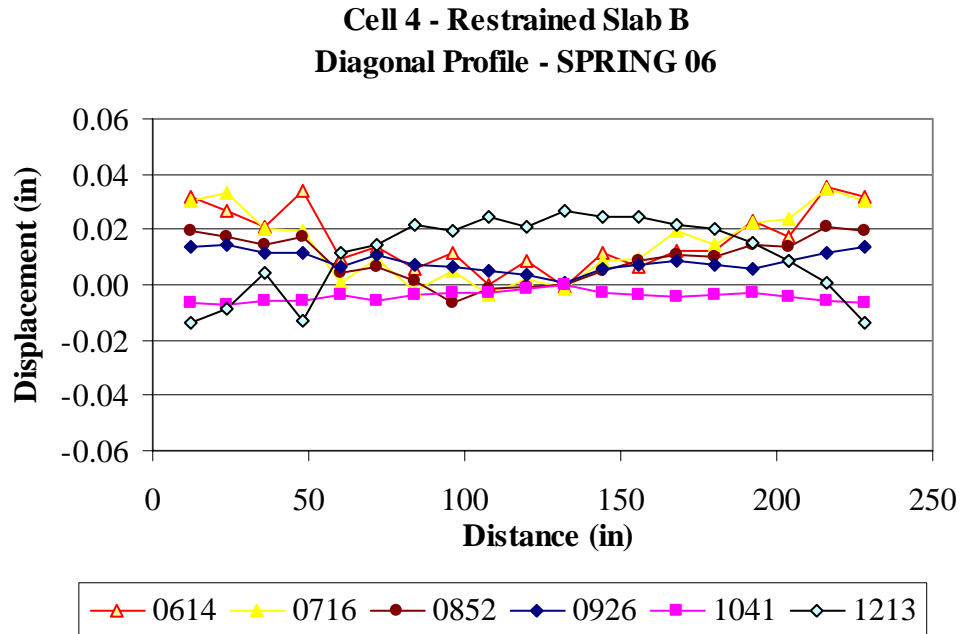


Figure E.5. Restrained Slab B diagonal surface profiles for the spring of 2006.

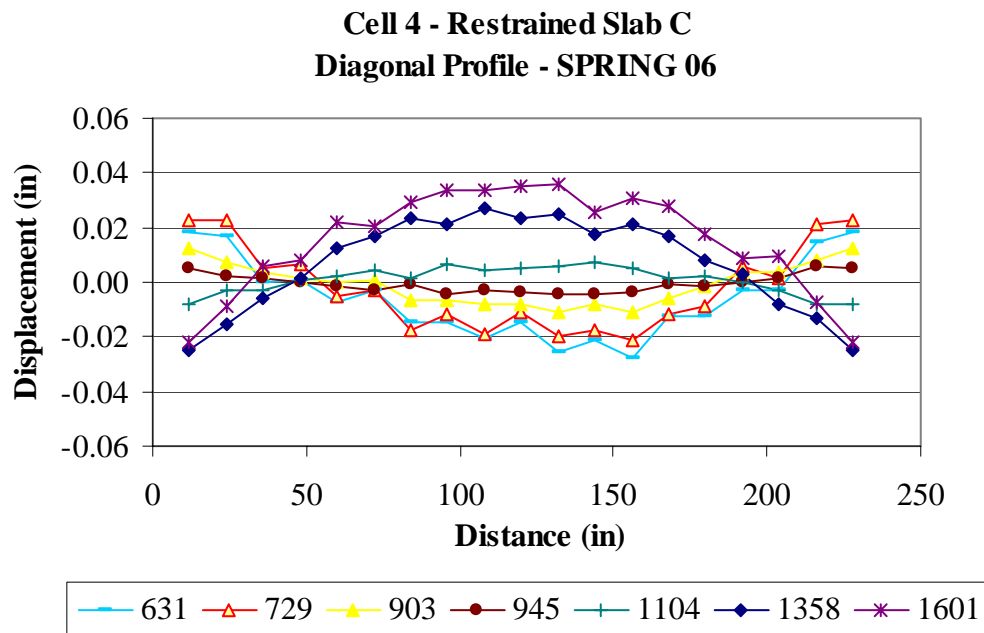


Figure E.6. Restrained Slab C diagonal surface profiles for the spring of 2006.

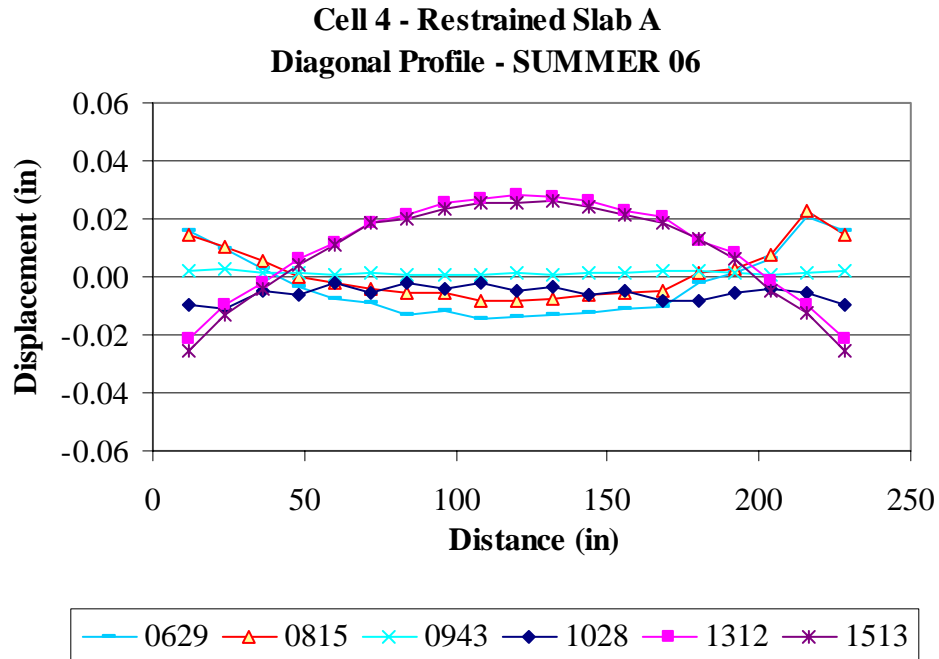


Figure E.7. Restrained Slab A diagonal surface profiles for the summer of 2006.

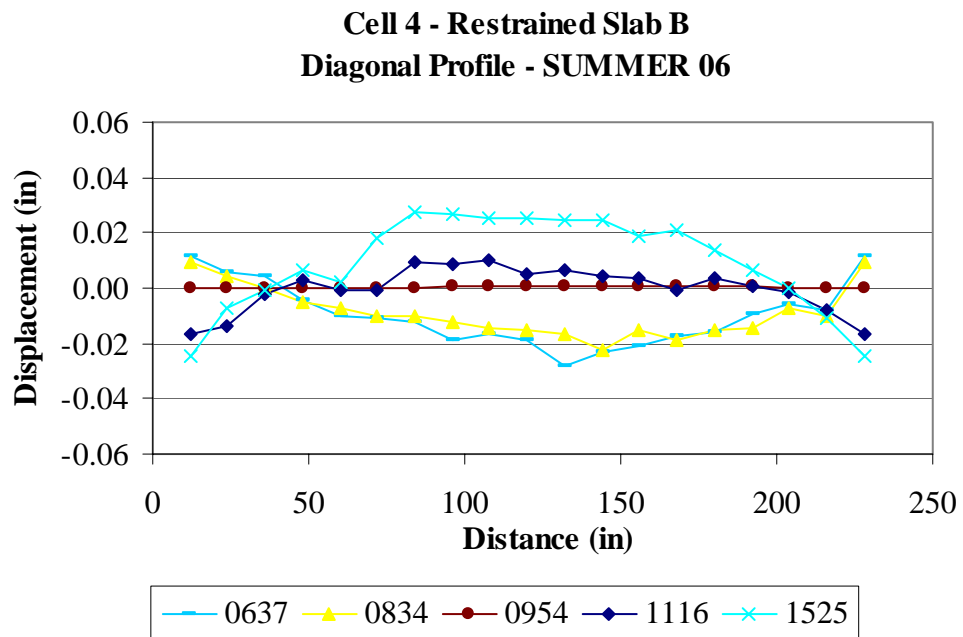


Figure E.8. Restrained Slab B diagonal surface profiles for the summer of 2006.

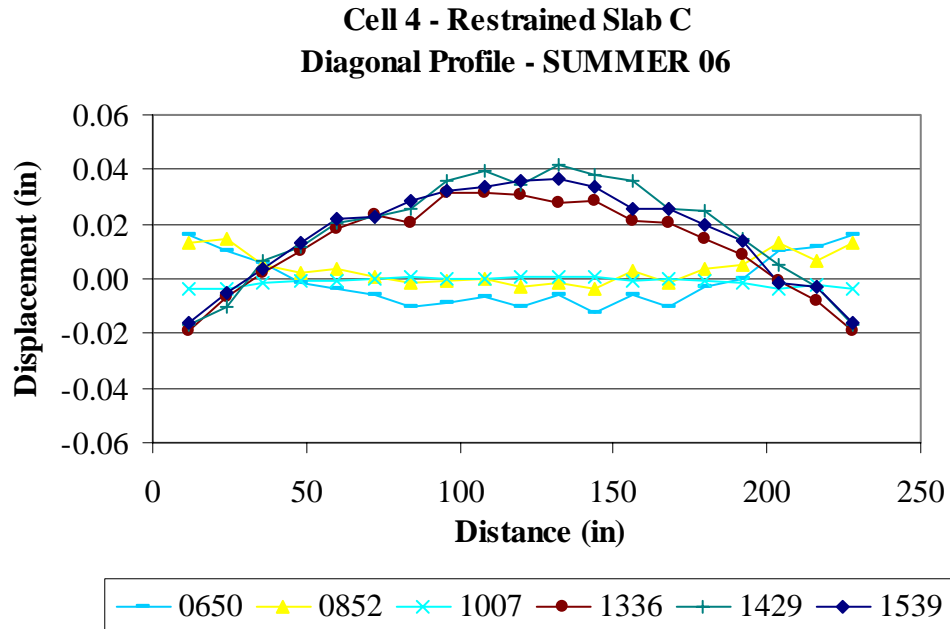


Figure E.9. Restrained Slab C diagonal surface profiles for the summer of 2006.

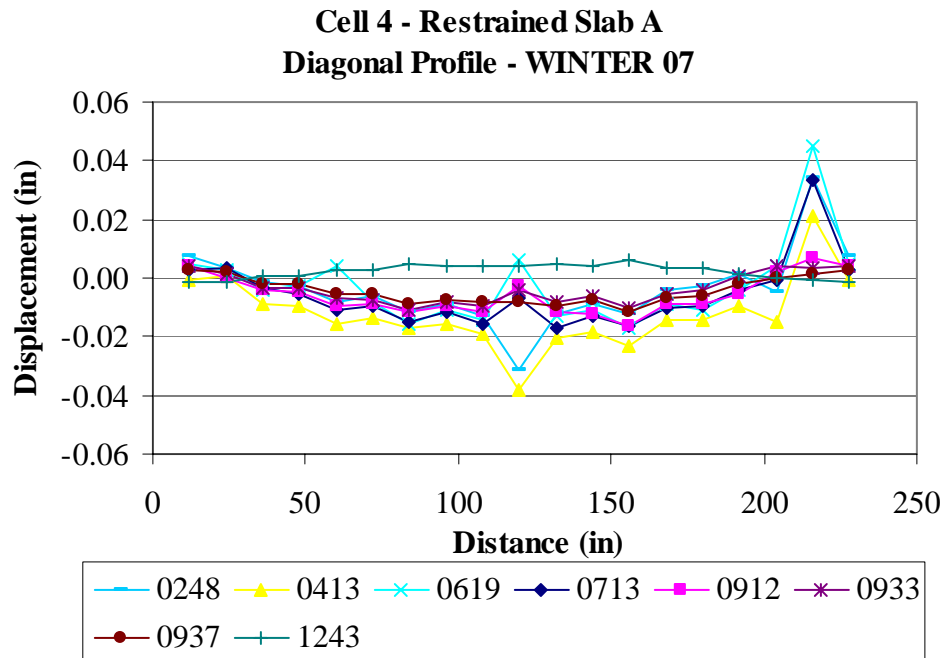


Figure E.10. Restrained Slab A diagonal surface profiles for the winter of 2007.

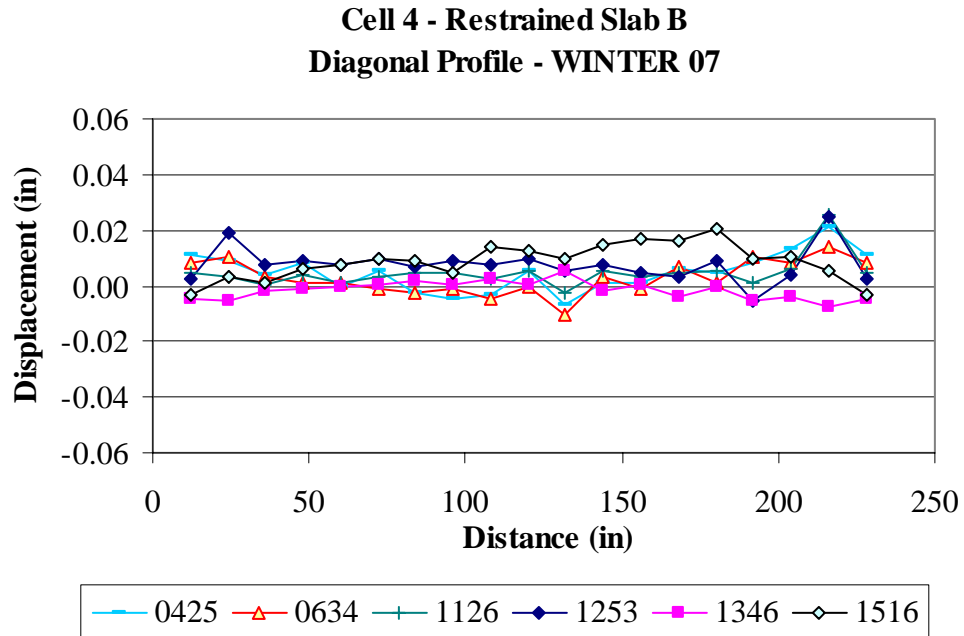


Figure E.11. Restrained Slab B diagonal surface profiles for the winter of 2007.

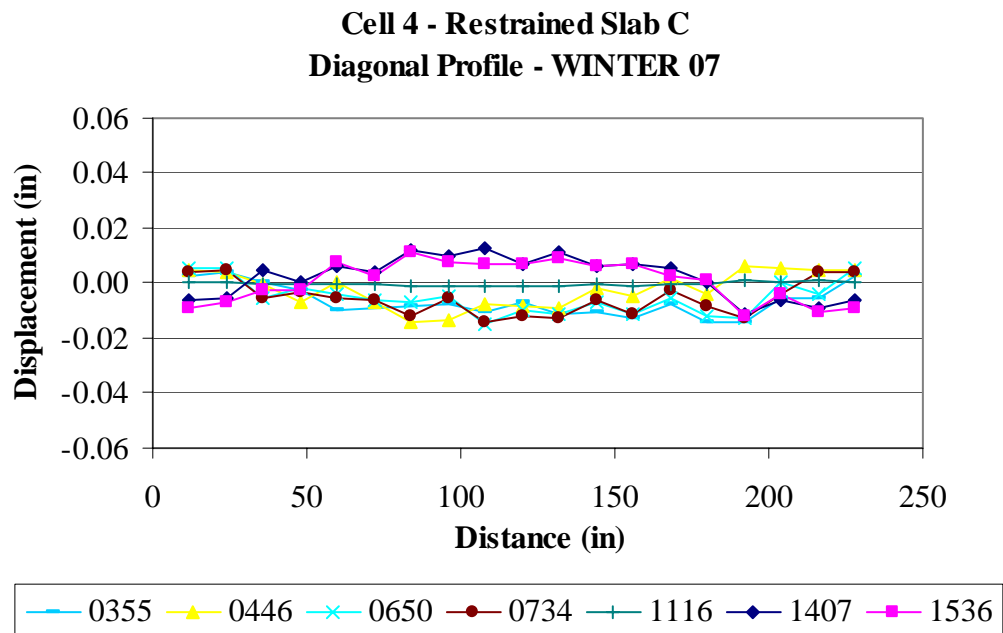


Figure E.12. Restrained Slab C diagonal surface profiles for the winter of 2007.

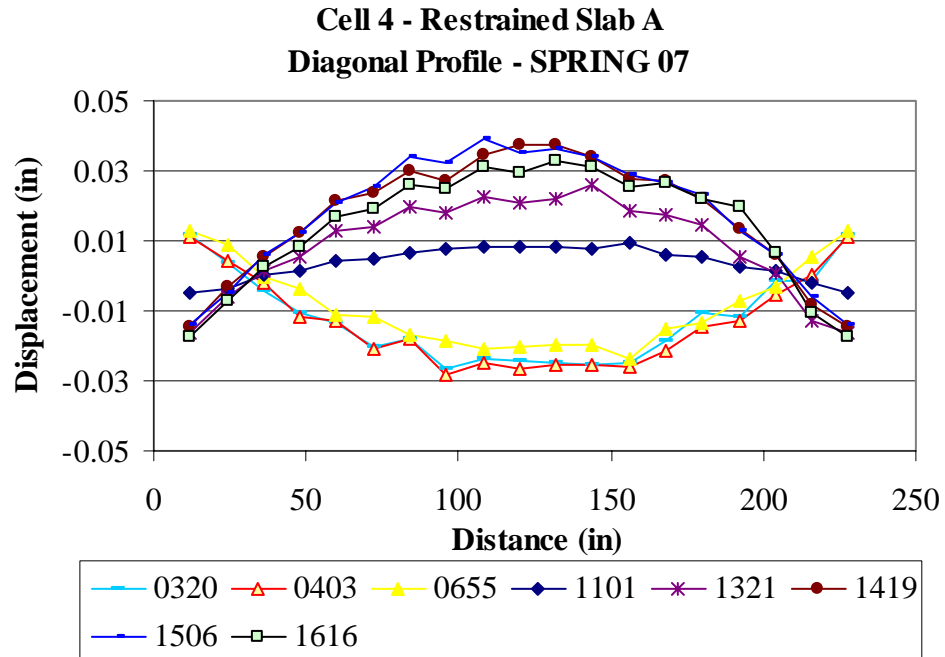


Figure E.13. Restrained Slab A diagonal surface profiles for the spring of 2007.

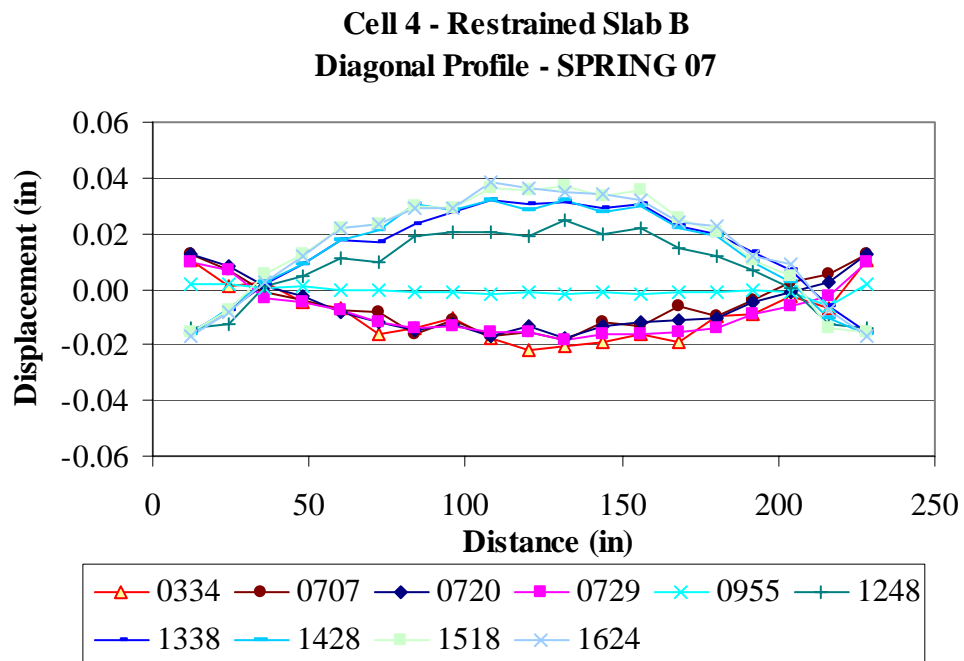


Figure E.14. Restrained Slab B diagonal surface profiles for the spring of 2007.

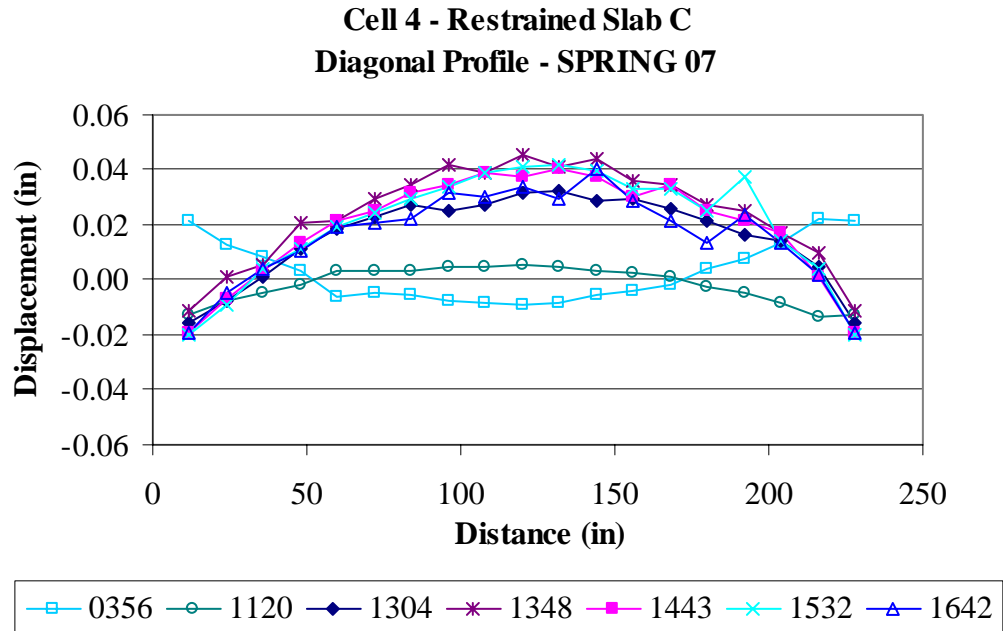


Figure E.15. Restrained Slab C diagonal surface profiles for the spring of 2007.

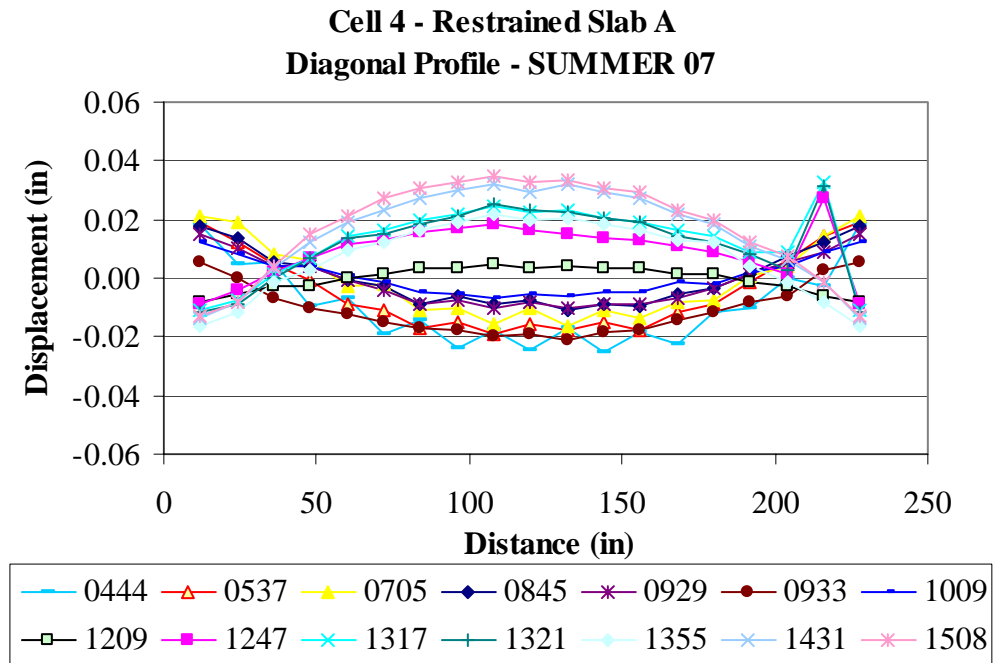


Figure E.16. Restrained Slab A diagonal surface profiles for the summer of 2007.

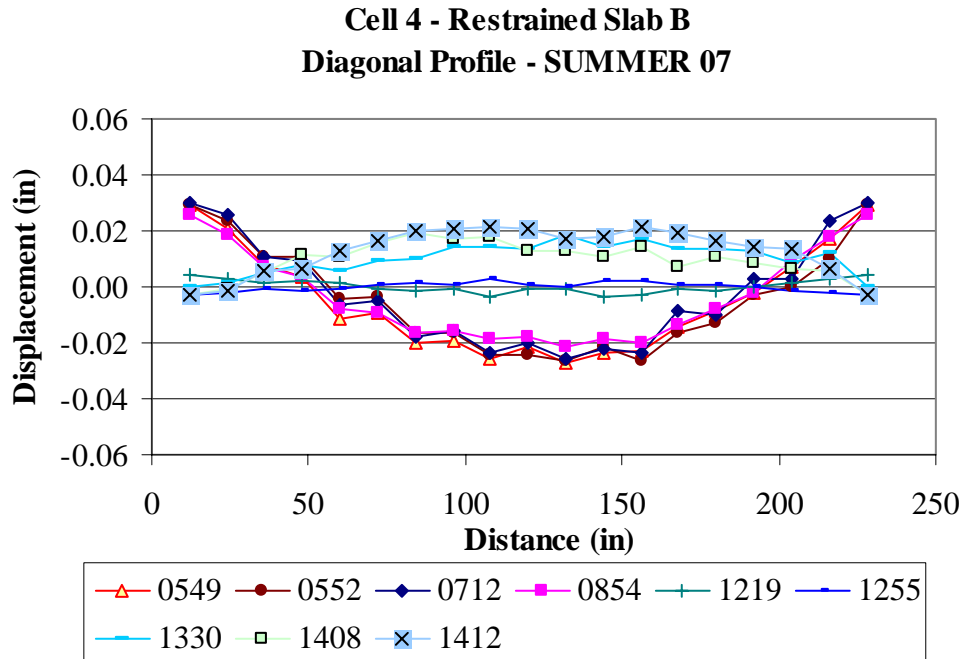


Figure E.17. Restrained Slab B diagonal surface profiles for the summer of 2007.

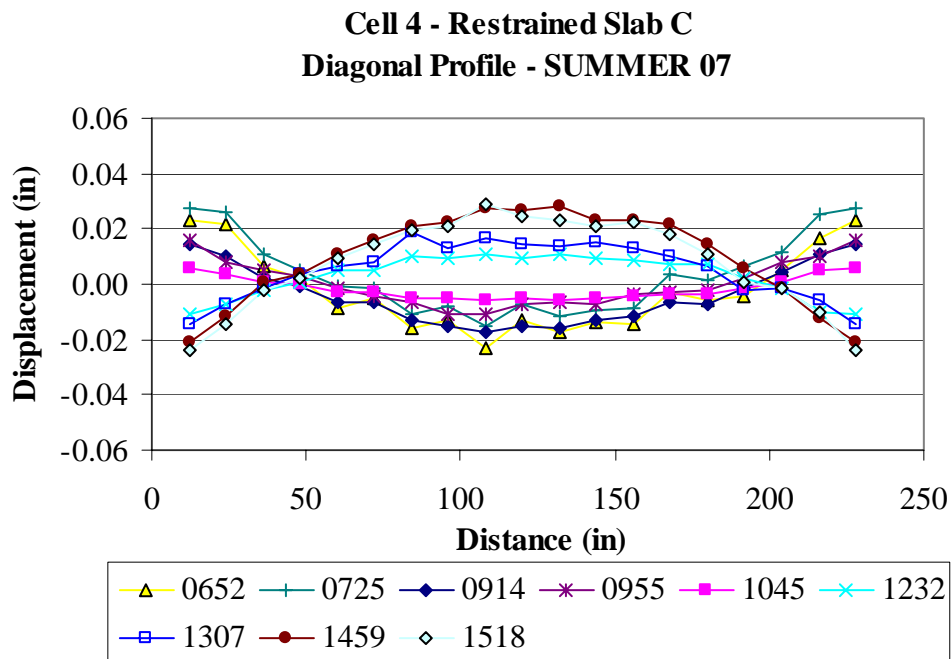


Figure E.18. Restrained Slab C diagonal surface profiles for the summer of 2007.

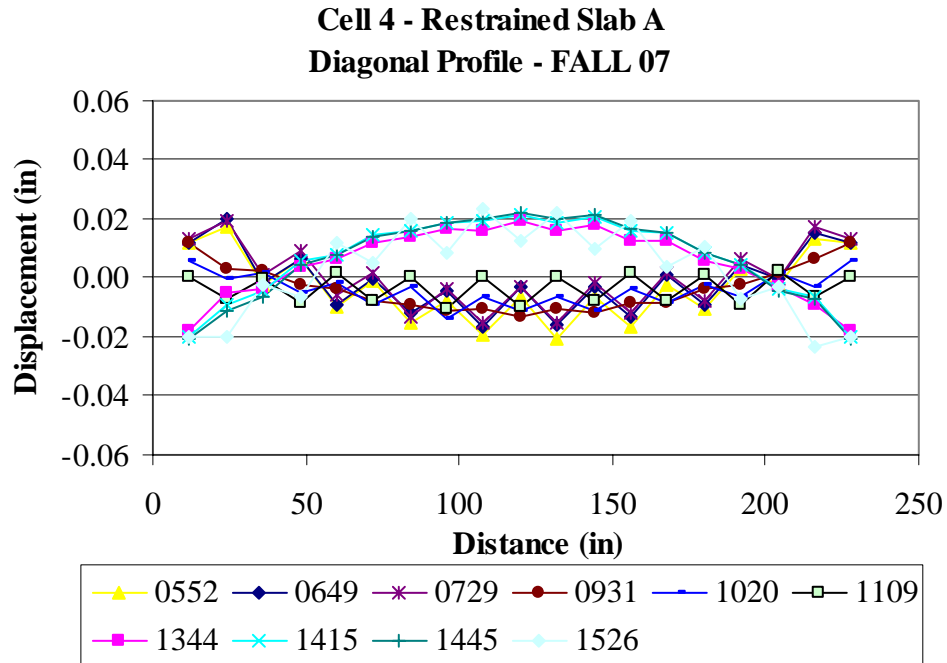


Figure E.19. Restrained Slab A diagonal surface profiles for the fall of 2007.

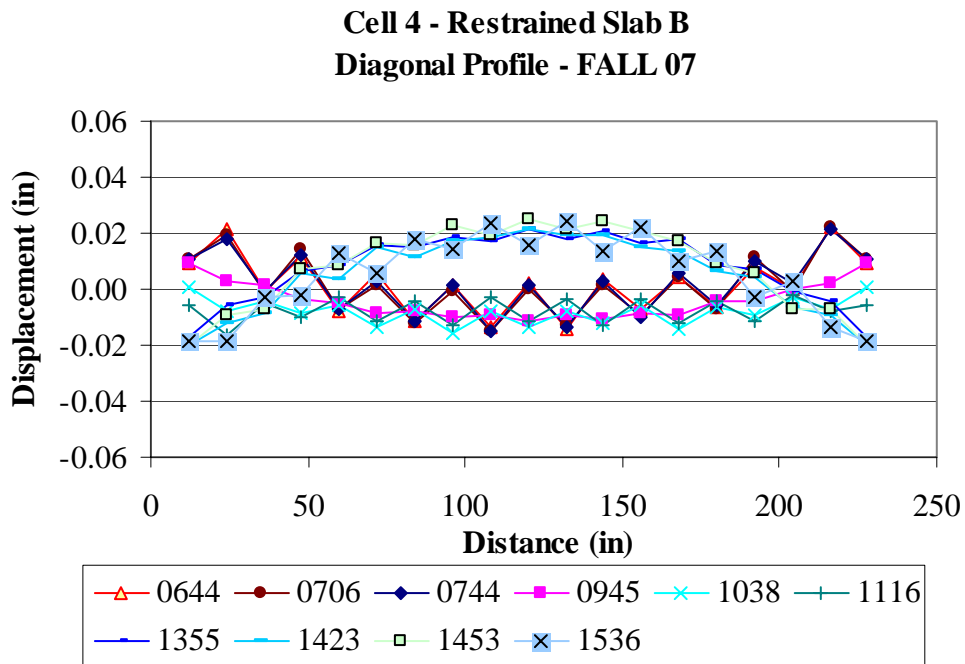


Figure E.20. Restrained Slab B diagonal surface profiles for the fall of 2007.

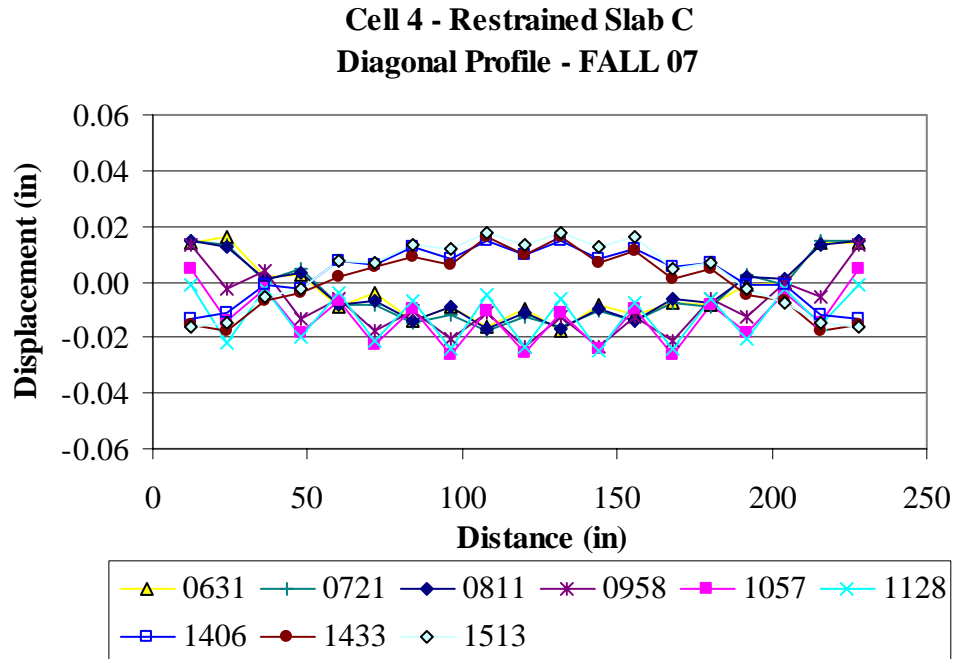


Figure E.21. Restrained Slab C diagonal surface profiles for the fall of 2007.

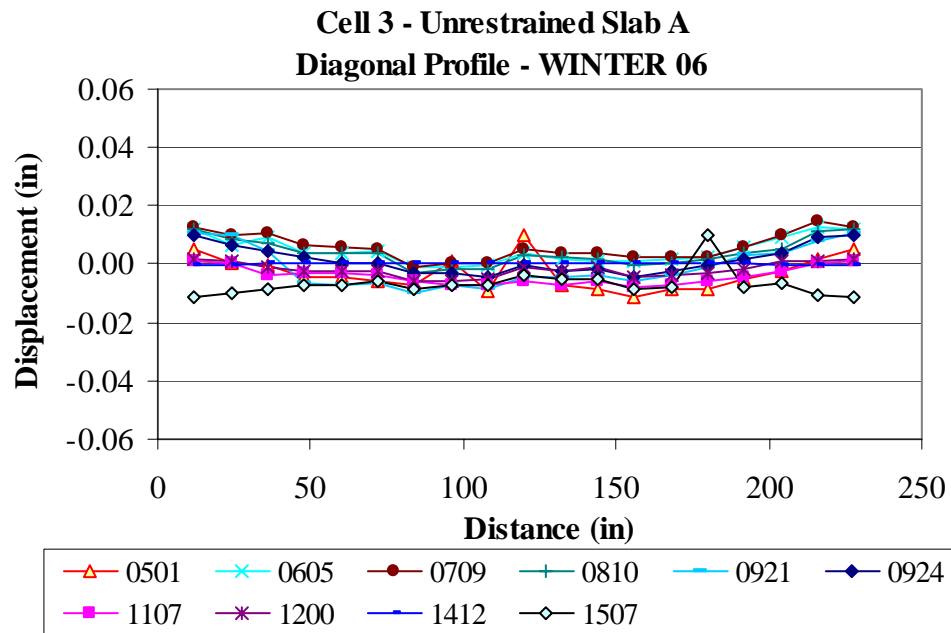


Figure E.22. Unrestrained Slab A diagonal surface profiles for the winter of 2006.

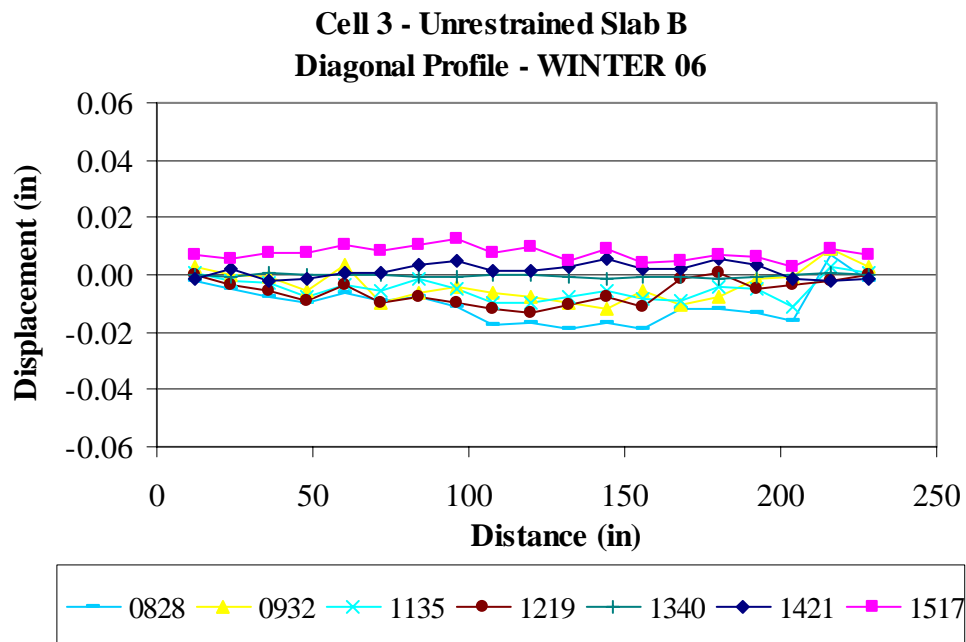


Figure E.23. Unrestrained Slab B diagonal surface profiles for the winter of 2006.

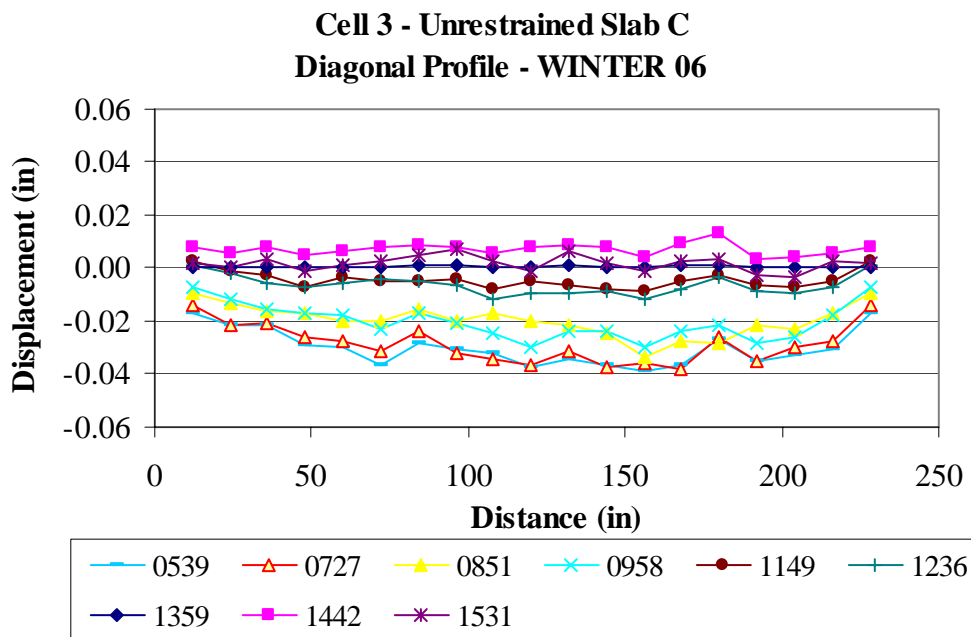


Figure E.24. Unrestrained Slab C diagonal surface profiles for the winter of 2006.

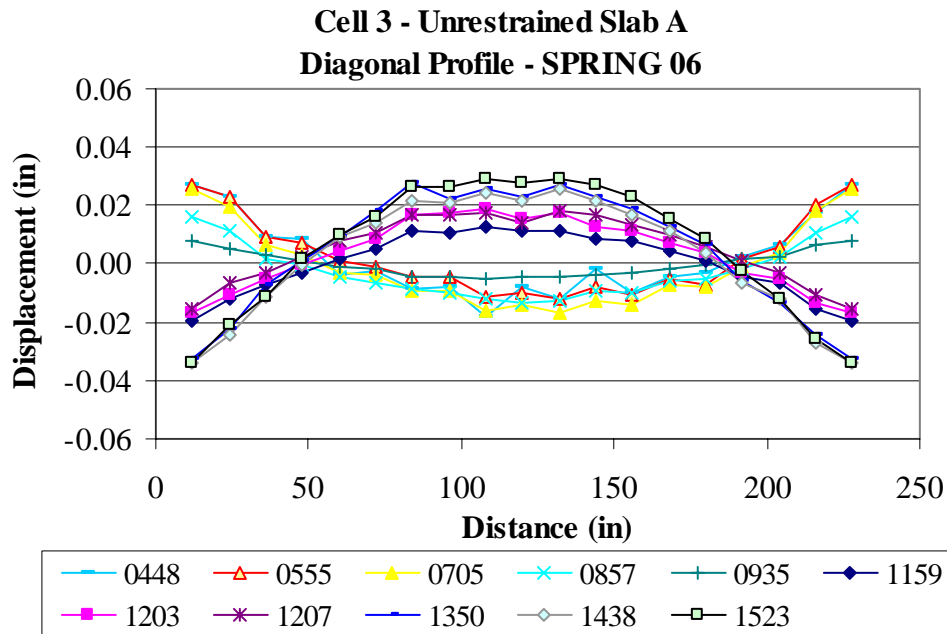


Figure E.25. Unrestrained Slab A diagonal surface profiles for the spring of 2006.

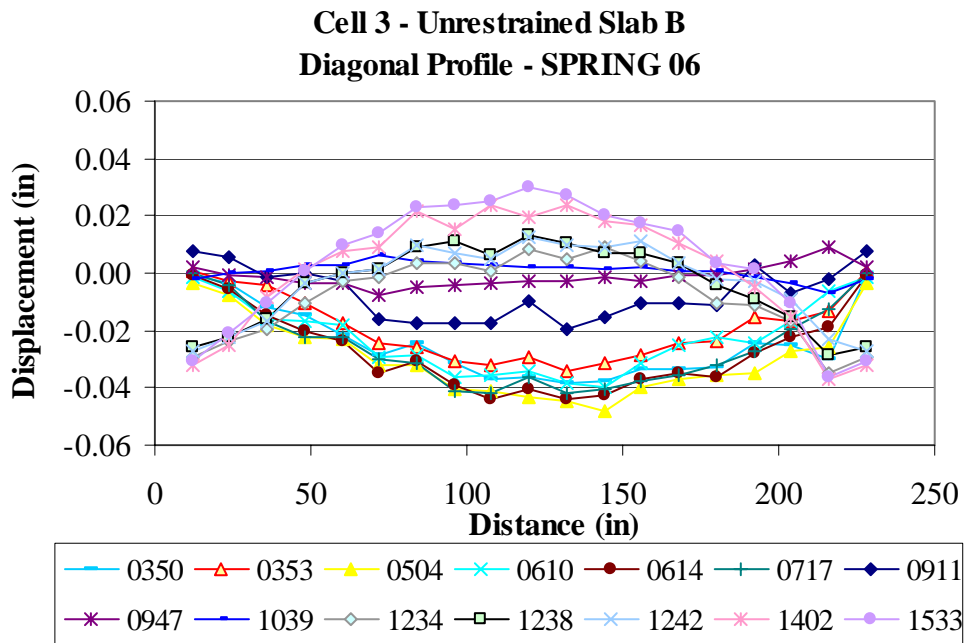


Figure E.26. Unrestrained Slab B diagonal surface profiles for the spring of 2006.

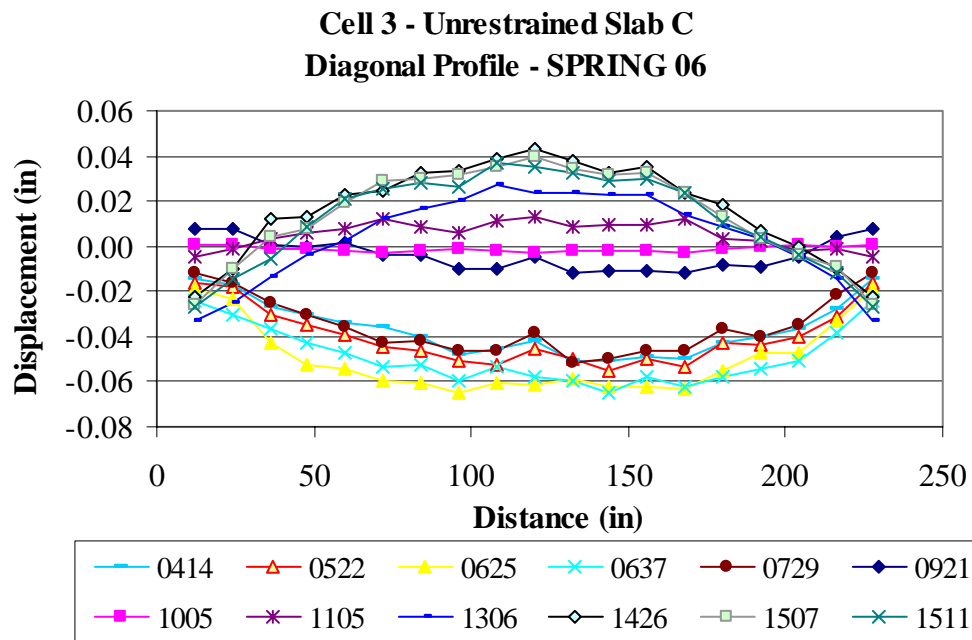


Figure E.27. Unrestrained Slab C diagonal surface profiles for the spring of 2006.

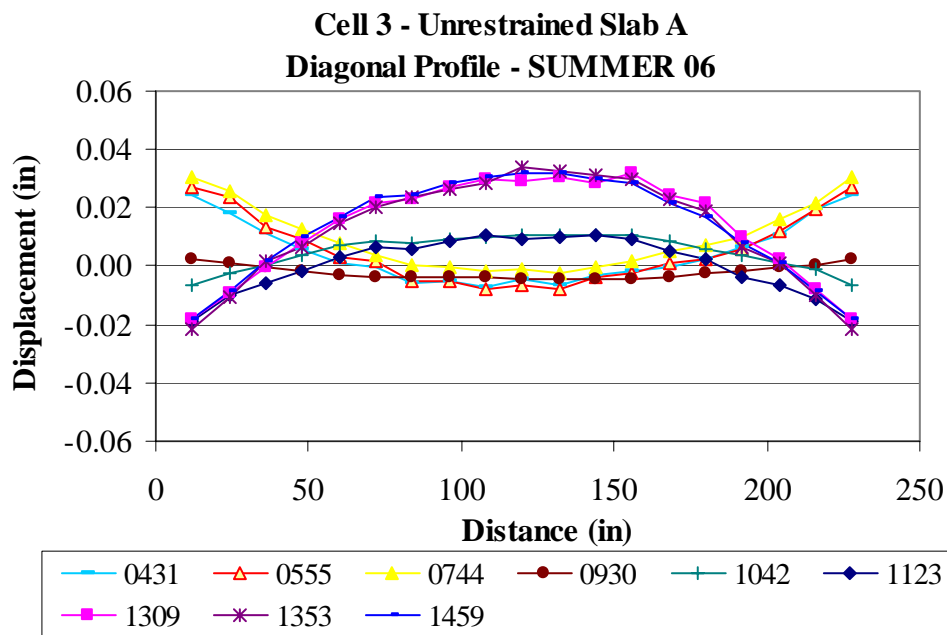


Figure E.28. Unrestrained Slab A diagonal surface profiles for the summer of 2006.

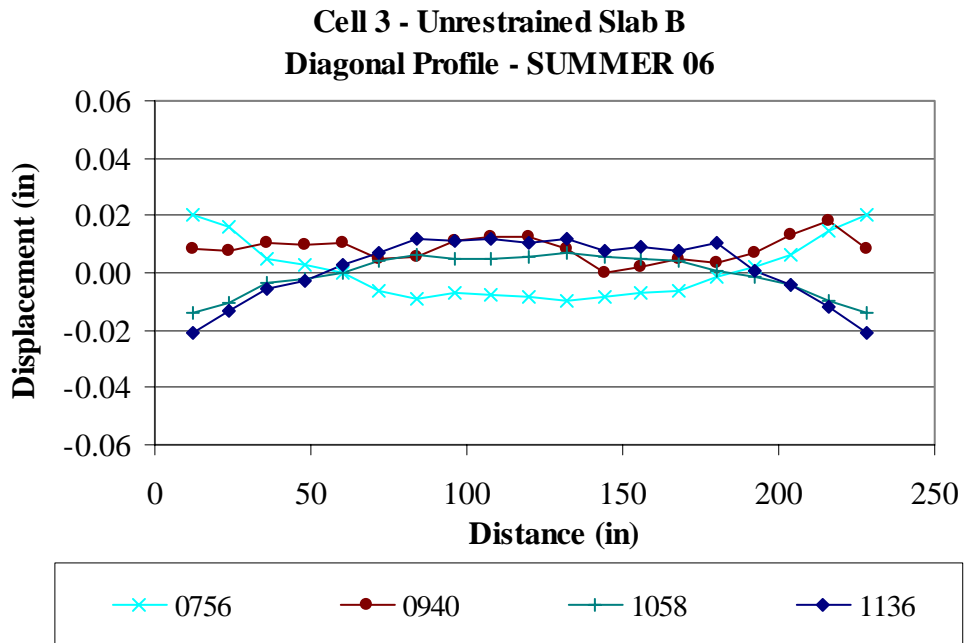


Figure E.29. Unrestrained Slab B diagonal surface profiles for the summer of 2006.

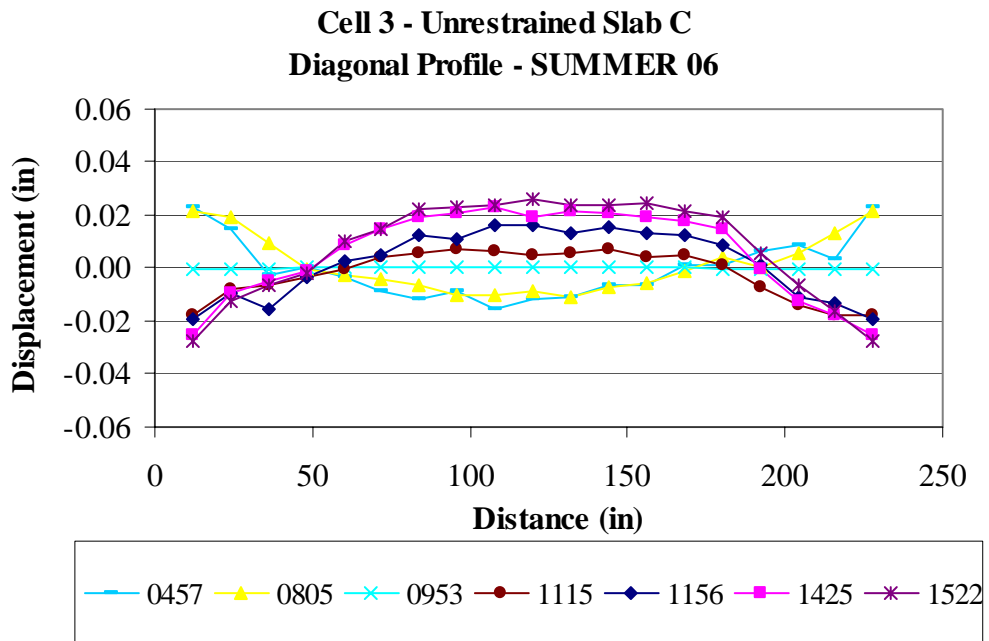


Figure E.30. Unrestrained Slab C diagonal surface profiles for the summer of 2006.

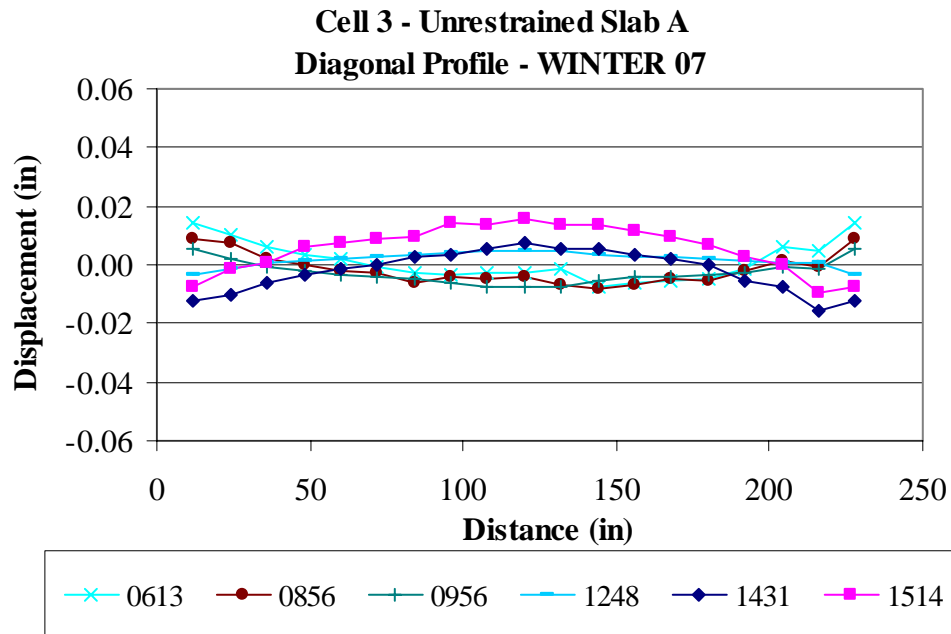


Figure E.31. Unrestrained Slab A diagonal surface profiles for the winter of 2007.

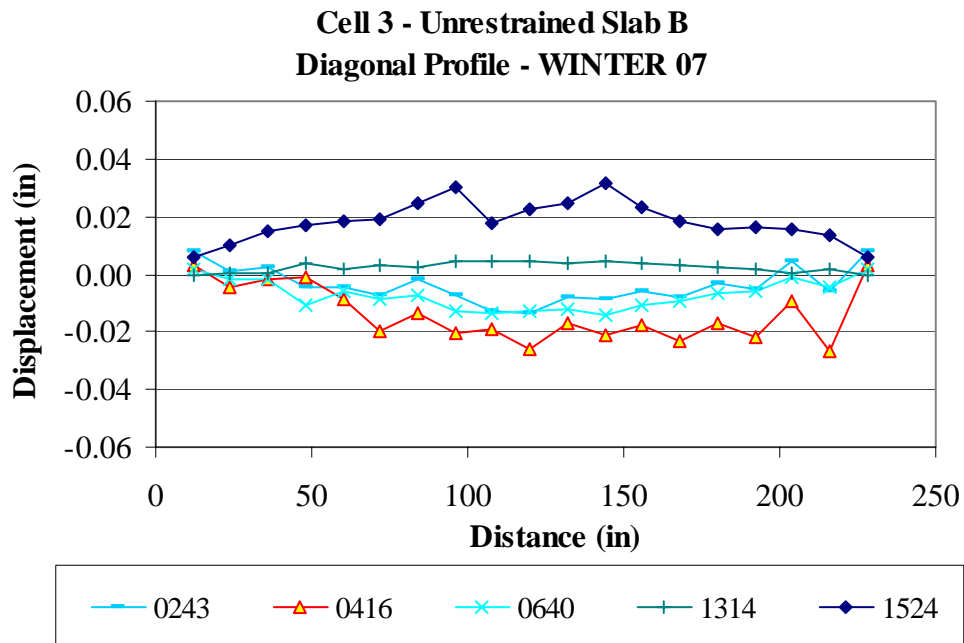


Figure E.32. Unrestrained Slab B diagonal surface profiles for the winter of 2007.

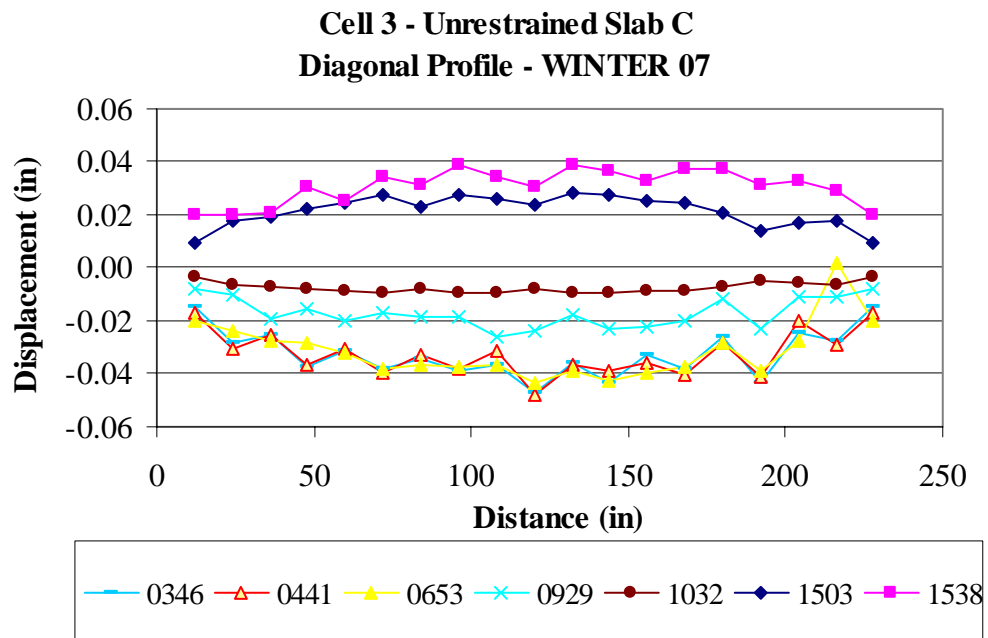


Figure E.33. Unrestrained Slab C diagonal surface profiles for the winter of 2007.

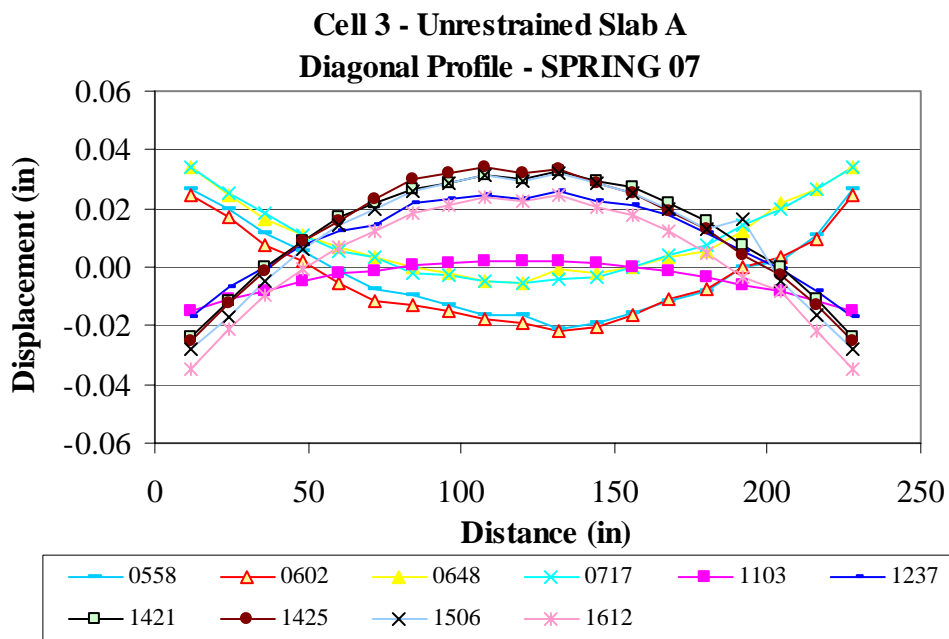


Figure E.34. Unrestrained Slab A diagonal surface profiles for the spring of 2007.

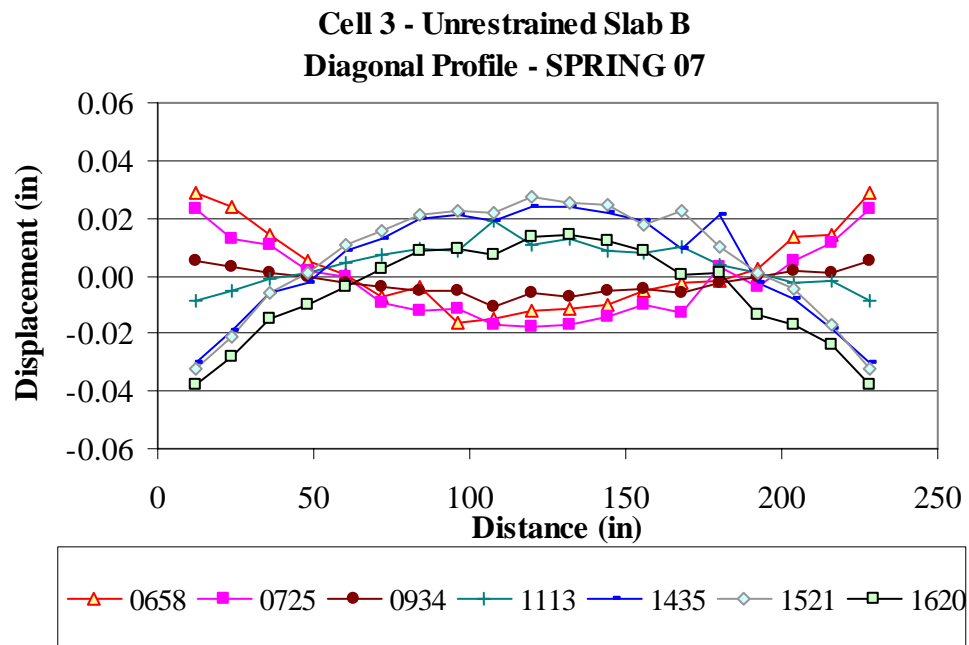


Figure E.35. Unrestrained Slab B diagonal surface profiles for the spring of 2007.

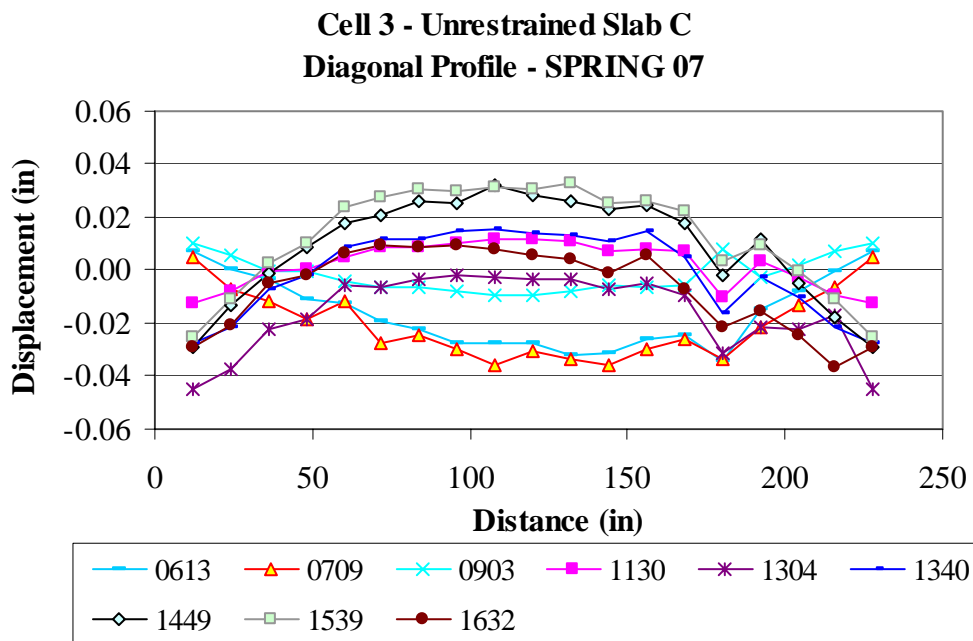


Figure E.36. Unrestrained Slab C diagonal surface profiles for the spring of 2007.

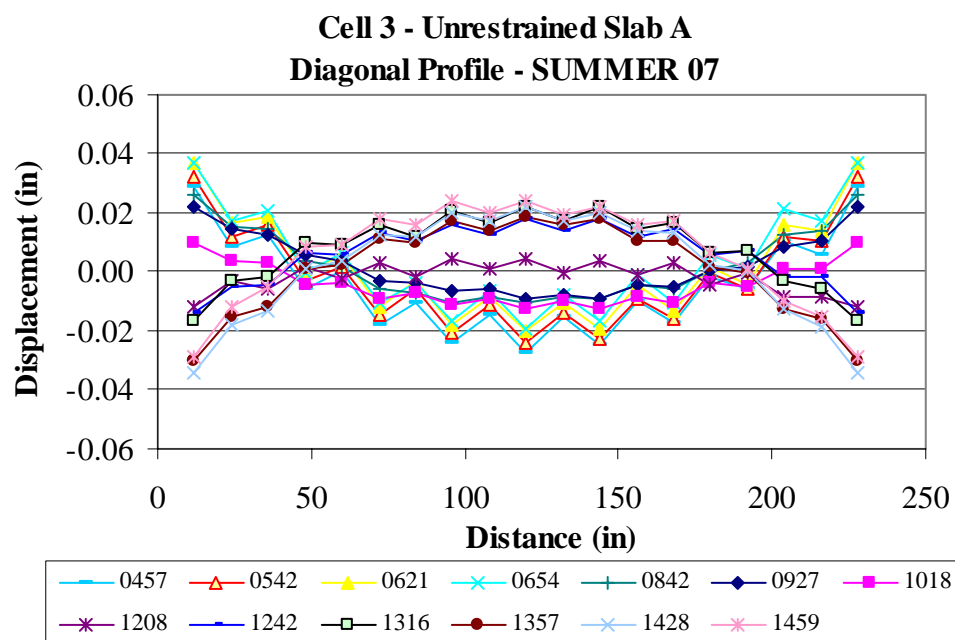


Figure E.37. Unrestrained Slab A diagonal surface profiles for the summer of 2007.

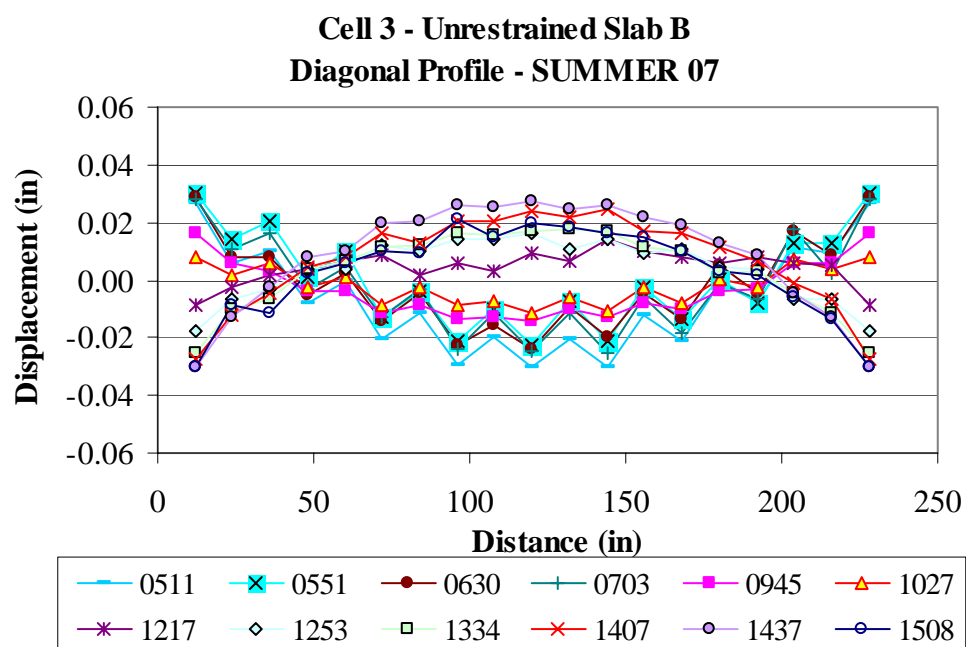


Figure E.38. Unrestrained Slab B diagonal surface profiles for the summer of 2007.

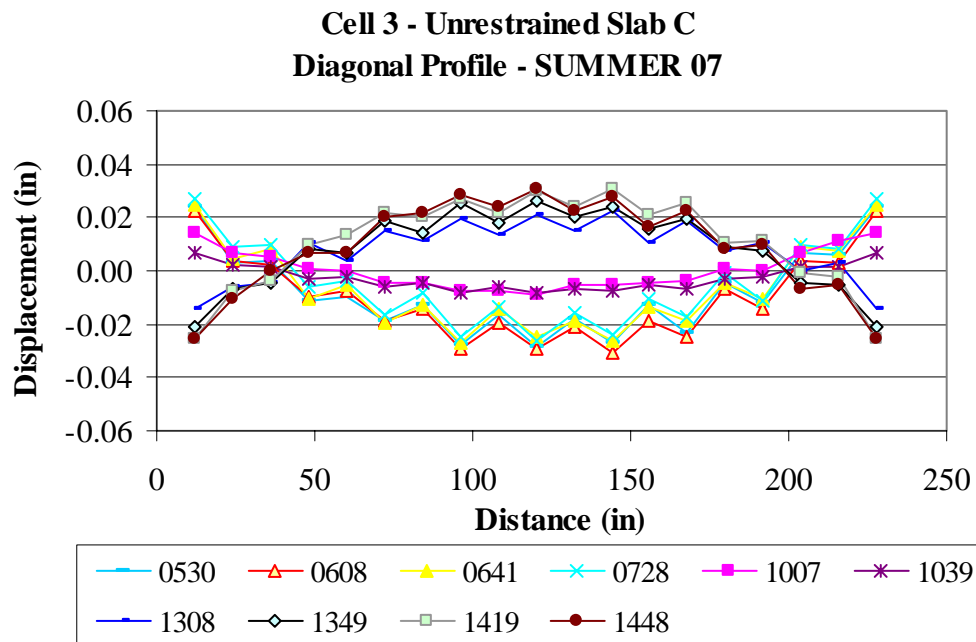


Figure E.39. Unrestrained Slab C diagonal surface profiles for the summer of 2007.

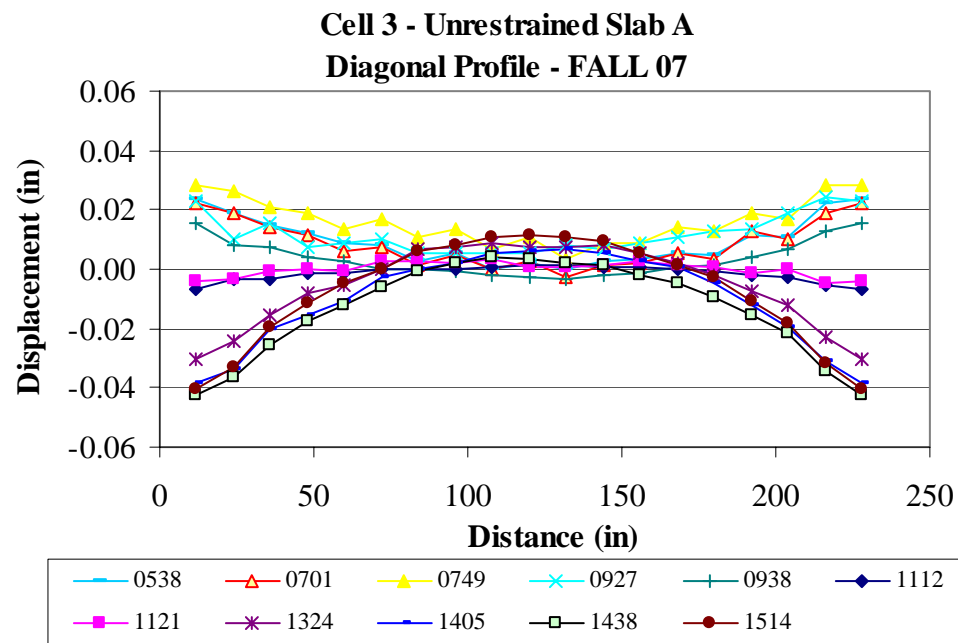


Figure E.40. Unrestrained Slab A diagonal surface profiles for the fall of 2007.

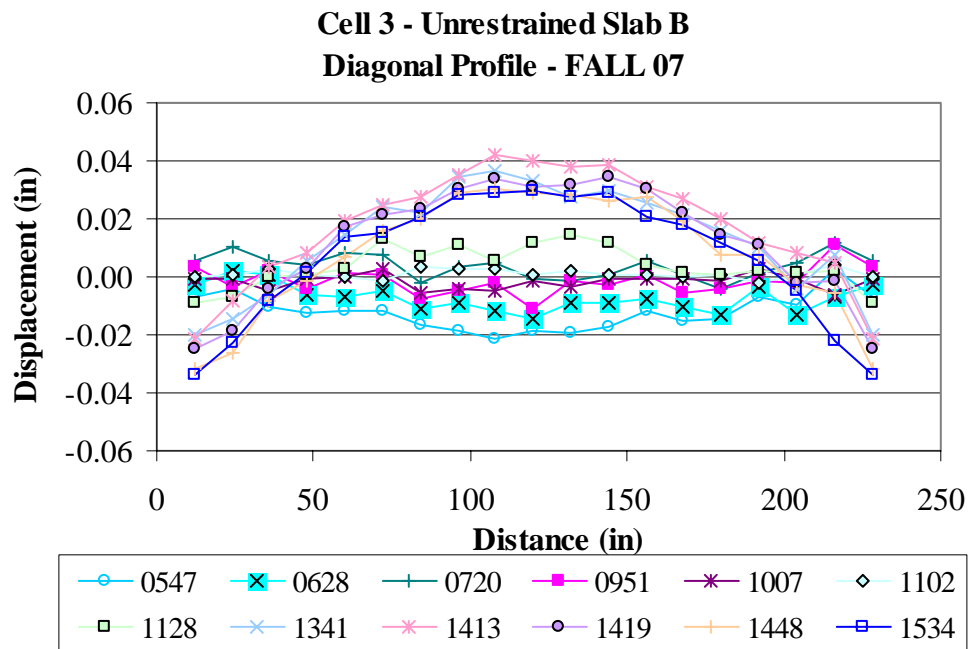


Figure E.41. Unrestrained Slab B diagonal surface profiles for the fall of 2007.

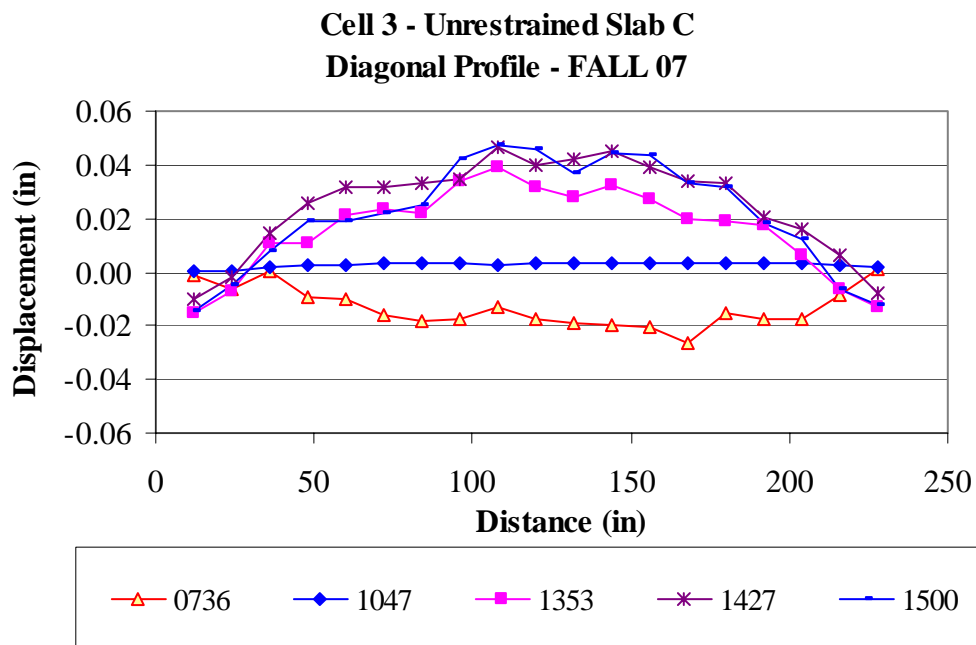


Figure E.42. Unrestrained Slab C diagonal surface profiles for the fall of 2007.

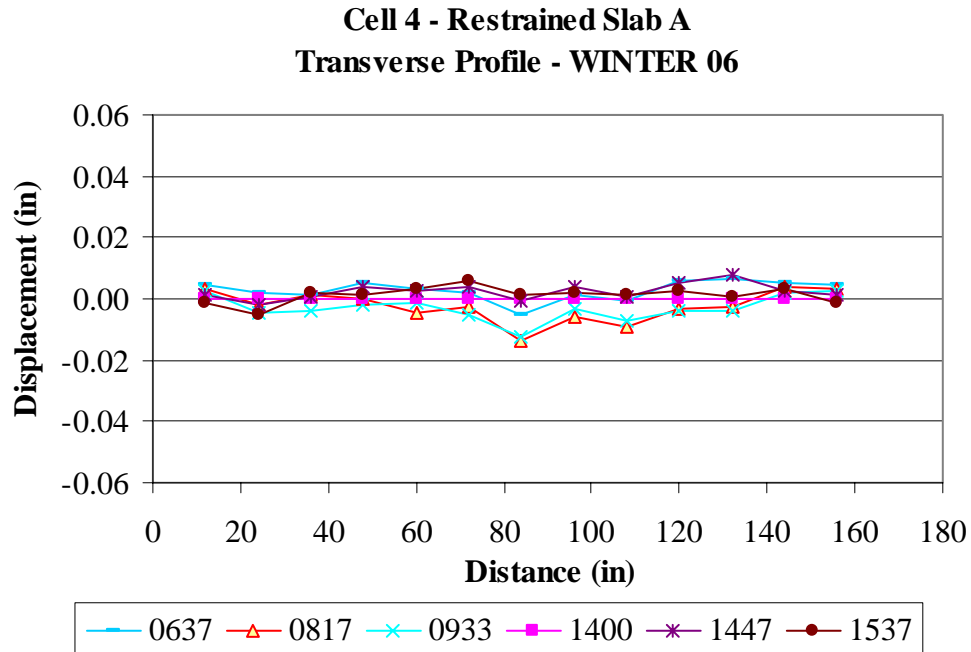


Figure E.43. Restrained Slab A Line A transverse surface profiles for the winter of 2006.

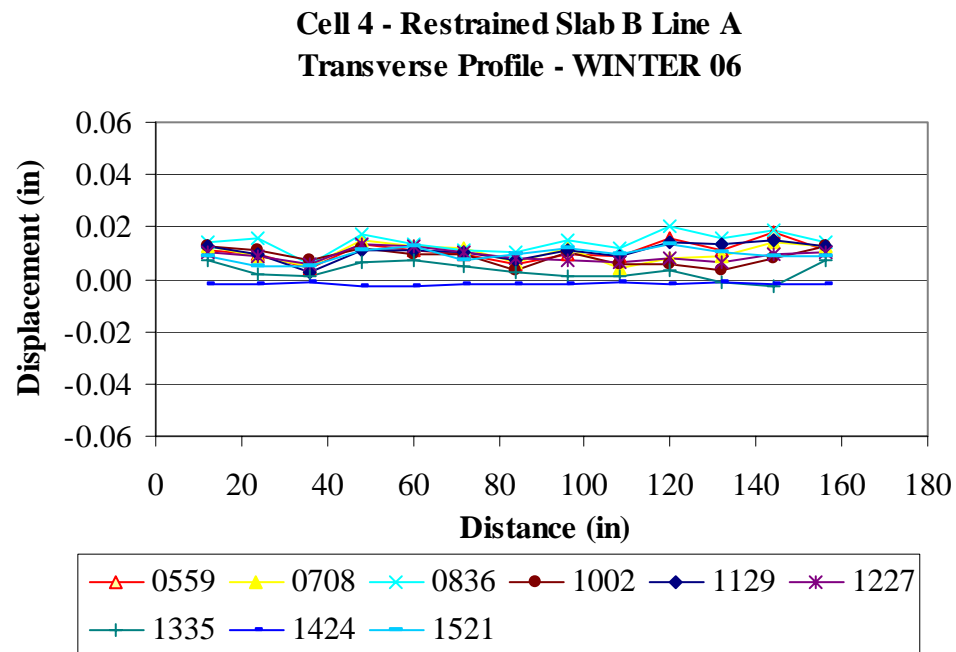


Figure E.44. Restrained Slab B Line A transverse surface profiles for the winter of 2006.

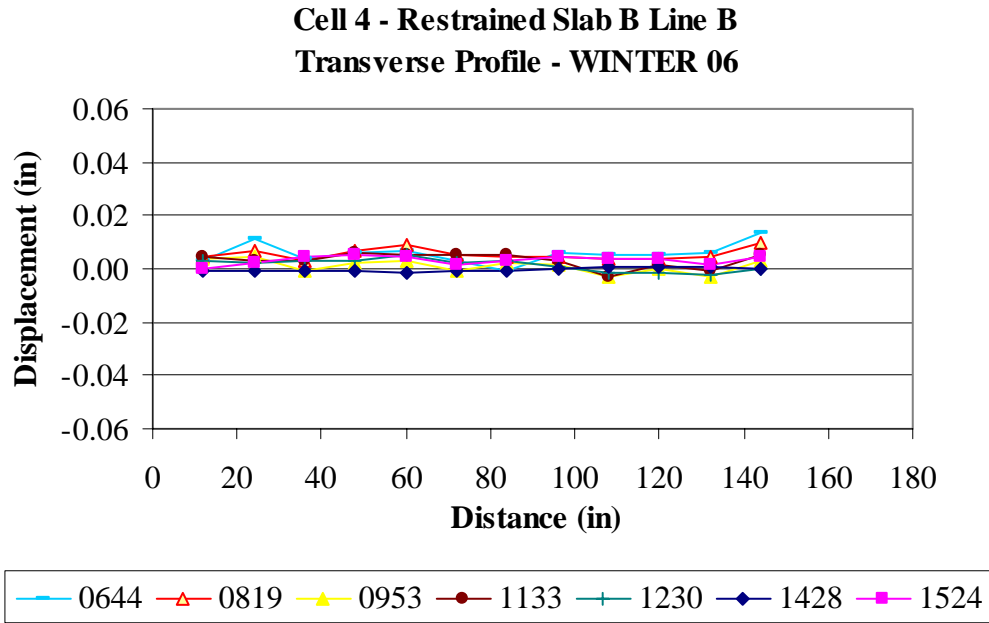


Figure E.45. Restrained Slab B Line B transverse surface profiles for the winter of 2006.

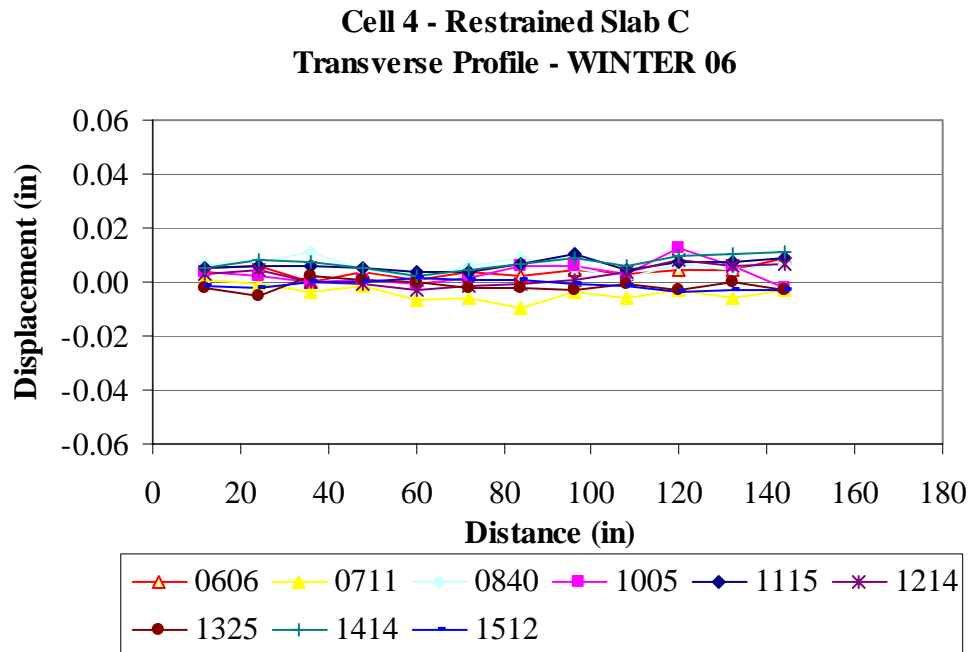


Figure E.46. Restrained Slab C Line B transverse surface profiles for the winter of 2006.

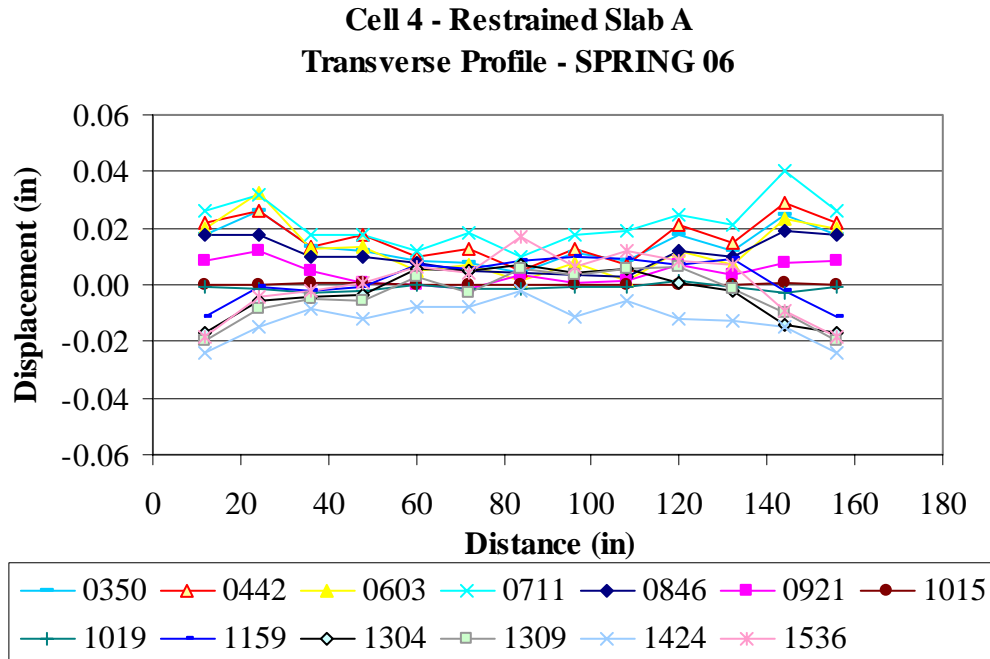


Figure E.47. Restrained Slab A Line A transverse surface profiles for the spring of 2006.

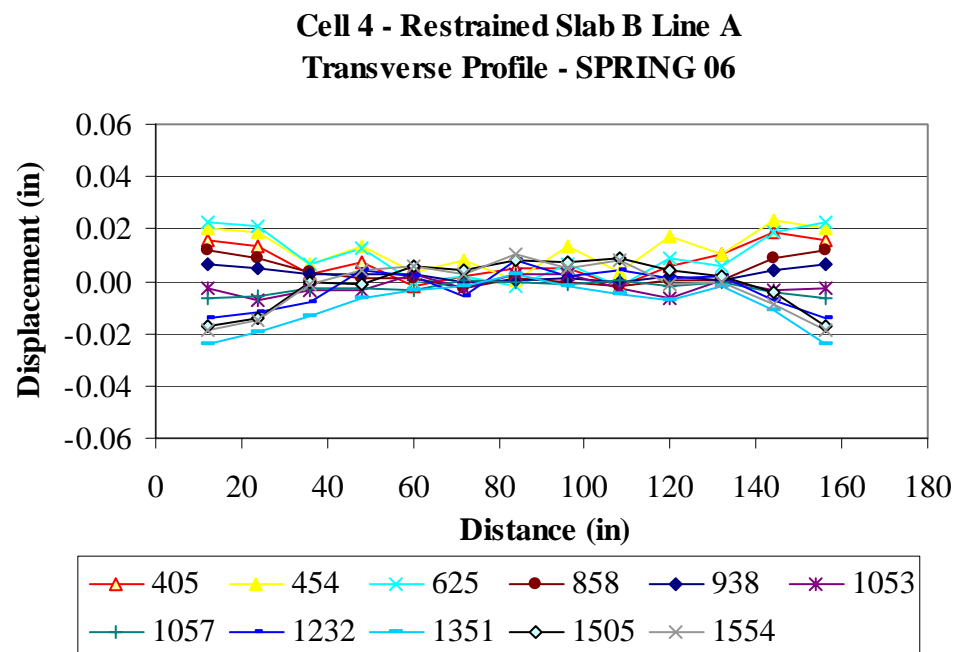


Figure E.48. Restrained Slab B Line A transverse surface profiles for the spring of 2006.

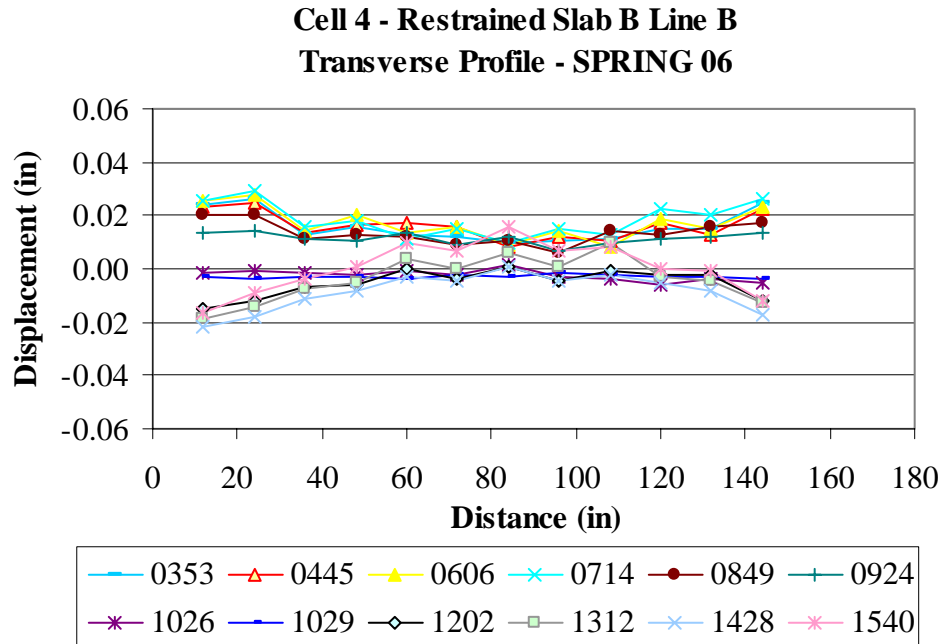


Figure E.49. Restrained Slab B Line B transverse surface profiles for the spring of 2006.

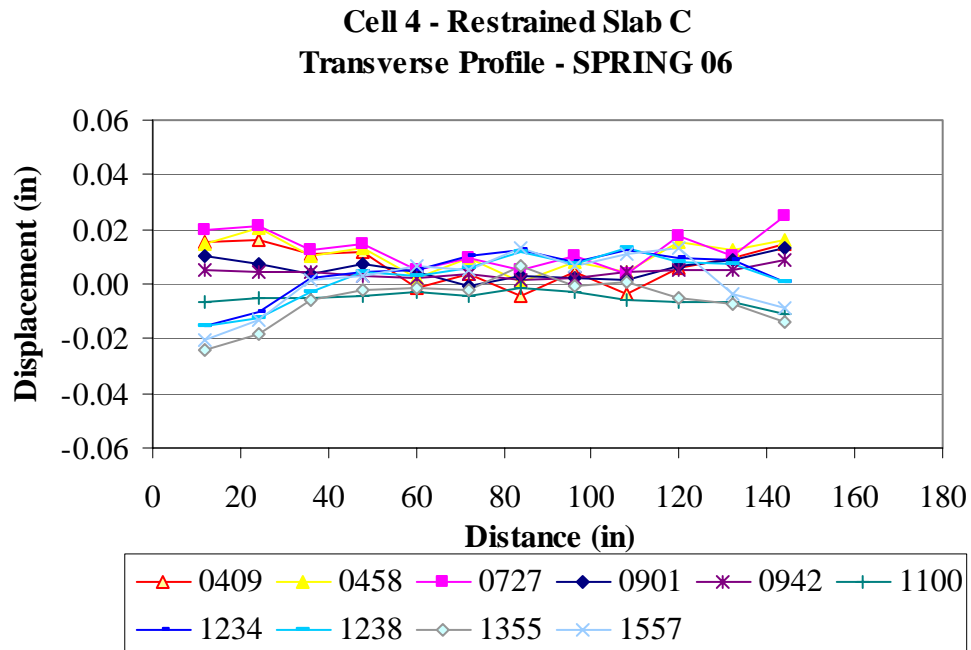


Figure E.50. Restrained Slab C Line B transverse surface profiles for the spring of 2006.

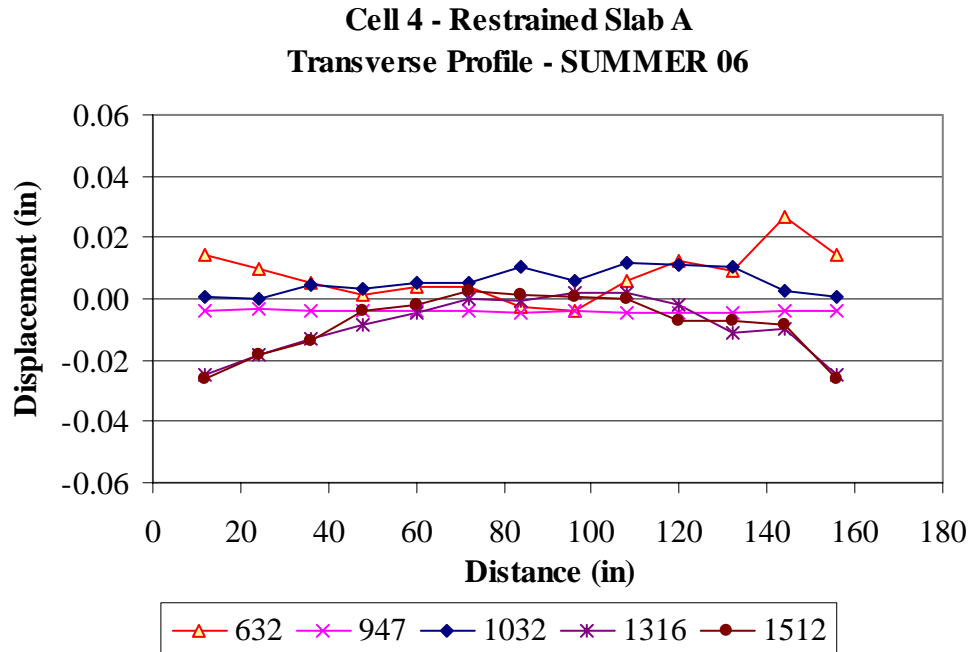


Figure E.51. Restrained Slab A Line A transverse surface profiles for the summer of 2006.

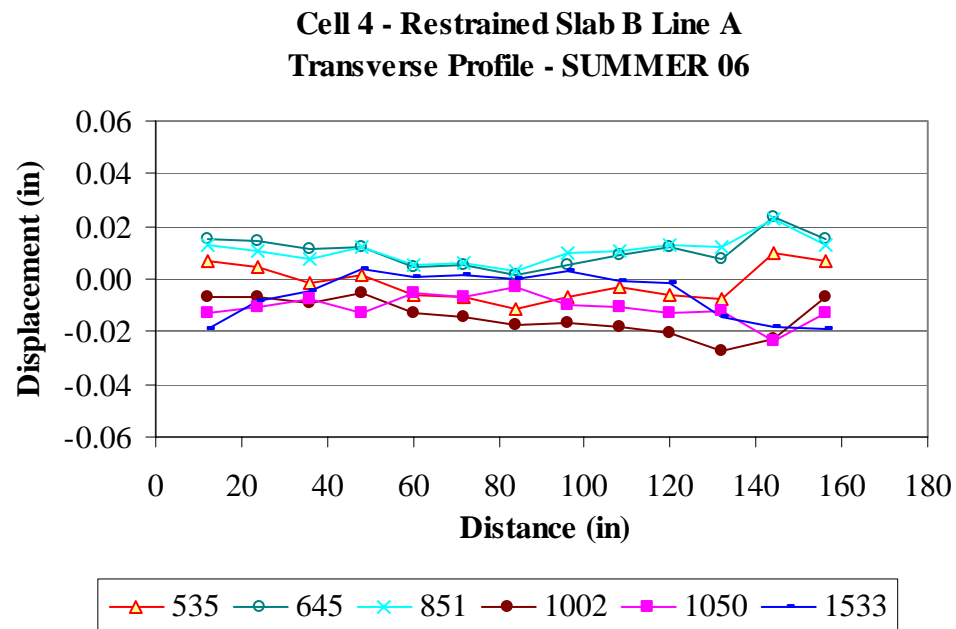


Figure E.52. Restrained Slab B Line A transverse surface profiles for the summer of 2006.

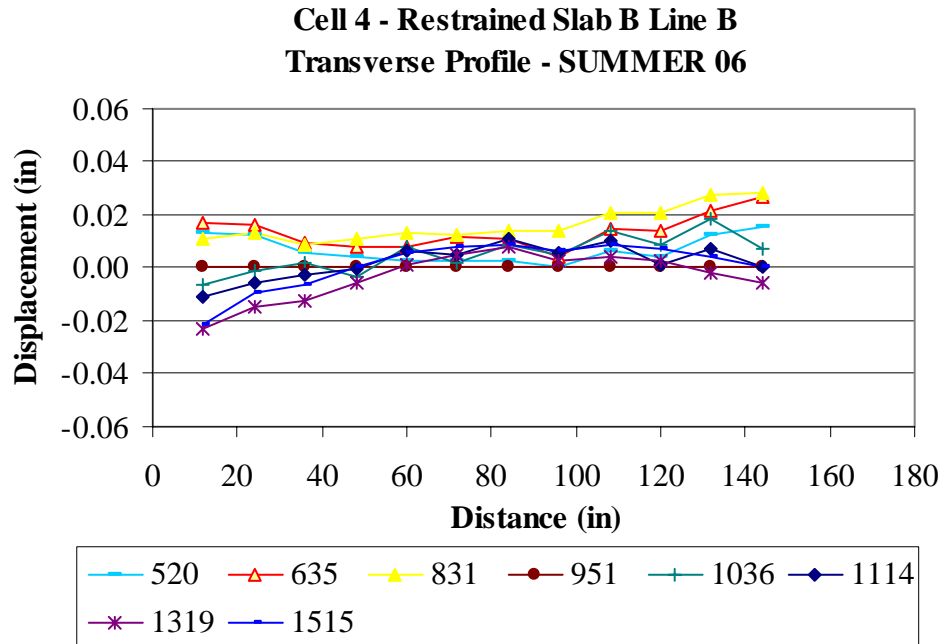


Figure E.53. Restrained Slab B Line B transverse surface profiles for the summer of 2006.

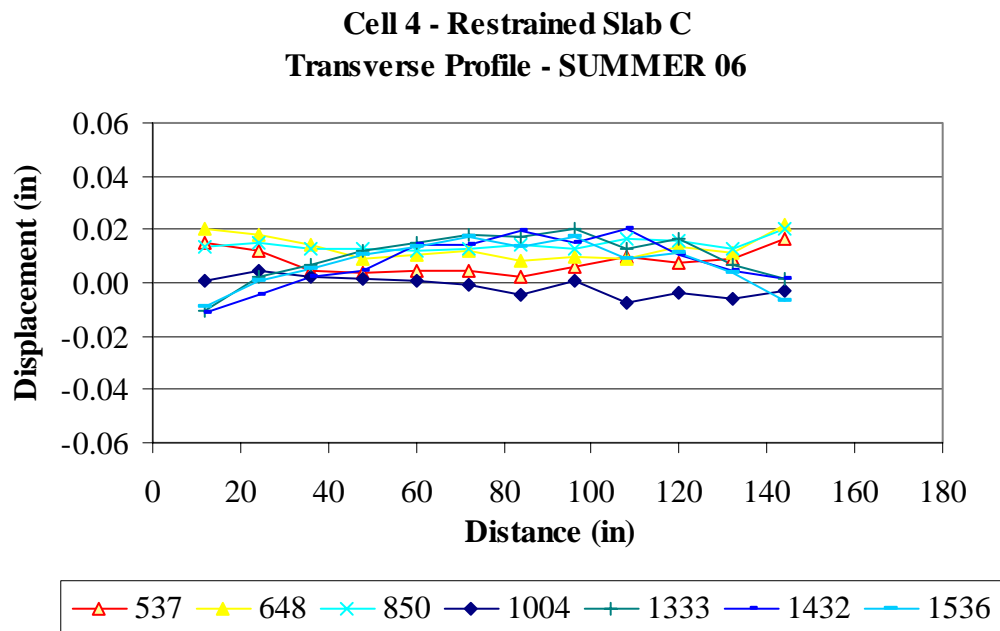


Figure E.54. Restrained Slab C Line B transverse surface profiles for the summer of 2006.

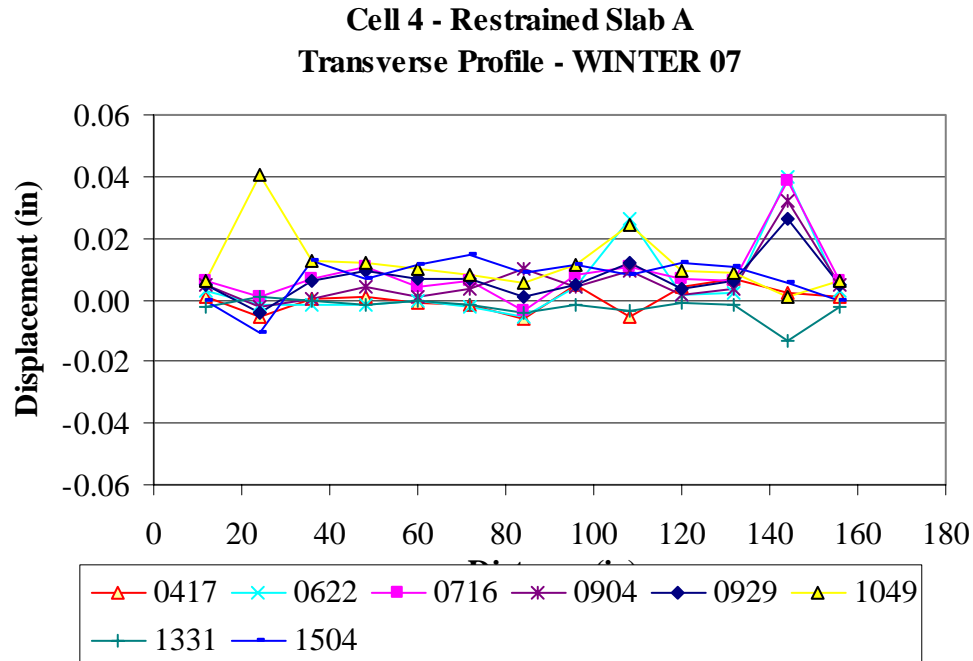


Figure E.55. Restrained Slab A Line A transverse surface profiles for the winter of 2007.

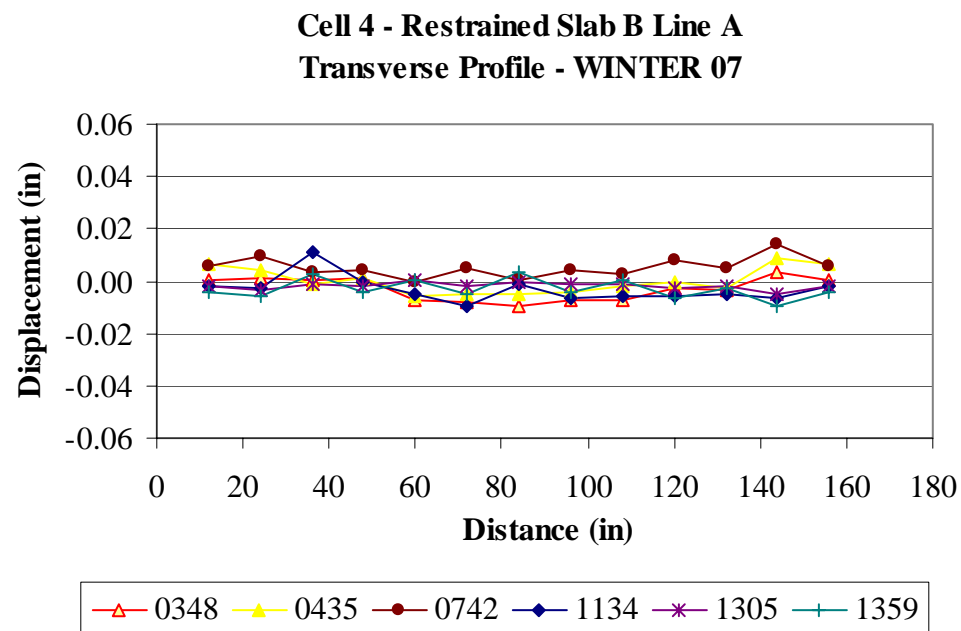


Figure E.56. Restrained Slab B Line A transverse surface profiles for the winter of 2007.

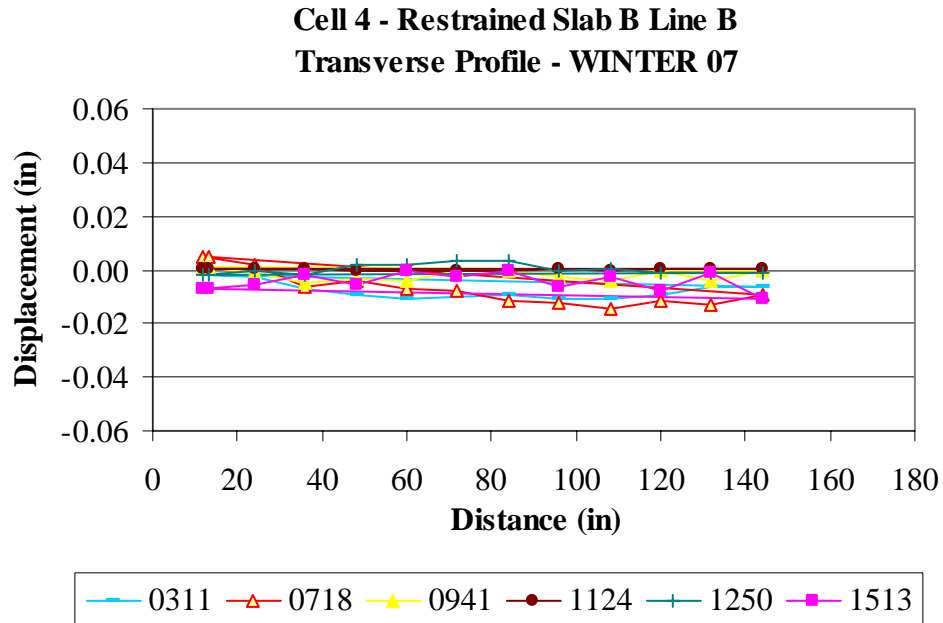


Figure E.57. Restrained Slab B Line B transverse surface profiles for the winter of 2007.

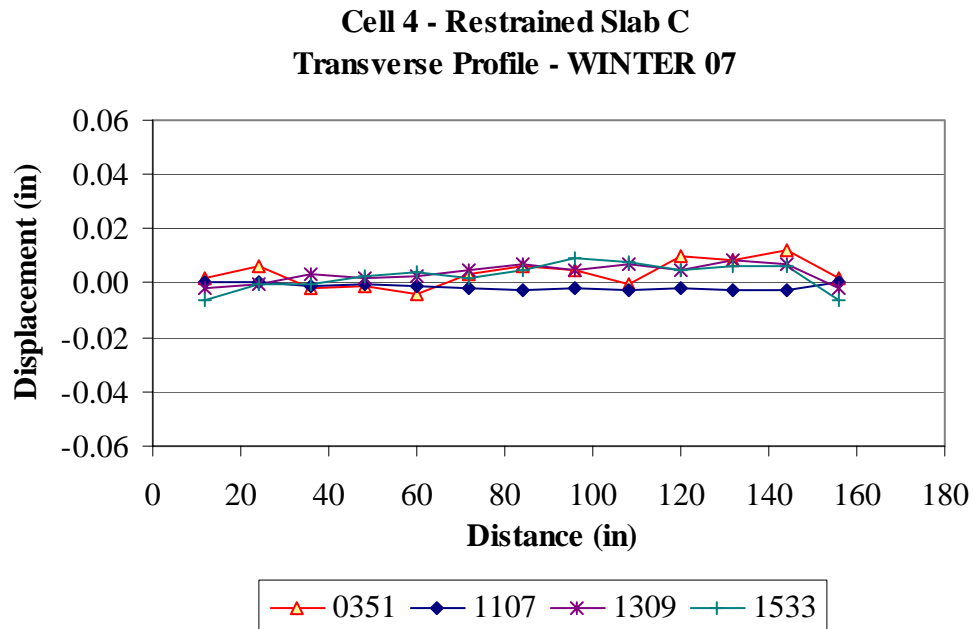


Figure E.58. Restrained Slab C Line B transverse surface profiles for the winter of 2007.

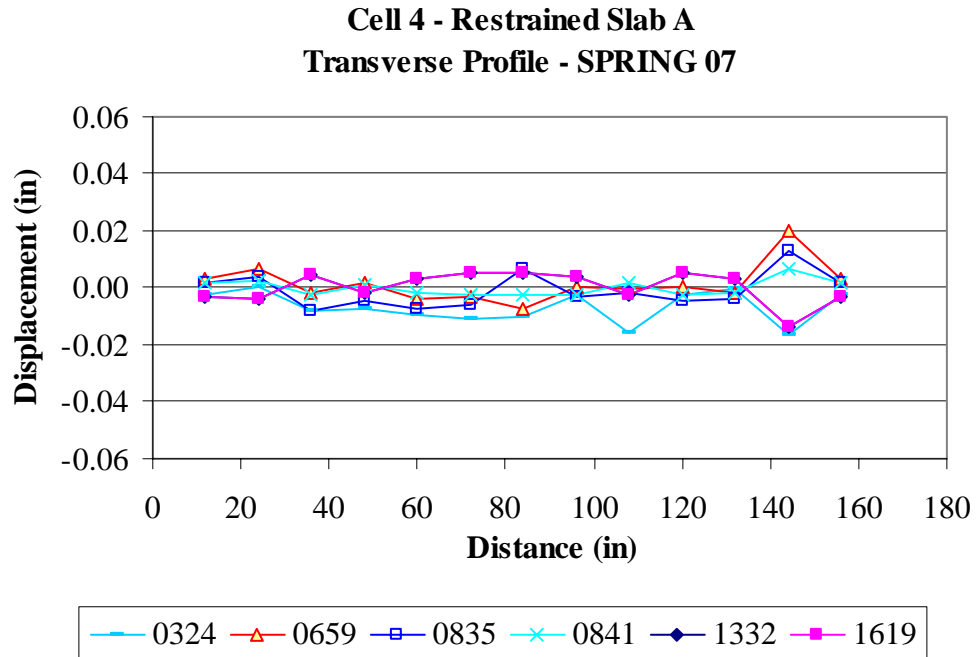


Figure E.59. Restrained Slab A Line A transverse surface profiles for the spring of 2007.

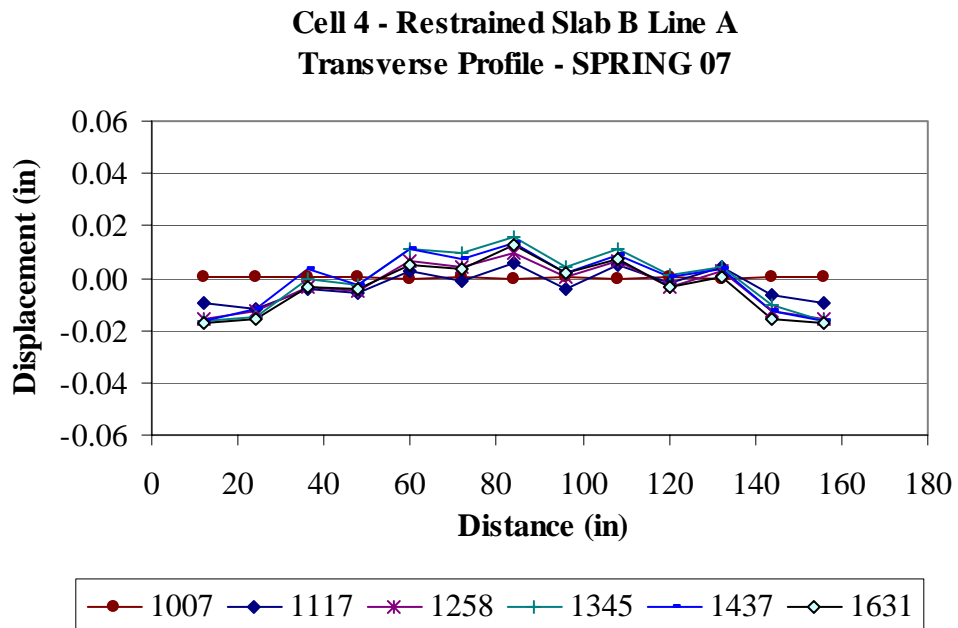


Figure E.60. Restrained Slab B Line A transverse surface profiles for the spring of 2007.

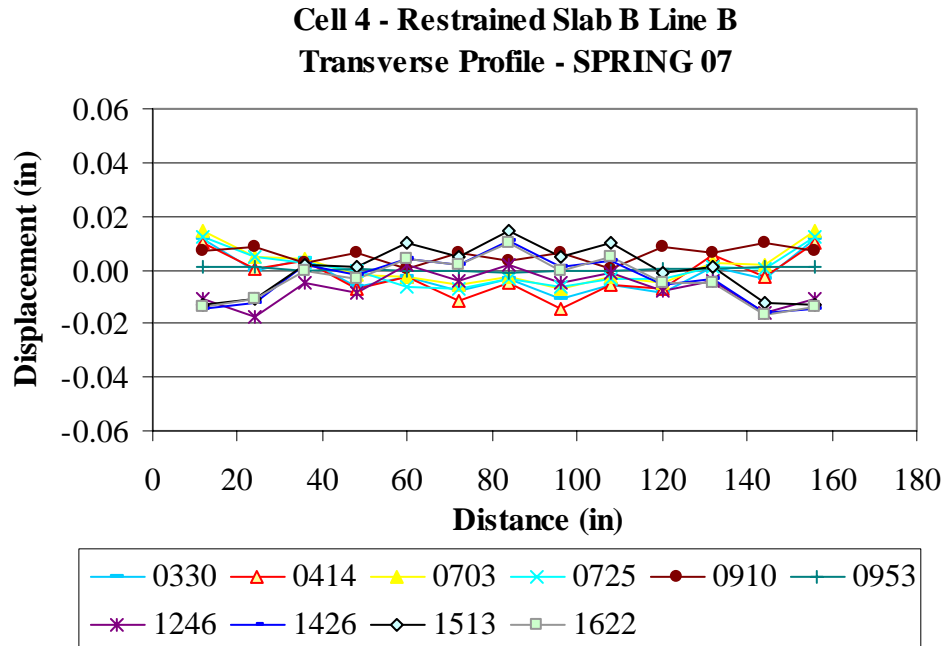


Figure E.61. Restrained Slab B Line B transverse surface profiles for the spring of 2007.

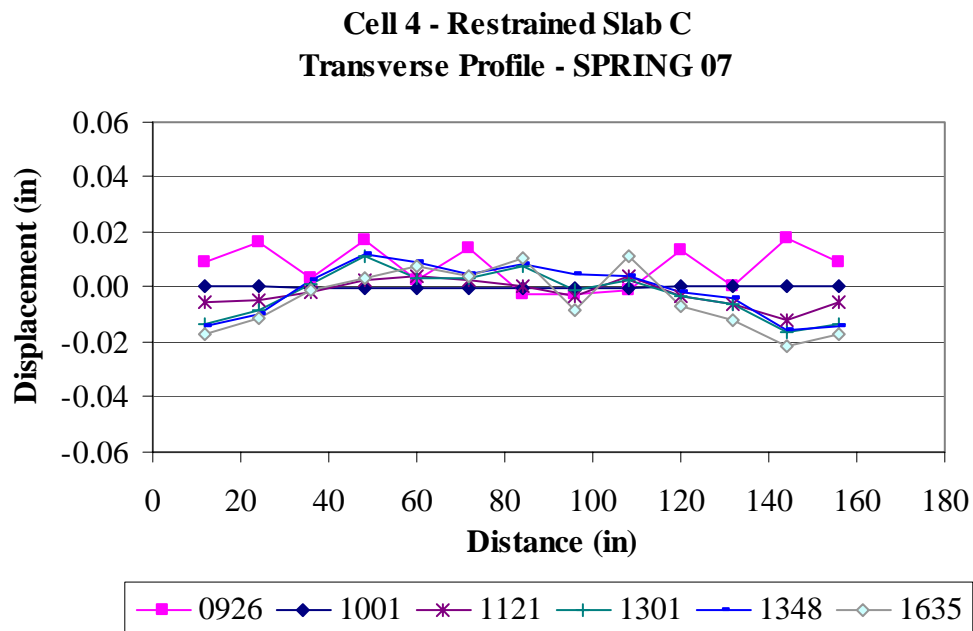


Figure E.62. Restrained Slab C Line B transverse surface profiles for the spring of 2007.

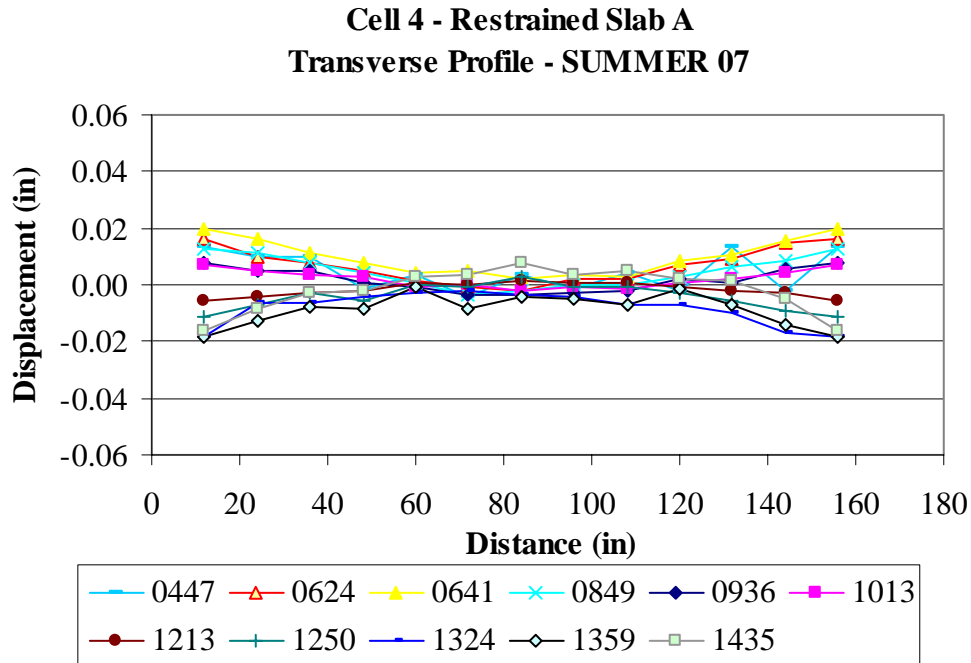


Figure E.63. Restrained Slab A Line A transverse surface profiles for the summer of 2007.

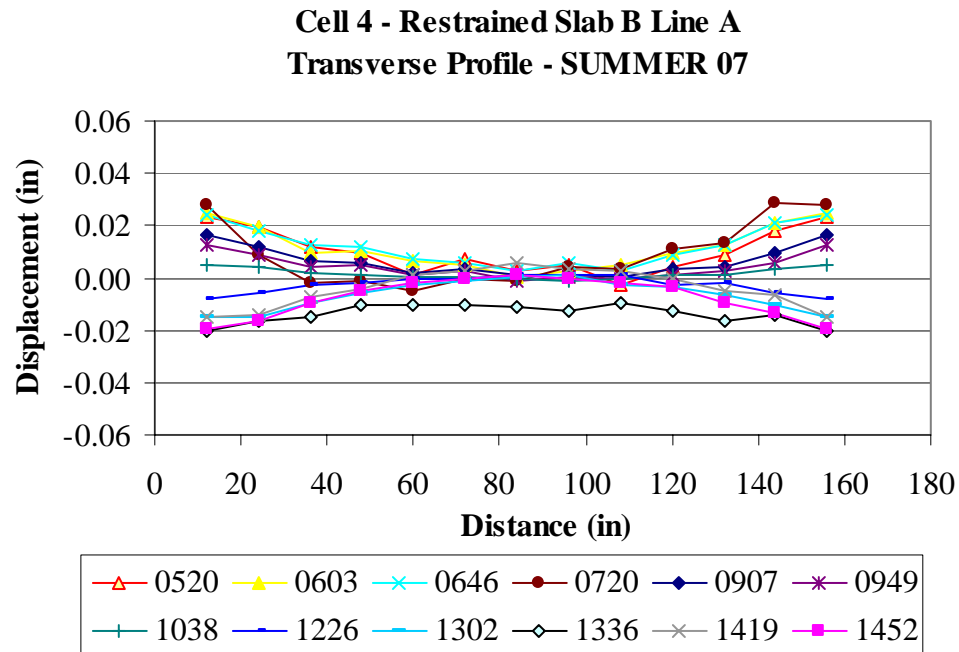


Figure E.64. Restrained Slab B Line A transverse surface profiles for the summer of 2007.

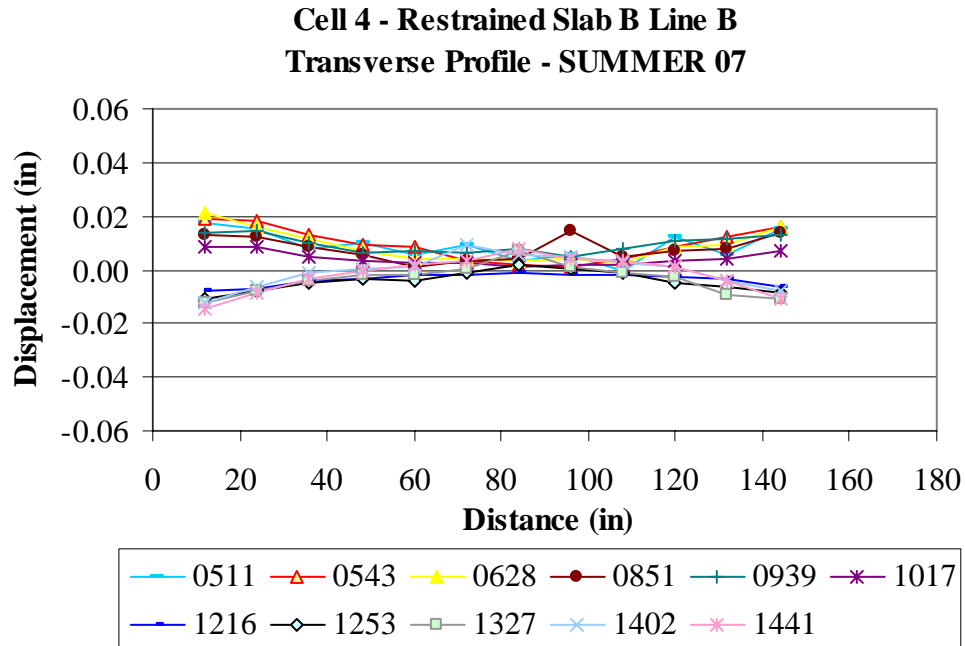


Figure E.65. Restrained Slab B Line B transverse surface profiles for the summer of 2007.

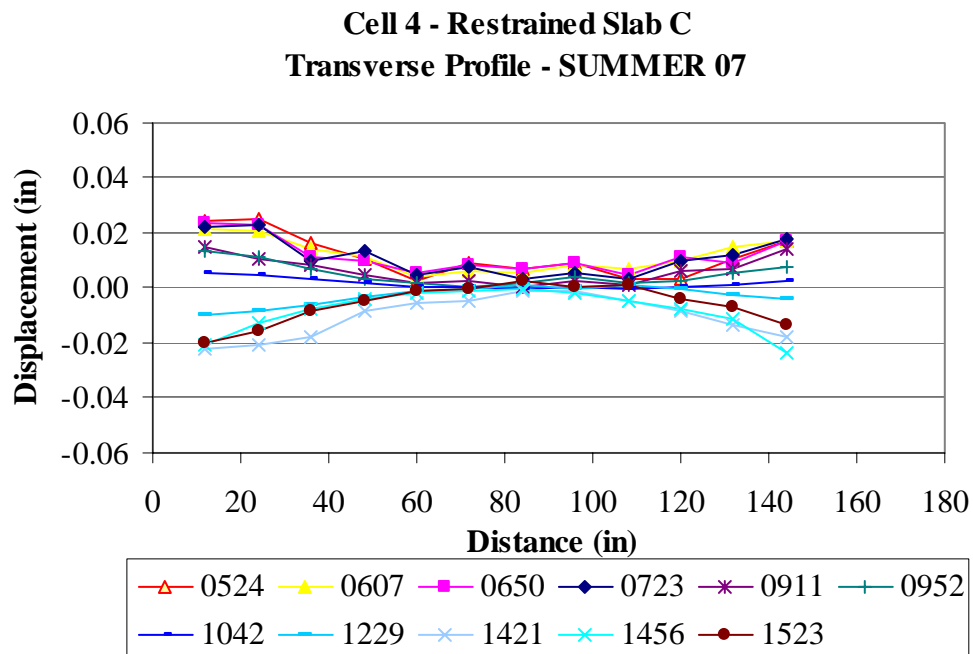


Figure E.66. Restrained Slab C Line B transverse surface profiles for the summer of 2007.

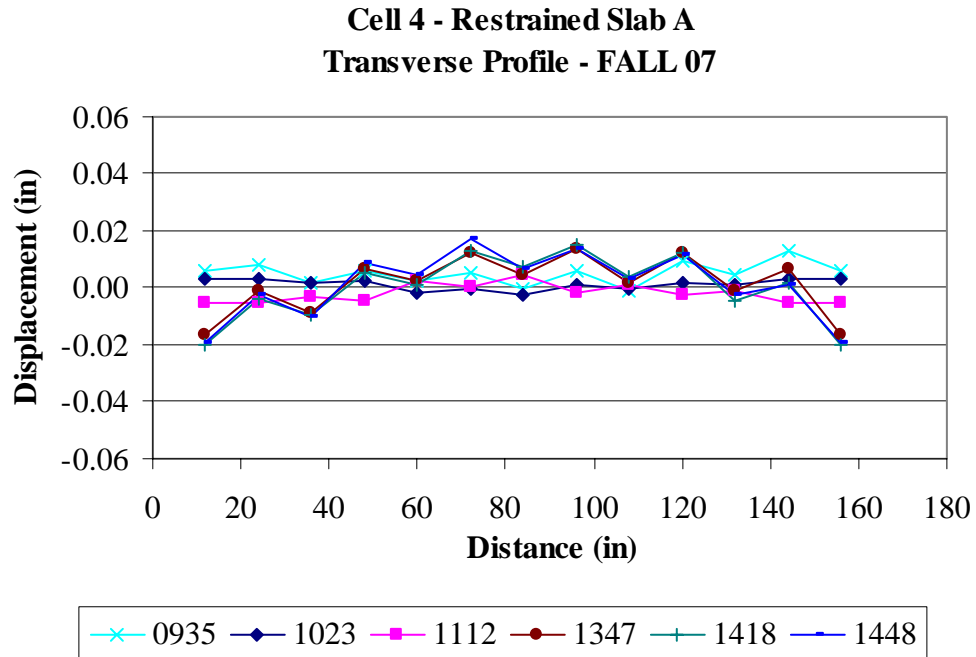


Figure E.67. Restrained Slab A Line A transverse surface profiles for the fall of 2007.

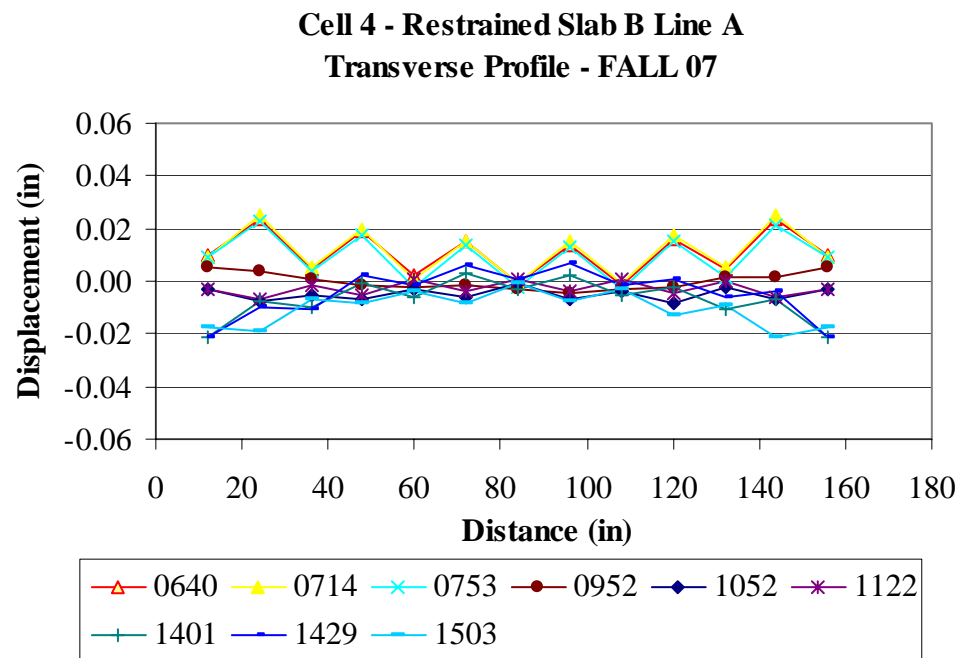


Figure E.68. Restrained Slab B Line A transverse surface profiles for the fall of 2007.

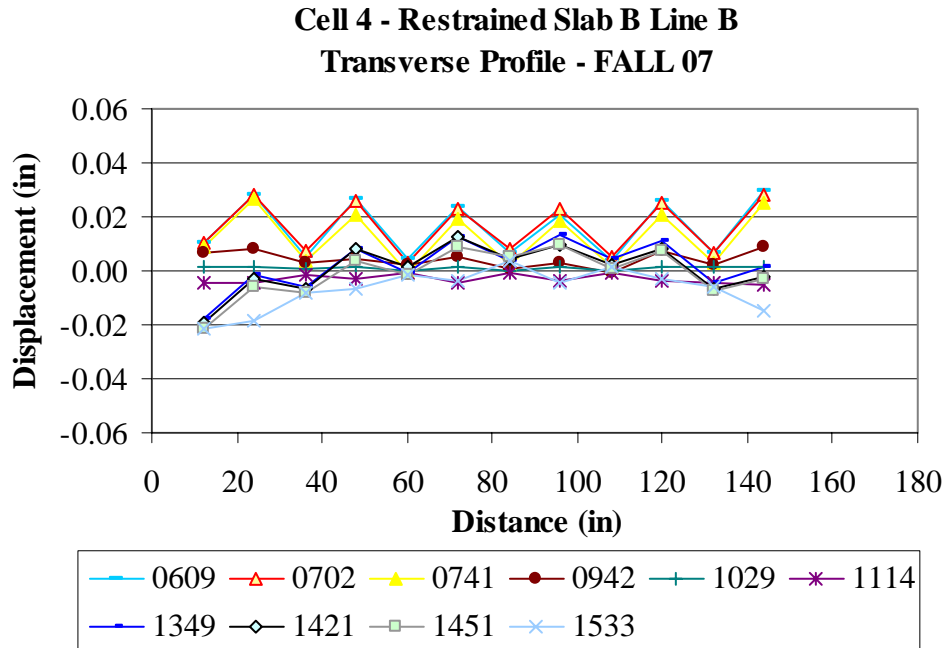


Figure E.69. Restrained Slab B Line B transverse surface profiles for the fall of 2007.

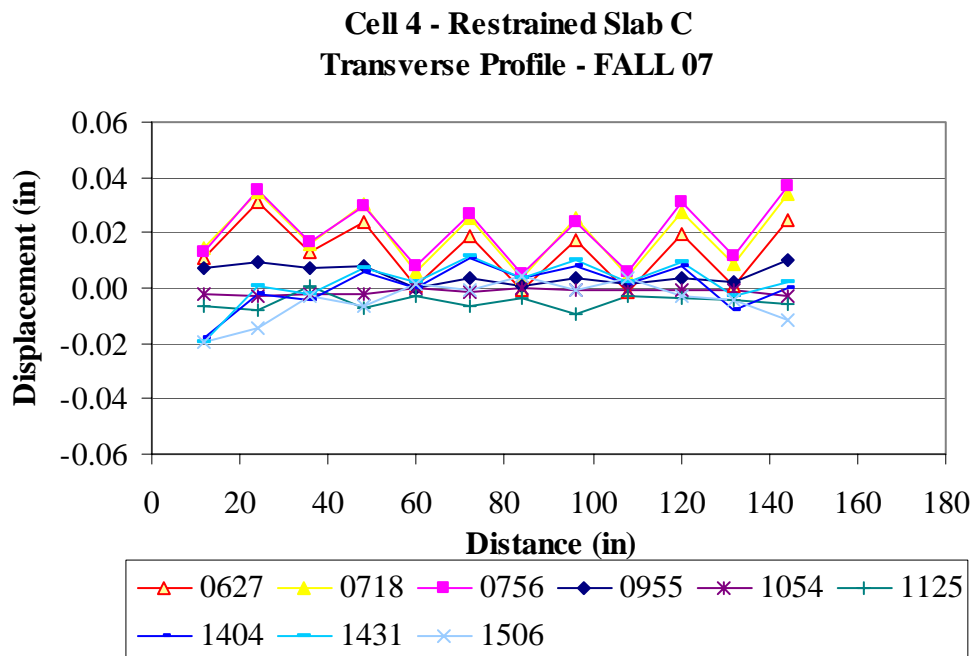


Figure E.70. Restrained Slab C Line B transverse surface profiles for the fall of 2007.

Cell 3 - Unrestrained Slab A
Transverse Profile - WINTER 06

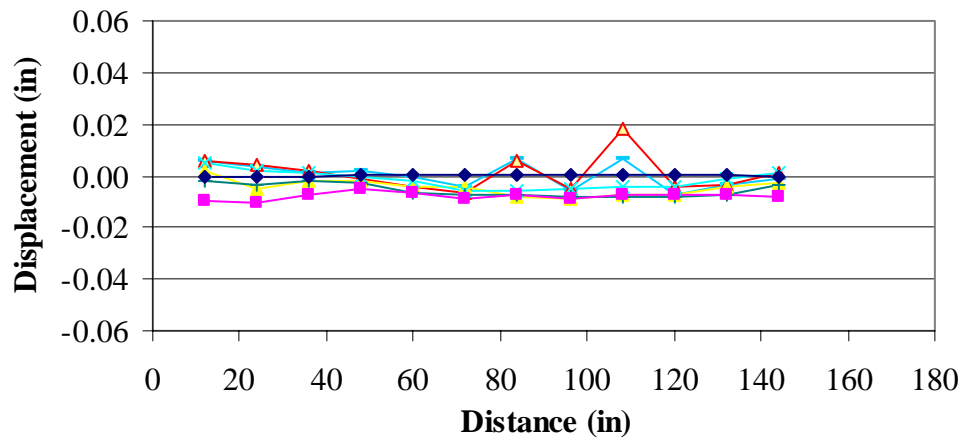


Figure E.71. Unrestrained Slab A Line A transverse surface profiles for the winter of 2006.

Cell 3 - Unrestrained Slab B Line A
Transverse Profile - WINTER 06

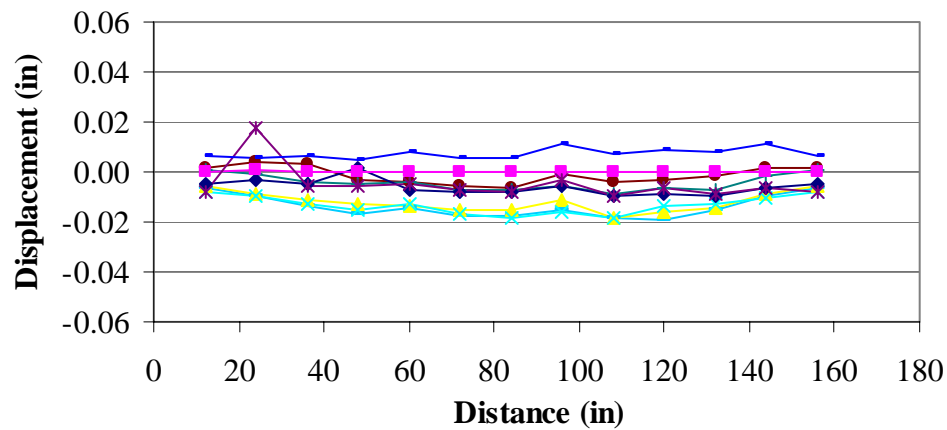


Figure E.72. Unrestrained Slab B Line A transverse surface profiles for the winter of 2006.

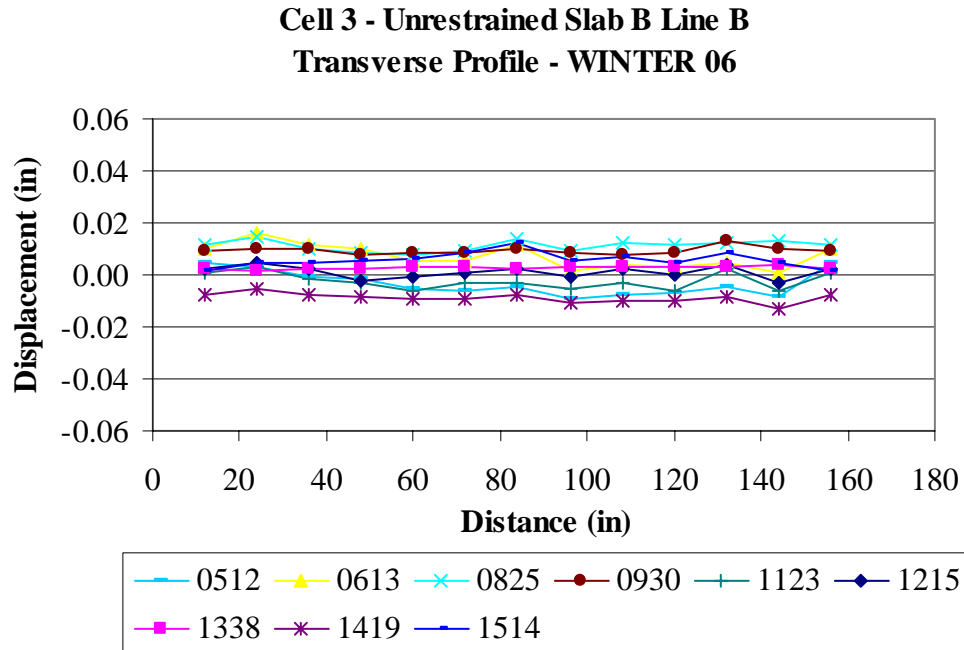


Figure E.73. Unrestrained Slab B Line B transverse surface profiles for the winter of 2006.

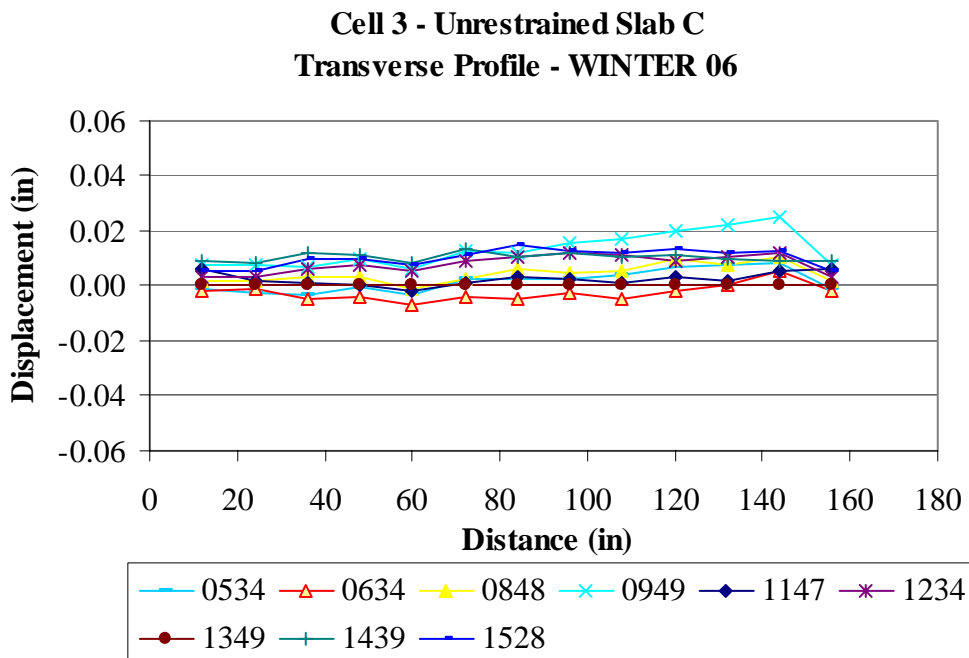


Figure E.74. Unrestrained Slab C Line B transverse surface profiles for the winter of 2006.

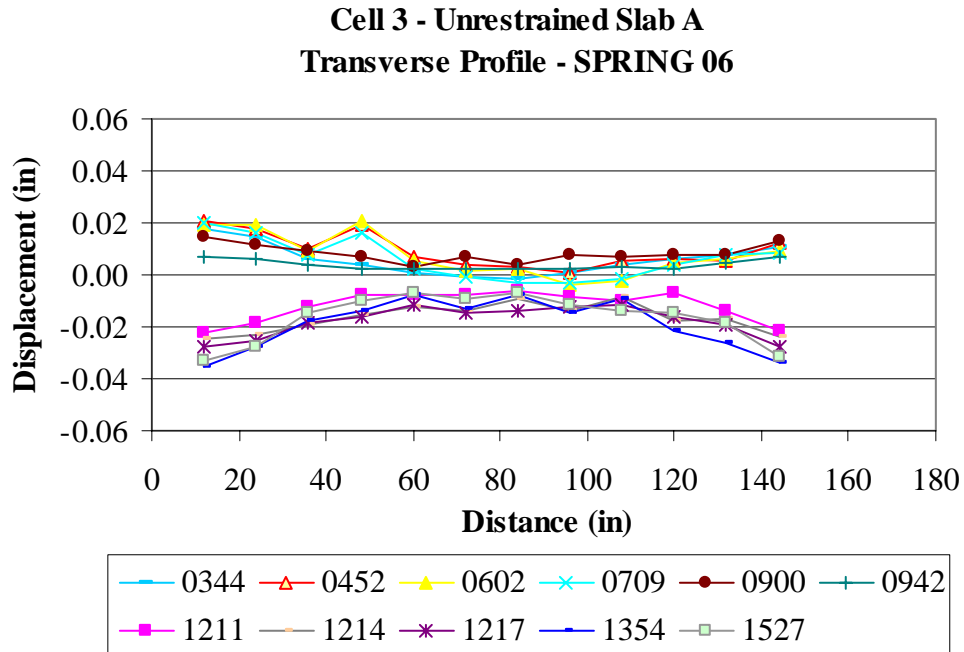


Figure E.75. Unrestrained Slab A Line A transverse surface profiles for the spring of 2006.

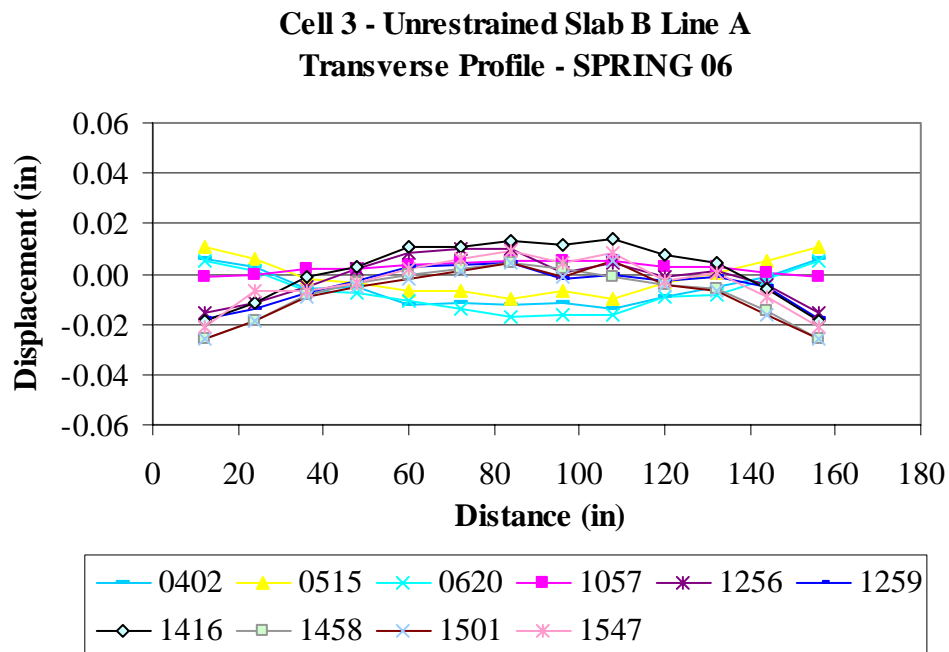


Figure E.76. Unrestrained Slab B Line A transverse surface profiles for the spring of 2006.

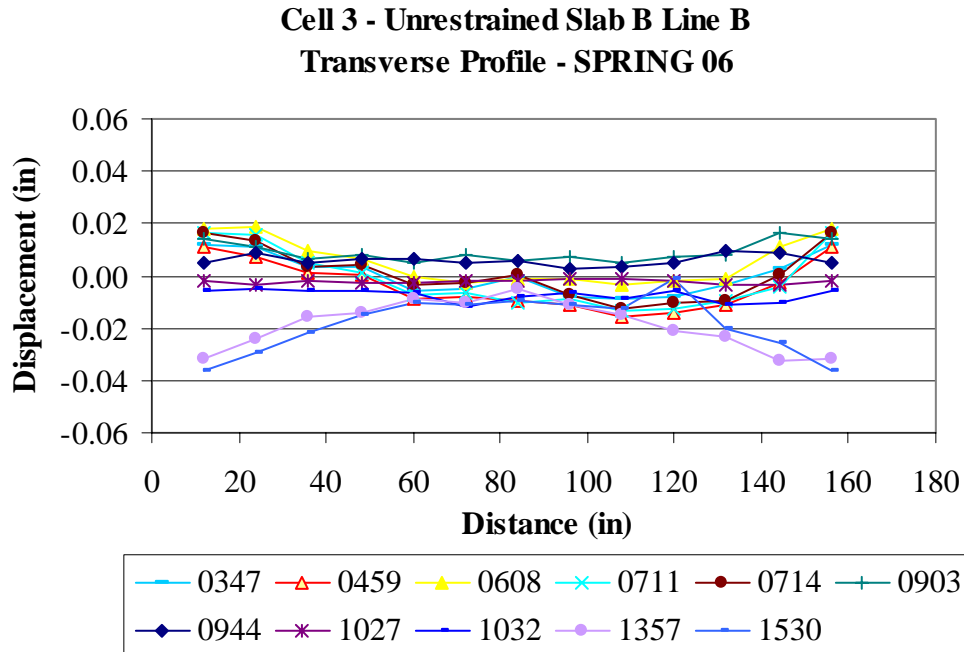


Figure E.77. Unrestrained Slab B Line B transverse surface profiles for the spring of 2006.

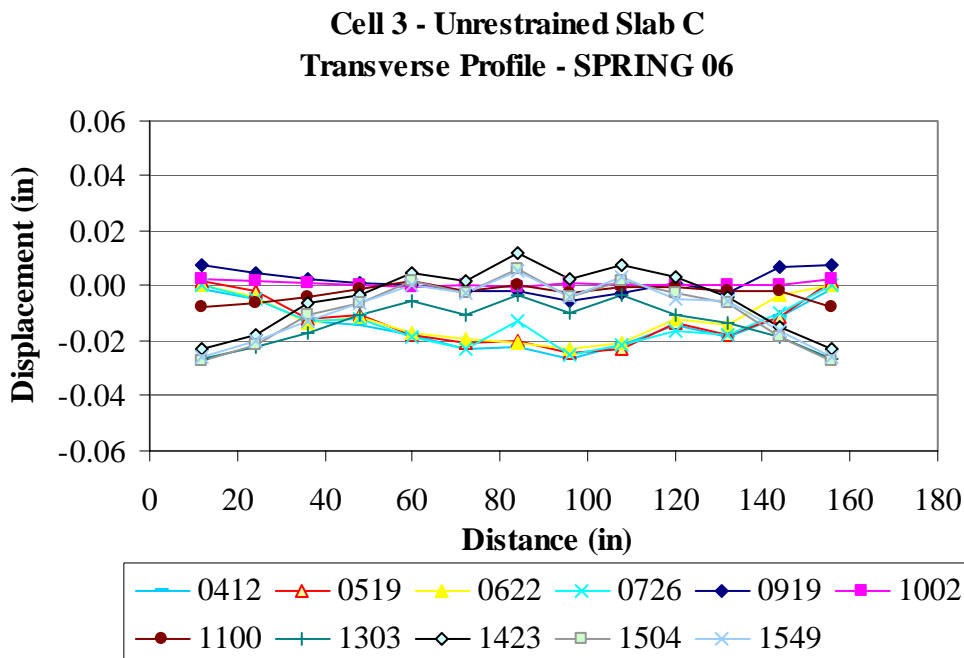


Figure E.78. Unrestrained Slab C Line B transverse surface profiles for the spring of 2006.

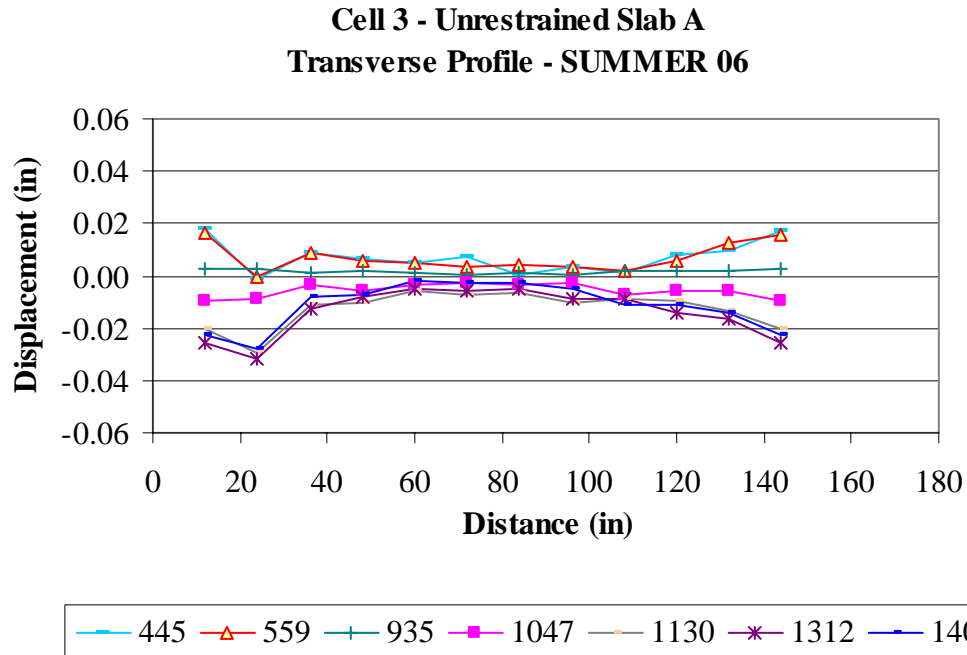


Figure E.79. Unrestrained Slab A Line A transverse surface profiles for the summer of 2006.

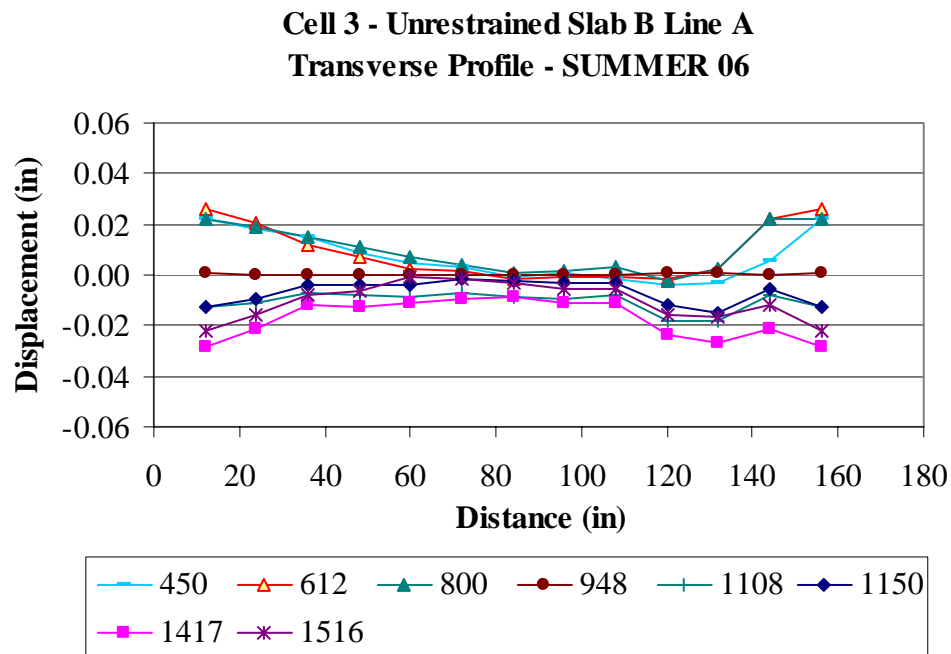


Figure E.80. Unrestrained Slab B Line A transverse surface profiles for the summer of 2006.

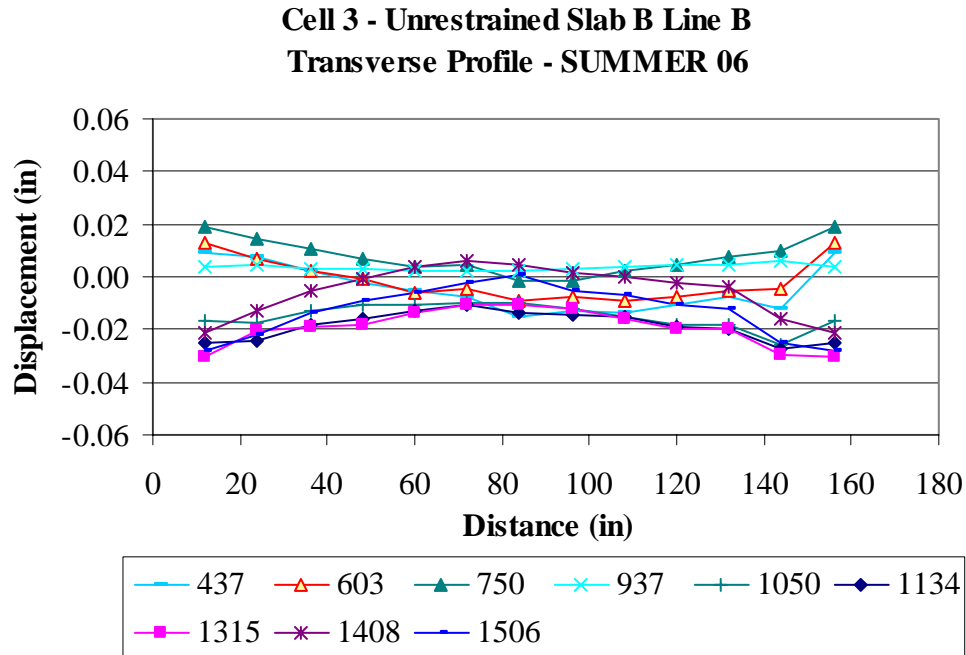


Figure E.81. Unrestrained Slab B Line B transverse surface profiles for the summer of 2006.

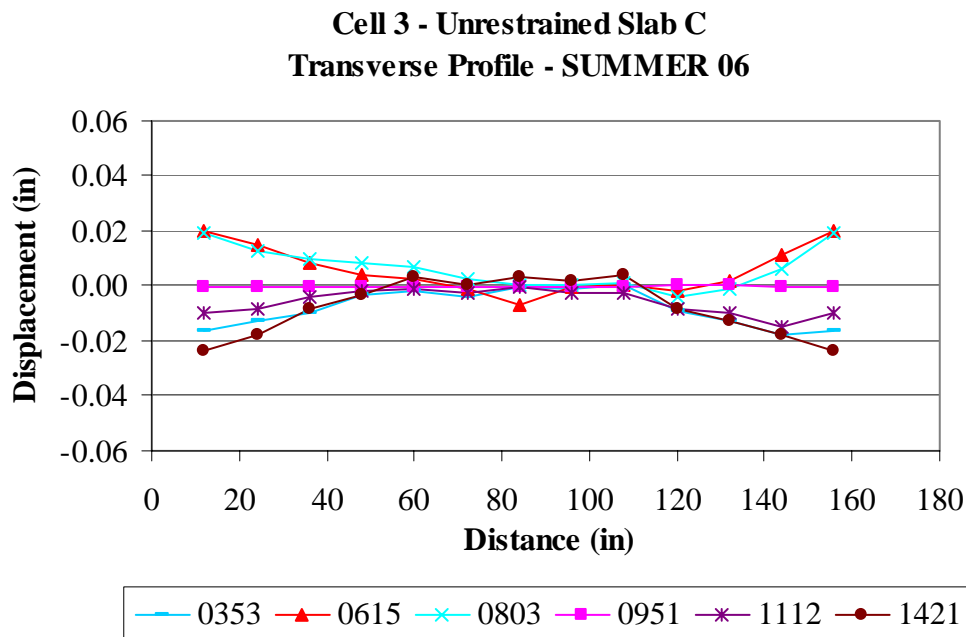


Figure E.82. Unrestrained Slab C Line B transverse surface profiles for the summer of 2006.

Cell 3 - Unrestrained Slab A
Transverse Profile - WINTER 07

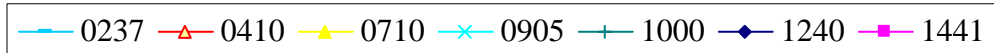
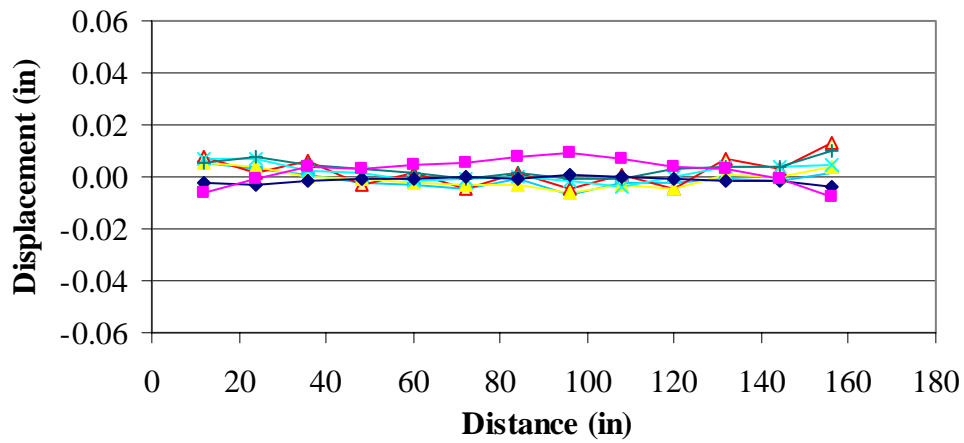


Figure E.83. Unrestrained Slab A Line A transverse surface profiles for the winter of 2007.

Cell 3 - Unrestrained Slab B Line A
Transverse Profile - WINTER 07

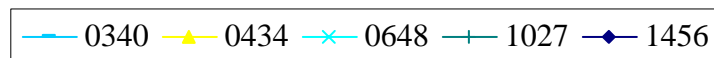
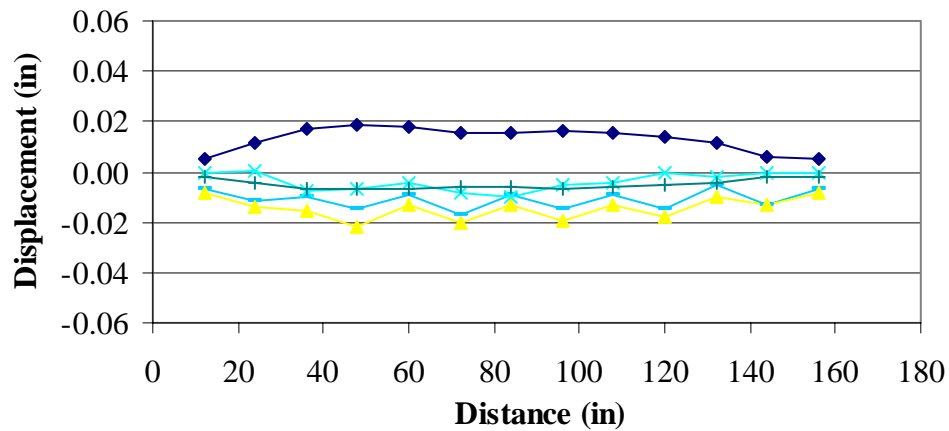


Figure E.84. Unrestrained Slab B Line A transverse surface profiles for the winter of 2007.

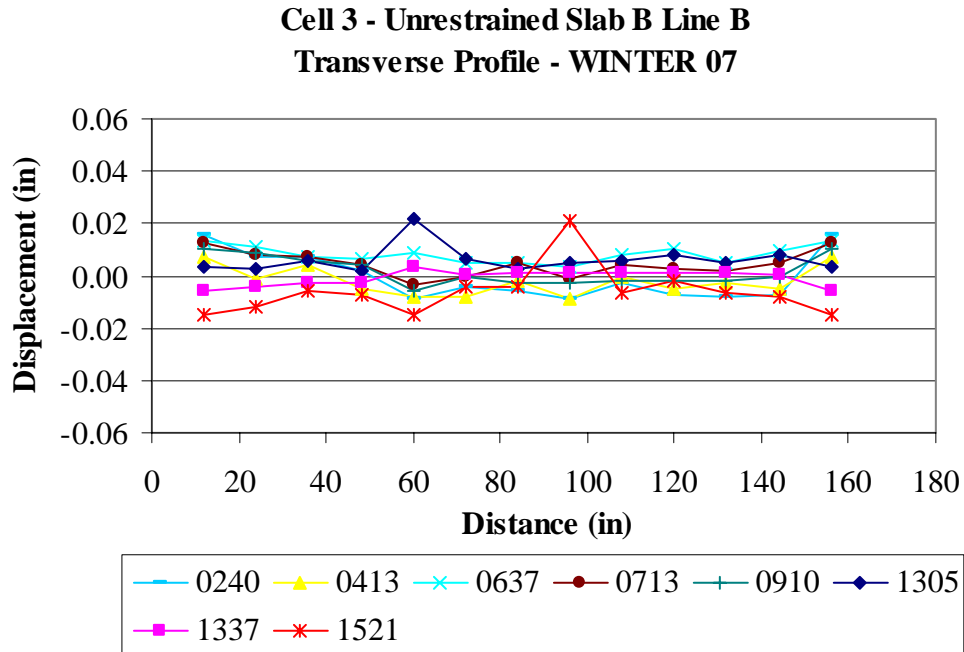


Figure E.85. Unrestrained Slab B Line B transverse surface profiles for the winter of 2007.

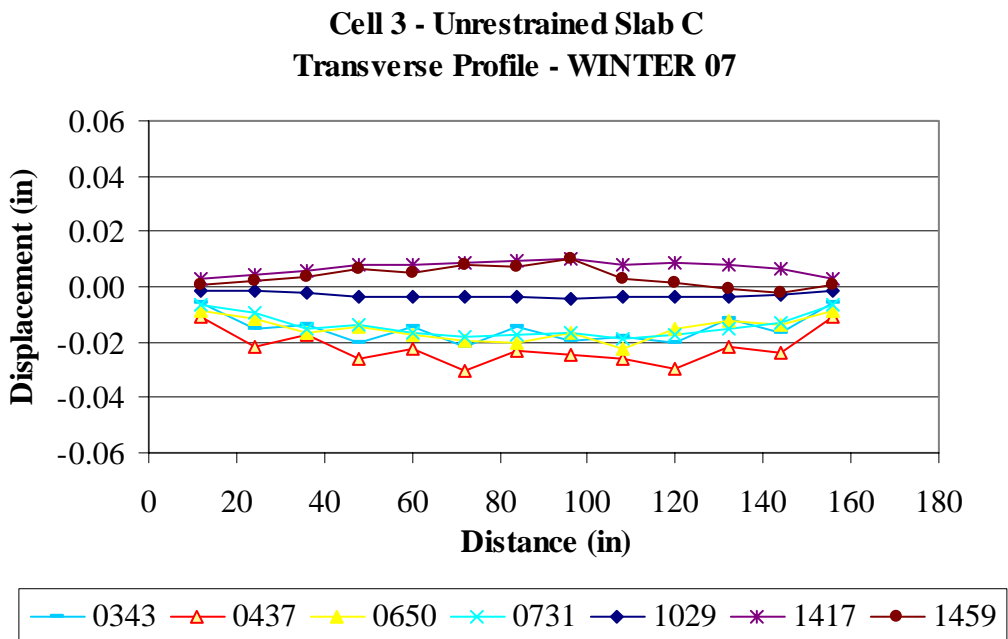


Figure E.86. Unrestrained Slab C Line B transverse surface profiles for the winter of 2007.

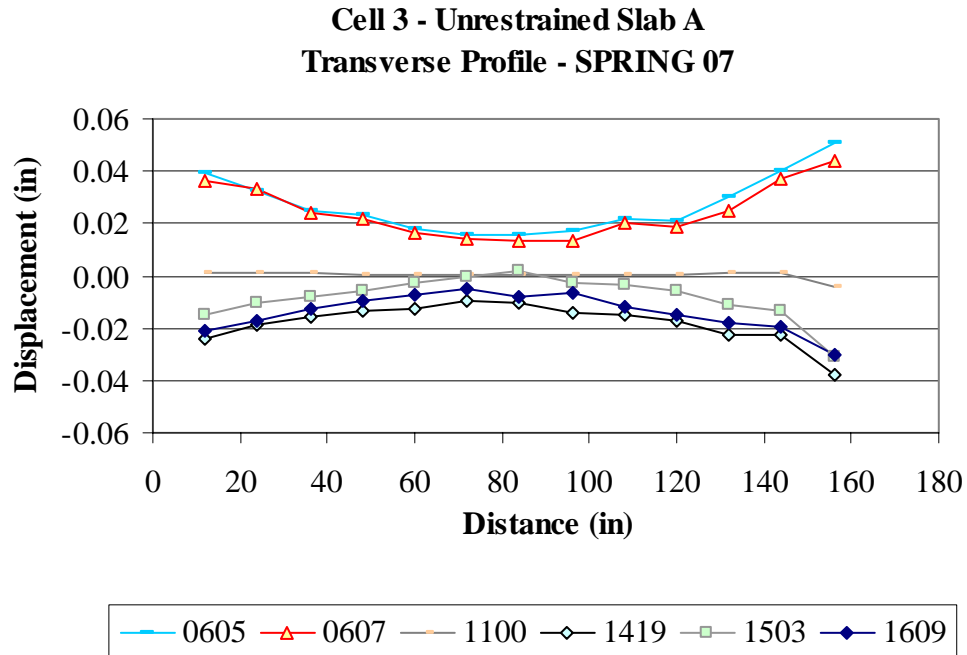


Figure E.87. Unrestrained Slab A Line A transverse surface profiles for the spring of 2007.

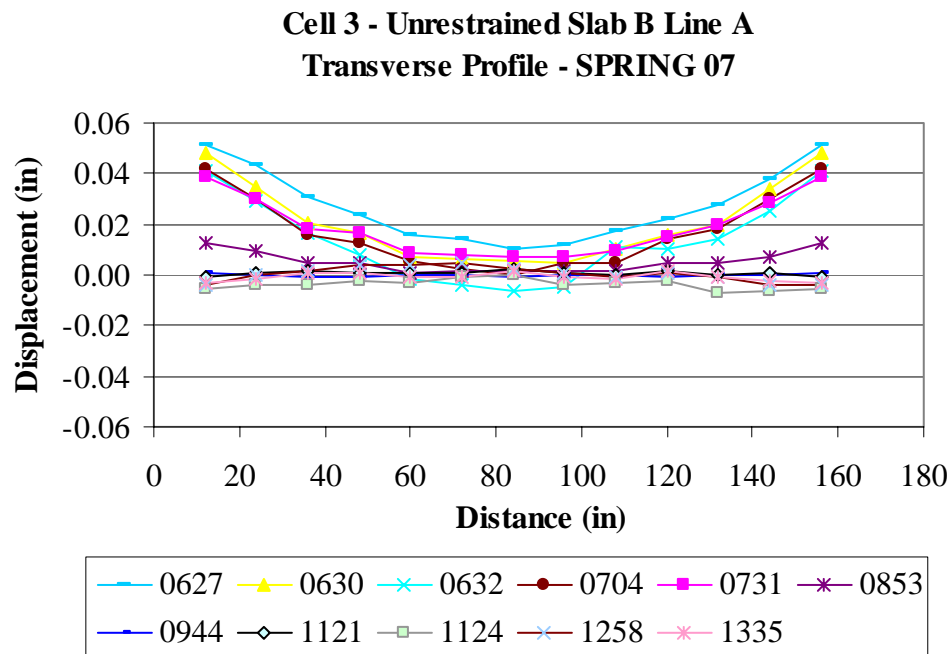


Figure E.88. Unrestrained Slab B Line A transverse surface profiles for the spring of 2007.

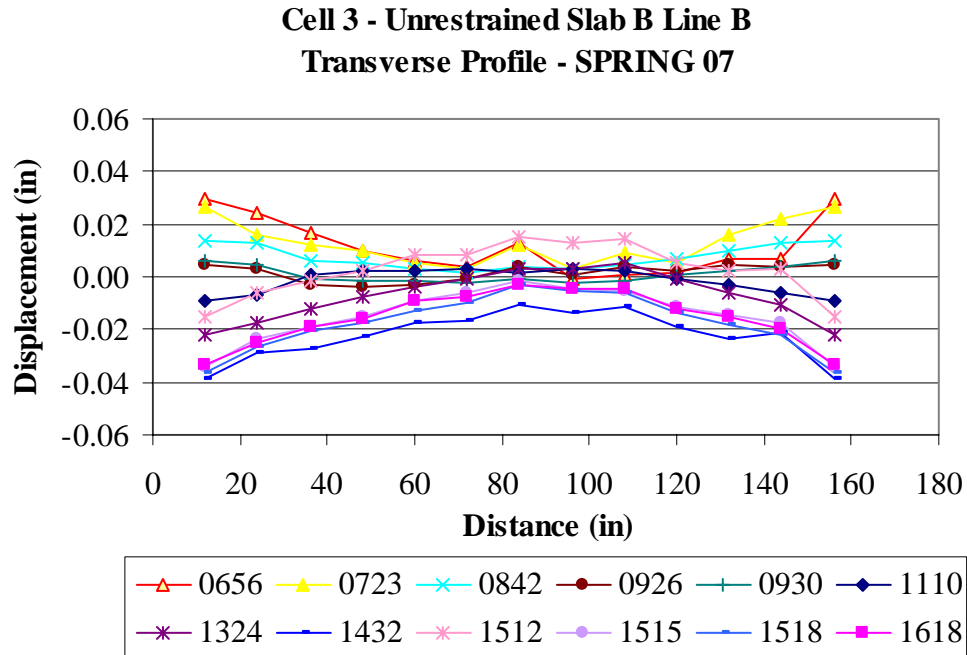


Figure E.89. Unrestrained Slab B Line B transverse surface profiles for the spring of 2007.

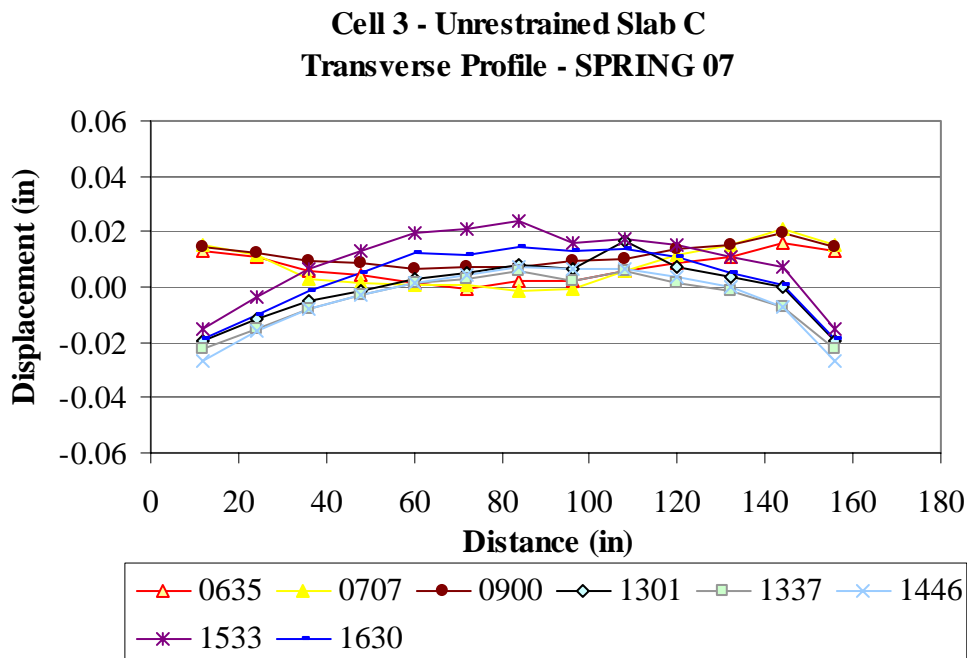


Figure E.90. Unrestrained Slab C Line B transverse surface profiles for the spring of 2007.

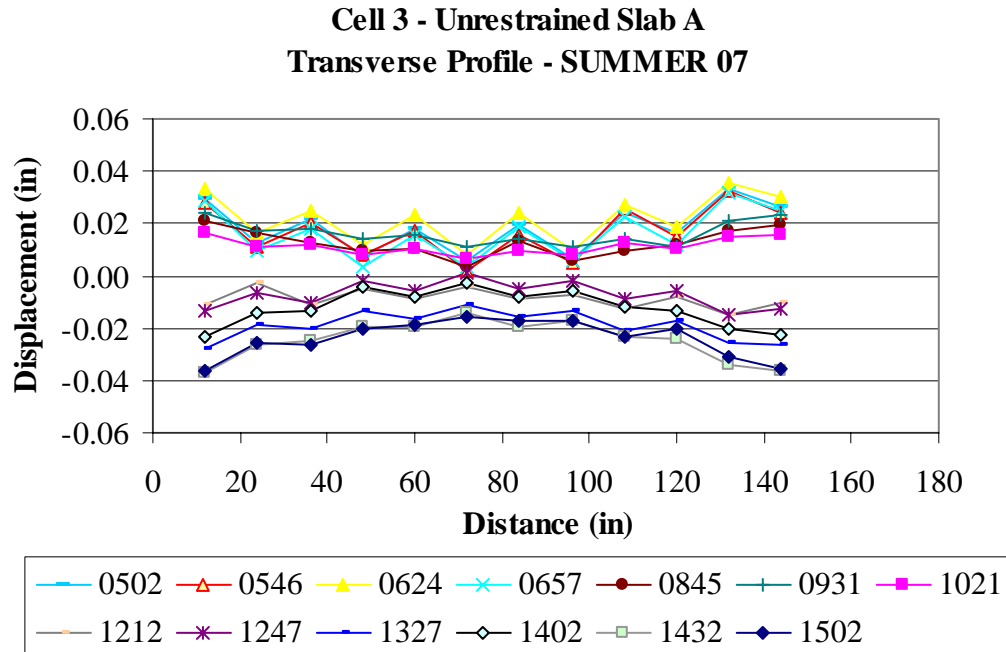


Figure E.91. Unrestrained Slab A Line A transverse surface profiles for the summer of 2007.

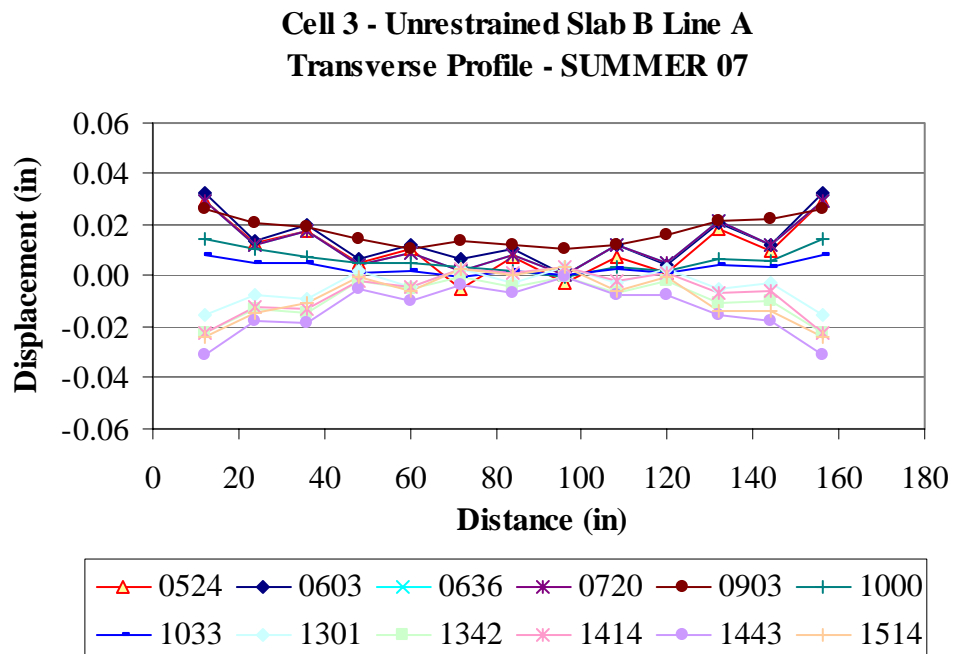


Figure E.92. Unrestrained Slab B Line A transverse surface profiles for the summer of 2007.

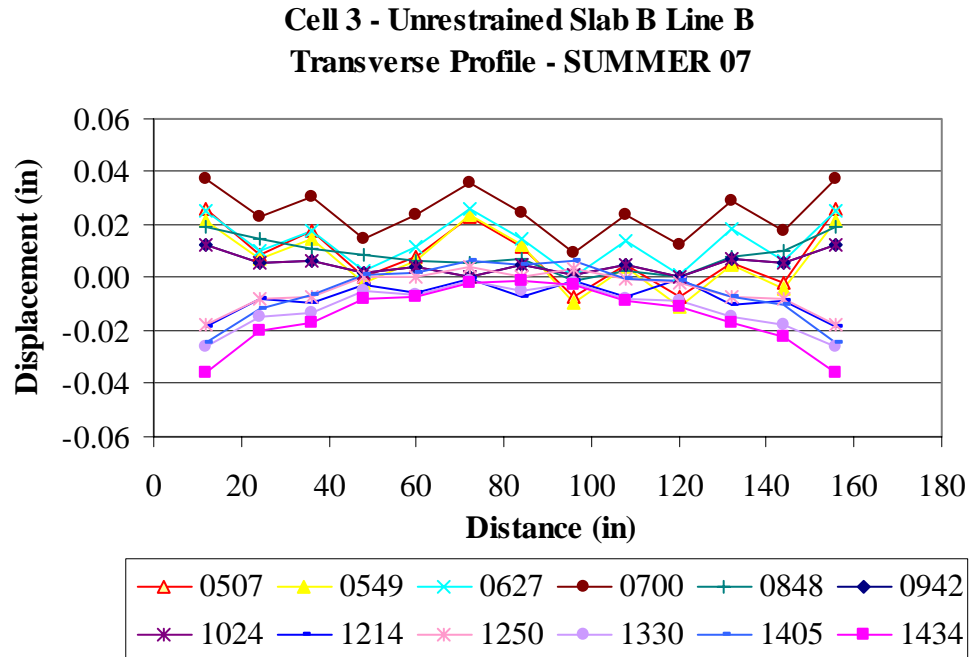


Figure E.93. Unrestrained Slab B Line B transverse surface profiles for the summer of 2007.

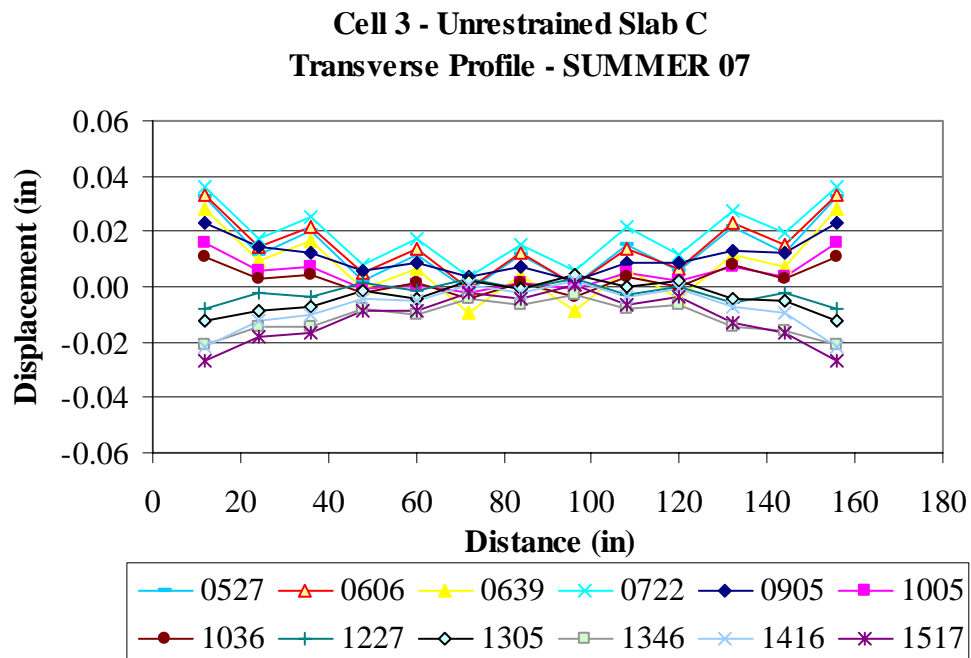


Figure E.94. Unrestrained Slab C Line B transverse surface profiles for the summer of 2007.

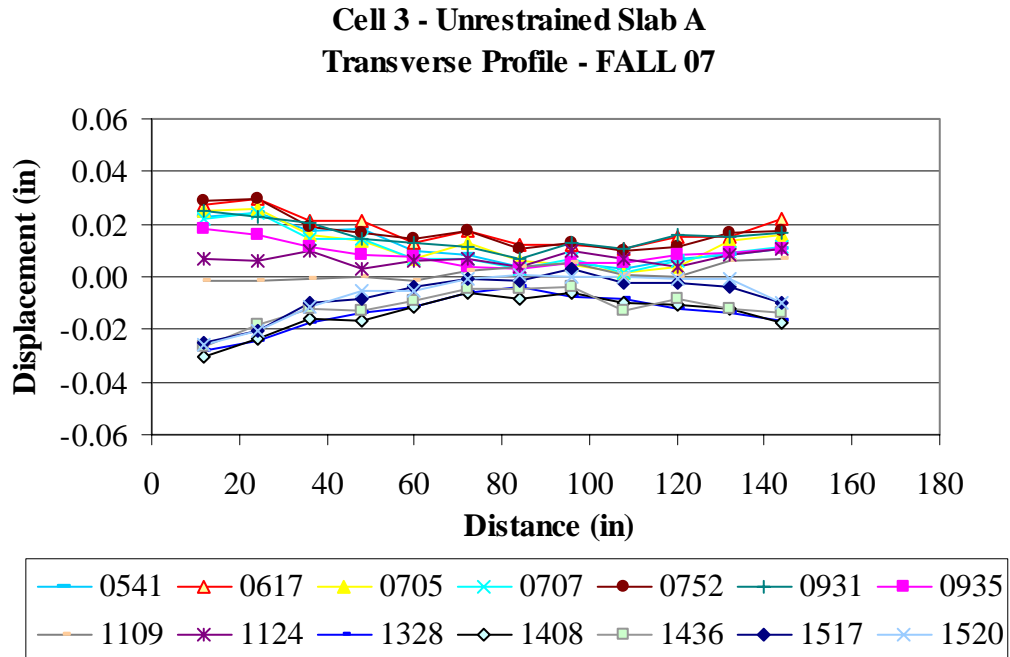


Figure E.95. Unrestrained Slab A Line A transverse surface profiles for the fall of 2007.

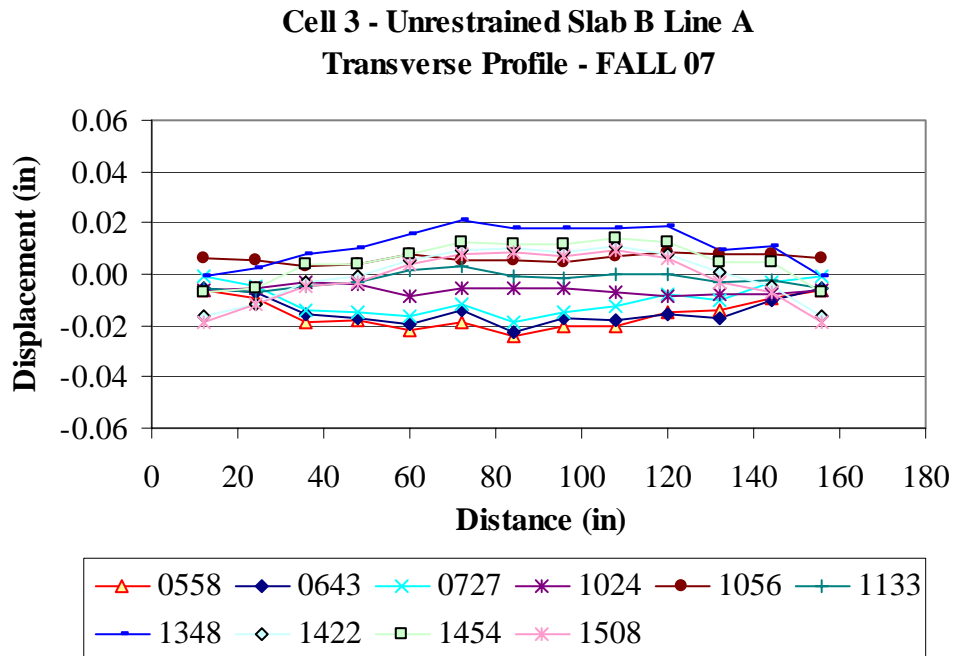


Figure E.96. Unrestrained Slab B Line A transverse surface profiles for the fall of 2007.

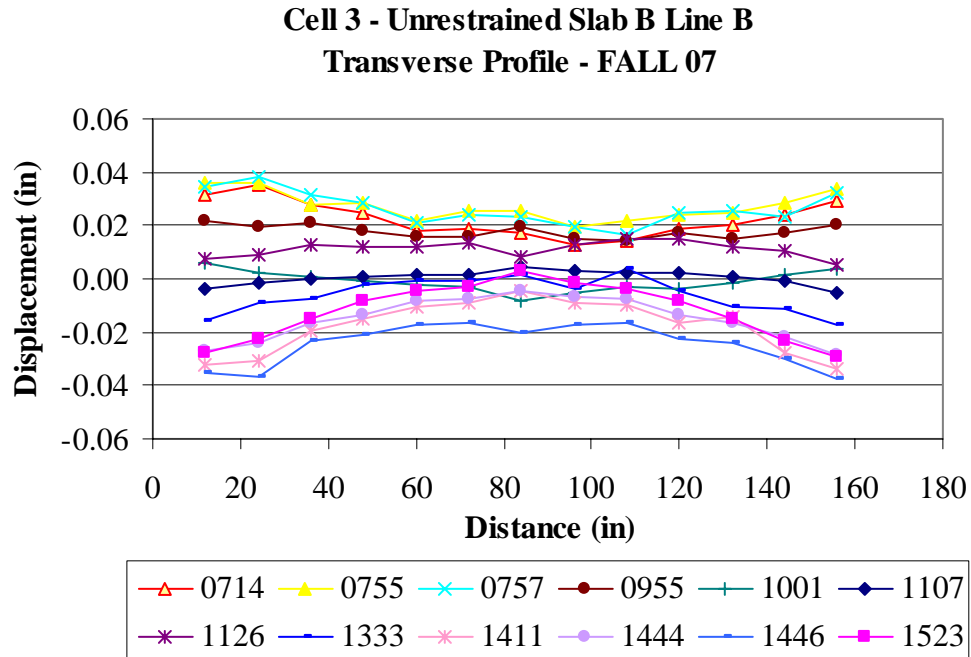


Figure E.97. Unrestrained Slab B Line B transverse surface profiles for the fall of 2007.

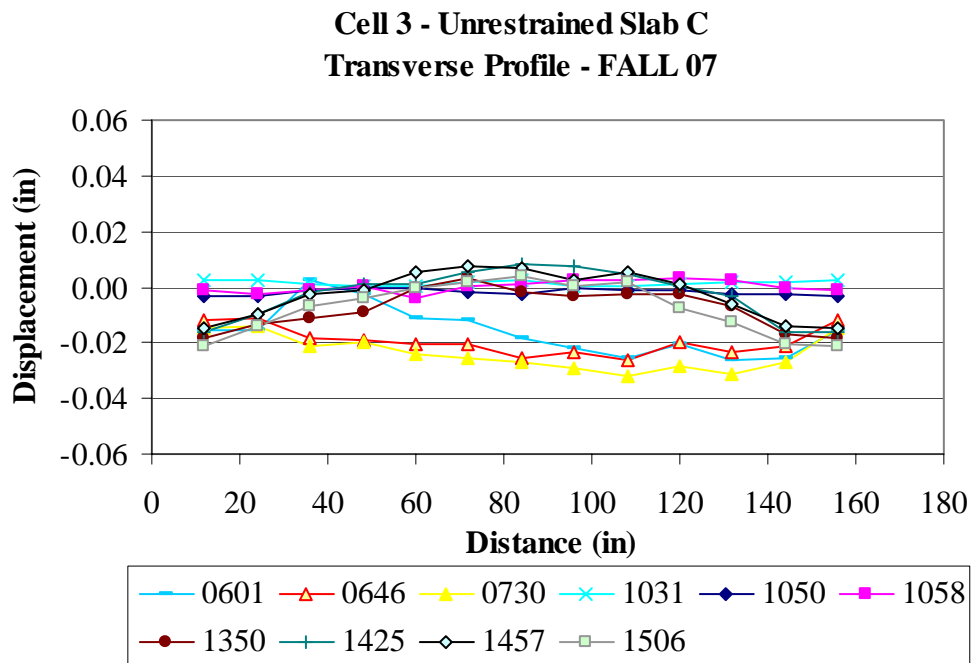


Figure E.98. Unrestrained Slab C Line B transverse surface profiles for the fall of 2007.

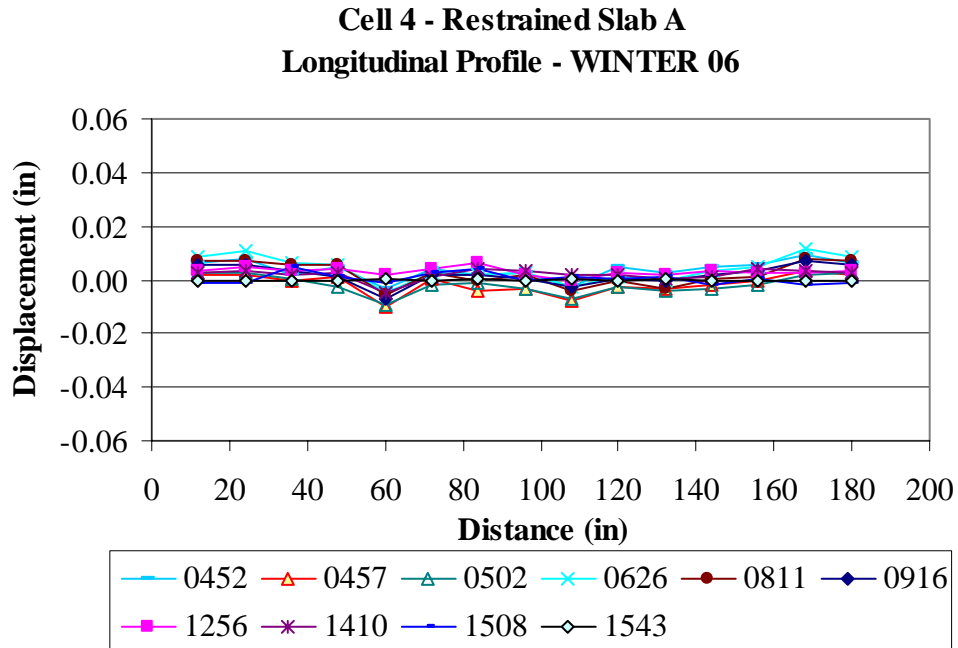


Figure E.99. Restrained Slab A longitudinal surface profiles for the winter of 2006.

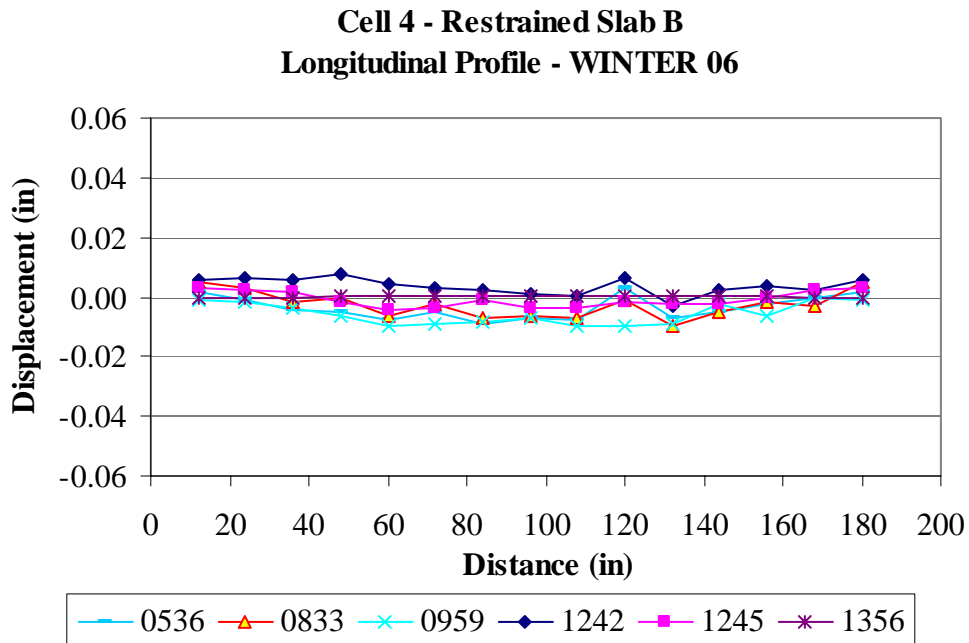


Figure E.100. Restrained Slab B longitudinal surface profiles for the winter of 2006.

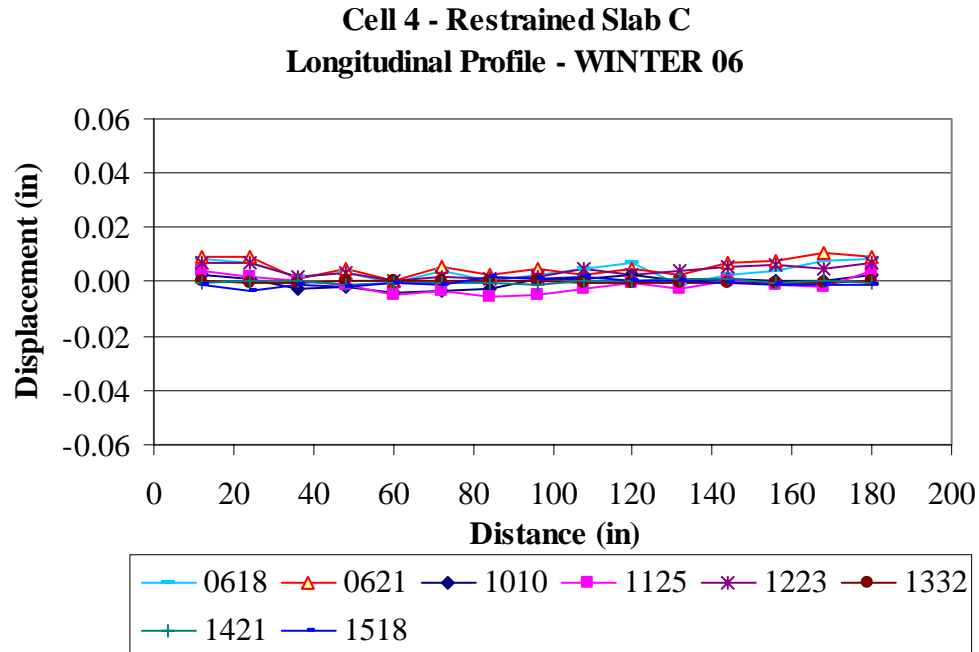


Figure E.101. Restrained Slab C longitudinal surface profiles for the winter of 2006.

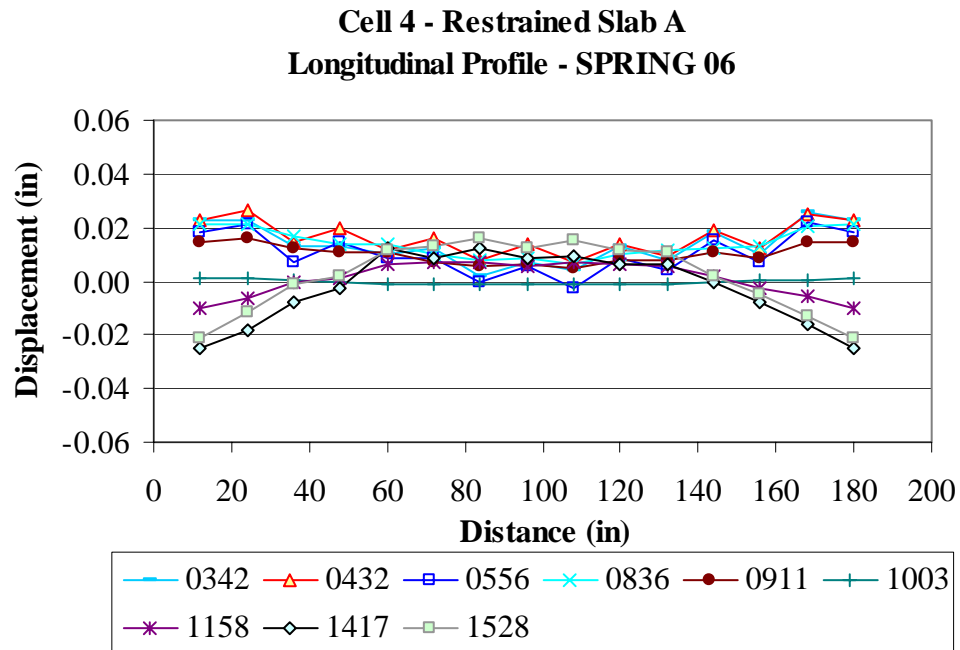


Figure E.102. Restrained Slab A longitudinal surface profiles for the spring of 2006.

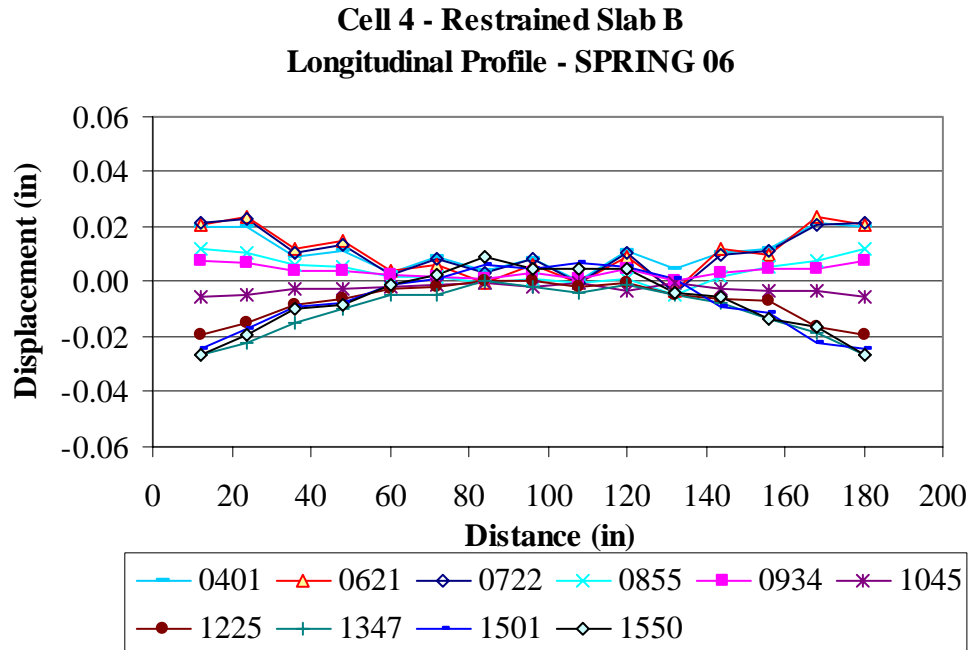


Figure E.103. Restrained Slab B longitudinal surface profiles for the spring of 2006.

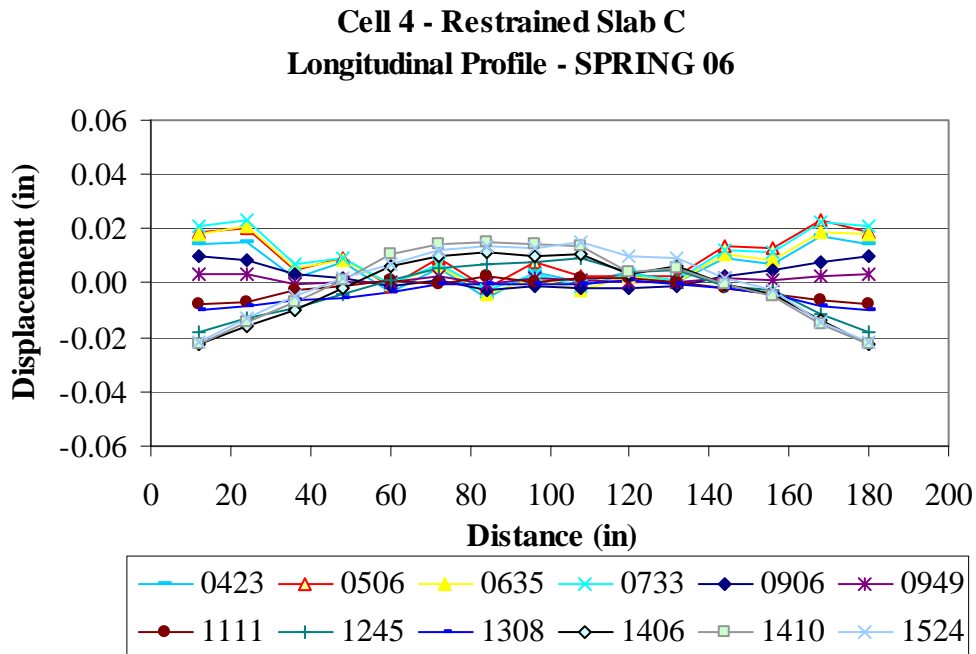


Figure E.104. Restrained Slab C longitudinal surface profiles for the spring of 2006.

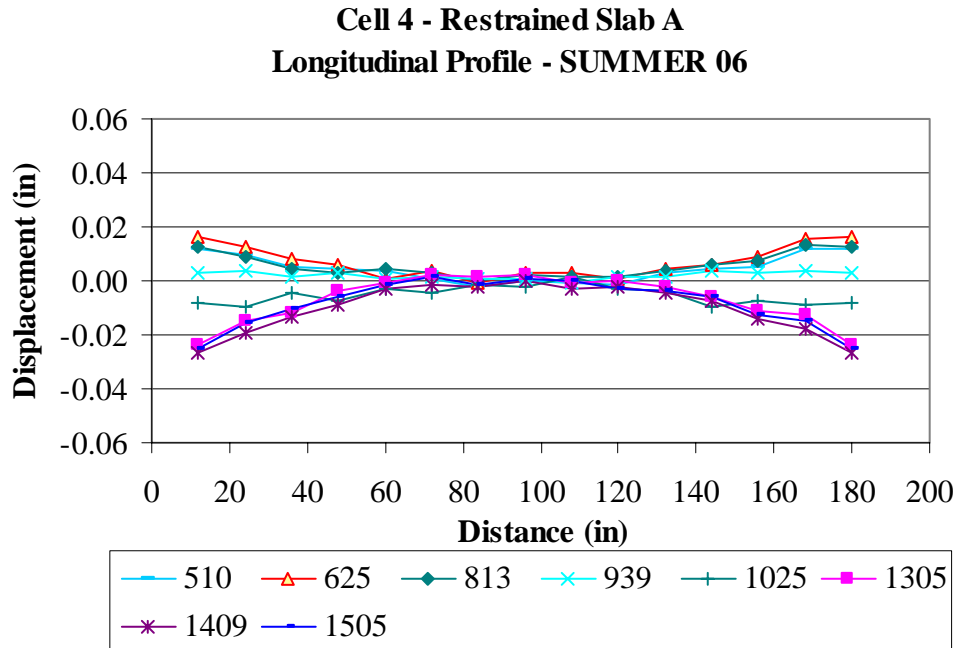


Figure E.105. Restrained Slab A longitudinal surface profiles for the summer of 2006.

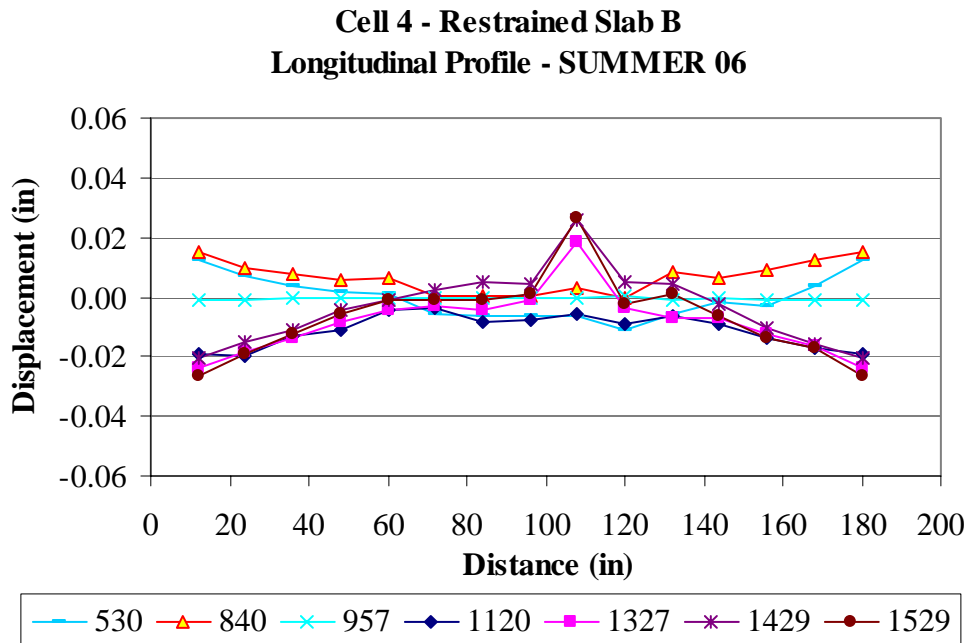


Figure E.106. Restrained Slab B longitudinal surface profiles for the summer of 2006.

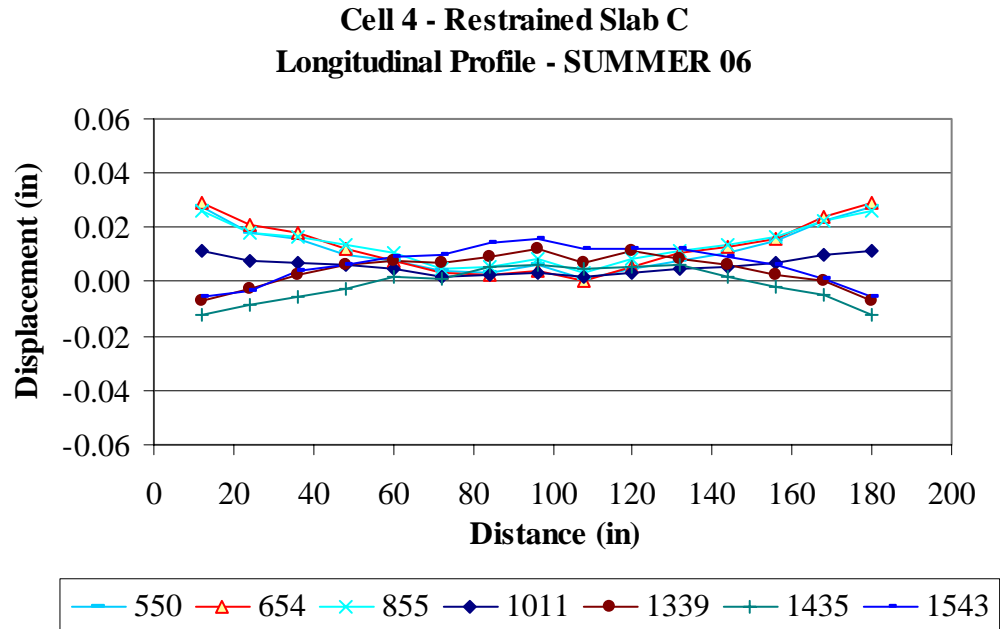


Figure E.107. Restrained Slab C longitudinal surface profiles for the summer of 2006.

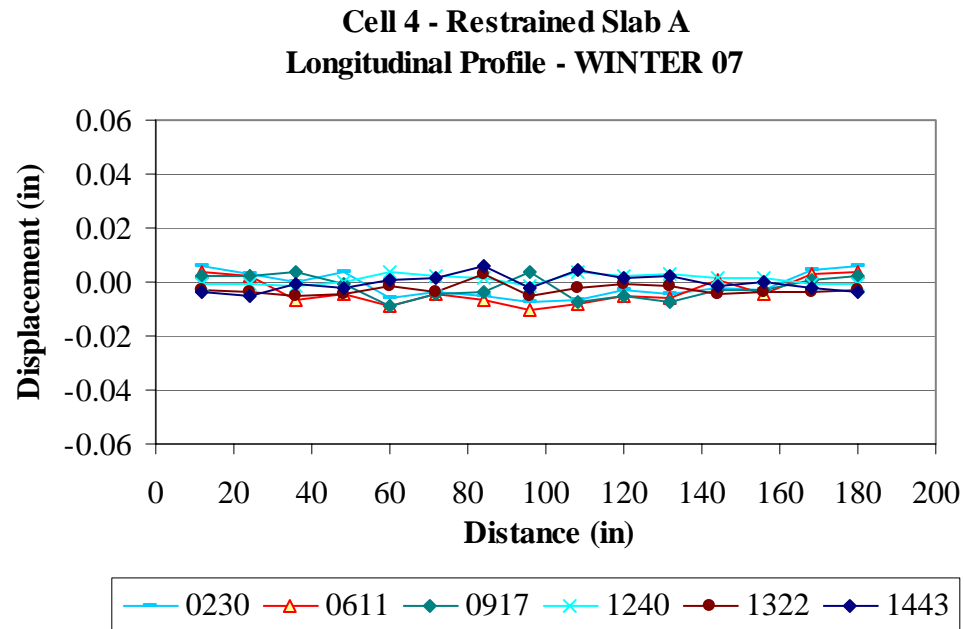


Figure E.108. Restrained Slab A longitudinal surface profiles for the winter of 2007.

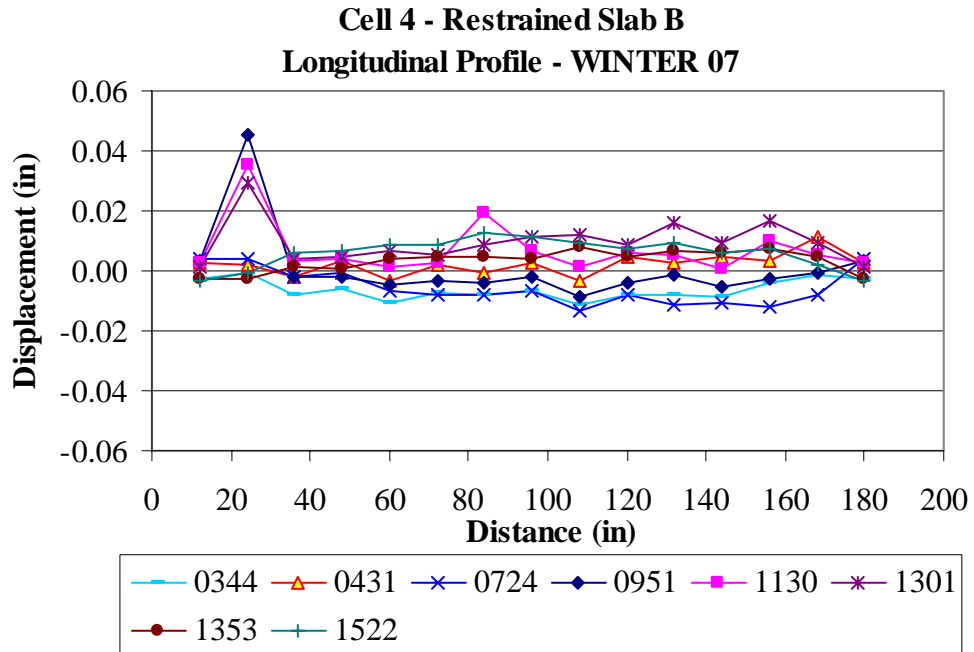


Figure E.109. Restrained Slab B longitudinal surface profiles for the winter of 2007.

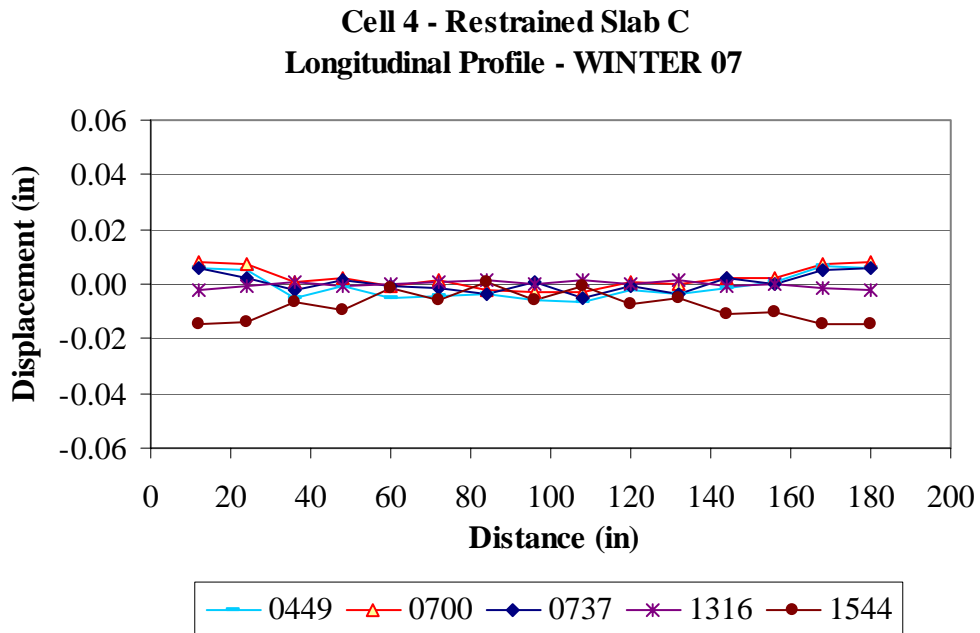


Figure E.110. Restrained Slab C longitudinal surface profiles for the winter of 2007.

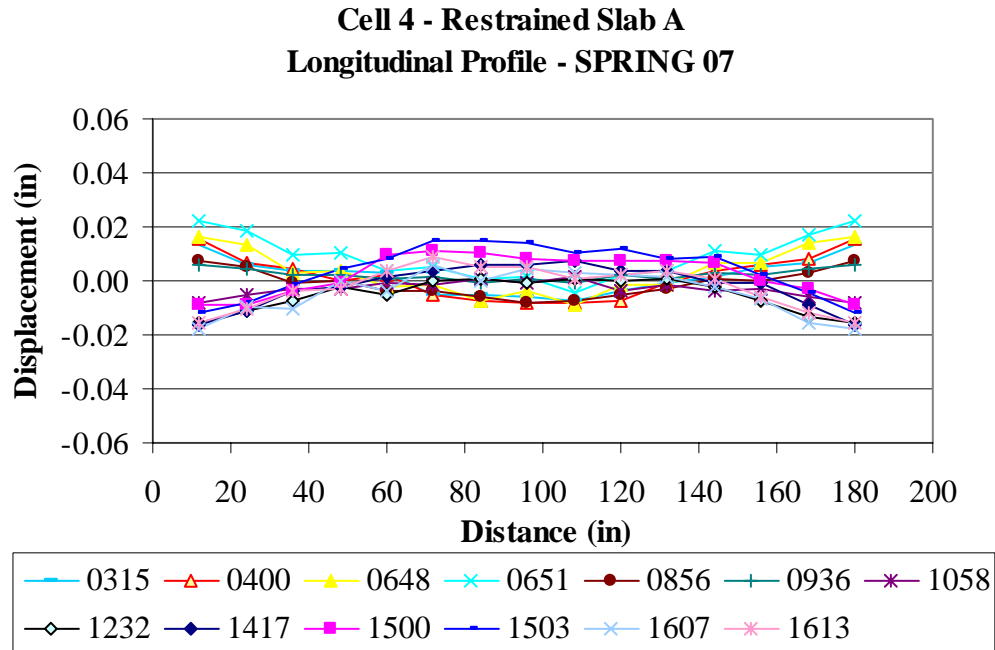


Figure E.111. Restrained Slab A longitudinal surface profiles for the spring of 2007.

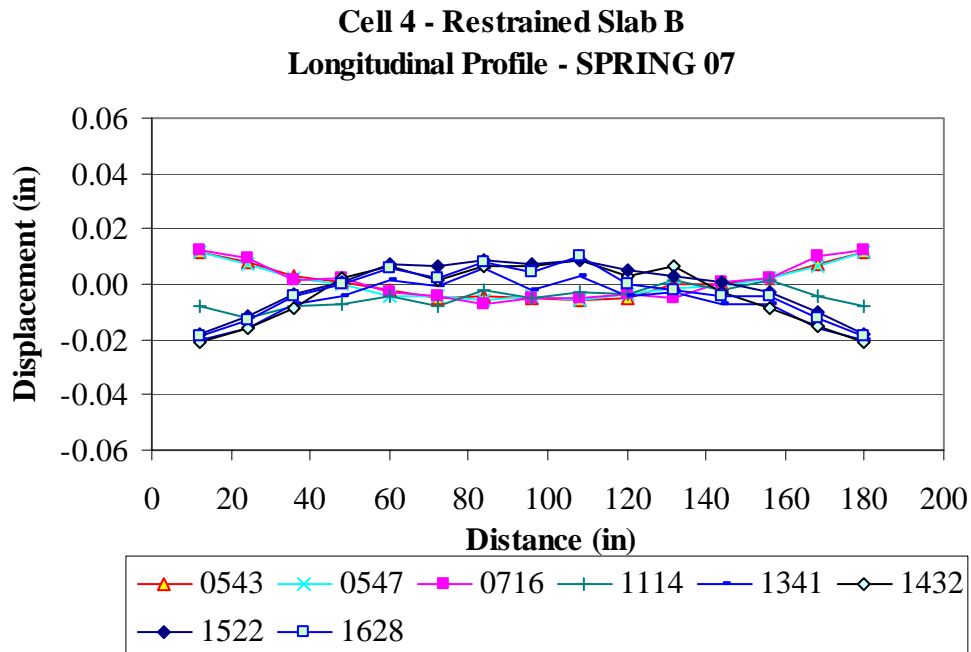


Figure E.112. Restrained Slab B longitudinal surface profiles for the spring of 2007.

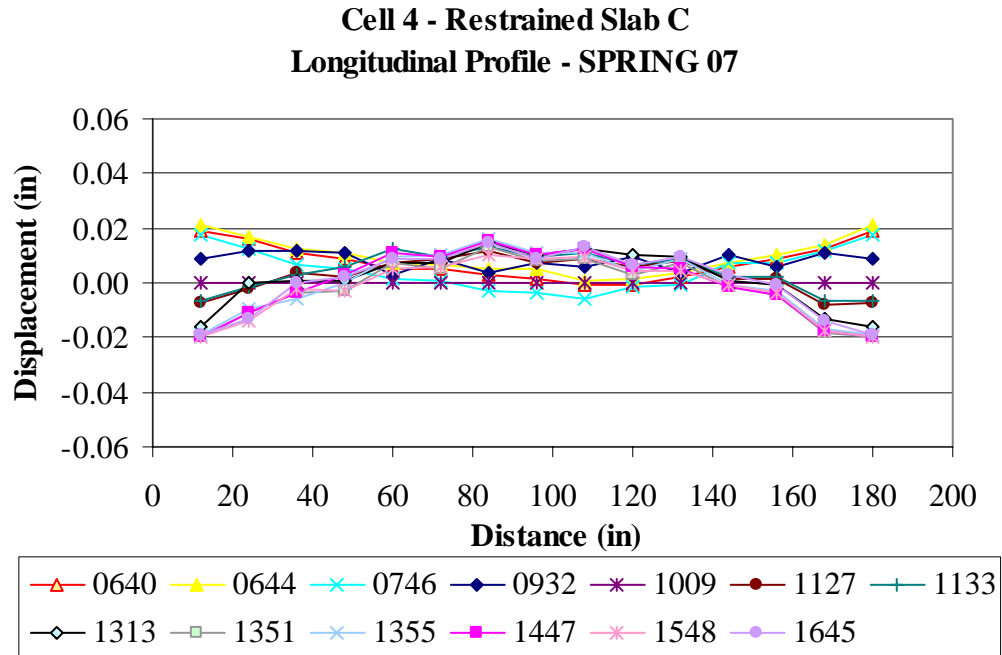


Figure E.113. Restrained Slab C longitudinal surface profiles for the spring of 2007.

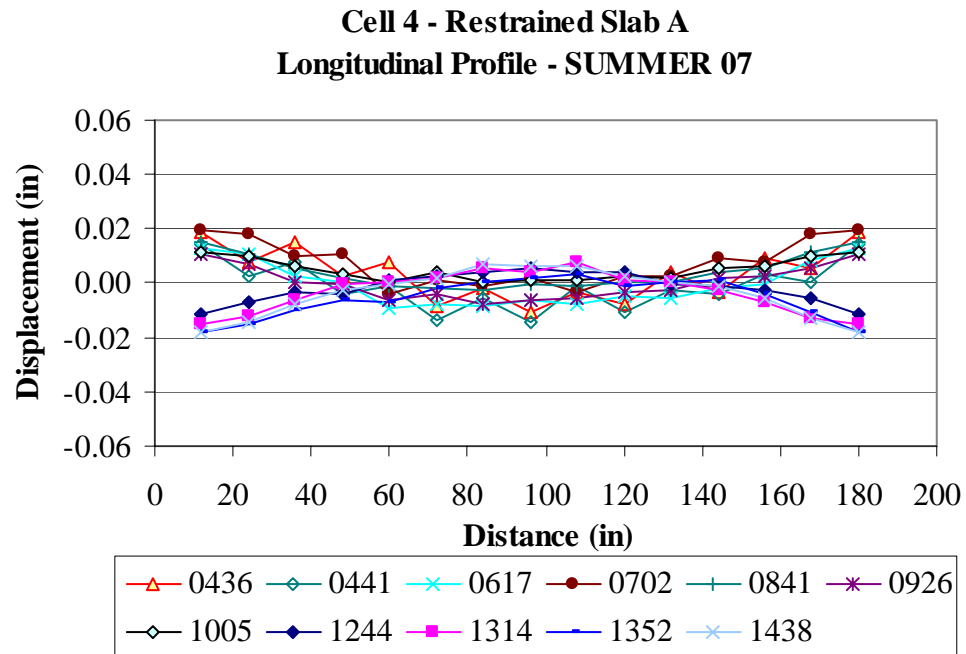


Figure E.114. Restrained Slab A longitudinal surface profiles for the summer of 2007.

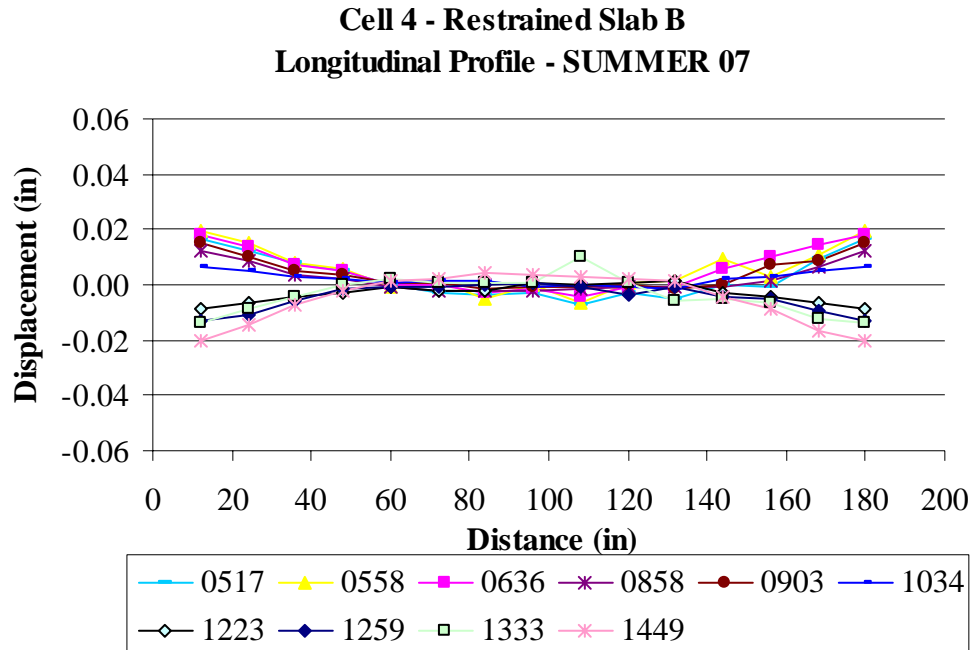


Figure E.115. Restrained Slab B longitudinal surface profiles for the summer of 2007.

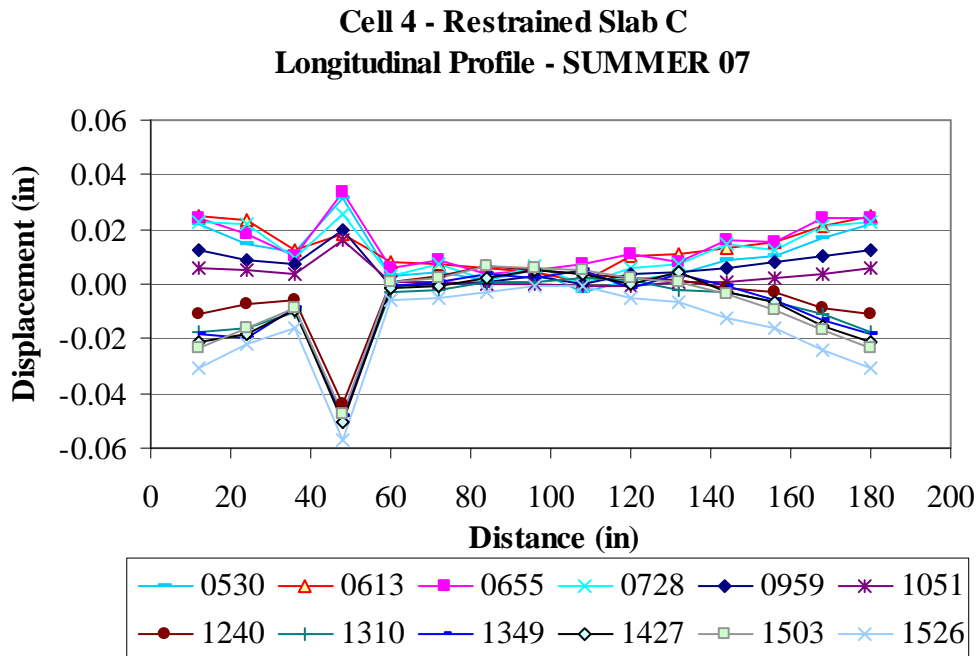


Figure E.116. Restrained Slab C longitudinal surface profiles for the summer of 2007.

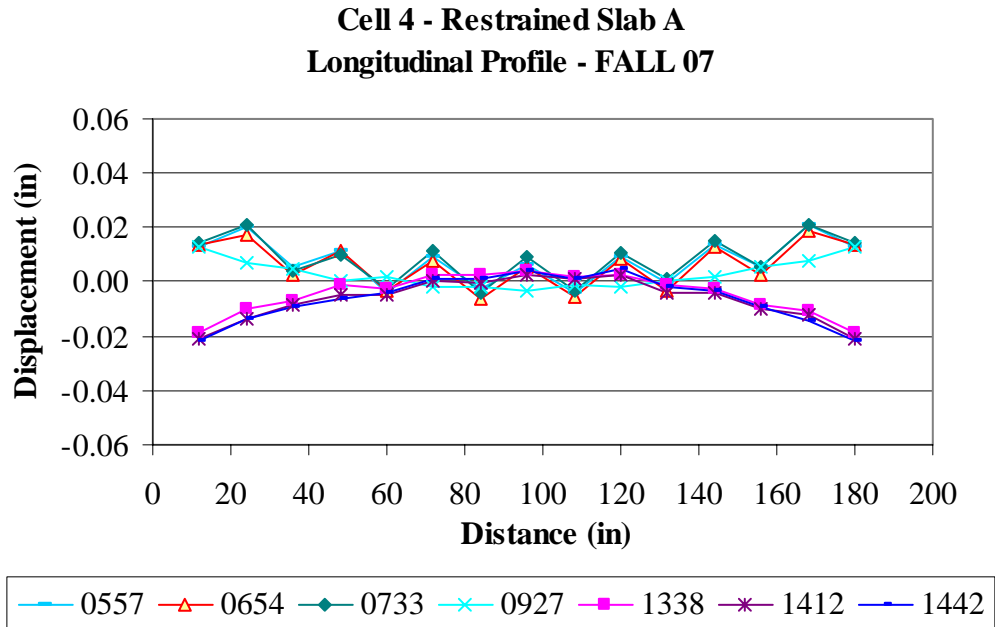


Figure E.117. Restrained Slab A longitudinal surface profiles for the fall of 2007.

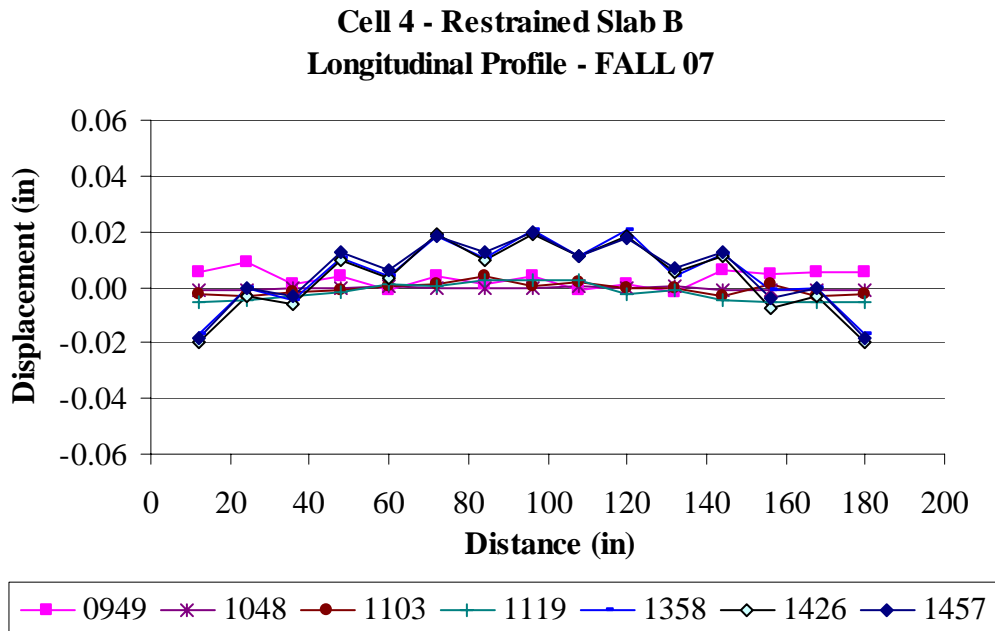


Figure E.118. Restrained Slab B longitudinal surface profiles for the fall of 2007.

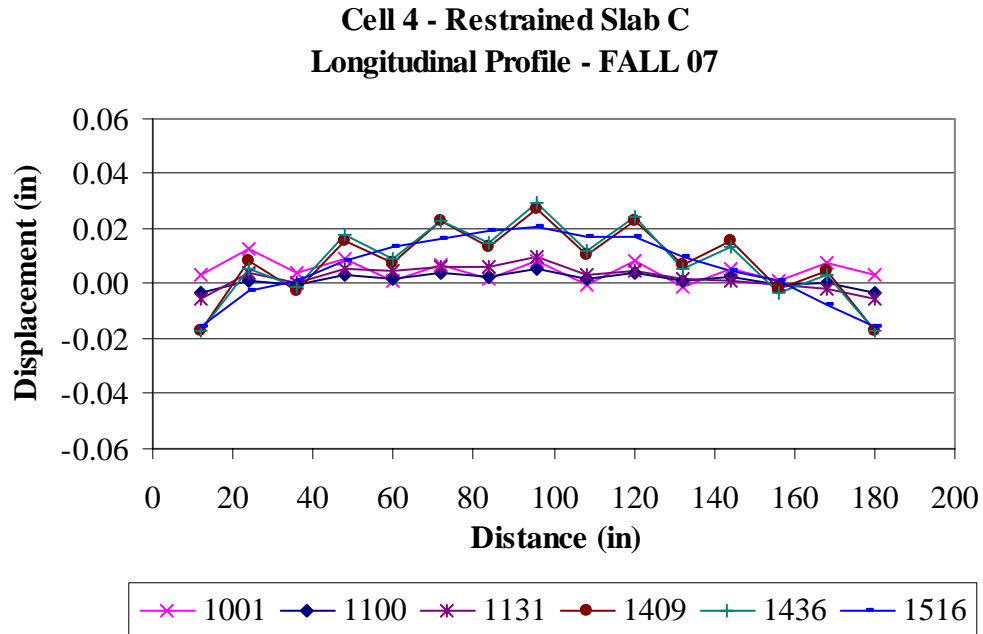


Figure E.119. Restrained Slab C longitudinal surface profiles for the fall of 2007.

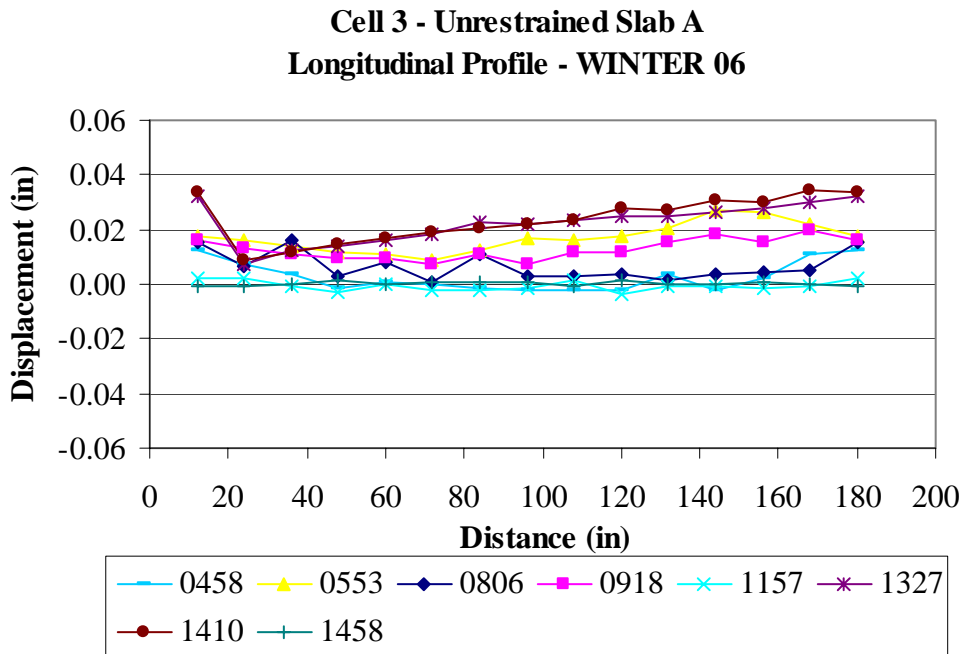


Figure E.120. Unrestrained Slab A longitudinal surface profiles for the winter of 2006.

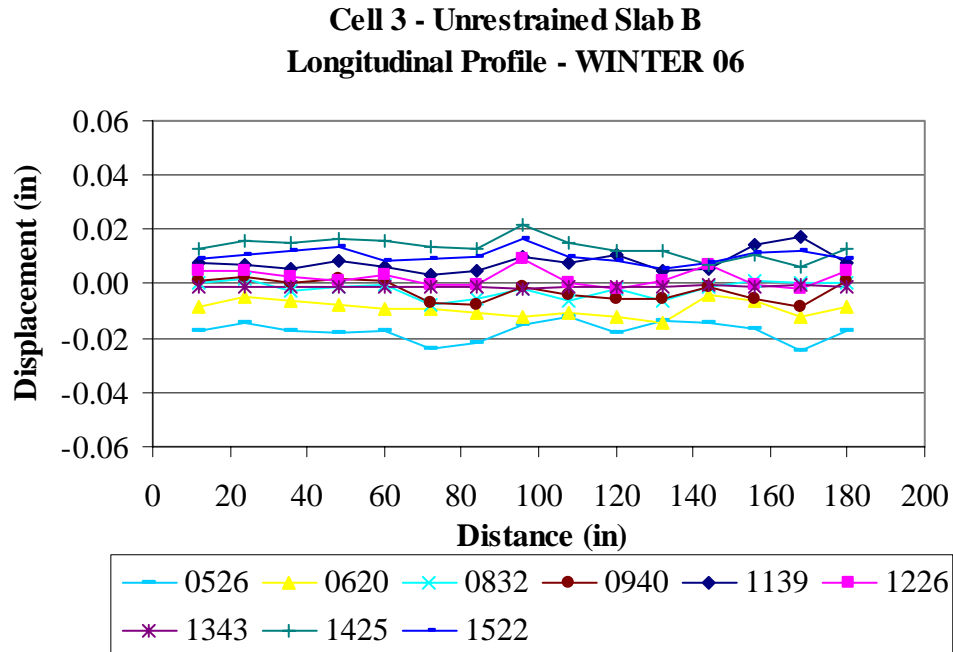


Figure E.121. Unrestrained Slab B longitudinal surface profiles for the winter of 2006.

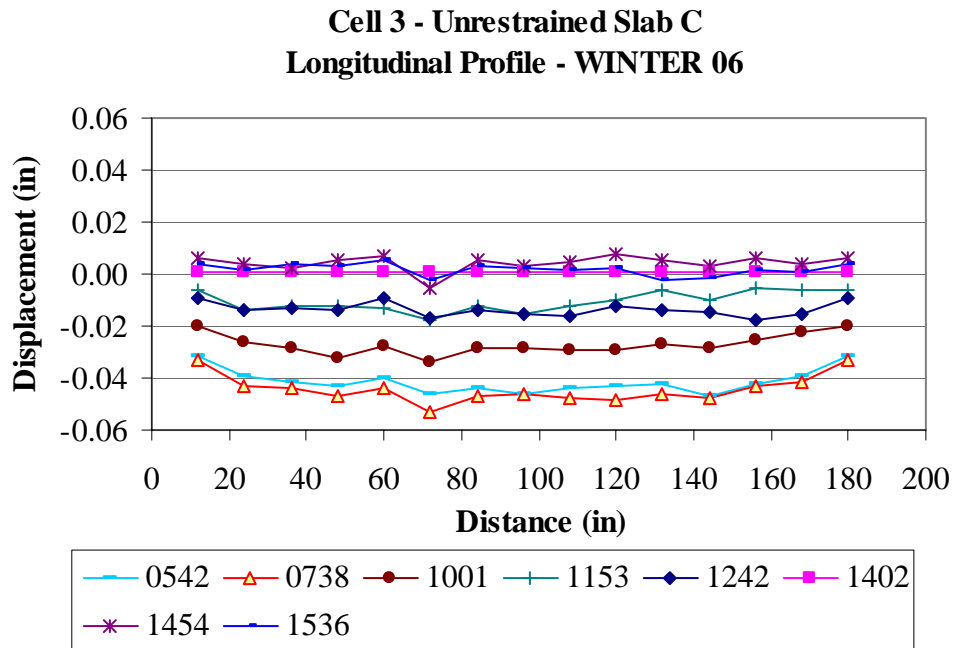


Figure E.122. Unrestrained Slab C longitudinal surface profiles for the winter of 2006.

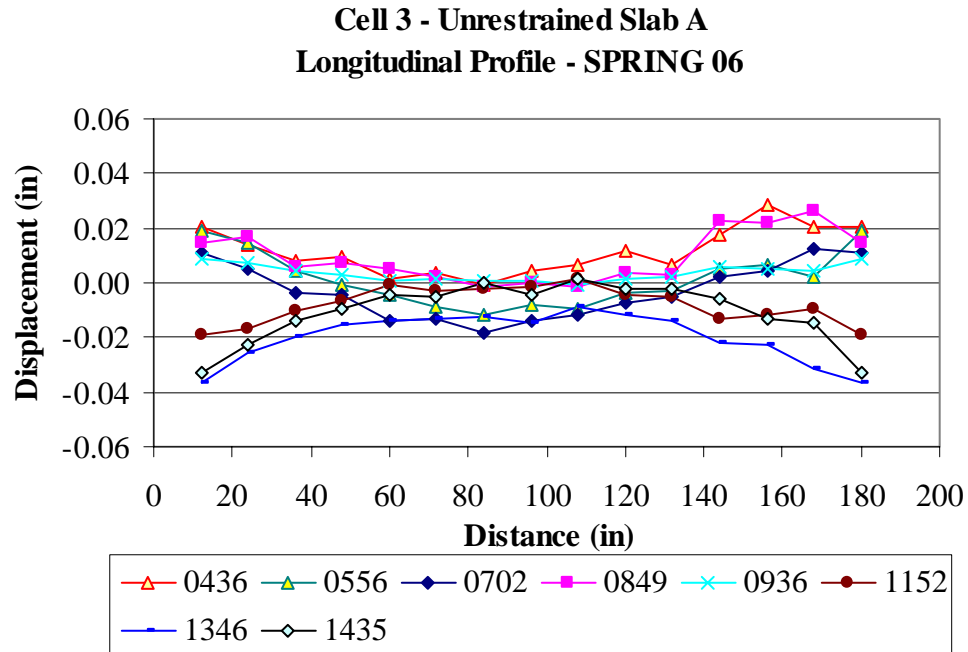


Figure E.123. Unrestrained Slab A longitudinal surface profiles for the spring of 2006.

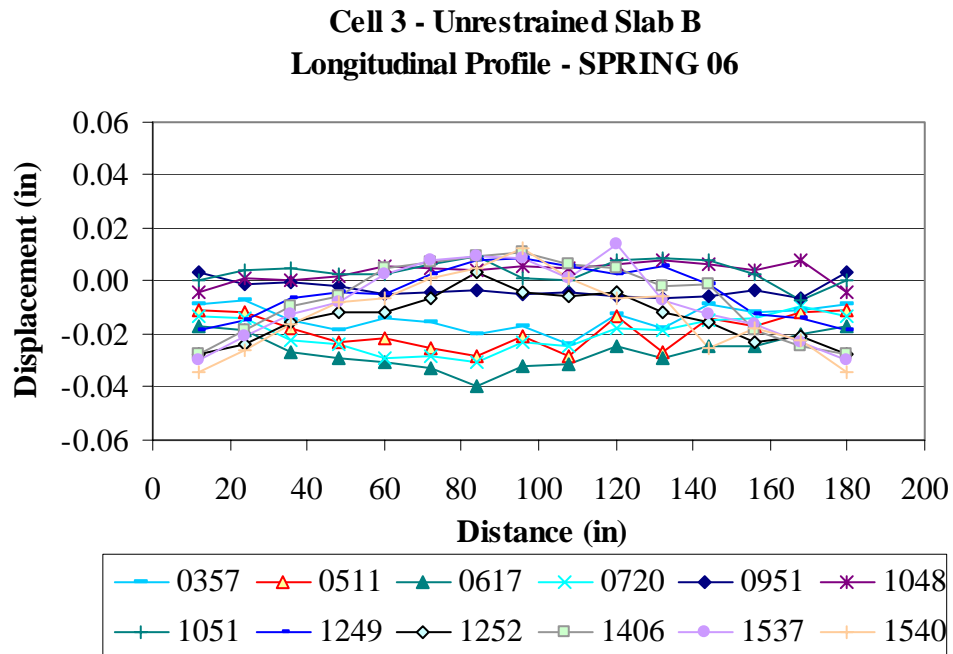


Figure E.124. Unrestrained Slab B longitudinal surface profiles for the spring of 2006.

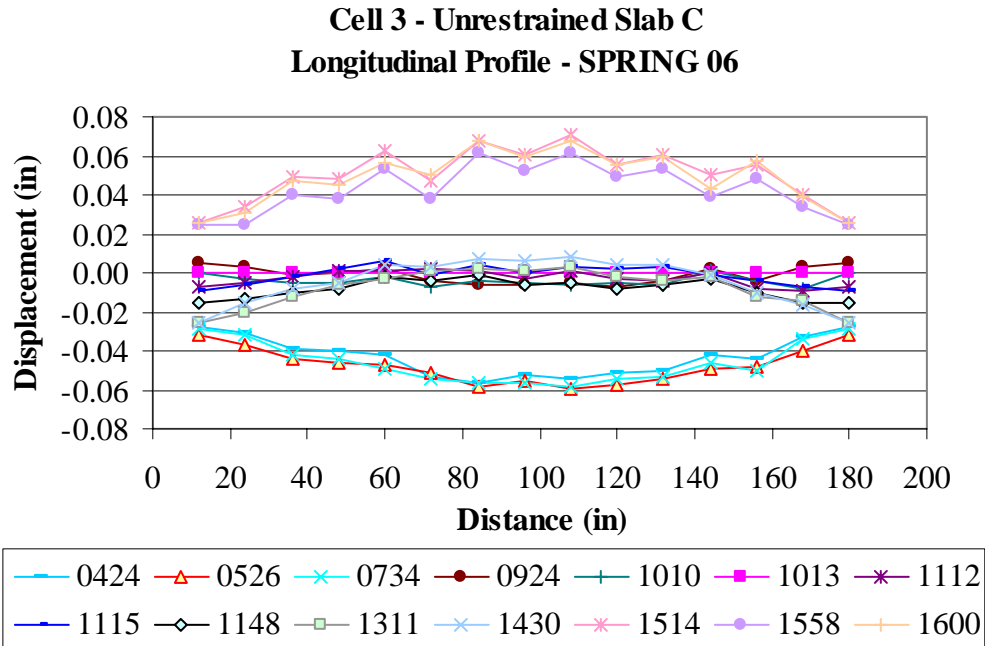


Figure E.125. Unrestrained Slab C longitudinal surface profiles for the spring of 2006.

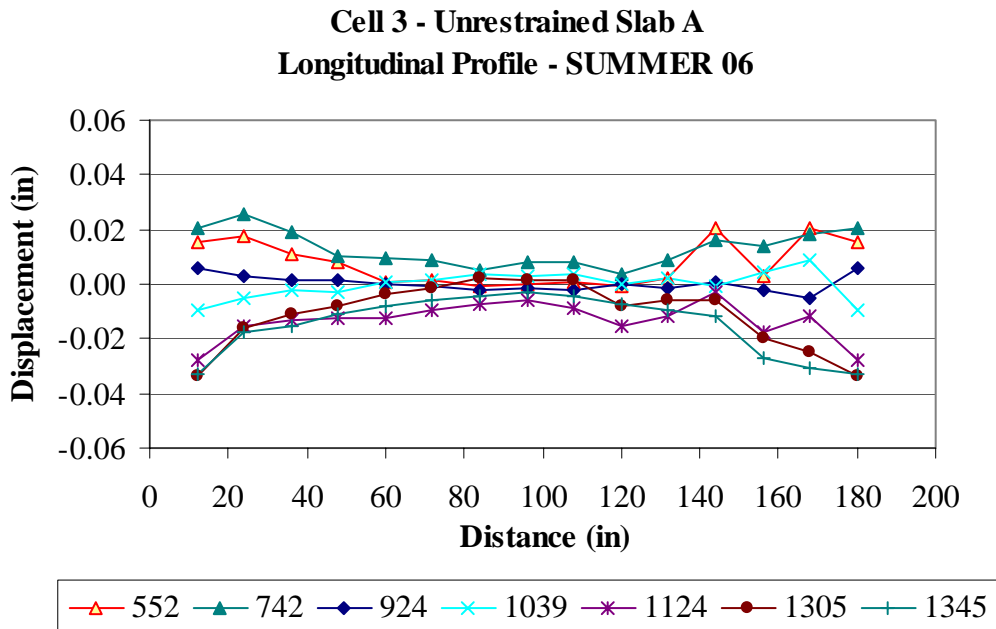


Figure E.126. Unrestrained Slab A longitudinal surface profiles for the summer of 2006.

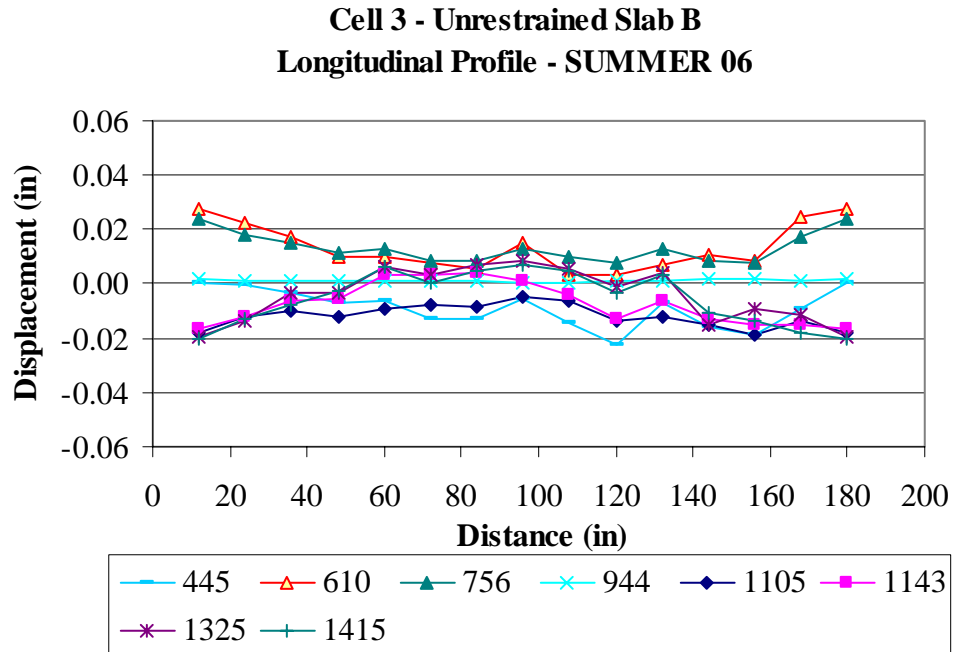


Figure E.127. Unrestrained Slab B longitudinal surface profiles for the summer of 2006.

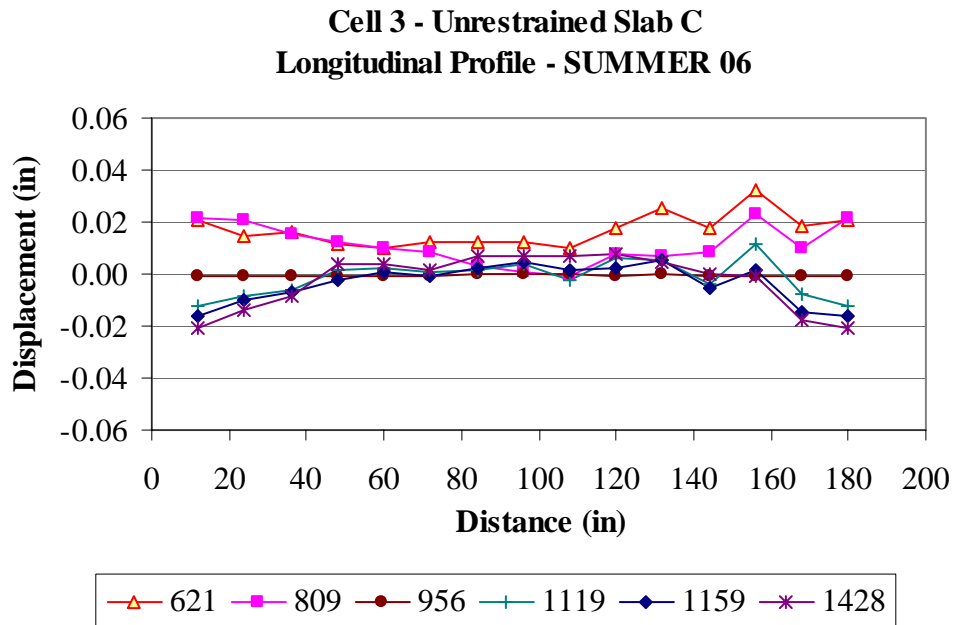


Figure E.128. Unrestrained Slab C longitudinal surface profiles for the summer of 2006.

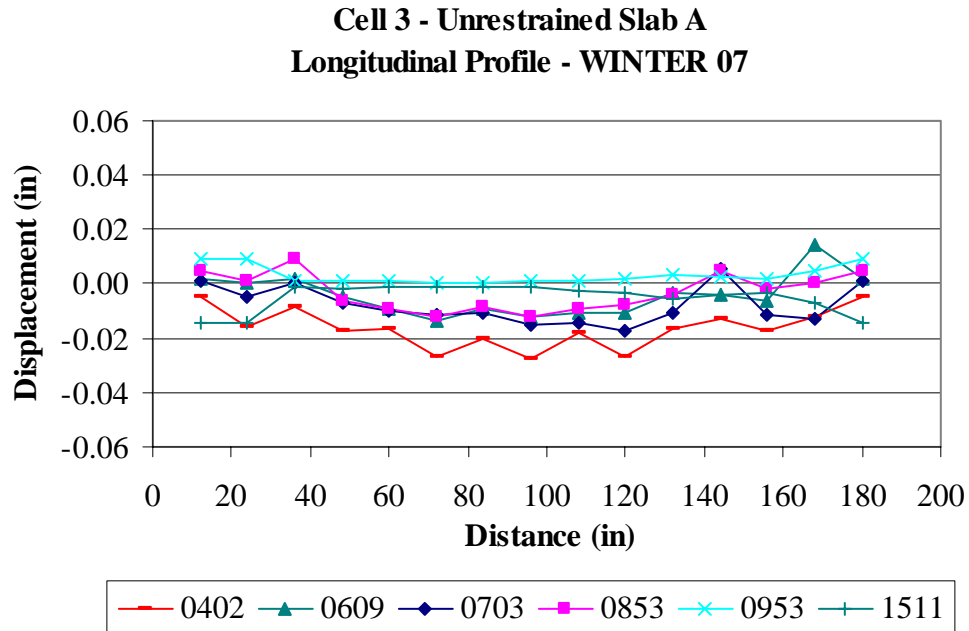


Figure E.129. Unrestrained Slab A longitudinal surface profiles for the winter of 2007.

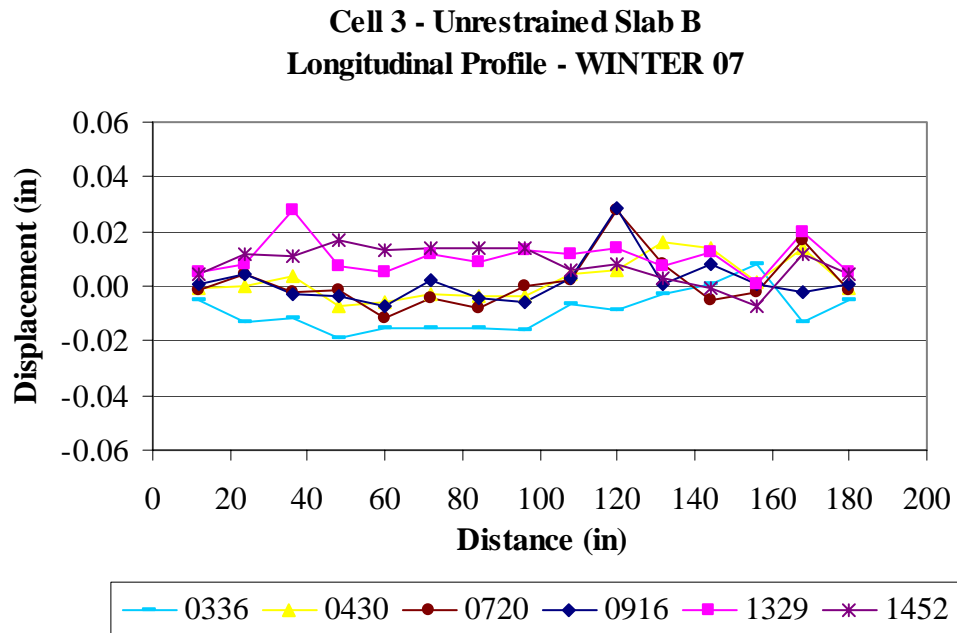


Figure E.130. Unrestrained Slab B longitudinal surface profiles for the winter of 2007.

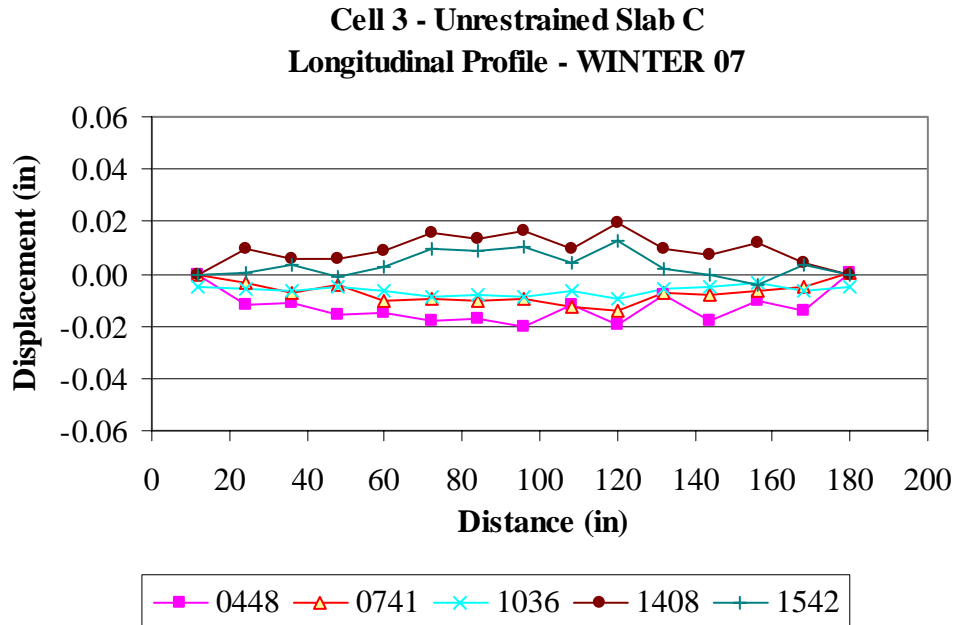


Figure E.131. Unrestrained Slab C longitudinal surface profiles for the winter of 2007.

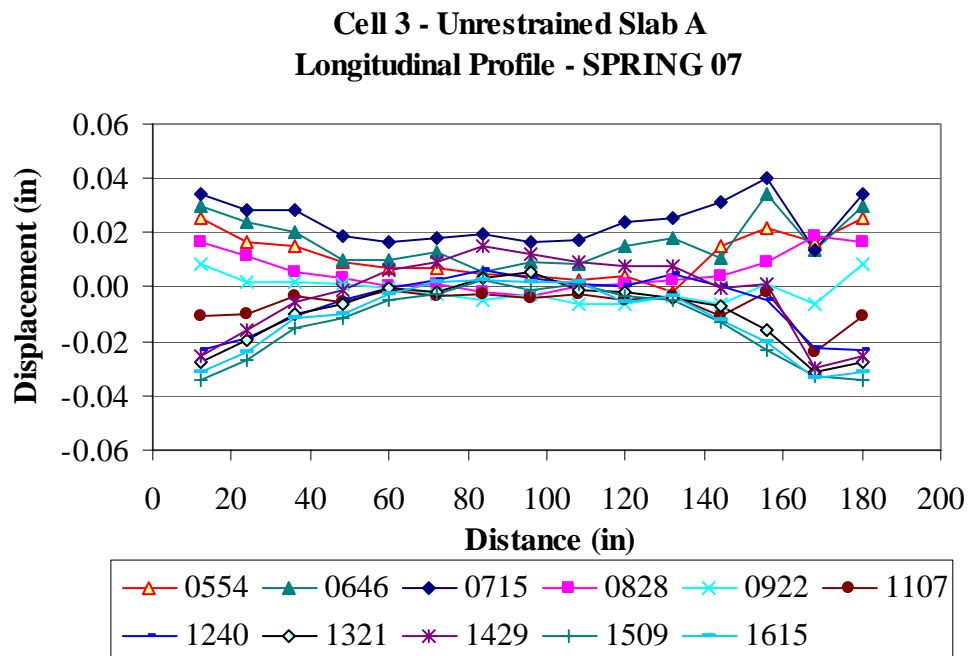


Figure E.132. Unrestrained Slab A longitudinal surface profiles for the spring of 2007.

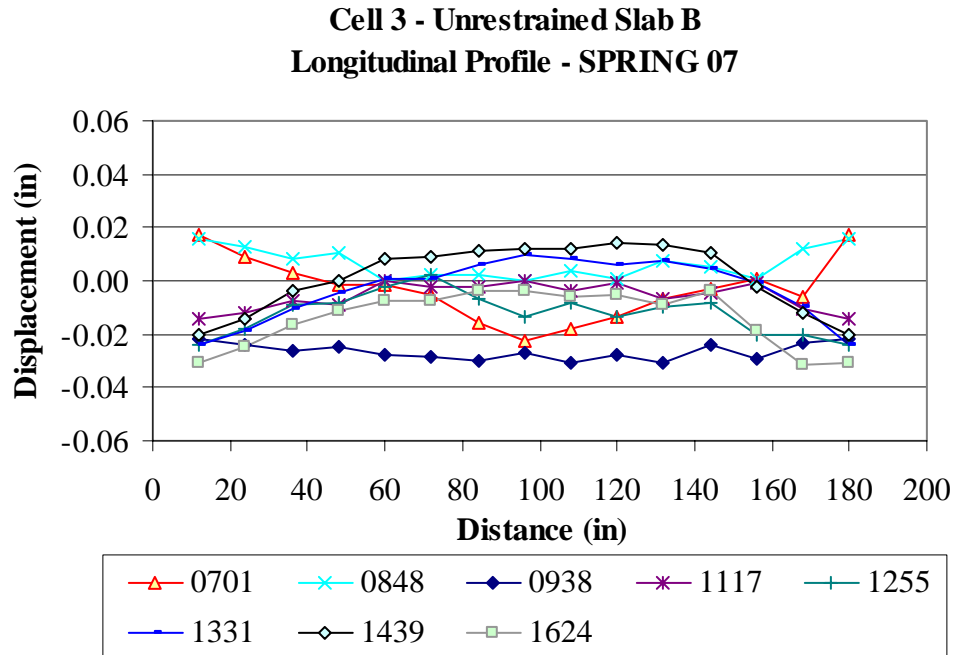


Figure E.133. Unrestrained Slab B longitudinal surface profiles for the spring of 2007.

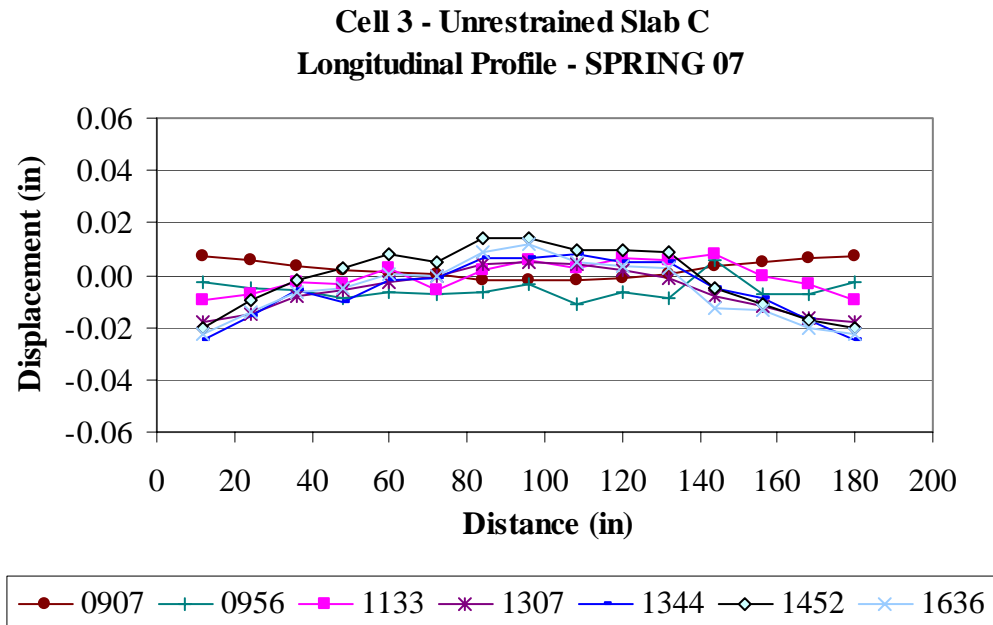


Figure E.134. Unrestrained Slab C longitudinal surface profiles for the spring of 2007.

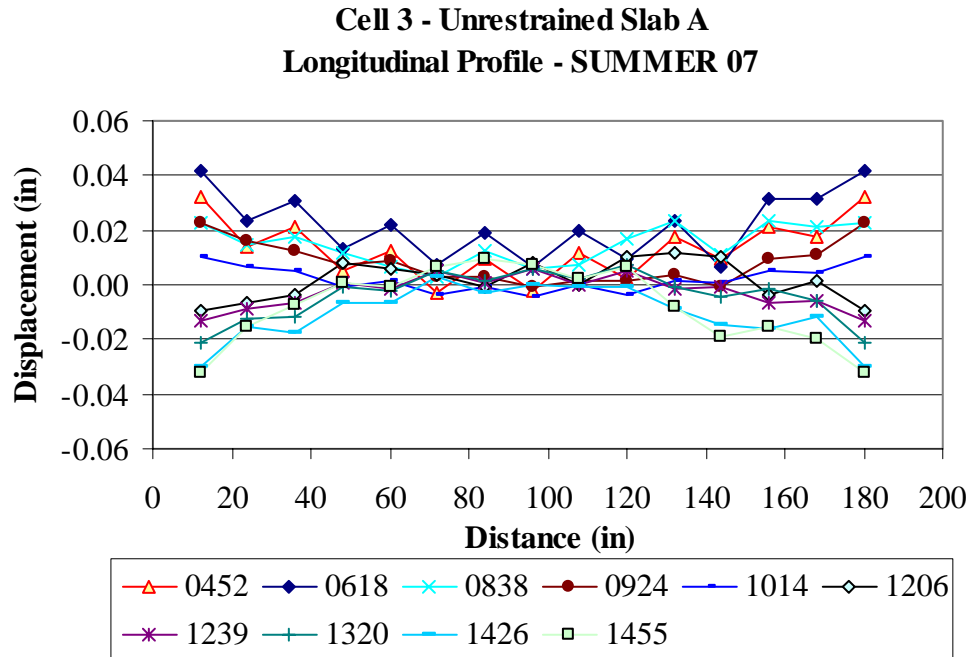


Figure E.135. Unrestrained Slab A longitudinal surface profiles for the summer of 2007.

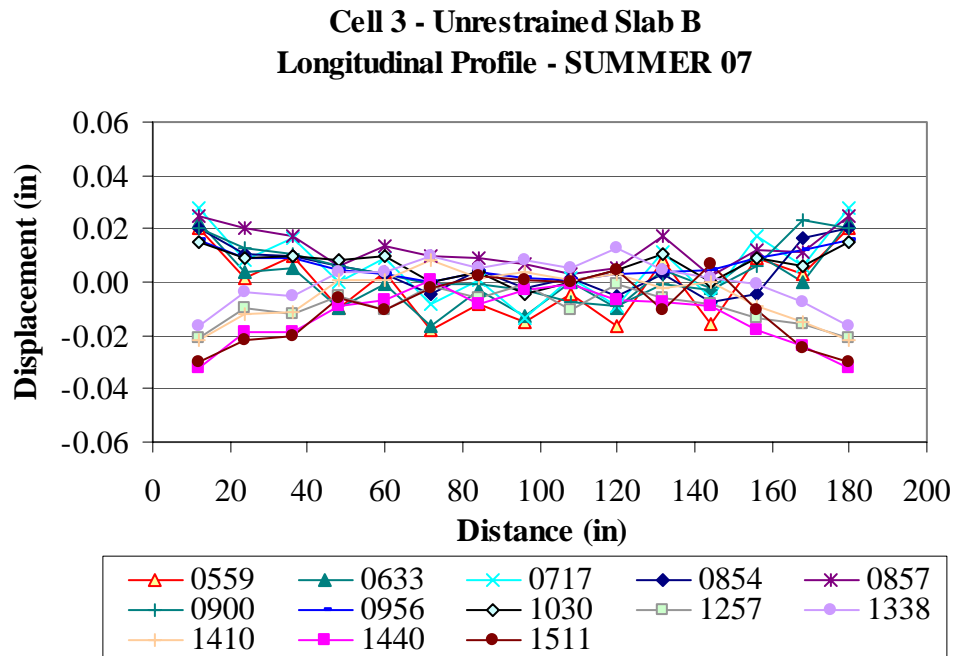


Figure E.136. Unrestrained Slab B longitudinal surface profiles for the summer of 2007.

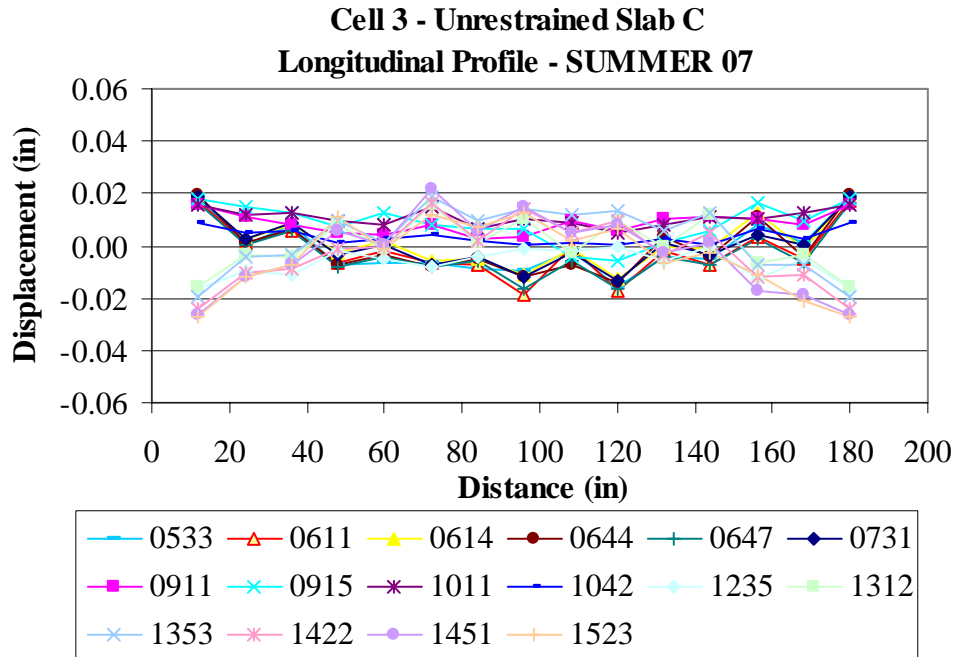


Figure E.137. Unrestrained Slab C longitudinal surface profiles for the summer of 2007.

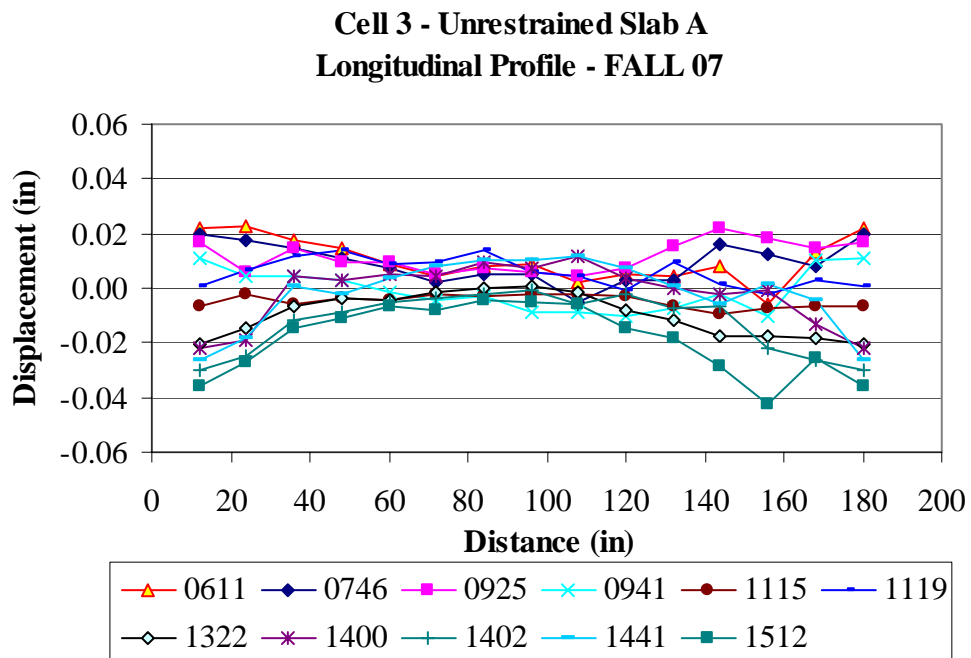


Figure E.138. Unrestrained Slab A longitudinal surface profiles for the fall of 2007.

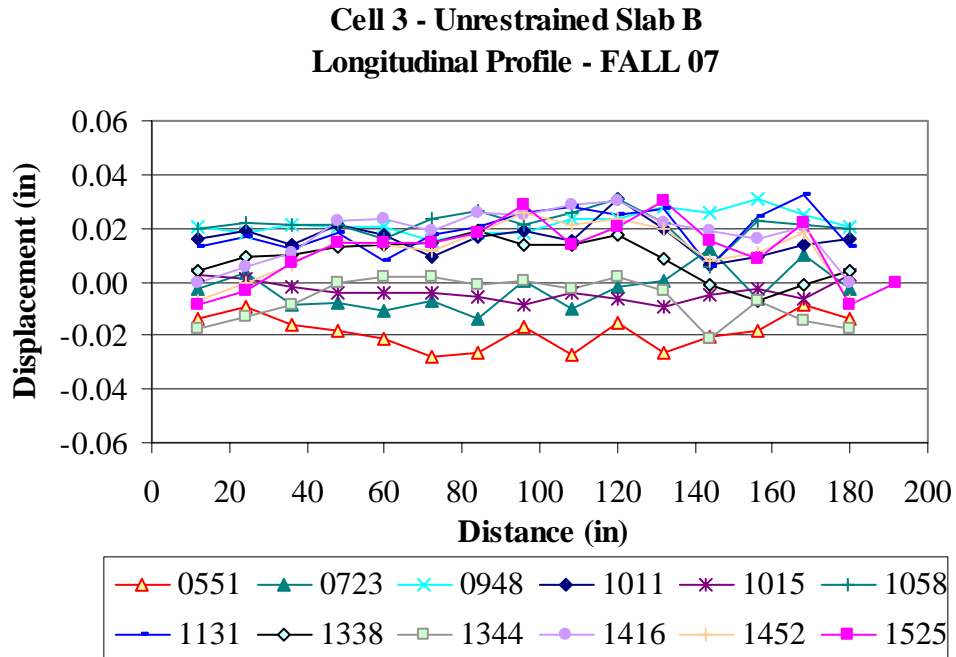


Figure E.139. Unrestrained Slab B longitudinal surface profiles for the fall of 2007.

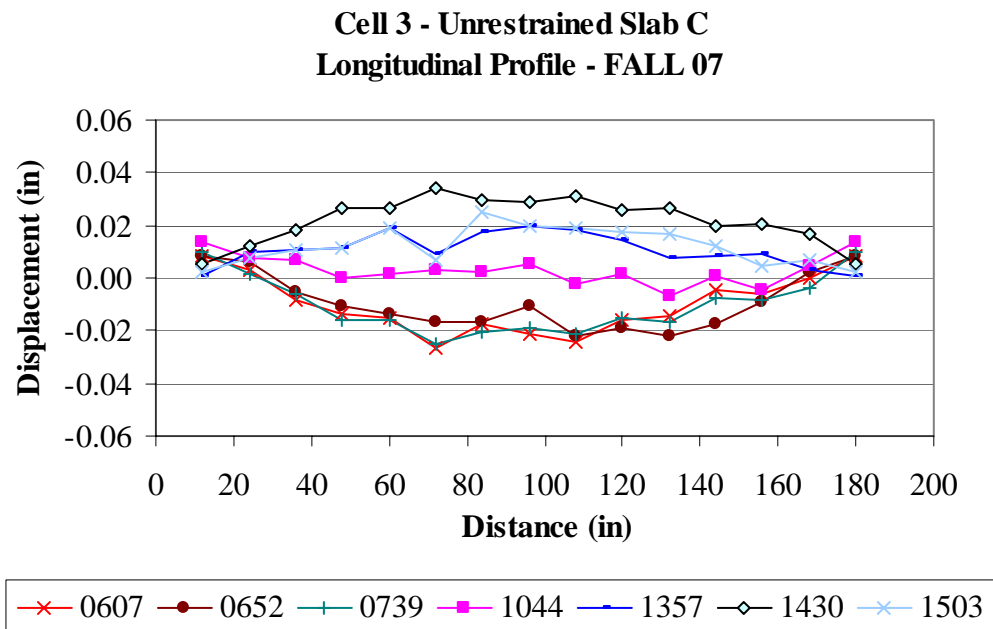


Figure E.140. Unrestrained Slab C longitudinal surface profiles for the fall of 2007.

Appendix F: Slab Curvature

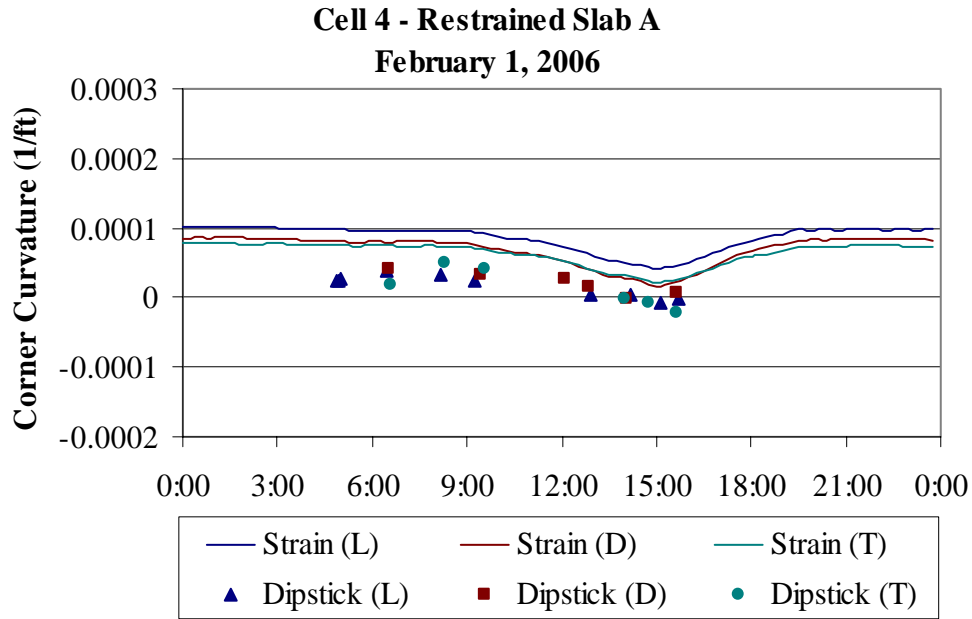


Figure F.1. Curvature estimated from surface profiles and vibrating wire gages for restrained Slab A during the winter of 2006.

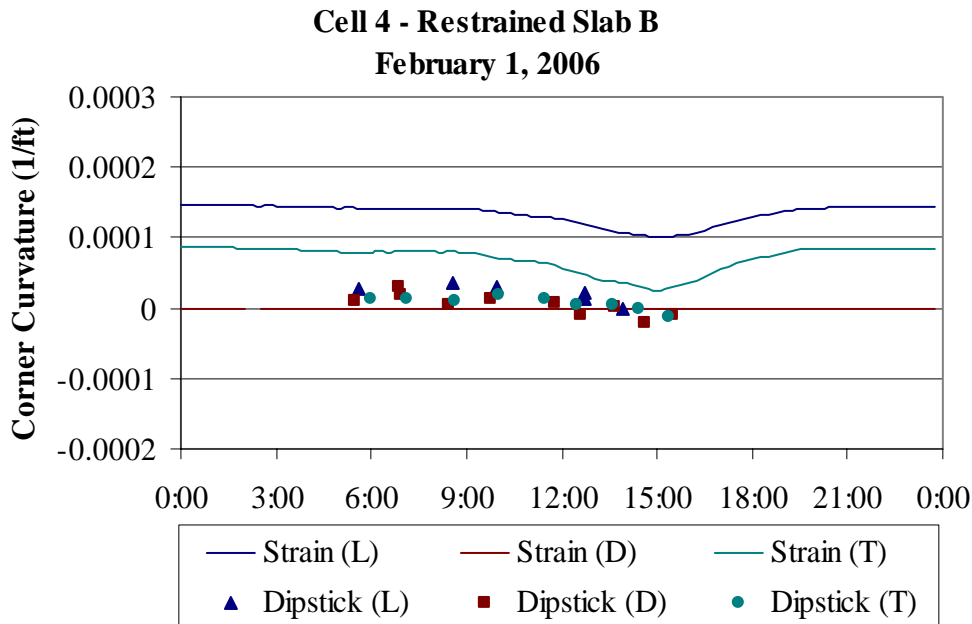


Figure F.2. Curvature estimated from surface profiles and vibrating wire gages for restrained Slab B during the winter of 2006.

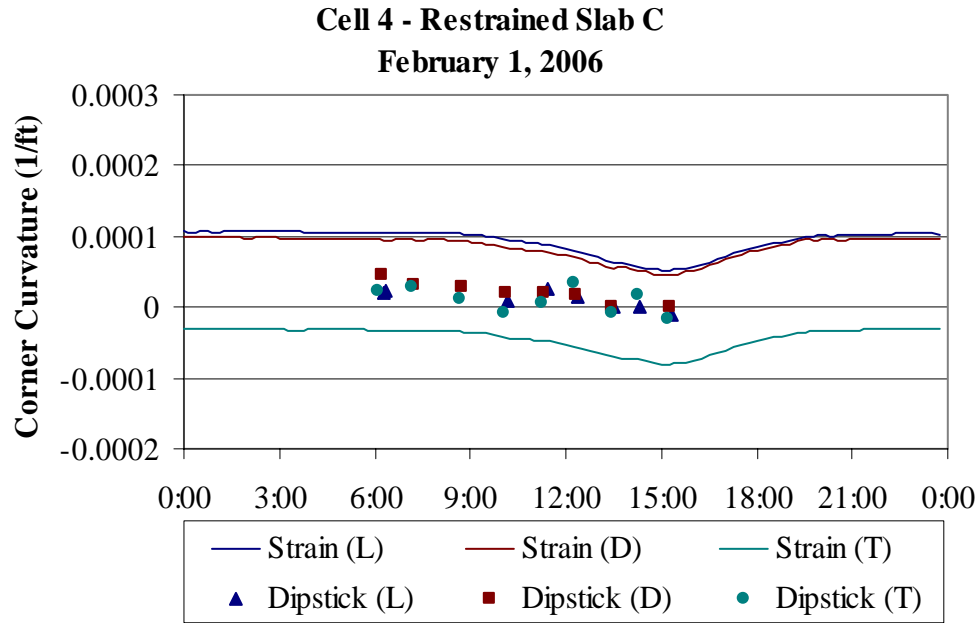


Figure F.3. Curvature estimated from surface profiles and vibrating wire gages for restrained Slab C during the winter of 2006.

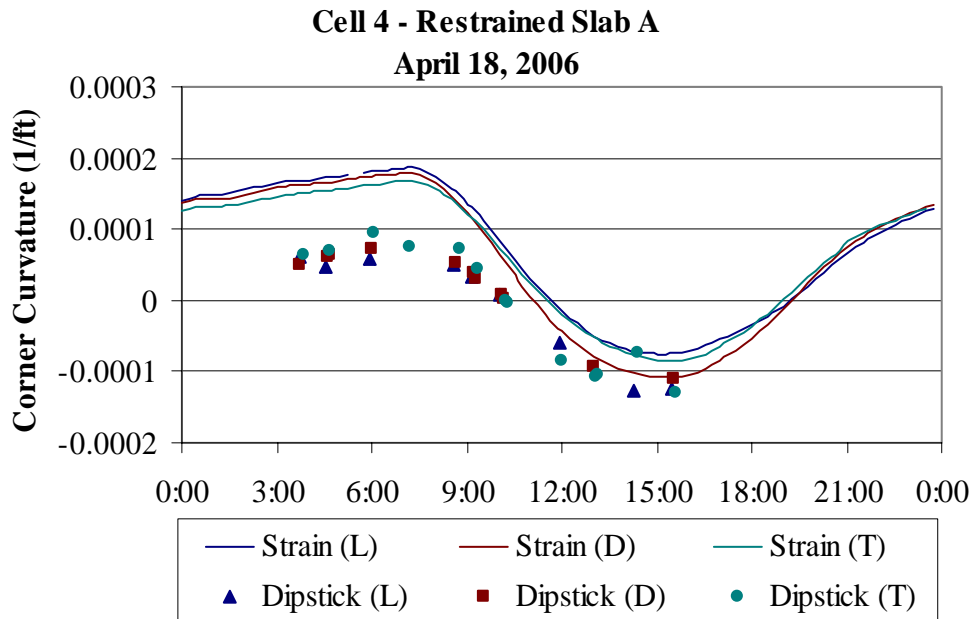


Figure F.4. Curvature estimated from surface profiles and vibrating wire gages for restrained Slab A during the spring of 2006.

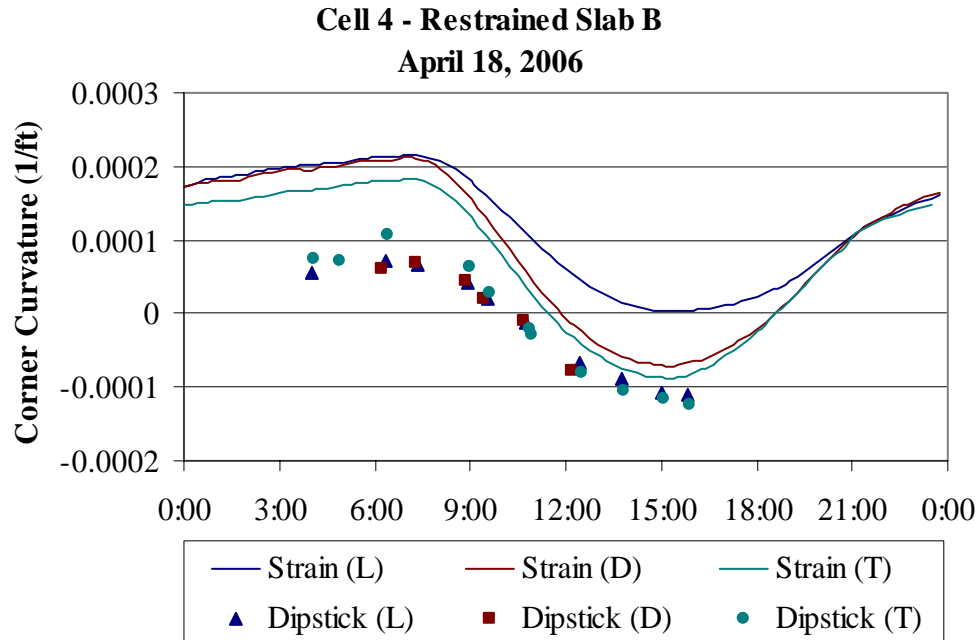


Figure F.5. Curvature estimated from surface profiles and vibrating wire gages for restrained Slab B during the spring of 2006.

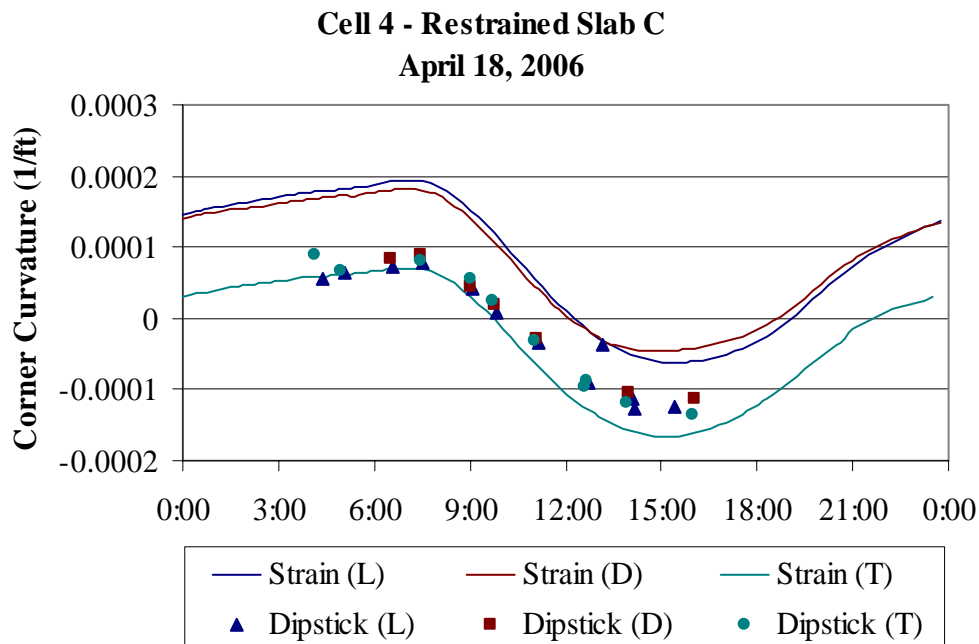


Figure F.6. Curvature estimated from surface profiles and vibrating wire gages for restrained Slab C during the spring of 2006.

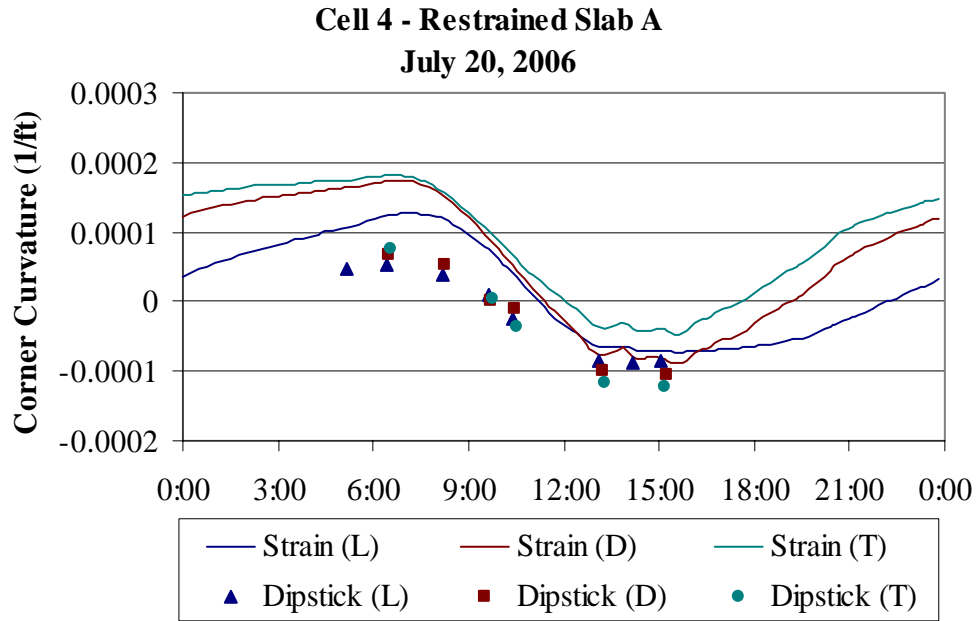


Figure F.7. Curvature estimated from surface profiles and vibrating wire gages for restrained Slab A during the summer of 2006.

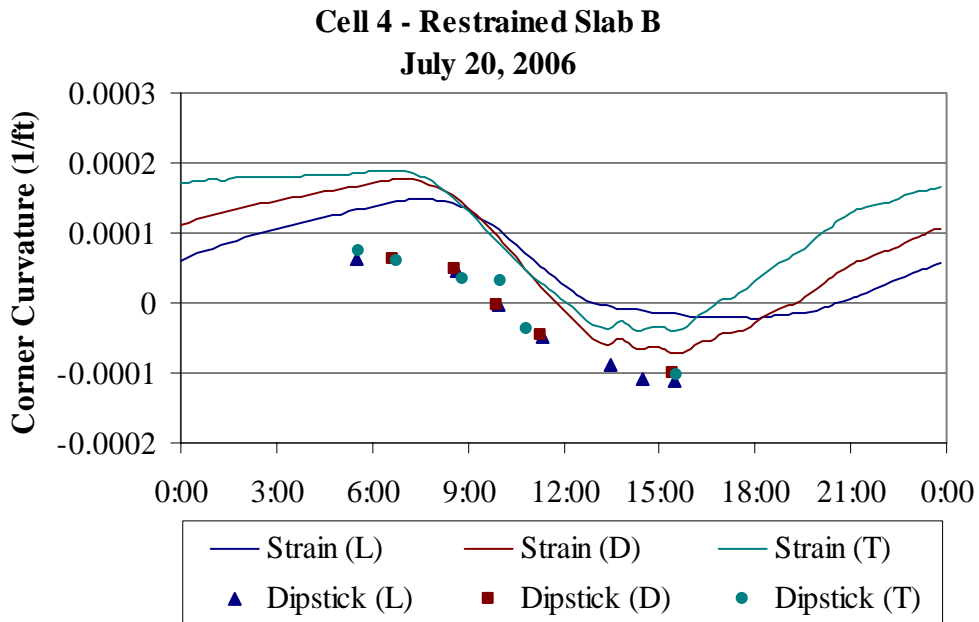


Figure F.8. Curvature estimated from surface profiles and vibrating wire gages for restrained Slab B during the summer of 2006.

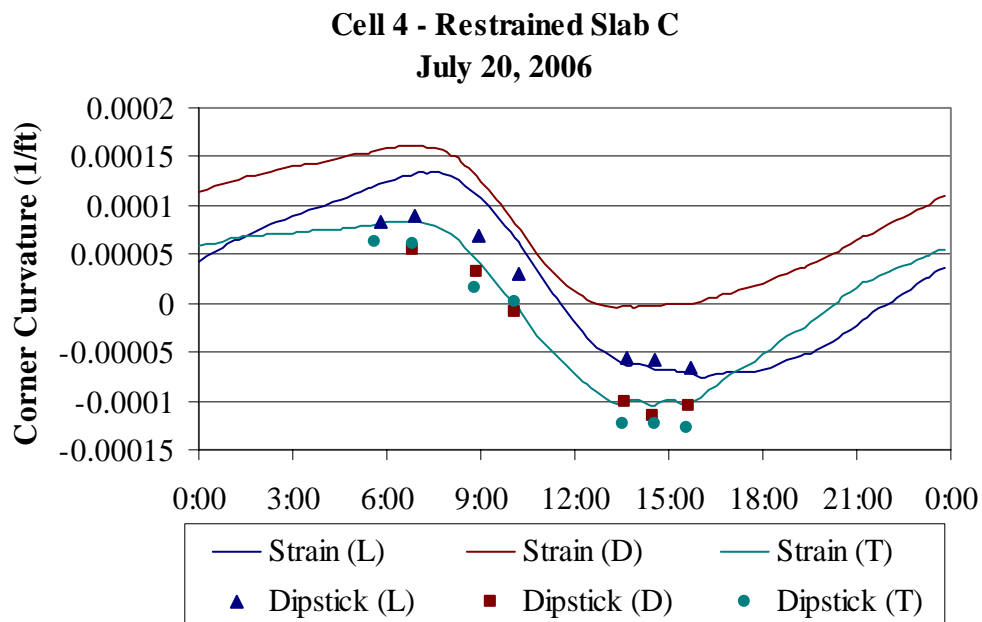


Figure F.9. Curvature estimated from surface profiles and vibrating wire gages for restrained Slab C during the summer of 2006.

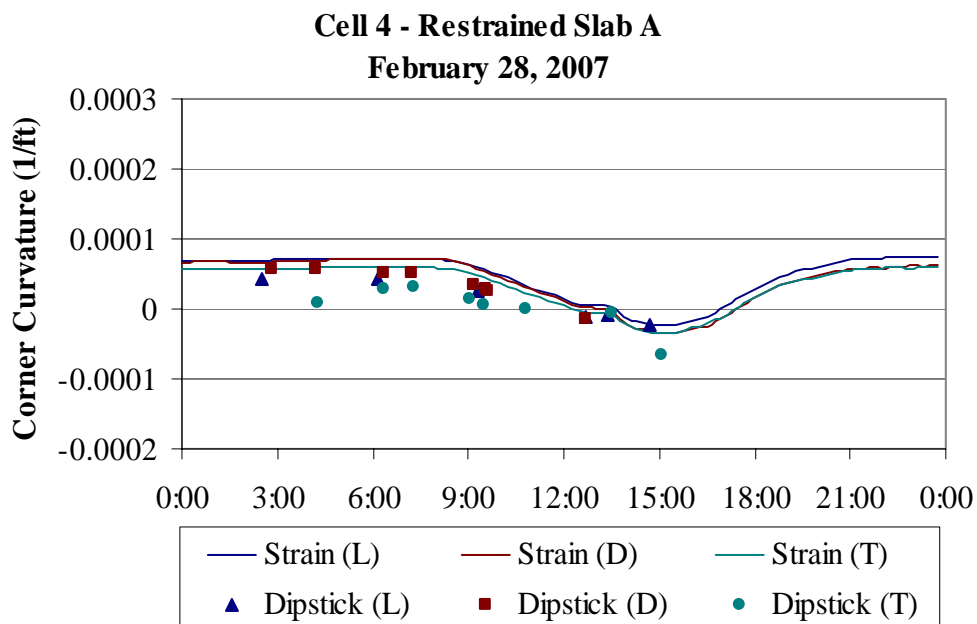


Figure F.10. Curvature estimated from surface profiles and vibrating wire gages for restrained Slab A during the winter of 2007.

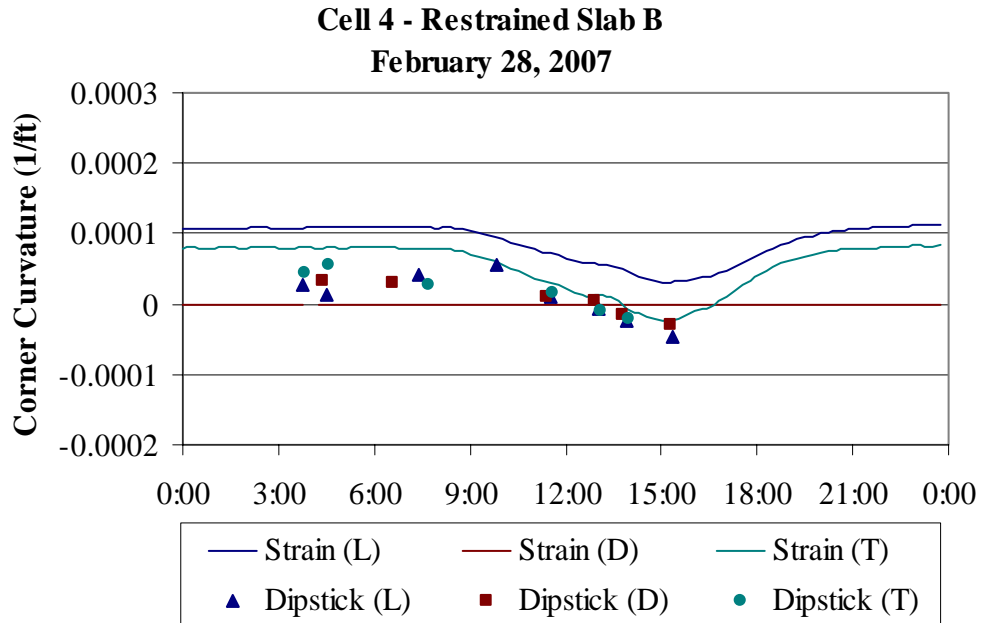


Figure F.11. Curvature estimated from surface profiles and vibrating wire gages for restrained Slab B during the winter of 2007.

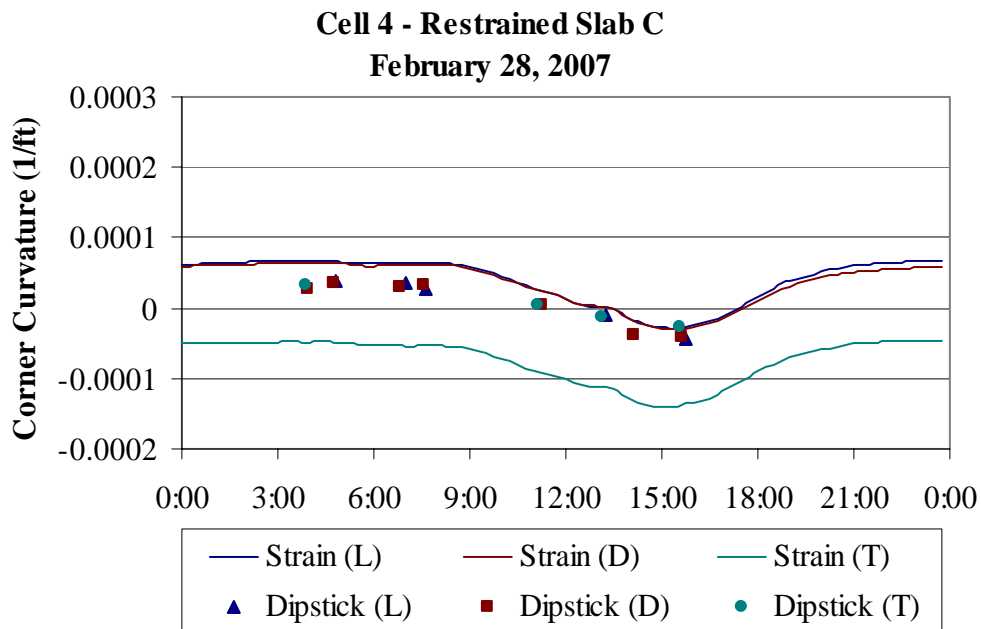


Figure F.12. Curvature estimated from surface profiles and vibrating wire gages for restrained Slab C during the winter of 2007.

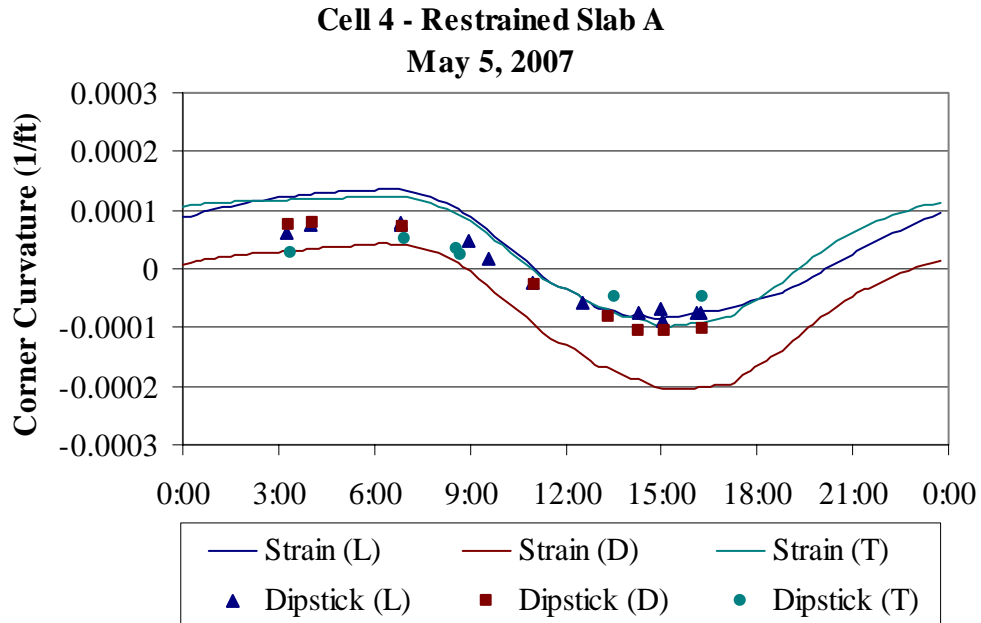


Figure F.13. Curvature estimated from surface profiles and vibrating wire gages for restrained Slab A during the spring of 2007.

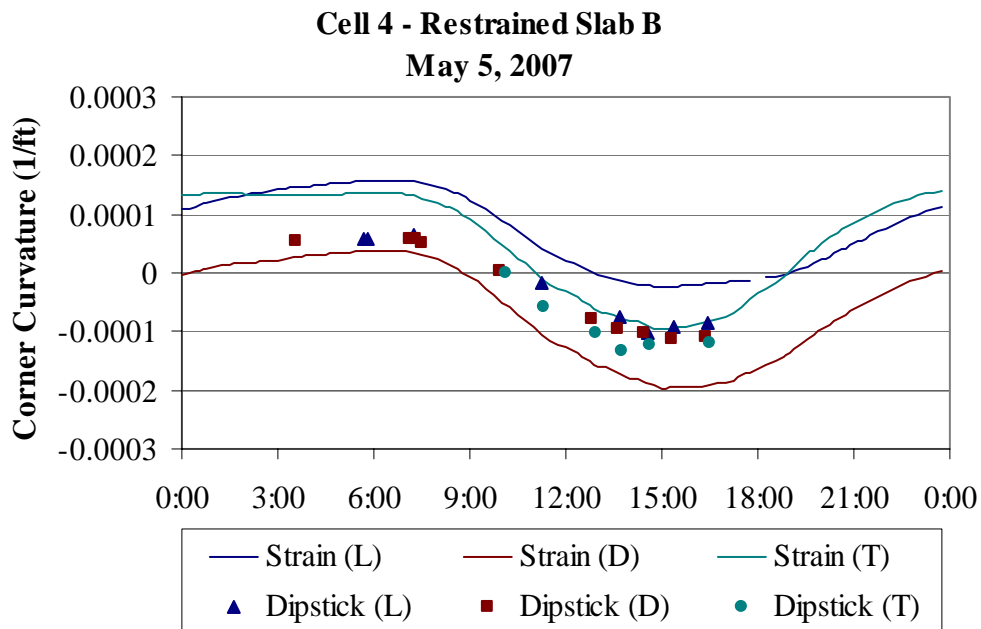


Figure F.14. Curvature estimated from surface profiles and vibrating wire gages for restrained Slab B during the spring of 2007.

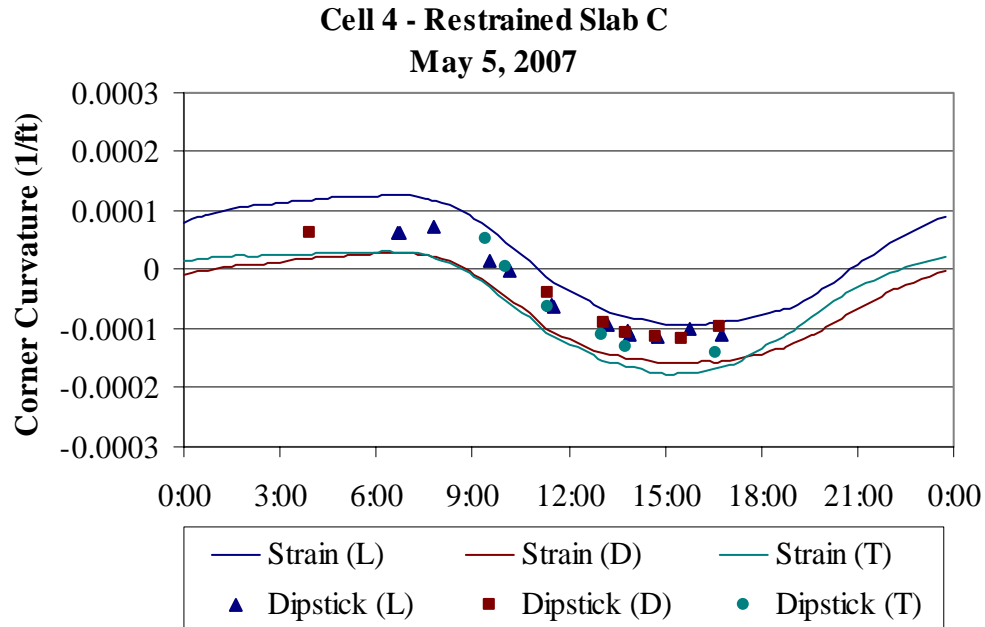


Figure F.15. Curvature estimated from surface profiles and vibrating wire gages for restrained Slab C during the spring of 2007.

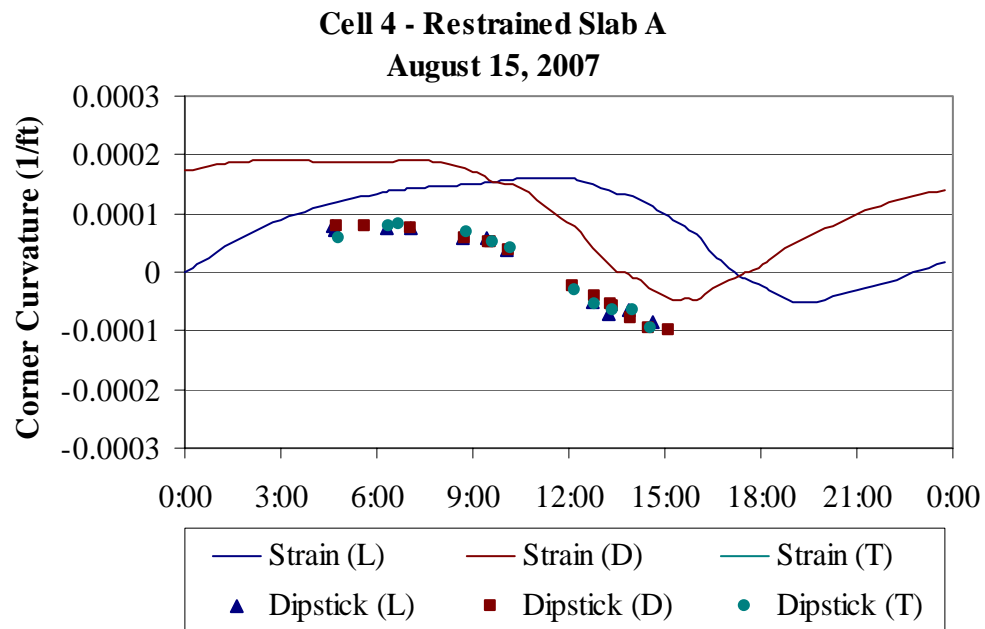


Figure F.16. Curvature estimated from surface profiles and vibrating wire gages for restrained Slab A during the summer of 2007.

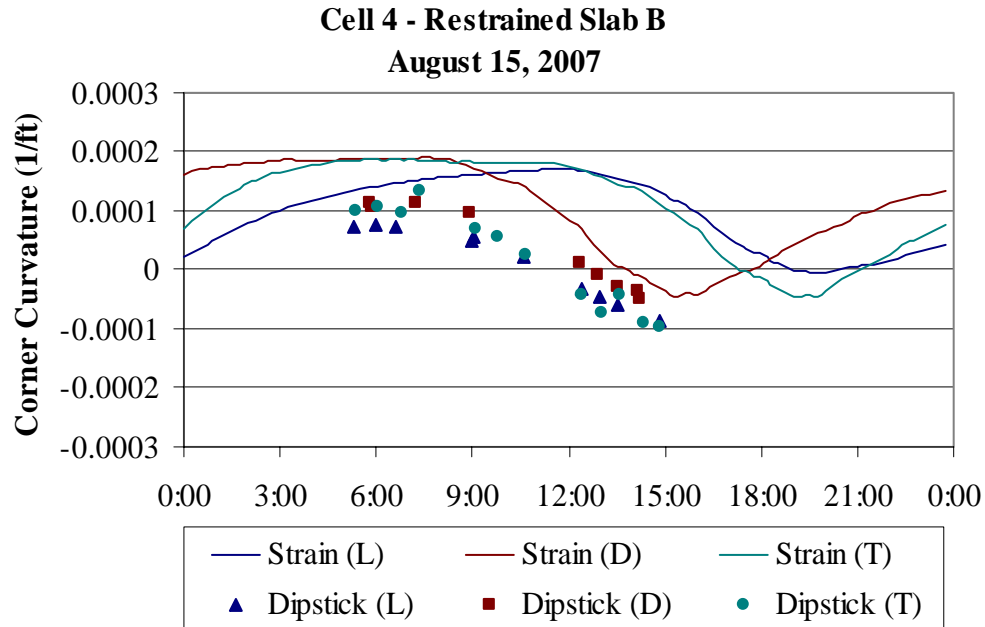


Figure F.17. Curvature estimated from surface profiles and vibrating wire gages for restrained Slab B during the summer of 2007.

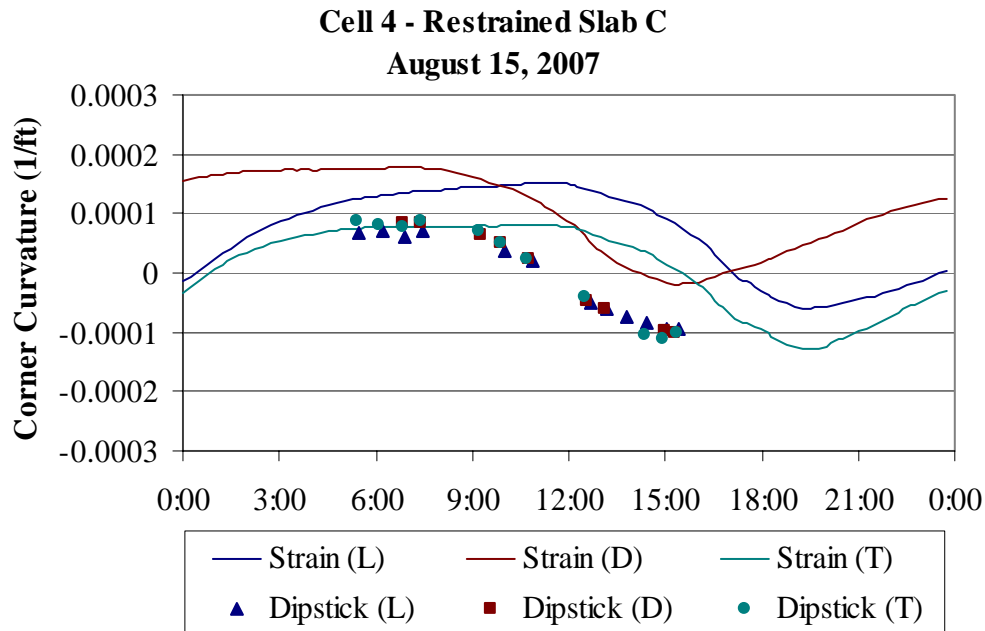


Figure F.18. Curvature estimated from surface profiles and vibrating wire gages for restrained Slab C during the summer of 2007.

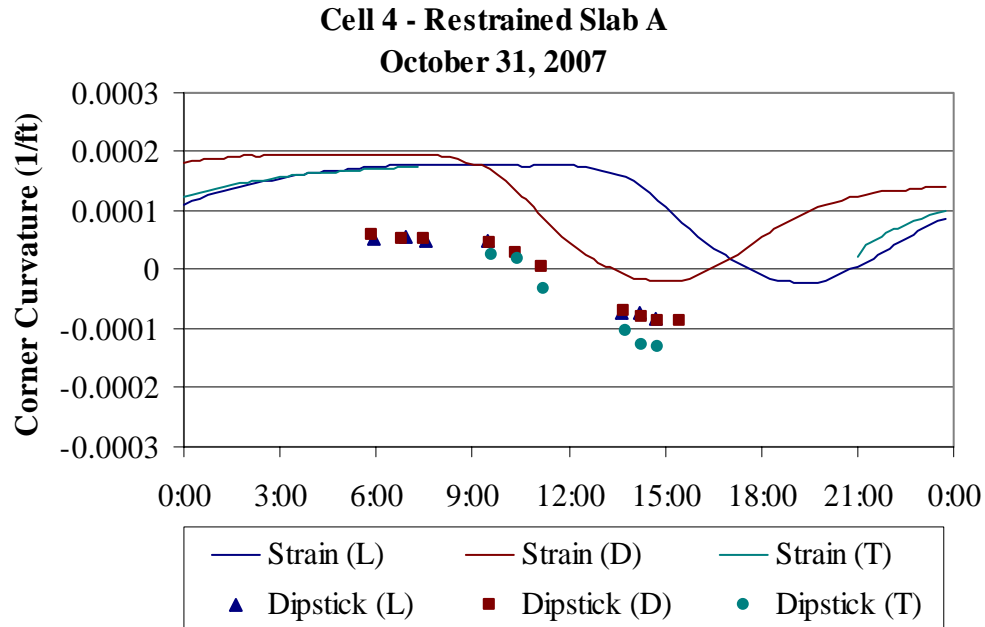


Figure F.19. Curvature estimated from surface profiles and vibrating wire gages for restrained Slab A during the fall of 2007.

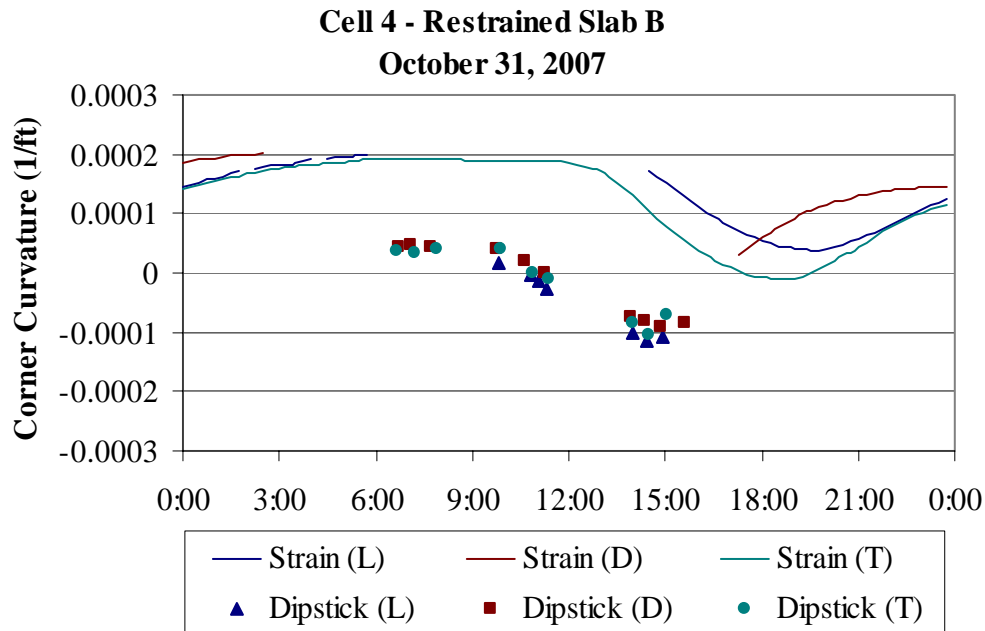


Figure F.20. Curvature estimated from surface profiles and vibrating wire gages for restrained Slab B during the fall of 2007.

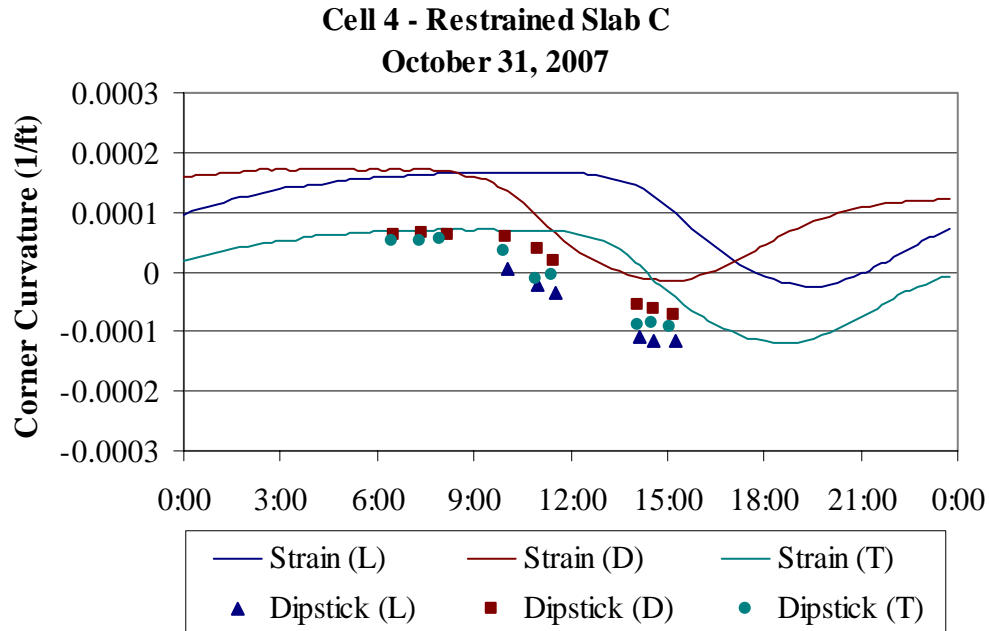


Figure F.21. Curvature estimated from surface profiles and vibrating wire gages for restrained Slab C during the fall of 2007.

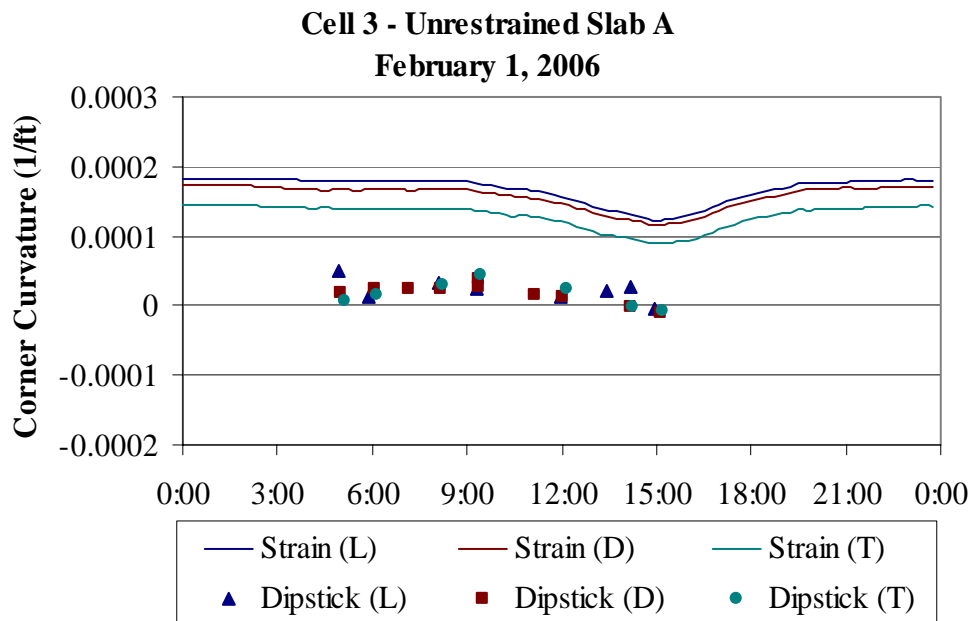


Figure F.22. Curvature estimated from surface profiles and vibrating wire gages for unrestrained Slab A during the winter of 2006.

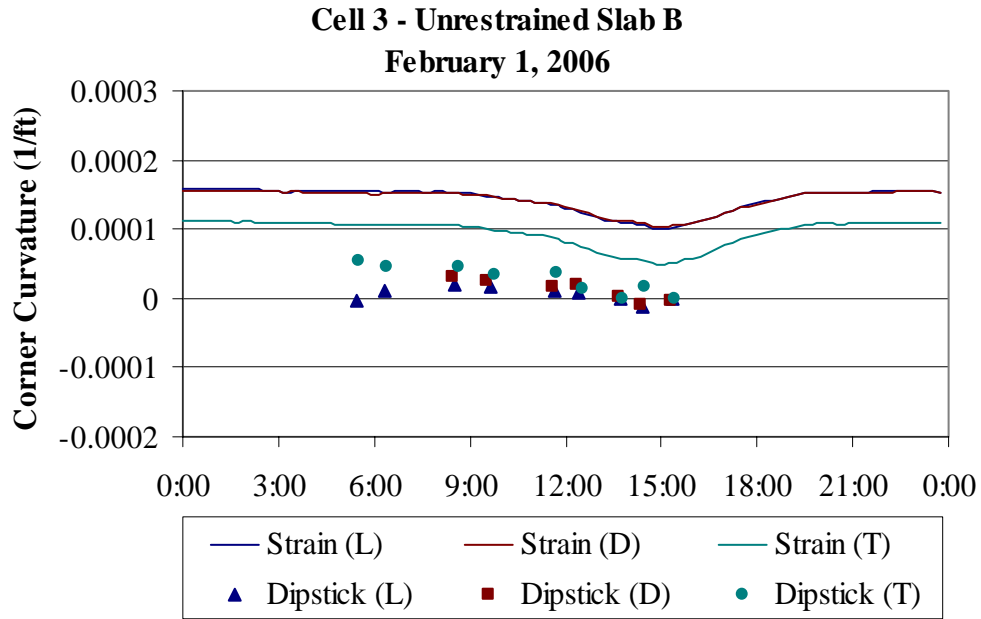


Figure F.23. Curvature estimated from surface profiles and vibrating wire gages for unrestrained Slab B during the winter of 2006.

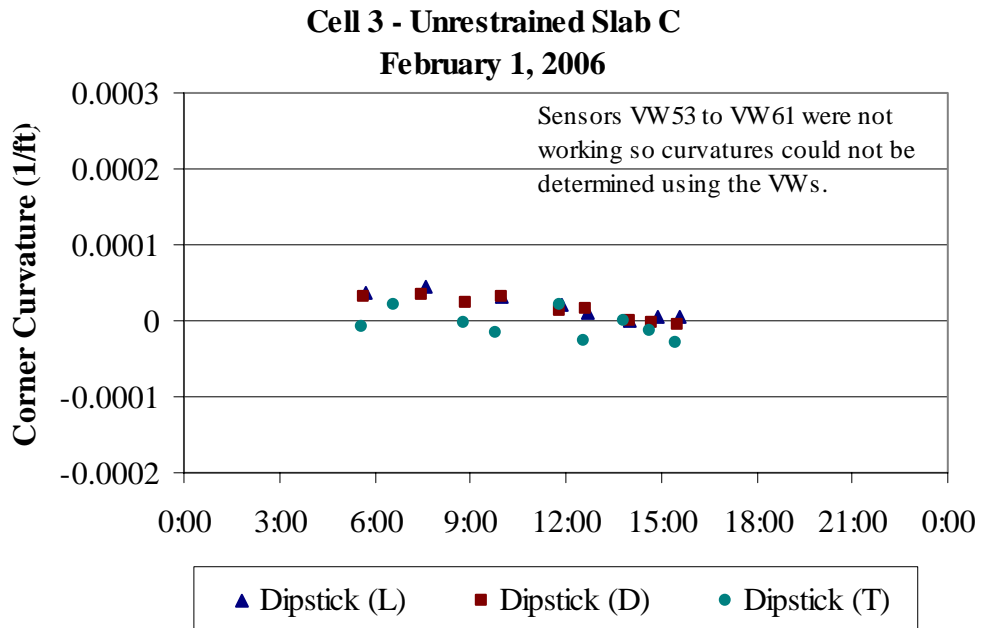


Figure F.24. Curvature estimated from surface profiles and vibrating wire gages for unrestrained Slab C during the winter of 2006 (VW Data is not available).

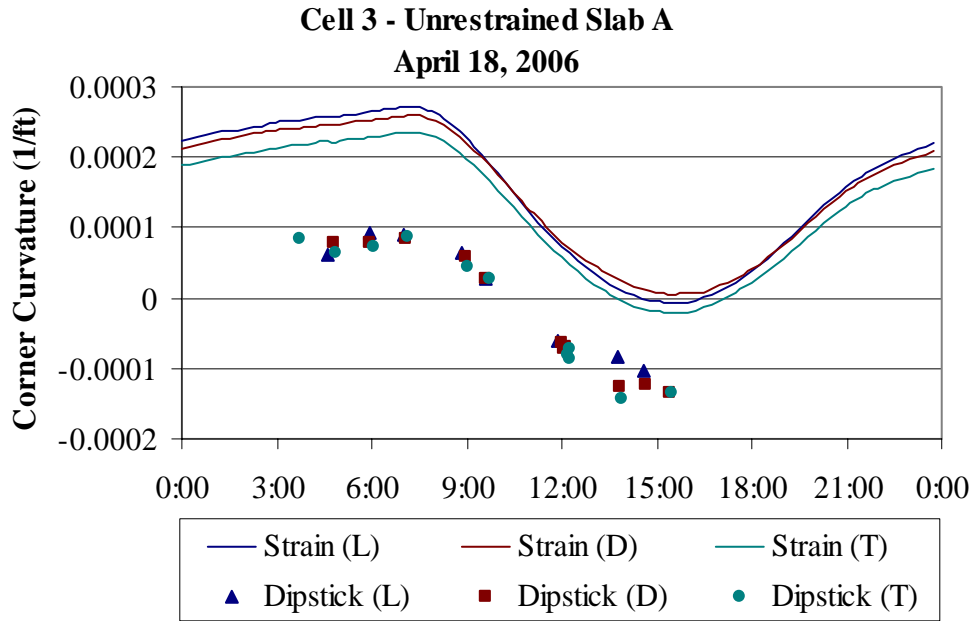


Figure F.25. Curvature estimated from surface profiles and vibrating wire gages for unrestrained Slab A during the spring of 2006.

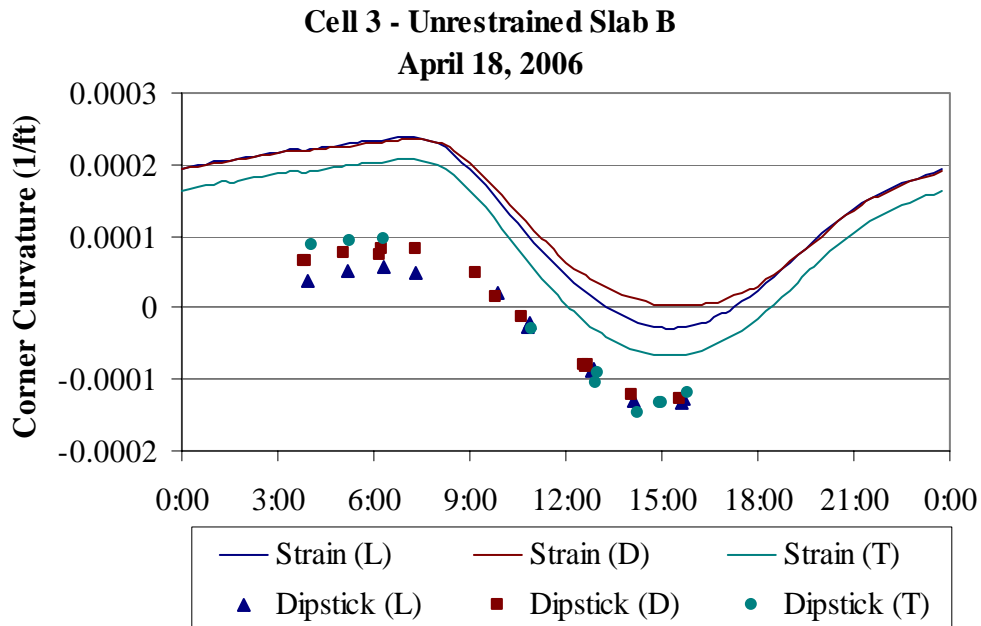


Figure F.26. Curvature estimated from surface profiles and vibrating wire gages for unrestrained Slab B during the spring of 2006.

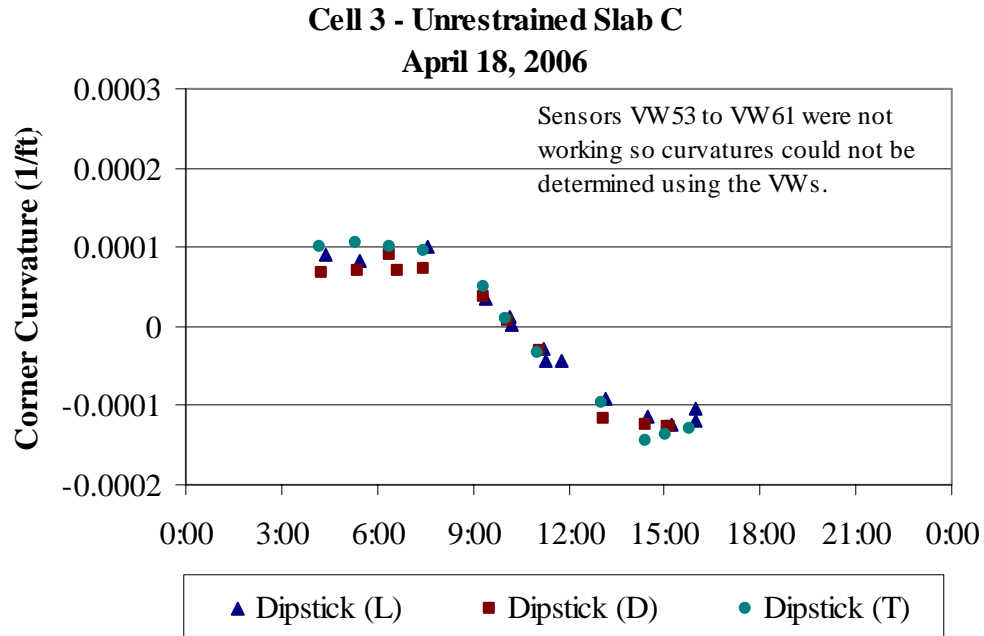


Figure F.27. Curvature estimated from surface profiles and vibrating wire gages for unrestrained Slab C during the spring of 2006 (VW Data is not available).

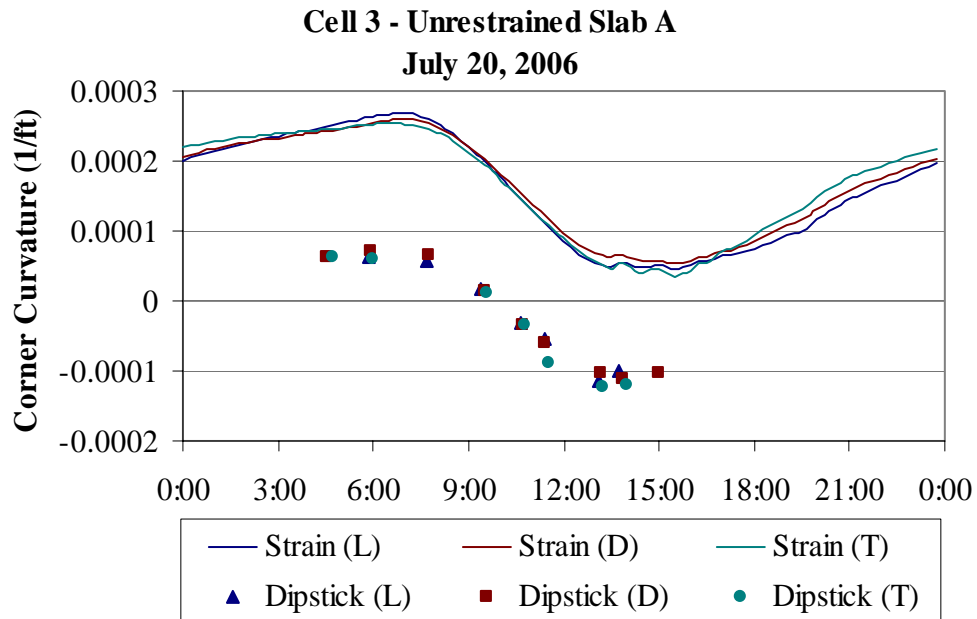


Figure F.28. Curvature estimated from surface profiles and vibrating wire gages for unrestrained Slab A during the summer of 2006.

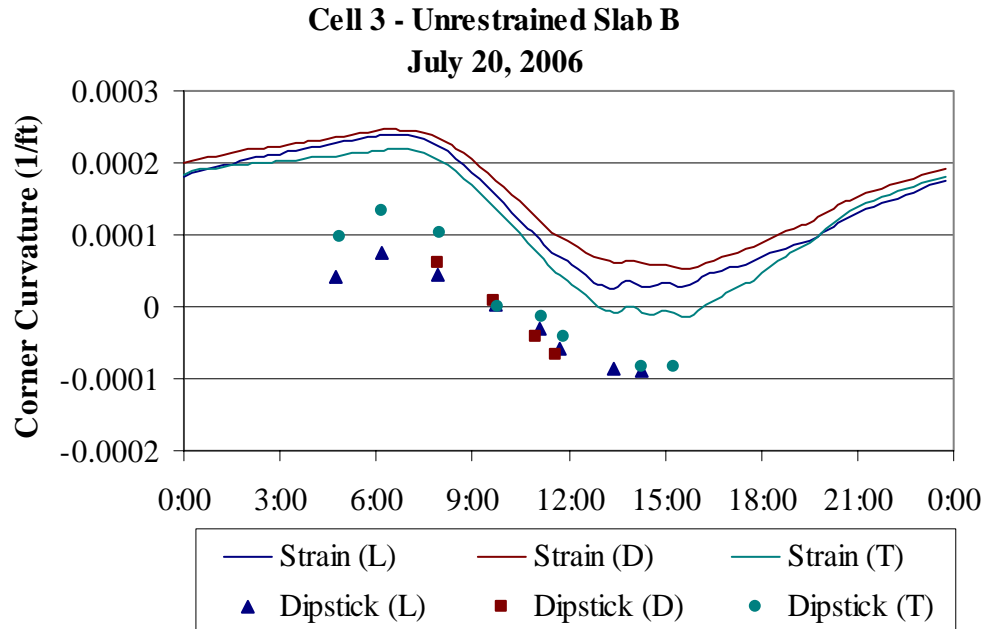


Figure F.29. Curvature estimated from surface profiles and vibrating wire gages for unrestrained Slab B during the summer of 2006.

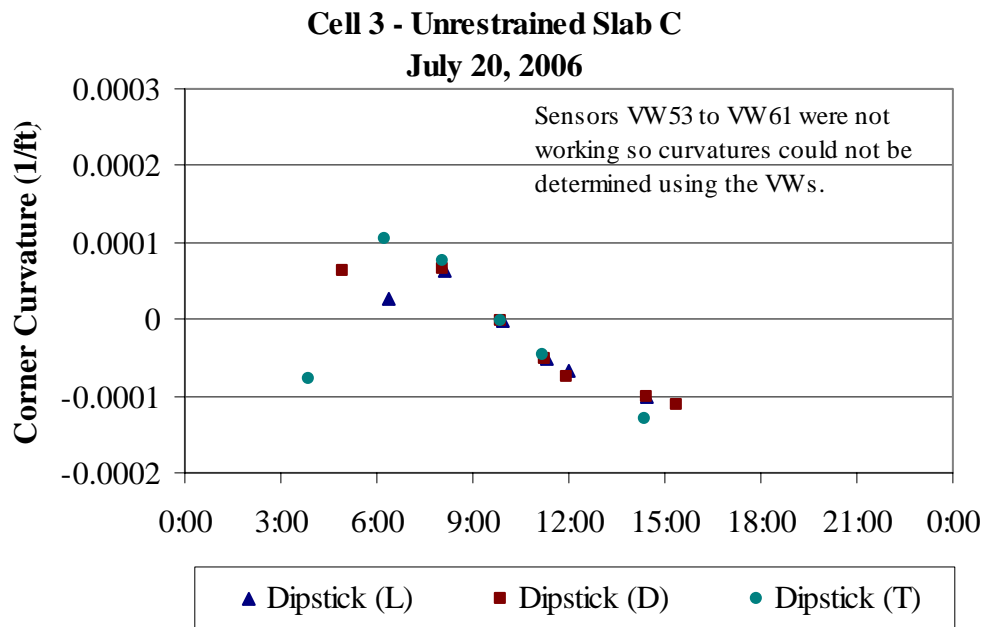


Figure F.30. Curvature estimated from surface profiles and vibrating wire gages for unrestrained Slab C during the summer of 2006 (VW Data is not available).

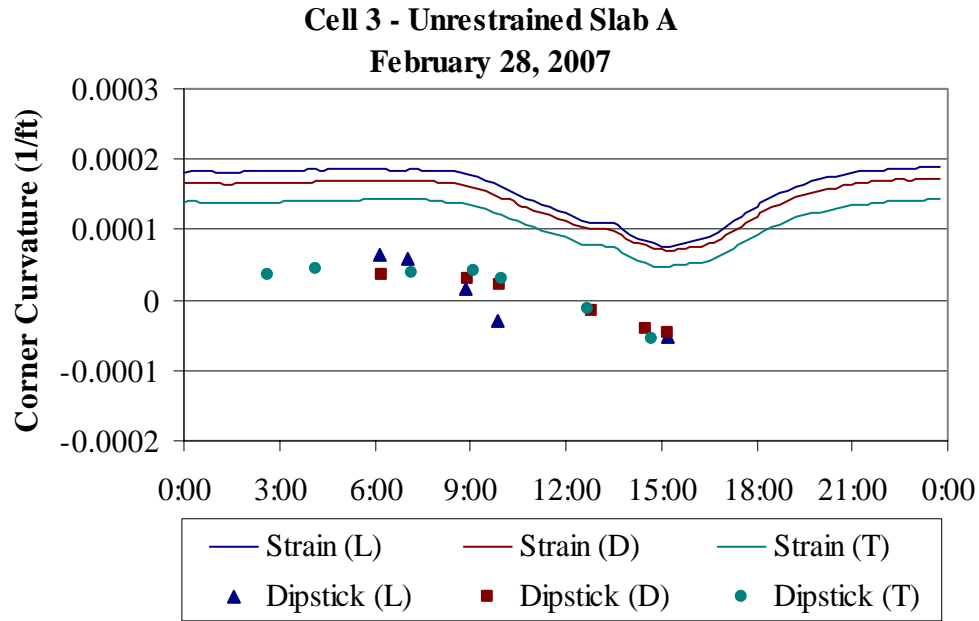


Figure F.31. Curvature estimated from surface profiles and vibrating wire gages for unrestrained Slab A during the winter of 2007.

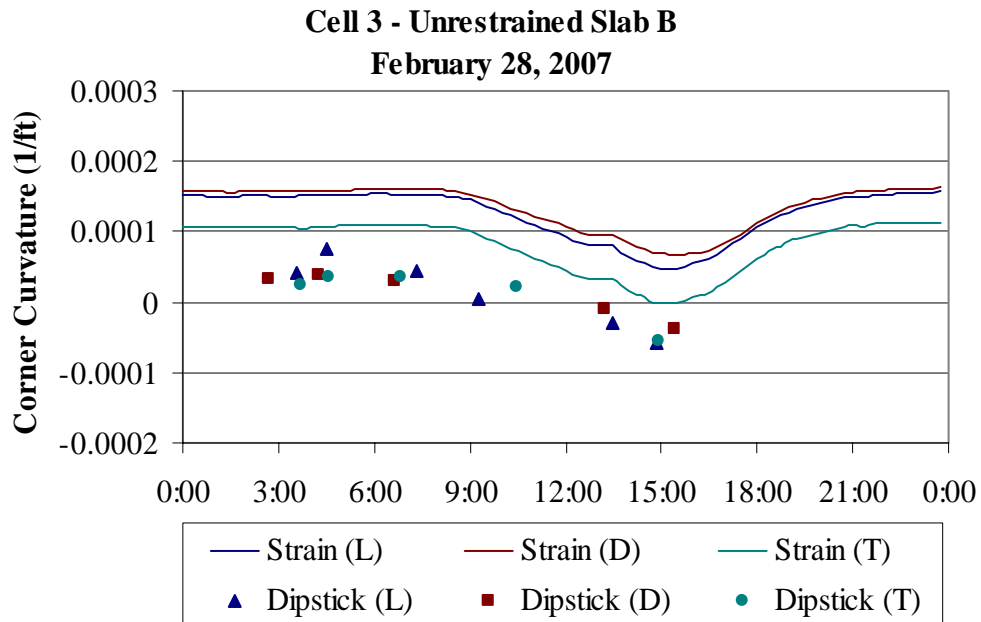


Figure F.32. Curvature estimated from surface profiles and vibrating wire gages for unrestrained Slab B during the winter of 2007.

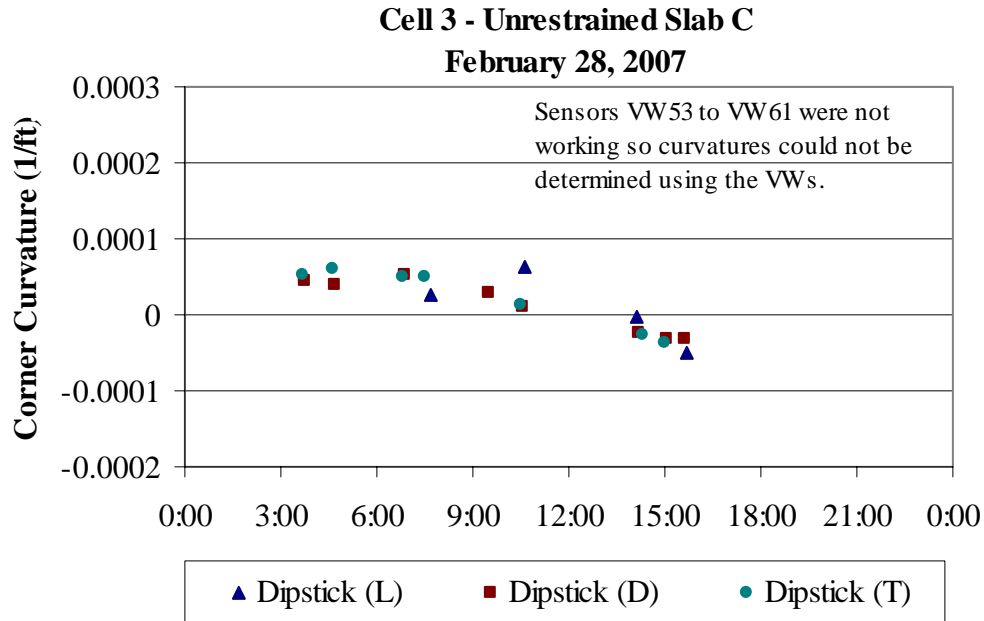


Figure F.33. Curvature estimated from surface profiles and vibrating wire gages for unrestrained Slab C during the winter of 2007 (VW Data is not available).

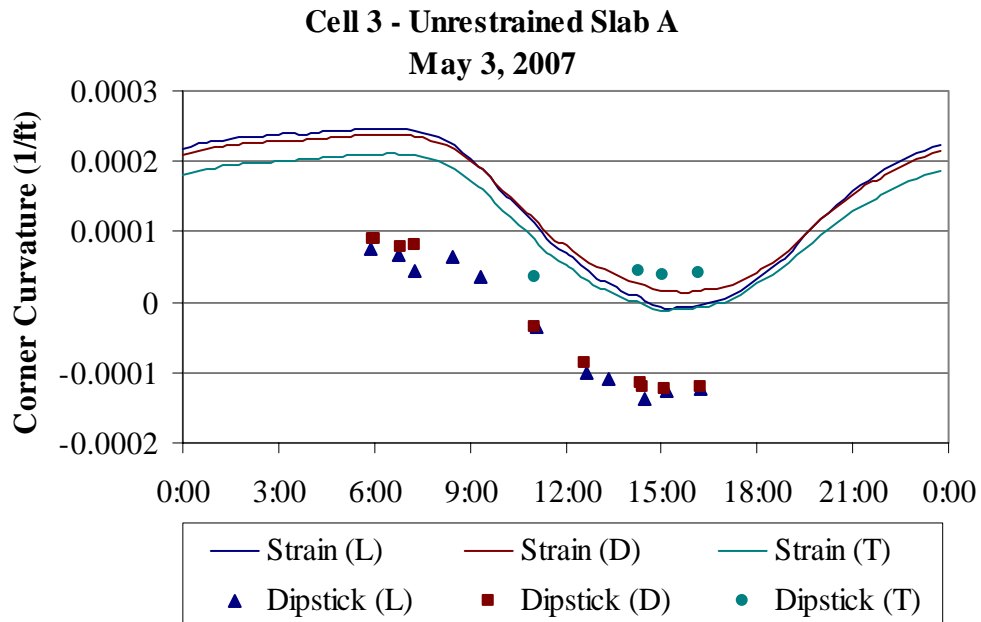


Figure F.34. Curvature estimated from surface profiles and vibrating wire gages for unrestrained Slab A during the spring of 2007.

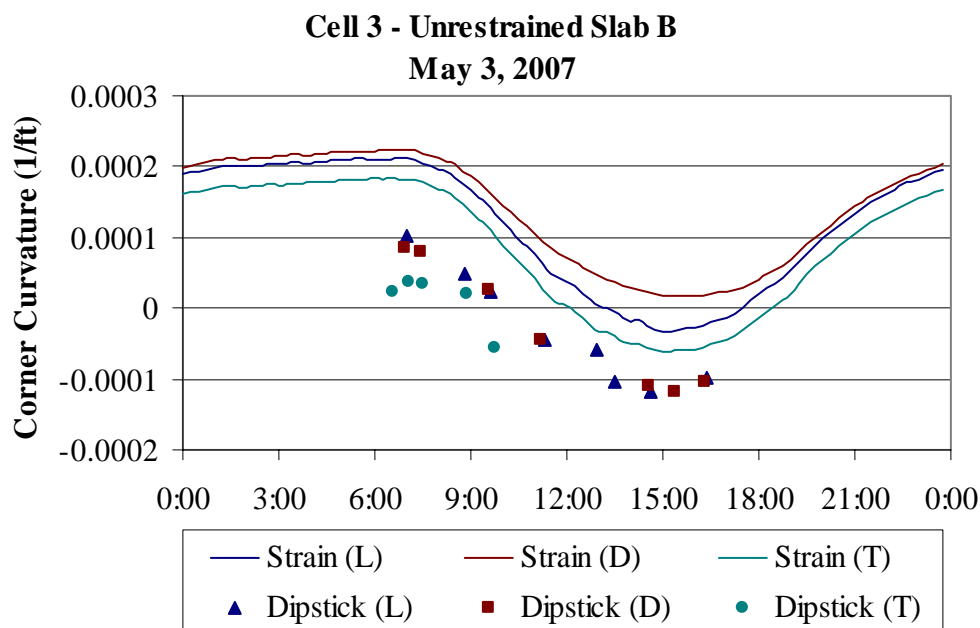


Figure F.35. Curvature estimated from surface profiles and vibrating wire gages for unrestrained Slab B during the spring of 2007.

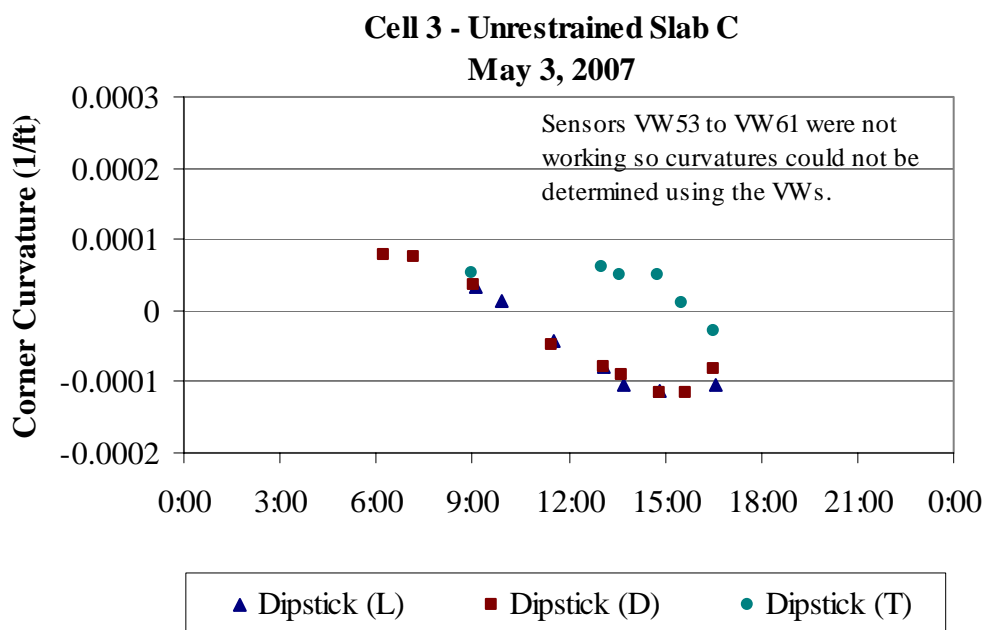


Figure F.36. Curvature estimated from surface profiles and vibrating wire gages for unrestrained Slab C during the spring of 2007 (VW Data is not available).

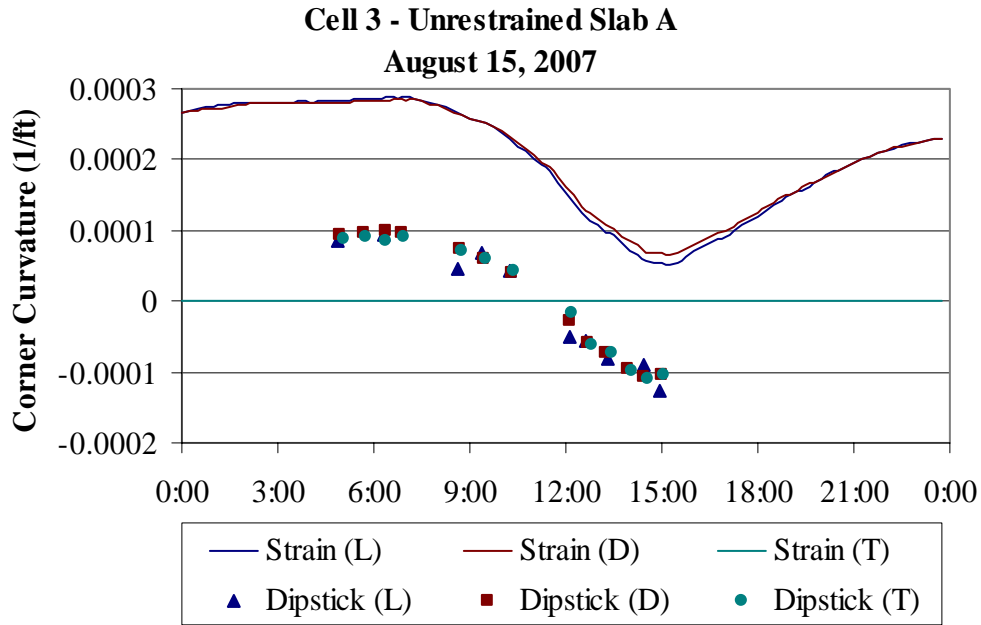


Figure F.37. Curvature estimated from surface profiles and vibrating wire gages for unrestrained Slab A during the summer of 2007.

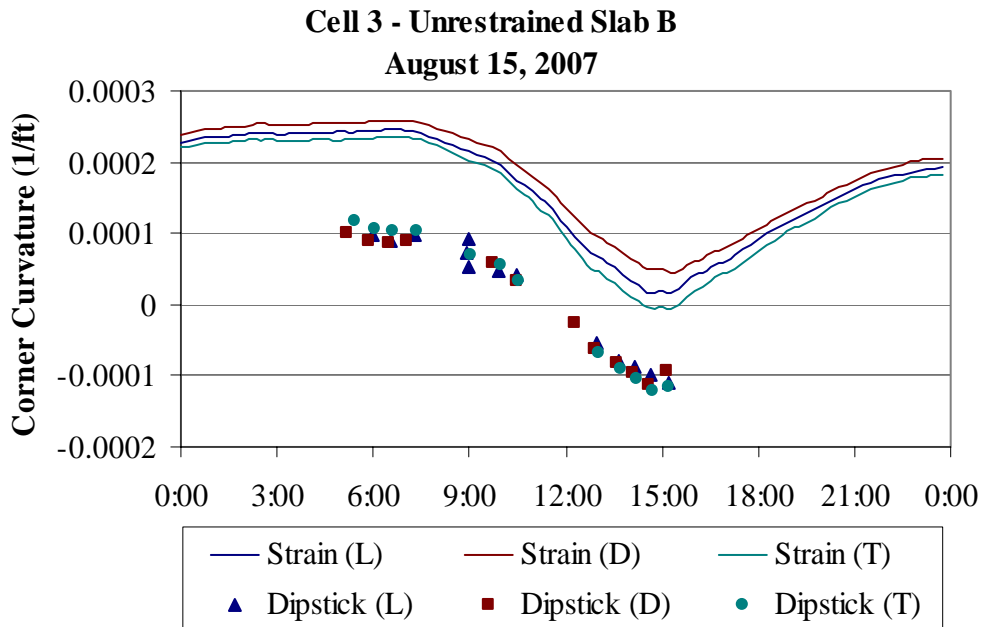


Figure F.38. Curvature estimated from surface profiles and vibrating wire gages for unrestrained Slab B during the summer of 2007.

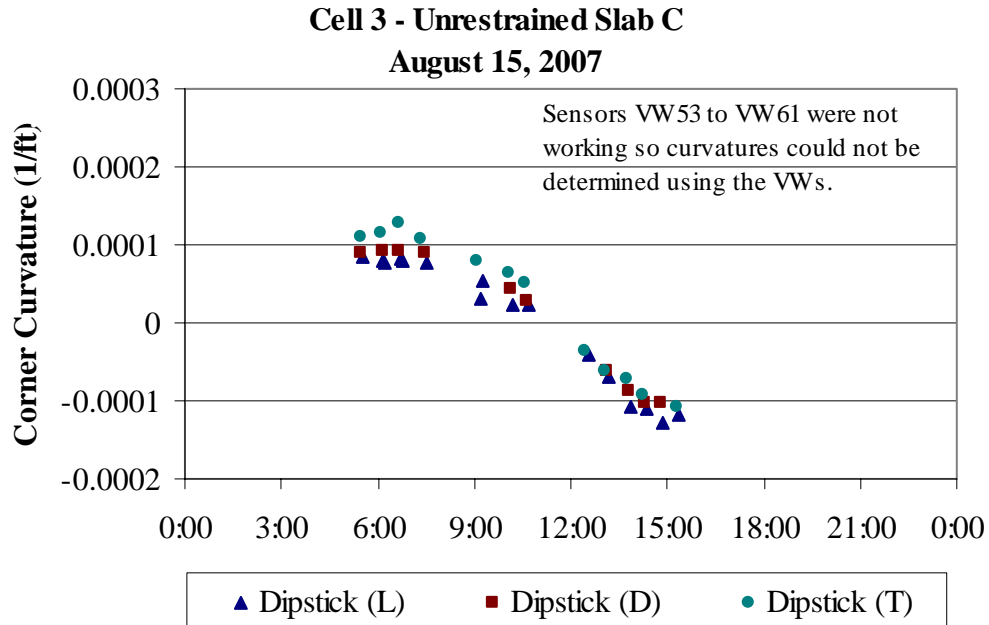


Figure F.39. Curvature estimated from surface profiles and vibrating wire gages for unrestrained Slab C during the summer of 2007 (VW Data is not available).

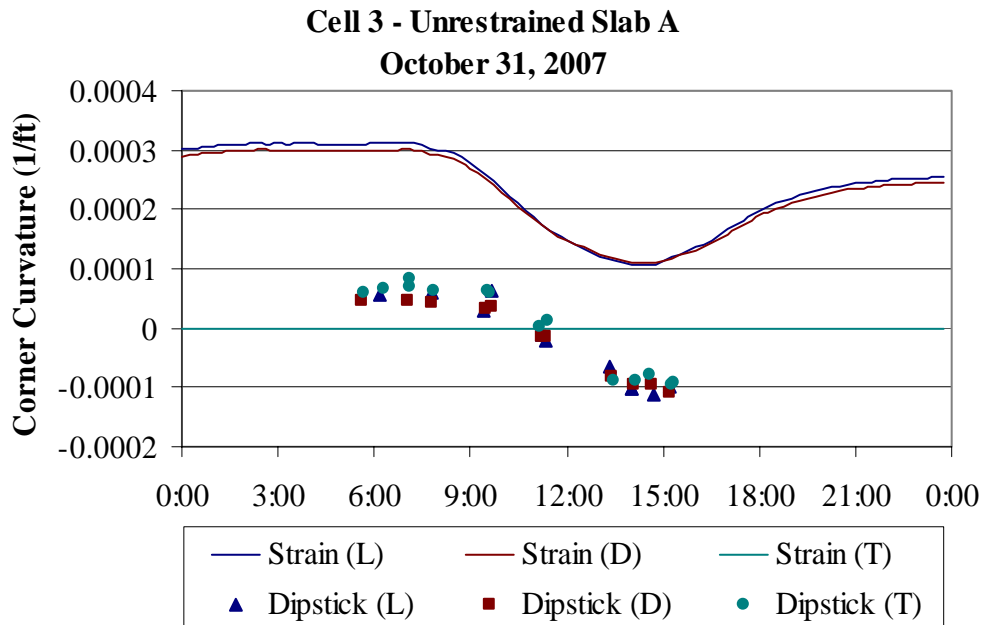


Figure F.40. Curvature estimated from surface profiles and vibrating wire gages for unrestrained Slab A during the fall of 2007.

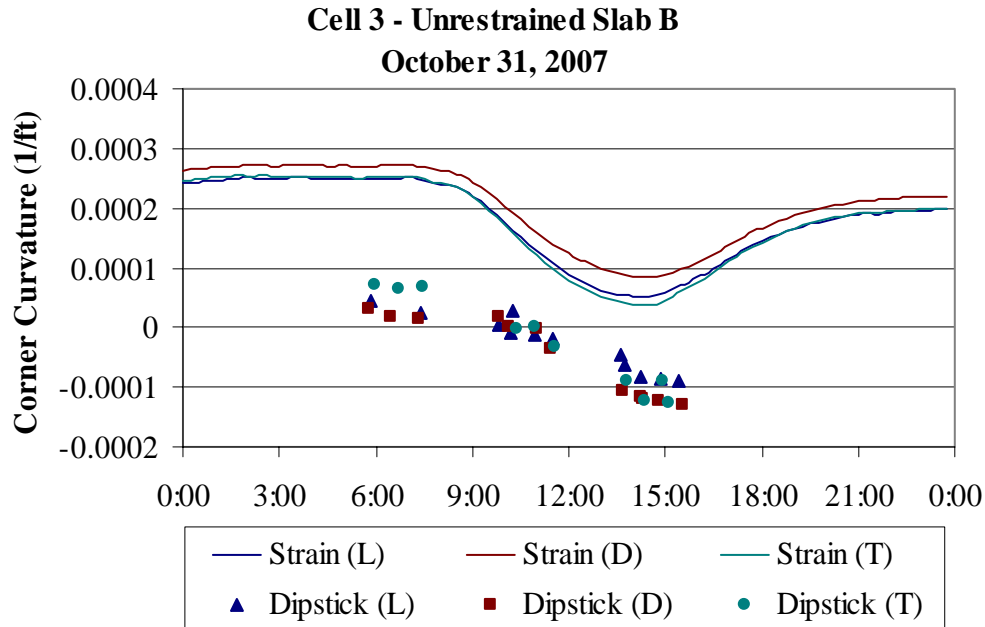


Figure F.41. Curvature estimated from surface profiles and vibrating wire gages for unrestrained Slab B during the fall of 2007.

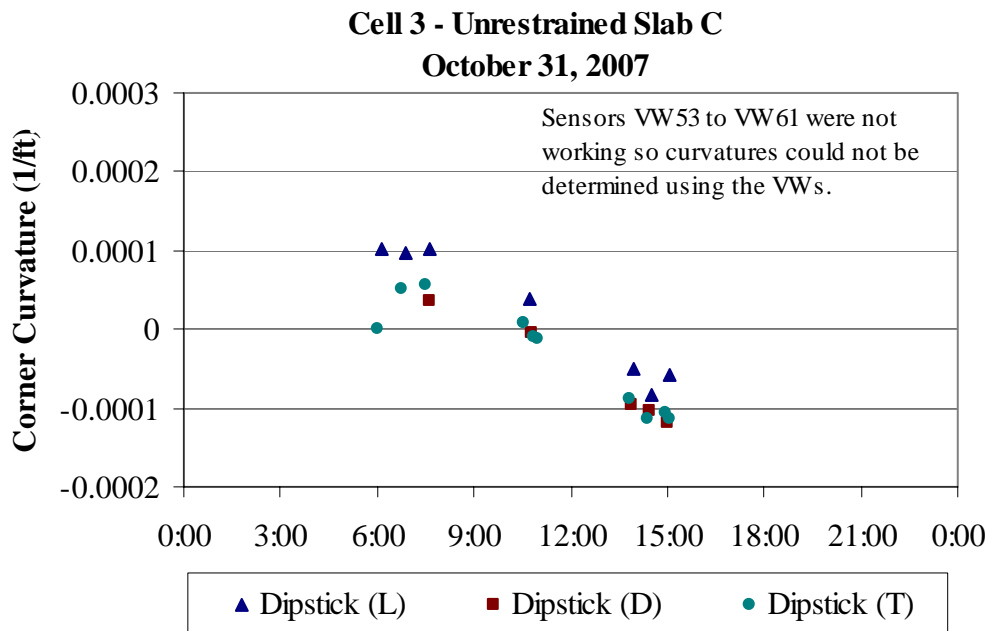


Figure F.42. Curvature estimated from surface profiles and vibrating wire gages for unrestrained Slab C during the fall of 2007 (VW Data is not available).

Appendix G: Pavement Response to Applied Loads

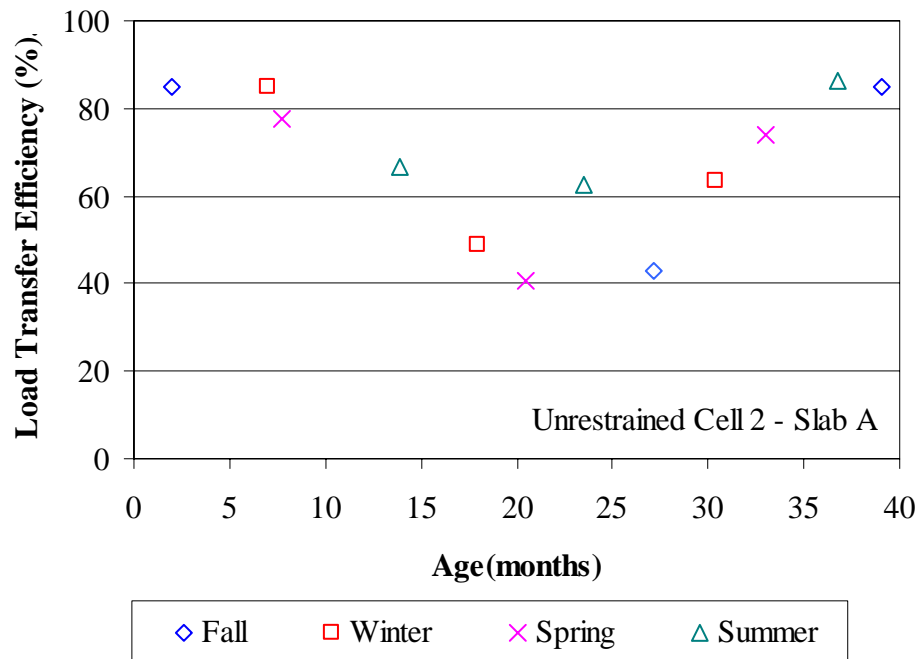


Figure G.1. Relationship between load transfer efficiency and age of the pavement for the unrestrained Cell 2.

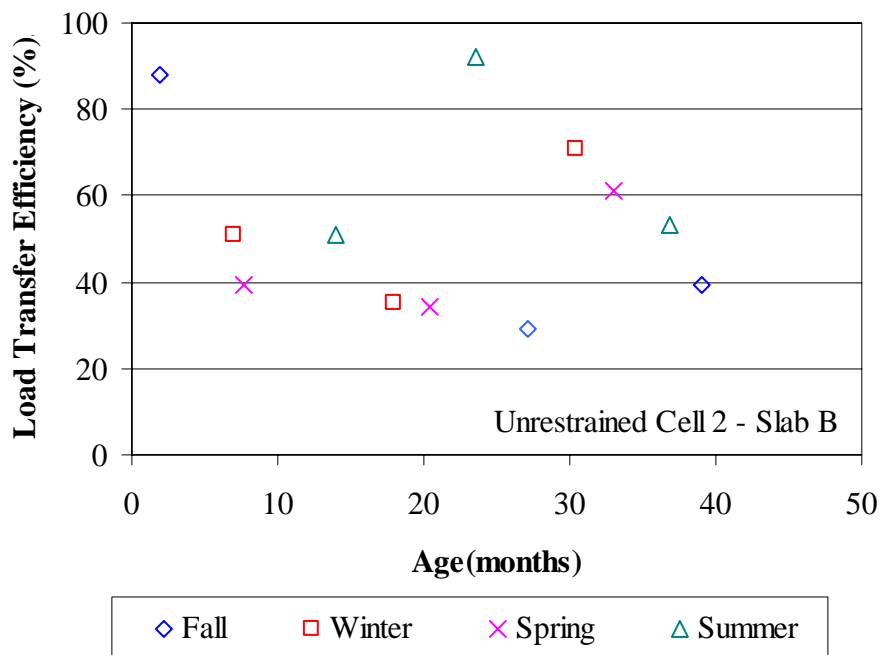


Figure G.2. Relationship between load transfer efficiency and age of the pavement for the unrestrained Cell 2.

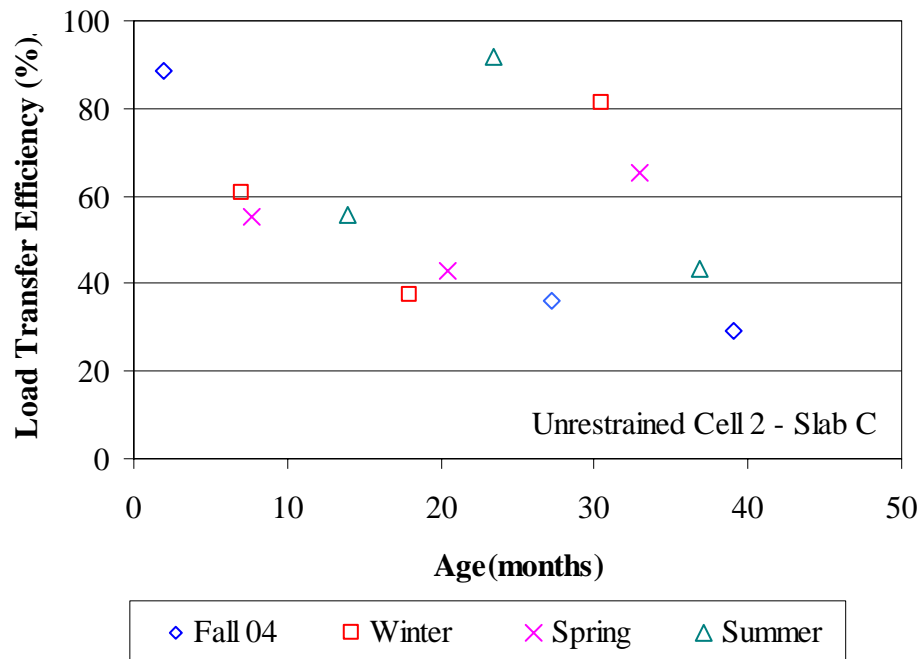


Figure G.3. Relationship between load transfer efficiency and age of the pavement for the unrestrained Cell 2

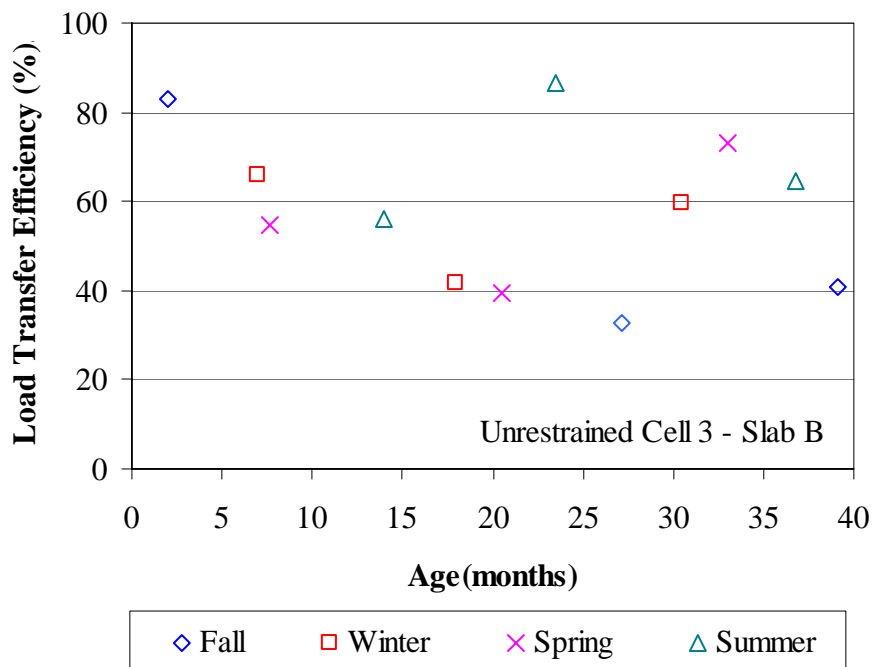


Figure G.4. Relationship between load transfer efficiency and age of the pavement for the unrestrained Cell 3

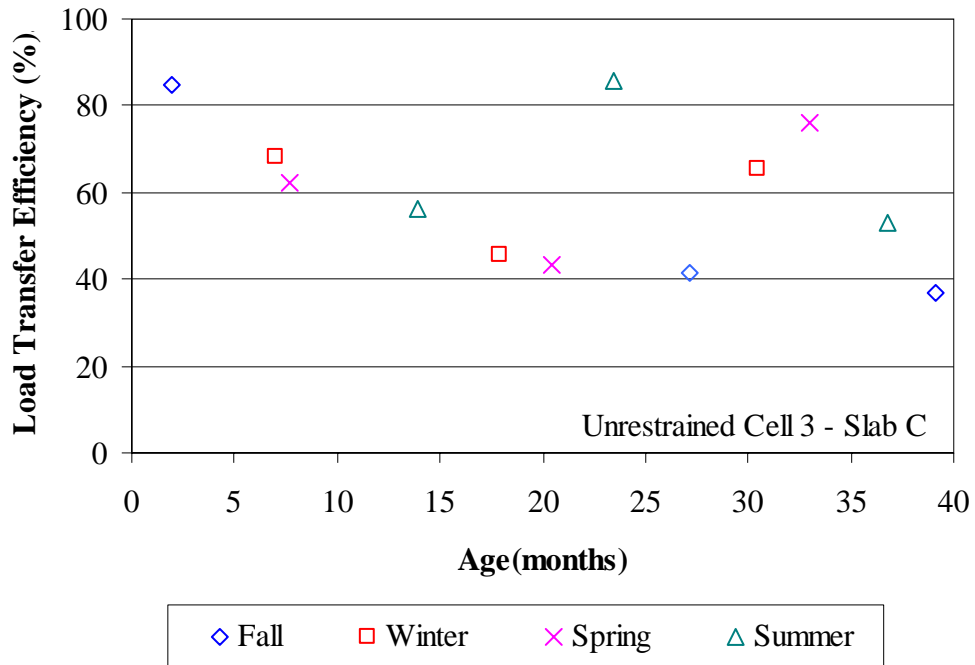


Figure G.5. Relationship between load transfer efficiency and age of the pavement for the unrestrained Cell 3.

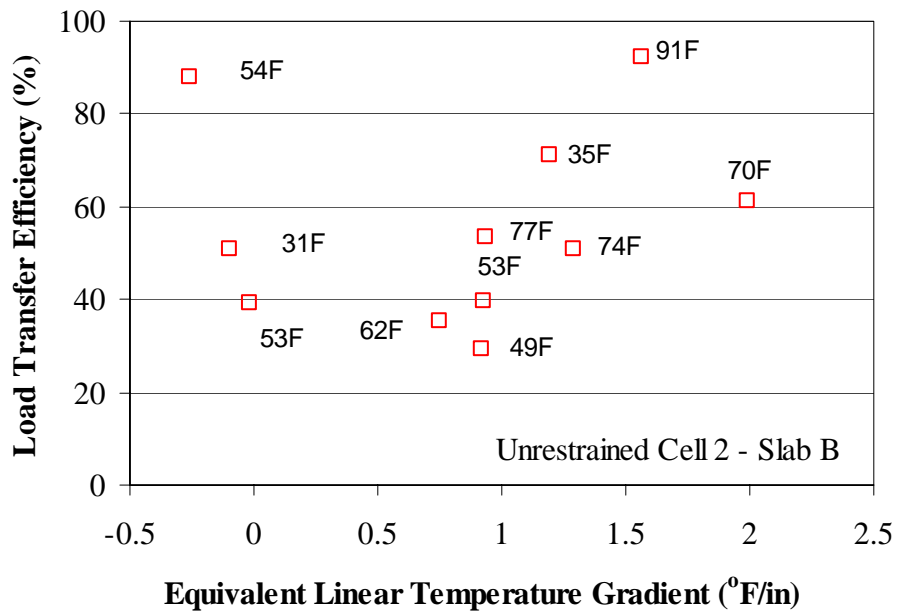


Figure G.6.. Relationship between load transfer efficiency and equivalent linear temperature gradient for the unrestrained Cell 2.

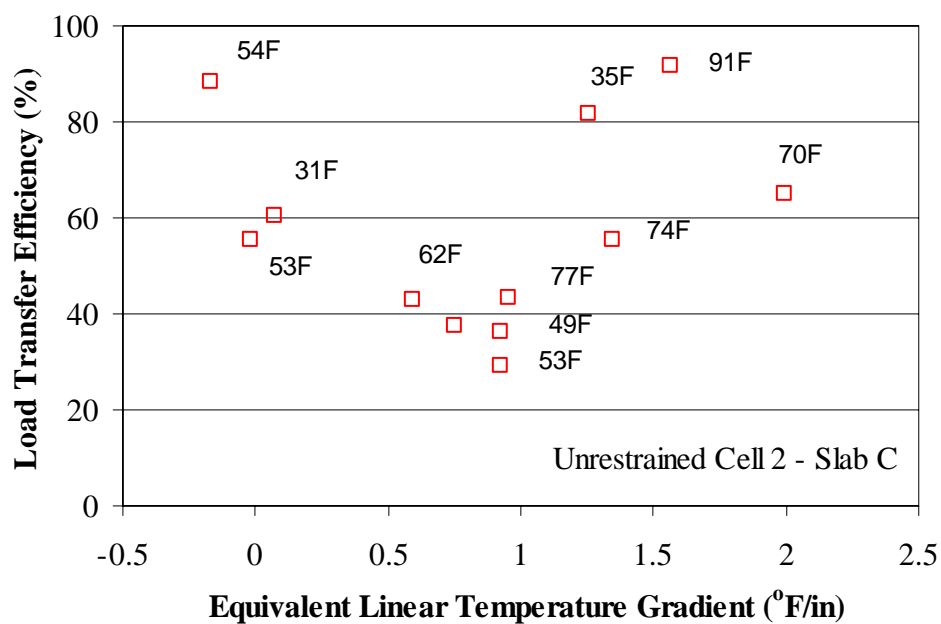


Figure G.7. Relationship between load transfer efficiency and equivalent linear temperature gradient for the unrestrained Cell 2.

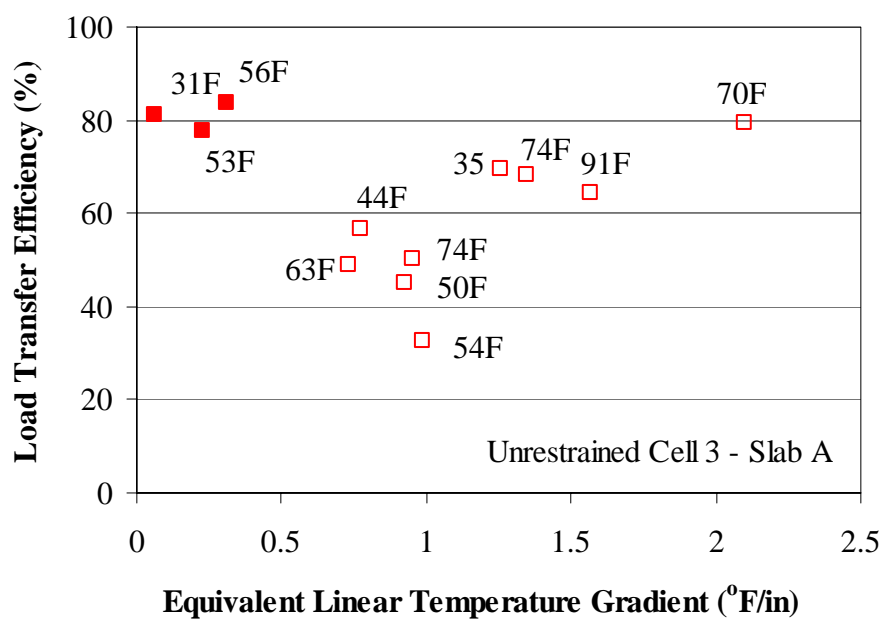


Figure G.8. Relationship between load transfer efficiency and equivalent linear temperature gradient for the unrestrained Cell 3.

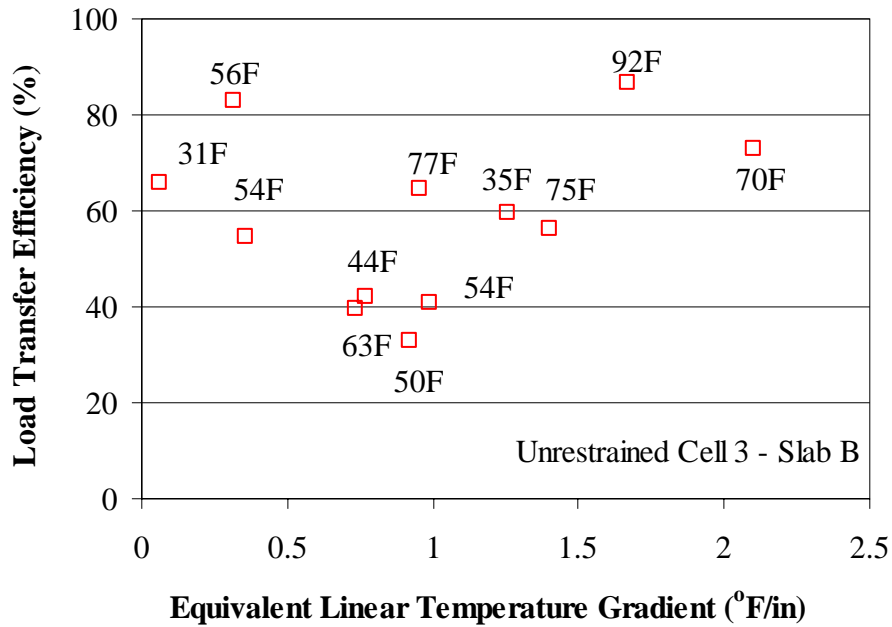


Figure G.9. Relationship between load transfer efficiency and equivalent linear temperature gradient for the unrestrained Cell 3.

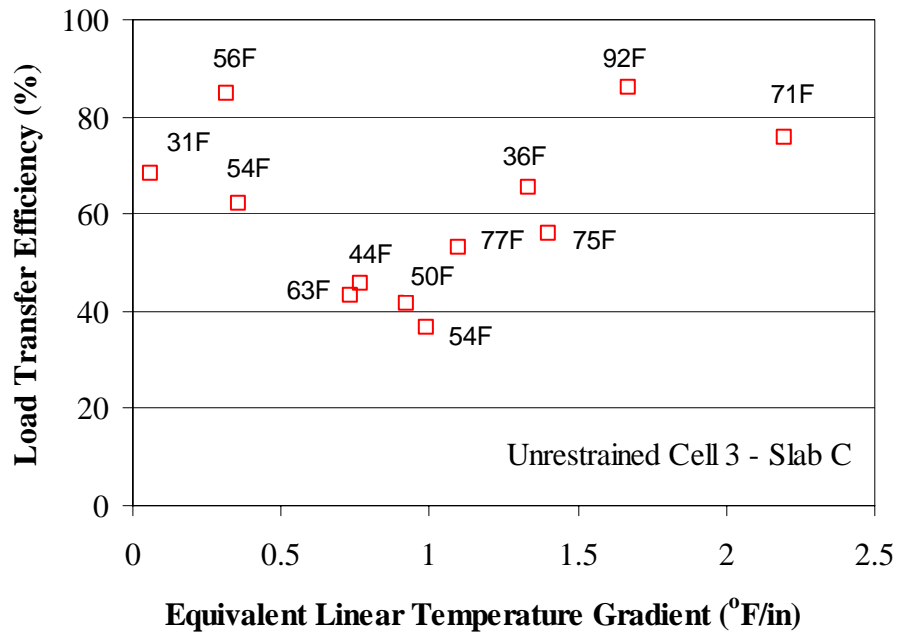


Figure G.10. Relationship between load transfer efficiency and equivalent linear temperature gradient for the unrestrained Cell 3.

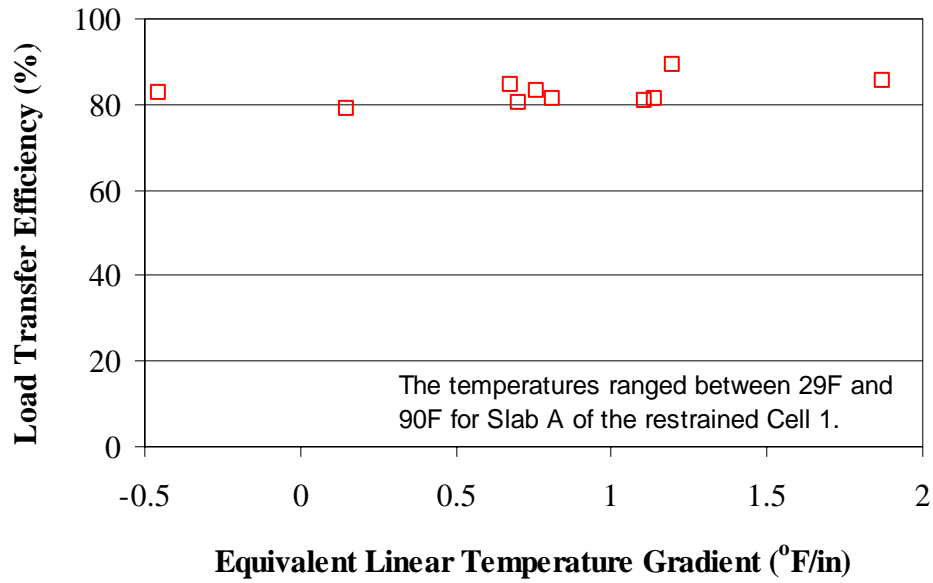


Figure G.11. Relationship between load transfer efficiency and equivalent linear temperature gradient for the restrained Cell 1.

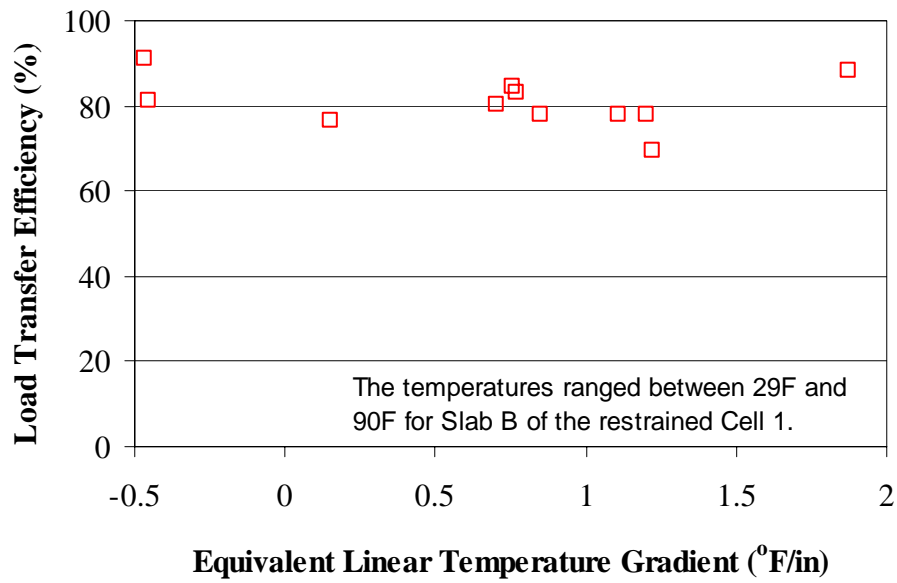


Figure G.12. Relationship between load transfer efficiency and equivalent linear temperature gradient for the restrained Cell 1.

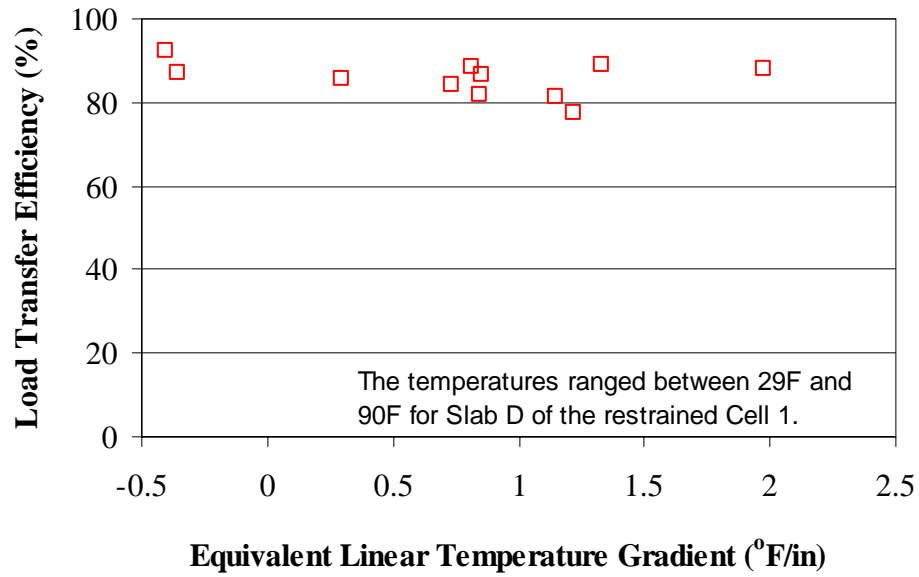


Figure G.13. Relationship between load transfer efficiency and equivalent linear temperature gradient for the restrained Cell 1.

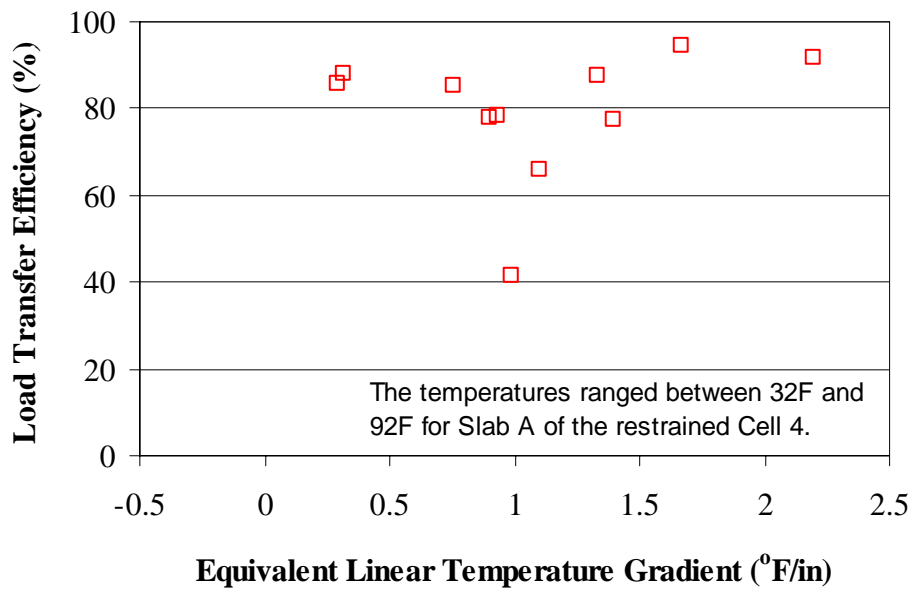


Figure G.14. Relationship between load transfer efficiency and equivalent linear temperature gradient for the restrained Cell 4.

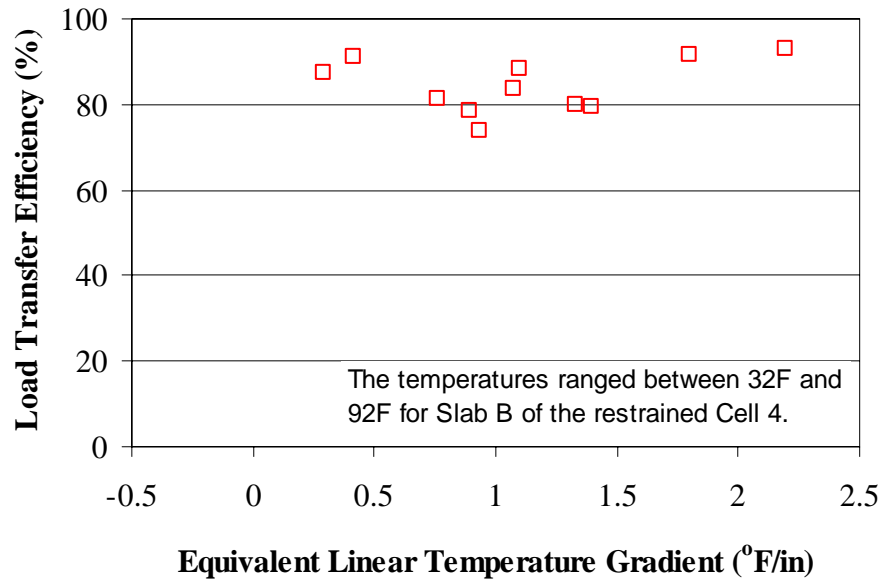


Figure G.15. Relationship between load transfer efficiency and equivalent linear temperature gradient for the restrained Cell 4.

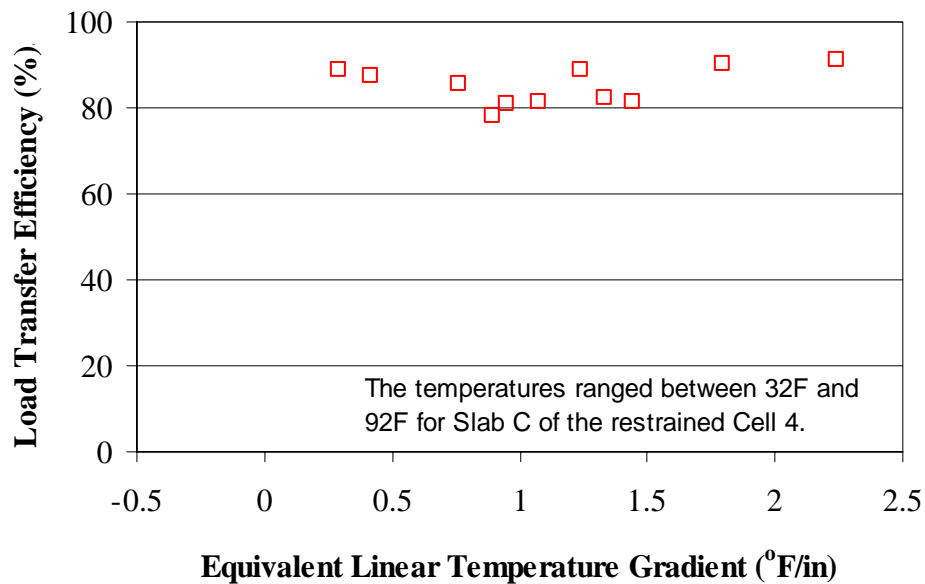


Figure G.16. Relationship between load transfer efficiency and equivalent linear temperature gradient for the restrained Cell 4.

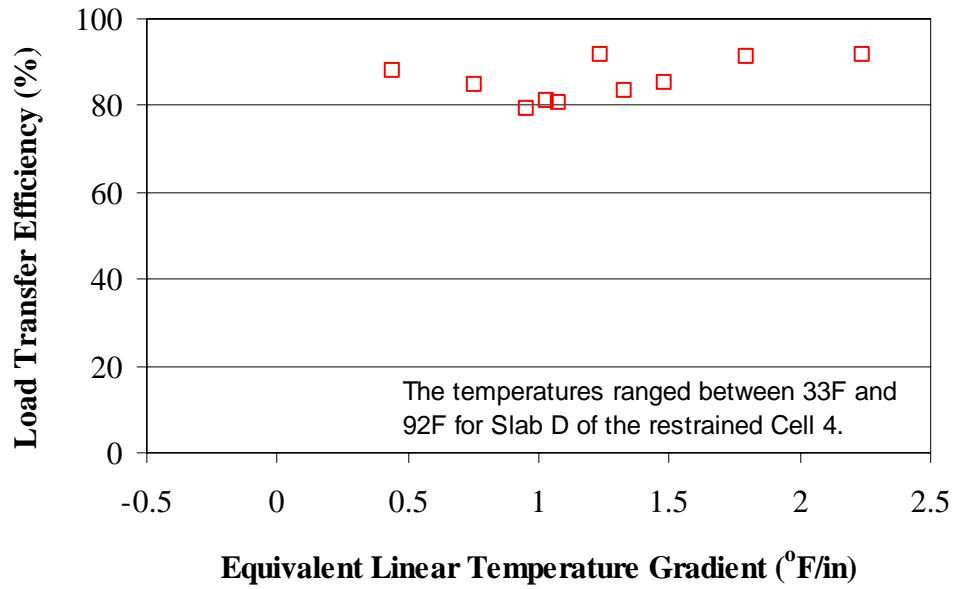


Figure G.17. Relationship between load transfer efficiency and equivalent linear temperature gradient for the restrained Cell 4.

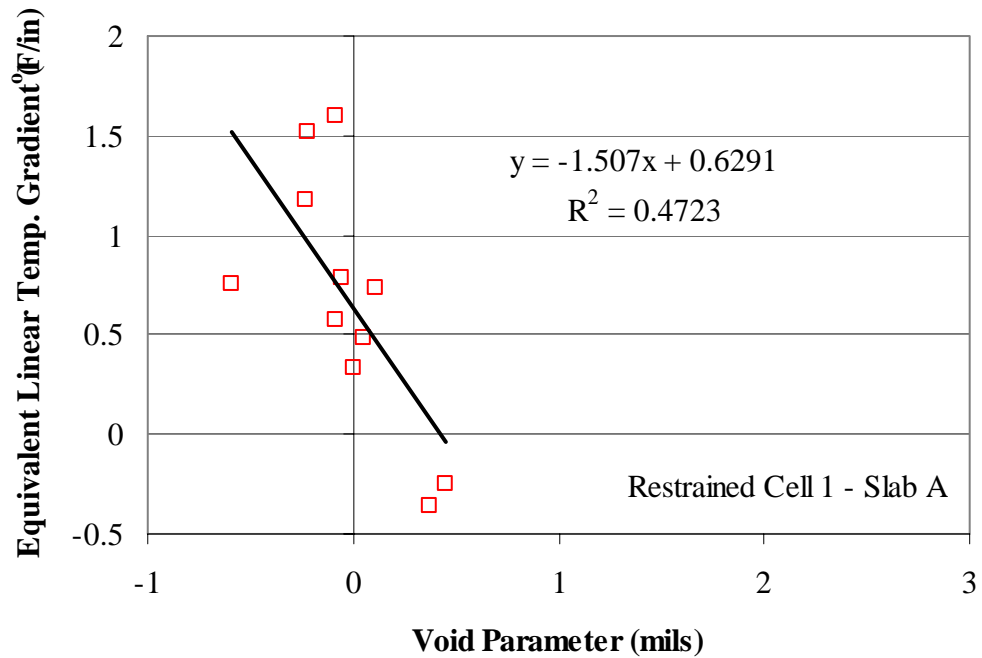


Figure G.18. Relationship between the Void parameter and the equivalent linear temperature gradient present during testing for the restrained Slab A in Cell 1.

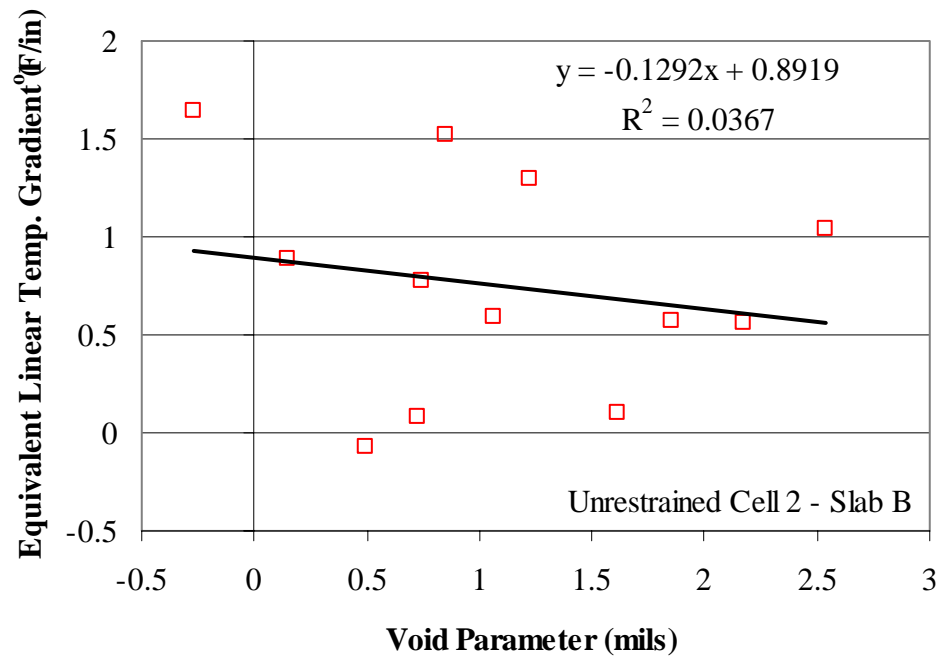


Figure G.19. Relationship between the Void parameter and the equivalent linear temperature gradient present during testing for unrestrained Slab B in Cell 2.

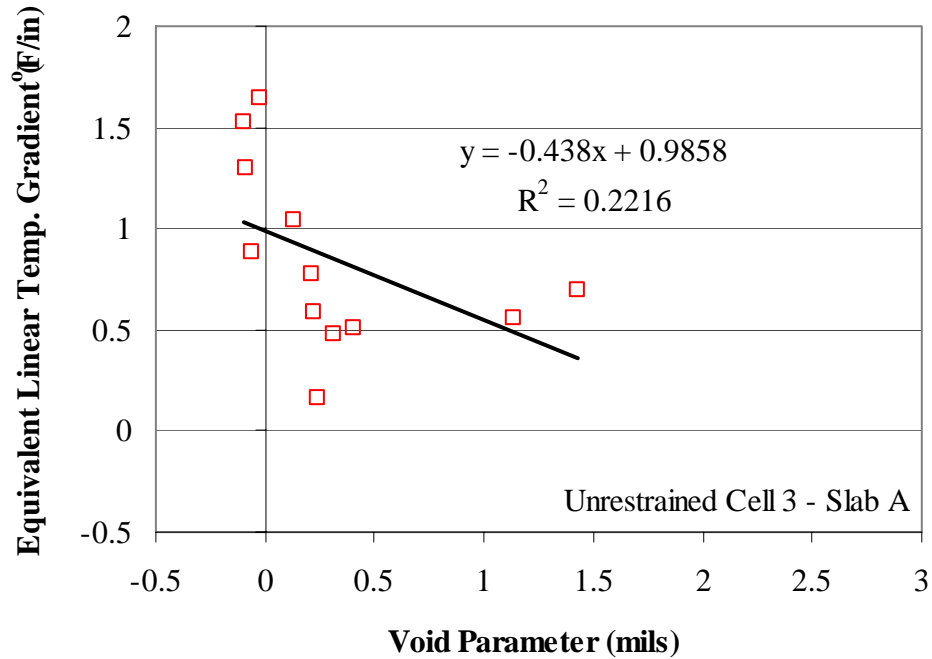


Figure G.20. Relationship between the Void parameter and the equivalent linear temperature gradient present during testing for the unrestrained Slab A in Cell 3.

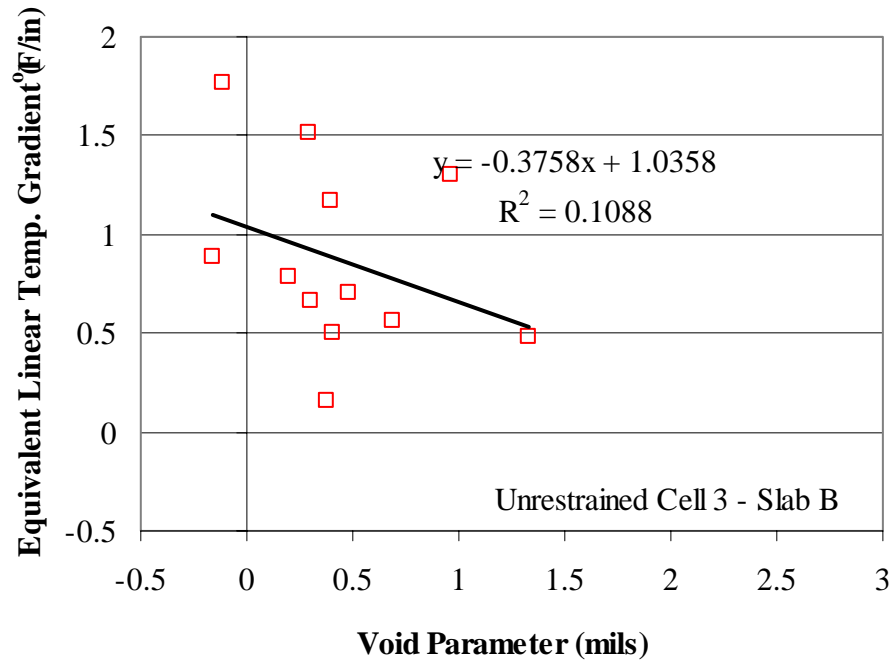


Figure G.21. Relationship between the Void parameter and the equivalent linear temperature gradient present during testing for the unrestrained Slab B in Cell 3.

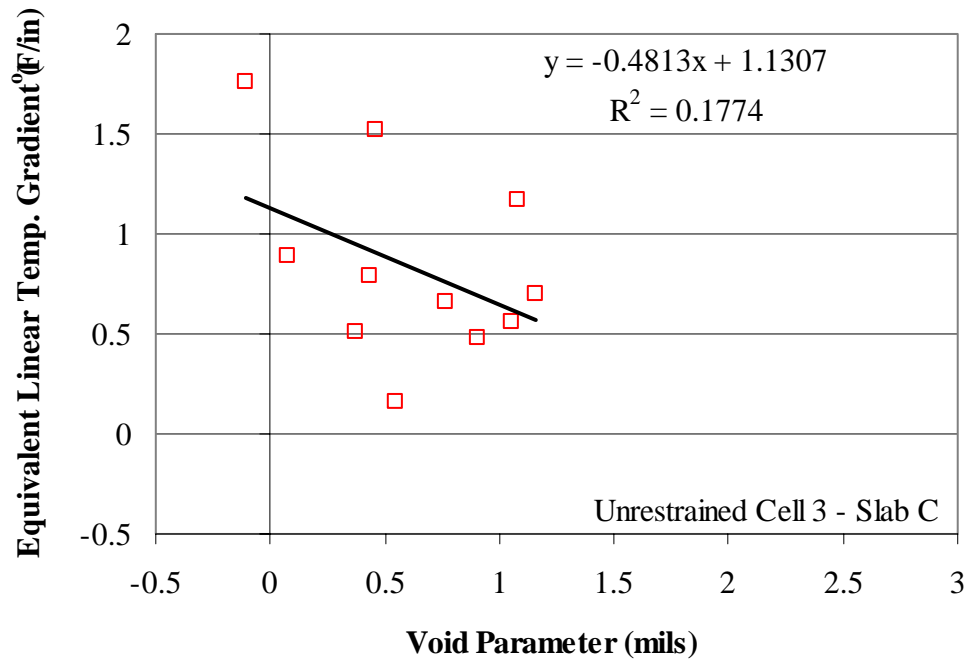


Figure G.22. Relationship between the Void parameter and the equivalent linear temperature gradient present during testing for unrestrained Slab C in Cell 3.

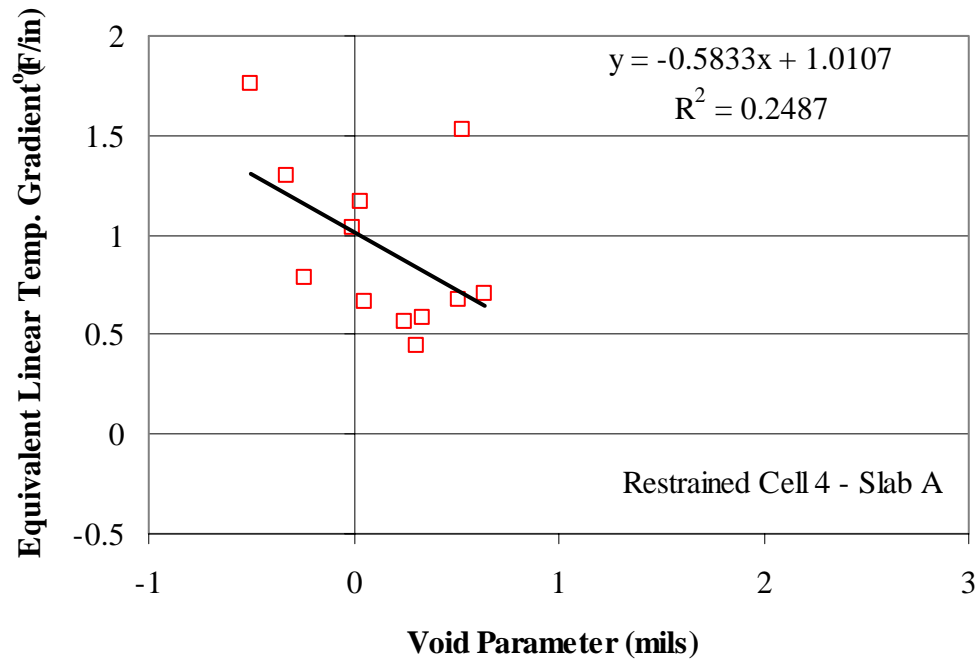


Figure G.23. Relationship between the Void parameter and the equivalent linear temperature gradient present during testing for the restrained Slab A in Cell 4.

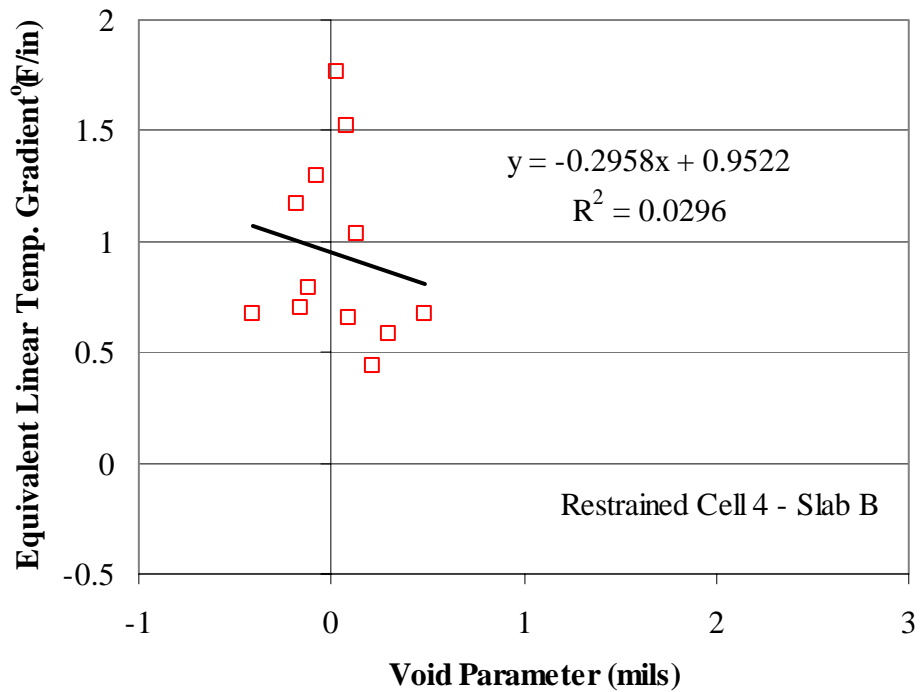


Figure G.24. Relationship between the Void parameter and the equivalent linear temperature gradient present during testing for the restrained Slab B in Cell 4.

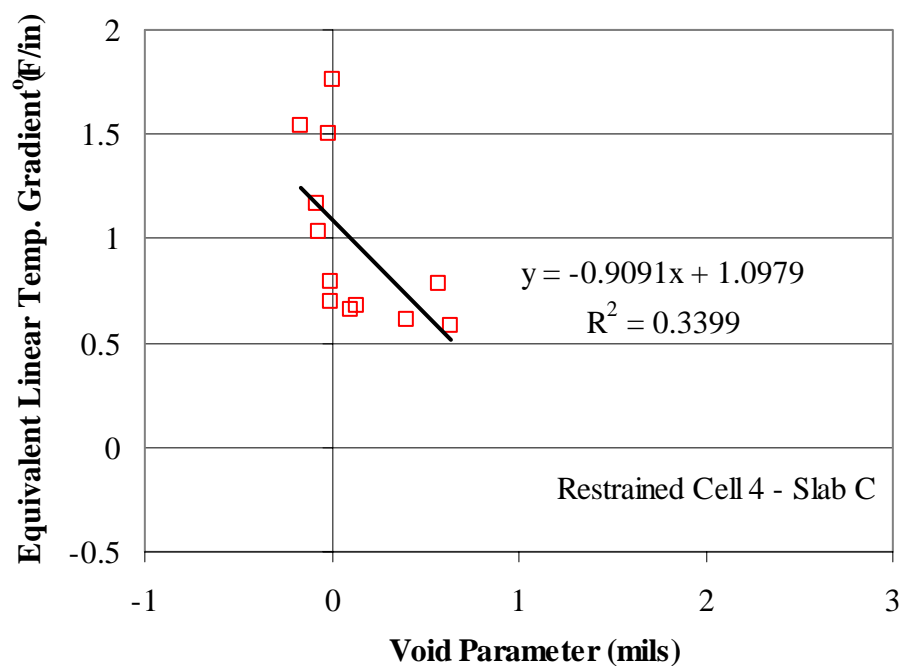


Figure G.25. Relationship between the Void parameter and the equivalent linear temperature gradient present during testing for the restrained Slab C in Cell 4.

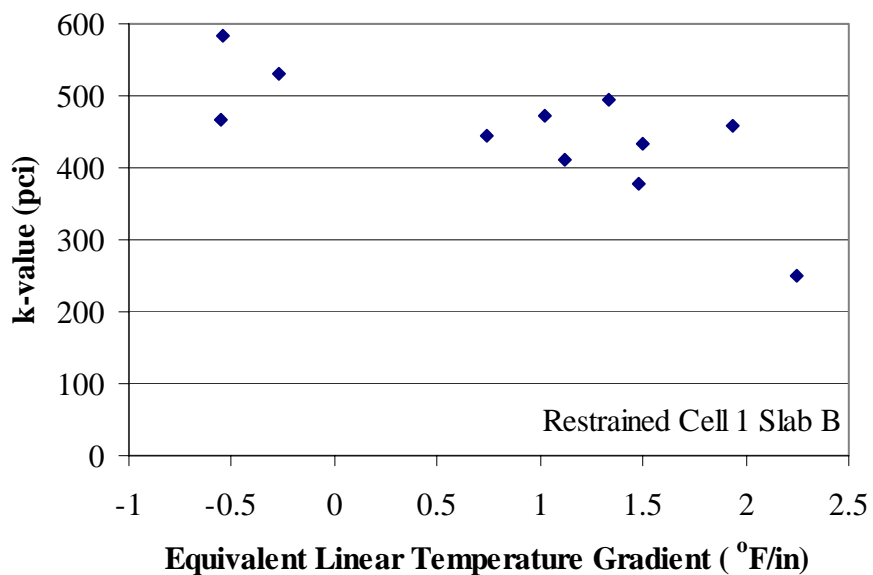


Figure G.26. Comparison of the support conditions beneath the slab and the equivalent linear temperature gradient of the slab during testing for restrained Slab B in Cell 1.

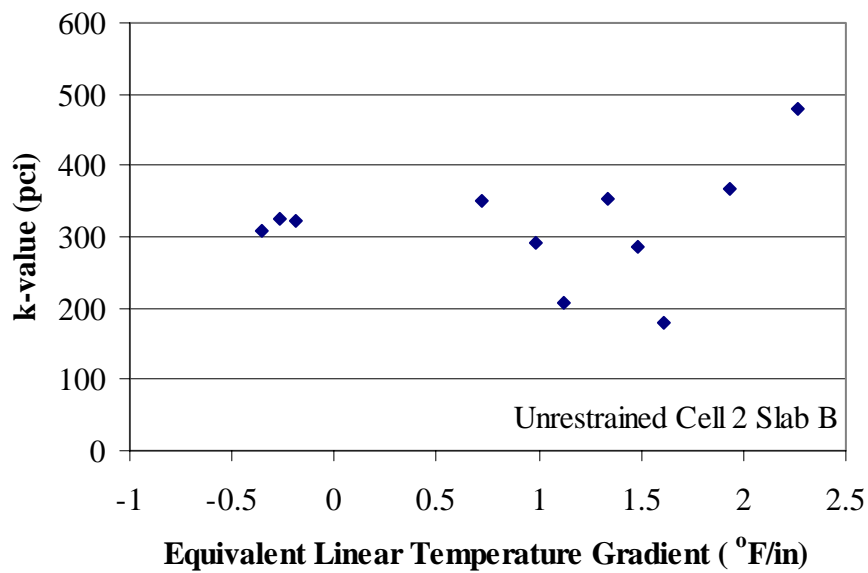


Figure G.27. Comparison of the support conditions beneath the slab and the equivalent linear temperature gradient of the slab during testing for unrestrained Slab B in Cell 2.

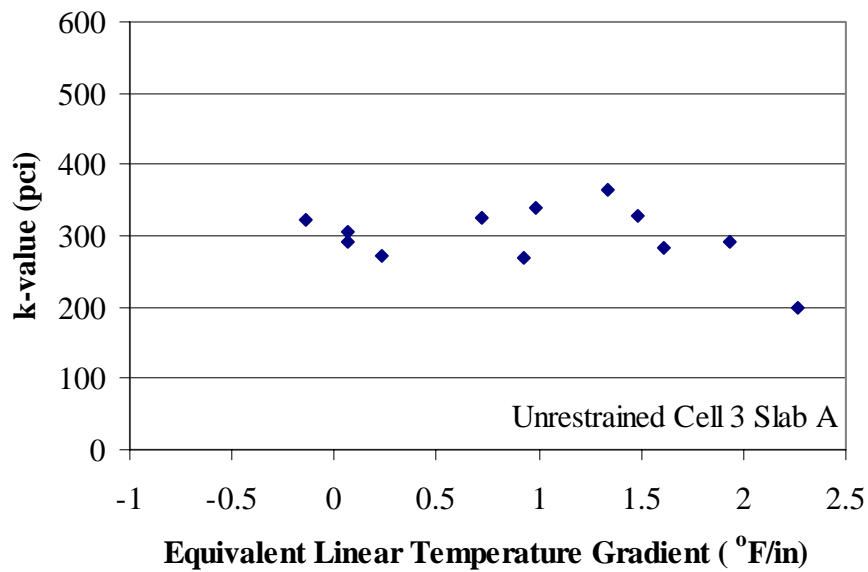


Figure G.28. Comparison of the support conditions beneath the slab and the equivalent linear temperature gradient of the slab during testing for unrestrained Slab A in Cell 3.

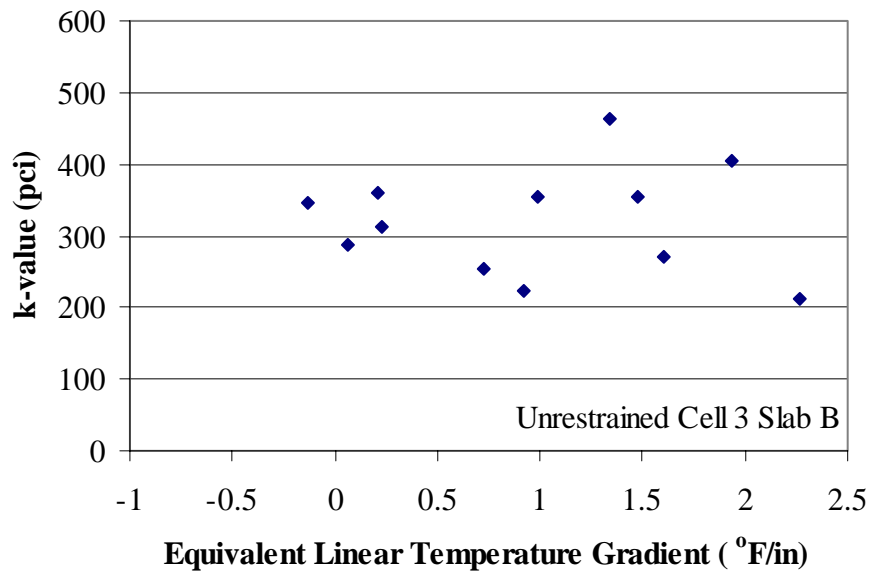


Figure G.29. Comparison of the support conditions beneath the slab and the equivalent linear temperature gradient of the slab during testing for unrestrained Slab B in Cell 3.

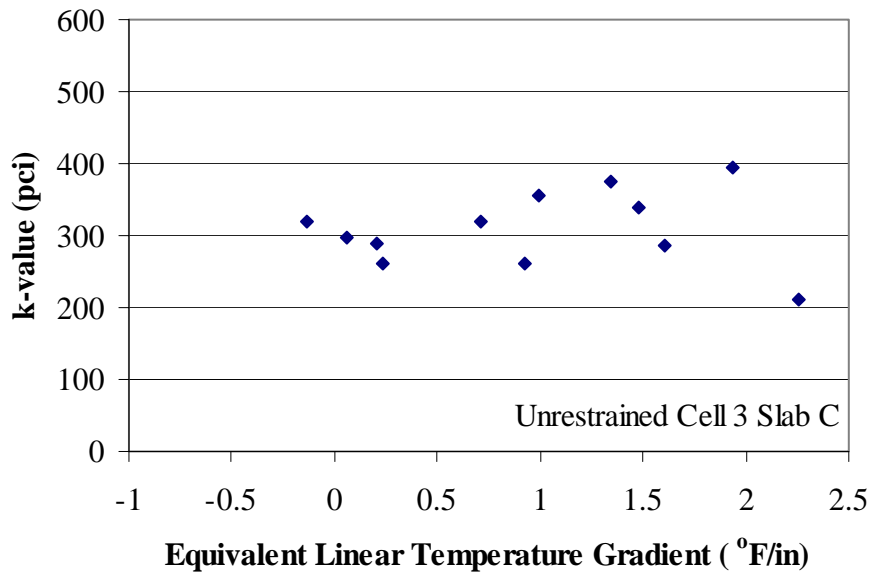


Figure G.30. Comparison of the support conditions beneath the slab and the equivalent linear temperature gradient of the slab during testing for unrestrained Slab C in Cell 3.

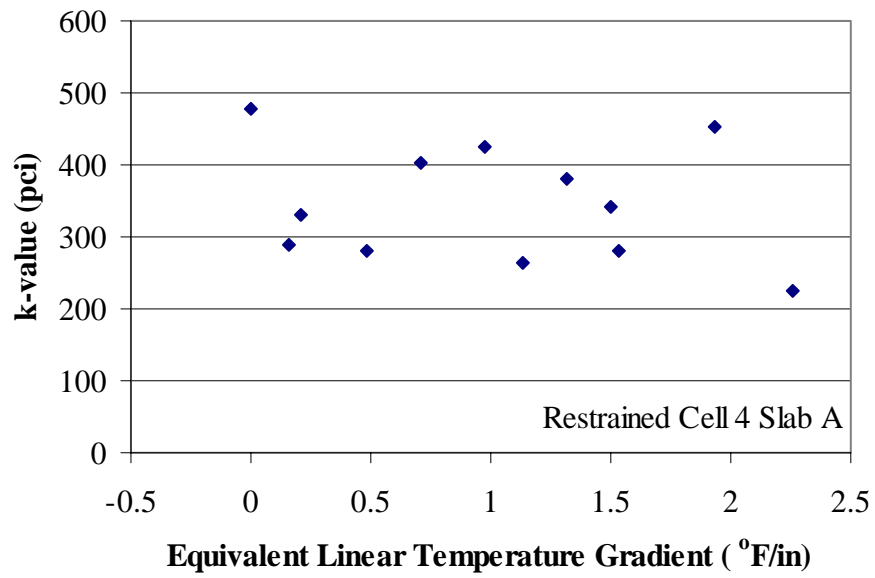


Figure G.31. Comparison of the support conditions beneath the slab and the equivalent linear temperature gradient of the slab during testing for restrained Slab A in Cell 4.

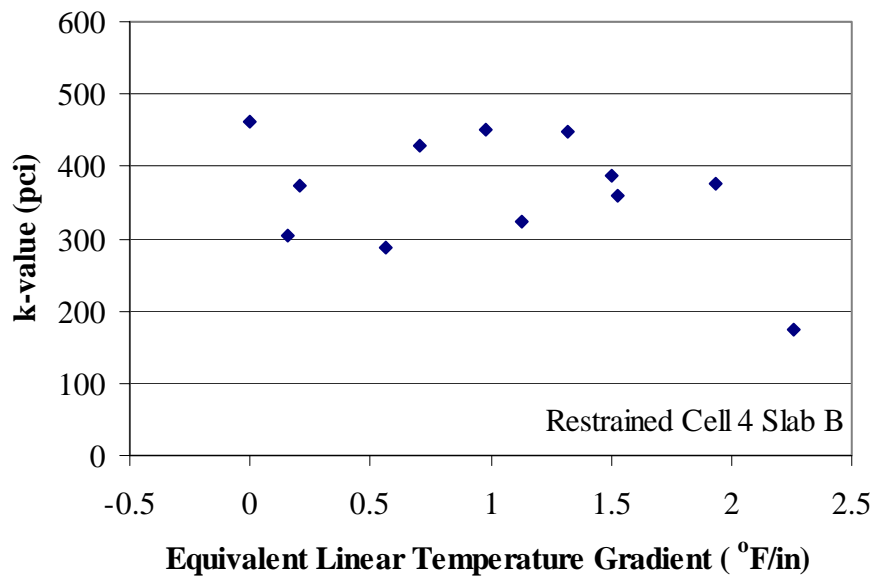


Figure G.32. Comparison of the support conditions beneath the slab and the equivalent linear temperature gradient of the slab during testing for restrained Slab B in Cell 4.

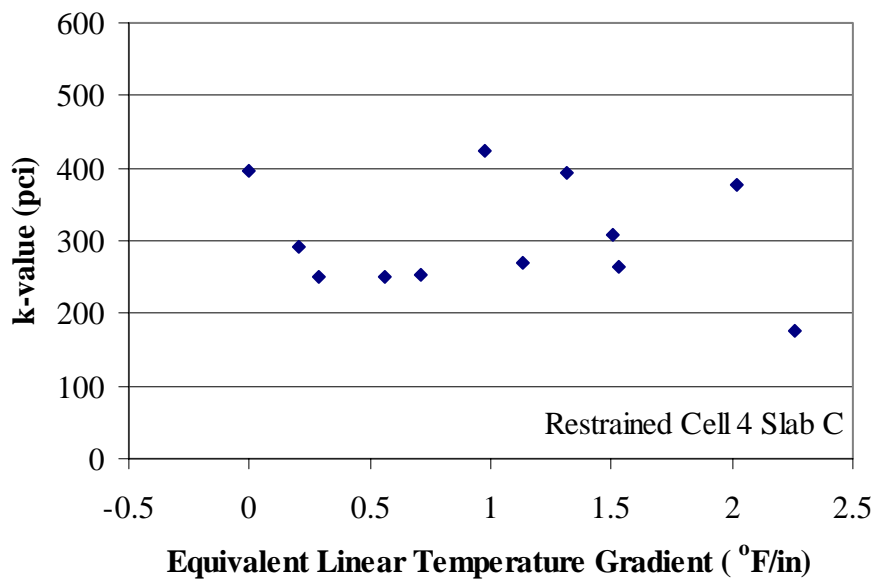


Figure G.33. Comparison of the support conditions beneath the slab and the equivalent linear temperature gradient of the slab during testing for restrained Slab C in Cell 4.

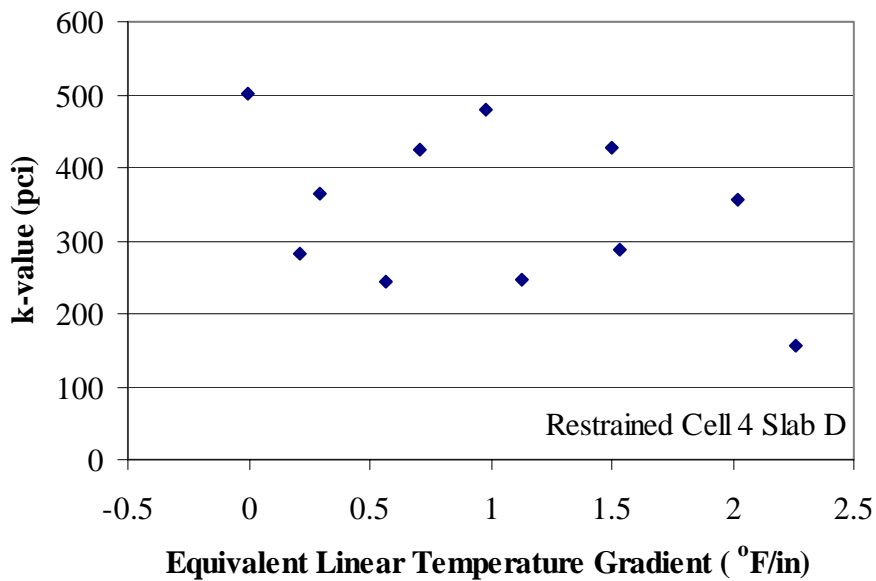


Figure G.34. Comparison of the support conditions beneath the slab and the equivalent linear temperature gradient of the slab during testing for restrained Slab D in Cell 4.

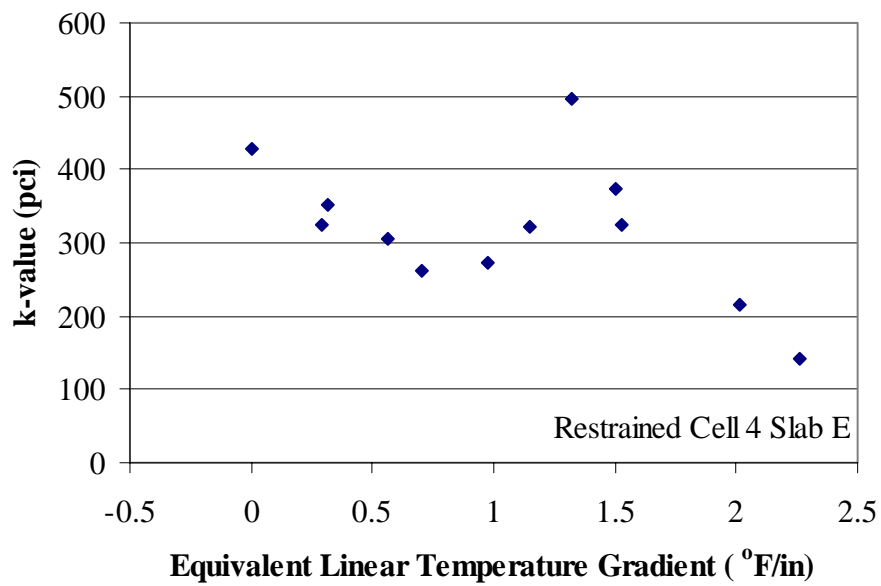


Figure G.35. Comparison of the support conditions beneath the slab and the equivalent linear temperature gradient of the slab during testing for restrained Slab E in Cell 4.

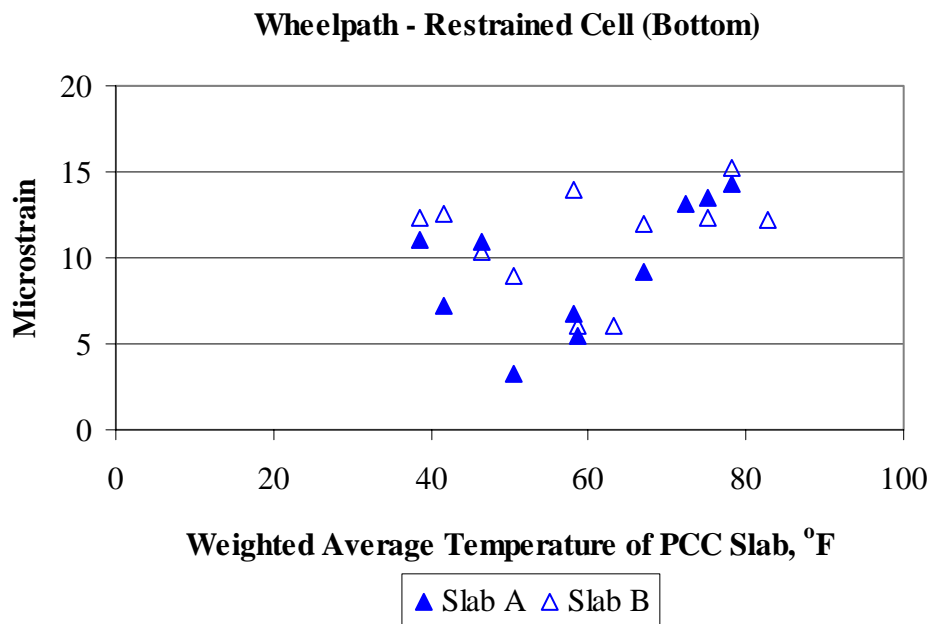


Figure G.36. Relationship between strain measured in the wheelpath at the bottom of the restrained slabs and slab temperature.

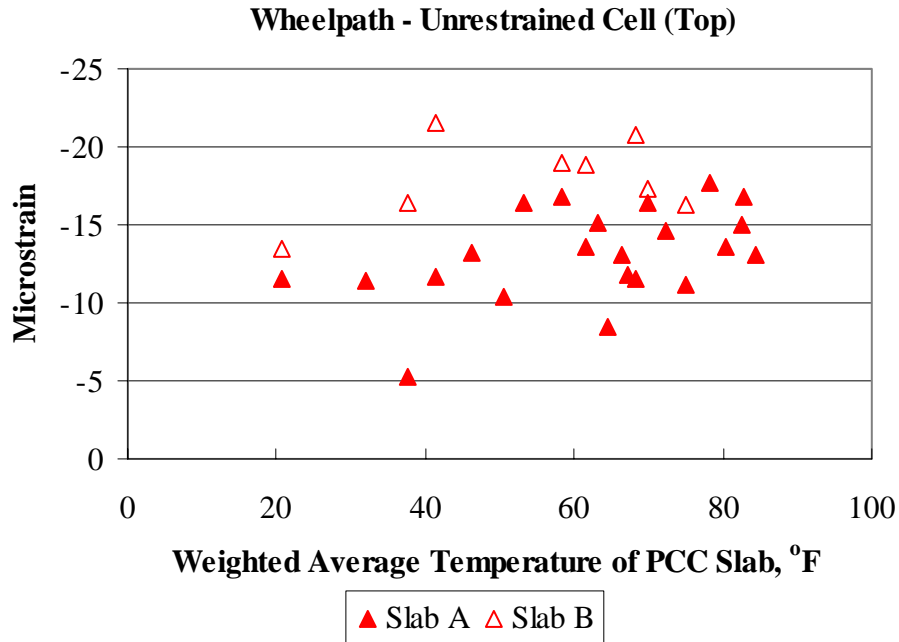


Figure G.37. Relationship between strain measured in the wheelpath at the top of the unrestrained slabs and slab temperature.

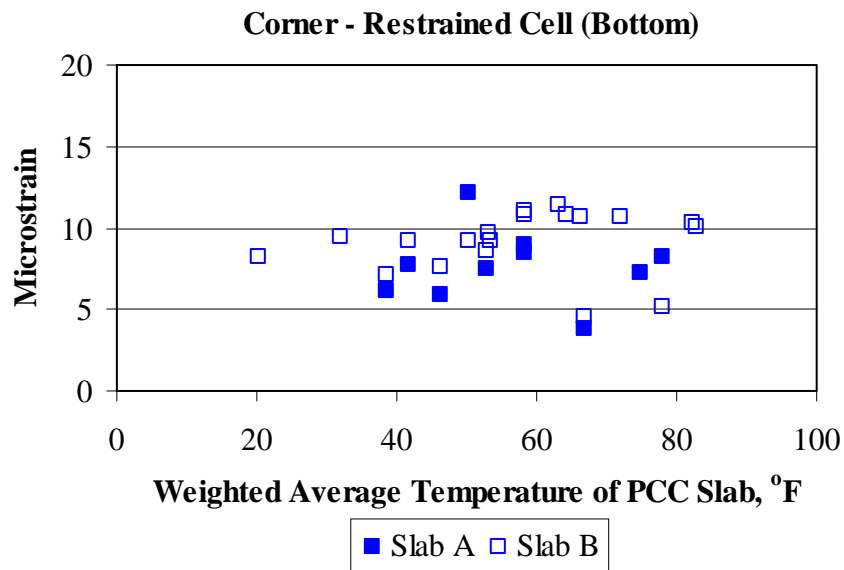


Figure G.38. Relationship between strain measured in the corner at the bottom of the restrained slabs and slab temperature.

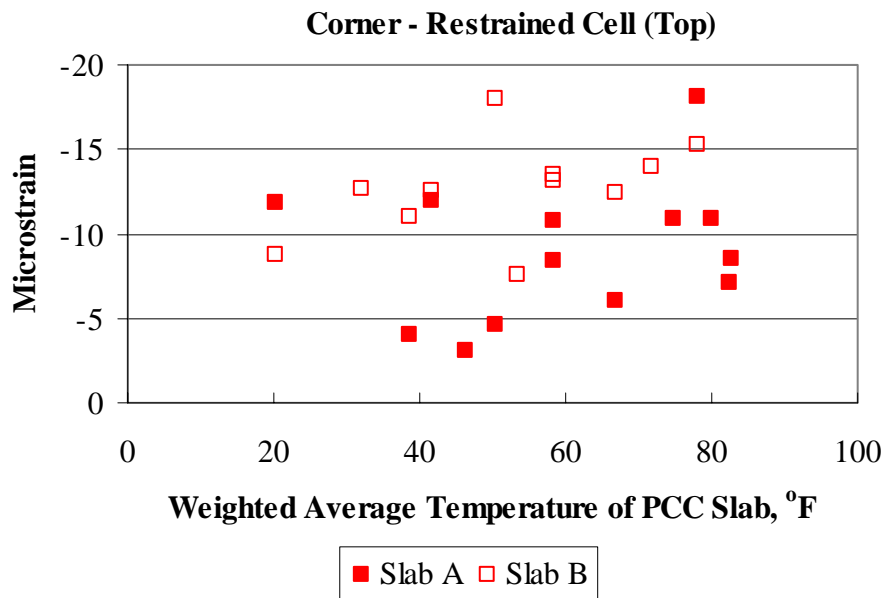


Figure G.39. Relationship between strain measured in the corner at the top of the unrestrained slabs and slab temperature.

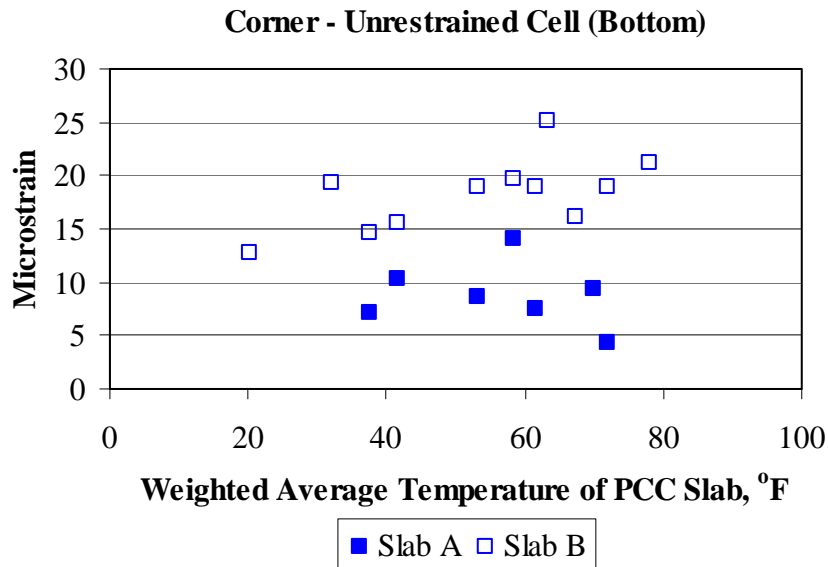


Figure G.40. Relationship between strain measured in the corner at the bottom of the unrestrained slabs and slab temperature.

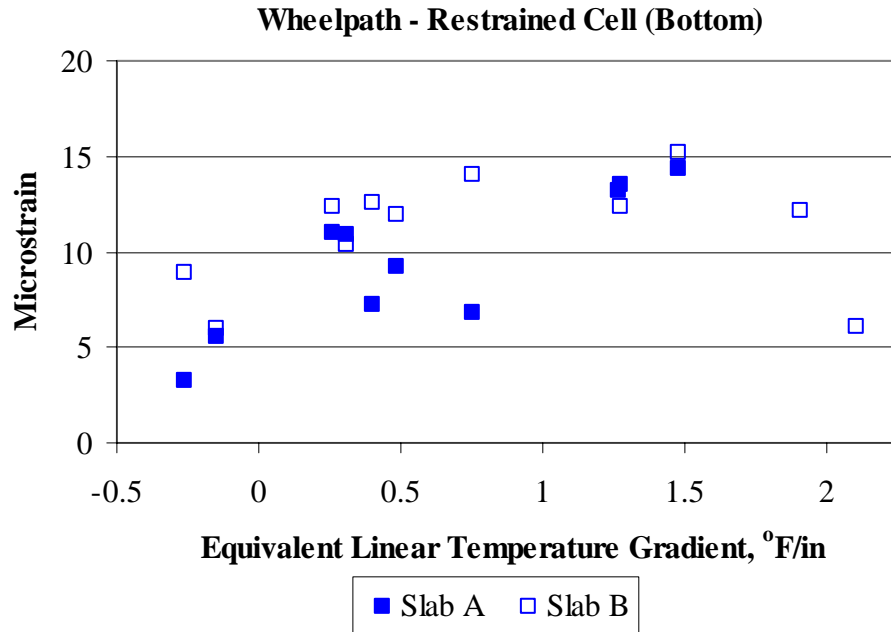


Figure G.41. Relationship between strain measured in the wheelpath at the bottom of the restrained slabs and the temperature gradient in the slab.

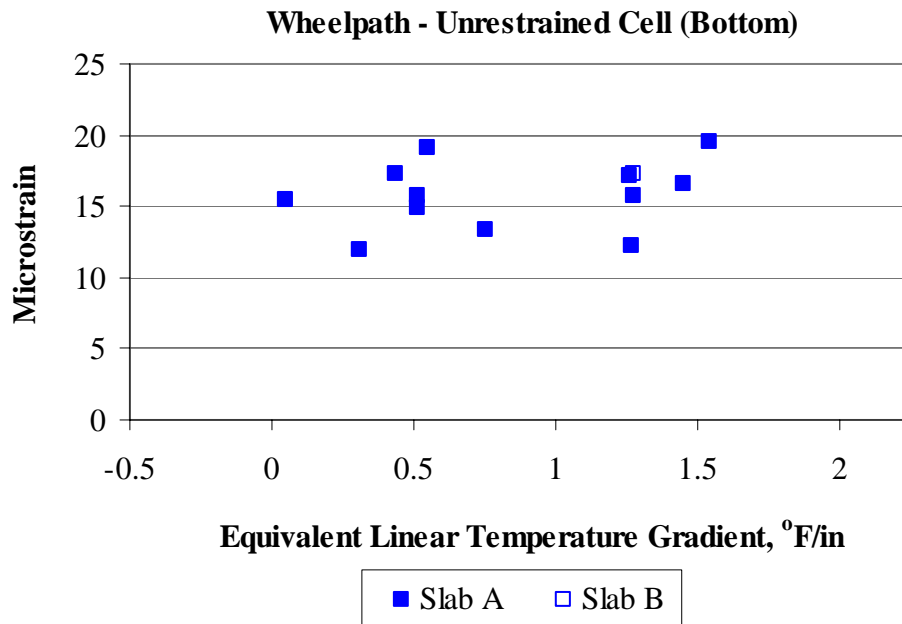


Figure G.42. Relationship between strain measured in the wheelpath at the bottom of the unrestrained slabs and the temperature gradient in the slab.

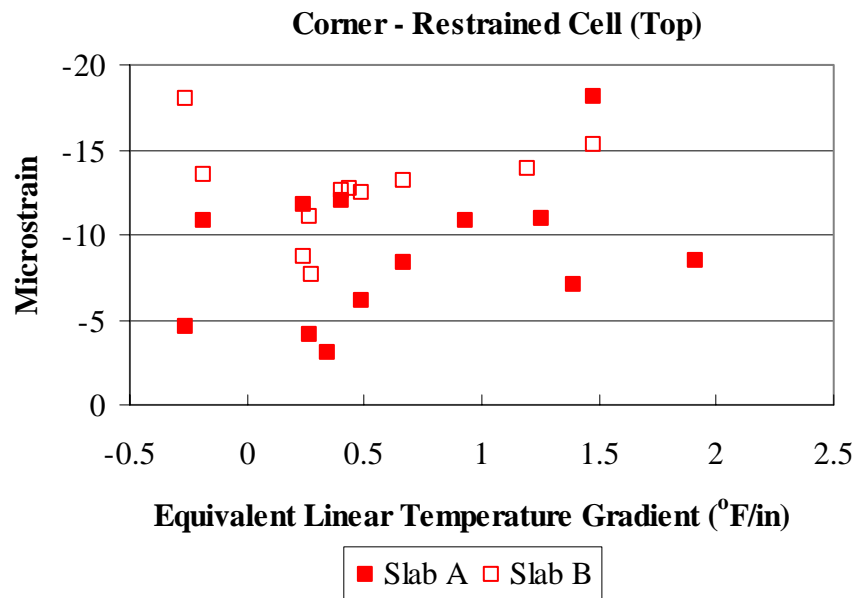


Figure G.43. Relationship between strain measured in the corner at the top of the restrained slabs and the temperature gradient in the slab.

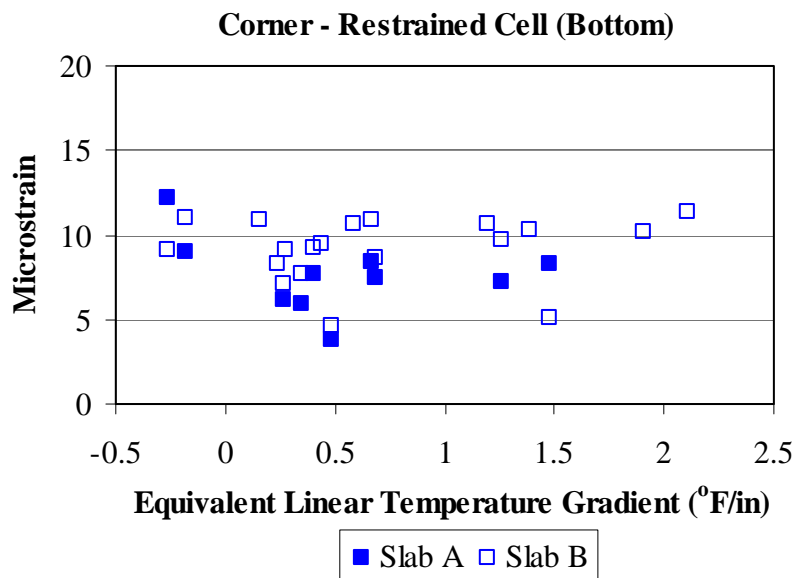


Figure G.44. Relationship between strain measured in the corner at the bottom of the restrained slabs and the temperature gradient in the slab.

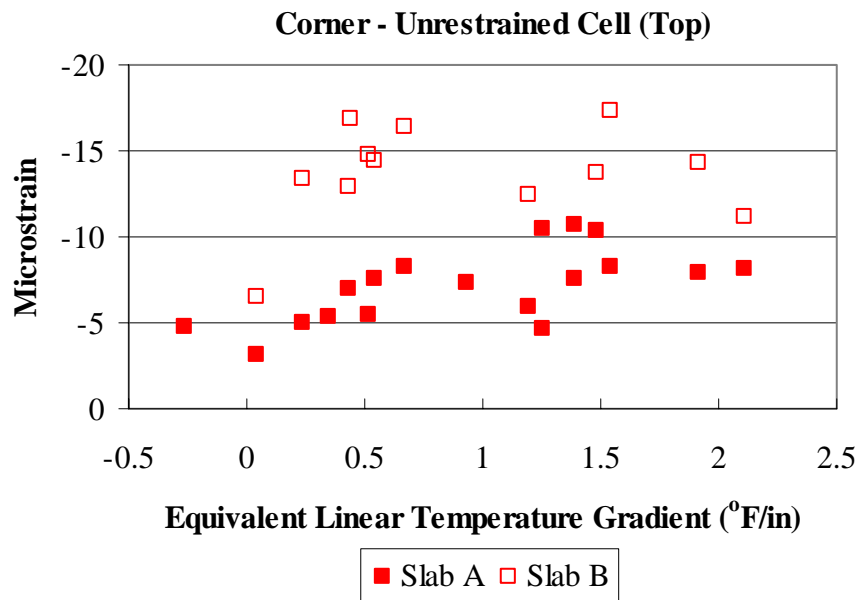


Figure G.45. Relationship between strain measured in the corner at the top of the unrestrained slabs and the temperature gradient in the slab.

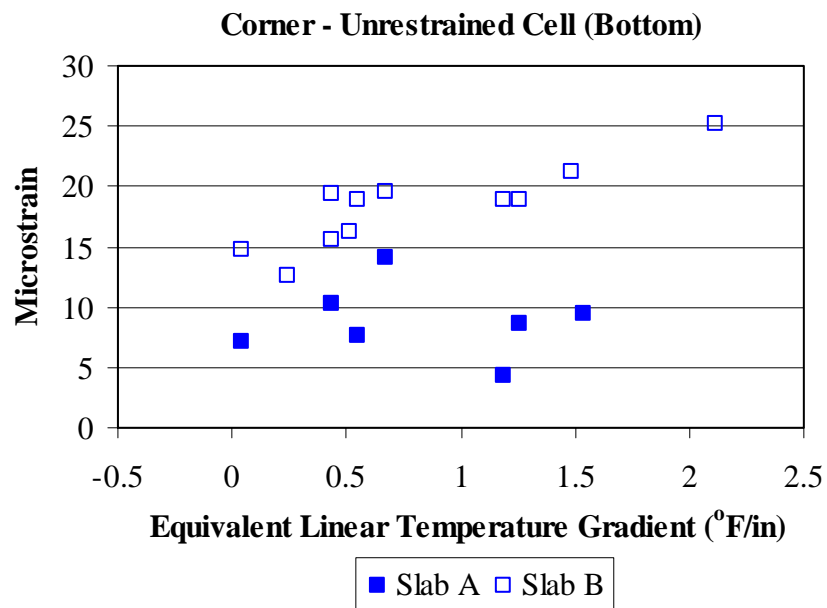


Figure G.46. Relationship between strain measured in the corner at the bottom of the unrestrained slabs and the temperature gradient in the slab.